Modeling of small-scale storage of cryogenic liquids

Nicolò Baiguini

To cite this version:

Nicolò Baiguini. Modeling of small-scale storage of cryogenic liquids. Thermics [physics.class-ph]. Université Paris sciences et lettres, 2023. English. NNT : 2023UPSLM090 . tel-04703658

HAL Id: tel-04703658
https://pastel.hal.science/tel-04703658v1

Submitted on 20 Sep 2024

PSL UNIVERSITÉ PARIS

THÈSE DE DOCTORAT
DE L'UNIVERSITÉ PSL

Préparée à MinesParis - PSL

Modélisation des cuves de petite taille pour le stockage des liquides cryogéniques

Modelling of small-scale storage of cryogenic liquids

Soutenue par

Nicolò BAIGUINI

Le 15 décembre 2023

Ecole doctorale n° 621

Ingénierie des systèmes, matériaux, mécanique, énergétique

Spécialité

Energétique et génie des procédés

Composition du jury :

Jean-Noël JAUBERT Professeur, Université de Lorraine	*Président*
Velisa VESOVIC Professeur, Imperial College London	*Rapporteur*
Hassan PEERHOSSAINI Professeur, Université Paris Diderot	*Rapporteur*
Stefania MOIOLI Professeure, Politecnico di Milano	*Examinatrice*
Rony TAWK Docteur, Engie Lab CRIGEN	*Examinateur*
Hugues MALVOS Docteur, Engie Lab CRIGEN	*Examinateur*
Marco CAMPESTRINI Docteur, Mines Paris	*Examinateur*
Paolo STRINGARI Directeur de recherché, Mines Paris	*Directeur de thèse*

MINES PARIS | PSL

Acknowledgments

I would like to express my gratitude to all the jury members. I am thankful to Pr. Velisa VESOVIC and Pr. Hassan PEERHOSSAINI for agreeing to read and evaluate my work. In addition, a thank you to Pr. Jean-Noël JAUBERT and to Dr. Hugues MALVOS for accepting to be members of this jury. I wish to thank Pr. Stefania MOIOLI, who inspired my PhD candidature, and to Pr. Laura AnnaMaria PELLEGRINI for encouraging me of doing a thesis at University PSL-MinesParis.

I would like to acknowledge the crucial role of Dr. Rony TAWK from the Engie Lab CRIGEN for the useful comments, remarks and engagement during the last five years, especially through analysis of the results and reviewing of the manuscript. I would like to express my gratitude to Dr. Djomice BREUGE for giving me advices on coding.

I would like to express my special appreciation and thanks to my *directeur de thès*e, Dr. Paolo STRINGARI, and my *maître de thèse*, Dr. Marco CAMPESTRINI. You have been important mentors for me and I thank you for your motivating guidance, invaluable constructive criticism and friendly advice during this work.

Special thanks go to my colleagues of the Center of Thermodynamics of Processes (CTP), Eric, Herve, David M., Hugo, Nicolas, Mauro, Snaide, Saleem, Serena and many others. I will not forget the paintball and the bets that we did for the FIFA world cup and for rugby world championship. Unfortunately, the final scores did not reflected the courage behind my bets. Special tanks to members of Engie Lab CRIGEN, Laurent, Florian, Audray, Hamza, Nicola, Stefano, Remi, Philippe and many others. I will not forget the *sortie de lab* and the Korean barbecue in our journey in South Korea.

Unique gratitude goes to my team mates, managers and coaches of Montgeron Bicross Club (MBC), and many others for these four years of happiness and reckness. Some of you can have good opportunities in BMX race and I hope being with you as long as possible. Special thanks go to my friends Jean, Aurelien and François, and many others for nights spent at the Glasgow. I hope we can make for lost time during the writing of the manuscript. Special thanks to Gabriele, Mattia, Daniele, Francesco and Filippo of *circolo folkloristico* for many adventures that cannot be told.

I want to express my endless gratitude to my dad, Cirillo, for being a good father. Special thanks go to my brother, Mattia, who has been my landmark for many years during my childhood, and to my little syster, Maria. Special thanks goes to Monica, my aunt, for the support received during the master degree. I would like to express my endless love for my mother, Eliana.

Least but not last, I want to thank me for spending holidays, week-ends and many hours of extra working to attempt as many objectives as possible.

Tables of content

List of figures

List of tables

Nomenclature

Index and exponent

B	Bottom
B,L	Bulk of the liquid sub-layer
BL	Bulk-to-boundary layer, boundary layer
BL,L	Boundary layer of the wet side wall
BOG	Boil-off gas
C	Computational, condensation
D	Descending
D,L	Descending in liquid
D,V	Descending in the vapour
E	Evaporation
EB	Energy balance
EFF	Effective
EV,ev	Evaporation or latent heat
ex	Experimental
F	Final
HL	Liquid height
I	Interface
i	General index
IN	Inlet
L	Liquid, wet surface
LOW	Lower
LV	Dry-to-wet
MAX	Maximum
MB	Mass balance
N	Last point, net

N-1	Second-last point
n_L	Liquid sub-layer
N^L	Interface sub-layer of the liquid, number of liquid sub-layer
n_V	Vapour virtual sub-layer
N^V	Roof virtual sub-layer, number of vapour virtual sub-layer
OUT	Outlet
P	Self-pressurisation, pressure
R	Roof, ring
S	Saturation
SL	Wet side wall or liquid side wall
SS	Steady state
SV	Dry side wall or vapour side wall
UP	Rising, upper
T	Thermal
t_i	Current time
t_{i-1}	Previous time
TL	Liquid temperature
TOT	Total
TV	Vapour temperature
V	Vapour, dry surface
w	Wall
0	Initial
1	Bottom sub-layer of the liquid, interface sub-layer of vapour

Acronym

A	Ageing
BC	Boundary condition
Bio-LNG	Liquefied bio-natural gas

BOG	Boil-off gas
BOGss	Boil-off produced at steady state
BOR	Boil-off rate
EQ	Equilibrium
ER	Empty ratio
Fl	Fluid
H	Homogenous
He	Test at different heat input (at constant filling ratio)
H 2.0	Homogeneous 2.0
IC	Test at different initial condition
IG	Internal geometry of the storage container
LBG	Liquefied biogas
Le	Tests at different liquid level
LF	Filling ratio, liquid level
LS	Large scale, liquid stratification
LH_2	Liquid hydrogen
LN_2	Liquid nitrogen
LNG	Liquefied natural gas
LSd	Liquid thermal de-stratification
LTE	Liquid thermal expansion
LVS	Liquid-vapour thermal stratification
LVNC	Liquid-vapour natural convection
MLI	Multi-layer insulation
Sc	Test at different scale (same geometry)
SeE	Score of experiment
TS	Total score
SP	Self-pressurisation
SS	Small scale

SoP	Score of physics
VSss	Vapour stratification at steady state

Latin alphabet

A	Surface, m^2, or coefficient
B	Coefficient
C	Coefficient
D	Diameter, m, or coefficient
E	Coefficient
e	Thickness, m
F	Coefficient
G	Coefficient
H	Height, m, or coefficient
$\tilde{H}$	Overall enthalpy, J
$\tilde{h}$	Specific enthalpy, J/kg
m	Mass, kg
$\dot{m}$	Mass flow, kg/s
P	Pressure, bar
$\dot{Q}$	Heat flow, W
$\dot{q}$	Heat flux, W/m^2
$\bar{\dot{Q}}$	Time-average heat flow, W
$\bar{\dot{q}}$	Time-average heat flux, W/m^2
t	Time, s
T	Temperature, K
V	Volume, m^3
x	Vertical coordinate, m

Greek alphabet

α	Coefficient of importance or corrective coefficient of dry side wall-to-vapour heat flow or thermal diffusivity, m^2/s
β	Overall score, elementary score or corrective coefficient of dry side wall-to-interface heat flow or volume expansion coefficient, K^{-1}
ε	Relative tolerance
η	Dynamic viscosity, Pa·s
Ω	Absolute ratio of the time-derivate
ρ	Density, kg/m^3
ν	Kinematic viscosity, m^2/s

Mathematical symbol

Δ	Difference or variation
d	Differential
$\frac{\partial}{\partial t}$	Partial derivative with respect to time
$\frac{\partial}{\partial x}$	Partial derivative with respect to coordinate x

Résumé

Les combustibles gazeux tels que le gaz naturel, le biogaz et l'hydrogène sont les principaux acteurs de la dé-carbonisation à moyen et long terme dans les secteurs de Petite Echelle (PE) de l'énergie et du transport (tel que la production d'électricité sur des sites hors réseau et le transport routier et maritime). Ces carburants sont souvent liquéfiés pour (i) augmenter leur densité énergétique et (ii) être stockés puis facilement transportés du site de production au site d'utilisation final. Le stockage de ces liquides est différent de celui des réservoirs de stockage à Grande Echelle (GE), car (i) le rapport surface/volume et (ii) la pression de fonctionnement sont supérieurs à ceux des réservoirs GE. La gestion du liquide cryogénique dans les réservoirs de stockage PE se fait en surveillant certains paramètres de stockage tels que le temps de rétention, la hauteur d'aspiration positive nette, l'indice de méthane et le pouvoir calorifique supérieur, qui sont calculés à partir de variables physiques (telles que la température, la pression, la composition et le niveau du remplissage). En raison des entrées thermiques et des opérations des réservoirs de stockage (comme la fermeture des réservoirs), les évolutions de ces variables dans le temps sont liées aux phénomènes qui se produisent dans les cuves de stockage PE : (i) la stratification thermique dans le liquide et dans la vapeur, (ii) l'auto-pressurisation et (iii) le vieillissement. Une prédiction fiable de leur évolution dans le temps est nécessaire pour définir une stratégie opérationnelle appropriée. Par conséquent, un modèle approprié capable de considérer les phénomènes de stockage est nécessaire pour des prédictions fiables des variables physiques (donc des variables de stockage) tout au long du temps de stockage.

Les modèles mathématiques existants ne prennent pas en compte toutes les contributions (telles que (i) l'influence du gradient de température liquide et gazeux sur la dynamique des fluides, (ii) la stratification de la vapeur, (iii) le couplage entre les mouvements du fluide et le transfert de chaleur aux parois du réservoir, et (iv) le transfert de chaleur/masse à l'interface vapeur-liquide), qui (i) déterminent les phénomènes du stockage et constituent le principal défi pour prédire le comportement d'un fluide cryogénique dans des cuves de stockage PE.

L'objectif de cette thèse est le développement d'un modèle capable de prendre en compte les phénomènes de stockage se produisant dans les cuves PE pour la prédiction des variables de stockage lors du stockage de fluides cryogéniques purs (azote liquide et hydrogène liquide). Quatre modèles d'une complexité croissante ont été développés. Chaque modèle a été conçu pour surmonter les faiblesses du précédent évaluées en comparant les résultats de modélisation aux valeurs expérimentales disponibles dans la littérature scientifique. Le premier modèle (modèle d'équilibre) considère les phases liquide et vapeur comme homogènes et à l'équilibre thermodynamique. Dans le deuxième modèle (modèle homogène), les phases liquide et vapeur sont homogènes, mais pas à l'équilibre. La vapeur est homogène, mais virtuellement stratifiée dans le troisième modèle (modèle homogène 2.0). Dans le dernier modèle (modèle de stratification liquide), la vapeur est traitée comme dans le modèle homogène 2.0 et le liquide est discrétisé en sous-couches.

Bien que les profils de température liquide ne soient pas bien prédits en raison de certaines hypothèses, le modèle de stratification liquide surmonte avec succès certains problèmes critiques des modèles précédents, notamment en matière de prévision de l'auto-pressurisation. Avant d'étendre le modèle au comportement des mélanges cryogéniques (comme le gaz naturel liquéfié) dans les réservoirs PE, d'autres améliorations telles que (i) la prise en compte de la stratification de température dans la vapeur et (ii) l'inclusion du transfert de chaleur par conduction le long de la paroi latérale humide et sèche, ont été suggérées. Une conception préliminaire d'un réservoir de stockage PE a été proposée pour mesurer toutes les propriétés nécessaires à la validation du modèle au vu de la disponibilité très limitée de données expérimentales.

Abstract

Gaseous fuels such as natural gas, bio-natural gas and hydrogen are the key drivers for mid-to-long term decarbonisation of energy and transport sectors. These fuels are often liquefied (i) to increase energy density, and (ii) to be compactly stored and easily transported from the production site to the end user's site. In small scale (SS) applications in energy and transport sectors, like road and maritime transportations or for power production in off-grid sites, the storage of these liquids is different from the one of large scale (LS) storage tanks, because (i) the surface-to-volume ratio and (ii) the operating pressure are higher than the ones of LS tanks.

The management of cryogenic liquid in SS storage tanks is done by monitoring some storage parameters such as holding-up time, net suction pressure head, methane number and gross heating value, which are computed from physical variables (like temperature, pressure, composition and filling ratio). Because of heat inputs and storage tank operations (such as the closing of the tanks), the time-evolutions of these variables are related to phenomena occurring within the SS storage containers, which are the (i) thermal stratification in liquid and in the ullage, (ii) the self-pressurisation and (iii) the ageing. A reliable prediction of their time-evolution are highly sought to define a proper operating strategy. A proper model capable of considering the storage phenomena is required for the reliable predictions of the physical variables (thus storage variables) all along the storage time.

Existing mathematical models developed for LS storage tanks cannot be applied for predicting the behaviour of cryogenic fluids in SS tanks. In fact, not all the contributions (such as (i) the influence of the liquid and vapour bulk temperature gradient on the fluid-dynamic, (ii) the vapour stratification, (iii) the coupling between fluid-motions and tank's wall heat transfer, and (iv) the heat/mass transfer at vapour-liquid interface) are considered in modelling the storage of cryogenic liquids in LS tanks. The modelling of these aspects is the main challenge to reproduce the behaviour of a cryogenic fluid in SS storage containers.

Hence, the objective of this thesis is the development of a model capable of taking into account the storage phenomena occurring in SS storage tanks for the prediction of the storage variables related to storage of pure cryogenic fluids, i.e. liquid nitrogen and liquid hydrogen. Four models of progressive increasing complexity have been developed. Each model has been conceived for overcoming the weaknesses of the previous one, which have been evaluated by comparing the modelling results to experimental values related to storage tanks of different geometries and sizes, containing different levels of liquid and submitted to different heat fluxes. The first model (equilibrium model) considers the liquid and the vapour phases as homogeneous and at thermodynamic equilibrium conditions. In the second model (homogenous model), the liquid and vapour phases are homogeneous, but not at equilibrium. The vapour is homogeneous, but virtually stratified in the third model (homogeneous model 2.0). In the last model (liquid stratification model), ullage is treated like in the homogeneous model 2.0 and the liquid is discretised in sub-layers.

Despite liquid temperature profiles are not well predicted because of some hypotheses, the liquid stratification model successfully overcomes some critical issues of the previous models especially in predicting the self-pressurisation. Before extending the model to the behaviour of cryogenic mixtures (like liquefied natural gas) in SS tanks, further modelling improvements such as (i) considering temperature stratification in the vapour, (ii) including the conduction heat transfer along the wet and dry side wall have been suggested. Furthermore, the lack of complete experimental datasets in the literature has been pointed out. A preliminary design of a SS storage tank has been proposed for measuring all the properties that are needed for model validation.

Chapter 1

Contexte, phénomènes, état de l'art et objectifs

Pour réduire les émissions anthropiques de dioxyde de carbone (CO_2), les carburants gazeux tels que le gaz naturel (GN), l'hydrogène (H_2) et le bio-méthane (BM) constituent une solution potentielle croissante pour réduire le CO_2 en remplaçant les carburants à base de pétrole dans le marché à Petite Echelle (PE). Ces carburants gazeux sont respectivement convertis en Gaz Naturel Liquéfié (GNL), en Hydrogène Liquide (LH_2) et en Bio-GNL pour (i) augmenter leur densité énergétique volumétrique et (ii) rendre ainsi leur transport et stockage plus efficaces. Les réservoirs de PE ont un rapport surface/volume plus élevé que les réservoirs de grande échelle qui sont utilisés dans les terminaux de liquéfaction et de regazéification de GNL/LH_2, d'où un taux d'apport de chaleur élevé par unité de masse de liquide. Pour pallier cet aspect, ces cuves PE de stockage sont équipées d’une isolation efficace.

Pour les applications de PE, le stockage de liquides cryogéniques contrôlé en surveillant certains paramètres tels que le temps de rétention, la hauteur d'aspiration positive nette, l'indice de méthane et le pouvoir calorifique supérieur. Ces paramètres sont fondamentales pour évaluer la (i) limite de sécurité et l'impact environnemental, (ii) les limites opérationnelles des équipements et (iii) la consommation des liquides cryogéniques quand utilisés comme carburants dans les véhicules.

De plus, ces paramètres varient dans le temps lors du stockage en raison de certains phénomènes physiques tels que la stratification thermique, l'auto-pressurisation et le vieillissement. Ces derniers dépendent du taux d'entrée de chaleur de l'environnement vers le fluide stocké dans le réservoir, des conditions opératoires des cuves et du gradient de température à proximité de l'interface. Par conséquent, ces phénomènes de stockage interagissent les uns avec les autres et ne peuvent être étudiés individuellement dans des cuves de stockage cryogéniques.

Les modèles computationnels de dynamique des fluides et de paramètres localisés avec des approches non-équilibre et à l'équilibre sont principalement utilisés dans la littérature pour modéliser le stockage de GNL et LH_2 dans des cuves de PE. Une méthode de table de score est développée et utilisée pour sélectionner les travaux de modélisation qui serviront de base de référence dans cette thèse. Les travaux sélectionnés souffrant certaines limites, cette thèse a pour objectif de développer un logiciel à usage industriel et d'améliorer la connaissance scientifique des phénomènes impactant la gestion des liquides cryogéniques lors du stockage PE. Le modèle qui développé dans cette thèse ne considère que les liquides cryogéniques purs, mais il a été conçu pour être étendu au GNL et à d'autres mélanges de liquides cryogéniques. Ce modèle s'appuie sur les théories conventionnelles de la dynamique des fluides et du transfert de chaleur.

Context, phenomena, state of art and objectives

To reduce the anthropogenic carbon dioxide (CO_2) emission, gaseous fuels such as Natural Gas (NG) Hydrogen (H_2), and Bio-methane (BM) are a growing potential solution to reduce the CO_2 by substituting oil-based fuels in Small Scale applications such heavy duty transport, shipping, production of electricity in remote areas, and for supplying power in industrial off-grid sites. These gaseous fuels are respectively converted to Liquefied Natural Gas (LNG), Liquid Hydrogen (LH_2), and Bio-LNG to be easily and compactly transported from the production sites to the end user sites, and to increase their volumetric energy density. LNG, LH_2, and bio-LNG are often stored in Small-Scale (SS) storage tanks. These tanks have a higher surface-to-volume ratio than large scale tanks used in LNG liquefaction and re-gasification terminals, thus a high heat input rate per unit mass of liquid. To mitigate this aspect, these storage containers are equipped with efficient insulation. For these applications, the cryogenic liquids are managed by controlling and monitoring some parameters such as Hold-up Time (HUT), the Net Positive Suction Head (NSPH), the Methane Number (MN) and the Gross Heating Value (GHV). These variables are fundamental to evaluate (i) the safety limit and the environmental impact, (ii) the operative limits of the equipment, and (iii) the use of cryogenic liquids, in particular LNG, as fuel in sparking engine. The parameters listed above are not constant in time during storage, because of some physical phenomena such as thermal stratification, self-pressurisation and ageing. Those phenomena depend on the rate of heat ingress from the ambient to the fluid stored in the tank, and the operating conditions, mainly the management of the pressure in the tank. The thermal stratification is developed due to the fluid-dynamics and the heat transfer at the side wall and at the liquid-vapour interface. The self-pressurisation and the ageing are controlled by the interfacial mass-heat transfer phenomena such as evaporation and condensation. These phenomena are affected by the temperature gradient near the interface, thus the thermal stratification. Hence, these storage phenomena interact with each other and they cannot be individually studied in cryogenic storage containers. Modelling works are available in scientific literature, mainly for LNG in large scale transport and storage and LH_2 used as fuel for rockets in aerospace industry. Computational Fluid-Dynamics (CFD) and Lumped Parameter (LP) model with non-equilibrium and equilibrium approaches are mainly used. A score-table method is developed and used to select the modelling works that will be used as a reference base in this thesis. Vliet et al. [1] was chosen because of the integrated heat transfer-fluid-dynamic model, which considers the bulk temperature gradient. Daigle et al. [2] was also selected because of their proposed discretisation approach, which was applied to liquid and to vapour. The model of Wang et al. [3] was considered to compute the heat transfer between each sub-layer. The works mentioned require modelling improvements because (i) they were not validated with a large data set and (ii) they cannot predict the behaviour at high values of heat ingress. The models also lack of a proper representation of the vapour thermal stratification. This thesis has the goals of developing a software for industrial uses and of improving the scientific knowledge of the phenomena impacting the management of cryogenic liquids during storage. The model to be developed in this thesis considers only pure cryogenic liquids, but it has been conceived to be extended to LNG and to other mixtures of cryogenic liquids. This model relies on the fluid-dynamics and heat transfer conventional theories.

Section 1 describes role of the cryogenic fuels in the energy transition. Section 2 presents the cryogenic small scale storage. Section 3 explains the features and the challenges of the small scale storage of cryogenic liquids. Section 4 describes the storage phenomena. Section 5 presents the analysis of the state of the art. Section 6 defines the objectives of the thesis.

1. Role of cryogenic fuels in the energy transition

In the last 40 years, the anomaly[1] in the average global temperature indicates that the Earth is becoming warmer [4]. Anthropogenic Greenhouse Gases (GHGs)[2] emissions, in particular CO_2 emissions, are extremely likely to be the cause of climate change[5]. This warming is having severe impacts on people and ecosystems such as surges, sea level rise, coastal and inland flooding, and period of extreme heat. As suggested by IPCC[6], the stabilization of GHGs concentration in the atmosphere can avoid these possible scenarios. This can be achieved by trasforming the fossil-based sources of the main CO_2 emissions[3] into ones with low or zero carbon dioxide emissions. This approach is called *energy transition*.

Gaseous fuels such as Natural Gas (NG), bio-methane or bio-natural gas (bio-NG) and green hydrogen (H_2) can play an important role in the de-carbonization of energy and transport sectors. NG can substitute coal and heavy oils for electricity production in large scale and for residential and industrial heating. Burning NG produces 20 % less carbon dioxide than oil and 45 % less than coal. NG and bio-NG can replace fossil fuels in small scale applications in energy and transport sectors such as maritime and heavy duty transport, and power production in off-grid industrial and residential sites in remote area. Green H_2 is also considered as an important energy vector to transport energy between the renewable energy production hubs and the final users. The contribution of bio-LNG in decarbonising the heavy-duty transport is remarkable since a 34 % reduction of GHG emission with respect to diesel, under the well to wheel perspective, is achieved in the heavy duty transport by using the 17 % of bio-LNG as blend with convecntion LNG[7]. A zero GHGs emissions scenario can be achieved with green H_2 in these small scale applications.

Natural gas, bio-methane and green hydrogen are, however, difficult to store because they are gases at ambient temperature, hence they have a very low volumetric energy density, as reported in Table 1. These values of density are computed using the thermodynamic models implemented in the software REFPROP V10[8].

Table 1. Density and energetic volumetric density at different storage conditions.

	Methane[4]			**Hydrogen**		
	Standard conditions[5]	**25 MPa**[9] **and 298.15 K**	**Saturated liquid at 1 bar**	**Standard conditions**	**70 MPa**[10] **and 298.15 K**	**Saturated liquid at 1 bar**
Density [kg/m^3]	0.64828	188.2	422.6	0.081272	39.223	70.899
Energetic volumetric density [MJ/m^3]	35.987	10447.5	23459.7	11.523	5561.43	10052.7

As consequence, these gaseous fuels are respectively liquefied into Liquefied Natural Gas (LNG), the bio-liquefied natural gas (b-LNG) and the liquid hydrogen (LH_2), to increases the density and the energetic volumetric density, instead of pressurising them, as reported in Table 1. Hence, the gaseous

---

[1] The anomaly in the average temperature is the difference between the current average temperature and the reference value. This reference temperature is usually the temperature before the first industrial revolution.

[2] GHGs are a family of gases that absorbs and emits radiant energy at thermal infrared wavelengths, causing the greenhouse effect. The main common GHGs are water vapour, CO_2 and methane.

[3] The heat and electricity production, the Agriculture, Forest and Other Land Use (AFOLU), the industry and transport sector are the main sources, with a production of 25 %, 24%, 21 % and 14 % of the overall GHGs production in 2010, respectively[5].

[4] Methane is the main component of natural gas and of bio-methane. Hence, it is used for estimating the NG and bio-NG properties.

[5] Standard conditions are the defined as the condition when the temperature is 298.15 K and the pressure is 1 bar.

fuels can be more compactly stored and transported as cryogenic liquids than pressurized gases, from the site of production to the site of the end user. These liquids are re-transformed in gases before being used as fuels because the direct uses of the liquid cannot be done. So, the cryogenic liquids are applied as energy carriers of low carbon gaseous fuels in the energy transition.

2. Small scale cryogenic liquids storage

Liquefied natural gas (LNG) and liquid nitrogen (LH_2) were historically stored in Large Scale (LS) storage containers, as described in Figure 1 (a) and (b). In Figure 1 (a), the storage tanks contain LNG for supply French gas-grid and for transferring LNG to ship. In Figure 1 (b), the storage container is filled with LH_2 for supplying rockets.

a) b)

Figure 1. a) LNG and b) LH_2 large scale storage tanks at Montoir de Bretagne (FR) [11] and Jonh F. Kennerdy Space Center (USA) [12].

Bio-liquefied natural gas (bio-LNG) does not have a large history of storage because it has been mainly produced in recent year. Its storage features are quite similar to LNG because both liquids are mainly made of methane.

Many applications, especially the use of the gases as fuel in transport vehicles (ships, trucks, etc.) and in producing power in off-grid sites require much smaller tanks, called Small Scale (SS) tanks. These storage tanks are described in Figure 2. In Figure 2 (a), the storage tank contains bio-LNG for supplying a local industry, which is not connected to the natilnal gas-grid. In Figure 2 (a), the storage container is designed for holding LNG as fuel for trucks.

a)

b)

Figure 2. a) An image of Small Scale tank that contains bio-LNG as industrial fuel in Valenton, France [13]. b) A picture of SS storage container of a truck fuelled with LNG [14].

Table 2 presents the main properties of the large and of the small scale storage tanks for LNG and LH_2. The storage properties of LH_2 small scale storage tanks are not reported because they are not documented in the open literature, to the author's knowledge.

Table 2. Properties of the large and small scale storage tanks.

Size	BOG[6] rate	BOG management	Operating pressure	Operating conditions	Insulation technology	Geometry
			LNG large scale			
0.12-0.2 Mm^3	0.05 – 0.15 %/d [15],[16]	Re-liquefied, inserted into gas-grid or burned in engines	Around 1 atm	Close to stationary, except during transferring	Perlite or insulation foam	Sphere, vertical cylinder and membrane
			LH_2 large scale			
0.54-4 km^3	0.1 – 0.18 %/d [17],[12]	Re-liquefied, inserted into gas-grid or burned in engines	Around 1 atm	Close to stationary, except during transferring	Vacuum and solid thermal insulation such as perlite and glass bubbles. [17],[12]	Sphere
			Small scale			
Change with the end use	Not found	They are often not available.	5 - 17 barg	Variable operations conditions: steady state, transferring, pressurisation, etc.	Vacuum chamber, multilayer insulation, glass bubble and vapour cooled shield (VCS) are usually applied.	Cylindrical vessels with rounded ends

The size, the operating pressure and the boil-off gas (BOG) management system strongly vary between the LS and SS storage containers. The volume-to-surface ratio is higher in SS tanks than in the LS container. As consequence, the heat fluxes per unit of volume of cryogenic liquid in SS storage containers are usually higher than in LS tanks. The pressure in SS containers is usually higher than in the LS tanks, because BOG management system, which regulates the pressure by withdrawing gas from the ullage, is often not available in SS tanks because it is not technically and economically advantageous.

---

[6] The Boil-off Gas (BOG) is the vapour that leaves the storage containers, due to cryogenic liquid evaporation.

3. Challenges of the storage of cryogenic fluids in small scale tanks

Due to the heat inputs, the variables such as temperatures, pressure, filling ratio and compositions can evolves during the storage of cryogenic liquid in open and closed storage containers. Operators of small scale (SS) storage containers are not partially interest in these physical variables, except for the filling ratio. To safely manage the storage of the cryogenic fuels, the operators prefers by monitoring the *storage variables*. These variables, which depends on the physical variables, are holding-up time (HUT), the net pressure suction head (NPSH), the gross heating value (GHV) and the methane number (MN), which are presented in Table 3.

Table 3. Storage variable: definition and physical variables that affect the storage variables.

Storage variables	Definition	physical variables
HUT	It is the time that is required by the pressure to go from a certain value to the maximum allowable operating pressure of the tank (MAOP)[7].	Pressure, temperatures and liquid level
NPSH	It is the difference in pressures between the pressure at the inlet of the pump and the saturated pressure of the liquid at the same inlet.	Liquid temperature at the inlet of cryogenic pump
GHV	GHV is the amount of heat realised per unit of fuel mass by the complete combustion with stoichiometric oxygen and with the condensation of the water.	Compositions of Liquefied natural Gas (LNG) and of the Boil-off Gas (BOG)
MN	MN is the anti-knocking property of LNG-fuelled sparkling engine. This property is measured as the equivalent anti-knocking property of a binary CH_4-H_2 mixture. CH_4 and H_2 have respectively a value equal to 100 and to 0.	

The HUT is computed from the pressure and it directly affects the techno-economic feasibility of cryogenic liquid storage. If the value of the pressure is above the MAOP, the storage container must be de-pressurized to restore the safe operating conditions. The reduction of pressure is often done by opening the relief valves and venting the vapour, thus the BOG, in the atmosphere. Venting is highly undesired because vapour fuel is lost, thus money is lost, and also because those gases usually have a greenhouse effect, such as methane (CH_4)[8] .

NPSH is estimated form the temperature profile in the liquid, and it gives a decisive indication on the breakdown of the cryogenic pump that send out the cryogenic liquid to the utility. The values of NPSH must be above the minimum value, which is given by the constructor of the cryogenic pump. When this condition is not respected, the cavitations[9] can damage the cryogenic pump. As consequence, the liquid fuels cannot be withdrawn and used until the NPSH value is within the accepted value. This can lead to a penalty on the quantity of cryogenic liquid that can be used in the system.

GHV and MN are computed form the composition of the fluid, and these parameters directly affect the operation of the engine and of other burning devices such as furnaces and boilers. In system fuelled with LNG and/or with the BOG, GHV and MN are highly controlled because the values of these parameters can change in time, due to the ageing phenomena. If the current values of these storage variables do not respect the range imposed by the constructors of the burning device, LNG and/or BOG cannot be fed to those units. Hence, the functioning of those units will be perturbed, leading to economical and maybe technical damages.

As consequence, the main challenge of the cryogenic storage is maintaining the storage variables in the applicability limits for supplying the engine or the power generation unit with the gaseous fuel. In particular, the trial of this thesis work is the development of a physical model to predict accurately the evolution of the value of the measured variables of Table 3 from the storage conditions, and then to establish a proper operating strategy.

---

[7] MAOP is the limit value of the pressure to guarantee the operation of the unit.

[8] Methane is a powerful GreenHouse Gases. Its GHG potential is around 28 times the one of CO_2.

[9] Cavitations are the formation of bubbles over the surface of the blades of the pump.

4. Phenomena in cryogenic storage containers

To properly develop a physical model, the main phenomena must be identified and understood. So, they can be well represented by this model. The phenomena that occur in small scale (SS) storage containers are mainly the results of the heat inputs and the operating conditions imposed by the user. These storage phenomena are the results of fundamental phenomena and they affect the behaviour of the storage variables, as it is indicated in Table 4.

Table 4. Storage and fundamental phenomena, and storage variables.

Storage phenomenon	Fundamental phenomenon	Storage variables
Thermal stratification (vapour and liquid)	Fluid-dynamic at side wall	Net suction pressure head (NSPH)
Self-pressurisation or natural pressure build-up	Condensation and evaporation at interface	Holding-up time (HUT)
Ageing or weathering	Condensation and evaporation at interface	Methane number (MN) and gross heating value (GHV)

The thermal stratification is the development of a bulk temperature gradient in a fluid confined space that is heated at the side and bottom boundary, and insulated or heated at the upper boundary. The temperature increases in same direction of the fluid motion at the side wall. The bulk temperature gradient is adverse because it disfavours the fluid motion. The self-pressurisation is the natural increment of the pressure in cryogenic storage containers due to the heat inputs, and due to the evaporation and condensation at the interface. Ageing is the time-variation of the composition of cryogenic liquid mixture due to the selective evaporation of the most volatile species.

Section 4.1 presents the pathway of the heat input in the storage container. Section 4.2 and 4.3 describes the fundamental phenomena of natural convection and, condensation and evaporation. Section 4.4 and 4.5 explains in details the thermal stratification in liquid and in vapour, respectively. Section 4.6 and 4.7 describes the self-pressurisation and the ageing, respectively.

4.1. Pathway of the heat input

In storage container with a cryogenic liquid, the heat leakage is always present due to the difference in temperature between the external surface of the storage tank and the cryogenic liquid. The heat inputs rate depends on the environmental conditions and the structure of the storage tank, in particular the thermal insulation and the geometry. The pathway of the heat input in a storage container can be approximately described with the electrical resistance analogy[10], using a scheme of three steps in series, as it is described in Figure 3. In Figure 3, the black rectangles are the external and internal walls. The green, yellow and the blue rectangles are respectively the air, the thermal insulation and the fluid stored (liquid and vapour). The white circles with purple border are the temperatures and the purple lines are the thermal resistances.

The three main steps of the environment-to-fluid heat transfer are:

a) Environment-external walls of the storage container;
b) The external walls- internal walls;
c) Internal walls-internal fluid (vapour and liquid);

The overall heat flows across these steps is equal to the heat flows in step a), b) and c). So, the rate of the overall heat input depends on the difference in temperatures between the environment and the

---

[10] The electrical resistance analogy is a method of representing the heat transfer in system by the analogous electrical system.

internal fluid, and on the overall thermal resistance. This resistance is composed by the sum of the thermal resistance of each step, which are described in Figure 3.

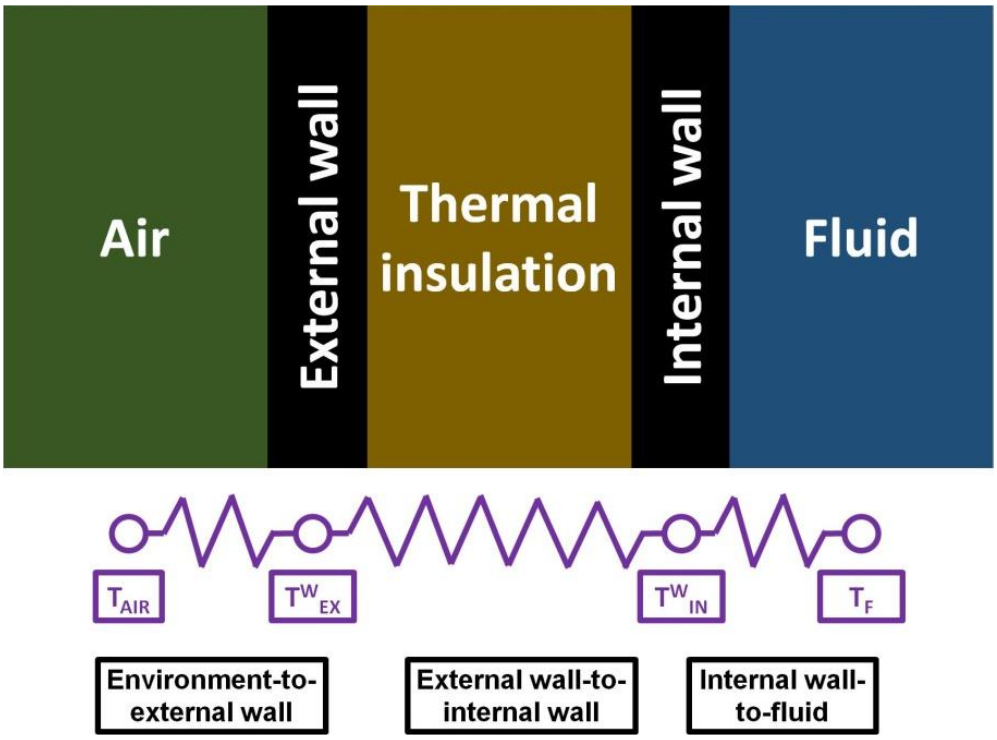

Figure 3. Pathway of heat transfer, explained with the electrical resistance analogy.

The overall heat flows across these steps is equal to the heat flows in step a), b) and c). So, the rate of the overall heat input depends on the difference in temperatures between the environment and the internal fluid, and on the overall thermal resistance. This resistance is composed by the sum of the thermal resistance of each step, which are described in Figure 3. Wind, rain and solar radiation can influence the thermal resistance, thus the amount of the heat transferred, between the air and the external shield. In absence of wind, natural convection characterizes the heat transfer in this step. When the wind is present, forced convection transfers the heat from the environment to the external shield. If the solar radiation is sufficiently strong, the external shield can be hotter than the air. In this case, the air contribution in heat transfer is lower. The thermal resistance between the external shield and the internal shield depends on the insulating technology, which affects environment-to-fluid heat transfer more than environmental-external shield and then internal shield-to-fluid (step a) and c) of Section 4.1). In presence of solid insulation such as perlite, multilayer or glass bubble, the heat is transferred only by conduction through this insulation. When thermal vacuum insulation is the only applied, the external shield transfers heat by conduction and by radiation. Complex mechanisms of conductive and irradiative heat transfer are present for insulation technologies that combine vacuum and solid insulation. The heat can be partially transferred by convection in storage containers with vapour cooled shield. The thermal resistance between the internal wall-to-vapour and internal wall-to-liquid heat transfers are affected by the fluid-dynamic phenomena occurring in the tank, which are quite similar to the one of fluid in confined spaces. This fluid-dynamic is affected by the heat fluxes, the geometry of the storage containers and by the bulk temperature gradient in liquid and in vapour phases. This bulk temperature gradient can evolve in time and it can disappear under certain storage conditions.

4.2.Fundamental phenomena: natural convection

The natural convection is the natural motion of a fluid over or along a surface due to the buoyancy forces. These forces are caused by a difference in temperature between the surface and the bulk. The velocity of the fluid motion is, so, produced by this difference. Three types of free-convection are discussed here:

a) Natural convection in homogeneous medium[11];
b) Natural convection in stratified medium[12];
c) Natural convection over upward and downward[13] heated horizontal surface.

These types of natural convection are respectively described in Section 4.2.1, 4.2.2 and 4.2.3.

4.2.1. Homogeneous medium

Let's consider a flat vertical surface subjected to a constant heat flux and immerged in a pure fluid. The temperature is uniform and the centre of gravity of the fluid medium is fixed. The boundary layer[14] and the temperature profile in this layer develop as illustrated in Figure 4 (a) and (b), respectively. In Figure 4, white arrows with red border are the heat inputs, blue and purple arrows and squares respectively indicate the cold and warm liquid. Green and red dashed lines individually indicate the velocity and the thermal boundary layers.

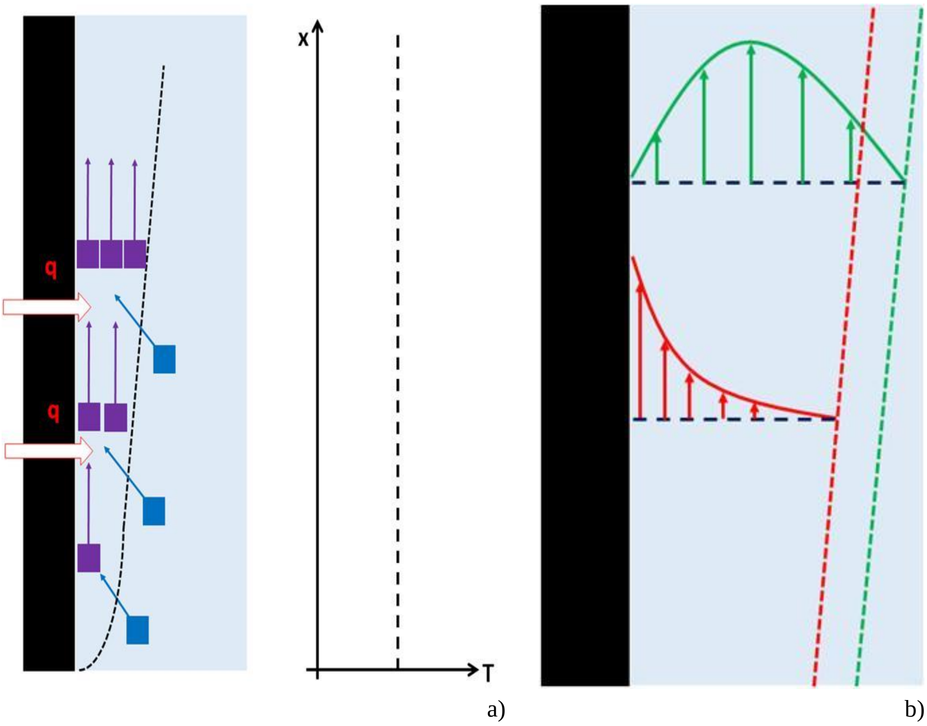

a) b)

Figure 4. a) fluid-dynamics of the boundary layer and b) the temperature (red) and the velocity (green) profiles in the boundary layer.

As illustrated in Figure 4 (a), the liquid is warmed by the heat flow at the wall. As the fluid moves upward, mass is entrained in the boundary layer, as indicated in Figure 4 (a). So, the speed and the size

---

[11] Homogeneous medium is an environment where the temperature is homogeneous.
[12] Stratified medium is a milieu where there is a he temperature gradient. This gradient is "adverse" when it disfavour the fluid motion. Hence, the temperature increases along the direction of the fluid motion.
[13] Upward and downward respectively indicate that the hot side of the surface looks upward and downward.
[14] Boundary layer is a thin layer of fluid near the surface where the velocity and temperature profiles change.

of the boundary layer are increased with the length of the surface, as reported in Figure 4 (b). In the boundary layer, the velocity profile has an inverted “U” shape curve, and the temperature profile monotonically decreases, as indicated in Figure 4 (b). The velocity increases by moving away from the wall until reaching a maximum value, because the viscous forces are reduced by the distance from the surface. After this peak, the velocity decreases because the fluid does not move in the bulk.

4.2.2. Stratified medium

The bulk is thermally stratified and the temperature gradient is adverse[12], as indicated in Figure 5. In Figure 5, white arrows with red border are the heat inputs, blue and purple arrows and squares respectively indicate the cold and warm liquid. Green and red dashed lines individually indicate the velocity and the thermal boundary layers. The dark and the light colours respectively indicate the high and low temperatures. The black rectangle is the wall of the vertical surface.

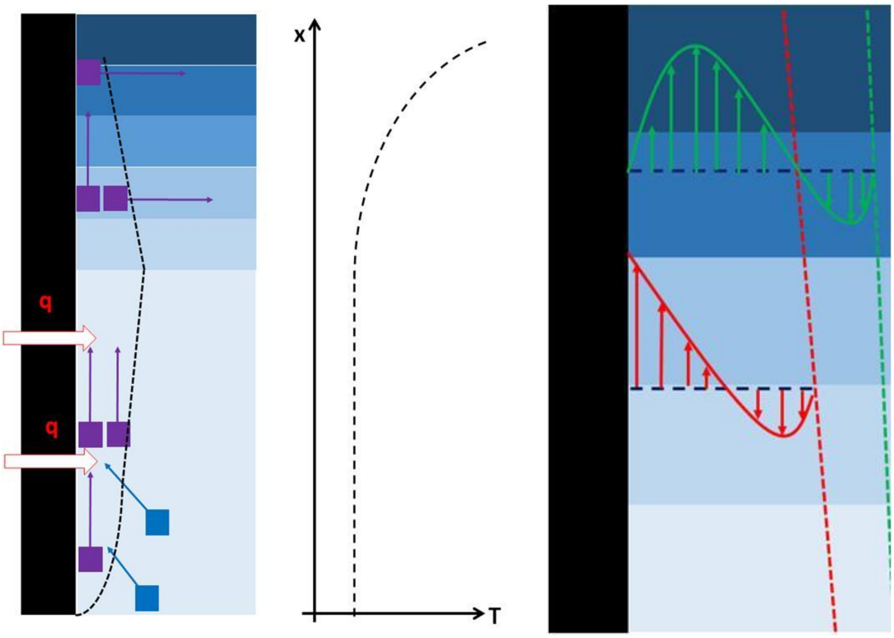

a) b)

Figure 5. a) fluid-dynamics of the boundary layer and b) the temperature (red) and the velocity (green) profiles in the boundary layer.

As described in Section 4.2.1, the fluid is pushed upward along the wall by the buoyancy forces. In the stratified medium, these forces are reduced due to the adverse temperature gradient, which creates an adverse density gradient. This density gradient reduces the buoyancy forces and the decrement of these forces produces:

a) Instability in the boundary layer.
b) Suppression of the natural convection.

The first scenario can occur when these forces become lower than the viscous forces, but they are sufficiently high to sustain the free-convection. In this situation, the shear tensor is partially inversed because the viscous forces dissipate more energy than the one produced by the buoyancy forces. So, the mass flow must reduce because there is not enough energy to move the fluid. As consequence, some mass exits the boundary layer as illustrated in Figure 5 (a). This instability perturbs the velocity and the temperature profiles, as shown in Figure 5 (b). The velocity decreases down to the minimum value due to the reversion of the shear tensor. This variable, then, increases to reach its value in the bulk. The temperature decreases because the shear tensor reversion mixes the fluid. The temperature, then, increases to reach the value of the bulk.

The second scenario can happen if the intensity of the bulk temperature gradient is very high. In this case, the buoyancy forces become so low that the viscous forces dissipate the momentum. So, the fluid motion stops and the natural convection are suppressed.

4.2.3. Upward and downward heated horizontal surface

The natural convection over upward and downward heated horizontal surfaces is illustrated in Figure 6 (a) and Figure 6 (b), respectively. In Figure 6, blue and red border arrows respectively indicate the cold and hot convective flows. The black rectangle is the wall of the horizontal surface and the red arrow is the heat flow.

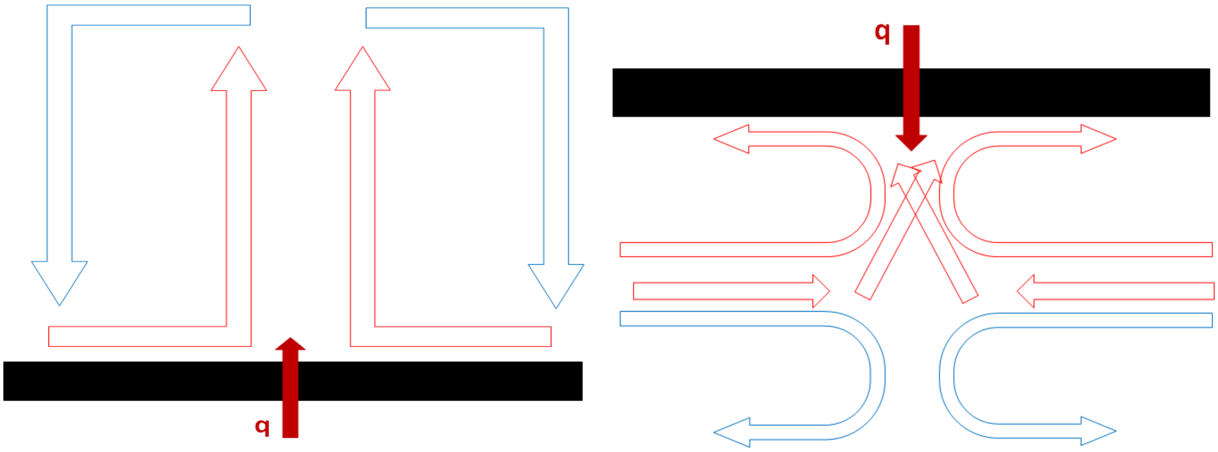

a) b)

Figure 6. a) Upward and b) downward heated horizontal surface.

The natural convection over heated upward horizontal surfaces is driven by the buoyancy forces, as for homogenous and stratified free-convection. The fluid attached to this surface becomes lighter and it is pushed upward by the buoyancy forces, as illustrated in Figure 6. The main difference is, however, the direction of the buoyancy forces respect to the surface. These forces are perpendicular to the surface and they are not parallels as in the previous cases. So, the boundary layer can be detached from the wall due to the buoyancy forces, as experimentally proved [18]. Two types of detachment can occur:

a) Distributed detachment of the boundary layer;
b) Central detachment of the boundary layer;

The first type of detachment occurs in all the point of the surface. The detached fluid moves upward and this movement entrain mass from the bulk. The warm fluid enters the cold bulk and it gets cold. So, it goes down to the boundary layer. As results, the fluid motion is chaotic and the macro vortexes are formed in every point where the detachment occurs. The second type of detachment occurs at the centre of the horizontal surface, as illustrated in Figure 6 (a). The fluid flows parallel to the surface from every direction to the centre of this surface. The streamlines converge in this point and the boundary layer detaches. So, the warm fluid moves upward and the cold fluid is entrained in the boundary layer from the edges of the surface. The warm liquid becomes cold when it reaches the bulk fluid above the surface and it goes down. As result, macro vortexes are generated over the surface, as illustrated in Figure 6 (a).

As for the upward heated horizontal surface, the free-convection is caused by the buoyancy forces. The buoyancy forces push the fluid against the wall of the horizontal surface, as presented in Figure 6 (b). The fluid cannot go upward because it is blocked by the surface. So, it randomly moves from left to right and form right to left. In this movement, the warm fluid entrains cold mass from the bulk, as illustrated in Figure 6 (b). At the same time, part of this warm fluid exits the boundary layer and it goes to the bulk, where it gets cold. As result, this configuration of the horizontal surface does not develop macro vortexes.

4.3. Fundamental phenomena: condensation and evaporation

Evaporation and condensation are non-equilibrium and unidirectional processes [19] of energy and of mass transfer. The evaporation is the movement of molecules form the liquid to the vapour. To do that, the liquid molecules have to break the intermolecular bounds. The condensation is the motion of particles from the vapour to the liquid. This motion occurs when the vapour molecules do not have enough kinetic energy to resist to the intermolecular forces. Evaporation and condensation occur through the free surface separating them, called the *liquid-vapour interface*. The latter is an infinitesimal space where these phenomena occur, and it is characterized by a temperature jump. This jump is a strong difference in temperatures between both vapour and liquid, and the interface [19]. Evaporation and condensation are always present in storage tanks, and often simultaneously. So, a net mass flow can be defined as the difference between the evaporation and the condensation flow rates. Three situations exist:

a) *Net evaporation*. The evaporation rate is governing and the liquid loses mass;
b) *Net condensation*. The condensation rate is dominant and the vapour loses mass;
c) *Dynamic equilibrium*. The net mass flow is equal to zero because the evaporation rate is equal to the condensation rate.

The net evaporation and condensation can alternate with each other. This can lead to the condensation dynamic effect. This affects determines the ageing and self-pressurisation in closed storage containers. Evidences of net condensation are not found in literature.

Section 4.3.1 describes the net evaporation. Section 4.3.2 presents the condensation blocking effect.

4.3.1. Net evaporation

Net evaporation is usually occurring in open storage containers, especially when the system reaches a steady state regime. Several experimental studies [20]–[22] investigated the net evaporation in open storage containers. The mechanism of this phenomenon is characterized by heat transfer between the bulk and the liquid interface, shown in Figure 7 (a). Figure 7 (b) presents the temperature profile in the tank. In Figure 7, the vapour-liquid interface is the yellow dashed line and the border between each zone is the purple dashed line. The heat fluxes are represented by the white arrows with red borders, the green line is the evaporative net mass flow at interface and the white arrows with blue borders indicate the free-convective flows. Low and high temperatures are respectively described by dark and light blue-green colour. T_S and T_B respectively refer to the saturation temperature and to the bulk temperature. The mechanism of net evaporation occurs in four successive steps. Each step corresponds to a specific region of the liquid that is placed near the interface. These regions are:

a) *Liquid interface*. This zone is named with the letter “A” in Figure 7. It is below the interface and, here, the evaporation takes place at molecular scale. The temperature is slightly above the saturation temperature of the liquid[21] and the interface is at quasi-equilibrium condition;
b) *Thermal conduction layer*. It is located below the liquid interface and it is described by the letter “B” in Figure 7. The temperature strongly changes with a gradient of around 50 K/cm [20]. So, this layer strongly controls the overall process. The heat is mainly transferred across this layer by conduction;

c) *Intermitted convective layer*. This zone is placed below the thermal conduction layer and this zone is indicated with the letter "C" in Figure 7. The temperature smoothly changes with a gradient of around 0.5 K/cm[20] and the heat is transferred by Rayleigh-Bernard convection[15]. Bernard cells are enclosed by the vortex lines and the vortexes radically move from the wall to the centre of the tank;

d) *The bulk of the liquid*. It is described by the letter "D" in Figure 7.

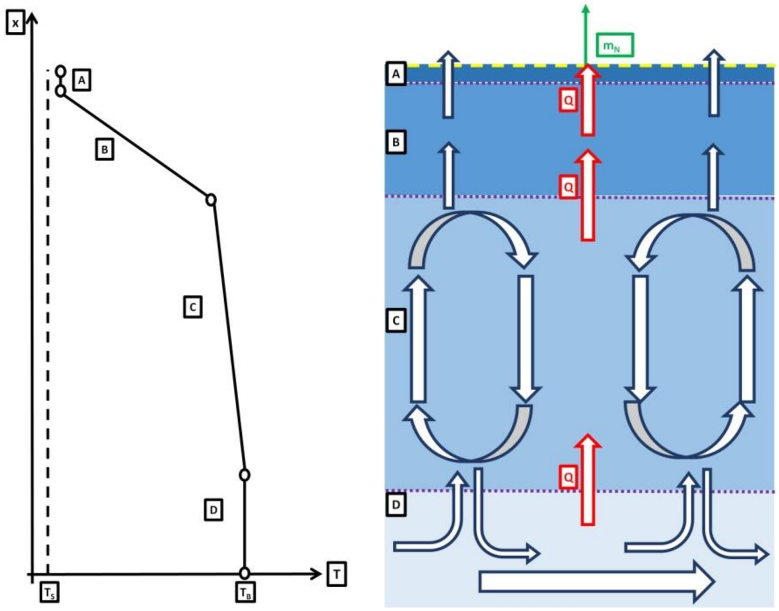

a) b)

Figure 7. (a) Liquid near the interface and (b) temperature profile.

The net evaporation rate can be reduced if impurities such as heavy species are present at interface [21]. This phenomenon can be strongly increased by the collapsing of the thermal conduction layer. This collapsing causes the explosive vaporization, as it happens during sloshing. Micro explosive vaporization can frequently occur due to the fluid-dynamic instability of the intermitted convective layer [21]. The net mass flow oscillates due to this micro vaporisation, but it is stable in average [21].

In closed storage containers, net evaporation can occur when the vapour-to-interface heat flow is higher than the interface-to-liquid heat flow. In this case, the interface temperature is higher than the bulk temperature. The Bernard cells are not formed in the intermitted convection layer. So, the heat is transferred by conduction in this step. However, experimental evidences of net evaporation during pressurisation are not found.

4.3.2. Dynamic condensation blocking

Dynamic condensation blocking was modelled by Osipov and Muratov [23] and it can be described as reported in Figure 8. In Figure 8, the light orange and light blue colours are the vapour and the liquid, respectively. The "cold" and the "warm" interface are respectively the blue and red rectangles. The evaporation and the condensation rate are the white arrows with green boarder, whose size indicates the magnitude of the rate.

---

[15] Rayleigh-Bernard convection is a type of free-convection that occurs over heated flat horizontal surface. This convection is characterized by regular patterns of convective cells, called Bernard cells.

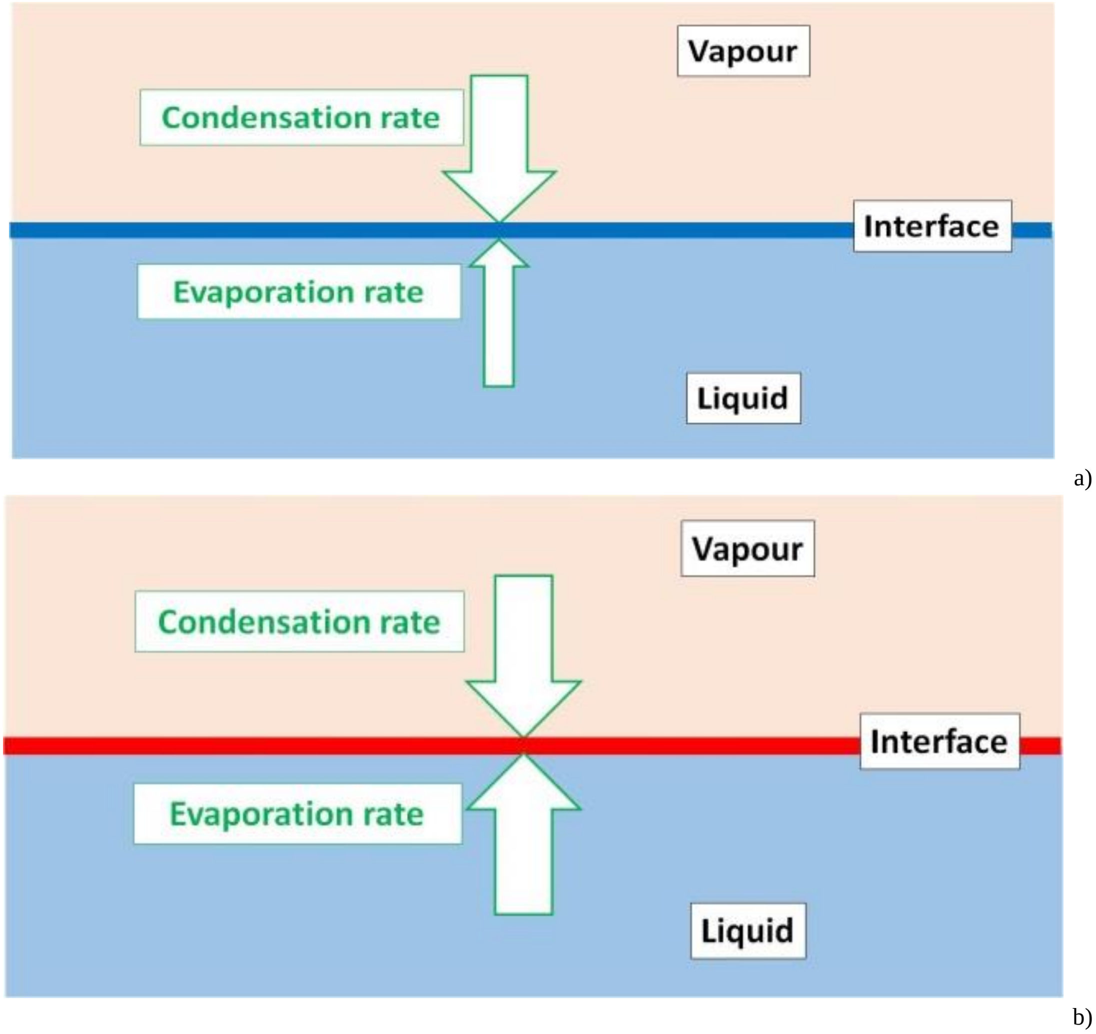

Figure 8. Condensation blocking effect: a) increment of condensation rate; b) increment of the evaporation rate.

As the pressure increases, the liquid becomes sub-cooled and the evaporation rate low, as indicated by the blue rectangle and the small arrows in Figure 8 (a), respectively. The collision rate of the vapour molecules increases, enhancing the condensation rate because the intermolecular bounds are easily formed. So, the condensation of the vapour releases heat at the interface. As described in Figure 8 (b) by the red rectangle, this heat increases the temperature of the interface and the evaporation rate, which can become higher than the condensation rate or it can be equal to this rate. The quasi-equilibrium condition is reached and net condensation is blocked, as illustrated by the size of the arrows in Figure 8 (b). To sum up, the dynamic condensation blocking [23] reduces the condensation rate, increasing the liquid-to-vapour mass flow and, possibly, the pressure.

4.4. Thermal stratification in liquids

The empirical evidences of thermal stratification in cryogenic liquids were reported in scientific literature, in particular by these authors [24]–[30]. From these works, it can be concluded that:

a) The temperature profile is flat in the liquid, except at the bottom, as especially indicated by Seo and Jeong [24], Kang et al. [25] and Perez et al. [26] during the steady state;
b) The development of the thermal stratification follows the mechanism for standard liquids[16] with side heating only (see Section 4.4.2 of Chapter 1);

---

[16] In this thesis, standard liquids are defined as fluids that are liquids at standard conditions (1 bar and 298.15 K).

c) The liquid temperature near the interface is close to the interface temperature, producing a small difference in temperatures between the interface and the liquid;
d) This phenomenon occurs in cryogenic liquids when they are in closed storage containers;
e) The development of the thermal stratification varies with the storage conditions;

Section 4.4.1 presents the similarities and the difference in thermal stratification between the standard and cryogenic liquids. Section 4.4.2 and 4.4.3 describes the thermal stratification of standard liquids with side heating only, and with bottom and side heating, respectively. Section 4.4.4 discusses the parameters that modify the thermal stratification. Section 4.4.5 describes the effect of the thermal stratification on the other storage phenomena.

4.4.1. Similarities and difference between cryogenic and standard liquids

As indicated by the conclusions a), b) and c) of Section 4.4 of Chapter 1, the mechanism of development of thermal stratification and the form of the temperature profile are common between cryogenic and standard liquids. For both liquids, the heat comes from the bottom and the side wall, producing the same mechanism of natural convection in stratified medium (see Section 4.2.2 of Chapter 1). This natural convection carries warm liquid to the interface where it is accumulated. The development of the thermal stratification starts from the interface in both types of liquid.

The main differences in thermal stratification between standard and cryogenic liquids are the role of the interface in developing this phenomenon and the effect of the storage conditions, as suggested by the observations d) and e) of Section 4.4 of Chapter 1. In standard liquid, the liquid-vapour interface is similar to a thermally insulated surface because the mass-heat transfer is extremely weak, almost negligible, except if they are at saturation. In cryogenic liquids, the interface can be respectively colder and warmer than the interface, when the storage container is open and closed. In open steady state storage containers, the net evaporation occurs and the interface remains cold because the warm liquid is not accumulated. In closed storage tanks, the net evaporation is almost suppressed and this surface is warm. The opening and closing of the storage container can produce the thermal stratification. As consequence, the storage conditions produce this phenomenon.

4.4.2. Thermal stratification in standard liquids: side heating only

As explained in Section 4.4.1 of Chapter 1, the evolution and the stationary states of the liquid thermal stratification in closed storage containers can be described with the experimental observations of standard liquids [31], [32], [33]. In particular, the observations with side heating only [32] shows the mechanism of this phenomenon, which is illustrated in Figure 9. In Figure 9, the interface is the yellow dashed line, the border between the stratified and the mixed region is the purple dashed line and the orange dashed line is the boundary layer. The heat fluxes are represented by the white arrows with red borders and the white arrows with blue borders indicate the free-convective flows. Low and warm temperatures are respectively described by dark and light blue colour.

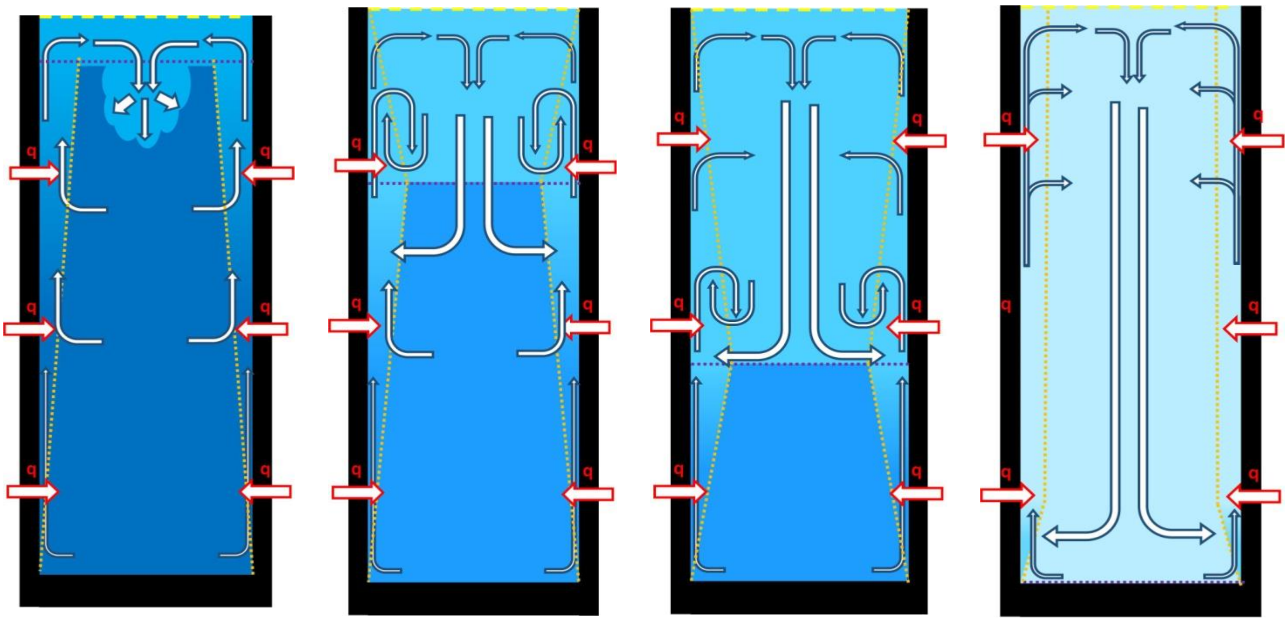

a) b) c) d)

Figure 9. The four steps (initial (a), quasi-steady (b), intermediate (c) and extended (d)) of the evolution of the thermal stratification of standard liquid in confined space, heated at the side only.

As illustrated in Figure 9, the thermal stratification of standard liquid in confined space, heated at side wall only, is formed in four steps [32]:

a) *Initial transient*. The liquid is initially sub-cooled and homogeneous, as described by Figure 9 (a). At the start of the experiment, the heating system is turned on and the liquid is heated at the side walls. The natural convection at the side walls carries warm liquid from the bottom to the interface. Here, the warm liquid does not evaporate because it is not at saturation condition. Hence, the liquid remains warm and, near the interface, it creates plumes and vortexes, as described by the white arrows with blue border in Figure 9 (a). These plumes and vortexes transfer the heat downward and sideward. The momentum of the moving liquid is partially dissipated by these vortexes;

b) *Quasi-steady stratification*. As time passes, the warm liquid is accumulated in the upper part of the fluid, which is close to the interface. So, a part of the side wall boundary layer is immerged in a stratified region, which is described by the light blue zone in Figure 9 (b). Here, a strongly temperature gradient is present and it is adverse to the direction of the rising liquid. The shear tensor and velocity are reversed because the buoyancy forces are reduced by the adverse temperature gradient, but the viscous forces at wall do not. The boundary layer is reduced and part of the flow rate is expulsed from the boundary layer. This expulsed mass goes to the bulk of the stratified region, as illustrated in Figure 9 (b). The stratified region expands downward, and a downward convective flow is present in the bulk of this zone*;*

c) *Intermediate stratification*. The fluid-dynamics mechanisms of quasi-steady state stratification continue in time. The stratified regions expand downward, due to mass accumulation, and the homogeneous initial region is progressively reduced. The liquid that rises at the boundary in this zone has less momentum and energy. Hence, the shear tensor and velocity reversion is less strong than the one in quasi-steady state stratification.

d) *Extended stratification*. The thermal stratification reaches the bottom of the confined space. Hence, the liquid is completely stratified. At the bottom, the liquid is entrained by the boundary layer at the side wall. In this boundary layer, the liquid rises, but it does not exit this layer as done in steps b) and c) of Section 4.4.2 of Chapter 1. The flow rate is almost constant in this layer and its thickness does not change.

The intensity of the bulk temperature gradient can be enough high to block the natural convection in the stratified region. This situation does not perturb the downward expansion of the stratified region.

4.4.3. Thermal stratification in standard liquids: effect of bottom heating

The fluid-dynamic mechanisms of this type of thermal stratification do not change when the bottom heating is added, except for the step of the extended stratification (step d) of Section 4.4.2 of Chapter 1). The development of the thermal distribution with side and bottom heating can be described as illustrated in Figure 10. In Figure 10, the interface is the yellow dashed line, the border between the stratified and the mixed region is the purple dashed line, and the orange dashed line is the boundary layer. The heat fluxes are described by the white arrows with red borders and the white arrows with blue borders represent the free-convective flows. Low and warm temperatures are respectively described by dark and light blue colour.

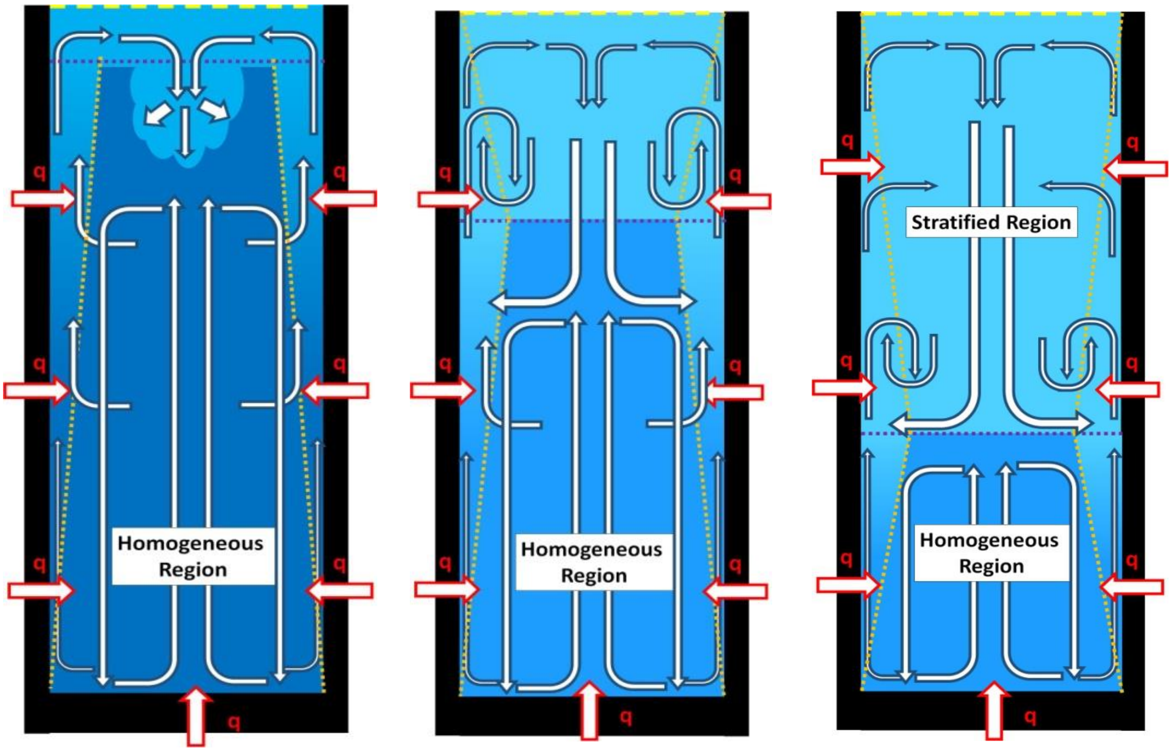

a) b) c)

Figure 10. Development of the thermal stratification with side and bottom heating in three steps: initial transient (a), quasi-steady stratification (b) and intermediate stratification (c).

As described in Figure 10, the development of this phenomenon is done in three steps: initial transient, quasi-steady stratification and intermediate stratification. These steps are similar to the ones of the thermal stratification with side heating only (see Section 4.4.2 of Chapter 1), except for the bottom vortexes. The vortexes are progressively compressed in the lower region as the time passes as described in Figure 10 (a) and (b). This compression ends when the stable condition of the intermediate stratification is reached as illustrated in Figure 10 (c). As reported by Anderson and Kolar [31], the bottom heating creates vortexes in the lower region of the liquid. These vortexes are pushed upward by the buoyancy forces because they are warm, thus lighter than the liquid. The upward movement of these vortexes is blocked by the descending flow produced by the thermal stratification and by the temperature gradient, which reduce the buoyancy forces. As consequence, the bottom heating creates two stable zones, respectively called *homogeneous region* and *stratified region*, as illustrated in Figure 10. The first region remains isothermal and homogeneous due to these vortexes. The region with the thermal stratification behaves as described in Section 4.4.2 of Chapter 1. This liquid region, however, does not expand as in the previous type of thermal stratification (with side heating only) because the vortexes of the homogeneous region block the expansion of this region.

4.4.4. Changes in thermal stratification in cryogenic liquids

Liquid level, heat inputs rate and heating configuration are the main variables that affect the thermal stratification in cryogenic liquids. The effects of these variables are reported in Figure 11. In Figure 11, the interface is the yellow dashed line, the border between the stratified and the mixed region is the purple dotted line and the orange dashed line is the boundary layer. The heat transfers are described by the white arrows with red borders and the white arrows with blue borders indicate the free-convective flows. The size of the white arrows with red border indicates the intensity of the heat fluxes. Low and warm temperatures are respectively described by dark and light blue colour. The vapour region is described by the orange colours.

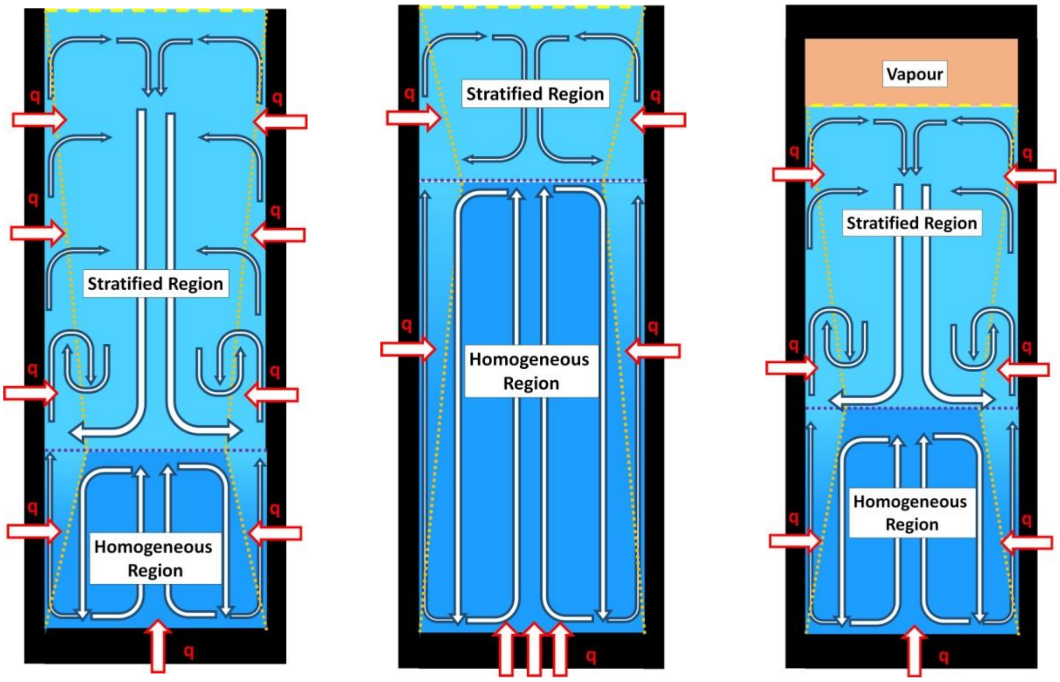

a) b) c)

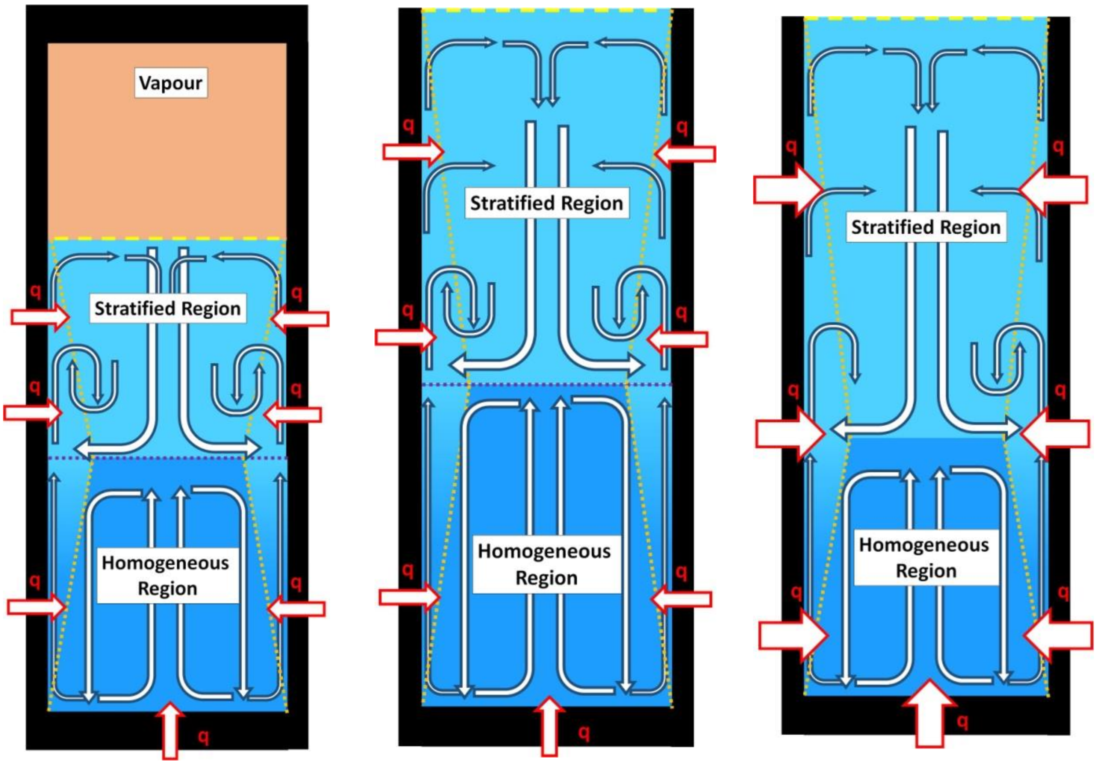

d) e) f)

Figure 11. Thermal stratification in different scenarios: a) high side heating; b) high bottom heating; c) high filling ratio; d) low filling ratio; e) low heat input; f) high heat input.

As observed by Anderson and Kolar [31], the heating configuration affects the thermal distribution, as reported in Figure 11 (a) and (b). When the liquid side heating is larger than the bottom, the stratified region is larger than the homogenous region. The bulk temperature gradient is present in almost all the liquid domain. As the bottom heating is increased, the homogenous region expands, reducing the stratified region. Hence, bottom heating enhances the homogenous region and side heating favours the thermal stratification.

The overall heat input in the storage container increases with the filling ratio, but the heat fluxes remains almost constant. As observed [25], the thermal stratification is not similar for different liquid levels due to the variation of the total heat ingress rates, as reported in Figure 11 (c) and (d). As the heat ingress rate increases, the mass flow in the boundary increases. As consequence, the volume of warm liquid transported to the interface is larger than the one at low liquid level. Hence, the steps b) and c) of Section 4.4.2 of Chapter 1 are intensified and the thermal stratification is more developed.

The thermal stratification can also vary for the same fixed filling ratio, the overall heat inputs are increased or reduced [24], [30]. If the heat inputs increase, the free-convective mass in the wet side wall flows faster than the one at low heat inputs and the bottom vortexes are larger than the ones at low heat input. Both increments cancel partially out and the homogeneous-to-stratified volume ratio does not significantly changes, as illustrated in Figure 11 (e) and (f). Since the free-convective mass flow increases, the thermal stratification develops more than the one at low heat input, and the bulk temperature gradient becomes sharper than the one at low heat inputs rate, as reported in Figure 11 (e) and (f).

4.4.5. Consequences of thermal stratification in cryogenic liquids

The thermal stratification impacts the mass-heat transfer at the interface, perturbing the self-pressurisation and the ageing. The relation between self-pressurisation and thermal stratification was proved by the experimental studies of Seo and Jeong [24] and Aydelott and Spuckler [30] at constant liquid level. In these conditions, the thermal stratification is stronger than the one at low heat fluxes because the side wall flow rate transports more energy to the interface. The bulk temperature gradient increases due to the accumulation of sensible energy, and this gradient reduces the natural convection of the side wall near the interface. As consequence, the temperature difference between the interface and the liquid decreases because the temperature of this liquid is closer to the interface temperature. The liquid-to-interface heat transfer and the condensation rate reduce. So, the natural pressure build-up is faster when the heat inputs rates are increased.

The effect of the thermal stratification on the ageing was studied by Al Ghafri et al. [3], [34]. They observed that the liquid and vapour compositions do not change in time in closed storage containers, while it does in open storage tanks. As the thermal stratification is developed in closed storage containers, sensible heat is accumulated near the interface because the net evaporation is reduced by condensing blocking effect (see Section 4.3.2 of Chapter 1). As consequence, the temperature gradient is developed and the convective flows at the side wall decrease. So, the evaporation rate decreases and the volatile components of the liquid are transferred with a lower rate than in an open system.

The thermal stratification has a considerable impact on the temperature of the cryogenic liquid at the inlet of the pump, as the temperature profile is a direct consequence of this phenomenon. So, the risks of cavitation9 are higher for storage container with sharp and large thermal stratification because of the high liquid temperature in the stratified region. Hence, the Net Positive Suction Head (NPSH) is affected by the thermal stratification.

4.5.Thermal stratification in vapour

The analysis of the work of Hasan et al. [27] and of Dresar et al. [28] on the storage of liquid hydrogen, revealed two main features of the ullage thermal stratification:

a) At any liquid level, the vapour temperature quickly increases at the beginning of the storage;
b) The vapour remains at quasi-steady state after this stage.

The vapour thermal capacity is lower than the one of the liquid due to the lower density, thus mass. As consequence, the vapour reaches the quasi-steady state condition faster than the liquid, and the vapour is mainly at the quasi-steady state during the self-pressurisation. Hence, the quasi-steady state condition is more of interest than the transient.

Section 4.5.1 and 4.5.2 respectively describe the quasi-steady state thermal stratification in open and closed tanks. Section 4.5.3 discusses the effect of some physical parameters on the behaviour of the vapour thermal stratification.

4.5.1. Vapour thermal stratification in open cryogenic columns

Islam and Scurlock [35], Boardman [36], and Beresford [37] studied the quasi-steady state thermal stratification of the vapour in open and closed cryogenic columns filled with liquid nitrogen. From those studies, the following can be concluded:

a) Thermo-siphon effect[17] was a remarkable source of heat flux;
b) The vapour thermal stratification is developed due to the cooling of the interface, and due to the free-convection at the side walls, as happens for the liquid;

---

[17] The thermo-siphon effect is the heat transferring between the hot and the cold sources by natural convection only, in a confined space.

c) The fluid moves upward in the boundary layer at the side wall;
d) A downward flow is detected in the core of the vapour phase.

The thermal stratification in vapour can be described by Figure 12 (a) and by Figure 12 (b) for the fluid motions and the velocity-temperature profiles, respectively. In Figure 12, the interface is the yellow dashed line, the border between each region is the purple dashed line and the dark red dashed line is the boundary layer. The heat fluxes are represented by the white arrows with red borders, the green line is the net mass flow at interface and the white arrows with blue borders indicate the free-convective flows. The darker is the colour of a layer, the higher is the temperature. The green indicates the direction of the velocity. The velocity and the temperature profiles are respectively described by the dashed green and dashed red lines. As described in Figure 12 (a), thermal stratification of the vapour can be divided into six regions:

a) *Turbulent*. It is represented by the dark red colour of Figure 12 (a) and it is called with letter A. It is located above the free-liquid surface. Here, vapour chaotically moves from the bulk to the side wall. The mass transfer phenomena at interface such as evaporation and condensation affect these chaotic motions of fluid. The temperature gradient is around 10-20 K/cm[35];
b) *Cold end mixing*. It is located above the turbulent region and it is indicated by the letter B in Figure 12 (a). The descending flow is indicated by the white arrows with the green-blue colour in Figure 12 (a). The descending flow mixes with the vapour of the turbulent region. The flow is entrained by the free-convection at the side wall and it moves from the bulk to the boundary layer.
c) *High gradient*. It is indicated by letter C. Here, the downward flow of the bulk is strongly cooled as it approaches the turbulent and the cold end mixing regions. The cooling of this flow causes a stable and high temperature gradient, whose values are between 5 and 10 K/cm[35]. In the bulk of this region, the velocity is directed downward and the profile is flat. A vapour flow rises between the bulk and the boundary layer to balance the reserving of the shear tensor in the boundary layer. This is explained by the green line in Figure 12 (b);
d) *Transition*. This region is represented by the letter D in Figure 12 (a). The temperature moderately changes along the vertical axis;
e) *Low gradient*. It is represented with letter E. Thermal stratification in this part is unstable because the downward flow of the bulk is not fully developed. In the bulk, a smaller part of the vapour moves downward. The remaining part moves upward in the bulk because it is entrained by the mass leaving the tank. The mass exiting the boundary layer contributes to this mechanism. Near the boundary layer, the phenomenon of the reversing of shear tensor occurs;
f) *Warm end mixing*. It is indicated by letter F. This region is characterized by a lower temperature gradient of around 1 K/cm[35]. The temperature is almost homogeneous due to the strong recirculation flows. These flows are created by the tank exit condition. The hot vapour of the boundary layer hits the roof and it changes direction. It moves to the centre of the tank and it is divided into two streams. The first descends, creating the downward flow of the bulk downward. This stream creates vortexes and it loses some of the momentum. The second stream is evacuated through the valve, if the tank is open.

The natural convection vapour motion can be blocked by the temperature gradient. This can happen in the upper region of the vapour, reducing the heat inputs. At the author’s knowledge, experimental evidences of this do not exit.

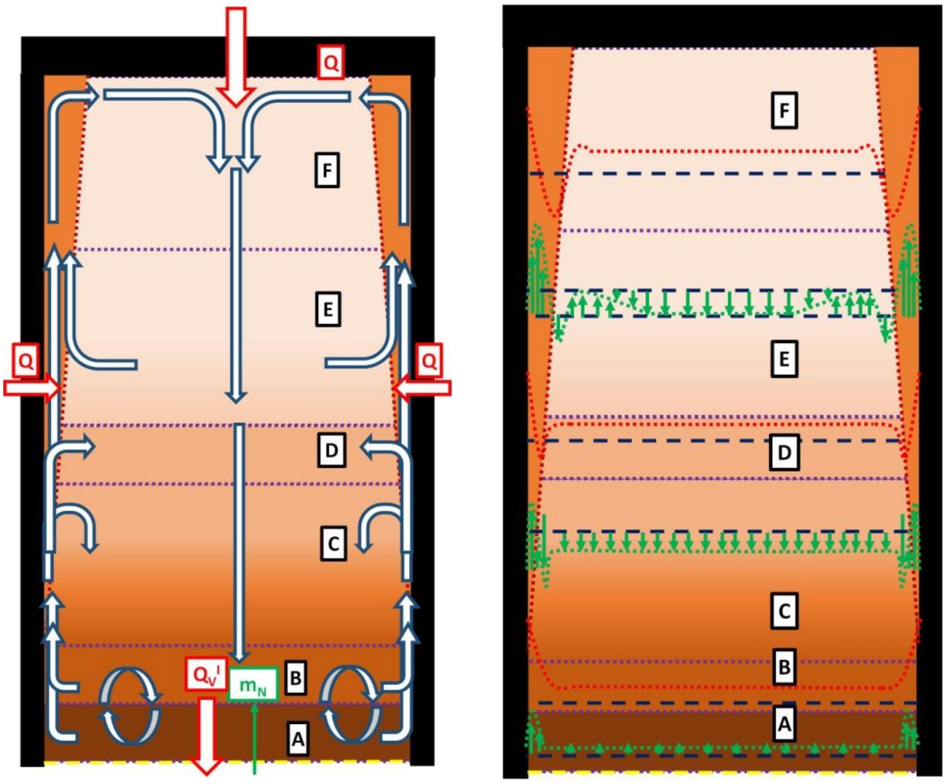

a) b)

Figure 12. (a) Subdivision of the vapour in six regions. (b) Velocity and temperature profiles.

The temperature and the velocity profiles in the boundary layer and in the bulk are reported in Figure 12 (b). The behaviour of the boundary layer differs in the different regions. The following aspects are observed:

a) In the turbulent and the low transition regions (A and B), the velocity increases in the boundary layer because the effect of the bulk temperature gradient is low;
b) In the high temperature gradient and the transition regions (C and D), the effect of the bulk temperature gradient is relevant, and the buoyancy forces are significantly reduced. Hence, the shear tensor and the velocity are reversed, as showed by the dotted green line in Figure 12 (b);
c) In the lower gradient region and in the warm end mixing (E and F), the instability increases up to the point where the flow is oriented downward with more speed in the boundary layer. Moreover, in the bulk, the vapour goes down in the centre line, but it rises near this line. The temperature profile seems flat along the radiant coordinate in the bulk. Cold spots can be detected near the boundary layer due to the mixing caused by the reversion of the shear tensor, which caused the reversion of the velocity.

As indicated by Beresford [37], the different upward and downward flows in these regions leads to a double recirculation process. Two macro recirculation processes can be detected: the low and the upper recirculation. The first recirculation occurs in the space between the turbulent and high gradient region. The second recirculation takes place between the low gradient region and the warm end mixing region. The transition region separates these macro recirculation processes.

4.5.2. Vapour thermal stratification in closed cryogenic columns

The description of the thermal stratification in Section 4.5.1 of Chapter 1 was done for open columns and it can be used for explaining this phenomenon in open storage containers. To the author’s knowledge, experimental evidences of fluid motions of vapour thermal stratification do not exist in closed storage container or closed columns. It is reasonable to believe that the sub-division of the vapour in six regions, as done in Section 4.5.1 of Chapter 1, is valid. In an open storage container or column, the vapour is removed from the top. As consequence, a part of the mass flow of the boundary layer can be sucked out, affecting the fluid-dynamics at the exit of the storage container. When the storage container is closed, the Boil-off Gas (BOG) rate is equal to zero because the vapour is not sucked. So, all the mass flow of the boundary layer of the dry side wall goes into the bulk. So, the warm and mixing regions (region F and E of Figure 12) can be qualitatively different from the ones of open storage containers (see Section 4.5.1 of Chapter 1) because the boundary conditions at the roof are different. The others regions are not perturbed because they are not influenced by the reduction of the BOG.

4.5.3. Variables affecting the thermal stratification

Storage parameters such as heat inputs and liquid level have an impact on the vapour thermal stratification, as underlined by Seo and Jeong [24], Kang et al. [25], Perez et al. [26], Hasan et al. [27], Dresar et al. [28], Aydelott [29] and Aydelott and Spuckler [30]. From these studies, it can be concluded that:

a) At fixed liquid level, the vapour temperature increases with the increment of the heat input;
b) As the filling ratio reduces, the vapour phase becomes hotter than the one at high filling ratio,
c) The shape of the temperature profiles is almost linear, and it barely changes with the heat inputs and liquid level.

With the increment of the heat input, the sensible heat accumulated in the ullage increases and the temperature rises. With the reduction of the filling ratio, the ullage heat input increases and the sensible thermal energy is accumulated.

4.6. Self-pressurisation

The natural increment of the pressure in a closed storage container has been experimentally studied and observed. The experimental works [24], [25], [26], [27], [28], [29], [30] shows the evolution of this phenomenon. Using the observations of these empirical investigations, it can be stated that:

a) The liquid thermal stratification influences the self-pressurisatio [24]–[30];
b) The natural pressure build-up is dependent from the mass-heat transfer at interface [28], [29];
c) The self-pressurisation occurs in two stages, respectively called *initial transient* and *constant pressurisation period*, when the heat fluxes are low (< 10W/m²) [24], [26]–[28]. The transient is short for liquid fraction above 70 % [24]. The transient becomes long when the heat input is increased [24], [27];
d) The pressure increases in case of high heat inputs rate at constant liquid level [24], [30].The pressure increases with the liquid level at high heat fluxes [25], [29] and it decreases with the filling ratio at low heat fluxes (10W/m²) [24], [26]–[28];

Figure 13 shows the pressure evolution in cryogenic containers filled with liquid nitrogen [24]–[26] and with liquid hydrogen [27]–[30] during self-pressurization experiments. Figure 13 (a) and (b) show the natural pressure build-up at low heat inputs (around 6 W/m²), respectively for liquid nitrogen and liquid hydrogen. Figure 13 (c) and (d) show the pressure evolution at medium heat inputs rate (around 60 W/m²), respectively for liquid nitrogen and liquid hydrogen. Figure 13 (e) shows the natural pressure build-up at high heat fluxes (around 180 W/m²). Figure 13 (f) presents the effect of the heat leakage rate on the pressure evolution at constant filling ratio. In Figure 13, the squat dots are the experimental data, the vertical dashed lines separate the initial transient form the constant pressurisation period. The arrows indicate the author of the experimental data when more authors are reported on the same graphs. The colours used are indicated in the legend of each graph.

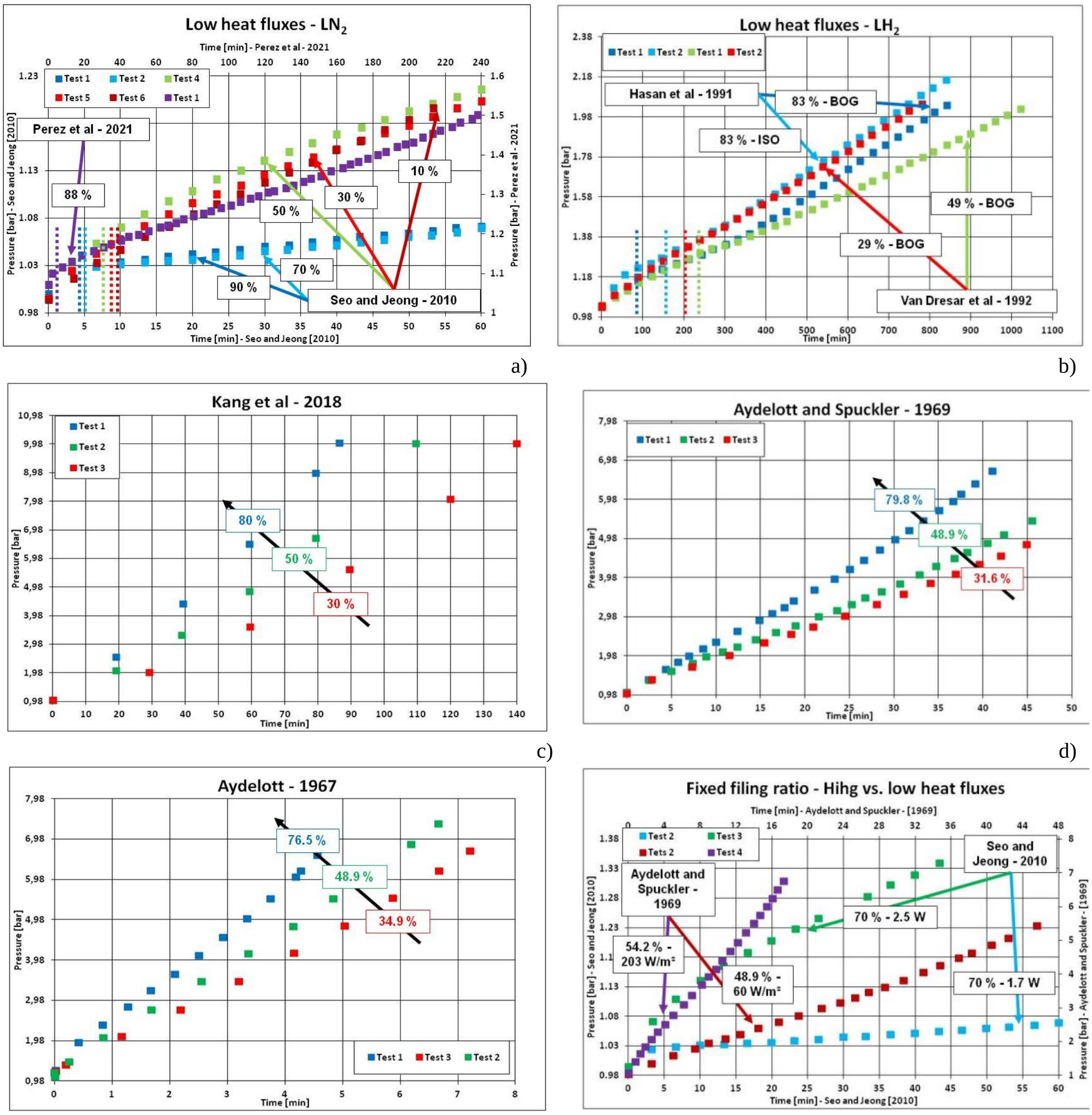

a) b)

c) d)

e) f)

Figure 13. Self-pressurisation in cryogenic tanks: low heat fluxes for LN_2 (a) and LH_2 (b); medium heat fluxes for LN_2 (c) and LH_2 (d); high heat fluxes (e); low vs. High heat fluxes (f).

The phenomena of evaporation and of condensation affect the self-pressurisation rate. The evaporation rate increases the mass in the ullage, thus the pressure. The condensation reduces the pressure because it removes mass form the ullage. In spherical and in ellipsoidal tanks, the surface area can change with the liquid level. Hence, low self-pressurisation rate are usually achieved when the interface surface area is the higher, thus near the value of 0.5 of filling ratio (Test 1 of Dresar et al. [28]), as reported in Figure 13 (b).

As indicated in Figure 13 (a) and (b), the <u>initial transient</u> of the pressure is caused by the liquid thermal expansion and due to the high evaporation rate. The liquid is initially homogeneous and it is close to the saturation point. Hence, this thermodynamic state of the liquid increases the thermal expansion and the evaporation rate, thus increases the pressure evolution in initial transient period. In the constant pressurisation period, the build-up rate decreases because the evaporation rate and the thermal expansion are reduced as result of the thermal stratification. As mentioned in Section 4.4.5, the thermal stratification increases the condensation rate, thus partially suppresses the evaporation and the pressure build-up. This behaviour is barely identified in case of medium heat fluxes[25], [30], as seen in Figure 13 (c) and (d).

At constant liquid level, the pressure increases with the heat inputs rate due to the mass-heat transfer at interface. The condensation rate decreases because of the thermal stratification. At the same time, the evaporation rate increases when the heat entering in the ullage increases, as seen in Figure 13 (f).

As said, the thermal stratification is related to the self-pressurisation, as it can be noted by comparing Figure 13 (a) and (b) (low heat fluxes), with Figure 13 (c) and (d) (medium heat fluxes) and with Figure 13 (e) (high heat fluxes). At medium and high heat fluxes, the thermal stratification develops more at high filling ratio than the one at low liquid level because the heat inputs at the wet side wall increases with the filling ratio. This increment of the thermal stratification produces a difference in temperatures between the interface and the liquid than is lower than the one at low heat fluxes. So, the condensation rate reduces and the pressure increases with the increment of the filling ratio. At low heat fluxes, the difference in temperature between the interface and the liquid is higher than the one at medium-high heat fluxes. Hence, the thermal stratification is weak and the condensation rate is higher than the one at high-medium heat fluxes. At low filling ratio, the ullage heat inputs are higher than the one at high liquid level. Hence, the evaporation rate is increased and the self-pressurisation rate increases with the reduction of the filling ratio.

The self-pressurisation directly influences the Holding-up time (HUT). Considering the behaviour of the self-pressurisation with the liquid level and heat inputs, it can be stated that:

a) High and low heat fluxes respectively produce short and long holding up time;
b) The increase of liquid level in the tank, extends the HUT at low heat fluxes;
c) At high heat fluxes, the increase of the filling ratio reduces the holding time;
d) The thermal stratification reduces the HUT;

So, to avoid venting, high liquid levels and low heat inputs are recommended.

4.7. Ageing

The ageing of cryogenic mixtures has been historically studied for Liquefied Natural Gas (LNG) in large scale storage containers, where the Boil-off Gas (BOG) is continuously removed. In these conditions, the storage container is almost at stationary state, and the evaporation is the main phenomenon affecting the evolution of the chemical composition in the liquid and in the ullage. Figure 14 describes the three main steps of the ageing of LNG. The yellow dashed line is the interface. The light and dark blue regions are respectively the vapour and the liquid. Yellow, green, orange and greys circles are respectively the nitrogen (N_2), the methane (CH_4), the ethane (C_2H_6) and the propane (C_3H_8).

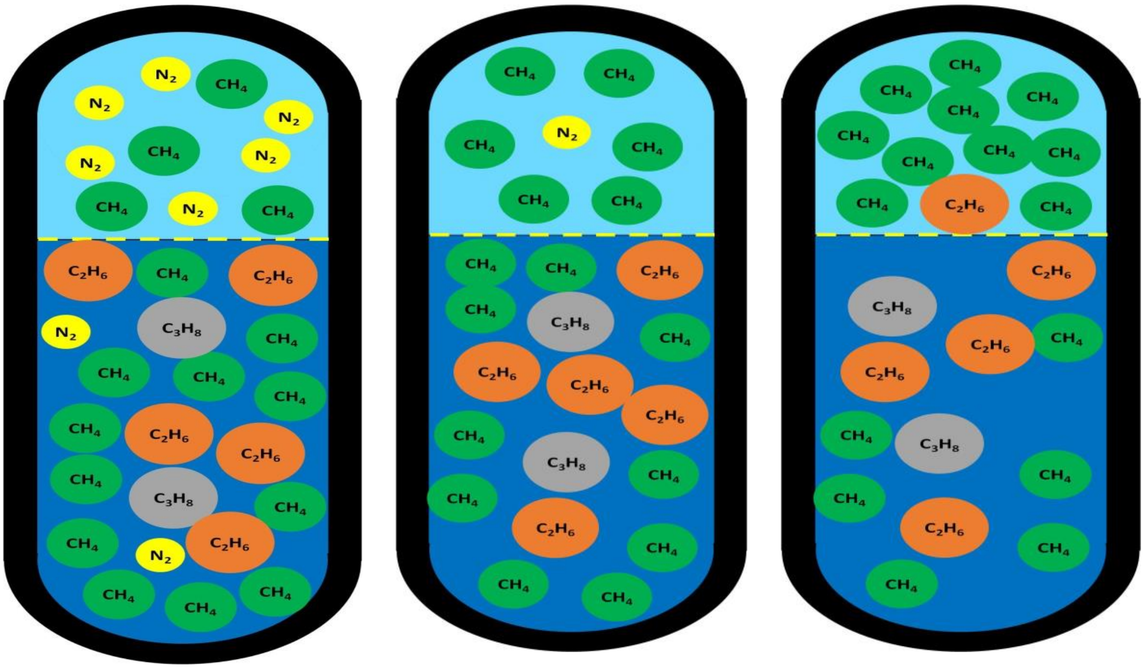

a) b) c)

Figure 14. Nitrogen evaporation (a), methane rich ullage (b) liquid density increment (c).

For LNG in large open storage containers, the ageing follows these steps:

a) *Nitrogen evaporation*. The nitrogen is the more volatile component in the mixture. Hence it is the first component to evaporate, thus its vapour concentration is very high, even for low content of nitrogen in the liquid. At the same time, methane occupies the remaining space in the ullage
b) *Methane rich ullage*. The ullage is almost pure methane with some traces of nitrogen and of heavy hydrocarbons such as ethane and propane;
c) *Liquid density increment*. The evaporation of methane increases the liquid concentrations of ethane and propane. The density and the gross heating value (GHV) increases and the methane number (MN) reduces.

In small scale closed storage containers, the ageing is not identical to large scale tanks, mainly because these units are often operated as closed systems. It should be noted that when small scale tanks are operated as an open system, the ageing phenomena is present and even more intense than in LS tanks, because the ratio of total heat ingress to liquid mass in the tank becomes much higher. Al Ghafri [3],[37] showed that the compositions of liquid and of vapour do not change in time, in a closed storage container of LNG-like mixture[18]. This is caused by the liquid thermal stratification which leads to a transfer of the heat from the interface to the liquid bulk. Hence, there is not enough heat at the interface to sustain the evaporation. At the same time, the condensation rate moves some of the evaporated mass back to the liquid.

Ageing can become a security issue, and it can limit the use of LNG as fuel. The ageing can cause rollover[19], when the nitrogen concentration is above 1%. This phenomenon can over-pressurize the storage container, leading to mechanical failures. Events of rollover in small scale tank are not found. The ageing changes the compositions, thus MN and GHV. So, these values can be out of the applicability range and LNG cannot be used as fuel.

---

[18] LNG-like mixture is a mixture of cryogenic liquids, composed by the main species of the LNG.

[19] Rollover is the rapid and large liquid evaporation that occurs after the density stratification. The latter is the formation of two or more zones at different density.

5. Analysis of scientific literature for modelling the storage of cryogenic liquids

A literature research is carried out to understand how the storage of cryogenic liquids has been historically modelled. A table-score method is developed to select the models that can better describe the phenomena that are involded in the storage of cryogenic liquids.

Section 5.1 presents the state of the art. Section 5.2 explains the score-table method used in this thesis. Section 5.3 describes the selected modelling work. Section 5.4 shows the conclusion.

5.1. State of the art

Many models have been developed for predicting the behaviour of cryogenic liquids in storage containers. These works can be grouped in function of the fluid studied, the size of the storage tanks, type of model used and the modelling approaches. Table 5 describes the different groups of the storage model and the modelling approach, and the main authors for each group.

Table 5. Storage and fundamental phenomena, and storage variables.

Subject	Type of model	Modelling approaches	Authors
LNG in LS tank	CFD	Fine discretisation of the whole storage containers	[1], [2]
	LP model with equilibrium-Evaporative rate approach	Liquid and vapour are at thermodynamic equilibrium. The heat inputs are empirically determined with the reference values of Boil-Off rate (BOR) of the tank.	[38]–[40]
	LP model with equilibrium-heat flow approach	Similar to the previous approach, but the heat inputs are calculated with a dedicated heat transfer model or by defining reasonable values.	[41]–[45]
	LP model with non-equilibrium and homogeneous approach	Liquid is at the bubble temperature and the vapour are overheated. Liquid and vapour are homogeneous.	[44], [46]–[49]
LNG in SS tank	CFD	Fine discretisation of the whole storage containers	[50], [51]
	LP model with non-equilibrium and homogeneous	Liquid is at the bubble temperature and the vapour are overheated. Liquid and vapour are homogenous.	[52]–[54]
LH_2 in SS tank	CFD	Fine discretisation of the whole storage containers	[55]–[60]
	LP model with Energy distribution function[20]	Liquid and vapour are homogenous. The vertical temperature profile is determined with energy distribution function. The stratified region is determined with the layer growth equations[21].	[61]–[68]
	LP model with non-equilibrium and homogeneous approach	The stratification region is not considered and, liquid and vapour are homogenous. Liquid is at saturation and the vapour is over-heated	[69], [70], [70]–[73]
	LP model with discretized	Liquid and vapour are discretized in sub-layers.	[1], [2], [74]–[76]
LN_2 in SS tank	LP model with non-equilibrium homogeneous	Liquid and vapour are homogeneous, but the vapour is overheated. The liquid is at saturation.	[3], [26], [34], [77], [78], [79]
	LP model - Discretized	Vapour and liquid are discretized in sub-layers.	[24], [80]

Computational Fluid-dynamics (CFD[22]) and Lumped Parameter (LP[23]) model with homogenous approach are the most common methods for modelling Liquefied Natural Gas (LNG). In these models,

---

[20] Energy distribution function is an empirical function that describes the accumulation of thermal energy in the stratified region of the liquid.

[21] Layer growth equation is a formula that computes the increment of the stratified region with free-convective correlations of mass flow rate in the boundary layer at side wall.

the liquid is often assumed at bubble point because they are applied for large scale (LS) storage containers. LP model is often used for modelling small scale (SS) storage container filled with liquid hydrogen (LH_2) and liquid nitrogen (LN_2), in particular with energy distribution approach and with the non-equilibrium homogeneous method. LP model with discretized approach is less developed than the other approaches.

Section 5.1.1 describes the models developed for LNG in LS storage containers. Section 5.1.1.5 presents the modelling approaches used for LNG in SS storage tanks. Section 5.1.2 explains the model for LH_2 is SS storage containers. Section 5.1.3 describes the modelling approaches for LN_2 in SS storage tanks. Section 5.1.4 presents the models of LN_2 used for modelling the LNG in SS storage containers.

5.1.1. Models developed for Liquefied Natural Gas in Large Scale storage tanks

As it is reported in Table 5, the behaviour of Liquefied Natural Gas (LNG) is in Large Scale (LS) storage tank is calculated with Computational Fluid Dynamics (CFD) models and with Lumped Parameter (LP) models with equilibrium-evaporative rate approach, equilibrium-heat flow approach and non-equilibrium and homogeneous approach.

Section 5.1.1.1 explains the modelling works with CFD. Section 5.1.1.2 presents the LP model with equilibrium-evaporative rate approach. Section 5.1.1.3 describes the modelling approach with equilibrium-heat flow approach. Section 5.1.1.4 explains the LP models with non-equilibrium and homogeneous approach.

5.1.1.1. Computational Fluid-Dynamics model

The Computational Fluid-Dynamics (CFD) works of Miana et al. [81] and of Saleem et al. [82] are found in the scientific literature of predicting the Liquefied Natural Gas (LNG) behaviour in Large Scale (LS) tanks.

Speaking about the CFD models, Miana et al. [81] studied the heat inputs though a storage tank of LNG carrier, called Mark III, using this type of model. They analyzed the temperature profiles across the insulation and they quantified the effect of the inclination of the some part of the side and the influence of the edge, to compute the overall heat transfer coefficient of the insulation barriers and the Boil-off Gas (BOG) production. The idea of simplifying the heat transfer process across the barrier with the overall heat transfer coefficient is a suitable approach for calculating the heat input rate. Using CFD for this estimation takes a lot of time and it is not flexible because a detailed study of the thermal distribution in the barrier should be done to estimate the overall heat transfer coefficient of each storage containers.

Saleem et al. [82] analysed the mechanism of liquid boiling in LS storage tank with LNG, by applying CFD. The convective flow of natural convection and the temperature distribution of both liquid and vapour were calculated by using this modelling approach. Saleem et al. [82] underlined that the uniformity of the liquid temperature is given by the circulation pattern that mixes LNG, but a thermal stratification in vapour is present. Large numerical grids are required for obtaining these results, resulting in a large computational time.

---

[22] CFD is the part of the fluid-dynamic science that numerically solves the problems of fluid motions.

[23] LP model is a numerical and analytical approach to solve spatially distributed physical system using discrete entities that are representative of the physical behaviour, under certain hypotheses.

5.1.1.2. Lumped Parameter model with equilibrium-evaporative rate approach

Dimopoulos et Frangopoulos [38], Wordu et Peterside [39] and Miana et al. [40] are the main references for Lumped Parameter (LP) model with equilibrium-evaporative approach.

Dimopoulos et Frangopoulos [38] modelled the evaporation of Liquefied Natural Gas (LNG) during ship transportation. The time-evolution of composition, which changes the thermodynamic properties during the storage, was considered in this model. The results of this model were not compared with the experimental data of behaviour of LNG. The short execution time and the ease of implementing this model are the main advantages of this model. This modelling approach can be only used for thermo-economic assessment because it does not describe the main phenomena of storage, except ageing, and it is not validated against experimental data.

Wordu et Peterside [39] estimated the Boil-off Gas (BOG) production from a LNG LS storage tank of liquefaction plants. The model can only be applied for thermo-economic assessment. It lacks of describing the storage phenomena and of comparing with experimental data.

Miana et al.[40] developed two type of models: a physical model (MOLAS) and an artificial intelligence model (i-model) with 10 neural networks. The first model is based on the mass and energy conservation equations of vapour and of liquid at equilibrium. It computes the ageing of LNG during ship transportation with fixed value of Boil-Off Rate (BOR), whose value was fixed at 0.15 %. Figure 15 describes the model proposed by Miana et al. [40] and its comparison with the experimental data of Kountz [83] (labelled with [2]) and with the results of the model of Aspelund et al. [84] (labelled with [3]).

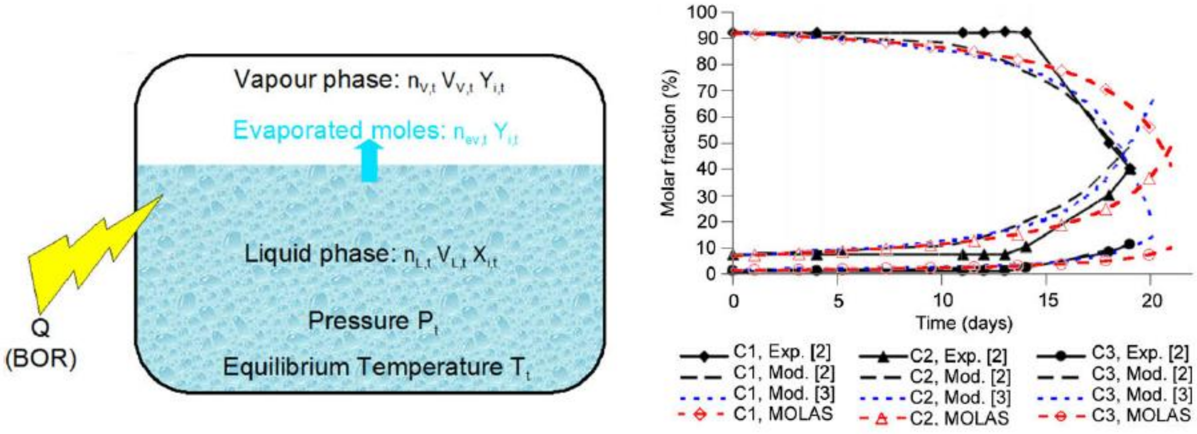

a) b)

Figure 15. (a) Concept of equilibrium model with evaporative rate approach (b) evolution of LNG molar fractions. Both pictures are taken from Miana et al. [40].

The physical model of Miana et al. [40] can predict the time-evolution of the concentration of methane (C1) in LNG, indicated as C1 in Figure 15 (b). This model fails in computing the time-evolution of ethane (C2) and propane (C3) after 12 days, as indicated by the different shapes of the calculated and measured curves of molar fraction in LNG. So, this model can be applied for computing the LNG composition at the discharging port, not for predicting the time-evolutions of the physical variables such as filling ratio, temperatures, pressure and compositions.

5.1.1.3. Lumped Parameter model with equilibrium-heat flow approach

Lumped Parameter (LP) model with equilibrium-heat flow approach were developed by Shah and Aarts [42], Migliore et al. [43], Cappello [44], Pellegrini et al. [45] and Miana et al. [41].

Shah and Aarts [42] studied the weathering (or ageing) of Liquefied Natural Gas (LNG) in storage containers of carrier and in “on-land” storage tanks. The heat leakage rate was calculated with a mathematical model that considered the environmental condition and the insulating barrier. This model was not validated against experimental data. Hence, the reliability of this model cannot be proved.

Migliore et al. [43] analyzed the weathering of LNG that is stored in “on-land” large scale (LS) storage containers. The heat input rate was calculated with a rigorous heat transfer model that is based on the main steps of the pathway of the heat input (see Section 4.1 of Chapter 1). The density of the LNG and the Vapour-Liquid-Equilibrium (VLE) at the interface was estimated with the Equation of State (EoS) of Peng-Robinson (PR) with Klosek Mc-Kinley method[24]. The proposed model was not validated against experimental data of LNG behaviour.

Cappello [44] studied the ageing of LNG in “on-land” LS storage container with the heat rate approach. The heat leakage was calculated considering the three main steps of the pathway of the heat input (see Section 4.1 of Chapter 1) and the thermodynamic properties were calculated with the PR-Eos. This model was compared with the values of LNG composition at the discharging port. Hence, the-evolution of the LNG composition was not proved.

Pellegrini et al. [45] analyzed the weathering of LNG in above-ground storage tanks, by using an equilibrium model with heat rate approach. The heat inputs were defined by the authors and they were fixed during the simulation of the LNG weathering. This model was compared with experimental data and with the equilibrium model with evaporative rate approach. Figure 16 describes the molar fraction of methane in the Boil-Off Gas (BOG) and in the liquid, computed with the evaporative and heat flow approach as function of the storage time. In Figure 16, circles are the experimental data of Kountz[83]. The dotted and the dashed lines individually refer to the evaporative and the heat flow approaches.

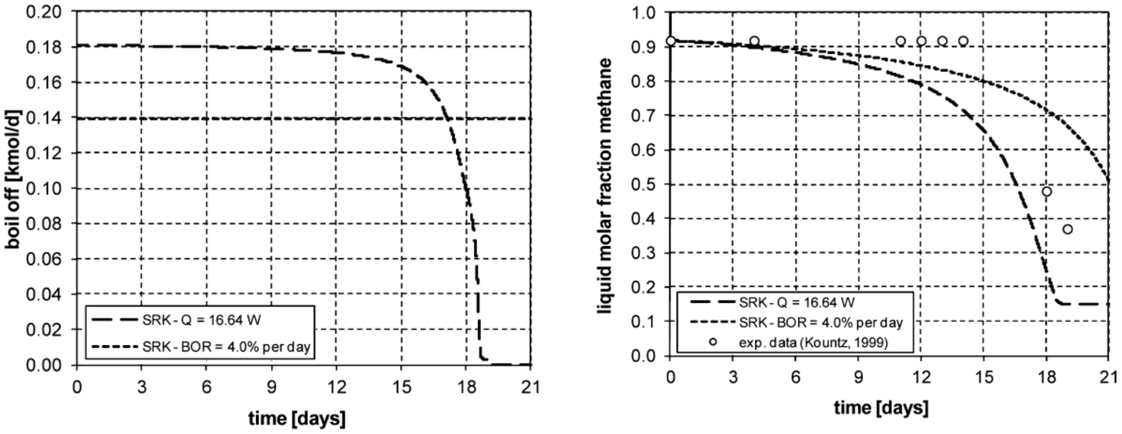

a) b)

Figure 16. (a) BOG and (b) liquid molar fraction for evaporative and heat flow approach as function of the storage time for a large scale tank filled with LNG. Both pictures are taken from Pellegrini et al.[45].

As described by Figure 16 (a), the BOG flow is always constant in the evaporative approach and the BOG flow computed with the heat flow approach decreases for long storage time. The liquid molar methane fraction in heat flow approach decreases faster in time than the values computed with the evaporative approach, as it is shown in Figure 16 (b). Both approaches fail in describing the time-evolution of the liquid composition after 12 days.

To predict the LNG ageing in marine transportation, Miana et al. [41] developed two equilibrium models: one with heat rate approach and one with the evaporative rate method. The heat input was

---

[24] The Klosek Mc-Kinley method computes the satureated density of LNG up to 115 K[85].

calculated with an energy balance, using some experimental data of LNG evaporation. The two models were compared with the experimental data of loading and of discharging at the ports, given by Shah and Aarts [42]. The two models are not suitable for short voyage, due to the non-equilibrium conditions formed during the initial period of the voyage. Both models cannot be considered validated because the results were not compared with the time-evolution of the LNG behaviour.

5.1.1.4. Lumped Parameter model with non-equilibrium and homogeneous approach

Lumped Parameter (LP) models with non-equilibrium and homogenous approach were developed by Cappello [44], Krikkis [47], Qu et al. [49], Huerta and Vesovic [48], and Migliore et al. [46].

Cappello [44] analyzed the ageing of Liquefied Natural Gas (LNG) in “on-land” large scale (LS) storage container with non-equilibrium and homogenous approach, considering the heat transfer with the environment and the vapour-to-liquid heat transfer. The heat input rate was calculated considering the three main steps of the pathway of the heat input (see Section 4.1). The vapour-to-liquid heat transfer is computed with a conductive model and vapour average temperature is computed with 1 dimension (1D) Fourier’s law. The interfacial heat transfer model does not consider the convection, lacking of being rigorous. The proposed model was not validated with experimental resutls. Hence, the reliability of the model cannot be proved.

Krikkis [47] studied the ageing of LNG in storage container of carrier, with a non-equilibrium and homogenous approach. The heat transfer with the environment was calculated with the approach of Migliore et al. [43]. The vapour-to-liquid was computed with the approach of Heestand et al. [86][25], by fixing the value of 95 % of the ratio between the vapour-to-liquid heat flow and the environmental-to-vapour heat flow. The model was compared with the experimental data of LNG behaviour recorded during the voyage, as reported in Figure 17. In Figure 17, CT1, CT2, CT3 and CT4 are the temperature thermocouples.

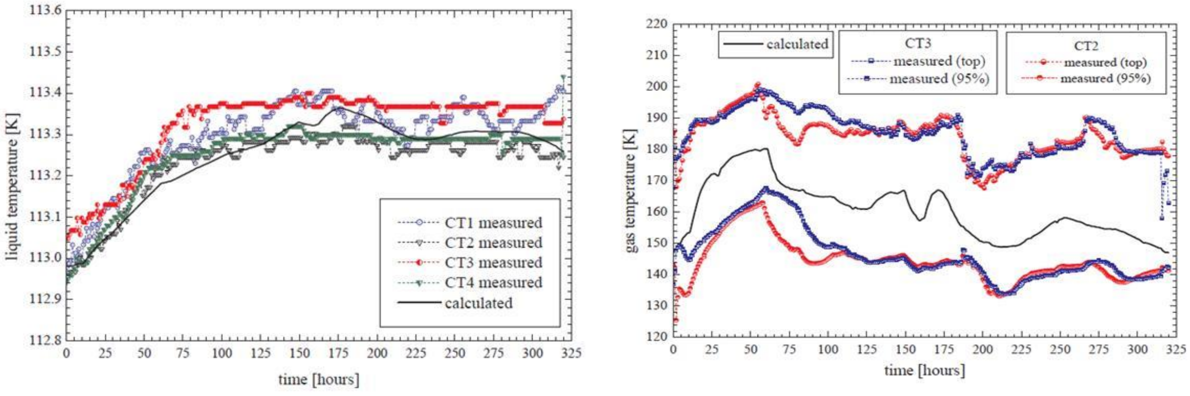

a) b)

Figure 17. (a) time-evolution of the liquid temperature and (b) vapour temperature against the experimental data. This images are taken from Krikkis [47].

As it is shown in Figure 17, the model predicts well the liquid temperature and the computed average temperature qualitatively behaves as the experimental one. Hence, LP model with non-equilibrium and homogeneous approach can predict the behaviour of LNG in large scale storage tanks. The approach of Heestand et al. [86] for the vapour-to-interface heat transfer cannot predict this heat flow from the physical phenomena. Hence, the ratio must be defined for each simulation, thus storage containers.

---

[25] Heestand et al.[86] computed the vapour-to-liquid heat flow as product between a constant and the environment-to-ullage heat flow. This approach was used for modelling the rollover of La Spezia.

Qu et al. [49] calculated the Boil-off Gas (BOG) production from storage containers of LNG carrier by considering the heat transfer with the environment, the vapour-to-liquid heat transfer and the sloshing. The heat transfer with the environment considers the weather condition, the insulating barrier, the ballast and the natural convection of both liquid and vapour inside the tank. The vapour-to-interface heat flow is calculated with a conductive model, as function of the LNG thermal layer. The condensation due to sloshing is modelled and the BOG production is computed with the Hertz-Knudsen formula[26]. The model was compared with the experimental data of LNG behaviour measured during the voyage of an LNG carrier, as reported in Figure 18. As it is indicated in Figure 18, the model predicts well the LNG temperature, the Natural Gas (NG) temperature and the pressure. Hence, this type of model can predict the behaviour of LNG. The value of LNG thermal layer was not reported in the paper, suggesting that this value could be computed by fitting the experimental data.

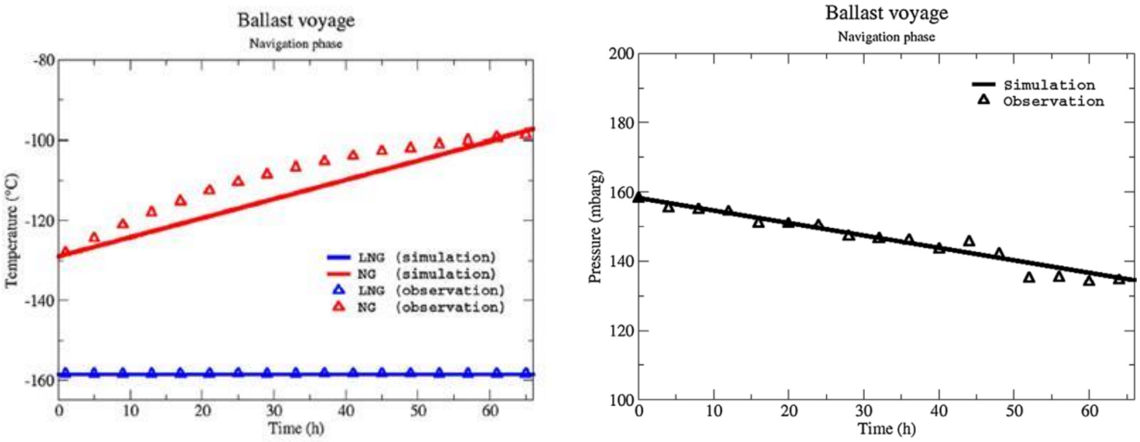

a) b)

Figure 18. (a) time-evolution of the liquid and vapour temperature and (b) pressure against the experimental data. this images are taken from Qu et al.[49].

Huerta and Vesovic [48] studied the weathering of LNG in LS storage tanks, by using a non-equilibrium and homogeneous approach. The thermodynamic properties and the Vapour-Liquid Equilibrium (VLE) were computed with the equation of state (EoS) of Peng-Robinson (PR), except for the liquid density, which is calcualted with the Enhanced Revised Klosek Mc-Kinley method[27]. The heat flow between the environments and the internal fluid (vapour and liquid) was calculated using the overall heat transfer coefficient. This coefficient was calculated considering the steps of the pathway of heat transfer (see Section 4.1 of Chapter 1). The vapour-to-liquid heat flow was calculated with the conductive law, using the temperature profile in the vapour. This temperature profile was calculated with the unsteady 1 dimensional (1D) advection-conduction equation. The results of this model were not compared with the experimental data. Hence, the reliability and the efficiency of predicting the behaviour of LNG cannot be proved.

Migliore et al. [46] studied the LNG weathering in LS storage container, using a non-equilibrium and homogeneous approach. The thermodynamics was modelled with the PR-EoS Klosek Mc-Kinley method[24] and the heat transfer between the environment and the liquid and vapour was computed with the overall heat transfer coefficients for the wet and dry surface. These coefficients were calculated by considering the convection of the air outside the tank, the conduction through the insulating barrier and the convection of liquid and vapour inside the tank. The vapour-to-liquid heat flow was computed

---

[26] Hertz-Knudsen formula is an equation to compute the mass transfer at liquid-vapour interface. This equation is deduced from the kinetic theory.

[27] Enhanced Revised Klosek Mc-Kinley method is quite similar to Klosek Mc-Kinley method and it the computes the saturated density of LNG for temperatures between the 115 and 135 K at pressures up to 10 MPa.

with the conductive and the convective model. In the conductive model, this heat flow was computed with the 1 dimension (1D) heat equation. In the convection model, the heat flow between the vapour and the liquid was computed with horizontal warm surface facing downward model of Kozanoglu and Rubio [87][28]. The results of this model were not compared with the experimental data. Hence, the reliability and the efficiency of predicting the behaviour of LNG cannot be proved.

5.1.1.5. Models developed for Liquefied Natural Gas in Small Scale storage tanks

The behaviour of Liquefied Natural Gas (LNG) in Small scale (SS) storage containers was studied with Computational Fluid-dynamics (CFD) and Lumped Parameter (LP) model with analytical and discretized approach. CFD were applied by Ovidi et al. [50] and Roh et al. [51]. Analytical approach was used by Chen et al. [52], and the non-equilibrium and homogeneous method was applied by Scarponi et al. [53].

Ovidi et al. [50] studied the behaviour of LNG, in particular the self-pressurisation, in a SS storage container of truck refuelling station under standard operating conditions and during upsets such as the case of damaged insulation. The temperature profile and the pressure rise were computed by using CFD, neglecting the interfacial mass and heat transfer. The self-pressurisation with damaged insulation increases faster than the one with intact insulation. The model was not compared with experimental data. Hence, it cannot be proved if this behaviour of the pressure is true or false.

Roh et al. [51] analyzed the transient of the free-convection in LNG that is contained in a SS storage tank, when the storage container is closed. The CFD model computed the thermal distribution and the fluid-motions in the liquid at constant pressure and during the pressurisation. The vapour phase was not described and the mass-heat transfers at interface are neglected. The results of the fluid-motion were not compared with the experimental data.

Chen et al.[52] studied the temperature and the pressure change in a SS storage tank filled with LNG in a fuelling station. The proposed model with analytical model considered the heat inputs form the equipment and the environment. The model can be only used for economical evaluation because the main phenomena occurign during the storage (see Section 4 of Chapter 1) are not considered.

Scarponi et al. [53] studied the thermal and the mechanical response of LNG in a SS storage tank, exposed to fire. The model considered the environment-to-internal fluid (liquid and vapour) and the vapour-to-liquid heat transfers. The environment-to-internal fluid heat flow was calculated (i) with convective heat transfer coefficients and (ii) by solving the energy balance equations at the walls of the storage container. The vapour-to-liquid heat flow was computed with the convective heat transfer coefficient of horizontal warm surface facing downward. The mass transfer at the interface was computed with the Hertz-Knudsen equation. The model predicted a fast increment of pressure when the storage container is exposed to fire, due to the increment of the internal temperature. The results of the model were not compared with experimental data and the reliability of the model could not be proved.

---

[28] The model of Kozanoglu and Rubio[87] computes the heat transfer coefficient of free-convection over an horizontal warm surface facing downward. The equation that compute this coefficient is obtained by fitting experimental data and it considers the thickness of the boundary layer as the characteristic length of heat transfer instead of using the length of the surface.

5.1.2. Models developed for Liquid Hydrogen in Small Scale storage tanks

The behaviour of liquid hydrogen (LH_2) in small scale (SS) storage containers has been studied with Computational Fluid-dynamics (CFD) and Lumped Parameter (LP) models. LP models can be divided into three main categories, according to the hypothesis on the liquid temperature gradient. These categories are energy distribution function approach, homogeneous approach and discretized approach.

Section 5.1.2.1 presents the CFD model. Sections 5.1.2.2, 5.1.2.3 and 5.1.2.4 explain the LP model with distribution function approach, homogeneous approach and discretized approach, respectively.

5.1.2.1. Computational Fluid-dynamics

Computational Fluid-dynamics (CFD) were used by Lin and Hasan [55], Hardy and Tomsik [56], Kassemi and Kartuzova [57], Grayson and Navickas [58], Kassemi et al. [59], Wang et al. [60], Stewart [66], Kumar et al. [68] and Stewart and Moder [67] for predicting the thermal stratification, self-pressurisation and fluid-motions neat the interface in Small scale (SS) storage tanks of Liquid Hydrogen (LH_2) .

Lin and Hasan [55] studied the flow patterns and the thermal stratification of LH_2 at constant temperature and at different rate of heat heating at the side. The conservation laws were solved with the finite-difference method in liquid and in vapour. The mass and heat transfer at the interface were neglected, decoupling the solution of vapour balance equations from the liquid ones. The maximum values of the temperature of the liquid were computed near the interface and the fluid pattern mainly contains a counter-clockwise vortex, which carries overheated liquid to the interface. The results were not compared with experimental data and this fluid-motion cannot be proved.

Hardy and Tomsik [56] used a commercial finite-difference fluid flow model (FLOW 3D) to predict the ullage gas thermal stratification in tank propellant for National Aero-Space Plane (NASP) vehicle at different values of gravity force and initial storage conditions. The temperature distribution and the amplitude of the final temperatures were respectively impacted by the initial tank pressure and initial temperature. These results were compared with the observations obtained of LH_2 behaviour. Tighter convergence criteria and smaller mesh sizes are required to assure computational stability, increasing the computational time.

Kassemi and Kartuzova [57] studied the effect of interfacial turbulence and accommodation coefficients on CFD predictions of pressurisation and pressure control in cryogenic storage tanks. The numerical prediction of CFD used the energy balance, the equality of the tangential component of the interfacial shear stress and tangential velocity to define the boundary condition at interface. The heat fluxes on the liquid and vapour side of the interface are computed with conductive model. The conductive model uses the effective thermal conductivity. Two approaches were applied at the interface: the saturation temperature and the Schrage kinetic relationship methods. The first approach assumed that the interface is at saturation and the energy balance equation at interface compute the interfacial mass transfer rate. The second approach uses the Schrage kinetic formula[29] to determine the interfacial mass transfer rate. In this approach, the interface temperature is computed with the energy balance. The heat transfer at the interface was modelled with an effective thermal conductivity, which is deduced from the natural convection in enclosure[83],[84]. The developed model was compared with experimental values of LH_2 self-pressurisation and thermal distribution in large tanks. The mass

---

[29] The Schrage kinetic formula computes the mass transfer at the interface with the kinetic theory, similarly as the formula of Hertz-Knudsen.

transfer kinetics may not be well described when the interface is largely at non-equilibrium and the interface is disturbed.

Grayson and Navickas [58] studied the interaction between the fluid-dynamic and the thermodynamic phenomena in the ullage of cryogenic tank, using FLOW 3D finite-difference program. The conservation laws of mass, momentum and energy were solved with the finite difference method. The temperature distribution of LH_2 can be disturbed by sloshing and by draining, causing the early ingestion of warm propellant. These results were not compared with experimental data.

Kassemi et al. [59] studied the self-pressurisation of LH_2, using CFD models for liquid and vapour and with Schrage equation. The model was compared with experimental data. The models cannot capture the turbulence in ullage and across the liquid-vapour interface. This fail occurs because the Schrage equation can only be applied to flat interface near equilibrium conditions with equivalent evaporation and condensation coefficient. These conditions do not exist in settled and unsettled configurations of the tank.

Wang et al. [60] studied the effect of the non-condensable helium in different pressurization situations of LH_2 tank, by using CFD model with Schrage equation together with Dalton's partial pressure model[30]. So, the influence of multi-component diffusion on phase change rate can be described, showing that the mass transfer of each species across interface influence the pressure and this influence increases as time passes. The model was not compared with experimental data.

Stewart [66] analysed the pressurisation of a flight-weight tank filled with liquid hydrogen by simulating both evaporation/condensation at liquid-vapour interface. The temperature at the interface, which defines the upper boundary of the liquid, is computed with the energy conservation law and the interfacial mass flows are calculated by the Hertz-Knudsen-Schrage[29] equation with unity accommodation coefficients. This concept of the numerical method for computing interface mass transfer can be applied to cryogenic storage container, as concluded by the author [66]. The results of the pressure is compared with the experimental data of forced pressurization with GH_2, followed by drainage.

Stewart and Moder [67] continued the previous study on pressurisation by comparing the CFD model with experimental data. Figure 19 (a) illustrates the natural convection at both liquid and vapour side wall and the conduction at the liquid-vapour interface. The orange and the white arrows in Figure 19 (a) respectively indicate the heat flow and the fluid motions. The model allowed obtaining good predictions of the heat flow and of the sensitivity of the initial pressure rise to the initial temperature profile. Surface tension, representation of saturation pressure and repair of mass loss in the simulation are the main challenges that limit the application of this model.

---

[30] In a gas mixture, Dalton's partial pressure model computes the partial pressure of the species "i" as the product between the molar fraction of the specie "i" and the overall pressure.

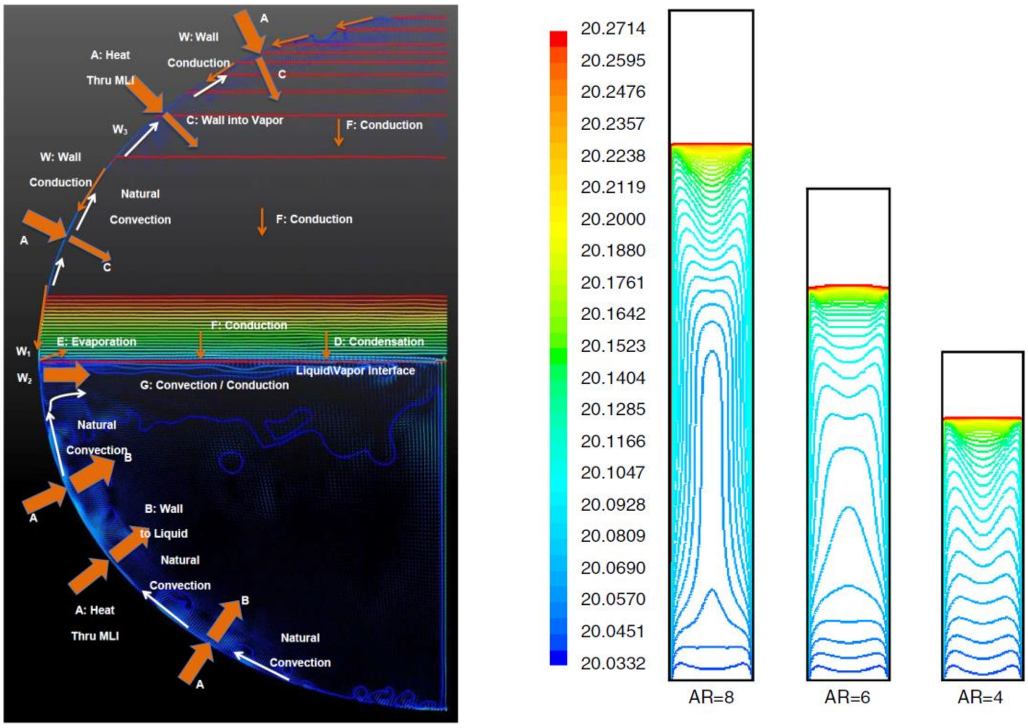

a) b)

Figure 19. (a) Heat flow and fluid motion in LH$_2$ tank [67]. (b) Temperature contours in the liquid zone [68].

Kumar et al. [68] studied the influence of surface evaporation on the thermal stratification in liquid hydrogen tanks having different value of the aspect ratio, which is the ratio between the height and the diameter of the storage container. Figure 19 (b) shows the thermal stratification obtained by Kumar et al. [68]. The contours are described with different colours from blue to red. Blue and red are respectively for low and high liquid temperature. As indicated by Figure 19 (b), the warm liquid is located at the interface due to the thermal stratification. Thermal stratification during the pre-evaporation and evaporation phases varies with the aspect ratio of the tank, defined as the height divided by the diameter. The thermal stratification seems enhanced by large aspect ratios, but the difference in this phenomenon is low for the different aspect ratios when surface evaporation takes place. These results were not compared with experimental data.

5.1.2.2. Lumped Parameter model with energy distribution function

Ruder [61], Barnett et al. [62], Gursu et al. [63], [64] and, Arnett and Voth [65] used Lumped Parameter (LP) model with energy distribution approach for modelling the behaviour of liquid hydrogen in (LH$_2$) in small scale (SS) storage tanks.

Ruder [61] modelled the stratification of the liquid in a pressurized container with side wall heating. He used straight-forward empirical approach based on liquid nitrogen data. He proved a good agreement with liquid hydrogen experimental data of thermal stratification. This model does not predict the behaviour of the vapour in the ullage and the bottom heating. The behaviour of the vapour and the bottom heating affect the behaviour of the liquid stored in small scale tanks.

Barnett et al. [62] investigated the thermal stratification of liquid hydrogen in a large cylindrical tank tank of the different configurations of the Saturn launch vehicle. In these configurations, the bottom of LH$_2$ tank is shared with the bulkhead of liquid oxygen containers. Figure 20 shows the conceptual drawing of the energy distribution function approach of Barnett et al. [62] and the comparison with the measured data of temperature profile of liquid hydrogen. In Figure 20 (a), the liquid phase is divided into boundary layer, stratified and bulk liquid. The heat fluxes come from the side and from the bottom.

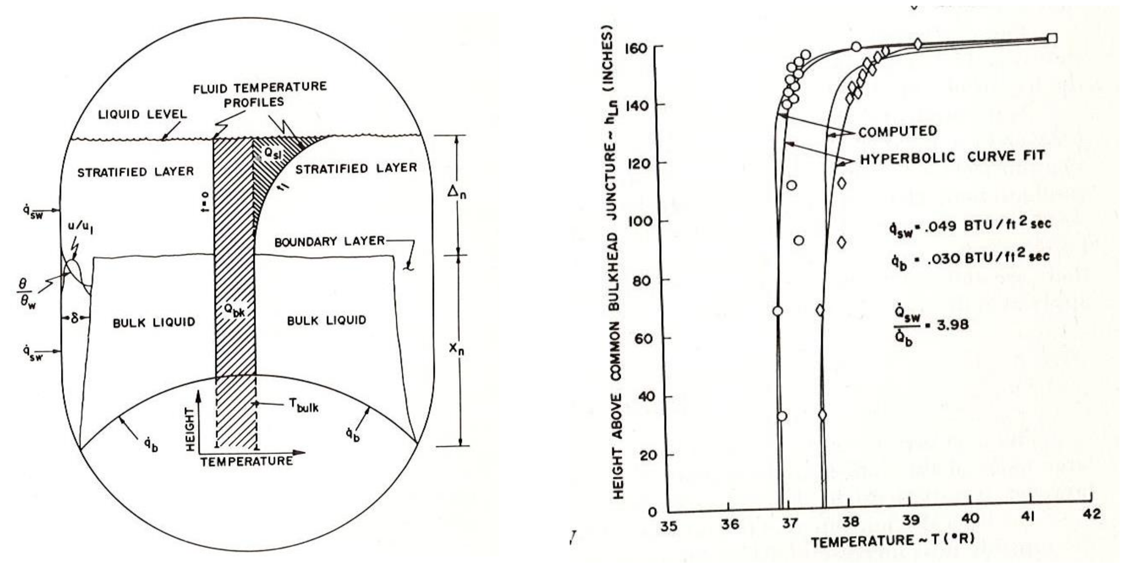

a) b)

Figure 20. (a) the analytical model of Barnett et al. [62] (b) the comparison with the experimental data temperature profile [62].

Barnett et al. [62] used a hyperbolic temperature profile to fit the energy distribution function with experimental thermal distribution in the liquid. The fraction of energy absorbed respect to the liquid heat inputs is experimentally determined with this energy distribution function. The stratified region (see Figure 20 (a)) is described with the overall mass and energy balance equation, as if it was homogeneous. Barnett et al. [62] combined the mass and energy conservation laws at the stratified region. The mass flow in the boundary layer of the bulk liquid was estimated with the fluid-dynamic model of free-convection in homogenous medium. They reported that significant thermal stratification exist in large tanks and that the liquid-to-vapour mass transfer decreases as the pressure increases in the storage container [62]. The model developed does not predict the behaviour of the vapour phase and it can be rarely applied to other system due to the fitting of the energy distribution function with the experimental data.

Gursu et al. [63], [64] analyzed the thermal stratification and the effect of the self-pressurisation in liquid hydrogen storage systems. They found that an increment in thickness of liquid stratified layer follows the pressurisation rate [63]. The latter is increased by the liquid level because the heat inputs increases with the filling ratio. They [64] concluded that the thermal stratification is one of the primary factors of pressure rise because the warm liquid at interface reduces the liquid-interface heat transfer. The proposed model does not match the experimental data.

Arnett and Voth [65] presented a computer program for computing the thermal stratification and the self-pressurisation in liquid hydrogen tanks. The classical approach for the solution of the turbulent boundary layer equations was used. The vertical distribution energy of the stratification region was described by an exponential function with parameters regressed on experimental data. The pressurisation rate is determined with the evaporative rate. The latter is computed considering that the energy of the stratified layer is partially converted into the phase change. Arnett and Voth [65] compared their model against experimental data and they obtained a good match, except for the ullage temperatures. The main drawback is the description of the vapour phase because the pressure of the ullage is the saturation pressure at the liquid temperature. Experimental evidences (see Section 4.5 of Chapter 1) indicate that the vapour is overheated and it cannot be at saturation.

5.1.2.3. Lumped Parameter model with non-equilibrium and homogeneous approach

Estey et al. [69], Osipov et al. [70], Osipov and Muratov [23], Petitpas [73], Liu and Li [71], and Al Ghafri et al. [72] used Lumped Parameter (LP) model with non-equilibrium and homogeneous approach to predict the behaviour of liquid hydrogen (LH_2) in small scale (SS) storage containers.

Estey et al. [69] predicted the evolution of the pressure in propellant tank with the scope of avoiding cavitations. Estey et al. [69] considered four control volumes: the ullage, the infinitesimal vapour-liquid interface, the liquid and the tank wall. The liquid and the vapour are treated as homogenous and isothermal. The heat is transferred by natural convection for upper surface of heated plate between the vapour and the interface. The model of film-wise condensation in the horizontal tubes determines the heat transfer coefficient between the liquid and the interface. The external heat flux was set to zero and the pressurisation was obtained by injecting helium. Estey et al. [69] concluded that the system of ordinal differential equations is applicable to any tank operating in blowdown mode and it lends itself to quick and efficient computer calculations. A comparison with experimental data is missing.

Osipov et al. [70] developed a dynamic model for loading rocket with liquid hydrogen as propellant. They used the work of Estey et al. [69] as base for developing this model. Figure 21 shows the control volumes and flows of the homogenous approach of Osipov et al. [70] and the heat transfer mechanisms at the interface.

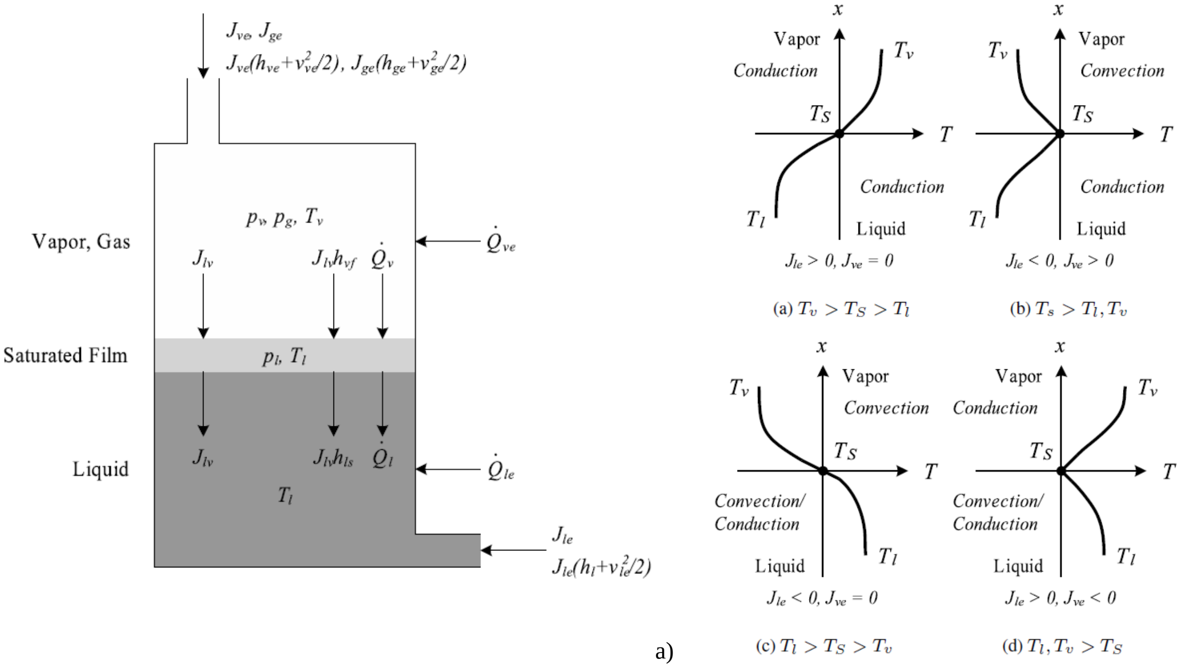

Figure 21. (a) control volumes and flows of homogenous approach [70]; (b) the heat transfer mechanism at interface.

This image describes very well this type of approach. The storage container can be divided into vapour, liquid, both homogenous, and into a saturated film at the interface, as indicated in Figure 21 (a). The vapour and the liquid are at non-equilibrium conditions and condensation/evaporation occurs at interface. Osipov et al. [70] considered the convective and conductive energy exchange. At this film, the heat is transferred with different mechanisms such as conduction and convection. The mechanism of heat transfer was chosen as function of the thermal gradients adjacent to the interface, as reported in Figure 21 (b). Even if the temperature of the interface coincides with the saturation temperature at the ullage pressure, this temperature differs from that of both liquid and vapour due to the non-equilibrium conditions. The heat transfer process directly impacts both evaporation and condensation. The evaporation is accompanied by heat removal and the condensation results in heating the interface. They used basic conservation laws and they applied the Hertz-Knudsen[26] equation for computing the condensation-evaporation mass fluxes. This model assumes that the gas is ideal and it predicts the evaporation and the condensation flow rate with the kinetic gas theory. Osipov et al. [70] simulated and compared the results of loading of LH_2 from the storage tank to the external tank, as reported in Figure 21 (a). The heat inputs were computed by defining a value of the heat transfer coefficient between the air and the liquid hydrogen in the external tank. The wall temperature is uniform and the value of this variable is the same in liquid and in vapour. The wall temperature is computed with the energy balance equation. They concluded that the low dimensional model was in good agreement with Space Shuttle refuelling data. This model does not consider the thermal stratification in liquid and in vapour. Liquid thermal stratification sternly affects the behaviour of cryogenic liquids for medium-high heat fluxes (see Section 4.6 of Chapter 1). Hence, the model is not suitable for medium-high heat fluxes at the walls of the storage container.

Osipov and Muratov [23] used an homogeneous model to study dynamic condensation blocking in cryogenic refuelling (see Section 4.3.2 of Chapter 1). This phenomenon is the reduction of the condensation rate due to the natural heating of the interface. They demonstrated that this phenomenon must be taken into account for the design of new generation spacecrafts. This model has several drawbacks. Firstly, it is not validated with experimental data. Second, the pressure coincides with the saturation pressure at interface. Finally, the behaviour of the vapour phase is neglected. The behaviour of the ullage strongly affects the time-evolution of pressure and of temperature in the liquid, especially at low filling ratio (see Section 4.4.4 and Section 4.6 of Chapter 1).

Liu and Li [71] investigated the pressurisation and the thermal stratification of LH_2 with the main assumption that the wall temperature is constant. The vapour-interface and the liquid-interface heat transfers were computed with the free-convective formulas of heat transfer for horizontal flat surfaces. The total phase change is computed with the energy balance equation at interface. They simulated a liquid hydrogen tank at different liquid level and gravity level. Liu and Li[71] concluded that the stratification is increased by the gravity level. The comparison with experimental data was not done and the physics of the phenomena occurring in the ullage were not deeply modelled and investigated.

Petitpas [73] focused on boil-off losses along LH_2 pathway. He quantified these losses with a model developed by Osipov et al. [70]. Petitpas [73] modified it with the equation of state implemented in the software REFPROP[8] to account for real gas behaviour. The energy equation is based on the variation of internal energies, and not on the temperatures. The bulk liquid temperature is fixed. The values of heat inputs were calibrated by comparing the measured and the simulated values of boil-off. The values of BOG were obtained from the measured values of liquid level of LH_2, recorded in winter, summer and in fall. Petitpas [73] predicted linear variations of liquid volume at heat inputs rate ranging from 30 to 70 W. He estimated the heat fluxes, whose value is between 1.0 W/m^2 and 2.5 W/m^2. Petitpas [73] used these values for his speculation on LH_2 behaviour. The model was not validated because the experimental data such as temperature variations, pressure and flow rates were not readily available. Petitpas[73] concluded that CFD analysis and experimental measurements should be carried out for validation of the model. The core of this model, which was developed by Osipov et al. [70], was validated against experimental data.

Al Ghafri et al. [72] tested the BoilFAST model with liquid hydrogen data of self-pressurisation from NASA's Kennedy Space Centre [27], [73], [90]. BoilFAST is the commercial name of a non-equilibrium model with vapour-liquid heat transfer. This model were developed by Perez et al. [26] and vapour-liquid heat transfer is defined as done for liquid nitrogen. Vapour-liquid heat transfer coefficient was empirically determined by fitting the experimental data of vapour temperature of LH_2.

Al Ghafri et al. [72] reported that this model exhibits excellent agreement with experimental and industrial data. The main drawback of this model is the fitting of heat transfer coefficients at interface with experimental data. So, the model cannot be used for other storage container and the use of the fitting indicates that the phenomena of mass-heat transfer at interface are not successfully described.

5.1.2.4. Lumped Parameter model with discretized approach

Schimdt et al. [74], Robbins and Robers [75], Epstein et al. [76], Vliet et al. [1] and Daigle et al. [2] havestudied the behaviour of liquid hydrogen (LH_2) in small scale (SS) storage tanks with Lumped Parameter (LP) model with discretized approach.

Schimdt et al. [74] experimentally studied the pressurisation and the stratification of liquid hydrogen in a 625 gallons Dewar at different pressurisation levels and filling ratios. The pressurisation levels were adjusted by changing the pressurisation gas consumption. They considered the liquid as a semi-infinite solid where the liquid-vapour interface is a constant temperature bounding face. The liquid thermal stratification was modelled with a partial-differential equation of Fourier. They reported that this approach is not suitable for higher heat flux due to the agitation of the liquid. The partial-differential equation of Fourier for semi-infinite solid was good to predict the liquid stratification. Schimdt et al. [74] concluded that the increment of the ullage pressure increases the heat transfer from the interface to the liquid stratified region.

Robbins and Robers [75] predicted the thermal stratification in liquid hydrogen in a vertical cylinder. They used an analytical model based on turbulent free-convective boundary layer. They assumed that the thermal strata and the free-convection boundary layer contain all the energy entering the fluid. The temperature outside these confines is uniform. To apply the boundary layer equations to non-uniform temperature fluid medium, Robbins and Robers [75] used the finite-difference technique. The model was compared with experimental data and the accuracy reported was reasonable. They underlined that modifications should be required to account the separation of the boundary layer, mass-energy exchange across liquid-vapour interface, and the interaction between the bottoms of the stratified region with the remaining liquid. The model does not consider the mass-energy heat transfer at interface and the bottom heating, which affect the storage of cryogenic liquid in small scale storage tank (see Section 4.4.3 and Section 4.4.4 of Chapter 1).

Epstein et al. [76] analyzed the tank pressurisation with a mathematical model that describes both liquid and vapour with space-variable heat transfer coefficients. The heat transferred across the sub-layers in liquid and in vapour was determined with effective thermal conductivity coefficients. The variation of the temperature and of the mass in heat sub-layer was calculated with the conservation laws. These equations account for the variation in time, the heat coming from the wall and the enthalpy fluxes due to the fluid motions. They reported that the calculations were in good agreement with the experimental data. The formulas of space-variable heat transfer coefficients were not deduced in the paper and it is reasonable to think that they were created to reproduce the experimental behaviour.

Vliet et al. [1] developed a stratified layer model for temperature stratification in liquids contained in heated vessels. Figure 22 shows the stratified layer model and its comparison with the experimental data of thermal distribution of liquid hydrogen.

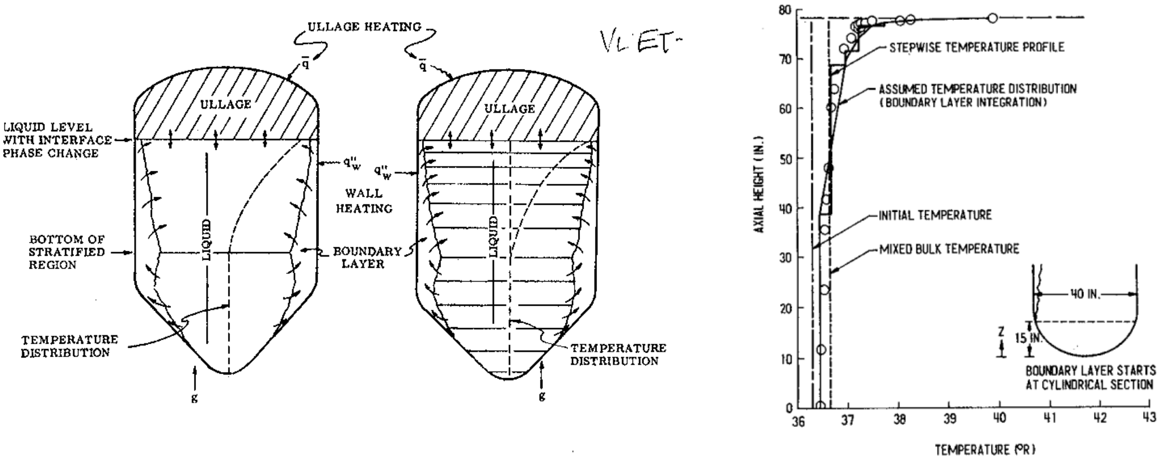

a) b)

Figure 22. (a) Model proposed by Vliet et al.[1]; (b) comparison with experimental data of liquid hydrogen[1].

The liquid volume was discretized in sub-layers (or sub-stratum). Each sub-stratum was decomposed into the bulk and into the boundary layer. The authors applied the energy and the momentum balance equations at the boundary of each sub-layer to compute the velocity and thermal boundary layer thickness. These conservations laws consider the contribution of the temperature gradient in the bulk. Vliet et al. [1] analytically solved these equations for different geometries of the side wall and for two types of temperature profiles. Firstly, the temperature was considered as uniform; then, it was assumed that the temperature is a power-law function of the vertical coordinate. Vliet et al. [1] considered four convection flow regimes: conduction, viscous flow, laminar and turbulent. They concluded that this approach and flow model gave good agreement with thermal profile of liquid hydrogen. Vliet et al. [1] underlined that further studies of natural convection on vertical and inclined surfaces are required. The vapour phase is described with the non-equilibrium and homogeneous approach. Considering that the ullage is stratified, this approach is the main drawback of the model of Vliet et al. [1].

Daigle et al. [2] modelled the temperature stratification in a cryogenic fuel tank and their modelling approach is similar to method of Vliet et al. [1]. Daigle et al. [2], however, discretized the liquid and the vapour in sub-layers and each sub-layer is composed by the bulk and the boundary. Figure 23 describes the control volumes of the vapour with the energy and mass flows, with a side and top views.

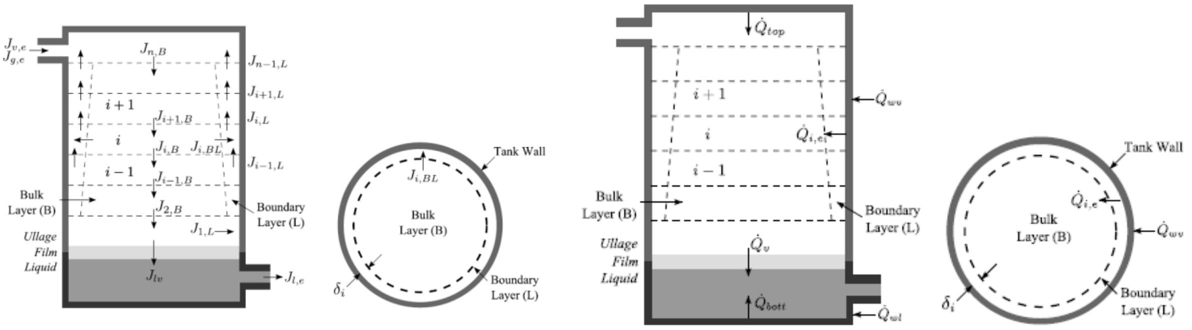

a) b)

Figure 23. Side and top view of control volume, mass flow (a) and energy flow (b) of the lumped model proposed by Daigle et al. [2]. This image refers to the vapour; the approach described is applied to the liquid too.

The general approach of modern lumped parameter models is described by Figure 23. As it is described in Figure 23, the whole vapour is divided into sub-layers of equal size and the boundary layer at the side wall is considered. At the bulk and at the boundary layer side wall, the conservation laws of mass and of energy are applied. The fluid-dynamic model computes the rising flows rate and the thickness at the boundary of each sub-layer. The heat inputs are determined at each sub-layer as function of the difference in temperature between the wall and the bulk. The flow model is based on the natural convection of homogeneous medium along a vertical wall, which is reported in Section 4.2.1. They did not considered the bulk temperature gradient in the conservation laws of energy and of momentum in the boundary layer. Daigle et al.[2] obtained a system of ordinary differential equations. This system was obtained by combining the basic conservation laws of each sub-layer. The liquid-interface and vapour-interface heat transfers are determined as the maximum value of conductive and of convective heat flux. The conductive flux is computed as done by Osipov et al.[70]. The natural convection formulas are used to compute the heat transfer coefficients at the side walls in liquid and in vapour. Since the heat fluxes are defined by the authors, the wall temperatures are determined with these coefficients. The convective flux is determined with formulas of natural convection over horizontal flat surface. They reported that this set of equations were capable of describing the temperature stratification. They underlined that these phenomenon is driven by natural convection and the condensation-evaporation phenomena at interface. The proposed model was not validated with experimental data. The boundary layer model does not consider the temperature gradient in the bulk and this neglect is the main drawback of this model.

5.1.3. Models developed for liquid nitrogen in small scale tanks

In the last decades, several experimental[24], [26], [91], [92] and numerical studies[24], [26], [34], [77], [80] of self-pressurisation and of thermal stratification were carried to understand the storage behaviour of liquefied natural gas (LNG). The use of liquid nitrogen (LN_2) instead of LNG or of liquid hydrogen (LH_2) is preferable for safety reasons and useful information such as stratification mechanism and fluid motions in both liquid and vapour can be obtained. Lumped Parameter (LP) model with non-equilibrium and homogeneous approach and with discretized approach have been developed to predict the behaviour of LN_2 is small scale (SS) storage tank.

Section 5.1.3.1 and Section 5.1.3.2 respectively describe the LP model with non-equilibrium and homogeneous approach and with discretized approach.

5.1.3.1. Lumped Parameter model with non-equilibrium and homogeneous approach

Perez et al. [26] experimentally investigated the behaviour of liquid nitrogen during the self-Pressurisation, de-pressurisation and steady state. They developed a model where the vapour and the liquid are homogeneous, but the vapour is overheated. Figure 24 shows the superheated model of Perez et al. [26] and the comparison with the experimental data of self-pressurisation. In Figure 24 (b), the continuous line refers to the computed values of pressure of the model. The measured value of self-pressurisation for experiment 1, 2, 3 and 4 are individually indicated by ○, ◊, □ and Δ, respectively. Black, blue, green and red are respectively experiments 1, 2, 3 and 4. In the model proposed by Perez et al. [26], the overall heat transfer coefficient of both liquid and vapour with the environment were tuned with the experimental data. The heat transferred between the vapour and the liquid through the interface was determined with the method of Heestand et al. [86]. The value of 97 % was used as specified factor. The model developed by Perez et al.[26] was used by Al Ghafri et al. [1], [2] for predicting the liquefied natural gas (LNG) behaviour.

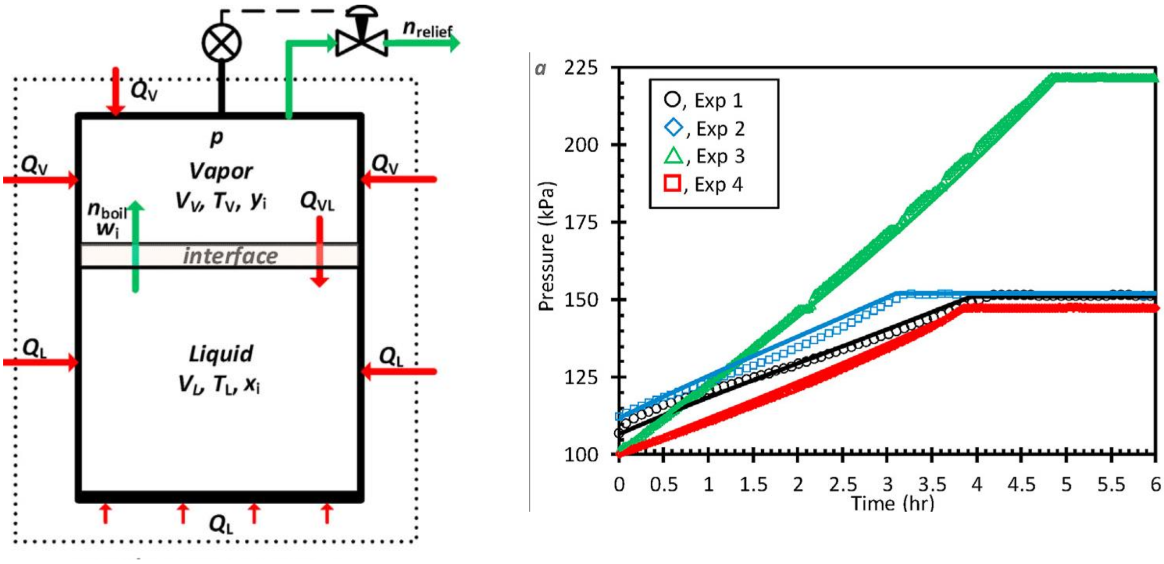

a) b)

Figure 24. (a) superheated model [26]. (b) Comparison with experimental data of self-pressurisation [26].

The models here reported are very simple and the model of Perez et al. [26] is reliable because the heat transfer coefficients were determined by fitting the experimental data. The method of Perez et al. [26] to estimate the heat transfer coefficient is interesting when the insulation properties are hard to determine. The approach of using the specified factor at liquid-vapour interface seems weak. The author thinks that this approach makes the model robust, but it loses applicability if the model is applied to other system. The specified factor approach can be overcome by studying the fluid-dynamics of vapour near the interface.

Seo and Jeong [79] developed a partial equilibrium model (PEM) for predicting the self-pressurisation in a closed cryogenic storage container. The liquid and the vapour are homogeneous, isothermal and at thermal equilibrium. The liquid-to-interface and the vapour-to-interface heat flows are computed with the heat transfer coefficients of natural convection at horizontal plates. The results of the PEM were compared with the experimental data of pressure at 13%, 28 % and 67 % of the filling ratio. The neglect of the thermal stratification, which controls the evaporation during the storage, is the main source of the deviation of the results with the experimental data.

5.1.3.2. Lumped Parameter model with discretized approach

Seo and Jeong [24] proposed the thermal diffusion model (TDM) to analyse the self-pressurisation. They compared the numerical results with experimental data. Figure 25 shows the thermal diffusion model proposed by Seo and Jeong [24] and the comparison with the experimental data of self-pressurisation. The pink line with “*” as symbol and the blue line with ♦ as symbol respectively indicate the measured value of pressure at 70 % filling ratio and 1.7 W heat input, and at 90 % filling ratio and 1.6 W heat input. The continuous and the dashed line individually refer to the computed values of pressure at 70 % filling ratio and 1.7 W heat input, and at 90 % filling ratio and 1.6 W heat input.

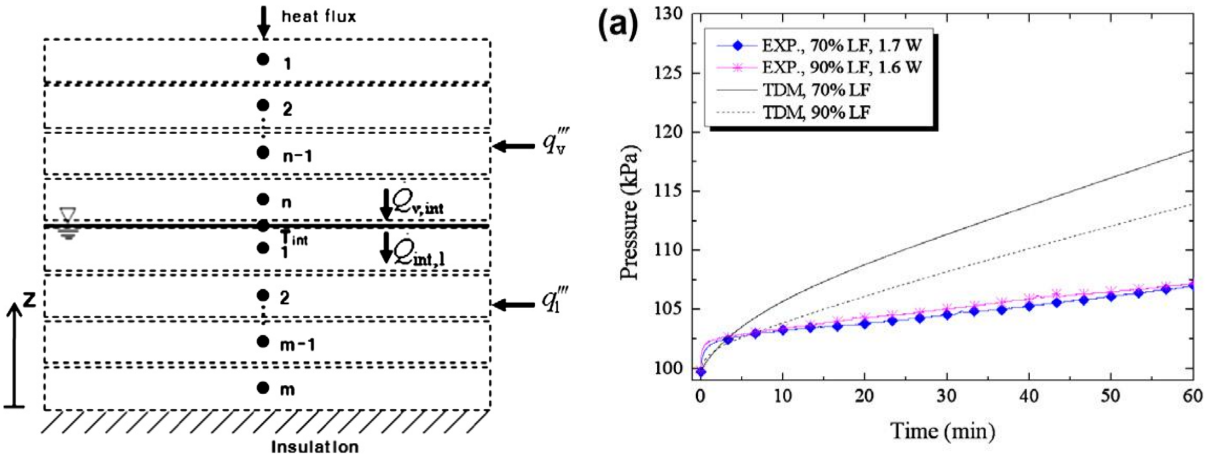

a) b)

Figure 25. (a) Thermal diffusion model [24]. (b) Comparison with experimental data of self-pressurisation [24].

This model is based on 1-dimensional thermal diffusion equation in liquid and in vapour. It is assumed that liquid and vapour are stagnant due to stratification. The heat is transferred between each layer by conduction up to the interface, where the net mass flow is computed with the energy conservation law. The developed model failed in the description of the pressurisation because this last was overestimated at high liquid level and it was underestimated for low and medium filling ratios. Seo and Jeong [24] assumed perfect stagnation in liquid and in vapour. This assumption is false because liquid and vapour move, as described by the experimental results from the literature presented in Section 4.4 and in Section 4.5 of Chapter 1. The result of this is a bad description of the experimental data as described in Figure 25 (b).

5.1.4. Models developed for liquid nitrogen in small scale tanks for predicting the behaviour of liquefied natural gas

Some of the most recent works [3], [34], [77], [78], [80] on liquefied natural gas (LNG) storage models were initially developed for liquid nitrogen (LN_2). Lumped Parameter (LP) model with non-equilibrium and homogeneous approach and with discretized approach have been developed to predict the behaviour of LN_2 is small scale (SS) storage tank.

Section 5.1.4.1 and Section 5.1.4.2 respectively describe the LP model with non-equilibrium and homogeneous approach and with discretized approach.

5.1.4.1. Lumped Parameter model with non-equilibrium and homogeneous approach

Al Ghafri et al. [34], Al Ghafri et al. [3], Wang et al. [77] and Wang et al. [78] used Lumped Parameter (LP) model with non-equilibrium and homogeneous approach for studying the behaviour of liquid nitrogen (LN_2) in small scale tank, to extend the model to liquefied natural gas (LNG).

Al Ghafri et al. [34] published an advanced studies of Boil-off Gas (BOG) generation in Liquefied Natural Gas (LNG) storage tanks. Their investigation reported a series of experiments with LNG-like binary mixtures of methane and of propane. The experimental data were collected in three storage conditions: self-pressurisation, de-pressurisation and homogenous or steady state. These data were compared with the results obtained from a non-equilibrium model with homogenous liquid and vapour. Figure 26 describes the conceptual drawing of the model of Al Ghafri et al. [34] and the comparison with the experimental data of the self-pressurisation. The continuous lines are the values computed by the model and the circles, triangles and squares individually indicate the measured values of pressure in experiments 1, 2 and 3. The author suggests to read the article of Al Ghafri et al.[34] for more details on experiments 1, 2 and 3.

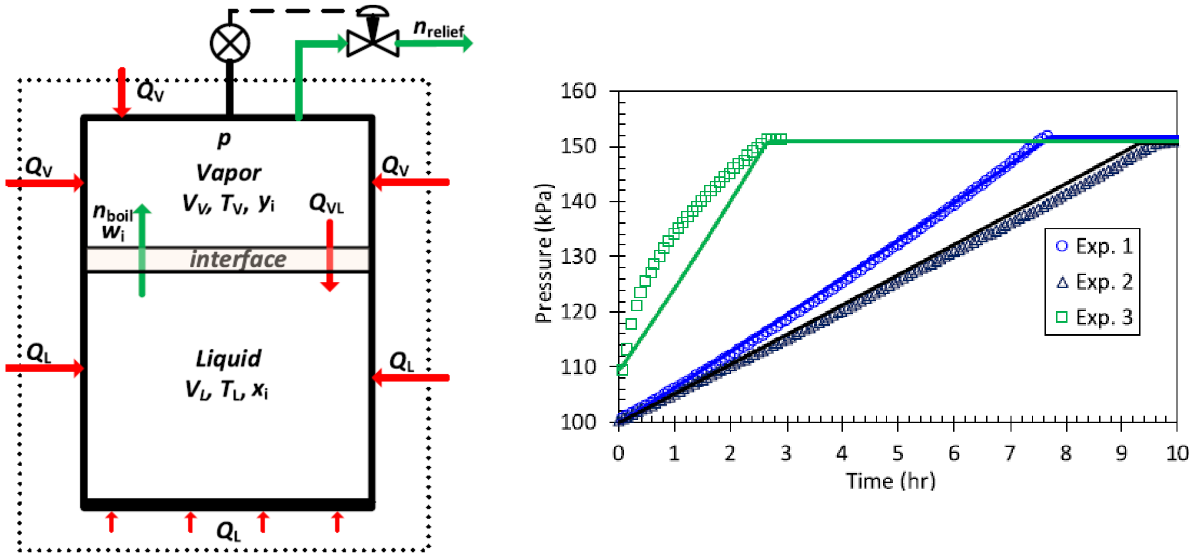

a) b)

Figure 26. (a) conceptual drawing of the model [34]; (b) comparison between the model and the experimental data during the self-pressurisation stage [34].

The vapour is overheated and the liquid is at saturation. The method used is similar to the approach of environmental-to-fluid heat transfer in three steps, as done by Migliore et al. [44], [46], and the approach of the liquid-vapour heat transfer, as done by Wang et al. [77]. Al Ghafri et al. [34] stated that the vapour-interface heat transfer can be computed with the heat transfer coefficient or using specified fraction of overall vapour heat inputs. They defined this heat transfer coefficient to be 4 W/m²/K and the heat transfer coefficients of liquid-environment and of vapour-environment were computed. These values were computed to fit the experimental data of liquid nitrogen and of LNG, depending of the comparison. The authors reported a good agreement between the proposed model and the experimental and literature data in the self-pressurisation and in the homogeneous stage. They underlined that neglecting the thermal stratification reduce the accuracy of the model, in particular during the de-pressurisation stage.

Al Ghafri et al. [3] continued the studies of the storage behaviour of LNG in the three storage configurations. They collected experimental data of ternary LNG-like mixture of methane, of ethane and of nitrogen. The model developed for binary LNG-like mixture was compared with the experimental data, but the heat transfer coefficients were manually computed from the experimental data, as for the heat inputs rate. The authors concluded that this model was in good agreement with the experimental data in all explored conditions. The main drawback of the model in Al Ghafri et al. [34] is the fitting of vapour-liquid heat transfer coefficient at interface, which limits the applicability of this model to other cryogenic fluids and storage containers.

Wang et al. [77] developed non-equilibrium thermodynamic model for liquefied natural gas storage tanks. Liquid and vapour were considered homogeneous and isothermal. The volumetric evaporation and condensation rates were computed with the Lee model [93]. The evaporation and the condensation coefficients of Lee model [93] were fixed at 0.1 to maintain the saturation temperature difference of the liquid and vapour phases below 3°C [77]. Figure 27 describes the homogeneous model of Wang et al. [77] and the comparisons of different models with the forced pressurisation experimental data of Ludwing et al.[92]. In Figure 27 (b), the symbol Δ indicate the experimental values of pressure. The continous red line, the continous black line and the yellowdashed line respectively indicate the values of pressure computed with the model of Wang et al. [77], the homogenous model and the CFD.

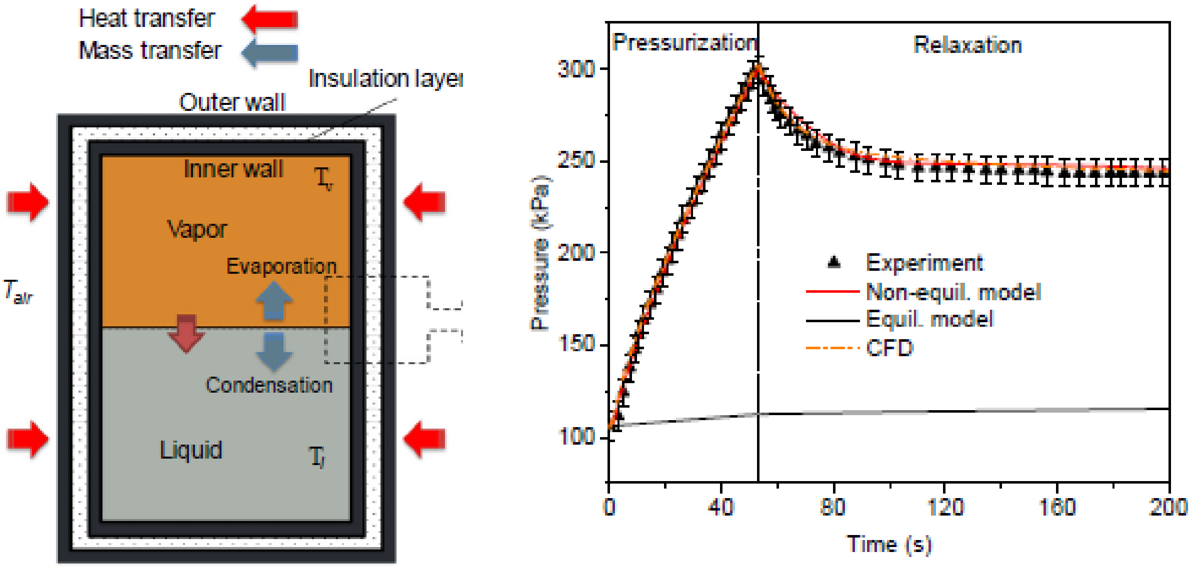

a) b)

Figure 27. (a) Homogenous model [77]; (b) comparison between the model [77] and the experimental data [92].

The heat transfer with the tank's walls was determined with the equivalent resistance-capacitance network. The heat transfer coefficients at the tank's wall were computed with the standard heat transfer correlation of free-convection. This type of correlations was used to estimate the heat transfer coefficient of liquid and of vapour at the interface. This type of model was in good agreement with the experimental data of liquid nitrogen given by Ludwing et al. [92] and by Harper and Powars [94]. They used pure methane to simulate the LNG experimental data of Harper and Powars [94]. After this validation, Wang et al. [77] used this model to predict the behaviour of LNG in two cryogenic tanks in refuelling stations and in truck refuelling. They concluded that the model predicted the pressure and the LNG temperature with good accuracy under stationary operating conditions. The model of Wang et al. [77] has two main drawbacks. Firstly, the vapour-to-interface heat flow is neglected. Second, the correction factor is applied to conductive model and the value of this factor is regressed with the experimental data. Hence, this model cannot be extended to other cryogenic liquids and storage containers.

Wang et al. [78] modelled and analyzed the pressurisation of LNG fuel tank under marine conditions. The liquid and the vapour were considered as homogenous and they are not at thermodynamic equilibrium. They considered the sloshing effect and the mass and the heat transfer at the liquid-vapour interface. Figure 28 shows the LNG fuel tank model of Wang et al. [78] and the comparison with the experimental data of pressure of Konopka et al. [95] in liquid nitrogen tank. In Figure 28 (a), "Q" and "G" respectively indicate the heat rate and the mass flow. In Figure 28 (a), the continuous red line is the measured values and the dashed black line is the values computed with the model.

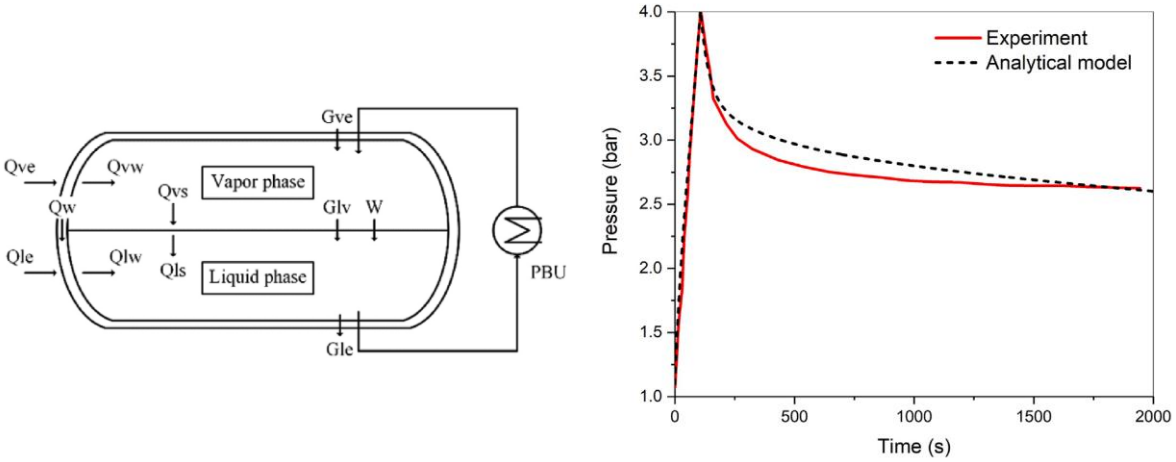

a) b)

Figure 28. (a) LNG fuel tank model [78] (b) comparison with experimental data [95].

Heat is transferred between the vapour and the interface by conduction. The Fourier's law is applied to model the liquid-interface heat transfer and a correction factor was used to determine the thickness of the liquid thermal boundary layer at interface. The phase change mass flow is computed with the energy balance equations at interface. The external heat flows were determined with an effective heat transfer coefficient. The latter is established with the Boil-off Rate (BOR), with the difference in temperatures between the liquid and the air, and with the overall surface of the tank. A correction factor was introduced to compute the heat transfer in the vapour phase to account for the enhancement due to the pressuring gas. This correction factor was determined by experimental data. The proposed model considers the thermal inertia of the tank walls in contact with the two phases. The variation of temperatures of the tank walls in vapour and in liquid are determined with the energy balance equations. The conductive heat flow along the tank wall is considered as ratio between the difference in wall temperatures between the vapour and the liquid and the difference between the diameter and the liquid level. The model of Wang et al. [78] was tested with the experimental data of liquid nitrogen of Ludwing et al. [92] and of Konopka et al. [95]. After this, the model was used to predict the behaviour of LNG during fuel gas supply and during sloshing, by considering LNG as pure methane. They concluded that the validity of the model was confirmed by the comparison with experimental data and that the pressurisation process strongly depends on the heat/mass transfer at interface and that the vapour condensation dominates the holding period and sloshing process. The main drawback of Wang et al. [78] is the use of experimental correction factor, which limit the applicability of this model to other cryogenic liquids and storage tanks.

5.1.4.2. Lumped Parameter model with discretized approach

Wang et al. [80] developed a non-equilibrium multilayer thermodynamic model for predicting the thermal stratification and rollover phenomena in liquefied natural gas tanks. The modelling approach is similar to the method used by Daigle et al. [2], but the introduction of the conduction layer is the main difference. Liquid and vapour are discretized in sub-layers and each sub-layer has a bulk and a boundary layer. Wang et al. [80] introduced the conduction layer in the liquid and it is located below the interface. The conduction layer corresponds to the stratified region of the liquid. Figure 29 describes the model of Wang et al. [80] and the comparison with the measured values of pressure of Perez et al. [26]. In Figure 29 (a), the red arrows are the heat inputs at bottom, side wall and roof. The orange, the light grey and the dark grey respectively indicate the vapour, the conduction layer and the liquid. In Figure 29 (b), the square points are the measured values and the lines indicate the computed values. the continuous, the dashed and the dot-dashed lines respectively indicate the computed values at the integration time step of 0.5, 1.0 and 2.0 seconds.

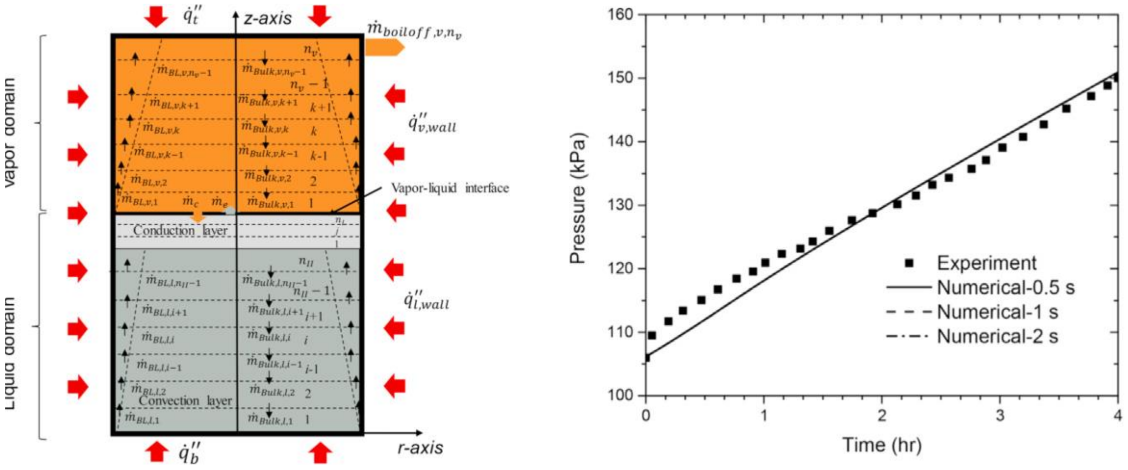

a) b)

Figure 29. (a) non-equilibrium multilayer thermodynamic model [80]; (b) comparison with experimental data [26].

This region is discretized in sub-strata and the heat is transferred across each layer by conduction. The thickness of the conduction layer is defined with the equation of stratified layer growth, as done in modelling the thermal stratification in LH_2 tanks [61]–[68]. Wang et al. [80] considered that convection occurs in the vapour and in the remaining volume of the liquid. Heat is transferred between each layer in both liquid and vapour. This heat flux is computed with the conduction model and with the free-convection in enclosure model. The latter uses the thickness of the sub-stratum as characteristic length of heat transfer. The fluid-dynamic is computed with the model of free-convection over vertical flat surface in homogenous medium. The heat transfer between the liquid and the vapour across the interface is computed with the formulas of natural convection over horizontal flat surfaces. A time adjustment factor was introduced in the liquid-vapour-interface heat transfer formula and in the equation of stratified layer growth. The value of this parameter was determined by experimental data. Lee model [93] was used to determine the evaporative and condensing volumetric flow and the volume of the interface was computed with the values of the interface thickness of 0.005 m. This value was reported by Beduz and Scurlock [20]. The evaporation and the condensation coefficients of Lee model [93] were determined by fitting the experimental data. The wall temperature in the vapour and in the liquid is respectively uniform and the heat transfer coefficients are calculated with free-convective formulas. The heat transfer models at roof and at the bottom are not specified. Wang et al. [80] estimated the liquid heat input from the temperature profile in liquid and the variation of temperatures in each liquid layers. The vapour heat inputs were estimated with the same method, but the enthalpy variation due to the vapour mass change was considered. Wang et al. [80] added the heat transfer rate from the walls in contact with the vapour phase to liquid-vapour interface because they underestimated the liquid heat inputs. The model was validated with the experimental data of liquid nitrogen of Perez et al. [26] and with rollover data of Sarsten [96]. They concluded that the accuracy of the model was good for both experimental series. The model of Wang et al.[80] has two drawbacks. Firstly, the temperature gradient is not considered in the boundary layer and this neglect is a drawback because this gradient affects the fluid-dynamics, thus the behaviour of cryogenic liquid. Second, the fitting of the parameters of the Lee model[31] [93] reduces the applicability of this model to other cryogenic liquids and storage containers.

---

[31] Lee model calcualtes the volumetric evaporation and condensation rates, with respect to the bubble point. These rates are computed as function of the evaoiratuionb and condensation coefficients, respectively.

5.2. Score-table method

The analysis of the scientific literature reveals that a large number of modelling works exists. Hence, a score table method is proposed to select the modelling approaches that better describe the physical phenomena. This method consists of:

a) Defining the categories to evaluate each modelling work;
b) Giving a score to each of these categories.

Each work gets one point if the proposed model has the features that are required in each category, and, then, an overall score is computed. Considering the storage phenomena, these categories are: the heat transfer within the storage system, and between the system and the ambient; the ageing in LS and SS storage tanks; the self-pressurisation, the stratification in liquid and in vapour; the flexibility to the operative conditions. Table 6 reports the main results of this score-table method.

Table 6. Main results of the score-table methods.

Author	**Heat Transfer with tank**	**Ageing in LS**	**Ageing in SS**	**Self-pressurisation**	**Stratification liquid**	**Stratification vapour**	**Flexible**	**Overall**
Ovidi et al. [50]	0	0	0	1	1	1	0	3
Roh et al. [51]	0	0	0	1	1	1	0	3
Osipov et al. [70]	1	0	0	1	0	0	1	3
Liu and Li [71]	1	0	0	1	1	0	0	3
Petitpas [73]	1	0	0	1	0	0	1	3
Al Ghafri et al. [3]	0	1	1	1	0	0	0	3
Vliet et al. [1]	1	0	0	1	1	0	0	3
Daigle et al. [2]	1	0	0	1	1	1	0	4
Wang et al. [80]	1	0	0	1	1	1	0	4

Daigle et al. [2] and Wang et al. [80] are the modelling works with the highest score because they can predict most of the main phenomena occurring during the storage. Vliet et al. [1] considered the bulk temperature gradient in the fluid-dynamic model. This approach is very important to predict the free-convection at side wall. Hence, Daigle et al. [2], Wang et al. [80] and Vliet et al. [1] are considered as reference for developing the storage model in this thesis.

Ovidi et al. [50] and Roh et al. [51] used CFD. Osipov et al. [70] developed a model to simulate the behaviour in cryogenic liquid transferring, with homogeneous approach. This model cannot predict the thermal stratification. Petitpas [73] modified the model of Osipov et al. [70], by using the internal energy to compute the liquid temperature. Hence, this model is not important in cryogenic storage modelling. Ghafri et al. [3] proposed an ageing model that can be applied in LS and SS tanks. They used the homogeneous approach to describe the liquid and the vapour. They did the regression of the vapour-heat transfer coefficient at interface to fit the experimental data. As consequence, this model cannot predict the thermal stratification and it requires experimental data to adjust the interface heat transfer. So, the works of Ovidi et al. [50], Roh et al. [51], Osipov et al. [70], Liu and Li [71], Liu and Li [71], Petitpas [73], Al Ghafri et al. [3] are not considered, even if they have the second best score. The results of the other modelling works are not reported because their scores is lower than 3. So, they are not of interest.

5.3. Summary of the selected modelling works

The score-table method allowed selecting three works as results: Daigle et al. [2], Wang et al. [80] and Vliet et al. [1]. The main characteristics of these works such as modelling approach fluid-dynamic model, heat transfer model and mass-heat transfer model at interface are reported in Table 7.

Table 7. Main features of the selected experimental work.

	Vliet et al. [1]	**Daigle et al. [2]**	**Wang et al. [80]**
Modelling approach	Discretisation of liquid	Discretisation of the whole volume	Division of liquid in region and discretisation of the whole volume
Intra liquid sub-layer heat transfer	Not present	Not present	Conductive and convective models
Fluid-dynamic model	Numerical integration of conservation laws.	Free-convective formulas for homogenous medium	Free-convective formulas for homogenous medium
Heat transfer model	Model based on the fluid-dynamic conservation laws	Free-convection in homogenous medium	Free-convection in homogenous medium
Interface – heat transfer	Not specified	Free-convection of over flat surface and conduction	Free-convection over flat surface
Interface – mass transfer	Not specified	Energy balance equation at interface	Lee[97] model

The discretisation approach consists of dividing the liquid or the vapour, or both into sub-layers[32]. Each sub-layer is, then, divided into the bulk[33] and the boundary layer[34]. Before using this method, Wang et al.[80] divided the liquid into the non-stratified region and the conductive layer. This layer corresponds to the liquid stratified region (see Section 4.2.2 of Chapter 1). This layer is computed with the layer growth equation, and this equation was corrected with a parameter adjusted on the basis of the experimental data. Heat transfer between sub-layers was considered only by Wang et al. [80]. They predicted this exchange with a pure conductive model in the conductive layer. The convective and conductive models were used for the non-stratified region and for the vapour. The convective model is based on free-convection in enclosed space. The heat transfer coefficient depends on the size of the sub-layer, that was defined by Wang et al. [80].

Daigle et al. [2] and Wang et al. [80] used the free-convective formulas for the boundary layer of Squire [98] and, of Eckert and Jackson [99] to develop the fluid-dynamic model. Hence, they did not consider the bulk temperature gradient in the conservation laws of energy and of momentum in the boundary layer. As consequence, Daigle et al.[2] and Wang et al. [80] used the free-convective heat transfer formulas in homogeneous medium. Only Vliet et al. [1] numerically integrated the conservation laws of boundary layer to develop the fluid-dynamic model. They analytically solved these equations only to obtain the initial solutions for the numerical integration. The heat transfer model of Vliet et al. [1] is directly based on the numerical solution of the boundary layer conservation laws. All the three authors, however, imposed the heat inputs in the storage container. Hence, the heat fluxes were used to obtain wall temperature and heat transfer coefficients at the wall.

Daigle et al. [2] and Wang et al. [80] used the free-convection heat transfer formula over horizontal surface to predict the heat transfer at interface. Daigle et al. [2] used these formulas and a conductive model. Daigle et al. [2] applied the energy balance equations at interface to predict the mass transfer. Wang et al. [80] used the Lee model[31] [93] and some of the parameters of this model were regressed to fit the experimental data.

---

[32] Sub-layer is a horizontal layer where temperature and composition are uniform.

[33] The bulk is the main part of the sub-layer.

[34] The boundary layer is the part of the sub-layer where the conservation laws of free-convective boundary layer are applied.

5.4.Conclusions

Several types of model have been developed to predict the behaviour of cryogenic liquids in storage containers, in particular for liquefied natural gas (LNG) and liquid hydrogen (LH_2). The main type of models are the computational fluid-dynamics (CFD), lumped parameter (LP) models with equilibrium and evaporative rate approach, LP models with equilibrium and heat flow approach, LP models with non-equilibrium and homogeneous approach, LP models with energy distribution approach and LP models with discretisation. This analysis reveals that the interaction between fluid-dynamics and heat transfer, and between fluid-dynamics and the heat-mass transfer at interface are not properly considered. These models are evaluated with a score-table method, where a score is given to each phenomenon that is described by the model. This approach is used to select the reference modelling works for the developing of the storage model in this thesis.

CFD models can describe the physical behaviours such as thermal stratification and fluid-dynamics, in absence of experimental data. The large computational time required in those models makes them unsuitable for industrial application. LP model with equilibrium (evaporative rate and heat flow approaches) can give good first guess estimation, in particular for LNG in large scale tanks at steady state conditions. They are, however, unsuitable to be applied in real situations since the equilibrium condition are rarely reached. Moreover, they do not describe the heat transfer between the liquid and the vapour with the tank. LP model with non-equilibrium and homogeneous approach can more realistically describe large scale (LS) storage tanks with LNG and small scale (SS) storage containers with LH_2. This approach is suitable when the heat inputs rate is low because thermal stratification is weak. Models [49], [50], [52] often determine the heat inputs, by considering three heat transfer steps: environment-to-tank, external-to-internal tank and internal-to-vapour-liquid. The heat transfer between the liquid and the vapour is considered and predicted with convective and conductive models. These models do not describe well this transfer because they are not based on the fluid-dynamics near the interface. Fitting the vapour-liquid heat transfer coefficient is usually done to improve the heat transfer at interface. The description of the interface can be improved by studying the fluid-dynamics in the vapour and the fluid-motions in the liquid near the interface. LP models with non-equilibrium and with homogeneous approach are not compared enough with experimental data and of physical evidence of heat transfer across the interface. In fact, some works [69], [73], [71] do not have a comparison with experimental data. LP models with energy distribution approach computes the liquid temperature profile from functions that have been regressed with experimental data. This procedure can hide some physical phenomena and it can limit the application of the model because experimental data of liquid thermal distribution do not exist for all the possible storage conditions.

LP model with discretisation does not require the energy distribution function to compute the thermal distribution in the liquid. This approach seems a good compromise between the spatial discretisation of CFD model and the simplicity of homogenous model. The discretisation approach of Daigle et al. [2] should be used for liquid and for vapour. The idea of Wang et al. [80] of introducing the conduction region is excise because the stratified region can be predicted with the fluid-dynamic and heat transfer model. The heat transfer between each sub-layer is crucial to determine how the heat is propagated in liquid and in vapour. The approach of Wang et al. [80] for this heat transfer should be modified because this transfer cannot directly depends on the size of the sub-layer, which is arbitrary defined. The heat transfer model with the tank should be computed form the fluid-dynamic model, as done by Vliet et al. [1]. This model should be based on the conservation laws of the boundary layer, for different geometries. The bulk temperature gradient should be considered in these equations and the balance equations should be numerically solved, as done by Vliet et al. [1]. In fact, the analytical solution is impossible when the bulk temperature gradient is considered.

6. Objectives of the thesis

As said in Section 3 of Chapter 1, the operating stategy is established as function of the time-evolution of the storage variables such as holding-up time (HUT), the net pressure suction head (NPSH), the gross heating value (GHV) and the methane number (MN). These variables depend on the physical variables such as vapour and liquid temperatures, pressure and filling ratio, which change in time during the storage of the cryogenic liquids. The physical variables are influenced by the phenomena occurring during the storage such as vapour and liquid thermal stratification, sel-pressurisation and ageing. To establish a proper operating stategy that maintains the storage variable inside the applicability limits, a physical model is required to directly compute the evolution of physical variables, thus to indirectly calculate the storage variables, from the storage conditions.

To this purpose, the scientific literature of models of storage of cryogenic liquids has been analyzed to find the modelling approaches that are suitable for computing these physical variables during the self-pressurisation. As reported in Section 5.4 of Chapter 1, the models of the behaviour of cryogenic liquids in small scale tank have some critical issues:

a) Many models have not been validated against experimental data. The few validated models have regressed some coefficients to reproduce the behaviour of experimental data;
b) The fluid-dynamic model rarely considers the bulk temperature gradient, the relation with the heat transfer and the effect of the geometry of the storage container;
c) The heat inputs are rarely computed with the difference in temperatures between the environment and the internal fluid;
d) The intra-layer heat transfer depends on the size of the sub-layer;

The industrial literature of models of storage of cryogenic liquids has been reviewed, in particular the one of Engie Lab Crigen. The model called LNGMaster$^{(R)}$ has been analyzed. This model predicts the behaviour of liquefied natural gas (LNG) in large scale tank. LNGMaster$^{(R)}$ cannot, however, describe the phenomena occurring during the storage (see Section 4 of Chapter 1) when this model is applied to small scale storage container, due to these critical issues:

a) Fixed integration time-step is used to solve the system of ordinary differential equations;
b) The heat inputs are defined by the user, instead of being computed from the insulating properties of the storage container and form the difference in temperature between the environment and the fluid stored;
c) The conservations laws of the model are not suitable for describing self-pressurisation and thermal stratification;
d) The interfacial heat transfer model does not consider the condensation rate.

To sum up, a sufficiently complete and predictive model do not exist for predicting the time-evolutions of the physical variables, thus for computing the time-evolutions of the storage variables, from the phenomena that occur during the storage. So, the challenges of the storage of cryogenic fluids in SS tank (see Section 3 of Chapter 1), cannot be overcome.

Collaboration between the center of thermodynamics of processe (CTP) of Mines Paris PSL and Engie Lab Crigen was established to develop a model for the behaviour of cryogenic liquids in small scale (SS) applications in energy and transport sectors. As consequence, a thesis was planned with the main objective of developing a model for pure cryogenic liquids in static SS storage containers, which can be extended to cryogenic mixture such as LNG. The developed model must be capable of:

a) Predicting the heat inputs knowing the insulation properties of the storage container, and the environmental conditions and the internal temperatures;

b) Considering a non-constant the time step for integrating system of ordinary differential equations, to optimise the computational time and to improve the precision;
c) Describing the thermal stratification in liquid and in vapour, and the self-pressurisation;
d) Computing the effect of the bulk temperature gradient and geometry on the fluid-dynamics, considering the relation between heat transfer and fluid-dynamics;
e) Predicting the interfacial heat transfer and the condensation rate;
f) Computing the intra-layer heat flow without using the size of the layer;

Objective a) can be achieved by using an approach where the heat transfer is composed of steps, similarly as done by Migliore et al. [46], Qu et al. [49], and Krikkis [47]. The thermal properties of the storage container can be described by the effective heat transfer coefficient, as proposed by Wang et al. [78]. Objective b) can be achieved with adaptive step size methods because they improve accuracy and reduce computational time, by changing the integration time-step when it is required. Objective c) can be fulfilled with the discretized approach of Daigle et al. [2] and objective d) can be achieved with the fluid-dynamics and heat transfer model of Vliet et al. [1]. Objective e) can be fulfilled with the interfacial model of Daigle et al. [2]. Objective f) can be achieved by with the same approach of Wang et al. [80], but with formulas that are independent from the size of the sub-layers.

Chapter 2

Données expérimentales et analyse de la distribution thermique

Les données expérimentales de pression et des profils de température dans les phases liquide et vapeur contenues dans une cuve de stockage à petite échelle (PE) sont importantes car quantifient indirectement la convection naturelle et le transfert de chaleur à l'interface et témoignent ainsi des phénomènes d'auto-pressurisation et de stratification thermique.

La recherche bibliographique effectuée dans le cadre de cette thèse a permis (i) de récolter les mesures expérimentales existants relatives à la stratification thermique et la pressurisation obtenues en étudiant le stockage de azote liquide (LN_2), de hydrogène liquide (LH_2), de mélanges de type gaz naturel liquéfies (GNL) et d'autres fluides non-cryogéniques, et (ii) de remarquer le manque d'informations sur la dynamique des fluides en présence de stratification thermique et d'auto-pressurisation. Une méthode de « table de notes » proposée dans cette thèse a permis de sélectionner 7 travaux expérimentaux (3 avec de l'azote liquide et 4 avec de l'hydrogène liquide) sur lesquels concevoir et valider le modèle.

L'analyse des données a montré que certaines informations fondamentales (les niveaux de liquide, la température d'interface, la température du Boil-off-Gas (BOG) et les températures moyennes du liquide et de la vapeur) pour la validation d'un modèle ne sont pas disponibles dans la littèrature. Ces variables sont par conséquent calculées à partir des valeurs expérimentales de profils de pression et de température.

Deuxièmement, la condition autour du réservoir de stockage doit être définie pour réaliser une comparaison modèle/donnée rigoureuse. Ces conditions sont principalement déterminées par les apports de chaleur dans les cuves de stockage. Comme indiqué dans la littérature, la valeur déclarée de l'apport thermique peut être très différente de celle calculée. Ainsi, les apports thermiques sont calculés pour chaque test de chaque travail expérimental. La méthode trouvée dans la littérature est revue et le résultat indique qu'elle n'est pas rigoureuse. Ainsi, une nouvelle approche est proposée, utilisant les lois de conservation de l'énergie et de la masse. Les valeurs calculées s'avèrent souvent très différentes de celles déclarées dans les articles et les entrées thermiques diminuent fortement avec la diminution du taux de remplissage.

Comme indiqué dans la littérature, les transferts de chaleur vapeur-liquide et entre parois sèches et mouillées affectent fortement la répartition thermique des échanges de chaleur entre le liquide et la vapeur, ce qui a un impact sur le comportement de stockage. Ainsi, l'analyse de la répartition thermique se fait en comparant la chaleur accumulée dans la vapeur et dans le liquide. Ces accumulations thermiques sont estimées avec les équations de bilan massique et énergétique en régime stationnaire et lors de l'auto-pressurisation. Les résultats montrent que la répartition thermique entre liquide et vapeur est fortement altérée par le transfert de chaleur à travers l'interface. Cette analyse ne pouvant pas déterminer le rôle du transfert de chaleur entre parois sèches et mouillées, une méthode basée sur la loi de Fourier de conduction thermique unidimensionnelle est proposée. Les résultats obtenus montrent que ce transfert de chaleur est aussi important que le transfert de chaleur à l'interface pour affecter le comportement des liquides cryogéniques dans les réservoirs de stockage cryogéniques.

Experimental data and thermal distribution analysis

Experimental data of pressure and of temperature profiles in liquid and in vapour directly describe the self-pressurisation and the thermal stratification. These variables indirectly quantify the natural convection and the heat-mass transfer at interface. Hence, these data are mandatory to fulfil the goal of this thesis in term of validating the model. These data are researched in the literature. Experimental studies of thermal stratification and of pressurisation were done with cryogenic (LN_2, LH_2 and LNG-like mixtures) and non-cryogenic fluids. The review of these articles reveals that experimental studies of fluid-dynamics with thermal stratification and self-pressurisation are missing. A score-table method is developed to select the papers with the most useful experimental data. Each storage phenomenon is classified with a score, as function of their importance in describing the storage and in fulfilling the goal of this research project. 7 experimental works with cryogenic liquids (3 with liquid nitrogen and 4 with liquid hydrogen[35]) were chosen because they describe better the storage phenomena and conditions. Then, the experimental devices, procedure and measurements uncertainties are described for each of these works. The measured values of pressure and of temperatures are the only available experimental data, but variables such as (i) liquid levels, (ii) interface temperature, (iii) BOG temperature, and (iv) average liquid and vapour temperatures are fundamental for evaluating the model. Hence, these variables are computed from the experimental values of pressure and of temperature profiles. To compare the model with the experimental data, the boundary condition must be defined. These conditions are mainly determined by the heat inputs in the storage containers. As proved in literature, the declared value of heat input can be very different from the calculated one. Hence, the heat inputs are computed for each test of each experimental work. The method found in literature is reviewed, revealing that it is not rigorous. So, a new approach is proposed, using the conservation laws of energy and of mass, and the results of this approach are analyzed. The values calculated are often very different from the one declared in the papers and the heat leakage strongly decreases with lowering the filling ratio. As reported in literature, vapour-liquid heat transfer and dry-wetted wall heat transfer strongly affect the thermal distribution of the heat leakage between the liquid and the vapour, impacting the storage behaviour. So, the analysis of thermal distribution is done by comparing the heat accumulated in the vapour and in the liquid. These thermal accumulations are estimated with the mass and energy balance equations at steady state and in self-pressurisation. The results show that the thermal distribution between liquid and vapour is strongly altered by the heat transfer across the interface. This analysis cannot determine the role of dry-wetted wall heat transfer. Hence, a method is proposed based on the Fourier's law of 1 dimensional heat conduction. The results show that this heat transfer is as important as the interfacial heat transfer in affecting the behaviour of cryogenic liquids in cryogenic storage tanks.

Section 1 explains the variables to have for validating the model. Section 2 presents the experimental data that was found in open literature on the storage of phenomena. Section 3 describes the table-score method and the criteria for selecting the experimental data. Section 4 presents the selected experimental works. The liquid level, the liquid-vapour interface temperature and the average temperatures in liquid and in vapour are described in Section 5. Section 6 presents the method for computing the heat inputs. Section 7 presents the thermal analysis and Section 8 explains the method to compute the dry-wetted walls heat transfer.

---

[35] The liquid hydrogen is considered as pure para-hydrogen.

1. Variables for validating the model

The goal of this thesis is the development of the model to predict the behaviour of cryogenic liquids in small scale (SS) storage containers. Hence, a hierarchy of the phenomena to study can be done. This hierarchy is described in Table 8 with five level of importance: mandatory, high, medium, low and negligible.

Table 8. Hierarchy of storage phenomena.

Phenomenon	Level of importance
Pressurisation (self) and thermal stratification (liquid and vapour)	Fundamental
Natural convection in stratified liquid and vapour, heat transfer with the wet and dry tank's walls and heat/mass transfer across interface	High
Thermal expansion	Medium
Forced pressurisation, sloshing and ageing	Low
Heat transfer phenomena outside the storage containers	Negligible

Thermal stratifications in liquid and in vapour are caused by fluid-dynamics and heat transfer at the side wall. Self-pressurisation is determined by the mass-heat transfer at interface. Thermal stratification influences the self-pressurisation and the ageing. Thermal stratification and self-pressurisation respectively affect the net pressure suction head (NPSH) and the hold-up time (HUT), which are two important storage variables (see Section 3 of Chapter 1). Hence, thermal stratification in liquid and in vapour and self-pressurisation are fundament for understanding and properly modelling the behaviour of cryogenic liquids. As consequence, they are classified of high importance. The thermal expansion influences the self-pressurisation, but the latter is more affected by the mass transfer at interface. So, its level of importance is medium. Forced pressurisation, sloshing, ageing and heat transfer phenomena outside the storage containers are respectively of low and of negligible importance because they are out of the scope of this thesis.

These storage phenomena are related to measurable variables such as ullage pressure, temperature profiles, velocity and thickness in boundary layer, liquid level. These variables can be organised, as reported in Table 9, with the same level of Table 8.

Table 9. Hierarchy storage variables.

Variable	Level of importance
Pressure and temperature profile (liquid and vapour)	Mandatory
Velocity, temperature and thickness in boundary layer at side wall	High
Heat inputs or BOR value at steady state	Medium
Initial liquid level and its evolution, liquid-vapour interface and BOG temperatures	Low
External surface temperatures	Negligible

Experimental data of pressure and of temperature profiles are mandatory because they directly connected with the phenomena of self-pressurisation, thermal stratification, natural convection in stratified liquid and vapour and, heat transfer with tank's wall and at interface. Velocity, temperature and thickness in boundary layer at side wall are of high importance cause of the relation between fluid-dynamic and heat transfer with pressure build-up and with thermal distribution in liquid and in vapour. Heat inputs or Boil-off Rate (BOR) value at steady state define the boundary conditions. These variables can be determined from the values of pressure and of temperature profile (see Section 6 of Chapter 2). So, they are not mandatory and they are classified as medium importance. Liquid level, liquid-vapour interface temperature and BOG temperature can be validate the models proposed in this thesis. They can be determined with the experimental values of pressure and of temperature profile, as described (see Section 5 of Chapter 2). Hence, they are of low importance. The environmental temperature and the external tank's surface temperature are negligible because they can be assumed being around 298.15 K, as done in this thesis.

2. Review of the experimental works

Many experimental works have been done to mainly understand the self-pressurisation and the thermal stratification in cryogenic storage containers. These investigations are classified for the different working fluids used and they are reviewed to underline the drawbacks and the advantages.

Section 2.1 presents the experimental works and Section 2.2 explains the conclusions.

2.1.Experimental works

The main experimental works with non-cryogenic fluids were done by Tellep and Harper [100], Vliet [101], Hurd and Harper [102], Shi et al. [103], [104] and Seo et al.[105]. Thermal stratification in liquid at different heating configurations was the main phenomenon studied by these authors. Tellep and Harper [100] investigated only side heating. Vliet [101], Hurd and Harper [102], Shi et al. [4],[5] and Seo et al. [105] applied the heat fluxes at bottom and at side wall with heaters. Vliet [101], and Hurd and Harper [102] did some tests at different bottom-to-side heating ratios. Shi et al. [4],[5] and Seo et al. [105] varied the overall heat power and liquid levels.

Barnett [106], Huntley [107], Seo and Jeong [24], Ludwig et al. [92], Ludwig and Dreyer [108], Konopka et al. [95], Kang et al. [91], Vishnu et al. [109], Perez et al.[26] and Muraleedharan et al. [110] used liquid nitrogen (LN_2) for understanding the storage phenomena. Barnett [106] focused on the liquid thermal stratification. Huntley [107] studied the thermal distribution and the natural pressure build-up under standard conditions and under stirring. Ludwig et al. [92], Ludwig and Dreyer [108], Konopka et al. [95] empirically examined the effect of the sloshing on forced pressurisation and thermal stratification. Seo and Jeong [24], Kang et al. [91], Vishnu et al. [109] experimentally investigated the self-pressurisation and the thermal stratification in liquid and in vapour. Perez et al. [26] experimentally studied the self-pressurisation, thermal stratification, the natural de-stratification and the BOG generation at quasi steady state. Muraleedharan et al. [110] tested the effect of bubbling to thermally de-stratify the liquid.

The storage of liquid hydrogen (LH_2) was experimentally studied for aerospace applications by Segel [111], Barnett et al. [62], Liebenberg and Edeskuty [112], Tatom et al. [113], Bailey and Fearn [114], Hasan et al.[27], Van Dresar et al.[28] Aydelott[24],[25], Aydelott and Spuckler [26], [27], Osipov et al. [70], Petitpas [73], Notardonato et al. [117], [90], [118] and Swanger et al. [119]. Segel [111], Barnett et al. [62], Tatom et al. [113], and Bailey and Fearn [114] mainly focused on the thermal stratification in the liquid under natural and forced pressure build-up. Liebenberg and Edeskuty [112] analyzed the consumption of pressuring gas during liquid hydrogen discharge. Hasan et al. [27], Van Dresar et al. [28] Aydelott[29], Aydelott and Spuckler [116] experimentally investigated the self-pressurisation and the thermal stratification in liquid and in vapour in LH_2 storage containers. Aydelott [25] analyzed these phenomena at different gravity level. Aydelott and Spuckler [27] did some boil-off test with liquid hydrogen. Petitpas [73] reported the variation of liquid levels in liquid hydrogen (LH_2) storage tank. Notardonato et al. [117], [90], [118] and Swanger et al. [119] reported a series of experimental tests on a new storage facility for containing liquid hydrogen at zero boil-off, for in loco-liquefaction and for liquid densification.

Some experimental data of liquefied natural gas (LNG) behaviour in large scale (LSà tanks and in small scale (SS) tanks were published. Dimopoulos and Frangopoulos[38], Miana et al. [40], Heestad et al. [86], Qu et al. [49], Krikkis [47] and Kountz [83] reported some experimental data of LNG ageing mainly during ship transportation. Temperature profile, pressurisation rate and LNG composition were measured in SS Dewar by Al Ghafri [3], [34] and by Jung et al. [54].

2.2. Summary and conclusions

The analysis of the literature shows that thermal stratification, natural convection in homogeneous medium[36] and evaporation-condensation have been mostly studied and measured by experiments. The experimental campaigns reported in literature were performed in different storage conditions, geometry of the tanks, working fluids and initial conditions. Cryogenic and non-cryogenic fluids are used in the experiments.

The experimental investigations at different heating modes show the fluid-dynamic interaction of liquid motions at bottom and at side walls. Self and forced pressurisation tests revealed the importance of the mass/heat transfer at liquid-vapour interface. The experimental investigations at different filling ratio and heat inputs describe how the thermal stratification in liquid evolves due to the fluid-dynamics.

The development of convective flow in stratified medium and the heat fluxes across the liquid-vapour interface have not been intensively investigated. This interaction strongly determines the thermal distribution in liquids. There are, however, not experiment that combines fluid-dynamics, thermal stratification and self-pressurisation. Without knowing the fluid motions, the cause of a particular shape of temperature profile cannot be established. The fluid-dynamics should be measured at different vertical and radial positions as done for the temperature. This should be done in liquid and in vapour at different heat input rates and filling ratios. So, the liquid-vapour interface heat transfer can be properly developed from these experimental evidences and the effect of the bulk temperature gradient on vapour-liquid convective flows can be understood. Hence, more experimental effort should be put on measuring the fluid-dynamics during thermal distribution and self-pressurisation.

The effect of the bulk temperature on the cryogenic boundary layer at side wall is similar to the one in standard fluids. Hence, the natural convection of confined liquid heated at side and at bottom is not expected to significantly change between a non-cryogenic and a cryogenic fluid in stratified medium[37] and homogenous medium. So, the using of these fluids is advantageous for studying these phenomena. However, Seo et al. [105] stated that it is better working with cryogenic liquids. In fact, the use of non-cryogenic liquids should be avoided because it fails in being representative of the heat-mass transfer at interface, of the self-pressurisation and of the thermal stratification in vapour. These phenomena cannot be reproduced in equivalent storage conditions because high heat fluxes are required to make the liquid evaporating, as naturally occurs in cryogenic liquids. The main drawbacks of non-cryogenic liquid can be overcome with liquid nitrogen because the cryogenic conditions are comparable with the one of liquefied natural gas (LNG) and of liquid hydrogen (LH_2). Thermal stratification, (natural and forced) pressure build-up, natural and forced de-stratification, boil-off gas (BOG) generation at steady condition can be properly determined with liquid nitrogen. Hence, the tests can be more representative of the real storage conditions and they can be more flexible for chaining stratification and de-stratification tests, as done by Perez et al. [26]. The normal gravity tests of liquid hydrogen are an important source of experimental data on the thermal distribution in liquid hydrogen storage tanks at different liquid levels and heat inputs. These tests represent the largest set of experimental data on the storage of cryogenic liquids in closed tanks. Experimental data LNG in storage containers are not open-source due to confidentiality. Some experiments of LNG-like mixtures at low heat inputs are freely accessible. They are, however, not enough to cover a wide range of storage conditions. So, the storage model of this thesis should be firstly tested with data of pure cryogenic liquids. Then, data of LNG-like mixtures can be applied to extend this model to cryogenic mixtures.

---

[36] The medium is homogenous when the bulk temperature is uniform.

[37] The medium is stratified when there is a bulk temperature gradient.

3. Selecting the experimental data

The previous review reveals that some of these experimental works give partial information on the storage conditions and on the measured variables. Hence, a method is required to select the experiments that will be used for validation of the model.

Section 3.1 presents the scorecard method used in this thesis. Section 3.2 explains the results and the conclusions.

3.1.Method of scorecard

The method of scorecard is based on the idea of computing the overall score for each experimental work. This score is composed by the rank of the physics studied and of the quality of the experimental work. This score is calculated by giving an elementary score for each category and by applying some coefficient of importance to each phenomenon studied and features of experiments. With this principle, the overall score is calculated with Equation 1.

Equation 1
$$\beta = \sum_{i=1}^{N_P} \alpha_i \cdot \beta_i + \sum_{i=1}^{N_E} \alpha_i \cdot \beta_i$$

β is the overall score, α is the coefficient of importance and β_i is the elementary score. N_P and N_E are respectively the number of phenomena and the number of the features of the experiments.

This elementary scores and the coefficient of importance are defined according to the objectives of the thesis. The values of α and β_i are respectively reported in Table 10 and in Table 11 for the physics and for the experiments. The values of α range between 1 and 2. The value of β_i can be 0 and 1.

Table 10. Values of elementary scores and coefficient of importance for ranking the experiments.

Experiment set-up	α	Score	
Type of liquid	2	Non-Cryogenic Cryogenic	0 1
Varying liquid level	2	NO YES	0 1
Changing heat input	1.5	NO YES	0 1
Internal Geometry	2	NO YES	0 1
External Geometry	1	NO YES	0 1
Changing scale	1.5	NO YES	0 1
Properties of insulation	1	NO YES	0 1
Boundary Condition (Heat Input or BOR)	1.5	NO YES	0 1
External Temperature	1	NO YES	0 1
Varying Initial condition	2	NO YES	0 1

Table 10 shows that the type of liquid, the test at different liquid level, the internal geometry, the initial condition and the availability of the experimental data are the most important features for ranking the quality of the experiments. The type of liquid is so important because only cryogenic liquids can reproduces the interaction between the storage phenomena, as reported in Section 2.2. The tests at different liquid levels are significant because the thermal stratification, thus the self-pressurisation, change a lot with this variable. The behaviour of the cryogenic liquid in SS tanks strongly depends on the initial condition, as reported by Hasan et al.[27] and by Dresar et al.[28]. Hence, the score is zero, if they are not available. One may notice that the elementary score of internal geometry is zero. Without them, the model cannot be compared with the experimental data.

The boundary conditions such as boil-off rate (BOR) or heat input and the tests at different heat input at constant liquid level are classified of second importance. BOR or heat input can be determined from the experimental data of pressure and of temperature profiles (see Section 6 of Chapter 2). The storage phenomena depend on the heat input, but the latter change with the liquid level. Hence, the tests at different heat inputs with constant filling ratio are quite important. The heat fluxes change with the scale of the storage container. So, the tests at different scale have the average value of the coefficient of importance.

The external temperatures can be taken as hypothesis. The properties of the insulation can be estimated with effective heat transfer coefficient, which is computed a mathematical model called BOR model. The assumption of the external temperature changes the value of the effective heat transfer coefficient, but not the heat input rate. Hence, the lowest importance is given to the external temperatures of the storage container, external geometry of the tank, and properties of the thermal insulation.

Table 11. Values of elementary scores and coefficient of importance for ranking the physics.

Phenomena	α	Measurement of evolution in time	Score	
Vapour and Liquid thermal stratification	2	Temperature Profile along the central axis	NO	0
			YES (Partial)	0.5
			YES (Complete)	1
Vapour thermal stratification (steady state)	1	Temperature Profile along the central axis	NO	0
			YES (Partial)	0.5
			YES (Complete)	1
Liquid de-stratification	1	Temperature Profile along the central axis	NO	0
			YES (Partial)	0.5
			YES (Complete)	1
BOG production at steady state	1	BOG flow rate	NO	0
			YES (Partial)	0.5
			YES (Complete)	1
Self-pressurisation	2	Pressure	NO	0
			YES (Partial)	0.5
			YES (Complete)	1
Liquid thermal Expansion	1.5	Liquid Level / Liquid height / Liquid mass	NO	0
			YES (Partial)	0.5
			YES (Complete)	1
Natural convection Liquid / vapour	2	Velocity profile in boundary layer at side wall	NO	0
			YES (Partial)	0.5
			YES (Complete)	1
		Velocity distribution along the centre axis of the tank	NO	0
			YES (Partial)	0.5
			YES (Complete)	1
		Thickness profile of boundary layer at side wall	NO	0
			YES (Partial)	0.5
			YES (Complete)	1
Ageing	2	Evolution of composition	NO	0
			YES (Partial)	0.5
			YES (Complete)	1

The measurements of a variable are defined as partial is the 15 % of the time evolution of this variable is not reported. The definition of complete is applied when this variable is measured during all the time evolution. Vapour/liquid thermal stratification and self-pressurisation are the phenomena to model in this thesis. Hence, their coefficient of importance is high. Liquid/vapour natural convection is almost as important as the thermal stratification and self-pressurisation due to the interaction between fluid-dynamic and these storage phenomena. So, they are highly ranked. The ageing can strongly affect the quality of liquefied natural gas (LNG) as fuel. Hence, it is considered as important as the self-pressurisation. Thermal expansion is of second importance in the natural build-up. So, the coefficient of importance is average. Vapour thermal stratification at steady state, boil-off gas (BOG) generation and de-stratification of liquid are important for modelling the storage behaviour, but they are not the main focus of this thesis. So, their coefficient of importance is low. Heat transfer across the tank, heat transfer outside the tank and forced pressurisation are not considered in this thesis and their coefficient of importance is zero.

Phase change, evaporation and condensation cannot be measured at the liquid and vapour interface, where they occur. Hence, they are not classified. They can be, however, indirectly determined from the values of pressure and of temperature profile.

3.2.Results and conclusions

The results of the score-table method are reported in Table 12. LVS, VSss, LSd, BOG, SP, LTE LVNC and A respectively indicate the liquid-vapour thermal stratification, the vapour stratification at steady state, the liquid thermal de-stratification, the boil-off gas (BOG) production at steady state, the self-pressurisation, the liquid thermal expansion, the liquid-vapour natural convection and the ageing. The words Fl, Le, He, IG, Sc, BC, IC respectively indicate the fluid, the test at different liquid level, the test at different heat input (at constant filling ratio), the internal geometry of the storage container, the test at different scale, the boundary condition and the test at different initial conditions. SoP, SeE and TS respectively mean the score of the physics, the score of the experiment and the total score.

Table 12. Results of the score table method.

Author	LVS	VSss	LSd	BOGss	SP	LTE	LVNC	A	SoP	Fl	Le	He	IG	Sc	BC	IC	SeE	TS
Non - cryogenic																		
Tellep and Harper[100]	0	0	0	0	0	0	0	0	0	0	0	1.5	2	0	1.5	0	5	5
Vliet[101]	0	0	0	0	0	0	0	0	0	0	0	1.5	2	0	1.5	0	5	5
Hurd and Harper[102]	0	0	0	0	0	0	0	0	0	0	0	1.5	2	0	1.5	0	5	5
Shi et al.[103]	0	0	0	0	0	0	0	0	0	0	2	1.5	2	0	1.5	0	7	7
Shi et al.[104]	0	0	0	0	0	0	0	0	0	0	2	1.5	2	0	1.5	0	7	7
Seo et al.[105]	2	0	0	0	0	0	0	0	2	0	2	1.5	2	0	1.5	0	7	9
Liquid nitrogen																		
Barnett[106]	0	0	0	0	0	0	0	0	0	2	2	1.5	2	0	1.5	0	9	9
Huntley[107]	1	0	0	0	2	0	0	0	3	2	0	0	2	0	1.5	0	5.5	8.5
Ludwing et al.[92]	2	0	1	0	0	0	0	0	3	2	0	0	2	0	1.5	0	5.5	8.5
Ludwing and Dreyer[108]	2	0	1	0	0	0	0	0	3	2	0	0	2	0	1.5	0	5.5	8.5
Konopka et al.[95]	2	1	0	0	0	0	0	0	3	2	0	0	2	0	0	0	4	7
Vishnu et al.[109]	0	1	0	0	2	0	0	0	3	2	0	0	2	0	1.5	0	5.5	8.5
Muraleedharan et al.[110]	2	0	0	0	0	0	0	0	2	2	0	0	2	0	1.5	0	5.5	7.5
Liquid hydrogen																		
Siegel[120]	0	0	0	0	0	0	0	0	0	2	0	1.5	2	0	1.5	0	7	7
Barnett et al.[62]	2	0	0	0	0	0	0	0	2	2	2	1.5	2	0	0	0	7.5	9.5
Liebenberg and Eduskuty[112]	2	0	0	0	0	0	0	0	2	2	0	0	2	0	0	0	4	6
Tatom et al.[113]	2	0	0	0	0	0	0	0	2	2	0	0	2	0	0	0	4	6
Bailey and Fearn[114]	2	0	0	0	0	0	0	0	2	2	0	0	2	0	0	0	4	6
Hasan et al.[27]	2	1	0	0	2	0	0	0	5	2	0	0	2	0	1.5	2	7.5	12.5
Dresar et al.[28]	2	1	0	0	2	0	0	0	5	2	2	0	2	0	1.5	0	7.5	12.5
Aydelott[115]	2	1	0	0	2	0	0	0	5	2	2	1.5	2	0	1.5	0	9	14
Aydelott and Spuckler[116]	0	1	0	0	0	0	0	0	1	2	2	0	2	0	1.5	0	9	10
Osipov et al.[70]	0	0	0	0	0	0	0	0	0	2	0	0	2	0	0	0	4	4
Notardonato et al.[118]	2	0	0	0	0	0	0	0	2	2	2	0	2	0	1.5	0	7.5	9.5
Notardonato et al.[90]	2	0	0	0	0	0	0	0	2	2	2	0	2	0	1.5	0	7.5	9.5
Notardonato et al.[117]	2	0	0	0	0	0	0	0	2	2	2	0	2	0	1.5	0	7.5	9.5
Swanger et al.[119]	2	0	0	0	0	0	0	0	2	2	2	0	2	0	1.5	0	7.5	9.5

Table 12. Results of the score table method.

LNG																		
Kountz[83]	2	0	0	0	2	0	0	2	6	2	0	1.5	2	0	0	0	5.5	11.5
Dimopoulos and Frangopoulos[38]	0	0	0	0	0	0	0	1	1	2	0	0	0	0	0	0	2	3
Miana et al.[40]	0	0	0	0	0	0	0	1	1	2	0	0	0	0	0	0	2	3
Qu et al.[49]	0	0	0	0	0	0	0	1	1	2	0	0	2	0	0	0	4	5
Krikkis[47]	0	1	0	0	0	0	0	2	3	2	0	0	2	0	0	0	4	7
Jung et al.[54]	0	0.5	0	1	0	0	0	2	3.5	2	0	0	2	0	0	0	4	7.5

The results with the best score are reported in Table 13. In Table 13, the availability is defined as the ratio between the tests that can be used and the total number of the tests done in by the author of the paper.

Table 13. Authors with the highest score.

Liquid Nitrogen				
Author	**Physics Score**	**Experiments Score**	**Overall Score**	**Availability**
Seo and Jeong[24]	4	7.5	11.5	6 / 6
Kang et al.[25]	4	5.5	9.5	3 / 3
Perez et al.[26]	7	7.5	14.5	1 / 4
Liquid hydrogen				
Author	**Physics Score**	**Experiments Score**	**Overall Score**	**Availability**
Hasan et al.[27]	5	7.5	12.5	2 / 6
Dresar et al.[28]	5	7.5	12.5	2 / 4
Aydelott[29]	5	9	14	3 / 21
Aydelott and Spuckler[30]	5	10.5	14	4 / 4
LNG				
Author	**Physics Score**	**Experiments Score**	**Overall Score**	**Availability**
Al Ghafri et al.[34]	9	11	20	7 / 7
Al Ghafri et al.[3]	9	11	20	4 / 4

Seo and Jeong [24] omitted part of the pressure build-up of experiment 70 % - 2.5W. Kang et al. [25] did not show the vapour temperature profile in all the ullage for the tests 50 % - 21.38 W and 30 % - 16.17 W. So, Seo and Jeong [24] and Kang et al. [25] have the lowest score in the description of physical phenomena, even if they studied self-pressurisation and thermal stratification. Al Ghafri et al. [34] and Al Ghafri et al. [3] studied the ageing and the BOG generation into more of the other authors. So, they have the highest score. Perez et al. [26] did four experimental tests, but pressure and temperature profiles can be extracted from only one of them. Aydelott [29] carried out 40 test, but only 3 tests can be used for validating. Hence, Perez et al. [26] and Aydelott [29] have the lowest availability score.

The other publications have scores too low for being used in this thesis. In fact, they mainly lack of available experimental data of self-pressurisation and of temperature profiles in vapour, and of tests at different liquid level. This experimental works can be used for extending the use of this model, but they are not useful for validating. Al Ghafri et al. [34] and Al Ghafri et al. [3] are not reported and analyzed because LNG is out of the scope of this thesis.

4. Selected experiments

7 sets of experimental data were selected for validating and for developing the storage model in small scale (SS) tanks for pure cryogenic and cryogenic mixtures. These data are obtained at low, medium and high heat fluxes. Kang et al. [25], Seo and Jeong [24] and Perez et al. [26] used liquid nitrogen as working fluid. Liquid hydrogen was applied in the experiments of Hasan et al. [27], Dresar et al. [28], Aydelott [29], Aydelott and Spuckler [30].

Section 4.1 describes the experimental devices and the measuring uncertainties. Section 4.2 presents the procedure used in each experimental work and the experimental tests done.

4.1.Experimental devices and measuring uncertainties

The description of the experimental devices is reported in Table 14 for each experimental work.

Table 14. Experimental device for each experimental work.

Author	Experimental device
Seo and Jeong[24]	The apparatus is composed by an outer storage container and an inner pressurized tank. Both tanks are vertical container with flat roof and flat bottom. The pressurized storage container has a 201 mm diameter and a 213 mm height, and it is suspended by an 850 mm length tubes. The vacuum chamber and the multi-layer insulation minimize heat ingress into the pressurized tank.
Kang et al.[25]	The storage container is made by the outer tank, with 406.4 mm in diameter, with 1200 mm in height and with 8 mm thickness, and by the pressurized tank with 130 mm in diameter, with 800 mm in height and with 5.1 mm in thickness. Both tanks are vertical container with flat roof and flat bottom. The inner and the outer tanks are separated by a vacuum chamber with a vacuum degree of 10^{-6} MPa. The overall thermal conductivity in the vacuum is around 0.024 W/m/K. The pressurized storage container is located above a plastic support. The latter prevents thermal conduction.
Perez et al.[26]	The Dewar contains a stainless steel (SS) can, a copper can, the radiation shield and the BOG cell. The SS can is partially immerged in a bath of liquid nitrogen to assure near-isothermal boundary around the equilibrium cells. The radiation shield is placed between the SS can and the copper can, and a vacuum of 2 kPa is established around the copper can to increases the thermal insulation. Heaters are placed in the copper can to monitor and to provide the heat fluxes to the BOG cell. The latter is vertical cylindrical tank with flat bottom and flat roof, with 200.5 mm diameter and with 213 mm height.
Hasan et al.[27]	The cryogenic storage container is an oblate spheroid with the major diameter of 2.2 m and the ratio major to minor axis is 1.2. Two blankets of multi-layer insulation wrapped the cryogenic tank and, fluid flow and instrumentation lines were routed through liquid hydrogen cold guard to reduce the heat transfer. This cryogenic tank was located in a cylindrical cryo-shroud and it was suspended by fibreglass composite struts. This cryo-shroud and the storage container were placed in a large size vacuum chamber at 10^{-4} Pa.
Dresar et al.[28]	As Hasan et al.[27]
Aydelott[29]	The storage container was made by three concentric spheres: inner, intermediate and outer. The inner tank has a diameter of 23 cm and it contains the liquid hydrogen. The intermediate sphere was a support for the electrical heating coils, which were mounted on its exterior surface. The external sphere was the vacuum jacket and coils with liquid nitrogen were located on its external surface to improve the thermal insulation.
Aydelott and Spuckler[30]	The same spherical tank of Aydelott[29], but the internal diameter is 56 cm.

These experimental devices were equipped with thermocouples, pressure and liquid level sensors, and gas flow meter. The thermocouples were not placed with the same method in each experimental work. Seo and Jeong [24] vertically placed 15 thermocouples near the central axis of the inner storage container. 6 sensors are located in the ullage at intervals of 3 mm and 9 thermocouples are placed at intervals of 20 mm below these six sensors. Kang et al. [25] vertically installed 38 thermocouples at intervals of 20 mm and at distance from wall of 30 mm. The level sensor is installed in the pressurized tank. Perez et al. [26] installed 33 thermocouples and they were distributed on the top and on the bottom lids. Each sensor was located in a different point of the lid and it had a different length to collect the value of temperature at a specific height. Hasan et al. [27] placed the thermocouples at 5%, 10%, 20%, 30%, 40%, 50%, 60%, 70%, 80%, 85%, 87% and 95 % of the filling ratio, in the centre line of the storage container. Dresar et al. [28] used the same spatial distribution of the thermocouples. Aydelott [29] and Aydelott and Spuckler [30] respectively installed 17 and 16 internal transducers of the temperature. Both authors ranked these thermocouples in four. The transducers of each group were placed at different values of the distance from the wall. The values of the distance from the wall for each thermocouple are reported in Table 15 for Aydelott [29] and for Aydelott and Spuckler [30].

Table 15. Positions of the thermocouples the inner sphere of the storage container.

Aydelott [29]					
Group – 1 (near the central axis)					
Transducer	**R - 5**	**R - 4**	**R - 3**	**R - 2**	**R - 1**
Distance from wall [cm]	2.59	4.72	5.59	7.37	11.43
Vertical position along the central axis [cm]	19.1233	17.8044	16.2658	14.5073	11.43
Group – 2 (near the central axis)					
Transducer	**R - 6**	**R - 7**	**R - 9**	**R - 8**	**R - 10**
Distance from wall [cm]	8.3	5.36	3	4.22	1.27
Vertical position along the central axis [cm]	9.8913	8.3527	7.4735	7.0338	5.715
Group – 3 (near the bottom)					
Transducer	**R - 11**	**R - 12**	**R - 15**		
Distance from wall [cm]	1.52	1.02	0.51		
Vertical position along the central axis [cm]	2.6377	2.4179	2.1981		
Group – 4 (near the side wall)					
Transducer	**R - 17**	**R - 18**	**R - 19**	**R - 20**	
Distance from wall [cm]	1.52	1.02	0.51	0.05	
Vertical position along the central axis [cm]	11.6498	10.7706	10.5508	10.1112	
Aydelott and Spuckler [30]					
Group – 1 (near the central axis)					
Transducer	**R - 4**	**R - 3**	**R - 2**	**R - 1**	
Distance from wall [cm]	5	12	20	30	
Vertical position along the central axis [cm]	46.4906	41.2075	34.8679	29.5849	
Group – 2 (near the central axis)					
Transducer	**R - 6**	**R - 7**	**R - 8**	**R - 9**	
Distance from wall [cm]	20	12	5	2.5	
Vertical position along the central axis [cm]	21.6604	15.3208	8.9811	6.3396	
Group - 3 (near the bottom)					
Transducer	**R - 16**	**R - 15**	**R - 12**	**R - 11**	
Distance from wall [cm]	0.5	1.5	2.3	3.8	
Vertical position along the central axis [cm]	24.2545	23.8364	23.4182	23	
Group - 4 (near the side wall)					
Transducer	**R - 20**	**R - 19**	**R - 18**	**R - 17**	
Distance from wall [cm]	0.5	1.5	2.3	3.8	
Vertical position along the central axis [cm]	25.9273	25.5091	25.0909	24.6727	

The measured values of pressure and of temperature profiles are reported in Appendix A. Pressure, temperatures, filling ratio and boil-off gas (BOG) flow were measured with the experimental uncertainties that are reported in Table 16.

Table 16. Experimental uncertainties for each of the selected experimental works.

Author	Pressure	Temperature	Filling ratio	BOG flow
Seo and Jeong[24]	Not specified	Not specified	Not specified	Not specified
Kang et al.[25]	± 0.7 %	± of 0.5 %	Not specified	Not specified
Perez et al.[26]	Below ± 0.01 %	Below ± 1 %	± 1 %	Below ± 0.4 %.
Hasan et al.[27]	±0.01 kPa	Between ±0.1 K and ±0.6 K	±1.9 cm	Below ±0.089 standard m^3/hr
Dresar et al.[28]	As Hasan et al.[27]	As Hasan et al.[27]	As Hasan et al.[27]	As Hasan et al.[27]
Aydelott[29]	Below ±2 psi (0.1378 bar)	±0.2 K	Not specified	Not specified
Aydelott and Spuckler[30]	Not specified	Not specified	Not specified	Not specified

Seo and Jeong [24] and Aydelott and Spuckler [30] did not reported the uncertainties. The uncertainties of Aydelott and Spuckler [30] are similar to the ones of Aydelott [29] because they used the same experimental device, but with different sizes. Kang et al. [25] did not specified the uncertainty of the filling ratio, even if they installed a liquid level sensor. They reported that this sensor is accurate when the liquid density is constant, thus not during the self-pressurisation.

4.2.Experimental procedure and experimental tests

These experimental data were obtained with tests. The experimental procedure is different for each author, but each experimental procedure follows these two main steps: the loading of cryogenic liquid and the stabilisation; the self-pressurisation test. Table 17 presents the details of each experimental procedure.

Table 17. Experimental procedure of each selected experimental work.

Author	Experimental Procedure
Seo and Jeong[24]	Firstly, the liquid nitrogen is filled at the charging level and the heat inputs are adjusted by modifying the vacuum degree. Finally, the valve on the supply line is closed, when the BOG flow is table. The self-pressurisation test is kept for 60 minutes.
Kang et al.[25]	The pressurized tank is filled with liquid nitrogen at 95 % and the venting valves are opened. The BOG is vented and monitored to detect the condition when the evaporation of the liquid is stable. Once the stationary conditions are reached, the venting valves are closed and the self-pressurisation begins. The pressurisation was ended by opening the venting valve, when the pressure reached the value of 1.0 MPa.
Perez et al.[26]	Firstly, continuous vacuum is created between the stainless steel (SS) can and the copper can, and liquid nitrogen was pumped into the Dewar to guarantee cryogenic conditions. During this stage, BOG cell is open to evacuate any vapour. Once the system was stable at 77 K, liquid nitrogen was directly pumped into the BOG cell at the desired level. The BOG cell was opened and it was left reaching the equilibrium at the pressure of 101 kPa. After this, heaters were switched on and the experiment began. Each experiment was composed by a pressure build-up period and by a constant pressure period. In the first stage, the BOG cell was closed and the pressure naturally increased up to the relief value, which was defined by Perez et al.[26]. Then, the relief valve was opened and the BOG was measured.
Hasan et al.[27]	An experimental procedure in two steps: boil-off test and a self-pressurisation test. The BOG test preceded the self-pressurisation test to conditioning the tank and to determine the overall heat input. Liquid hydrogen was filled into the tank up to 95 % of filling ratio. The pressure valve is open until the top section of the storage container is cooled down. Then, this valve is partially closed to reach the operating pressure of 117 kPa. The storage container remained in this configuration until the boil-off rate was stable. When this condition is reached, the self-pressurisation test started. The pressure valve is closed and the liquid hydrogen is drained to 85 % and the pressure dropped to 103 kPa. In the self-pressurisation test with isothermal initial condition, the experiment immediately began because draining liquid caused a fast bulk boiling of the liquid. For the second type of initial

Table 17. Experimental procedure of each selected experimental work.

	condition, the pressure valve was opened until a stable BOG was detected.
Dresar et al.[28]	As Hasan et al. [27]
Aydelott[29]	Firstly, the vacuum was produced between the inner and the outer spheres, and the outer sphere was cooled down by circulating liquid nitrogen in the coils. Then, liquid hydrogen was pumped in the storage container and the venting valves were opened. The heaters maintained the desired heat fluxes and the stable conditions were reached. At zero time, the inner sphere was closed and the tank self-pressurized up to the nominal pressure of 100 psia (6.89476 bar).
Aydelott and Spuckler[30]	As Aydelott [29].

Table 18 reports the name of the tests done by these authors and the values of filling ratio, heat inputs-heat fluxes that are reported in the paper. Aydelott[29] carried out the experiments at high heat fluxes, whose declared values are between 283 W/m² and 191 W/m². Kang et al. [25] and Aydelott and Spuckler [30] respectively did the experiments at medium heat fluxes. the values of these heat fluxes of Kang et al. [25] are between 84 W/m², and 50 W/m². The values of these heat fluxes of Aydelott and Spuckler [30] are between 69 W/m² and 53 W/m², except for Test 4. Seo and Jeong [24], Perez et al. [26], Hasan et al. [27] and Dresar et al. [28] carried out the experimental tests at low heat fluxes. The heat fluxes values of Seo and Jeong [24] are between 7 W/m² and 3.5 W/m², except for Test 3. The value of these fluxes of Perez et al. [26] is around 6 W/m². Hasan et al.[27] did the experimental tests with an heat fluxes of 6.1 W/m². Dresar et al. [28] used an heat fluxes between 5.2 W/m² and 4.6 W/m². The values of heat inputs of Kang et al. [25], Perez et al. [26], Hasan et al. [27] and Dresar et al. [28] were obtained with BOG calorimetry[38]. Seo and Jeong [24] calculated the heat inputs as average value between the values at steady state and at the moment after the self-pressurisation. The value of heat inputs of Test 2 is clearly wrong because this value is not in agreement with the other values of heat inputs.

Table 18. Name of the tests for the selected experimental works filling ratio, heat inputs and heat fluxes that are declared in the papers.

	Seo and Jeong [24]					
Test	1	2	3	4	5	6
Filling ratio	90 %	70 %	70 %	50 %	30 %	10 %
Heat Input	1.6 W	1.7 W	2.5 W	1.2 W	1.0 W	0.8 W

	Kang et al. [25]			**Perez et al. [26]**
Test	1	2	3	1
Filling ratio	80 %	50 %	30 %	88 %
Heat Input	28.84 W	21.38 W	16.17 W	2.2 W
Bottom Input	9.07 W	7.94 W	8.00 W	/
Side Input	19.78 W	13.45 W	8.17 W	/
Upper Input	9.95e-15 W	1.07e-14 W	1.11e-14 W	/

	Hasan et al. [27]		**Dresar et al. [28]**	
Test	1	2	1	2
Filling ratio	83 %	83 %	49 %	29 %
Heat Flux	3.5 W/m²	3.5 W/m²	3.5 W/m²	3.5 W/m²
Heat Input	47.42 W	47.42 W	47.42 W	47.42 W
Initial condition	Steady BOG	Isothermal	Steady BOG	Steady BOG

---

[38] BOG calorimetry is technique that computes the heat inputs from the stationary values of boil-off gas flow rate. These values are measured with a gas flow meter.

Table 18. Name of the tests for the selected experimental works filling ratio, heat inputs and heat fluxes that are declared in the papers.

Aydelott [29]			
Test	1	2	3
Filling ratio	76.5 %	48.9 %	34.9 %
Heat Flux	229 W/m²	204 W/m²	189 W/m²
Heat Input	38.0576 W	33.9028 W	31.41 W

Aydelott and Spuckler [30]				
Test	1	2	3	4
Filling ratio	79.8 %	48.9 %	31.6 %	54.2 %
Heat Flux	69 W/m²	60 W/m²	53 W/m²	203 W/m²
Heat Input	67.9790 W	59.1122 W	52.2158 W	199.9963 W

Kang et al. [25] recorded the values of BOG and these values were used to compute the heat inputs at steady state. The values of heat inputs from this technique were compared with the thermal results of the Finite Element Analysis (FEA). Almost the same values were obtained with the experimental technique and with the FEA. Heat fluxes at the bottom, computed with this numerical technique, indicate a value is around 600 W/m². As it is described by Kang et al. [25], there is not any manipulations of the device that can cause this value of the heat flux. Hence, this technique fails in determine this heat flux.

Seo and Jeong [24] and Aydelott and Spuckler [30] did one test at different heat inputs with fixed filling ratio. Hasan et al. [27] carried out experiments at different initial conditions: at steady BOG and at isothermal liquid and vapour at the saturation temperature. All the authors tested the self-pressurisation and the thermal stratification at different liquid levels, thus heat inputs rate.

5. Computing interface temperatures, filling ratios and other variables

The variables such as interface temperatures, filling ratios, boil-off gas (BOG) temperature and average temperatures are important for validating the storage model. The values of these variables were, however, not reported in the papers. So, these values can be deduced and calculated from the measured values of temperature profiles and of pressure, and form the thermo-physical properties. These properties are computed at the average liquid and vapour temperatures, and at the liquid and ullage pressure. REFPROP®[39] is used for computing these properties.

Section 5.1, 5.2, 5.3 and 5.4 describe the method of computing the interface temperature, the BOG temperatures, the average temperatures and the filling ratios, respectively.

5.1. Interface temperatures

Direct measures of the vapour-liquid interface are usually inaccurate because placing the thermocouples at the exact position of the interface is difficult. Some evidences has, however, proved that the vapour-liquid interface is at quasi-equilibrium conditions [23]. So, it can be assumed that the interface is at thermodynamic equilibrium, as done in literature [28], [45]. For pure cryogenic liquids, the vapour-liquid interface is at saturation. So, the temperature can be computed with the saturation temperature relation at the ullage pressure. This relation is obtained with the thermodynamic model based on Helmholtz free energy, as it is implemented in REFPROP®.

The values of the interface temperature are reported in Table 19 at different times. These values are presented for the different experiments of each series of experimental data.

Table 19. Values of the interface temperatures for the selected experimental works.

Seo and Jeong - 2010					
Test 1		**Test 2**		**Test 3**	
Time [m]	**T [K]**	**Time [m]**	**T [K]**	**Time [m]**	**T [K]**
0	77.243	0	77.205	0	77.205
20	77.584	20	77.541	20	78.884
40	77.71967	40	77.680	40	79.683
60	77.830	60	77.818	60	80.447
Test 4		**Test 5**		**Test 6**	
Time [m]	**T [K]**	**Time [m]**	**T [K]**	**Time [m]**	**T [K]**
0	77.205	0	77.205	0	77.192
20	78.127	20	78.021	20	77.9265
40	78.581	40	78.468	40	78.454
60	78.935	60	78.845	60	78.966
Kang et al. - 2018					
Test 1		**Test 2**		**Test 3**	
Time [m]	**T [K]**	**Time [m]**	**T [K]**	**Time [m]**	**T [K]**
0	77.601	0	77.601	0	77.601
20	86.528	20	84.313	30	83.896
40	92.599	40	89.222	60	90.0776
60	97.657	60	93.779	90	95.567
80	102.239	80	97.983	120	100.551
87	103.947	109	103.553	140	103.765
Perez et al. - 2021					
Test 1					
Time [m]			**T [K]**		

---

[39] REFPROP is software to compute the thermo-physical properties and the transport properties of pure fluid and mixtures. This software is developed by NIST. [121]

Table 19. Values of the interface temperatures for the selected experimental works.

0	77.829
120	79.5438
240	80.913

Hasan et al. - 1991

Test 1		**Test 2**	
Time [m]	**T [K]**	**Time [m]**	**T [K]**
0	20.327	0	20.3276
240	21.115	240	21.331
720	22.548	720	22.815

Dresar et al. - 1992

Test 1		**Test 2**	
Time [m]	**T [K]**	**Time [m]**	**T [K]**
0	20.327	0	20.327
240	21.144	240	21.325
720	22.196	720	22.739

Aydelott - 1967

Test 1		**Test 2**		**Test 3**	
Time [m]	**T [K]**	**Time [m]**	**T [K]**	**Time [m]**	**T [K]**
0	20.856	0	20.856	0	20.856
1	23.845	1	23.197	1	22.776
2	25.367	2	24.586	2	23.971
3	26.704	4	26.791	4	26.007
4	27.954	6.5	29.177	6.5	28.171

Aydelott and Spuckler - 1969

Test 1		**Test 2**	
Time [m]	**T [K]**	**Time [m]**	**T [K]**
0	20.397	0	20.393
5	22.202	5	21.906
15	24.433	15	23.635
25	26.194	30	25.656
35	27.827	40	26.915
Test 3		**Test 4**	
Time [m]	**T [K]**	**Time [m]**	**T [K]**
0	20.318	0	20.499
5	21.781	2.5	22.897
15	23.326	5	24.219
30	25.253	10	26.267
40	26.391	15	27.993

The values in Table 19 are used to compute the average temperatures in liquid and in vapour. The interface temperature increases in time for all the experimental series, because of the dynamic condensation blocking effect. When pressure builds-up, the condensation releases thermal energy at the interface and the temperature increases, maintaining the equilibrium condition at the interface.

5.2. BOG temperatures

The boil-off gas (BOG) receives heat from the dry walls of the storage container, when it moves from the interface to the roof. The BOG temperature is the temperature at the exit of the ullage of the storage container. The BOG temperature is computed from the experimental temperature profile. A linear profile is assumed between the last experimental point and the venting valve of the storage container. This linear relation is described by Equation 2.

Equation 2
$$T_{BOG} = \frac{T_N - T_{N-1}}{x_N - x_{N-1}} \cdot (100 - x_N) + T_N$$

T_{BOG} is the BOG temperature, and T_N and T_{N-1} are respectively the experimental values of the vapour temperature at the last and second-last point. x_N and x_{N-1} are respectively the last and second-last measurement points, as relative values respect to the internal height of the storage container.

The values of the BOG temperature are reported in Table 20 at different times, for all the selected experimental works. These values are used to calculate the average temperatures in liquid and in vapour.

Table 20. Values of the BOG temperatures for the 7 series of experimental data.

Seo and Jeong - 2010					
Test 1		**Test 2**		**Test 3**	
Time [m]	**T [K]**	**Time [m]**	**T [K]**	**Time [m]**	**T [K]**
0	78.026	0	81.536	0	85.527
20	78.997	20	82.493	20	85.957
40	78.252	40	82.521	40	87.131
60	79.047	60	83.232	60	87.989
Test 4		**Test 5**		**Test 6**	
Time [m]	**T [K]**	**Time [m]**	**T [K]**	**Time [m]**	**T [K]**
0	84.579	0	86.388	0	87.262
20	84.672	20	86.246	20	88.925
40	85.070	40	86.497	40	88.277
60	84.772	60	87.197	60	89.519
Kang et al. - 2018					
Test 1		**Test 2**		**Test 3**	
Time [m]	**T [K]**	**Time [m]**	**T [K]**	**Time [m]**	**T [K]**
0	121.261	0	166.082	0	156.157
20	128.931	20	167.826	30	162.362
40	130.732	40	174.345	60	173.890
60	133.128	60	184.952	90	182.328
80	134.391	80	189.203	120	196.029
87	135.816	109	207.654	140	211.639
Perez et al. - 2021					
Test 1					
Time [m]	**T [K]**				
0	79.202				
120	81.124				
240	82.575				
Hasan et al. - 1991					
Test 1		**Test 2**			
Time [m]	**T [K]**	**Time [m]**	**T [K]**		
0	25.938	0	20.197		
240	48.069	240	47.346		
720	49.314	720	46.871		
Dresar et al. - 1992					
Test 1		**Test 2**			
Time [m]	**T [K]**	**Time [m]**	**T [K]**		
0	28.248	0	28.188		
240	50.397	240	49.867		
720	54.718	720	57.168		
Aydelott - 1967					
Test 1		**Test 2**		**Test 3**	
Time [m]	**T [K]**	**Time [m]**	**T [K]**	**Time [m]**	**T [K]**
0	58.0276	0	89.977	0	97.926
1	125.062	1	116.150	1	125.789
2	167.637	2	134.796	2	143.268
3	203.503	4	178.647	4	179.746
4	224.637	6.5	216.269	6.5	218.128

Table 20. Values of the BOG temperatures for the 7 series of experimental data.

Aydelott and Spuckler - 1969			
Test 1		**Test 2**	
Time [m]	**T [K]**	**Time [m]**	**T [K]**
0	38.621395	0	59.164
5	83.6219808	5	79.366
15	134.49098	15	108.137
25	157.478458	30	137.588
35	179.693745	40	154.031
Test 3		**Test 4**	
Time [m]	**T [K]**	**Time [m]**	**T [K]**
0	84.802	0	62.678
5	98.573	2.5	98.113
15	119.120	5	122.353
30	146.332	10	160.352
40	157.193	15	192.575

The BOG temperature increases in time and with the reduction of the filling ratio. During the self-pressurisation, part of the heat transferred at the dry walls of the tank is accumulated as sensible heat. As time passes, the sensible heat is progressively accumulated, thus increasing the temperature. This accumulation increases with the increment of the ullage volume because surface area at the dry walls increases.

5.3. Average temperatures

The average temperatures of vapour and of the liquid are important for estimating the heat leakages and for comparing the model with the experimental data. The heat leakages are determined from the enthalpies variation between the beginning and the end of the self-pressurisation. The values of average temperature compute the specific enthalpies of vapour and of liquid. The values of the average temperatures are required for comparing the results of the homogeneous model with the experimental data.

The average temperatures of liquid and of vapour are computed with the numerical integrations. This integration is based on the trapezoidal rule[40]. These temperatures are respectively determined with Equation 3 and with Equation 4.

Equation 3

$$\bar{T}^L = \frac{1}{LF}\cdot\left\{dx_1\cdot T_1^L + \sum_{i=2}^{N_{ex}^L}\left[\left(T_i^L + T_{i-1}^L\right)\cdot\frac{dx_i}{2}\right] + \left[\left(T^I + T_{N_L}^L\right)\cdot\frac{dx_{N_{ex}^L+1}}{2}\right]\right\}$$

Equation 4

$$\bar{T}^V = \frac{1}{100-LF}\cdot\left\{\left[\left(T^I + T_1^V\right)\cdot\frac{dx_1}{2}\right] + \sum_{i=2}^{N_{ex}^V}\left[\left(T_i^V + T_{i-1}^V\right)\cdot\frac{dx_i}{2}\right] + \left[\left(T_{BOG} + T_{N_{ex}^V}^V\right)\cdot\frac{dx_{N_{ex}^V+1}}{2}\right]\right\}$$

N_{ex}^L and N_{ex}^V are respectively the number of experimental points in the liquid and in the vapour. dx_i is the absolute distance between two experimental points, x_i and $x_{(i-1)}$. dx_1 is the absolute distance between the first point of liquid and the bottom in Equation 3, and it is the absolute distance between the liquid level and the first point of vapour in Equation 4. $dx_{N_{ex}^L+1}$ is the absolute distance between the liquid level and the last point of the liquid. $dx_{N_{ex}^V+1}$ is the absolute distance between the roof and the last point of the vapour. LF is the liquid level.

---

[40] Trapezoidal rule is a numerical integration method where the integral is approximated with the area below the curve.

The values of the liquid and vapour average temperatures are reported in Table 21 as function of time.

Table 21. Values of the average liquid and vapour temperatures for the 7 series of experimental data.

Seo and Jeong - 2010								
Test 1			**Test 2**			**Test 3**		
Time [m]	$\bar{T}^L$ [K]	$\bar{T}^V$ [K]	**Time [m]**	$\bar{T}^L$ [K]	$\bar{T}^V$ [K]	**Time [m]**	$\bar{T}^L$ [K]	$\bar{T}^V$ [K]
0	77.025	77.412	0	77.038	78.908	0	77.143	80.488
20	77.218	78.150	20	77.220	79.504	20	77.612	81.695
40	77.318	78.135	40	77.327	79.846	40	77.889	82.558
60	77.480	78.535	60	77.524	80.196	60	78.201	83.340
Test 4			**Test 5**			**Test 6**		
Time [m]	$\bar{T}^L$ [K]	$\bar{T}^V$ [K]	**Time [m]**	$\bar{T}^L$ [K]	$\bar{T}^V$ [K]	**Time [m]**	$\bar{T}^L$ [K]	$\bar{T}^V$ [K]
0	76.931	80.474	0	76.841	81.056	0	76.768	81.687
20	77.040	81.003	20	77.091	81.797	20	77.221	82.528
40	77.228	81.411	40	77.219	82.207	40	77.652	83.152
60	77.434	81.895	60	77.628	82.705	60	78.078	83.533

Kang et al. - 2018								
Test 1			**Test 2**			**Test 3**		
Time [m]	$\bar{T}^L$ [K]	$\bar{T}^V$ [K]	**Time [m]**	$\bar{T}^L$ [K]	$\bar{T}^V$ [K]	**Time [m]**	$\bar{T}^L$ [K]	$\bar{T}^V$ [K]
0	77.033	100.612	0	77.684	121.156	0	77.638	116.614
20	79.836	110.916	20	80.853	128.224	30	82.422	126.122
40	82.129	115.426	40	83.422	135.113	60	86.893	135.706
60	84.652	118.488	60	85.764	141.939	90	91.287	143.102
80	86.361	120.289	80	88.614	146.463	120	95.489	151.435
87	87.101	121.240	109	92.253	156.537	140	98.489	159.448

Perez et al. - 2021		
Test 1		
Time [m]	$\bar{T}^L$ [K]	$\bar{T}^V$ [K]
0	77.7611	78.352
120	78.526	80.439
240	79.560	81.680

Hasan et al. - 1991					
Test 1			**Test 2**		
Time [m]	$\bar{T}^L$ [K]	$\bar{T}^V$ [K]	**Time [m]**	$\bar{T}^L$ [K]	$\bar{T}^V$ [K]
0	20.245	22.827	0	20.351	20.246
240	20.650	33.833	240	20.737	33.776
720	21.405	35.643	720	21.492	34.476

Dresar et al. - 1992					
Test 1			**Test 2**		
Time [m]	$\bar{T}^L$ [K]	$\bar{T}^V$ [K]	**Time [m]**	$\bar{T}^L$ [K]	$\bar{T}^V$ [K]
0	20.132	23.5003	0	20.097	23.668
240	20.712	33.483	240	20.833	33.162
720	21.691	36.743	720	21.986	39.038

Aydelott - 1967								
Test 1			**Test 2**			**Test 3**		
Time [m]	$\bar{T}^L$ [K]	$\bar{T}^V$ [K]	**Time [m]**	$\bar{T}^L$ [K]	$\bar{T}^V$ [K]	**Time [m]**	$\bar{T}^L$ [K]	$\bar{T}^V$ [K]
0	20.708	32.212	0	20.322	50.147	0	20.586	48.901
1	21.635	71.223	1	21.43	73.620	1	21.435	74.543
2	22.007	91.459	2	22.139	89.487	2	22.443	88.807
3	22.522	104.762	4	23.458	113.817	4	23.773	108.551
4	23.127	113.832	6.5	25.031	132.092	6.5	26.496	125.045

Aydelott and Spuckler - 1969	
Test 1	**Test 2**

Table 21. Values of the average liquid and vapour temperatures for the 7 series of experimental data.

Time [m]	$\bar{T}^L$ $[K]$	$\bar{T}^V$ $[K]$	Time [m]	$\bar{T}^L$ $[K]$	$\bar{T}^V$ $[K]$
0	20.903	29.474	0	20.784	40.038
5	21.180	55.865	5	21.349	58.127
15	21.853	82.699	15	22.207	79.0133
25	22.948	94.889	30	23.378	97.737
35	23.034	103.760	40	24.003	105.295
	Test 3			**Test 4**	
Time [m]	$\bar{T}^L$ $[K]$	$\bar{T}^V$ $[K]$	**Time [m]**	$\bar{T}^L$ $[K]$	$\bar{T}^V$ $[K]$
0	19.554	53.343	0	21.055	39.027
5	21.512	67.751	2.5	21.872	68.011
15	21.818	84.657	5	22.577	86.877
30	22.614	100.875	10	23.952	112.637
40	22.954	107.822	15	24.897	131.441

As reported in Table 21, the values of the average temperatures in liquid and in vapour increase in time due to the accumulation of heat. The liquid average temperatures in the liquid do not change with the liquid level, thus heat inputs, for low heat fluxes [9], [22], [23]. For medium [26], [43] and high heat fluxes [29], these variables increases reducing the liquid level, thus lowering the thermal capacity[41]. The average temperatures of the vapour increase when liquid level decreases. This behaviour does not always occur when the filling ratio is below 50 %. In fact, the temperature of the vapour does not increase a lot or it is slightly reduced with the filling ratio. As the volume of the vapour increases, the dry surface areas increases and heat enters in the ullage with a flow that is higher than the one at high filling ratio. The heat transfer coefficient with the dry walls is, however, reduced and the thermal capacity of the vapour is increased. These two factors balance the effect of the dry surface area. In Test 4, 5 and 6 of Seo and Jeong [24], the liquid temperature is strongly sub-cooled. The degree of sub-cooling increases with the reduction of the liquid level.

5.4. Filling ratios

The initial filling ratio is given in each experiment of the seven selected experimental publications. The time-evolution of this variable cannot be obtained from the papers of the selected experimental works, except for Seo and Jeong [24] and Perez et al. [26]. These authors reported the position of liquid interface, thus the filling ratio, in their graphs of the temperature profile evolution. The values of filling ratio indicated in the graphs do not coincide with the values declared in the papers. In fact, Seo and Jeong [24] respectively reported the values of 92.2 %, 71.8 %, 70.9 %, 51.5 %, 27.7 % and 9.6 % for the Test 1, 2, 3, 4, 5 and 6. Perez et al. [26] indicated a liquid level around 86 %, even if the reference value is 88 %. Hence, this inconsistency in filling ratio values suggests finding a procedure to estimate the initial liquid level and its time-evolution.

5.4.1. Approach to compute the filling ratio

At the beginning of the test, the liquid is homogeneous and the fluctuations of the measured values make the determination of the initial filling ratio almost impossible. Due to these fluctuations, the temperature profiles are more precise at the end of the pressurisation. so, the proposed method to compute the filling ratio is based two hypotheses:

a) The mass conservation laws can compute the evolution of the filling ratio;
b) Temperature profile at the end of pressurisation gives the exact value of the filling ratio.

---

[41] Thermal capacity is the product between the mass and the specific heat at constant pressure. This variable indicates the capacity of accumulating heat.

The mass balance equation in a closed tank is described by Equation 5.

Equation 5 $$(\rho^L \cdot V^L)|_{t_i} + (\rho^V \cdot V^V)|_{t_i} = (\rho^L \cdot V^L)|_{t_{i-1}} + (\rho^V \cdot V^V)|_{t_{i-1}}$$

ρ is the density and V is the volume. The exponents "L" and "V" respectively indicate the liquid and the vapour. t_i is the current time and t_{i-1} is the previous time step. Equation 5 implicitly considers evaporation-condensation at the interface and the variation of the liquid volume due to the thermal expansion[42]. This expansion is caused by the accumulation of sensible heat in the liquid. The method to compute the liquid level is reported in Appendix D.

5.4.2. Results of the filling ratio

Table 22 describes the values of the filling ratio as function of the time for the selected experimental work. These data are computed with the algorithm of Appendix D.

Table 22. Values of the filling ratio for the selected experimental works.

Seo and Jeong - 2010					
Test 1		**Test 2**		**Test 3**	
Time [m]	**LF [%]**	**Time [m]**	**LF [%]**	**Time [m]**	**LF [%]**
0	93.780	0	75.649	0	73.608
20	93.881	20	75.722	20	73.772
40	93.933	40	75.765	40	73.87
60	94.019	60	75.848	60	73.987
Test 4		**Test 5**		**Test 6**	
Time [m]	**LF [%]**	**Time [m]**	**LF [%]**	**Time [m]**	**LF [%]**
0	55.6204	0	36.555	0	23.998
20	55.626	20	36.593	20	24.048
40	55.6715	40	36.6136	40	24.085
60	55.726	60	36.682	60	24.117

Kang et al. - 2018					
Test 1		**Test 2**		**Test 3**	
Time [m]	**LF [%]**	**Time [m]**	**LF [%]**	**Time [m]**	**LF [%]**
0	79.638	0	50.010	0	30.791
20	80.780	20	50.753	30	31.442
40	81.719	40	51.353	60	32.006
60	82.809	60	51.878	90	32.557
80	83.472	80	52.576	120	33.106
87	83.770	109	53.483	140	33.588

Perez et al. - 2021	
Test 1	
Time [m]	**LF [%]**
0	84.568
120	84.918
240	85.412

Hasan et al. - 1991			
Test 1		**Test 2**	
Time [m]	**LF [%]**	**Time [m]**	**LF [%]**
0	75.242	0	74.972
240	75.778	240	75.491
720	76.682	720	76.363

Dresar et al. - 1992			
Test 1		**Test 2**	
Time [m]	**LF [%]**	**Time [m]**	**LF [%]**

---

[42] Thermal expansion is the variation of the volume due to the increment of the internal temperature.

Table 22. Values of the filling ratio for the selected experimental works.

0	49.372	0	34.657
240	49.761	240	34.972
720	50.233	720	35.216

Aydelott - 1967					
Test 1		**Test 2**		**Test 3**	
Time [m]	**LF [%]**	**Time [m]**	**LF [%]**	**Time [m]**	**LF [%]**
0	62.432	0	48.052	0	24.896
1	63.131	1	48.535	1	25.032
2	63.496	2	48.861	2	25.206
3	63.679	4	49.512	4	25.352
4	64.096	6.5	50.322	6.5	25.996

Aydelott and Spuckler - 1969			
Test 1		**Test 2**	
Time [m]	**LF [%]**	**Time [m]**	**LF [%]**
0	72.479	0	51.291
5	72.779	5	51.604
15	73.443	15	52.077
25	74.751	30	52.745
35	74.536	40	53.068
Test 3		**Test 4**	
Time [m]	**LF [%]**	**Time [m]**	**LF [%]**
0	34.086	0	50.968
5	34.680	2.5	51.412
15	34.691	5	51.821
30	34.809	10	52.684
40	34.791	15	53.256

The values calculated at Test 5 and Test 6 of Seo and Jeong[24] indicate that this method does not work for strong sub-cooled liquid, at low filing ratio and low heat fluxes. At these conditions, the hypothesis b) of Section 5.4.1 of Chapter 2 cannot be applied because the fluctuations of the measured variables are strong. Hence, the algorithm of Appendix D is modified by assuming that the exact value of the initial filling ratio is the one reported in the paper, thus 27.7 % and 9.6 %, for Test 5 and Test 6 respectively. The mass conservation law and the structure of the algorithm of Appendix D do not change. Table 23 reports the new values of the filling ratio at Test 5 and at Test 6 of Seo and Jeong [24].

Table 23. Values of the filling ratio at Test 5 and at Test 6 of Seo and Jeong**[24]**.

Test 5		**Test 6**	
Time [m]	**LF [%]**	**Time [m]**	**LF [%]**
0	27.791	0	9.684
20	27.794	20	9.670
40	27.792	40	9.665
60	27.840	60	9.657

As indicated in Table 22 and Table 23, the filling ratio increases in time due to the thermal expansion, except for Test 6 of Seo and Jeong [24]. In closed storage mode, the net evaporation is strongly reduced and sensible heat is accumulated in the liquid. The liquid thermally expands and, at the same time, it loses masses. So, thermal expansion and net evaporation are in competition. The values in Table 22 clearly indicate that the liquid level always increase during self-pressurisation. Hence, this increment is caused by thermal expansion, which is higher than the evaporation of liquid.

6. Estimation of the heat input from experimental data

The boundary conditions of the storage container are crucial to properly model the behaviour of cryogenic liquid. The boundary conditions are the environmental temperature and pressure, and the heat leakage. In this thesis, the environmental conditions are defined: temperature is 298.15 K and pressure is 1 atm. Hence, the heat input is a boundary condition to be determined. In each of the seven experimental works, the values of heat leakage are reported. Wang et al. [122] computed the heat input of Test 1 of Perez et al. [122] and they, showed that the reported values are fake. So, heat input must be calculated for each experimental works.

Three methods can be used for estimating the heat input and they are: the calorimetric approach, the steady state approach, the method of Wang et al. [122] and the overall enthalpy variation method, which is proposed in this thesis. The calorimetric and the steady state approach require the values of boil-off gas (BOG) flow at steady state. These values are not reported in the selected experimental works. So, these two methods cannot be used and the heat inputs are estimated during the self-pressurisation, even if the temperatures change in time. The method of Wang et al. [122] can compute the heat inputs during the stage of natural pressure build-up, from the experimental data. This approach is not rigorous due to the estimation of the thermal expansion coefficient of the liquid and the consistency of the conservation laws. As consequence, the overall enthalpy variation method is developed and used in this thesis.

Section 6.1 describes the new method for estimating the heat inputs. Section 6.2 presents the results and Section 6.3 discusses these results. Section 6.4 presents the conclusion.

6.1. Overall enthalpy variation approach

A new method was developed in this work to compute the overall heat input and this method is called *overall enthalpy variation approach.* This method assumes that the storage container is a closed[43] isochoric[44] system. Hence, the first principle of the thermodynamics for this system can be applied, by neglecting the work, and it is expressed by Equation 6.

Equation 6
$$\int_{t_0}^{t_F} \dot{Q}(t)dt = \Delta\widetilde{H}$$

$\dot{Q}(t)$ is the heat inputs. $\Delta\widetilde{H}$ is the enthalpy variation between the beginning (t_0) and the end of the self-pressurisation (t_F). Hence, it is the difference in the overall enthalpy[45] between the time t_F and t_0. The variation of the enthalpy can be computed with Equation 7.

Equation 7
$$\Delta\widetilde{H} = \widetilde{H}_{t_F} - \widetilde{H}_{t_0} = \left[m^L \cdot \tilde{h}^L + m^V \cdot \tilde{h}^V\right]_{t_F} - \left[m^L \cdot \tilde{h}^L + m^V \cdot \tilde{h}^V\right]_{t_0}$$

$\tilde{h}$ is the specific enthalpy[46] and m is the mass[47]. The exponents "L" and "V" indicate the liquid and the vapour, respectively. The time integrals of the heat inputs can be solved with the theorem of the mean

---

[43] Close system is system where only energy can enter and exit.

[44] Isochoric means that the volume is constant.

[45] The overall enthalpy is the sum of the liquid and vapour enthalpies.

[46] The specific enthalpy indicates the enthalpy per unit of mass. For a pure fluid, this variable depends on the temperature and on the pressure only. For mixtures, this variable depends on the composition too.

[47] The mass is the product between the volume and the density.

integral value[48]. Hence, the first principle of the thermodynamics for isochoric closed system (Equation 6) can be written with Equation 8.

Equation 8 $$\bar{\dot{Q}} \cdot \Delta t = \left[m^L \cdot \tilde{h}^L + m^V \cdot \tilde{h}^V\right]_{t_F} - \left[m^L \cdot \tilde{h}^L + m^V \cdot \tilde{h}^V\right]_{t_0}$$

$\bar{\dot{Q}}$ is the average heat input during the self-pressurisation and Δt is the pressurisation period. From Equation 8, the average heat input can be computed and the overall average heat fluxes can be estimated with Equation 9.

Equation 9 $$\bar{\dot{q}} = \frac{\bar{\dot{Q}}}{A^{TOT}}$$

$\bar{\dot{q}}$ is the average heat fluxes during the self-pressurisation and A^{TOT} is the overall internal surface of the storage container (see Appendix B).

6.2.Results of the overall enthalpy variation approach

The values of the heat inputs, of heat fluxes and of the self-pressurisation time are reported in Table 24 for all the experimental works considered in these thesis.

Table 24. Values of heat inputs, heat fluxes and self-pressurisation period.

	Seo and Jeong - 2010					
Test	**1**	**2**	**3**	**4**	**5**	**6**
$\bar{\dot{Q}}\ [W]$	1.3308	1.1635	2.6184	1.0339	0.9183	0.7119
$\bar{\dot{q}}\ [W/m^2]$	6.7223	5.8773	13.2265	5.2225	4.6387	3.5962
$\Delta t\ [min]$	60	60	60	60	60	60

	Kang et al. - 2018			***Perez et al. - 2021***
Test	**1**	**2**	**3**	**1**
$\bar{\dot{Q}}\ [W]$	29.912	23.856	17.886	1.201
$\bar{\dot{q}}\ [W/m^2]$	84.671	67.528	50.629	6.088
$\Delta t\ [min]$	87	109	140	240

	Hasan et al. - 1991		***Dresar et al. - 1992***	
Test	**1**	**2**	**1**	**2**
$\bar{\dot{Q}}\ [W]$	82.966	83.081	70.300	62.591
$\bar{\dot{q}}\ [W/m^2]$	6.1243	6.1328	5.1894	4.6203
$\Delta t\ [min]$	720	720	720	720

	Aydelott - 1967		
Test	**1**	**2**	**3**
$\bar{\dot{Q}}\ [W]$	48.182	46.465	33.680
$\bar{\dot{q}}\ [W/m^2]$	289.92	279.59	202.66
$\Delta t\ [min]$	4	6.5	6.5

	Aydelott and Spuckler - 1969			
Test	**1**	**2**	**3**	**4**
$\bar{\dot{Q}}\ [W]$	75.582	73.098	56.363	242.24
$\bar{\dot{q}}\ [W/m^2]$	76.718	74.196	57.209	245.87
$\Delta t\ [min]$	35	40	40	15

As indicated in Table 24, the heat inputs and the heat fluxes decrease with the reduction of the liquid level, except for Test 3 of Seo and Jeong [24] and the Test 4 of Aydelott and Spuckler [30]. These tests were done by intentionally modifying the boundary conditions of the storage containers, thus the heat inputs.

---

[48] The theorem of the mean integral value states that the integral of function of f in the interval Δx is equal to the product of the mean value and the interval.

6.3. Discussion of the results

The heat inputs and the heat fluxes have the same behaviour because the internal surface of the storage container does not change with the filling ratio. Hence, the only the behaviour of the heat inputs are discussed.

The heat input can be computed as the sum of the product between the liquid heat fluxes and liquid surface areas, and of the product between the vapour heat fluxes and vapour surface areas, as described by Equation 10.

Equation 10
$$\bar{\dot{Q}} = \dot{q}^L \cdot A^L + \dot{q}^V \cdot A^V$$

$\dot{q}$ is the heat fluxes. The exponents L and V are respectively the liquid and the vapour. A^L and A^V are respectively the wetted and dry surface areas, computed as reported in Appendix B.

As the liquid level decreases, the surface area of the wetted walls becomes low. The difference in temperature between the liquid and the wetted walls is usually small due to the high transport properties. So, the liquid heat fluxes are slightly reduced when the filling ratio become low. As the liquid level becomes low, the dry wall surfaces area is increased, compensating the reduction of the liquid surface areas. Because the overall heat input reduces, the heat fluxes in the vapour must lower. As the liquid level is reduced, the evaporation rates decreases and the temperature gradient in the bulk of the vapour increases. Hence, the rising flow rate is reduced in the boundary layer. As consequence, the speed in the boundary layer is lower and the heat transfer rate too. The reduction of $\dot{q}_V$ with the decrement of the filing ratio can be caused by the reduction of the average heat transfer coefficient between the vapour and the tank's walls.

6.4. Summary and conclusions

The boundary conditions are fundamental to determine the behaviour of the stored cryogenic liquid. The heat input is the main variable to consider and it can be determined with calorimetric method, the method of Wang et al. [122] and with the overall enthalpy variation approach. The first method requires the experimental values of boil-off gas (BOG) flow at steady state. These values are, however, not available, hence this method cannot be used. The method of Wang et al. [122] can estimate the heat inputs during the self-pressurisation. The method is, however, sloppy because the overall conservation of energy is not respected. Hence, the overall enthalpy variation approach is proposed. This approach computes the heat leakage from the overall enthalpy variation during the self-pressurisation. The enthalpy is estimated with experimental values of pressure and of temperature profile, and with the calculated values of liquid level and of average temperatures. As proved by Wang et al. [122], the calculated values are very different from the values reported in the papers, except for Kang et al. [25]. So, this confirms the effort of computing the heat input, instead of relying on the reference values. Moreover, the calculated values indicate that the heat leakage strongly decreases with the lowering the filling ratio. This is caused by the reduction of the heat transfer coefficient between the dry walls and the vapour.

The discussion of the results reveals that the repartition of the heat into the storage containers is not related to the surface area. The evaluation of thermal distribution is fundamental to properly model the storage of cryogenic liquids. Hence, a thermal analysis is required to determine which factors cause the thermal distribution, and it is done in Chapter 7.

7. Analysis of the thermal distribution: experimental approach

The heat inputs and their distribution in the storage tank control the storage phenomena. Section 6 shows that the heat fluxes in vapour determine the heat inputs in the storage container, alternating the thermal distribution. Hence, a thermal analysis is required to evaluate how these heat fluxes change with the storage conditions such as liquid levels and heat inputs, and between the steady state and self-pressurisation stage. At this stage of the development of the storage model, only the experimental data can be used because the heat transfer model is not validated yet, even if this model can theoretically predict the thermal distribution. The heat transfer model is developed in the next chapters, using the results of the thermal distribution analysis. Hence, an approach with experimental data is developed with the goal of determining these heat fluxes, even if a theoretical method[123] exists. This approach is called *experimental approach of thermal analysis*.

Section 7.1 explains the hypotheses, the mathematical and the pseudo-variables. Section 7.2 describes the equations of the pseudo-variables. Section 7.3 presents the results. Section 7.4 and 7.5 discusses the results at steady state and during the self-pressurisation. Section 7.6 explains the conclusions.

7.1. Definition of the problems: hypotheses, equations and variables

The experimental approach of the thermal analysis is based on the following hypotheses:

a) Liquid and vapour are homogeneous and isothermal;
b) The interface is at thermodynamic equilibrium;
c) The heat is transferred between the liquid and the interface and between the vapour and the interface;
d) The heat is transferred from the dry side wall to the interface;
e) Only the conservation laws of energy and of mass can describe the thermal distribution;
f) No flow rate enters or exits the storage containers, except for the BOG;
g) The steady state conditions are reached before the self-pressurisation stage.

As consequence, the storage container can be described with three control volumes. These control volumes are liquid, vapour and interface, as described by Figure 30. Figure 30 shows the heat fluxes that are considered in the storage containers for this analysis. The light orange and light blue colours respectively indicate the ullage and the liquid. The dashed yellow line is the liquid-vapour interface and the red arrows are the heat fluxes. The green arrows are the mass flow rates.

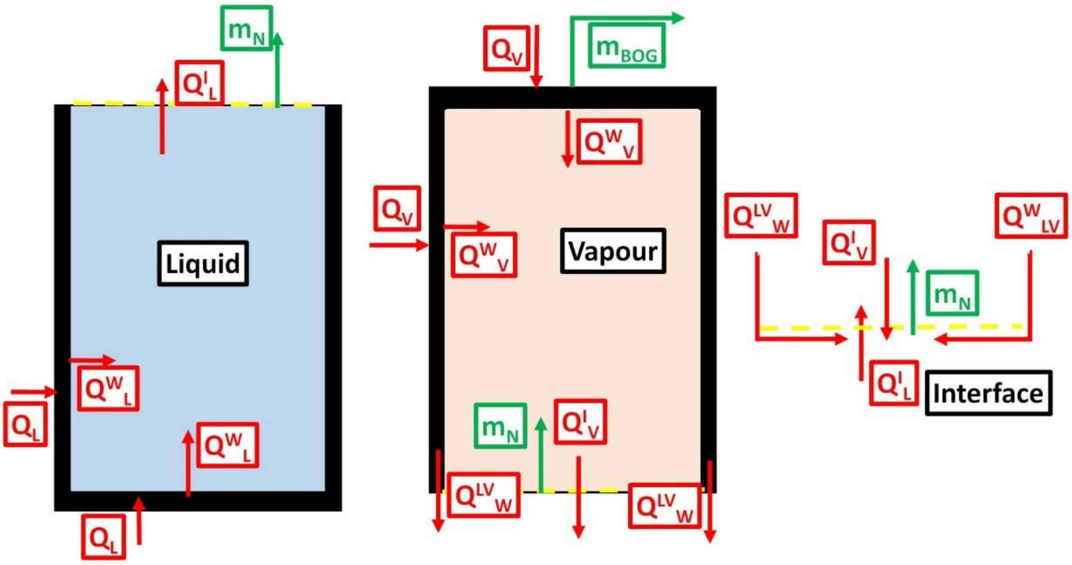

Figure 30. The storage container in the experimental approach of the thermal analysis.

As reported in Figure 30, the main variables of the thermal analysis are the heat inputs and the mass flows. These variables are described in Table 25.

Table 25. Variables of experimental approach of the thermal analysis.

Variables	Name
Overall heat input at the wetted walls[49]	$\dot{Q}_L$
Heat entering the liquid from the wetted walls	$\dot{Q}_L^W$
Overall heat inputs at the dry walls[50]	$\dot{Q}_V$
Heat entering the vapour from the vapour from the dry walls	$\dot{Q}_V^W$
Liquid-to-interface heat transfer	$\dot{Q}_L^I$
Vapour-to-interface heat transfer	$\dot{Q}_V^I$
Dry wall-to-interface heat transfer	$\dot{Q}_W^{LV}$
BOG flow rate	$\dot{m}_{BOG}$
Net mass flow	$\dot{m}_N$

The variables of Table 25 are coupled with the mathematical system of the thermal distribution analysis. This mathematical system is reported in Table 26 for the steady state and for the self-pressurisation. This mathematical system is obtained with the procedure of Appendix E.

Table 26. Mathematical system of the thermal distribution analysis.

	Steady state
Equation 11	$\dot{m}_{BOG} = \dfrac{\dot{Q}_L^I + \dot{Q}_V^I + \dot{Q}_W^{LV}}{\Delta\tilde{H}_{ev}(P)}$
Equation 12	$\dot{Q}_L^W + \dot{Q}_V^I + \dot{Q}_W^{LV} = \dot{m}_{BOG} \cdot \{\Delta\tilde{H}_{ev}(P) - [\tilde{h}_L(T^L, P^L) - \tilde{h}_L(P^V)]\}$
Equation 13	$\dot{Q}_V^W - \dot{Q}_V^I = \dot{m}_{BOG} \cdot [\tilde{h}_V(T_{BOG}, P^V) - \tilde{h}_V(P^V)]$
	Self-pressurisation
Equation 14	$\Delta t \cdot \left[\tilde{H}^L\big\|_{t_F} - \tilde{H}^L\big\|_{t_0}\right] = \int_{t_0}^{t_F} [\dot{Q}_L^W - \dot{Q}_L^I] \cdot dt - \sum_{i=1}^{N-1} [m_N \cdot \tilde{h}^L(P^V)]\big\|_i$
Equation 15	$\Delta t \cdot \left[\tilde{H}^V\big\|_{t_F} - \tilde{H}^V\big\|_{t_0}\right] = \int_{t_0}^{t_F} [\dot{Q}_V^W - \dot{Q}_V^I] \cdot dt + \sum_{i=1}^{N-1} [m_N \cdot \tilde{h}^V(P^V)]\big\|_i$
Equation 16	$m_{N,i} = \dfrac{m_i^V - m_{i-1}^V}{t_i - t_{i-1}}$

---

[49] Wetted walls are the bottom and the side wall that is in contact with the liquid.

[50] Dry walls are the roof and the side wall that is in contact with the vapour.

N is the number of time steps and t is the time. For both situations, this mathematical system is undetermined because the variables $\dot{Q}_L^I$, $\dot{Q}_W^{LV}$ and $\dot{Q}_V^I$ have to be computed with the heat transfer model. Hence, the new variables are defined for the steady state and the self-pressurisation. These variables are called pseudo-heat variables and they are reported in Table 27.

Table 27. Pseudo-heat variables, name and formulas.

Pseudo-heat variables	**Name**	**Equation**	**Formula**
Overall heat entering the liquid in self-pressurisation	$\bar{\dot{Q}}_L^P$	Equation 17	$\bar{\dot{Q}}_L^P = \frac{1}{\Delta t} \cdot \int_{t_0}^{t_F} [\dot{Q}_L^W - \dot{Q}_L^I] \cdot dt$
Net heat input in the vapour in self-pressurisation	$\bar{\dot{Q}}_V^P$	Equation 18	$\bar{\dot{Q}}_V^P = \frac{1}{\Delta t} \cdot \int_{t_0}^{t_F} [\dot{Q}_V^W - \dot{Q}_V^I] \cdot dt$
Overall heat entering the liquid at steady state	$\dot{Q}_L^{SS}$	Equation 19	$\dot{Q}_L^{SS} = \dot{Q}_L^W + \dot{Q}_V^I + \dot{Q}_W^{LV}$
Net heat input in the vapour at steady state	$\dot{Q}_V^{SS}$	Equation 20	$\dot{Q}_V^{SS} = \dot{Q}_V^W - \dot{Q}_V^I$

$\bar{\dot{Q}}_L^P$and $\bar{\dot{Q}}_V^P$are calculated during the self-pressurisation. $\dot{Q}_L^{SS}$and $\dot{Q}_V^{SS}$ are estimated at the steady state.

7.2.Calculation of the pseudo-variables

The pseudo-heat variables of Table 27 can be determined with the equations of Table 28.

Table 28. Equations for the pseudo-heat variables.

Equation	**Formula**
Equation 21	$\bar{\dot{Q}}_L^P = \left[\tilde{H}^L\big\|_{t_F} - \tilde{H}^L\big\|_{t_0}\right] + \frac{1}{\Delta t} \cdot \sum_{i=1}^{N-1} [m_N \cdot \tilde{h}_S^L(P^V)]\big\|_i$
Equation 22	$\bar{\dot{Q}}_V^P = \left[\tilde{H}^V\big\|_{t_F} - \tilde{H}^V\big\|_{t_0}\right] - \frac{1}{\Delta t} \cdot \sum_{i=1}^{N-1} [m_N \cdot \tilde{h}_S^V(P^V)]\big\|_i$
Equation 23	$\dot{Q}_L^{SS} = \dot{m}_{BOG} \cdot \{\Delta\tilde{H}_{ev}(P^V) + [\tilde{h}_L(T^L, P^L) - \tilde{h}_S^L(P^V)]\}$
Equation 24	$\dot{Q}_V^{SS} = \dot{m}_{BOG} \cdot [\tilde{h}_V(T_{BOG}, P^V) - \tilde{h}_S^V(P^V)]$

The equations of Table 28 are obtained from the formulas of Table 26. The specific enthalpies are obtained as explained in Section 5. The enthalpies and the masses are computed form the liquid level.

7.3.Results of the thermal analysis

The results of the experimental approach of the thermal analysis are presented in terms of heat fluxes and the values of heat fluxes of the pseudo-heat variables are reported in Table 29.

Table 29. Heat fluxes of the pseudo-heat variables.

			Seo and Jeong - 2010			
Test	**1**	**2**	**3**	**4**	**5**	**6**
$\bar{q}_L^{SS}$ $[W/m^2]$	8.3928	8.5109	19.1433	9.3225	12.6453	15.069
$\bar{q}_V^{SS}$ $[W/m^2]$	0.14513	0.42572	1.72005	0.44443	0.34434	0.24459
$\bar{q}_L^P$ $[W/m^2]$	8.4150	8.5457	18.707	8.2697	9.9217	8.8663
$\bar{q}_V^P$ $[W/m^2]$	0.014098	0.042872	0.113933	0.069040	0.098555	0.12287

		Kang et al. - 2018		***Perez et al. - 2021***
Test	**1**	**2**	**3**	**1**
$\bar{q}_L^{SS}$ $[W/m^2]$	88.528	91.602	110.48	8.21820
$\bar{q}_V^{SS}$ $[W/m^2]$	71.452	43.445	22.157	0.17711
$\bar{q}_L^P$ $[W/m^2]$	102.87	115.07	122.36	8.1371
$\bar{q}_V^P$ $[W/m^2]$	3.1404	6.0489	5.2116	0.019470

Table 29. Heat fluxes of the pseudo-heat variables.

	Hasan et al. - 1991		***Dresar et al. - 1992***	
Test	**1**	**2**	**1**	**2**
$\bar{q}_L^{SS}$ $[W/m^2]$	7.1201	8.1801	8.7639	11.131
$\bar{q}_V^{SS}$ $[W/m^2]$	3.0982	0.0000	1.7034	1.1671
$\bar{q}_L^{P}$ $[W/m^2]$	7.8766	7.8583	9.2024	9.1133
$\bar{q}_V^{P}$ $[W/m^2]$	0.77265	0.97114	1.2575	1.7751
	Aydelott - 1967			
Test	**1**	**2**	**3**	
$\bar{q}_L^{SS}$ $[W/m^2]$	243.87	214.46	275.64	
$\bar{q}_V^{SS}$ $[W/m^2]$	366.45	339.83	178.47	
$\bar{q}_L^{P}$ $[W/m^2]$	366.62	394.79	323.69	
$\bar{q}_V^{P}$ $[W/m^2]$	152.32	149.34	139.53	
	Aydelott and Spuckler - 1969			
Test	**1**	**2**	**3**	**4**
$\bar{q}_L^{SS}$ $[W/m^2]$	72.812	74.377	65.531	237.15
$\bar{q}_V^{SS}$ $[W/m^2]$	87.004	74.004	52.906	254.94
$\bar{q}_L^{P}$ $[W/m^2]$	93.453	107.13	84.415	350.09
$\bar{q}_V^{P}$ $[W/m^2]$	30.026	33.447	34.435	125.19

For the variable $\bar{q}_L^{SS}$, the reduction of the filling ratio increases the value of this variables, except for Aydelott [29] and Aydelott and Spuckler [30]. For these two experimental works, $\bar{q}_L^{SS}$ has a minimum near the value of filling ratio of 50 %. $\bar{q}_V^{SS}$ descreases with the liquid level, except for Seo and Jeong [24] and for Aydelott and Spuckler [30]. In Seo and Jeong [24], this variables has a maximum around 50 % of liquid level. Near the same value of the filling ratio, there is a minimum of $\bar{q}_V^{SS}$ in Aydelott and Spuckler [30].

The values of $\bar{q}_L^{P}$ are usually higher than $\bar{q}_L^{SS}$. This variable increases with the reduction of the filling ratio in Kang et al. [25]. In the experimental work of Seo and Jeong[24], this variable is irregularly behaves and the maximum value is obtained at 30%. $\bar{q}_L^{P}$ has a minimum and a maximum at 50 % filling ratio, respectively in Aydelott and Spuckler [30] and in Aydelott [29]. The values of $\bar{q}_V^{P}$ are usually lower than $\bar{q}_V^{SS}$. $\bar{q}_V^{P}$ increases with the reduction of the filling ratio in the low heat fluxes experimental works [9],[22],[23]. $\bar{q}_V^{P}$ has a maximum near the filling ratio of 50 % at medium heat fluxes [27],[43]. This variables decreases with the liquid level in the experimental work of Aydelott [29].

7.4.Discussion of steady state results

During the steady state, the heat enters the storage container and this energy goes into the liquid and into the vapour. The heat fluxes at the wet surfaces are directly transferred to the liquid, as indicated by the low overheated state of this phase. The heat fluxes in the ullage are distributed between the dry walls and the vapour, between the side dry wall and the interface, and between the vapour and the interface. Due to the overheated state of the ullage, a part of the ullage heat fluxes is accumulated as sensible heat in the vapour.

The wet surface-to-liquid heat transfer coefficient is not affected by the bulk temperature, cause the liquid is homogeneous, and by the filling ratio, due to the high transport properties. As consequence, the heat fluxes $\bar{q}_L^{SS}$ should remain constant with the liquid level, but it does not. Hence, the variables $\dot{Q}_V^{I}$ and $\dot{Q}_W^{LV}$ have to change, according to Equation 19, and they increase with the reduction of the filling ratio. The minimum value of the heat fluxes at Test 2 of Aydelott [29] and Test 2 of Aydelott and Spuckler [30] can be explained with Equation 25.

Equation 25
$$\frac{\partial \bar{q}_L^{SS}}{\partial LF} = \frac{\frac{\partial \dot{Q}_L^{SS}}{\partial LF} \cdot A^L - \frac{\partial A^L}{\partial LF} \cdot \dot{Q}_L^{SS}}{{A^L}^2}$$

Equation 25 is the derivate of the variable $\bar{q}_L^{SS}$ respect to the filling ratio. $\frac{\partial A^L}{\partial LF}$ strongly change with the filling ratio. $\frac{\partial \dot{Q}_L^{SS}}{\partial LF}$ weakly varies between Test 1 and Test 2, as indicated by the overall heat input of Aydelott [29] and Test 2 of Aydelott and Spuckler[30] (see Table 24). So, the minimum of $\bar{q}_L^{SS}$ is caused by the negative value of the numerator of Equation 25 because the overall heat input slowly change between Test 1 and Test 2 of both experiments [29],[30].

The dry side wall-to-vapour heat transfer is affected by the bulk temperature gradient because the ullage is fully thermally stratified. As the filling ratio is reduced, the boundary layer convective flows at the side wall are reduced by the bulk temperature gradient. As consequence, the heat transfer coefficient lowers and the heat fluxes too. Hence, the variable $\bar{q}_V^{SS}$ decreases with the filling ratio as indicated by Equation 20. So, the environment-ullage heat flow prefers moving along the side wall to reach the interface. The role of $\dot{Q}_V^I$ cannot be defined in the steady state due to the lack of experiments. The maximum value of $\bar{q}_V^{SS}$ at Test 4 of Seo and Jeong [24] and the minimum value of $\bar{q}_V^{SS}$ at Test 2 of Aydelott and Spuckler [30] can be explained with Equation 26, as done for $\bar{q}_L^{SS}$.

Equation 26
$$\frac{\partial \bar{q}_V^{SS}}{\partial LF} = \frac{\frac{\partial \dot{Q}_V^{SS}}{\partial LF} \cdot A^V - \frac{\partial A^V}{\partial LF} \cdot \dot{Q}_V^{SS}}{{A^V}^2}$$

Equation 26 is the derivate of the variable $\bar{q}_V^{SS}$ respect to the filling ratio. If there is a maximum, the numerator of Equation 26 is positive when the filling ratio is decreased. $\frac{\partial A^V}{\partial LF}$ is always negative, so the terms $\frac{\partial \dot{Q}_V^{SS}}{\partial LF} \cdot A^V$ is sometime positive. This condition is caused by the change of $\dot{\bar{Q}}$ between Test 2, Test 4 and Test 5 of Seo and Jeong [24]. When there is a minimum, $\frac{\partial \dot{Q}_V^{SS}}{\partial LF} \cdot A^V$ is lower than the term $\frac{\partial A^V}{\partial LF} \cdot \dot{Q}_V^{SS}$ as the filling ratio increases from the minimum value. Hence, $\dot{Q}_V^{SS}$ is almost constant between Test 2 and Test 3 of Aydelott and Spuckler [30].

7.5. Discussion of self-pressurisation results

In the self-pressurisation, the thermal stratification is developed in the upper region of liquid. The bulk temperature gradient reduces the convective flow near the interface, causing a reduction of the heat transfer coefficient, thus reducing the wet surface-to-liquid heat transfer. So, $\dot{Q}_L^W$ decreases and it should be expected that $\bar{q}_L^P$ is lower than $\bar{q}_L^{SS}$. This condition, however, does not occur. Hence, the interface-to-liquid heat transfer has to give energy to the liquid phase, as indicated by Equation 17. The variable $\dot{Q}_I^L$ removes heat from the interface and, the dry side wall-to-interface and the dry side wall-to-interface heat transfers have to increase. With the reduction of the filling ratio, the thermal stratification is lower and the liquid convective flow is higher than the one at high liquid level. Hence, this convective flow transfers heat better and $\bar{q}_L^P$ increases with the reduction of the filling ratio. The irregular behaviour of $\bar{q}_L^P$ in Seo and Jeong [24] can be caused by the estimation of the filling ratio. If the values of $\bar{q}_L^P$ at Test 1 and at Test 6 are considered, the variable $\bar{q}_L^P$ increases with the reduction of the filling ratio. The maximum value of $\bar{q}_L^P$ near 50 % of liquid level occurs only in oblate ellipsoidal [27], [28] and spherical [29], [116] tanks. At this filling ratio, the interfacial area is the largest. Hence, this maximum is caused by the interfacial area that increases the interface-to-liquid heat transfer, thus $\dot{\bar{Q}}_L^P$.

In the self-pressurisation, the net mass flow lowers due to the condensation rate. So, the descending flow in the ullage can reaches the interface, enhancing the heat exchange. At the same time, the bulk temperature gradient increases due to the accumulation of sensible heat in the vapour. Hence, the convective flow at the side wall reduces. As consequence, $\dot{Q}_V^W$ slightly decreases and $\dot{Q}_V^I$ increases. So, $\bar{\dot{q}}_V^P$ reduces between the steady state and the self-pressurisation, as reported by Equation 18. As low heat fluxes, the convective flow at the dry side wall and the descending flow in the bulk are low because there is not enough heat input at the dry side surfaces. In this condition, the reduction of the filling ratio increases the heat input at the dry surfaces, increasing $\bar{\dot{q}}_V^P$ for Seo and Jeong [27], Hasan et al. [27] and Dresar et al. [28]. As the overall heat fluxes are increased to the medium level, the heat input in the ullage and the vapour-to-interface heat transfer increases due to the convective flow. Hence, a maximum is present as indicated by the results for the experimental works Kang et al. [124] and Aydelott and Spuckler [30]. For the experimental series of Aydelott [115] at high heat inputs, the vapour-to-interface heat transfer reduces $\bar{\dot{q}}_V^P$ due to the descending flow, which is enhanced by these heat fluxes.

7.6. Summary and conclusions

The distribution of the heat between the liquid and the ullage determines the behaviour of cryogenic liquid in storage container. A thermal analysis is developed using only the experimental data due to the lack of validate models of heat transfer. The mathematical system, based on conservation laws, is undetermined and the pseudo-heat transfer variables are introduced. These variables are calculated for conservation laws at steady state and during the self-pressurisation. The results indicate that the liquid-to-interface, the vapour-to-interface and the dry side wall-to-interface heat transfer determine the thermal distribution. These interface heat transfers are related to the fluid-dynamics in liquid and vapour. Hence, the interface heat transfer model has to be set on the fluid-dynamics near the interface. The relative importance of the vapour-to-interface and the dry side wall-to-interface heat transfer in the thermal distribution of the ullage is not clear due to the lack of experimental information. Hence, the dry side wall-to-interface heat transfer must be analyzed to understand if it is crucial in the behaviour of the cryogenic liquid in storage containers.

8. Heat transfer between dry and wetted walls

As stated in Section 7.6, the relative importance between the vapour-to-interface and the dry side wall-to-interface heat transfers cannot be determined with the thermal analysis. The dry wall-to-interface heat transfer can be computed from the experimental data, using the 1 dimensional Fourier's law.

Section 8.1 presents the dry wall-to-interface heat transfer. Section 8.2 illustrates the results. Section 8.3 presents the discussions.

8.1. The dry wall-to-interface heat transfer

Let's imagine cutting horizontally the storage container at the liquid-vapour. So, a ring can be obtained. This ring has the thickness of the storage container. Figure 31 (a) and Figure 31 (b) respectively shows the storage container and the ring obtained from cutting it. In Figure 31 (a), the light orange and blue semi-circles are respectively the vapour and the liquid phases. The dashed yellow line is the interface, the vertical and horizontal green lines are respectively the filling ratio and the internal diameter. The red arrows are the heat exchanged between the dry and the wetted walls. In Figure 31 (b), the green lines are the thickness of the storage containers and the internal diameter at the liquid level, respectively. Red "x" indicates the direction of the dry side wall-to-interface heat transfer, which is directed into the ring. The yellow are is the interfacial area at the interface.

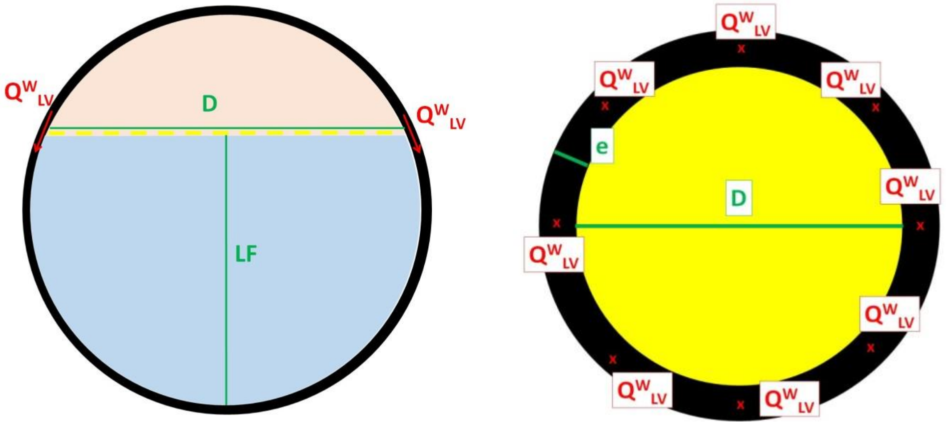

a) b)

Figure 31. (a) Drawing of spherical storage container; (b) the ring obtained from cutting the storage tank at interface.

The dry wall-to-interface heat transfer is perpendicular to this ring. Hence, the dry-wetted heat transfer can be estimated with Equation 27, which is the Fourier's law of heat conduction.

Equation 27
$$\dot{Q}_{w}^{LV} = A_R \cdot k \cdot \frac{\partial T}{\partial x}$$

A_R is the surface area of the ring, k is the thermal conductivity of the walls of the storage container and $\frac{\partial T}{\partial x}$ is the temperature gradient between the dry wall vapour and the walls at the interface. This temperature gradient is estimated with Equation 28.

Equation 28
$$\frac{\partial T}{\partial x} = \frac{T_{BOG} - T^{I}}{x_{BOG} - x^{I}}$$

Equation 28 is quite accurate because the difference in temperature between the wall and the vapour bulk is low and constant with the vertical position, as experimentally proved by Hasan et al. [27] and by Dresar et al. [28].

8.2. Results

Table 30 reports the values of the bulk temperature gradient ($\frac{\partial T}{\partial x}$) computed with Equation 28 at steady state (SS) and the end of the pressurisation (P). The values of $\dot{Q}_{W}^{LV}$ for these two storage conditions are illustrated in Table 30.

Table 30. Values of $\frac{\partial T}{\partial x}$ and of $\dot{Q}_{LV}^{W}$ at the steady state and at the end of the self-pressurisation.

			Seo and Jeong - 2010			
Test	**1**	**2**	**3**	**4**	**5**	**6**
$\frac{\partial T}{\partial x}\Big\vert_{SS}$ $[K/m]$	59.062	83.510	148.047	78.014	59.708	52.343
$\frac{\partial T}{\partial x}\Big\vert_{P}$ $[K/m]$	95.567	105.26	136.13	61.896	54.336	54.841
$\dot{Q}_{LV}^{W}\vert_{SS}$ $[W]$	0.13938	0.19708	0.34939	0.18411	0.14091	0.12353
$\dot{Q}_{LV}^{W}\vert_{P}$ $[W]$	0.22554	0.24840	0.32126	0.14607	0.12823	0.12943

		Kang et al. - 2018		***Perez et al. - 2021***
Test	**1**	**2**	**3**	**1**
$\frac{\partial T}{\partial x}\Big\vert_{SS}$ $[K/m]$	268.04	221.25	141.88	41.766
$\frac{\partial T}{\partial x}\Big\vert_{P}$ $[K/m]$	245.46	279.74	203.04	53.534
$\dot{Q}_{LV}^{W}\vert_{SS}$ $[W]$	3.7683	3.1106	1.9947	0.096304
$\dot{Q}_{LV}^{W}\vert_{P}$ $[W]$	3.4509	3.9329	2.8546	0.12344

	Hasan et al. - 1991		***Dresar et al. - 1992***	
Test	**1**	**2**	**1**	**2**
$\frac{\partial T}{\partial x}\Big\vert_{SS}$ $[K/m]$	12.3640	-0.28268	8.5353	6.5625
$\frac{\partial T}{\partial x}\Big\vert_{P}$ $[K/m]$	62.610	55.515	35.645	28.987
$\dot{Q}_{LV}^{W}\vert_{SS}$ $[W]$	0.36598	-0.0083978	0.33558	0.24562
$\dot{Q}_{LV}^{W}\vert_{P}$ $[W]$	1.8158	1.6176	1.4016	1.0889

		Aydelott - 1967	
Test	**1**	**2**	**3**
$\frac{\partial T}{\partial x}\Big\vert_{SS}$ $[K/m]$	430.20	578.52	446.17
$\frac{\partial T}{\partial x}\Big\vert_{P}$ $[K/m]$	2381.8	1637.4	1116.0
$\dot{Q}_{LV}^{W}\vert_{SS}$ $[W]$	4.0552	5.6219	3.7653
$\dot{Q}_{LV}^{W}\vert_{P}$ $[W]$	22.244	15.924	9.5489

		Aydelott and Spuckler - 1969		
Test	**1**	**2**	**3**	**4**
$\frac{\partial T}{\partial x}\Big\vert_{SS}$ $[K/m]$	118.25	142.14	174.70	153.61
$\frac{\partial T}{\partial x}\Big\vert_{P}$ $[K/m]$	1065.0	483.66	358.20	628.74
$\dot{Q}_{LV}^{W}\vert_{SS}$ $[W]$	5.2562	7.0525	8.2298	7.6228
$\dot{Q}_{LV}^{W}\vert_{P}$ $[W]$	46.206	23.962	16.955	31.142

As reported in Table 30, the bulk gradient is higher during the self-pressurisation than in the steady state. $\dot{Q}_{LV}^{W}$ increases when the storage containers is closed. The values of this heat transfer are of the same order of magnitude of the overall heat input for the experimental works of Seo and Jeong [24] and of Perez et al. [26]. In the other experimental works, $\dot{Q}_{LV}^{W}$ is lower than the heat input in the ullage.

8.3. Discussions and conclusions

As the storage container is closed, the sensible heat is accumulated in the ullage as time passes. This accumulation increases the bulk temperature gradient, reducing the dry side wall-to-interface heat transfer coefficient. Hence, the wall temperature of the dry side and the gradient at the wall increase. As consequence, more heat is transferred via the dry side wall during self-pressurisation than in the steady state. The absolute value of $\dot{Q}_{w}^{LV}$ are not enough to transfer all the heat entering the ullage at medium and high overall heat fluxes [30], [115], [124]. Hence, the vapour-to-interface heat transfer must contribute to transfer heat to the interface.

The thermal analysis cannot determine the role of the dry side wall-to-interface heat transfer. Hence, this variable is modelled with the 1 dimension Fourier's law. The temperature gradient is estimated with the experimental values of the ullage temperature and of the filling ratio. The results indicate that this variable strongly increases between the steady state and the self-pressurisation. Moreover, this heat transfer can transfer all the heat entering the ullage at low overall heat input. As the overall heat inputs are increased, the vapour-to-interface should be considered. Hence, the dry side wall-to-interface heat transfer must be considered in the storage model.

Chapter 3

Modèle à l'équilibre

Le modèle à l'équilibre (modèle EQ) est développé pour prédire le comportement des liquides cryogéniques dans des réservoirs à petite échelle pour différents modes de stockage. Ces modes de stockage sont le régime stationnaire et l'auto-pressurisation. Le modèle proposé est basé sur l'hypothèse d'équilibre thermodynamique instantané et d'homogénéité du liquide et de la vapeur. En conséquence, le système mathématique du modèle EQ est composé de six variables et six équations. Certaines d'entre elles sont différentes pour les deux modes de stockage. Le système mathématique est composé d'équations algébriques et d'équations différentielles ordinaires obtenues à partir des lois de conservation de l'énergie et de la masse.

Les équations de bilan énergétique et massique nécessitent les valeurs des entrées thermiques et les valeurs des propriétés thermodynamiques du liquide et de la vapeur. Les apports thermiques sont calculés au moyen du modèle Storage Heat Transfer (SHT). Ce modèle estime un coefficient de transfert de chaleur effectif entre le liquide cryogénique et l'environnement (i) qui reflète la propriété isolante de la cuve de stockage et (ii) qui est calculé au moyen du modèle Boil-Off Rate (BOR).

Les propriétés thermodynamiques et de transport sont respectivement calculées avec les équations d'état de référence et avec les équations dédiées telles qu'implémentées dans le logiciel REFPROP 9.0. Ces équations déterminent les propriétés thermo-physiques (thermodynamiques et de transport) avec une précision comparable à l'erreur de mesure de ces propriétés, pour les fluides considérés dans ce travail de thèse et aux conditions de température et de pression les plus courantes dans le stockage cryogénique à petite échelle.

Le système d'équations différentielles ordinaires est résolu avec la méthode Runge-Kutta-Fehlberg du 5ème ordre avec paramètres Cash-Karp (RKF-CKp). Cette méthode explicite avec une taille de pas adaptative et peut réduire le temps de calcul et augmenter la précision lorsque cela est nécessaire. Le modèle d'équilibre est comparé aux données expérimentales de l'azote liquide et de l'hydrogène liquide sous flux thermiques faibles, moyens et élevés. Cette comparaison montre que le modèle d'équilibre sous-estime l'auto-pressurisation, du fait de l'hypothèse d'un équilibre thermodynamique instantané. L'état de surchauffe de la vapeur n'est pas prédit par ce modèle. La température et le volume du liquide sont généralement prédits avec une erreur moyenne inférieure à 1 %.

Equilibrium model

The Equilibrium model (EQ model) is developed to predict the behaviour of cryogenic liquids in small scale tanks for different storage modes. These storage modes are the steady state and the self-pressurisation, and they are respectively called 1.b and 4. The predictions of the model will then be compared with the experimental data reported in Chapter 2. The proposed model is based on the assumption of instantaneous thermodynamic equilibrium and homogeneity of both liquid and vapour. As consequence, the mathematical system of the EQ model is composed of six variables and six equations. Some of them are different for the two storage modes. The mathematical system is composed of algebraic equations and Ordinary Differential Equations (ODE), which are obtained from the energy and mass conservation laws. Energy and mass balance equations require the values of the heat inputs and the values of the thermodynamic properties of both liquid and vapour. The heat inputs are calculated by means of the Storage Heat Transfer (SHT) model. This model estimates an effective heat transfer coefficient between the cryogenic liquid and the ambient. This coefficient reflects the insulating property of the storage container, and it is computed by means of the Boil-Off Rate (BOR) model. The thermodynamic and the transport properties are respectively computed with the reference equations of state and with the dedicated equations as implemented in the software REFPROP 9.0 [8]. These equations determine the thermo-physical (thermodynamic and transport) properties with a precision comparable to the measurement error of these properties, for the fluids considered in this thesis work and at the temperature and pressure conditions most common in cryogenic small scale storage. The Ordinary Differential Equations system is solved with the 5th order Runge-Kutta-Fehlberg method with Cash-Karp parameters (RKF-CKp), which is an explicit method with an adaptive step size. This method can reduce the computational time and it can increase the accuracy when it is required. The equilibrium model is compared with the experimental data of liquid nitrogen and of liquid hydrogen under low, medium and high heat fluxes. This comparison shows that the equilibrium model underestimates the self-pressurisation, because of the hypothesis of instantaneous thermodynamic equilibrium. The overheated state of the vapour is not predicted by this model. The liquid temperature and volume are usually predicted with an average error below 1 %.

In this chapter, Section 1 describes the hypothesis, the variables, the mathematical system and the block structure. Section 2 explains the mathematical procedure to obtain the equations of EQ model. Section 3 presents the approach of boil-off rate (BOR) model and the storage heat transfer (SHT) model. Section 4 describes the reference models to compute the thermo-physical properties. Section 5 presents the algorithm of the ODE solver. Finally, Section 6 shows the comparison between the experimental data and the results of the EQ model. Section 7 presents the discussion of the results and the perspective.

1. Introduction

As underlined in the analysis of the scientific literature (see Section 5 of Chapter 1), Lumped Parameter (LP) models with equilibrium approach were firstly developed for large scale storage tanks of Liquefied Natural Gas (LNG). To the author's knowledge, this type of models has not been developed for pure cryogenic liquids in small scale (SS) storage container. Hence, in this work, the equilibrium model (EQ model) is created to validate this type of approach for pure cryogenic liquids in SS storage tanks.

Section 1.1 and 1.2 describe the hypothesis and the variables, respectively. Section 1.3 explains the block structure of the EQ model. Section 1.4 presents the mathematical system for the two storage modes.

1.1. Hypothesis

The storage behaviour of the cryogenic liquid is mainly determined by the heat input from the environment. This thermal energy enters in the storage containers due to the difference in temperature between the external surface and the liquid. As consequence, the storage container is not at thermodynamic equilibrium during the whole self-pressurisation. This behaviour can be determined with the equilibrium model, with the following hypotheses:

a) *Hypothesis of instantaneous thermodynamic equilibrium:* Both liquid and vapour are at thermodynamic equilibrium at the ullage pressure at any time of the storage;
b) *Global homogeneity hypothesis:* Both liquid and vapour are isothermal;

With these assumptions, the storage model can be described by Figure 32, in which the grey colour is the vapour and the liquid. In Figure 32, the green arrow shows the net mass flow of fluid across the liquid-vapour interface represented by the yellow dashed line (phase change). The black arrows indicate the mass flows of gas entering and leaving the storage tank. The white arrow with red border, which is named Q, is the overall heat input rate flowing into the tank through its walls. The white circle with purple border is the external wall temperature.

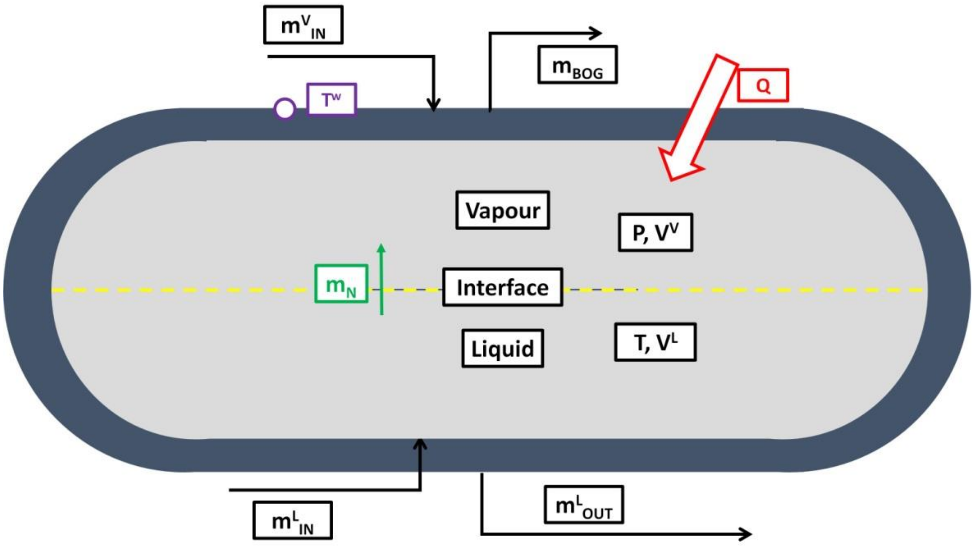

Figure 32. Description of the equilibrium model.

As illustrated in Figure 32, the vapour temperature is equal to the liquid temperature. Both temperatures are equal to the saturation temperature at ullage pressure, as consequence of hypothesis of instantaneous thermodynamic equilibrium (assumption a) of Section 1.1 of Chapter 3). Hence, the heat input in the ullage is completely transferred to the liquid. The natural convection does not occur, due to the hypothesis of instantaneous thermodynamic equilibrium (assumption a) of Section 1.1 of Chapter 3). The internal temperature is uniform in both liquid and vapour, due to hypothesis of global homogeneity (assumption b) of Section 1.1 of Chapter 3). The heat fluxes, which depend on the thermal resistance of the insulation, are uniform in the storage container because the liquid and vapour have the same temperature. Temperature gradients at the walls of the storage container, and at the interface are absent because the system is at equilibrium. Mass is, however, transferred at the interface at each time step, due to the heat inputs. This mass flow maintains the equilibrium condition at any time step, by transferring mass between the liquid and the vapour.

1.2. Variables

The variables of the equilibrium model (EQ model) can be grouped in five categories:

- State: these variables describe the state of the behaviour and they are the temperature, the pressure, and the liquid and vapour volumes;
- Differential: these variables are the time-derivates of the state variables and they describe the time-variation of the state variables;
- Boundary: variable that define the boundary conditions of the system such as heat flows, wall temperature, inlet and outlet flow rate, etc.;
- Geometrical: variable that describe the geometry of the storage container;
- Thermo-physical: variables that quantify the thermophysical properties, which can be computed from the state variables such as temperature and pressure;

The variables of the equilibrium model (EQ) are explained and classified in Table 31, which include the type, the name, the symbol and the unit of each variable.

Table 31. Nomenclature of the variables of the EQ model.

Type of variable	Name of the variable	Symbol	Unit
State	Ullage pressure	P^V	[kPa]
	Temperature	T	[K]
	Liquid volume	V^L	[m^3]
	Ullage volume	V^V	[m^3]
	Time	t	[s]
Differential	Time derivate of ullage pressure	$\frac{\partial P^V}{\partial t}$	[kPa/s]
	Time derivate of the liquid volume	$\frac{\partial V^L}{\partial t}$	[m^3/s]
	Time derivate of the overall enthalpy	$\frac{\partial \tilde{H}}{\partial t}$	[J/s]
	Time derivate of the overall mass	$\frac{\partial m}{\partial t}$	[kg/s]
	Time derivate of the liquid mass	$\frac{\partial m^L}{\partial t}$	[kg/s]
	Time derivate of the vapour mass	$\frac{\partial m^V}{\partial t}$	[kg/s]
	Net mass flow[51]	$\dot{m}_N$	[kg/s]
Boundary	External wall temperature	T^W	[K]
	Overall heat inputs	$\dot{Q}$	[W]
	Effective heat transfer coefficient	h_{EFF}	[W/m²/K]
	Inlet vapour mass flow	$\dot{m}_{IN}^V$	[kg/s]
	Inlet liquid mass flow	$\dot{m}_{IN}^L$	[kg/s]
	Boil-off Gas (BOG) flow	$\dot{m}_{BOG}$	[kg/s]

---

[51] The net mass flow is defined as the difference in mass flow rate between the evaporation and the condensation.

Table 31. Nomenclature of the variables of the EQ model.

	Outlet liquid mass flow	$\dot{m}_{OUT}^{L}$	[kg/s]
	Temperature of inlet vapour mass flow	T_{IN}^{V}	[K]
	Pressure of inlet vapour mass flow	P_{IN}^{V}	[kPa]
	Temperature of inlet liquid mass flow	T_{IN}^{L}	[K]
	Pressure of inlet liquid mass flow	P_{IN}^{L}	[kPa]
	Temperature of BOG	T_{BOG}	[K]
	Pressure of BOG	P_{BOG}^{V}	[kPa]
	Temperature of outlet liquid mass flow	T_{OUT}^{L}	[K]
	Pressure of outlet liquid mass flow	P_{OUT}^{L}	[kPa]
Geometrical	Internal height	H	[m]
	Internal diameter	D	[m]
	Internal surface area	A^{TOT}	[m^2]
	Internal volume	V^{TOT}	[m^3]
	Volume	V	[m^3]

The geometrical variables are computed as described in Appendix B. The thermo-physical variables are divided into thermodynamic and transport properties. Both properties are described in Section 4 of Chapter 3.

1.3. Block structure of the equilibrium model

The input and the output of the equilibrium model (EQ model) are reported in Table 32.

Table 32. Input and output of the EQ model.

Input	Geometry, overall heat input, experimental data, simulation time, values of tolerance, type of fluid and physical constants.
Output	The time-evolution of the state variables (see Table 31).

The equilibrium model can be described with the block structure, which is reported in Figure 33. In Figure 33, “y” is the vector of the state variables, “t_{SS}” is the steady state time, “t_{MAX}” is the maximum simulation time and “dt” is the time-step.

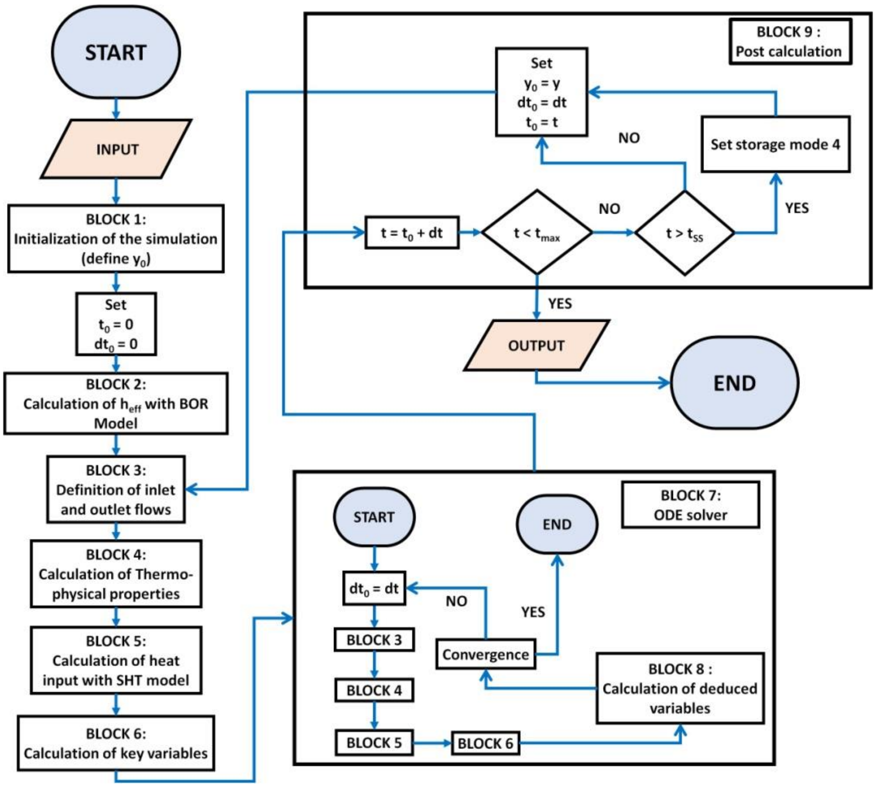

Figure 33. Algorithm of the EQ model.

As indicated in Figure 33, the EQ model is composed by 9 blocks:

a) BLOCK 1. In this block, the vector of the initial values of the state variables (y_0), the initial time (t_0) and the initial time step (dt_0) values, the storage mode (see Table 35) and the nominal heat input or the nominal Boil-Off Rate (BOR) of the storage container are defined by the user. More details are given in Section 1.3.1;

b) BLOCK 2. The effective heat transfer coefficient is computed with the BOR model. This coefficient is used in the Storage Heat Transfer (SHT) model to compute the heat inputs during the simulation. More details on the BOR model are given in Section 3;

c) BLOCK 3. The boundary variables such as the inlet and outlet mass flow, the temperatures and pressure of these flows and the wall temperature are determined, as described in Section 1.3.2.

d) BLOCK 4. The thermo-physical properties are calculated at the saturation temperature and pressure, for liquid and vapour phases. Reference models are used to calculate these variables and they are explained in Section 4.

e) BLOCK 5. The heat inputs entering the storage container are determined with the SHT model. More details about SHT model are given in Section 3.

f) BLOCK 6. The indipendent variables of the mathematical (see Table 36) system are computed with the target equations, which are equations that are derived from the energy and mass conservation laws. More details on the indipendent variables and on the equations to use are given in Section 1.4;

g) BLOCK 7. The liquid volume and the pressure are computed with the Ordinary Differential Equations (ODEs) solver, which is an iterative procedure that ends when the value of the relative tolerance of the numerical error is respected. In this procedure, integration time step (dt) is adjusted to match the value of this tolerance. At each iteration, the Blocks 3, 4, 5 6 and 8 are executed to compute the time-derivates of the liquid volume and of the pressure, as it is shown in Figure 33. More details of the ODE solver are given in Section 5;

h) BLOCK 8. The dipendent variables of the mathematical (see Table 36) system, which are a type of variables of the EQ model, are computed with the target equations. More details on the dipendent variables and on the equations to use are given in Section 1.4;

i) BLOCK 9. This block is composed by a series of control steps to determine if the storage mode can be shifted from steady state to self-pressurisation.

Section 1.3.1, 1.3.2 and 1.3.3 respectively describe Block 1, 3 and 9.

1.3.1. Block 1: Initialisation of the simulation

The Equilibrium model (EQ model) is developed for the steady state and the self-pressurisation. The initial storage mode can be defined by the user, which can select the steady state or self-pressurisation. The initial values of pressure and of filling ratio are defined by the user. The initial values of the other state variables can be calculated from these values of pressure and of filling ratio. This calculation is done using the target equations of Table 36. After this calculation, the vector of the initial values of the state variables (y_0) can be defiend. The initial time and the initial time step values are equal to zero by defaults. The overall heat inputs must be given by the user for the calculation of the effective heat transfer coefficient in the Boil-off Rate (BOR) model.

1.3.2. Block 3: Outlet and inlet flow

Table 33 reports the value of the outlet and inlet flow, the temperature and the pressure.

Table 33. Boundary variables defined in BLOCK 3 of EQ model.

Variables	$\dot{m}_{IN}^{V}$	$\dot{m}_{OUT}^{L}$	T_{IN}^{V}	P_{IN}^{V}	T_{IN}^{L}	P_{IN}^{L}	T_{BOG}	P_{BOG}^{V}	T_{OUT}^{L}	P_{OUT}^{L}	T^{W}
Values	0	0	T	P	T	P	T	P	T	P	298.15 K

As indicated in Table 33, $\dot{m}_{IN}^{V}$ and $\dot{m}_{OUT}^{L}$ are equal to zero because only the storage mode steady sate (1.b) and self-pressurisation (4) are used[52]. T_{IN}^{V} and T_{IN}^{L}, and P_{IN}^{V} and P_{IN}^{L} are respectively equal to the saturation temperature (T) and pressure (P) to not add other unknowns to the boundary conditions. The boundary variables $\dot{m}_{IN}^{L}$ and $\dot{m}_{BOG}$ are determined with the algebraic equations of mathematical systems (see Table 36). The value of the wall temperature is determined by the hypothesis of external wall temperature (see Section 6.4 of Chapter 3).

1.3.3. Block 9: Post calculation

If the self-pressurisation is simulated after the steady state, the initial storage mode is changed when the steady state conditions are reached. This change is done evaluating the current time (t) against the maximum time (t_{MAX}) and the steady state time (t_{SS}). These variables are calculated with the equations of Table 34.

Table 34. Equations to compute $\boldsymbol{t}$, $\boldsymbol{t_{MAX}}$ and $\boldsymbol{t_{SS}}$.

Variable	**Equation**	**Formula**
t	Equation 29	$t = t_0 + dt$
t_{MAX}	Equation 30	$t_{MAX} = t_{SP} + t_{SS}$
t_{SS}	Equation 31	$t_{SS} = t_{SP} \cdot \tau_{SS}$

t_{SP} is the self-pressurisation time, which can be equal to the experimental time of the self-pressurisation if the equilibrium model (EQ model) is used to simulate an experiment. τ_{SS} is the ratio between the steady state time and the self-pressurization time. The value of this ratio is 30 % of self-pressurisation time. The value of this ratio is arbitrary chosen. This value can be zero if the self-pressurisation is simulated without beginning from the steady simulation.

If the time t is higher than t_{MAX}, the calculation ends and the output are printed. Otherwise, the time t is compared with the steady state time. If the time is lower than t_{SS}, the new initial values of the state variables, of the time and of the time step are defined as equal to the values computed after Block 8. When t is higher than t_{SS}, the storage mode is changed from 1.b (steady state) to 4 (self-pressurisation), before the initialization of the new values of the initial variables.

1.4. Mathematical system

The equilibrium model (EQ model) is compared with the experimental data, as described in Section 6. These data (see Section 4 of Chapter 2) are obtained by measuring the variables such as temperatures and pressure during the self-pressurisation. This pressurisation occurs after the steady state period, where the liquid storage container reaches the steady conditions as open tank. Hence, the mathematical system of the EQ model is developed for predicting the behaviour of cryogenic liquids in two storage modes to be compared with the experimental data. These storage modes are defined and described in Table 35.

Table 35. Storage modes.

Storage mode	**Description**

---

[52] 9 storage modes have been developed and implemented in the code of the EQ model. For the purposes of this thesis, only two of them are of interest.

Table 35. Storage modes.

Steady state (1.b)	Open storage container with liquid filling and boil-off gas (BOG) removing. Pressure and filling ratio remains constant.
Self-pressurisation (4)	Closed storage containers.

The storage mode 1.b is introduced to simulate the steady state to simulate the steady state phase that can be present before the self-pressurization. The storage mode 4 is created to predict the behaviour during the self-pressurisation because the experimental data are mainly measured during this pressurisation. The mathematical system describing each storage mode is composed by the target variables and the target equations, as indicated by Figure 34.

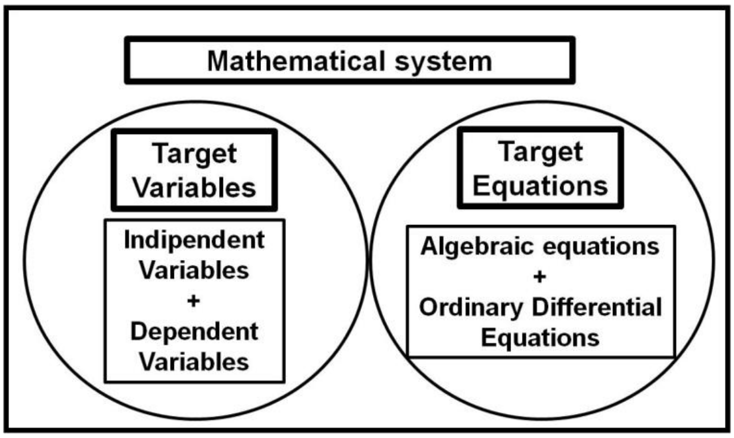

Figure 34. Mathematical system of EQ model for both storage modes.

These variables are the variables that have to be computed for determining all the variables of Table 31. Target variables are composed by the indipendent variables and the dipendent variables, as illustrated in Figure 34. The target equations are the formulas to calculate the values of the target variables. These equations are divided into algebraic and Ordinary Differential Equations (ODEs), as described in Figure 34. These differential equations compose the ODE system of the EQ model (see Table 52). The algebraic and differential equations, and the indipendent and dipendent variables of the mathematical system are reported in Table 36 both the storage modes.

Table 36. Equations and target variables of mathematical system of EQ model.

Target variables		***Target equations***	
Type	**Symbol**	**Type**	**Name**
indipendent	$\frac{\partial P^V}{\partial t}$	Differential	Pressure evolution equations (Equation 69 and Equation 70)
	$\frac{\partial V^L}{\partial t}$	Differential	Liquid volume evolution equations (Equation 71 and Equation 72)
	$\dot{m}_{BOG}$	Algebraic	Boil-off Gas equations (Equation 73 and Equation 74)
	$\dot{m}_{IN}^L$	Algebraic	Inlet Liquid Flow equations (Equation 75 and Equation 76)
dependent	V^V	Algebraic	Volume conservation equation (Equation 654)
	T	Algebraic	Saturation pressure equation (Equation 738)

The pressure evolution, the liquid volume evolution, the Boil-off Gas and Inlet Liquid flow equations are obtained from the conservations laws, as reported in Section 2. Equation 69, Equation 71, Equation 73 and Equation 75 are used in the storage mode 4 (self-pressurisation). Equation 70, Equation 72, Equation 74 and Equation 76 are applied during the steady state (storage mode 1.b). The saturation pressure equation is obtained from the thermodynamic model, as described in Section 4. The ullage volume is obtained with the geometrical formulas of Appendix B. Equation 654 and Equation 738 are used in storage mode 4 and 1.b.

2. Mathematical procedure to deduce the pressure evolution, liquid volume evolution, inlet liquid flow and Boil-Off Gas equations

Pressure evolution (P-e), liquid volume evolution (V^L-e), the inlet liquid flow (ILF) and the Boil-off Gas (BOG) equations of the mathematical system of the equilibrium model (EQ model) (see Table 36) are deduced from the conservations laws of mass and of energy. These equations are determined with an approach that is described in Figure 35.

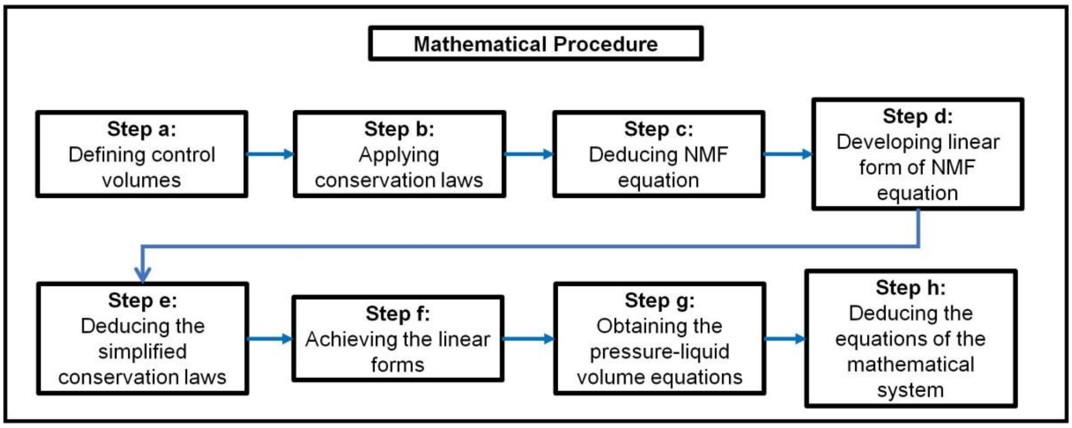

Figure 35. Mathematical procedure to deduce P-e, V^L-e, ILF and BOG equations.

As indicated by Figure 35, the approach is composed by the following steps:

a) Defining the control volumes;
b) Applying the conservation laws to the control volumes;
c) Deducing the net mass flow (NMF) equation;
d) Developing the linear form of (NMF) equation;
e) Deducing the simplified form of conservation laws;
f) Achieving the linear form of conservation laws;
g) Obtaining the pressure-liquid volume (P-V^L) equations;
h) Deducing the P-e, V^L-e, ILF and BOG equations;

Section 2.1 describes the control volume of EQ model. Section 2.2 presents the conservation laws of EQ model. Section 2.3 and 2.4 respectively explain the NMF equation and its linear form. Section 2.5 and 2.6 respectively describe the simplified form of conservation laws and their linear form. Section 2.7 presents the P-V^L equation. Section 2.8 explains the P-e, V^L-e, ILF and BOG equations.

2.1. Control volumes of the equilibrium model

The definition of the control volumes is the first step (step a) of Section 2 of Chapter 3), as illustrated in Figure 35. To deduce the conservation laws form the fundamental formulas of Table 192, it is crucial to define the control volume where these formulas are applied. The control volumes required for the EQ model are shown in Figure 36. In Figure 36, the grey colour indicates the vapour, liquid and the overall system. The green arrows represent the net mass flow across the liquid-vapour interface. This mass flow is the difference between the evaporative and the condensing flow rates at the interface. The black arrows represent the inlet and outlet mass flows through the tank vents. The red arrows refer to the enthalpy flows. The white arrow with red border is the overall heat input rate.

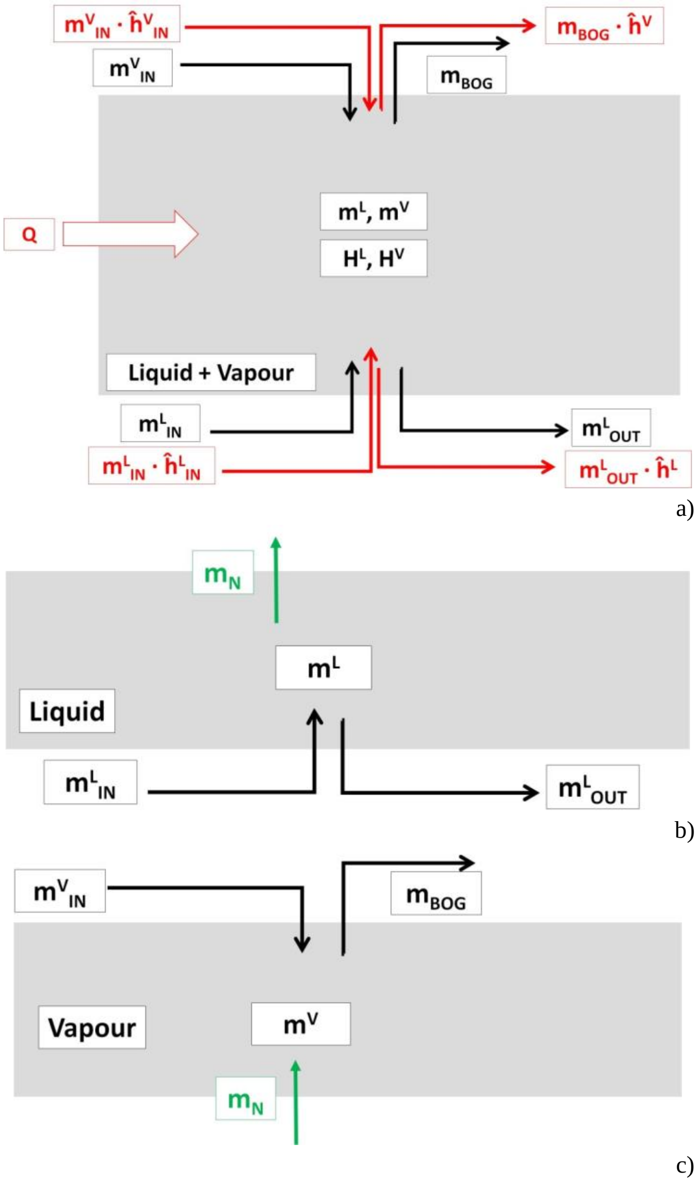

Figure 36. Control volumes of the EQ model: a) overall mass and energy; b) liquid mass; c) vapour mass.

As described by Figure 36, the EQ model can be decomposed into three control volumes: overall mass and energy, liquid mass and vapour mass. These volumes are reported and described in Table 37.

Table 37. Number and description of the control volumes.

Control volume	Description
“overall”	It considers the overall internal volume, thus the liquid and the vapour. The overall enthalpy and mass changes due to the inlet and outlet mass and enthalpy flows, and due to the heat inputs.
“liquid mass”	It is formed by the liquid only. The net mass flow and, the liquid inlet and outlet flows cause the variation of the mass.
“vapour mass”	It considers only the ullage. The variation of the mass is caused by the net mass, the inlet and outlet flows.

The control volumes are a direct consequence of the hypotheses of global homogeneity (hypothesis b) of Section 1.1) of Chapter 3) and of instantaneous thermodynamic equilibrium (hypothesis a) of Section 1.1 of Chapter 3).

2.2. Conservation laws

The second step of the mathematical procedure (step b) of Section 2 of Chapter 3) is the deduction of the balance equations, as indicated in Figure 35. The conservations laws of the EQ model are deduced from the first principle of the thermodynamics (Equation 685) and from the principle of conservation of the mass (Equation 686), as reported in Table 192 (see Appendix F). Equation 685 is applied to the control volume “overall”. Equation 686 is used for the control volumes “overall”, “liquid mass” and “vapour mass”. So, the conservation laws of the EQ model are reported in Table 38.

Table 38. Conservation laws of EQ model.

Name	Equation	Formulas
Overall energy balance equation	Equation 32	$\frac{\partial \tilde{H}}{\partial t} = \dot{Q} + \dot{m}_{IN}^{L} \cdot \tilde{h}_{IN}^{L} - \dot{m}_{OUT}^{L} \cdot \tilde{h}_{S}^{L} + \dot{m}_{IN}^{V} \cdot \tilde{h}_{IN}^{V} - \dot{m}_{BOG} \cdot \tilde{h}_{S}^{V}$
Overall mass balance equation	Equation 33	$\frac{\partial m}{\partial t} = \dot{m}_{IN}^{L} - \dot{m}_{OUT}^{L} + \dot{m}_{IN}^{V} - \dot{m}_{BOG}$
Liquid mass balance equation	Equation 34	$\frac{\partial m^{L}}{\partial t} = -\dot{m}_{N} + \dot{m}_{IN}^{L} - \dot{m}_{OUT}^{L}$
Vapour mass balance equation	Equation 35	$\frac{\partial m^{V}}{\partial t} = \dot{m}_{N} + \dot{m}_{IN}^{V} - \dot{m}_{BOG}$
Volume balance equation	Equation 36	$\frac{\partial V^{V}}{\partial t} + \frac{\partial V^{L}}{\partial t} = 0$

$\tilde{h}_{IN}^{L}$ and $\tilde{h}_{IN}^{V}$ are respectively the liquid and the vapour specific enthalpies at the temperature and pressure of the liquid and vapour inlet flow rate. $\tilde{h}_{S}^{L}$ and $\tilde{h}_{S}^{V}$ are the saturation specific enthalpies of liquid and of vapour at the ullage pressure, respectively.

2.3. Net mass flow equation

The third step of the mathematical procedure (step c) of Section 2) is the development of the net mass flow (NMF) equation. NMF equation is the mathematical formula that computes the variable $\dot{m}_N$ from the values of pressure and liquid volume time-derivates. This equation is described as follows:

Equation 37
$$\dot{m}_N = -\left[V^L \cdot \frac{\partial P^V}{\partial t} \cdot \left(\left.\frac{\partial \rho_S^L}{\partial T}\right|_{P^V} \cdot \left.\frac{\partial T}{\partial P^V}\right|_{S} + \left.\frac{\partial \rho_S^L}{\partial P^V}\right|_{T} \right) + \frac{\partial V^L}{\partial t} \cdot \rho_S^L \right] + \dot{m}_{IN}^{L} - \dot{m}_{OUT}^{L}$$

Equation 37 is the NMF equation. This equation is mandatory for deducing the pressure-liquid volume equations (see Section 2.7 of Chapter 3). The mathematical steps to obtain Equation 37 are described in Section 2 of Appendix F.

2.4. Linear form of Net mass flow equation

The fourth step of the mathematical procedure (step d) of Section 2 of Chapter 3) is the development of the linear form of the net mass flow (NMF) equation. The linear form of NMF equation can be described as follows.

Equation 38
$$\dot{m}_N = -\left[\frac{\partial P^V}{\partial t} \cdot A_{MB}^{L} + \frac{\partial V^L}{\partial t} \cdot C_{MB}^{L} + \dot{m}_{IN}^{L} \cdot D_{MB}^{L} + \dot{m}_{OUT}^{L} \cdot E_{MB}^{L}\right]$$

The coefficients of Equation 38 are given in Table 39.

Table 39. Coefficients of the linear form of the NMF equation (Equation 38).

Coefficients	Equations	Formulas	Coefficients	Equations	Formulas
A_{MB}^{L}	Equation 39	$A_{MB}^{L} = \left[V^{L} \cdot \left(\left.\frac{\partial \rho_S^L}{\partial T}\right\|_{P^V} \cdot \left.\frac{\partial T}{\partial P^V}\right\|_{S} + \left.\frac{\partial \rho_S^L}{\partial P^V}\right\|_{T}\right)\right]$	D_{MB}^{L}	Equation 40	$D_{MB}^{L} = -1$
C_{MB}^{L}	Equation 41	$C_{MB}^{L} = \rho_S^L$	E_{MB}^{L}	Equation 42	$E_{MB}^{L} = 1$

Equation 38 is obtained with the mathematical procedure of Section 3 of Appendix F. The linear form of NMF equation is used to obtain the pressure-liquid volume equations.

2.5. Simplified form of conservation laws

Deducing the simplified conservation laws is the fifth step of the mathematical procedure (step e) of Section 2). The number of conservation laws of equilibrium model (EQ model) is five, as indicated in Table 38. The number of indipendent variables that are computed with conservation laws is 4, as described in Table 36. Two of these variables are defined by the user for each storage mode. So, the number of indipendent variables that are computed with conservation laws becomes 2. Hence, 3 of the conservation laws of EQ model (Table 38) are redundant and they are the conservation laws of liquid and vapour mass (Equation 34 and Equation 35), and of volume (Equation 36). As consequence, the system of conservation laws of EQ model is simplified and only the overall energy and mass balance conservation laws (Equation 658 and Equation 33) are used. Equation 658 and Equation 33 can be written as function of the pressure and liquid volume time-derivates ($\frac{\partial P^V}{\partial t}$ and $\frac{\partial V^L}{\partial t}$), and of the net mass flow ($\dot{m}_N$). This form of the conservation laws is reported in Table 40.

Table 40. Simplified form of the conservation laws.

Name	Equation	Formula
Simplified form energy conservation law	Equation 43	$\sum_{i=L,V} \left\{m^{i} \cdot \frac{\partial P^V}{\partial t} \cdot \left[C_{P_S}^{i} \cdot \left.\frac{\partial T}{\partial P^V}\right\|_{S} + \left.\frac{\partial \tilde{h}_S^i}{\partial P^V}\right\|_{T}\right]\right\} + \dot{m}_N \cdot \Delta\widetilde{H}_{EV} = \dot{Q} + \dot{m}_{IN}^{L} \cdot \left[\tilde{h}_{IN}^{L} - \tilde{h}_{S}^{L}\right] + \dot{m}_{IN}^{V} \cdot \left[\tilde{h}_{IN}^{V} - \tilde{h}_{S}^{V}\right]$
Simplified form of mass conservation law	Equation 44	$\sum_{i=L,V} \left[V^{i} \cdot \frac{\partial P^V}{\partial t} \cdot \left(\left.\frac{\partial \rho_S^i}{\partial T}\right\|_{P^V} \cdot \left.\frac{\partial T}{\partial P^V}\right\|_{S} + \left.\frac{\partial \rho_S^i}{\partial P^V}\right\|_{T}\right)\right] + \frac{\partial V^L}{\partial t} \cdot (\rho_S^L - \rho_S^V) = \dot{m}_{IN}^{L} - \dot{m}_{OUT}^{L} + \dot{m}_{IN}^{V} - \dot{m}_{BOG}$

Equation 43 and Equation 44 are used to develop the liner form of the conservation laws, thus the pressure-liquid volume equations. The mathematical steps to obtain these equations are described in Section 3.1 of Appendix F.

2.6. Linear form of the simplified form of conservation laws

The development of the linear form of the simplified conservation laws (see Table 40) is the sixth step of the mathematical procedure (step f) of Section 2). To reduce the computation time, the target variable of the mathematical system of EQ model (see Table 36) must be analytically determined. Hence, the conservations laws are written as a linear combination of the target variables and the conservation coefficients to make easier the analytical solution. The linear form of the simplified conservation laws (Equation 43 and Equation 44) can be described by Equation 45 and Equation 46, which are reported in Table 41.

Table 41. Linear form of the simplified conservation laws.

Equation	Formula
Equation 45	$\frac{\partial P^V}{\partial t} \cdot A_{EB} + \dot{m}_N \cdot B_{EB} + \frac{\partial V^L}{\partial t} \cdot C_{EB} + \dot{m}_{IN}^{L} \cdot D_{EB}^{L} + \dot{m}_{IN}^{V} \cdot D_{EB}^{V} + \dot{m}_{OUT}^{L} \cdot E_{EB}^{L} + \dot{m}_{BOG} \cdot E_{EB}^{V} + F_{EB} = 0$
Equation 46	$\frac{\partial P^V}{\partial t} \cdot A_{MB} + \dot{m}_N \cdot B_{MB} + \frac{\partial V^L}{\partial t} \cdot C_{MB} + \dot{m}_{IN}^{L} \cdot D_{MB}^{L} + \dot{m}_{IN}^{V} \cdot D_{MB}^{V} + \dot{m}_{OUT}^{L} \cdot E_{MB}^{L} + \dot{m}_{BOG} \cdot E_{MB}^{V} + F_{MB} = 0$

The coefficients D_{MB}^{L} and E_{MB}^{L} are given in Table 39. The coefficients of Equation 45 and Equation 46 are reported in Table 42.

Table 42. Coefficients of linear form of the simplified conservation laws.

Coefficients	Equations	Formulas	Coefficients	Equations	Formulas
A_{EB}	Equation 47	$A_{EB}=\sum_{i=L,V}\left\{m^{i}\cdot\left[C_{P_S}^{i}\cdot\left.\frac{\partial T}{\partial P^{V}}\right\|_{S}+\left.\frac{\partial\tilde{h}_{S}^{i}}{\partial P^{V}}\right\|_{T}\right]\right\}$	D_{MB}^{L}	Equation 48	$D_{MB}^{L}=-1$
A_{MB}	Equation 49	$A_{MB}=\sum_{i=L,V}\left[V^{i}\cdot\left(\left.\frac{\partial\rho_{S}^{i}}{\partial T}\right\|_{P^{V}}\cdot\left.\frac{\partial T}{\partial P^{V}}\right\|_{S}+\left.\frac{\partial\rho_{S}^{i}}{\partial P^{V}}\right\|_{T}\right)\right]$	D_{MB}^{V}	Equation 50	$D_{MB}^{V}=-1$
B_{EB}	Equation 51	$B_{EB}=\Delta H_{EV}$	E_{EB}^{L}	Equation 52	$E_{EB}^{L}=0$
B_{MB}	Equation 53	$B_{MB}=0$	E_{EB}^{V}	Equation 54	$E_{EB}^{V}=0$
C_{EB}	Equation 55	$C_{EB}=0$	E_{MB}^{L}	Equation 56	$E_{MB}^{L}=1$
C_{MB}	Equation 57	$C_{MB}=(\rho_{S}^{L}-\rho_{S}^{V})$	E_{MB}^{V}	Equation 58	$E_{MB}^{V}=1$
D_{EB}^{L}	Equation 59	$D_{EB}^{L}=-\left[\tilde{h}_{IN}^{L}-\tilde{h}_{S}^{L}\right]$	F_{EB}	Equation 60	$F_{EB}=-\dot{Q}$
D_{EB}^{V}	Equation 61	$D_{EB}^{V}=-\left[\tilde{h}_{IN}^{V}-\tilde{h}_{S}^{V}\right]$	F_{MB}	Equation 62	$F_{MB}=0$

The linear forms of the conservation laws, thus Equation 45 and Equation 46, are used for developing the pressure-liquid volume equations. The mathematical steps to obtain Equation 45 and Equation 46 are reported in Section 3.2 of Appendix F.Appendix F

2.7. Pressure-Liquid Volume Equations

The deduction of the pressure-liquid volumes (P-V^L) equations is the seventh step of the mathematical procedure (step g) of Section 2). The P-V^L equations are the key formulas to obtain the pressure-evolution (P-e), liquid volume-evolution (V^L-e), inlet liquid flow (ILF) and boil-off gas (BOG) equations of the mathematical system of the EQ model (see Table 36). The P-V^L equations are so-called because only the differential variables $\frac{\partial P^{V}}{\partial t}$ and $\frac{\partial V^{L}}{\partial t}$ are present. The pressure-liquid volume equations are reported in Table 43.

Table 43. Pressure-Liquid Volume (P-V^L) equations.

Name	Equation	Formula
Energy P-V^L equations	Equation 63	$\frac{\partial P^{V}}{\partial t}\cdot A'_{EB}+\frac{\partial V^{L}}{\partial t}\cdot C'_{EB}+\dot{m}_{IN}^{L}\cdot D'^{L}_{EB}+\dot{m}_{IN}^{V}\cdot D_{EB}^{V}+\dot{m}_{OUT}^{L}\cdot E'^{L}_{EB}+\dot{m}_{BOG}\cdot E_{EB}^{V}+F_{EB}=0$
Mass P-V^L equations	Equation 64	$\frac{\partial P^{V}}{\partial t}\cdot A_{MB}+\frac{\partial V^{L}}{\partial t}\cdot C_{MB}+\dot{m}_{IN}^{L}\cdot D_{MB}^{L}+\dot{m}_{IN}^{V}\cdot D_{MB}^{V}+\dot{m}_{OUT}^{L}\cdot E_{MB}^{L}+\dot{m}_{BOG}\cdot E_{MB}^{V}+F_{MB}=0$

The coefficients of Equation 64 are reported in Table 42 and the coefficients of Equation 63 are given in Table 44.

Table 44. Coefficients of pressure-liquid volume equations.

Coefficients	Equations	Formulas
A'_{EB}	Equation 65	$A'_{EB}=A_{EB}-A_{MB}^{L}\cdot B_{EB}$
C'_{EB}	Equation 66	$C'_{EB}=C_{EB}-\rho_{S}^{L}\cdot C_{EB}$
D'^{L}_{EB}	Equation 67	$D'^{L}_{EB}=D_{EB}^{L}-C_{EB}\cdot D_{MB}^{L}$
E'^{L}_{EB}	Equation 68	$E'^{L}_{EB}=E_{EB}^{L}-C_{EB}\cdot E_{MB}^{L}$

The mathematical steps for obtaining the equations of Table 43 are described in Section 4 of Appendix F.Appendix F

2.8. Pressure evolution, liquid volume evolution, inlet liquid flow and boil-off gas equations

The last step of the mathematical procedure (step h) of Section 2) is the deduction of pressure-evolution (P-e), liquid volume-evolution (V^L-e), inlet liquid flow (ILF) and boil-off gas (BOG) equations from the pressure-liquid volume (P-V^L) equations (see Table 43). P-e, V^L-e, ILF and BOG equations are reported in Table 45 for the two storage modes.

Table 45. Target equations of the indipendent variables.

	Storage mode 4		***Storage mode 1.b***	
Name	**Equations**	**Formulas**	**Equations**	**Formulas**
P-e equation	Equation 69	$\frac{\partial P^V}{\partial t} = -\frac{Z''_{EB}}{A''_{EB}}$	Equation 70	$\frac{\partial P^V}{\partial t} = 0$
V^L-e equation	Equation 71	$\frac{\partial V^L}{\partial t} = \frac{\partial P^V}{\partial t} \cdot A''_{MB} + Z''_{MB}$	Equation 72	$\frac{\partial V^L}{\partial t} = 0$
BOG equation	Equation 73	$\dot{m}_{BOG} = 0$	Equation 74	$\dot{m}_{BOG} = -\frac{Z''_{EB}}{E''_{EB}}$
ILF equation	Equation 75	$\dot{m}^L_{IN} = 0$	Equation 76	$\dot{m}^L_{IN} = \dot{m}_{BOG} \cdot D''_{MB} + Z''_{MB}$

Z''_{EB}, E''_{EB}, D''_{MB}, Z''_{MB}, A''_{EB} and A''_{MB} are given in Table 46.

Table 46. Coefficients for P-e, V^L-e, ILF and BOG equations in storage mode1.b and 4.

Storage mode 1.b			***Storage mode 4***		
Coefficients	**Equations**	**Formulas**	**Coefficients**	**Equations**	**Formulas**
E''^V_{EB}	Equation 77	$E''^V_{EB} = E^V_{EB} + D''_{MB} \cdot D'^L_{EB}$	A''_{EB}	Equation 78	$A''_{EB} = A'_{EB} + C'_{EB} \cdot A''_{MB}$
Z''^L_{EB}	Equation 79	$Z''^L_{EB} = Z_{EB} + D'^L_{EB} \cdot Z''_{MB}$	Z''_{EB}	Equation 80	$Z''_{EB} = Z_{EB} + C'_{EB} \cdot Z''_{MB}$
D''_{MB}	Equation 81	$D''_{MB} = -\frac{E^V_{MB}}{D^L_{MB}}$	A''_{MB}	Equation 82	$A''_{MB} = -\frac{A_{MB}}{C_{MB}}$
Z''_{MB}	Equation 83	$Z''_{MB} = -\frac{Z_{MB}}{D^L_{MB}}$	Z''_{MB}	Equation 84	$Z''_{MB} = -\frac{Z_{MB}}{C_{MB}}$

The coefficients Z_{MB} and Z_{EB} of Table 46 are reported in Table 47.

Table 47. Coefficients $\boldsymbol{Z_{MB}}$ and $\boldsymbol{Z_{EB}}$ for storage mode 1.b and 4.

Coefficients	**Equations**	**Formulas**
		Storage mode 1.b
Z_{EB}	Equation 85	$Z_{EB} = \frac{\partial P^V}{\partial t} \cdot A'_{EB} + \frac{\partial V^L}{\partial t} \cdot C'_{EB} + \dot{m}^V_{IN} \cdot D^V_{MB} + \dot{m}^L_{OUT} \cdot E'^L_{EB} + F_{EB}$
Z_{MB}	Equation 86	$Z_{MB} = \frac{\partial P^V}{\partial t} \cdot A_{MB} + \frac{\partial V^L}{\partial t} \cdot C_{MB} + \dot{m}^V_{IN} \cdot D^V_{MB} + \dot{m}^L_{OUT} \cdot E^L_{MB} + F_{MB}$
		Storage mode 4
Z_{EB}	Equation 87	$Z_{EB} = \dot{m}^L_{IN} \cdot D'^L_{EB} + \dot{m}^V_{IN} \cdot D^V_{EB} + \dot{m}^L_{OUT} \cdot E'^L_{EB} + \dot{m}_{BOG} \cdot E^V_{EB} + F_{EB}$
Z_{MB}	Equation 88	$Z_{MB} = \dot{m}^L_{IN} \cdot D^L_{MB} + \dot{m}^V_{IN} \cdot D^V_{MB} + \dot{m}^L_{OUT} \cdot E^L_{MB} + \dot{m}_{BOG} \cdot E^V_{MB} + F_{MB}$

In storage mode 4 (self-pressurisation), the BOG and the liquid inlet flow rates are equal to zero because the storage container is closed. Hence, the pressure-liquid volume equations (see Table 43) can be used to determine the evolution of pressure and liquid volume. In storage mode 1.b (steady state), the pressure and the liquid volume remain constant and the derivates of these variables are equal to zero. So, the pressure-liquid volume equations (see Table 43 of Section 2.7) can determine the inlet liquid flow rate and the BOG flow rate. The mathematical steps of P-e, V^L-e, ILF and BOG equations are reported in Section 5 of Appendix F.Appendix F

3. Boil-Off Rate (BOR) and Storage Heat Transfer (SHT) models

The Storage Heat Transfer (SHT) model is the Block 5 and the boil-off rate (BOR) model is Block 2, as illustrated in the structure of the equilibrium model (Figure 33). These models are required to determine the boundary conditions of both liquid and vapour, in particular the heat inputs and the insulating properties.

Section 3.1 and 3.2 describe the BOR model and the SHT model, respectively.

3.1. Storage Heat Transfer Model

The heat inputs are the only sources that determine the behaviour of the cryogenic liquids in the storage containers. The heat ingress rates mainly depend on three factors: the environmental conditions, the insulation property of the tank walls, and the tank's geometry. Hence, the heat ingress rate can be computed from these factors. So, a model is required to calculate the heat input rate. This model is called Storage Heat Transfer (SHT) model and it is developed for the EQ model. As explained in Section 1.1, the temperature gradients at the walls are neglected due to the hypotheses of instantaneous thermodynamic equilibrium and of total homogeneity (assumptions a) and b) of Section 1.1 of Chapter 3). As consequence, the *hypothesis of negligible thermal resistance* can be assumed. This assumption states that the heat transfer coefficients at the walls are so high that the value of their thermal resistance[53] is equal to zero. Hence, the heat input can be estimated with Equation 89.

Equation 89
$$\dot{Q} = h_{eff} \cdot A^{TOT} \cdot (T^{W} - T)$$

As results, the heat inputs can be estimated from the environmental and internal conditions, geometry and effective heat transfer coefficient. The overall internal surface (A^{TOT}) is estimated as reported in Appendix B.

3.2. Boil-Off Rate model

The type of the fluid in the storage container determines the internal temperature, thus the driving force of the heat transfer process between the environment and the liquid. Hence, the insulating properties are designed, as function of the internal temperature, to maintain the target value of Boil-Off Rate (BOR), which is around 0.05-0.15 %/d [15], [16] and 0.1-0.18 %/d [17], [12] for LNG and LH_2, respectively. The insulating properties are, however, rarely available. Hence, these properties must be computed from other parameters, such as the BOR[54] or the measured heat input. So, a model is required to calculate the insulating properties and it is called Boil-Off Rate (BOR) model. This model is based on the *hypothesis of the overall thermal insulation*. This assumption states that the whole insulating system can be simplified with the overall insulation, as described in Figure 37. In Figure 37, the light blue and the light orange are respectively the liquid and the vapour. The dashed yellow line is the interface. The dark circles are the walls of the storage container. The circles with blue, purple, green and red colours are the multi-layer insulation (MLI). The grey zone is the overall insulation.

---

[53] The thermal resistance is the struggle to transfer heat from a hot source to a cold one.

[54] Boil-Off Rate (BOR) is the percentage of evaporated liquid volume respect to the initial liquid volume in one day. This value is often expressed in [% vol./vol./day]. The BOR is often experimentally estimated by measuring the variation of the liquid volume over 24 hours at constant pressure of 1 bar, in the storage container that is filled at 98 %.

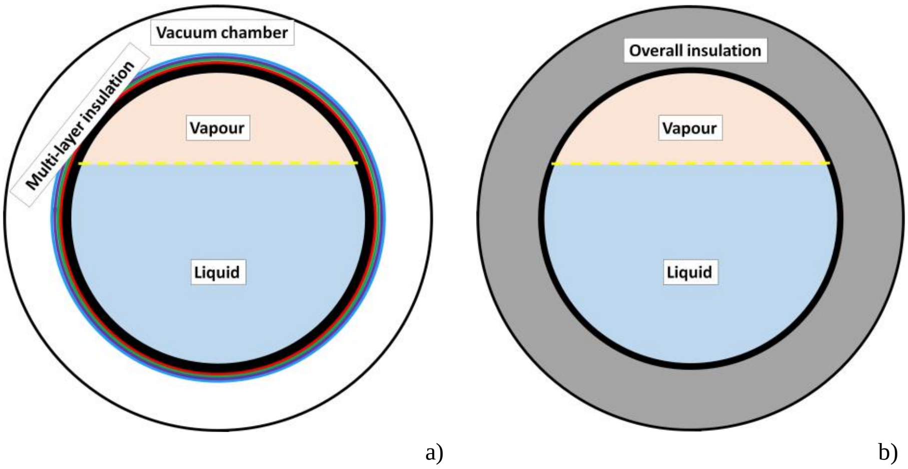

Figure 37. a) Insulation system; b) overall insulation.

As consequence, the properties of the overall insulation can be described by the effective heat transfer coefficient, called h_{eff}. Considering the hypothesis of negligible thermal resistance of in the SHT model (see Section 3.1 of Chapter 3), h_{eff} is calculated with Equation 90 for the EQ model.

Equation 90 $$h_{eff} = \frac{\dot{Q}_{IN}}{A^{TOT} \cdot (T^W - T_S)}$$

T_S is the saturation temperature of the liquid at the pressure of storage container during the BOR test. $\dot{Q}_{IN}$ is the measured heat leakage rate in this test.

3.3.Estimation of the heat leakage rate

The heat inputs make the liquid evaporating, causing the variation of the liquid mass. In an open storage container, this variation causes the reduction of the liquid volume, as occurs in the boil-off rate (BOR) test. Hence, the heat leakage rate of BOR test ($\dot{Q}_{IN}$) can be estimated from the value of the BOR. To do that, it must be assumed:

a) The liquid must be a saturation at the pressure of the BOR test. So, all the heat entering the liquid is coverted into evaporation, thus latent heat;
b) The vapour has the same temperature of the liquid;
c) The storage container is at quasi-steady state, except for the variation of the liquid volume;

As consequence, the overall energy and mass balance equations (Equation 658 and Equation 33) can be substituted with the conservation laws of Table 48.

Table 48. Conservation laws of the BOR model.

Name	Equation	Formulas
Energy conservation law of BOR model	Equation 91	$-\dot{m}_{BOG} \cdot \tilde{h}_S^L = \dot{Q}_{IN} - \dot{m}_{BOG} \cdot \tilde{h}_S^V$
Mass conservation law of BOR model	Equation 92	$\rho \cdot \frac{\partial V^L}{\partial t} = \rho \cdot {V_{IN}}^L \cdot BOR = \dot{m}_{BOG}$

If Equation 91 and Equation 92 are combined, heat leakage rate ($\dot{Q}_{IN}$) can be estimated as follows:

Equation 93 $$\dot{Q}_{IN} = \rho \cdot {V_{IN}}^L \cdot BOR \cdot \Delta\widetilde{H}_{EV}$$

ρ is the liquid density at T_S and ${V_{IN}}^L$ is the initial liquid volume. $\Delta\widetilde{H}_{EV}$ is the latent heat of evaporation. BOR of Equation 93 is in s^{-1}.

4. Reference models for the thermo-physical properties

The calculation of the thermo-physical properties is the Block 4 of the structure of the equilibrium model (EQ) model, as illustrated in Figure 33. The thermodynamic properties are required for computing the thermal behaviour of liquid hydrogen[55] and nitrogen, and their corresponding vapour phase. Moreover, the fluid-dynamics and the heat transfer models require the evaluation of transport properties. Hence, the models of thermo-physical[56] properties are crucial for properly predicting the behaviour of cryogenic liquids. The list of the thermo-physical properties used in the model is reported in Table 49.

Table 49. List of the thermodynamic and transport properties.

Property	Name	Symbol	Unit
Thermodynamic	Specific enthalpy	$\tilde{h}$	[J/kg]
	Latent heat of evaporation	$\Delta\tilde{H}_{EV}$	[J/kg]
	Isobaric heat capacity	C_P	[J/kg/K]
	Derivate of the temperature respect to pressure at saturation	$\left.\frac{\partial T}{\partial P}\right\|_S$	[K/kPa]
	Derivate of specific enthalpy respect to pressure, at constant temperature	$\left.\frac{\partial \tilde{h}}{\partial P}\right\|_T$	[J/kg/kPa]
	Density	ρ	[kg/m^3]
	Derivate of density respect to pressure, at constant temperature	$\left.\frac{\partial \rho}{\partial P}\right\|_T$	[kg/m^3/kPa]
	Derivate of specific enthalpy respect to pressure, at constant temperature	$\left.\frac{\partial \tilde{h}}{\partial T}\right\|_P$	[kg/m^3/K]
	Volume expansion coefficient	β	[1/K]
	Saturation pressure	P_S	[kPa]
Transport	Thermal conductivity	λ	[W/m/K]
	Dynamic viscosity	η	[Pa·s]
	Kinematic viscosity	ν	[m²/s]
	Thermal diffusivity	α	[m²/s]

Kinematic viscosity and thermal diffusivity can be deduced from the dynamic viscosity and thermal conductivity, as reported in Section 3 of Appendix G. The thermodynamic properties can be obtained from the Helmholtz free energy (see Section 1 of Appendix G), which are implemented in REFPROP[57] [8]. The models of REFPROP are considered as the reference for a certain number of pure fluids and their mixtures because:

a) Their parameters have been regressed and regularly updated against primary datasets. These datasets are selected among all the available literature data[125];
b) Their functional forms allow the best representation of the thermo-physical properties of such fluids [125].

The use of REFPROP [8] offers the advantages of flexibly in describing the thermo-physical properties because this software can compute these properties for many fluids in a large range of pressure and temperatures. REFPROP [8] contains the numerical algortimh to compute these physical properties. Hence, this software simplifies the implementation of the algorithms to estimate these properties. So, REFPROP [8] is used to compute the thermo-physical properties in this thesis.

The thermodynamic model is described in Section 4.1. The reference models of the transport properties are explained in Section 4.2.

---

[55] In this thesis, hydrogen is considered as pure para-hydrogen..

[56] Thermo-physical property are divided into thermodynamic and transport property.

[57] REFPROP is a software proposed by the National Institute of Standard and Technology (NIST)[8]. This software is implemented in the Matlab$^{(R)}$ code of this thesis via a function developed by (NIST)[8]. The version of REFPROP used is 9.1.

4.1. Thermodynamic model

In literature, several Equations of State (EoSs) exist to predict the thermodynamic properties of pure fluids and mixtures. The fundamental equations explicit in Helmholtz free energy (see Section 1 of Appendix G), as implemented in the software REFPROP, are used in this thesis. These EoSs have the following advantages [125]:

a) The error of computing the thermodynamic properties is within the experimental uncertainty of the respective property for the considered fluid;
b) The coefficients of the equation are obtained with the multi-property fitting[58];
c) These equations are valid over a wide range of pressure and temperature;

Table 50 reports the uncertainty in the representation of some of the thermodynamic properties of interest in this thesis for nitrogen and for normal hydrogen in the range of interest of this thesis (pressure is below 1 MPa).

Table 50. Uncertainty of fundamental EoS of nitrogen**[126]** and of para-hydrogen**[127]**.

	Para-hydrogen	
Variables	**Uncertainty**	**Range**
Density	Below ± 0.5 %	20-100K and 0.1-10 bar
Ideal gas heat capacity	Below ± 10 %	Below 100 K
	Nitrogen	
Variables	**Uncertainty**	**Range**
Density	0.02 %	70-200 K and 1-10 bar
Vapour Isobaric heat capacity	± 0.3 % (vapour)	70-200 K and 1-10 bar
Liquid Isobaric heat capacity	± 0.8% (liquid)	70-200 K and 1-10 bar

The EoS of Span et al. [126] for nitrogen and the EoS of Leachman et al. [127] for hydrogen are enough precise to estimate the thermodynamic properties of in small scale (SS) storage tanks.

4.2. Transport properties model

As recommended by REFPROP [8] authors, the viscosity and the thermal conductivity of nitrogen are calculated with the model of Lemmon and Jacobsen [128]. The models of Muzny et al. [129] and of Assael et al. [130] respectively determine the viscosity of the normal hydrogen[59] and the thermal conductivity of para-hydrogen. These models are based on the same principle of the fundamental EoS. So, the transport property is decomposed in ideal and real contribution (see Section 3 of Appendix G). Table 51 reports the uncertainty of these transport properties for normal hydrogen and nitrogen for the temperature and pressure range of interest of this thesis.

Table 51. Uncertainty of the models of transport properties.

	Normal hydrogen	
Variables	**Uncertainty**	**Range**
Viscosity	Between 15% and -8 %	0-100K
Thermal conductivity	Below 5%	0-200K
	Nitrogen	
Variables	**Uncertainty**	**Range**
Viscosity	Mainly below 2% Up to 5 % around 90 K	66-220K and 0.1-10 bar
Thermal conductivity	Below 2%	64-220K and 0.1-10 bar

As consequence of uncertainty of Table 51, the proposed models are suitable to calculate the viscosity and the thermal conductivity under storage conditions. The uncertainties are, however, higher than the ones for thermodynamic properties.

---

[58] The EoS parameters were regressed on the experimental data of different properties.

[59] The viscosity of para-hydrogen is computed with the viscosity of the normal hydrogen.

5. Solution of the Ordinary Differential Equations Systems

The solution of the Ordinary Differential Equations (ODEs) system is the Block 7 of the structure of the equilibrium model (EQ model), as explained in Figure 33. During the self-pressurisation, the variables such as pressure, temperatures and liquid level change in time due to the heat inputs. The time-variation of these variables is determined with differential equations. The exact solution of these equations cannot be analytically obtained. An approximated solution can be, however, determined with a numerical method. Hence, an ODE solver is required to calculate the values of these variables from their time-variation. This solver is chosen to fulfil the objectives of this thesis. One of the sub-objectives of this thesis is the implementation of a method to solve the Ordinary Differential Equation Systems (ODEs), which is suitable for industrial applications. For these applications, the computational time must be reduced as much as possible, maintaining a reasonable accuracy. So, the ODE solver must be chosen to optimize the computational time. This time depends on the stiffness[60] of the differential equations and the accuracy, thus the tolerance[61]. Hence, the time step and the tolerance should be determined with the purposes of:

a) Increasing the number of iteration, thus the precision, when it is required. High precision, thus low tolerance, are required when the derivates significantly changes in time;
b) Reducing the computational time, when the derivates are more or less numerically constant, by increasing the time step and the tolerance;

The method of Runge-Kutta-Fehlberg with Cash-Karp parameters [131] (RKF-CKp) is chosen to solve the Ordinary Differential Equations (ODEs) system, because it is a good compromise between accuracy and computational time.

Section 5.1 presents the ODEs system of the EQ model. Section 5.2 describes the theory of the RKF-CKp method and Section 5.3 presents the algorithm of this approach.

5.1. Ordinary Differential Equations system of equilibrium model

The mathematical system of equilibrium model (EQ model) (see Table 36) is composed by algebraic and differential equations. The differential equations compose the Ordinary Differential Equations (ODEs) system for the self-pressurisation (storage mode 4) and for the steady state (styorage mode 1.b), as reported in Table 52.

Table 52. ODE system of equilibrium model.

Storage mode	Steady state (1.b)	Self-pressurisation (4)
Equations	P-e equation (Equation 70) P-e equation (Equation 72)	V^L-e equation (Equation 69) V^L-e equation (Equation 71)

The ODE system is solved to determine the liquid volume and the pressure, thus the state variables V^L and P^V. These variables are used to determine the dipendent variables of Table 36. As indicated in Table 52, the ODE system is determined because the number of equations is equal to the number of variables. Hence, only the initial conditions are required to solve his system. According to Cauchy's theorem[62], the initial conditions of the ODEs must be defined to assure the uniqueness and the existence of the solution. The method to define the initial conditions is defined in Block 1 (see Section 1.3.1 of Chapter 3).

---

[60] Stiffness is defined as the feature of the equation to change the solution, as the parameters are modified.

[61] Tolerance is the numerical error that can be accepted.

[62] Chauchy's theorem states that the solution of an ODEs system exists and is unique, if and only if the initial conditions are defined.

5.2.Runge-Kutta-Felhberg with Cash-Karp parameters

The Runge-Kutta-Fehlberg with Cash-Karp parameters [131] (RKF-CKp) method is an explicit[63] Runge-Kutta (RK) method of 5th order with adaptive step size[64]. This method is based on the idea of decomposing the time-evolution of the variable y_n in intervals, called integration time-step (dt_i), and in point, called time-point (t_i), as illustrated in Figure 38. Each interval is divided into sub-time-point ($t_{i,j}$), as described in Figure 38. In Figure 38, the black arrows are the horizontal and vertical axis. The dark line is the time-evolution of the variable y_n. The blue braces are the integration time-step. The orange and the red dashed lines connect the time-points with the values of the variable y_n, and the sub-time-point with the same variable, respectively. The green and the purple circles are the time-points and the sub-time-points, respectively. The orange and the red circles are the values of the variable y_n at the time-points and at the sub-time-points.

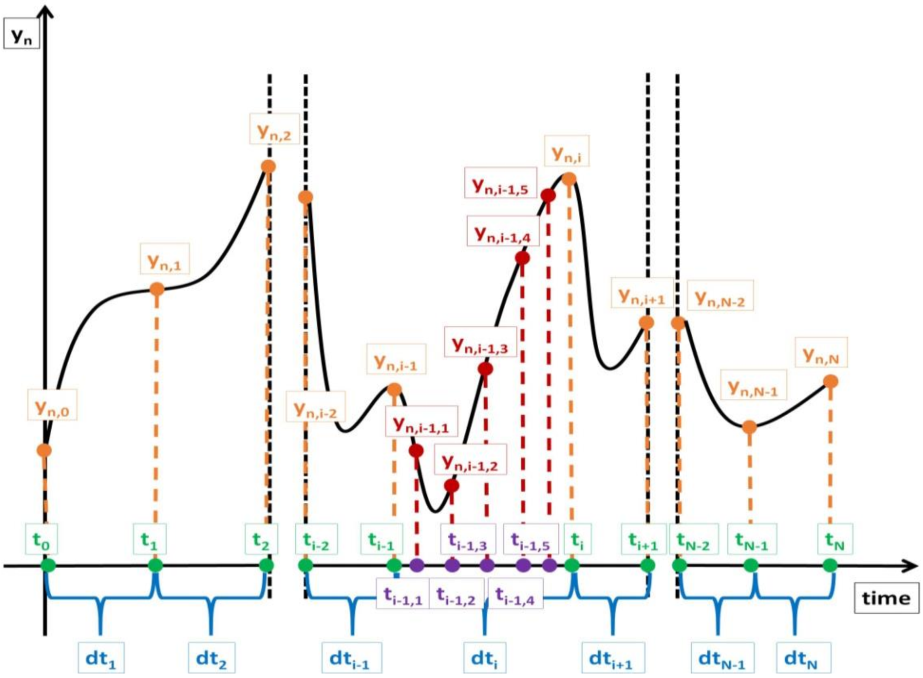

Figure 38. Division of the time-evolution of the variable $\boldsymbol{y_n}$.

As illustrated in Figure 38, the integration time-step is not fixed and it changes for every time-points. The value of this step is low when the time-evolution of the variable y_n rapidly changes because the potential numerical error is high. If the time-evolution of this variable is almost constant, the potential numerical error is low and the value of the integration time-step increases. Hence, the reduction of the computation time can be obtained with this type of adaptive step size method. As described in Figure 38, the integration time-step is decomposed into five sub-time-points because the ODE solver is a 5th order Runge-Kutta. For each sub-time-point, the value of the variable y_n is estimated with formulas that uses the values of the derivates of y_n this variable at the previous sub-time-point. Hence, the approximate value of the variable y_n at the time point t_{i+1} is more accurate than the one obtained by Eulero Forward (EF) method[65]. So, this RK approach is suitable for the industrial applications of the equilibrium model.

---

[63] In Explicit method, the derivates are calculated with the values of the solutions at the previous time step.

[64] Adaptive time step means that the time step is determined before the integration of the ODE and it is not fixed.

[65] Eulero Forward method: $y_{n,t_i+1} = y_{n,t_i} + \left.\frac{\partial y}{\partial t}\right|_{t_i,n}$

5.3. Algorithm of the Ordinary Differential Equations system solver

The method of Runge-Kutta-Fehlberg with Cash-Karp parameters[131] (RKF-CKp) compute the integration time-step at every time-point, to match the desired value of the numerical error. This numerical error is estimated with the approximated solution, as described by Equation 788 [131] of Appendix H. This approximated solution is determined as function of this integration time-step, as explained by Equation 779. Hence, the method of RKF-CKp is an iterative procedure where the integration time-step is computed until the desired value of the numerical error is achieved.

The equations of the algorithm of the solver of the Ordinary Differential Equations (ODEs) system are reported in Table 211 of Appendix H. The inputs and the output variables are given in Table 53.

Table 53. Input and output of the algorithm of RKF-CKp.

Input
Relative tolerance (ε)[66], approximated solution at the previous time-point ($\tilde{y}_{n,i-1}$), values of the derivates at the previous time-point ($\frac{\partial y}{\partial t}\Big|_{n,i-1}$), the value of the integration time-step of the previous time point (dt_{i-1}).
Output
Approximated solution at the current time-point ($\tilde{y}_{n,i}$), integration time-step (dt_i) and the integration time step at the next time-point (dt_{i+1}).

Figure 39 describes the algorithm of method of RKF-CKp.

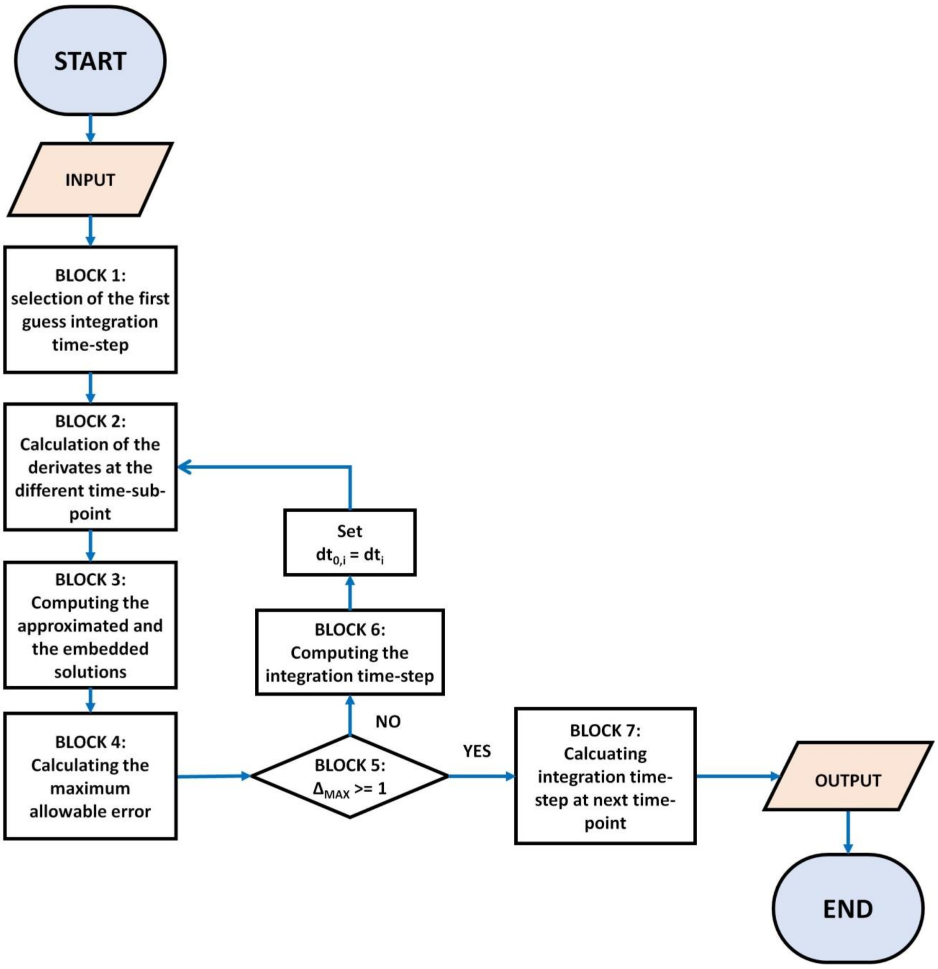

Figure 39. Algorithm of the method of RKF-CKp.

---

[66] The relative tolerance is fixed at the values of 10^{-10}.

This algorithm is an iterative procedure and it is composed by the following steps:

a) BLOCK 1: the first guess value of the integration time-step ($dt_{0,i}$) at the current time-point (t_i) is calcualted with two methods, respectively called M1 and M2:
  - M1: if the current time-point is the first time-point (t_1), $dt_{0,i}$ is computed with Equation 792 of Appendix H;
  - M2: when the current time-point is not t_1, $dt_{0,i}$ is equal to the integration time-step of the previous time point (t_{i-1}) that is computed with Equation 791.

b) BLOCK 2: the values of the derivates ($\left.\frac{\partial y}{\partial t}\right|_{1,n}$, $\left.\frac{\partial y}{\partial t}\right|_{2,n}$, $\left.\frac{\partial y}{\partial t}\right|_{3,n}$, $\left.\frac{\partial y}{\partial t}\right|_{4,n}$ and $\left.\frac{\partial y}{\partial t}\right|_{5,n}$) are computed at each sub-time-point ($t_{i-1,1}$, $t_{i-1,2}$, $t_{i-1,3}$, $t_{i-1,4}$ and $t_{i-1,5}$), using $dt_{0,i}$, with Equation 781, Equation 782, Equation 783, Equation 784 and Equation 785, respectively. To compute the values of these derivates, the state variables, the thermo-physical properties and the heat inputs are required. Hence, Block 3, 4, 5, 6 and 8 of block structure of equilibrium model are executed, as reported in Figure 33.

c) BLOCK 3: the approximated solution and the embedded solution are respectively computed with Equation 779 and Equation 789 of Appendix H.

d) BLOCK 4: the maximum allowable error (Δ_{MAX}) is determined with Equation 787.

e) BLOCK 5: two patterns of the algorithm are developed as function of Δ_{MAX} and they are respectively called P 1.5 and P 2.5:
  - P 1.5: if the value of Δ_{MAX} is lower than 1, the algorithm executes BLOCK 7;
  - P 2.5: when the value of this error is higher than 1, the algorithms runs BLOCK 6;

f) BLOCK 6: the integration time-step (dt_i) of t_i is computed with Equation 786. The algorithm re-starts the calculation form BLOCK 2, after setting that $dt_{0,i}$ is equal to dt_i;

g) BLOCK 7: the integration time-step (dt_{i+1}) of next time-point (t_{i+1}) is computed with Equation 791. The output exits the algorithm and the iterative procedure stops;

The algortimh of the ODE solver converges in 1 iterations, if the first guess value of the time-step produces a numerical error that is lower than the defined one. If this situtiaon does not occur, this algorithm usually converge in 10 iterations.

6. Comparison with experimental data

The results of the equilibrium model (EQ model) are compared with the experimental data. The data considered in this comparison covers different levels of overall heat fluxes ingress into the tank (low, medium and high). The values of these fluxes are obtained as explained in Section 6 of Chapter 2. The results of the EQ model are obtained by the structure of Figure 33, but BLOCK 1 (the initialisation of the variable) and BLOCK 2 (Boil-Off Rate Model) are changed from the ones proposed in Section 1.3.1 and in Section 3.2, respectively.

Section 6.1 presents the cases and Section 6.2 explains the simulation procedure. Section 6.3 and Section 6.4 describes the modifications of BLOCK 1 and BLOCK 2, respectively. Section 6.5, 6.6 and 6.7 presents the results of the EQ model and the comparison with experimental data of pressure, ullage and liquid temperatures, and filling ratio for the study cases at low, medium and high heat fluxes, respectively.

6.1. Definition of the study cases, initial and boundary conditions

The different study cases are reported and classified as function of the heat fluxes, as described in Table 54. In Table 54, SS and ISO respectively indicate steady state and isothermal. LN_2 and LH_2 are the liquid nitrogen and the liquid hydrogen, respectively. H and D are the maximum internal height and the maximum internal dimater, respectively. the heat fluxes are computed as ratio between the overall heat input and the overall internal surface.

Table 54. Definition of the Study case and classification.

Type	Study case	Authors	Fluid	Geometry	Sub-case	Initial conditions	Heat fluxes $[W/m^2]$
Low heat fluxes	1	Seo and Jeong [24]	LN_2	Vertical cylinder with flat bottom and roof (0.201mx0.213m – DxH)	Test 1	SS	6.722
					Test 2	SS	5.877
					Test 3	SS	13.23
					Test 4	SS	5.222
					Test 5	SS	4.638
					Test 6	SS	3.596
	2	Perez et al. [3]	LN_2	Vertical cylinder with flat bottom and roof (0.2005mx0.213m – DxH)	Test 1	SS	6.087
	3	Hasan et al. [27]	LH_2	Oblate ellipsoid with equals horizontal semi-axis (2.2mx1.833m–DxH)	Test 1	SS	6.141
					Test 2	ISO	6.170
	4	Dresar et al. [28]	LH_2	Oblate ellipsoid with equals horizontal semi-axis (2.2mx1.833m–DxH)	Test 1	SS	5.201
					Test 2	SS	4.667
Medium heat fluxes	5	Kang et al. [25]	LN_2	Vertical cylinder with flat bottom and roof (0.13mx0.8m – DxH)	Test 1	SS	84.67
					Test 2	SS	97.53
					Test 3	SS	50.63
	6	Aydelott and Spuckler [30]	LH_2	Sphere with internal diameter of 56 cm	Test 1	SS	75.92
					Test 2	SS	72.69
					Test 3	SS	55.73
					Test 4	SS	237.5
High heat fluxes	7	Aydelott [29]	LH_2	Sphere with internal diameter of 23 cm	Test 1	SS	283.91
					Test 2	SS	269.62
					Test 3	SS	191.36

Except for Study Case 7, experimental data of liquid nitrogen and liquid hydrogen are available at medium and low heat fluxes.

6.2. Simulation procedure for the comparison with the experimental data

To reproduce the self-pressurisation, it is required that the initial conditions of the simulation are at steady state, as done in the experiments. Hence, the simulation of the self-pressurisation must start from the stationary point that is obtained from the equilibrium model (EQ model). To achieve this steady state point, a simulating procedure is developed to reproduce the initial conditions of the self-pressurisation as similarly as it is done in the experiments. These stages are respectively called the steady state stage and by the self-pressurisation stage. These stages are described in Table 55.

Table 55. Description of the simulation stages.

Stage	Description
Steady state	The behaviour of the cryogenic liquid is simulated for an open storage container at constant pressure and liquid level. The storage mode of steady state (1.b) is used. The storage container is initially at thermodynamic equilibrium at the pressure and liquid level of the experiment that is simulated. The initial time (t_0) is equal to zero. The filling ratio is kept constant by adding a liquid at the same temperature and pressure of the liquid stored. So, the thermal behaviour of the liquid is not perturbed by this inlet flow rate. This stage lasts the 30% of the experimental time of the self-pressurisation.
Self-pressurisation	The storage container is virtually closed and the storage tank is simulated as a closed system[67]. The storage mode of the self-pressurisation (4) is applied. The self-pressurisation starts at the conditions at the end of the previous stage.

As described in Table 55, the steady state stage defines the initial conditions of the self-pressurisation. This procedure is applied for all the storage models and for all the experiments, except for the Test 2 of Study case 3. In this case, the steady state stage is skipped and the self-pressurisation stage immediately starts with the storage container at equilibrium condition, because the experiment started at the isothermal condition, without the steady state stage

6.3. Initialisation of the simulation (BLOCK 1) for comparison

The initial value of the state variable must be defined due to the Chauchy's theorem (see Section 5.1 of Chapter 3). These values are determined as explained in Section 1.3.1 of Chapter 3, except for the comparison with the experimental data. For this purpose, the initial value of pressure and the initial value of filling ratio are equal to the experimental ones at the beginning of the self-pressurisation. The internal temperature is equal to the saturation one at the initial experimental pressure of the self-pressurisation.

6.4. Boil-off Rate Model (BLOCK 2) for comparison

To describe the storage of cryogenic liquids in storage container with equilibrium model (EQ model), the boundary conditions of the storage containers must be determined. These conditions are the external wall temperature and the insulating properties of the storage containers. These properties are described with the effective heat transfer coefficient, which is computed with the Boil-Off Rate (BOR) model. The BOR model estimates this coefficient with the heat inputs rate or with the value of the BOR, as explained in Section 3.2. The experimental values of the BOR of the Study case are not available. Hence, the experimental values of the heat leakage rate are used in Equation 90 instead of measured heat flow ($\dot{Q}_{IN}$) that is deduced from the BOR. In Equation 90, the temperature T_S is computed as the saturation temperature at the experimental initial pressure of the self-pressurisation. The external wall temperature is constant and its value is equal to 298.15 K. The value of this

---

[67] Closed system is a system that can exchange only energy and work.

temperature is used in Equation 89 of Storage Heat Transfer (SHT) model (see Section 3.1 of Chapter 3).

6.5.Low heat fluxes study cases

The experimental and numerical model's initial and boundary conditions of the self-pressurisation stage are described in Table 56, for the cases at low heat fluxes (Study case 1, 2, 3 and 4 presented in Table 54). In Table 56, h_{eff} is the effective heat transfer of the storage container. $\dot{Q}$ is the overall heat input at steady state, LF is the filling ratio, P is the pressure, and T^V and T^L are respectively the ullage and the liquid temperature. The experimental and the calculated values of these variables are respectively indicated with "Exp" and with "EQ", at the start of the self-pressurisation.

Table 56. Initial conditions and boundary conditions for the self-pressurisation stage.

Sub-case	$h_{eff}\ \left[\frac{W}{m^2\cdot K}\right]$	$\dot{Q}$ [W]		LF [%]		P [bar]		T^V [K]		T^L [K]	
		Exp	**EQ**	**Exp**	**EQ**	**Exp**	**EQ**	**Exp**	**EQ**	**Exp**	**EQ**
Study case 1											
Test 1	0.03043	1.331	1.331	93.78	93.78	1	1	77.41	77.24	77.02	77.24
Test 2	0.02660	1.163	1.163	75.65	75.65	0.9954	0.9954	78.91	77.20	77.03	77.20
Test 3	0.05968	2.618	2.618	73.61	73.61	0.9954	0.9954	80.48	77.20	77.14	77.20
Test 4	0.02363	1.034	1.033	55.62	55.62	0.9954	0.9954	80.47	77.20	76.93	77.20
Test 5	0.02099	0. 9183	0.9183	27.79	27.79	0.9954	0.9954	81.05	77.20	76.84	77.20
Test 6	0.01627	0.7119	0.7119	9.684	9.684	0.9939	0.9939	81.68	77.19	76.77	77.19
Study case 2											
Test 1	0.02763	1.201	1.201	84.57	84.57	1.071	1.071	78.35	77.83	77.76	77.83
Study case 3											
Test 1	0.02204	82.96	82.96	75.48	75.48	1.03	1.03	22.83	20.33	20.24	20.33
Test 2	0.02207	83.08	83.08	75.19	75.19	1.03	1.03	20.46	20.33	20.35	20.33
Study case 4											
Test 1	0.01867	70.30	70.30	49.37	49.37	1.03	1.03	23.50	20.33	20.13	20.33
Test 2	0.01663	62.59	62.59	34.65	34.65	1.03	1.03	23.66	20.33	20.09	20.33

As indicated in Table 56, the EQ and Exp values of heat inputs, filling ratio and pressure are equal at the start of the self-pressurisation. A small difference in the value between the Exp and EQ liquid temperatures exists because the liquid is close to the saturation conditions. On the other hand, the EQ vapour temperature is lower than the Exp value of this variable because the vapour is overheated. The value of the effective heat transfer coefficient (h_{eff}) changes for every sub-case because it is computed for every test.

Section 6.5.1, 6.5.2, 6.5.3, 6.5.4 and 6.5.6 presents the results of the effective heat transfer coefficient, the net mass flow and the heat inputs, the pressure, the temperature and the filling ratio, respectively. In the title of these graphs of these sections, the words LN_2 and LH_2 respectively indicate the liquid nitrogen and the liquid hydrogen. The words "Vert. Cyl.", "Obl. Elip." and "Sph." means vertical cylinder, oblate ellipsoid and sphere, respectively. The isothermal and steady Boil-off Gas initial conditions are indicated by the words "ISO" and "SS" respectively. The initial values of filling ratio and heat input, calculated in this thesis, are reported in each graph. The word “Exp” indicates the experimental values.

6.5.1. Presentation of the results: Heat inputs

Figure 40 shows the time evolution of the heat inputs computed with Equation 89 (see Section 3.1 of Chapter 3). The continuous lines are the values computed with the equilibrium model. The colour of each line corresponds to the experimental tests, as indicated in each graphs.

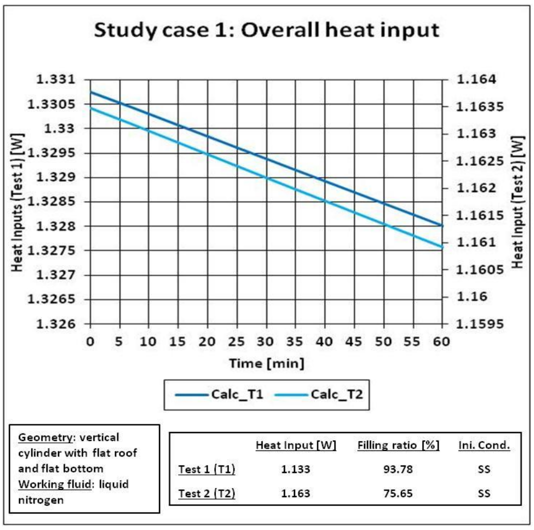

	Heat Input [W]	Filling ratio [%]	Ini. Cond.
Test 1 (T1)	1.133	93.78	SS
Test 2 (T2)	1.163	75.65	SS

a)

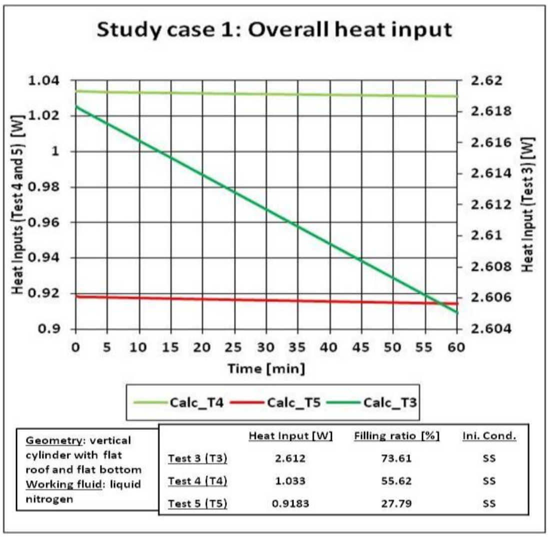

	Heat Input [W]	Filling ratio [%]	Ini. Cond.
Test 3 (T3)	2.612	73.61	SS
Test 4 (T4)	1.033	55.62	SS
Test 5 (T5)	0.9183	27.79	SS

b)

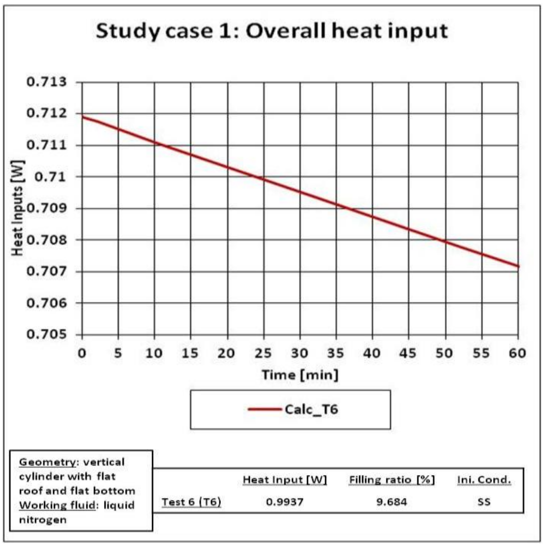

	Heat Input [W]	Filling ratio [%]	Ini. Cond.
Test 6 (T6)	0.9937	9.684	SS

c)

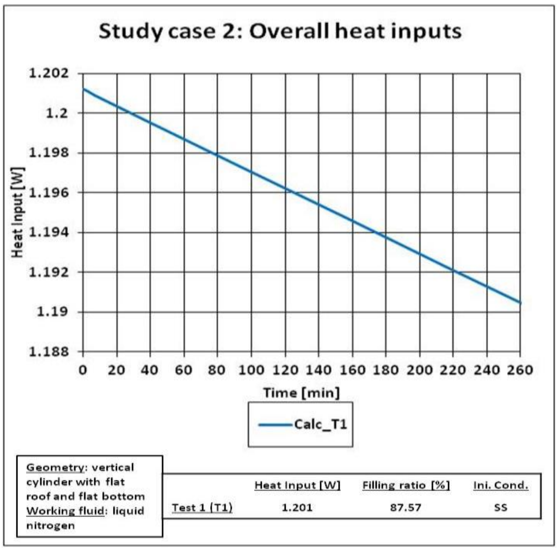

	Heat Input [W]	Filling ratio [%]	Ini. Cond.
Test 1 (T1)	1.201	87.57	SS

d)

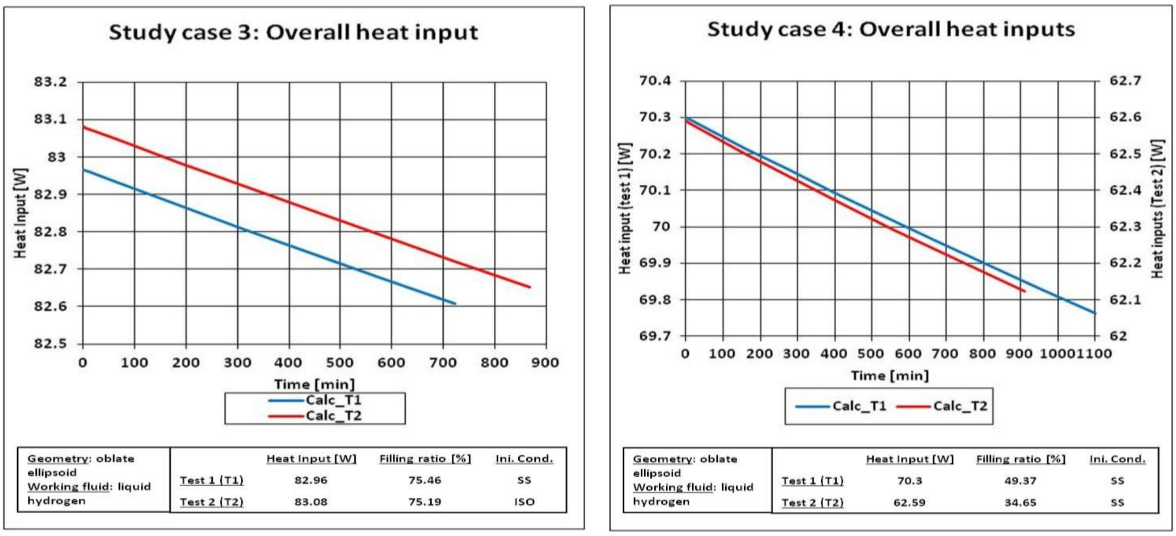

Geometry: oblate ellipsoid
Working fluid: liquid hydrogen

	Heat Input [W]	Filling ratio [%]	Ini. Cond.
Test 1 (T1)	82.96	75.46	SS
Test 2 (T2)	83.08	75.19	ISO

Geometry: oblate ellipsoid
Working fluid: liquid hydrogen

	Heat Input [W]	Filling ratio [%]	Ini. Cond.
Test 1 (T1)	70.3	49.37	SS
Test 2 (T2)	62.59	34.65	SS

e) f)

Figure 40. Heat inputs computed with EQ model for the study cases at low heat fluxes: a) Study case 1 (Test 1 and Test 2), b) Study case 2 (Test 3, 4 and 6), c) Study case 3 (Test 6), d) Study case 2, e) Study case 3 and f) Study case 4.

The heat inputs decrease during the self-pressurisation, with a rate that depends on the natural pressure build-up. As the natural pressure build-up rate increases, the heat entering is reduced. At the same time-point, the heat leakage decreases with the reduction of the filling ratio, except for Test 3 of Study case 1.

6.5.2. Presentation of the results: Net Mass flow

Figure 41 shows the time-evolution of the net mass flow ($\dot{m}_N$), which is computed with Equation 37 (see Section 2.3 of Chapter 3). The continuous lines are the values computed with the equilibrium model. The different curves in each graph correspond to the different tests conducted in each study case.

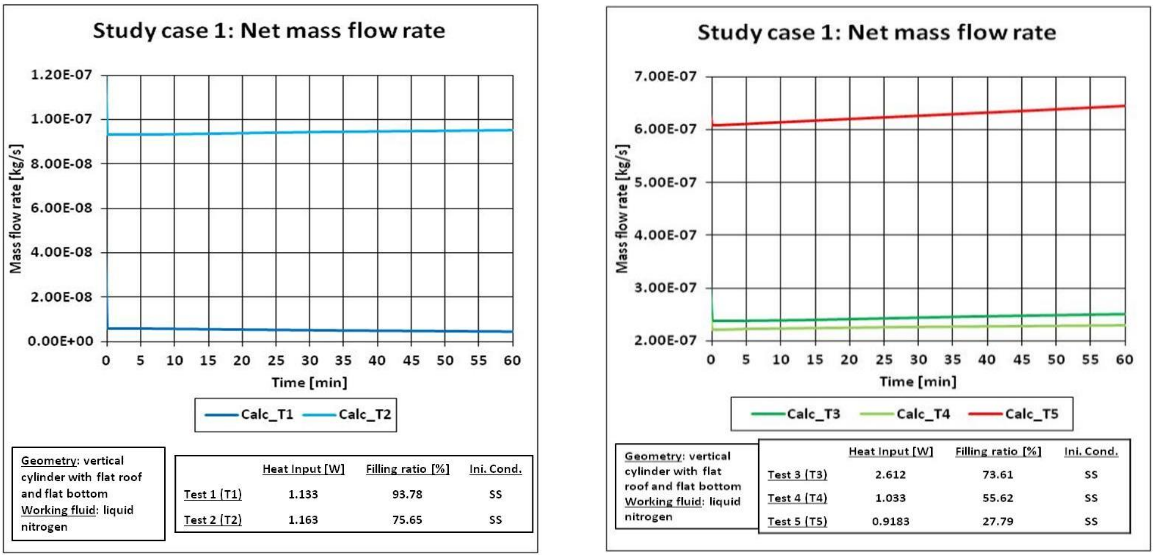

Geometry: vertical cylinder with flat roof and flat bottom
Working fluid: liquid nitrogen

	Heat Input [W]	Filling ratio [%]	Ini. Cond.
Test 1 (T1)	1.133	93.78	SS
Test 2 (T2)	1.163	75.65	SS

Geometry: vertical cylinder with flat roof and flat bottom
Working fluid: liquid nitrogen

	Heat Input [W]	Filling ratio [%]	Ini. Cond.
Test 3 (T3)	2.612	73.61	SS
Test 4 (T4)	1.033	55.62	SS
Test 5 (T5)	0.9183	27.79	SS

a) b)

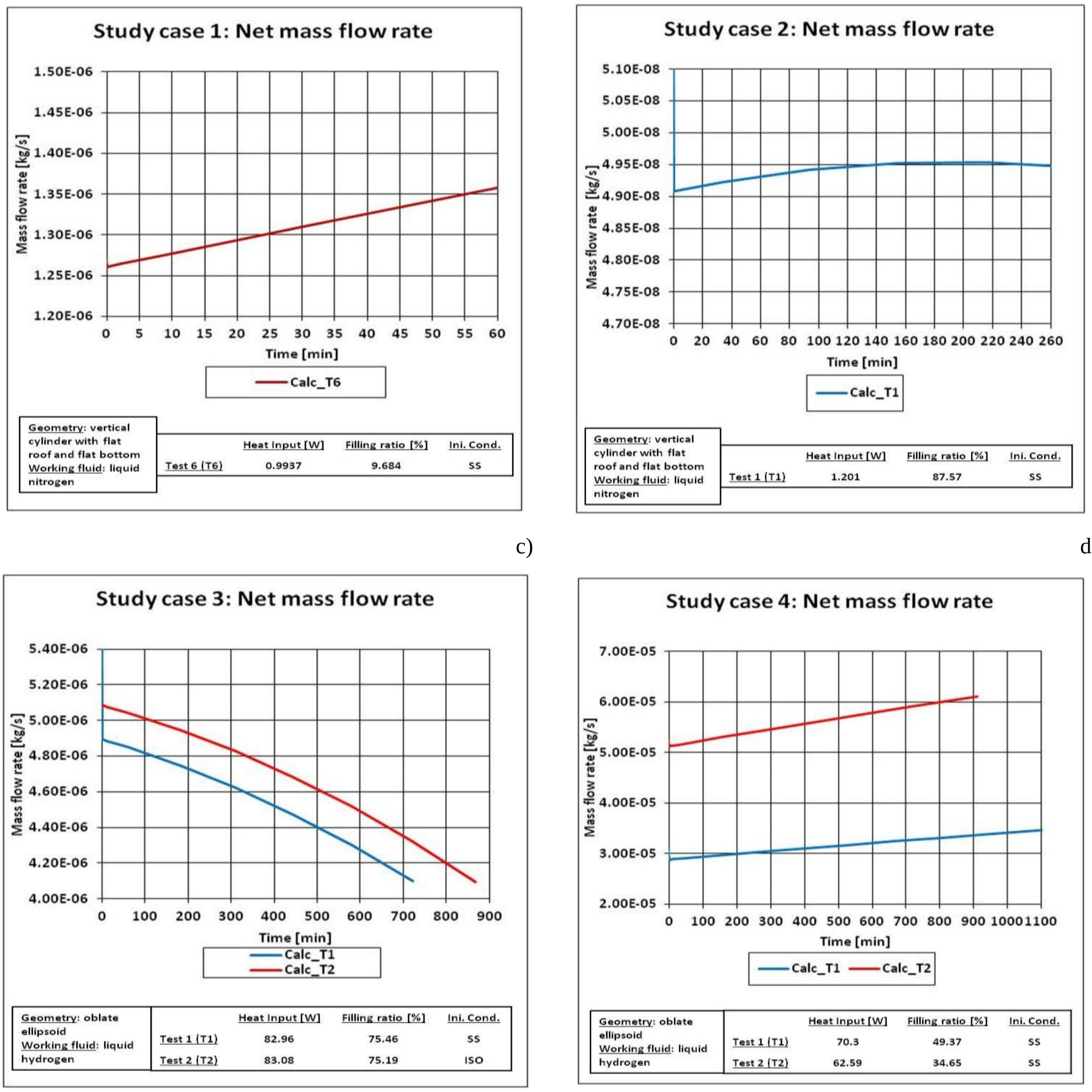

c) d)

e) f)

Figure 41. Net mass flow with EQ model for the study cases at low heat fluxes: a) Study case 1 (Test 1 and Test 2), b) Study case 2 (Test 3, 4 and 5), c) Study case 3 (Test 6), d) Study case 2, e) Study case 3; f) Study case 4.

$\dot{m}_N$ can strongly decrease between the steady state and the self-pressurisation stage, as reported in Table 57.

Table 57. Values of the net mass flow at steady state and at the beginning of the self-pressurisation for the Study cases at flow heat fluxes (1, 2, 3 and 4).

	Study case 1					
	Test 1	**Test 2**	**Test 3**	**Test 4**	**Test 5**	**Test 6**
$\dot{m}_N^{SS}\ [kg/s]$	$6.6765\cdot10^{-6}$	$5.8358\cdot10^{-6}$	$1.3133\cdot10^{-5}$	$5.1856\cdot10^{-6}$	$4.6059\cdot10^{-6}$	$3.5705\cdot10^{-6}$
$\dot{m}_N^{SP}\ [kg/s]$	$5.9303\cdot10^{-9}$	$9.3228\cdot10^{-8}$	$2.3769\cdot10^{-7}$	$2.222\cdot10^{-7}$	$6.0833\cdot10^{-7}$	$1.261\cdot10^{-6}$
	Study case 2		***Study case 3***		***Study case 4***	
	Test 1		**Test 1**	**Test 2**	**Test 1**	**Test 2**
$\dot{m}_N^{SS}\ [kg/s]$	$6.0494\cdot10^{-6}$		$1.861\cdot10^{-4}$	0	$1.5769\cdot10^{-4}$	$1.404\cdot10^{-4}$
$\dot{m}_N^{SP}\ [kg/s]$	$4.908\cdot10^{-8}$		$4.8937\cdot10^{-6}$	$5.0854\cdot10^{-6}$	$2.88506\cdot10^{-5}$	$5.1223\cdot10^{-5}$

As indicated in Table 57, this reduction of the mass flow is enhanced by the increment of the filling ratio. After the initial reduction, $\dot{m}_N$ weakly increases during the self-pressurisation, except for Study case 3 and for Test 1 of Study case 1. The rate of this increment is enhanced when the filling ratio is reduced and when the heat input increases. For Study case 3 and for Test 1 of Study case 1, $\dot{m}_N$ decreases in time. For Study case, this mass flow is higher at the isothermal condition than at the steady state, as illustrated by Figure 41 (e).

6.5.3. Presentation of the result: Pressure

Figure 42 shows the comparison between the evolution of the measured pressure, and the one computed with the EQ model. The continuous lines are the values computed with the equilibrium model. The square symbols are the experimental values. The colour of each line corresponds to the experimental tests, as indicated in each graphs.

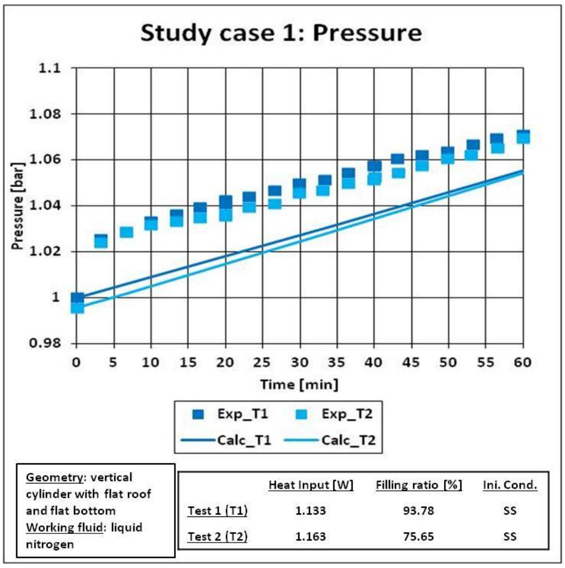

Geometry: vertical cylinder with flat roof and flat bottom
Working fluid: liquid nitrogen

	Heat Input [W]	Filling ratio [%]	Ini. Cond.
Test 1 (T1)	1.133	93.78	SS
Test 2 (T2)	1.163	75.65	SS

a)

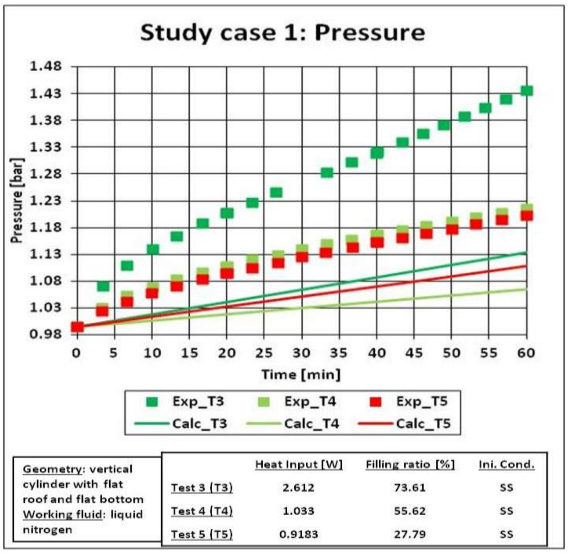

Geometry: vertical cylinder with flat roof and flat bottom
Working fluid: liquid nitrogen

	Heat Input [W]	Filling ratio [%]	Ini. Cond.
Test 3 (T3)	2.612	73.61	SS
Test 4 (T4)	1.033	55.62	SS
Test 5 (T5)	0.9183	27.79	SS

b)

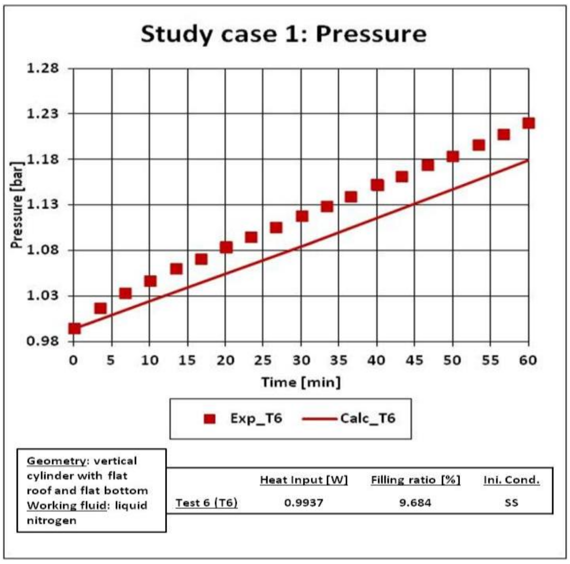

Geometry: vertical cylinder with flat roof and flat bottom
Working fluid: liquid nitrogen

	Heat Input [W]	Filling ratio [%]	Ini. Cond.
Test 6 (T6)	0.9937	9.684	SS

c)

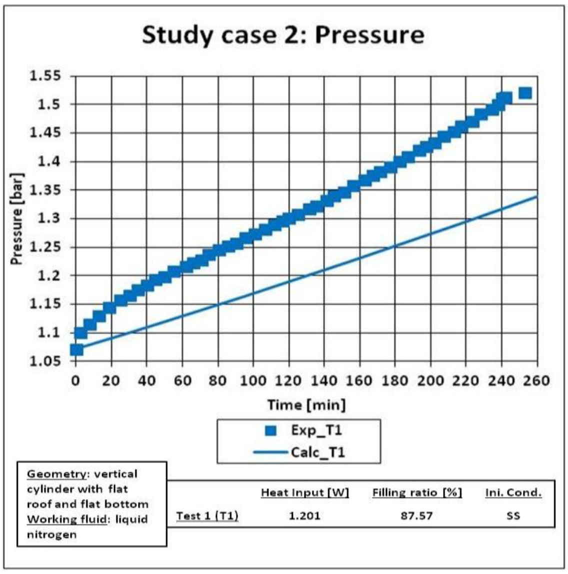

Geometry: vertical cylinder with flat roof and flat bottom
Working fluid: liquid nitrogen

	Heat Input [W]	Filling ratio [%]	Ini. Cond.
Test 1 (T1)	1.201	87.57	SS

d)

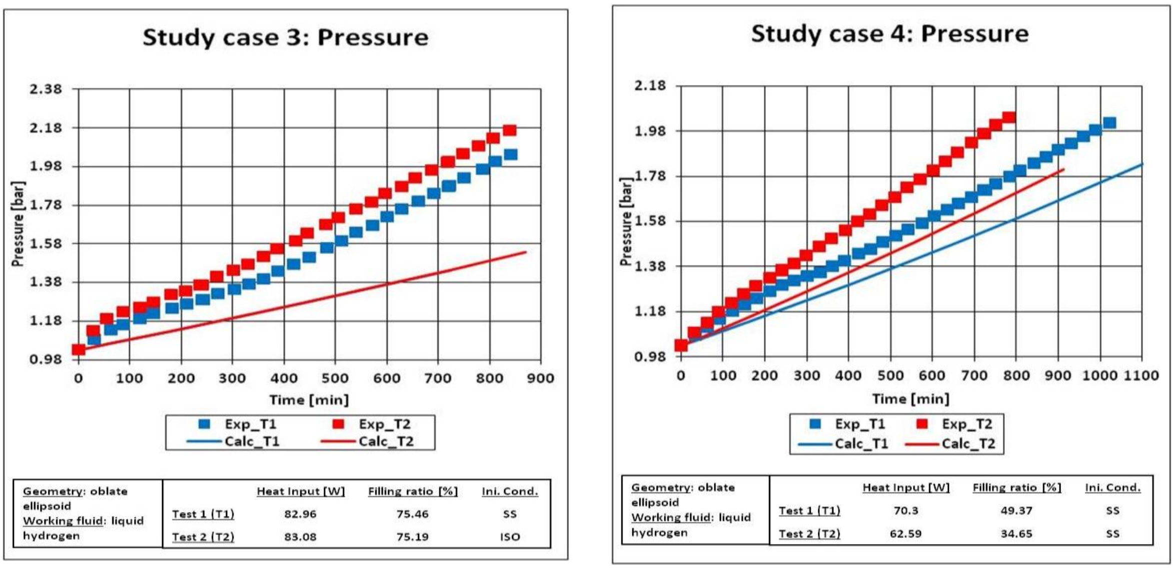

e) f)

Figure 42. Comparison between the measured pressure and the one computed with EQ model for the study cases at low heat fluxes: a) Study case 1 (Test 1 and Test 2), b) Study case 2 (Test 3, 4 and 5), c) Study case 3 (Test 6), d) Study case 2, e) Study case 3; f) Study case 4.

For all the study cases, the computed pressure increases in time, coherently with the experimental data. The predicted natural pressure build-up is, however, lower than the one observed in the experiments. The increment of the pressure with the heat inputs, and with the increasing liquid level, is qualitatively predicted by the EQ model, as indicated in Study case 1, except Test 4, 5 and 6. For Test 4, 5 and 6 of Study case 1, the computed pressure changes with the filling ratio, but the experiments shows that the pressure is almost constant with the liquid level. In Study case 3, the time-evolution of the pressure of Test 1 (steadys state initial conditions) is superposed to the one of Test 2 (isothermal initial conditions). Thus, the EQ model predicts the same increment of pressure for the isothermal and the steady state initial conditions, thus Test 1 and Test 2, respectively, even if the experimental observation indicates a faster increment when both liquid and vapour are isothermal.

6.5.4. Presentation of the results: Vapour Temperature

Figure 43 shows the comparison between the experimental time-evolution of the ullage temperature, and the one obtained from the EQ model. The continuous lines are the values computed with the equilibrium model. The full square symbols are the experimental values of the vapour average temperature.

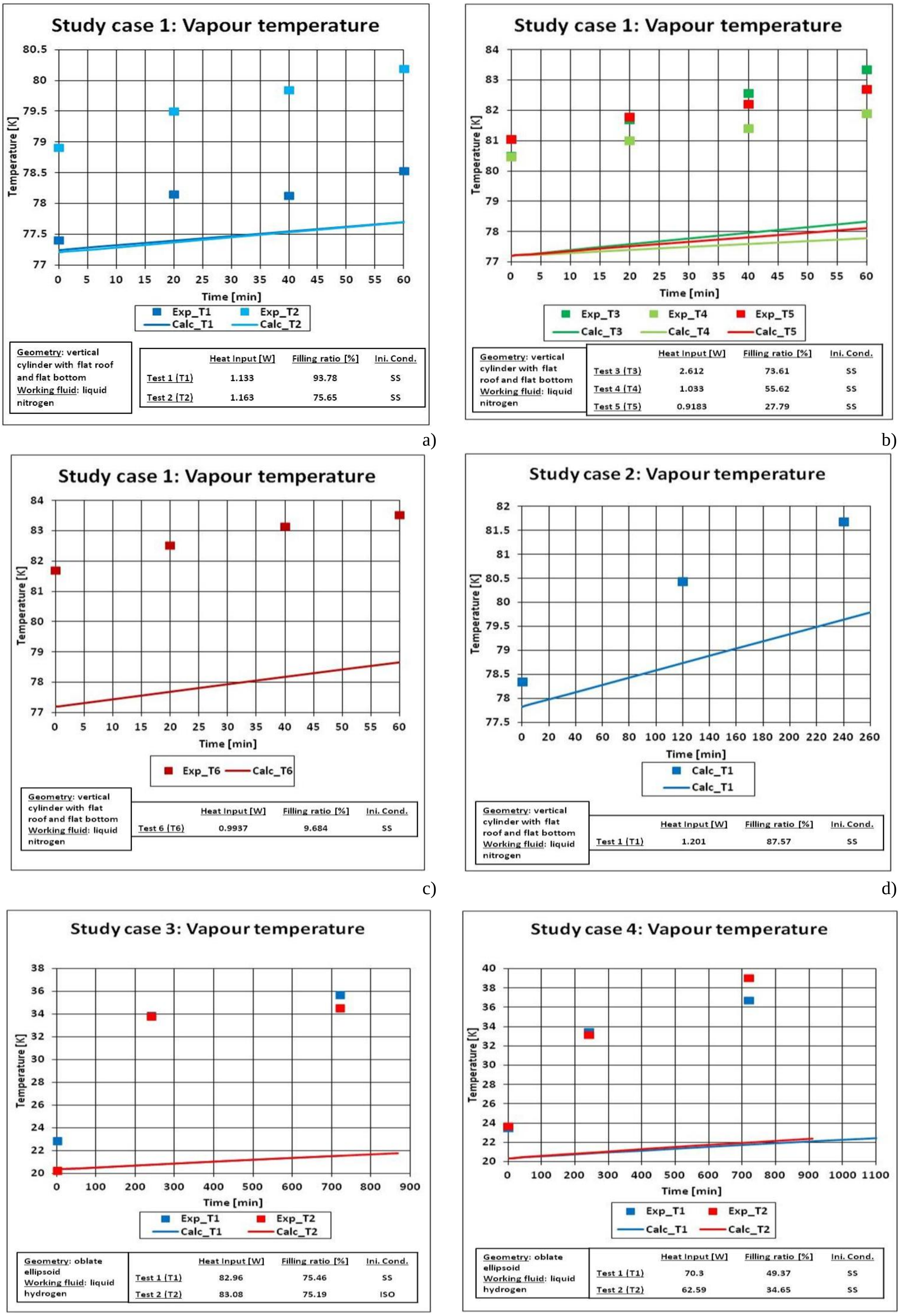

Study case 1: Vapour temperature

Geometry: vertical cylinder with flat roof and flat bottom
Working fluid: liquid nitrogen

	Heat Input [W]	Filling ratio [%]	Ini. Cond.
Test 1 (T1)	1.133	93.78	SS
Test 2 (T2)	1.163	75.65	SS

a)

Study case 1: Vapour temperature

Geometry: vertical cylinder with flat roof and flat bottom
Working fluid: liquid nitrogen

	Heat Input [W]	Filling ratio [%]	Ini. Cond.
Test 3 (T3)	2.612	73.61	SS
Test 4 (T4)	1.033	55.62	SS
Test 5 (T5)	0.9183	27.79	SS

b)

Study case 1: Vapour temperature

Geometry: vertical cylinder with flat roof and flat bottom
Working fluid: liquid nitrogen

	Heat Input [W]	Filling ratio [%]	Ini. Cond.
Test 6 (T6)	0.9937	9.684	SS

c)

Study case 2: Vapour temperature

Geometry: vertical cylinder with flat roof and flat bottom
Working fluid: liquid nitrogen

	Heat Input [W]	Filling ratio [%]	Ini. Cond.
Test 1 (T1)	1.201	87.57	SS

d)

Study case 3: Vapour temperature

Geometry: oblate ellipsoid
Working fluid: liquid hydrogen

	Heat Input [W]	Filling ratio [%]	Ini. Cond.
Test 1 (T1)	82.96	75.46	SS
Test 2 (T2)	83.08	75.19	ISO

e)

Study case 4: Vapour temperature

Geometry: oblate ellipsoid
Working fluid: liquid hydrogen

	Heat Input [W]	Filling ratio [%]	Ini. Cond.
Test 1 (T1)	70.3	49.37	SS
Test 2 (T2)	62.59	34.65	SS

f)

Figure 43. Comparison between the measured ullage temperature and the one computed with EQ model for the study cases at low heat fluxes: a) Study case 1 (Test 1 and Test 2), b) Study case 2 (Test 3, 4 and 5), c) Study case 3 (Test 6), d) Study case 2, e) Study case 3 and f) Study case 4.

The computed and the measured temperature increases in time, for all the Study cases. This increment depends on the self-pressurisation and it is linear for all the Study cases. The slope of the curve of the time-increment of the computed vapour temperature is quite similar to the experimental one, for Study case 1 and 2. The increment is, however, lower than the experimental one for Study case 3 and 4. The relations between the heat input and vapour temperature, and between filling ratio and vapour temperature is qualitatively correct. In fact, as the heat inputs increase, the ullage becomes hotter than the case at low heat input, as indicated by Test 3 of Study case 1. The vapour temperature rises with the reduction of the filing ratio, as described by Test 1, 2, 4, 5 and 6 of Study case 1. This computed increment is very low for Study case 4, coherently with the experimental data. The isothermal initial condition does not affect the computed temperature.

6.5.5. Presentation of the results: Liquid temperature

Figure 44 shows the comparison between the experimental time-evolution of the liquid temperature and the one obtained from the EQ model. The continuous lines are the values computed with the equilibrium model. The full square symbols are the experimental values of the vapour average temperature.

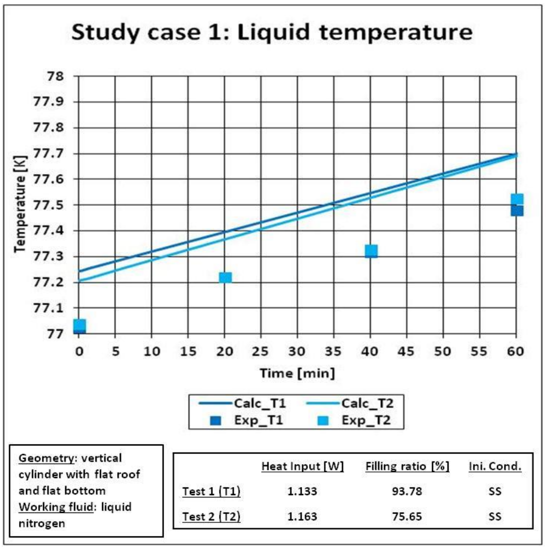

	Heat Input [W]	Filling ratio [%]	Ini. Cond.
Test 1 (T1)	1.133	93.78	SS
Test 2 (T2)	1.163	75.65	SS

a)

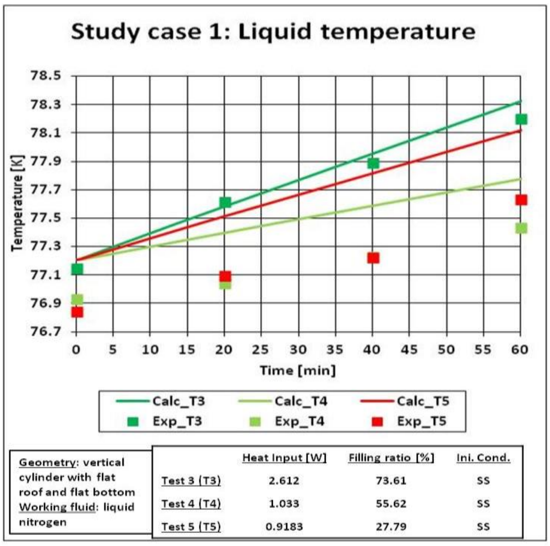

	Heat Input [W]	Filling ratio [%]	Ini. Cond.
Test 3 (T3)	2.612	73.61	SS
Test 4 (T4)	1.033	55.62	SS
Test 5 (T5)	0.9183	27.79	SS

b)

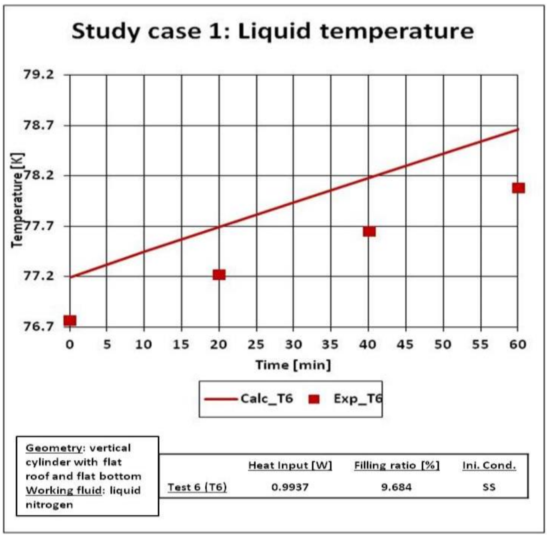

	Heat Input [W]	Filling ratio [%]	Ini. Cond.
Test 6 (T6)	0.9937	9.684	SS

c)

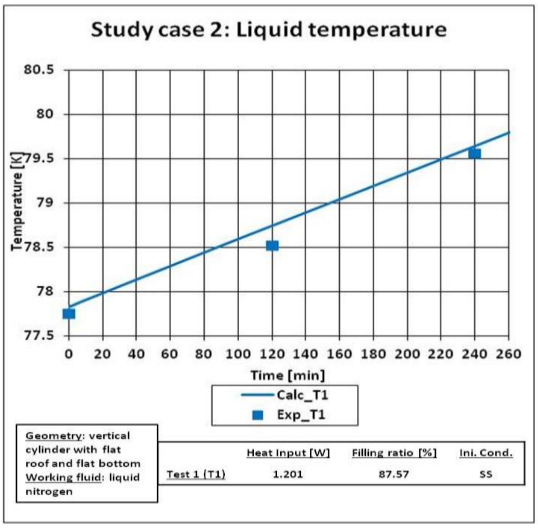

	Heat Input [W]	Filling ratio [%]	Ini. Cond.
Test 1 (T1)	1.201	87.57	SS

d)

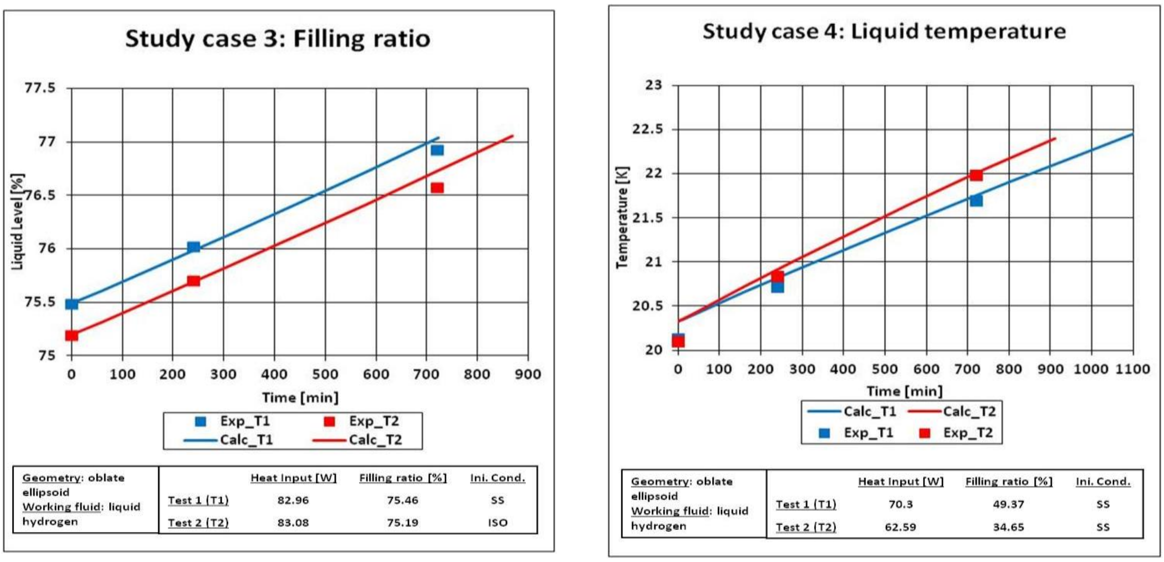

e) f)

Figure 44. Comparison between the measured liquid temperature and the one computed with EQ model for the study cases at low heat fluxes: a) Study case 1 (Test 1 and Test 2), b) Study case 2 (Test 3, 4 and 5), c) Study case 3 (Test 6), d) Study case 2, e) Study case 3 and f) Study case 4.

The computed and the measured temperatures increase during the self-pressurisation. The difference in values between the observed and the calculated values are low. Hence, the EQ model can well predict the time-increment of the liquid temperature, and the overall liquid is close to the saturation condition. The main difference between the experimental data and the EQ model are seen at the beginning of the self-pressurisation, because the measured temperature is often below the saturated one. The liquid cannot be sub-cooled at the steady state in an open storage container where only the Boil-Off Gas is evacuated. The liquid can be sub-cooled in this type of storage tank if frigories are added to the liquid phase. So, sub-cooled state is caused due to measuring uncertainties. The liquid temperature increases with the heat input and with the reduction of the filling ratio, as experimentally observed.

6.5.6. Presentation of the results: Filling ratio

Figure 45 indicates the experimental (full square symbols) and the computed (continous line) time-evolutions of the filling ratio for the Study cases at low heat fluxes.

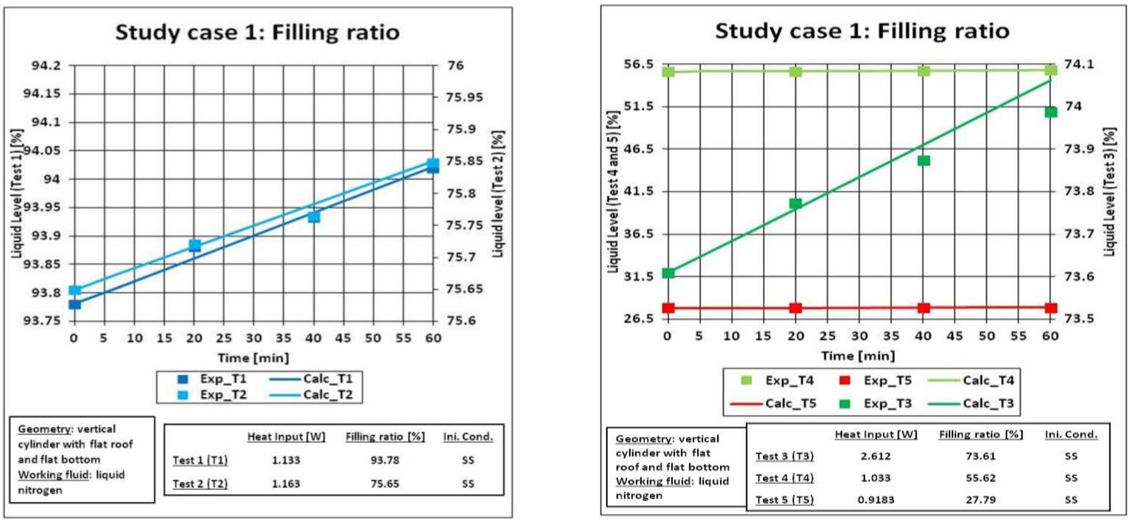

a) b)

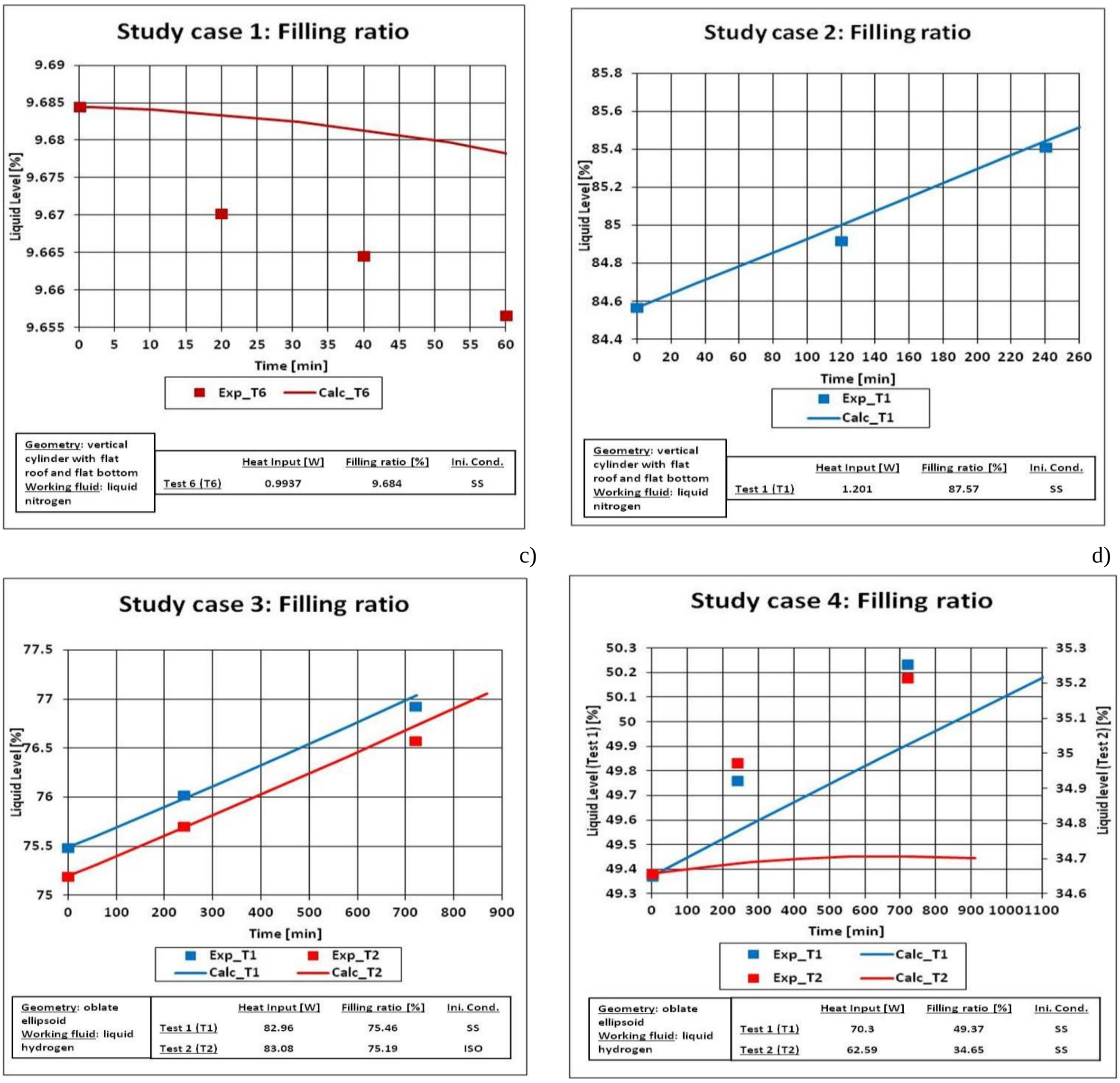

c) d)

e) f)

Figure 45. Comparison between the measured filling ratio and the one computed with EQ model for the study cases at low heat fluxes: a) Study case 1 (Test 1 and Test 2), b) Study case 2 (Test 3, 4 and 5), c) Study case 3 (Test 6), d) Study case 2, e) Study case 3 and f) Study case 4.

The computed filling ratio increases in time, except for Test 6 of Study case 1 and for Test 2 of Study case 4. For these tests, the liquid level decreases during the self-pressurisation. The EQ model's results are coherent with the experimental data, except for Test 2 of Study case 4. The difference in values of filling ratio between the experimental and the calculated is low. For Test 2 of Study case 4, the computed liquid level has a maximum, instead of monotonically increasing as occurs in the experiment.

6.6. Medium heat fluxes study cases

Table 58 reports the initial and the boundary conditions of the experiments, and the one of the equilibrium model (EQ model) of the Study cases 5 and 6, which were obtained at medium heat fluxes.

Table 58. Initial conditions and boundary conditions for the self-pressurisation stage.

Sub-case	$\dot{Q}$ $[W]$	LF [%]	P $[bar]$	T^V $[K]$	T^L $[K]$

Table 58. Initial conditions and boundary conditions for the self-pressurisation stage.

		Exp	EQ	Exp	EQ	Exp	EQ	Exp	EQ	Exp	EQ
					Study case 5						
Test 1	0.3839	29.91	29.91	79.63	79.63	1.042	1.042	100.6	77.60	77.03	77.60
Test 2	0.3062	23.85	23.85	50.01	50.01	1.042	1.042	121.2	77.60	77.68	77.60
Test 3	0.2296	17.88	17.88	30.79	30.79	1.042	1.042	116.6	77.60	77.64	77.60
					Study case 6						
Test 1	0.2762	75.58	75.58	72.45	72.45	1.051	1.051	29.47	20.39	20.90	20.39
Test 2	0.2671	73.09	73.09	51.29	51.29	1.050	1.050	40.04	20.39	20.78	20.39
Test 3	0.2059	56.36	56.36	34.08	34.08	1.027	1.027	53.34	20.32	19.55	20.32
Test4	0.8855	242.2	242.2	50.96	50.96	1.083	1.083	39.03	20.49	21.05	20.49

Only the vapour and liquid initial temperature of the EQ model are not equal to the ones of the experiments. The effective heat transfer coefficient (h_{eff}) change for every test, due to the approach to compute the boundary condition (see Section 6.1 of Chapter 3).

Section 6.6.1, 6.6.2, 6.6.3, 6.6.4, 6.6.5 and 6.6.6 presents the results of the effective heat transfer coefficient, the net mass flow and the heat inputs, the pressure, the temperature and the filling ratio, respectively.In the title of these graphs of these sections, the words LN_2 and LH_2 respectively indicate the liquid nitrogen and the liquid hydrogen. The words “Vert. Cyl.”, “Obl. Elip.” and “Sph.” means vertical cylinder, oblate ellipsoid and sphere, respectively. The isothermal and steady Boil-off Gas initial conditions are indicated by the words “ISO” and “SS” respectively. The initial values of filling ratio and heat input, calculated in this thesis, are reported in each graph. The word “Exp” indicates the experimental values.

6.6.1. Presentation of the results: Heat inputs

Figure 46 shows the time evolution of the heat inputs. The heat leakages are computed with Equation 89 (see Section3.1 of Chapter 3). The continuous lines are the values computed with the equilibrium model.

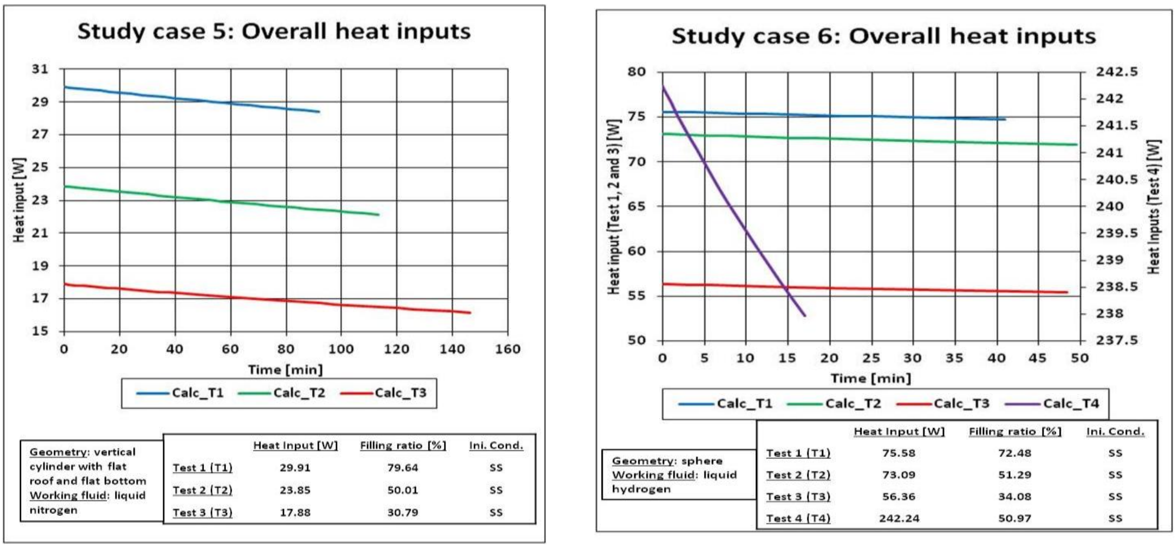

Geometry: vertical cylinder with flat roof and flat bottom
Working fluid: liquid nitrogen

	Heat Input [W]	Filling ratio [%]	Ini. Cond.
Test 1 (T1)	29.91	79.64	SS
Test 2 (T2)	23.85	50.01	SS
Test 3 (T3)	17.88	30.79	SS

Geometry: sphere
Working fluid: liquid hydrogen

	Heat Input [W]	Filling ratio [%]	Ini. Cond.
Test 1 (T1)	75.58	72.48	SS
Test 2 (T2)	73.09	51.29	SS
Test 3 (T3)	56.36	34.08	SS
Test 4 (T4)	242.24	50.97	SS

a) b)

Figure 46. Heat inputs computed with EQ model at medium heat fluxes: a) Study case 5, b) Study case 6.

The overall heat inputs decreases during the self-pressurisation, as it occurs for the Study cases at low heat fluxes (see Section 6.5.1 of Chapter 3). The rate of this decrement depends on the self-pressurisation rate, and it is higher than the one of the study cases at low heat fluxes (see Section 6.5.1 of Chapter 3).

6.6.2. Presentation of the results: Net mass flow

Figure 47 shows the time evolution of the net mass flow ($\dot{m}_N$), which is computed with Equation 37 of Section 2.3. The continuous lines are the values computed with the equilibrium model.

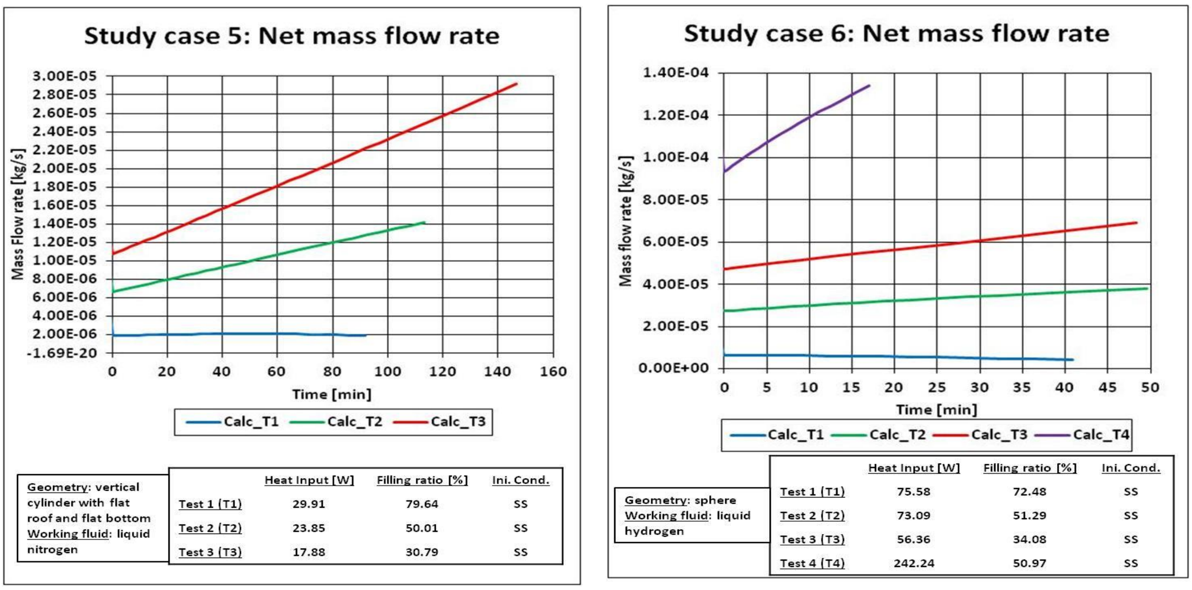

a) b)

Figure 47. Net mass flow computed with EQ model at medium heat fluxes: a) Study case 5, b) Study case 6.

$\dot{m}_N$ strongly decreases between the steady state and the self-pressurisation, as described in Section 6.5.2 of Chapter 3 for the cases at low heat fluxes. This reduction is reported in Table 59.

Table 59. Values of the net mass flow at steady state and at the beginning of the self-pressurisation for the Study cases at medium heat fluxes (5 and 6).

	Study case 5		
	Test 1	**Test 2**	**Test 3**
$\dot{m}_N^{SS}\ [kg/s]$	$1.5042\cdot10^{-4}$	$1.1996\cdot10^{-4}$	$8.9943\cdot10^{-5}$
$\dot{m}_N^{SP}\ [kg/s]$	$1.8714\cdot10^{-6}$	$6.6399\cdot10^{-6}$	$1.0728\cdot10^{-5}$

	Study case 6			
	Test 1	**Test 2**	**Test 3**	**Test 4**
$\dot{m}_N^{SS}\ [kg/s]$	$1.6966\cdot10^{-4}$	$1.6408\cdot10^{-4}$	$1.2642\cdot10^{-4}$	$5.4435\cdot10^{-4}$
$\dot{m}_N^{SP}\ [kg/s]$	$6.3395\cdot10^{-6}$	$2.7349\cdot10^{-5}$	$4.723\cdot10^{-5}$	$9.3347\cdot10^{-5}$

This reduction decreases with the reduction of the filing ratio, as for the cases at low heat fluxes (Section 6.5.2 of Chapter 3). However, this reduction is enhanced by the increment of the heat input, contrary to Test 3 of Study case 1.

After this initial reduction, $\dot{m}_N$ always increases in time. The rate of this increment increases with the reduction of the filling ratio and with the increment of the heat input, as for the cases at low heat fluxes (Section 6.5.2 of Chapter 3).

6.6.3. Presentation of the results: Pressure

Figure 48 shows the comparison between the measured and EQ model's computational results of the tank's ullage pressure. The continuous lines are the values computed with the equilibrium model. The square symbols are the experimental values.

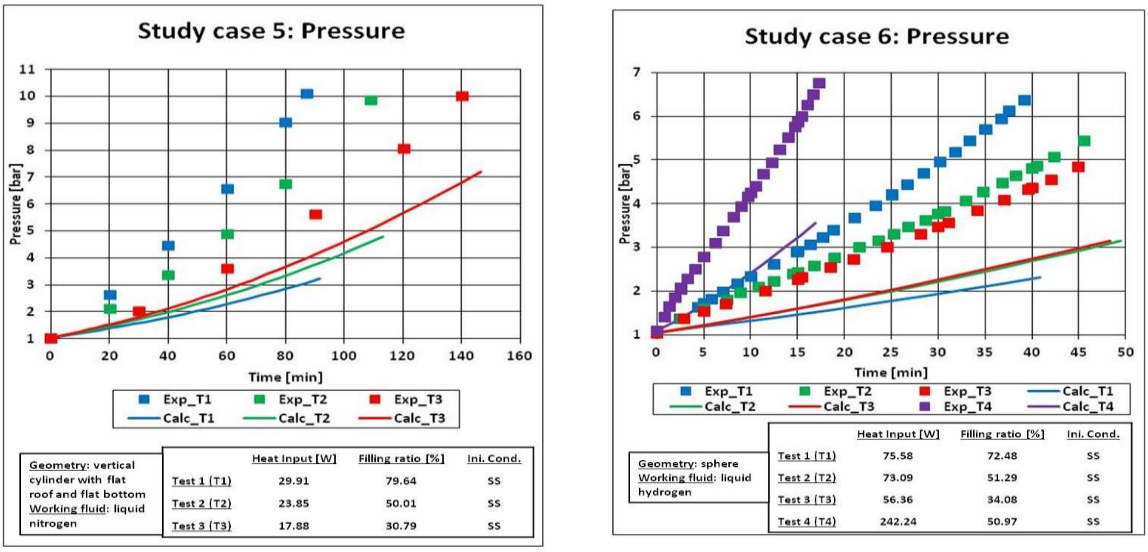

Geometry: vertical cylinder with flat roof and flat bottom
Working fluid: liquid nitrogen

	Heat Input [W]	Filling ratio [%]	Ini. Cond.
Test 1 (T1)	29.91	79.64	SS
Test 2 (T2)	23.85	50.01	SS
Test 3 (T3)	17.88	30.79	SS

Geometry: sphere
Working fluid: liquid hydrogen

	Heat Input [W]	Filling ratio [%]	Ini. Cond.
Test 1 (T1)	75.58	72.48	SS
Test 2 (T2)	73.09	51.29	SS
Test 3 (T3)	56.36	34.08	SS
Test 4 (T4)	242.24	50.97	SS

a) b)

Figure 48. Comparison between the experimental pressure and the one computed with EQ model for the study cases at medium heat fluxes: a) Study case 5, b) Study case 6.

The pressure predicted by the EQ model increases in time, similarly to the experimental values. The computed rate of natural pressure build-up is increased at high heat input, as indicated the experimental values. This behaviour is similar to the one of the previous study cases (see Section 6.6.3). The calculated pressure increases with the reduction of the filling ratio, but this behaviour is opposite to the one of the experimental data.

6.6.4. Presentation of the results: Vapour temperature

Figure 49 shows the comparison between the time-evolution of the ullage temperature computed by means of the EQ model, and the same parameter measured experimentally. The continuous lines are the values computed with the equilibrium model. The square symbols are the experimental values.

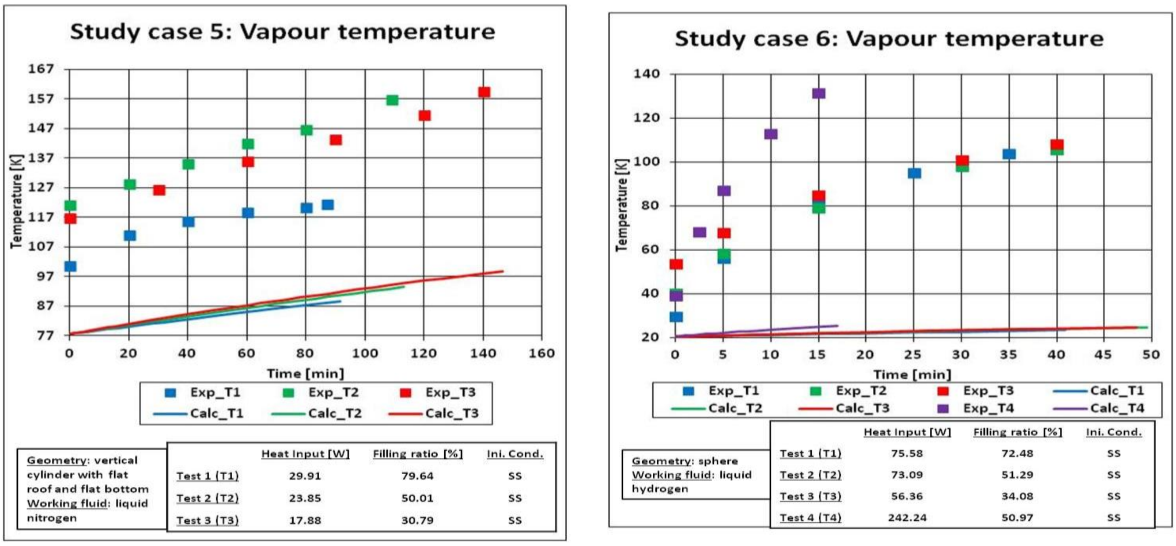

Geometry: vertical cylinder with flat roof and flat bottom
Working fluid: liquid nitrogen

	Heat Input [W]	Filling ratio [%]	Ini. Cond.
Test 1 (T1)	29.91	79.64	SS
Test 2 (T2)	23.85	50.01	SS
Test 3 (T3)	17.88	30.79	SS

Geometry: sphere
Working fluid: liquid hydrogen

	Heat Input [W]	Filling ratio [%]	Ini. Cond.
Test 1 (T1)	75.58	72.48	SS
Test 2 (T2)	73.09	51.29	SS
Test 3 (T3)	56.36	34.08	SS
Test 4 (T4)	242.24	50.97	SS

a) b)

Figure 49. Comparison between the experimental ullage temperature and the one computed with EQ model for the study cases at medium heat fluxes: a) Study case 5, b) Study case 6.

As for the previous study cases (see Section 6.5.4 of Chapter 3), the computed temperature increases in time as happen for the measured one. The difference in value between the measured and the computed is very high, indicating that the vapour is strongly overheated. The EQ model qualitatively predicts the increment of the temperature when the heat inputs increases, as indicated by the comparison of Test 4 of Study case 6. The relation between the filling ratio and the ullage temperature of the EQ model do not match the experimental one, as indicated by the comparison of Study case 5.

6.6.5. Presentation of the results: Liquid temperature

Figure 50 shows the comparison between the time-evolution of the liquid temperature calculated by means of the EQ model, with respect to the experimental measurements. The continuous lines are the values computed with the equilibrium model. The square symbols are the experimental values. The colour of each line corresponds to the experimental tests, as indicated in each graphs.

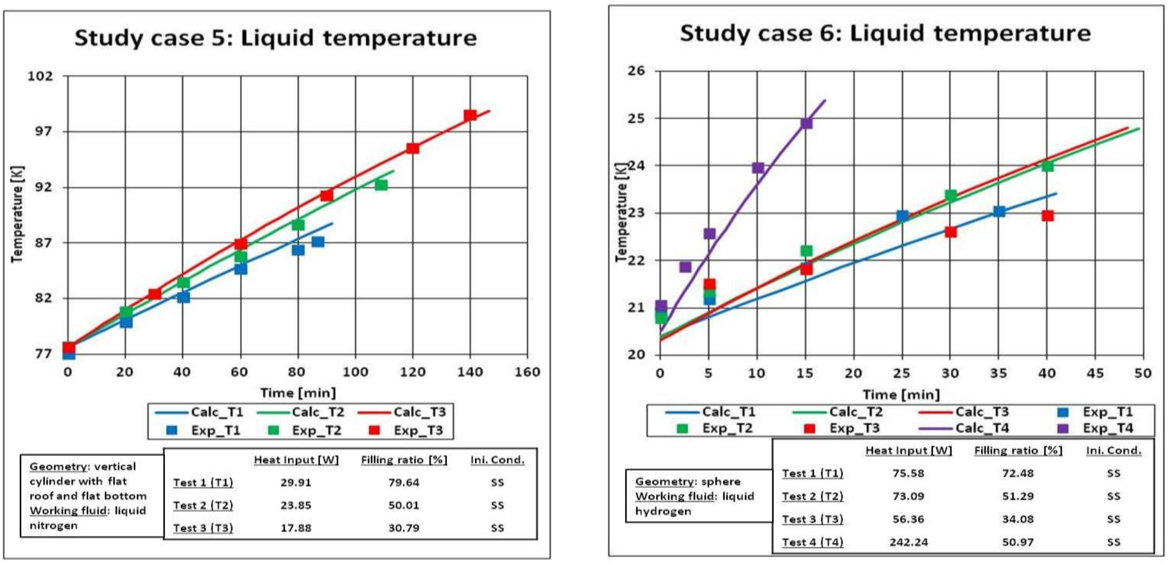

Geometry: vertical cylinder with flat roof and flat bottom
Working fluid: liquid nitrogen

	Heat Input [W]	Filling ratio [%]	Ini. Cond.
Test 1 (T1)	29.91	79.64	SS
Test 2 (T2)	23.85	50.01	SS
Test 3 (T3)	17.88	30.79	SS

Geometry: sphere
Working fluid: liquid hydrogen

	Heat Input [W]	Filling ratio [%]	Ini. Cond.
Test 1 (T1)	75.58	72.48	SS
Test 2 (T2)	73.09	51.29	SS
Test 3 (T3)	56.36	34.08	SS
Test 4 (T4)	242.24	50.97	SS

a) b)

Figure 50. Comparison between the experimental liquid temperature and the one computed with EQ model for the study cases at medium heat fluxes: a) Study case 5, b) Study case 6.

The computed temperature increases in time as happen for the measured one. The absolute difference is between the measured and the computed value is very low, indicating that the liquid is close to the saturation, even at medium heat fluxes. The liquid temperature increases with the reduction of the initial filling ratio, except for the Test 3 of Study case 6. Except for this case, the EQ model is in agreement with the experimental filling ratio-liquid temperature relation. For Test 3 of Study case 6, the temperature of the model is lower than the experimental one. These observations, except for Test 3 of Study case 6, are similar to the one found for study cases at the low heat fluxes (see Section 6.5.5 of Chapter 3).

6.6.6. Presentation of the results: Filling ratio

Figure 51 indicates the experimental and the computed time-evolutions of the filling ratio for the Study cases at medium heat fluxes. The continuous lines are the values computed with the equilibrium model. The square symbols are the experimental values of filling ratio.

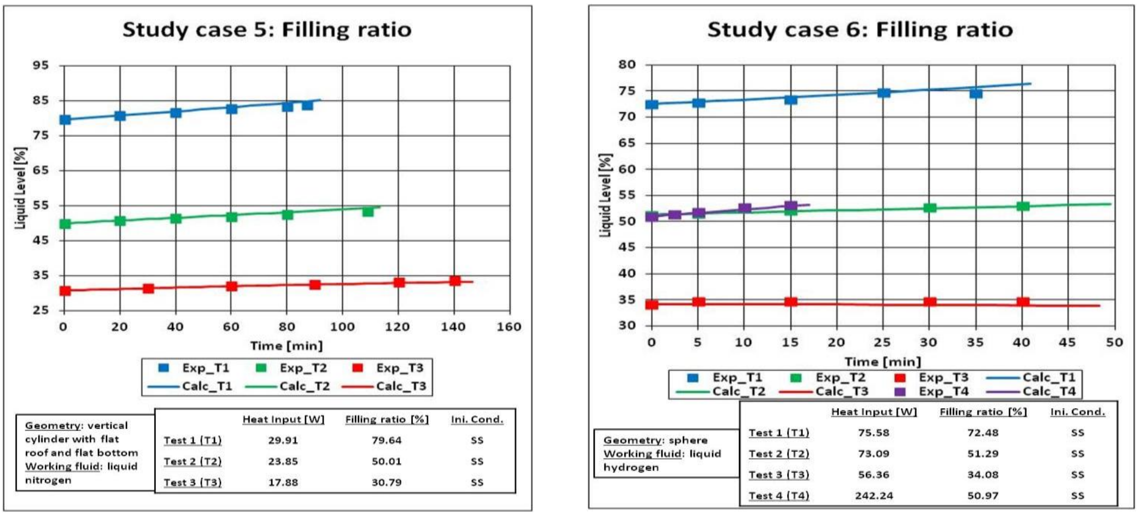

Geometry: vertical cylinder with flat roof and flat bottom
Working fluid: liquid nitrogen

	Heat Input [W]	Filling ratio [%]	Ini. Cond.
Test 1 (T1)	29.91	79.64	SS
Test 2 (T2)	23.85	50.01	SS
Test 3 (T3)	17.88	30.79	SS

Geometry: sphere
Working fluid: liquid hydrogen

	Heat Input [W]	Filling ratio [%]	Ini. Cond.
Test 1 (T1)	75.58	72.48	SS
Test 2 (T2)	73.09	51.29	SS
Test 3 (T3)	56.36	34.08	SS
Test 4 (T4)	242.24	50.97	SS

a) b)

Figure 51. Comparison between the measured filling ratio and the one computed with EQ model for the study cases at medium heat fluxes: a) Study case 5, b) Study case 6.

The computed filling ratio increases in time, except for Test 3 of Study case 6. For this test, the liquid level decrease during the self-pressurisation. As for the previous Study cases (see Section 6.5.6), the difference in values between the observed and the calculated is low. The effect of the initial filling ratio and heat inputs on the evolution of the liquid level is coherent with the experimental observations. At medium heat fluxes, the filling ratio always increases in time, even for low filling ratios. This behaviour is different from the one of the Study case at low heat fluxes (see Section 6.5.6).

6.7. High heat fluxes study case

For the study cases at high heat fluxes (Study case 7), the initial and the boundary conditions of the experiments and of the equilibrium model (EQ model) are reported in Table 60.

Table 60. Initial conditions and boundary conditions for the self-pressurisation stage.

Sub-case	$h_{eff}\ \left[\frac{W}{m^2\cdot K}\right]$	$\dot{Q}\ [W]$		LF [%]		$P\ [bar]$		$T^V\ [K]$		$T^L\ [K]$	
		Exp	**EQ**	**Exp**	**EQ**	**Exp**	**EQ**	**Exp**	**EQ**	**Exp**	**EQ**
Study case 7											
Test 1	1.045	48.18	48.18	62.43	62.43	1.199	1.199	32.21	20.85	20.70	20.85
Test 2	1.008	46.46	46.46	48.05	48.05	1.199	1.199	50.14	20.85	20.35	20.85

Table 60. Initial conditions and boundary conditions for the self-pressurisation stage.

Test 3	0.7308	33.68	33.68	24.89	24.89	1.199	1.199	48.90	20.85	20.58	20.85

As for the previous study cases (Section 6.5 and 6.6), the initial conditions of the self-pressurisation for the vapour and liquid temperatures are not equal to the ones of the experiments. In particular, the experimental liquid temperature is below of its corresponding value in the EQ model, due to measuring uncertainties. The boundary conditions are defined with the effective heat transfer coefficient (h_{eff}), as done for the previous study cases (Section 6.5 and 6.6).

Section 6.7.1, 6.7.2, 6.7.3, 6.7.4, 6.7.5 and 6.7.6 presents the results of the effective heat transfer coefficient, the net mass flow and the heat inputs, the pressure, the temperature and the filling ratio, respectively. In the title of these graphs of these sections, the words LN_2 and LH_2 respectively indicate the liquid nitrogen and the liquid hydrogen. The words “Vert. Cyl.”, “Obl. Elip.” and “Sph.” means vertical cylinder, oblate ellipsoid and sphere, respectively. The isothermal and steady Boil-off Gas initial conditions are indicated by the words “ISO” and “SS” respectively. The initial values of filling ratio and heat input, calculated in this thesis, are reported in each graph. The word “Exp” indicates the experimental values.

6.7.1. Presentation of the results: Heat inputs

Figure 52 shows the time evolution of the heat inputs computed with Equation 89 (see Section 2.3 of Chapter 3), for the Study case at high heat fluxes (Study case 7). The continuous lines are the values computed with the equilibrium model.

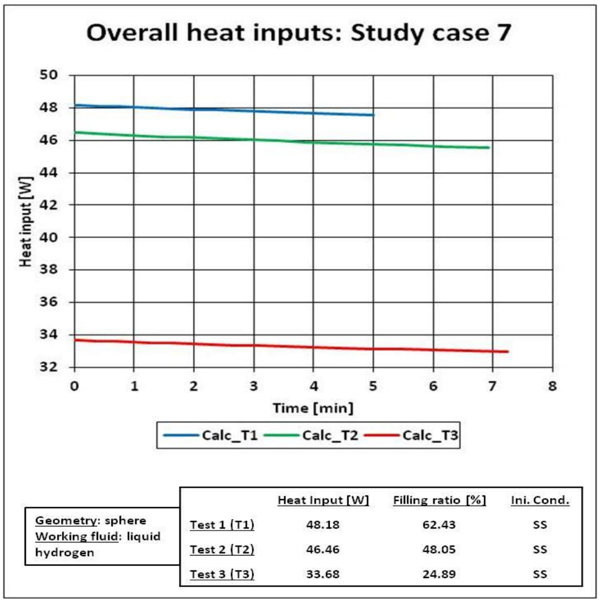

Geometry: sphere
Working fluid: liquid hydrogen

	Heat Input [W]	Filling ratio [%]	Ini. Cond.
Test 1 (T1)	48.18	62.43	SS
Test 2 (T2)	46.46	48.05	SS
Test 3 (T3)	33.68	24.89	SS

Figure 52. Heat inputs computed with EQ model for the study cases at high heat fluxes: Study case 7.

The EQ model predicts that the heat inputs decreases in time, during the self-pressurisation. The rate of decrement increases with the self-pressurisation rate. These observations are similar to the previous ones seen in Section 6.5.1 and 6.6.1 of Chapter 3, for the Study cases at low and medium heat fluxes.

6.7.2. Presentation of the results: Net mass flow

igure 53 shows the time evolution of the net mass flow ($\dot{m}_N$) computed with Equation 37 (see Section 2.3 of Chapter 3). For the Study case at high heat fluxes (Study case 7), the continuous lines are the values computed with the equilibrium model (EQ model).

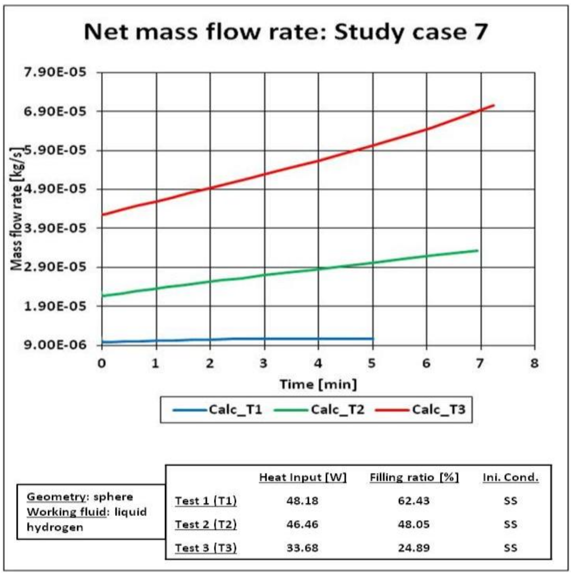

Figure 53. Net mass flow computed with EQ model for the study cases at high heat fluxes: Study case 7.

The computational results of the EQ model show that $\dot{m}_N$ increases in time and with the reduction of the initial filling ratio. The rate of this increment is stronger at low heat input than at high heat input. $\dot{m}_N$ changes between the steady state and the self-pressurisation, and the variation is described in Table 61.

Table 61. Values of the net mass flow at steady state and at the beginning of the self-pressurisation for the Study cases at high heat fluxes.

		Study case 7	
	Test 1	**Test 2**	**Test 3**
$\dot{\boldsymbol{m}}_N^{SS}$ $[\boldsymbol{kg/s}]$	$1.0872 \cdot 10^{-4}$	$1.0485 \cdot 10^{-4}$	$7.5999 \cdot 10^{-5}$
$\dot{\boldsymbol{m}}_N^{SP}$ $[\boldsymbol{kg/s}]$	$9.7858 \cdot 10^{-6}$	$2.1663 \cdot 10^{-5}$	$4.2473 \cdot 10^{-5}$

These behaviours are similar to the ones of the Study cases at medium heat fluxes (see Section 6.6).

6.7.3. Presentation of the results: Pressure

igure 53 shows the time-evolution of the pressure computed with the equilibrium model (EQ model), and the experimental data, for the Study case 7 (high heat fluxes). The continuous lines are the values computed with the EQ model. The square symbols are the experimental values.

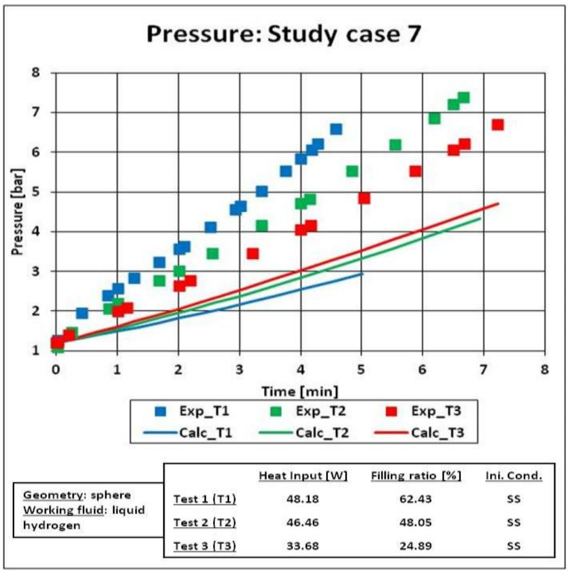

	Heat Input [W]	Filling ratio [%]	Ini. Cond.
Test 1 (T1)	48.18	62.43	SS
Test 2 (T2)	46.46	48.05	SS
Test 3 (T3)	33.68	24.89	SS

Figure 54. Pressure computed with EQ model for the study cases at high heat fluxes: Study case 7.

As for the experimental data, the computed pressure increases in time, similarly to the previous study cases (see Section 6.5.3 and 6.6.3 of Chapter 3). This increment is, however, quantitatively lower than the experimental one. The pressure calculated by EQ model barely increases with the reduction of the filling ratio. This behaviour is opposite to the one experimentally observed. The behaviour of the computed pressure is similar to the one of the previous study cases (see Section 6.5.3 and 6.6.3 of Chapter 3).

6.7.4. Presentation of the results: Vapour temperature

The experimental measurements of the ullage temperature, and the values of the same parameter computed by the equilibrium model (EQ model) are shown in Figure 55 for the Study case 7 (high heat fluxes). The continuous lines are the values computed with the equilibrium model. The square symbols are the experimental values.

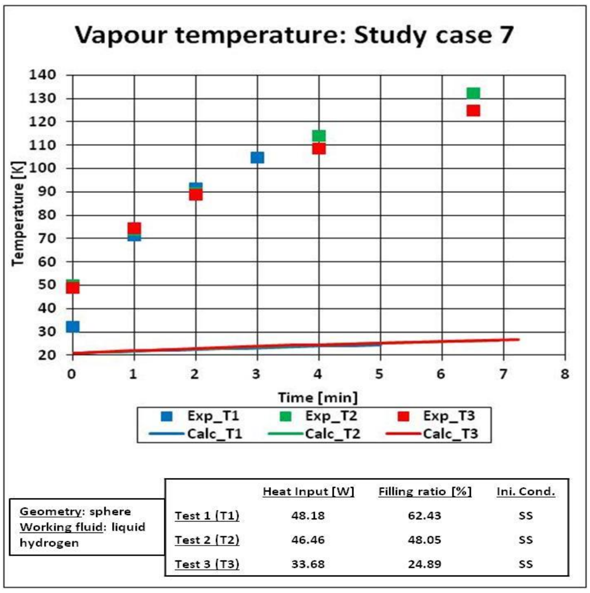

	Heat Input [W]	Filling ratio [%]	Ini. Cond.
Test 1 (T1)	48.18	62.43	SS
Test 2 (T2)	46.46	48.05	SS
Test 3 (T3)	33.68	24.89	SS

Figure 55. Comparison between the experimental ullage temperature and the one computed with EQ model for the study case at high heat fluxes: Study case 7.

The computed temperature increases in time. This increment is lower than the one recorded in the experiments, and the difference in temperature between the computed and the observed is high. These behaviours are similar to one of the medium heat fluxes Study cases (see Section 6.7.4 of Chapter 3).

6.7.5. Presentation of the results: Liquid temperature

The time-evolution of the liquid temperature is presented in Figure 56, for both the experiments and the calculations of the equilibrium model (EQ model) for the Study case at high heat fluxes (Study case 7). The continuous lines are the values computed with the equilibrium model. The square symbols are the experimental values.

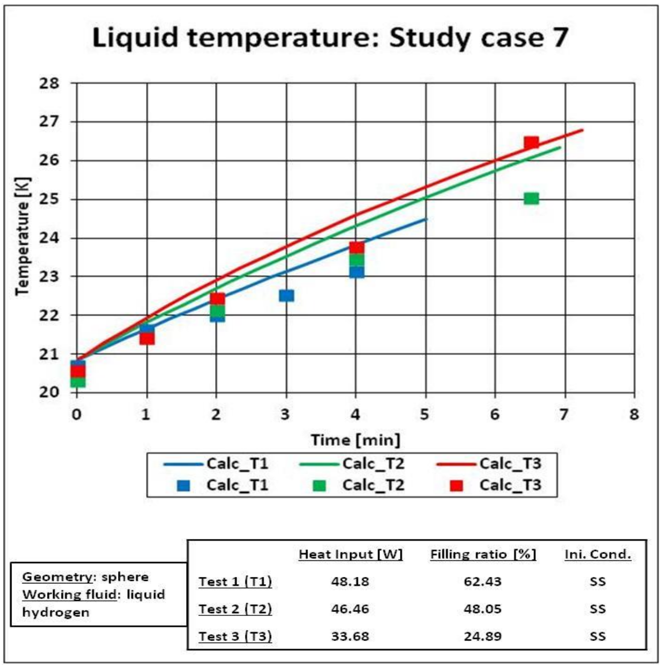

	Heat Input [W]	Filling ratio [%]	Ini. Cond.
Test 1 (T1)	48.18	62.43	SS
Test 2 (T2)	46.46	48.05	SS
Test 3 (T3)	33.68	24.89	SS

Figure 56. Comparison between the experimental liquid temperature and the one computed with EQ model for the study case at high heat fluxes: Study case 7.

The liquid temperature of the EQ model increases in time and this increment is qualitatively correct, as explained by the experimental data. This increment is, however, overestimated by the EQ model and it is higher than the one of the previous cases at medium and low heat fluxes (see Section 6.5.5 and 6.6.5 of Chapter 3). The computed liquid temperature increases with the reduction of the filling ratio, as occurs in the experiments. This behaviour is similar to the one of the previous case at medium heat fluxes (see Section 6.6.5 of Chapter 3).

6.7.6. Presentation of the results: Filling ratio

Figure 57 presents the experimental and the computed time-evolutions of the filling ratio for the Study cases at high heat fluxes. The continuous lines are the values computed with the equilibrium model. The square symbols are the experimental values of filling ratio.

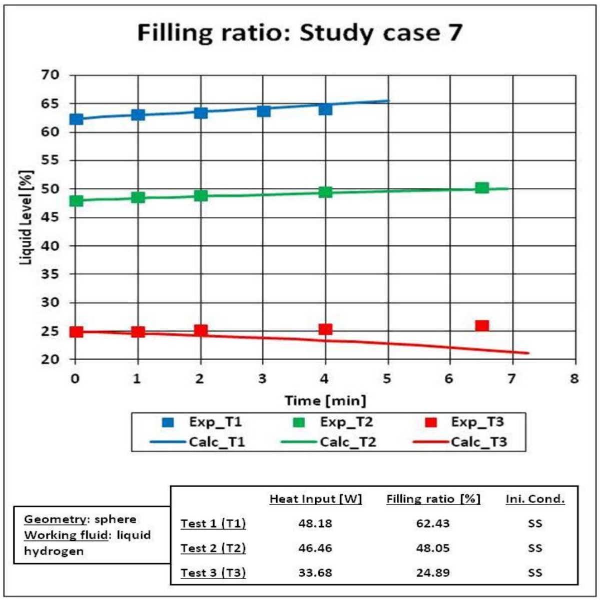

	Heat Input [W]	Filling ratio [%]	Ini. Cond.
Test 1 (T1)	48.18	62.43	SS
Test 2 (T2)	46.46	48.05	SS
Test 3 (T3)	33.68	24.89	SS

Figure 57. Comparison between the experimental filling ratio and the one computed with EQ model for the study case at high heat fluxes: Study case 7.

Except for Test 3, the filling ratio of the EQ model increases in time. This increment is qualitatively and quantitatively in agreement with the experimental data. Except for Test 3, the computed filling ratio decreases in time, as indicated by the experimental observations. These behaviours are similar to the ones seen in Study case 1 at low heat fluxes (see Section 6.5.6 of Chapter 3).

7. Discussion of the results and main conclusions

Due to the structure and the hypotheses of the equilibrium (EQ model), the discussion on the observations of the model's performance starts with the analysis of the behaviour of the effective heat transfer coefficient and of the pressure. The other variables such as internal temperature, heat inputs, liquid level and $\dot{m}_N$ are then discussed.

Section 7.1 presents the causes of the behaviour of the effective heat transfer coefficient. Section 7.2 explains the factors affecting the computed pressure. Section 7.3 describes the reasons of the behaviour of the internal temperature (vapour and liquid). Section 7.4 presents the sources of the time-evolution of the heat inputs. Section 7.5 discusses the behaviour of the filing ratio. Section 7.6 explains the causes of the time-evolution of the net mass flow. Section 7.7 explains the effect of the heat fluxes. Section 7.8 explains the difference between the storage of liquid nitrogen and the liquid hydrogen. Section 7.9 presents the summary and the perspective.

7.1. Behaviour of the computed effective heat transfer coefficient

The results of effective heat transfer coefficient (h_{eff}) are firstly discussed because the heat inputs, which affect the behaviour of the cryogenic liquid, are estimated from this variable. This coefficient quantifies the insulating properties of the storage container. h_{eff} is computed by the Boil-Off Rate (BOR) model (see Section 3.2 of Chapter 3) for each test with Equation 90, using the experimental value of the overall heat input. Equation 90 is derived from the hypothesis of negligible thermal resistance of Storage Heat transfer (SHT) model (see Section 3.1 of Chapter 3).

As reported in Table 56, Table 58 and Table 60, the values of h_{eff} increase with the rise of the heat leakage rate, as explained by Equation 90 of Section 3.2. Except for Test 4 of Study case 6 and of Test 3 of Study case 1, the value of this coefficient increases with the increment of the filling ratio because the experimental value of the overall heat leakage increases with the liquid level. This increment is caused by the rise of the dry side wall-to-vapour heat transfer coefficient (see Section 7 of Chapter 2). To the author's knowledge, the insulating properties of the storage container of Test 4 of Study case 6 and of Test 3 of Study case 1 were changed to increase the heat input rates respect to Test 2 of Study case 6 and to Test 2 of Study case 1, respectively. The insulating properties of the storage tanks of the remaining tests and Study cases were not changed when the filling ratio was reduced.

Hence, the behaviour of the effective heat transfer coefficient is wrong because the insulating properties cannot change with the filling ratio, except if these properties are manipulated as done in Test 4 of Study case 6 and of Test 3 of Study case 1. The BOR model cannot predict the decrement of the dry side wall-to-vapour heat transfer coefficient with the reduction of the filling ratio (see Section 7 of Chapter 2) because this heat transfer coefficient is neglected by the hypothesis of negligible thermal resistance of SHT model (see Section 3.1 of Chapter 3) So, this assumption should not be used for estimating h_{eff}.

7.2. Behaviour of the computed pressure

The computed value of the pressure is obtained with Ordinary Differential Equations (ODEs) system solver (see Section 5 of Chapter 3). During the self-pressurisation (storage mode 4), the time-derivate of the pressure is calculated with the Pressure-evolution (P-e) equation (Equation 69), as explained in Section 2.8. Equation 69 is deduced form the conservation laws of the EQ model (see Table 38 of Section 2.2 of Chapter 3), under the hypotheses of instantaneous thermodynamic equilibrium and total homogeneity (assumptions a) and b) of Section 1.1 of Chapter 3). Hence, the behaviour of the computed pressure is determined by two variables: the heat inputs rate and by the overall thermal capacity[68]. The total heat leakage decreases with the filling ratio, due to the reduction of the dry side wall-to-vapour heat transfer coefficient (see Section 7 of Chapter 2). As the heat input rises, at fixed thermal capacity, the liquid temperature, thus the internal temperature, increases. As consequence, the pressure increases due to the hypothesis of instantaneous thermodynamic equilibrium (assumptions a) of Section 1.1 of Chapter 3). The overall thermal capacity is mainly controlled by the liquid, and its total thermal capacity decreases with the reduction of the initial filling ratio. The increment of the thermal capacity reduces the self-pressurisation rate, at fixed heat input, because a larger amount of energy can be stored in the liquid than the one at low liquid level. As results, the heat leakage and the thermal capacity have two different effects on the pressure, and these effects are in competitions.

As illustrated in Figure 42, Figure 48 and Figure 54, the computed pressure increases in time and it is always lower than the experimental one. At low heat fluxes, the computed pressure increases as the filling ratio decreases. The calculated pressure increases with the isothermal condition as done with the steady state conditions, as illustrated in Figure 42 (f). At medium and high heat fluxes, the computed pressure increases as the initial liquid level reduces, as shown in Figure 48 and Figure 54. The pressure increases with the heat input as indicated by Test 3 of Study case 1 (see Figure 42 (b)) and by Test 4 of Study case 6 (see Figure 48 (b)).

Hence, the effect of the overall thermal capacity is stronger than the one of the heat input. So, the pressure remains lower than the experimental one and the pressure increases with the reduction of the filing ratio, instead of decreasing. The EQ model predict the wrong self-pressurisation rate and the wrong filling ratio-pressure relation due to the (P-e) equation (Equation 69), thus due to the hypothesis of instantaneous equilibrium (assumptions a) of Section 1.1 of Chapter 3). Hence, the pressure must be computed with a different conservation law.

7.3. Behaviour of the computed temperature

In the equilibrium model (EQ model), the liquid and the vapour temperatures are equal to the saturation temperature of the component at the ullage pressure, due to the hypothesis of instantaneous (assumptions a) of Section 1.1 of Chapter 3). The internal temperature is computed with the saturation relation (Equation 738). Hence, the behaviour of the temperature is related to the behaviour of the pressure.

The internal temperature increases in time, as reported in Figure 43, Figure 49 and Figure 55 for the comparison with the experimental vapour temperature data, and in Figure 44, Figure 50 and Figure 56 for the comparison with the experimental liquid temperature data. The increment rate of the internal temperature is lower than the one of the experimental data of the vapour temperature because the calculated self-pressurisation rate is lower than the experimental one. The computed values of the internal temperature are, however, close to the experimental values of the liquid temperature.

Hence, the internal temperature, in particular the vapour one, cannot be computed from the saturation relation (Equation 738). So, the hypothesis of instantaneous equilibrium (assumptions a) of Section 1.1 of Chapter 3) should not be used for modelling the ullage temperature. As consequence, this temperature must be estimated with the energy conservation law of the ullage.

---

[68] The thermal capacity is the product between the mass and the isobaric heat capacity. The overall thermal capacity is the sum of the thermal capacity of the liquid and the one of the vapour. For the same volume, the thermal capacity of the liquid is higher than the one of the vapour.

7.4. Behaviour of the computed heat inputs

The heat inputs are computed with Equation 89 of the storage heat transfer (SHT) model (see Section 3.1 of Chapter 3), under the hypothesis of the negligible thermal resistance. Equation 89 depends on the difference in temperatures between the external surface and the internal fluid. Hence, the time-evolution of the heat leakage is directly affected by the behaviour of the internal temperature.

As illustrated in Figure 40, Figure 46 and Figure 52, the values of heat input decrease during the self-pressurisation. The rate of this decrement increases with the increment of self-pressurisation rate because the value of the internal temperature increases. The increment of the internal temperature reduces the difference of temperatures of Equation 89 and this increment is higher at low initial filling ratio than the one at high liquid level.

Hence, the behaviour of the computed heat input is qualitatively correct because this variable decreases during the self-pressurisation.

7.5. Behaviour of the computed filling ratio

The calculated values of the filling ratio are obtained from the values of the liquid volume with the geometrical formulas of Appendix B.Appendix FThe values of liquid volume are calculated with the Ordinary Differential Equations (ODE) solver (see Section 5 of Chapter 3), as done for the calculated pressure. During the self-pressurisation (storage mode 4), the time-derivate of the liquid volume computed with liquid volume-evolution (V^L-e) equation (Equation 71), as explained in Section 2.8. Equation 71 is deduced form the conservation laws of the equilibrium model (EQ model) (see Table 38), under the hypotheses of instantaneous thermodynamic equilibrium and total homogeneity (assumptions a) and b) of Section 1.1 of Chapter 3). Hence, this variable depends on two factors: the time-derivate of the pressure and the overall density expansion respect to the pressure. Hence, the time-evolution of the filling ratio is directly connected to the pressure. The second factor is described by the coefficient A_{MB} (see Table 42), which is composed by the density expansion respect to the pressure of liquid and of vapour. The absolute values of the liquid density expansion respect to pressure, which is the term $V^L \cdot \left(\frac{\partial \rho_S^L}{\partial T}\Big|_{P^V} \cdot \frac{\partial T}{\partial P^V}\Big|_S + \frac{\partial \rho_S^L}{\partial P^V}\Big|_T \right)$ in Equation 49, increases with the liquid volume, thus initial filling ratio. The contribution $\frac{\partial \rho_S^L}{\partial T}\Big|_{P^V} \cdot \frac{\partial T}{\partial P^V}\Big|_S$ is negative and its absolute value is higher than $\frac{\partial \rho_S^L}{\partial P^V}\Big|_T$, which is positive. Hence, the term $V^L \cdot \left(\frac{\partial \rho_S^L}{\partial T}\Big|_{P^V} \cdot \frac{\partial T}{\partial P^V}\Big|_S + \frac{\partial \rho_S^L}{\partial P^V}\Big|_T \right)$ decreases with the filling ratio. The vapour density expansion respect to pressure is described by the term $V^V \cdot \left(\frac{\partial \rho_S^V}{\partial T}\Big|_{P^V} \cdot \frac{\partial T}{\partial P^V}\Big|_S + \frac{\partial \rho_S^V}{\partial P^V}\Big|_T \right)$ in Equation 49 and the absolute value of this term increases with the reduction of the initial liquid level. The contribution $\frac{\partial \rho_S^V}{\partial T}\Big|_{P^V} \cdot \frac{\partial T}{\partial P^V}\Big|_S$ is negative and its absolute value is lower than the contribution $\frac{\partial \rho_S^V}{\partial P^V}\Big|_T$, which is positive. Hence, the vapour density expansion respect to pressure increases with the reduction of the initial filling ratio.

As indicated in Figure 45, Figure 51 and Figure 57, the values of the calculated filling ratio are close to the experimental one. The value of the liquid level increases during the self-pressurisation. This increment is caused by the increment of pressure, as indicated by Equation 71. Test 6 of Study case 1, Test 3 of Study case 4, Test 3 of Study case 6 and Test 3 of Study case 7 are the exceptions of this increment. In these testes, the liquid level decreases or it is almost constant during the self-pressurisation. The initial filling ratio of these tests is around 30 % or lower. The decrement is caused by the density expansion because the coefficient A_{MB} is positive in these tests, instead of being negative as occurs at high values of the initial liquid level. The values of this coefficient are positive because the contribution of the vapour density expansion respect to pressure is stronger than the liquid one.

The filling ratio is dependent from two phenomena: the thermal expansion[69] and the mass transfer at the interface. During the self-pressurisation, the liquid absorbs heat and its density decreases. Hence, its volume increases. Regarding the mass transfer, it can decrease or increase the liquid volume because it is leads to a change in the total liquid mass. The mass decreases if $\dot{m}_N$ is positive and it increases if this flow rate is negative. Hence, the EQ model can predict the effect of the thermal expansion on the time-evolution of the filling ratio. The effect of the mass transfer at interface are not modelled by the EQ model, due to the hypothesis of instantaneous thermodynamic equilibrium (assumptions a) of Section 1.1 of Chapter 3). So, the time-evolution of the liquid volume should be computed from the conservation law of the liquid mass, instead of the Equation 71.

7.6.Behaviour of the computed net mass flow

The net mass flow ($\dot{m}_N$) is determined from Equation 38 of Section 2.4, which is obtained from the liquid mass conservation law (Equation 34). Hence, this variable depends on two factors: the time derivates of the pressure and of the liquid volume, as described in Section 2.3 of Chapter 3. The time-derivate of the pressure increases the net mass flow, as indicated by the term $\frac{\partial P^V}{\partial t} \cdot A^L_{MB}$ in Equation 38. The time-derivate of the liquid volume decreases the values of this mass flow, as suggested by the term $\frac{\partial V^L}{\partial t} \cdot C^L_{MB}$ of Equation 38. Hence, the effects of these time-derivates are opposite and they are in competition.

As described by Figure 41, Figure 47 and igure 53, this flow rate always increases in time. The rate of this increment increases with the heat inputs and the reduction of the initial liquid level. Hence, the impact of the time-derivate of pressure on $\dot{m}_N$ is always more intense than the impact of the time-derivate of the liquid volume because this mass flow increases in time. As the filling ratio is reduced, the effect of the term $\frac{\partial V^L}{\partial t} \cdot C^L_{MB}$ is lower than the one at high liquid level. Hence, the mass flow rate increases with the reduction of the filling ratio.

As reported by Table 57, Table 59 and Table 61, the values of $\dot{m}_N$ reduces when the storage container move from the steady state (storage mode 1.b) to the self-pressurisation (storage mode 4). At steady state, $\dot{m}_N$ is equal to the inlet liquid flow, thus Boil-Off Gas flow rate, as indicated by Equation 38, because the time-derivates of pressure and liquid volume are equal to zero. At the self-pressurisation, $\dot{m}_N$ is calculated from the values of these derivates, causing a reduction of the value of this flow rate.

Hence, the hypothesis of instantaneous thermodynamic equilibrium (assumptions a) of Section 1.1 of Chapter 3) is not suitable for predicting $\dot{m}_N$ because the influence of the temperature gradient at the interface are considered.

7.7.Effect of the overall heat fluxes

The experimental data of the comparison are obtained at different rate of the overall heat input, thus heat flux, as described in Table 54 of Section 6.1. In Study case 1, 2, and 5 of liquid nitrogen (LN_2)

---

[69] The thermal expansion is the increment of the volume due to the rise of internal temperature.

[24]–[26], the storage containers are quite similar because they are vertical cylinder with flat bottom and roof. In Study case 3, 4, 6 and 7 of liquid hydrogen (LH_2) [27]–[30], the geometry of the oblate ellipsoid is quite similar to the one of the sphere. Hence, the effect of the overall heat fluxes can be evaluated.

The heat fluxes affect the overall heat inputs. In the EQ model, this variable affects the evolution of the pressure, due to the hypothesis of instantaneous thermodynamic equilibrium (assumptions a) of Section 1.1 of Chapter 3). As observed in Section 6.5.3, 6.6.3 and 6.7.3 of Chapter 3, the self-pressurisation rate increases when the value of overall heat flux rises. As consequence, the increment of the filling ratio and of the internal temperature is higher than the one at low overall heat fluxes. That effect of the overall heat flux is not in agreement with the experimental observation due to the hypothesis of instantaneous thermodynamic equilibrium (assumptions a) of Section 1.1 of Chapter 3). Hence, this hypothesis should be removed.

7.8. Difference between liquid nitrogen and liquid hydrogen

The equilibrium model (EQ model) is compared with the experimental data of liquid nitrogen (LN_2) [24]–[26] (Study case 1, 2, and 5) and liquid hydrogen (LH_2) [27]–[30] (Study case 3, 4, 6 and 7), as reported in Table 54. The experimental data of LN_2 are obtained in a vertical cylinder with flat bottom and roof. The experimental data of LH_2 are measured in oblate ellipsoid and sphere, respectively for Study case 3 and 4, and for Study case 6 and 7. The heat inputs and the initial liquid level of the LN_2 are different from the one of LH_2, even if the values of these variables are quite similar. Hence, the behaviour of the two cryogenic fluids cannot be compared because the initial condition, the heat input and the geometry are different.

7.9. Summary and perspective

The equilibrium model (EQ model) is developed to predict the behaviour of cryogenic liquids in small scale (SS) storage container, using the thermodynamic approach that is found the scientific literature as basis for developing the EQ model. The equilibrium model (EQ model) is based on the hypotheses of instantaneous thermodynamic equilibrium and total homogeneity (assumptions a) and b) of Section 1.1 of Chapter 3). The mathematical system of this model is developed for two storage modes 1.b (steady state) and 4 (self-pressurisation), as described in Section 1.4 of Chapter 3. This system is composed by key and dipendent variables, and by Ordinary Differential Equations (ODEs) and algebraic equations. Some of these equations are obtained from the conservation laws of mass and of energy. The differential equations are solved with the adaptive steps size method for explicit Runge-Kutta method, as presented in Section 5 of Chapter 3. The thermodynamic properties and the transport properties are determined with the reference models of Section 4.1 and of Section 4.2 of Chapter 3. The EQ model is compared with the experimental data of liquid nitrogen and liquid hydrogen at different overall heat fluxes and in storage containers of different geometry. The main critical issues of the EQ model are:

a) The estimation of the effective heat transfer coefficient (h_{eff}). The values of the effective heat transfer coefficient are wrong because they change with the filling ratio;
b) The prediction of the pressure. The self-pressurisation rate is lower than the experimental one;
c) The calculation of the ullage temperature. The difference in vapour temperature between the calculated and the experimental is high;

The cause of the weak prediction capacity of these experimental data is the hypothesis of instantaneous thermodynamic equilibrium (assumptions a) of Section 1.1 of Chapter 3). Hence, a new version of the storage model, called homogeneous model, must be created, by removing this hypothesis. The new model should be developed with these axes of improvement:

a) The hypothesis of negligible thermal resistance of storage heat transfer (SHT) model (see Section 3.1 of Chapter 3) should be removed. Hence, the dry side wall-to-vapour and the wet walls-to-liquid heat transfer coefficients must be considered in the estimation of the effective heat transfer coefficient of the boil-off rate (BOR) model, and in the SHT model. As consequence, a new BOR model and heat transfer model must be proposed;
b) The overheated state of the vapour and the sub-cooled state of the liquid must be considered because the hypothesis of instantaneous thermodynamic equilibrium is removed. Hence, the temperature of liquid and vapour should be estimated with the energy conservation laws, instead of using the saturation relation of the EQ model;
c) The temperature gradients at the interface, thus the heat transfer, should be considered to predict the net mass flow. Hence, net mass flow ($\dot{m}_N$) should be calculated from the interfacial heat transfer;

These actions will be further explaining in the next chapter model.

Chapter 4

Modèle homogène

Le modèle à l’équilibre (EQ) ne peut pas prédire (i) l'auto-pressurisation et (ii) l'état de surchauffe de la vapeur ni (iii) estimer le coefficient de transfert de chaleur effectif, en raison de l'hypothèse d'équilibre thermodynamique instantané. Le modèle homogène (modèle H) a été par conséquent développé tel que décrit dans ce chapitre.

Ce modèle suppose que le liquide et la vapeur sont homogènes et isothermes mais ne sont pas à l’équilibre thermodynamique. Par conséquent, le transfert de chaleur au niveau des parois des cuves de stockage doit être calculé avec une approche différente, tandis que le transfert de chaleur à l’interface doit être pris en compte dans le modèle H.

Il s’ensuit qu’un nouveau système mathématique doit être développé. Les sous-modèles tels que le modèle de taux d'évaporation (BOR) et le modèle de transfert de chaleur de stockage (SHT) doivent être modifiés pour être cohérents avec les nouvelles hypothèses et les nouveaux modèles tels que le modèle de couche limite de stockage (SBL) et le transfert de chaleur à l’interface (IHT) doit être introduit. Cette version du modèle BOR calcule (i) le coefficient de transfert thermique effectif, (ii) le coefficient correctif du coefficient de transfert thermique paroi sèche-vapeur et (iii) le coefficient correctif du transfert thermique paroi sèche-interface. Les entrées thermiques au niveau de chaque surface sont respectivement déterminées avec le modèle SHT. Ce dernier utilise les lois de conservation des flux thermiques et les valeurs moyennes des coefficients de transfert thermique. Ces coefficients sont estimés avec les formules semi-empiriques et avec l'approche de la couche limite. qui détermine les coefficients de transfert de chaleur en fonction des variables de la couche limite telles que l'épaisseur de la couche et la vitesse de la couche limite extérieure d'un écoulement à convection forcée comparable. Ces variables sont estimées au moyen du modèle SBL, avec deux approches différentes : (i) les solutions exactes et (ii) numériques des équations de bilan d'énergie et de quantité de mouvement de la couche limite. Ces équations sont obtenues à partir de la théorie de Prandtl et de la méthode intégrale de von Karman. La solution numérique est obtenue par discrétisation de la couche limite en sous-couches de même hauteur. Certaines équations du système mathématique sont obtenues à partir des lois de conservation de la masse et de l'énergie, appliquées au liquide et à la vapeur. Ces équations d'équilibre sont développées à l'aide d'une procédure mathématique pour expliciter les dérivées temporelles de la pression, du volume de liquide et des températures du liquide et de la vapeur, créant ainsi le système mathématique du modèle H. Ce système est obtenu pour les différents modes de stockage et il est composé d’équations algébriques et d’un système d’équations différentielles ordinaires, résolu avec la même approche du modèle EQ. Le système mathématique est combiné au modèle d'interface qui détermine le débit massique net en utilisant l'approche thermodynamique.

Les résultats du modèle H sont comparés aux données expérimentales de l'azote liquide et de l'hydrogène liquide, ainsi qu'aux résultats du modèle EQ. La comparaison révèle que l’équation du bilan énergétique de la vapeur et le transfert de chaleur vapeur-interface doivent être modélisés différemment. La prédiction de la température de vapeur à faibles flux thermiques est améliorée par rapport à celle du modèle EQ.

Homogeneous model

The equilibrium model (EQ model) cannot predict (i) the self-pressurisation, (ii) the overheated state of the ullage and (iii) estimating the effective heat transfer coefficient, due to the hypothesis of instantaneous thermodynamic equilibrium. Hence, the homogeneous model (H model) is introduced in this chapter. This model assumes that both liquid and vapour are homogenous and isothermal, thus omitting the hypothesis of instantaneous thermodynamic equilibrium. Hence, the heat transfer at the walls of the storage containers must be computed with a different approach, and the interfacial mass-heat transfer must be considered in the H model. As consequence, a new mathematical system must be developed. The sub-models such as the Boil-off Rate (BOR) and the Storage Heat Transfer (SHT) model must be modified to be coherent with new assumptions and new models such as Storage Boundary Layer (SBL) model and the Interfacial Heat Transfer (IHT) model must be introduced. This version of BOR model computes (i) the effective heat transfer coefficient, (ii) the corrective coefficient of the dry side wall-to-vapour heat transfer coefficient and (iii) the corrective coefficient of the dry side wall-to-interface heat transfer. The heat inputs at each surface are respectively determined with the SHT model. The latter uses the conservation laws of heat fluxes and the average values of the heat transfer coefficients. These coefficients are estimated with the semi-empirical formulas and with the boundary layer approach. This approach determines the heat transfer coefficients as function of the boundary layer variables such as the thickness of the layer and the velocity the outside boundary layer of comparable forced-convection flow[70]. These variables are estimated by means of SBL model, with two different approaches: the exact and the numerical solutions of the energy and momentum balance equations of the boundary layer. These equations are obtained from the Prandtl’s theory and the von Karman integral method. The numerical solution is obtained with the discretization of the boundary layer in sub-layers that have the same height. Some of the equations of the mathematical system are obtained from the mass and energy conservations laws, which are applied for the liquid and the vapour. These balance equations are developed with a mathematical procedure to explicit the time derivates of pressure, liquid volume, and liquid and vapour temperatures, creating the mathematical system of the H model. This system is obtained for the different storage modes and it is composed by the algebraic equations and the Ordinary Differential Equations (ODE). The system of ODE is solved with the same approach of the EQ model. The mathematical system is combined with the interface model, which determines the net mass flow, using the thermodynamic approach. The results of the H model are compared with the experimental data of liquid nitrogen and of liquid hydrogen, and with the results of the EQ model. The comparison reveals that the energy balance equation of the vapour, and the vapour-to-interface heat transfer should be modelled differently. The prediction of the vapour temperature at low heat fluxes is improved respect to the one of the EQ model.

Section 1 introduces the homogeneous model. Section 2 describes the mathematical procedure to deduce the equations of the mathematical system of the H model. Section 3 and 4 present the SBL and SHT models, respectively. Section 5 and 6 describes the IHT and BOR models, respectively. Section 7 discusses the comparison between the results of the model and the experimental data. Section 8 introduces the discussion of the results of the H model. Section 9 presents the the comparison between the results of the H model and the one of EQ model.

---

[70] The theory of natural convection was developed using some formulas and hypotheses of the forced convection. The velocity outside boundary layer of comparable forced-convection flow is the velocity of the forced convective flow outside the boundary layer, if the free-convection occurs as the forced-convection.

1. Introduction

The equilibrium model (EQ model) (see Chapter 3) was developed with the hypotheses of instantaneous thermodynamic equilibrium and of total homogeneity. The results of this model were compared with the experimental data of liquid nitrogen and of liquid hydrogen (see Chapter 2). The EQ model cannot predict the behaviour of the cryogenic liquids in storage containers, in particular the pressure, the ullage temperature and the effective heat transfer coefficient, with an acceptable reliability. This non-accurate description is caused by the hypothesis of instantaneous thermodynamic equilibrium and from the sub-models of EQ model such as Boil-off rate (BOR) and the Storage Heat Transfer (SHT) model, which are directly derived by this assumption. As consequence, a new model is proposed and developed and it is called *homogeneous model (H model)*. In this model, a new set of hypotheses is used to overcome the critical issues of the EQ model, modifying the sub-models and developing new ones. Hence, a new mathematical and a new Ordinary Differential Equation (ODEs) systems are formulated. As consequence of the new hypotheses, the block structure of the H model is changed from the one of the EQ model.

Section 1.1 explains the hypotheses of the H model. Section 1.2 presents the variables of the EQ model. Section 1.3 describes the block structure of the H model. Section 1.4 explain the mathematical system of EQ model.

1.1. Hypothesis

As mentioned before, the hypothesis of the instantaneous thermodynamic equilibrium must be removed to increase the reliability of the model. So, the actual thermodynamic states of the liquid and the vapour in the tank must be considered in the homogeneous model (H model). The behaviour of the cryogenic liquids in storage container depends on the phenomena of heat and of mass transfer across the vapour-liquid interface. As shown in experiments [1],[2], the liquid-vapour interface is close to the thermodynamic equilibrium, in a state called "quasi-equilibrium". Hence, the H model can be based on the following assumptions:

a) Liquid and vapour are homogenous, thus isothermal;
b) The thermodynamic state of the liquid and of the vapour can be over-heated, sub-cooled or at saturation
c) The interface is at thermodynamic equilibrium at the pressure of the ullage;

Assumption a) is called *hypothesis of total homogeneity* and it is similar to the one used in the EQ model. So, the thermal stratification is neglected in both liquid and vapour. Assumption b) is called the *hypothesis of actual thermodynamic state*. Assumption c) is called *local equilibrium condition*.

Figure 58 shows the H model. The blue and red zones are respectively the liquid and the ullage. The yellow dashed line is the interface, the green arrow is the net mass flow at interface, and the black arrows are the inlet and outlet flows of the fluid. The white arrows with red boarders are the heat fluxes, and the white points with purple boarders are the wall temperatures. The orange and light blue arrows represent the convective flows in vapour and in liquid, respectively. As shown in Figure 58, the heat inputs at the side walls, at the bottom and at the roof causes the phenomenon of the natural convection. The convective flows of this phenomenon mix the liquid and the vapour mass, respectively, making the liquid and the vapour isothermal, as illustrated in Figure 58. The heat ingress across the wet side and the bottom walls entirely ends up in the liquid, accumulating sensible heat. This energy is transferred to the interface, when the interface temperature is lower than the liquid one. In the opposite situation, the interface moves energy to the liquid.

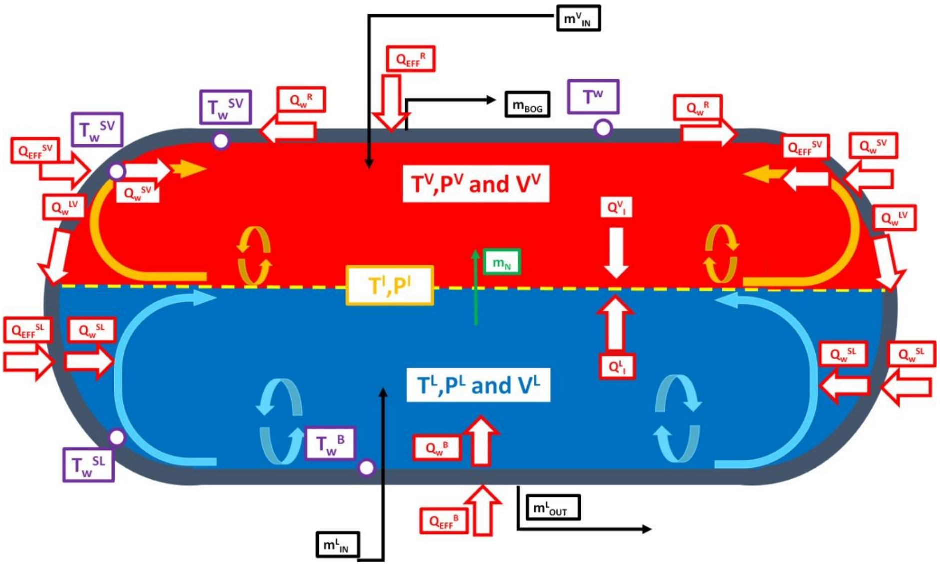

Figure 58. H model.

Regarding the ullage, the heat coming from the environment is partially transferred to the interface by conduction at the dry side wall. The remaining part ends up in the vapour, as sensible heat, causing the over-heated state of the vapour. Part of this sensible heat is transferred to the interface, as seen in Figure 58. This energy is then converted into evaporative and condensing mass flows, which end up in a net mass flow.

1.2. Variables

The homogeneous model (H model) uses the hypotheses of actual thermodynamic state and of local thermodynamic equilibrium (assumptions b) and c) of Section 1.1 of Chapter 4). Hence, these hypotheses increase the number of the variables because the thermodynamic state is not the same in the liquid as in the vapour. The variables of the H model can be grouped in seven categories:

- State: variables that describe the state of the behaviour;
- Differential: variables that represent the variation in time;
- Border: variables that define the boundary conditions;
- Heat transfer: variables that describe the heat transfer;
- Boundary layer: variables that represent the natural convection;
- Geometrical: variables that describe the geometry of the storage container;
- Interface: variables of the transport phenomena at the interface;
- Thermo-physical: variables that quantify the transport and thermodynamic properties;

These seven categories are described in Table 62.

Table 62. Nomenclature of the variables of the H model.

Type of variable	Name of the variable	Symbol	Unit
State	Liquid pressure	P^L	[kPa]
	Liquid Temperature	T^L	[K]
	Liquid volume	V^L	[m^3]
	Interface pressure	P^I	[kPa]
	Interface temperature	T^I	[K]
	Ullage pressure	P^V	[kPa]
	Ullage temperature	T^V	[K]
	Ullage volume	V^V	[m^3]
	Time	t	[s]

Table 62. Nomenclature of the variables of the H model.

Differential	Time derivate of liquid pressure	$\frac{\partial P^L}{\partial t}$	[kPa/s]
	Time derivate of liquid temperature	$\frac{\partial T^L}{\partial t}$	[K/s]
	Time derivate of ullage pressure	$\frac{\partial V^L}{\partial t}$	[m^3/s]
	Time derivate of ullage pressure	$\frac{\partial P^V}{\partial t}$	[kPa/s]
	Time derivate of vapour temperature	$\frac{\partial T^V}{\partial t}$	[K/s]
	Time derivate of the vapour volume	$\frac{\partial V^V}{\partial t}$	[m^3/s]
	Time derivate of the liquid enthalpy	$\frac{\partial \tilde{H}^L}{\partial t}$	[J/s]
	Time derivate of the vapour enthalpy	$\frac{\partial \tilde{H}^V}{\partial t}$	[J/s]
	Time derivate of the liquid mass	$\frac{\partial m^L}{\partial t}$	[kg/s]
	Time derivate of the vapour mass	$\frac{\partial m^V}{\partial t}$	[kg/s]
Border	External wall temperature	T^W	[K]
	Overall heat inputs	$\dot{Q}$	[W]
	Effective heat transfer coefficient	h_{EFF}	[W/m²/K]
	Corrective coefficient of dry side wall-to-vapour heat transfer coefficient	α	[-]
	Corrective coefficient of dry side wall-to-interface heat transfer	β	[-]
	Inlet vapour mass flow	$\dot{m}_{IN}^V$	[kg/s]
	Inlet liquid mass flow	$\dot{m}_{IN}^L$	[kg/s]
	Boil-off Gas (BOG) flow	$\dot{m}_{BOG}$	[kg/s]
	Outlet liquid mass flow	$\dot{m}_{OUT}^L$	[kg/s]
	Temperature of inlet vapour mass flow	T_{IN}^V	[K]
	Pressure of inlet vapour mass flow	P_{IN}^V	[kPa]
	Temperature of inlet liquid mass flow	T_{IN}^L	[K]
	Pressure of inlet liquid mass flow	P_{IN}^L	[kPa]
	Temperature of BOG	T_{BOG}	[K]
	Pressure of BOG	P_{BOG}^V	[kPa]
	Temperature of outlet liquid mass flow	T_{OUT}^L	[K]
	Pressure of outlet liquid mass flow	P_{OUT}^L	[kPa]
Heat transfer	Bottom wall temperature	T_w^B	[K]
	Wet side wall temperature	T_w^{SL}	[K]
	Dry side wall temperature	T_w^{SV}	[K]
	Roof wall temperature	T_w^R	[K]
	Effective Bottom-to-liquid heat input	$\dot{Q}_{EFF}^B$	[W]
	Effective Wet side wall-to-liquid heat input	$\dot{Q}_{EFF}^{SL}$	[W]
	Effective Dry side wall-to-vapour heat flux	$\dot{Q}_{EFF}^{SV}$	[W]
	Effective Roof-to-dry side wall heat flux	$\dot{Q}_{EFF}^R$	[W]
	Bottom-to-liquid heat input	$\dot{Q}_w^B$	[W]
	Wet side wall-to-liquid heat input	$\dot{Q}_w^{SL}$	[W]
	Dry side wall-to-vapour heat flux	$\dot{Q}_w^{SV}$	[W]
	Roof-to-dry side wall heat flux	$\dot{Q}_w^{R-SV}$	[W]
	Dry side wall-to-interface heat flux	$\dot{Q}_w^{S-L}$	[W]
	Bottom-to-liquid heat transfer coefficient	h_w^B	[W/m²/K]
	Wet side wall-to-liquid heat transfer coefficient	h_w^{SL}	[W/m²/K]
	Dry side wall-to-liquid heat transfer coefficient	h_w^{SV}	[W/m²/K]
Boundary layer	Velocity outside boundary layer of comparable forced-convection flow	U	[m]

Table 62. Nomenclature of the variables of the H model.

	Average velocity in the boundary layer	$\bar{u}$	[m]
	Thickness of the boundary layer	δ	[m]
	Thermal thickness of the boundary layer	δ_T	[m]
	Momentum thickness of the boundary layer	δ_M	[m]
	Mass flow in the boundary layer	$\dot{m}^{UP}$	[kg/s]
	Temperature in the boundary layer	T^{BL}	[K]
Geometrical	Bottom surface area	A^B	[m²]
	Wet side wall surface area	A^{SL}	[m²]
	Dry side wall surface area	A^{SV}	[m²]
	Roof surface area	A^R	[m²]
	Interface surface area	A^I	[m²]
	Internal surface area	A^{TOT}	[m²]
	Internal volume	V^{TOT}	[m³]
	Liquid internal volume	V^L	[m³]
	Vapour internal volume	V^V	[m³]
	Volume	V	[m³]
Interface	Net mass flow	$\dot{m}_N$	[kg/s]
	Vapour-to-interface heat transfer	$\dot{Q}_I^V$	[W]
	Liquid-to-interface heat transfer	$\dot{Q}_I^L$	[W]

The thermo-physical properties of the H model are the same as in the equilibrium model and they are computed with the reference models of the equilibrium model (see Section 4 of Chapter 3). Hence, they are not reported in Table 31. The number of the state variable is 9 and it is increased of 4 variables respect to the equilibrium model due to the hypotheses of actual thermodynamic state and of local thermodynamic equilibrium (assumptions b) and c) of Section 1.1 of Chapter 4). The time-derivates of liquid pressure, liquid temperature and vapour temperature are added to the differential variables. The time-derivates of the overall enthalpy and mass are omitted. The corrective coefficients α and β are added to the border variables. The heat transfer, the boundary layer and the interface variables were not presented in the equilibrium model and they are introduced for the H model. The geometrical variables such as side walls, bottom and roof, and interface surface are considered in the H model, instead of being neglected as done the equilibrium model. These variables are computed with the formulas of Appendix B.

1.3.Block structure of the homogeneous model

The input of the homogeneous model (H model) is similar to the one of the equilibrium model (EQ model), except for the tolerance of the numerical error. This tolerance is required for the Block 2, where the number of the sub-layers is calcualted. The output of the H model is the same of the EQ model (see Table 32). The block structure of the H model is described in Figure 59.

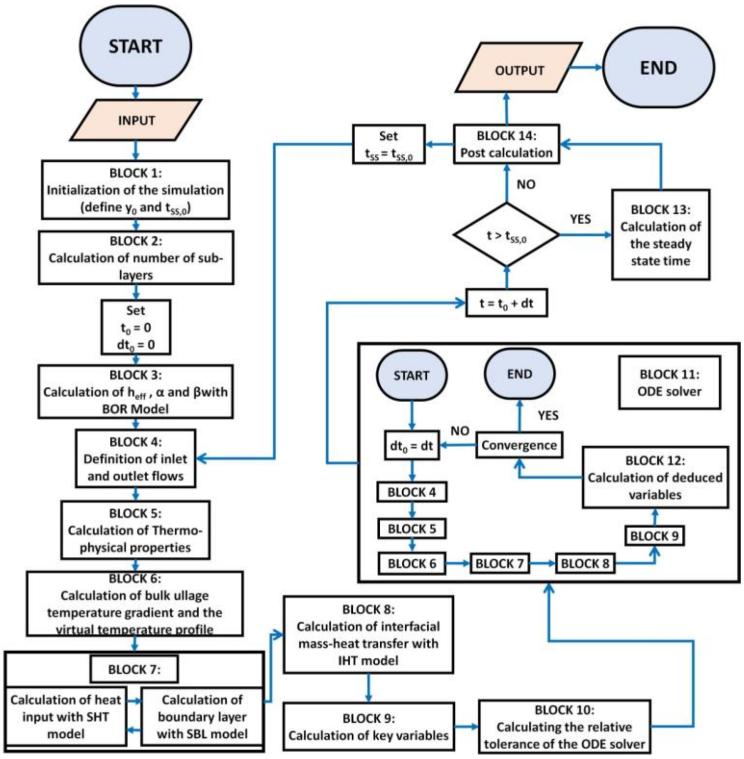

Figure 59. Block structure of H model.

The block strucuture is composed by 13 blocks:

a) BLOCK 1. This block is the initialisation of the state variables (y_0), the definition of the heat input rate, and the initial value of the integration step (dt_0) and of time (t_0), and the first guess value and the maximum value of the steady-state time ($t_{SS,0}$ and $t_{SS,MAX}$). The first guess value and the maximum value of the steady state time can be computed with the equations of Table 63.

Table 63. Equations to compute the first guess value and the maximum value of the steady state time.

Variables	Name	Equation	Formula
first guess value of the steady state time	$t_{SS,0}$	Equation 94	$t_{SS,0} = t_{SP} \cdot \tau_{SS}$
the maximum value of the steady state time	$t_{SS,MAX}$	Equation 95	$t_{SS,MAX} = 1.5 \cdot t_{SP}$

In Equation 94, t_{SP} is the self-pressurisation time and τ_{SS} is steady state ratio. The value of this ratio is 30 %. This maximum value of steady state time is the 3/2 of the self-pressurisation time. This value and the value of τ_{SS} are arbitrarily defined. $t_{SS,0}$ and $t_{SS,MAX}$ are required in BLOCK 11 (step k) of Section 1.3 of Chapter 4). This block is similar to the one of the EQ model (see Section 1.3 of Chapter 3);

b) BLOCK 2. The Storage Boundary Layer (SBL) and the Storage Heat Transfer (SHT) models require the numbers of the sub-layers of the wet and dry side walls, respectively. In this block, these numbers are computed with the approach of Section 1.3.1 of Chapter 4;

c) BLOCK 3. The effective heat transfer coefficient (h_{eff}), and the corrective coefficients α and β are computed with the Boil-Off Rate (BOR) model. These coefficients are used in the SHT model to compute the heat inputs and the thermal distribution. More details on the BOR model are given in Section 4;

d) BLOCK 4. The border variables such as the inlet and outlet mass flow, the temperatures and pressure of these flows and the wall temperature are determined. The approach to define this variable is the one used for the EQ model (see Section 1.3.2 of Chapter 3).

e) BLOCK 5. The thermo-physical properties are determined at the vapour temperature and pressure, and at the liquid temperature and pressure, respectively for liquid and vapour phases. The reference models, which are used to calculate these variables, are the ones used in the EQ model (see Section 4 of Chapter 3);

f) BLOCK 6. The SHT model is coupled with the SBL model because the interaction between the fluid-dynamic and the heat transfer is considered in the H model. Hence, these models are simultaneously used in this block to compute the heat inputs at each surface and the boundary layer variables, respectively. The SBL and the SHT models are respectively described in Section 3 and 4;

g) BLOCK 7. The mass and the heat transfers at the interface are calculated with the Interface Heat Transfer (IHT) model, as it is explained in Section 5. This model is placed after the SHT and SBL model because it requires the variables of the wet side wall to compute the interfacial mass and heat transfer.

h) BLOCK 8. The indipendent variables of the mathematical (see Table 64) system are computed with the target equations. More details on the indipendent variables and on the equations to use are given in Section 1.4;

i) BLOCK 9. The value of the relative tolerance of the Ordinary Differential Equation (ODEs) system is calculated with the procedure explained in Section 1.3.3;

j) BLOCK 10. The pressure, the liquid volume, and the vapour and liquid temperatures are computed with the Ordinary Differential Equations (ODEs) solver. The ODE solver is the one used in the EQ model (see Section 5 of Chapter 3). The numbers of the variable and of differential equation are higher than the ones of the EQ model. The value of the relative tolerance changes during the simulation to reduce the computational time, instead of being constant as done in the EQ model. At each iteration of the ODE solver, Block 4, 5, 6 7 and 9 are executed;

k) BLOCK 11. The dipendent variables of the mathematical (see Table 64) system are computed with the target equations. More details on the dipendent variables and on the equations to use are given in Section 1.4;

l) BLOCK 12. This block calculates the steady state time[71], which is used in Block 11 (step l) of Section 1.3 of Chapter 4). This calculation is done as explained Section 1.3.3;

m) BLOCK 13. This block is composed by a series of logical steps to determine if the storage mode can be shifted from steady state (storage mode 1.b) to self-pressurisation (storage mode 4). This change of the storage mode is done is the simulated time is above the steady state time. This block is identical to the post-calculation block of EQ model (see Section 1.3.3 of Chapter 3).

As illustrated in Figure 59, Block 2, 3, 6 and 7 are the main differences respect to the EQ model because these blocks are affected by the new set of hypotheses of the H model (see Section 1.1 of Chapter 4), which indirectly change the SHT model, and require the introduction of SBL and IHT models.

The Block 2, 8 and 10 are respectively explained in Section 1.3.1, 1.3.2 and 1.3.3.

1.3.1. BLOCK 2: Computation of the numbers of sub-layers

The modelling approach of the Storage Boundary Layer (SBL) and Storage Heat Transfer (SHT) model require the number of sub-layer of the liquid and vapour side walls. This modelling approach

---

[71] The steady state time is the time required to reach the steady state conditions.

discretizes the boundary layer of the side walls in sub-layers of equal height. Hence, the numerical method used in the SBL model introduces an error in estimating the boundary layer variables δ_M and U (see Table 31), respect to the exact approach. This error increases with the augmentation of the heat inputs and the length of the side wall. This error decreases with the increment of the number of the sub-layers. The increment of the number of the sub-layers augments the computational time because the number of the iterations of the SBL algorithm is higher than the one at low number of sub-layers. Hence, these numbers are determined with a computation method to assure accuracy and reasonable computational time.

The numbers of sub-layers are computed for the liquid and the vapour side walls, and these numbers are respectively named N^L and N^V. These numbers are computed with an iterative procedure. This procedure minimizes the numerical error of one of the boundary layer variables (see Table 62). Mass flow rate in the boundary layer is computed as product of the variables δ_M and U, with the formulas reported in Section 2 of Appendix P. Hence, this variable can be used to minimize the numerical errors of the variables δ_M and U, thus the numerical error of the discretisation approach of the Storage Boundary Layer (SBL) model. The structure, the inputs and output variables of the algorithm to compute N^L and N^V are given in Section 1 of Appendix L.

1.3.2. BLOCK 9: relative tolerance

The homogenous (H) model is more complex than the equilibrium model (EQ model), as reported in Figure 59, due to the Storage Heat Transfer (SHT) and Storage Boundary Layer (SBL) models, in particular for the discretisation approach of the SBL model. Hence, the computation time of the H model is potentially higher than the one of the EQ model. Hence, the values of the relative tolerance of the H model is not fixed during the self-pressurisation and the steady state to reduce the computation time. To avoid loss of accuracy due to the increment of the value of the relative tolerance, a procedure is developed. This procedure is roughly composed by the steps:

a) The ratio of the time-derivates between the current value and the maximum possible one is computed for all the variables of the ODE system, thus the differential indipendent variables (see Table 64) ;
b) The values of the relative tolerance are defined as function of the value of this ratio. If the value of this ratio decreases, the value of the relative tolerance increases because the numerical error of the ODE solver reduces. When the value of this ratio increases, the value of this tolerance reduces to decrease the numerical error of the ODE solver.

The details of the described procedure are reported in Section 2 of Appendix L.

1.3.3. BLOCK 12: computing the steady state time

The homogenous (H) model describes the steady state and the self-pressurisation of cryogenic liquids in small scale tanks. When the self-pressurisation is simulated, the H model computes the time-evolution of the time-derivates until the simulated time is equal or above the steady state time, as explained in Section 3 of Appendix L. Once this constrain is respected, the steady state conditions are reached. The attainment of this condition is the mandatory to calculate the initial conditions of the self-pressurisation, except for the cases where these initial conditions are known by default and the self-pressurisation can be immediately simulated.

These steady state conditions cannot be calculated before starting the simulation because the liquid and the vapour temperature, pressure and volume can reach these conditions at different simulation time. As consequence, there are potentially more than one steady state times. Hence, the time required to reach steady state conditions can only be computed during the simulation of the steady state. A method, called *steady state algorithm*, is developed to compute the steady state time.

A dynamic system is at the steady state when the values of the variables of this system are constant. This condition implies that the values of the time-derivates of these variables are equal to zero. The values of the time derivates computed by the model cannot, however, be equal to zero. Hence, the condition of steady state can be defined as the condition at which the values of the time-derivates are lower than a defined value. This value must be sufficiently low to guarantee that the variable imperceptibly changes in time. Hence, the steady state algorithm can be developed with these steps:

a) Computing the average value of time-derivate of pressure, liquid volume, liquid and vapour temperatures in the last 10 time-points[72];
b) Calculating the relative ratio between the values of these time-derivates and the maximum values of same derivates during the steady state;
c) Increasing the steady state time if this difference is higher than the desired value;

The maximum value of the steady state time is required for avoiding that the H model is blocked in the steady state model. The details of this procedure and the maximum value of the steady state time are described in Section 3 of Appendix L.

1.4. Mathematical system

As for the equilibrium model (EQ model), the mathematical system of the homogeneous model (H model) is developed for predicting the behaviour of cryogenic liquid in two storage modes: steady state (mode 1.b) and self-pressurisation (mode 4) (see Table 35). The mathematical system of the H model is composed by the target variables[73] and target equations[74], as for the EQ model (see Figure 34). The target variables are composed by the key[75] and the deduced[76] variables, and the target equations are divided into algebraic equations and Ordinary Differential Equations (ODEs). The algebraic and differential equations, and the key and dipendent variables of the mathematical system are reported in Table 64 for both the storage modes.

Table 64. Equations and target variables of mathematical system of H model.

Target variables		***Target equations***	
Type	**Symbol**	**Type**	**Name**
Independent	$\frac{\partial P^V}{\partial t}$	Differential	Pressure evolution (P-e) equation (Equation 149 and Equation 150)
	$\frac{\partial V^L}{\partial t}$	Differential	Liquid volume evolution (V^L-e) equation (Equation 151 and Equation 152)
	$\frac{\partial T^L}{\partial t}$	Differential	Liquid temperature evolution (T^L-e) equation (Equation 133)
	$\frac{\partial T^V}{\partial t}$	Differential	Liquid temperature evolution (T^V-e) equation (Equation 134)

---

[72] The numerical integration of solver of the ODE system discretises the simulation time in steps. Each step is characterized by a time-point.

[73] The target variables are the variables that have to be compute to characterize the behaviour of the cryogenic liquids and their vapours in storage containers.

[74] Target equations are formulas used to calculate the target variables.

[75] The key variables are the one computed from the target equations that are obtained from the conservation laws.

[76] The deduced variables are the variables that can be obtained from the key variables.

Table 64. Equations and target variables of mathematical system of H model.

	$\dot{m}_{BOG}$	Algebraic	Boil-off Gas (BOG) equation (Equation 153 and Equation 154)
	$\dot{m}_{IN}^{L}$	Algebraic	Inlet Liquid Flow (ILF) equation (Equation 155 and Equation 156)
Dependent	V^V	Algebraic	Volume conservation equation (Equation 654)
	P^L	Algebraic	Hydrostatic pressure equation (Equation 880)
	P^I	Algebraic	Pressure equality equation
	T^I	Algebraic	Saturation pressure equation (Equation 738)

P-e equation, V^L-e equations, T^L-e equation and T^V-e equation respectively compute the time-derivates of pressure, liquid volume, liquid temperature and vapour temperature. BOG equation and ILF equation respectively calculate the boil-off gas and the inlet liquid flow rate. Equation 149, Equation 151, Equation 153 and Equation 155 are used in the storage mode 4. Equation 150, Equation 152, and Equation 156 are applied on storage mode 1.b. Equation 133 and Equation 134 are used in both storage modes. P-e equation, V^L-e equations, T^L-e equation and T^V-e equation, BOG equation and ILF equation are obtained from the conservation laws of energy and mass with a mathematical procedure that is reported in Section 2. The volume conservation equation, hydrostatic pressure equation and pressure equality equation and the saturation pressure equation are used in storage mode 1.b and 4. The ullage volume is obtained with the geometrical formulas of Appendix B. The liquid pressure is computed with the hydrostatic pressure equation (Equation 880), using an iterative procedure. This iterative procedure is reported in Section 4 of Appendix L. Pressure equality equation states that the pressure at the interface is equal to the pressure of the ullage. The saturation pressure equation is obtained from the thermodynamic model, as described in Appendix G.

1.5. System of ordinary differential equations

As indicated in Table 64, only the time-derivates of liquid and vapour temperatures, the pressure and the liquid volume can be computed. So, some state variables such as the liquid and vapour temperatures, the pressure and the liquid level, cannot be directly deduced from the mathematical system of the homogeneous model (H model). These variables can be determined by solving the Ordinary Differential Equations (ODE) system. This system is composed by the differential equations of Table 10 for steady state (mode 1.b) and self-pressurisation (mode 4), respectively, as reported in Table 65.

Table 65. ODE systems for H model.

Storage modes	4	1.b
Equations	Equation 149	Equation 150
	Equation 151	Equation 152
	Equation 133	Equation 133
	Equation 134	Equation 134

As it is described in Table 65, the ODE system is composed from four equations and four variables. Hence, the number of variables and equation of the ODE system is increased with respect to the one of the equilibrium model (EQ model) (see Table 52). The ODE system of the H model is explicit because each target variable can be explicitly computed. The ODE system is integrated and solved with the method of Runge-Kutta-Fehlberg with Cash-Karp parameters (RKF-CKp) [131], as done in the EQ model (see Section 5 of Chapter 3).

2. Procedure to determine the pressure-evolution, the liquid volume-evolution, the liquid and vapour temperature-evolution, the boil-off and the inlet flow rate equations

The mathematical system of the homogeneous model (H model) is composed by several equations (see Table 64). Among them, the pressure-evolution (P-e), the liquid volume (V^L-e), liquid temperature (T^L-e), vapour temperature (T^V-e), the boil-off gas (BOG) equation and the inlet liquid flow (ILF) equations respectively can be deduced from the conservations laws of energy and of mass, applied to liquid and vapour. The deduction of these equations requires a mathematical procedure where the conservation laws are modified to explicitly obtain the indipendent variables of the H model (see Table 64). This procedure is described in Figure 60.

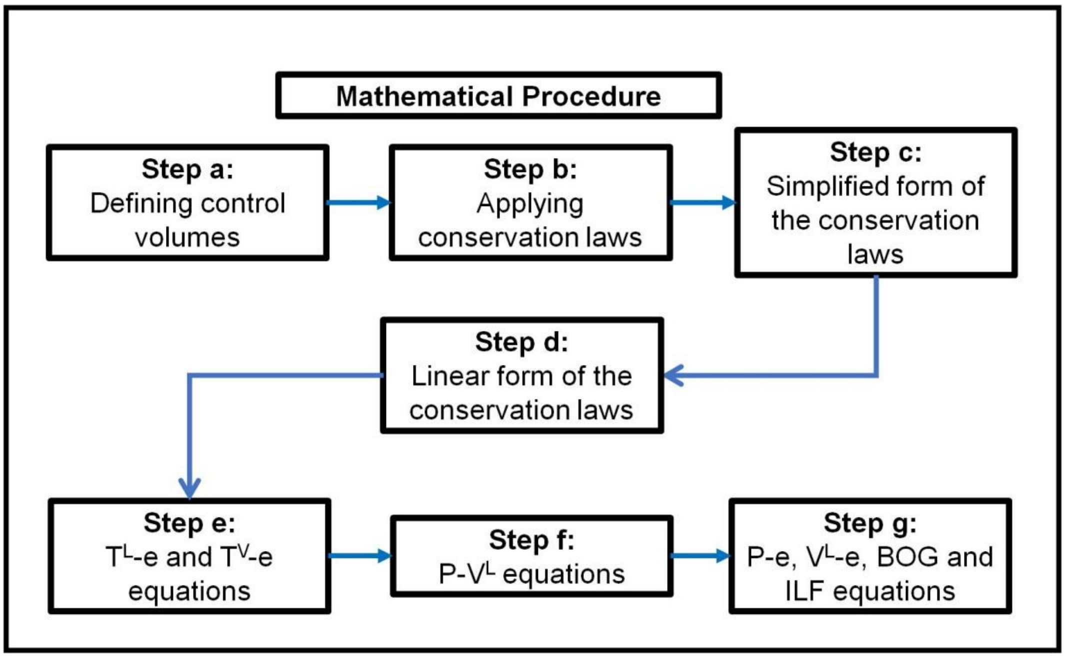

Figure 60. Mathematical procedure to deduce P-e, V^L-e, T^L-e and T^V-e, ILF and BOG equations.

As it is illustrated in Figure 60, this procedure is based on the following steps:

a) Defining the control volumes;
b) Applying the conservation laws;
c) Simplified form of the conservation laws;
d) Linear form of the conservation laws;
e) Deducing the T^L-e and T^V-e equations;
f) Obtaining the pressure-liquid volume (P-V^L) equations;
g) Deducing the P-e, the V^L-e, the BOG and the ILF equations

Section 2.1 describes the control volume of the H model. Section 2.2 explains the conservation laws of energy and of mass. Section 2.3 presents the simplified form of the conservation laws. Section 2.4 describes the linear form of these conservation laws. Section 2.5 describes the T^L-e and T^V-e equations. Section 2.6 explains the P-V^L equations. Section 2.7 presents the P-e, the V^L-e, the BOG and the ILF equations.

2.1. Control volumes

The definition of the control volume is the first step of the mathematical procedure (step a) of Section 2 of Chapter 4), as it is illustrated in Figure 60. To determine the conservation laws, it is crucial to define the control volumes where the first principle of the thermodynamics and the mass-conservation law are applied. The control volumes required for the homogeneous model are presented in Figure 61. In Figure 61, the blue and the orange colours respectively indicate the liquid and the vapour. The green and black arrows are respectively the net mass flow and the inlet and outlet mass flows. The red arrows refer to the enthalpy flows. The white arrows with red border are the heat leakage rates. The yellow dashed line is the interface.

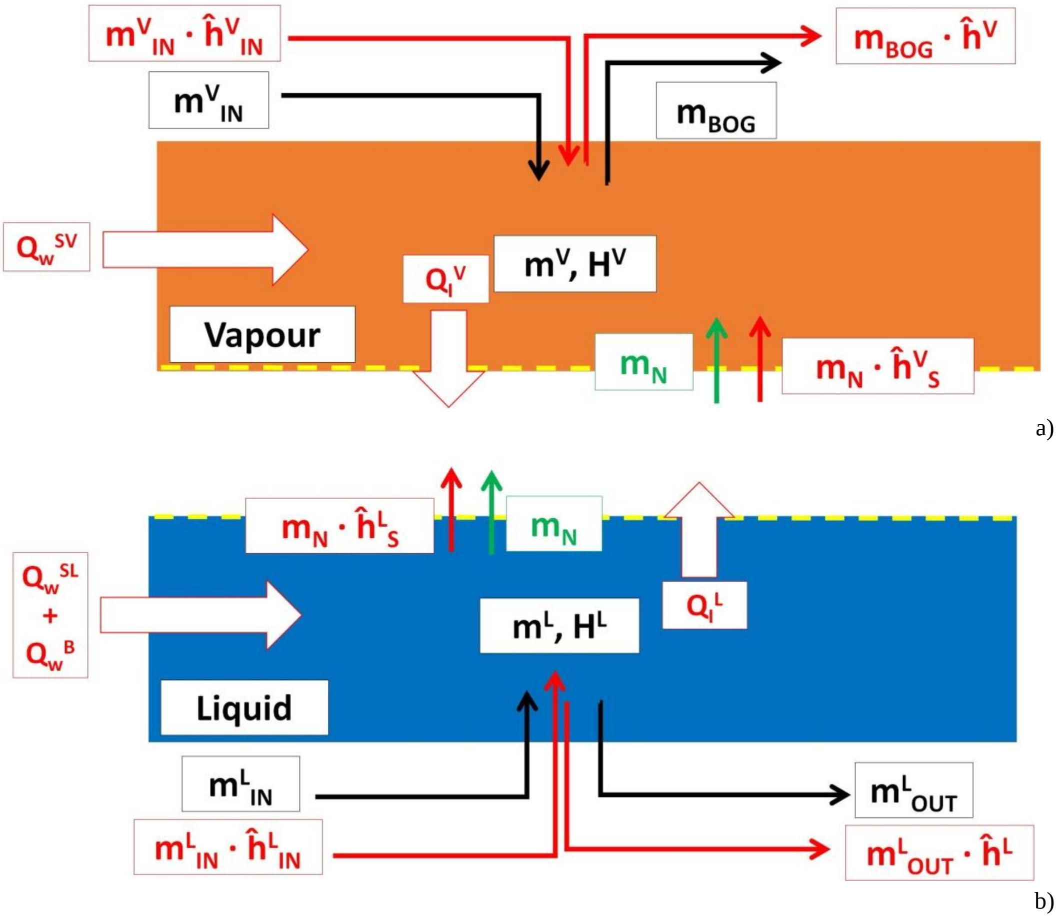

Figure 61. Control volumes of the homogeneous model: a) vapour energy and mass; b) liquid energy and mass.

As described in Figure 61, the homogeneous model can be decomposed into two control volumes: *liquid energy-mass* and *vapour energy-mass*. These control volumes consider only the liquid and the vapour, respectively, without including the interface and the walls of the storage container. In these control volumes, the inlet, outlet and the net mass flows are considered. The heat entering from the walls and the heat exchanged at the interface are included in these control volumes, along with the enthalpy content of the mass flows that enter and exits the liquid and the vapour, respectively.

2.2. Conservation laws

The second step of the mathematical procedure (step b) of Section 2 of Chapter 4) is the application of the conservation laws to the control volumes, as it is illustrated in Figure 60. The conservation laws of the homogeneous model can be determined, after applying the fundamental formulas (see Table 192) to the control volumes. These balance equations are illustrated in Table 66.

Table 66. Conservation laws of the homogeneous model.

Conservation law		Equation
Liquid energy balance	Equation 96	$\frac{\partial \tilde{H}^L}{\partial t} = \dot{Q}_w^B + \dot{Q}_w^{SL} - \dot{Q}_I^L + \dot{m}_{IN}^L \cdot \tilde{h}_{IN}^L - \dot{m}_N \cdot \tilde{h}_S^L - \dot{m}_{OUT}^L \cdot \tilde{h}^L$
Liquid mass balance	Equation 97	$\frac{\partial m^L}{\partial t} = \dot{m}_{IN}^L - \dot{m}_N - \dot{m}_{OUT}^L$
Vapour energy balance	Equation 98	$\frac{\partial \tilde{H}^V}{\partial t} = \dot{Q}_w^{SV} - \dot{Q}_I^V + \dot{m}_{IN}^V \cdot \tilde{h}_{IN}^V + \dot{m}_N \cdot \tilde{h}_S^V - \dot{m}_{BOG} \cdot \tilde{h}^V$
Vapour mass balance	Equation 99	$\frac{\partial m^V}{\partial t} = \dot{m}_{IN}^V + \dot{m}_N - \dot{m}_{BOG}$
Volume balance	Equation 100	$\frac{\partial V^V}{\partial t} + \frac{\partial V^L}{\partial t} = 0$

$\tilde{h}_S^L$ and $\tilde{h}_S^V$ are the saturation specific enthalpies of liquid and of vapour.

2.3. Simplified form of the conservation laws

The third step of the mathematical procedure (step c) of Section 2 of Chapter 4) is the simplification of the system of conservation laws of Table 66, as it is illustrated in Figure 60. The conservation equations of Table 66 cannot directly compute the indipendent variables (see Table 64). So, these balance equations are modified to directly compute these variables. This modification is done (i) by making explicit the indipendent variables from the enthalpy and the mass, and (ii) by removing the time-derivate of the ullage volume from the vapour mass balance (Equation 99). The details of these mathematical steps are reported in Section 2 of Appendix M. The modified form of the conservation laws of Table 66 is called the *simplified form of conservations laws*, because the volume balance (Equation 100) is removed from the system of conservation equations. The simplified form of the conservation laws are reported in Table 67.

Table 67. Simplified conservation laws of the homogeneous model.

Name	Equation	Formula
Simplified form of liquid energy balance equation	Equation 101	$m^L \cdot \left[C_P^L \cdot \frac{\partial T^L}{\partial t} + \left. \frac{\partial \tilde{h}^L}{\partial P^V} \right\vert_{T^L} \cdot \frac{\partial P^V}{\partial t} \right] =$ $\dot{Q}_w^B + \dot{Q}_w^{SL} - \dot{Q}_I^L + \dot{m}_{IN}^L \cdot \left(\tilde{h}_{IN}^L - \tilde{h}^L \right) - \dot{m}_N \cdot \left(\tilde{h}_S^L - \tilde{h}^L \right)$
Simplified form of liquid mass balance equation	Equation 102	$\rho^L \cdot \frac{\partial V^L}{\partial t} + V^L \cdot \left[\left. \frac{\partial \rho^L}{\partial T^L} \right\vert_{P^V} \cdot \frac{\partial T^L}{\partial t} + \left. \frac{\partial \rho^L}{\partial P^V} \right\vert_{T} \cdot \frac{\partial P^V}{\partial t} \right] = \dot{m}_{IN}^L - \dot{m}_N - \dot{m}_{OUT}^L$
Simplified form of vapour energy balance equation	Equation 103	$m^V \cdot \left[C_P^V \cdot \frac{\partial T^V}{\partial t} + \left. \frac{\partial \tilde{h}^V}{\partial P^V} \right\vert_{T} \cdot \frac{\partial P^V}{\partial t} \right] =$ $\dot{Q}_w^{SV} - \dot{Q}_I^V + \dot{m}_{IN}^V \cdot \left(\tilde{h}_{IN}^V - \tilde{h}^V \right) + \dot{m}_N \cdot \left(\tilde{h}_S^V - \tilde{h}^V \right)$
Simplified form of vapour mass balance equation	Equation 104	$-\rho^V \cdot \frac{\partial V^L}{\partial t} + V^V \cdot \left[\left. \frac{\partial \rho^V}{\partial T^V} \right\vert_{P^V} \cdot \frac{\partial T^V}{\partial t} + \left. \frac{\partial \rho^V}{\partial P^V} \right\vert_{T^V} \cdot \frac{\partial P^V}{\partial t} \right] = \dot{m}_{IN}^V + \dot{m}_N - \dot{m}_{BOG}$

In comparison with the equations of Table 66, the simplified conservation of Table 67 explicitly depend on the target variables $\frac{\partial T^L}{\partial t}$, $\frac{\partial T^V}{\partial t}$, $\frac{\partial V^L}{\partial t}$ and $\frac{\partial P^V}{\partial t}$. The number of the simplified balance equations is lower than the number equations of Table 66.

2.4. Linear form of the conservation laws

Obtaining the linear form of the conservation laws is the fourth step of the mathematical procedure (step d) of Section 2 of Chapter 4). To reduce the computation time, an explicit Ordinary Differential Equation (ODE) system is required. The explicit ODE system can be obtained from the simplified form of the conservations equations (see Table 67). To do that, the equations of Table 67 are reorganized as a linear combination of the indipendent variables and coefficients. The linear forms of the conservation laws are reported in Table 68.

Table 68. Linear forms of the conservation laws.

Conservation law	Equation	Formula
Linear form of liquid energy balance	Equation 105	$A^{TL} \cdot \frac{\partial P^V}{\partial t} + B^{TL} \cdot \frac{\partial T^L}{\partial t} + C^{TL} \cdot \frac{\partial V^L}{\partial t} + D^{TL} \cdot \dot{m}_{IN}^L + E^{TL} \cdot \dot{m}_{OUT}^L + F^{TL} = 0$
Linear form of liquid mass balance	Equation 106	$A^{HL} \cdot \frac{\partial P^V}{\partial t} + B^{HL} \cdot \frac{\partial T^L}{\partial t} + C^{HL} \cdot \frac{\partial V^L}{\partial t} + D^{HL} \cdot \dot{m}_{IN}^L + E^{HL} \cdot \dot{m}_{OUT}^L + F^{HL} = 0$
Linear form of vapour energy balance	Equation 107	$A^{TV} \cdot \frac{\partial P^V}{\partial t} + B^{TV} \cdot \frac{\partial T^V}{\partial t} + C^{TV} \cdot \frac{\partial V^L}{\partial t} + D^{TV} \cdot \dot{m}_{IN}^V + E^{TV} \cdot \dot{m}_{BOG} + F^{TV} = 0$
Linear form of vapour mass balance	Equation 108	$A^{P} \cdot \frac{\partial P^V}{\partial t} + B^{P} \cdot \frac{\partial T^V}{\partial t} + C^{P} \cdot \frac{\partial V^L}{\partial t} + D^{P} \cdot \dot{m}_{IN}^V + E^{P} \cdot \dot{m}_{BOG} + F^{P} = 0$

The coefficients A, B, C, D, E and F are reported in Table 69. The exponents "TL", "HL", "TV" and "P" respectively indicate the liquid energy balance (Equation 101), the liquid mass balance (Equation 102), the vapour temperature balance (Equation 103) and the vapour mass balance (Equation 104) equations.

Table 69. Coefficients of the linear form of the conservation laws.

Coefficients	Equation	Formula
Liquid energy conservation laws (Equation 105)		
A^{TL}	Equation 109	$A^{TL} = m^L \cdot \left. \frac{\partial \tilde{h}^L(T^L, P^L)}{\partial P^V} \right\|_{T^L}$
B^{TL}	Equation 110	$B^{TL} = m^L \cdot C_P^L(T^L, P^L)$
C^{TL}	Equation 111	$C^{TL} = 0$
D^{TL}	Equation 112	$D^{TL} = -\left[\tilde{h}_{IN}^L(T_{IN}^L, P_{IN}^L) - \tilde{h}^L(T^L, P^L)\right]$
E^{TL}	Equation 113	$E^{TL} = 0$
F^{TL}	Equation 114	$F^{TL} = -\left\{\dot{Q}_w^B + \dot{Q}_w^{SL} - \dot{Q}_I^L - \dot{m}_N \cdot \left[\tilde{h}_S^L(P^V) - \tilde{h}^L(T^L, P^L)\right]\right\}$
Liquid mass conservation laws (Equation 106)		
A^{HL}	Equation 115	$A^{HL} = V^L \cdot \left. \frac{\partial \rho^L(T^L, P^L)}{\partial P^V} \right\|_{T^L}$
B^{HL}	Equation 116	$B^{HL} = V^L \cdot \left. \frac{\partial \rho^L(T^L, P^L)}{\partial T^L} \right\|_{P^V}$
C^{HL}	Equation 117	$C^{HL} = \rho^L(T^L, P^L)$
D^{HL}	Equation 118	$D^{HL} = -1$
E^{HL}	Equation 119	$E^{HL} = 1$
F^{HL}	Equation 120	$F^{HL} = -[-\dot{m}_N]$
Vapour energy conservation laws (Equation 107)		
A^{TL}	Equation 121	$A^{TV} = m^V \cdot \left. \frac{\partial \tilde{h}^V(T^V, P^V)}{\partial P^V} \right\|_{T^V}$

Table 69. Coefficients of the linear form of the conservation laws.

B^{TV}	Equation 122	$B^{TV} = m^V \cdot C_P^V(T^V, P^V)$
C^{TV}	Equation 123	$C^{TV} = 0$
D^{TV}	Equation 124	$D^{TV} = -\left[\tilde{h}_{IN}^V(T_{IN}^V, P_{IN}^V) - \tilde{h}^V(T^V, P^V)\right]$
E^{TV}	Equation 125	$E^{TV} = 0$
F^{TV}	Equation 126	$F^{TV} = -\left\{\dot{Q}_W^{SV} - \dot{Q}_I^V + \dot{m}_N \cdot \left[\tilde{h}_S^V(P^V) - \tilde{h}^V(T^V, P^V)\right]\right\}$
	Vapour mass conservation laws (Equation 108)	
A^P	Equation 127	$A^P = V^V \cdot \left.\frac{\partial \rho^V(T^V, P^V)}{\partial P^V}\right\vert_{T^V}$
B^P	Equation 128	$B^P = V^L \cdot \left.\frac{\partial \rho^V(T^V, P^V)}{\partial T^V}\right\vert_{P^V}$
C^P	Equation 129	$C^P = -\rho^V(T^V, P^V)$
D^P	Equation 130	$D^P = -1$
E^P	Equation 131	$E^P = 1$
F^P	Equation 132	$F^P = -[\dot{m}_N]$

The equations of Table 68 are obtained by substituting each term of the simplified form of conservation laws with the coefficients of Table 69, as described in Section 2.6 of Chapter 3.

2.5. Liquid temperature-evolution and vapour temperature-equations

The fifth step of the mathematical procedure (step e) of Section 2 of Chapter 4) is the deduction of the liquid temperature-evolution (T^L-e) and vapour temperature-evolution (T^V-e) equations from the linear form of the conservation laws (see Table 68). These equations explicitly compute the indipendent variables $\frac{\partial T^L}{\partial t}$ and $\frac{\partial T^V}{\partial t}$ and they are reported in Table 70.

Table 70. T^L-e and T^V-e equations.

Name	Equation	Formula
T^L-e equation	Equation 133	$\frac{\partial T^L}{\partial t} = -\frac{1}{B^{TL}} \cdot \left[A^{TL} \cdot \frac{\partial P^V}{\partial t} + C^{TL} \cdot \frac{\partial V^L}{\partial t} + D^{TL} \cdot \dot{m}_{IN}^L + E^{TL} \cdot \dot{m}_{OUT}^L + F^{TL}\right]$
T^V-e equation	Equation 134	$\frac{\partial T^V}{\partial t} = -\frac{1}{B^{TV}} \cdot \left[A^{TV} \cdot \frac{\partial P^V}{\partial t} + C^{TV} \cdot \frac{\partial V^L}{\partial t} + D^{TV} \cdot \dot{m}_{IN}^V + E^{TL} \cdot \dot{m}_{BOG} + F^{TV}\right]$

The mathematical steps to obtain the T^L-e and the T^V-e equations are described in Section 3 of Appendix M.

2.6. Pressure-liquid volume equations

The sixth step of the mathematical procedure (step f) of Section 2 of Chapter 4) is the deduction of the pressure-liquid volume (P-V^L) equations, from the linear form of the conservation laws (see Table 68). As said in Section 2.4 of Chapter 4, the explicit Ordinary Differential Equations (ODEs) system can reduce to computational time. Indipendent variables $\frac{\partial T^L}{\partial t}$ and $\frac{\partial T^V}{\partial t}$ are explicitly computed with liquid temperature-evolution (T^L-e) and vapour temperature-evolution (T^V-e) equations (Equation 133 and Equation 134). The indipendent variables $\frac{\partial P^V}{\partial t}$, $\frac{\partial V^L}{\partial t}$, $\dot{m}_{IN}^L$ and $\dot{m}_{BOG}$ cannot, however, be explicitly computed at this point of the mathematical procedure. To do that, the indipendent variables $\frac{\partial T^L}{\partial t}$ and $\frac{\partial T^V}{\partial t}$ should be removed from the linear form of the liquid mass and vapour mass conservation laws, respectively (Equation 106 and Equation 108). The details of the mathematical steps to do that are described in Section 4 of Appendix M. The equations obtained are called the P-V^L equations because only the key differential variables $\frac{\partial P^V}{\partial t}$ and $\frac{\partial V^L}{\partial t}$ are present. These equations are reported in Table 71.

Table 71. P-V^L equations.

Name	Equation	Formula
Vapour P-V^L equations	Equation 135	$A'^P \cdot \frac{\partial P^V}{\partial t} + C'^P \cdot \frac{\partial V^L}{\partial t} + D'^P \cdot \dot{m}_{IN}^V + E'^P \cdot \dot{m}_{BOG} + F'^P = 0$
Liquid P-V^L equations	Equation 136	$A'^{HL} \cdot \frac{\partial P^V}{\partial t} + C'^{HL} \cdot \frac{\partial V^L}{\partial t} + D'^{HL} \cdot \dot{m}_{IN}^L + E'^{HL} \cdot \dot{m}_{OUT}^L + F'^{HL} = 0$

The coefficients A', C', D', E' and F' are reported in Table 72.

Table 72. Coefficients of pressure-volume equations.

Coefficients	Equations	Formulas
Vapour liquid-volume equations (Equation 135)		
A'^P	Equation 137	$A'^P = A^P - B^P \cdot \frac{A^{TV}}{B^{TV}}$
B'^P	Equation 138	$B'^P = 0$
C'^P	Equation 139	$C'^P = C^P - B^P \cdot \frac{C^{TV}}{B^{TV}}$
D'^P	Equation 140	$D'^P = D^P - B^P \cdot \frac{D^{TV}}{B^{TV}}$
E'^P	Equation 141	$E'^P = E^P - B^P \cdot \frac{E^{TV}}{B^{TV}}$
F'^P	Equation 142	$F'^P = F^P - B^P \cdot \frac{F^{TV}}{B^{TV}}$
Liquid liquid-volume equations (Equation 136)		
A^{HL}	Equation 143	$A'^{HL} = A^{HL} - B^{HL} \cdot \frac{A^{TL}}{B^{TL}}$
B^{HL}	Equation 144	$B'^{HL} = 0$
C^{HL}	Equation 145	$C'^{HL} = C^{HL} - B^{HL} \cdot \frac{C^{HL}}{B^{HL}}$
D^{HL}	Equation 146	$D'^{HL} = D^{HL} - B^{HL} \cdot \frac{D^{HL}}{B^{HL}}$
E^{HL}	Equation 147	$E'^{HL} = E^{HL} - B^{HL} \cdot \frac{E^{HL}}{B^{HL}}$
F^{HL}	Equation 148	$F'^{HL} = F^{HL} - B^{HL} \cdot \frac{F^{HL}}{B^{HL}}$

Equation 135 and Equation 136 are respectively called the vapour pressure-liquid volume and the liquid pressure-liquid volume equations because they are respectively obtained from the linear form of the vapour mass and liquid mass conservation laws, respectively (Equation 108 and Equation 106).

.

2.7. Pressure evolution, liquid volume evolution, inlet liquid flow and boil-off gas equations

The last step of the mathematical procedure (step g) of Section 2 of Chapter 4) is the deduction of pressure-evolution (P-e), liquid volume-evolution (V^L-e), inlet liquid flow (ILF) and boil-off gas (BOG) equations from the pressure-liquid volume (P-V^L) equations (see Table 71). The procedure to obtain P-e, V^L-e, ILF and BOG equations is described in Section 5 of Appendix M. P-e, V^L-e, ILF and BOG equations explicitly compute the indipendent variables $\frac{\partial P^V}{\partial t}$, $\frac{\partial V^L}{\partial t}$, $\dot{m}_{IN}^L$ and $\dot{m}_{BOG}$. Hence, the explicit form of the Ordinary Differential Equation (ODEs) system can be obtained, reducing the computational time. P-e, V^L-e, ILF and BOG equations are reported in Table 73 for the two storage modes.

Table 73. P-e, V^L-e, ILF and BOG equations.

	Storage mode 4 (self-pressurisation)		***Storage mode 1.b (steady state)***	
Name	**Equation**	**Formula**	**Equation**	**Formula**
P-e equation	Equation 149	$\frac{\partial P^V}{\partial t} = -\frac{Z^P - Z^{HL} \cdot \frac{C'^P}{C'^{HL}}}{A'^P - A'^{HL} \cdot \frac{C'^P}{C'^{HL}}}$	Equation 150	$\frac{\partial P^V}{\partial t} = 0$
VL-e equation	Equation 151	$\frac{\partial V^L}{\partial t} = -\frac{1}{C'^{HL}} \cdot \left[Z^{HL} + A'^{HL} \cdot \frac{\partial P^V}{\partial t}\right]$	Equation 152	$\frac{\partial V^L}{\partial t} = 0$
BOG equation	Equation 153	$\dot{m}_{BOG} = 0$	Equation 154	$\dot{m}_{BOG} = -\frac{Z^P}{E'^P}$
ILF equation	Equation 155	$\dot{m}_{IN}^L = 0$	Equation 156	$\dot{m}_{IN}^L = -\frac{Z^{HL}}{D'^{HL}}$

The coefficients A'^P, A'^{HL}, C'^P, C'^{HL}, E'^P and D'^{HL} are reported in Table 72. The coefficients Z^P and Z^{HL} are defined as reported in Table 74.

Table 74. Coefficients $\boldsymbol{Z^P}$ and $\boldsymbol{Z^{HL}}$.

Storage mode	Coefficient	Equation	Formula
1.b	Z^P	Equation 157	$Z^P = A'^P \cdot \frac{\partial P^V}{\partial t} + C'^P \cdot \frac{\partial V^L}{\partial t} + D'^P \cdot \dot{m}_{IN}^V + F'^P$
	Z^{HL}	Equation 158	$Z^{HL} = A'^{HL} \cdot \frac{\partial P^V}{\partial t} + C'^{HL} \cdot \frac{\partial V^L}{\partial t} + E'^{HL} \cdot \dot{m}_{OUT}^L + F'^{HL}$
4	Z^P	Equation 159	$Z^P = D'^P \cdot \dot{m}_{IN}^V + E'^P \cdot \dot{m}_{BOG} + F'^P$
	Z^{HL}	Equation 160	$Z^{HL} = D'^{HL} \cdot \dot{m}_{IN}^L + E'^{HL} \cdot \dot{m}_{OUT}^L + F'^{HL}$

The coefficient F'^P and F'^{HL} are reported in Table 72.

As it is indicated in Table 10, the BOG and the liquid inlet flow rates are equal to zero because the storage container is closed during the self-pressurisaiton (storage mode 4). Hence, the pressure-liquid volume equations (see Table 71) can be used to determine the evolution of pressure and liquid volume during the self-pressurisation. In storage mode 1.b (steady state), the pressure and the liquid volume remain constant. So, time derivates $\frac{\partial P^V}{\partial t}$ and $\frac{\partial V^L}{\partial t}$ are equal to zero, as it is indicated in Table 10. So, the pressure-liquid volume equations (see Table 71) can be used to compute the inlet liquid flow rate and the BOG flow rate. The mathematical steps of the equations of Table 73 are described in Section 5 of Appendix M.

3. Storage boundary layer model: homogenous model

The Storage Boundary Layer (SBL) model composes the Block 6 of the structure of the Homogeneous model (H model), as explained in Figure 59. As indicated by Figure 59, the SBL model is connected with the Storage Heat Transfer (SHT) model and vice versa. Hence, the SBL model is discussed before all the other sub-models of the H model because it is directly required in the SHT model and indirectly in the Boil-off Rate (BOR) model.

Cryogenic liquids can be placed in storage containers of different geometries, depending on the use of these fluids. The heat leakage rate is affected by the geometry, by the liquid and vapour fluid-dynamics, and by the thermal stratification. The liquid and vapour fluid-dynamics and the thermal stratification change as the heat inputs vary, creating interdependence between heat transfer and fluid-dynamics, as explained in Section 4 of Chapter 1. As obtained from the analysis of the scientific literature (see Section 5 of Chapter 1), the proposed fluid-dynamic models [2], [101], [122] are de-coupled by the heat transfer model because the heat inputs are often defined as input parameters of the model. So, they are not computed form the difference in temperature between the environment and the internal fluid. These fluid-dynamic models [1], [2] are often developed for vertical storage containers and they cannot consider the effect of the bulk temperature gradient, thus the effect of the thermal stratification, because they are based on the theory of fluid-dynamics in homogeneous medium[77]. So, the modelling of the fluid-dynamics of storage container should be done with the following criteria:

a) To be easily adapted to the different geometries;
b) To consider the interdependence between heat transfer and fluid-dynamics;
c) To be suitable for homogeneous medium, as well as for stratified medium[78];

As consequence, the *storage boundary layer (SBL) model* is developed for fulfilling these criteria, in particular for coupling this model with the heat transfer model. Due to the different geometries of the storage containers, this model is divided into the *exact boundary layer (EBL) approach* and the *integrated boundary layer (IBL) approach*. To be easily coupled with the heat transfer model, the analytical and the numerical methods can use the heat fluxes and the difference in temperatures between the wall and the bulk as input parameters. Hence, two modes are developed and they are respectively called *heat flux mode* (HF mode) and *difference in temperatures mode* (ΔT mode).

Section 3.1 describes the hypotheses of the SBL model. Section 3.3 and 3.4 describe the EBL and IBL approaches, respectively.

3.1.Hypotheses

The Storage Boundary Layer (SBL) model is based on fluid-dynamics works [98], [99], [132], [133] of vertical surface with homogeneous wall temperature or homogeneous heat fluxes, immerged in homogeneous [98], [99] and stratified [132], [133] media. These works uses the Prandtl's theory of the boundary layer and the von Karman integrals method to simplify the physical description of the boundary layer. As consequence, the SBL model is developed with these approaches and with the following assumptions:

a) The temperature and velocity can vary only in the boundary layer[79];

---

[77] Homogeneous medium is an environment that is isothermal and homogeneous.

[78] Stratified medium in an environment where there is a bulk temperature gradient.

[79] Boundary layer is a small region of the fluid, near the surface, that determines the transfer of momentum, energy and mass between the surface and the fluid.

b) The thickness of the boundary layer is lower than the characteristic dimension[80] of the surface. Hence, the curvature of walls of the storage container can be ignored[134];
c) The phenomenon of natural convection is described in rectangular coordinates x and y. The x axis is parallel to the surface and y axis is perpendicular to the surface;
d) The fluid is incompressible[81];
e) The Boussinesq approximation[82] is valid ;
f) The Newton's law of shear tensor[83] computes the viscous forces in the boundary layer;
g) The boundary layer is at steady state;
h) The kinetic and the dissipated energy, and the work can be neglected in the Navier-Stokes equations[84] ;
i) The fluid layer in direct contact with the solid surface of the wall does not slip [135];
j) The thermal and the momentum boundary layers are equal.

The hypotheses i) and j) are respectively called unique boundary layer and no-slip condition. The unique boundary layer assumption simplifies the analytical and numerical solutions of the conservation laws of the boundary layer. The hypothesis of no-slip condition reduces the complexity of these conservation laws because the displacement of the boundary layer is neglected.

3.2. Algorithm of the Storage Boundary Layer model

The Storage Boundary Layer (SBL) model computes the boundary layer variables of Table 62, using the Exact Boundary Layer (EBL) and the Integral Boundary Layer (IBL) approaches. The input and the output variables of the algorithm of the SBL model are reported in Table 75.

Table 75. Input and output of the SBL model.

Variable	Description
Input	Type of surface (side wall or flat ends), state variables (see Table 62) and thermo-physical properties (see Table 31), heat flows at the surface or the surface wall temperature, and geometry
Output	boundary layer variables

The structure of the algorithm of the SBL model is reported in Figure 62.

---

[80] The characteristic dimension is dimension that defines the scale of the fluid-dynamics.
[81] A fluid is defined incompressible if the density does not change with the pressure, at constant temperature.
[82] The Boussinesq approximation states that the density variation only affects the buoyancy forces. This approximation is usually applied in fluid-dynamics of incompressible fluids.
[83] The Newton's law states the stresses are proportional to the rate of change of the fluid's velocity vector.
[84] Navier-Stokes equations are fundamental conservation laws of energy, mass and momentum of fluid motion.

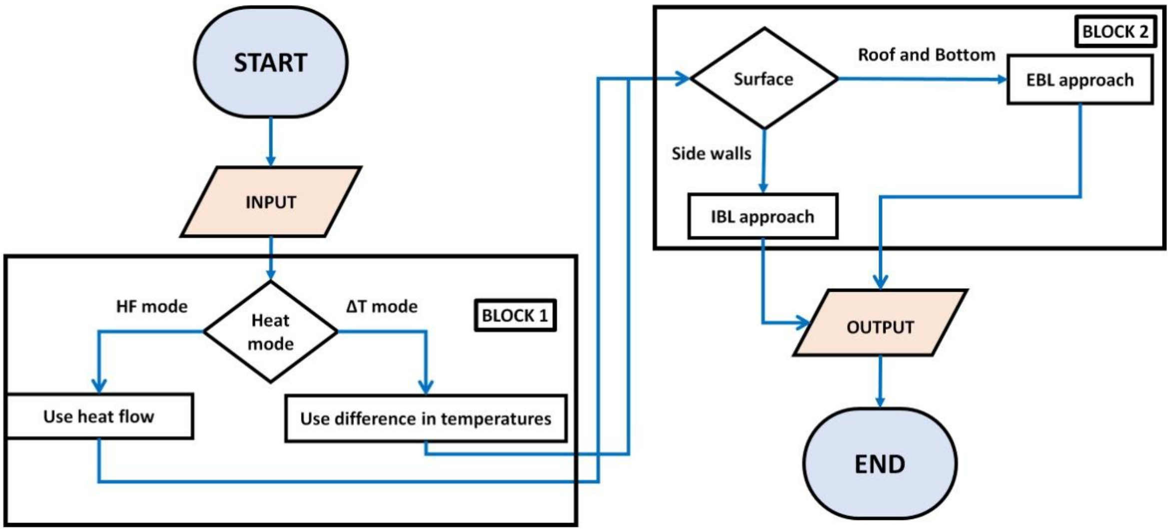

Figure 62. Algorithm of SBL model.

As it is illustrated by Figure 62, the algorithm is mainly composed by these steps:

a) BLOCK 1: selection of the heat mode between the heat flux mode (HF mode) and difference in temperatures mode (ΔT mode). As said in Section 3, the EBL and the IBL approaches can use the heat fluxes and the difference in temperatures between the wall and the bulk as input parameters. If this difference in temperatures is given as input parameter, the ΔT mode is chosen. When the heat flow is used as input, the HF mode is applied;
b) BLOCK 2: selection of the approach. The approach is selected as function of the type of surfaces. If the SBL model is applied to flat ends such as roof and bottom, the EBL approach is used. When the SBL model describes the boundary layer of side walls, the IBL approach is selected.

The algortimh of tyhe SBL is not iterative, but iterative procedures are present for computing the bottom-to-liquid, the wet side wall-to-liquid and the dry side wall-to-vapour heat flows.

3.3.Exact boundary layer approach

The geometry of the storage containers can be various: sphere, ellipsoid, vertical or horizontal cylinder with rounded ends or with flat ends[85]. In particular for vertical cylinder with flat ends, the geometry of these storage containers creates a discontinuity of the fluid-motions at the corner between the side wall and the flat ends, as it is described in Figure 63. In Figure 63, the dark rectangles are the side and the flat ends. The blue and green arrows respectively indicate the fluid motions at the side wall and the flat ends.

---

[85] Flat ends are usually the bottom and the roof of vertical cylinder.

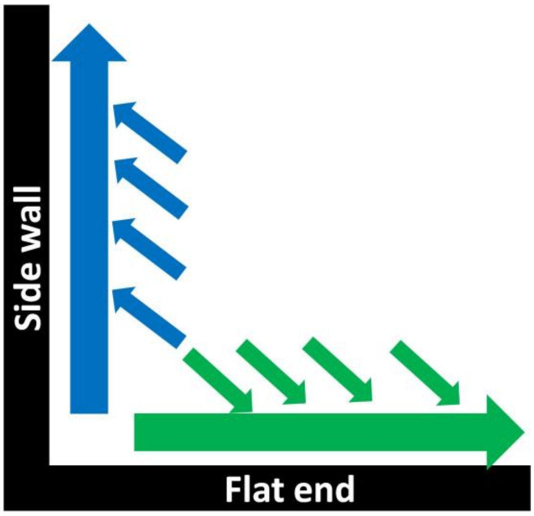

Figure 63. Hypothesis of no interaction.

Hence, an approach to describe the boundary layer of the flat ends (bottom and roof) is required and it is called *exact boundary layer (EBL) approach*. Due to the discontinuity of the fluid-motion at the corner, it can be assumed that fluid-motion of the flat ends (roof or bottom) remain separated from the one of the side wall. This assumption of separation of fluid-motion is called *hypothesis of no interaction* and it is the basement of the EBL approach. As consequence, the flat end can be seen as a vertical surface with a uniform wall temperature or wall heat flux, and the theory [98], [99] of the free-convection over vertical surface can be applied. In this theory, the boundary layer variables (see Table 62) such as temperature (T_{BL}), mass flow ($\dot{m}_{BL}$), average speed ($\bar{u}$) and thermal thickness (δ_T) can be deduced from the momentum thickness (δ_M) and from the velocity the outside boundary layer of comparable forced-convection flow[70] (U). δ_M and U can be computed with the equations of Table 76 for the difference in temperature and heat fluxes modes, and at different fluid-dynamics regime.

Table 76. Equations to compute $\boldsymbol{\delta_M}$ and $\boldsymbol{U}$ in the EBL approach of SBL model.

Variable	Equation	Formula	Regime
		Difference in temperatures mode	
U	Equation 161 [98]	$U(x) = \frac{5.17 \cdot \nu}{\left(Pr + \frac{20}{21}\right)^{0.5}} \cdot ({Gr^S}_{\Delta T})^{0.5} \cdot x^{0.5}$	Laminar
	Equation 162	$U(x) = U^L \cdot \left[\frac{x}{x^L}\right]^{\frac{\ln\left(\frac{U^T}{U^L}\right)}{\ln\left(\frac{x^T}{x^L}\right)}}$	Transition
	Equation 163 [99]	$U(x) = 1.185 \cdot \nu \cdot \frac{({Gr^S}_{\Delta T})^{0.5}}{\left[1 + 0.494 \cdot (Pr)^{\frac{2}{3}}\right]^{0.5}} \cdot x^{0.5}$	Turbulent
δ	Equation 164 [98]	$\delta(x) = \frac{3.93}{Pr^{0.5}} \cdot \left(Pr + \frac{20}{21}\right)^{0.25} \cdot ({Gr^S}_{\Delta T})^{-0.25} \cdot x^{0.25}$	Laminar
	Equation 165	$\delta(x) = \delta^L \cdot \left[\frac{x}{x^L}\right]^{\frac{\ln\left(\frac{\delta^T}{\delta^L}\right)}{\ln\left(\frac{x^T}{x^L}\right)}}$	Transition
	Equation 166 [99]	$\delta(x) = 0.565 \cdot x^{\frac{7}{10}} \cdot \frac{\left[1 + 0.494 \cdot (Pr)^{\frac{2}{3}}\right]^{0.1}}{\left[({Gr^S}_{\Delta T})^{0.1} \cdot (Pr)^{\frac{8}{15}}\right]^{0.5}}$	Turbulent
		Heat fluxes mode	
U	Equation 167	$U(x) = 6.5129 \cdot \frac{\nu}{(Pr)^{\frac{1}{5}}} \cdot \left(\frac{{Gr^S}_q}{Pr + 1}\right)^{\frac{2}{5}} \cdot x^{\frac{3}{5}}$	Laminar

Table 76. Equations to compute $\boldsymbol{\delta_M}$ and $\boldsymbol{U}$ in the EBL approach of SBL model.

	Equation 168	$U(x) = U^L \cdot \left[\frac{x}{x^L}\right]^{\frac{\ln\left(\frac{U^T}{U^L}\right)}{\ln\left(\frac{x^T}{x^L}\right)}}$	Transition
	Equation 169	$U(x) = 4.3063 \cdot v \cdot Gr_{s_q}^{\frac{5}{14}} \cdot Pr^{-\frac{67}{42}} \cdot \left[\left(1 + 0.509 \cdot Pr^{\frac{2}{3}}\right)\right]^{-\frac{5}{14}} \cdot x^{\frac{3}{7}}$	Turbulent
δ	Equation 170	$\delta(x) = 3.3935 \cdot \left(\frac{1}{Pr}\right)^{\frac{2}{5}} \cdot \left[\frac{Pr+1}{{Gr^S}_q}\right]^{\frac{1}{5}} \cdot x^{\frac{1}{5}}$	Laminar
	Equation 171	$\delta(x) = \delta^L \cdot \left[\frac{x}{x^L}\right]^{\frac{\ln\left(\frac{\delta^T}{\delta^L}\right)}{\ln\left(\frac{x^T}{x^L}\right)}}$	Transition
	Equation 172	$\delta(x) = 0.4547 \cdot \left[\frac{Pr^{-3}}{{Gr^S}_q} \cdot \left(1 + 0.509 \cdot Pr^{\frac{2}{3}}\right)\right]^{\frac{1}{14}} \cdot x^{\frac{5}{7}}$	Turbulent

Pr is the Prandtl's number, ${Gr^S}_{\Delta T}$ and ${Gr^S}_q$ are the pseudo-Grashof's number, respectively for the difference in temperatures and heat fluxes modes. These dimensionless numbers are reported in Section 1 of Appendix N. x is the length of the characteristic dimension and it is half of the internal diameter for flat ends of vertical cylinders. x^L, x^T, δ^L, δ^T, U^L and U^T are the limit values of length, momentum thickness and velocity outside the boundary layer between the laminar and the turbulent regime. The fluid-dynamics conditions that define the regime are discussed in Section 3 of Appendix N. Equation 161, Equation 163, Equation 164 and Equation 166 are obtained by analytically solving the momentum and the energy conservation laws in the boundary layer, for vertical flat surface in homogeneous medium with uniform wall temperature, as reported by Squire [98] and Eckert and Jackson [99]. Equation 162, Equation 165, Equation 167, Equation 168, Equation 169, Equation 170, Equation 171 and Equation 172 are analytically obtained in this thesis, by doing a power-law interpolation between the laminar and turbulent regime. The algorithm of the EBL approach is reported in Section 1 of Appendix O.

3.4. Integral boundary layer approach

The fluid-dynamics at the side wall play a crucial role in developing the thermal stratification in both liquid and vapour (see Section 4 of Chapter 1) because it affects the free-convective fluid motions. These convective flows depend on the geometry of the storage container and on the heat fluxes at the side wall. As said in Section 3, the storage tank can be vertical cylinder, oblate, sphere and horizontal cylinder, and the Storage Boundary Layer (SBL) model must describe the fluid-dynamics in these systems.

To adapt the SBL model to the different geometries, the Integral Boundary Layer (IBL) approach is applied. In this approach, the *hypothesis of discretized boundary layer* is used. This hypothesis states that the boundary layer at the side walls can be discretized in sub-layers of each thickness, as it is described in Figure 64. Hence, the side wall is discretized in sub-layers. In Figure 64, the white arrows with red boarder are the heat inputs at the side wall. The black square with the yellow boarder and the white square with green boarder are the sub-layers of the wall and of the boundary layer, respectively. The orange points and the white points with the purple boarder are the points of the sub-layer and the wall temperatures, respectively.

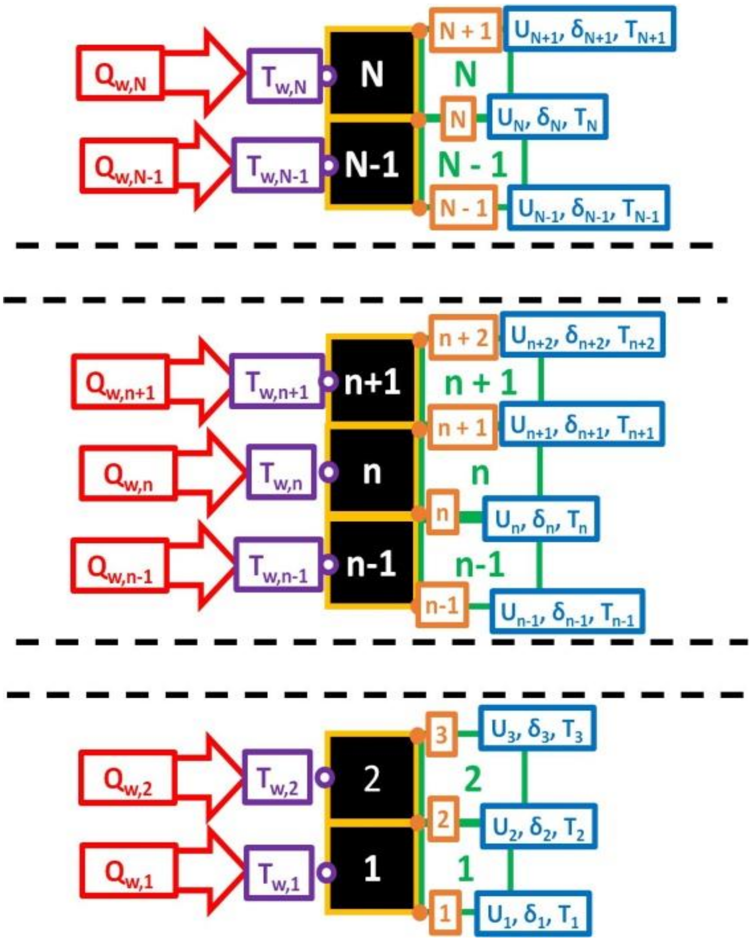

Figure 64. Discretization of the side wall and of the boundary layer.

The boundary layer variables (see Table 62), in particular the momentum thickness (δ_M) and from the velocity outside boundary layer of comparable forced-convection flow (U), cannot be analytically computed from the momentum and energy conservation layer. So, the IBL approach is required to compute these variables from these laws. Due to the hypothesis of discretized boundary layer, the IBL approach can be used for liquid and vapour side walls in vertical cylinder, sphere and oblate ellipsoid.

Section 3.4.1 describes the discretized side wall. Section 3.4.2 presents the conservation law of the numerical approach.

3.4.1. Discretized side wall

The Storage Boundary Layer (SBL) model uses the Prandtl's theory and the van Karman approach and conservation laws of momentum and energy must be used in rectangular coordinate, as it is described in Section 3.1. As already mentioned, the Integrated Boundary Layer (IBL) approach of the SBL model can be adapted to the different geometries of the storage containers due to the hypothesis of discretized boundary layer. By using this hypothesis, any curved surface of the side wall can be approximated as an series of inclined surfaces, as it is described in Figure 65 (a). So, the hypotheses of Section 3.1 of Chapter 4 can be applied to this series and the vertical surfaces can be described with rectangular coordinate by default. In Figure 65 (a), the dark line is the curved surface and the light blue dashed line is the series of inclined surfaces. In Figure 65 (b), the black line is the arc of the side wall, and the orange line is the angle with the horizontal. The white points with purple circles are the points on the ellipse that correspond to a specific value of the liquid height in each layer. The green and the blue lines indicate respectively the distance of each point from the vertical axis of the tank and the distance along the vertical axis of the storage container between each point.

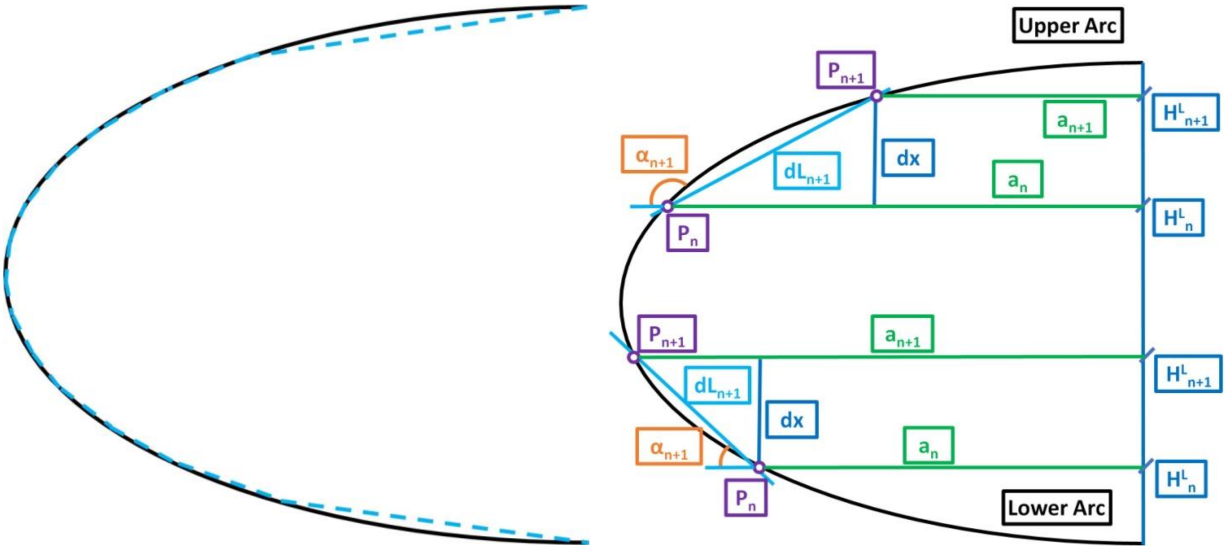

a) b)

Figure 65. Infinitesimal series of inclined surface; b) lower and upper arc or curved surface.

As it is illustrated in Figure 65 (b), the total liquid height, which is called H^L, is divided into a number of equal size sub-layers, called N_S. This number is equal to the number of sub-layer of the boundary layer. Along the lower arc of the ellipse, the points P_{i+1} and P_i can be respectively placed at the liquid height H_{i+1}^L and H_i^L. Hence, a_{i+1} and a_i are respectively the diameter of the section of the ellipse at liquid height H_{i+1}^L and H_i^L. When the points P_{i+1} and P_i are placed in the upper arc, a_i is bigger than a_{i+1}, and if the points P_{i+1} and P_i are located in the lower arc, a_i is smaller than a_{i+1}. The distance between these points is the line of inclined surface that is perpendicular to the paper. The angle and length of this line can be computed with the equations of Table 77.

Table 77. Thickness, angle and length in the discretized curved surface.

Variable	Name	Equation	Formula
thickness of each sub-layer	dx	Equation 173	$dx = \frac{H^L}{N_S} = H_{i+1}^L - H_i^L$
the length of each inclined surface	dL	Equation 174	$dL = \sqrt{dx^2 + (a_{i+1} - a_i)^2}$
the angle of each inclined surface (lower arc)	α	Equation 175	$\alpha = \tan^{-1}\left[\frac{dx}{(a_{i+1} - a_i)}\right]$
the angle of each inclined surface (upper arc)	α	Equation 176	$\alpha = \pi - \tan^{-1}\left[\frac{dx}{(a_i - a_{i+1})}\right]$

Equation 175 and Equation 176 are respectively applied to the lower and upper arc. The approach of the infinitesimal series of inclined surface is applied for sphere, ellipsoid and vertical cylinder. In vertical cylinder, the length of each inclined surface coincides with the thickness of the sub-layer because the angle is equal to 90°.

3.4.2. Conservation laws

With the hypothesis of the discretized boundary layer, the conservation laws in rectangular coordinate can be applied to curved surface because this surface is approximated as a series of inclined surfaces, as it is explained in Section 3.4.1 of Chapter 4. The angles of these surfaces change along the entire side surface of the storage container, as reported in Figure 65 (b). Four types of inclined surfaces can be found: horizontal, upward, vertical and downward. These surfaces are respectively described in Figure 66 (a), Figure 66 (b), Figure 66 (c) and Figure 66 (d). The thick black and light blue lines respectively indicate the wall and the horizontal line. The black arrows respectively define the x axis and the y axis. The thick green and purple arrows respectively indicate the buoyancy forces and the gravity acceleration. The orange arc represents the angle of the inclined surface. The blue square is the part of the fluid where the viscous and the buoyancy forces are applied.

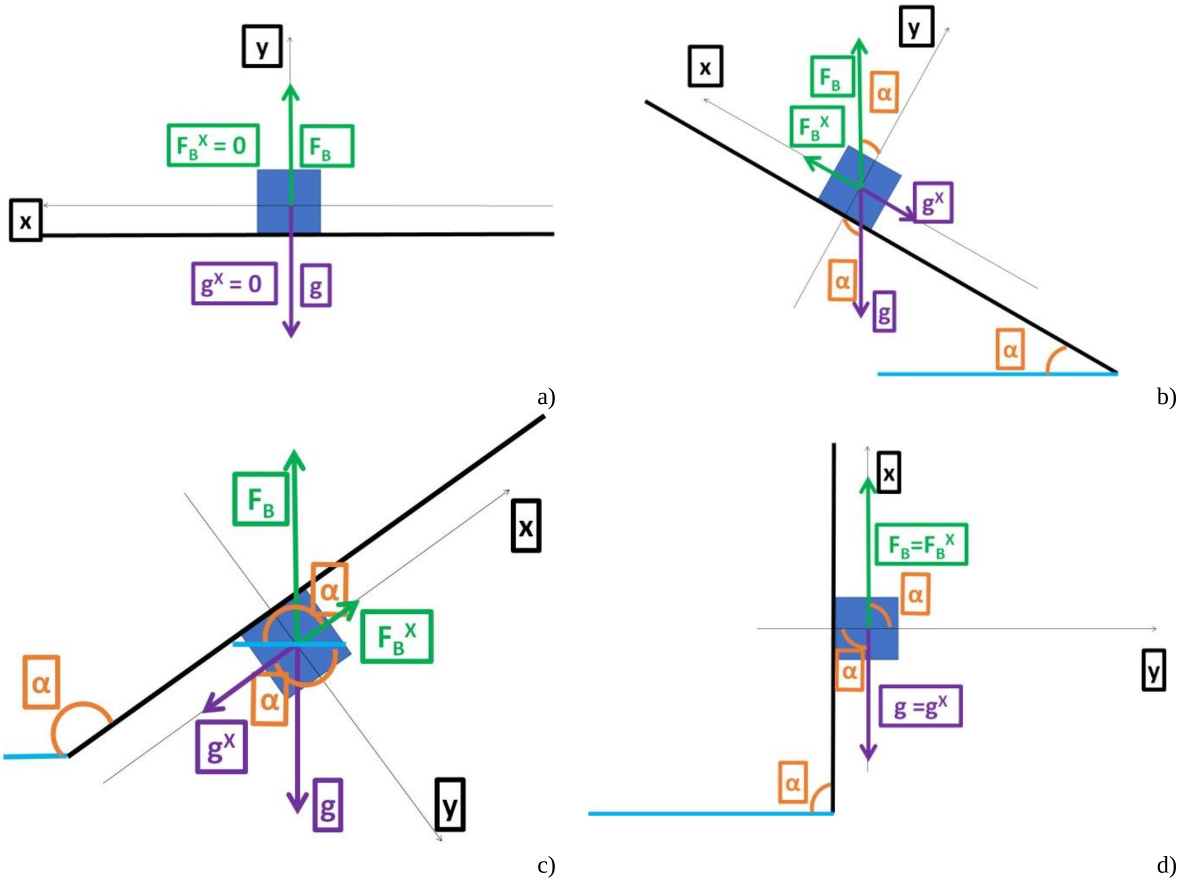

Figure 66. Four types of inclined surfaces: a) horizontal, b) upward, c) vertical and d) downward.

If the surface is inclined from the position of Figure 66 (a) to the position of Figure 66 (d), the angle of this surface changes. As consequence, the horizontal component of the vector of the gravity acceleration ($\vec{g}$) varies, modifying the intensity of the buoyancy forces (F_B) that pushes the fluid along the surface. The horizontal component of $\vec{g}$, which is called g_x, is calculated with Equation 177.

Equation 177
$$g_x = |\vec{g}| \cdot \sin(\alpha)$$

$|\vec{g}|$ is the magnitude of the gravity acceleration, which is 9.81 m/s². The shear tensor (τ_w) does not change in magnitude because it is always parallel to the motion of the fluid. Hence, the conservation laws proposed by of Evans et al. [132] and by Drake [133] for stratified medium can be applied in the IBL approach, by considering the change of the horizontal component of $\vec{g}$ of the bounyancy forces. These modified balance equations of momentum and of energy are respectively described by Equation 178 and Equation 179.

Equation 178
$$\frac{\partial(U^2 \cdot \delta_M)}{\partial x} = \frac{\left(F_{B,x} - \tau_w\right)}{\rho \cdot \Lambda}$$

Equation 179
$$\frac{\partial(U \cdot \delta_M)}{\partial x} = \frac{\left(\dot{q}_w - \dot{q}_\infty - \dot{q}_{\theta_w}\right)}{C_P \cdot \rho \cdot \theta_w \cdot \Upsilon}$$

$F_{B,x}$ is the buoyancy and τ_w is the viscous forces. $\dot{q}_\infty$ is the heat due to the transferring of mass between the bulk and the boundary layer. $\dot{q}_w$ is the heat fluxes at the wall. $\dot{q}_{\theta_w}$ is the heat fluxes due to the temperature gradient on the side wall. Λ and Υ are respectively the momentum and the energy constants. F_B, τ_w, $\dot{q}_\infty$, Λ and Υ are computed using different formulas summarized in Table 78.

Table 78. Boundary and viscous forces, boundary-to-bulk and wall temperature gradient heat flows and coefficients.

Regime	Equation	Formula	Equation	Formula
		Bouyancy forces		**Viscous forces**
Laminar	Equation 180[99]	$F_B = g_x \cdot \beta \cdot \theta_w \cdot \frac{\delta}{3} \cdot \rho$	Equation 181[98]	$\tau_w = \mu \cdot \frac{U}{\delta_M}$
Transition	Equation 182	$F_B = \frac{F_B^T - F_B^L}{Ra_{\Delta T}^T - Ra_{\Delta T}^L} \cdot \left(Ra_{\Delta T} - Ra_{\Delta T}^L\right) + F_B^L$	Equation 183	$\tau_w = \frac{\tau_w^T - \tau_w^L}{{Ra_T}^{TUR} - {Ra_T}^{LAM}} \cdot \left(Ra_T - Ra_{\Delta T}^L\right) + \tau_w^L$
Turbolent	Equation 184[98]	$F_{B,x} = 0.125 \cdot g_x \cdot \beta \cdot \theta_w \cdot \delta_M \cdot \rho$	Equation 185[99]	$\tau_w = 0.0225 \cdot \rho \cdot U^2 \cdot \left(\frac{v}{U \cdot \delta_M}\right)^{0.25}$
		Boundary-to-bulk heat flow		**Wall temperature gradient heat flow**
Laminar	Equation 186[132]	$\dot{q}_\infty = 0.0833 \cdot \rho \cdot C_P \cdot U \cdot \delta_M \cdot \frac{\partial T_\infty}{\partial x}$	Equation 187	$\dot{q}_{\theta_w} = 0.0833 \cdot \rho \cdot C_P \cdot U \cdot \delta_M \cdot \frac{\partial \theta_w}{\partial x}$
Transition	Equation 188	$\dot{q}_\infty = \frac{\dot{q}_\infty^T - \dot{q}_\infty^L}{Ra_{\Delta T}^T - Ra_{\Delta T}^L} \cdot \left(Ra_{\Delta T} - Ra_{\Delta T}^L\right) + \dot{q}_\infty^L$	Equation 189	$\dot{q}_{\theta_w} = \frac{\dot{q}_{\theta_w}^T - \dot{q}_{\theta_w}^L}{Ra_{\Delta T}^T - Ra_{\Delta T}^L} \cdot \left(Ra_{\Delta T} - Ra_{\Delta T}^L\right) + \dot{q}_{\theta_w}^L$
Turbolent	Equation 190[132]	$\dot{q}_\infty = 0.1464 \cdot \rho \cdot C_P \cdot U \cdot \delta_M \cdot \frac{\partial T_\infty}{\partial x}$	Equation 191	$\dot{q}_{\theta_w} = 0.1464 \cdot \rho \cdot C_P \cdot U \cdot \delta_M \cdot \frac{\partial \theta_w}{\partial x}$
		Momentum constant		**Energy constant**
Laminar	Equation 192[98]	$\Lambda = \frac{1}{105}$	Equation 193[98]	$\Upsilon = \frac{1}{30}$
Transition	Equation 194	$\Lambda = \frac{\Lambda^T - \Lambda^L}{Ra_{\Delta T}^T - Ra_{\Delta T}^L} \cdot \left(Ra_{\Delta T} - Ra_{\Delta T}^L\right) + \Lambda^L$	Equation 195	$\Upsilon = \frac{\Upsilon^T - \Upsilon^L}{Ra_{\Delta T}^T - Ra_{\Delta T}^L} \cdot \left(Ra_{\Delta T} - Ra_{\Delta T}^L\right) + \Upsilon^L$
Turbolent	Equation 196[99]	$\Lambda = 0.0523$	Equation 197[99]	$\Upsilon = 0.0366$

Equation 182, Equation 183, Equation 188, Equation 189, Equation 194 and Equation 195 are obtained this thesis. If Equation 178 and Equation 179 are applied to a homogeneous medium, as for the homogeneous model (H model), $\dot{q}_{\theta_w}$and $\dot{q}_\infty$ are equal to zero because the bulk temperature and the wall temperature gradient are neglected due to the total homogeneity hypothesis (assumption a) of Section 1.1 of Chapter 4). The numerical integration of Equation 178 and Equation 179 can compute the boundary layer can compute the momentum thickness (δ_M) and the velocity outside boundary layer of comparable forced-convection flow (U). The algorithms of the numerical integration are reported in Section 2 of Appendix O. From the values of δ_M and U, the other boundary layer variables of Table 62, except the temperature, can be deduced as it is explained in Section 2 of Appendix O. The boundary layer temperature is computed as described in Section 2.1 of Appendix O.

4. Storage heat transfer model: homogeneous model

The Storage Heat Transfer (SHT) model is the Block 6 of the homogeneous model (H model), as it is described in Figure 59. The SHT model computes the heat flows from the internal walls to the internal fluid (liquid and vapour). This model is connected with the Storage Boundary Layer (SBL) model, as it in shown in Figure 59.

The heat leakage rate is the main factor that controls the behaviour of cryogenic liquids in storage container. As it is explained in Section 4.4 and 4.5 of Chapter 1, the heat input produces the vapour and liquid thermal stratifications, which affect the self-pressurisation and the ageing. The value of the heat rate is affected by the geometry of the storage containers, the thermal distribution in liquid and in vapour, and by the environmental conditions. In particular at the side walls, the heat transfer is directly dependent of the fluid-dynamics of the free-convective boundary layer. So, the heat transfer between the environment and the internal fluid is connected to the fluid-dynamics at the side walls.

As it is underlined in Section 5 of Chapter 1, the Lumped Parameter Models (LPM) with discretized approach [1], [2], [122] do not compute the heat transfer between the environment and the internal fluid because the heat leakages are defined by the developer of the model. In LPM with non-equilibrium approach [46], [47], [49], the heat transfer between the environment and the internal fluid is computed considering the geometry of the storage containers and the environmental conditions. In LPM with discretized and non-equilibrium approaches, the interaction between fluid-dynamics and heat transfer is neglected. As consequence, the heat input should be computed with a method that considers these criteria:

a) Being adaptable to the different geometries;
b) Considering the effect of the thermal distribution on the heat transfer;
c) Being flexible to the variation of the environmental conditions;

To fulfil these goals, *storage heat transfer (SHT) model* is developed. The heat transfer at the side wall is connected to the fluid-dynamics by computing the heat transfer coefficients from the boundary layer variables. Doing that, the adaptability to the geometry, and the link between fluid-dynamic and heat transfer are considered in the boundary variables. The flexibility to the variation of the environmental conditions is considered by computing the heat inputs on the basis of the difference in temperatures between the external and the internal walls of the storage container.

Section 4.1 describes the hypotheses. Section 4.2 explains the distribution of the heat flows in the storage container. Section 4.3 presents the control volumes at the side wall, due to this distribution. Section 4.4 describes the balance equations that are deduced from these volumes. Section 4.5 presents the heat flow between the dry and the wet side walls. Section 4.6 describes the model of the heat transfer coefficients. Section 4.7 presents the algorithm of the SHT model.

4.1.Hypotheses

After reviewing some modelling works [46], [47], [49], the heat transfer between the environment and the internal fluid (liquid and vapour) can be simplified as the thermal energy flows in three steps:

a) the environment-to-external wall transfer;
b) the external wall-to-internal wall transfer;
c) the internal wall-to-internal fluid transfer.

Due to the wind, sun and the air temperature, the energy of the environment passes to the external wall, which is usually uniform in temperature. The difference in temperature between the air and the external wall is usually very low because the storage containers are well thermally insulated. From the external walls, the heat is transferred to the internal walls and small part of the energy is trapped in the insulation because the thermal inertia of the storage container is usually low. The heat mainly enters from the bottom, the side walls and roof into the internal fluids. As underlined by the thermal analysis of Kang et al. [25] and by the experimental observation of vapour temperature profile in vertical storage cylinders [24], [25], [26], the roof-to-vapour heat transfer is negligible. As it is proved in Section 7 of Chapter 2, the heat coming from the walls is distributed between the vapour and the liquid as function of the thermal conduction of the walls, and on the vapour-to-interface heat transfer. So, in the Storage Heat Transfer (SHT) model, it can be assumed that:

a) The external wall temperature of the storage container is equal to the air temperature;
b) The external wall temperature is homogenous over the whole surface of the storage container;
c) The heat transfer process of the SHT model is composed by external wall-to-internal wall and by the internal wall-to-internal fluid (steps b) and c) of Section 4.1 of Chapter 4);
d) External walls-to-internal walls heat transfer is described as pseudo-convective process, using the effective heat transfer coefficient to quantify the rate of this transfer;
e) The thermal inertia of the walls can be neglected;
f) The wall temperature, thus the heat ingress flow, is uniform at each surface;
g) The heat exchanged between the dry and the wet walls by conduction is transferred at the interface and it is not transferred to the wet side wall;
h) The roof does not exchange heat with the vapour;
i) The roof temperature is equal to the dry side wall temperature;

With assumption a) of Section 4.1 of Chapter 4, a fixed temperature boundary condition is assumed at the external walls of the storage container. As consequence, the environment-to-external wall heat transfer can be neglected, as explained by assumption c) of Section 4.1 of Chapter 4. The effect of the environment can be considered by changing the value of the external wall temperature of the storage container.

Hypothesis h) of Section 4.1 is a consequence of the experimental observation of vapour temperature profiles. Assumption i) of Section 4.1 of Chapter 4 is deduced from hypotheses h) of Section 4.1 of Chapter 4. If the roof-to vapour heat input is equal to zero, the heat coming from the external wall to the internal wall of the roof must goes to the dry side wall by conduction.

The ullage is thermally stratified, independently from the storage conditions, as it is explained in Section 4.5 of Chapter 1. In the homogeneous model (H model), the vapour is isothermal due to the hypothesis of total homogeneity (assumption a) of Section 1.1 of Chapter 4). Hence, the dry side walls-to-vapour heat flow rate is corrected with the coefficient α, which is computed with the Boil-off Rate (BOR) model.

As said, the dry side wall-to-wet side wall heat transfer affects the thermal distribution inside the storage container, thus the behaviour of the cryogenic liquids. Due to the hypothesis of total homogeneity (assumption a) of Section 1.1 of Chapter 4), the temperature of the dry side wall is homogeneous, even if a gradient is present due to the thermal stratification. Considering the thickness of the wall is not known, this heat transfer is corrected with the coefficient β, which is computed with the BOR model.

4.2. Distribution of the heat flows

The Storage Heat Transfer (SHT) model can be applied to storage containers of different geometry such as vertical cylinder with flat ends, oblate ellipsoid and sphere, because it is connected to the Storage Boundary Layer (SBL) model, as explained in Section 4 of Chapter 4. In the SHT model, the heat flows in the storage container are shown in Figure 67 for these geometries. This distribution of the heat flows is a direct consequences of the hypotheses of Section 4.1 of Chapter 4. The red arrows indicate the heat fluxes and the green lines represent the characteristic length of heat transfer. The white arrow with red border is the overall heat input. The dashed yellow line is the interface. The light orange and the light blue colours are respectively the ullage and the liquid. The white circles with purple borders are the wall temperatures.

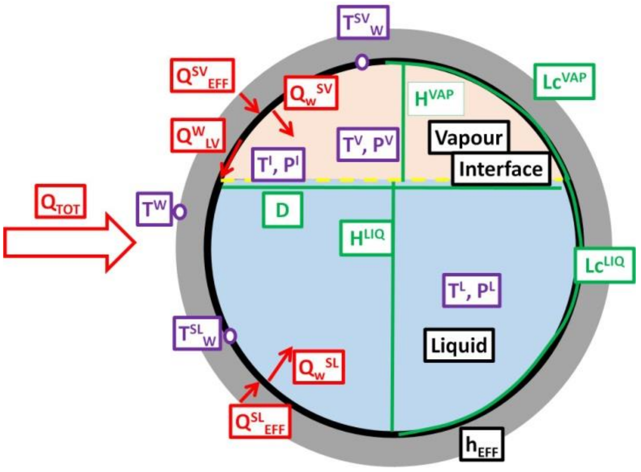

a)

Figure 67. Heat transfer problems in oblate ellipsoid and sphere (a) and for vertical cylinder with flat bottom and roof (b).

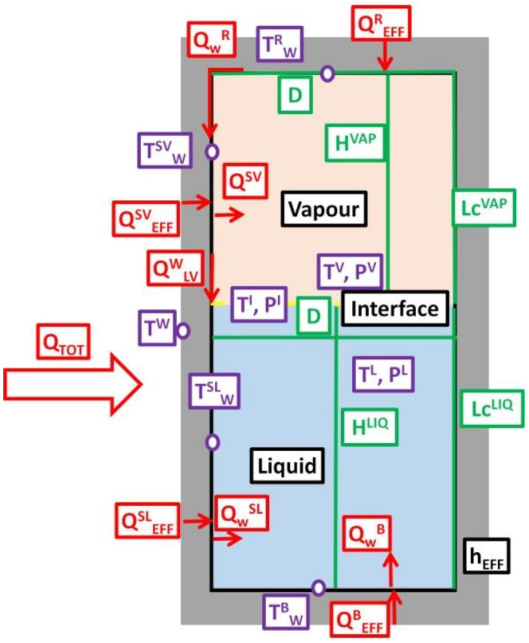

b)

As it is shown in Figure 67, the heat flows at the bottom and at the roof are considered only for vertical cylinders with flat ends because these ends create a discontinuity in the fluid-dynamics as described in Section 3.3 of Chapter 4. As shown in Figure 67, the heat flow between the external wall and the internal wall of the roof ($\dot{Q}^{R}_{EFF}$) is completely transferred to the side wall by conduction. This conductive heat flow ($\dot{Q}^{R-SV}_{w}$) is added to the heat flow between the external wall and the dry side wall ($\dot{Q}^{SV}_{EFF}$). $\dot{Q}^{R-SV}_{w}$ and $\dot{Q}^{SV}_{EFF}$ warms the dry side wall, creating a temperature gradient in the wall. The heat of the wall is transferred to the interface ($\dot{Q}^{LV}_{w}$) by conduction and to the vapour ($\dot{Q}^{SV}_{w}$) by free-convection. In the liquid phase, the heat pathway is simpler than the one of the vapour. The heat flow between the external wall and at the wet side wall ($\dot{Q}^{SL}_{EFF}$), and the one between the external wall and the bottom wall ($\dot{Q}^{B}_{EFF}$) are totally transferred to the liquid.

4.3. Control volumes at the walls

As consequence of the distribution of the heat flows (see Section 4.2 of Chapter 4), three control volumes can be defined for the Storage Heat Transfer (SHT) model. These control volumes are the wet side wall (or liquid side wall), the dry side wall (or vapour side wall) and the bottom, as it is shown in Figure 68. In Figure 68, the dark rectangles are the walls. The heat flows are the white arrows with red borders. The wall temperatures are the white circle with the purple borders.

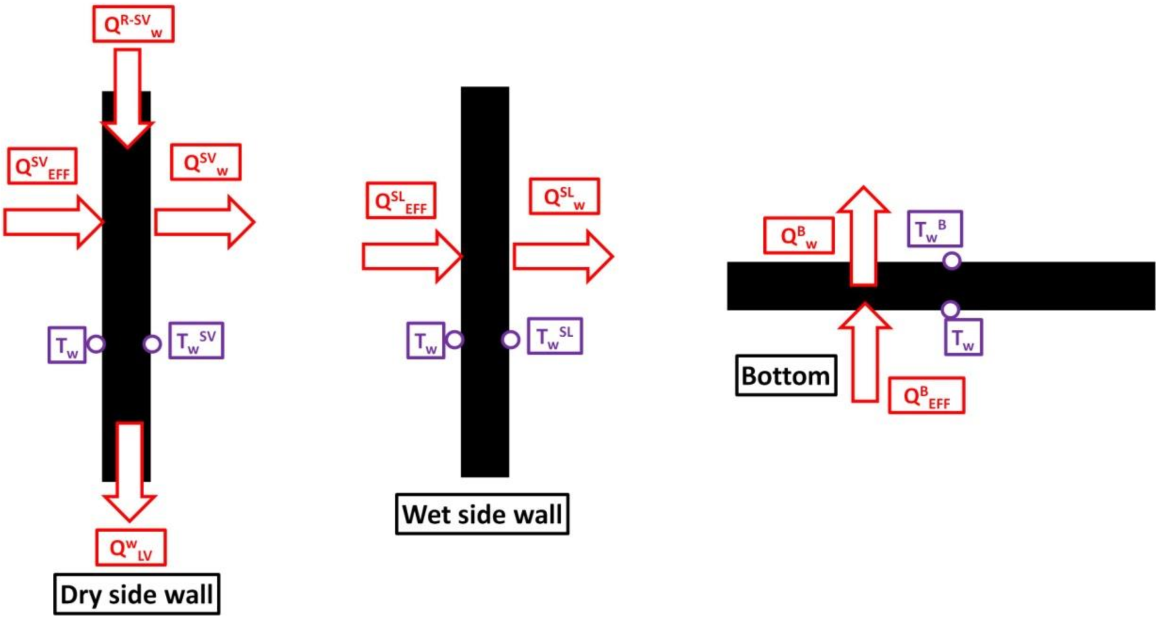

Figure 68. Control volumes of the SHT model.

The control volume of the roof is not considered because there is not heat transfer with the vapour, due to hypotheses i) and h) of Section 4.1 of Chapter 4.

4.4.Energy Balance equations at the walls of the storage container

Due to hypothesis (assumption e) of Section 4.1 of Chapter 4), the thermal inertia of the walls can be neglected. Hence, the heat flows from the environments to the internal walls are immediately transferred, without accumulating heat in the walls. At the bottom, the heat flows between the external wall and the internal wall ($\dot{Q}_{EFF}^{B}$) must be equal to the heat exchange with the liquid ($\dot{Q}_w^B$), as it is illustrated in Figure 68. At the wet side wall, the same occurs and the heat flow between the liquid and the internal wall ($\dot{Q}_w^{SL}$) is equal to the heat exchanged between the external and the internal walls ($\dot{Q}_{EFF}^{SL}$). At the dry side wall, the heat exchange between the external and the internal wall ($\dot{Q}_{EFF}^{SV}$), and the heat coming from the roof ($\dot{Q}_w^{R-SV}$) are balanced by the heat transferred to the interface by conduction ($\dot{Q}_w^{LV}$) and by convection to the vapour ($\dot{Q}_w^{SV}$). Hence, the energy balance equations at the walls of the storage container can be described with the equations of Table 79.

Table 79. Energy balance equations at each control volume of SHT model.

Control volume	Equations	Formula
bottom wall	Equation 198	$h_w^B \cdot A^B \cdot (T_w^B - T^L) - h_{eff} \cdot A^B \cdot (T^w - T_w^B) = 0$
liquid side wall	Equation 199	$h_w^{SL} \cdot A^{SL} \cdot (T_w^{SL} - T^L) - h_{eff} \cdot A^{SL} \cdot (T^w - T_w^{SL}) = 0$
vapour side wall	Equation 200	$\dot{Q}_w^{LV} \cdot \beta + \alpha \cdot h_w^{SV} \cdot A^{SV} \cdot (T_w^{SV} - T^V) - h_{eff} \cdot (A^{SV} + A^R) \cdot (T^w - T_w^{SV}) = 0$

The energy balance equation at the wall of the roof is not written due to hypotheses i) and h) of Section 4.1. The heat transfer coefficient h_w^B is computed as function of the heat flow $\dot{Q}_w^B$. The heat transfer coefficients h_w^{SV} and h_w^{SL} are respectively calculated from the difference in temperature between the dry side wall and the vapour, and between the wet side wall and the liquid. So, the heat flows $\dot{Q}_w^B$, $\dot{Q}_w^{SL}$ and $\dot{Q}_w^{SV}$ can only be computed with iterative procedures where Equation 198, Equation 199 and Equation 200 are respectively solved. These iterative procedures are respectively explained in Section 1, 2 and 3 of Appendix Q. The wall temperatures T_w^B, T_w^{SL} and T_w^{SV} are computed through these procedures.

4.5. Dry side wall-to-interface heat transfer

The heat flows between the dry and the wet side wall due to the difference in temperatures between these side walls, as it is illustrated in Figure 69. The light orange and the black cords are the vapour space and the dry wall, respectively. The interface is the yellow dashed line. The green lines indicate the diameter at the interface, the bulk temperature and the wall temperature positions. The grey dashed line is the projection of the bulk temperature on the dry wall. The white circles with purple boarders are the temperatures. The red arrow is the dry side wall-to-interface heat flow.

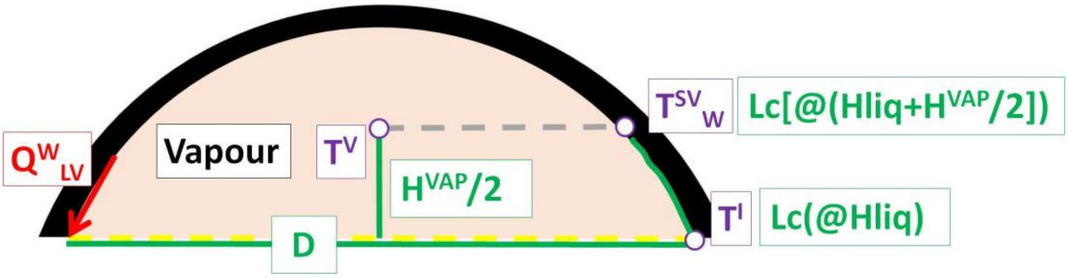

Figure 69. Model of dry side wall-to-interface heat transfer.

As it is shown in Figure 69, the heat flow between the dry and the wet side wall ($\dot{Q}_W^{LV}$) affects the thermal distribution in the storage container. This heat is transferred by conduction, as indicated by the Fourier'law[86]. This heat flow can be computed as function of the wall temperature gradient at the interface and of the thickness of the side wall, as it follows:

Equation 201
$$\dot{Q}_W^{LV} = -k \cdot A_R \cdot \left.\frac{\partial T_W^{SV}}{\partial x}\right|_{x=H^L}$$

In Equation 201, k is the wall thermal conductivity computed as indicated in Appendix C. A_R is the surface of the metallic ring obtained by cutting the storage container at the interface and it is computed with the geometrical formulas of Appendix B. $\left.\frac{\partial T_W^{SV}}{\partial x}\right|_{x=H^L}$ is the temperature gradient of the dry side wall at the temperature.

Due to the hypothesis of homogeneity (assumption a) of Section 1.1 of Chapter 4), the dry side wall is isothermal and the gradient cannot be estimated from the temperature profile of the dry side wall. As it is shown in Figure 69, the position of the reference point for evaluating the bulk ullage temperature is placed at halfway between the liquid-vapour interface and the highest point of the roof. The evaluation point for the dry side wall temperature evaluation point is at the same horizontal level of the ullage temperature, as seen in Figure 69. Hence, the dry wall temperature gradient at the interface is computed with Equation 202.

Equation 202
$$\left.\frac{\partial T_W^{SV}}{\partial x}\right|_{x=H^L} = -\frac{T_W^{SV} - T^I}{L_c\left(H^{LIQ} + \frac{H^{VAP}}{2}\right) - L_c(H^{LIQ})}$$

$L_c(H^{LIQ})$ is the length of the wet side wall from the bottom to the free-surface of the liquid. $L_c\left(H^{LIQ} + \frac{H^{VAP}}{2}\right)$ is the length of the side wall from the bottom to the reference point of the bulk ullage temperature.

---

[86] Fourier's law state that the conductive heat flux can be computed as : $\dot{q} = -k \cdot \frac{\partial T}{\partial x}$

4.6. Heat transfer coefficient

To solve the balance equations of Table 79, the heat transfer coefficients have to be computed. These coefficients can be calculated using semi-empirical formulas or using the fluid-dynamics theory. The semi-empirical formulas calculate the heat transfer coefficient from the Nusselts's number (see Section 1 of Appendix N), with mathematical expressions that are obtained by regressing the experimental data of heat transfer. With the fluid-dynamics theory, the heat transfer coefficient can be calculated from the values of the momentum thickness (δ_M) and the velocity outside boundary layer of comparable forced-convection flow (U). These variables are obtained from the Storage Boundary Layer (SBL) model. Hence, the SBL and the SHT are connected. So, SHT model can be easily adapted to different geometries of the storage container and this model can consider the effect of the bulk temperature gradient on the heat transfer.

The equations to compute the heat transfer coefficient are reported in Table 80.

Table 80. Heat transfer coefficients for the semi-empirical and boundary layer approaches.

Equation	Formula	Regime
	Semi-empirical approach	
Equation 203 [135]	$\bar{h} = \frac{\overline{Nu} \cdot k}{L_C}$	Laminar, transition and turbulent
	Boundary layer method	
Equation 204	$h_x = \frac{2 \cdot k}{\delta_M(x)}$	Laminar
Equation 205	$h_x = \frac{{h_x}^{TUR} - {h_x}^{LAM}}{{Ra_x}^{TUR} - {Ra_x}^{LAM}} \cdot (Ra_x - Ra\_x^{\ LAM}) + {h_x}^{LAM}$	Transition
Equation 206	$h_x = 0.0225 \cdot \rho \cdot C_P \cdot U(x) \cdot \left(\frac{\nu}{U(x) \cdot \delta_M(x)}\right)^{\frac{1}{4}}$	Turbulent

Equation 204 and Equation 206 are obtained in this thesis from formulas of the heat fluxes in laminar and turbulent regimes (Equation 953 and Equation 956), respectively. Equation 205 is obtained in this thesis as linear interpolation between the turbulent and laminar regime. $\bar{h}$ and h_x are the average and the local heat transfer coefficients. $\overline{Nu}$ is the average Nusselt's number and it can be computed with the formulas reported in Table 231. L_C is the characteristic length of the heat transfer. For the flat ends, this length is half of the diameter. For side wall, this length is the length of the side. The semi-empirical approach calculates the heat transfer coefficient for the flat ends (roof and bottom). The boundary layer method computes this coefficient for the side walls (wet and dry). This approach gives the values of the local heat transfer coefficient because it uses the values of δ_M and of U at every sub-layer of the boundary layer.

If the values of δ_M and of U are equal to zero, the fluid does not flows in the boundary layer and the natural convection vanishes. So, Equation 204, Equation 205 and Equation 206 cannot be used. As consequence, the heat of the side wall (wet and dry) is transferred by conduction to the fluid (liquid and vapour). Hence, the heat transfer coefficient can be computed as it follows:

Equation 207
$$h_x = \frac{k}{\frac{D}{2}}$$

k is the thermal conductivity of the fluid (vapour and liquid). D is the diameter of the storage container at the height of the sub-layer, where the heat transfer coefficient is computed.

In the homogeneous model (H model), the side walls are isothermal due to the hypothesis of homogeneity (assumption a) of Section 1.1) and the average heat transfer coefficient is required. Hence, this coefficient can be calculated with theorem of the mean integral[87], as follows:

Equation 208 $$\bar{h} = \frac{1}{L_C} \cdot \int_0^{L_C} h_x(x) \cdot dx$$

L_C is the length of the side wall. The integral of Equation 208 is numerically solved with the trapezoidal rule (see Section 3 of Appendix F) because h_x cannot be computed from the position x with an analytical formula.

4.7. Algorithm of storage heat transfer model

The algorithm of the Storage Heat Transfer (SHT) model is the mathematical procedure to calculate the heat inputs at the surfaces of the storage container. The algorithm of SHT model is composed by three sub-algorithms, which are respectively called $\dot{Q}_w^B$, $\dot{Q}_w^{SL}$ and $\dot{Q}_w^{SV}$ algorithms. These three mathematical procedures respectively compute the bottom-to-liquid ($\dot{Q}_w^B$), the wet side wall-to-liquid ($\dot{Q}_w^{SL}$) and the dry side wall-to-vapour ($\dot{Q}_w^{SV}$) heat flows.

The input and the output variables of the SHT model are reported in Table 81.

Table 81. Input and output of the algorithm of the SHT model.

Variable	Description
Input	Geometry, state variable (see Table 62) and thermo-physical properties (see Table 31).
Output	Heat transfer and boundary layer variables (see Table 62) for each surface

a) The outputs of the SHT model are the heat transfer and the boundary layer variables because the Storage Boundary Layer (SBL) model is directly connected to the SHT model. Due to this interaction between the SHT and the SBL models, the algorithm to compute the heat flows can be described by Figure 70.

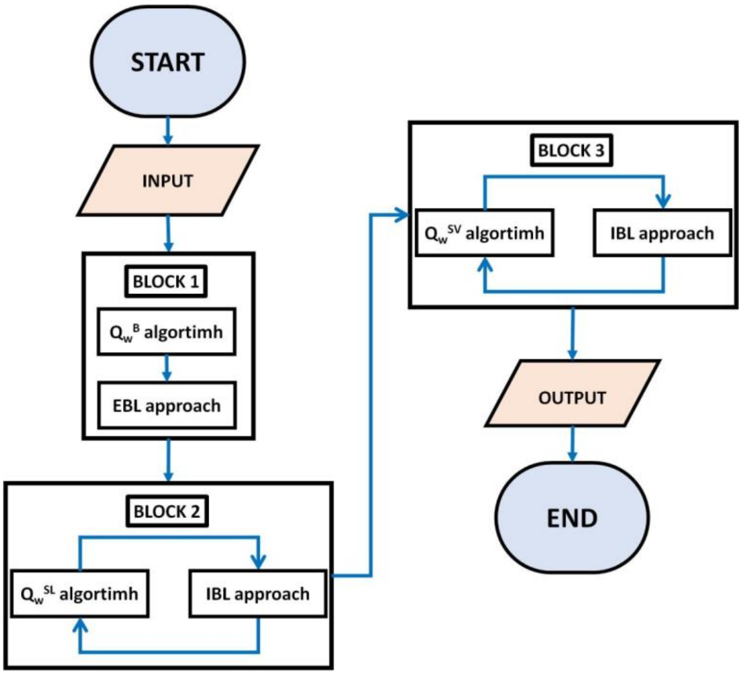

Figure 70. Algorithm of the SHT model.

---

[87] Mean integral values : $L \cdot \bar{y} = \int_0^L y(x) \cdot dx$

As it is shown in Figure 70, the algorithm is composed by the following steps:

a) BLOCK 1. The heat transfer is calculated with the $\dot{Q}_w^B$ algorithm. The boundary layer variables at the bottom are calculated, using Exact Boundary Layer (EBL) approach (see Section 3.3 of Chapter 4). In the $\dot{Q}_w^B$ algorithm, the average heat transfer coefficients are computed with the semi-empirical approach. Hence, this algorithm does not depend on the EBL approach;
b) BLOCK 2. The heat transfer is computed with the $\dot{Q}_w^{SL}$ algorithm. The boundary layer variables at the bottom are calculated, using the Integrated Boundary Layer (IBL) approach (see Section 3.4 of Chapter 4). In the $\dot{Q}_w^{SL}$ algorithm, the average heat transfer coefficients are calculated with the boundary layer approach. Hence, the values of boundary layer variables δ_M and U at every sub-layer are required. These variables are computed with the IBL approach with the value of the heat transfer variables of the $\dot{Q}_w^{SL}$ algorithm. Hence, $\dot{Q}_w^{SL}$ algorithm and the IBL approach are strictly connected. The first guess values of the heat transfer variables are required to start the calculation in this block.

BLOCK 3. The heat transfer is calculated with the $\dot{Q}_w^{SV}$ algorithm. The boundary layer variables at the bottom are computed, using the IBL approach (see Section 3.4 of Chapter 4). In the $\dot{Q}_w^{SV}$ algorithm, the average heat transfer coefficients are computed with the boundary layer approach, using δ_M and U at every sub-layer, as done in Block 2. $\dot{Q}_w^{SV}$ algorithm and the IBL approach are strictly connected and first guess values of the heat transfer variables are required to start the calculation in this block, as done in Block 2.

The heat input at the roof is equal to zero, due to hypothesis h). Hence, an algorithm is not required to compute the heat transfer variables at this wall.

5. Interface heat transfer model

Due to the hypothesis of actual thermodynamic state (assumption b) of Section 1.1 of Chapter 4), the vapour and the liquid can be sub-cooled, overheated and at saturation. Hence, heat can be transferred across the interface because the vapour and liquid temperatures are different from the one of the interface. As consequence, mass is exchanged at the interface, and evaporative and condensing mass flows are present. The difference in these mass flows produces a net mass flow. The Interface Heat Transfer (IHT) model is developed to calculate the heat transfer between the liquid and the interface, and between the vapour and the interface, and the net mass flow. The IHT is the Block 7 of the homogeneous model (H model), as it is described in Figure 59.

In the scientific literature, the behaviour of the interface, in particular the mass transfer, has been studied with two approaches: the saturation approach [2], [46]–[48], [78] and with the kinetic approach [49], [66], [67], [122], [136]. The kinetic approach can be separated into the Lee model [93] and the Hertz-Knudsen model [137]. The phenomena of liquid and vapour heat transfer at the interface have been described with the theory of natural convection over horizontal surfaces [2], [47], [49], [70], [78], [122], [136]. Due the hypothesis of local equilibrium condition (assumption c) of Section 1.1 of Chapter 4), the temperature of the interface is equal to the saturation one at the pressure of the ullage. Hence, the saturation approach is chosen because the interface is at saturation as it is imposed by this assumption. In this thesis, the theory of natural convection over horizontal surfaces computes the vapour-to-interface heat transfer. The liquid-to-interface heat transfer is described with an approach based on the fluid-dynamics of the wet side wall.

Section 5.1 presents the hypotheses and the conservation laws at the interface. Section 5.2 and 5.3 respectively describe the vapour-to-interface and the liquid-to-interface heat transfers. Section 5.4 explains the net mass flow.

5.1. Hypothesis and conservations laws

The mass-heat transfer rates depend on the surface area of the interface. Natural convection at the liquid side wall can deform the surface of interface near the wall. This surface can be distorted by the oscillation of the storage containers. Hence, the *hypothesis of rigid mass-less surface* is applied. This assumption states that the liquid-vapour interface is a rigid and mass-less surface, which is permeable to mass flow surface. With this hypothesis, the interface can be described as indicated in Figure 71. The light orange and the light blue are respectively the vapour and the liquid. The yellow dashed line is the interface. The white arrows with red borders are the heat transfer. The green and the bourdon dashed arrows are the mass and enthalpy flows, respectively. The continuous-line arrow is the net mass flow.

As illustrated in Figure 71, the evaporation and the condensation rates respectively transfers mass from the liquid to the interface and from the vapour to the interface. As consequence, these mass flows carry sensible energy inside and outside the interface. The interface temperature is equal to the saturation temperature at vapour’s pressure, due to the hypothesis of local equilibrium condition (assumption c) of Section 1.1 of Chapter 4). So, there are temperature gradients between the liquid and the interface, and between the vapour and the interface. Due to these temperature gradients, thermal energy is transferred from the vapour, the liquid and the dry side wall to the interface. These heat flows balance the enthalpy flows of the evaporative and condensing mass flows.

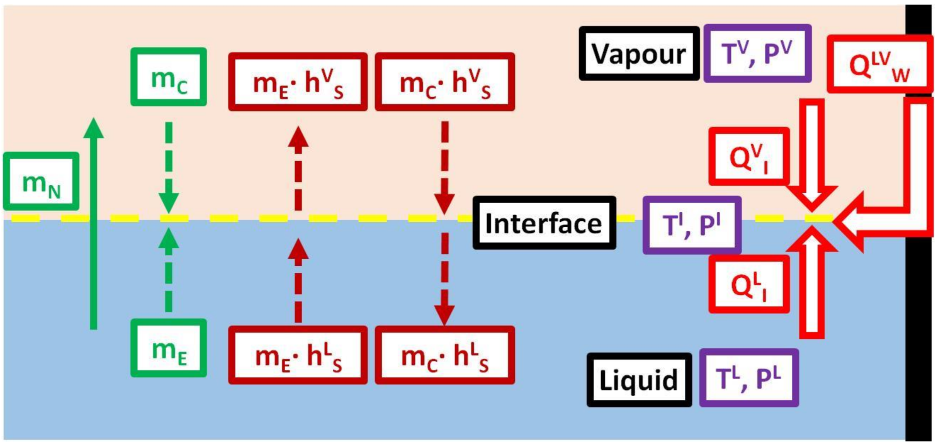

Figure 71. Interface in IHT model.

The inertia of the interface is neglected, due to the hypothesis of rigid mass-less surface. Hence, only the energy conservation equation is required and it is described as follows:

Equation 209
$$\dot{m}_E \cdot \tilde{h}_S^L(P^V) + \dot{m}_C \cdot \tilde{h}_S^V(P^V) + \dot{Q}_I^V + \dot{Q}_I^L + \beta \cdot \dot{Q}_W^{LV} = \dot{m}_E \cdot \tilde{h}_S^V(P^V) + \dot{m}_C \cdot \tilde{h}_S^L(P^V)$$

$\dot{m}_E$ and $\dot{m}_C$ are respectively the evaporation and the condensation rate. $\dot{Q}_W^{LV}$ is computed as it is explained in Section 4.5 of Chapter 4.

5.2. Vapour-to-interface heat transfer

The vapour transfers heat to the interface because a temperature gradient exists between the ullage bulk and the interface. The vapour is always hotter than the interface during the self-pressurisation and the steady state, as experimentally proved [3], [24]–[30], [34], [72]. Due to the hypothesis of rigid mass-less surface (see Section 5.1 of Chapter 4), the interface is a flat cold horizontal surface facing upward for the heat is transferred between the vapour and the interface. This heat transfer can be computed with the theory of natural convection over horizontal surfaces, as it is said in Section 5. So, the vapour-to-interface heat transfer is computed as follows:

Equation 210
$$\dot{Q}_I^V = h_I^V \cdot A^I \cdot (T^V - T^I)$$

In Equation 210, A^I is the interface surface area and it depends on the filling ratio in spherical and ellipsoidal tanks. This variable is computed with the geometrical formulas of Appendix B. h_I^V is the heat transfer coefficient between the vapour and the interface. This coefficient is estimated with the Equation 203 of the semi-empirical approach (see Section 4.6 of Chapter 4). The Nusselt's number in Equation 203 is estimated with as it is described in Section 2 of Appendix N, for flat cold horizontal surface facing upward. If the surface is hotter than the vapour, the Nusselt's number is described with the formulas of Section 2 of Appendix N, for flat warm horizontal surface facing upward. This condition rarely occurs.

5.3. Liquid-to-interface heat transfer

As experimentally observed during the steady state [1], [2], the liquid moves from the wall to the centre of the storage container near the free-surface. This movement is proportional to the mass flow rate of the wet side wall boundary layer. During this movement, the heat is transferred to interface in different steps as explained in Section 4.3.1 of Chapter 1.The heat transferred depends on the energy carried by this flow, thus the temperature in this boundary layer. Each of these steps is characterized by a region where the heat is transferred from the lower region to the upper one by conduction or convection. Each of these regions causes a resistance in transferring the heat from the wall-to-centre mass flow to the interface. Due to the lack of experiments and models for describing the heat transfer in these regions, the liquid-to-interface heat transfer is proportional to the mass flow of the wet side wall, and to the difference in temperatures between the interface and the temperature in the side wall. Hence, the liquid-to-interface heat transfer is calculated as follows:

Equation 211 $$\dot{Q}_I^L = \dot{m}_{BL}^I \cdot C_P^L \cdot (T_{BL}^I - T^I)$$

In Equation 211, $\dot{m}_{BL}^I$ and T_{BL}^I are the boundary layer mass flow and temperature of the wet boundary layer at the last sub-layer. These variables are computed with the Integral Boundary layer (IBL) approach of the Storage Boundary Layer (SBL) model (see Section 3.4 of Chapter 4). Hence, the liquid-to-interface heat transfer can be estimated after the SBL model, as explained in Figure 59.

5.4.Net mass flow

As said in Section 5, the net mass flow ($\dot{m}_N$) is the difference in mass flow between the evaporation and the condensation. Hence, this flow can be computed as follows.

Equation 212 $$\dot{m}_N = \dot{m}_E - \dot{m}_C$$

In Equation 212, the mass flow $\dot{m}_E$ and $\dot{m}_C$ cannot be computed because the saturation approach is chosen, due to the hypothesis of local equilibrium condition (assumption c) of Section 1.1 of Chapter 4). Hence, the net mass flow must be deduced from the energy balance equation at the interface (Equation 209). In Equation 209, the mass flow $\dot{m}_E$ and $\dot{m}_C$ can be grouped in the right part of energy balance equation at the interface and this conservation laws can be written as follows:

Equation 213 $$\dot{Q}_I^V + \dot{Q}_I^L + \beta \cdot \dot{Q}_W^{LV} = \dot{m}_E \cdot \left[\tilde{h}_S^V(P^V) - \tilde{h}_S^L(P^V)\right] + \dot{m}_C \cdot \left[\tilde{h}_S^L(P^V) - \tilde{h}_S^V(P^V)\right]$$

In Equation 213, the difference $\left[\tilde{h}_S^V(P^V) - \tilde{h}_S^L(P^V)\right]$ is the latent heat of evaporation ($\Delta\widetilde{H}_{EV}(P^V)$). Hence, Equation 213 can be written as follows:

Equation 214 $$\dot{Q}_I^V + \dot{Q}_I^L + \beta \cdot \dot{Q}_W^{LV} = \dot{m}_E \cdot \Delta\widetilde{H}_{EV}(P^V) - \dot{m}_C \cdot \Delta\widetilde{H}_{EV}(P^V)$$

In the right part of Equation 214, the latent heat of evaporation can be grouped and the difference $\dot{m}_E - \dot{m}_C$ can be substituted by the net mass flow of Equation 212. Equation 214 can be written as follows:

Equation 215 $$\dot{Q}_I^V + \dot{Q}_I^L + \beta \cdot \dot{Q}_W^{LV} = \dot{m}_N \cdot \Delta\widetilde{H}_{EV}(P^V)$$

If the left and the right parts of Equation 215 are divided by the latent heat of evaporation, the net mass flow can be computed as follows:

Equation 216 $$\dot{m}_N = \frac{\dot{Q}_I^V + \dot{Q}_I^L + \beta \cdot \dot{Q}_W^{LV}}{\Delta\widetilde{H}_{EV}}$$

To compute the net mass flow from Equation 216, the values of $\dot{Q}_I^V$, $\dot{Q}_I^L$ and $\dot{Q}_W^{LV}$ are required. $\dot{Q}_W^{LV}$ is computed with the Storage Heat Transfer (SHT) model (see Section 4.5 of Chapter 4). So, the Interface heat transfer (IHT) model is computed after the SHT model, as described in Figure 59. In the IHT model, this mass flow is calculated after computing $\dot{Q}_I^V$ and $\dot{Q}_I^L$ with the equations of Section 5.2 and 5.3 of Chapter 4.

6. Boil-off rate Model: approach for homogeneous model

The Boil-Off Rate (BOR) model is the Block 3 of the homogeneous model (H model), as it is described in Figure 59. This model computes the effective heat transfer coefficient (h_{eff}) and the corrective coefficients α and β. Block 3 of the homogeneous model (H model) is presented after the Storage Boundary Layer (SBL) and the Storage Heat transfer (SHT) models because they are used in the BOR model.

The effective heat transfer coefficient of the BOR model of the equilibrium model (EQ model) reduces with the decrement of filling ratio for the same storage container, as proved when this model was applied to the experimental data (see Section 7.1 of Chapter 3). This behaviour is physically inaccurate and a new BOR model for the H model is proposed, respecting the coherency with the hypotheses of the H model and of the SHT model. As explained in Section 4, the hypothesis of total homogeneity (assumption a) of Section 1.1 of Chapter 4) neglects the bulk and wall temperature gradient in the ullage. The thickness of the side wall is usually unknown. So, the corrective coefficients α and β are applied at the dry side wall-to-vapour and at the dry side wall-to-interface heat transfers. These coefficients (α and β) and the effective heat transfer coefficient (h_{eff}) are computed with the energy balance equations at wall and at the ullage during the experiments for obtaining the value of the nominal BOR or heat input at low and at high filling ratio.

Section 6.1 presents the hypothesis of the BOR model. Section 6.2 discusses the energy balance equations to compute the effective heat transfer coefficient and the corrective coefficients. Section 6.2.2 explains the structure of the BOR model.

6.1.Hypotheses

The heat input is the main factor that controls the behaviour of the cryogenic liquids in small scale storage containers. After building the storage container, the Boil-off Rate is measured as average value of the amount of liquid evaporated over a steady state evaporation of 24 hours. At least two experimental tests are required, respectively at high and low filling ratio. Three coefficients, which are the effective heat transfer coefficient (h_{eff}) and the corrective coefficients α and β, must be computed. The following assumptions are required:

a) The ullage and the liquid are at steady state;
b) The liquid is at the saturation point at the pressure of the ullage;
c) The wet side wall and the bottom wall are considered as one wall, which is called wet walls;
d) The values of BOR and of ullage temperature are measured at high and low filling ratio, at least. The liquid level is high when the value is above 80 %. The filling ratio is low if the value is below 30 %. The test at high and low filling ratio are respectively called Test 1 and 2;
e) For the highest filling ratio, the corrective coefficient α is equal to 1;
f) The Storage Boundary Layer (SBL) model can predict the fluid-dynamics in the liquid and in the vapour;
g) The Storage Heat Transfer (SHT) model can describe the heat transfer at the walls of the storage container;

Assumption a) of Section 6.1 is called *hypothesis of steady state*. Assumption b) of Section 6.1 is called *hypothesis of saturated liquid*. Assumption c) of Section 6.1 is called *hypothesis of unique wet wall*. As consequence of this hypothesis, the vapour can be overheated. Assumption e) of Section 6.1 is called the *hypothesis of the exact heat transfer coefficient* because the dry side wall-to-vapour heat transfer coefficient of the SHT model is not adjusted with the coefficient α.

With these hypotheses, the storage container can be described by Figure 72. Figure 72 describes the storage container that results from these assumptions. In Figure 72, the orange and blue are respectively the thermally stratified ullage and the liquid. The green arrow is the net mass flow. The yellow dashed line is the interface. The black arrow is the BOG. The red arrows are the internal heat transfers and the white arrows with red borders are the heat transfer from the environment to the internal surface. The white circles with the purple borders are the wall temperatures.

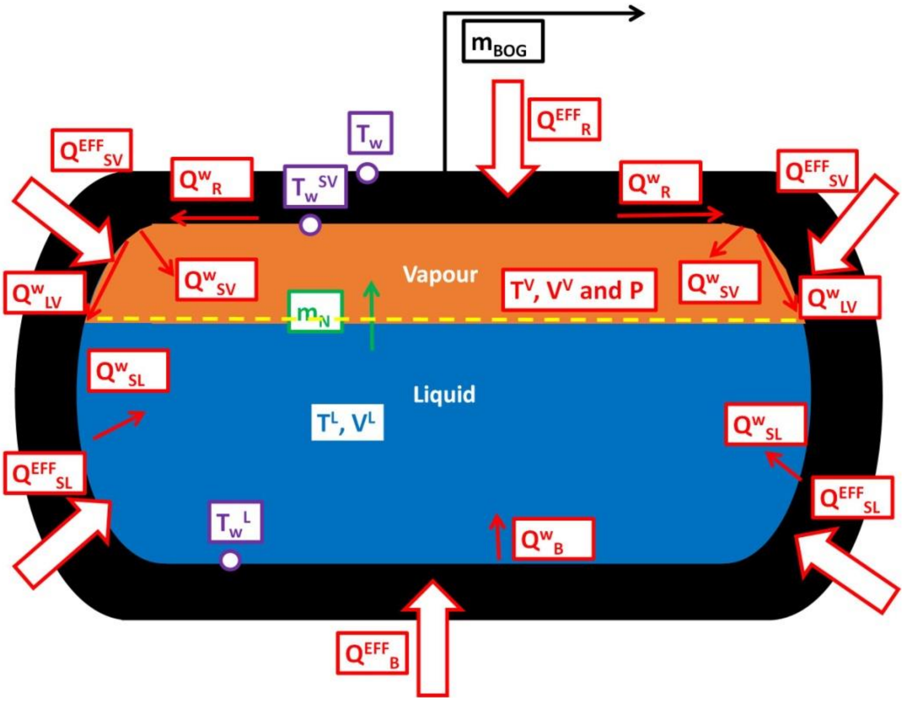

Figure 72. Storage containers in the BOR model for H model.

As shown in Figure 72, the heat ingress across the wet side and the bottom walls entirely ends up in the liquid and they are completely evacuated at the interface, due to the hypothesis of saturated liquid (Assumption b) of Section 6.1 of Chapter 4). Regarding the ullage, the heat flows as it is described by Figure 58 (see Section 1.1 of Chapter 4). The heat of the environment is partially transferred to the interface by conduction at the dry side wall and the remaining part ends up in the vapour, as sensible heat. Part of this sensible heat is transferred to the interface, as seen in Figure 72.

6.2. Balance equations of the Boil-Off Rate model

The Boil-Off Rate (BOR) model computes the effective heat transfer coefficient (h_{eff}) and the corrective coefficients α and β. Hence, three equations are required, at least, to determine the mathematical system. These equations can be deduced from the balance equations of energy at the control volumes of the storage containers. Six control volumes are defined in the storage container for the BOR model, as it illustrated in Figure 73. In Figure 73 (a), the white arrows with red border indicate the heat flows. The red, the green and the black lines respectively refer to the BOG flow, the enthalpy flows and the net mass flow. The yellows dashed line is the interface. In Figure 73 (b) and (c), the black rectangles are the wall, the white circles white purple border are the wall temperatures.

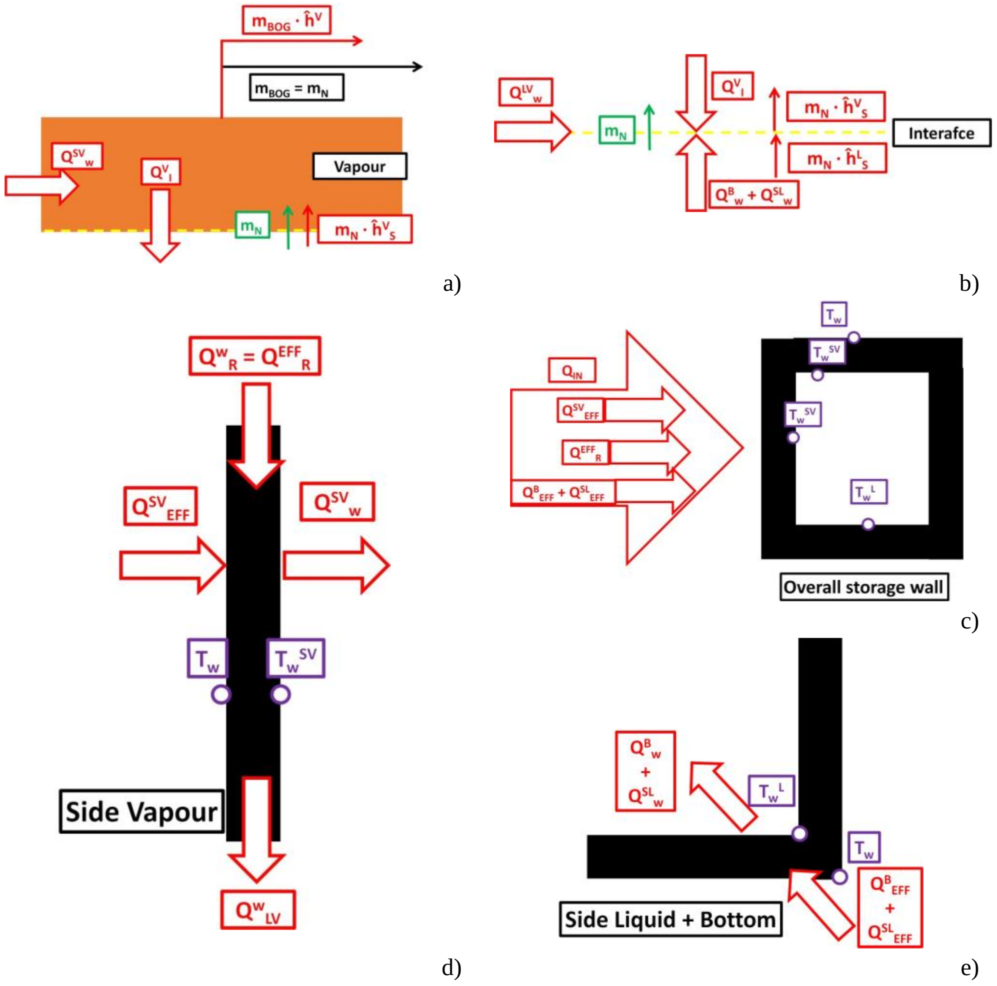

Figure 73. Control volumes of the BOR model: a) Vapour at steady state; b) Interface c) overall wall of the storage container; d) Dry side wall; e) wet walls (bottom and side wall).

Due to the hypothesis of steady state vapour (assumption a) of Section 6.1 of Chapter 4), the mass and energy cannot be accumulated in the ullage. Hence, the net mass flow is equal to the Boil-off Gas (BOG) flow, as it is illustrated in Figure 73 (a). The heat transferred between the dry side wall and the vapour is absorbed by the enthalpy flows. The remaining part is exchanged at the interface. As described in Figure 73 (b) and (c), the heat entering in the walls of the storage container is not accumulated due to the hypothesis of negligible thermal inertia (assumption e) of Section 4.1 of Chapter 4). As consequence, the heat coming from the environment to the wet walls is completely transferred to the liquid. Due to the hypothesis of saturated liquid (assumption b) of Section 6.1 of Chapter 4), this energy flow is entirely exchanged at the interface, as it is shown in Figure 73 (b). The vapour side receives heat from the roof by conduction and from the environment. Due to the hypothesis of negligible thermal inertia (assumption e) of Section 4.1 of Chapter 4), the overall entering heat is divided into the dry side wall-to-interface flow and into the dry side wall-to-vapour flow. As consequence, the energy conservation laws at these control volumes are the ones reported in Table 82.

Table 82. Energy conservation laws of the BOR model.

Control volume	Equation	Formula
Steady state vapour energy balance	Equation 217	$(A^{SV}+A^{R})\cdot(T^{W}-T_{W}^{SV})-\beta\cdot\dot{Q}_{W}^{LV}-\dot{Q}_{I}^{V}=\dot{m}_{BOG}\cdot\left[\tilde{h}^{V}(T^{V},P^{V})-\tilde{h}_{S}^{V}(P^{V})\right]$
Steady state mass balance	Equation 218	$\dot{m}_{N}=\dot{m}_{BOG}$
Interface energy balance	Equation 219	$\dot{Q}_{I}^{V}+h_{eff}\cdot[(A^{SL}+A^{B})\cdot(T^{W}-T_{W}^{L})]+\beta\cdot\dot{Q}_{W}^{LV}=\dot{m}_{N}\cdot\Delta\widetilde{H}_{EV}(P^{V})$

Table 82. Energy conservation laws of the BOR model.

Overall storage wall energy balance	Equation 220	$\dot{Q}_{IN} = h_{eff} \cdot [(A^{SL} + A^{B}) \cdot (T^{W} - T_{w}^{L}) + (A^{SV} + A^{R}) \cdot (T^{W} - T_{w}^{SV})]$
Wet walls energy balance	Equation 221	$\left(h_{w}^{SL} \cdot A^{SL} + h_{w}^{B} \cdot A^{B}\right) \cdot (T_{w}^{L} - T^{L}) = h_{eff} \cdot [(A^{SL} + A^{B}) \cdot (T^{W} - T_{w}^{L})]$
Dry side wall energy balance	Equation 222	$\alpha \cdot h_{w}^{SV} \cdot A^{SV} \cdot (T_{w}^{SV} - T^{V}) + \beta \cdot \dot{Q}_{LV}^{w} = h_{eff} \cdot (A^{SV} + A^{R}) \cdot (T^{W} - T_{w}^{SV})$

$\dot{Q}_{I}^{V}$ and $\dot{Q}_{W}^{LV}$ are respectively computed as described in Section 5.2 and 4.5. As it is indicated in Table 82, the value of the Boil-Off Rate (BOR) is not present in any equation. The values of the overall heat input ($\dot{Q}_{IN}$) can be given as input parameter or it can be calculated from the value of the BOR, as it is explained in Section 6.2.1.

6.2.1. Calculation of the overall heat inputs

Due to the hypothesis of steady state vapour (assumption a) of Section 6.1 of Chapter 4) and the hypothesis of saturated liquid (assumption b) of Section 6.1 of Chapter 4), all the heat coming from the environment evaporates the liquid and it warms up the ullage. Hence, the overall energy balance equation of the storage container can be described as follows:

Equation 223
$$\dot{Q}_{IN} = \dot{m}_{BOG} \cdot \left[\Delta\widetilde{H}_{EV}(P^{V}) + \Delta\widetilde{H}_{V}\right]$$

$\Delta\widetilde{H}_{V}$ is the enthalpy of the overheated vapour and it is equal to $\left[\tilde{h}^{V}(T^{V}, P^{V}) - \tilde{h}_{S}^{V}(P^{V})\right]$. As explained in Section 3.2 of Chapter 3, the Boil-Off Gas flow ($\dot{m}_{BOG}$) can be calculated from the Boil-Off Rate (BOR) as follows:

Equation 224
$$\dot{m}_{BOG} = BOR \cdot \rho_{S}^{L} \cdot V^{L}$$

ρ_{S}^{L} is the saturated density of the liquid at the pressure of the ullage and V^{L} is the initial liquid volume. Hence, the of the overall heat input ($\dot{Q}_{IN}$) can be computed from the BOR as follows:

Equation 225
$$\dot{Q}_{IN} = BOR \cdot \rho_{S}^{L} \cdot V^{L} \cdot \left[\Delta\widetilde{H}_{EV}(P^{V}) + \Delta\widetilde{H}_{V}\right]$$

In Equation 255, BOR is given in 1/s.

6.2.2. Algorithm of the Boil-Off Rate model

As indicated in Table 82, the mathematical system is composed of six equations. The number of the variables of the BOR model is seven: h_{eff}, α, β, $\dot{m}_{N}$, T_{w}^{L}, and T_{w}^{SV}. So, this system is under defined because there are more variables than equations. Due to hypotheses d) and e) of Section 6.1 of Chapter 4, the calculation of these variables can be separated into two algorithms, respectively called h_{eff} algorithm and α algorithm. In both algorithms, β, $\dot{m}_{N}$, T_{w}^{L}, and T_{w}^{SV} are computed. The corrective variable β is calculated with the β algorithm in the h_{eff} algorithm.

The structure of the algorithm of BOR model is described in Figure 74.

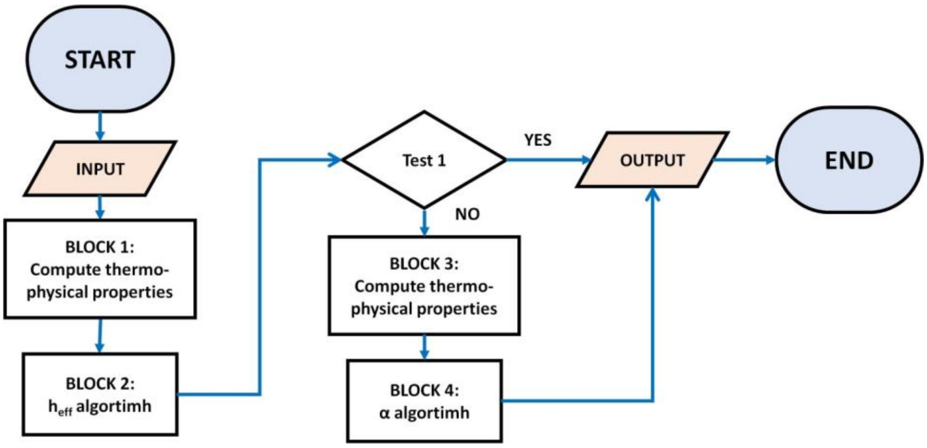

Figure 74. Algorithm of BOR model.

This algorithm is composed by the following steps:

a) BLOCK 1. The thermo-physical properties of liquid and vapour are calculated with the value of pressure, vapour temperature and saturated liquid temperature of the test at the high filling ratio (Test 1). This calculation is done with the reference models of Chapter 3;

b) BLOCK 2. The effective heat transfer (h_{eff}) algorithm is applied for Test 1. This mathematical procedure computes the values of the effective heat transfer coefficient and of the corrective coefficient β, under the hypothesis of the exact heat transfer coefficient. In this algorithm, the variables $\dot{m}_N$, T_w^L, and T_w^{SV} are calculated too. Two pathways are present:
   - Pathway 1.2 (P 1.2). If the BOR model is applied just for Test 1, the algorithm stops;
   - Pathway 2.2 (P 2.2). when the BOR model is used just for Test 2, the algorithm goes to Block 3 (step c) of Section 6.2.2 of Chapter 4)

c) BLOCK 3. The thermo-physical properties of liquid and vapour are computed with the value of pressure, vapour temperature and saturated liquid temperature of the Test 2 (test at low filling ratio). This calculation is done with the reference models of Chapter 3;

d) BLOCK 4. The α algorithm is used for the test at low filling ratio (Test 2) to compute the corrective coefficients α and β. In this algorithm, the variables $\dot{m}_N$, T_w^L, and T_w^{SV} are calculated too. After this block, the algorithm stops;

The details of the h_{eff}, α and β algortimhs are given in Appendix R.

7. Comparison with experimental data

As done for the equilibrium model (EQ model), the results of the homogeneous model (H model) are compared with the experimental, average temperatures and of filling ratios of the different study cases (see Table 54). These data are grouped in three categories: low, medium and high heat fluxes. The results of the pressure, liquid and vapour average temperatures, net mass flow and heat transfer at interface are discussed because these variables describe the main differences with the EQ model. Firstly, the heat transfer at interface is described because it affects the net mass flow. Then, the time-evolution of this mass flow rate is discussed because it causes the self-pressurisation. At the end, the results of the pressure and the temperatures are presented and discussed. The computational results of heat inputs and filling ratio are not presented because they are similar to the ones obtained from the EQ model. The procedures to set the initial conditions and to simulate the storage containers are the same used for the EQ model. The effective heat transfer coefficient, the corrective coefficients α and β, which define the obundayr conditions, are computed with the Boil-Off Rate (BOR) model. Test 1 and 3 of Study case 1, Test 1 of Study case 2, Test 1 and 2 of Study case 3, Test 1 of Study case 5, Test 1 and 4 of Study case 6 and Test 1 of Study case 7 are considered as the Test 1 of BOR model. The other tests of the Study cases are considered as Test 2 of BOR model. Only the initial values of the temperatures, heat inputs, effective heat transfer coefficient and the corrective coefficients are reported.

Section 7.1, 7.2 and 7.3 present the results of the H model and the comparison with experimental data of ullage and liquid temperatures, and pressure for the study cases at low, medium and high heat fluxes, respectively.

7.1. Study cases: low heat fluxes

The study cases at low heat fluxes are reported in Table 54. In Table 83, the boundary and the initial condition of temperature are reported at the beginning of the self-pressurisation.

Table 83. Initial conditions and boundary conditions for the self-pressurisation stage for Study cases at low heat fluxes.

Sub-case	$h_{eff}\left[\frac{W}{m^2\cdot K}\right]$	$\alpha\,[-]$	$\beta\,[-]$	$\dot{Q}\,[W]$		$T^V\,[K]$		$T^L\,[K]$	
				Exp	**H**	**Exp**	**H**	**Exp**	**H**
Study case 1									
Test 1	0.03045	1	2.042	1.331	1.331	77.41	77.41	77.02	77.24
Test 2	0.03045	$2.863\cdot10^{-3}$	$2.141\cdot10^{-2}$	1.163	1.163	78.91	78.92	77.03	77.21
Test 3	0.06033	1	1.572	2.618	2.618	80.48	80.54	77.14	77.19
Test 4	0.03045	$2.568\cdot10^{-3}$	$1.644\cdot10^{-2}$	1.034	1.033	80.47	80.49	76.93	77.21
Test 5	0.03045	$1.685\cdot10^{-3}$	$5.523\cdot10^{-2}$	0. 9183	0.9182	81.05	81.08	76.84	77.20
Test 6	0.03045	$1.144\cdot10^{-3}$	$2.434\cdot10^{-2}$	0.7119	0.7119	81.68	81.59	76.77	77.22
Study case 2									
Test 1	0.02766	1	2.482	1.201	1.201	78.35	78.35	77.76	77.82
Study case 3									
Test 1	0.02211	1	0	82.96	83.04	22.83	21.69	20.24	20.33
Test 2	0.02211	1	0	83.08	83.14	20.25	20.33	20.35	20.33
Study case 4									
Test 1	0.02211	$5.554\cdot10^{-3}$	0	70.30	71.18	23.50	21.89	20.13	22.28
Test 2	0.02211	$3.624\cdot10^{-3}$	0	62.59	63.68	23.66	20.32	20.09	20.33

The values of the effective heat transfer coefficient do not change with the initial filling ratio, except for Test 3 of Study case 1. The values of alpha coefficient decrease as the initial filling ratio reduce.

The value of beta coefficient with the filling ratio is irregular because, for Study case 3 and 4, the values of this variable are equal to zero. The initial values of temperature and heat inputs are almost similar to the experimental ones. The largest difference in initial vapour temperature between the experimental and the model occurs for Test 1 of Study cases 3 and 4, in which the value of beta is equal to zero.

7.1.1. Presentation of the results: heat transfer at interface

Figure 75 shows the evolution in time of heat transfers at interface, computed with the Interface Heat Transfer (IHT) model (see Section 5 of Chapter 5). The heat transfer at the interface is composed by three heat flows: liquid-to-interface ($\dot{Q}_I^L$), the vapour-to-interface ($\dot{Q}_I^V$) and the dry side wall-to-interface ($\dot{Q}_w^{LV}$). These flows are respectively computed with Equation 211, Equation 210 and Equation 201. The solid, the dotted and the dashed lines respectively indicate the $\dot{Q}_I^L$, the $\dot{Q}_I^V$ and $\dot{Q}_w^{LV}$. These heat inputs at the interface are noted as QLI, QVI and QwLV, respectively. The colours refer to the different tests, and the use of these colours is reported in each graphs.

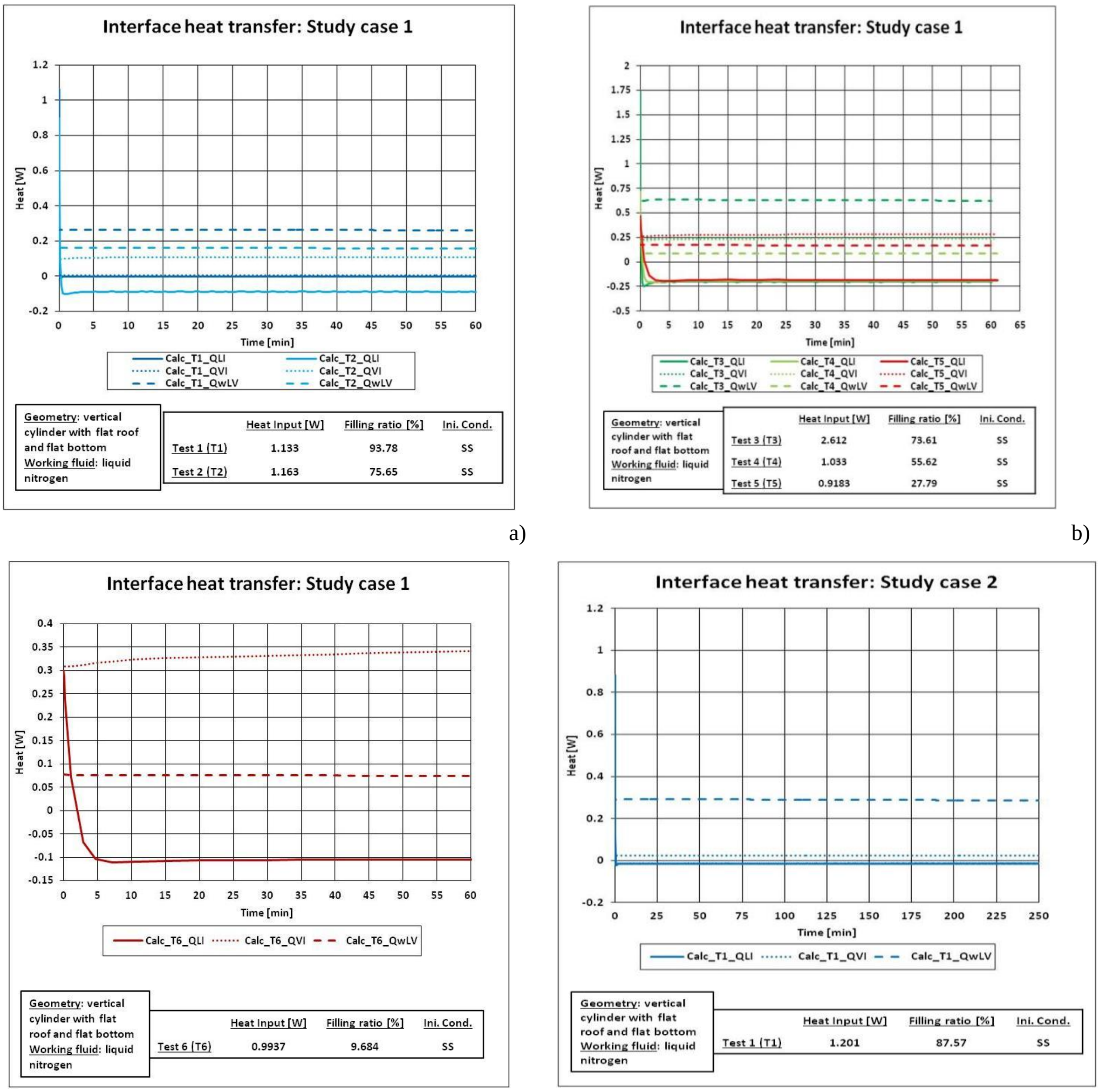

a) **Geometry**: vertical cylinder with flat roof and flat bottom **Working fluid**: liquid nitrogen

	Heat Input [W]	Filling ratio [%]	Ini. Cond.
Test 1 (T1)	1.133	93.78	SS
Test 2 (T2)	1.163	75.65	SS

b) **Geometry**: vertical cylinder with flat roof and flat bottom **Working fluid**: liquid nitrogen

	Heat Input [W]	Filling ratio [%]	Ini. Cond.
Test 3 (T3)	2.612	73.61	SS
Test 4 (T4)	1.033	55.62	SS
Test 5 (T5)	0.9183	27.79	SS

c) **Geometry**: vertical cylinder with flat roof and flat bottom **Working fluid**: liquid nitrogen

	Heat Input [W]	Filling ratio [%]	Ini. Cond.
Test 6 (T6)	0.9937	9.684	SS

d) **Geometry**: vertical cylinder with flat roof and flat bottom **Working fluid**: liquid nitrogen

	Heat Input [W]	Filling ratio [%]	Ini. Cond.
Test 1 (T1)	1.201	87.57	SS

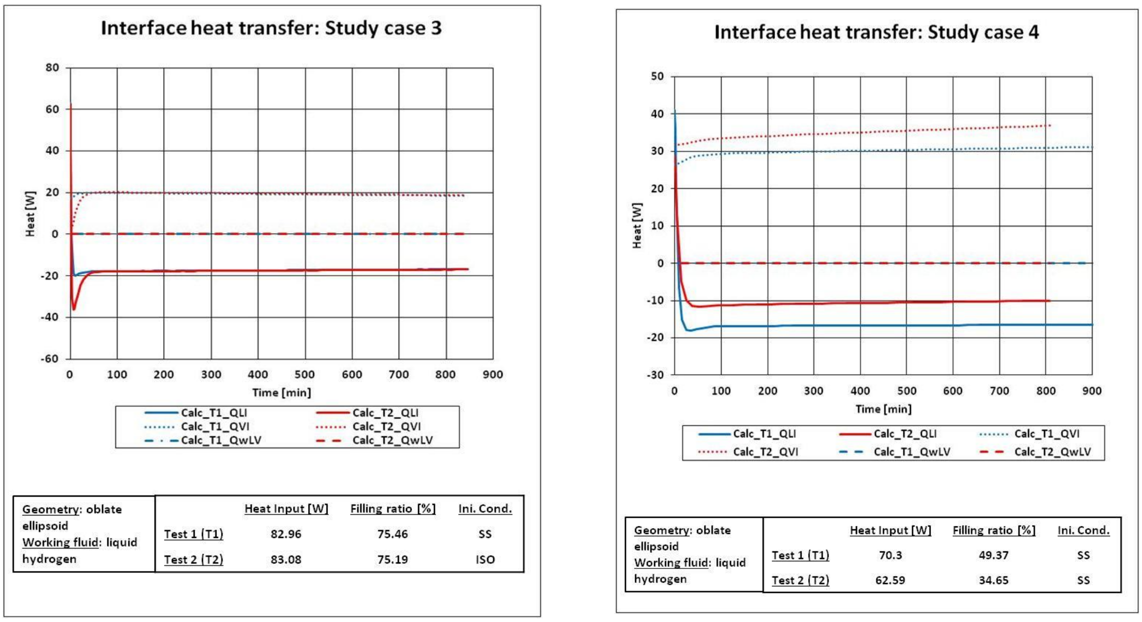

e) f)

Figure 75. Heat transfer at the interface for the Study cases at low heat fluxes: a) Study case 1 (Test 1 and Test 2), b) Study case 1 (Test 3, 4 and 5), c) Study case Test 6, d) Study case 2, e) Study case 3 and f) Study case 4.

The time-evolution of $\dot{Q}_I^L$ can be decomposed into two phases: *initial transient* and *constant behaviour*. In this stage, the heat is initially transferred from the liquid to the interface. Then, $\dot{Q}_I^L$ decreases, reaching negative values. Hence, the heat is transferred from the interface to the liquid. This decrement occurs when the thermodynamic state of the liquid changes from overheated to sub-cooled (see Section 7.1.5 of Chapter 4). When the initial filling ratio increases, the initial is short and the shape of this transient is sharp. At fixed filling ratio, the increment of the heat input reduces the initial transient and the decrement of $\dot{Q}_I^L$ is quicker than the one at low heat leakage. When the self-pressurisation starts at isothermal condition, $\dot{Q}_I^L$ decreases more than the one at the steady state condition. Hence, the decrement of $\dot{Q}_I^L$ is increased with the incrcement of the heat inputs and with the increment of the filling ratio. The isothermal initial conditions increases the decrement of $\dot{Q}_I^L$. This decrement of the $\dot{Q}_L^l$ stops when the steady state or the minimum values are reached. Then, the constant behaviour stage occurs. In this stage, $\dot{Q}_I^L$ remains constant with time.

$\dot{Q}_I^V$ is almost constant during the self-pressurisation and a small initial transient is observed for Study case 3 and 4. This transient occurs during the initial increment of the ullage temperature (see Section 7.1.4 of Chapter 4). The values of $\dot{Q}_I^V$ are higher at low filling ratio than the ones at high liquid level.

$\dot{Q}_W^{LV}$ is constant during the self-pressurisation. The value of this heat flow is usually lower than the one of $\dot{Q}_I^V$, except for Test 1 and 3 of Study case 1, for Test 1 of Study case 2. In these tests, the value of the corrective coefficient α is equal to 1 (see Table 83) and the interfacial surface area is lower than the one computed for Study case 3 and 4. The value of the dry side wall-to-interface heat transfer is equal to zero for Study case 3 and 4 because beta is null.

7.1.2. Presentation of the results: net mass flow

Figure 76 describes how the net mass flow ($\dot{m}_N$) changes during the self-pressurisation for the Study cases at low heat fluxes. The colours used in each graphs is reported in the corresponding legend. The net mass flow is computed with Equation 216, applying the Interface Heat Transfer (IHT) model (see Section 5.4 of Chapter 4).

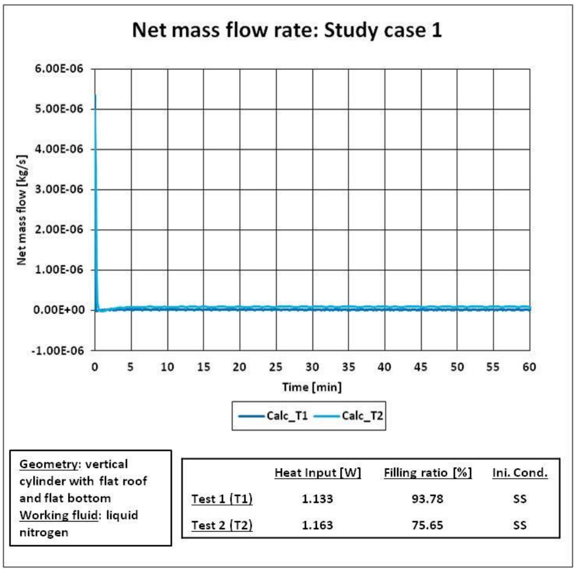

Geometry: vertical cylinder with flat roof and flat bottom
Working fluid: liquid nitrogen

	Heat Input [W]	Filling ratio [%]	Ini. Cond.
Test 1 (T1)	1.133	93.78	SS
Test 2 (T2)	1.163	75.65	SS

a)

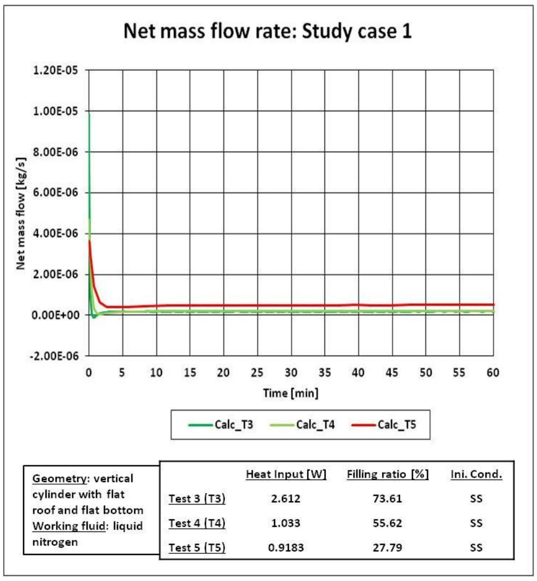

Geometry: vertical cylinder with flat roof and flat bottom
Working fluid: liquid nitrogen

	Heat Input [W]	Filling ratio [%]	Ini. Cond.
Test 3 (T3)	2.612	73.61	SS
Test 4 (T4)	1.033	55.62	SS
Test 5 (T5)	0.9183	27.79	SS

b)

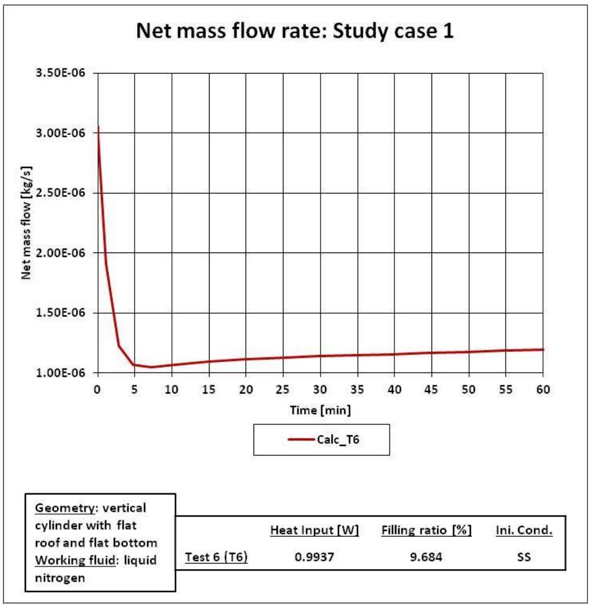

Geometry: vertical cylinder with flat roof and flat bottom
Working fluid: liquid nitrogen

	Heat Input [W]	Filling ratio [%]	Ini. Cond.
Test 6 (T6)	0.9937	9.684	SS

c)

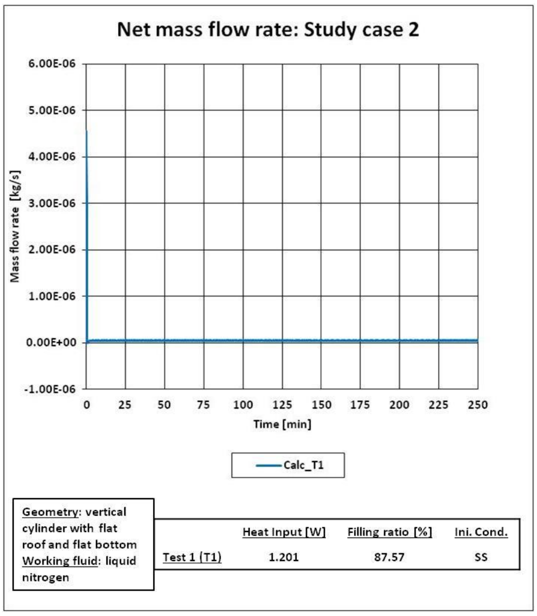

Geometry: vertical cylinder with flat roof and flat bottom
Working fluid: liquid nitrogen

	Heat Input [W]	Filling ratio [%]	Ini. Cond.
Test 1 (T1)	1.201	87.57	SS

d)

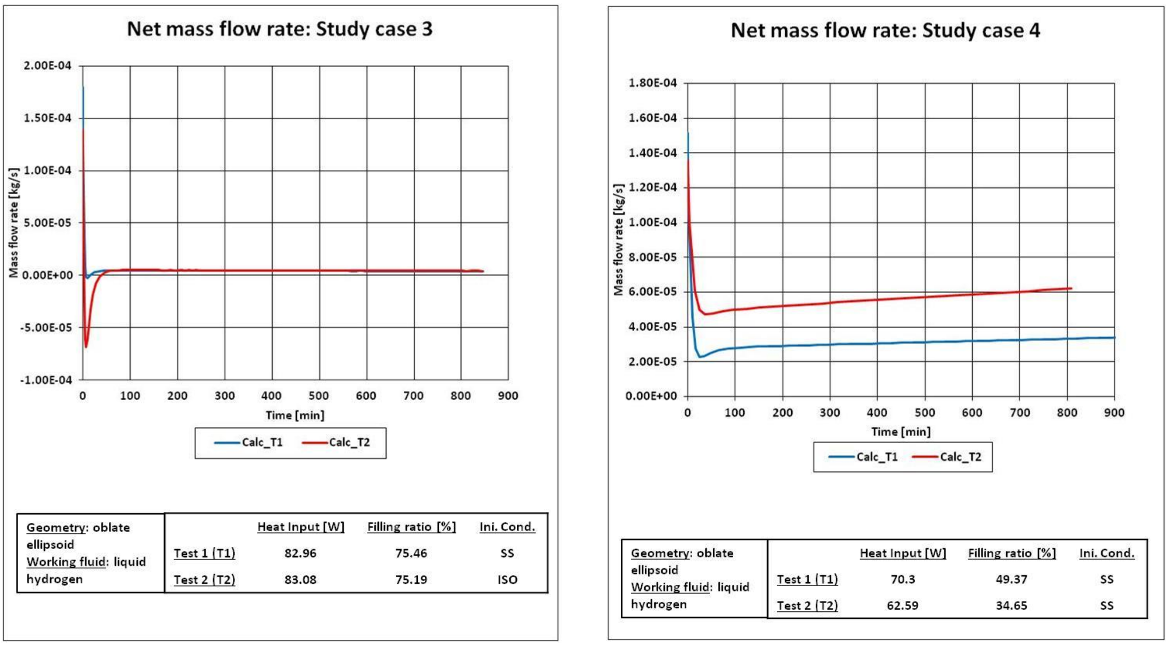

e) f)

Figure 76. Net mass flow for the Study cases at low heat fluxes: a) Study case 1 (Test 1 and Test 2), b) Study case 1 (Test 3, 4 and 5), c) Study case Test 6, d) Study case 2, e) Study case 3 and f) Study case 4.

As for the liquid-to-interface heat transfer, the behaviour of the net mass flow ($\dot{m}_N$) can be decomposed into the stages: *initial transient* and *constant behaviour*.

In the initial transient, $\dot{m}_N$ decreases from the steady state value to the stationary value of the self-pressurisation. During this decrement, the values of $\dot{m}_N$ can be negative, as occurs for Study case 3, Study case 2 and Test 1 and 3 of Study case 1. In these tests, $\dot{m}_N$ reaches a minimum in the initial transient. The shape of the initial transient and the slope of this decrement are very similar to the one observed for the liquid-to-interface heat flow ($\dot{Q}_I^L$). Hence, $\dot{m}_N$ is mainly controlled by $\dot{Q}_I^L$ heat transfer during the initial transient. The initial decrement is faster at isothermal condition than at steady state condition. This decrement is faster at high filling ratio than at low liquid level.

In the constant behaviour stage, $\dot{m}_N$ remains positive in the constant behaviour stage, similarly to the vapour-to-interface ($\dot{Q}_I^V$) and dry side wall-to-interface ($\dot{Q}_W^{LV}$) heat flows. Hence, $\dot{m}_N$ is controlled by these heat flows rather than $\dot{Q}_I^L$. In this stage, the net mass flow at low filling ratio is higher than the one at high filing ratio.

7.1.3. Presentation of the results: pressure

Figure 77 describes the time-evolution of the computed and experimentally measured values of pressure. The solid lines are the values computed with homogeneous model (H model), using the pressure evolution (P-e) equation (Equation 149). This equation is obtained from the mass conservation law, as it is described in Section 2 of Chapter 4. The square dots are the experimental data.

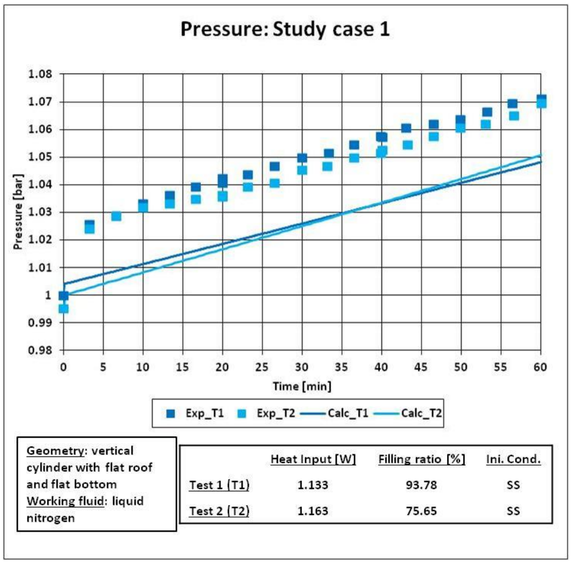

Geometry: vertical cylinder with flat roof and flat bottom
Working fluid: liquid nitrogen

	Heat Input [W]	Filling ratio [%]	Ini. Cond.
Test 1 (T1)	1.133	93.78	SS
Test 2 (T2)	1.163	75.65	SS

a)

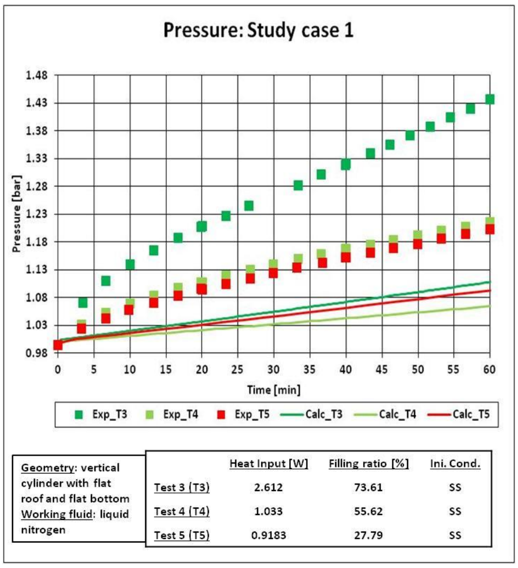

Geometry: vertical cylinder with flat roof and flat bottom
Working fluid: liquid nitrogen

	Heat Input [W]	Filling ratio [%]	Ini. Cond.
Test 3 (T3)	2.612	73.61	SS
Test 4 (T4)	1.033	55.62	SS
Test 5 (T5)	0.9183	27.79	SS

b)

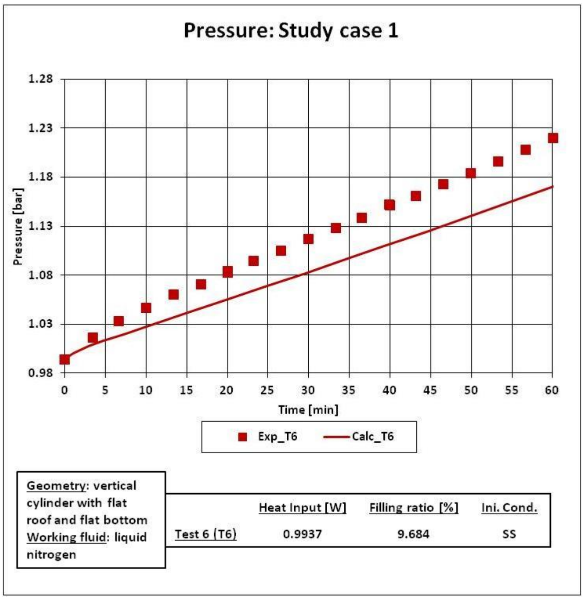

Geometry: vertical cylinder with flat roof and flat bottom
Working fluid: liquid nitrogen

	Heat Input [W]	Filling ratio [%]	Ini. Cond.
Test 6 (T6)	0.9937	9.684	SS

c)

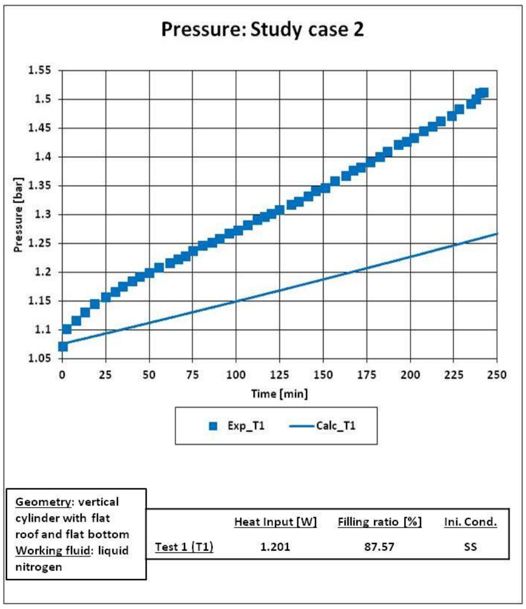

Geometry: vertical cylinder with flat roof and flat bottom
Working fluid: liquid nitrogen

	Heat Input [W]	Filling ratio [%]	Ini. Cond.
Test 1 (T1)	1.201	87.57	SS

d)

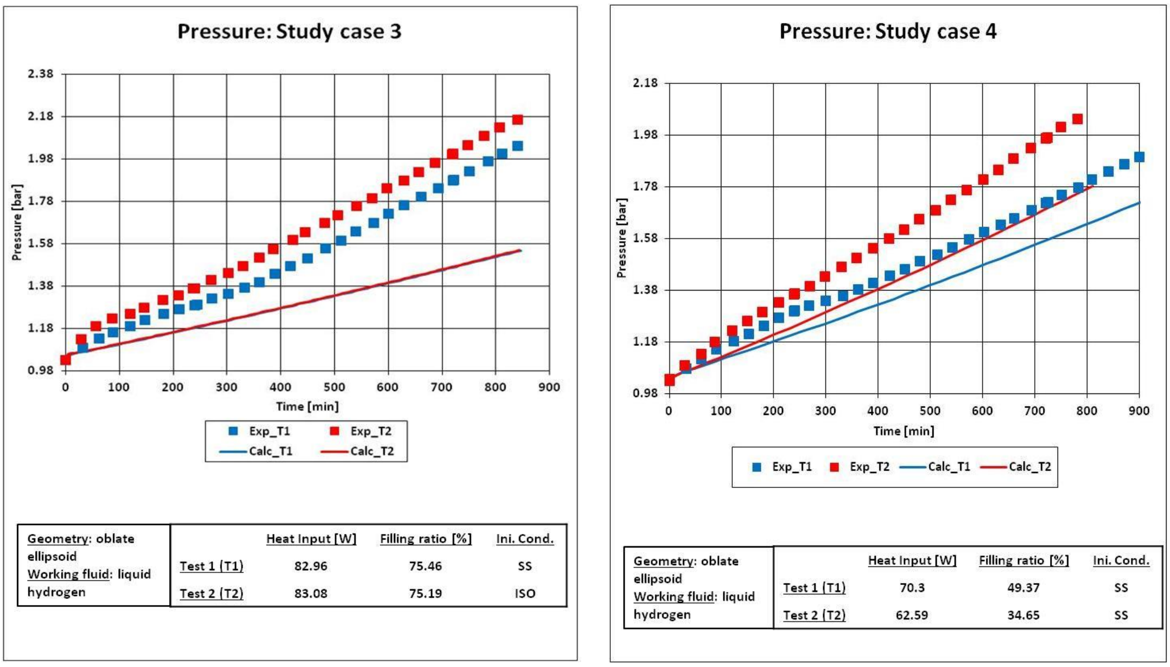

e) f)

Figure 77. Computed and experimental pressure at low heat fluxes: a) Study case 1 (Test 1 and Test 2), b) Study case 1 (Test 3, 4 and 5), c) Study case Test 6, d) Study case 2, e) Study case 3 and f) Study case 4.

The computed pressure always increases in time during the self-pressurisation. The increment of this variable is regular, and it is linear with the time. A small initial transient is calculated for the Study cases at low heat fluxes, but it is almost negligible. The values of the computed pressure are lower than the measured ones. The difference in pressure between the data and the modelling resutls reduces as the initial filling ratio decreases. In particular, at Test 6 of Study case 1, the H model well predicts the self-pressurisation. The self-pressurisation at isothermal initial condition is equal to the one at steady state, as observed for Study case 3. So, the effect of the initial conditions on the self-pressurisation is not correctly described by the homogeneous model (H model). The self-pressurisation at isothermal initial condition is equal to the one at steady state, as observed for Study case 3. For Study case 4, the effect of the interface surface area on the natural pressure build-up of the H model is qualitatively in agreement with the data, as shown by Figure 77 (d).

7.1.4. Presentation of the results: ullage temperature

Figure 78 describes the time-evolution of the computed and of experimentally measured values of the ullage temperature. The ullage temperature is computed with the homogeneous model (H model), using Equation 134, which is deduced from the energy conservation law of the ullage (see Section 2 of Chapter 4). The solid lines are the values computed with H model and the square dots are the experimental data.

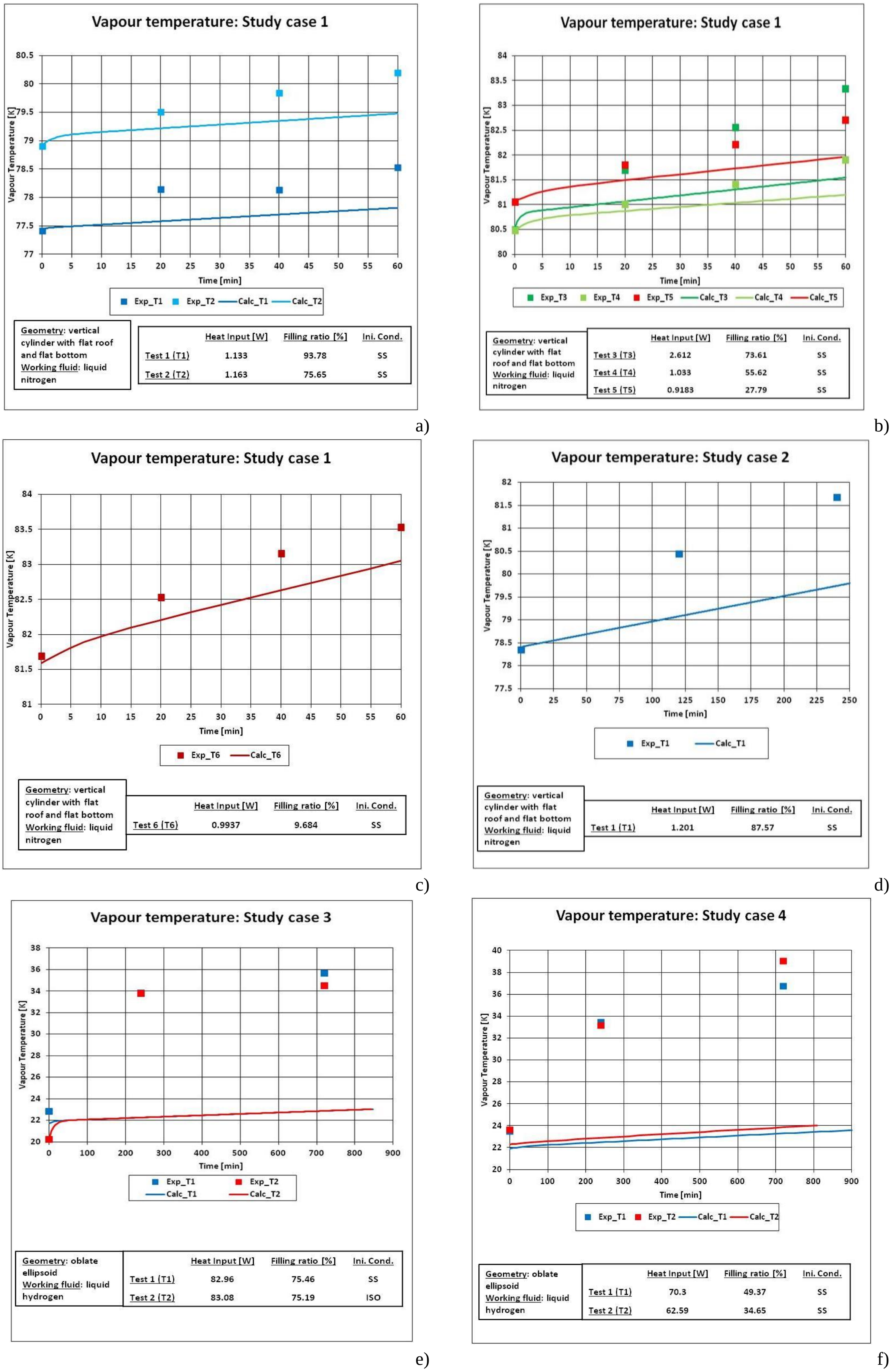

Geometry: vertical cylinder with flat roof and flat bottom
Working fluid: liquid nitrogen

	Heat Input [W]	Filling ratio [%]	Ini. Cond.
Test 1 (T1)	1.133	93.78	SS
Test 2 (T2)	1.163	75.65	SS

a)

Geometry: vertical cylinder with flat roof and flat bottom
Working fluid: liquid nitrogen

	Heat Input [W]	Filling ratio [%]	Ini. Cond.
Test 3 (T3)	2.612	73.61	SS
Test 4 (T4)	1.033	55.62	SS
Test 5 (T5)	0.9183	27.79	SS

b)

Geometry: vertical cylinder with flat roof and flat bottom
Working fluid: liquid nitrogen

	Heat Input [W]	Filling ratio [%]	Ini. Cond.
Test 6 (T6)	0.9937	9.684	SS

c)

Geometry: vertical cylinder with flat roof and flat bottom
Working fluid: liquid nitrogen

	Heat Input [W]	Filling ratio [%]	Ini. Cond.
Test 1 (T1)	1.201	87.57	SS

d)

Geometry: oblate ellipsoid
Working fluid: liquid hydrogen

	Heat Input [W]	Filling ratio [%]	Ini. Cond.
Test 1 (T1)	82.96	75.46	SS
Test 2 (T2)	83.08	75.19	ISO

e)

Geometry: oblate ellipsoid
Working fluid: liquid hydrogen

	Heat Input [W]	Filling ratio [%]	Ini. Cond.
Test 1 (T1)	70.3	49.37	SS
Test 2 (T2)	62.59	34.65	SS

f)

Figure 78. Computed and experimental ullage temperature at low heat fluxes: a) Study case 1 (Test 1 and Test 2), b) Study case 1 (Test 3, 4 and 5), c) Study case Test 6, d) Study case 2, e) Study case 3 and f) Study case 4.

The initial values of the ullage are almost equal to the experimental one. The largest differences in the initial values between the computed and measured ullage temperature are observed for Study cases 3 and 4, where the corrective coefficient β is equal to zero (see Table 83). The computed temperature increases in time with a rate that is lower than the one that is experimentally observed. As a consequence, the calculated temperature always remains lower than the experimental one. A small initial transient is calculated for Study case 1 and 3. For Study case 1, except Test 3, the H model is quantitatively accurate because the difference in ullage temperatures between the calculated and the experimental values is lower than the one of the other Study cases. For Study case 3 and 4, this difference is very high and the computed temperature is much lower than the experimental one.

7.1.5. Presentation of the results: liquid temperature

Figure 79 shows the calculated and the experimental results of liquid temperature, during the self-pressurisation. The liquid temperature is computed with the homogeneous model (H model), using Equation 801, which is deduced from the energy conservation law of the liquid (see Section 2 of Chapter 4). The solid lines are the values computed with H model and the square dots are the experimental data.

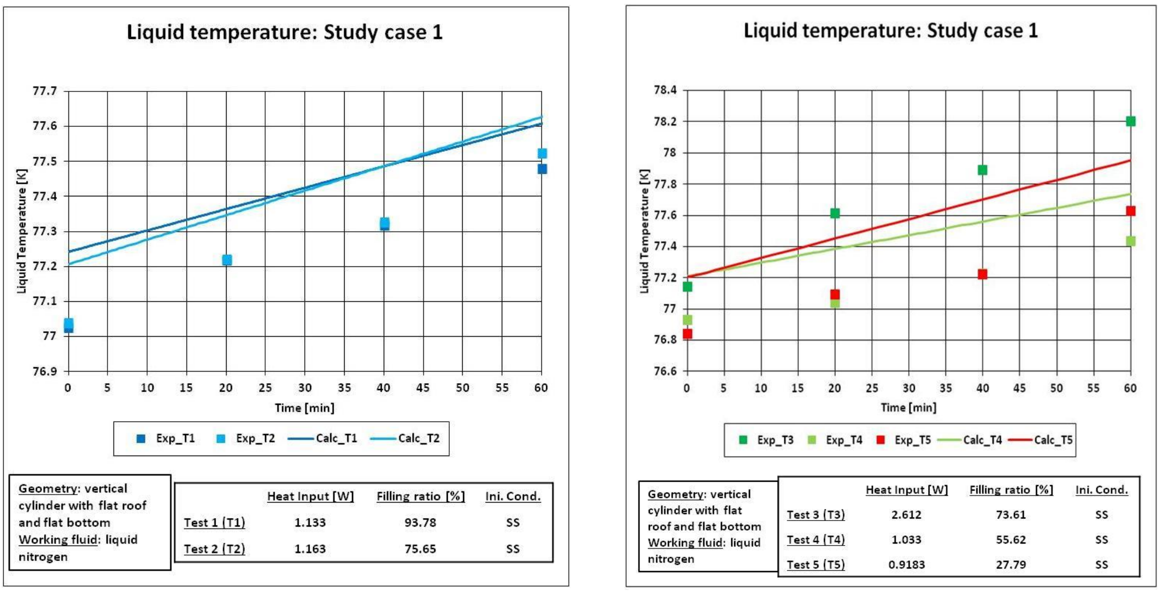

Geometry: vertical cylinder with flat roof and flat bottom
Working fluid: liquid nitrogen

	Heat Input [W]	Filling ratio [%]	Ini. Cond.
Test 1 (T1)	1.133	93.78	SS
Test 2 (T2)	1.163	75.65	SS

Geometry: vertical cylinder with flat roof and flat bottom
Working fluid: liquid nitrogen

	Heat Input [W]	Filling ratio [%]	Ini. Cond.
Test 3 (T3)	2.612	73.61	SS
Test 4 (T4)	1.033	55.62	SS
Test 5 (T5)	0.9183	27.79	SS

a) b)

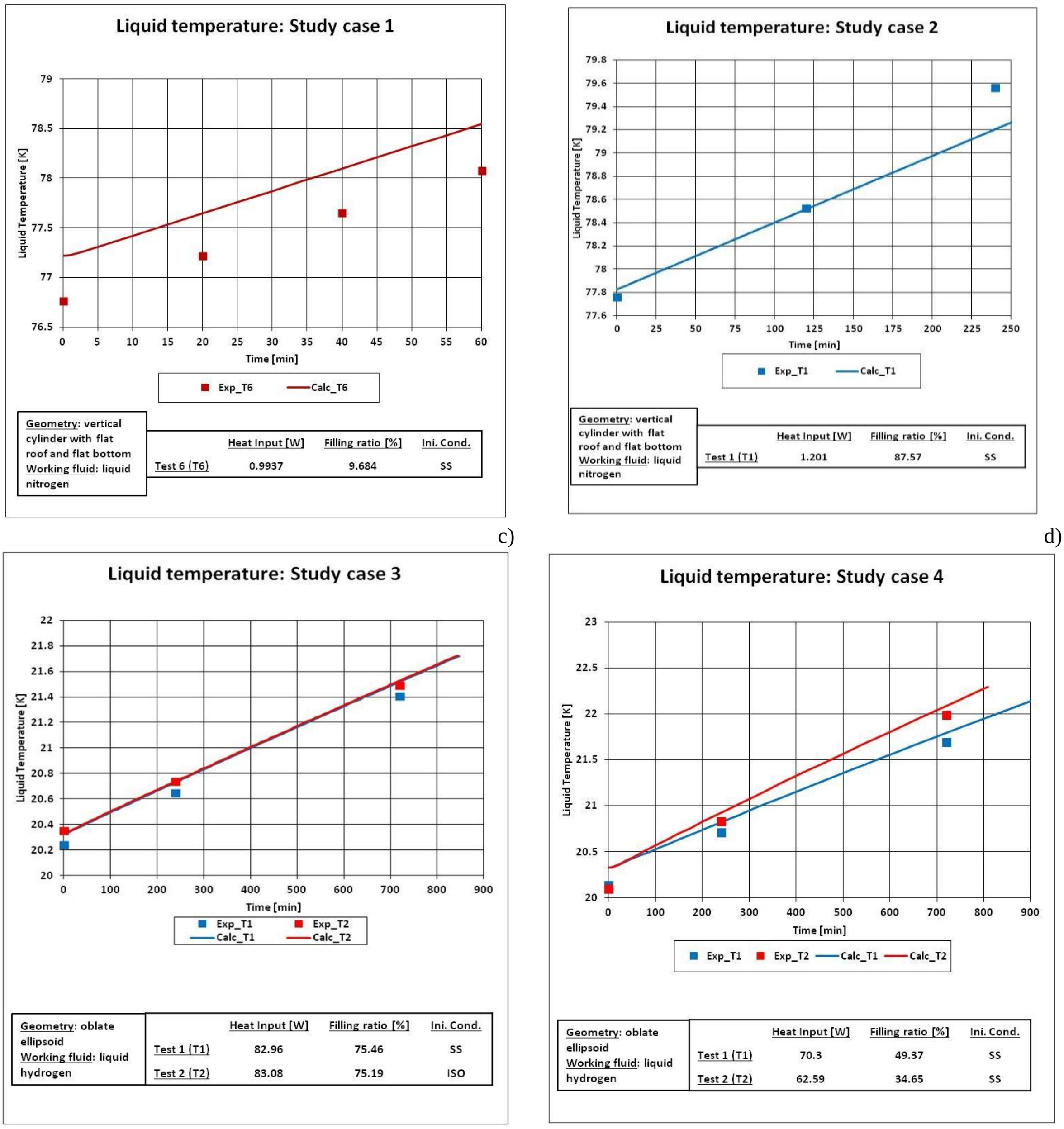

Geometry: vertical cylinder with flat roof and flat bottom
Working fluid: liquid nitrogen

	Heat Input [W]	Filling ratio [%]	Ini. Cond.
Test 6 (T6)	0.9937	9.684	SS

c)

Geometry: vertical cylinder with flat roof and flat bottom
Working fluid: liquid nitrogen

	Heat Input [W]	Filling ratio [%]	Ini. Cond.
Test 1 (T1)	1.201	87.57	SS

d)

Geometry: oblate ellipsoid
Working fluid: liquid hydrogen

	Heat Input [W]	Filling ratio [%]	Ini. Cond.
Test 1 (T1)	82.96	75.46	SS
Test 2 (T2)	83.08	75.19	ISO

e)

Geometry: oblate ellipsoid
Working fluid: liquid hydrogen

	Heat Input [W]	Filling ratio [%]	Ini. Cond.
Test 1 (T1)	70.3	49.37	SS
Test 2 (T2)	62.59	34.65	SS

f)

Figure 79. Computed and experimental liquid temperature at low heat fluxes: a) Study case 1 (Test 1 and Test 2), b) Study case 1 (Test 3, 4 and 5), c) Study case Test 6, d) Study case 2, e) Study case 3 and f) Study case 4.

The computed liquid temperature always increases in time and this temperature is lower than the saturation one. Hence, the liquid is slightly in sub-cool state during the self-pressurisation. The self-pressurisation starts after the steady state, except for Test 2 of Study case 3. The computed liquid temperature is slightly higher than the saturation one. Hence, the initial value of this variable is higher than the one experimentally observed. As a consequence, the thermodynamic state of the liquid changes form overheated to sub-cool during the self-pressurisation. The rate of the temperature increment that is calculated by the H model is similar to the experimental one. Hence, the difference in the initial temperature mainly determines the difference between the computed and observed liquid temperature. The value of the difference in temperature between the calculated and the measured is, however, lower respect to the one of the ullage (see Section 7.1.4 of Chapter 4).

7.2. Study cases: medium heat fluxes

The study cases at medium heat fluxes are presented in Table 54. The boundary and the initial condition of temperature are reported at the beginning of the self-pressurisation in Table 84, for the Study case at medium heat fluxes.

Table 84. Initial conditions and boundary conditions for the self-pressurisation stage for Study cases at medium heat fluxes.

Sub-case	$h_{eff}\left[\frac{W}{m^2\cdot K}\right]$	$\alpha\,[-]$	$\beta\,[-]$	$\dot{Q}\,[W]$		$T^V\,[K]$		$T^L\,[K]$	
				Exp	**H**	**Exp**	**H**	**Exp**	**H**
Study case 5									
Test 1	0.3987	1	0.3199	29.91	29.89	100.6	101.3	77.03	77.59
Test 2	0.3987	$6.772\cdot10^{-2}$	0.2615	23.85	23.78	121.2	122.4	77.68	77.59
Test 3	0.3987	$1.668\cdot10^{-2}$	0.4941	17.88	17.76	116.6	119.1	77.64	77.57
Study case 6									
Test 1	0.2807	1	0	75.58	75.85	29.47	26.53	20.90	20.39
Test 2	0.2807	0.6918	0	73.09	74.67	40.03	31.19	20.78	20.9
Test 3	0.2807	$1.861\cdot10^{-2}$	0	56.39	63.02	53.34	32.04	19.55	20.32
Test 4	0.9373	1	0	242.2	242.2	39.03	38.02	21.05	20.49

For Study case 5, the initial values of heat inputs and temperatures are close to the experimental values at the beginning of the self-pressurisation. The value of the effective heat transfer is constant with the filling ratio. The values of the corrective coefficient β decrease between Test 1 and Test 2, but it increases between Test 2 and Test 3. Hence, there is a minimum around the value of filling ratio of 50 %. The values of the corrective coefficient α decrease with the reduction of the filling ratio.

For Study case 6, the differences of both vapour temperature and heat input between the computed and the experimental values are higher than the one of Study case 5. The effective heat transfer coefficient is constant with the filling ratio, except for Test 4 of Study case 6. So, the behaviour of this coefficient is similar to the one of Study case 5. The values of corrective coefficient α decrease with the reduction of the filling ratio, except for Test 4 of Study case 6. Hence, the behaviour of this coefficient is quite similar to the one of Study case 5. The values of the corrective coefficient β are equal to zero, contrarily to the behaviour of β of Study case 5.

The behaviours of the effective heat transfer coefficient, of the corrective coefficient α and beta are quite similar to the ones observed for the Study cases at low heat fluxes (see Section 7.1 of Chapter 4).

7.2.1. Presentation of the results: heat transfer at interface

Figure 80 shows the time-evolution of heat transfers at interface, computed with the Interface Heat Transfer (IHT) model (see Section 5 of Chapter 4). The heat transfer at the interface is composed by three heat flows: liquid-to-interface ($\dot{Q}_I^L$), the vapour-to-interface ($\dot{Q}_I^V$) and the dry side wall-to-interface ($\dot{Q}_W^{LV}$). These flows are respectively computed with Equation 211, Equation 210 and Equation 201. The solid, the dotted and the dashed lines respectively indicate $\dot{Q}_I^L$, $\dot{Q}_I^V$ and $\dot{Q}_W^{LV}$. These heat inputs at the interface are noted as QLI, QVI and QwLV, respectively. The colours refer to the different tests, and the use of these colours is reported in each graphs.

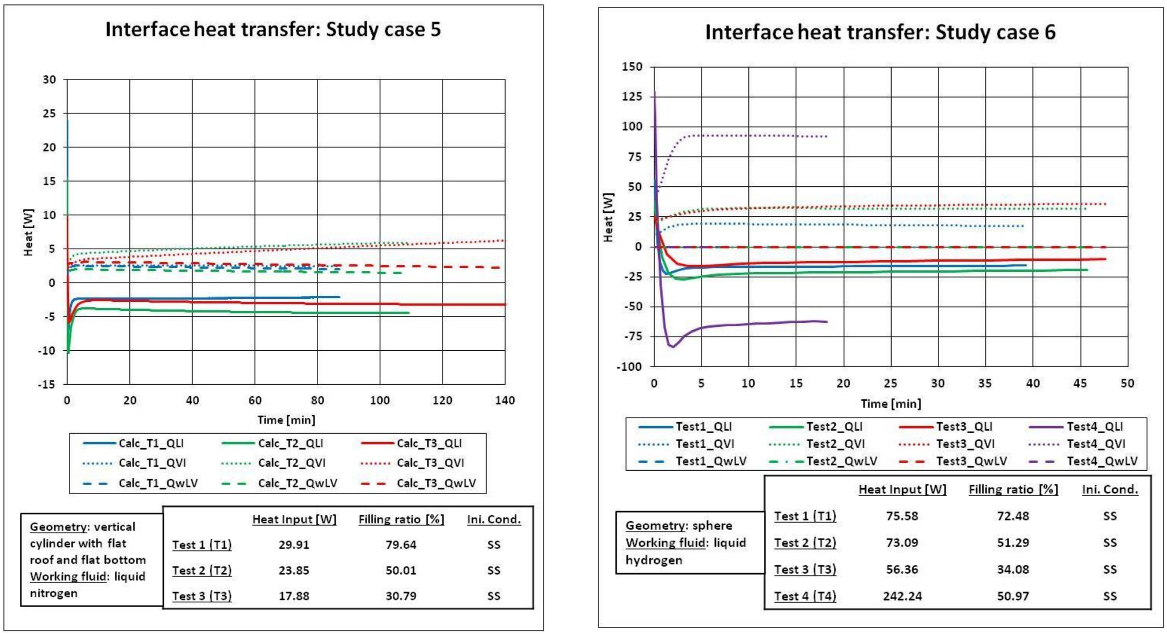

Geometry: vertical cylinder with flat roof and flat bottom
Working fluid: liquid nitrogen

	Heat Input [W]	Filling ratio [%]	Ini. Cond.
Test 1 (T1)	29.91	79.64	SS
Test 2 (T2)	23.85	50.01	SS
Test 3 (T3)	17.88	30.79	SS

a)

Geometry: sphere
Working fluid: liquid hydrogen

	Heat Input [W]	Filling ratio [%]	Ini. Cond.
Test 1 (T1)	75.58	72.48	SS
Test 2 (T2)	73.09	51.29	SS
Test 3 (T3)	56.36	34.08	SS
Test 4 (T4)	242.24	50.97	SS

b)

Figure 80. Heat transfer at the interface for the Study cases at medium heat fluxes: a) Study case 5, b) Study case 6.

As for the Study cases at low heat fluxes (see Section 7.1.1 of Chapter 4), the behaviour of $\dot{Q}_I^L$can be composed into two stages: *initial transition* and *constant rate*. At the steady state, $\dot{Q}_I^L$ is positive, indicating that energy moves from the liquid to the interface. When the storage container is closed, $\dot{Q}_I^L$ rapidly decreases and it becomes negative, which means the heat moves from the interface to the liquid. At the same time, the thermodynamic state of the liquid changes from over-heated to sub-cooled (see Section 7.2.4 of Chapter 4). The rate of this decrement does not change with the filling ratio for Study case 5. The lowest value of $\dot{Q}_I^L$ is, however, reached for Test 2 of Study case 5. For Study case 6, the decrement of $\dot{Q}_I^L$ is sharper and faster at high filling ratio than the one at low filling ratio. As the heat inputs increase, the values of $\dot{Q}_I^L$ are lower than the one at low heat leakage. The relations between filling ratio and liquid-to-interface heat flow and between heat input and liquid-to-interface heat flow are quite similar to the ones of the Study cases at low heat fluxes (see Section 7.1.1 of Chapter 4).

$\dot{Q}_I^V$ has a small initial transient, which can be particularly seen at high heat inputs (Test 4 of Study case 6). This initial transient occurs at the same moment of the increment of the ullage temperature (see Section 7.2.4 of Chapter 4). After this small transient, $\dot{Q}_I^V$ remains constant. The steady state values increase with the reduction of the initial filling ratio and with the heat inputs for Study case 5 and 6. The time-evolution of $\dot{Q}_I^V$ at medium heat fluxes is quite similar to the one at low heat fluxes (see Section 7.1.1 of Chapter 4), but the initial transient is more visible for Study case 5 and 6 than the one of Study cases 1, 2, 3 and 4.

The time-evolution of $\dot{Q}_W^{LV}$ is quite similar to the one of the vapour-to-interface heat flow, but the initial transient of $\dot{Q}_W^{LV}$ is almost negligible. For Study case 5, the values of $\dot{Q}_W^{LV}$ are lower than the ones of $\dot{Q}_I^V$. $\dot{Q}_W^{LV}$ increases with the reduction of the initial filling ratio. For Test 6, the values of $\dot{Q}_W^{LV}$ are equal to zero because the values of the corrective coefficient β are equal to zero (see Table 84). The time-evolution of $\dot{Q}_W^{LV}$ at medium heat fluxes is quite similar to the one at low heat fluxes (see Section 7.1.1 of Chapter 4).

7.2.2. Presentation of the results: net mass flow

The time-evolution of the net mass flow ($\dot{m}_N$) is described in Figure 81. The net mass flow is computed with Equation 216, applying the Interface Heat Transfer (IHT) model (see Section 5.4 of Chapter 4).

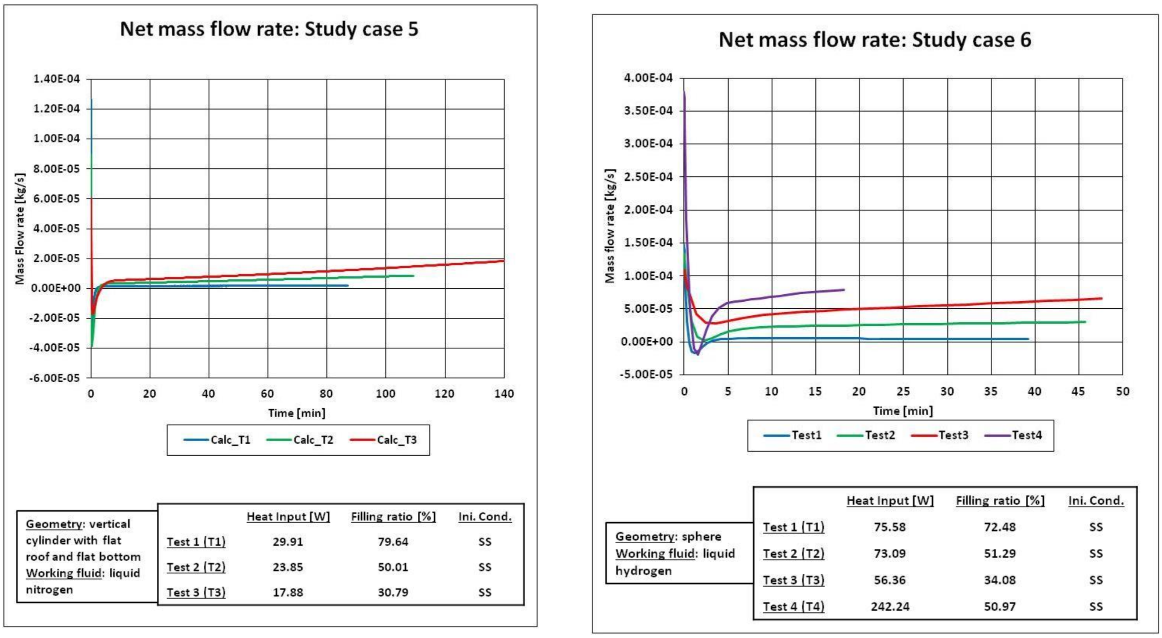

Geometry: vertical cylinder with flat roof and flat bottom
Working fluid: liquid nitrogen

	Heat Input [W]	Filling ratio [%]	Ini. Cond.
Test 1 (T1)	29.91	79.64	SS
Test 2 (T2)	23.85	50.01	SS
Test 3 (T3)	17.88	30.79	SS

a)

Geometry: sphere
Working fluid: liquid hydrogen

	Heat Input [W]	Filling ratio [%]	Ini. Cond.
Test 1 (T1)	75.58	72.48	SS
Test 2 (T2)	73.09	51.29	SS
Test 3 (T3)	56.36	34.08	SS
Test 4 (T4)	242.24	50.97	SS

b)

Figure 81. Net mass flow for the Study cases at medium heat fluxes: a) Study case 5, b) Study case 6.

The time-evolution of $\dot{m}_N$ can be decomposed into two stages: the *initial transient* and *constant rate*. $\dot{m}_N$ rapidly decreases as the storage container is closed, reaching a minimum value. For Study case 5, the value of this minimum is negative, indicating that net condensation occurs in this initial transient. The lowest value of $\dot{m}_N$ occurs for Test 2, thus at the value of the initial filling ratio of 50 %. The decrement of $\dot{m}_N$ is fast for all the test of Study case 5. For Study case 6, the minimum values of $\dot{m}_N$ are negative for Test 1 and Test 4 and the rate of the decrement of $\dot{m}_N$ is lower than the one of Study case 6. As the initial filling ratio increases, the minimum value of $\dot{m}_N$ increases and it is positive in Study case 6. Hence, net condensation only occurs for Test 1 and Test 4 of Study case 6. Hence, the behaviour of $\dot{m}_N$ is similar to the one of the liquid-to-interface heat flow ($\dot{Q}_I^L$) in the initial transient. These behaviours of $\dot{m}_N$ are quite similar to the ones of the Study cases at low heat fluxes (see Section 7.1.2 of Chapter 4). The initial transition at medium heat fluxes is, however, sharper than the one at low heat fluxes.

During the constant rate period, the value of $\dot{m}_N$ slightly increases in time. The rate of this increment augments with the reduction of the initial filling ratio and with the heat input, for Study case 5 and 6. This shape of $\dot{m}_N$ in the constant rate period is quite similar to the ones of vapour-to-interface and dry side wall-to-interface heat flows ($\dot{Q}_I^V$ and $\dot{Q}_W^{LV}$) (see Section 7.2.1 of Chapter 4). Hence, the time-evolution of $\dot{m}_N$ is controlled by $\dot{Q}_I^V$ and $\dot{Q}_W^{LV}$ in the constant rate period. This time-evolution is quite similar to the one at low heat fluxes (see Section 7.1.2 of Chapter 4).

7.2.3. Presentation of the results: pressure

The values of the computed and of the measured pressures are illustrated in Figure 82, during the self-pressurisation. The solid lines are the values computed with homogeneous model (H model), using the pressure evolution (P-e) equation (Equation 149 of Chapter 4). This equation is obtained from the mass conservation law, as it is described in Section 2. The square dots are the experimental data.

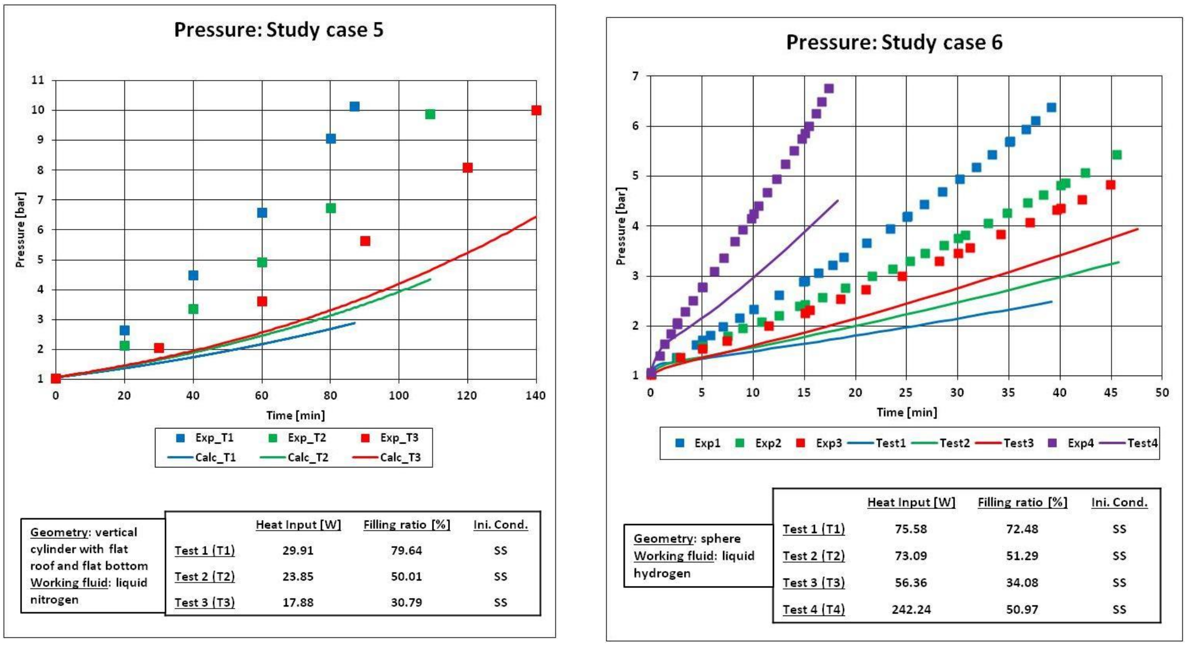

Geometry: vertical cylinder with flat roof and flat bottom
Working fluid: liquid nitrogen

	Heat Input [W]	Filling ratio [%]	Ini. Cond.
Test 1 (T1)	29.91	79.64	SS
Test 2 (T2)	23.85	50.01	SS
Test 3 (T3)	17.88	30.79	SS

Geometry: sphere
Working fluid: liquid hydrogen

	Heat Input [W]	Filling ratio [%]	Ini. Cond.
Test 1 (T1)	75.58	72.48	SS
Test 2 (T2)	73.09	51.29	SS
Test 3 (T3)	56.36	34.08	SS
Test 4 (T4)	242.24	50.97	SS

a) b)

Figure 82. Computed and experimental pressure for the Study cases at medium heat fluxes: a) Study case 5, b) Study case 6.

The computed pressure increases in time with a rate that is lower than the measured one. For Study case 5, the shape of the time-evolution of the computed pressure is qualitatively similar to the experimental one. The difference between the computed and the measured values is high, and the H model under-estimates the increment of the pressure. As the initial filling ratio is reduced, the pressure increases, contrary to the experimental data.

For Study case 6, the time-evolution of the calculated pressure has a small initial transient. This transient increases with the increment of the initial liquid level and heat inputs. The calculated pressure increases with the reduction of the initial filling ratio and with the increment of the heat inputs. The first behaviour is opposite to what is observed in the experiments. The second behaviour is qualitatively correct.

Hence, the Hmodel cannot predict the time-evolution of the pressure and the relation between the initial filling ratio and the pressure. The rate of the pressure build-up is under-estimated by the H model, as for the previous cases (see Section 7.2.3 of Chapter 4).

7.2.4. Presentation of the results: ullage temperature

Figure 83 shows the time-evolution of the computed and of experimentally measured values of the ullage temperature. The ullage temperature is computed with the homogeneous model (H model), using Equation 134, which is deduced from the energy conservation law of the ullage (see Section 2 of Chapter 4). The solid lines are the values computed with H model and the square dots are the experimental data.

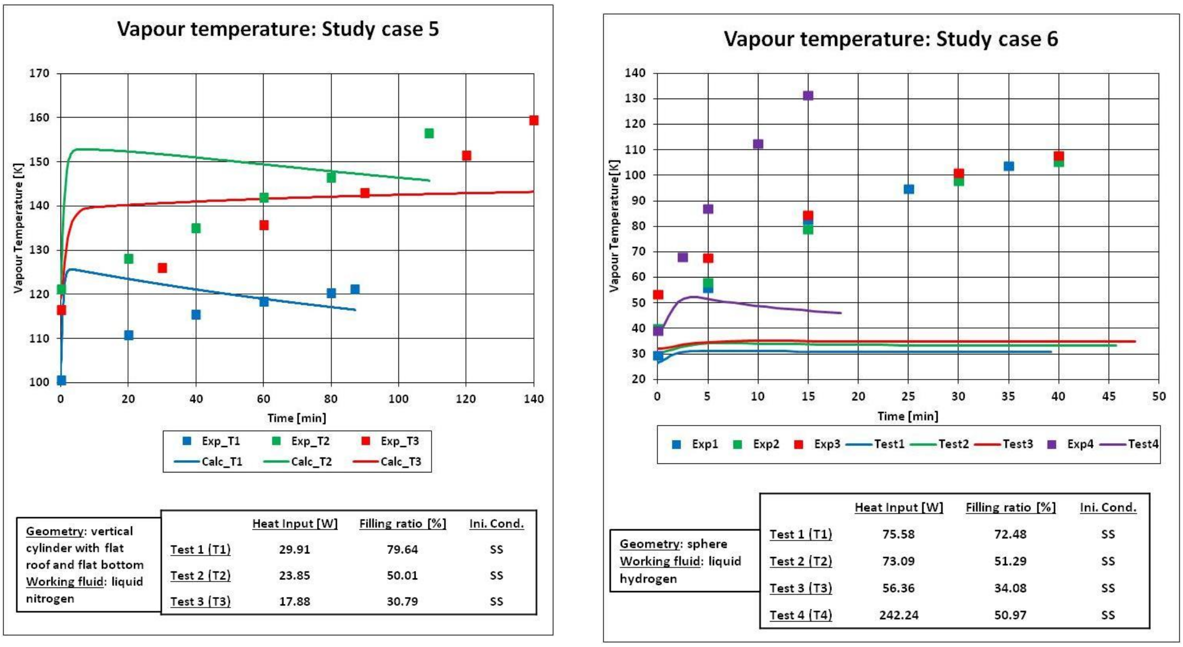

Geometry: vertical cylinder with flat roof and flat bottom
Working fluid: liquid nitrogen

	Heat Input [W]	Filling ratio [%]	Ini. Cond.
Test 1 (T1)	29.91	79.64	SS
Test 2 (T2)	23.85	50.01	SS
Test 3 (T3)	17.88	30.79	SS

Geometry: sphere
Working fluid: liquid hydrogen

	Heat Input [W]	Filling ratio [%]	Ini. Cond.
Test 1 (T1)	75.58	72.48	SS
Test 2 (T2)	73.09	51.29	SS
Test 3 (T3)	56.36	34.08	SS
Test 4 (T4)	242.24	50.97	SS

a) b)

Figure 83. Computed and experimental ullage temperature at medium heat fluxes: a) Study case 5, b) Study case 6.

For Study case 5, the calculated temperature quickly increases at the beginning of the self-pressurisation. Then, the temperature slowly decreases, producing a peak, except for Test 3. For this test, the temperature slowly increases after the initial fast increment. Hence, the time-evolution of the ullage pressure can be decomposed in two periods: *initial transient* and *constant rate*. This decomposition is similar to the ones of the liquid-to-interface heat flow ($\dot{Q}_I^L$) and of the net mass flow ($\dot{m}_N$) (see Sections 7.2.1 and 7.2.2 of Chapter 4). Hence, the time-evolution of the ullage temperature is controlled by $\dot{m}_N$, thus $\dot{Q}_I^L$. The calculated relation between the initial filling ratio and the ullage temperature is similar to the measured one because the calculated temperature of Test 2 is higher than the one at Test 3, which is in turn higher than the one of Test 1, as experimentally observed.

For Study case 6, the time-evolution of the calculated ullage temperature is quite similar to the one of Study case 5, but these peaks are reduced by the scale of the graphs, due to the low initial values of the vapour temperature. These peaks are increased by the heat inputs, as indicated in Test 4 of Study case 6. The calculated temperature increases with the reduction of the initial filling ratio and with the increment of the heat inputs as experimentally occurs.

These shapes of calculated temperature curves are not quantitatively and neither qualitatively similar to the experimental ones for both the Study cases. These peaks are not present at low heat fluxes (see Section 7.1.4 of Chapter 4). Hence, the H model fails in qualitatively and quantitatively calculating the time-evolution of the ullage temperature during the self-pressurisation.

7.2.5. Presentation of the results: liquid temperature

Figure 84 shows the calculated and the experimental results of liquid temperature, during the self-pressurisation. The liquid temperature is computed with the homogeneous model (H model), using Equation 801, which is deduced from the energy conservation law of the liquid (see Section 2 of Chapter 4). The solid lines are the values computed with H model and the square dots are the experimental data.

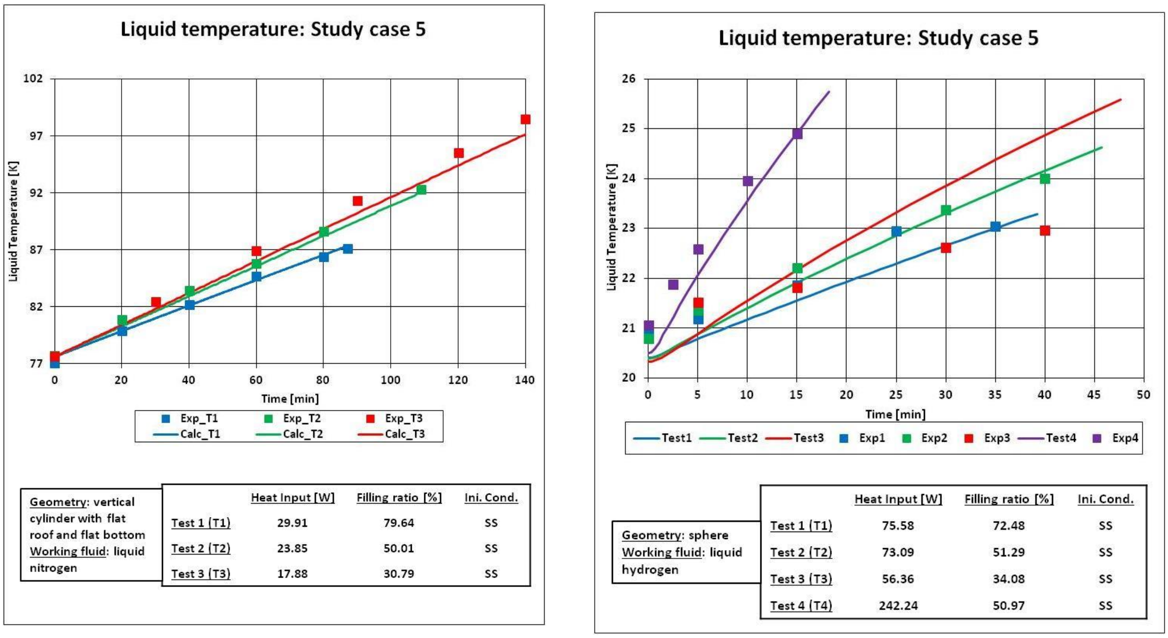

a) b)

Figure 84. Computed and experimental liquid temperature at medium heat fluxes: a) Study case 5, b) Study case 6.

For Study case 5, the computed liquid temperature increases with the time and with the reduction of the initial filling ratio. The time-evolution and the liquid temperature-filling ratio relation are very similar to the experimental ones. The rate of the computed temperature increment is almost linear, as the experimental one. This behaviour is qualitatively and quantitatively close to the experimental data, except for Test 3. For this test, the difference in temperatures between the experimental and the computed value is around 1.3 K, at the end of the self-pressurisation.

For study case 6, the computed temperature increases with the time, the heat inputs and the reduction of the initial filling ratio. The relation between the calculated liquid temperature and the initial liquid level is quite different from the experimental one. The increment of the liquid temperature is quite similar to the experimental one. The difference in the initial temperature between the model and the experiment is higher than the one of the Study case 5.

The homogeneous model well computes the liquid temperature at medium heat fluxes and the results are quite similar to the ones calculated at low heat fluxes (see Section 7.2.5 of Chapter 4). As observed with the Study cases at low heat fluxes (see Section 7.2.5 of Chapter 4), the initial liquid temperature is higher than the one of the interface, which is at saturation. Then, the liquid temperature becomes lower than the interface one. Hence, the liquid thermodynamic state changes from over-heated to sub-cooled during the self-pressurisation.

7.3. Study cases: high heat fluxes

The study cases at high heat fluxes are presented in Table 54. Table 85 describes the boundary conditions and the initial condition of temperature at the beginning of the self-pressurisation for the Study case at high heat fluxes.

Table 85. Initial conditions and boundary conditions for the self-pressurisation stage for Study cases at high heat fluxes.

Sub-case	$h_{eff}\left[\frac{W}{m^2\cdot K}\right]$	α [−]	β [−]	$\dot{Q}$ [W] Exp	$\dot{Q}$ [W] H	T^V [K] Exp	T^V [K] H	T^L [K] Exp	T^L [K] H
				Study case 7					
Test 1	1.086	1	0.904	48.18	48.19	32.12	32.42	20.71	20.82

Table 85. Initial conditions and boundary conditions for the self-pressurisation stage for Study cases at high heat fluxes.

Test 2	1.086	2.675	0	46.46	47.56	50.17	38.82	20.32	20.85
Test 3	1.086	$5.735{\cdot}10^{-2}$	0	33.68	34.85	48.9	44.95	20.58	20.85

The initial values of the liquid temperatures are close to the experimental values at the beginning of the self-pressurisation. For Test 1, the values the ullage temperature and of the heat inputs are close to the experimental ones. The initial values of heat leakage are higher than the measured ones for Test 2 and Test 3. For the same tests, the initial values of ullage temperature are lower than the experimental one. The beta coefficient is equal to zero for Test 2 and Test 3. The values of alpha coefficient increase between Test 1 and Test 2, and they decrease between Test 2 and Test 3. Hence, the alpha coefficient has a maximum in the initial filling ratio. This behaviour is not detected for the Study case at medium and low heat fluxes (see Section 7.1 and 7.2 of Chapter 4).

7.3.1. Presentation of the results: heat transfer at interface

Figure 85 illustrates the evolution in time of heat transfers at interface, computed with the Interface Heat Transfer (IHT) model (see Section 5 of Chapter 4). The heat transfer at the interface is composed by three heat flows: liquid-to-interface ($\dot{Q}_I^L$), the vapour-to-interface ($\dot{Q}_I^V$) and the dry side wall-to-interface ($\dot{Q}_w^{LV}$). These flows are respectively computed with Equation 211, Equation 210 and Equation 201. The solid, the dotted and the dashed lines respectively indicate the $\dot{Q}_I^L$, the $\dot{Q}_I^V$ and $\dot{Q}_w^{LV}$. These heat inputs at the interface are noted as QLI, QVI and QwLV, respectively. The colours refer to the different tests, and the use of these colours is reported in each graphs.

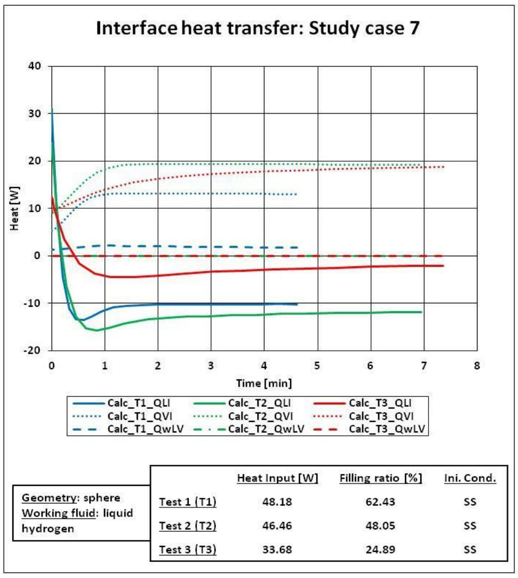

Figure 85. Heat transfer at the interface for the Study cases at high heat fluxes.

As for the Study cases at medium and low heat fluxes (see Section 7.1.1 and 7.2.1 of Chapter 4), the behaviour of $\dot{Q}_I^L$ can be decomposed into the *initial transient* and the *constant rate* stages. This heat flow decreases at the beginning of the self-pressurisation, indicating that the heat is progressively transferred from the interface to the liquid. The rate of this decrement of Test 1 is quite similar to the one of Test 2 and, for Test 3, this rate reduces. Hence, the slope of initial transient of $\dot{Q}_I^L$ becomes steeper as the filling ratio increases from 30 % to 50 %, but it does not change between the values liquid level of 60 % and 50 %. The minimum value of Test 2 is lower than the one of Test 1, which is lower than the one of Test 3. This behaviour is different from the one observed for the Study case 6, but it is similar to the one of Study case 5 (see Section 7.2.1 of Chapter 4). As for the Study case at low and medium heat fluxes (see Section 7.1.1 and 7.2.1 of Chapter 4), the initial transient occurs during the change of the thermodynamic state of the liquid. In the constant rate period, the $\dot{Q}_I^L$ is almost constant. The value of this steady state is higher at Test 3, than at Test 1, than at Test 2. Hence, the value of the steady state has a maximum in the initial filling ratio. This behaviour is not present at low and medium heat fluxes (see Section 7.1.1 and 7.2.1 of Chapter 4).

$\dot{Q}_I^V$ has an initial transient as happens for the for the Study cases at medium heat fluxes (see Section 7.2.1 of Chapter 4). This transient is more visible and longer than the one of Study case 5 and 6, and it occurs during the initial ullage temperature rise (see Section 7.3.4 of Chapter 4). $\dot{Q}_I^V$ is higher than the $\dot{Q}_w^{LV}$. The time-evolution of $\dot{Q}_I^V$ is qualitatively similar to the calculated ones at low and medium heat fluxes (see Section 7.1.1 and 7.2.1 of Chapter 4). $\dot{Q}_w^{LV}$ is equal to zero for Test 2 and 3 because the beta coefficient is equal to zero for these tests.

7.3.2. Presentation of the results: net mass flow

Figure 86 presents how the net mass flow ($\dot{m}_N$) changes during the self-pressurisation for the Study cases at low heat fluxes. The colours used in each graphs is reported in the corresponding legend. The net mass flow is computed with Equation 216, applying the Interface Heat Transfer (IHT) model (see Section 5.4 of Chapter 4).

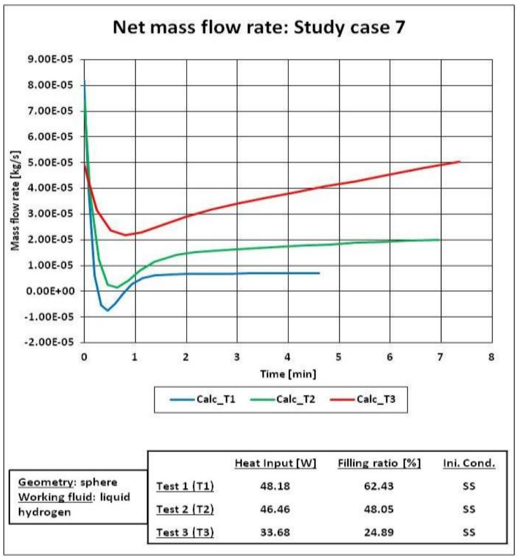

	Heat Input [W]	Filling ratio [%]	Ini. Cond.
Test 1 (T1)	48.18	62.43	SS
Test 2 (T2)	46.46	48.05	SS
Test 3 (T3)	33.68	24.89	SS

Figure 86. Net mass flow for the Study cases at high heat fluxes.

$\dot{m}_N$ rapidly decreases when the storage container is closed, reaching a minimum value. Then, $\dot{m}_N$ increases, until reaching quasi-constant value. Hence, the behaviour of this variable can be decomposed into two stages: the *initial transient* and *constant rate*. The slope of the initial transient is stepper at Test 1 than at Test 3 and the value of the minimum is lower at Test 1 than at Test 2. Hence, the increment of the initial filling ratio reduces the minimum and it increases the rate of the net mass flow reduction in the initial transient. This steady state value is almost constant in Test 1 (high filling ratio), and it increases in time in Test 3 (low filling ratio). Hence, $\dot{m}_N$ increases faster at low liquid level than at high filling ratio, in the constant rate period. The behaviour of $\dot{m}_N$ is similar to the one at medium heat fluxes (see Section 7.2.2 of Chapter 4).

7.3.3. Presentation of the results: pressure

The values of the computed and measured pressure are illustrated in Figure 87, during the self-pressurisation. The solid lines are the values computed with homogeneous model (H model), using the pressure evolution (P-e) equation (Equation 149). This equation is obtained from the mass conservation law, as it is described in Section 2 of Chapter 4. The square dots are the experimental data.

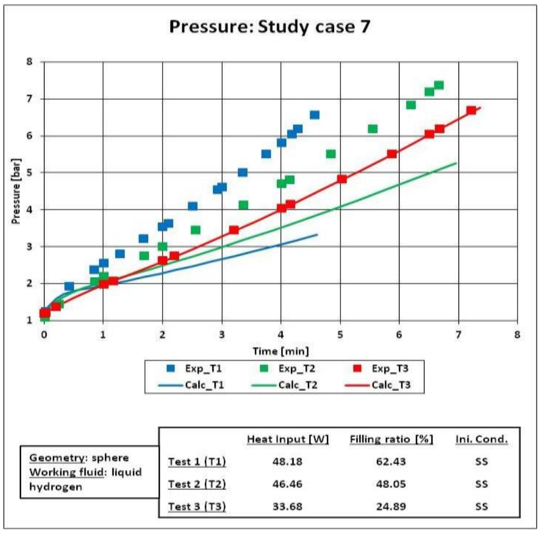

Geometry: sphere
Working fluid: liquid hydrogen

	Heat Input [W]	Filling ratio [%]	Ini. Cond.
Test 1 (T1)	48.18	62.43	SS
Test 2 (T2)	46.46	48.05	SS
Test 3 (T3)	33.68	24.89	SS

Figure 87. Computed and experimental pressure for the Study cases at high heat fluxes.

The computed pressure increases with the time and it has a small initial transient. This transient is more visible for Test 1 than Test 2 than Test 3. So, the initial transient reduces with the reduction of the filling ratio, as for the net mass flow (see Section 7.3.2 of Chapter 4). As the initial filling ratio is reduced, the values of the calculated pressure increase. This increment is not coherent with the experimental data because these data indicate that the pressure increases with the filling ratio. At Test 3, the calculated pressure perfectly follows the experimental data. Hence, the H model cannot predict this behaviour, similarly to the cases of medium heat fluxes (see Section 7.2.3 of Chapter 4), except for the test at low filling ratio (Test 3). So, the liquid is close to the homogeneity at low filling ratio.

7.3.4. Presentation of the results: ullage temperature

Figure 88 shows the time-evolution of the computed and of experimentally measured values of the ullage temperature. The ullage temperature is computed with the homogeneous model (H model), using Equation 134, which is deduced from the energy conservation law of the ullage (see Section 2 of Chapter 4). The solid lines are the values computed with H model and the square dots are the experimental data.

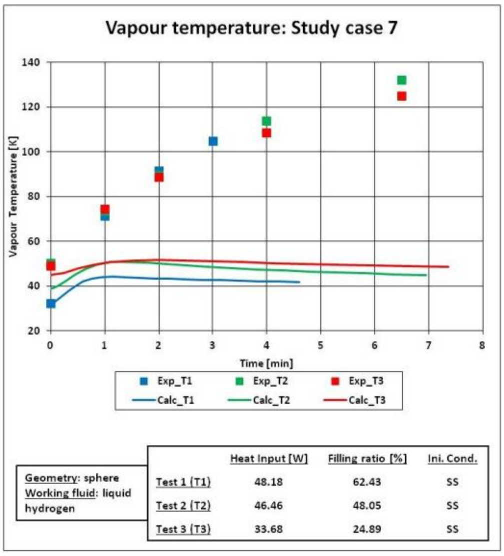

	Heat Input [W]	Filling ratio [%]	Ini. Cond.
Test 1 (T1)	48.18	62.43	SS
Test 2 (T2)	46.46	48.05	SS
Test 3 (T3)	33.68	24.89	SS

Figure 88. Computed and experimental ullage temperature for the Study cases at high heat fluxes.

The initial computed temperature of the ullage is close to the experimental one for Test 1. At Test 2 and 3, the computed temperature is lower than the experimental one because the values of the beta coefficient are equal to zero (see Table 85). The computed ullage temperature initially increases and the rate of this increment decreases from Test 1 to Test 3, as occurs for the net mass flow (See Section 7.3.2 of Chapter 4). Hence, the initial rate of temperature increment increases with the initial filling ratio. After this initial increment, the ullage temperature decreases, producing a peak. The rate of this decrement is quite constant with the filling ratio. The computed temperature is, however, lower than the experimental one. The computed temperature increases with the reduction of the filling ratio. The behaviour of the vapour temperature is quite similar to the one at medium heat fluxes (see Section 7.2.4 of Chapter 4).

7.3.5. Presentation of the results: liquid temperature

Figure 89 shows the calculated and the experimental results of liquid temperature, during the self-pressurisation. The liquid temperature is computed with the homogeneous model (H model), using Equation 801, which is deduced from the energy conservation law of the liquid (see Section 2 of Chapter 4). The solid lines are the values computed with H model and the square dots are the experimental data.

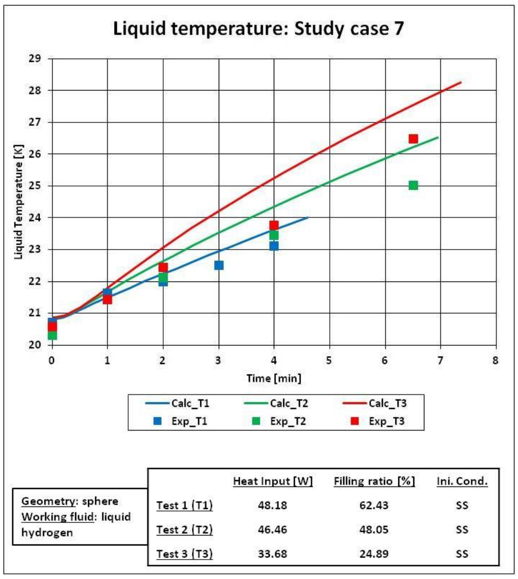

Geometry: sphere
Working fluid: liquid hydrogen

	Heat Input [W]	Filling ratio [%]	Ini. Cond.
Test 1 (T1)	48.18	62.43	SS
Test 2 (T2)	46.46	48.05	SS
Test 3 (T3)	33.68	24.89	SS

Figure 89. Computed and experimental liquid temperature for the Study cases at high heat fluxes.

The computed liquid temperature increases in time and the rate of this increment is higher at Test 3 than Test 2 than Test 1. So, the rate of the temperature increment increases with the reduction of the filling ratio. These behaviours are qualitatively correct because the experimental liquid temperature also increases with the reduction of the liquid level. The rise of computed liquid temperature is, however, higher than the one of the experimental data. This overestimation is quite similar to the one observed for the Study case at medium heat fluxes (see Section 7.2.5 of Chapter 4). The initial liquid temperature is higher than the interface one, which is at saturation. Then, the liquid temperature is sub-cooled. Hence, the H model computes the change of the thermodynamic state from over-heated to sub-cooled, as occurs at low and medium heat fluxes (see Section 7.1.5 and 7.2.5 of Chapter 4).

8. Discussion of the results

The discussion of the results is presented in different sections for each aspects of the homogeneous model (H model). The Interface Heat Transfer (IHT), the Boil-Off Rate (BOR), the Storage Heat Transfer (SHT) and the Storage Boundary Layer (SBL) models are the main aspects of the H model. The BOR model computes the boundary conditions, which are described by the effective heat transfer coefficient (h_{eff}) and by the corrective coefficients α and β. The IHT model calculates the heat flows at the interface ($\dot{Q}_I^L$, $\dot{Q}_I^V$ and $\dot{Q}_w^{LV}$) and the net mass flow ($\dot{m}_N$). The SHT and SBL models compute the heat inputs at each wall of the storage containers. The interfacial heat flows, net mass flow and the heat inputs determine the time-evolution of the state variables (see Table 62). Hence, the results of interfacial heat flows, net mass flow and state variables such as liquid and ullage temperatures, and pressure are discussed to underline these causes. As explained in Chatper 3, the differences between in the storage behaviour between liquid nitrogen (LN_2) and liquid hydrogen (LH_2) is not discussed due to the lack of experimental evidences.

Section 8.1 and 8.2 explain the results of the boundary conditions and of the initial conditions, respectively. Section 8.3 and 8.4 present the causes of the interfacial heat flows and of the net mass flow, respectively. Section 8.5 analyses the results of the pressure. Section 8.6 and 8.7 present the causes of the time-evolution of the ullage temperature and liquid temperature, respectively. Section 8.8 presents the conclusions. Section 8.9 summarises Chapter 4 and it presents the perspective.

8.1. Boundary conditions

The boundary conditions are defined with the effective heat transfer coefficient (h_{eff}) and by the corrective α and β coefficients, which are computed with the Boil-Off Rate (BOR) Model (see Section 6). These coefficients are computed with iterative procedures (see Appendix R), which are based on the conservation laws given in Table 82. These conservation laws are deduced from the hypotheses of total homogeneity, local thermodynamic equilibrium and actual thermodynamic states (assumptions a), b) and c) of Section 1.1 of Chapter 4).

Section 8.1.1, 8.1.2 and 8.1.3discuss the results of the effective heat transfer coefficient, the alpha coefficient and the beta coefficient.

8.1.1. Effective heat transfer coefficient

The effective heat transfer coefficient (h_{eff}) describes the insulating properties of the storage container. This coefficient is calculated with the h_{eff} algorithm (see Section 1 of Appendix R), only for Test 1 and 3 of Study case 1, Test 1 of Study case 2, Tests 1 and 2 of Study case 3, Test 1 of Study case 5, Test 1 and 4 of Study case 6 and Test 1 of Study case 7.

As it is gathered in Table 83, Table 84 and Table 85, the value of h_{eff} remains constant with the filling ratio, except for the Test 3 of Study case 1 and Test 4 of Study case 5. For these tests, the insulating properties of the storage container were modified to increase the heat leakage. Hence, the behaviour of h_{eff} remains constant because it is calculated only for one test of each experimental series.

8.1.2. Alpha corrective coefficient

The dry side wall-to-vapour heat transfer coefficient ($\bar{h}_w^{SV}$) depends on the bulk temperature gradient of the ullage, which affects the fluid-dynamics and the heat transfer at the dry side wall. Due to the hypothesis of total homogeneity (assumption a) of Section 1.1 of Chapter 4), the gradient is neglected and the corrective coefficient α is computed to correct the neglect of the bulk ullage temperature gradient. This coefficient is equal to 1, due to the hypothesis of the exact heat transfer coefficient (assumption e) of Section 6.1 of Chapter 4). This coefficient is computed with $\boldsymbol{\alpha}$ algorithm (see Section 2 of Appendix R) for the tests where this hypothesis is not applied. This algorithm computes the corrective coefficient with Equation 1055, which is deduced from the energy balance equation of the dry side wall (Equation 222). So, the value of this coefficient increases with the reduction of corrective coefficient β and of the wet walls-to-liquid heat flow ($\dot{Q}_w^L$) and with the increment of the overall heat input ($\dot{Q}_{IN}$). This heat leakage decreases with the reduction of the initial filling ratio. The reduction of the liquid level increases the dry side wall surface area (A^{SV}), the wall and bulk temperature of the ullage (T_w^{SV} and T^V) and the heat transfer coefficient between the dry side wall and the vapour ($\bar{h}_w^{SV}$). The increments of these variables reduce the denominator of Equation 1055. The filling ratio reduces wet walls-to-liquid heat flow, thus the numerator of Equation 1055. Hence, the increment of the numerator can potentially increase the corrective coefficient α, if overall heat input does not reduce with the filling ratio.

As it is observed in Table 83, Table 84 and Table 85, the value of the alpha coefficient decreases with the reduction of the initial filling ratio, except for Test 3 of Study case 1 and Test 4 of Study case 5 and for the Study case 7. Hence, the values of corrective coefficient α decrease because the denominator of Equation 1055 becomes higher than the numerator when the initial liquid level reduces. In other words, α must reduce to assure the value of overall heat input, compensating the increment of the heat transfer due to the neglect of the ullage bulk gradient (assumption a) of Section 1.1 of Chapter 4). In the Study case 7, the corrective coefficient α has a maximum near the filling ratio of 50 %. So, the increment of alpha coefficient is caused by the increment of the numerator of Equation 1055 because the difference in the overall heat input between Test 1 (60 %) and Test 2 (50 %) is lower than the one of the other Study cases.

8.1.3. Beta corrective coefficient

The dry side wall-to-interface heat flow ($\dot{Q}_w^{LV}$) affects the thermal distribution of the heat inputs between the liquid and the vapour, influencing the behaviour the cryogenic liquid. This heat flow is estimated with Equation 201, which is obtained from the Fourier'law (see Section 4.5 of Chapter 4), using the thickness of the side wall and the temperature gradient in the dry side wall. The coefficient $\boldsymbol{\beta}$ is required because this thickness is unknown and this gradient is neglected due to the hypothesis of total homogeneity (assumption a) of Section 1.1 of Chapter 4). This coefficient is computed with the $\boldsymbol{\beta}$ algorithm (see Section 1.2 of Appendix R) in the h_{eff} algorithm. The beta coefficient is calcualted with Equation 1042 in α algorithm algorithm (see Section 2 of Appendix R). β algorithm and Equation 1042 are based on the energy and mass balance equation of the ullage at steady state (Equation 217 and Equation 218) and on the interface energy balance (Equation 219). The values of β potentially increases with the values of the effective heat transfer coefficient (h_{eff}) and with the dry side wall and roof surface area (A^{SV} and A^R). The values of beta coefficient decrease, if the values of wet walls-to-liquid heat flow ($\dot{Q}_w^L$), vapour-to-interface heat flow ($\dot{Q}_I^V$) and dry side wall-to-interface heat flow ($\dot{Q}_w^{LV}$) increase. When the initial filling ratio is reduced, $\dot{Q}_w^L$ descreases, $\dot{Q}_I^V$ increases if the interfacial area remains constant, A^{SV} increases and $\dot{Q}_w^{LV}$ slightly increases. So, the value of beta can potentially increases with the reduction of the initial liquid level.

As it is reported in Table 83, Table 84 and Table 85, the values of the corrective coefficient β are equal to zero for Study cases 3, 4, 6 and 7 (except Test 1) for any values of heat inputs and filling ratio, indicating that the numerator of Equation 1042 is potentially negative or equal to zero. This can happens if $\dot{Q}_I^V$ is much higher than the heat coming from the dry walls, which is described be the term $h_{eff} \cdot (A^{SV} + A^R) \cdot (T^W - T_w^{SV})$. Hence, the $\dot{Q}_I^V$ is higher than the value that it should be at steady state. The anomaly of Test 1 of Study case 7 is determined by the high heat fluxes that makes the numerator positive, thus term $h_{eff} \cdot (A^{SV} + A^R) \cdot (T^W - T_w^{SV})$ is greater than the heat flow $\dot{Q}_I^V$. The values of β has a minimum at Test 2 of Study case 5 (filling ratio of 50 %) because $\dot{Q}_I^V$ and the term $h_{eff} \cdot (A^{SV} + A^R) \cdot (T^W - T_w^{SV})$ increase with the reduction of the filling ratio. The beta coefficient is irregular at Study case 1 because $\dot{Q}_w^{LV}$, thus the denominator, increases as the filling ratio is reduced, changing the effect of the numerator, thus the effect of $\dot{Q}_I^V$ and the term $h_{eff} \cdot (A^{SV} + A^R) \cdot (T^W - T_w^{SV})$ on Equation 1042.

8.2. Initial conditions

The initial conditions are calculated during the steady state, except for Test 2 of Study case 3, with the homogeneous model (H model). As it is reported in Table 83, Table 84 and Table 85, the values of ullage temperature, liquid temperature and heat inputs are close to the experimental one, except for Study cases 3, 4, 6 and 7 (except Test 1). For these Study cases, the values of the beta coefficient are equal to zero. Hence, the wrong prediction of the initial condition is caused by the wrong estimation of the beta coefficient, which is equal to zero due to the over-estimation of the vapour-to-interface heat flow ($\dot{Q}_I^V$) at steady state.

8.3. Interfacial heat flows

The interfacial heat flows are composed of 3 elements: liquid-to-interface ($\dot{Q}_I^L$), vapour-to-interface ($\dot{Q}_I^V$) and dry side wall-to-interface ($\dot{Q}_w^{LV}$) heat flows. $\dot{Q}_I^L$ and $\dot{Q}_I^V$ are computed with the Interface Heat Transfer (IHT) model, which is based on the hypothesis of local thermodynamic equilibrium (assumptions c) of Section 1.1 of Chapter 4). The heat flow $\dot{Q}_w^{LV}$ respectively computed with the Storage Heat Transfer (SHT) model, which is added to the homogeneous model (H model) due to the hypotheses of total homogeneity and of actual thermodynamic states (assumptions a) and b) of Section 1.1 of Chapter 4).

Sections 8.3.1, 8.3.2 and 8.3.3 respectively discuss the results of heat flows $\dot{Q}_I^L$, $\dot{Q}_I^V$ and $\dot{Q}_w^{LV}$.

8.3.1. Liquid-to-interface heat flow

The liquid-to-interface heat flow ($\dot{Q}_I^L$) is computed with the Interface Heat Transfer (IHT) model, using Equation 211, as it is explained in Section 5.3. Equation 211 depends on the mass flow rate of the last sub-layer of the boundary layer of the wet side wall ($\dot{m}_{BL}^I$) and on the difference in temperatures between the boundary layer at this sub-layer and the interface ($T_{BL}^I - T^I$). The temperature and the mass flow rate in the boundary layer are calculated with the Storage Boundary Layer (SBL) model (see Section 3 of Chapter 4). The absolute value of $\dot{Q}_I^L$ increases with the increment of the mass flow in the boundary layer and the aforementioned difference in the temperatures. $\dot{Q}_I^L$ can be negative when this difference in temperature is negative because the boundary mass flow is always positive and not equal to zero due to the hypothesis of total homogeneity (assumption a) of Section 1.1 of Chapter 4). The absolute value of liquid-to-interface heat flow increases with the liquid level and with the heat inputs, as described by the SBL model.

As it is shown in Sections 7.1.1, 7.2.1 and 7.3.1 of Chapter 4, the time-evolution of liquid-to-interface heat flow ($\dot{Q}_I^L$) is decomposed into the initial transient, where the values of $\dot{Q}_I^L$ decreases, and the constant rate, where the values of $\dot{Q}_I^L$ remains almost constant. The initial decrement is caused by the reduction of the difference in temperatures between the interface and the last sub-layer of the boundary layer. This difference can become negative at high filling ratio and heat inputs, changing the direction of the heat transfer, which passes from liquid-to-interface to interface-to-liquid. The steady state is caused by the fact that this difference in temperature remains almost constant during the self-pressurisation because the mass flow in the last sub-layer of the boundary layer does not significantly change in the self-pressurisation. As the heat input or the filling ratio increases, the initial transient is steep because the mass flow rate in the last sub-layer of the boundary layer increases.

8.3.2. Vapour-to-interface heat flow

The vapour-to-interface heat flow ($\dot{Q}_I^V$) is computed with Interface Heat Transfer (IHT) model, using Equation 210, as it is explained in Section 5.2. Equation 210 depends on the interfacial surface area (A^I), which can change with the filling ratio in sphere and oblate ellipsoid, the vapour-to-interface heat transfer coefficient (h_I^V) and difference in temperatures between the vapour and the interface ($T^V - T^I$). h_I^V is computed as function of $T^V - T^I$, as it is described in the semi-empirical approach (see Section 4.6 of Chapter 4). Hence, $\dot{Q}_I^V$ increases with the increment of the difference $T^V - T^I$ and A^I.

As it is described in Sections 7.1.1, 7.2.1 and 7.3.1 of Chapter 4, $\dot{Q}_I^V$ has a small initial transient and it remains almost constant during the self-pressurisation. This initial increment is caused by the increment of the difference in temperatures, which rises the values of h_I^V. As consequences, the values of $\dot{Q}_I^V$ increases with the reduction of the filling ratio because this $T^V - T^I$ is higher, even if A^I are reduces with the filling ratio in spherical and oblate ellipsoidal storage tanks. $\dot{Q}_I^V$ increases with the heat fluxes because the ullage vapour temperature is high.

8.3.3. Dry side wall-to-interface heat flow

The dry side wall-to-interface heat flow ($\dot{Q}_W^{LV}$) is calculated with Equation 201, using the Storage Heat Transfer (SHT) model, as it is explained in Section 4.5 of Chapter 4. $\dot{Q}_W^{LV}$ depends on the surface area of the metallic ring (A^R) on the corrective coefficient and on the temperature gradient in the dry side wall. This gradient is calculated with Equation 202 according to hypothesis of total homogeneity (assumption a) of Section 1.1 of Chapter 4).

As it is described in Sections 7.1.1, 7.2.1 and 7.3.1 of Chapter 4, the value of $\dot{Q}_W^{LV}$ is often zero because the beta coefficient is equal to zero in Study case 3, 4, 6 and 7 (except Test 1). When this does not occur, $\dot{Q}_W^{LV}$ has a small transient and it remains almost constant. This transient is caused by the increment of the side wall temperature, due to the rise of the ullage temperature. Hence, this transient is increased by the reduction of initial filling ratio and of heat inputs, which increases the ullage temperature. $\dot{Q}_W^{LV}$ can increase with the reduction of the filling ratio due to the increment of the ullage temperature, as occurs at Study case 5. The value of $\dot{Q}_W^{LV}$ can be higher at the highest filling ratio than the ones at the lowest due to the value of beta coefficient, as it happens at Study cases 1 and 2.

8.4. Net mass flow

The net mass flow ($\dot{m}_N$) is the difference between the evaporation and the condensation rates. $\dot{m}_N$ is computed with Equation 216, using the Interface Heat Transfer (IHT) model (see Section 5 of Chapter 4). Equation 216 is deduced from the interfacial energy balance equation (Equation 209), which is obtained from the hypothesis of local thermodynamic equilibrium (assumption c) of Section 1.1 of Chapter 4). As it is described by Equation 216, the mass flow $\dot{m}_N$ is a function of sum of the three interfacial heat flows: liquid-to-interface ($\dot{Q}_I^L$), vapour-to-interface ($\dot{Q}_I^V$) and dry side wall-to-interface ($\dot{Q}_W^{LV}$).

As observed in Section 7.1.2, 7.2.2 and 7.3.2 of Chapter 4, the time-evolution of $\dot{m}_N$ is composed by the initial transient and the constant rate period. In the transient, $\dot{m}_N$ decreases at the beginning of the self-pressurisation down to a minimum. Then, $\dot{m}_N$ increases up to the steady state value. This initial transient is similar to the one of $\dot{Q}_I^L$, due to Equation 216. $\dot{Q}_I^L$ removes energy from the interface. The vapour must condense to compensate the heat removed by the $\dot{Q}_I^L$ for maintaining the thermodynamic equilibrium, which is imposed by hypothesis (assumption c) of Section 1.1 of Chapter 4). Hence, the condensation rate increases and $\dot{m}_N$ reduces. After this initial decrement, $\dot{m}_N$ remains constant or it slightly increases because $\dot{Q}_I^L$ is stable. In the constant rate period, $\dot{m}_N$ is positive, indicating a net evaporation of the liquid. This occurs because the sum of $\dot{Q}_I^V$ and $\dot{Q}_W^{LV}$ is higher than $\dot{Q}_I^L$, as indicated by Equation 216. Hence, $\dot{Q}_I^V$ and $\dot{Q}_W^{LV}$ enhances the evaporation rate at the interface, sustaining the self-pressurisation. As a consequence, $\dot{m}_N$ increases with the reduction of the filling ratio because the absolute value of the heat flow $\dot{Q}_I^L$ reduces and the values of heat flows $\dot{Q}_I^V$ and $\dot{Q}_W^{LV}$ increase.

8.5. Pressure

The pressure is calculated with the homogeneous model (H model) using the pressure evolution (P-e) equation (Equation 149). This equation is obtained from the energy and mass conservation laws of liquid and vapour, as it is described in Section 2 of Chapter 4. If the time-derivates of ullage temperature and liquid volume ($\frac{\partial T^V}{\partial t}$ and $\frac{\partial V^L}{\partial t}$) are knows, the pressure can be computed with Equation 108, which is the linear form of the ullage mass conservation law. During the self-pressurisation, the terms $B^P \cdot \frac{\partial T^V}{\partial t}$, $C^P \cdot \frac{\partial V^L}{\partial t}$ and F^P (see Table 69) are of particular interest for the time-evolution of the pressure because the mass flows $\dot{m}_{IN}^V$, $\dot{m}_{BOG}$, $\dot{m}_{IN}^L$ and $\dot{m}_{OUT}^L$ are equal to zero. The values of these terms at the beginning and at the end of the self-pressurisation are reported in Table 86.

Table 86. Values of $\boldsymbol{B^P \cdot \frac{\partial T^V}{\partial t}}$, $\boldsymbol{C^P \cdot \frac{\partial V^L}{\partial t}}$ and $\boldsymbol{F^P}$ during the self-pressurisation.

			Study case 1			
	Test 1	**Test 2**	**Test 3**	**Test 4**	**Test 5**	**Test 6**
			At the beginning of self-pressurisation			
$B^P \cdot \frac{\partial T^V}{\partial t}$	$-2.313 \cdot 10^{-7}$	$-1.92457 \cdot 10^{-7}$	$-3.43122 \cdot 10^{-7}$	$-1.59813 \cdot 10^{-7}$	$-1.34679 \cdot 10^{-7}$	$-2.41743 \cdot 10^{-7}$
$C^P \cdot \frac{\partial V^L}{\partial t}$	$7.087 \cdot 10^{-8}$	$3.5174 \cdot 10^{-8}$	$6.6618 \cdot 10^{-8}$	$2.7994 \cdot 10^{-8}$	$2.0183 \cdot 10^{-8}$	$1.6286 \cdot 10^{-8}$
F^P	$-5.352 \cdot 10^{-6}$	$-4.9844 \cdot 10^{-6}$	$-9.8401 \cdot 10^{-6}$	$-4.6695 \cdot 10^{-6}$	$-3.6584 \cdot 10^{-6}$	$-3.0551 \cdot 10^{-6}$
			At the end of self-pressurisation			
$B^P \cdot \frac{\partial T^V}{\partial t}$	$-3.559 \cdot 10^{-9}$	$-1.1772 \cdot 10^{-8}$	$-2.3012 \cdot 10^{-8}$	$-2.5672 \cdot 10^{-8}$	$-6.0524 \cdot 10^{-8}$	$-1.4395 \cdot 10^{-7}$
$C^P \cdot \frac{\partial V^L}{\partial t}$	$-1.691 \cdot 10^{-8}$	$-1.5199 \cdot 10^{-8}$	$-3.0840 \cdot 10^{-8}$	$-1.3126 \cdot 10^{-8}$	$-7.4634 \cdot 10^{-9}$	$5.0801 \cdot 10^{-10}$
F^P	$-2.682 \cdot 10^{-8}$	$-8.5884 \cdot 10^{-8}$	$-1.9057 \cdot 10^{-7}$	$-2.1337 \cdot 10^{-7}$	$-5.1177 \cdot 10^{-7}$	$-1.2070 \cdot 10^{-6}$
			Study case 2			

Table 86. Values of $\boldsymbol{B^P \cdot \frac{\partial T^V}{\partial t}}$, $\boldsymbol{C^P \cdot \frac{\partial V^L}{\partial t}}$ and $\boldsymbol{F^P}$ during the self-pressurisation.

	Test 1
At the beginning of self-pressurisation	
$B^P \cdot \frac{\partial T^V}{\partial t}$	$-1.9668\cdot10^{-7}$
$C^P \cdot \frac{\partial V^L}{\partial t}$	$4.1102\cdot10^{-8}$
F^P	$-4.5632\cdot10^{-6}$
At the end of self-pressurisation	
$B^P \cdot \frac{\partial T^V}{\partial t}$	$-7.7513\cdot10^{-9}$
$C^P \cdot \frac{\partial V^L}{\partial t}$	$-1.7484\cdot10^{-8}$
F^P	$-4.5839\cdot10^{-8}$

Study case 3

	Test 1	**Test 2**
At the beginning of self-pressurisation		
$B^P \cdot \frac{\partial T^V}{\partial t}$	$-1.6293\cdot10^{-5}$	-0.0001374
$C^P \cdot \frac{\partial V^L}{\partial t}$	$6.7635\cdot10^{-6}$	$7.5265\cdot10^{-6}$
F^P	-0.00017973	-0.0001393
At the end of self-pressurisation		
$B^P \cdot \frac{\partial T^V}{\partial t}$	$-1.3676\cdot10^{-6}$	$-1.405\cdot10^{-6}$
$C^P \cdot \frac{\partial V^L}{\partial t}$	$-3.4078\cdot10^{-6}$	$-3.391\cdot10^{-6}$
F^P	$-3.8792\cdot10^{-6}$	$-4.219\cdot10^{-6}$

Study case 4

	Test 1	**Test 2**
At the beginning of self-pressurisation		
$B^P \cdot \frac{\partial T^V}{\partial t}$	$-1.7866\cdot10^{-5}$	$-1.16\cdot10^{-5}$
$C^P \cdot \frac{\partial V^L}{\partial t}$	$3.1901\cdot10^{-6}$	$2.5124\cdot10^{-6}$
F^P	-0.00015156	-0.0001358
At the end of self-pressurisation		
$B^P \cdot \frac{\partial T^V}{\partial t}$	$-7.5836\cdot10^{-6}$	$-1.231\cdot10^{-5}$
$C^P \cdot \frac{\partial V^L}{\partial t}$	$-1.9089\cdot10^{-6}$	$-6.623\cdot10^{-8}$
F^P	$-3.4645\cdot10^{-5}$	$-6.201\cdot10^{-5}$

Study case 5

	Test 1	**Test 2**	**Test 3**
At the beginning of self-pressurisation			
$B^P \cdot \frac{\partial T^V}{\partial t}$	$-2.1458\cdot10^{-6}$	$-1.2394\cdot10^{-6}$	$-1.4654\cdot10^{-6}$
$C^P \cdot \frac{\partial V^L}{\partial t}$	$8.2003\cdot10^{-7}$	$3.71966\cdot10^{-7}$	$2.3705\cdot10^{-7}$
F^P	-0.00012638	$-8.9757\cdot10^{-5}$	$-6.0362\cdot10^{-5}$
At the end of self-pressurisation			
$B^P \cdot \frac{\partial T^V}{\partial t}$	$2.1303\cdot10^{-7}$	$3.7646\cdot10^{-7}$	$-2.5774\cdot10^{-7}$
$C^P \cdot \frac{\partial V^L}{\partial t}$	$-9.1244\cdot10^{-7}$	$-8.1710\cdot10^{-7}$	$-6.4898\cdot10^{-7}$
F^P	$-1.8176\cdot10^{-6}$	$-8.5895\cdot10^{-6}$	$-1.8449\cdot10^{-5}$

Study case 6

	Test 1	**Test 2**	**Test 3**	**Test 4**
At the beginning of self-pressurisation				
$B^P \cdot \frac{\partial T^V}{\partial t}$	$-7.9349\cdot10^{-6}$	$-5.1790\cdot10^{-6}$	$-3.5537\cdot10^{-6}$	$-8.5922\cdot10^{-6}$

Table 86. Values of $\boldsymbol{B^P} \cdot \frac{\partial T^V}{\partial t}$, $\boldsymbol{C^P} \cdot \frac{\partial V^L}{\partial t}$ and $\boldsymbol{F^P}$ during the self-pressurisation.

$C^P \cdot \frac{\partial V^L}{\partial t}$	$4.4709\cdot10^{-6}$	$2.2013\cdot10^{-6}$	$1.3829\cdot10^{-6}$	$5.3499\cdot10^{-6}$
F^P	-0.000147	-0.0001344	-0.0001093	-0.0003798
At the end of self-pressurisation				
$B^P \cdot \frac{\partial T^V}{\partial t}$	$-3.6899\cdot10^{-8}$	$1.1304\cdot10^{-7}$	$-1.3319\cdot10^{-6}$	$1.0432\cdot10^{-5}$
$C^P \cdot \frac{\partial V^L}{\partial t}$	$-3.7921\cdot10^{-6}$	$-2.9736\cdot10^{-6}$	$6.1739\cdot10^{-8}$	$-1.0617\cdot10^{-5}$
F^P	$-3.986\cdot10^{-6}$	$-3.005\cdot10^{-5}$	$-6.572\cdot10^{-5}$	$-7.877\cdot10^{-5}$
Study case 7				
	Test 1	**Test 2**	**Test 3**	
At the beginning of self-pressurisation				
$B^P \cdot \frac{\partial T^V}{\partial t}$	$-3.0468\cdot10^{-6}$	$-1.7539\cdot10^{-6}$	$1.8142\cdot10^{-6}$	
$C^P \cdot \frac{\partial V^L}{\partial t}$	$1.8423\cdot10^{-6}$	$1.095\cdot10^{-6}$	$-5.3522\cdot10^{-5}$	
F^P	$-8.1842\cdot10^{-5}$	$-7.40782\cdot10^{-5}$	$4.9284\cdot10^{-5}$	
At the end of self-pressurisation				
$B^P \cdot \frac{\partial T^V}{\partial t}$	$7.7838\cdot10^{-7}$	$2.3510\cdot10^{-6}$	$-3.208\cdot10^{-5}$	
$C^P \cdot \frac{\partial V^L}{\partial t}$	$-1.9606\cdot10^{-6}$	$-2.271\cdot10^{-6}$	$-2.4471\cdot10^{-5}$	
F^P	$-6.9335\cdot10^{-6}$	$-1.9862\cdot10^{-5}$	$5.0462\cdot10^{-5}10^{-5}$	

At the beginning of the self-pressurisation, the value of the term F^P is always higher than $B^P \cdot \frac{\partial T^V}{\partial t}$ and $C^P \cdot \frac{\partial V^L}{\partial t}$, except when the self-pressurisation starts at isothermal initial condition (Test 2 of Study case 3). Hence, the net mass flow ($\dot{m}_N$) affects more the self-pressurisation than the warming of the ullage and the thermal expansion of the liquid. For Test 2 of Study case 3, the value of the term F^P has the same order of magnitude of $B^P \cdot \frac{\partial T^V}{\partial t}$, suggesting that the warming of the ullage has the same influence of $\dot{m}_N$ on the self-pressurisation.

At the end of the self-pressurisation, the value of the term F^P has the same order of magnitude of $C^P \cdot \frac{\partial V^L}{\partial t}$, while $B^P \cdot \frac{\partial T^V}{\partial t}$ is lower than these two terms for Tests 1 and 2 of Study case 1, and Test 1 of Study case 2 (tests at high filling ratio and low heat fluxes), Test 1 of Study case 6 (medium heat fluxes and high filling ratio) and Test 1 of Study case 7 (high heat fluxes and high filling ratio). The term F^P is higher than the terms $C^P \cdot \frac{\partial V^L}{\partial t}$ and $B^P \cdot \frac{\partial T^V}{\partial t}$ at Tests 3, 4, 5 and 6 of Study case 1 (low heat fluxes medium-low filling ratio), Study case 5 (medium heat fluxes), at Tests 2 and 3 of Study case 6 (medium heat flux and medium-low filling ratio) and Test 1 of Study case 7 (high heat fluxes and high filling ratio). For the remaining tests, the terms $B^P \cdot \frac{\partial T^V}{\partial t}$, $C^P \cdot \frac{\partial V^L}{\partial t}$ and F^P have the same order of magnitude. Hence, the term F^P is always the main actor of the self-pressurisation. The warming of the ullage, thus $B^P \cdot \frac{\partial T^V}{\partial t}$, is important at low filling ratio and when liquid hydrogen (LH_2) is stored in the cryogenic container because the derivate of the vapour density respect to the temperature ($\left.\frac{\partial \rho^V}{\partial T^V}\right|_P$) of the hydrogen is higher than the one of the nitrogen[88]. The thermal expansion, thus $C^P \cdot \frac{\partial V^L}{\partial t}$, is relevant on the self-pressurisation when the filling ratio is high.

---

[88] $\left.\frac{\partial \rho^V}{\partial T^V}\right|_P$ of LH_2 at saturation of 1 bar is -0.0842 kg/m^3/K. $\left.\frac{\partial \rho^V}{\partial T^V}\right|_P$ of LN_2 at saturation of 1 bar is -0.0672 kg/m^3/K

As presented in Section 7.1.3, 7.2.3 and 7.3.3 of Chapter 4, the computed pressure is always lower than the experimental one, except for Test 3 of Study case 7. The ullage temperature, which can influence the time-evolution of the pressure, is often over-estimated (Study case 5) or under-estimated (Study case 3, 4, 5 and 6). Hence, the under-estimation of the pressure is mainly caused by the low values of $\dot{m}_N$ for liquid nitrogen and liquid hydrogen, due to the behaviour of the liquid-to-interface heat flow ($\dot{Q}_I^L$). The under-estimation of the ullage temperature can reduce the self-pressurisation computed with the homogeneous model for liquid hydrogen storage containers.

8.6. Ullage temperature

The time-evolution of the ullage temperature is calculated with the vapour temperature evolution (T^V-e) equation (Equation 134) of the homogeneous model (H model). This equation is deduced from the conservation law of vapour energy (Equation 98), as it is explained in Section 2. As it is indicated by T^V-e equation, the variation of the vapour temperature mainly depends on the coefficients B^{TV} and F^{TV}, and on the terms $A^{TV} \cdot \frac{\partial P^V}{\partial t}$ and $C^{TV} \cdot \frac{\partial V^L}{\partial t}$ because the mass flows $\dot{m}_{IN}^V$ and $\dot{m}_{BOG}$ are equal to zero during the self-pressurisation. The coefficient B^{TV} is proportional to the vapour mass, thus on the ullage volume, as it is indicated in Table 69. The coefficient F^{TV}, which describes the accumulation of sensible heat, is calculated from the dry side wall-to-vapour heat flow ($\dot{Q}_W^{SV}$), the vapour-to-interface heat flow ($\dot{Q}_I^V$) and on the enthalpy flow of the net mass flow ($\dot{m}_N \cdot \left[\tilde{h}_S^V(P^V) - \tilde{h}^V(T^V, P^V)\right]$), as it is described in Table 42. The term $A^{TV} \cdot \frac{\partial P^V}{\partial t}$, which describes the increment of temperature due to the increment of pressure, is proportional to the mass, thus the ullage volume. The term $C^{TV} \cdot \frac{\partial V^L}{\partial t}$ does not affect the time-evolution of the ullage, as indicated in Table 69. As a consequence, the increment of the ullage temperature can increase with the reduction of B^{TV}, thus with the reduction of the vapour mass, with the increment of the pressure and with the increments of the dry side wall-to-vapour heat flow ($\dot{Q}_W^{SV}$). The vapour temperature can reduce with the increment of the net mass flow ($\dot{m}_N$) and of the vapour-to-interface heat flow ($\dot{Q}_I^V$). The values of $A^{TV} \cdot \frac{\partial P^V}{\partial t}$ and B^{TV} are reported in Table 87 at the beginning and at the end of the self-pressurisation.

Table 87. Values of $\boldsymbol{A^{TV}} \cdot \frac{\partial P^V}{\partial t}$ and $\boldsymbol{F^{TV}}$ during the self-pressurisation.

Study case 1						
	Test 1	**Test 2**	**Test 3**	**Test 4**	**Test 5**	**Test 6**
At the beginning of self-pressurisation						
$A^{TV} \cdot \frac{\partial P^V}{\partial t}$	$-1.59304 \cdot 10^{-2}$	$-1.4186 \cdot 10^{-2}$	$-2.6640 \cdot 10^{-2}$	$-1.2664 \cdot 10^{-2}$	$-9.7889 \cdot 10^{-3}$	$-8.3808 \cdot 10^{-3}$
F^{TV}	$-3.5321 \cdot 10^{-4}$	$-8.3572 \cdot 10^{-4}$	$-7.653 \cdot 10^{-4}$	$-8.9788 \cdot 10^{-5}$	$-1.0481 \cdot 10^{-3}$	$-1.1208 \cdot 10^{-2}$
At the end of self-pressurisation						
$A^{TV} \cdot \frac{\partial P^V}{\partial t}$	$-1.4249 \cdot 10^{-4}$	$-3.245 \cdot 10^{-4}$	$-7.015 \cdot 10^{-4}$	$-7.009 \cdot 10^{-4}$	$-1.6242 \cdot 10^{-3}$	$-3.9853 \cdot 10^{-3}$
F^{TV}	$-1.3021 \cdot 10^{-4}$	$-5.9907 \cdot 10^{-4}$	$-1.152 \cdot 10^{-3}$	$-1.3614 \cdot 10^{-3}$	$-3.2826 \cdot 10^{-3}$	$-7.8254 \cdot 10^{-3}$
Study case 2						
	Test 1					
At the beginning of self-pressurisation						
$A^{TV} \cdot \frac{\partial P^V}{\partial t}$	$-1.4319 \cdot 10^{-2}$					
F^{TV}	$-8.4817 \cdot 10^{-4}$					
At the end of self-pressurisation						

Table 87. Values of $\boldsymbol{A^{TV}}\cdot\frac{\partial P^V}{\partial t}$ and $\boldsymbol{F^{TV}}$ during the self-pressurisation.

$A^{TV}\cdot\frac{\partial P^V}{\partial t}$	$-2.4797\cdot10^{-4}$
F^{TV}	$-3.5635\cdot10^{-4}$

Study case 3		
	Test 1	**Test 2**
At the beginning of self-pressurisation		
$A^{TV}\cdot\frac{\partial P^V}{\partial t}$	-3.3217	-5.381
F^{TV}	$-6.1147\cdot10^{-3}$	-20.607
At the end of self-pressurisation		
$A^{TV}\cdot\frac{\partial P^V}{\partial t}$	$-2.1771\cdot10^{-1}$	$-2.2697\cdot10^{-1}$
F^{TV}	$-6.9464\cdot10^{-2}$	$-6.8221\cdot10^{-2}$

Study case 4		
	Test 1	**Test 2**
At the beginning of self-pressurisation		
$A^{TV}\cdot\frac{\partial P^V}{\partial t}$	-2.8697	-2.4236
F^{TV}	$-8.1802\cdot10^{-1}$	$-2.0263\cdot10^{-2}$
At the end of self-pressurisation		
$A^{TV}\cdot\frac{\partial P^V}{\partial t}$	-1.27033	-2.03339
F^{TV}	$-3.5422\cdot10^{-1}$	$-6.4647\cdot10^{-1}$

Study case 5			
	Test 1	**Test 2**	**Test 3**
At the beginning of self-pressurisation			
$A^{TV}\cdot\frac{\partial P^V}{\partial t}$	$-2.1939\cdot10^{-1}$	$-1.0951\cdot10^{-1}$	$-7.82376\cdot10^{-2}$
F^{TV}	$-4.9068\cdot10^{-4}$	$-4.5574\cdot10^{-2}$	$-9.9909\cdot10^{-2}$
At the end of self-pressurisation			
$A^{TV}\cdot\frac{\partial P^V}{\partial t}$	$-9.3959\cdot10^{-3}$	$-3.3699\cdot10^{-2}$	$-1.1245\cdot10^{-1}$
F^{TV}	$3.3857\cdot10^{-2}$	$8.8313\cdot10^{-2}$	$7.6622\cdot10^{-2}$

Study case 6				
	Test 1	**Test 2**	**Test 3**	**Test 4**
At the beginning of self-pressurisation				
$A^{TV}\cdot\frac{\partial P^V}{\partial t}$	-1.9569	-1.4876534	-1.0871	-3.1086
F^{TV}	$-8.9101\cdot10^{-2}$	$-5.7724\cdot10^{-2}$	$-4.6299\cdot10^{-2}$	$-1.8232\cdot10^{-2}$
At the end of self-pressurisation				
$A^{TV}\cdot\frac{\partial P^V}{\partial t}$	$-2.0193\cdot10^{-1}$	-1.0125	-2.3018	-2.0327
F^{TV}	$1.9131353\cdot10^{-1}$	1.04736438	1.87178328	6.73130272

Study case 7			
	Test 1	**Test 2**	**Test 3**
At the beginning of self-pressurisation			
$A^{TV}\cdot\frac{\partial P^V}{\partial t}$	$-9.333\cdot10^{-1}$	$-6.5224\cdot10^{-1}$	$-3.5078\cdot10^{-1}$

Table 87. Values of $\boldsymbol{A^{TV}\cdot\frac{\partial P^V}{\partial t}}$ and $\boldsymbol{F^{TV}}$ during the self-pressurisation.

F^{TV}	-4.5284·10^{-2}	-3.3472·10^{-2}	-3.1297·10^{-2}
At the end of self-pressurisation			
$A^{TV}\cdot\frac{\partial P^V}{\partial t}$	-0.1777	-0.6166	-1.6207
F^{TV}	0.4955	1.6351	3.18868

At the beginning of the self-pressurisation, the term $A^{TV}\cdot\frac{\partial P^V}{\partial t}$ is higher than the ones of coefficient F^{TV} for Tests 1, 2, 3 and 4 of Study case 1, Test 1 of Study case 2, Test 1 of Study case 3, Study case 4, Test 1 and 2 of Study case 5, Study case 6 and 7. The values of term $A^{TV}\cdot\frac{\partial P^V}{\partial t}$ has the same order of magnitude of the one of the coefficient F^{TV} or lower, for Tests 5 and 6 of Study case 1, and Test 2 of Study case 3 and Test 3 of Study case 5. Hence, the increment of the pressure affects more the increment of the vapour temperature than the accumulation of sensible heat in the ullage because the ullage is at steady state when the self-pressurisation starts. Low filling ratios and isothermal initial conditions can inverse this behaviour because the ullage mass reduce and sensible heat can be accumulated in large quantity.

At the end of the self-pressurisation, the term $A^{TV}\cdot\frac{\partial P^V}{\partial t}$ is almost equal or lower than the ones of coefficient F^{TV} for every Study cases, except Study case 3 and 4. Hence, the accumulation of the sensible heat in the ullage affects more the increment of the vapour temperature than the increment of the pressure, after the beginning of the self-pressurisation, if the storage container is relatively small. For large mass of vapour (Study cases 3 and 4), the increment of pressure is more important than the accumulation of sensible heat in the ullage on the warming of the vapour phase.

As reported in Section 7.1.4, 7.2.4 and 7.3.4 of Chapter 4, the calcualted ullage temperature increases with a small transient at low heat fluxes (Study cases 1, 2, 3 and 4), but the rate of this increment is lower than the experimental one. At medium and high heat fluxes (Study cases 5, 6 and 7), the calculated ullage temperature initially increases. Then, it decreases or it remains almost constant, creating a peak. Except for Study cases 3 and 4, the initial increment of the temperature occurs when the net mass flow ($\dot{m}_N$) decreases. When $\dot{m}_N$ is stable, the ullage temperature slightly increases. When this mass flow is stable, the ullage temperature remains slightly increases or decreases. Hence, the time-evolution of ullage temperature is quite similar to the time-evolution of the net mass flow, indicating that the enthalpy flow of the net mass flow affect more the coefficient F^{TV} than the dry side wall-to-vapour and vapour-to-interface heat flows. This influence of enthalpy flow of the net mass flow is particularly relevant at medium and high heat fluxes.

8.7.Liquid temperature

The time-evolution of the liquid temperature is calculated with the liquid temperature evolution (T^L-e) equation (Equation 134) of the homogeneous model (H model). This equation is deduced from the energy conservation law of liquid (Equation 96), as it is explained in Section 2 of Chapter 4. As it is indicated by T^L-e equation, the variation of the liquid temperature mainly depends on the coefficients B^{TL} and F^{TL}, and on the terms $A^{TL}\cdot\frac{\partial P^V}{\partial t}$ and $C^{TL}\cdot\frac{\partial V^L}{\partial t}$ because the mass flows $\dot{m}_{IN}^L$ and $\dot{m}_{OUT}^L$ are equal to zero during the self-pressurisation. The coefficient F^{TL} describes the accumulation of sensible heat and it is composed by the bottom-to-liquid heat flow ($\dot{Q}_W^B$), the wet side wall-to-liquid heat flow ($\dot{Q}_W^{SL}$), the liquid-to-interface heat flow ($\dot{Q}_I^L$) and the enthalpy flow of the net mass flow ($\dot{m}_N\cdot$

$\left[\tilde{h}_S^L(P^V) - \tilde{h}^L(T^L,P^L)\right]$). As shows in Sections 7.1.1, 7.2.1 and 7.3.1 of Chapter 4, the liquid temperature monotonically increases, indicating that the coefficient F^{TL} affects more this increment than the term $A^{TL} \cdot \frac{\partial P^V}{\partial t}$. The calculated values are close to the experimental data of liquid temperature.

During the self-pressurisation, the liquid receives energy from the environment and from the interface. This sensible energy cannot be released at the interface as occurs in the steady state. Hence, the liquid temperature increases in time due to the accumulation of sensible heat. The enthalpy flow $\dot{m}_N \cdot \left[\tilde{h}_S^L(P^V) - \tilde{h}^L(T^L,P^L)\right]$) affects less the increment of temperature than the heat flows $\dot{Q}_w^B$, $\dot{Q}_w^{SL}$ and $\dot{Q}_I^L$ because the different in temperature between the interface and the liquid is very low. As the filling ratio is reduced, the thermal capacity, which depends on the mass, is lower than the one at high filling ratio. Hence, the derivate of the liquid temperature (Equation 134) increases and the liquid temperature is higher at low liquid level than at a high filling ratio. The liquid temperature is very close to the interface temperature, thus the saturation one. The rise of the liquid temperature is, however, not enough high to reach the equilibrium condition due to the thermal resistance of the liquid-to-interface heat transfer.

8.8. Conclusion

The comparison of the results of the homogeneous model (H model) with the experimental data has revealed some drawbacks concerning the Interface Heat Transfer (IHT), Storage Heat Transfer (SHT) and Storage Boundary Layer (SBL) models and some advantages given by the Boil-Off Rate (BOR) model. The values of the effective heat transfer coefficient (h_{eff}) are physically coherent because the insulating properties do not change with the filling ratio. The values of alpha coefficient reduce with the initial filling ratio as it should be due to the decrement of the heat inputs with the initial liquid level. This coefficient can properly compensate the over-estimation of the heat coming into the ullage caused by the hypothesis of total homogeneity (assumption a) of Section 1.1 of Chapter 4). The values of beta coefficient are irregular and they are often equal to zero, indicating that the heat cannot be transferred via conduction through the dry side wall. This is physically impossible because there is a temperature gradient in the dry side wall, which produces a heat flow from the dry side to the interface ($\dot{Q}_w^{LV}$). The negative values of beta coefficient are caused by the over-estimation of the vapour-to-interface heat flow ($\dot{Q}_I^V$) at the steady state. Hence, the BOR model is well developed, but Equation 210 of the IHT model, which calculates $\dot{Q}_I^V$, is the main of problems for estimating the beta coefficient.

The initial values of vapour temperature and heat inputs are not properly computed before the self-pressurisation. This occurs when the value of the beta coefficient are equal to zero. Hence, the H model can fail in computing the initial conditions of the self-pressurisation due to the over-estimation of the heat flow $\dot{Q}_I^V$, thus due to Equation 210 of the IHT model.

The H model cannot calculate the time-evolution of pressure. The values of the calculated pressure are always lower than the experimental ones, except for high heat fluxes and low filling ratio. The calculated value of the temperature are lower than the experimental ones at low heat fluxes and they are qualitatively wrong at medium and high heat fluxes, due to the presence of peaks. The increment of the pressure is mainly controlled by the net mass flow at the interface ($\dot{m}_N$). This increment can be affected by the rise of ullage temperature at low filling ratio, if storage container is filled with liquid hydrogen. The time-evolution of the net mass flow is controlled by the liquid-to-interface heat flow ($\dot{Q}_I^L$), which is computed with Equation 211 of IHT model. The negative values of this heat flow are too low due to the hypothesis of total homogeneity (assumption a) of Section 1.1 of Chapter 4). Hence, the hypothesis of total homogeneity (assumption a) of Section 1.1 of Chapter 4) is unsuitable for calculating the self-pressurisation because it excessively decreases the values of $\dot{Q}_I^L$ that are computed with Equation 211 of IHT model.

The H model cannot compute the time-evolution of ullage temperature. The calculated values of the temperature are lower than the experimental one at low heat fluxes. These values are qualitatively wrong at medium and high heat fluxes, due to peaks. The rise of temperature is only controlled by the accumulation of sensible heat in the ullage, in particular by the enthalpy flow of the net mass flow at high and medium heat fluxes, as it is described by the coefficient F^{TV} of Equation 134. The coefficient F^{TV} is calculated with a formula obtained from the conservation law of ullage energy (Equation 98), which is deduced from the assumption a) of Section 1.1 of Chapter 4. Hence, this hypothesis is not suitable for calculating the rise of the ullage temperature because the enthalpy flow of the net mass flow affects too much this coefficient, thus the accumulation of the sensible heat.

The calculated liquid temperature is close to the experimental value. Hence, the H model is suitable for predicting the rise of the temperature in the liquid.

8.9. Summary and perspectives

The homogenous (H) model is developed under the hypotheses of total homogeneity, actual thermodynamic state and local equilibrium condition (assumption a), b) and c) of Section 1.1 of Chapter 4). The equations that compute the time-evolution of pressure, ullage temperature, liquid temperature and liquid volume are deduced from these hypotheses, using the conservation laws of mass and energy. The Boil-Off Rate (BOR), the Storage Heat Transfer (SHT), the Storage Boundary Layer (SBL) and the Interface Heat Transfer (IHT) models are required because the boundary conditions, the heat inputs, and the heat and mass flows at the interface have to be computed, as consequence of the hypotheses of the H model. The comparison with the experimental data indicates that the calculated time-evolution of pressure and the vapour temperature are not in agreement with the experimental ones. The computed the coefficient beta, the liquid-to-interface heat flow and the coefficient F^{TV} of the vapour-temperature evolution equation (Equation 134) are the factors that cause this deviation between the H model and the experimental data. These factors are not estimated with accuracy and often not qualitatively correct because of the hypothesis of total homogeneity (assumption a) of Section 1.1 of Chapter 4) and of Equation 210 of the IHT model.

Hence, the H model must be improved, in particular in the prediction of the time-evolution of the ullage temperature, which is the weakest point of this model. This improvement can be done by removing the hypothesis of total homogeneity (assumption a) of Section 1.1 of Chapter 4) for the ullage and changing the equation that computes the vapour-to-interface heat flow ($\dot{Q}_I^V$). So, new vapour temperature-evolution equation will be deduced from the conservation laws. A new equation of $\dot{Q}_I^V$ will be obtained from the fluid-dynamics of the ullage. The improvement of the calculation of the pressure is not as urgent as the ullage temperature one. So, Equation 211 of the IHT model will be coupled with another equation for the reducing the over-estimation of the liquid-o-interface heat flow during the self-pressurisation.

9. Comparison with the results of equilibrium model

The homogeneous model (H model) is developed because the equilibrium model (EQ model) cannot calculate the time-evolutions of vapour temperature and pressure that are in agreement with the experimental data, because of the hypothesis of instantaneous thermodynamic equilibrium (assumption a) of Section 1.1 of Chapter 3). This assumption is removed and a new set of hypotheses is done in the H model. These hypotheses increase the complexity of the storage model, increasing the computational time. Hence, the computational time and the accuracy of H model are compared with the ones of EQ model. The accuracy is evaluated using the statistical errors: Average Absolute Deviation (AAD), the Bias and the Maximum Absolute Deviation (MAD), which are reported in Section 1 of Appendix S.

Section 9.1 presents the computational time of H and EQ models. Section 9.2, 9.3, 9.4 and 9.5 discusses the accuracy of both models in describing the pressure, the ullage temperature, the liquid temperature and the filling ratio. Section 9.6 explains the causes of these results and it presents the conclusions. Section 9.7 summarizes the comparison between the two models and it describes the perspective for improving the H model.

9.1. Computational time

The computational time is an important features of the storage model (equilibrium and homogeneous) because these models should be used for industrial and commercial applications. In this thesis, the computational time is the time required to execute the whole structure of the storage model (equilibrium and homogeneous), form the Boil-Off Rate (BOR) model to the calculation at the last time-point. The computational time of equilibrium model (EQ model) and the one of homogeneous model (H model) are reported in Table 88.

Table 88. Values of $\boldsymbol{t_C^{EQ}}$ and $\boldsymbol{t_C^{H}}$.

	Study case 1					
	Test 1	**Test 2**	**Test 3**	**Test 4**	**Test 5**	**Test 6**
$t_C^{EQ}\ [s]$	3.8075	4.1900	3.5462	3.0890	2.9731	3.7029
$t_C^{H}\ [s]$	5327.7	4160.8	1429.1	3443.1	1137.8	1032.1
	Study case 2					
	Test 1					
$t_C^{EQ}\ [s]$	3.0932					
$t_C^{H}\ [s]$	5929.41					
	Study case 3					
	Test 1	**Test 2**				
$t_C^{EQ}\ [s]$	3.3251	3.4984				
$t_C^{H}\ [s]$	1212.6	1033.1				
	Study case 4					
	Test 1	**Test 2**				
$t_C^{EQ}\ [s]$	3.7736	2.8355				
$t_C^{H}\ [s]$	802.73	513.32				
	Study case 5					
	Test 1	**Test 2**	**Test 3**			
$t_C^{EQ}\ [s]$	5.6265	3.4442	3.4997			
$t_C^{H}\ [s]$	19681.4	11786.6	7164.9			
	Study case 6					
	Test 1	**Test 2**	**Test 3**	**Test 4**		
$t_C^{EQ}\ [s]$	4.6289	1.9285	1.6453	3.8802		
$t_C^{H}\ [s]$	1285.5	804.5	1361.4	1478.9		
	Study case 7					
	Test 1	**Test 2**	**Test 3**			

Table 88. Values of $\boldsymbol{t_C^{EQ}}$ and $\boldsymbol{t_C^{H}}$.

$t_C^{EQ}\ [s]$	3.3884	8.6683	3.9810
$t_C^{H}\ [s]$	1258.7	1313.6	2056.7

As it is indicated by Table 88, the EQ model takes around 3 seconds to simulate the storage container. The H model takes a time that is at least 3 orders of magnitude more than the computational time of EQ model, on average. The H model simulates the storage container in less than 1 hour. The computational time of H model is lower than the experimental time that is simulated.

The H model takes more time than the EQ model due to the Storage Boundary Layer (SBL) model seeing that this model is used at each iteration of Storage Heat Transfer (SHT) model to compute the heat transfer coefficient. As a consequence, the values of computational times of Study cases at medium and high heat fluxes are usually higher than the ones at low heat fluxes because more sub-space-points, thus iteration, are required in the SBL model.

9.2.Accuracy in computing the pressure

The Average Absolute Deviation (AAD), BIAS and Maximum Absolute Deviation (MAD) of the calculated pressure of homogeneous (H) and equilibrium model (EQ model)s are reported in Figure 90 for all the study cases.

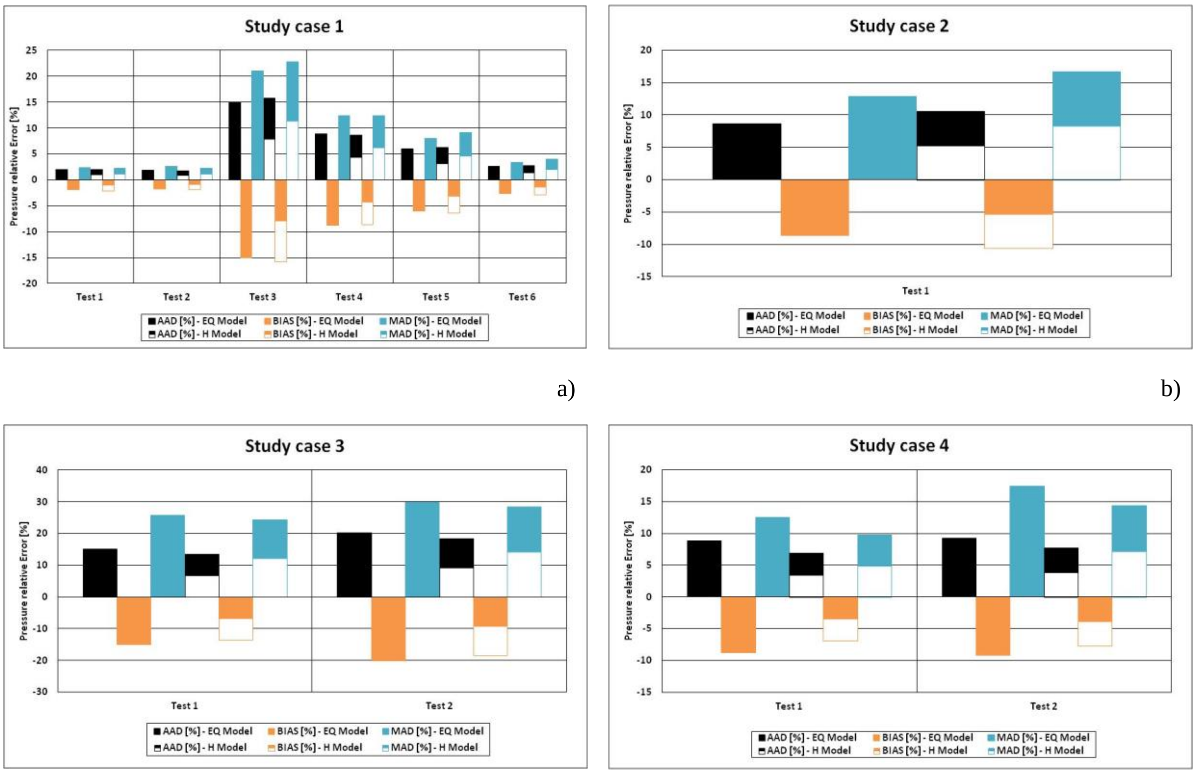

a)

b)

c)

d)

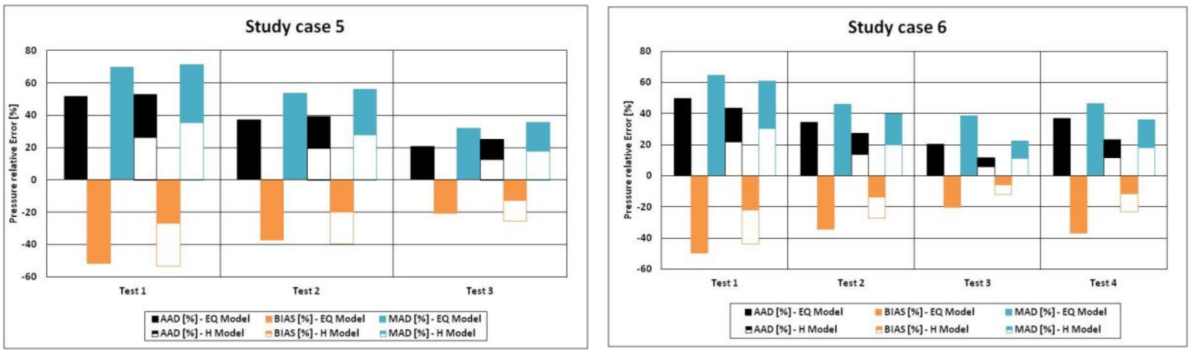

e)

f)

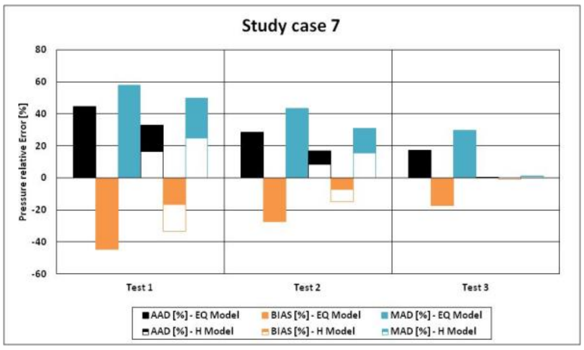

Figure 90. The values of AAD, BIAS and MAD of the calculated pressure of H and EQ models for Study case 1 (a), 2 (b), 3 (c), 4 (d), 5 (e), 6 (f) and 7 (g).

g)

For the Study case 1, the highest value of AAD, BIAS and MAD are calculated for Test 3 (high heat inputs). The lowest values of these statistical errors are computed for Test 1 and Test 3 (high filling ratio). The values of AAD, BIAS and MAD decreases from Test 4 to Test 6, thus they decrease from medium to low filling ratio. The difference in the values of these statistical errors between the H and the EQ models is small.

For Study case 2, the difference in the values of these statistical errors between the H and the EQ models is small as for the previous case.

For Study case 3, the EQ and the H models are less accurate at Test 2 (isothermal initial conditions) than at Test 1 (steady state initial conditions) because the highest values of AAD, BIAS and MAD are calculated for Test 2. The difference in the values of these statistical errors between the H and the EQ models is small.

For Study case 4, the values of AAD, BIAS and MAD are lower than the ones of the Study case 3. The values of these statistical errors are higher at Test 2 (low filling ratio) than Test 1 (medium filling ratio). As it is indicated by Figure 90 (d), the H model is slightly more accurate than the EQ model because the values of AAD, BIAS and MAD of H model are lower than the ones of the EQ model.

For Study case 5, the values of AAD, BIAS and MAD decrease from Test 1 to Test 3, thus they decreases from high to low filling ratio. The difference in the values of these statistical errors between the H and the EQ models is small. The values of these statistical errors increase for H and EQ model, passing from low to medium heat fluxes.

For Study case 6, the same behaviour of Study case 5 is observed, but the H model is slightly better than EQ model. For high heat input (Test 4), the values of AAD, BIAS and MAD are higher than the one at low heat input (Test 1, 2 and 3) for H and EQ models.

For Study case 7, the same behaviour of Study case 5 and 6 is observed. The values of AAD, BIAS and MAD decrease from Test 1 to Test 3, thus from high to low filling ratio. The values of these statistical errors are higher than the one sat low heat fluxes and they are almost equal to the ones at medium heat fluxes. The differences in values of AAD, BIAS and MAD between the H and EQ models are more visible than the ones of at low and medium heat fluxes.

9.3. Accuracy in computing the ullage temperature

The Average Absolute Deviation (AAD), BIAS and Maximum Absolute Deviation (MAD) of the calculated ullage temperature of homogeneous (H) and equilibrium model (EQ model)s are reported in Figure 91 for all the study cases.

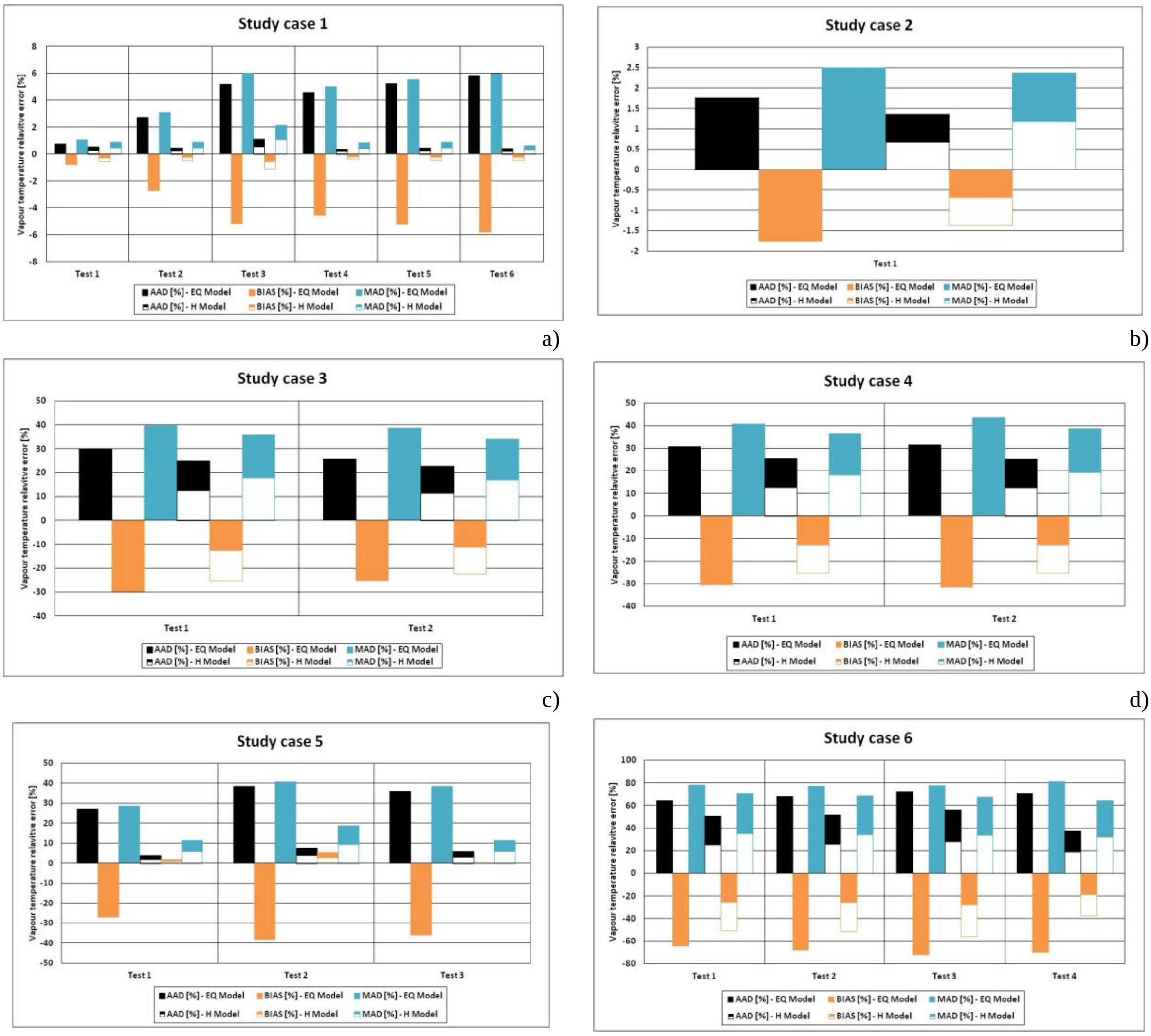

a) b)

c) d)

e) f)

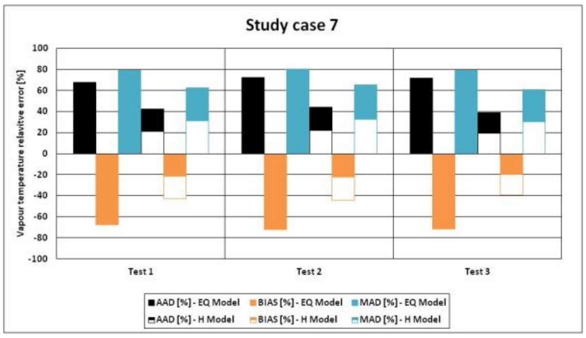

g)

Figure 91. The values of AAD, BIAS and MAD of the calculated ullage temperature of H and EQ models for Study case 1 (a), 2 (b), 3 (c), 4 (d), 5 (e), 6 (f) and 7 (g).

For Study case 1, the values of AAD, BIAS and MAD of EQ model increase from Test 1 to Test 6, thus they increase from high to low filling ratio. The values of these statistical errors of the EQ model at Test 3 (high heat inputs) are the highest values. The values of AAD, BIAS and MAD of H model are much lower than the ones of EQ model for all the tests. The highest values of these statistical errors of the H model are computed at Test 3. Hence, the H model is more accurate than EQ model. The accuracy of H model decreases with the increment of the heat input.

For Study case 2, the values of AAD, BIAS and MAD of H model are lower than the ones of EQ model, but the difference in these statistical errors between the two models is lower than the one observed for Study case 1. The H model is more accurate than the EQ model.

For Study case 3, the values of AAD, BIAS and MAD of the EQ and H models decrease from Test 1 (steady state initial conditions) to Test 2 (isothermal initial conditions) because the calculated initial temperature of both models at Test 2 is closer to the experimental value than the one of Test 1. The values of these numerical errors of H model are slightly lower than EQ model. So, the H model is slightly more accurate than EQ model.

For Study case 4, the values of AAD, BIAS and MAD of the EQ model slightly increase from Test 1 (medium filling ratio) to Test 2 (low filling ratio) because the difference in temperatures between the calculated and the measured ullage temperature is higher at Test 2 than Test 1. The values of these statistical errors of H model are lower than the one of EQ model, but the differences in values of AAD, BIAS and MAD of H model between Test 1 and Test 2 is almost null. Hence, the H model is more accurate than EQ model.

For Study case 5, the values of AAD, BIAS and MAD of the EQ model increase from Test 1 (high filling ratio) to Test 2 (medium filling ratio) and they slightly decrease from Test 2 to Test 3 (low filling ratio). Hence, the maximum values of these statistical errors of EQ model are calculated at Test 2. The values of AAD, BIAS and MAD of the H model increase from Test 1 to Test 2 and they decrease from Test 2 to Test 3, creating a maximum at the medium filling ratio, as for EQ model. The values of these statistical errors of the H model are much lower than the one of EQ model. The values of BIAS are lower than the values of AAD and MAD due to the peaks of vapour temperature. The H model is more accurate than the EQ model and the maximum deviations occur at medium filling ratio.

For Study case 6, the values of AAD, BIAS and MAD of the EQ model are almost constant with the filling ratio and heat inputs, and they do not significantly change from Test 1 to Test 4. The values of these statistical errors of the H model are almost constant from Test 1 to Test 3, and a small decrement is calculated for Test 4. The values of AAD, BIAS and MAD of the H model are lower than the one of EQ model. Hence, the H model is more accurate than the EQ model.

For study case 7, the values of AAD, BIAS and MAD of the EQ model are constant at any filling ratio and they do not change between Test 1 and Test 3. The same behaviour is observed for the statistical errors of H model, but the values of AAD, BIAS and MAD of H model are lower than the one of the EQ model. So, the H model is more accurate than the EQ model.

9.4. Accuracy in computing the liquid temperature

The Average Absolute Deviation (AAD), BIAS and Maximum Absolute Deviation (MAD) of the calculated liquid temperature of homogeneous (H) and equilibrium model (EQ model)s are reported in Figure 92 for all the study cases.

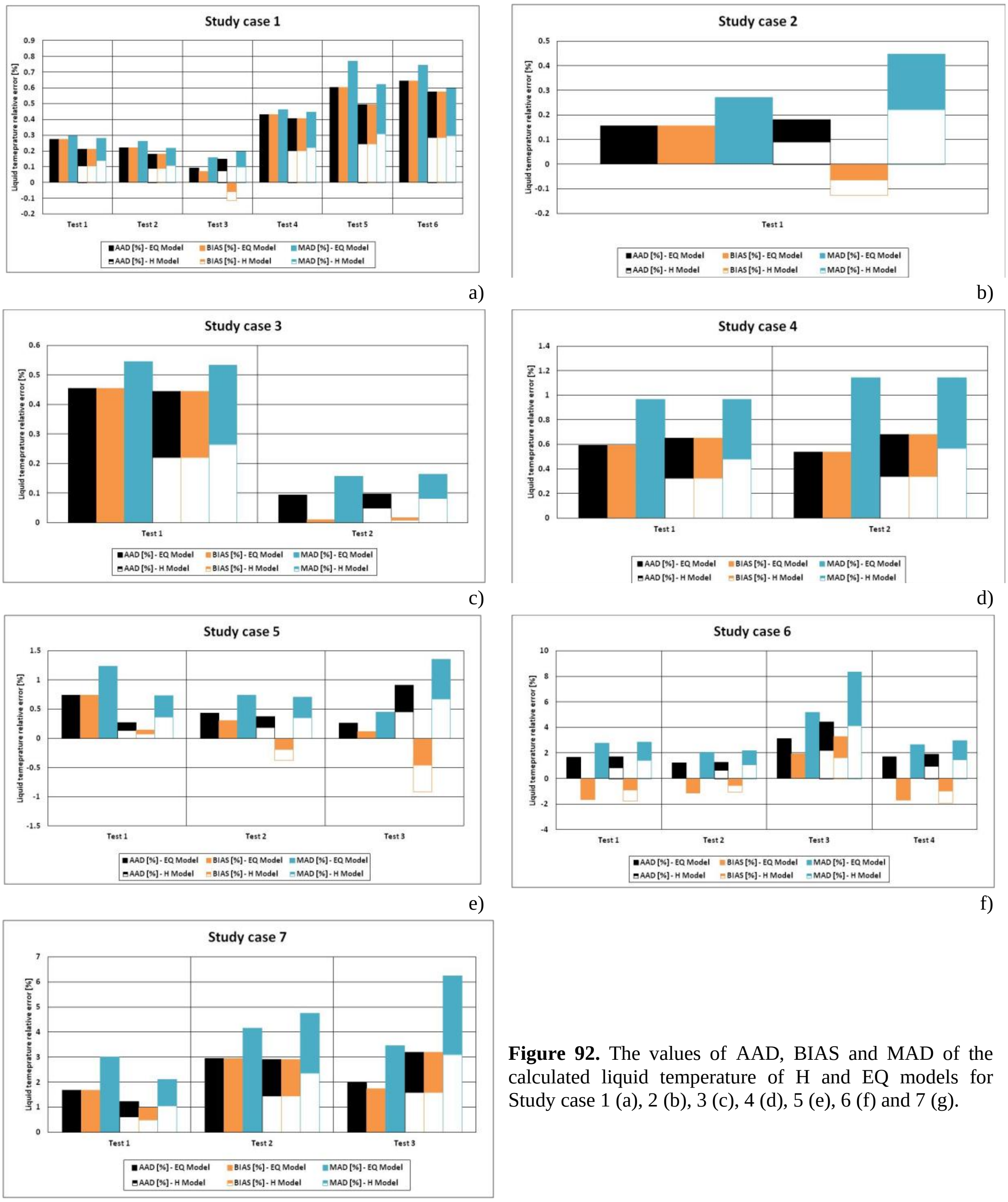

a)

b)

c)

d)

e)

f)

g)

Figure 92. The values of AAD, BIAS and MAD of the calculated liquid temperature of H and EQ models for Study case 1 (a), 2 (b), 3 (c), 4 (d), 5 (e), 6 (f) and 7 (g).

For Study case 1, the values of AAD, BIAS and MAD of EQ and H models decrease from Test 1 to Test 2. These values increase from Test 4 to Test 5 and they slightly decrease from Test 5 to Test 6. Hence, the values of statistical errors have a minimum value at Test 2 and a maximum value at Test 5. The lowest values of AAD, BIAS and MAD of EQ and H models are calculated for Test 3 (high heat inputs). The values of the statistical errors of H model are lower than the one of EQ model. Hence, the H model is slightly more accurate than EQ model.

For Study case 2, the values of AAD of EQ model is slightly lower than the one of H model. The value of MAD of H model is higher than the one of EQ model because the difference in temperature between the H model and the zxperimental liquid temperature is higher than the one of EQ model at the end of the self-pressurisation. The value of BIAS of H model is negative because the calculated temperature is lower than the experimental one at the end of the self-pressurisation.

For Study case 3, the values of AAD, BIAS and MAD of EQ model are equal to the one of H model. The values of these statistical errors of Test 1 are lower than the one of Test 2. The EQ model is as accurate as the H model.

For study case 4, the values of AAD and BIAS of EQ model slightly decrease from Test 1 (medium filling ratio) to Test 2 (low filling ratio). The values of MAD of EQ model increase from Test 1 to Test 2. The values of these statistical errors are higher than the ones of EQ model. The EQ model is more accurate than H model.

For Study case 5, the values of AAD and BIAS of EQ model decrease from Test 1 to Test 3, thus from high to low filling ratio because the pressure, thus the temperature, increases with the reduction of the filling ratio. The values of these statistical errors of H model increases from Test 1 to Test 3 because the liquid temperature at low filling ratio is slightly under-estimated since it does not receive enough energy from the interface. It cannot be stated if EQ model is better than H model or not.

For Study 6, the values of AAD, BIAS and MAD of EQ and H models are higher than the ones of the previous study cases (1, 2, 3, 4 and 5). The statistical errors of EQ and H models are almost constant between Test 1 and Test 2, and they increase between Test 2 and Test 3. The values of these statistical errors at Test 4 are slightly higher than the one of Test 1 and 2, and they are lower than the ones of Test 3, for both H and EQ models. The values of AAD, BIAS and MAD of H model are slightly lower than the ones of EQ model, except for Test 3. Hence, it cannot be stated if EQ model is better than H model or not.

For Study case 7, the values of AAD, BIAS and MAD of EQ and H model are the highest of all the study case. The values of AAD, BIAS and MAD of EQ model increase from Test 1 to Test 3, thus they increases from high to low filling ratio because the experimental temperature decreases with the reduction of the filing ratio. The values of these statistical errors of H model are lower than the ones of EQ model for Test 1. The values of AAD and BIAS of EQ model are equal to the one of H model. The values of AAD, BIAS and MAD of H model are higher of the ones of EQ model at Test 3. Hence, it cannot be stated if H model is better than EQ model.

9.5.Accuracy in computing the liquid level

The Average Absolute Deviation (AAD), BIAS and Maximum Absolute Deviation (MAD) of the calculated filling ratio of homogeneous (H) and equilibrium model (EQ model)s are reported in Figure 93 for all the study cases.

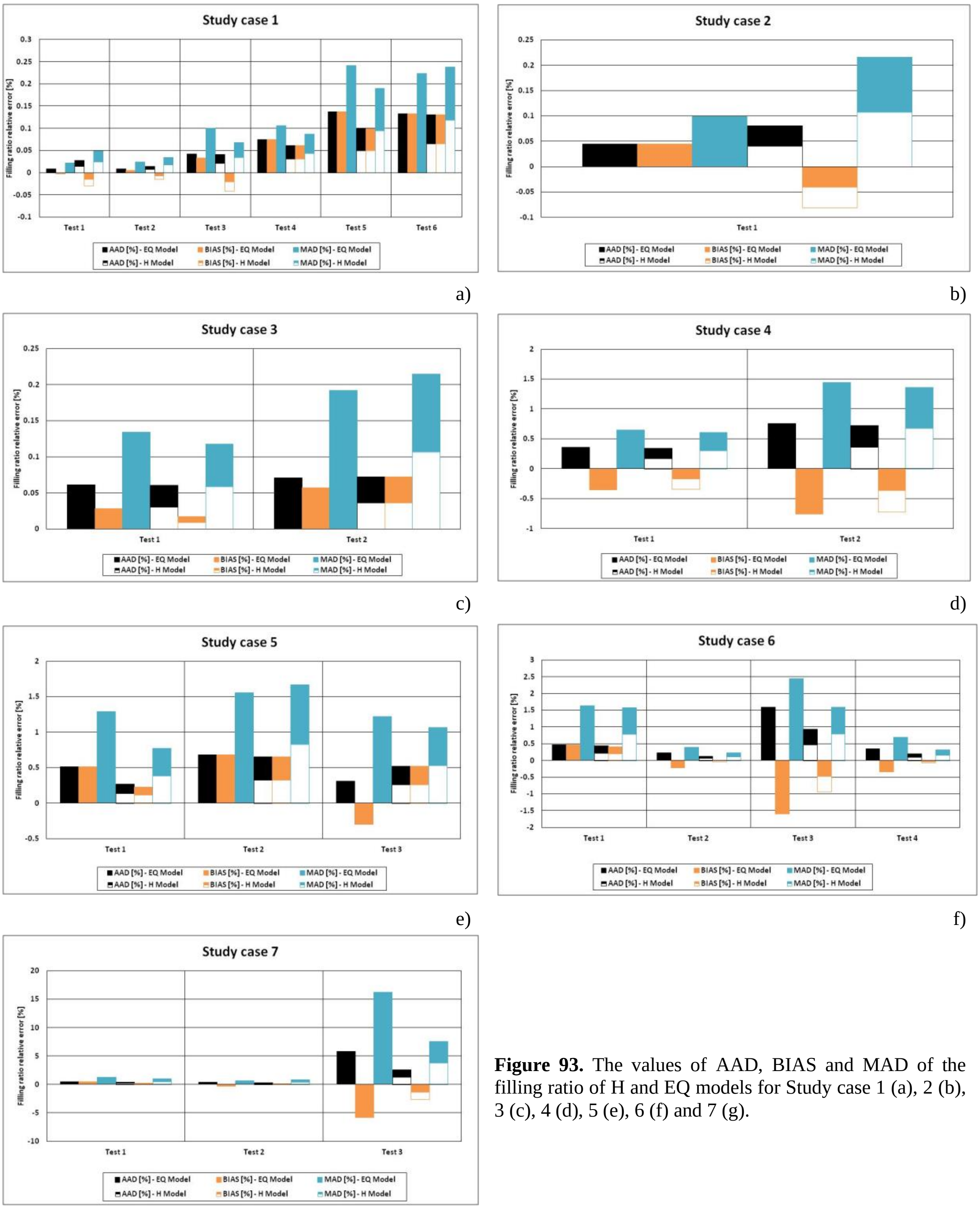

a)

b)

c)

d)

e)

f)

g)

Figure 93. The values of AAD, BIAS and MAD of the filling ratio of H and EQ models for Study case 1 (a), 2 (b), 3 (c), 4 (d), 5 (e), 6 (f) and 7 (g).

For Study case 1, the values of AAD, BIAS and MAD of EQ model increase from Test 1 to Test 5 and they slightly decrease from Test 5 to Test 6, creating a small maximum at Test 5. The values of these statistical errors of H model follow the same trend of the ones of EQ model. The highest values of AAD, BIAS and MAD of EQ and H models are calculated at Test 5 and 6. At Test 5, both models calculate a rate of thermal expansion faster than the experimental one. At Test 6, both models compute the rate of filling ratio decrement lower than the experimental one. The values of AAD, BIAS and MAD of H model are lower than the ones of EQ model. Hence, the H model is slightly more accurate than EQ model.

For Study case 2, the values of AAD, BIAS and MAD of EQ model are lower than the one of H model. The value of BIAS of H model is negative, indicating the liquid thermal expansion is lower than the experimental one. The values of AAD and MAD of H model are high because this model computes a lower value of the rate of thermal expansion than the experimental one. The EQ model is more accurate than H model.

For Study case 3, the values of AAD, BIAS and MAD of EQ and of H models increase from Test 1 (steady state initial condition) to Test 2 (isothermal initial condition). At Test 1, the values of these statistical errors of EQ model are slightly higher than the ones of H model. At Test 2, the values of AAD, BIAS and MAD of EQ model are slightly lower than the ones of H model. Hence, it cannot be stated if H model is more accurate than EQ model.

For Study case 4, the values of AAD, BIAS and MAD of EQ and of H models increase from Test 1 (medium filling ratio) to Test 2 (low filling ratio). The values of these statistical errors of EQ model are slightly higher than the ones of H model. So, the H model is slightly more accurate than EQ model.

Foes Study case 5, the values of AAD, BIAS and MAD of EQ model increase from Test 1 (high filling ratio) to Test 2 (medium filling ratio).These values decrease from Test 2 to Test 3 (low filling ratio), creating a maximum at medium filling ratio. The same behaviour of EQ model is observed for the statistical errors of H model. The values of AAD, BIAS and MAD of H model are lower than the ones of EQ model, indicating that the homogeneous modelling approach is more accurate than the equilibrium one.

For Study case 6, the values of AAD, BIAS and MAD of EQ model decrease from Test 1 (high filling ratio) to Test 2 (medium filling ratio) and they increase from Test 2 to Test 3 (low filling ratio), creating a minimum at medium filling ratio. The values of these statistical errors of EQ model at Test 4 (high heat input) are slightly higher than the ones of Test 2. The values of AAD, BIAS and MAD of H model have the same behaviour of the ones of EQ. The values of these statistical errors of H model are lower than the ones of EQ model, indicating that the homogeneous modelling approach is more accurate than the equilibrium one.

For Study case 7, the lowest values of AAD, BIAS and MAD of EQ and H models are calculated for Test 2 (medium filling ratio) and the highest values of these statistical errors are computed for Test 3 (low filling ratio). Hence, there is a minimum at the medium filling ratio. The values of AAD, BIAS and MAD of EQ model are lower than the ones of H model. Hence, the H model is slightly more accurate than EQ model.

9.6. Discussions and conclusions

The homogenous (H) model is evaluated against the equilibrium model (EQ model), by comparing the values of the statistical errors, computed for the pressure, liquid and vapour temperature, and filling ratio.

Section 9.6.1, 9.6.2, 9.6.3 and 9.6.4 discusses the results for the pressure, ullage temperature, liquid temperature and filling ratio, respectively.

9.6.1. Pressure

The Average Absolute Deviation (AAD) related to the pressure of equilibrium model (EQ model) is between 2.5 and 15 % for low heat fluxes (Study cases 1, 2, 3 and 4) and it is between 20 and 40 % for medium and high heat fluxes (Study cases 5, 6 and 7). The values of this statistical error are comprised in the same intervals of EQ model because the AAD value of H model is slightly lower than the one of H model. Hence, there is not a significant improvement in the calculation of the pressure, passing from the EQ model to the H model. The hypothesis of actual thermodynamic state (assumption b) of Section 1.1 of Chapter 4) of H model gives results that are quite similar to the one obtained with the hypothesis of instantaneous thermodynamic state of EQ model. This similarity of computing the pressure of both models is caused by the neglect of the bulk temperature gradient, which is a consequence of the hypothesis of total homogeneity. This neglect over-estimates the mass flow rate in the boundary layer of the wet side wall in the H model.

9.6.2. Ullage temperature

The Average Absolute Deviation (AAD) of the ullage temperature of equilibrium model (EQ model) does not overcome the value of 30 % at low heat fluxes (Study cases 1, 2, 3 and 4) and it is between 25 % and 70 % at medium and high heat fluxes (Study cases 5, 6 and 7). The AAD of ullage temperature of H model does not overcome the values of 25 % at low heat fluxes (Study cases 1, 2, 3 and 4) and it is bounded between 5 and 50 %. Hence, the hypothesis of actual thermodynamic state (assumption b) of Section 1.1 of Chapter 4) of H model improves the description of the ullage temperature. The AAD of H model strongly changes between each Study case, due to the value of beta coefficient. The highest value of this statistical error occurs when the value of beta coefficient is equal to zero, due to the overestimation of the vapour-to-interface heat flow.

9.6.3. Liquid temperature and filling ratio

The Average Absolute Deviation (AAD) of the liquid temperature of equilibrium model (EQ model) are bounded between 0.15 % and 0.6 % at low heat fluxes (Study cases 1, 2, 3 and 4). These values are between 0.15 and 3 % at medium and high heat fluxes (Study cases 5, 6 and 7). The AAD of the liquid temperature of H model are slightly above the limits of EQ at low heat fluxes. The values of this statistical error of H model are between 0.2 and 3 % at medium and high heat fluxes. Hence, there is not a significant difference in accuracy between the H and the EQ models. This negligible difference is caused by the hypothesis of total homogeneity of H model (assumption a) of Section 1.1 of Chapter 4). This hypothesis increases the heat flow entering in the liquid from the interface, closing the difference in temperature between the saturated liquid and the sub-cooled one.

9.6.4. Filling ratio

The values of the Average Absolute Deviation (AAD) of the filling ratio of equilibrium model (EQ model) are lower than 0.75 % at low heat fluxes (Study cases 1, 2, 3 and 4). These values are below 0.5 % at medium and high heat fluxes (Study cases 5, 6 and 7), except for Test 3 of Study case 7 where the value of AAD is around 5 %. The AAD of the filling ratio of H model is below the 0.75 % at low, medium and high heat fluxes, expect for Test 3 of Study case 7 where the value of AAD is around 2.5 %. Hence, the H model is as accurate as the EQ model because the difference in AAD values between these models is very low. This low difference is caused by the heat flow entering in the liquid from the interface, which reduces the sub-cooled state of the liquid. Hence, the hypothesis of total homogeneity of H model (assumption a) of Section 1.1 of Chapter 4) is quite similar to the hypothesis of instantaneous thermodynamic equilibrium of EQ model, in term of deviation.

9.7.Summary and perspectives

The statistical errors are computed with the results of the equilibrium (EQ model) and homogeneous model (H model)s and these models are compared to determine which modelling approach is accurate. The comparison indicates that H model is more accurate than EQ because the errors of H model between the experimental and computed values of ullage temperature are lower than the ones of the EQ model. The values of the errors of H model in calculating the pressure and the ullage temperature suggests that effort has to be put on describing the interfacial heat transfer and the accumulation of sensible heat in the ullage. The approach of increasing the complexity that is done in H model is worth because some improvement has been obtained. Hence, the approach of increasing the complexity will be used in the next model, in particular for the description of the accumulation of sensible heat in the ullage.

Chapter 5

Modèle homogène 2.0

Le modèle homogène (modèle H) présente trois problèmes critiques principaux intervenant dans la phase vapeur : (i) les valeurs du coefficient bêta sont égales à zéro ; (ii) la température de la vapeur présente des pics irréalistes pour des cuves soumises à des flux de chaleur moyens et élevés ; (iii) le taux d'auto-pressurisation est inférieur à celui observé.

Le modèle H 2.0 est développé pour pallier les problèmes (i) and (ii), qui sont plus critiques que le (iii), et repose sur la même théorie du modèle précédent à l'exception de l'hypothèse de stratification virtuelle de vapeur. Pour résumer, (i) l'équation d'évolution de la température de vapeur, (ii) le modèle de couche limite de stockage (SBL) de la paroi latérale sèche, (iii) le modèle Storage Heat Transfer (SHT) de la paroi latérale sèche et (iv) le transfert de chaleur d'interface (IHT) sont modifiés par rapport à ceux du modèle H.

Une nouvelle équation de bilan pour la vapeur est proposée pour mieux calculer l'accumulation de chaleur sensible dans le ciel gazeux.

Le gradient de température global du ciel gazeux est pris en compte dans l'intégration numérique des lois de conservation de la couche limite. Seules les lois de conservation du régime turbulent sont résolues pour améliorer la stabilité des algorithmes numériques du modèle Storage Boundary Layer (SBL).

Étant donné que le modèle SHT est basé sur le modèle SBL, l'algorithme permettant de déterminer le flux thermique paroi sèche-vapeur est modifié pour augmenter la stabilité de l'intégration numérique et réduire le temps de calcul. Le nouveau modèle SHT de la paroi latérale sèche est basé sur la méthode de Netwon-Raphson aux différences finies, au lieu d'utiliser la méthode de substitution directe comme dans le modèle H.

Le flux thermique liquide-interface est estimé selon deux approches : (i) la première considère la dynamique des fluides de la paroi latérale humide ; (ii) la seconde suppose la convection naturelle d'une surface plane près de l'interface. Le flux thermique vapeur-interface est calculé à partir des flux convectifs dans la vapeur. Ces flux convectifs sont estimés avec une discrétisation virtuelle du ciel gazeux en sous-couches. Puisque ces flux dépendent du taux d'évaporation net, ce taux massique est estimé avec une procédure itérative au lieu d'utiliser une formule analytique comme pour le modèle précédent. En raison des modifications apportées, le coefficient correctif paroi sèche-interface du modèle BOR doit être modifié. Ce coefficient correcteur est estimé avec un algorithme qui utilise l'équation du bilan énergétique de la vapeur à l'état stationnaire, au lieu d'utiliser une formule analytique comme pour le modèle précédent.

Les résultats du modèle H 2.0 sont comparés aux données expérimentales de l'azote liquide et de l'hydrogène liquide à des flux thermiques faibles, moyens et élevés. Le modèle H 2.0 améliore l'estimation des valeurs initiales de température de la vapeur et d'apports thermiques ainsi que l'évolution temporelle de la température de la vapeur lors de l'auto-pressurisation, sauf pour les essais à faibles flux thermiques et faible taux de remplissage. La prédiction de la pression est sous-estimée à cause de la surestimation des valeurs absolues du flux thermique liquide-interface lors de l'auto-pressurisation. Il s'ensuit que la prévision de l'évolution temporelle de la pression devrait être améliorée de toute urgence.

Homogeneous model 2.0

The homogeneous model (H model) has three main critical issues: (i) the values of the beta coefficient are equal to zero; (ii) vapour temperature creates unrealistic peaks at medium and high heat fluxes; (iii) the self-pressurisation rate is lower than the observed one. The first critical issue is caused by the over-estimation of the vapour-to-interface heat flow at the steady state. The peaks seen in the curves of ullage temperature are produced by the enthalpy flow of the net mass flow across the liquid-vapour interface. The first and the second critical issues are more important than the third one. So, homogeneous model 2.0 (H 2.0 model) is developed to overcome these issues of the vapour phase. The H 2.0 model is based on the same theory of the previous model, except for the hypothesis of vapour virtual stratification. So, (i) the vapour temperature evolution equation, (ii) the Storage Boundary Layer (SBL) model of the dry side wall, (iii) the Storage Heat Transfer (SHT) model of the dry side wall and (iv) the Interface Heat Transfer (IHT) are changed from the ones of the H model. A new balance equation of the ullage is proposed to better compute the accumulation of the sensible heat in the ullage. The bulk temperature gradient of the ullage is considered in the numerical integration of the conservation laws of the boundary layer. Only the conservations laws of turbulent regime are solved to improve the stability of the numerical algorithms of the Storage Boundary Layer (SBL) model. Since the Storage Heat Transfer (SHT) model is based on SBL model, the algorithm to determine the dry side wall-to-vapour heat flow is modified to increase the stability of the numerical integration and to reduce the computational time. The new SHT model of the dry side wall is based on the method of Netwon-Raphson method with finite difference, instead of using the method of direct substitution as done in H model. The liquid-to-interface heat flow is estimated with two approaches: (i) the first one considers the fluid-dynamic of the wet side wall; (ii) the second one assumes the natural convection of flat surface near the interface. The vapour-to-interface heat flow is calculated with the convective flows of the ullage. These convective flows are estimated with a virtual discretisation of the ullage in sub-layers. Since these flows depend on the net evaporation rate, this mass rate is estimated with an iterative procedure, instead of using an analytical formula as done for the previous model. Due to the modifications done, the dry side wall-to-interface corrective coefficient of the BOR model has to be changed. This corrective coefficient is estimated with an algorithm that uses the vapour energy balance equation at steady state, instead of using an analytical formula as done for the previous model. The results of the H 2.0 model are compared with the experimental data of liquid nitrogen (LN_2) and liquid hydrogen (LH_2) at low, medium and high heat fluxes. The H 2.0 model improves the estimation of the initial values of ullage temperature and heat inputs, except for the tests at low heat fluxes and low filling ratio. The calculation of the time-evolution of the vapour temperature during the self-pressurisation is improved with the hypothesis of the vapour virtual stratification. The prediction of the pressure remains a critical issue due to the over-estimation of absolute values of the liquid-to-interface heat flow in the self-pressurisation. As consequence, the prediction of the time-evolution of the pressure should be urgently improved.

Section 1 explains the features of the H 2.0 model. Seciton 2 presents the new energy balance equation of hte uallge. Section 3 presents the new algorithm of the dry side wall-to-vapour heat flow. Section 4 describes the interface model. Section 5 explains the BOR model. Section 6 compares the results with the experimental data. Section 7 analyses the results, and it presents the main aspect and conclusions. Section 8 describes the comparison between the results of the H 2.0 and H models.

1. Introduction

In Chapter 4, the homogeneous model (H model) was developed under the hypotheses of total homogeneity, actual thermodynamic state and local thermodynamic equilibrium. The differential equations were deduced from the corresponding mass and enrgy conservations laws. The differential equations computed the time-derivates of pressure, liquid and vapour temperatures, and liquid volume. These equations were coupled with the formulas related to the mass and heat flows at the interface. The results of the H model were compared with the experimental data and with the results of equilibrium model (EQ model). Even if H model is more accurate in description of the ullage temperature than the EQ model, the homogeneous model (i) computes null values of the beta coefficient, (ii) under-estimates the self-pressurisation rate and (iii) calculates peaks of ullage temperature, which are unrealistic. The vapour-to-interface heat flow is the cause of the null values of the beta coefficient and the low rate of natural pressure build-up is caused by the over-estimation of the interface-to-liquid heat flow, due to the homogeneity of the liquid phase. The variation of the vapour enthalpy flow of the net mass flow during the self-pressurisation is the main cause of the peaks of the ullage temperature. The homogeneous model 2.0 (H 2.0 model) is developed to overcome some of thesecritical issues.

Section 1.1 describes objectives of the H 2.0 model. Section 1.2 presents the hypotheses and the variables of H 2.0 model. Section 1.3 explains the block structure of the H 2.0 model.

1.1. Objectives of the homogeneous model 2.0

The main critical issues of the homogenous (H) model come from the interface heat transfer (IHT) model, in particular from the calculation of liquid-to-interface heat flow during the self-pressurisation, and the differential equations that compute the ullage temperature increment, thus the accumulation of sensible heat in the the ullage. The H model has to be improved in computing the accumulation of sensible heat in the ullage and in calculating the heat flows at the interface. The accumulation of the sensible heat depends on the thermal stratification, which affects the vapour-to-interface heat flow and the enthalpy flow of the net mass flow. The heat flows at the interface, in particular the liquid-to-interface, depends on the fluid-motion of the liquid near the interface during the self-pressurisation. So, these improvements can be done by fulfilling these objectives:

a) Obtaining a new differential equation of the vapour temperature from the physics of the thermal stratification of the ullage, as suggested by some experimental evidences [35]–[37];
b) Deducing an alternative of the liquid-to-interface and vapour-to-interface heat transfer models from the fluid-dynamics of liquid and of vapour during the self-pressurisation;

As consequence, new version (with respect to H model) of the Storage Heat Transfer (SHT), the Storage Boundary Layer (SBL), the Boil-off Rate (BOR) and Interface Heat Transfer (IHT) model have been proposed in the H 2.0 model.

1.2. Hypotheses and variables

The ullage is always thermally stratified during the self-pressurisation and when it reaches the steady state in an open storage container. The thermal stratification in the liquid develops when the pressure in the ullage increases because the storage container is closed. So, the assumption of total homogeneity of homogeneous model (H model) excessively simplifies the accumulation of the heat in the ullage. Hence, the thermal stratification of the ullage must be considered and the homogeneous model 2.0 (H 2.0 model) is based on the following assumptions:

a) *Hypothesis of iquid homogeneity*: the liquid is homogenous and isothermal;
b) *Hypothesis of vapour virtual stratification*: the vapour is virtually stratified;
c) *Hypothesis of actual thermodynamic state*: The vapour and the liquid can be over-heated, sub-cooled and saturated.
d) *Hypothesis of local thermodynamic equilibrium*: he interface is at thermodynamic equilibrium;

The hypothesis of total homogeneity of H model is replaced by the assumptions a) and b). This hypothesis considers the vapour as homogenous and isothermal, but a virtual discretisation is done to obtain a new differential equation of the vapour temperature for describing the accumulation of heat in the ullage. The assumptions c) and d) are the same of the H model. As consequence, the storage container can be outlined as in Figure 94. The blue zone is the liquid and the red zone with colour degradation is the ullage. The yellow dashed line is the interface. The green arrow is the net mass flow at interface. The black arrows are the inlet and outlet flows of the fluid. The white arrows with red boarders are the heat fluxes, and the white points with purple boarders are the wall temperatures. The orange and light blue arrows represent the convective flows in vapour and in liquid, respectively.

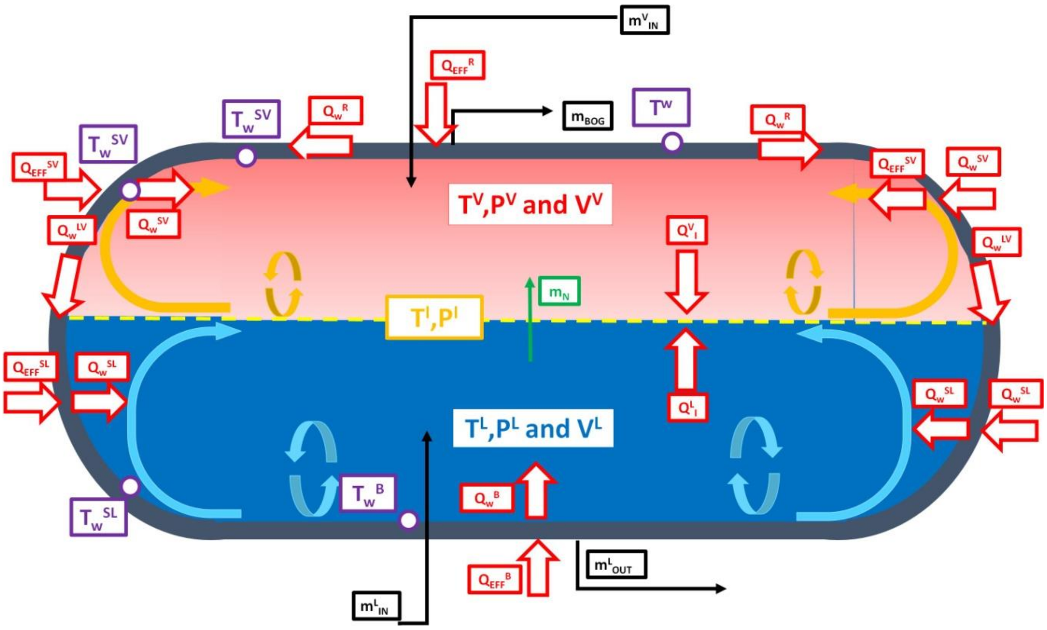

Figure 94. H 2.0 model.

As shown in Figure 94, the description of the phenomena of natural convection and heat transfer at the walls of the storage containers are similar to the ones of the H model. The main difference is the ullage, which is virtually discretized. As a consequence, the enthalpy flow of the net mass flow reduces because the difference in temperatures between the interface and vapour near the free surface is lower than the one of the H model. The enthalpy flow of the inlet vapour flow and the BOG depends on the virtual vapour temperature near the roof, instead of the bulk temperature of the ullage as in the H model.

The variables of the H 2.0 model are those of the H model (see Table 62) plus the bulk temperature of the ullage and the virtual temperature profile. The number of state variables does change between these models. As a consequence, the H 2.0 model can be described with the same mathematical system and Ordinary Differential Equation (ODEs) system of the H model (see Table 64 and Table 65), except for the ullage temperature-evolution equation (T^V-e equation). The coefficients of this equation are different form the one of the H model.

1.3. Block structure of the homogeneous model 2.0

According to what stated in Section 1.2 of Chapter 5, the structure of homogeneous model 2.0 (H 2.0 model) is similar to the structure of homogeneous model (H model), with with the addition of Blocks 6 and 7 for the calculation of bulk temperature gradient and the virtual temperature profile, as it is shown in Figure 95.

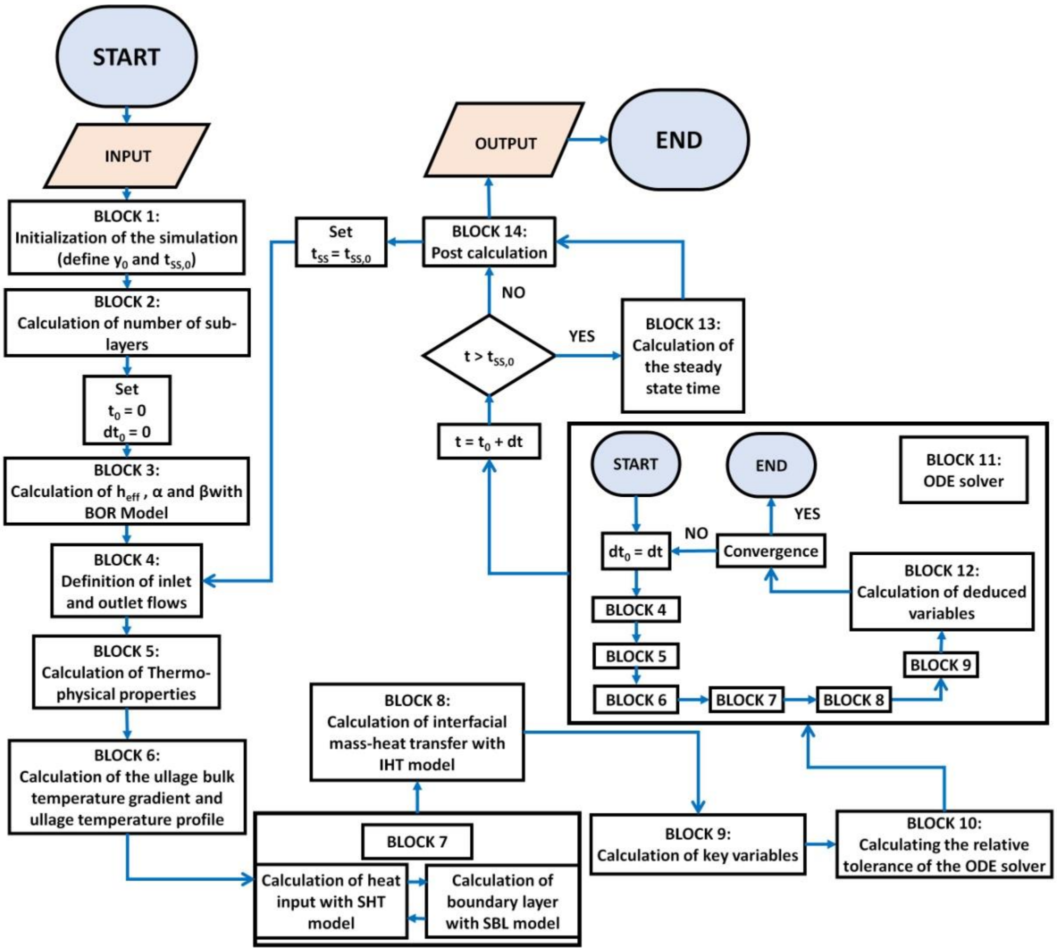

Figure 95. Block structure of H 2.0 model.

In Block 6, the ullage temperature gradient and the virtual temperature profile are calculated. The calculations of Block 6 are done before using the Storage Heat Transfer (SHT) and Storage Boundary Layer (SBL) models because ullage temperature gradient and the virtual temperature profile are required in these models. As consequence, the Boil-off Rate (BOR), SHT, SBL Interface Heat Transfer (IHT) models are modified to improve the calculation of the accumulation of the sensible heat in the ullage and the mass and heat transfer at the interface. The indipendent variables of the mathematical system are calculated with same equation of the H model, except for the differential equation of the ullage temperature.

The ullage bulk temperature and the virtual temperature profile are described in Section 1.3.1 and 1.3.2, respectively.

1.3.1. Bulk ullage temperature gradient

During the self-pressurisation, the accumulation of sensible heat in the ullage depends on three factors: the dry side wall-to-vapour heat flow ($\dot{Q}_W^{SV}$), the vapour-to-interface heat flow ($\dot{Q}_I^V$) and the vapour enthalpy flow of the net mass flow. This enthalpy flow directly depends on the difference in temperatures between the vapour near the free surface and the liquid-vapour interface, thus it depends on the ullage bulk temperature gradient. The heat flow $\dot{Q}_w^{SV}$ is affected by the free-convection at the dry side, which depends on the ullage temperature gradient. The heat flow $\dot{Q}_I^V$ is controlled by the fluid-dynamics in the core of the ullage, which is characterized by a descending mass flow [1], [2]. The fluid motions in the core of the ullage depends on the free-convection at the dry side wall, thus on the bulk ullage temperature gradient. Hence, this gradient must be computed to improve the prediction of the accumulation of sensible heat in the ullage.

The bulk vapour temperature gradient can be calculated from the temperature of the points shown in Figure 96 and their distance "dx". In Figure 96, the light blue zone is the liquid and the red zone with colour degradation is the ullage. The yellow dashed line is the interface, the red points are the vapour temperatures and the orange braces "{" are the distances between each temperature.

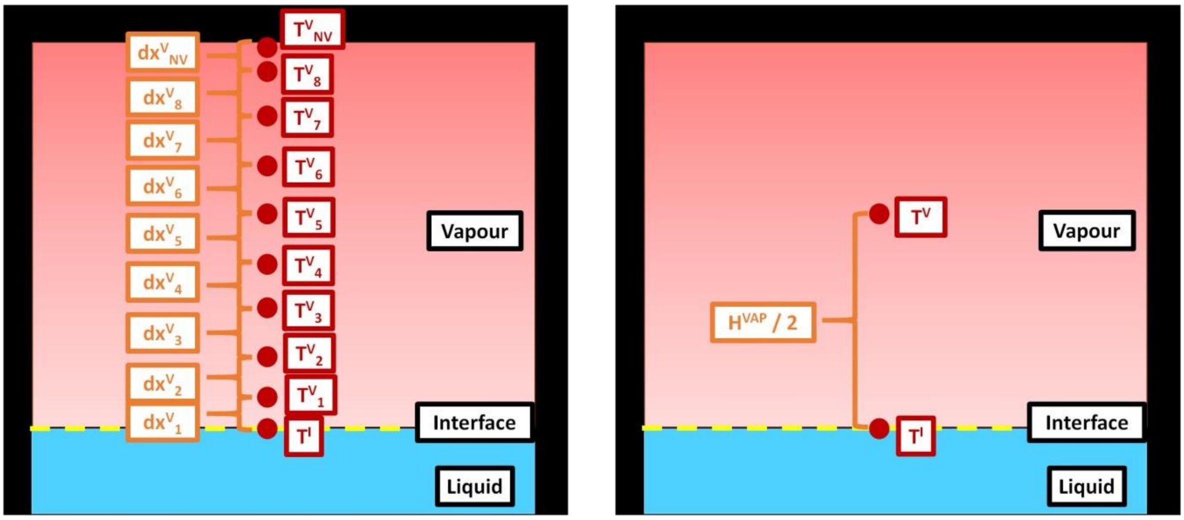

a) b)

Figure 96. Distribution of the temperature in the ullage: a) real case; b) H 2.0 model.

The approach illustrated in Figure 96 (a) requires a real discretisation of the ullage to calculate the vapour temperature in each point of the ullage, in particular along the vertical axis. Due to the hypothesis of vapour virtual stratification (assumption b) of Section 1.1 of Chapter 5), the vapour is homogeneous and the temperature is equal in every point of the ullage, thus the real discretisation of Figure 96 (a) cannot be applied. Hence, this temperature gradient can only be computed using the bulk variables of the ullage such as the temperature and the height of the ullage, as it is illustrated in Figure 96 (b). This gradient is then computed as follows:

Equation 226
$$\frac{\partial T^V}{\partial x} = 2 \cdot \frac{T^V - T^I}{H^V}$$

In Equation 226, $\frac{\partial T^V}{\partial x}$ is the bulk ullage temperature gradient. T^V and T^I are the ullage and interface temperature. H^V is the height of the ullage and it is calculated with the geometrical formulas given in Appendix B.

1.3.2. Vapour virtual temperature profile

The vapour ullage temperature profile could be computed knowing the temperatures of all the points in the vertical axis of the discretized ullage, as it is illustrated in Figure 96 (a). In the homogenous (H 2.0) model 2.0, the stratification in the vapour phase is only virtual, thus only a virtual temperature profile can only be computed. The experimental data [1]–[5],[9],[10] show that the vapour temperature profile is almost linear in the ullage, as it is described in Figure 97.

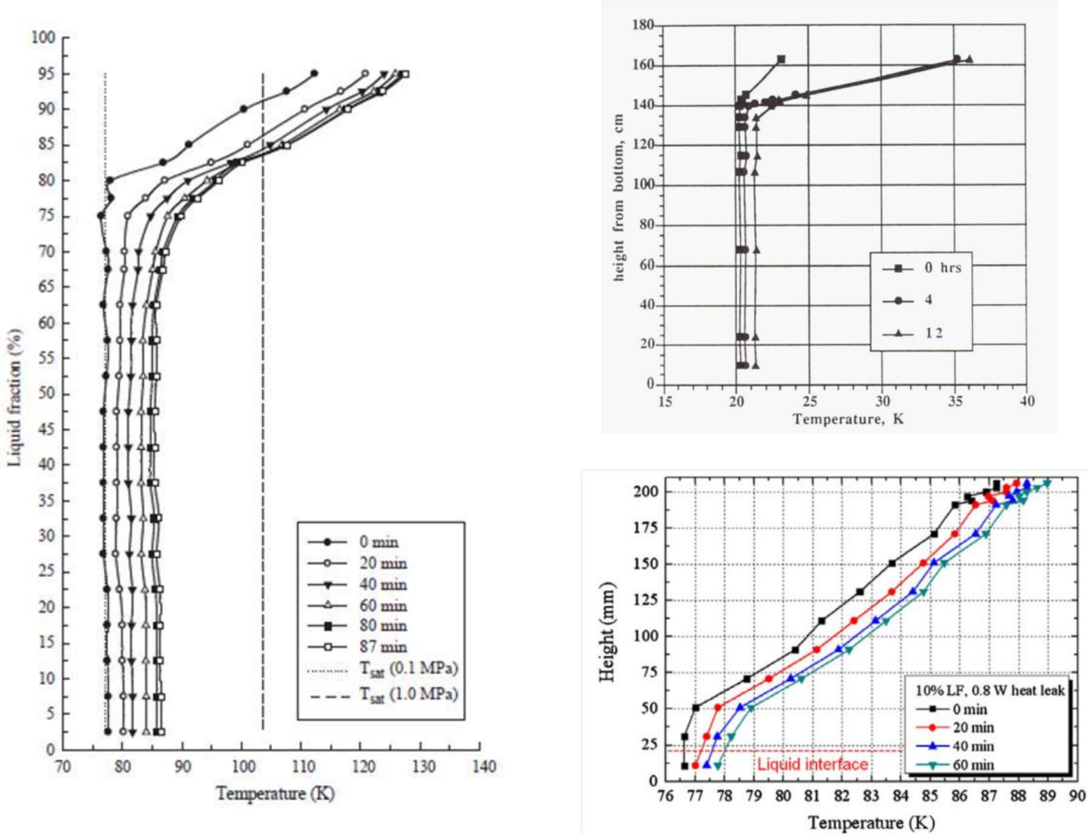

b)

a) c)

Figure 97. Temperature profile in the storage container: a) Kang et al. [1] (Test 1); b) Hasan et al. **[27]** (Test 1); c) Seo and Jeong **[24]** (Test 6).

So, the vapour virtual temperature profile can be computed as follows:

Equation 227
$$T_i^V = T^I + \frac{\partial T^V}{\partial x} \cdot H_i^V$$

In Equation 227, H_i^{VAP} is the vapour height at the point “i” and $\frac{\partial T^V}{\partial x}$ is the bulk temperautre gradien from Equation 226.

2. New differential equation of the ullage temperature

One of the objective of the homogeneous model 2.0 (H 2.0 model) (objective a) of Section 1.1 of Chapter 5) is the development of a new differential equation to compute the time-derivate of the ullage temperature. This differential equation can be deduced from the conservation laws of the ullage. The deducing procedure of time-derivate of the ullage temperature is described in Figure 98.

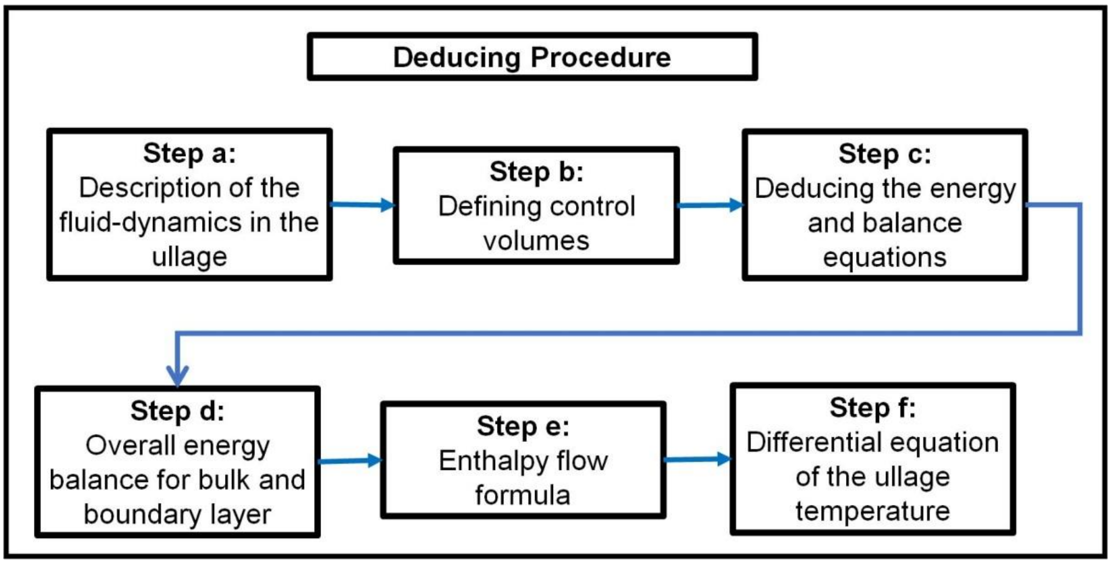

Figure 98. Procedure to deduce the formula that computes vapour-to-interface heat flow.

This procedure is divided into the following steps:

a) Description of the fluid-dynamics in the ullage;
b) Defining the control volume;
c) Writing the mass and of energy conservation laws for the control volumes;
d) Determining the overall energy balance equation of the ullage;
e) Determining the enthalpy flow formula of ullage balance equation;
f) Solving the differential equation of the ullage temperature

These steps are respectively explained in Section 2.1, 2.2, 2.3, 2.4, 2.5 and 2.6.

2.1. Description of the fluid-dynamics in the ullage

The description of the fluid-dynamics in the ullage is the first step (step a) of Section 4.2 of Chapter 5) for deducing differential equation of the ullage temperature, as it is described in Figure 98. The fluid motions in the ullage can be described as in Figure 99. The light blue is the liquid, while the different gradations of yellow and orange colours indicate the dry side boundary layer and the ullage, respectively. The light and the dark colours respectively describe the high and low temperature in the ullage and in the dry side boundary layer. The yellow dashed line is the interface and the black zone is the storage container's wall. The white arrows with red boarders are the heat inputs in the ullage and the heat transfer at the interface. The black arrows are the inlet and outlet vapour mass flow. The green arrow is the the net mass flow at the interface. The grey arrows indicates the mass flow in the boundary layer and in the core of the ullage.

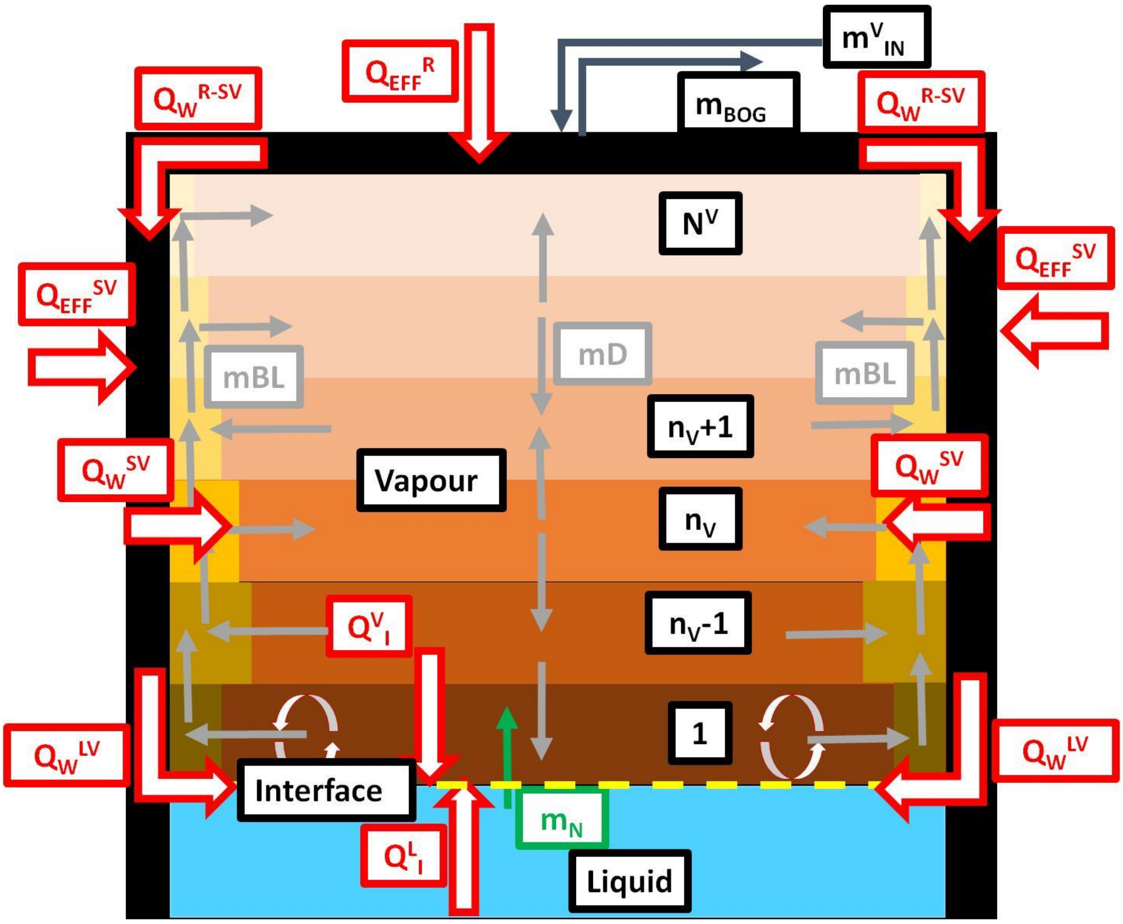

Figure 99. Description of ullage.

As described in Figure 99, the vapour moves upward along the vertical walls of the storage containers, due to the buoyancy forces that are generated by the difference in vapour density between the vapour at the wall and the vapour in the bulk. This difference is caused by the heat ingress through the dry side wall. As the vapour moves upward, the buoyancy forces are reduced by the bulk temperature gradient and the velocity in the boundary layer reduces. Part of the mass flow exits the boundary layer, while the remaining part reaches the end of the dry side wall. The upward mass flow at the side wall is balanced by a descending flow in the core of the ullage [35], [37]. The bulk temperature gradient can reduce the velocity of the boundary layer if the mass flow vanishes in the boundary layer. Experimental evidences of this block of the natural convection have not been found. Near the interface, phenomena of natural convection and conduction can occur.

2.2.Control volumes in the virtual discretisation of the ullage

The definition of the control volume is the second step (step b) of Section 4.2 of Chapter 5) for deducing differential equation of the ullage temperature, as it is described in Figure 98. Due to the hypothesis of vapour virtual stratification (assumption b) of Section 1.2 of Chapter 5), the ullage can be divided into sub-layers of equal thickness. Each sub-layer is separated into the bulk and the boundary layer. The mass, the enthalpy and the heat flows are determined for each sub-layer. As said in Section 2 of Chapter 5, there is a descending flow in the core of the ullage, which carries sensible heat. This descending flow can be directed upward, under certain fluid-dynamics conditions of the dry side wall and storage conditions. Hence, the control volumes of the virtual discretisation of the ullage can be described with Figure 100. In Figure 100, the green, the grey and the red arrows are respectively the net mass flow, the convective mass flow and the enthalpy flows. The white arrows with red border are the dry side wall-to-vapour heat flows. The black, the dark yellow and the dark orange rectangles are respectively the wall, the boundary layer of the sub-layers and the bulk of the sub-layers.

Figure 100. Description of control volumes: a) vapour-interface, b) roof-vapour; c) core-vapour.

The sub-layer near the interface is called interface-vapour and it is indicated with the number 1, as it is reported in Figure 100. The sub-layer in contact with the roof is named roof-vapour and it is labelled with the word “N^V”, where N^V the number of the sub-layer of the dry side wall (see Section 1 of Appendix L for computing this number). The remaining sub-layers are defined as core-vapour and they are indicated with the word “n_V”, as it is shown in Figure 100. The variables of Figure 100 are reported in Table 89.

Table 89. Nomenclature of the variables of the control volumes.

Name	Symbol	Unit
Downward mass flow between sub-layer “$n_V + 1$” and sub-layer “n_V”	$\dot{m}^D_{n_v+1}$	[kg/s]
Downward mass flow between sub-layer “n_V” and sub-layer “$n_V - 1$”	$\dot{m}^D_{n_v}$	[kg/s]

Table 89. Nomenclature of the variables of the control volumes.

Downward mass flow between sub-layer “2” and interface sub-layer	$\dot{m}_2^D$	[kg/s]
Downward mass flow between roof sub-layer and sub-layer “N^V - 1” (second last sub-layer)	$\dot{m}_{N^V}^D$	[kg/s]
Upward mass flow at the sub-layer “n$_V$”	$\dot{m}_{n_v}^{UP}$	[kg/s]
Upward mass flow at the sub-layer “n$_V$ - 1”	$\dot{m}_{n_v-1}^{UP}$	[kg/s]
Upward mass flow at the interface sub-layer	$\dot{m}_2^{UP}$	[kg/s]
Upward mass flow at the sub-layer “N^V - 1” (second last sub-layer)	$\dot{m}_{N^V-1}^{UP}$	[kg/s]
Bulk-to-boundary layer mass flow, at sub-layer “n$_V$”	$\dot{m}_{n_v}^{BL}$	[kg/s]
Bulk-to-boundary layer mass flow, at interface sub-layer	$\dot{m}_1^{BL}$	[kg/s]
Bulk-to-boundary layer mass flow, at roof sub-layer	$\dot{m}_{N^V}^{BL}$	[kg/s]
Temperature in the boundary layer of the sub-layer “n$_V$”	$T_{n_v}^{BL,V}$	[K]
Temperature in the boundary layer of the interface sub-layer	$T_1^{BL,V}$	[K]
Temperature in the boundary layer of the roof sub-layer	$T_{N^V}^{BL,V}$	[K]
Temperature in the bulk of the sub-layer “n$_V$”	$T_{n_v}^V$	[K]
Temperature in the bulk of the interface sub-layer	T_1^V	[K]
Temperature in the bulk of the roof sub-layer	$T_{N^V}^V$	[K]
Specific enthalpy in the boundary layer of the sub-layer “n$_V$”	$\tilde{h}_{n_v}^{BL,V}$	[J/kg]
Specific enthalpy in the boundary layer of the interface sub-layer	$\tilde{h}_1^{BL,V}$	[J/kg]
Specific enthalpy in the boundary layer of the roof sub-layer	$\tilde{h}_{N^V}^{BL,V}$	[J/kg]
Specific enthalpy in the bulk of the sub-layer “n$_V$”	$\tilde{h}_{n_v}^V$	[J/kg]
Specific enthalpy in the bulk of the interface sub-layer	$\tilde{h}_1^V$	[J/kg]
Specific enthalpy in the bulk of the roof sub-layer	$\tilde{h}_{N^V}^V$	[J/kg]

The temperature in the boundary layer ($T_{NV}^{BL,V}$, $T_1^{BL,V}$ and $T_{nv}^{BL,V}$) and the mass flow ($\dot{m}_{nv}^{BL}$, $\dot{m}_1^{BL}$ and $\dot{m}_{NV}^{BL}$) in the boundary layer are calculated with the Integral Boundary Layer (IBL) approach of the Storage Boundary Layer (SBL) model, as it is reported in Section 2.1 of Appendix O. In this approach, the mass $\dot{m}_1^{UP}$ is calculated with the Exact Boundary Layer (EBL) approach, thus without considering the ullage bulk temperature gradient, to start the numerical calculation of IBL approach (see Section 2 of Appendix P).

As reported in Figure 100, the downward mass flows and of the bulk-to-boundary layer mass flow can change direction. Hence, different control volumes are present and each variation of the direction corresponds to a case, which in reported in Table 90.

Table 90. Cases of the control volumes.

	Vapour-interface sub-layer (Figure 100 (a))
Case 1	$\dot{m}_2^D$ is directed downward.
Case 2	$\dot{m}_2^D$ is directed upward.
	Roof-vapour sub-layer (Figure 100 (c))
Case 1	$\dot{m}_{N^V}^D$ is directed downward.
Case 2	$\dot{m}_{N^V}^D$ is directed upward.
Case 3	$\dot{m}_{N^V-1}^{UP}$ is equal to zero.
	Core-vapour sub-layer (Figure 100 (b))
Case 1	$\dot{m}_{n_V+1}^D$ and $\dot{m}_{n_V}^D$ are directed downward. $\dot{m}_{n_V}^{BL}$ enters the boundary layer.
Case 2	$\dot{m}_{n_V+1}^D$ is directed downward and $\dot{m}_{n_V}^D$ is directed downward. $\dot{m}_{n_V}^{BL}$ enters the boundary layer.
Case 3	$\dot{m}_{n_V+1}^D$ and $\dot{m}_{n_V}^D$ are directed downward. $\dot{m}_{n_V}^{BL}$ exits the boundary layer.
Case 4	$\dot{m}_{n_V+1}^D$ is directed downward and $\dot{m}_{n_V}^D$ is directed upward. $\dot{m}_{n_V}^{BL}$ exits the boundary layer.
Case 5	$\dot{m}_{n_V+1}^D$ and $\dot{m}_{n_V}^D$ are directed upward. $\dot{m}_{n_V}^{BL}$ enters the boundary layer.
Case 6	$\dot{m}_{n_V+1}^D$ and $\dot{m}_{n_V}^D$ are directed upward. $\dot{m}_{n_V}^{BL}$ exits the boundary layer.

Table 90. Cases of the control volumes.

Case 7	$\dot{m}_{n_V+1}^{D}$ is directed downward and $\dot{m}_{n_V}^{D}$ is directed upward. $\dot{m}_{n_V}^{BL}$ exits the boundary layer. $\dot{m}_{n_V}^{UP}$ is equal to zero.
Case 8	$\dot{m}_{n_V+1}^{D}$ and $\dot{m}_{n_V}^{D}$ are directed upward. $\dot{m}_{n_V}^{BL}$ exits the boundary layer. $\dot{m}_{n_V}^{UP}$ is equal to zero.
Case 9	$\dot{m}_{n_V+1}^{D}$ and $\dot{m}_{n_V}^{D}$ are directed upward. $\dot{m}_{n_V}^{BL}$, $\dot{m}_{n_V}^{UP}$ and $\dot{m}_{n_V-1}^{UP}$ are equal to zero.

In Case 3 of roof-vapour and in cases 7, 8 and 9 of core-vapour sub-layers, the mass flow vanishes in the boundary layer of the dry side wall. This condition can occurs when the ullage bulk temperature gradient reduces the buoyancy forces at the point of vanishing the rising flow in the boundary layer ($\dot{m}_{n_V}^{UP}$), as it is explained in Section 2.1 of Chapter 5. In this situation, the only mass flow that moves in the ullage bulk is caused by the venting of the Boil-Off gas (BOG), if the storage container is open, or by the net mass flow ($\dot{m}_N$). The condition of the block of mass flow in the boundary layer is not calculated by the SBL model at the first sub-layer, which is the vapour-interface sub-layer, because the the rising mass flow in the boundary layer ($\dot{m}_2^{UP}$) is calculated with the EBL approach.

2.3. Mass and energy conservation laws

The writing the mass and energy conservation laws is the third step (step c) of Section 4.2) for deducing differential equation of the ullage temperature, as it is described in Figure 98. These conservation laws are divided into two classes: the conservation laws of the boundary layer and the conservation laws of the bulk.

Section 2.3.1 and 2.3.2 respectively describe the conservation laws of the boundary layer and of the bulk, respectively.

2.3.1. Conservation laws of the boundary layer

As it is shown in Figure 100, the boundary layer of each sub-layer is very smaller than the bulk. Hence, the mass and the energy are accumulated and dispersed faster than in the bulk. As a consequence, the boundary layer of each sub-layer is at steady state, and the mass and energy accumulations are neglected in the boundary layer. The mass and energy equations of mass and of energy of the boundary layer of the sub-layers are described with the equations in Table 234 (see Section 2.1 of Appendix O), as it is reported in Table 91.

Table 91. Energy and mass balance equations in the boundary layer of the sub-layers.

Case	Conservation law	Equation	Comments
Vapour-interface sub-layer			
1 and 2	Mass balance equation	Equation 958	/
1 and 2	Energy balance equation	Equation 959	$\tilde{h}_1^{B}$, $\tilde{h}_1^{BL}$and $\dot{Q}_{W,1}$ are respectively sustituted by $\tilde{h}_1^{V}$, $\tilde{h}_1^{BL,V}$ and $\dot{Q}_{W,1}^{SV}$
Roof-vapour sub-layer			
1 and 2	Mass balance equation	Equation 964	$\dot{m}_N^{BL}$ and $\dot{m}_N^{UP}$ are respectively substituted by $\dot{m}_{N^V}^{BL}$ and $\dot{m}_{N^V}^{UP}$
1 and 2	Energy balance equation	Equation 965	$\tilde{h}_N^{B}$, $\tilde{h}_{N-1}^{BL}$and $\dot{Q}_{W,N}$ are respectively substituted by $\tilde{h}_{N^V}^{BL,V}$, $\tilde{h}_{N^V-1}^{BL,V}$ and $\dot{Q}_{W,N^V}^{SV}$
Core-vapour sub-layer			
1, 2 and 5	Mass balance equation	Equation 960	$\dot{m}_n^{BL}$, $\dot{m}_{n+1}^{UP}$ and $\dot{m}_n^{UP}$ are respectively substituted by $\dot{m}_{n_V}^{BL}$, $\dot{m}_{n_V+1}^{UP}$ and $\dot{m}_{n_V}^{UP}$.
1, 2 and 5	Energy balance equation	Equation 961	$\tilde{h}_n^{B}$, $\tilde{h}_n^{BL}$, $\tilde{h}_{n-1}^{BL}$ and $\dot{Q}_{W,n}$ are respectively substituted by $\tilde{h}_{n_V}^{V}$, $\tilde{h}_{n_V}^{BL,V}$, $\tilde{h}_{n_V-1}^{BL,V}$ and $\dot{Q}_{W,n_V}^{SV}$
3, 4 and 6	Mass balance equation	Equation 962	$\dot{m}_n^{BL}$, $\dot{m}_{n+1}^{UP}$ and $\dot{m}_n^{UP}$ are respectively substituted by $\dot{m}_{n_V}^{BL}$, $\dot{m}_{n_V+1}^{UP}$ and $\dot{m}_{n_V}^{UP}$.

Table 91. Energy and mass balance equations in the boundary layer of the sub-layers.

3, 4 and 6	Energy balance equation	Equation 963	$\tilde{h}_n^{BL}$, $\tilde{h}_{n-1}^{BL}$ and $\dot{Q}_{W,n}$ are respectively substituted by $\tilde{h}_{n_V}^{BL,V}$, $\tilde{h}_{n_V-1}^{BL,V}$ and $\dot{Q}_{W,n_V}^{SV}$.
7 and 8	Mass balance equation	Equation 962	$\dot{m}_n^{BL}$and $\dot{m}_n^{UP}$ are respectively substituted by $\dot{m}_{n_V}^{BL}$ and $\dot{m}_{n_V}^{UP}$. $\dot{m}_{n+1}^{UP}$, thus $\dot{m}_{n_V+1}^{UP}$, is equal to zero.
7 and 8	Energy balance equation	Equation 963	$\tilde{h}_n^{BL}$, $\tilde{h}_{n-1}^{BL}$ and $\dot{Q}_{W,n}$ are respectively substituted by $\tilde{h}_{n_V}^{BL,V}$, $\tilde{h}_{n_V-1}^{BL,V}$ and $\dot{Q}_{W,n_V}^{SV}$. The enthalpy flow of $\dot{m}_{n+1}^{UP}$ is removed.

As reported in Table 91, the mass and the energy balance equation of the boundary layer of case 3 of roof-vapour and case 9 of core-vapour are not reported because there are not mass and enthalpy flows inthese sub-layers. Since the mass flows $\dot{m}_2^{UP}$, $\dot{m}_{n_V-1}^{UP}$, $\dot{m}_{n_V}^{UP}$ and $\dot{m}_{N^V-1}^{UP}$ are computed with the Integral Boundary Layer (IBL) approach, the mass flows between the bulk and the boundary layer can be calculated with the formulas that are deduced from the mass conservation laws of Table 234. These formulas are reported in Table 235 (see Section 2.1 of Appendix O) and they are adapted to the boundary layer of the dry side wall as it is reported in Table 92.

Table 92. Formulas to compute $\dot{\boldsymbol{m}}_1^{BL}$, $\dot{\boldsymbol{m}}_{n_V}^{BL}$ and $\dot{\boldsymbol{m}}_{N^V}^{BL}$.

Case	Equation	Comments
	Vapour-interface sub-layer	
1 and 2	Equation 966	/
	Roof-vapour sub-layer	
1 and 2	Equation 972	$\dot{m}_N^{BL}$ and $\dot{m}_N^{UP}$ are respectively substituted by $\dot{m}_{N^V}^{BL}$ and $\dot{m}_{N^V}^{UP}$
	Core-vapour sub-layer	
1, 2 and 5	Equation 968	$\dot{m}_n^{BL}$, $\dot{m}_{n+1}^{UP}$ and $\dot{m}_n^{UP}$ are respectively substituted by $\dot{m}_{n_V}^{BL}$, $\dot{m}_{n_V+1}^{UP}$ and $\dot{m}_{n_V}^{UP}$.
3, 4 and 6	Equation 970	$\dot{m}_n^{BL}$, $\dot{m}_{n+1}^{UP}$ and $\dot{m}_n^{UP}$ are respectively substituted by $\dot{m}_{n_V}^{BL}$, $\dot{m}_{n_V+1}^{UP}$ and $\dot{m}_{n_V}^{UP}$.
7 and 8	Equation 970	$\dot{m}_n^{BL}$and $\dot{m}_n^{UP}$ are respectively substituted by $\dot{m}_{n_V}^{BL}$ and $\dot{m}_{n_V}^{UP}$. $\dot{m}_{n+1}^{UP}$, thus $\dot{m}_{n_V+1}^{UP}$, is equal to zero.

The mass and energy balance equations of the boundary layer of the sub-layers depends on the term $\dot{m}_{n_V}^{BL}$ and $\tilde{h}_{n_V}^{BL,V}$. In particular, this specific enthalpy is affected by the vapour temperature in the bulk, which can be calculated with the mass and energy conservation laws of the bulk of the sub-layer.

2.3.2. Conservation laws of the bulk

The natural convection at the dry side wall produces a descending flow in the core of the ullage. As it is described in Figure 100, this descending flow can be upward or dowanward directed. The mass flow in the boundary layer of the dry side wall changes as function of the bulk temperature gradient. When this gradient is low, this mass flow increases and mass moves from the bulk to the boundary layer. If the gradient is high, this mass flow decreases and the mass moves from the boundary layer to the bulk. As a consequence, the direction of the descending flow ($\dot{m}_{n_V}^D$) and of the boundary layer-to-bulk mass flow ($\dot{m}_{n_V}^{BL}$) can change ineach sub-layer, affetting the mass and energy conservation laws of the bulk. These equations are reported in Table 93.

Table 93. Energy and mass balance equations in the bulk of the sub-layers.

	Vapour-interface sub-layer	
Case 1	Equation 228	$m_1^V \cdot \frac{\partial \tilde{h}_1^V}{\partial t} + \tilde{h}_1^V \cdot \frac{\partial m_1^V}{\partial t} = -\dot{Q}_I^V + \dot{m}_2^D \cdot \tilde{h}_2^V - \dot{m}_1^{BL} \cdot \tilde{h}_1^V + \dot{m}_N \cdot \tilde{h}_S^V$

Table 93. Energy and mass balance equations in the bulk of the sub-layers.

	Equation 229	$\frac{\partial m_1^V}{\partial t} = \dot{m}_2^D - \dot{m}_1^{BL} + \dot{m}_N$
Case 2	Equation 230	$m_1^V \cdot \frac{\partial \tilde{h}_1^V}{\partial t} + \tilde{h}_1^V \cdot \frac{\partial m_1^V}{\partial t} = -\dot{Q}_I^V - \dot{m}_2^D \cdot \tilde{h}_1^V - \dot{m}_1^{BL} \cdot \tilde{h}_1^V + \dot{m}_N \cdot \tilde{h}_S^V$
	Equation 231	$\frac{\partial m_1^V}{\partial t} = -\dot{m}_2^D - \dot{m}_1^{BL} + \dot{m}_N$
		Roof-vapour sub-layer
Case 1	Equation 232	$m_{N^V}^V \cdot \frac{\partial \tilde{h}_{N^V}^V}{\partial t} + \tilde{h}_{N^V}^V \cdot \frac{\partial m_{N^V}^V}{\partial t} = -\dot{m}_{N^V}^D \cdot \tilde{h}_{N^V}^V + \dot{m}_{N^V}^{BL} \cdot \tilde{h}_{N^V}^{BL,V} - \dot{m}_{BOG} \cdot \tilde{h}_{N^V}^V + \dot{m}_{IN}^V \cdot \tilde{h}_{IN}^V$
	Equation 233	$\frac{\partial m_{N^V}^V}{\partial t} = -\dot{m}_{N^V}^D + \dot{m}_{N^V}^{BL} - \dot{m}_{BOG} + \dot{m}_{IN}^V$
Case 2	Equation 234	$m_{N^V}^V \cdot \frac{\partial \tilde{h}_{N^V}^V}{\partial t} + \tilde{h}_{N^V}^V \cdot \frac{\partial m_{N^V}^V}{\partial t} = \dot{m}_{N^V}^D \cdot \tilde{h}_{N^V-1}^V + \dot{m}_{N^V}^{BL} \cdot \tilde{h}_{N^V}^{BL,V} - \dot{m}_{BOG} \cdot \tilde{h}_{N^V}^V + \dot{m}_{IN}^V \cdot \tilde{h}_{IN}^V$
	Equation 235	$\frac{\partial m_{N^V}^V}{\partial t} = \dot{m}_{N^V}^D + \dot{m}_{N^V}^{BL} - \dot{m}_{BOG} + \dot{m}_{IN}^V$
Case 3	Equation 236	$m_{N^V}^V \cdot \frac{\partial \tilde{h}_{N^V}^V}{\partial t} + \tilde{h}_{N^V}^V \cdot \frac{\partial m_{N^V}^V}{\partial t} = \dot{Q}_{W,N^V}^{SV} + \dot{m}_{N^V}^D \cdot \tilde{h}_{N^V-1}^V - \dot{m}_{BOG} \cdot \tilde{h}_{N^V}^V + \dot{m}_{IN}^V \cdot \tilde{h}_{IN}^V$
	Equation 237	$\frac{\partial m_{N^V}^V}{\partial t} = \dot{m}_{N^V}^D - \dot{m}_{BOG} + \dot{m}_{IN}^V$
		Core-vapour sub-layer
Case 1	Equation 238	$m_{n_V}^V \cdot \frac{\partial \tilde{h}_{n_V}^V}{\partial t} + \tilde{h}_{n_V}^V \cdot \frac{\partial m_{n_V}^V}{\partial t} = -\dot{m}_{n_V}^D \cdot \tilde{h}_{n_V}^V - \dot{m}_{n_V}^{BL} \cdot \tilde{h}_{n_V}^V + \dot{m}_{n_V+1}^D \cdot \tilde{h}_{n_V}^V$
	Equation 239	$\frac{\partial m_{n_V}^V}{\partial t} = -\dot{m}_{n_V}^D - \dot{m}_{n_V}^{BL} + \dot{m}_{n_V+1}^D$
Case 2	Equation 240	$m_{n_V}^V \cdot \frac{\partial \tilde{h}_{n_V}^V}{\partial t} + \tilde{h}_{n_V}^V \cdot \frac{\partial m_{n_V}^V}{\partial t} = \dot{m}_{n_V}^D \cdot \tilde{h}_{n_V-1}^V - \dot{m}_{n_V}^{BL} \cdot \tilde{h}_{n_V}^V + \dot{m}_{n_V+1}^D \cdot \tilde{h}_{n_V}^V$
	Equation 241	$\frac{\partial m_{n_V}^V}{\partial t} = \dot{m}_{n_V}^D - \dot{m}_{n_V}^{BL} + \dot{m}_{n_V+1}^D$
Case 3	Equation 242	$m_{n_V}^V \cdot \frac{\partial \tilde{h}_{n_V}^V}{\partial t} + \tilde{h}_{n_V}^V \cdot \frac{\partial m_{n_V}^V}{\partial t} = -\dot{m}_{n_V}^D \cdot \tilde{h}_{n_V}^V + \dot{m}_{n_V}^{BL} \cdot \tilde{h}_{n_V}^{BL,V} + \dot{m}_{n_V+1}^D \cdot \tilde{h}_{n_V}^V$
	Equation 243	$\frac{\partial m_{n_V}^V}{\partial t} = -\dot{m}_{n_V}^D + \dot{m}_{n_V}^{BL} + \dot{m}_{n_V+1}^D$
Case 4	Equation 244	$m_{n_V}^V \cdot \frac{\partial \tilde{h}_{n_V}^V}{\partial t} + \tilde{h}_{n_V}^V \cdot \frac{\partial m_{n_V}^V}{\partial t} = -\dot{m}_{n_V}^D \cdot \tilde{h}_{n_V}^V + \dot{m}_{n_V}^{BL} \cdot \tilde{h}_{n_V}^{BL,V} - \dot{m}_{n_V+1}^D \cdot \tilde{h}_{n_V}^V$
	Equation 245	$\frac{\partial m_{n_V}^V}{\partial t} = -\dot{m}_{n_V}^D + \dot{m}_{n_V}^{BL} - \dot{m}_{n_V+1}^D$
Case 5 and case 8	Equation 246	$m_{n_V}^V \cdot \frac{\partial \tilde{h}_{n_V}^V}{\partial t} + \tilde{h}_{n_V}^V \cdot \frac{\partial m_{n_V}^V}{\partial t} = \dot{m}_{n_V}^D \cdot \tilde{h}_{n_V-1}^V - \dot{m}_{n_V}^{BL} \cdot \tilde{h}_{n_V}^V - \dot{m}_{n_V+1}^D \cdot \tilde{h}_{n_V}^V$
	Equation 247	$\frac{\partial m_{n_V}^V}{\partial t} = \dot{m}_{n_V}^D - \dot{m}_{n_V}^{BL} - \dot{m}_{n_V+1}^D$
Case 6 and case 7	Equation 248	$m_{n_V}^V \cdot \frac{\partial \tilde{h}_{n_V}^V}{\partial t} + \tilde{h}_{n_V}^V \cdot \frac{\partial m_{n_V}^V}{\partial t} = \dot{m}_{n_V}^D \cdot \tilde{h}_{n_V-1}^V + \dot{m}_{n_V}^{BL} \cdot \tilde{h}_{n_V}^{BL,V} - \dot{m}_{n_V+1}^D \cdot \tilde{h}_{n_V}^V$
	Equation 249	$\frac{\partial m_{n_V}^V}{\partial t} = \dot{m}_{n_V}^D + \dot{m}_{n_V}^{BL} - \dot{m}_{n_V+1}^D$
Case 9	Equation 250	$m_{n_V}^V \cdot \frac{\partial \tilde{h}_{n_V}^V}{\partial t} + \tilde{h}_{n_V}^V \cdot \frac{\partial m_{n_V}^V}{\partial t} = \dot{Q}_{W,n_V}^{SV} + \dot{m}_{n_V}^D \cdot \tilde{h}_{n_V-1}^V - \dot{m}_{n_V+1}^D \cdot \tilde{h}_{n_V}^V$
	Equation 251	$\frac{\partial m_{n_V}^V}{\partial t} = \dot{m}_{n_V}^D - \dot{m}_{n_V+1}^D$

Due to the hypothesis of the virtual discretisation (assumption b) of Section 1.2 of Chapter 5), the transient of the ulllage mass of the bulk of the sub-layer can be neglected. $\dot{m}_{N^V}^D$ in case 3 of roof-vapour, $\dot{m}_{n_V}^D$ and $\dot{m}_{n_V+1}^D$ of case 9 of core-vapour, and $\dot{m}_{n_V+1}^D$ of case 8 of core-vapour are equal to $\dot{m}_{BOG}$ because the bulk of the virtual sub-layer are at steady state.

2.4.Overall energy balance equations of ullage

The writing the mass and energy conservation laws is the fourth step (step d) of Section 4.2 of Chapter 5) for deducing differential equation of the ullage temperature, as it is described in Figure 98.

The vapour is virtually stratified due to the hypothesis of the vapour virtual stratification (assumption b) of Section 1.2 of Chapter 5). Hence, the systems of mass and energy balance equations of Table 91 and Table 93 should be simplified with the overall energy and mass balance equations of the ullage. The energy balance equation can be deduced from the energy balance equations of Table 91 and Table 93. The overall enthalpy variation of the ullage bulk is the sum of the enthalpy variations of the bulk of each sub-layer, which are reported in Table 91 for the different case. Hence, the overall enthalpy variation of the ullage bulk can be computed as follows:

Equation 252

$$\sum_{i=1}^{N^V}\left[m_i^V\cdot\frac{\partial\tilde{h}_i^V}{\partial t}+\tilde{h}_i^V\cdot\frac{\partial m_i^V}{\partial t}\right]=\dot{m}_N\cdot\tilde{h}_S^V-\dot{Q}_I^V-\dot{m}_{BOG}\cdot\tilde{h}_{N^V}^V$$

$$+\dot{m}_{IN}^V\cdot\tilde{h}_{IN}^V-\sum_{i=1}^{N^+}\left[\dot{m}_i^{BL}\cdot\tilde{h}_i^V\right]+\sum_{i=1}^{N^-}\left[\dot{m}_i^{BL}\cdot\tilde{h}_i^{BL,V}\right]+\sum_{i=1}^{N_0}\dot{Q}_{w,i}^{SV}$$

In Equation 252, N^+ and N^- are respectively the number of sub-layers where the $\dot{m}_{nV}^{BL}$ enters and exits the boundary layer. N_0 is the number of sub-layer where $\dot{m}_{nV}^{BL}$ is equal to zero. Hence, Equation 252 considers the different cases of Table 93. As done for the bulk, the energy conservation laws of Table 93 can be used to compute the overall energy balance equation of the boundary layer. The overall energy conservation law of the boundary layer is expressed as follows:

Equation 253

$$\sum_{i=1}^{N}\dot{Q}_{W,i}^{SV}+\sum_{i=1}^{N^+}\left[\dot{m}_i^{BL}\cdot\tilde{h}_i^V\right]-\sum_{i=1}^{N^-}\left[\dot{m}_i^{BL}\cdot\tilde{h}_i^{BL,V}\right]=0$$

In Equation 253, N is the number of the sub-layer where $\dot{m}_{nV}^{BL}$ is different from zero. The overall energy balance of the ullage can be obtained as sum of Equation 252 and of Equation 253, as follows:

Equation 254

$$\sum_{i=1}^{N^V}\left[m_i^V\cdot\frac{\partial\tilde{h}_i^V}{\partial t}+\tilde{h}_i^V\cdot\frac{\partial m_i^V}{\partial t}\right]=$$

$$\dot{m}_N\cdot\tilde{h}_S^V-\dot{Q}_I^V-\dot{m}_{BOG}\cdot\tilde{h}_{N^V}^V+\dot{m}_{IN}^V\cdot\tilde{h}_{IN}^V+\sum_{i=1}^{N_0}\dot{Q}_{w,i}^{SV}+\sum_{i=1}^{N}\dot{Q}_{W,i}^{SV}$$

The sum of the terms $\sum_{i=1}^{N_0}\dot{Q}_{w,i}^{SV}$ and $\sum_{i=1}^{N}\dot{Q}_{W,i}^{SV}$ is equal to the dry side wall-to-vapour heat flow ($\dot{Q}_W^{SV}$). N_0 is the number of the virtual vapour sub-layer where $\dot{m}_i^{BL}$ is equal to zero ($\dot{m}_i^{BL}=0$).

2.5.Enthalpy flow formula of the overall energy balance equation

The deducing of the enthalpy flow formula of the overall energy balance equation (Equation 255) the fifth step (step e) of Section 4.2 of Chapter 5) for deducing differential equation of the ullage temperature, as it is described in Figure 98.

Descending mass flows and the boundary layer-to-bulk mass describe the fluid motions in the ullage, which is caused by the natural convection at the dry side wall. In order to explicit these flows in Equation 254, the mass conservation laws of Table 93 can be used to replace the term $\frac{\partial m_i^V}{\partial t}$, obtaining:

Equation 255

$$\begin{aligned}\sum_{i=1}^{N^V}\left[m_i^V\cdot\frac{\partial\tilde{h}_i^V}{\partial t}\right] &= \dot{m}_N\cdot\left(\tilde{h}_S^V-\tilde{h}_1^V\right)-\dot{Q}_I^V+\dot{m}_{IN}^V\cdot\left(\tilde{h}_{IN}^V-\tilde{h}_{N^V}^V\right)\\ &+\dot{Q}_w^{SV}+\sum_{i=1}^{N^+}\left[\dot{m}_i^{BL}\cdot\tilde{h}_i^V\right]-\sum_{i=1}^{N^-}\left[\dot{m}_i^{BL}\cdot\tilde{h}_i^V\right]+\sum_{i=1}^{N^V}\left[F_{i+1}^{D,+}\cdot\dot{m}_{i+1}^D\cdot\left(\tilde{h}_{i+1}^V-\tilde{h}_i^V\right)\right]\\ &-\sum_{i=1}^{N^V}\left[F_{i+1}^{D,-}\cdot\dot{m}_{i+1}^D\cdot\left(\tilde{h}_i^V-\tilde{h}_{i+1}^V\right)\right]\end{aligned}$$

In Equation 255, the term $\dot{m}_{BOG}\cdot\tilde{h}_{N^V}^V$ is removed as a consequence of substituting $\frac{\partial m_i^V}{\partial t}$ with the conservation laws of mass of Table 91. $F_{i+1}^{D,+}$ is equal to 1 when $\dot{m}_{i+1}^D$ is downward and it is equal to 0 if $\dot{m}_{i+1}^D$ is upward. $F_{i+1}^{D,-}$ is equal to 0 when $\dot{m}_{i+1}^D$ is downward and it is equal to 1 if $\dot{m}_{i+1}^D$ is upward.

2.6.Differential equation of the ullage temperature

The differential equation of the ullage temperature is deduced from the enthalpy flow formula of the overall energy balance equation (Equation 255) at the sixth step (step f) of Section 4.2 of Chapter 5) of the procedure of Figure 98.

The term $\sum_{i=1}^{N^V}\left[m_i^V\cdot\frac{\partial\tilde{h}_i^V}{\partial t}\right]$ of the Equation 255 must be equal to the variation of the overall vapour enthalpy vapour due to the change of the ullage temperature (T^V) and pressure (P^V). The overall enthalpy is the product between the overall ullage mass (m^V) and the overall specific enthalpy ($\tilde{h}^V$). m^V it is calculated as product between the ullage volume and the vapour density. Hence, the term $\sum_{i=1}^{N^V}\left[m_i^V\cdot\frac{\partial\tilde{h}_i^V}{\partial t}\right]$ can be computed as follows:

Equation 256

$$\sum_{i=1}^{N^V}\left[m_i^V\cdot\frac{\partial\tilde{h}_i^V}{\partial t}\right]=m^V\cdot\frac{\partial\tilde{h}^V}{\partial t}=m^V\cdot\left[C_P^V\cdot\frac{\partial T^V}{\partial t}+\left.\frac{\partial\tilde{h}^V}{\partial P^V}\right|_{T^V}\cdot\frac{\partial P^V}{\partial t}\right]$$

$\frac{\partial P^V}{\partial t}$ is the time-derivate of the pressure. As a consequence, the enthalpy flow formula of the overall energy balance equation can be written as follows:

Equation 257

$$\begin{aligned}m^V\cdot\left[C_P^V\cdot\frac{\partial T^V}{\partial t}+\left.\frac{\partial\tilde{h}^V}{\partial P^V}\right|_{T^V}\cdot\frac{\partial P^V}{\partial t}\right] &= \dot{m}_N\cdot\left(\tilde{h}_S^V-\tilde{h}_1^V\right)-\dot{Q}_I^V+\dot{m}_{IN}^V\cdot\left(\tilde{h}_{IN}^V-\tilde{h}_{N^V}^V\right)\\ &+\dot{Q}_w^{SV}+\sum_{i=1}^{N^+}\left[\dot{m}_i^{BL}\cdot\tilde{h}_i^V\right]-\sum_{i=1}^{N^-}\left[\dot{m}_i^{BL}\cdot\tilde{h}_i^V\right]+\sum_{i=1}^{N^V}\left[F_{i+1}^{D,+}\cdot\dot{m}_{i+1}^D\cdot\left(\tilde{h}_{i+1}^V-\tilde{h}_i^V\right)\right]\\ &-\sum_{i=1}^{N^V}\left[F_{i+1}^{D,-}\cdot\dot{m}_{i+1}^D\cdot\left(\tilde{h}_i^V-\tilde{h}_{i+1}^V\right)\right]\end{aligned}$$

The structure of Equation 257Equation 255 is similar to the energy balance equation of the vapour in the H model. Hence, it can be subjected to the same mathematical procedure to obtain the vapour temperature-evolution (T^V-e) equation. So, the T^V-e equation of the H 2.0 model can be computed as follows:

Equation 258

$$\frac{\partial T^V}{\partial t}=-\frac{1}{B^{TV}}\cdot\left[A^{TV}\cdot\frac{\partial P^V}{\partial t}+C^{TV}\cdot\frac{\partial V^L}{\partial t}+D^{TV}\cdot\dot{m}_{IN}^V+E^{TV}\cdot\dot{m}_{BOG}+F^{TV}\right]$$

$\frac{\partial V^L}{\partial t}$ is the time-derivate of the liquid volume. The coefficients A^{TV}, C^{TV} and E^{TV} (see Table 69) are the ones of the T^V-e equation of H model (Equation 133). The coefficients F^{TV} and D^{TV} of Equation 258 have to be modified because the enthalpy flow of the net mass flow [$\dot{m}_N \cdot \left(\tilde{h}_S^V - \tilde{h}_1^V\right)$] and the enthalpy flow of the inlet vapour flow [$\dot{m}_{IN}^V \cdot \left(\tilde{h}_{IN}^V - \tilde{h}_{N^V}^V\right)$] of the H 2.0 model are different from the ones of the H model. The coefficient D^{TV} and F^{TV} of T^V-e equation of the H 2.0 model are respectively computed as follows:

Equation 259
$$D^{TV} = -\left[\left(\tilde{h}_{IN}^V - \tilde{h}_{N^V}^V\right)\right]$$

Equation 260
$$F^{TV} = -\left\{\dot{Q}_W^{SV} - \dot{Q}_I^V + \dot{m}_N \cdot \left(\tilde{h}_S^V - \tilde{h}_1^V\right) + \sum_{i=1}^{N^+}\left[\dot{m}_i^{BL} \cdot \tilde{h}_i^V\right] - \sum_{i=1}^{N^-}\left[\dot{m}_i^{BL} \cdot \tilde{h}_i^V\right] + \sum_{i=1}^{N^V}\left[F_{i+1}^{D,+} \cdot \dot{m}_{i+1}^D \cdot \left(\tilde{h}_{i+1}^V - \tilde{h}_i^V\right)\right] - \sum_{i=1}^{N^V}\left[F_{i+1}^{D,-} \cdot \dot{m}_{i+1}^D \cdot \left(\tilde{h}_i^V - \tilde{h}_{i+1}^V\right)\right]\right\}$$

As indicated by Equation 260, the enthalpy flow of the net mass flow of H 2.0 model is lower than the one of H model because the difference $\left(\tilde{h}_S^V - \tilde{h}_1^V\right)$ is lower than the difference in the specific enthalpy that is used in the H model. Hence, the Equation 258 theoretically fulfils the objective of improving the prediction of the ullage warming by precisely computing this enthalpy flow on the physics of the vapour thermal stratification (objective a) of Section 1.1 of Chapter 5).

3. Storage heat transfer and storage boundary layer models for the homogeneous model 2.0

The Storage Boundary Layer (SBL) and the Storage Heat Transfer (SHT) models are the Block 7 of the structure of the homogeneous model 2.0 (H 2.0 model), as it is illustrated in Figure 95. The introduction of the bulk temperature gradient of the ullage has an impact on the SBL model. Since the SBL model is used in the SHT model, the latter is indirectly impacted by the ullage bulk temperature gradient. Hence, both models have to be modified.

Section 3.1 and 3.2 respectively describe the SBL model and the SHT model of H 2.0 model.

3.1. Storage Boundary Layer model

The Storage Boundary Layer (SBL) model computes the boundary layer variables, which are reported in Table 62. The variables $\bar{u}$, δ, δ_T, $\dot{m}_{BL}$ and T_{BL} can be computed from the variables U and δ_M, as it is described in Appendix O. These variables can be calculated by solving the conservation laws of momentum and of energy of the boundary layer (Equation 178 and Equation 179, see Section 3.4.2 of Chapter 4 for more details on these equations).

As done for the homogeneous model (H model), these conservation laws can be solved with two approaches: (i) the Exact Boundary Layer (EBL) and (ii) the Integral Boundary Layer (IBL) approaches. EBL uses the exact solution of these conservation laws and it analytically computes the variables U and δ_M. This approach can only be used for the flat ends of the storage tanks (bottom and roof). The IBL approach discretizes the boundary layer of the side wall in sub-layer, which are divided into sub-space-points, and it numerically solve these conservation laws with integration, calculating the variable U and δ_M. Heat fluxes due to the transferring of mass between the bulk and the boundary layer (variable $\dot{q}_\infty$ in Equation 179) is not equal to zero when the IBL is applied to the dry side wall, due to the ullage bulk temperature gradient (Equation 226). The denominator of Equation 179 (energy conservation law) can be negative, creating instability in the numerical algorithm. Hence, only the IBL approach of the dry side wall is impacted by the bulk ullage temperature gradient and the IBL approach of the dry side wall has to be improved to increase the stability. Two adjustments have been done:

a) Only the turbulent fluid-dynamic regimes is considered;
b) The number of sub-space-points is fixed;

Section 3.1.1 explains the reasons of the turbulent fluid-dynamic regime. Section 3.1.2 explains the new approach to determine the sub-space-points.

3.1.1. Turbulent fluid-dynamic regime

The viscous forces (τ_w) of Equation 178 (momentum conservation law) are calculated with different formulas, as function of the fluid-dynamic regime, as it is reported in Table 78. In the equation that computes the turbulent viscous forces (Equation 180), the viscosity forces depend on the quantity $U^2 \cdot \left(\frac{1}{U \cdot \delta_M}\right)^{0.25}$. So, the viscous forces goes to zero when the values of U and δ_M reduce. In the equation that computes the laminar viscous forces (Equation 184), the viscous forces are functions of the ratio $\frac{U}{\delta_M}$. As consequence, the viscous force cannot be computed when the values of U and δ_M are close to zero, because the ratio $\frac{U}{\delta_M}$ goes to the undefined value 0/0.

The homogeneous model 2.0 (H 2.0 model) considers the bulk temperature gradient in the ullage (Equation 226). In the Integration Boundary Layer (IBL) approach of the dry side wall, the energy conservation law (Equation 179) depends on the ullage bulk temperature gradient, which affects the heat flux due to the transferring of mass between the bulk and the boundary layer (variable $\dot{q}_\infty$ in Equation 179). The vaiable $\dot{q}_\infty$ reduces the derivate $\frac{\partial(U\cdot\delta_M)}{\partial x}$, decreasing the values of the variables U and δ_M. Hence, the numerical integration becomes instable when the ullage bulk temperature is considered due to Equation 184. As a consequence, it is reasonable to consider that the fluid-dynamics regime at the dry side wall is turbulent. Using this assumption, the numerical integration is stable because Equation 180 goes to zero as the variable U and δ_M decreases, instead of going to an undefined value as done by Equation 184.

The assumption of turbulent boundary layer was used by Vliet et al. [1], which used a numerical method to integrate the conservation laws of the boundary layer to compute the variables U and δ_M. This assumption is robust for storage containers with low filling ratio or medium-high heat fluxes because the values of these variables create turbulence in the boundary layer of the dry side wall.

3.1.2. Number of the sub-space-points

The conservation laws of the boundary layer (Equation 178 and Equation 179) are numerically solved by the Integration Boundary Layer (IBL) approach. In the IBL approach, the side wall is divided into sub-layer and these equations are numerically integrated in each sub-layer. To increases the stability, each sub-layer is spatially divided into sub-space-points, as done in the homogeneous model (H model). The number of sub-space-points of each sub-layer is calculated as function of the ratio between the derivates and the critical derivates[89] of the pseudo-boundary layer variables[90], called E and M, . These variables are used to stabilize the numerical integration of IBL approach and they are computed from the variables U and δ_M (see Section 2 of Appendix P). When this ratio is high, the number of sub-space-points is high to improve the accuracy. The number of sub-space-points decreases if this ratio is low.

The ullage bulk temperature gradient is added in the energy conservation law (Equation 179), reducing the derivates of the pseudo-boundary layer variables. As a consequence, the ratio between these derivates and the critical derivates is close to 1 and the number of sub-space-points, thus the accuracy, increases. Considering that the IBL approach is used to compute the heat transfer coefficient at the side wall with an iterative procedure, the number of sub-space-points can change at each iteration, modifying the values of these coefficients. The ullage bulk temperature gradient increases the change of the number of sub-space-points at each iteration, creating instability in the calculation of the heat transfer coefficient. Hence, the number of sub-space-point is fixed at 10, when the IBL approach is used for the dry side wall. When the IBL is applied at the wet side wall, the number of sub-space-points is calculated as done in the H model.

3.2. Storage Heat Transfer model

The Storage Heat Transfer (SHT) model computes the heat transfer variables at each surface of the storage container. These variables are reported in Table 62. Since the SHT model (i) must be adaptable to different geometry of the storage container and (ii) must consider the relation between the fluid-dynamics and the heat transfer, the heat transfer coefficient of each surface is computed with two

---

[89] Critical derivate is the derivate that makes the variables E and M equal to zero.

[90] $E = U\cdot\delta_M$; $M = U^2\cdot\delta_M$.

approaches: semi-empirical and the boundary layer approaches (see Section 4.6 of Chapter 4). The semi-empirical calculates the heat transfer coefficient of the flat ends of the storage container (bottom and roof) using formulas that are functions of the Nusselt's number. The boundary layer approach calculates the heat transfer coefficient at the dry and wet side walls, from the values of the variables U and δ_M. Hence, the instabilities of the Integration Boundary Layer (IBL) approach of dry side wall of Storage Boundary Layer (SBL) model propagate to the SHT model when the heat transfer coefficient of the dry side wall ($\bar{h}_w^{SV}$) is calculated in the algorithm of the dry side wall (see Section 3 of Appendix Q). To improve the stability of this algorithm, which computes the heat inputs at the dry side wall, the following modifications are proposed:

a) The dry side wall-to-vapour heat inputs ($\dot{Q}_w^{SV}$) is calculated with Newton-Raphson with finite difference method (see Section 2 of Appendix I);
b) The dry side wall temperature is calculated from the heat definition of the heat flow[91].

Section 3.2.1 explains the calculation of the dry side wall temperature. Section 3.2.2 describes the theory of the new algorithm of the dry side wall heat flow.

3.2.1. Dry side wall temperature

The dry side wall temperature (T_w^{SV}) is calculated from the energy balance equation of the dry side wall in the algorithm of the dry side wall (see Section 3 of Appendix Q) in the homogeneous model (H model). Since the dry side wall-to-vapour heat inputs ($\dot{Q}_w^{SV}$) is calculated with Newton-Raphson with finite difference method in the homogeneous model 2.0 (H 2.0 model), the temperature T_w^{SV} cannot be computed with the energy balance equation of the dry side wall. The heat flow $\dot{Q}_w^{SV}$ depends (i) on the difference in temperature between the dry side wall and the bulk, and (ii) on the heat transfer coefficient $\bar{h}_w^{SV}$. Hence, the dry side wall temperature (T_w^{SV}) can be computed with the definition of the heat flow, as follows:

Equation 261
$$T_w^{SV} = T^V + \frac{\dot{Q}_w^{SV}}{\alpha \cdot \bar{h}_w^{SV} \cdot A^{SV}}$$

α is the corrective coefficient and it is calculated with the Boil-Off Rate (BOR) model (see Section 5 of Chapter 5). A^{SV} is the surface area of the dry side wall (see Appendix B). The coefficient $\bar{h}_w^{SV}$ is calculated in the boundary layer approach, using the variables U and δ_M (see Section 4.6 of Chapter 4). In the H model, these variables were calculated with the Storage Boundary Layer (SBL) model, using the difference in temperature between the dry side wall (T_w^{SV}) and the bulk (T^V) as input parameter. In H 2.0 model, these variables are calculated with SBL model, using the dry side wall-to-vapour heat flow as input parameter. The use of this heat flow to compute U and δ_M gives more stability to the numerical integration than the method that use the difference in temperatures between T_w^{SV} and T^V because the value of the heat flow changes a bit during each iteration of the algorithm of the dry side wall.

3.2.2. Theory of the algorithm of the dry side wall

Due to the hypothesis of the vapour virtual discretisation (assumption b) of Section 1.2 of Chapter 5), the vapour phase is homogeneous and isothermal, with a virtual temperature profile. Hence, dry side wall can be considered as isothermal and the distribution of the heat flows in this wall can be described with Figure 68, as done for the homogeneous model (H model). Since the hypothesis of

---

[91] Heat flow : $\dot{Q} = h \cdot A \cdot \Delta T$

negligible thermal inertia of the side wall (assumption e) of Section 4.1 of Chapter 4) is valid, the energy conservation law at the dry side wall of H model (Equation 200) can be used. This conservation law can be written as follows:

Equation 262 $$h_{eff} \cdot (A^{SV} + A^{R}) \cdot (T^{w} - T_{w}^{SV}) = \alpha \cdot \bar{h}_{w}^{SV} \cdot A^{SV} \cdot (T_{w}^{SV} - T^{V}) + \beta \cdot \dot{Q}_{w}^{LV}$$

In Equation 262, T^{w} is the external wall temperature. h_{eff} is the effective heat transfer coefficient. β is the corrective coefficient of the dry side wall-to-interface heat flow. $\dot{Q}_{w}^{LV}$ is the dry side wall-to-interface heat flow and it is computed as function of T_{w}^{SV}, as done in the H model (see Section 4.5 of Chapter 4). T_{w}^{SV} is computed with Equation 261 and $\bar{h}_{w}^{SV}$ depends on the dry side wall-to-vapour heat flow ($\dot{Q}_{w}^{SV}$). So, the dry side wall-to-vapour heat flow ($\dot{Q}_{w}^{SV}$) can be only computed with the iterative procedure, based on the Newton-Raphson method with finite difference approach (see Section 2 of Appendix I). To use this approach the first guess value of the heat flow $\dot{Q}_{w}^{SV}$ and the intermediate variables have to be computed. To assure a fast convergence, the first guess value have to be calculated as close as possible to the value of $\dot{Q}_{w}^{SV}$. Hence, the equations of Table 94 are used.

Table 94. First guess value and intermediate variables of $\dot{Q}_{w}^{SV}$.

Variables	Name	Equation	Formula
first guess value of the heat flow	$\dot{Q}_{w}^{SV,0}$	Equation 263	$\dot{Q}_{w}^{SV,0} = h_{eff} \cdot (A^{SV} + A^{R}) \cdot \left(T^{w} - T_{w}^{SV,0}\right) - \beta \cdot \dot{Q}_{w}^{LV}$
First intermediate variable of the heat flow	$\dot{Q}_{w}^{SV,1}$	Equation 264	$\dot{Q}_{w}^{SV,1} = 0.999 \cdot \dot{Q}_{w}^{SV,0}$
Second intermediate variable of the heat flow	$\dot{Q}_{w}^{SV,2}$	Equation 265	$\dot{Q}_{w}^{SV,2} = 1.001 \cdot \dot{Q}_{w}^{SV,0}$

The values 0.999 and 1.001 are arbitrary taken. $T_{w}^{SV,0}$ is the first guess value of the dry side wall vapour temperature and it is equal to the value of the dry side wall temperature at the previous time-point. This variable is equal to the ullage temperature (T^{V}) at the first time-point. The details of the algorithm of the dry side wall are given in Appendix U. As indicated by Equation 263, the first guess value of the dry side wall-to-vapour heat flow ($\dot{Q}_{w}^{SV,0}$) can be lower than zero for certain values of coefficient β and of first guess value of the dry side wall vapour temperature. If this occurs, the first guess value of the dry side wall-to-vapour heat flow is computed as follows:

Equation 266 $$\dot{Q}_{w}^{SV,0} = h_{eff} \cdot (A^{SV} + A^{R}) \cdot \left(T^{w} - T_{w}^{SV,0}\right)$$

Equation 266 is obtained from Equation 263, by setting the beta coefficient equal to zero.

To improve the stability of the algorithm of the dry side wall, a value of $\dot{Q}_{w}^{SV,0}$ that is close to the final solution is not enough. Range of values where the solution of $\dot{Q}_{w}^{SV}$ can exist should be calculated. This limit is determined considering the physics of the heat transfer. The dry side wall-to-interface heat flow removes heat from the dry side wall and the environment-to-dry walls (side wall and roof) gives energy to this wall. Hence, the maximum value of the dry side wall-to-vapour heat flow occurs when the dry side wall-to-interface heat flow is equal to zero. The maximum value is calculated as follows:

Equation 267 $$\dot{Q}_{w,MAX}^{SV} = h_{eff} \cdot (A^{SV} + A^{R}) \cdot (T^{w} - T^{V})$$

Equation 267 is deduced by the energy balance equation at the dry side wall (Equation 262). The ullage receives heat from the dry side wall and the opposite pathway of the heat transfer cannot occur. Hence, the value of $\dot{Q}_{w}^{SV}$ must be higher than zero. so, the value of $\dot{Q}_{w}^{SV}$ must be between zero and the values of $\dot{Q}_{w,MAX}^{SV}$.

4. Interface Heat Transfer model

The Interface Heat Transfer (IHT) model is the Block 8 of the structure of the homogeneous model 2.0 (H 2.0 model), as it is illustrated in Figure 95.

The homogenous (H 2.0) model 2.0 is developed for improving the description of the liquid-to-interface and vapour-to-interface heat transfers (objective b) of Section 1.1 of Chapter 5), by using the fluid motions of liquid and of vapour near the interface. Hence, the formulas for computing the liquid-to-interface and vapour-to-interface heat flows in the homogeneous model (H model) cannot be used and new formulas are nedded. To contrary, the formula to compute the net mass flow of the H 2.0 model is the same of the H model seeing that the hypothesis of local thermodynamic equilibrium (assumption d) of Section 1.2 of Chapter 5) is applied in both models.

Section 4.1 presents the new model of the liquid-to-interface heat transfer. Section 4.2 explains the model of the vapour-to-interface heat flow. The algorithm of the IHT model for computing the net mass flow is reported in Appendix U.

4.1. Liquid-to-Interface heat transfer

During the steady state, the liquid moves to the interface due to the convective flow on the side wall. When the self-pressurisation starts, the thermal stratification in the liquid reduces the convective flow of the side wall near the interface. So, this convective flow can be blocked near the interface, causing local convective motion of fluid. Hence, two different heat transfer mechanisms (boundary layer convection and local natural convection) can occur, as it is described in Figure 101. In Figure 101, the orange zone is the vapour and the yellow dashed line is the interface. The light blue and the dark blue zones are the bulk of the liquid and the boundary layer of the wet side wall near the interface. The white arrows with blue border are the convective mass flow. The white arrows with red border are the heat flow and the enthalpy flow of the convective flows.

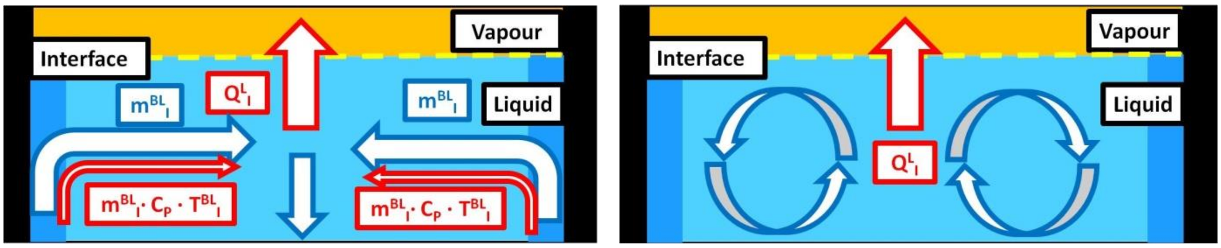

a) b)

Figure 101. a) Boundary layer convection and b) local natural convection.

The mechanism of Figure 101 can affect the liquid-to-interface heat flow during the self-pressurisation. Due to the hypothesis of liquid homogeneity (assumption a) of Section 1.2 of Chapter 5), the fluid-dynamic condition of the block of the convective flow at the wet side wall cannot be determined because the liquid bulk temperature is equal to zero. So, this blocking condition is based on thermodynamic conditions. When the interface temperature (T^I) is higher than the boundary layer temperature at the interface (T^I_{BL}), the model of local natural convection occurs. If T^I_{BL} is higher than T^I, the model of the boundary layer convection is used. These models are reported in Table 95.

Table 95. Equations of the models of boundary layer convection and local natural convection.

Conditions	Equation	Formula	Heat transfer mechanism
$T^I_{BL} \geq T^I$	Equation 268	$\dot{Q}^L_I = \dot{m}^{BL}_I \cdot C^L_P \cdot (T^I_{BL} - T^I)$	Boundary layer convection
$T^I_{BL} < T^I$	Equation 269	$\dot{Q}^L_I = A^I \cdot h^L_I \cdot (T^L - T^I)$	Local natural convection

A^I is the interface surface area. $\dot{m}_I^{BL}$ and T_{BL}^I are the boundary layer mass flow and temperature at the interface. These variables are computed with the Storage Boundary Layer (SBL) model, by means of the Integral Boundary Layer (IBL) approach of the SBL model, applied at the wet side wall. h_I^L is the liquid-to-interface heat transfer coefficient and it is computed with the semi-empirical approach (see Section 4.6 of Chapter 4). The Nusselt's number for the semi-empirical approach is determined with the model of Fishenden and Saunders [138] for horizontal warm flat surface that faces downward.

4.2. Vapour-to-Interface heat transfer

In the homogeneous model (H model), the vapour-to-interface heat transfer was described with the mechanism of natural convection over horizontal cooled surface facing upward, due to the hypothesis of total homogeneity (assumption a) of Section 1.1 of Chapter 4). This type of mechanism is unsuitable and the vapour-to-interface heat transfer should be deduced from the fluid-dynamics in the ullage. Hence, a new formula of the vapour-to-interface heat flow is required, based on the fluid-dynamics near the interface (see Figure 71).

As said in Section 2.1 of Chapter 5, the heat can be transferred to the interface with conduction or with local natural convection in the vapour near the interface, with the fluid-motions in the ullage and with the heat that is transferred between each sub-layer of the vapour phase. Hence, the vapour-to-interface heat flow can be computed as sum of these three contributions, as follows:

Equation 270
$$\dot{Q}_I^V = \dot{Q}_{I,1}^V + \dot{Q}_{I,2}^V + \dot{Q}_{I,3}^V$$

$\dot{Q}_{I,1}^V$ is vapour-to-interface heat flow due to the conduction-local natural convection. $\dot{Q}_{I,2}^V$ is the vapour-to-interface heat flow due to fluid-motions in the ullage. $\dot{Q}_{I,3}^V$ is the vapour-to-interface heat flow due to the heat transfer between sub-layers. Experimental evidences of these types of mechanisms near the interface are not available.

Section 4.2.1, 4.2.2 and 4.2.3 respectively describe these heat flows.

4.2.1. Vapour-to-interface heat flow: conduction-local natural convection

Daigle et al. [2] considered the conduction and the local natural convection when they modelled the heat flow between the vapour and the interface. They used the approach of maximum heat flow to determine which mechanism is dominant. In this approach, the vapour-to-interface heat flow is calculated with the conduction heat transfer mechanism if the heat flow of this mechanism is higher than the one of the local natural convection. The local natural convection is used when the heat flow of this mechanism is higher than the one of the conduction. In the homogenous (H 2.0) model 2.0, the heat transfer coefficients of these mechanisms are compared and the selected heat transfer mechanism is the one having the higher heat transfer coefficient. Hence, the vapour-to-interface heat flow due to conduction-local natural convection can be computed as follows:

Equation 271
$$\dot{Q}_{I,1}^V = \begin{cases} \dot{Q}_{I,C}^V, & h_{I,V}^V < h_{I,C}^V \\ \dot{Q}_{I,V}^V, & h_{I,V}^V \geq h_{I,C}^V \end{cases}$$

$\dot{Q}_{I,C}^V$ is the vapour-to-interface heat flow due to conduction and $h_{I,C}^V$ is the heat transfer coefficient of this heat flow. $\dot{Q}_{I,V}^V$ is the vapour-to-interface heat flow due to local natural convection and $h_{I,V}^V$ is the heat transfer coefficient of this heat flow. $\dot{Q}_{I,C}^V$ and $\dot{Q}_{I,V}^V$ are respectively computed as follows:

Equation 272 $$\dot{Q}^V_{I,C} = A^I \cdot h^V_{I,C} \cdot (T^V_1 - T^I)$$

Equation 273 $$\dot{Q}^V_{I,V} = A^I \cdot h^V_{I,V} \cdot (T^V_1 - T^I)$$

In Equation 272, heat transfer coefficient of conduction is calculated as follows:

Equation 274 $$h^V_{I,C} = \frac{k^V}{dx^V}$$

In Equation 274, $k^V$is the thermal conductivity and dx^V the thickness of the vapour sub-layer. In Equation 273, $h^V_{I,V}$ is computed with the semi-empirical approach of the Storage Heat Transfer (SHT) model (see Section 4.6 of Chapter 4). In this approach, the heat transfer coefficient is calculated from the Nusselt's number. This number is computed with the model of Fishenden and Saunders [138] for horizontal warm flat surface that faces downward.

4.2.2. Vapour-to-interface heat flow: fluid-motions in the ullage

As experimentally demonstrated, the rate of temperature increment in the ullage is low because most of the heat is transferred to the interface via the wall and via the vapour bulk. Considering the physics presented in Figure 71, most of the vapour bulk heat flow must come from the enthalpy of the descending mass flow in the core of the ullage. These enthalpy flows can be deduced from Equation 255. Hence, the vapour-to-interface heat flow due to fluid-motions can be computed as follows:

Equation 275 $$\dot{Q}^V_{I,2} = \sum_{i=1}^{M^+} \left[\dot{m}^D_i \cdot \left(\tilde{h}^V_{i+1} - \tilde{h}^V_i\right)\right]$$

M^+ is the number of sub-layer where $\dot{m}^D_i$ is directed downward. The mass accumulation in the ullage can be neglected due to the hypothesis of vapour virtual stratification (assumption b) of Section 1.2 of Chapter 5). So, the descending mass flow of Equation 275 is calculated as follows:

Equation 276 $$\dot{m}^D_{i+1} = \dot{m}^D_i + \dot{m}^{BL}_i - \dot{m}^{BL}_{i-1}$$

In Equation 276, $\dot{m}^{BL}_i$and $\dot{m}^{BL}_{i-1}$ are computed with the equations of Table 92. At the first sub-layer, the value of the descending mass flow $\dot{m}^D_i$ is substituted by $-\dot{m}_N$, as it is indicated in Figure 100.

4.2.3. Vapour-to-interface heat flow: heat transfer between sub-layer

It can happen that $\dot{m}^{BL}_{n_V}$ is can be equal to zero in the sub-layer, as it is illustrated in Figure 100. If this happens, the dry side wall-to-vapour heat flow of the sub-layer ($\dot{Q}^{SV}_{w,n_V}$) is absorbed by the bulk, as it is described in Figure 100. This energy is, then, transferred to theunderheath sub-layers that are below, up to the interface. So, the energy transferred in this way is equal to the sum of the dry side wall-to-vapour heat flow of the sub-layer where $\dot{m}^{BL}_{n_V}$ is equal to zero. Hence, the vapour-to-interface heat flow due to the heat transfer between sub-layer is calculated as follows:

Equation 277 $$\dot{Q}^V_{I,3} = \sum_{i=1}^{N_0} \dot{Q}^{SV}_{w,i}$$

N_0 is defined in Equation 254.

5. Boil-Off Rate Model: approach for homogeneous model 2.0

The Boill-off Rate (BOR) model is the Block 3 of the structure of the homogeneous model 2.0 (H 2.0 model), as it is illustrated in Figure 95.

Taking into account that most of the hypotheses of the homogeneous model (H model) are applied also for the homogeneous model 2.0 (H 2.0 model), the Boil-off Rate (BOR) model of H 2.0 model is quite similar to the one of the H model. The main difference between the two BOR models is the different energy conservation law of the ullage at steady state, which require a new beta algorithm in the computation of the alpha coefficient.

Section 5.1 recaps the BOR model of H model. Section 5.2 explains the BOR model of H 2.0 model.

5.1. Recap of the boil-off rate model of the homogeneous model

The Boil-Off Rate (BOR) model of the homogeneous model (H model) computes the effective heat transfer coefficient (h_{eff}), and the corrective coefficients α and β, using the values of vapour temperature, Boil-Off Rate (BOR) or overall heat input, pressure and filling ratio. These values have to be measured for two types of steady state experiments: one at high filling ratio (Test 1), and one at low filling ratio (Test 2).

The heat transfer coefficient is calculated with the h_{eff} algorithm (see Section 1 of Appendix R), using the experimental values of these variables of Test 1. In this algorithm, the value of the corrective coefficient α is equal to 1 for hypothesis. The h_{eff} algorithm is based on the energy conservation law at the walls of the storage container and it uses the substitution method (see Section 1 of Appendix I) for the iterative procedure. The beta coefficient is calculated with the β algorithm (see Section 1.2 of Appendix R) using the steady state energy and mass conservation laws at the ullage and the Newton-Raphson with finite difference method (see Section 2 of Appendix I). In the β algorithm, the dry side wall temperature (T_w^{SV}) is calculated with T_w^{SV} algorithm (see Section 1.3 of Appendix R). This algorithm uses the energy conservation law at the dry side wall and it is based on Newton-Raphson with finite difference method (see Section 2 of Appendix I).

If the BOR model is applied for Test 2, the corrective coefficients α and β are computed with the α algorithm. The effective heat transfer coefficient of Test 2 is the one computed with the h_{eff} algorithm, applied at Test 1. The α algorithm is based on formulas that are deduced from the conservation laws of energy at the wall of the storage containers (Equation 222) and from the steady state conservation laws of energy and mass at the ullage (Equation 217 and Equation 218). The dry side wall temperature is computed with Equation 1043, which is deduced from the energy conservation law at the dry side wall. The β coefficient is calculated with Equation 1042, which is obtained from the steady state conservation laws of energy and mass at the ullage. The α coefficient is computed from the energy conservation law of the overall storage container (Equation 1055).

In each algorithm of the BOR model, the heat transfer coefficients at each wall of the storage container are required and they are computed with the Storage Heat Transfer (SHT) model. The heat transfer coefficient at the wet and dry side walls are calculated with the boundary layer approach (see Section 4.6 of Chapter 4) and the Storage Boundary Layer (SBL) model is required.

5.2.Boil-Off Rate model

In the homogeneous (H 2.0) model, the bulk ullage temperature gradient is considered, due to the hypothesis of vapour virtual stratification (assumption b) of Section 1.2 of Chapter 5). As a consequence, the storage container of the Boil-Off Rate (BOR) model can be described as it is illustrated in Figure 102. The blue zone is the liquid and the red zone with colour degradation is the ullage. The yellow dashed line is the interface. The green arrow is the net mass flow at interface and the black arrows are the inlet and outlet flows of the fluid. The white arrows with red boarders are the heat fluxes, and the white points with purple boarders are the wall temperatures.

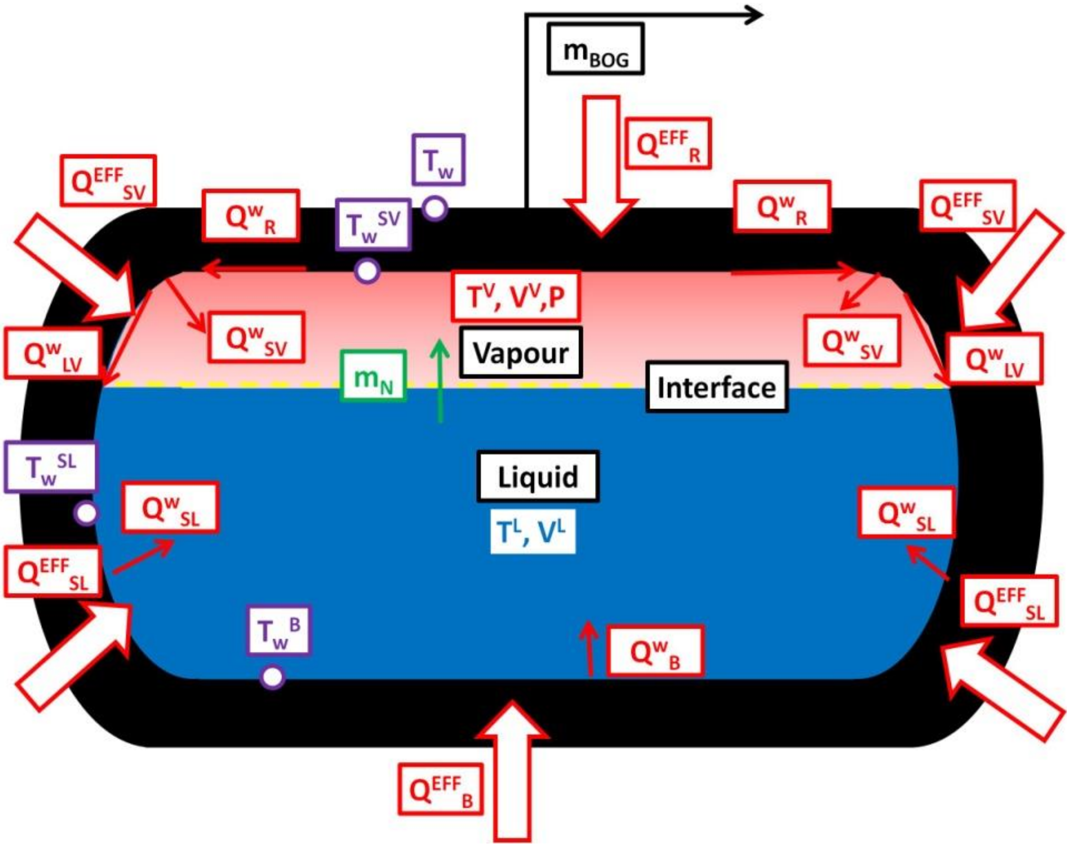

Figure 102. BOR model

This hypothesis of vapour virtual stratification requires a new the energy conservation law of the steady state ullage. The liquid is described as done in the H model. So, only the α algorithm and the energy conservation law of the steady state ullage of β algorithms are changed from the ones of the H model. The h_{eff} algortimh of BOR model of H 2.0 model is similar to the one used in the H model (see Section 1 of Appendix R).

The value of beta coefficient is computed form the steady state conservation laws of mass and energy at the ullage in h_{eff} and α algorithms. The mass balance equations, which states that the net mass flow ($\dot{m}_N$) is equal to the Boil-Off Gas flow ($\dot{m}_{BOG}$), is the one of the BOR model of H model (Equation 218). The energy conservation law of the ullage at the steady state can be deduced from the enthalpy flow formula of the overall energy balance equation (Equation 255). The energy balance equations of the BOR model of H 2.0 model at steady state can be described as follows:

Equation 278

$$\begin{aligned}&\dot{m}_N \cdot \left(\tilde{h}_S^V - \tilde{h}_1^V\right) - \dot{Q}_I^V + \dot{m}_{IN}^V \cdot \left(\tilde{h}_{IN}^V - \tilde{h}_{N^V}^V\right) + \dot{Q}_w^{SV} \\ &+ \sum_{i=1}^{N^+}\left[\dot{m}_i^{BL} \cdot \tilde{h}_i^V\right] - \sum_{i=1}^{N^-}\left[\dot{m}_i^{BL} \cdot \tilde{h}_i^V\right] + \sum_{i=1}^{N^V}\left[F_{i+1}^{D,+} \cdot \dot{m}_{i+1}^D \cdot \left(\tilde{h}_{i+1}^V - \tilde{h}_i^V\right)\right] \\ &- \sum_{i=1}^{N^V}\left[F_{i+1}^{D,-} \cdot \dot{m}_{i+1}^D \cdot \left(\tilde{h}_i^V - \tilde{h}_{i+1}^V\right)\right] = 0\end{aligned}$$

In Equation 278, $\dot{m}_{IN}^V$, which is the inlet vapour flow, is equal to zero by hypothesis. $\dot{m}_N$ is computed with the net mass flow algorithm (see Appendix V) and $\dot{Q}_I^V$ is calculated with the Interface Heat Transfer (IHT) model (Section 4.2 of Chapter 5). $\dot{Q}_w^{SV}$ is computed with the dry side wall heat flow algorithm (see Appendix V). As consequence, a new β algorithm has to be developed for α algorithm. β algorithm of α algorithm is described in Appendix Z.

In the BOR model of H 2.0 model, the dry side wall temperature is computed with the dry side wall energy conservation law (Equation 262). Since Equation 262 is equal to the one of H model (Equation 222), this temperature is computed with T_w^{SV} algorithm of BOR model of H model (see Section 1.3 of Appendix R) in the BOR model of H 2.0 model for the h_{eff} algorithm. For the α algortimh of BOR model of H 2.0 model, this temperature is computed with same equation of BOR model of H model (Equation 1043).

6. Comparison with experimental data

The results of the homogeneous model 2.0 (H 2.0 model) are compared with the experimental data of the Study case of Table 54, as done for the previous models. In H 2.0 model, the fluid-dynamic and the heat transfer modelling approach of the dry side wall, the modelling approach of the vapour-to-interface heat transfer and the energy conservation laws of the ullage are changed with respect to the homogeneous model (H model). Hence, the results of the pressure and ullage temperature are coompated with the experimental data. The discussions focus on the fluid-dynamics and the heat transfer at the dry side wall, the interfacial heat transfer and net mass flow. The computed values of liquid temperature and of filling ratio are not compared with measured values, because the modifications introduced in the H 2.0 model do not have any significant impact on these variables.

It should be reminded that the self-pressurization phase is preceded by a steady state phase in all experimental works considered in this thesis, except for Test 2 of Study case 3. The steady state is also simulated by the models. In Test 2 of Study case 3, the simulation directly starts from the self-pressurisaiton, without the steady state as done in the experiment.

Section 6.1, 6.2 and 6.3 presents the comparison between the results of the H 2.0 model and the comparison with experimental data of ullage temperature and pressure for Study cases at low, medium and high heat fluxes, respectively.

6.1. Study cases: low heat fluxes

The study cases at low heat fluxes are reported in Table 54. In Table 96, the boundary conditions and the initial condition of temperature at the beginning of the self-pressurisation phase are presented. The data in Table 96 are the values of the parameters at the transition point between the steady state and the self-pressurization phases.

Table 96. Initial conditions and boundary conditions for the self-pressurisation stage.

Sub-case	$h_{eff}\left[\frac{W}{m^2\cdot K}\right]$	$\alpha\,[-]$	$\beta\,[-]$	$\dot{Q}\,[W]$		$T^V\,[K]$	
				Exp	**H 2.0**	**Exp**	**H 2.0**
Study case 1							
Test 1	0.3047	1	0.6951	1.331	1.331	77.41	77.41
Test 2	0.3047	$1.683\cdot10^{-2}$	$2.054\cdot10^{-2}$	1.163	1.163	78.91	78.87
Test 3	0.06041	1	1.365	2.618	2.618	80.48	80.48
Test 4	0.3047	$1.368\cdot10^{-2}$	$2.043\cdot10^{-2}$	1.034	1.037	80.47	79.95
Test 5	0.3047	$1.030\cdot10^{-2}$	$7.159\cdot10^{-2}$	0. 9183	0.9318	81.05	79.26
Test 6	0.3047	$7.581\cdot10^{-3}$	$4.799\cdot10^{-2}$	0.7119	0.7344	81.68	79.46
Study case 2							
Test 1	0.02768	1	1.573	1.201	1.201	78.35	78.34
Study case 3							
Test 1	0.02210	1	63.57	82.96	82.96	22.83	22.83
Test 2	0.02210	1	63.57	83.08	83.14	20.25	20.33
Study case 4							
Test 1	0.02210	$3.227\cdot10^{-3}$	5.406	70.30	70.36	23.50	23.24

Table 96. Initial conditions and boundary conditions for the self-pressurisation stage.

Test 2	0.02210	$1.997\cdot10^{-3}$	7.293	62.59	62.89	23.66	22.58

For Study case 1, the overall heat inputs of Test 1 (high filling ratio), 2 (high-medium filling ratio) and 3 (high heat input) at the end of the steady state, thus at the beginning of the self-pressurisation, are equal to the experimental one. For Test 4 (medium filling ratio), there is a small difference in the heat input between the homogeneous model 2.0 (H 2.0 model) and the experimental one. The values of this difference of Tests 5 (medium low filling ratio) and 6 (low filling ratio) are higher than the ones of Test 4. Hence, the values of overall heat input are properly computed at high filling ratio and high heat input. A divergence of the overall heat input is observed between the experimental data and the H 2.0 model at medium and flow filling ratios. The values of the ullage temperature of Tests 1 and 3 at the beginning of the self-pressurisation are equal to the experimental one. The difference in ullage temperature between the computed and the measured is observed for Tests 2, 4, 5 and 6 and the value of this difference increases with the reduction of the filling ratio. So, the ullage temperature at the beginning of the self-pressurisation is better calculated at high filling ratio and heat input than at low-medium filling ratio. Except for Tests 1 and 3, the values of the alpha coefficient decreases with the reduction of the initial liquid level. The values of beta coefficient increase from Tests 1 to 3, if the values of alpha coefficient are equal to 1 (Test 1 and 3). The value of beta coefficient (i) is almost constant between Tests 2 and 4, (ii) increases between Tests 4 and 5 and (iii) decreases at Test 6. Hence, the value of beta increases with the heat input and it decreases with the reduction of the filling ratio, creating a minimum near 50 % (Test 4) and maximum near 30 % (Test 5).

For Study case 2, the overall heat input at the end of the steady state is equal to the experimental one. At the beginning of the self-pressurisation, the difference in ullage temperature between the calculated and the experimental value is around 0.01 K. The initial value of overall heat input and ullage temperature are computed with the H 2.0 model with a negligible error.

For Study case 3, the values of overall heat input and ullage temperature at the end of the steady state are equal to the experimental ones, at Test 1 (steady state initial condition). The difference in the overall heat input between the experimental data and the H 2.0 model is around 0.6 W at Test 2 (isothermal initial condition). The computed ullage temperature at the beginning of the self-pressurisation is slightly higher than the experimental one, at Test 2. The values of beta and alpha coefficient do not change between Tests 1 and 2.

For Study case 4, the value of overall heat input at the end of the steady state is almost equal to the experimental one, at Test 1 (medium filling ratio), and the difference in heat input between the calculated and measured one is around 0.06 W. The computed ullage temperature of Test 1 is slightly lower than the experimental one, with a difference of 0.26 K at the beginning of the self-pressurisation. The value of the overall heat input of Test 2 (low filling ratio) is slightly higher than the experimental one at the end of the steady state. The difference in ullage temperature between H 2.0 model and the experimental value is 1.08 K at the beginning of the self-pressurisation of Test 2. The values of alpha coefficient decrease with the reduction of the initial filling ratio. The values of beta coefficient increase between Tests 1 and 2, thus with the reduction of the initial liquid level.

To sum up for the Study cases at low heat fluxes, the computed values of overall heat input and of ullage temperature are equal to the experimental ones at high filling ratio and high heat input, with steady state initial condition. At medium and low filling ratios, or at isothermal steady state condition, the difference in overall heat input between the calculated and measured one is less than 3.2 %, whereas the difference in ullage temperature between the calculated and measured one is less than 4.6 %. The values of alpha coefficient always decrease with the reduction of the initial filling ratio. The values of beta coefficient decrease from high to medium filling ratio. These values increases between medium and low liquid level, creating a minimum around 50 %.

Section 6.1.1, 6.1.2, 6.1.3 and 6.1.4, present the results (i) the fluid-dynamics at the dry side wall, (ii) the heat transfer at the dry side wall, (iii) the heat transfer at the interface and (iv) the net mass flow, respectively. Section 6.1.5 and 6.1.6 illustrate the comparison of the pressure and of the ullage temperature with the experimental data, respectively.

6.1.1. Presentation of the results: fluid-dynamics at the dry side wall

Figure 103 describes the fluid-dynamics at the dry side wall, by showing the time-evolutions of the bulk temperature gradient ($\frac{\partial T^V}{\partial x}$) and the boundary layer average mass flow[92] at the dry side wall ($\dot{m}_{BL}^{SV}$). The values of $\frac{\partial T^V}{\partial x}$ and $\dot{m}_{BL}^{SV}$ are reported on the left and right vertical axis, respectively.

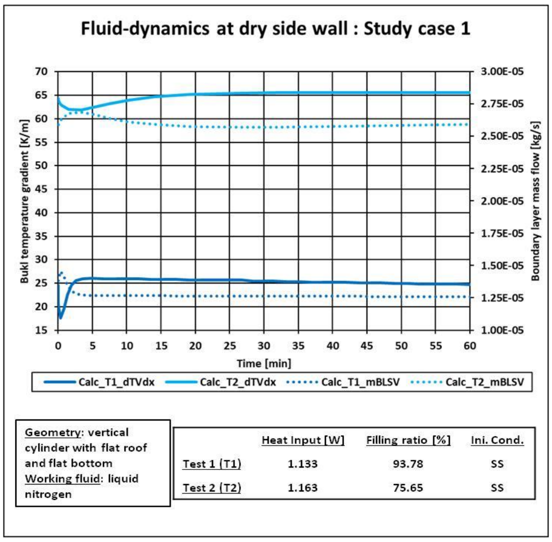

	Heat Input [W]	Filling ratio [%]	Ini. Cond.
Test 1 (T1)	1.133	93.78	SS
Test 2 (T2)	1.163	75.65	SS

a)

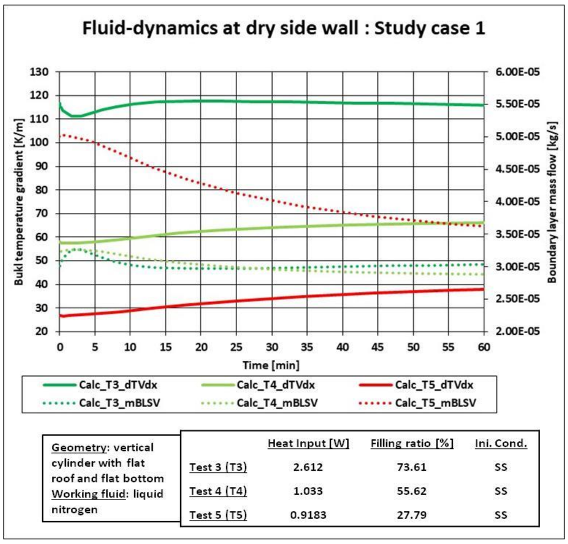

	Heat Input [W]	Filling ratio [%]	Ini. Cond.
Test 3 (T3)	2.612	73.61	SS
Test 4 (T4)	1.033	55.62	SS
Test 5 (T5)	0.9183	27.79	SS

b)

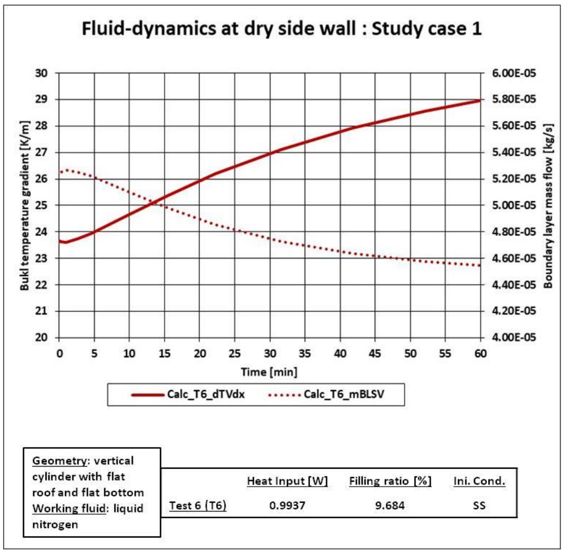

	Heat Input [W]	Filling ratio [%]	Ini. Cond.
Test 6 (T6)	0.9937	9.684	SS

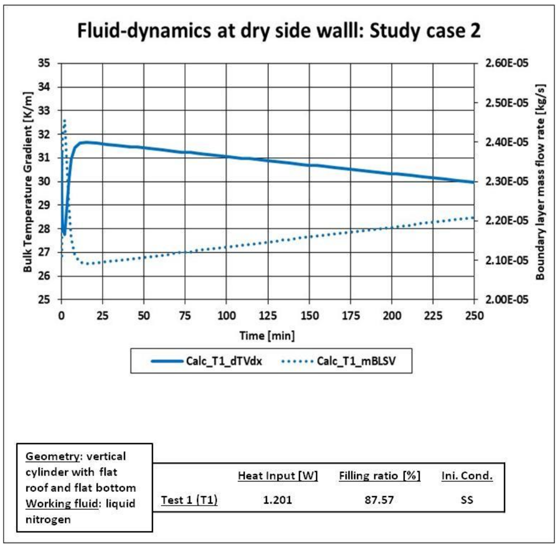

	Heat Input [W]	Filling ratio [%]	Ini. Cond.
Test 1 (T1)	1.201	87.57	SS

---

[92] The average mass flow is computed with the trapezoidal rule, using the value of the boundary layer mass flow at each sub-layer of the dry side wall. Hence, this value is directly depends on the value of the boundary layer variable U and δ_M.

c) d)

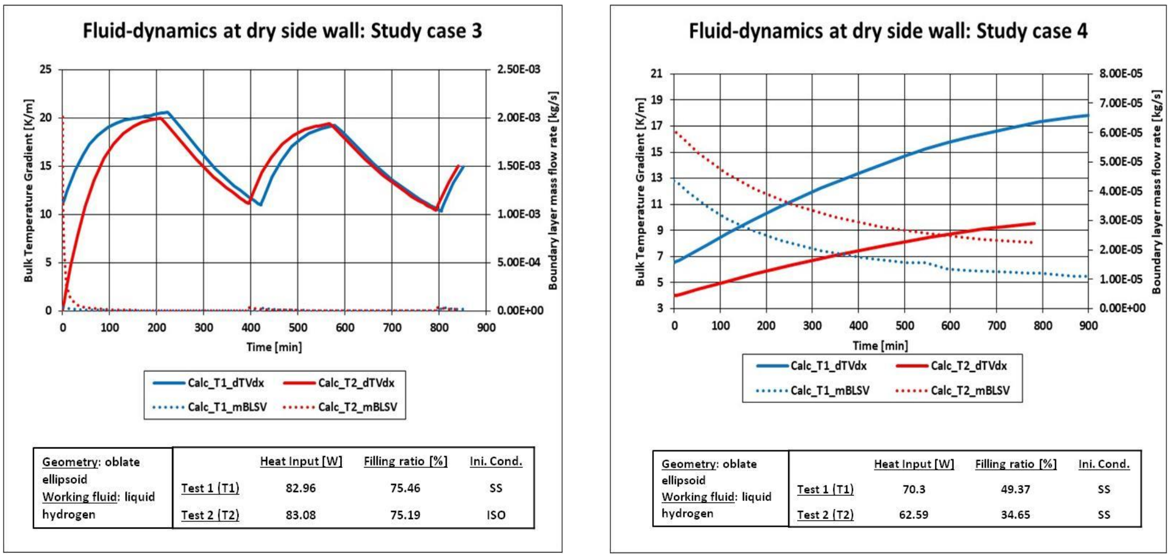

e) f)

Figure 103. Fluid-dynamics at the dry side wall: a) Study case 1 (Test 1 and Test 2), b) Study case 1 (Test 3, 4 and 5), c) Study case 1 (Test 6), d) Study case 2, e) Study case 3 and f) Study case 4.

For Study case 1, $\frac{\partial T^V}{\partial x}$ initially decreases during the self-pressurisation and the shape of this decrement is particularity sharp at Test 1 (high filling ratio). The shape of this decrement becomes smooth at Test 2 (high-medium filling ratio) and Test 3 (high heat input). This initial decrement is almost absent at Tests 4 (medium filling ratio), 5 (medium-low filling ratio) and 6 (low filling ratio). Thus, this initial decrement decreases with the reduction of the low filing raito. After this initial transient, $\frac{\partial T^V}{\partial x}$ increases. This increment lasts for all the self-pressurisation for Tests 4, 5 and 6. For Tests 1, 2 and 3, this increment stops and $\frac{\partial T^V}{\partial x}$ remains almost constant. For the same time-point of the self-pressurisation, $\frac{\partial T^V}{\partial x}$ increases from Test 1 to Test 2 and it decreases from Test 4 to Test 6. $\dot{m}_{BL}^{SV}$ initially increases during the self-pressurisation, creating a peak for Test 1 (high filling ratio), Test 2 (high-medium filling ratio) and Test 3 (high heat input). This peak of Test 1 is sharper than the ones of Tests 2 and 3. This initial increment is less relevant at Tests 4 (medium filling ratio), 5 (medium-low filling ratio) and 6 (low filling ratio) than at Tests 1, 2 and 3. Thus, this peak reduces as the initial filling ratio decreases. After this initial transient, $\dot{m}_{BL}^{SV}$ decreases. For Tests 1, 2 and 3, this decrement stops and $\dot{m}_{BL}^{SV}$ remains almost constant. For Tests 4, 5 and 6, this decrement continues for all the self-pressurisation. The rate of this reduction increases as the initial filling ratio decreases. At fixed time-point of the self-pressurisation, $\dot{m}_{BL}^{SV}$ increases between Test 1 and Test 6.

For Study case 2, the time-evolution of $\frac{\partial T^V}{\partial x}$ is qualitatively similar to the one of the Test 1 of Study case 1. So, $\frac{\partial T^V}{\partial x}$ initially decreases and, then, it increases. After the increment, $\frac{\partial T^V}{\partial x}$ constantly decreases, contrarily to the ones of Test 1 of Study case 1. The time-evolution of $\dot{m}_{BL}^{SV}$ is symmetrical with the one of $\frac{\partial T^V}{\partial x}$. Hence, it initially increases, and, then, it decreases. After this decrement, it constantly increases.

For Study case 3, $\frac{\partial T^V}{\partial x}$ increases during the first 200 minutes of the self-pressurisation. This initial increment of Test 2 (isothermal initial condition) is faster than the one of Test 1 (steady state initial condition). $\frac{\partial T^V}{\partial x}$ of Test 1 is higher than the one of Test 2. After 200 minutes, $\frac{\partial T^V}{\partial x}$ decreases up to 400 minutes. Between 400 and 580 minutes of the self-pressurisation, $\frac{\partial T^V}{\partial x}$ increases. $\frac{\partial T^V}{\partial x}$ decreases up to 800 minutes and it increases up to the end of the self-pressurisation. At the end of the natural pressure build-up, the difference in $\frac{\partial T^V}{\partial x}$ between Tests 1 and 2, is lower than the one at the beginning. $\dot{m}_{BL}^{SV}$ quickly and massively decreases at the beginning of the self-pressurisation. The rate of decrement of Test 2 (isothermal initial condition) is higher than the one of Test 1 (steady state initial condition). At 200 minutes, $\dot{m}_{BL}^{SV}$ is almost zero. Between 200 and 400 minutes, $\dot{m}_{BL}^{SV}$ increases and, at 400 minutes, there is a peak. Between 400 and 580 minutes of the self-pressurisation, $\dot{m}_{BL}^{SV}$ decreases. At 580 minutes, there is drop of $\dot{m}_{BL}^{SV}$. $\dot{m}_{BL}^{SV}$ increases up to 800 minutes and it decreases up to the end of the self-pressurisation.

For Study case 4, $\frac{\partial T^V}{\partial x}$ almost constantly increases during the self-pressurisation. $\frac{\partial T^V}{\partial x}$ of Test 1 (medium filling ratio) is higher than the one of Test X (low filling ratio). $\dot{m}_{BL}^{SV}$ decreases during the self-pressurisation and this decrement is symmetrical to the increment of $\frac{\partial T^V}{\partial x}$. $\dot{m}_{BL}^{SV}$ of Test 2 is higher than the one of Test 1.

To sum up, the time-evolution of the boundary layer average mass flow ($\dot{m}_{BL}^{SV}$) is symmetrical to the one of $\frac{\partial T^V}{\partial x}$. After the initial transient, $\frac{\partial T^V}{\partial x}$ increases during the self-pressurisation and the rate of this increment increases with the reduction of the filling ratio. The highest values of $\frac{\partial T^V}{\partial x}$ are often observed at medium filling ratio. The values of $\dot{m}_{BL}^{SV}$ decrease during the self-pressurisation, after the initial transient. $\dot{m}_{BL}^{SV}$ increases with the heat input and the reduction of the initial filling ratio.

6.1.2. Presentation of the results: heat transfer at dry side wall

Figure 104 illustrates the heat transfer at the dry side wall during the self pressurisation, showing the evolution of dry side wall-to-vapour heat transfer coefficient ($\bar{h}_W^{SV}$) and of the dry side wall-to-vapour heat flow ($\dot{Q}_W^{SV}$). The values of $\bar{h}_W^{SV}$ and $\dot{Q}_W^{SV}$ are reported on the left vertical and right vertical axis, respectively.

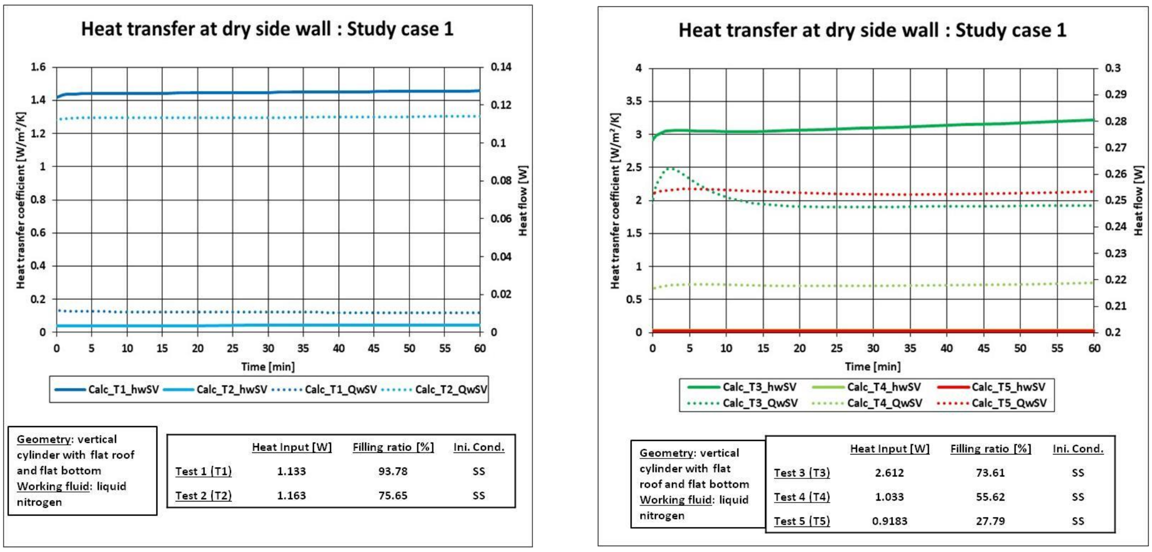

a)

b)

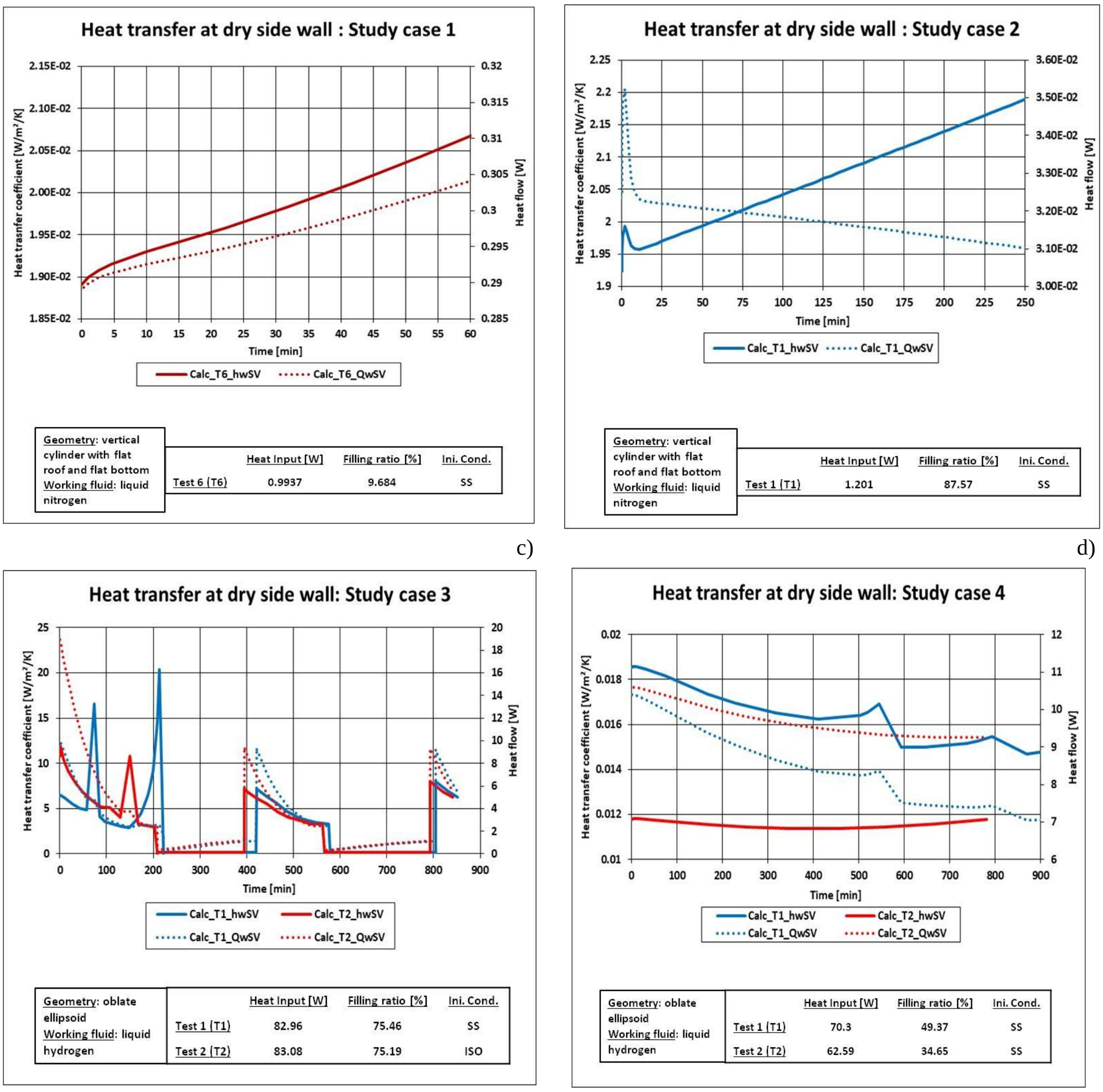

Geometry: vertical cylinder with flat roof and flat bottom Working fluid: liquid nitrogen	Heat Input [W]	Filling ratio [%]	Ini. Cond.
Test 6 (T6)	0.9937	9.684	SS

c)

Geometry: vertical cylinder with flat roof and flat bottom Working fluid: liquid nitrogen	Heat Input [W]	Filling ratio [%]	Ini. Cond.
Test 1 (T1)	1.201	87.57	SS

d)

Geometry: oblate ellipsoid Working fluid: liquid hydrogen	Heat Input [W]	Filling ratio [%]	Ini. Cond.
Test 1 (T1)	82.96	75.46	SS
Test 2 (T2)	83.08	75.19	ISO

e)

Geometry: oblate ellipsoid Working fluid: liquid hydrogen	Heat Input [W]	Filling ratio [%]	Ini. Cond.
Test 1 (T1)	70.3	49.37	SS
Test 2 (T2)	62.59	34.65	SS

f)

Figure 104. Heat transfer at the dry side wall for Study cases at low heat fluxes: a) Study case 1 (Test 1 and Test 2), b) Study case 1 (Test 3, 4 and 5), c) Study case 1 (Test 6), d) Study case 2, e) Study case 3 and f) Study case 4.

For Study case 1, $\bar{h}_w^{SV}$ is constant during the self-pressurisation, except for Test 3 (high heat input) and Test 6 (low filling ratio). In these tests, $\bar{h}_w^{SV}$ increases in time. $\bar{h}_w^{SV}$ decreases from Test 1 (high filling ratio) to Test 6, thus it decreases with the reduction of the initial filling ratio. $\bar{h}_w^{SV}$ increases with the increment of the heat input. $\dot{Q}_w^{SV}$ is constant during the self-pressurisation for Tests 1 and 2 (high-medium filling ratio). For the other tests, $\dot{Q}_w^{SV}$ slightly increases during the self-pressurisation. For Test 3 (high heat input), there is a peak at the beginning of the self-pressurisation. $\dot{Q}_w^{SV}$ increases from Test 1 to Test 6, thus it increases with the reduction of the filling ratio.

For Study case 2, $\bar{h}_w^{SV}$ has a peak at the beginning of the self-pressurisation, thus at the end of the steady state. After this peak, $\bar{h}_w^{SV}$ constantly decreases in time. $\dot{Q}_w^{SV}$ has a peak at the end of the steady state, as done by $\bar{h}_w^{SV}$. After this peak, $\dot{Q}_w^{SV}$ constantly increases.

For Study case 3, $\bar{h}_w^{SV}$ decreases between the beginning of the self-pressurisation and the 200 minutes. $\bar{h}_w^{SV}$ and the rate of this decrement of Test 2 (isothermal initial condition) are higher than the ones of Test 1 (steady state initial condition). For Test 1, there are two peaks in this period of time and, for

Test 2, one peak is observed. At 200 minutes, $\bar{h}_w^{SV}$ decreases up to zero, whereas it. increases between 200 minutes and 400 minutes. Then, a peak is observed, then it decreases up to 580 minutes. At this time, $\bar{h}_w^{SV}$ drops and it increases between 580 and 800 minutes. At 800 minutes, there is a peak, which constantly reduces up to the end of the self-pressurisation. The time-evolution of $\dot{Q}_w^{SV}$ is quite similar to the one of $\bar{h}_w^{SV}$. $\dot{Q}_w^{SV}$ decreases between 0 and 200 minutes, between 400 and 580 minutes, and between 800 minutes up to the end of the self-pressurisation. $\dot{Q}_w^{SV}$ increases between 200 and 400 minutes, and between 580 and 800 minutes. The peaks of $\dot{Q}_w^{SV}$ are observed at 400 and 800 minutes, and the drops are located at 200 and 580 minutes. Contrarily to profile of $\bar{h}_w^{SV}$, there are no significant peaks for $\dot{Q}_w^{SV}$ from the beginning of the self-pressurisation up to 200 minutes.

6.1.3. Presentation of the results: heat transfer at interface

Figure 105 shows the time-evolution in time of liquid-to-interface heat flow ($\dot{Q}_I^L$), of dry side wall-to-interface heat flow ($\dot{Q}_w^{LV}$) and of the vapour-to-interface heat flow ($\dot{Q}_I^V$).

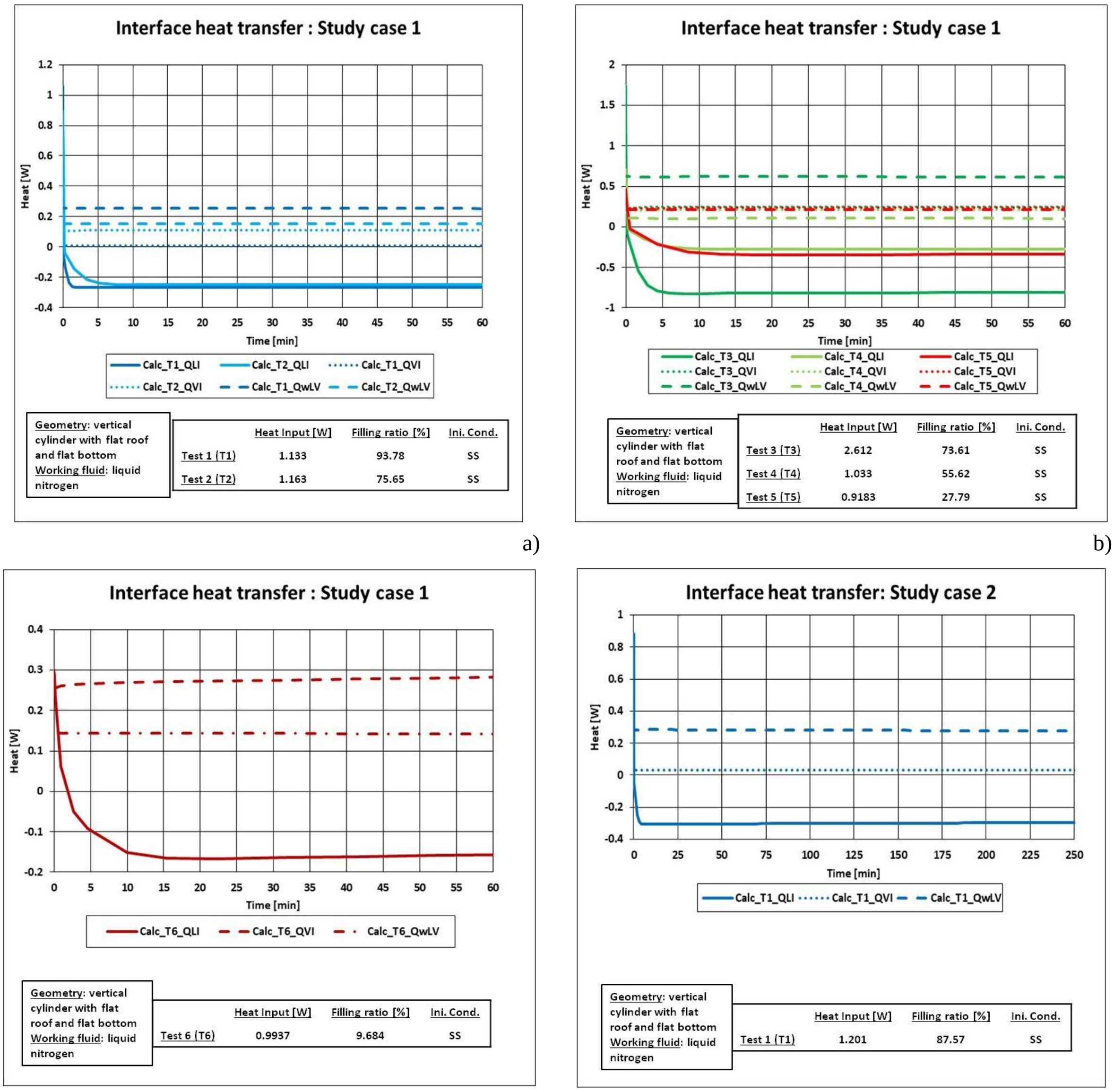

	Heat Input [W]	Filling ratio [%]	Ini. Cond.
Test 1 (T1)	1.133	93.78	SS
Test 2 (T2)	1.163	75.65	SS

a)

	Heat Input [W]	Filling ratio [%]	Ini. Cond.
Test 3 (T3)	2.612	73.61	SS
Test 4 (T4)	1.033	55.62	SS
Test 5 (T5)	0.9183	27.79	SS

b)

	Heat Input [W]	Filling ratio [%]	Ini. Cond.
Test 6 (T6)	0.9937	9.684	SS

c)

	Heat Input [W]	Filling ratio [%]	Ini. Cond.
Test 1 (T1)	1.201	87.57	SS

d)

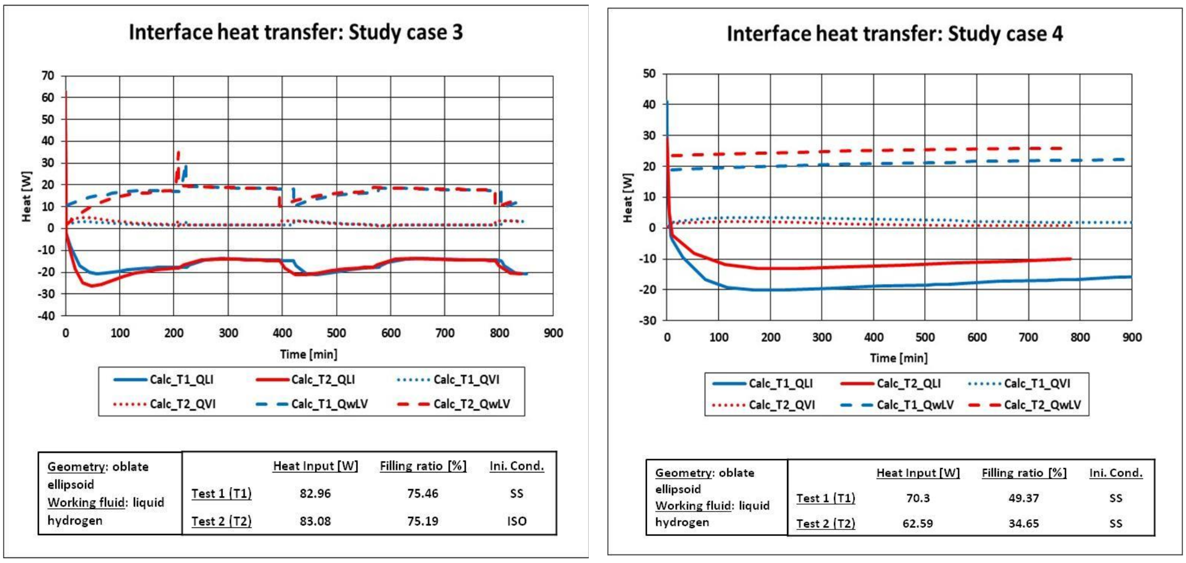

e) f)

Figure 105. Heat transfer at the interface for the Study cases at low heat fluxes: a) Study case 1 (Test 1 and Test 2), b) Study case 1 (Test 3, 4 and 5), c) Study case 1 (Test 6), d) Study case 2, e) Study case 3 and f) Study case 4.

For Study case 1, $\dot{Q}_I^L$ decreases at the beginning of the self-pressurisation and it reaches negative values. So, the heat flows from the interface to the liquid, instead of flowing from the liquid to the interface as occurs during the steady state. The shape of this decrement of Test 1 (high filling ratio) is sharper than the one of Test 6 (low filling ratio). After this initial decrement, $\dot{Q}_I^L$ remains constant. Hence, the $\dot{Q}_I^L$ profile is like a "L" shape. $\dot{Q}_I^L$ decreases with the increment of the filling ratio and with the increment of the heat flow. $\dot{Q}_w^{LV}$ and $\dot{Q}_I^V$ are constant during the self-pressurisation. $\dot{Q}_w^{LV}$ is higher than $\dot{Q}_I^V$ for Test 1, 2 (high-medium filling ratio) and 3 (high heat input). $\dot{Q}_w^{LV}$ is lower than $\dot{Q}_I^V$ for Test 4 (medium filling ratio), 5 (medium-low filing ratio) and 6. $\dot{Q}_w^{LV}$ decreases from Test 1 to Test 6, thus it decreases with the reduction of the filling ratio. $\dot{Q}_I^V$ increases from Test 1 to Test 6.

For Study case 2, $\dot{Q}_I^L$ decreases at the end of the steady state. and it profile forms a"L" shape profile as for Study case 1. After this decrement, $\dot{Q}_I^L$ is negative, indicating that the energy moves from the interface to the liquid, instead of flowing from the liquid to the interface as occurs during the steady state. $\dot{Q}_I^L$ is constant after the initial decrement. $\dot{Q}_w^{LV}$ and $\dot{Q}_I^V$ are constant during the self-pressurisation, but $\dot{Q}_w^{LV}$ is higher than $\dot{Q}_I^V$.

For Study case 3, $\dot{Q}_I^L$ decreases at the beginning of the self-pressurisation and the rate of this decrement of Test 2 (isothermal initial condition) is higher than the one of Test 1 (steady state initial condition). Instead of forming the "L" shape, this decrement creates a minimum. After this minimum, $\dot{Q}_I^L$ irregularly increases. Uplifts of $\dot{Q}_I^L$ are observed between 200 and 400 minutes and between 580 and 800 minutes. Steps-downs are located between 400 and 580 minutes, and from 800 minutes to the end of the self-pressurisation. $\dot{Q}_w^{LV}$ initially increases, forming an initial transient. At 200 minutes, a peak is observed. Then, $\dot{Q}_w^{LV}$ remains constant up to the "hole", which occurs at 400 minutes. After the hole, $\dot{Q}_w^{LV}$ increases and it remains constant. A second hole is observed at 800 minutes. $\dot{Q}_w^{LV}$ has a small initial transient andremains almost constant, except for the small irregularities. These irregularities occur at the same time of the hole and peak of $\dot{Q}_w^{LV}$. There are two small peaks at 400 minutes and at 800 minutes, and there is a small peak at 200 minutes. $\dot{Q}_w^{LV}$ is higher than $\dot{Q}_I^V$.

For Study case 4, $\dot{Q}_I^L$ drops at the end of the steady state. The profile of $\dot{Q}_I^L$ is quite similar to an "L" shape, as for the Study cases 1, 2 and 3. Contrary to Study cases 1 and 2, $\dot{Q}_I^L$ slightly increases during the self-pressurisation, after the initial decrement. $\dot{Q}_I^L$ of Test 2 (low filling ratio) is higher than the one of Test 1 (medium filling ratio). $\dot{Q}_W^{LV}$ and $\dot{Q}_I^V$ are constant during the self-pressurisation, but $\dot{Q}_W^{LV}$ is higher than the $\dot{Q}_I^V$. $\dot{Q}_W^{LV}$ of Test 2 is higher than in Test 1. $\dot{Q}_I^V$ of Test 1 is slightly higher than in Test 2.

To sum up, $\dot{Q}_I^L$ initially decreases and a "L" shape profile is formed. After the initial decrement, $\dot{Q}_I^L$ can slightly increase. During the self-pressurisation, the energy goes from the interface to the liquid. $\dot{Q}_I^L$ increases with the reduction of the initial filling ratio and it decreases with the increment of the heat input. Isothermal initial condition can create a minimum of $\dot{Q}_I^L$. The behaviour of $\dot{Q}_I^L$ in the H 2.0 model is quite similar to the one of H model (the initial decrement of the H odel was shaper). $\dot{Q}_W^{LV}$ and $\dot{Q}_I^V$ are constant during the self-pressurisation, as for the H model, with $\dot{Q}_W^{LV}$ usually higher than $\dot{Q}_I^V$.

6.1.4. Presentation of the results: net mass flow

Figure 106 presents the evolution of the calculated net mass flow ($\dot{m}_N$) during the self-pressurization phase for the Study case at low heat fluxes (Study cases 1, 2, 3 and 4).

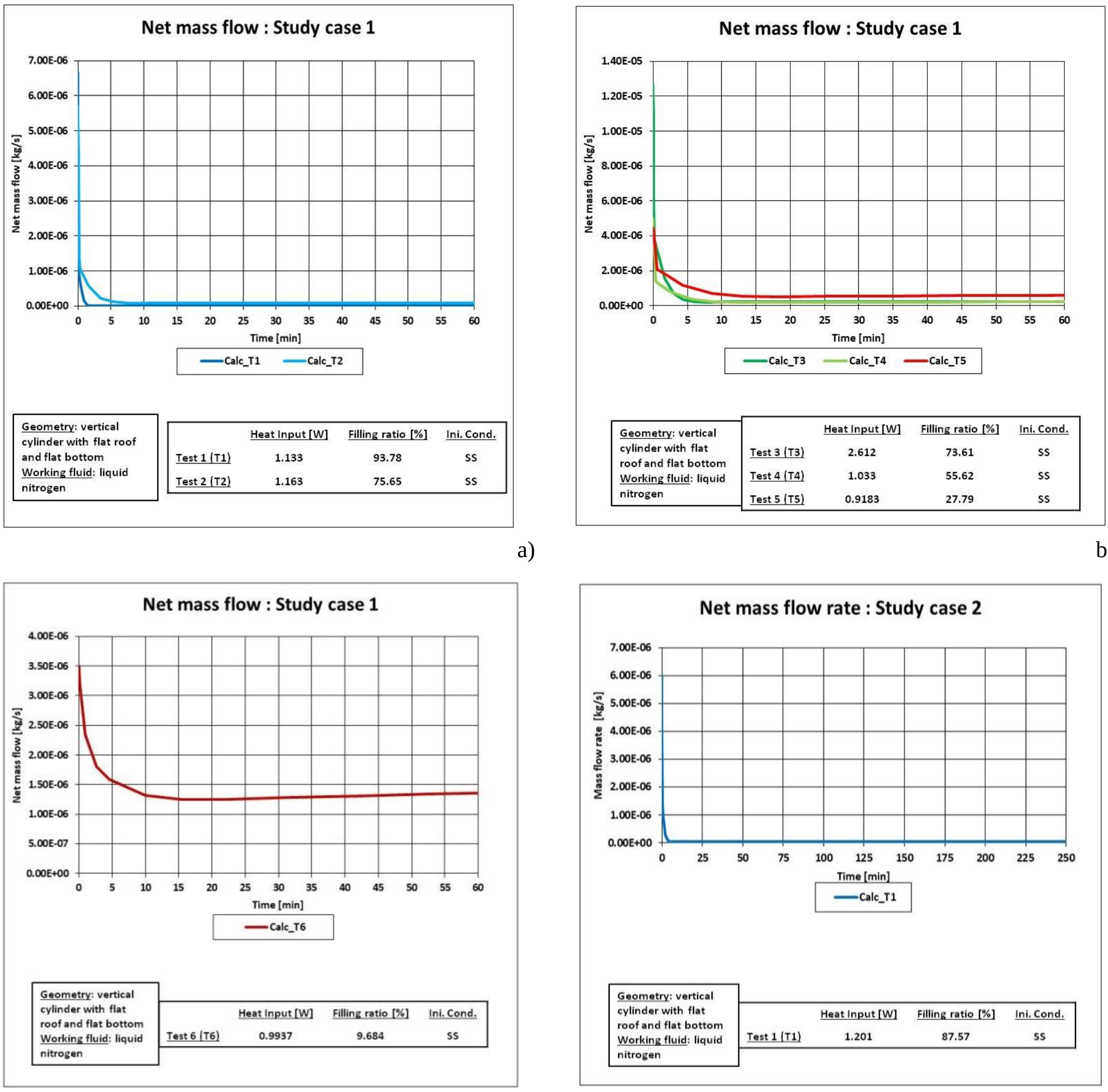

Geometry: vertical cylinder with flat roof and flat bottom
Working fluid: liquid nitrogen

	Heat Input [W]	Filling ratio [%]	Ini. Cond.
Test 1 (T1)	1.133	93.78	SS
Test 2 (T2)	1.163	75.65	SS

a)

Geometry: vertical cylinder with flat roof and flat bottom
Working fluid: liquid nitrogen

	Heat Input [W]	Filling ratio [%]	Ini. Cond.
Test 3 (T3)	2.612	73.61	SS
Test 4 (T4)	1.033	55.62	SS
Test 5 (T5)	0.9183	27.79	SS

b)

Geometry: vertical cylinder with flat roof and flat bottom
Working fluid: liquid nitrogen

	Heat Input [W]	Filling ratio [%]	Ini. Cond.
Test 6 (T6)	0.9937	9.684	SS

c)

Geometry: vertical cylinder with flat roof and flat bottom
Working fluid: liquid nitrogen

	Heat Input [W]	Filling ratio [%]	Ini. Cond.
Test 1 (T1)	1.201	87.57	SS

d)

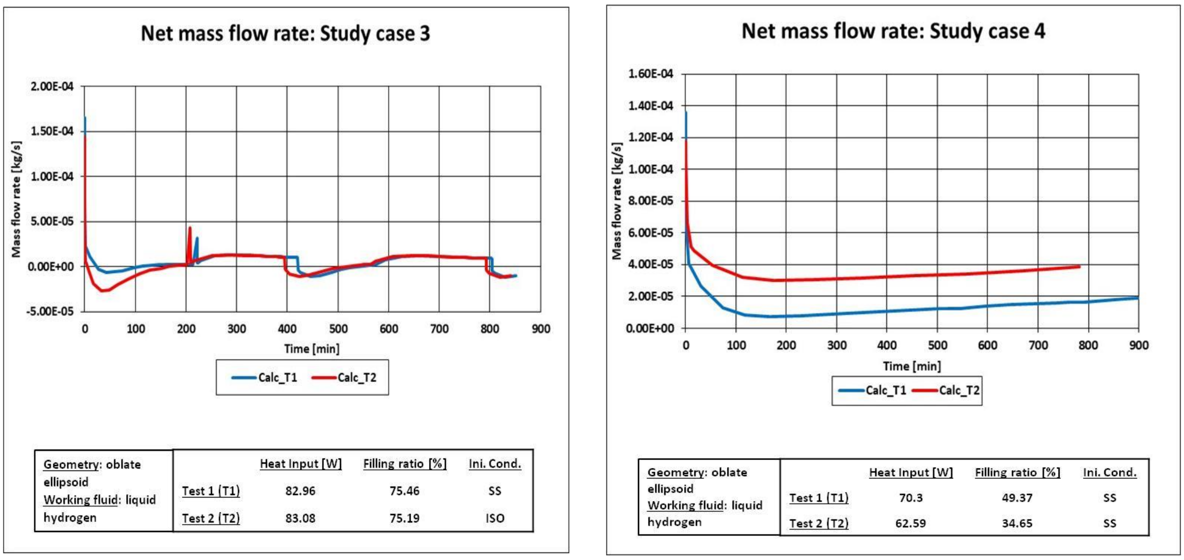

Geometry: oblate ellipsoid Working fluid: liquid hydrogen		Heat Input [W]	Filling ratio [%]	Ini. Cond.
	Test 1 (T1)	82.96	75.46	SS
	Test 2 (T2)	83.08	75.19	ISO

Geometry: oblate ellipsoid Working fluid: liquid hydrogen		Heat Input [W]	Filling ratio [%]	Ini. Cond.
	Test 1 (T1)	70.3	49.37	SS
	Test 2 (T2)	62.59	34.65	SS

e) f)

Figure 106. Net mass flow for the Study cases at low heat fluxes: a) Study case 1 (Test 1 and Test 2), b) Study case 1 (Test 3, 4 and 5), c) Study case 1 (Test 6), d) Study case 2, e) Study case 3 and f) Study case 4.

For Study case 1, $\dot{m}_N$ initially decreases, forming a vertical drop. After this drop, $\dot{m}_N$ remains constant. Hence, the shape of the time-evolution of the net mass flow is similar to an "L" shape, as for the liquid-to-interface heat flow ($\dot{Q}_I^L$). $\dot{m}_N$ increases from Test 1 (high filling ratio) to Test 6 (low filling ratio), thus it increases with the reduction of the filling ratio. The profile of the "L" shape is smoother at Test 6 than in Test 1. $\dot{m}_N$ is never negative, contrarily to the values of the H model.

For Study case 2, the time-evolution of $\dot{m}_N$ is similar to the one of Test 1 of Study case 1. Hence, the shape of the profile of this mass flow is similar to an "L" shape, with a strong decrement at the end of the steady state. After this decrement, the net mass flow remains constant.

For Study case 3, $\dot{m}_N$ initially decreases, creating a negative minimum. The minimum of Test 2 (isothermal initial condition) is lower than the one of Test 1 (steady state initial condition). After this minimum, $\dot{m}_N$ increases. There is a peak t 200 minutes and there are two small drops, respectively placed at 400 and 800 minutes, as for $\dot{Q}_I^L$.

For Study case 4, $\dot{m}_N$ decreases at the end of the steady state, thus at the beginning of the self-pressurisation. After the initial decrement, the mass flow slightly increases in time. So, the profile of the net mass flow is not a perfect "L" shape as for Study cases 1 and 2. The mass flow of Test 2 (low filling ratio) is higher than in Test 1 (high filling ratio). For both Tests, the values of the net mass flow are never negative.

To sum up, the time-evolution of $\dot{m}_N$ is quite similar to the one of $\dot{Q}_I^L$, with an initial decrement and a "plateau". A minimum can appear in the initial decrement. $\dot{m}_N$ increases with the reduction of the initial filling ratio and with the increment of the heat input. Under isothermal initial conditions, the initial drop is faster than in steady state initial conditions. In comparison with the hogeneous (H) model, the initial decrement of the net mass flow is smoother. The values of $\dot{m}_N$ of the homogeneous model 2.0 (H 2.0 model) are sometime higher than the ones of H model. the difference in the net mass flow between these two models is usually small.

6.1.5. Presentation of the results: pressure

Figure 107 shows the time-evolution of the computed and experimental values of the ullage pressure, during the self-pressurisation.

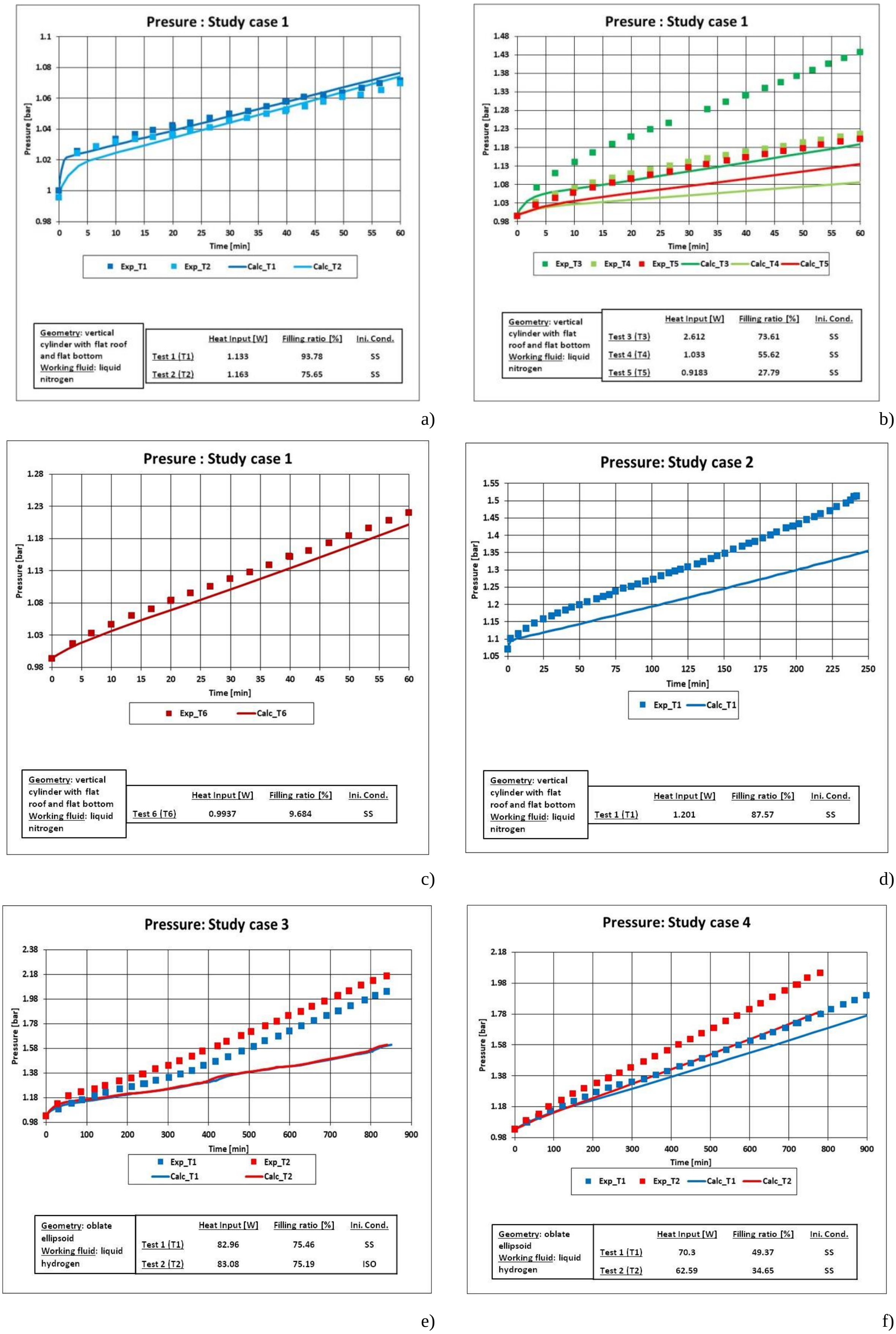

Geometry: vertical cylinder with flat roof and flat bottom
Working fluid: liquid nitrogen

	Heat Input [W]	Filling ratio [%]	Ini. Cond.
Test 1 (T1)	1.133	93.78	SS
Test 2 (T2)	1.163	75.65	SS

a)

Geometry: vertical cylinder with flat roof and flat bottom
Working fluid: liquid nitrogen

	Heat Input [W]	Filling ratio [%]	Ini. Cond.
Test 3 (T3)	2.612	73.61	SS
Test 4 (T4)	1.033	55.62	SS
Test 5 (T5)	0.9183	27.79	SS

b)

Geometry: vertical cylinder with flat roof and flat bottom
Working fluid: liquid nitrogen

	Heat Input [W]	Filling ratio [%]	Ini. Cond.
Test 6 (T6)	0.9937	9.684	SS

c)

Geometry: vertical cylinder with flat roof and flat bottom
Working fluid: liquid nitrogen

	Heat Input [W]	Filling ratio [%]	Ini. Cond.
Test 1 (T1)	1.201	87.57	SS

d)

Geometry: oblate ellipsoid
Working fluid: liquid hydrogen

	Heat Input [W]	Filling ratio [%]	Ini. Cond.
Test 1 (T1)	82.96	75.46	SS
Test 2 (T2)	83.08	75.19	ISO

e)

Geometry: oblate ellipsoid
Working fluid: liquid hydrogen

	Heat Input [W]	Filling ratio [%]	Ini. Cond.
Test 1 (T1)	70.3	49.37	SS
Test 2 (T2)	62.59	34.65	SS

f)

Figure 107. Comparison between the computed and experimental values of the pressure for the Study cases at low heat fluxes: a) Study case 1 (Test 1 and Test 2), b) Study case 1 (Test 3, 4 and 5), c) Study case 1 (Test 6), d) Study case 2, e) Study case 3 and f) Study case 4.

For Study case 1, the computed pressure increases during the self-pressurisation, with an initial transient and a constant rate period, as it is experimentally observed. For Test 1 (high filling ratio) and Test 2 (high-medium filling ratio), the computed values are close to the experimental data. For Tests 3 (high heat input), 4 (medium filling ratio) and 5 (medium-low filling ratio), the pressures of the homogeneous model 2.0 (H 2.0 model) are lower than the experimental ones. The computed pressures at Test 3 are higher than the ones of Test 4, which is contrary to what can be inferred from the experimental data. The pressures of H 2.0 model of Test 6 (low filling ratio) are close to the experimental values.

For Study case 2, the computed pressure increases in time. In the first 5 minutes of the self-pressurisation, the values of the pressure of the H 2.0 model are close to the experimental ones, indicating that the computed initial transient is similar to the experimental one. After this initial transient, the computed rate of self-pressurisation is lower than the experimental one. The computed time-evolution is qualitatively correct.

For Study Case 3, the computed pressure has a small transient within the first 50 minutes of the self-pressurisation (here the pressure difference between the experimental values and the H 2.0 model is small). After this transient, the computed rate of self-pressurisation is lower than the experimental one. The computed pressures are lower than the experimental ones. The computed rate of self-pressurisation is almost constant, except for small variations at 400 and 800 minutes. Contrary to the experimental data, the pressure difference between Test 1 (steady state initial condition) and Test 2 (isothermal initial condition) is negligible.

For Study case 4, the computed pressure regularly increases in time, without forming any initial transient. In the first 100 minutes, the computed pressure is close to the experimental data. Then, thepressures of the H 2.0 model are lower than the experimental data. The computed pressures of Test 2 (low filling ratio) are higher than the ones of Test 1 (medium filling ratio), coherently with the experimental data.

To sum up, the computed pressures are sometime close to the experimental values. The calculate pressures are, however, often lower than the measured ones, even if the calculated initial transient is often similar to the experimental one. The H 2.0 model computes the same rate of self-pressurisation for isothermal and steady state initial conditions. The pressures of the H 2.0 model are often higher than the one of homogeneous model (H model).

6.1.6. Presentation of the results: ullage temperature

Figure 108 shows the evolution of the computed and the experimental values of the ullage temperature during the natural pressure build-up.

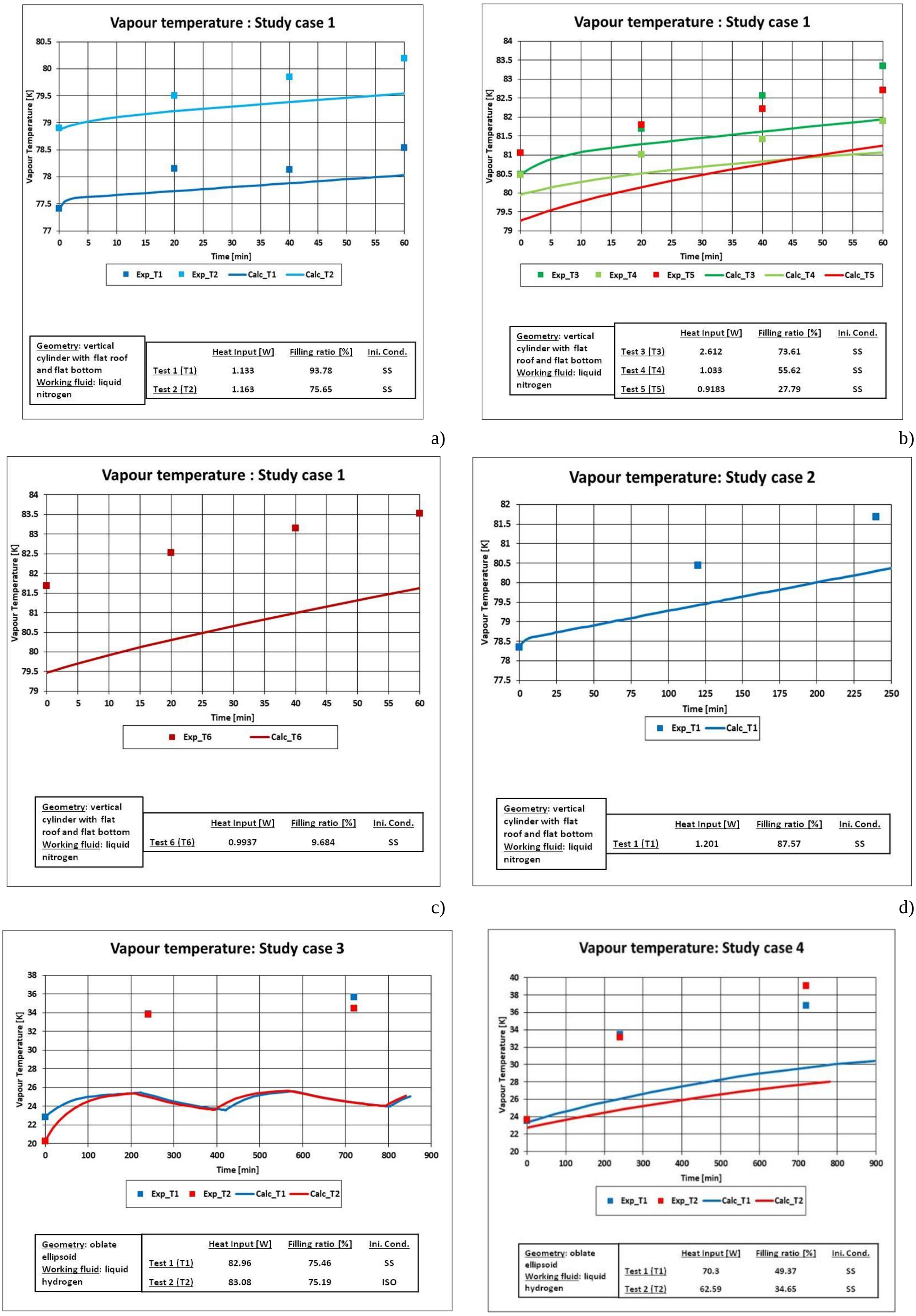

a)

Geometry: vertical cylinder with flat roof and flat bottom
Working fluid: liquid nitrogen

	Heat Input [W]	Filling ratio [%]	Ini. Cond.
Test 1 (T1)	1.133	93.78	SS
Test 2 (T2)	1.163	75.65	SS

b)

Geometry: vertical cylinder with flat roof and flat bottom
Working fluid: liquid nitrogen

	Heat Input [W]	Filling ratio [%]	Ini. Cond.
Test 3 (T3)	2.612	73.61	SS
Test 4 (T4)	1.033	55.62	SS
Test 5 (T5)	0.9183	27.79	SS

c)

Geometry: vertical cylinder with flat roof and flat bottom
Working fluid: liquid nitrogen

	Heat Input [W]	Filling ratio [%]	Ini. Cond.
Test 6 (T6)	0.9937	9.684	SS

d)

Geometry: vertical cylinder with flat roof and flat bottom
Working fluid: liquid nitrogen

	Heat Input [W]	Filling ratio [%]	Ini. Cond.
Test 1 (T1)	1.201	87.57	SS

e)

Geometry: oblate ellipsoid
Working fluid: liquid hydrogen

	Heat Input [W]	Filling ratio [%]	Ini. Cond.
Test 1 (T1)	82.96	75.46	SS
Test 2 (T2)	83.08	75.19	ISO

f)

Geometry: oblate ellipsoid
Working fluid: liquid hydrogen

	Heat Input [W]	Filling ratio [%]	Ini. Cond.
Test 1 (T1)	70.3	49.37	SS
Test 2 (T2)	62.59	34.65	SS

Figure 108. Comparison between the computed and experimental values of the ullage temperature for the Study cases at low heat fluxes: a) Study case 1 (Test 1 and Test 2), b) Study case 1 (Test 3, 4 and 5), c) Study case 1 (Test 6), d) Study case 2, e) Study case 3 and f) Study case 4.

For Study case 1, the computed ullage temperature increases in time. For Tests 1 (high filling ratio), 2 (high-medium filling ratio) and 3 (high heat input), the calculated rate of temperature increment is lower than the experimental one, even if the computed initial ullage temperature is equal to the experimental one. For Tests 4 (medium filling ratio), 5 (medium-low filling ratio) and 6 (low filling ratio), the computed rate of temperature increment is quite close to the measured one.

For Study case 2, the computed initial ullage temperature is equal to experimental one. The rate of temperature increment is lower than he experimental one.

For Study case 3, the computed initial ullage temperature is reasonable equal to the experimental one. At the beginning of the self-pressurisation, the computed temperature increases in time and the rate of this increment of Test 2 (isothermal initial condition) is faster than the one of Test 1 (steady state initial condition). The maximum value of temperature increment is reached around 200 minutes. Then, the temperature decreases until the simulation time of the self-pressurisation reaches the value of 400 minutes, creating a local minimum. After this minimum, the ullage temperature increases for simumation time up to 580 minutes. This temperature decreases, creating a local maximum at 580 minutes. Between this time-point and 800 minutes, the computed ullage temperature decreases, creating a local minimum at 800 minutes. Then, the computed temperature increases up to the end of the self-pressurisation. The time-evolution of the computed ullage temperature is qualitatively and quantitatively different from the experimental one. This time-evolution is quite similar to the time-evolution of bulk temperature gradient.

For Study case 4, the computed initial ullage temperatures are slightly lower than the experimental ones. The rate of the temperature increment is lower than the measured one, even if it is qualitatively correct. The values of the computed temperature of Test 1 (medium filling ratio) are higher than the one of Test 2 (low filling ratio), contrarily to the experimental data.

To sum up, the computed rate of temperature increment is lower than the experimental one. The calculated initial ullage temperature is often lower than the experimental value. Except for the initial temperature, the rate of temperature increment of the homogeneous model 2.0 (H 2.0 model) is similar to the one of the H model for Study cases 1 and 2. The same rate of H 2.0 model is higher than the one of homogeneous model (H model) for Study case 4. For Study case 3, the H 2.0 model computes a time-evolution of the ullage temperature that is completely different from the one of H model.

6.2. Study cases: medium heat fluxes

Table 97 reports the boundary and the initial conditions of temperature at the beginning of the self-pressurisation, thus at the end of the steady state, for the study cases at medium heat fluxes (see Table 54). It should be reminded that the self-pressurization phase is preceded by a steady state phase, which is also simulated by the homogeneous model 2.0 (H 2.0 model).

Table 97. Initial conditions and boundary conditions for the self-pressurisation stage.

Sub-case	$h_{eff}\left[\frac{W}{m^2\cdot K}\right]$	$\alpha\,[-]$	$\beta\,[-]$	$\dot{Q}\,[W]$ Exp	$\dot{Q}\,[W]$ H 2.0	$T^V\,[K]$ Exp	$T^V\,[K]$ H 2.0
			Study case 1				
Test 1	0.400	1	$6.641\cdot10^{-16}$	29.91	29.93	100.6	99.86
Test 2	0.400	0.1747	0.1213	23.85	23.85	121.2	121.2
Test 3	0.400	0.06217	0.4617	17.88	17.88	116.6	116.6
			Study case 2				

Table 97. Initial conditions and boundary conditions for the self-pressurisation stage.

Test 1	0.2806	1	$4.118 \cdot 10^{-15}$	75.58	75.76	29.47	27.46
Test 2	0.2806	0.8781	$1.684 \cdot 10^{-15}$	73.09	73.47	40.03	37.62
Test 3	0.2806	$7.529 \cdot 10^{-2}$	$2.832 \cdot 10^{-16}$	56.39	59.01	53.34	45.09
Test 4	0.9401	1	$8.368 \cdot 10^{-15}$	242.2	242.7	39.03	38.17

For Study case 5, the initial values of vapour temperature and heat inputs are similar to the experimental data. The alpha coefficients decrease with reduction of the initial filling ratio; the values are higher and closer to 1 than the ones computed with the homogeneous model (H model). The beta coefficients increase from Test 1 (high filling ratio) to Test 3 (low filling ratio), as the filling ratio reduces; the values are lower than the ones of H model. In particular for Test 1 (high filling ratio), the beta coefficient is equal to zero, contrarily to the H model. The increment of beta coefficient with the reduction of the filling ratio is not present in the H model, where the minimum value of this coefficient is for Test 2 (medium filling ratio).

For Study case 6, the initial values of vapour temperature are lower than the experimental ones. The difference in the initial vapour temperature between the H 2.0 model and the experiment is, however, lower than the one of the previous model, in particular for Test 2 (medium filling ratio) and Test 3 (low filling ratio). The overall heat inputs of H 2.0 model are higher than experimental ones, due to the lower vapour temperature that is calculated by the model. The difference in heat input between the measureements and the values calculated with the H 2.0 model is lower than the one obtained for the H model. The alpha coefficients decrease with the reduction of the initial filling ratio and they are higher than the ones of the H model. As for the H model, the beta coeffiecients are close to zero.

To sum up, there is not a significant difference in the effective heat transfer coefficient between the H 2.0 and the H models. The difference in the ullage vapour temperature, thus in the overall heat input, between the H 2.0 model and the experimental values is lower than the one of H model. The alpha coefficients are higher than the ones of H model.

Section 6.2.1, 6.2.2, 6.2.3 and 6.2.4 present the results of (i) the fluid-dynamics at the dry side wall, (ii) the heat transfer at the dry side wall, (iii) the heat transfer at the interface and (iv) the net mass flow, respectively. Section 6.2.5 and 6.2.6 explain the comparison of the pressure and of the ullage temperature with the experimental data, respectively.

6.2.1. Presentation of the results: fluid-dynamics at the dry side wall

Figure 109 describes the fluid-dynamics at the dry side wall, by showing the time-evolutions of the bulk temperature gradient ($\frac{\partial T^V}{\partial x}$) and the boundary layer average mass flow at the dry side wall ($\dot{m}_{BL}^{SV}$). The values of $\frac{\partial T^V}{\partial x}$ and $\dot{m}_{BL}^{SV}$ are reported on the left and right vertical axis, respectively.

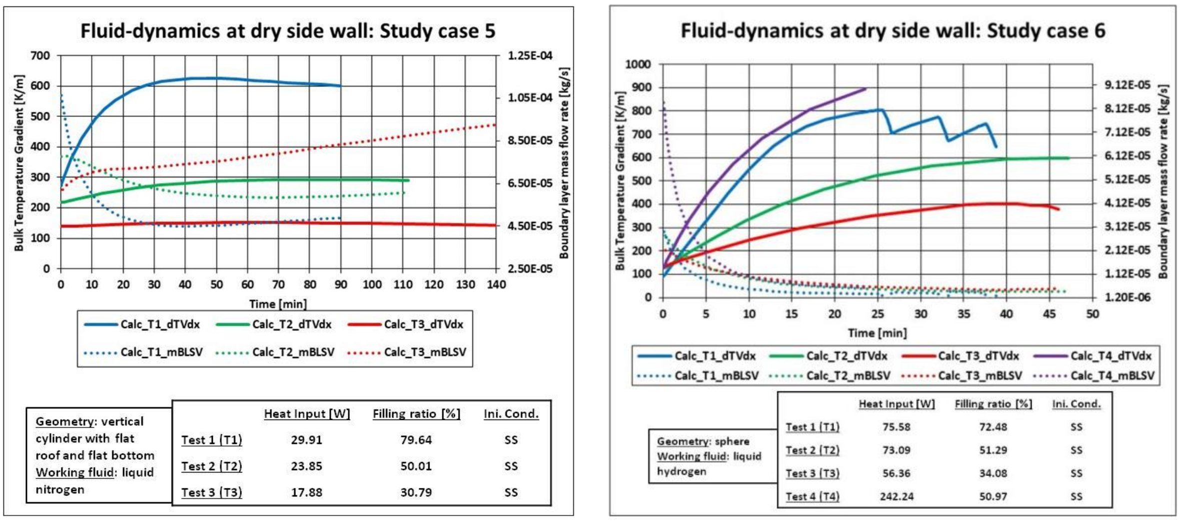

a) b)

Figure 109. Fluid-dynamics at the dry side wall for Study cases at medium heat fluxes: a) Study case 5; b) Study case 6.

For Study case 5, $\frac{\partial T^V}{\partial x}$ of Test 1 (high filling ratio) increases during the self-pressurisation up to 50 minutes, creating a maximum. After this time-point, $\frac{\partial T^V}{\partial x}$ slowly decreases. $\frac{\partial T^V}{\partial x}$ of Test 2 (medium filling ratio) has an initial increment, with a rate that is lower than the one of Test 1. After the initial increment, $\frac{\partial T^V}{\partial x}$ of Test 2 remains almost constant. For Test 3 (low filling ratio), $\frac{\partial T^V}{\partial x}$ is almost constant during the self-pressurisation. Hence, the initial increment of $\frac{\partial T^V}{\partial x}$ decreases with the reduction of the initial liquid level. The rate of increment of $\frac{\partial T^V}{\partial x}$ decreases from Test 1 to Test 3, thus it decreases with the reduction of the initial liquid level. $\dot{m}_{BL}^{SV}$ decreases in the first part of the self-pressurisation for Test 1 and Test 2. The rate of this decrement of Test 1 is higher than the one of Test 2. After this initial decrement, $\dot{m}_{BL}^{SV}$ remains almost constant. For Test 3, $\dot{m}_{BL}^{SV}$ continuously increases during the self-pressurisation. So, $\dot{m}_{BL}^{SV}$ increases with the reduction of the initial filling ratio during the self-pressurisation. The initial decrement increases with the increment of the initial liquid level.

For Study case 6, $\frac{\partial T^V}{\partial x}$ regularly increases during the self-pressurisation, except for Test 1 (high filling ratio). For Test 1, two peaks are observed at 32 and 37 minutes. Two holes are present and 26 and 33 minutes. The values of $\frac{\partial T^V}{\partial x}$ and the increment of this gradient increase from Test 1 to Test 3 (low filling ratio), thus they increases with the reduction of the initial filling ratio. $\frac{\partial T^V}{\partial x}$ of Test 4 (high heat input) is higher than the one of Test 1. $\dot{m}_{BL}^{SV}$ decreases during the self-pressurisation. The rate of this decrement of Test 1 is higher of the one of Test 3. The rate of decrement of Test 4 is the highest of the Study case. Hence, $\dot{m}_{BL}^{SV}$ decreases with the increment of the heat input and with the reduction of the initial filling ratio.

To sum up, the $\frac{\partial T^V}{\partial x}$ increases during the self-pressurisation, contrarily to one of the Study cases at low heat fluxes (see Section 6.1.2 of Chapter 5). The rate of this increment increases with the increment of the initial filling ratio and with the increment of the heat input. The values of $\frac{\partial T^V}{\partial x}$ are higher than the one of low heat fluxes. $\dot{m}_{BL}^{SV}$ decreases in time. The rate of this decrement increases with the increment of the initial filling ratio and with heat input, contrarily to that of the Study cases at low heat fluxes.

6.2.2. Presentation of the results: heat transfer at dry side wall

Figure 110 illustrates the heat transfer at the dry side wall during the self pressurisation, showing the evolution of dry side wall-to-vapour heat transfer coefficient ($\bar{h}_w^{SV}$) and of the dry side wall-to-vapour heat flow ($\dot{Q}_w^{SV}$). The values $\bar{h}_w^{SV}$ and $\dot{Q}_w^{SV}$ are reported on the left and right vertical axis, respectively.

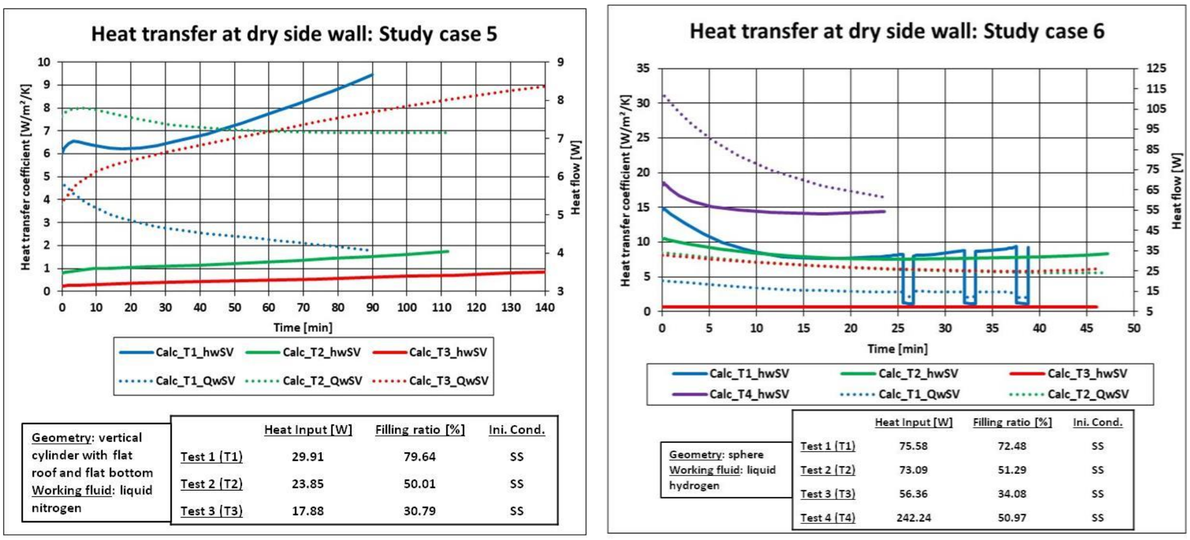

Geometry: vertical cylinder with flat roof and flat bottom
Working fluid: liquid nitrogen

	Heat Input [W]	Filling ratio [%]	Ini. Cond.
Test 1 (T1)	29.91	79.64	SS
Test 2 (T2)	23.85	50.01	SS
Test 3 (T3)	17.88	30.79	SS

Geometry: sphere
Working fluid: liquid hydrogen

	Heat Input [W]	Filling ratio [%]	Ini. Cond.
Test 1 (T1)	75.58	72.48	SS
Test 2 (T2)	73.09	51.29	SS
Test 3 (T3)	56.36	34.08	SS
Test 4 (T4)	242.24	50.97	SS

a) b)

Figure 110. Heat transfer at the dry side wall for Study cases at medium heat fluxes: a) Study case 5; b) Study case 6.

For Study case 5, $\bar{h}_w^{SV}$ constantly increases in time, except for Test 1 thigh filling ratio). For Test 1, there is a small peaks at 4 minutes and, then, $\bar{h}_w^{SV}$ decreases up to 20 minutes. After this time-point, it constantly increases. $\bar{h}_w^{SV}$ increases from Test 3 (low filling ratio) to Test 1, thus they increase with the increment of the initial filling ratio. $\dot{Q}_w^{SV}$ of Test 1 decreases during the self-pressurisation. $\dot{Q}_w^{SV}$ of Test 2 (medium filling ratio) has a small peaks at 5 minutes. Then, $\dot{Q}_w^{SV}$ decreases. For Test 3, $\dot{Q}_w^{SV}$ increases during the self-pressurisation.

For Study case 6, $\bar{h}_w^{SV}$ decreases in time, except for Test 3 (low filling ratio). At this test, $\bar{h}_w^{SV}$ is constant. For Test 1 (high filling ratio), $\bar{h}_w^{SV}$ produces some holes at 26, 33 and 37 minutes. $\bar{h}_w^{SV}$ increases from Test 3 to Test 1, thus it increases with the increment of the initial filling ratio. $\bar{h}_w^{SV}$ of Test 4 (high heat input) is the highest of the one of Study case 6. $\dot{Q}_w^{SV}$ decreases in time. The rate of this decrement of Test 4 is higher than the ones of the other tests. $\dot{Q}_w^{SV}$ of Test 1 is lower than the one of Test 2 (medium heat flow) and Test 3. The difference in $\dot{Q}_w^{SV}$ between Test 2 and Test 3 is almost negligible.

To sum up, the time-evolution of $\bar{h}_w^{SV}$ and $\dot{Q}_w^{SV}$ of Study case 5 are different from the ones of Study case 6. Common features are not observed between these study cases. The time-evolutions of these variables are different from the ones at low heat fluxes.

6.2.3. Presentation of the results: heat transfer at interface

Figure 111 shows the time-evolution in time of liquid-to-interface heat flow ($\dot{Q}_I^L$), of dry side wall-to-interface heat flow ($\dot{Q}_w^{LV}$) and of the vapour-to-interface heat flow ($\dot{Q}_I^V$).

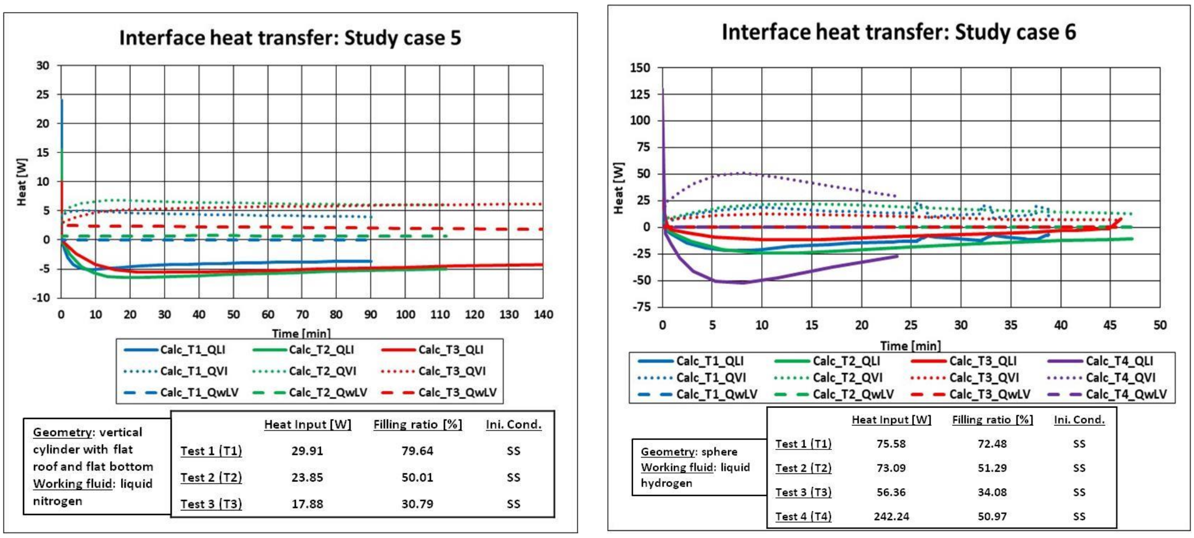

Geometry: vertical cylinder with flat roof and flat bottom
Working fluid: liquid nitrogen

	Heat Input [W]	Filling ratio [%]	Ini. Cond.
Test 1 (T1)	29.91	79.64	SS
Test 2 (T2)	23.85	50.01	SS
Test 3 (T3)	17.88	30.79	SS

Geometry: sphere
Working fluid: liquid hydrogen

	Heat Input [W]	Filling ratio [%]	Ini. Cond.
Test 1 (T1)	75.58	72.48	SS
Test 2 (T2)	73.09	51.29	SS
Test 3 (T3)	56.36	34.08	SS
Test 4 (T4)	242.24	50.97	SS

a) b)

Figure 111. Heat transfer at the interface for the Study cases at medium heat fluxes: a) Study case 5; b) Study case 6.

For Study case 5, $\dot{Q}_I^L$ initially decreases towards negative values. The rate of this reduction increases from Test 1 (high filling ratio) to Test 3 (low filling ratio), thus it increases with the initial liquid level. After the initial transient, $\dot{Q}_I^L$ remains almost constant, except for Test 1. For this test, $\dot{Q}_I^L$ slightly increases during the self-pressurisation. Hence, the shape of the time-evolution of $\dot{Q}_I^L$ is quite similar to an "L" shape, for Tests 1, 2 and 3. $\dot{Q}_I^V$ has a small initial increment. After this initial transient, $\dot{Q}_I^V$ remains almost constant. $\dot{Q}_I^V$ of Test 2 (medium filling ratio) is higher than the one of Test 1 and quite similar to the one of Test 3. $\dot{Q}_W^{LV}$ is constant during the self-pressurisation. $\dot{Q}_W^{LV}$ increases from Test 1 to Test 3, thus it increases with the increment of the initial filling ratio.

For Study case 6, $\dot{Q}_I^L$ decreases and is negative. This decrement creates a "basin", which reduces from Test 1 (high filling ratio) to Test 3 (low filling ratio). So, this decrement reduces with the reduction of the initial liquid level. The deepest basin of the Study case 6 occurs for Test 4 (high heat input). For Test 1, small peaks can be observed at 26 and 33 minutes; $\dot{Q}_W^{LV}$ is equal to zero and $\dot{Q}_I^V$ initially increases during the self-pressurisation. The increment of Test 3 is lower than those of Tests 1 and 2 (medium filling ratio). The increment of $\dot{Q}_I^V$ of Test 4 is the highest of the Study case 6; this increment produces a maximum and, after it, $\dot{Q}_I^V$ decreases.

To sum up, the time-evolution of $\dot{Q}_I^L$ follows a quasi-"L" shape profile, contrarily to the ones of the H model. These quasi-"L" shape profiles are similar to the one observed for the low heat fluxes. The increment of the heat input reduces $\dot{Q}_I^L$. The effect of the initial filling ratio is less significant than the one of the H model. The dry side wall-to-interface heat flow is zero and $\dot{Q}_I^V$ has an initial increment which can result in a maximum. This was not observed at low heat fluxes.

6.2.4. Presentation of the results: net mass flow

The time-evolution of the net mass flow ($\dot{m}_N$) is described in Figure 112.

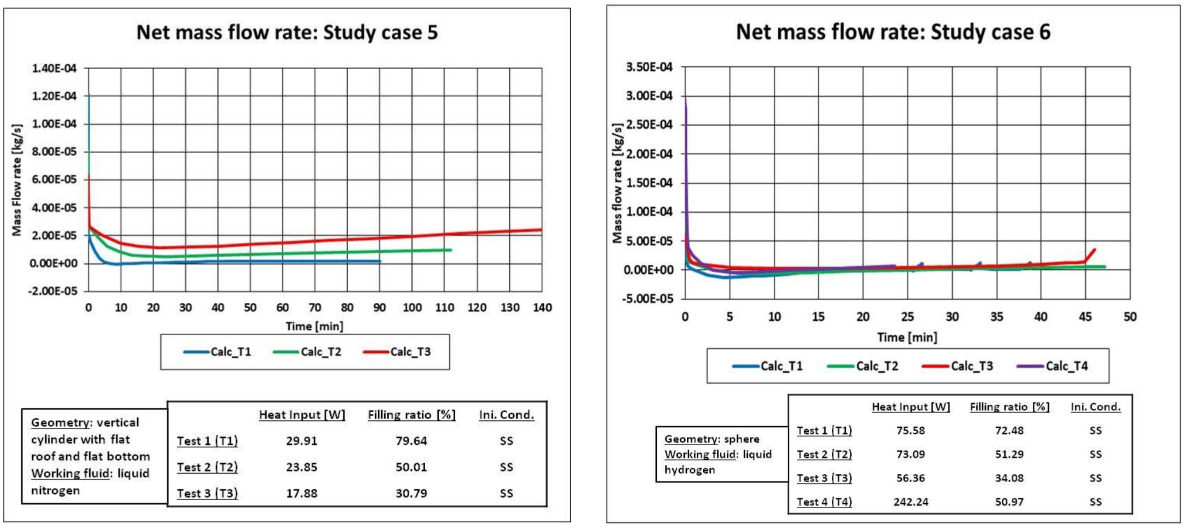

Geometry: vertical cylinder with flat roof and flat bottom
Working fluid: liquid nitrogen

	Heat Input [W]	Filling ratio [%]	Ini. Cond.
Test 1 (T1)	29.91	79.64	SS
Test 2 (T2)	23.85	50.01	SS
Test 3 (T3)	17.88	30.79	SS

Geometry: sphere
Working fluid: liquid hydrogen

	Heat Input [W]	Filling ratio [%]	Ini. Cond.
Test 1 (T1)	75.58	72.48	SS
Test 2 (T2)	73.09	51.29	SS
Test 3 (T3)	56.36	34.08	SS
Test 4 (T4)	242.24	50.97	SS

a) b)

Figure 112. Net mass flow for the Study cases at medium heat fluxes: a) Study case 5, b) Study case 6.

For Study case 5, $\dot{m}_N$ decreases at the end of the steady state. This decrement increases from Test 3 (low filling ratio) to Test 1 (high filling ratio), thus it increases with the increment of the initial liquid level. After this decrement, the net mass flow slightly increases. $\dot{m}_N$ increases from Test 1 to Test 3, thus it increases with the reduction of the initial filling ratio. The time-evolution of the net mass flow is similar to the one of the liquid-to-interface heat flow ($\dot{Q}_I^L$)

For Study case 6, $\dot{m}_N$ drops and it remains almost constant, after the initial transient. This mass flow increases from Test 3 (low filling ratio) to Test 1 (high filling ratio), thus it increases with the increment of the initial liquid level. The net mass flow of Test 4 is quite similar to the one of the other tests.

To sum up, the time-evolution of $\dot{m}_N$ is quite similar to the one of $\dot{Q}_I^L$. Hence, the shape of the time-evolution of this mass flow is of an "L" shape type, as for the ones of the Study cases at low heat fluxes. The reduction of the initial filling ratio increases the values of $\dot{m}_N$. The values of this mass flow are slightly negative and they are higher than the ones of the homogeneous model (H model).

6.2.5. Presentation of the results: pressure

Figure 113 shows the time-evolution of the computed and experimental values of the ullage pressure, during the self-pressurisation.

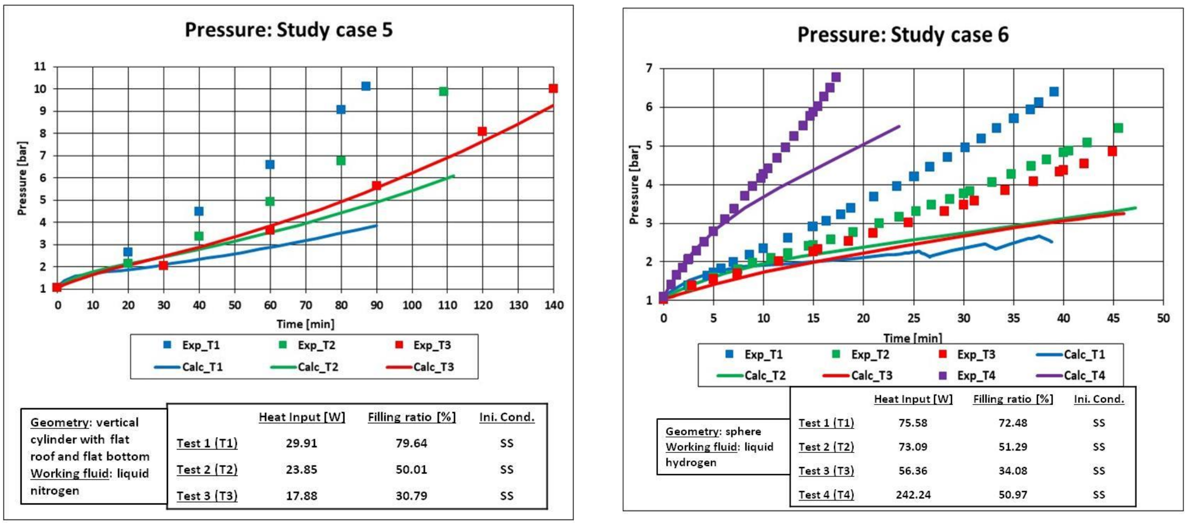

Geometry: vertical cylinder with flat roof and flat bottom
Working fluid: liquid nitrogen

	Heat Input [W]	Filling ratio [%]	Ini. Cond.
Test 1 (T1)	29.91	79.64	SS
Test 2 (T2)	23.85	50.01	SS
Test 3 (T3)	17.88	30.79	SS

a)

Geometry: sphere
Working fluid: liquid hydrogen

	Heat Input [W]	Filling ratio [%]	Ini. Cond.
Test 1 (T1)	75.58	72.48	SS
Test 2 (T2)	73.09	51.29	SS
Test 3 (T3)	56.36	34.08	SS
Test 4 (T4)	242.24	50.97	SS

b)

Figure 113. Computed and experimental pressure at medium heat fluxes: a) Study case 5, b) Study case 6.

For Study case 5, the computed pressure increases in time. The rate of this increment increases from Test 1 (high filling ratio) to Test 3 (low filling ratio), thus it increases with reducing the filling ratio. The rate of the self-pressurisation is, however, lower than the experimental one for Test 1 and Test 2 (medium filling ratio). For Test 3, the computed pressures are similar to the experimental ones. At given time-point, the computed pressure increases from Test 1 to Test 3, thus it increases with reducing the filling ratio, contrarily to the experimental behaviour.

For Study case 6, the computed pressure increases in time. In the first 5 minutes of the self-pressurisation, the computed values are similar to the experimental ones. After this period, the rate of the self-pressurisation is lower than the experimental one and the computed pressure is lower than the measured one. Computed pressures of Test 4 (high heat input) are the highest of the Study case 6, as experimentally observed. The calculated pressures of Test 1 (high filling ratio) are lower than the ones of Test 2 (medium filling ratio) and Test 3 (low filling ratio), contrarily to the experimental data. The difference in computed pressure between Test 2 and Test 3 is low, as it is observed for the measured pressures.

To sum up, the rate of self-pressurisation is under-estimated by the homogeneous model 2.0 (H 2.0 model). The calculated initial filling ratio-pressure is dissimilar to the experimental one, as it occurs with the homogeneous model (H model). The calculated pressures of the H 2.0 model are higher than the ones of H model.

6.2.6. Presentation of the results: ullage temperature

Figure 114 shows the evolution of the computed and the experimental values of the ullage temperature during the natural pressure build-up.

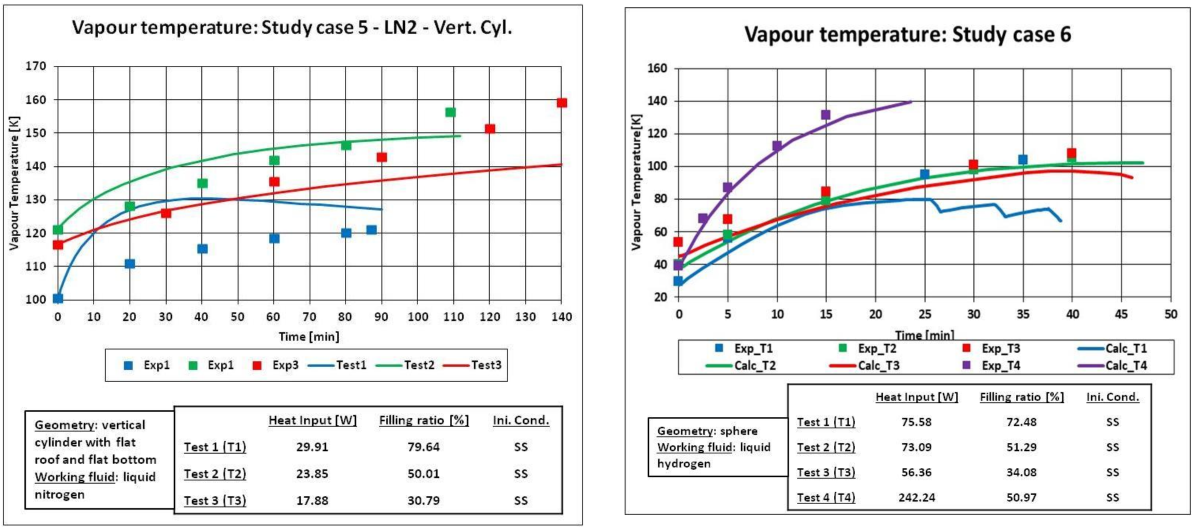

a) b)

Figure 114. Computed and experimental ullage temperature for the Study cases at medium heat fluxes: a) Study case 5, b) Study case 6.

For Study case 5, the computed initial ullage temperature is equal to the experimental one. The computed temperature of Test 2 (medium filling ratio) and of Test 3 (low filling ratio) monotonically increases as done by the experimental data. The computed temperature of Test 1 (high filling ratio) increases at the beginning of the self-pressurisation, producing a maximum at 40 minutes. Then, the temperature decreases. This evolution is not coherent with the experimental data. The computed ullage temperature increases from Test 1 to Test 2. The temperature decreases from Test 2 to Test 3, thus the highest values of the temperature are computed at medium filling ratio, as experimentally observed.

For Study case 6, the initial calculated ullage temperature is lower than the experimental one, except for Test 4 (high heat input). The computed temperature monotonically increases in time, except for Test 1 (high filling ratio). The values of this variables are close to the experimental ones. For Test 1, two drops are observed at 26 and 33 minutes, and two peaks are present at 32 and 37 minutes.

To sum up, the compute ullage temperature monotonically increases, except for Test 1 of Study case 1. So, the computed time-evolution of the ullage temperature is more coherent with the experimental data than the one of the homogeneous model (H model). The computed values are often close to the experimental ones.

6.3.Study cases: high heat fluxes

The Study cases at high heat fluxes are presented in Table 54. Table 98 describes the boundary and the initial conditions of temperature at the beginning of the self-pressurisation. It should be reminded that the self-pressurization phase is preceded by a steady state phase, which is also simulated by the homogeneous model 2.0 (H 2.0 model).

Table 98. Initial conditions and boundary conditions for the self-pressurisation stage.

Sub-case	$h_{eff}\left[\frac{W}{m^2\cdot K}\right]$	$\alpha\,[-]$	$\beta\,[-]$	$\dot{Q}\,[W]$		$T^V\,[K]$	
				Exp	**H 2.0**	**Exp**	**H 2.0**
			Study case 7				
Test 1	1.086	1	$3.053\cdot10^{-15}$	48.18	48.22	32.12	31.83
Test 2	1.086	2.489	$1.504\cdot10^{-4}$	46.46	47.47	50.17	40.58
Test 3	1.086	0.1308	0.3600	33.68	33.69	48.9	48.87

The initial values of the temperature are close to the experimental one, except for Test 2 (medium filling ratio) where the value of the difference in temperature between the modelling and the experimental results is around 10 K. The initial values of the heat input are quite similar to the experimental data, except for Test 2. For this test, the different in the heat input between the model and the calculated one is around 1 W. The values of alpha coefficient increase from Test 1 (high filling ratio) to Test 2, and they decrease from Test 2 to Test 3 (low filling ratio), as in the H model. The values of alpha coefficient approach 1 more than the ones of the H model. The values of beta coefficient increase from Test 1 to Test 3, namely they increase with the reduction of the initial filling ratio, contrary to those of the H model.

To sum up, the H 2.0 model predicts heat inputs, initial ullage temperature, alpha and beta coefficients better than the H model.

Section 6.3.1, 6.3.2, 6.3.3 and 6.3.4 present the results of (i) the fluid-dynamics at the dry side wall, (ii) the heat transfer at the dry side wall, (iii) the heat transfer at the interface and (iv) the net mass flow, respectively. Section 6.3.5 and 6.3.6 explain the comparison of the pressure and of the ullage temperature with the experimental data, respectively.

6.3.1. Presentation of the results: fluid-dynamics at the dry side wall

Figure 115 describes the fluid-dynamics at the dry side wall, by showing the time-evolutions of the bulk temperature gradient ($\frac{\partial T^V}{\partial x}$) and the boundary layer average mass flow at the dry side wall ($\dot{m}_{BL}^{SV}$); the values of $\frac{\partial T^V}{\partial x}$ and $\dot{m}_{BL}^{SV}$ are reported on the left and right vertical axis, respectively.

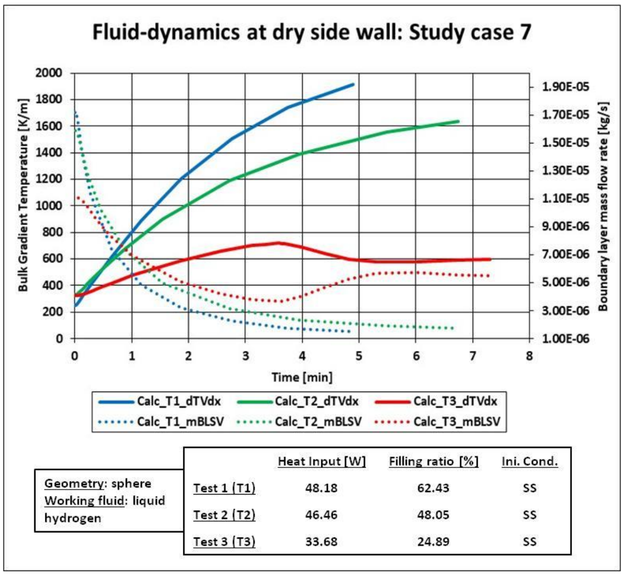

	Heat Input [W]	Filling ratio [%]	Ini. Cond.
Test 1 (T1)	48.18	62.43	SS
Test 2 (T2)	46.46	48.05	SS
Test 3 (T3)	33.68	24.89	SS

Figure 115. Fluid-dynamics at the dry side wall for Study case at high heat fluxes.

$\frac{\partial T^V}{\partial x}$ constantly increases during the self-pressurisation, except for Test 3 (low filling ratio). For this test, $\frac{\partial T^V}{\partial x}$ decreases after 3.5 minutes, creating a maximum. After the decrement, $\frac{\partial T^V}{\partial x}$ remains constant. At fixed time-point, $\frac{\partial T^V}{\partial x}$ increases from Test 3 to Test 1 (high filling ratio), thus it increases with the increment of the initial filling ratio. $\dot{m}_{BL}^{SV}$ in time. This decrement increases from Test 3 to Test 1, thus it increases with the increment of the initial filling ratio. For Test 3, $\dot{m}_{BL}^{SV}$ increases after 3.5 minutes, creating a minimum. After this increment, $\dot{m}_{BL}^{SV}$ remains constant.

To sum up, the time-evolutions of $\frac{\partial T^V}{\partial x}$ and $\dot{m}_{BL}^{SV}$ are quite similar to the one observed for the Study case at medium heat fluxes (see Section 6.2.1 of Chapter 5), except for Test 1.

6.3.2. Presentation of the results: heat transfer at dry side wall

Figure 116 illustrates the heat transfer at the dry side wall during the self pressurisation, showing the evolution of dry side wall-to-vapour heat transfer coefficient ($\bar{h}_w^{SV}$) and of the dry side wall-to-vapour heat flow ($\dot{Q}_w^{SV}$). The values of $\bar{h}_w^{SV}$ and $\dot{Q}_w^{SV}$ are reported on the left and right vertical axis, respectively.

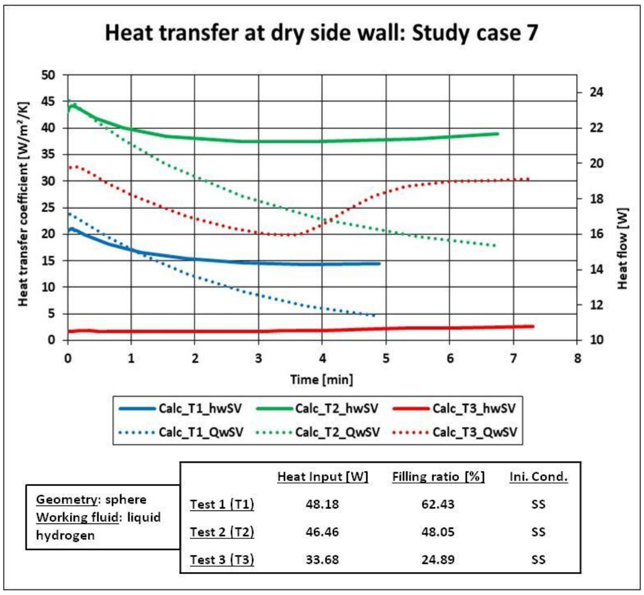

	Heat Input [W]	Filling ratio [%]	Ini. Cond.
Test 1 (T1)	48.18	62.43	SS
Test 2 (T2)	46.46	48.05	SS
Test 3 (T3)	33.68	24.89	SS

Figure 116. Heat transfer at the dry side wall for Study case at high heat fluxes.

After a very small peak, $\bar{h}_w^{SV}$ decreases in time for Test 1 (high filling ratio) and Test 2 (medium filling ratio). For Test 3 (low filling ratio), $\bar{h}_w^{SV}$ slightly increases. $\bar{h}_w^{SV}$ of Test 2 is the highest of the Study case. $\bar{h}_w^{SV}$ of Test 1 is higher than the one of Test 3. $\dot{Q}_w^{SV}$ monotonically decreases in time, except for Test 3. For this test, $\dot{Q}_w^{SV}$ increases after 3.5 minutes, reaching a plateau near 6 minutes. $\dot{Q}_w^{SV}$ of Test 2 is the highest of the Study case. $\dot{Q}_w^{SV}$ of Test 1 is higher than the one of Test 3.

To sum up, $\bar{h}_w^{SV}$ and $\dot{Q}_w^{SV}$ decrease, except for Test 3. These decrements are similar to the ones of the Study cases at medium heat fluxes (see Section 6.2.2 of Chapter 5), except for Test 3. The highest values of $\bar{h}_w^{SV}$ and $\dot{Q}_w^{SV}$ are computed at medium filling ratio, contrarily to the Study cases at medium heat fluxes (see Section 6.2.2 of Chapter 5).

6.3.3. Presentation of the results: heat transfer at interface

Figure 117 shows the time-evolution in time of liquid-to-interface heat flow ($\dot{Q}_I^L$), of dry side wall-to-interface heat flow ($\dot{Q}_w^{LV}$) and of the vapour-to-interface heat flow ($\dot{Q}_I^V$).

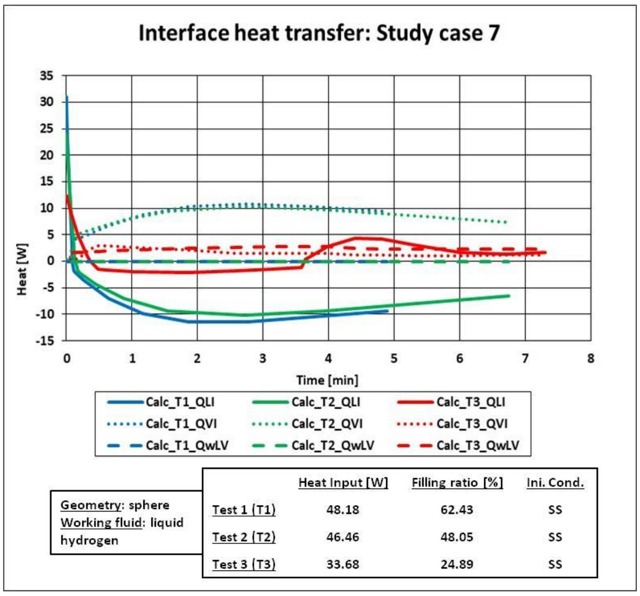

Geometry: sphere
Working fluid: liquid hydrogen

	Heat Input [W]	Filling ratio [%]	Ini. Cond.
Test 1 (T1)	48.18	62.43	SS
Test 2 (T2)	46.46	48.05	SS
Test 3 (T3)	33.68	24.89	SS

Figure 117. Heat transfer at the interface for the Study case at high heat fluxes.

$\dot{Q}_I^L$ initially decreases and is negative, creating a "basin". After this decrement, $\dot{Q}_I^L$ remains almost constant except for Test 3 (low filling ratio). The "basin" caused by this initial decrement is smaller at Test 3 than the ones of Tests 1 (high filling ratio) and 2 (medium filling ratio). $\dot{Q}_w^{LV}$ is equal to zero for Test 1 and 2. $\dot{Q}_w^{LV}$ of Test 3 is constant. $\dot{Q}_I^V$ of Test 1 and of Test 2 increases at the beginning of the self-pressurisation, creating a maximum. After this maximum, $\dot{Q}_I^V$ decreases for Test 1 and Test 2. For Test 3, there is a small peak of $\dot{Q}_I^V$ at the end of the steady state. Then, $\dot{Q}_I^V$ slightly decreases.

To sum up, the behaviour of the liquid-to-interface heat transfer is similar to the one observed for the Study cases at low and medium heat fluxes (see Section 6.1.3 and 6.2.3 of Chapter 5). This decrement is smoother than the one of the homogeneous model (H model). The dry side wall-to-interface heat flow is of secondary importance due to the values of the coefficient beta, as occurs for the H model. Contrarily to the H model, the lowest values of this heat flow are observed for Test 3.

6.3.4. Presentation of the results: net mass flow

Figure 118 presents the time-evolution of the calculated net mass flow ($\dot{m}_N$).

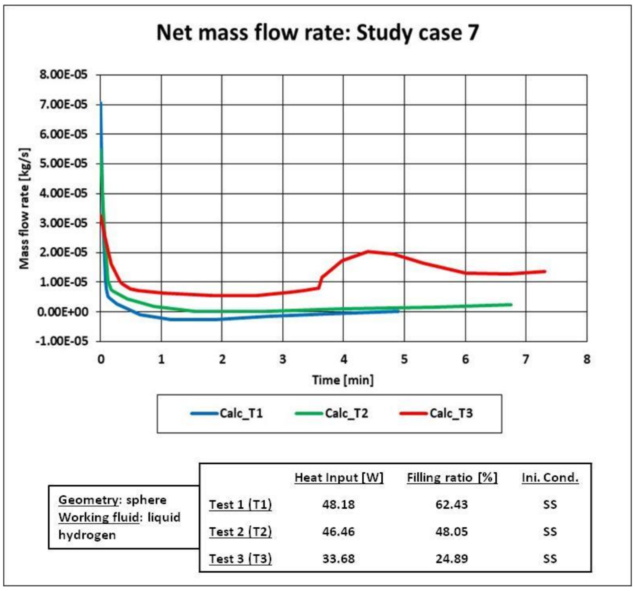

	Heat Input [W]	Filling ratio [%]	Ini. Cond.
Test 1 (T1)	48.18	62.43	SS
Test 2 (T2)	46.46	48.05	SS
Test 3 (T3)	33.68	24.89	SS

Figure 118. Net mass flow for the Study cases at high heat fluxes.

$\dot{m}_N$ drops at the end of the self-pressurisation. The rate of this decrement increases from Test 3 (low filling ratio) to Test 1 (high filling ratio), thus it increases with the increment of the initial filling ratio. After this initial decrement, $\dot{m}_N$ slightly increases, except for Test 3. In this test, $\dot{m}_N$ rapidly increases at 3.5 minutes, creating a maximum. After this maximum, this mass flow decreases and it reaches a plateau. The net mass flows of Test 1 and of Test 2 (medium filling ratio) are always positive. In Test 1, the net mass flow is negative between 0.5 and 4 minutes.

To sum up, as for the Study cases at low and medium heat fluxes (see Section 6.1.3 and 6.2.3 of Chapter 5), the time-evolution of $\dot{m}_N$ is very similar to the one of the liquid-to-interface heat flow. The initial decrement of $\dot{m}_N$ is smoother than the one of the homogeneous model (H model). The net mass flow is higher than the one of H model.

6.3.5. Presentation of the results: pressure

Figure 119 shows the time-evolution of the computed and experimental values of the ullage pressure, during the self-pressurisation.

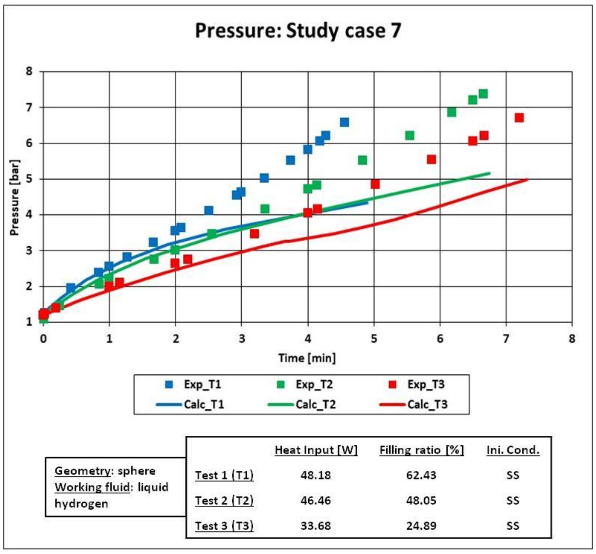

	Heat Input [W]	Filling ratio [%]	Ini. Cond.
Test 1 (T1)	48.18	62.43	SS
Test 2 (T2)	46.46	48.05	SS
Test 3 (T3)	33.68	24.89	SS

Figure 119. Computed and experimental pressure for the Study cases at high heat fluxes.

The calculated pressure increases in time as it occurs for the experimental data. The computed rate of pressurisation is quite similar to the measured one within 1.5 minutes, thenit becomes lower than the experimental one. As a result, the computed pressures are lower than experimental ones for all the tests of this study case. The computed pressure increases with the increment of the initial filling ratio, in agreement with experimental evidence. In Test 3 (low filling ratio), the computed rate of self-pressurisation rate at 3.5 minutes becomes slightly steeper than at the beginning of the pressurisation.

To sum up, the computed pressure increases with the increment of the initial filling ratio, contrarily to the homogeneous model (H model). The calculated pressure rates are lower than the experimental ones, except in the first 1.5 minutes. In the H model, the computed pressure of Test 3 are similar to the measured ones. This does not occur in the homogeneous model 2.0 (H 2.0 model).

6.3.6. Presentation of the results: ullage temperature

Figure 120 shows the evolution of the computed and the experimental values of the ullage temperature during the self-pressurisation.

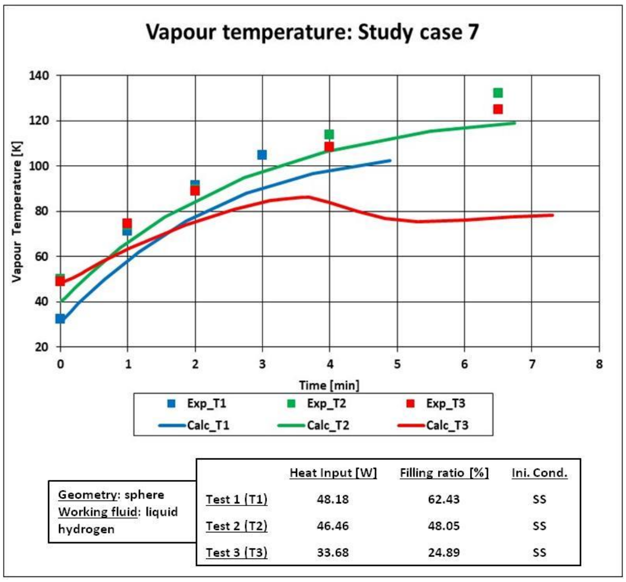

Geometry: sphere
Working fluid: liquid hydrogen

	Heat Input [W]	Filling ratio [%]	Ini. Cond.
Test 1 (T1)	48.18	62.43	SS
Test 2 (T2)	46.46	48.05	SS
Test 3 (T3)	33.68	24.89	SS

Figure 120. Computed and experimental ullage temperature for the Study cases at high heat fluxes.

The computed ullage temperature monotonically increases during the self-pressurisation and the such an increment is quite similar to the experimental one, except for Test 3 (low filling ratio). The computed rate of temperature increment is, on average, lower than the experimental one. For Test 3, the ullage temperature decreases after 3.5 minutes, contrarily to the experimental data, before reaching a basically constant value.

To sum up, the computed temperatures are closer to the experimental ones (except for Test 3) and the time-evolution of the computed temperature is qualitatively correct, which is a major progression with respect to the homogneous (H) model.

7. Discussions of the results

The time-evolutions of the pressure and of the ullage temperature depends on the fluid-dynamics and on the heat transfer at the dry side wall and on the neat-mass transfer at the interface. Here, the relations between these variables and these phenomena are discussed.

Section 7.1 and 7.2 discuss the results of the boundary and initial conditions, respectively. Section 7.3 and 7.4 analyse the fluid-dynamics and the heat transfer at the dry side wall. Section 7.5 and 7.6 discuss the interfacial heat transfer and the time-evolution of the net mass flow, respectively. Section 7.7 and 7.8 respectively analyse the comparison of the pressure and of the ullage temperature with the experimental data.

7.1. Initial conditions of the self-pressurisation

The initial conditions of the self-pressurisation are defined by the steady state values of ullage pressure, filling ratio, ullage and liquid temperatures, and heat input. The computed initial values of pressure and filling ratio are always equal to the experimental one. The difference in the initial liquid temperature between the homogeneous model 2.0 (H 2.0 model) and the experiments is negligible. Hence, only the initial values of ullage temperature and heat input are discussed.

Section 7.1.1 and 7.1.2 respectively describe the initial values of the self-pressurisation of the ullage temperature and of the heat input.

7.1.1. Initial ullage temperature of the self-pressurisation

For simulating the self-pressurisation, the initial values of liquid and vapour temperature, filling ratio and pressure are the steady state values, which are obtained by computing the time-evolution of these variables from the isothermal condition up to the stationary point. Only the self-pressurisation of Test 2 of Study case 3 directly starts from the isothermal initial condition.

At low heat fluxes (see Section 6.1 of Chapter 5), the computed initial values of the ullage temperature are equal to the experimental data, except for the Test 4, 5 and 6 of Study case 1 and for Study case 4. Hence, the difference in the initial ullage temperature between the homogeneous model 2.0 (H 2.0 model) and the measured data increases with the reduction of the initial filling ratio. At medium heat fluxes (see Section 6.2 of Chapter 5), the computed ullage temperature is equal to the experimental one for Test 2 and 3 of Study case 5. For the remaining tests, the difference in initial vapour temperature between the H 2.0 model and the experiments range between 1 and 8 K. This difference is present when the values of beta coefficient are equal to zero. This difference increases with the reduction of alpha coefficient, thus it increases with the reduction of the filling ratio. At high heat fluxes (see Section 6.3 of Chapter 5), the initial temperature of Test 3 is equal to the experimental one. The difference in initial temperature between the H 2.0 model and the experiments is lower at Test 1 than the one of Test 2, which is around 10 K. The values of beta of Test 1 and Test 2 are almost equal to zero.

As a consequence, the difference in initial temperature between H 2.0 model and experiments is present when the values of beta are equal to zero at medium-high heat fluxes. If the values of beta are equal to zero, this difference would increase with the reduction of the filling ratio. Hence, the initial values of ullage temperature are not equal to the experimental ones because the values of the beta coefficient, thus the boundary condition, are not correctly computed. This disparity increases with the reduction of the filling ratio because the hypothesis of vapour virtual stratification (assumption b) of Section 1.2 of Chapter 5) cannot describe the stratified vapour at high ullage volume.

7.1.2. Initial heat input of the self-pressurisation

The heat inputs are computed with the Storage Heat Transfer (SHT) model. In SHT model, the overall heat leakage is computed as the sum of the environment-to-internal wall heat flow at each surface of the storage container. These heat flows are computed as function of the difference in temperature between the fluid in contact with the wall and the external wall temperature.

As for the initial ullage temperature, the initial heat input of homogeneous model 2.0 (H 2.0 model) is usually higher than the experimental one when the values of beta are equal to zero. If the values of beta are equal to zero, this difference increases with the reduction of the filling ratio. This difference is, however, lower than the one of the initial temperature because it does not exceed the 3 W.

As a consequence, the heat inputs are often over-estimated because the initial ullage temperature of H 2.0 is lower than the experimental one. Hence, the difference in temperature between the external wall and the vapour increases, growing up the heat inputs at the dry walls (dry side wall and roof). The difference in the heat input is low because the environmental-to-tank heat transfer is mainly controlled by the liquid, which has higher heat transfer properties than the vapour.

7.2. Boundary conditions of the self-pressurisation

The boundary conditions are defined by three coefficients: the effective heat transfer coefficient, the alpha corrective coefficient and the beta corrective coefficient. The effective heat transfer coefficient does not significantly change between the homogeneous model and the homogeneous model 2.0. Hence, only the alpha and beta coefficient are discussed.

Section 7.2.1 discusses the results of the alpha coefficient. Section 7.2.2 examines the computed values of the beta coefficient.

7.2.1. Alpha coefficient

The alpha coefficient is introduced because the vapour is isothermal due to the hypothesis of vapour virtual stratification (assumption b) of Section 1.2 of Chapter 5), instead of being thermally stratified as experimentally observed. The values of the alpha coefficient are calculated with the α algorithm of the Boil-Off Rate (BOR) model. This algorithm is used for all the tests of medium and low filling ratio because the value of this coefficient is equal to 1, by hypothesis, for the test at high filling ratio. In α algorithm, this coefficient is computed using a formula that is deduced from the overall energy conservation law of the dry side wall (Equation 262). In this formula, the dry side wall temperature and the dry side wall-to-vapour heat transfer coefficient ($\bar{h}_w^{SV}$) are required at the dry side. This coefficient is computed with the boundary layer approach (see Section 4.6 of Chapter 4), with the bulk temperature gradient of the ullage. Hence, the value of alpha coefficient reduces with the increment of $\bar{h}_w^{SV}$ and of the difference in temperature between the external wall and the dry side wall. This difference increases with the reduction of the initial liquid level because the dry side wall surface area, thus the heat input in the ullage, increases. Due to the increment of this difference in temperature and of the heat transfer coefficient, the values of alpha have to reduce to respect the overall energy conservation law of the dry side wall. Hence, the values of alpha decrease with the reduction of the filling ratio at low, medium and high heat fluxes as it is observed in Section 6.1, 6.2 and 6.3 of Chapter 5

The introduction of this gradient reduces the values of $\bar{h}_w^{SV}$, because the values of the boundary layer variables U and δ_M decrease. Hence, the homogenous (H 2.0) model 2.0 computes values of alpha that are closer to 1 than the one of the homogeneous model (H model).

7.2.2. Beta coefficient

The thickness of the side wall is merely computed rather being set equal to experimental values, that are missing. Due to the hypothesis of vapour virtual stratification (assumption b) of Section 1.2 of Chapter 5), the bulk temperature gradient of the dry side wall is computed with the temperature of this wall, which is uniform. So, the beta coefficient is introduced. This is computed with the β algorithm of h_{eff} algorithm (see Section 1 of Appendix R) and with the β algorithm of α algorithm (see Appendix Z). Both β algorithms are based on the energy conservation laws of steady state ullage (Equation 278). This equation depends on (i) the vapour-to-interface heat flow ($\dot{Q}_I^V$), (ii) on the dry side wall-to-vapour heat flow ($\dot{Q}_w^{SV}$) and (iii) on the enthalpy flow of the convective mass flow of the ullage. As consequence, the value of beta coefficient decreases if the vapour-to-interface heat low increases.

At low heat fluxes (see Section 6.1 of Chapter 5), the values of beta are never equal to zero, even if they are lower or almost equal to 10^{-2}. At medium heat fluxes (see Section 6.2 of Chapter 5) the values of this coefficient are equal to zero for Test 1 of Study case 5 and for Study case 6. At high heat fluxes (see Section 6.3 of Chapter 5), only beta coefficient of Test 3 is not equal to zero. Hence, the dry side wall-to-interface heat flow is often equal to zero because vapour-to-interface heat low at steady state is higher than it should be. As a consequence, the beta coefficient is reduced as much as possible to respect the energy conservation laws of steady state ullage (Equation 278). This reduction is often unphysical.

7.3. Fluid-dynamics at the dry side wall

The fluid-dynamics at the side wall is characterized by the mass flow in the boundary layer of this side wall. This mass flow depends on the bulk ullage temperature gradient.

Section 7.3.1 discusses the time-evolution of the bulk ullage temperature gradient. Section 7.3.2 anlyses the evolution of the mass flow in the boundary layer during the self-pressurisation.

7.3.1. Bulk ullage temperature gradient

Due to the hypothesis of vapour virtual stratification (assumption b) of Section 1.2 of Chapter 5), the bulk temperature gradient of the ullage ($\frac{\partial T^V}{\partial x}$) is considered and it is calculated with Equation 226. This gradient depends on the difference in temperature between the ullage and the interface, and on the height of the the ullage, thus on the volume of the ullage. As consequence, $\frac{\partial T^V}{\partial x}$ increases with the increment of this difference. This gradient reduces when the ullage volumes increases.

At low heat fluxes (see Section 6.1.1 of Chapter 5), $\frac{\partial T^V}{\partial x}$ increases during the self-pressurisation, even if it can decreases in the initial transient. The rate of this increment increases with the reduction of the filling ratio. The highest values of this gradient are often observed at medium filling ratio. At medium and high heat fluxes (see Section 6.2.1 and 6.3.1 of Chapter 5), $\frac{\partial T^V}{\partial x}$ increases during the self-pressurisation. The rate of this increment increases with the increment of the initial filling ratio and with the increment of the heat input.

As a consequence, the initial transient of the bulk ullage temperature gradient is caused by the reduction of the difference in temperature between the ullage and the interface, at low heat fluxes. As the filling ratio is reduced, the ullage temperature and the ullage height increase. Hence, the highest values of this gradient are often at medium filling ratio, at low heat fluxes. The values of the bulk ullage temperature gradient increase from low to high heat fluxes because the ullage temperature increases with the heat fluxes. As the filling ratio is reduced, the ullage volume and the ullage height increase. This increment reduces $\frac{\partial T^V}{\partial x}$ as it is observed for medium and high filling ratio.

7.3.2. Mass flow in the boundary layer of the dry side wall

The boundary layer mass flow of the dry side wall ($\dot{m}_{BL}^{SV}$) is calculated with the Storage Boundary Layer (SBL) model by numerically integrating the energy and momentum conservation laws along the length of the dry side wall. In the homogeneous model 2.0 (H 2.0 model), the bulk temperature gradient ($\frac{\partial T^V}{\partial x}$) is considered in the energy conservation law. The numerical integration is done as for the homogeneous model (H model), except for the fluid-dynamic regime and the number of sub-space-points of the sub-layer. In the H 2.0 model, only the turbulent regime is considered at the dry side wall and the number of the sub-space-points is fixed (see Section 3.1 of Chapter 5). So, the $\dot{m}_{BL}^{SV}$ decreases with the increment of the bulk ullage temperature gradient. This mass flow increases with the increment of the heat flux and the increment of the length of the dry side wall.

At low, medium and high heat fluxes (see Section 6.1.1, 6.2.1 and 6.3.1 of Chapter 5), the values of the boundary layer average mass flow decrease during the self-pressurisation. At low heat fluxes, the values of this mass flow increase with the heat input and the reduction of the initial filling ratio. At medium and high heat fluxes, the rate of this decrement increases with the increment of the initial filling ratio and with heat input.

The $\dot{m}_{BL}^{SV}$ decreases during the self-pressurisation. The bulk ullage temperature gradient reduces the energy in the boundary layer, decreasing the values of the boundary layer variables U and δ_M. The initial transient at low heat fluxes (see Section 6.1.1 of Chapter 5) is caused by the transient of the bulk ullage temperature gradient. At low heat fluxes, the bulk ullage temperature gradient is low and it affects $\dot{m}_{BL}^{SV}$ less than the length of the dry side wall. So, this mass flow increases because the natural convection can be developed over a longer length than the one at high initial liquid level. At medium and high heat fluxes (see Section 6.2.1 and 6.3.1 of Chapter 5), the bulk ullage temperature gradient is high and it affects $\dot{m}_{BL}^{SV}$ more than the length of the dry side wall. Hence, this mass flow decreases with the increment of the initial filling ratio. For Study case 3, the time-evolution of $\dot{m}_{BL}^{SV}$ is not monotonically and this mass flow increases and decreases up to values that are close to zero. This situation occurs because the SBL model predicts the absence of natural convection since $\frac{\partial T^V}{\partial x}$ vanishes the mass flow in the boundary layer of the dry side wall.

7.4. Heat transfer at the dry side wall

The heat transfer at the dry side wall can be described with two variables: the heat transfer coefficient and the heat flow.

Section 7.4.1 discusses the time-evoltuion of the dry side wall heat transfer coefficient. Section 7.4.2 analyses the evolution of the dry side wall-to-vapour heat flow during the self-pressurisation.

7.4.1. Dry side wall-to-vapour heat transfer coefficient

The dry side wall-to-vapour heat transfer coefficient ($\bar{h}_w^{SV}$) is calculated with the Storage Heat Transfer (SHT) model, using the boundary layer approach. Hence, this variable directly depends on the boundary layer variables U and δ_M. These variables are affected by the bulk ullage boundary layer ($\frac{\partial T^V}{\partial x}$). As a consequence, this variable similarly behaves to the mass flow rate in the boundary layer. So, the heat transfer coefficient is reduced $\frac{\partial T^V}{\partial x}$. This coefficient increases with the increment of the heat fluxes and the increment of the length of the dry side wall. The heat fluxes at the dry side wall depend on the value of alpha coefficient.

At low and medium heat fluxes (see Section 6.1.2 and 6.2.2 of Chapter 5), the time-evolution of $\bar{h}_w^{SV}$ is different for each test and increases with the heat input. At low heat fluxes, this heat transfer coefficient decreases with the reduction of the initial filling ratio. At high heat fluxes (see Section 6.3.2 of Chapter 5), $\bar{h}_w^{SV}$ decreases during the self-pressurisation and the highest values of this coefficient are computed at medium filling ratios.

As a consequence, the decrement of $\bar{h}_w^{SV}$ is caused by the decrement of the boundary layer mass flow of the dry side wall, which is produced by the reduciotn of the of the boundary layer variables U and δ_M. If this gradient reduces, the heat transfer coefficient increases because the boundary layer variables U and δ_M increase. So, this coefficient decreases with the increment of the bulk ullage temperature gradient. If alpha decreases, the dry side wall-to-vapour heat flow reduces because the heat fluxes at the dry side wall decreases. As a consequence, instead of increasing with the reduction of the initial liquid level, the heat transfer coefficient increases with the filling ratio. The irregularities of Study case 3 and of Test 1 of Study case 7 are caused by the anomalies of the mass flow rate due to the fail of the numerical integration.

7.4.2. Dry side wall-to-vapour heat flow

The dry side wall-to-vapour heat flow ($\dot{Q}_w^{SV}$) is computed with the Storage Heat Transfer (SHT) model using an iterative procedure, as it is reported in Appendix U. This iterative procedure is based on the energy conservation law at the dry side wall (Equation 262). Hence, $\dot{Q}_w^{SV}$ increases with the increment of the dry side wall surface area and with the of the difference in temperature between the external wall surface (T^w) and the dry side wall (T_w^{SV}). This heat flow decreases with the increment of the dry side wall temperature because the dry side wall-to-interface increases with this increment.

At low heat fluxes (see Section 6.1.2 of Chapter 5), $\dot{Q}_w^{SV}$ increases with the reduction of filling ratio because the surface area dry side wall increases. At medium and high heat fluxes (see Section 6.2.2 and 6.3.2 of Chapter 5), the decrement of the initial filling ratio increases the temperature of the dry side wall and the the difference in temperature between the external wall and the dry side wall reduces. At the same time, the surface area of the dry walls increases and this increment partially cancels out the reduction of the difference in temperaturebetween the external wall and the dry side wall. Hence, $\dot{Q}_w^{SV}$ at medium filling ratio is sometime higher than the one at high filling ratio. The dry side wall heat flow decreases during the self-pressurisation due to the decrement of the heat transfer coefficient.

7.5. Heat transfer at the interface

The heat transfer at the interface is calculated with the Interface Heat Transfer (IHT) model under the hypothesis of local thermodynamic equilibrium (assumption d) of Section 1.2 of Chapter 5). This heat transfer is composed by three heat flows: liquid-to-interface heat flows ($\dot{Q}_I^L$) of dry side wall-to-interface heat flow ($\dot{Q}_W^{LV}$) and of the vapour-to-interface heat flow ($\dot{Q}_I^V$).

Section 7.5.1, 7.5.2 and 7.5.3 respectively discuss the $\dot{Q}_I^L$, $\dot{Q}_I^V$ and $\dot{Q}_W^{LV}$.

7.5.1. Liquid-to-interface heat flow

The liquid-to-interface heat flow ($\dot{Q}_I^L$) is calculated with two approaches, as it is described in Section 4.1 of Chapter 5. The first approach, called boundary layer convection (Equation 268), is applied when the boundary layer temperature of the last sub-layer of the wet side wall (T_{BL}^I) is higher than the interface temperature (T^I). The second approach, called local natural convection (Equation 269), is used when the interface temperature is higher than this boundary layer temperature.

As the storage container is closed, the interface temperature increases due to the self-pressurisation. The difference in temperature between the interface and the boundary layer of the wet side wall reduces, causing the reduction of $\dot{Q}_I^L$ at the beginning. Boundary layer convection (Equation 268) is used because the interface is colder than the boundary layer temperature of the last sub-layer of the wet side wall. As a consequence, at low, medium and high heat fluxes (see Section 6.1.3, 6.2.3 and 6.3.3 of Chapter 5), the liquid-to-interface heat transfer initially decreases in time. Then, the boundary layer temperature of the wet side wall becomes lower than the interface one, and Equation 269 is applied. Hence, the liquid-to-interface remains almost constant and the time-evolution is quite similar to the shape of an “L”. The rate of decreasing is usually smoother than the one of the homogeneous model (H model) because Equation 269 computes a lower value of $\dot{Q}_I^L$ than the one of Equation 268, which is used by H model in all test of the self-pressurisation.

7.5.2. Dry side wall-to-interface heat flow

At low heat fluxes (see Section 6.1.3 of Chapter 5), the dry side wall-to-interface heat flow ($\dot{Q}_W^{LV}$) remains constant during the self-pressurisation because the heat fluxes are low and the dry side wall temperature is constant. At medium and high heat fluxes (see Section 6.2.3 and 6.3.3 of Chapter 5), $\dot{Q}_W^{LV}$ is equal to zero because the beta coefficient is equal to zero.

7.5.3. Vapour-to-interface heat flow

The vapour-to-interface heat transfer is calculated using Equation 270, as function of the local natural convection near the interface, the convective flows in the bulk and the heat transferred across the sub-layer of the ullage. These convective flows increases with the heat fluxes at the dry side wall. As the storage container is closed, these convective flows are mainly directed to the interface, increasing the vapour-to-interface heat flows.

At low heat fluxes (see Section 6.1.3 of Chapter 5), $\dot{Q}_I^V$ remains constant during the self-pressurisation because the intensity of these convective flows is low. At medium and high heat fluxes (see Section 6.2.3 and 6.3.3 of Chapter 5), $\dot{Q}_I^V$ initially increases because these convective flows are mainly directed to the interface, increasing the energy transferred at the interface.

7.6. Net mass flow

The net mass flow is calculated with an iterative procedure, which is based on the energy conservation laws at the interface (see Appendix V). Hence, this mass flow directly depends on the three heat flows at the interface.

At low, medium and high heat fluxes (see Section 6.1.4, 6.2.4 and 6.3.4 of Chapter 5), the net mass flow initially decreases during the self-pressurisation and, then, it remains almost constant. Hence, the liquid-to-interface heat flow ($\dot{Q}_I^L$) affects more the net mass flow than the vapour-to-interface, because this mass flow has the same shape of $\dot{Q}_I^L$. In Test 3 of Study case 7, the net mass flow increases due to the increment of $\dot{Q}_I^L$. The values of the net mass flow are higher than the one of the homogeneous model (H model) because the absolute values of liquid-to-interface heat flow are lower than the one of the H model, due to the local natural convection approach (Equation 269).

7.7. Pressure

The pressure is determined by solving the Ordinary Differential Equations (ODEs) system of the mathematical system of the homogeneous model 2.0 (H 2.0 model), which is similar to the one of the homogeneous model (H model). The time-derivate of pressure mainly depends on the net mass flow, which is affected by the interfacial heat flows. The effect of the increment of the ullage temperature is of secondary importance in the increment of the pressure, except for the liquid hydrogen (LH_2) (see Section 8.5 of Chapter 4).

As the storage container is closed, the liquid-to-interface heat flow ($\dot{Q}_I^L$) is directed to the liquid phase, removing energy from the interface. This removed energy is balanced by the condensation and the net mass flow is lower than the one at steady state. Since the H 2.0 model computes a lower value of the QLI than the H model, the net mass flow increases. So, the pressure is higher than in the H model at the beginning of the self-pressurisation. After the initial transient, the difference in temperatures between the bulk and the interface increases. $\dot{Q}_I^L$ goes up and the condensation rate grows. So, the pressure remains lower than he experimental data because the net mass flow is not enough to sustain the storage pressure build-up as it is experimentally observed at low, medium and high heat fluxes (see Section 6.1.5, 6.2.5 and 6.3.5 of Chapter 5).

7.8. Ullage temperature

The ullage temperature is calculated with the Ordinary Differential Equations (ODEs) system, which numerically integrates the vapour temperature-evolution (T^V-e) equation (Equation 258). The T^V-e equation depends on the increment of the ullage pressure and on the accumulation of the sensible heat, which is computed with the coefficient F^{TV}. The accumulation is affected by the dry side wall-to-vapour heat flow and on the vapour-to-interface heat flow. The dry side wall-to-vapour heat flow ($\dot{Q}_W^{SV}$) is calculated considering turbulent regime at the dry side wall.

At low, medium and high heat fluxes (see Section 6.1.6, 6.2.6 and 6.3.6 of Chapter 5), the computed ullage temperature monotonically increases, except for Test 1 of Study case 5, Test 3 of Study case 7 and for Study case 3. During the self-pressurisation, the ullage receives heat from the dry side wall and the vapour transfers energy to the interface. A small part of the incoming heat flow is accumulated in the ullage, causing the monotonic increment of the temperature.

For Test 3 of Study case 7 and for Study case 3, the increment of the temperature is not monotonic due to the variations of the boundary layer mass flow of the dry side wall. As indicated by the comparison with the experimental data, the vapour-to-interface model (see Section 4.2 of Chapter 5) works well at medium and high heat fluxes, and at high filling ratio at low heat fluxes because the heat inputs rate is enough high to guarantee a good prediction of the convective flow in the ullage. At low heat fluxes, the turbulent fluid-dynamics regime overestimates the convective flows, increasing the vapour-to-interface heat flow and reducing the initial temperature. The proposed model better estimates the vapour-to-interface heat transfer than the homogeneous model (H model).

7.9.Conclusion and perspective

The homogeneous model 2.0 (H 2.0 model) is based on the hypothesis of vapour virtual stratification (assumption b) of Section 1.2 of Chapter 5). The temperature gradient in the vapour is considered in the Storage Boundary Layer (SBL) model for computing the boundary layer variables at the dry side wall. This gradient produces numerical instability in the numerical algortimh set up to compute these variables. This instaibilty is transferred to the algorithm that calculates the dry side wall-to-vapour heat flow ($\dot{Q}_w^{SV}$) because the heat transfer ceofficent is calculated with the boundary layer variables. Thus, the stability is increased by considering only the turbulent regime and using the a new algortimh for $\dot{Q}_w^{SV}$, which is based on the Newton-Raphson method. The accumulation of the sensible heat in the ullage is computed with the vapour temperature-evolution (T^V-e) equation (Equation 258). This equation is deduced from the mass and energy conservation laws of the virtual sub-layers of the vapour. Due to the hypothesis of vapour virtual stratification (assumption b) of Section 1.2 of Chapter 5), T^V-e equation is less affected by the enthalpy flow of the net mass flow than the one of the homogeneous model (H model). The net mass flow is computed with an iterative procedure because the vapour-to-interface heat flow ($\dot{Q}_I^V$) directly depend on this mass flow. The H 2.0 model computes $\dot{Q}_I^V$ on the basis of the local convection near the interface, of the convective motions in the ullage and of the heat transferred across the virtual sub-layer. The convective motions in the ullage depend on the net mass flow. The liquid-to-interface heat transfer is estimated with two approaches, respectively called boundary layer and local natural convection.

The agreement of the ullage temperature with the experimental data indicates that this model can better predict the behaviour of the ullage than the H model. Hence, the vapour bulk temperature gradient and the temperature profile in the ullage must be considered for modelling the behaviour of the ullage. The comparison with the experimental data reveals that the pressurisation rate is still underestimated. Hence, the different mechanism of liquid-to-interface heat transfer is not enough to properly predict the rate of self-pressurisation, even if this rate is higher than the one of the H model. This underestimation is produced because the effect of the liquid bulk temperature gradient on the liquid-to-interface heat transfer is neglected. The values of beta coefficient are often equal to zero and these values are not physically possible. $\dot{Q}_I^V$ at steady state is the main responsible of these values of the beta coefficient. So, a new model of $\dot{Q}_I^V$ should be proposed. Even if the description of the ullage must be improved, this aspect is of secondary importance because the time-evolution of the ullage temperature, which was a critical issued of the H model, has been largely solved. Hence, it is worth to improve the calculation of the ullage pressure, which is under-estimated in H and in H 2.0 model. So, it is mandatory to consider the bulk temperature gradient in the liquid to compute the evolution of the fluid-dynamics at the interface, which affect the self-pressurisation rate. This can be done by discretizing the liquid in sub-layers.

8. Comparison with the results of homogenous model

The homogeneous model 2.0 (H 2.0 model) is developed because the homogeneous model (H model) cannot calculate the time-evolution of vapour temperature that is in agreement with the experimental data because the H model computes peaks of ullage temperature, instead of the monotonic increment of temperature. The hypothesis of total homogeneity of the H model is removed and the hypothesis of the vapour virtual stratification (assumption b) of Section 1.2 of Chapter 5) is introduced in the H 2.0 model. So, the H 2.0 model is more complex than the H model, and the computational time and the accuracy could increase. The accuracy is evaluated using the statistical errors: Average Absolute Deviation (AAD), the Bias and the Maximum Absolute Deviation (MAD) (see Section 1 of Appendix S). The accuracy in computing the liquid temperature and filling ratio is not computed because these variables are not significantly impacted by the hypotheses of H 2.0 model.

Section 8.1presents the computational time of H 2.0 and H models. Section 8.2 and 8.3 discuss the accuracy of both models in describing the pressure and the ullage temperature. Section 8.4 explains the causes of these results and it presents the conclusions. Section 8.5 summarizes the comparison between the two models and it describes the perspective for improving the homogeneous model.

8.1.Computational time

The objective of the thesis is the development of a model that can be used in industrial application. So, the computational time of homogeneous model 2.0 (H 2.0 model) is compared to the one of the homogeneous model (H model). In this thesis, the computational time is the time required to execute the whole structure of the H 2.0 model form the Boil-Off Rate (BOR) model to the calculation at the last time-point. The computational time of H 2.0 model ($t_C^{H\ 2.0}$) and the difference in computational time ($\Delta t_C^{H-H2.0}$) between the H 2.0 and the H models are reported in Table 99.

Table 99. Values of $\boldsymbol{\Delta t_C^{H-H2.0}}$ and $\boldsymbol{t_C^{H\ 2.0}}$.

Study case 1

	Test 1	**Test 2**	**Test 3**	**Test 4**	**Test 5**	**Test 6**
$\Delta t_C^{H-H2.0}\ [s]$	-3051.7	-2968.0	290.6	-2147.6	551.7	1137.3
$t_C^{H\ 2.0}\ [s]$	2276.0	1192.8	1719.7	1295.5	1689.5	2169.4

Study case 2

	Test 1
$\Delta t_C^{H-H2.0}\ [s]$	-4758.8
$t_C^{H\ 2.0}\ [s]$	1170.6

Study case 3

	Test 1	**Test 2**
$\Delta t_C^{H-H2.0}\ [s]$	8576.2	5951.3
$t_C^{H\ 2.0}\ [s]$	9788.8	6984.4

Study case 4

	Test 1	**Test 2**
$\Delta t_C^{H-H2.0}\ [s]$	4031.5	1823.3
$t_C^{H\ 2.0}\ [s]$	4834.2	2336.6

Study case 5

	Test 1	**Test 2**	**Test 3**
$\Delta t_C^{H-H2.0}\ [s]$	-15682	-7888.4	-2327.0
$t_C^{H\ 2.0}\ [s]$	3999.6	3898.2	4838.0

Study case 6

	Test 1	**Test 2**	**Test 3**	**Test 4**
$\Delta t_C^{H-H2.0}\ [s]$	12268	2669.06	65.413	1053.0
$t_C^{H\ 2.0}\ [s]$	13554	3473.6	1426.8	2532.0

Study case 7

	Test 1	**Test 2**	**Test 3**
$\Delta t_C^{H-H2.0}\ [s]$	2337.7	301.09	149.87

Table 99. Values of $\Delta t_C^{H-H2.0}$ and $t_C^{H\ 2.0}$.

$t_C^{H\ 2.0}$ $[s]$	3596.4	1614.7	2206.6

As it is indicated by Table 99, the computational time of the H 2.0 model is usually higher than the one of H model because the difference in the computational time is positive. The increment of the computational time ranges between the 5 % and the 950 % of the time required by the H model. The average value of the increment is around 240 %. The values of the computational time of Test 1 of Study case 6, of Study case 3 and Test 1 of Study case 3 are the highest values for the H 2.0 model. The H 2.0 model is faster than H model for Test 1, 2 and 4 of Study case 1, for Study case 2 and for Study case 5.

The Storage Boundary Layer (SBL) model uses a fixed number of sub-space-points to numerically compute the boundary layer variables U and δ_M. If this number is lower (higher) than the one used in the H model, the computational time of the H 2.0 model is lower (higher) than the one of the H model. As a consequence, the computational time of H 2.0 model is lower than the one of H model due to the low number of sub-space-points, for Tests 1, 2 and 4, and Study cases 1, 2 and 5. The SBL computes the absence of the natural convection at the dry side wall for Test 1 of Study case 6, of Study case 3 and Test 1 of Study case 3, which have the highest increment of the computation time. Hence, the absence of the natural convection increases the computational time.

8.2. Accuracy in computing the pressure

The Average Absolute Deviation (AAD), BIAS and Maximum Absolute Deviation (MAD) of the calculated pressure of homogeneous model 2.0 (H 2.0 model) and homogeneous model (H model) are reported in Figure 121 for all the study cases.

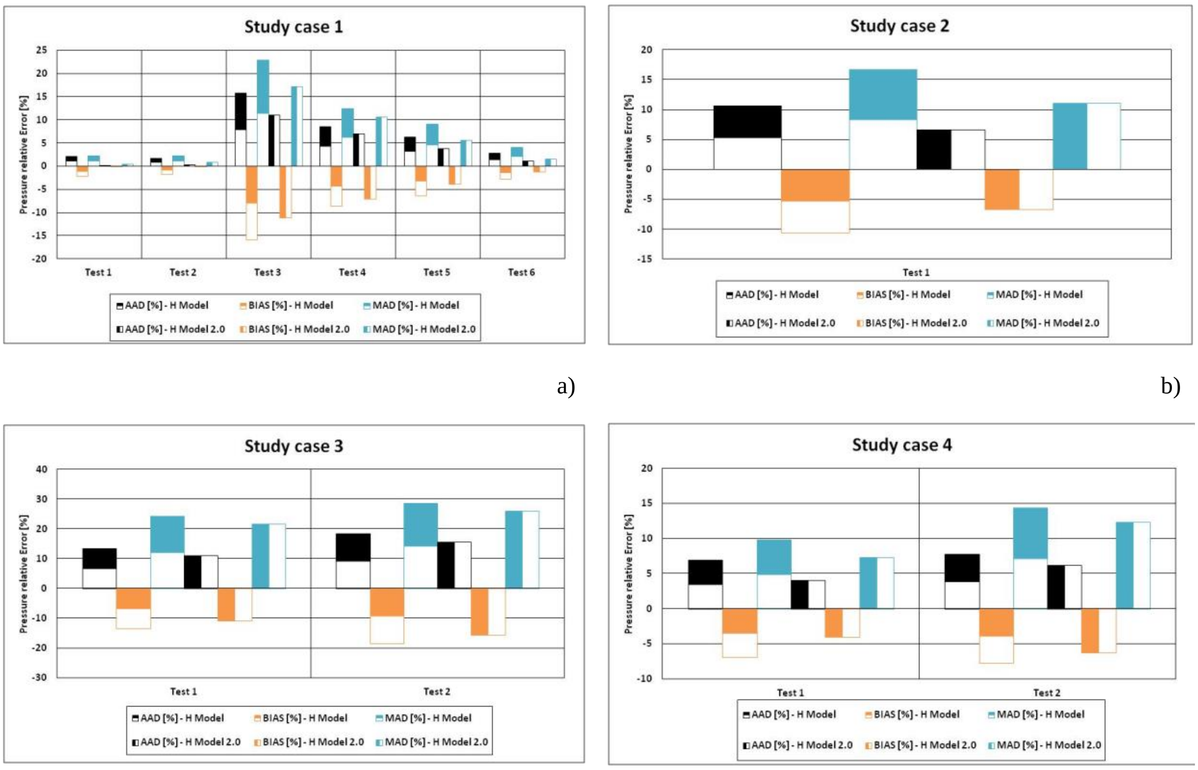

a) b)

c) d)

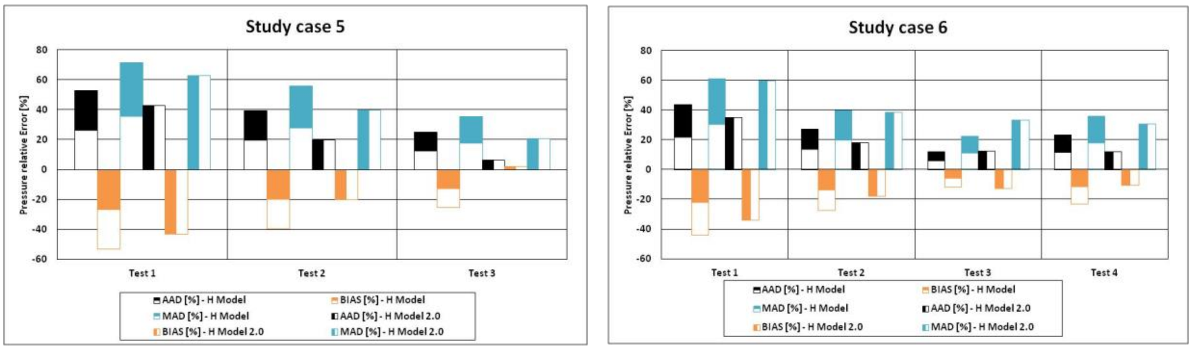

e) f)

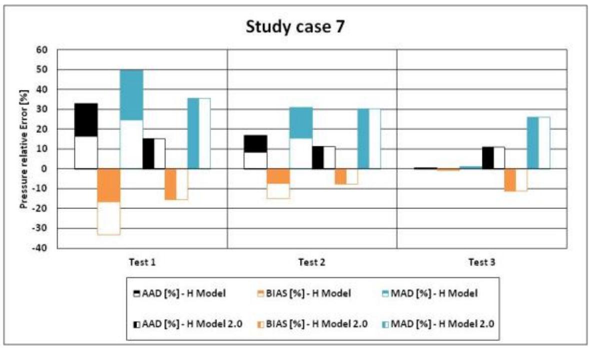

g)

Figure 121. The values of AAD, BIAS and MAD of the calculated pressure of H 2.0 and H models for Study case 1 (a), 2 (b), 3 (c), 4 (d), 5 (e), 6 (f) and 7 (g).

For the Study case 1, the AAD, the BIAS and the MAD of the H 2.0 model decreases from Test 4 (medium filling ratio) to Test 6 (low filling ratio). The values of these statistical errors are almost constant between Test 1 (high filling ratio) and Test 2 (high-medium filling ratio). The highest values of AAD, the BIAS and the MAD of the H 2.0 model are computed for Test 3 (high heat input). These statistical errors are lower than the one of the H model and the relative variation[93] of these statistical errors is reported in Table 100.

Table 100. Relative variation of AAD, BIAS and MAD between H 2.0 and H model for ullage pressure of Study case 1.

Test	1	2	3	4	5	6
AAD [%]	-90.766	-82.272	-29.342	-17.950	-38.509	-55.935
BIAS [%]	-98.048	-97.093	-29.342	-17.950	-38.509	-55.935
MAD [%]	-79.140	-62.497	-24.526	-14.664	-37.877	-61.208

The relative variation reduces with the reduction of the filling ratio, and the average relative variations of AAD, the BIAS and the MAD are respectively -52.5 %, -56.1 % and -46.6 %.

For Study case 2, the values of the AAD, BIAS and MAD of H 2.0 model are lower than the one of H model. The relative variation of these statistical errors is reported in Table 101.

Table 101. Relative variation of AAD, BIAS and MAD between H 2.0 and H model for ullage pressure of Study case 2.

Test	1
AAD [%]	-36.903
BIAS [%]	-36.903
MAD [%]	-33.840

The values of the relative variation of AAD, the BIAS and the MAD of Study case 2 are lower than the average values of one of Study case 1.

---

[93] The relative decrement is computed as : $\frac{y_{H\,2.0}-y_H}{y_H}\cdot 100$. y can be ADD, BIAS and MAD.

For Study case 3, the AAD, BIAS and MAD of H 2.0 model of Test 1 (steady state initial condition) are lower than the one of Test 2 (isothermal initial condition). The differences in AAD, in BIAS and MAD between Test 1 and Test 2 are respectively -4.7 %, 4.8 % and -4.3 %. The AAD, BIAS and MAD of H 2.0 model are lower than the one of H 2.0 model and the relative variation of these statistical errors is reported in Table 102.

Table 102. Relative variation of AAD, BIAS and MAD between H 2.0 and H model for ullage pressure of Study case 3.

Test	1	2
AAD [%]	-18.741	-15.194
BIAS [%]	-19.818	-15.194
MAD [%]	-10.524	-8.834

The relative variation of Test 2 is lower than the one of Test 1 and the average relative variations of AAD, the BIAS and the MAD are respectively -16.9 %, -17.5 % and -9.67 %.

For Study case 4, the AAD, BIAS and MAD of H 2.0 model of Test 1 (medium filling ratio) are lower than the one of Test 2 (low filling ratio). The differences in AAD, in BIAS and MAD between Test 1 and Test 2 are respectively -2.2%, 2.1 % and -5.0 %. Thus, the calculation at medium liquid level are more accurate than the one at low filling ratio. The AAD, BIAS and MAD of H 2.0 model are lower than the one of H 2.0 model and the relative variation of these statistical errors is reported in Table 103.

Table 103. Relative variation of AAD, BIAS and MAD between H 2.0 and H model for ullage pressure of Study case 4.

Test	1	2
AAD [%]	-41.433	-19.506
BIAS [%]	-41.489	-19.506
MAD [%]	-25.077	-14.181

The relative variation of Test 2 is lower than the one of Test 1 and the average relative variations of AAD, the BIAS and the MAD are respectively -30.5 %, -30.5 % and -19.7 %. The absolute values of the relative variation of Study case 4 are higher than the one of Study case 3.

For Study case 5, the values of the AAD, BIAS and MAD of H 2.0 model decreases from Test 1 (high filling ratio) to Test 3 (low filling ratio). The values of these statistical values are lower than the one of H model and the relative variation is reported in Table 104.

Table 104. Relative variation of AAD, BIAS and MAD between H 2.0 and H model for ullage pressure of Study case 5.

Test	1	2	3
AAD [%]	-19.296	-49.443	-73.341
BIAS [%]	-19.296	-49.829	-108.393
MAD [%]	-12.190	-29.108	-41.948

The values of the relative variation of AAD, BIAS and MAD decreases from Test 1 to Test 3, indicating the that H 2.0 model is more accurate at low filling ratio than at high liquid level. The average values of the relative variation of AAD, BIAS and MAD are respectively -47.4 %, -59.2% and -27.7%.

For Study case 6, the values of the AAD and of MAD decrease from Test 1 (high filling ratio) to Test 3 (low filling ratio). The differences in AAD and in MAD between Test 3 and Test 4 (high heat input) are almost negligible. The BIAS increases from Test 1 to Test 3. The values of this statistical error of Test 4 are slightly lower than the ones of Test 3. MAD and BIAS are lower than the ones of H model, except for Test 3. For this test, the differences in AAD and in BIAS are almost negligible. The values of MAD of H 2.0 model are lower than the ones of H model. The values of the relative variation of these statistical errors are reported in Table 105.

Table 105. Relative variation of AAD, BIAS and MAD between H 2.0 and H model for ullage pressure of Study case 6.

Test	1	2	3	4
AAD [%]	-20.266	-33.936	6.1236	-49.086
BIAS [%]	-22.482	-35.069	6.1236	-55.399
MAD [%]	-2.0276	-2.7298	48.309	-14.220

As it is reported in Table 105, the values of relative variation of Test 4 are the lowest. Only for Test 3 these values are positive, indicating that the H model is better than the H 2.0 model. The average values of these relative variations of AAD, BIAS and MAD are respectively -24.3%, -26.7% and 7.3 %. These average values are lower than the ones of Study case 5.

For Study case 7, the values of AAD, BIAS and MAD decrease from Test 1 (high filling ratio) to Test 2 (medium filling ratio). The values of AAD of Test 2 are quite similar to the one of Test 3 (low filling ratio). The values of MAD of Test 3 are lower than the ones of Test 2. The BIAS decreases from Test 2 to Test 3. The values of these statistical errors are lower than the ones of H model, except for Test 3. For this test, the absolute values of AAD, BIAS and MAD of H 2.0 model are higher than the one of H model. The values of the relative variation of these statistical errors are reported in Table 106.

Table 106. Relative variation of AAD, BIAS and MAD between H 2.0 and H model for ullage pressure of Study case 7.

Test	1	2	3
AAD [%]	-53.639	-32.288	1613.7
BIAS [%]	-53.639	-48.272	1613.7
MAD [%]	-28.262	-2.0773	1874.8

The average values of the relative variation of AAD, BIAS and MAD are respectively 509 %, 503 % and 614 %. Hence, the H 2.0 does not improve the calculation of the ullage pressure for Study case 7, on average.

To sum up, the H 2.0 model globally improves the calculation of the ullage pressure, except Study case 7. The AAD reduces of a value that ranges between -90 % and – 15 %, neglecting Test 3 of Study case 6 and Test 3 of Study case 7. The highest improvements are observed for storage containers with high filling ratio and low heat fluxes, and with low filling ratio and medium heat fluxes.

8.3. Accuracy in computing the ullage temperature

The Average Absolute Deviation (AAD), BIAS and Maximum Absolute Deviation (MAD) of the calculated ullage temperature of homogeneous model 2.0 (H 2.0 model) and homogeneous model (H model) are reported in Figure 122 for all the study cases.

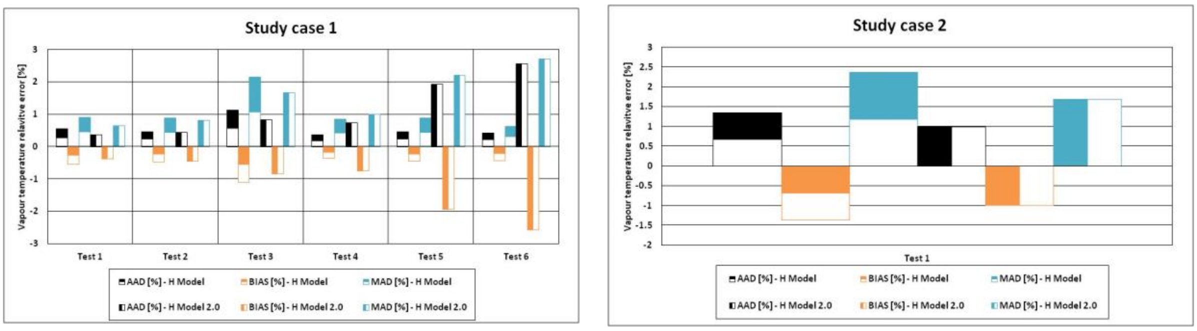

a) b)

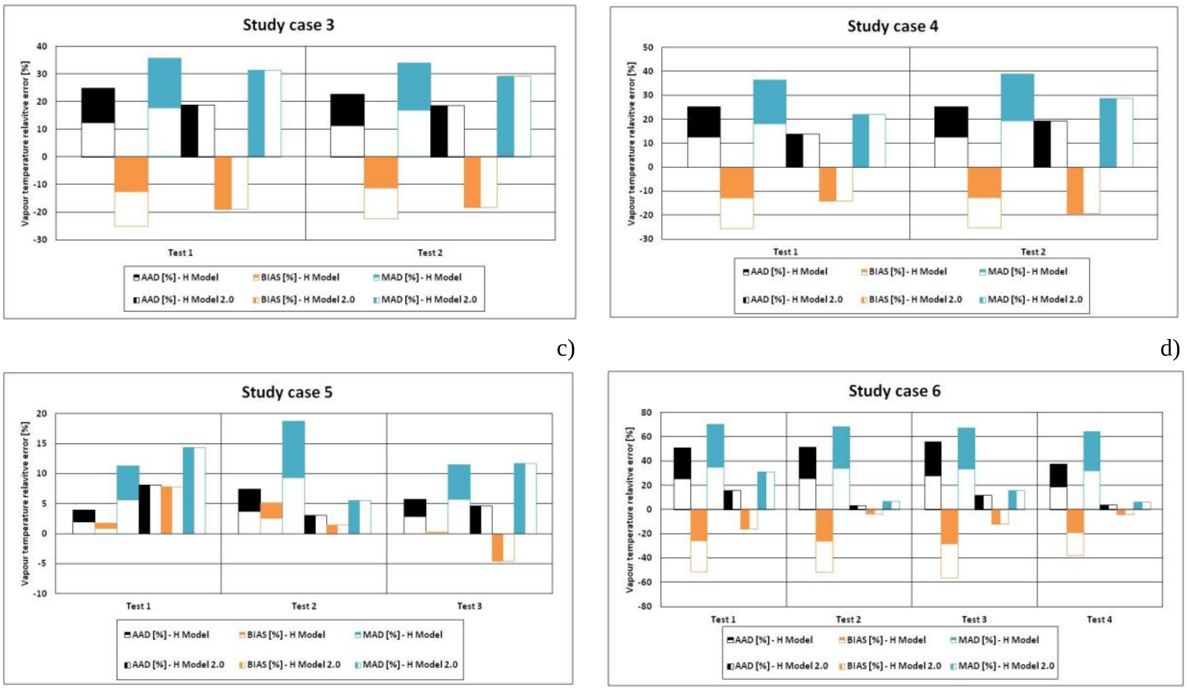

c) d)

e) f)

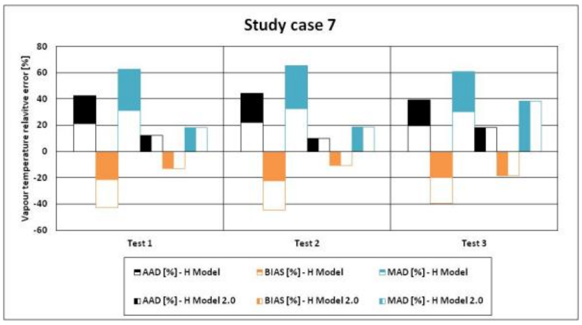

g)

Figure 122. The values of AAD, BIAS and MAD of the calculated ullage temperature of H 2.0 and H models for Study case 1 (a), 2 (b), 3 (c), 4 (d), 5 (e), 6 (f) and 7 (g).

For Study case 1, the absolute values of AAD, BIAS and MAD of H 2.0 model increases from Test 4 (medium filling ratio) to Test 6 (low filling ratio). The difference in these statistical errors between Test 1 (high filling ratio) and Test 2 (high-medium filling ratio) is low. The absolute values of AAD, BIAS and MAD of H 2.0 model are lower than the one of H model for Test 1, 2 and 3 (high filling ratio). The absolute values of these statistical errors of H model are lower than the one of H 2.0 model for Tests 4, 5 and 6. The relative variation of AAD, BIAS and MAD are reported in Table 107.

Table 107. Relative variation of AAD, BIAS and MAD between H 2.0 and H model for ullage temperature of Study case 1.

Test	1	2	3	4	5	6
AAD [%]	-31.843	-4.5881	-26.288	99.169	310.70	500.26
BIAS [%]	-31.843	-3.4437	-23.728	104.66	326.32	500.26
MAD [%]	-29.556	-8.6626	-22.082	17.999	145.90	333.00

The average values of the relative variation of AAD, BIAS and MAD are respectively 141 %, 145 % and 73 %, indicating the H model is in general better than H 2.0 model.

For Study case 2, the absolute values of AAD, BIAS and MAD of H 2.0 model are lower than the one of H model, indicating that H 2.0 model improves the calculation of the ullage temperature. The relative variations of these statistical errors are reported in Table 108.

Table 108. Relative variation of AAD, BIAS and MAD between H 2.0 and H model for ullage temperature of Study case 2.

Test	1

Table 108. Relative variation of AAD, BIAS and MAD between H 2.0 and H model for ullage temperature of Study case 2.

AAD [%]	-27.091
BIAS [%]	-27.062
MAD [%]	-28.711

For Study case 3, the value of AAD of Test 1 (steady state initial condition) is almost equal to the one of Test 2 (isothermal initial condition). The value of BIAS of Test 1 is lower than the one of Test 2. The value of MAD of Test 1 is higher than the one of Test 2. The absolute values of AAD, BIAS and MAD of H 2.0 model are lower than the ones of H model. The values of the relative variation of these statistical errors are reported in Table 109.

Table 109. Relative variation of AAD, BIAS and MAD between H 2.0 and H model for ullage temperature of Study case 3.

Test	1	2
AAD [%]	-24.161	-18.265
BIAS [%]	-24.161	-18.481
MAD [%]	-12.025	-14.168

The values of Table 109 are negative, indicating that the H 2.0 model improves the calculation of the ullage temperature of Study case 3. The average values of the relative variations of AAD, BIAS and MAD are respectively -21.2%, 21.3 % and -13.1%.

For Study case 4, the absolute values of AAD, BIAS and MAD of H 2.0 model of Test 1 (medium filling ratio) are higher than the ones of Test 2 (low filling ratio). The values of these statistical errors of H 2.0 model are lower than the ones of H model. The relative variations are reported in Table 110.

Table 110. Relative variation of AAD, BIAS and MAD between H 2.0 and H model for ullage temperature of Study case 4.

Test	1	2
AAD [%]	-45.007	-23.218
BIAS [%]	-45.007	-23.218
MAD [%]	-39.684	-25.792

The average values of the relative variation of AAD, BIAS and MAD are respectively -34%, - 34 % and 32 %, indicating the H 2.0 model is better than H model in computing the ullage temperature.

For Study case 5, the absolute values of AAD, BIAS and MAD of H 2.0 model decrease from Test 1 (high filling ratio) to Test 2 (medium filling ratio). These values increase from Test 2 to Test 3 (low filling ratio). So, the lowest absolute values of these statistical errors are the ones of medium filling ratio. The absolute values of AAD, BIAS and MAD of H 2.0 model are higher than the one of H model at Test 1. At Test 2, the absolute values of these statistical errors of H 2.0 model are lower than the ones of Test 2. At Test 3, the value of AAD of H 2.0 model is lower than the one of H model. The absolute values of BIAS and MAD of H 2.0 model are higher than the one of H model. The relative variation of AAD, BIAS and MAD are reported in Table 111.

Table 111. Relative variation of AAD, BIAS and MAD between H 2.0 and H model for ullage temperature of Study case 5.

Test	1	2	3
AAD [%]	104.03	-58.892	-17.662
BIAS [%]	335.68	-71.631	-1808.1
MAD [%]	27.466	-70.202	2.1827

The average values of the relative variations of AAD, BIAS and MAD are respectively 9.2 %, -514 % and -13.5 %. Hence, the calculation of the ullage temperate of H 2.0 model is not quantitatively improved respect to the one of the H model.

For Study case 6, the absolute values of AAD, BIAS and MAD of H 2.0 model decrease from Test 1 (high filling ratio) to Test 2 (medium filling ratio). These values increase from Test 2 to Test 3 (low filling ratio). So, the lowest absolute values of these statistical errors are the ones of medium filling ratio, as it is observed for Study case 5. The absolute values of these statistical errors of Test 4 (high heat input) are quite similar to the ones of Test 2. The absolute values of AAD, BIAS and MAD of H 2.0 model are lower than the ones of H model. The relative variations of AAD, BIAS and MAD are reported in Table 112.

Table 112. Relative variation of AAD, BIAS and MAD between H 2.0 and H model for ullage temperature of Study case 6.

Test	1	2	3	4
AAD [%]	-68.793	-93.186	-78.556	-89.509
BIAS [%]	-68.793	-93.186	-78.556	-89.509
MAD [%]	-55.902	-89.644	-76.863	-90.180

The average values of the relative variations of AAD, BIAS and MAD are respectively -82.5 %, -82.5 % and -78.1 %. Hence, the H 2.0 model significantly improves the description of the ullage temperature for Study case 6.

For Study case 7, the absolute values of AAD, BIAS and MAD of H 2.0 model of Test 1 (high filling ratio) are quite similar to the one of Test 2 (medium filling ratio). The absolute values of these statistical errors of H 2.0 model of Test 3 (low filling ratio) are higher than the ones of Tests 1 and 2. The absolute values of AAD, BIAS and MAD of H 2.0 model are lower than the ones of H model and the relative differences are reported in Table 113.

Table 113. Relative variation of AAD, BIAS and MAD between H 2.0 and H model for ullage temperature of Study case 7.

Test	1	2	3
AAD [%]	-70.602	-76.752	-53.684
BIAS [%]	-70.424	-76.752	-53.684
MAD [%]	-70.743	-71.017	-36.908

The average values of the relative variations of AAD, BIAS and MAD are respectively -67 %, -66.9 % and -59.5 %. Hence, the H 2.0 model significantly improves the description of the ullage temperature for Study case 7.

To sum up, the absolute values of AAD, BIAS and MAD of H 2.0 model are usually lower than the ones of H model. The AAD reduces of a value that ranges between -93 % and -4 %, except for Test 1 of Study case 5 and for Tests 4, 5 and 6 of Study case 1. The highest improvements are observed for storage container with medium and high filling ratio. On the other hand, the there is not a significant improvement of computing the ullage temperature at low heat fluxes.

8.4. Discussions and conclusions

The homogenous (H 2.0) model is evaluated against the homogeneous (H), by comparing the values of the statistical errors, computed for the pressure and vapour temperature.

Section 8.4.1 and 8.4.2 discuss the results for the pressure and ullage temperature, respectively.

8.4.1. Pressure

The values of the vapour-to-interface heat flow ($\dot{Q}_I^V$) and of the liquid-to-interface heat flow ($\dot{Q}_I^L$) are higher than the ones of the homogeneous model (H model), due to the new formulas of computing these heat flows (see Section 4.1 and 4.2 of Chapter 5). As consequence, more energy than the one of H model remains in the interface and this excess of heat is converted into evaporation. So, the evaporation rate, thus the net mass flow, increases and more mass is accumulated in the ullage in the H 2.0 model than in the H model. So, the values of Absolute Deviation (AAD) of the pressure of H 2.0 model are usually lower than the ones of the H model. The values of this reduction is usually between

-90 % and -15 % of the relative variation, except for Test 3 of Study case 6 and for Test 3 of Study case 7. The best improvements are observed for storage container with high filling ratio and low heat fluxes, and with low filling ratio and medium heat fluxes.

To sum up, the model of $\dot{Q}_I^L$ with two approaches is suitable for modelling the behaviour of cryogenic liquids, indicating that mechanism of the liquid-to-interface heat transfer can change from boundary layer convection to local natural convection. The neglect of the bulk temperature gradient of the liquid is the main issues to solve for improving the representation of the storage pressure.

8.4.2. Ullage temperature

Due to the hypothesis of vapour virtual stratification (assumption b) of Section 1.2 of Chapter 5), the accumulation term (coefficient F^{TV}) of the vapour temperature-evolution (T^V-e) equation (Equation 258) in the homogneous (H 2.0) model 2.0 is changed from the one of the homogeneous model (H model). The effect of the enthalpy of the net mass flow is lower than the of the H model. As a consequence, the time-evolution of the ullage temperature is monotonic, except for Test 1 of Study case 5 and for Test 4, 5 and 6 of Study case 1. So, the Average Absolute Deviation (AAD) of the ullage temperature of H 2.0 model is lower than the one of the H model. The relative reduction of the AAD ranges from -93 % to -4 %, and the best improvements are observed for observed for storage container at medium and high filling ratios. The computed absence of natural convection at the dry side wall (of Study case 3) is one of the reasons behind the low improvements for liquid hydrogen at low heat fluxes.The low computed initial temperature of the ullage is the main causes of the weak improvement of H 2.0 model at low heat fluxes.

8.5. Summary and perspectives

The statistical errors are computed with the results of the homogeneous model 2.0 (H 2.0 model) and homogeneous model (H model)s. These models are compared to state if the increment of the complexity is worthy. The comparison indicates that H 2.0 model is more accurate than H in computing the ullage pressure and temperature, due to the hypothesis of vapour virtual stratification (assumption b) of Section 1.2 of Chapter 5) and due to the modelling of liquid-to-interface with two approaches. Hence, the approach of the H 2.0 is enough accurate to calculate the behaviour of the ullage temperature, but the pressure remains under-estimated. So, the improvement of the pressure is the next step that has benn sought.

The hypothesis of vapour virtual stratification (assumption b) of Section 1.2 of Chapter 5) can be used in the next version of the storage model. As a consequence, the mathematical model of the ullage is the same of H 2.0 model. The number of the sub-space-points of the Storage Boundary Layer (SBL) model should be increased to make the numerical integration at the dry side wall more stable than the one of the H 2 model, due to the irregularities of the average mass boundary layer of Study case 3 and Test 1 of Study case 6. The laminar fluid-dynamics regime should be considered in the boundary layer model of the dry side wall. The modelling approach of the liquid has to be changed from the one of the H 2.0 model. The new modelling approach consists of introducing the bulk temperature gradient in the liquid by discretizing the liquid in sub-layers of equal height. This new approach will be considered in the liquid stratification model.

Chapter 6

Modèle de la stratification liquide

Le modèle homogène 2.0 ne peut pas en général prédire correctement l'augmentation de la pression dans le ciel gazeux en accord avec les données expérimentales. La sous-estimation de l'auto-pressurisation est causée par le taux de condensation élevé produit par les valeurs sous-estimées du flux thermique liquide-interface. L'intensité de ce flux de chaleur est supérieure à celle qui devrait l'être, car la différence de température entre l'interface et le liquide est utilisée au lieu d'appliquer la différence de température entre l'interface et le liquide proche de l'interface.

La température du liquide à proximité de l'interface peut être calculée (i) en discrétisant le liquide en sous-couches et (ii) en appliquant les lois de conservation de la masse et de l'énergie. Par conséquent, le gradient de température global du liquide est calculé à chaque sous-couche. Ces lois de conservation considèrent (i) le flux de chaleur au niveau des parois, (ii) les flux de chaleur à travers les sous-couches, et (iii) les flux convectifs du liquide.

Les flux de chaleur au niveau des parois sont calculés avec le modèle Storage Heat Transfer (SHT). Les coefficients de transfert de chaleur sont calculés avec les valeurs des variables de la couche limite calculées avec le modèle Storage Boundary Layer (SBL). Le gradient global de température du liquide est ajouté à l'équation de conservation d'énergie de la couche limite. Seul le régime fluide-dynamique turbulent est considéré pour améliorer la stabilité de l'intégration numérique et des algorithmes du modèle SHT. Les flux de chaleur au niveau des parois sont calculés à partir du coefficient de transfert thermique effectif et des coefficients correcteurs alpha et bêta, qui sont calculés avec le modèle Boil-Off Rate. Ce modèle est similaire à celui du modèle H 2.0, sauf pour l'utilisation des modèles SHT et SBL de la paroi latérale humide du modèle de la stratification liquide (LS). Le flux de chaleur paroi latérale sèche-vers-interface rentre dans la paroi latérale humide, au lieu d'être directement absorbé par l'interface, du fait de la discrétisation. Par conséquent, l'équation du bilan énergétique de l'interface ne prend en compte que les flux de chaleur liquide-interface et vapeur-interface.

Les flux de chaleur à travers les sous-couches sont calculés à l'aide du modèle de transfert de chaleur intra-couche, qui prend en compte différents mécanismes de transfert de chaleur, respectivement appelés statique, semi-statique et non statique. En statique, les flux thermiques sont calculés en se rapprochant du flux thermique maximum entre la conduction et la convection. En mode non statique, la chaleur est transférée entre chaque sous-couche par conduction uniquement. Dans le mécanisme semi-statique, il est composé de l'approche du flux thermique maximal et de l'approche de la conduction uniquement.

Les écoulements convectifs dans le cœur du liquide se déduisent du débit massique de la couche limite de la paroi latérale humide et du débit massique au fond.

Les résultats du modèle LS sont comparés aux données expérimentales et aux résultats du modèle H 2.0. La pression calculée est souvent surestimée à faible taux de remplissage, en raison (i) de la négligence du régime dynamique des fluides laminaire et (ii) de l'accumulation excessive de chaleur sensible près de l'interface. Le modèle LS est qualitativement en accord avec les données expérimentales en décrivant l'auto-pressurisation et l'effet des apports thermiques et du taux de remplissage initial sur la pression, mais il n'est pas plus précis que le modèle H 2.0 car le gain de prédiction de la pression est perdu à un taux de remplissage élevé et à de faibles flux thermiques.

Liquid stratification model

The homogeneous model 2.0 (H 2.0 model) cannot properly predict rise of the ullage[94] pressure that is in agrrement with the experimental data, except for certain cases. The under-estimation of the self-pressurisation is caused by the high condensation rate, which is produced by the under-estimated values of the liquid-to-interface heat flow. The intensity of this heat flow is higher than the one that should be because the temperature difference between the interface and the liquid bulk is applied instead of using the difference in temperature between the interface and the liquid near the interface. The liquid temperature near the interface can be computed (i) discretizing the liquid into sub-layers and (ii) applying the mass and energy conservation laws. Hence, the bulk temperature gradient of the liquid is computed at each sub-layer. These laws consider (i) the heat flow at the walls, (ii) the heat flows across the sub-layers, and (iii) the convective flows of the liquid. The heat flows at the walls are computed with the Storage Heat Transfer (SHT) model. the heat transfer coefficients are computed with the values of the boundary layer variables, which are calculated with the Storage Boundary Layer (SBL) model. The bulk liquid temperature gradient is added to the energy conservation equation of the boundary layer. Only the turbulent fluid-dynamic regime is considered to improve the stability of the numerical integration and of the algorithms of SHT model. The heat flows at the walls are calculated from the effective heat transfer coefficient, and from the alpha and beta corrective coefficients, which are computed with the Boil-Off Rate (BOR) model. This model is similar to the one of the H 2.0 model, except for using the SHT and the SBL models of the wet side wall of the liquid stratification model (LS model). The dry side wall-to-interface heat flow goes to the wet side wall, instead of being directly absorbed by the interface, due to the discretisation. Hence, the energy balance equation of the interface considers only the liquid-to-interface and the vapour-to-interface heat flows. The heat flows across the sub-layers are calculated with the Intra-Layer Heat Transfer (ILHT) model, which consider different heat transfer mechanisms, respectively called static, semi-static and no-static. In static, the heat flows are computed with the approach of maximum heat flow between the conduction and the convection. In no-static, the heat is transferred between each sub-layer by conduction only. In the semi-static mechanism is composed by the approach of maximum heat flow and the approach of conduction only. The convective flows of the liquid bulk are deduced from the mass flow of the boundary layer of the wet side wall and from the mass flow at the bottom. The results of the LS model are compared with the experimental data and with the results of the H 2.0 model. The computed pressure is often over-estimated at low filling ratio, (i) due to the neglect of the laminar fluid-dynamic regime and (ii) due to the excessive calculated accumulation of sensible heat near the interface. The LS model qualitatively agrees with the experimental data in describing the self-pressurisation and the effect of the heat inputs and the initial filling ratio on the pressure. LS model is not more accurate than the H 2.0 model because the gain in predicting the pressure is lost at high filling ratio and low heat fluxes, even if the LS model is always qualitatively in line with the experimental data of pressure.

Section 1 introduces the LS model. Section 2 describes how the equations of the LS model are deduced from the mass and energy conservation laws. Section 3 presents the fluid-dynamics in the liquid. Section 4, 5, 6 and 7 respectively describes the ILHT, the SHT, the SBL and the interface heat transfer models. Section 8 compares the experimental data with the results of the LS model. Section 9 discusses the results and presents the conclusions. Section 10 compares the LS model with the H 2.0 model.

---

[94] The ullage is the empty space of the storage container, thus it is synonym of vapour phase.

1. Introduction

The the homogeneous (H 2.0) model under-estimates the rate of sel-pressurisation because the difference in temperature between the interface and hte liquid bulk is higher than the one that should be. During self-pressurisation, sensible energy accumulating in the liquid near the interface makes the liquid temperature at the interface higher than the one in the bulk. Hence the heat flow from liquid to the interface shall be lower than the one that is estimated by the homogeneous (H 2.0) model. In the liquid stratificaiotn (LS) model, the liquid temperature near the interface is calculated by discretizing the liquid region in sub-layers and applying the energy and mass conservation laws.

Section 1.1 presents the main critical issue of the H 2.0 model. Section 1.2 describes the hypotheses used. Section 1.3 explains the discretisation approach. Section 1.4 presents the variables of the LS model. Section 1.5 describes the block structure of the LS model. Section 1.6 and Section 1.7 respectively explains the mathematical system and the Ordinary Differential Equation (ODE) system of the LS model.

1.1. Critical issues of homogeneous model 2.0 and objective of the liquid stratification model

The homogeneous model 2.0 (H 2.0 model) was developed with the goal of computing the time-evolution[95] of the ullage temperature that at least qualitatively agrees with the experimental one. Even if this goal is achieved, the computed rate of self-pressurisation is lower than the experimental one, in particular at medium and high heat fluxes. The raise of the pressure mainly depends on the increment of the mass in the ullage, thus on the net mass flow[51]. This mass flow decreases during the self-pressurisation because the heat flows from the interface to the liquid instead of flowing from the liquid to the interface. Hence, the condensation mass flow increases to balance the energy subtracted by the liquid-to-interface heat flow. In the H 2.0 model, this heat flow is computed with the boundary layer and the local convection approaches. For the local convection approach, which is mainly used during the self-pressurisation, the liquid-to-interface heat flow is calculated as function of the difference in temperature between the interface and the liquid bulk, which is homogeneous by hypothesis. During the self-pressurisation, sensible energy is accumulated in the liquid, near the interface. The liquid temperature at the interface is higher than the one of the bulk. The liquid is thermally stratified. The liquid-to-interface heat transfer depends on the difference in temperatures between the interface and the liquid near the interface. this difference is lower tha the one between the interface and the liquid bulk. So, the intensity of the liquid-to-interface heat flow is over-estimated by the H 2.0 model and the accumulation of mass in the ullage is not enough to sustain the self-pressurisation.

Consequently, the LS model is developed to solve the aforementioned inconsistency that stems from the isothermal hypothesis of the liquid region of the H 2.0 model. The self-pressurisation can be properly computed (i) if a more accurate value of the difference in temperatures between the interface and the liquid near the interface is employed, and (ii) if the fluid-dynamics of the dominant heat transfer mechanism is correctly computed. In literature, the liquid temperature near the interface can be computed with the approach of the energy distribution function [61]–[68] and with the approach of discretisation [1], [2], [24], [74], [76], [80]. In the first approach, energy distribution function is regressed from experimental data. So, this approach cannot be used if the storage conditions are different from the experimental ones, as it can occur in industrial applications. As a consequence, the modelling approach of the discretisation of the liquid in sub-layers of equal height is suitable for industrial applications and it used in this thesis.

---

[95] Time-evolution of the variable “A” is the variation of the variable “A” during the storage of cryogenic liquids.

1.2. Hypotheses

Except for the small temperature gradient at the interface and at the walls of the storage container, the liquid phase is almost isothermal during the steady state phase in the open storage operation. The ullage is thermally stratified due to the thermo-siphon effect[96]. When the storage container is closed, the sensible heat of the liquid is accumulated near the interface, because of the natural convective flow of the wet side wall. This convective flow transfers this sensible heat to the core of the liquid, producing the thermal stratification. At the same time, the convective flow at the bottom mixes the lower part of the liquid core, maintaining the isothermal condition in a limited part of the liquid. Due to the liquid thermal stratification, the mass flow reduces in the boundary layer of the wet side wall. This reduction changes the fluid-dynamics of the liquid near the interface from the one of isothermal liquid. As a consequence, the intensity of the liquid-to-interface heat flow reduces. Hence, the liquid stratification model (LS model) has been developed with the following assumptions:

a) *vapour virtual stratification* : the ullage is virtually stratified (like in the homogeneous model 2.0 (H 2.0 model));
b) *liquid discretization* : the liquid can be discretized in sub-layer of equal height;
c) *actual thermodynamic equilibrium:* the liquid in each sub-layer and the vapour can be sub-cooled, over-heated, or at saturation (similarly to the homogeneous model (H model))
d) *local thermodynamic equilibrium:* the interface is always at thermodynamic equilibrium;

Figure 123 shows the storage volume discratization used as reference for the development of the LS model. The blue and red zones are respectively the liquid and the ullage. The gradation of blue colour indicates the region of the thermal stratification in the liquid. The darker is the blue colour, the colder is the liquid. The yellow dashed line is the interface, the green arrow is the net mass flow at interface and the black arrows are the inlet and outlet flows. The white arrows with red boarders are the heat fluxes and the white points with purple boarders are the wall temperatures. The orange and light blue arrows indicate the convective flows in vapour and in liquid, respectively.

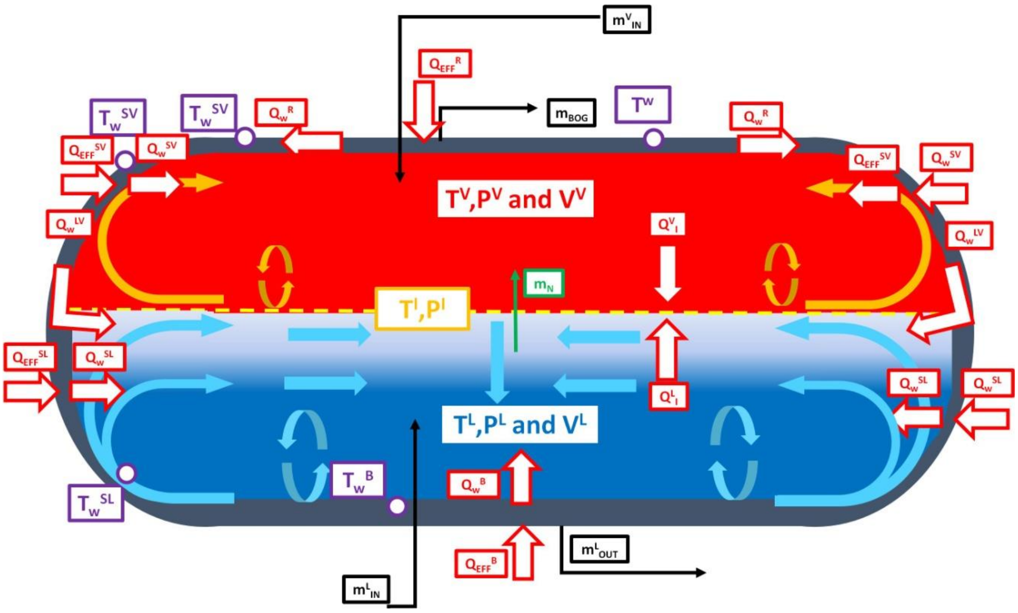

Figure 123. Liquid stratification model.

As illustrated by Figure 123, the description of the vapour phase is similar to the one of the H 2.0 model. The ullage receives heat from the side wall and it transfers part of this energy to the interface.

---

[96] Thermo-siphon effect is the natural convection that is caused by the heat exchange at the dry side wall.

The remaining part is absorbed by the ullage and by the enthalpy flow of the net mass flow. The dry side wall is warmed by the heat from environment and from the heat transferred through the roof. The thermal energy is transferred to the vapour and to the liquid walls. Hence, the interface is differently modelled than in the H 2.0 model, as reported in Figure 123.

The dry side wall-to-interface heat flow goes to the wet side wall instead of being directly absorbed by the interface. The liquid-to-interface and the vapour-to-interface heat flows are the only heat flows that produce the net mass flow at the interface. In the lower part of the liquid, the mass in entrained in the boundary layer by the natural convection at the side wall. As the boundary layer mass flow enters the stratification region (zone with gradation of blue in Figure 123), part of the mass is expulsed due to the adverse temperature gradient[97], which is present due to the hypothesis of liquid discretisation (assumption b) of Section 1.2 of Chapter 6). The expulsed flow exchanges heat with the bulk, increasing the thermal stratification. This flow goes down in the liquid bulk until it meets the upcoming flow of natural convection at the bottom, as indicated by the light blue arrows of Figure 123. Liquid can be filled and withdraw by the storage container, as indicated by the inlet and outlet liquid flows ($\dot{m}_{IN}^{L}$ and $\dot{m}_{OUT}^{L}$). Vapur can be added and removed from the storage tank, respectively using the inlet vapour flow and boil-off gas (BOG) flow ($\dot{m}_{IN}^{V}$ and $\dot{m}_{BOG}$).

1.3. Discretisation approach

In the homogeneous model (H model) and in the homogeneous model 2.0 (H 2.0 model), the dry and wet side walls are discretized in sub-layers. Hence, each liquid sub-layer is composed by the bulk and the boundary layers in liquid stratification model (LS model), as it is illustrated in Figure 124 (a), due to the hypothesis of liquid discretisation (assumption b) of Section 1.2 of Chapter 6). In Figure 124 (a), the blue rectangle is the bulk and the light blue rectangle is the boundary layer. In Figure 124 (b), the light orange rectangle is the ullage and the dashed yellow line is the interface. The rectangles with the degradation of the colour blue are the liquid sub-layers.

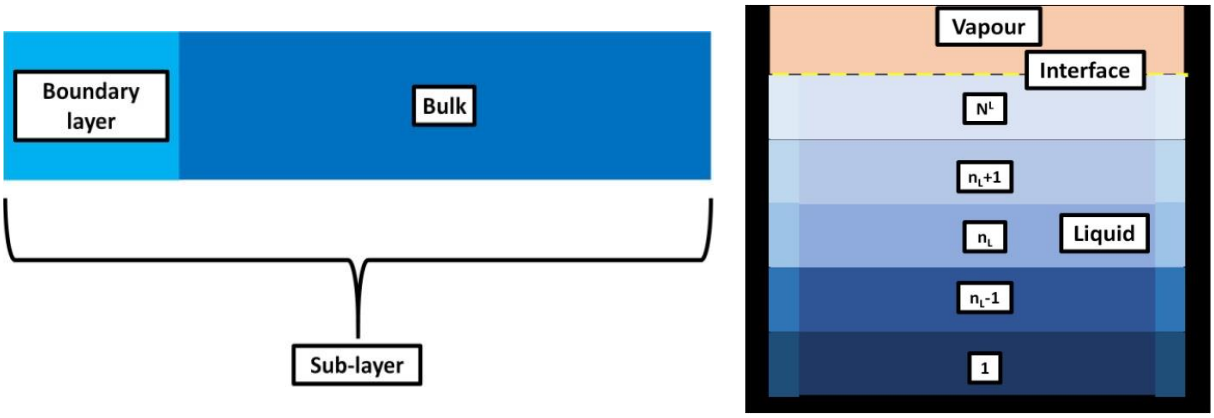

a) b)

Figure 124. a) sub-layer; b) discretized liquid.

As for the H and H 2.0 models, the volume of the boundary layer is much lower than the one of the bulk, and the mass and energy transient can be neglected in this part of the sub-layer. So, the transient of mass and of energy is only considered for the bulk of the sub-layer. As it is indicated in Figure 124 (b), the liquid is discretized in sub-layers, whose number is N^L. The first sub-layer is the one at the bottom and this sub-layer is called *bottom sub-layer*. The last sub-layer is the one near the interface and it is called *interface sub-layer*. Each of the remaining sub-layers is called *core sub-layer*.

---

[97] Adverse temperature gradient is a temperature gradient opposite to the direction of the fluid flow.

1.4. Variables

All the variables of the liquid stratification model (LS model) can be grouped in seven categories. These categories are the one of the homogeneous model (H model) (see Section 1.2 of Chapter 4). Due to the hypothesis of liquid discretisation (assumption b) of Section 1.2 of Chapter 4), the volume, the temperature, and the pressure of the bulk of each sub-layer are considered as well as side surface of the sub-layer, andwall temperature, heat transfer coefficient and heat flow of the sub-layer. So, the number of total variables of the LS model increases. The new variables of the LS model are given in Table 114 according to their category, their name, their symbol, and their unit.

Table 114. Nomenclature of the new variables of the liquid stratification model.

Type of variable	**Name of the variable**	**Symbol**	**Unit**
State	Liquid pressure of the sub-layer n_L	P^L_{nL}	[kPa]
	Liquid temperature of the bulk of the sub-layer n_L	$T^{B,L}_{nL}$	[K]
	Liquid volume of the sub-layer n_L	V^L_{nL}	[m^3]
	Liquid volume of thebulk of the sub-layer n_L	$V^{B,L}_{nL}$	[m^3]
	Thickness of the sub-layer	dxL	[m]
Differential	Time derivate of liquid pressure of the sub-layer n_L	$\frac{\partial P^L_{nL}}{\partial t}$	[kPa/s]
	Time derivate of liquid temperature of the sub-layer n_L	$\frac{\partial T^{B,L}_{nL}}{\partial t}$	[K/s]
	Time derivate of ullage pressure of the sub-layer n_L	$\frac{\partial V^L_{nL}}{\partial t}$	[m^3/s]
	Time derivate of the liquid enthalpy of the sub-layer n_L	$\frac{\partial \widetilde{H}^L_{nL}}{\partial t}$	[J/s]
	Time derivate of the liquid mass of the sub-layer n_L	$\frac{\partial m^L_{nL}}{\partial t}$	[kg/s]
	Time derivate of thickness of the sub-layer n_L	$\frac{\partial dxL}{\partial t}$	[m/s]
	Bulk descending flow rate of sub-layer n_L	$\dot{m}^D_{n_L}$	[kg/s]
	Bulk rising flow rate of the bottom of sub-layer n_L	$\dot{m}^B_{n_L}$	[kg/s]
Heat transfer	Wet side wall temperature of the sub-layer n_L	$T^{SL}_{w,nL}$	[K]
	Effective Wet side wall-to-liquid heat input of the sub-layer n_L	$\dot{Q}^{SL}_{EFF,nL}$	[W]
	Wet side wall-to-liquid heat input of the sub-layer n_L	$\dot{Q}^{SL}_{w,nL}$	[W]
	Wet side wall-to-liquid heat transfer coefficient of the sub-layer n_L	$h^{SL}_{w,nL}$	[W/m^2/K]
Geometrical	Wet side wall surface area of the sub-layer n_L	dA^{SL}_{nL}	[m^2]

The boundary layer variables of the LS model are the same of the H model because the dry and wet side walls are discretized in sub-layer in both the LS and H models. The thermo-physical variables are computed with the reference models (see Chapter 3). For the liquid, these properties are computed at the average temperature and pressure of the liquid, as it is explained later in Section 1.5.1 of Chapter 6. The volume of the liquid sub-layers and the volume of the ullage are computed with the geometrical formulas given in Appendix AA.

1.5. Block structure of the liquid stratification model

The inputs of the liquid stratification model (LS model) are the geometry of the storage containers, the measured values of Boil-Off Rate (BOR), ullage temperature and pressure of Test 1 and Test 2 of the BOR experimental tests, the simulation time of the self-pressurisation, and the initial value of the ullage pressure and of the liquid level, as done for the previous models. Test 1 and Test 2 are respectively done at high and low filling ratio and they are required to define the boundary conditions of the storage container, due to the hypothesis of vapour virtual discretisation (assumption a) of Section 1.2 of Chapter 6). The block structure of the LS model is described in Figure 125.

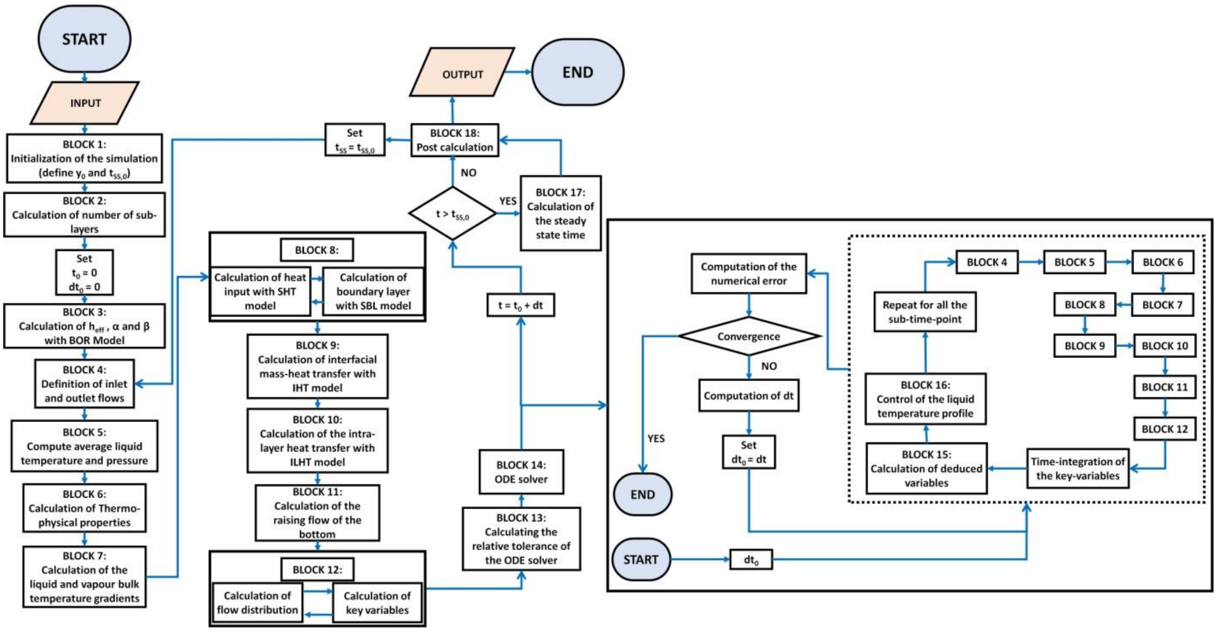

Figure 125. Algorithm of the LS model.

The block structure of the LS model is composed by the following steps:

a) BLOCK 1. The initial values of the vector of state variables is calculated with the initial values of the pressure and of the filling ratio, which are input values of the LS model (see Section 1.3.1 of Chapter 3). The value of first try of the steady state time is computed as it is explained in Section 1.3.3 of Chapter 4.

b) BLOCK 2. The numbers of sub-layers of the dry and wet side walls are calculated with the same approach that is described in Section 1.3.1 of Chapter 4. In this approach, the number of sub-layers is increased from the first try value to the value at which the relative numerical error is lower than the defined relative tolerance. The increment of the number of sub-layers increases the accuracy and the computational time. Being more complex than the others, the computational time needed for simulating the storage by means of the LS model is expected to he higher. So, the relative numerical error of the liquid is reduced as seen in Table 115.

Table 115. Values of tolerance.

Sub-layer	Tolerance
Liquid	10^{-3}
Vapour	10^{-4}

The Storage Heat Transfer (SHT) and Storage Boundary Layer (SBL) models of the LS model, which are used in calculation, are the same of the homogeneous model 2.0 (H 2.0 model) for the dry side wall. Whereas dedicated SHT and SBL models have been developed for the wet side wall of the LS model.

c) BLOCK 3. The effective heat transfer coefficient (h_{eff}) of the storage container, and the alpha and beta corrective coefficients (α and β) are computed with the Boil-Off rate (BOR) model. The algorithms and the theory of the BOR model are the ones developed for the H 2.0 model

d) BLOCK 4. The inputs and the output flows of the storage containers are defined as explained in Chapter 3. Thus, the inlet vapour and the outlet liquid mass flows are equal to zero. Temperature and pressure of inlet vapour and Boil-Off Gas (BOG) flow are respectively equal to the ullage temperature at the roof ($T^V_{N^V}$) and to the pressure of the ullage. The temperature and the pressure of the liquid inlet and outlet mass flows are the ones of the bottom sub-layer.

e) BLOCK 5. The average liquid temperature and pressure are calculated as it is explained later in Section 1.5.1 of Chapter 6.

f) BLOCK 6. The thermo-physical properties of liquid (vapour) (see Table 49) are calculated with the reference models (see Section 4 of Chapter 3) at the average (ullage) temperature and pressure;

g) BLOCK 7. The ullage bulk temperature gradient is computed considering the temperature difference between the ullage and the interface, as it is explained in Section 1.3.1 of Chapter 5. The liquid bulk temperature gradient is computed in every sub-layer with the approach of the finite difference, as it is explained later in Section 1.5.2 of Chapter 6;

h) BLOCK 8. The heat transfer variables at the walls of the storage container are calculated with the SHT model, which computes the heat transfer coefficients at the wet and dry side walls from the values of the thickness and of velocity in the boundary layer. The boundary layer variables are computed with the SBL model at each surface of the storage containers. So, the SHT and the SBL models are simultaneously executed due to the relation between the heat transfer and the boundary layer variables (see Section 4.6 of Chapter 4);

i) BLOCK 9. The vapour-to-interface and the liquid-to-interface heat flows, and the net mass flow are calculated with the Interface Heat Transfer (IHT) model, which is described in Section 4 of Chapter 6. The algorithms and the theory to compute the vapour-to-interface heat flow are the same used in the H 2.0 model. The net mass flow and the liquid-to-interface heat flows are computed with a different theory than the one used for the H 2.0 model.

j) BLOCK 10. The heat flow across the sub-layers of the liquid is computed with the intra-layer heat transfer (ILHT) model, which is later explained in Section 4 of Chapter 6;

k) BLOCK 11. The behaviour of the cryogenic liquids depends on the distribution of the convective flows in the liquid. these convective flows are the descending flows ($\dot{m}^{D,L}_{n_L+1}$) and the rising flow of hte bottom ($\dot{m}^{B}_{n_L}$). This disctribution is calculated with the fluid-dynamics at the wet side wall and by the fluid-dynamics at the bottom. The fluid-dynamics at the bottom is characterized by the bottom rising flows, which rise in the liquid bulk. These flows are calculated as it is later explained in Section 3 of Chapter 6;

l) BLOCK 12. The indipendent variables of the LS model (see Table 118) are computed solving the corresponding system of equations. The indipendent variables and these equations are reported in Section 1.6 of Chapter 6. Being the value of the direction of descending flow ($\dot{m}^{D,L}_{n_L+1}$) needed in the system of equation and a function of the indipendent variables (see Section 1.6 of Chapter 6), the calculation of the indipendent variables. The resolution of the equations are simultaneously done with an iterative procedure (as explained in Appendix AD);

m) BLOCK 13. To reduce the computational time, the values of the relative tolerance should increase when the values of time-derivate of the state variables are low and it should reduce if these values are high. Using this idea, the relative tolerance of the Ordinary Differential Equations (ODEs) system is computed at every time-point, similarly to the homogeneous model (H model). To reduce the computational time, the values of the relative tolerance are increased. The values of the relative tolerance and the conditions to select them are reported in Table 116.

Table 116. Values of the relative tolerance.

Condition	$\Omega_{MAX} \geq 5 \cdot 10^{-1}$	$5 \cdot 10^{-2} \leq \Omega_{MAX} < 5 \cdot 10^{-1}$	$\Omega_{MAX} < 5 \cdot 10^{-2}$

Tolerance	10^{-4}	10^{-3}	10^{-3}

Ω_{MAX} is the absolute maximum ratio of the time-derivates (see Section 1.3.2 of Chapter 4).

n) BLOCK 14. The ODEs system of the LS model is still solved with the method of Runge-Kutta-Fehlberg with Cash-Karp parameters (RKF-CKp) [131] (see Section 5 of Chapter 3). When this method is used, the Block 4, 5, 6, 7, 8, 9, 10, 11 and 12 are used to compute the variables of the ODEs system at the different sub time-point of this method. The variables of the ODEs system are the differential variables of the mathematical system, as described later in Section 1.6 of Chapter 6. The Block 15 and Block 16 are used at each sub-time step:
    a. BLOCK 15. The dipendent variables of the mathematical system (see Table 118) are calculated with the values of the state variables that are obtained from the ODEs solver;
    b. BLOCK 16: the computed values of the temperature liquid temperature profiles are analyzed to understand if these values are physically or not. This "control" will be explained in Section 1.5.3 of Chapter 6;

o) BLOCK 17. If the computed time is higher than first try of the steady state time of Block 1 (step a) of Section 1.5 of Chapter 6), the steady state time is calculated. If the storage container is at steady state, the steady state time is equal to the values of first try, as it is explained in Section 1.3.3 of Chapter 4.

p) BLOCK 18. This block is composed by a series of logical steps to determine if the storage mode can be shifted from steady state to self-pressurisation. This change of the storage mode is done if the simulated time is above the steady state time. This block is identical to the post-calculation block of EQ model (see Section 1.3.3 of Chapter 3).

Block 5, 7 and 16 are respectively described in Section 1.5.1, in Section 1.5.2 and in Section 1.5.3.

1.5.1. Block 5: average liquid temperature and pressure

Seeing that this work deals only with pure fluids, the thermo-physical properties depend only on the temperature and pressure. To reduce the computational time, the thermo-physical properties of the liquid are computed at the average liquid temperature and pressure, instead of being computed at the temperature and pressure of each sub-layer.

Section 1.5.1.1 explains how the average liquid temperature is computed. Section 1.5.1.2 presents the equation to compute the average liquid pressure.

1.5.1.1. Average liquid temperature

Liquid discretisation (assumption b) of Section 1.2 of Chapter 6) means that the temperature is heterogeneous in the liquid and a temperature profile is present. So, the overall energy of the liquid can be computed as follows:

Equation 279 $$U^L = \sum_{n_L=1}^{N^L} U^L_{n_L}$$

In Equation 279, U^L is the overall internal energy of the liquid and $U^L_{n_L}$ is the internal liquid energy of each sub-layer. Due to the theorem of the mean integral value[98], the overall internal energy can be computed as the product between the overall mass and the mean value of the overall specific internal

---

[98] Theorem of the mean integral value : $(a-b)\cdot\bar{y} = \int_b^a y(x)dx$

energy. The specific internal energy can be computed asproduct between the isochoric specific heat (C_V^L) and the temperature. The mass is the product between the volume and the density (ρ^L). Hence, Equation 279 can be written as follows:

Equation 280 $$\rho^L \cdot V^L \cdot C_V^L \cdot T^L = \sum_{n_L=1}^{N^L} \rho^L \cdot C_V^L \cdot V_{n_L}^{SL} \cdot T_{n_L}^{B,L}$$

The density and the isochoric specific heat are computed at the average liquid temperature and pressure. So, the values of these variables of the left term are equal to the one of the right term. So, Equation 281 can be written as follows:

Equation 281 $$V^L \cdot T^L = \sum_{n_L=1}^{N^L} V_{n_L}^{SL} \cdot T_{n_L}^{B,L}$$

Thus, the average liquid temperature (T^L) can be computed as follows:

Equation 282 $$T^L = \frac{1}{V^L} \cdot \sum_{n_L=1}^{N^L} V_{n_L}^{SL} \cdot T_{n_L}^{B,L}$$

V^L is the overall liquid volume and it is calculated as it is described in Appendix AA.

1.5.1.2. Average liquid pressure

Liquid discretization (assumption b) of Section 1.2 of Chapter 6) also means a pressure profile in the liquid phase, with pressure increasing from the interface to the bottom due to the hypostatic pressure effect[99]. Using the theorem of the integral mean value, the average liquid pressure can be computed as follows:

Equation 283 $$P^L = \frac{1}{V^L} \cdot \sum_{n_L=1}^{N^L} V_{n_L}^{SL} \cdot P_{n_L}^{L}$$

$P_{n_L}^L$ is computed with the algorithm of the liquid pressure of the homogeneous model (H model) (see Section 4 of Appendix L), applied at each sub-layer

1.5.2. Block 7: ullage and liquid bulk temperature gradient

Due to the hypotheses of vapour virtual stratification and of liquid discretisation (assumption a) and b) of Section 1.2 of Chapter 6), the ullage and the liquid bulk temperature gradient have to be computed and considered in the fluid-dynamics of the dry and wet side walls, respectively. The hypothesis of vapour virtual stratification (assumption a) of Section 1.2 of Chapter 6) is the one used in the homogeneous (H 2.0) model, thus the ullage bulk temperature gradient is computed as it is explained in see Section 1.2 of Chapter 5. The liquid bulk temperature gradient has to be computed for each sub-layer, due to the hypothesis of liquid discretisation (assumption b) of Section 1.2 of Chapter 6). Since the liquid is discretized, these gradients can be computed with the finite difference approach[100], as follows:

---

[99] Hypostatic pressure : $\Delta P = H \cdot \rho \cdot g$

[100] The finite difference approach is a numerical method that computes the derivate as the ratio between the difference of variables an interval and the length of this interval.

Equation 284 $$\frac{\partial T^{L}_{n_L}}{\partial x} = \frac{T^{B,L}_{n_L} - T^{B,L}_{n_L-1}}{dxL}$$

dxL is reported in Table 114. For the bottom sub-layer, Equation 284 cannot be used because the variable $T^{B,L}_{0}$ does not exit. So, the bulk temperature gradient at the bottom sub-layer is calculated as follows:

Equation 285 $$\frac{\partial T^{L}_{1}}{\partial x} = \frac{T^{B,L}_{2} - T^{B,L}_{1}}{dxL}$$

$T^{B,L}_{2}$ is the liquid temperature of the sub-layer above the bottom sub-layer.

1.5.3. Block 16: control of the temperature profile

As it is experimentally observed [24]–[30], the liquid temperature profile is flat, except for some fluctuations during the steady state of a cryogenic storage container at constant pressure. During the self-pressurisation, the liquid temperature monotonically increases from the core to the interface. In the core, the temperature is homogeneous and can slightly increases near the bottom. In the liquid stratification model (LS model), the temperature profile is deduced from the values of the liquid temperature of the bulk of the sub-layer. These values are computed with the Ordinary Differential Equations (ODEs) solver from the equations of the mathematical system (see Table 119). So, the computed temperature profile cannot monotonically increase due to possible hot and cold spots that are produced from the ODEs solver. These hot and cold spots are respectively described in Figure 126 for the steady state and for the self-pressurisation. In Figure 126, the black rectangles are the walls of the storage container. The light blue is the liquid. The yellow dashed line is the interface. The purple points are the measured experimental data. The green line is the computed temperature profile. The green points are the hot-cold spots. The blue and the red circles are respectively the cold and the hot spot. The orange circle is the interface temperature.

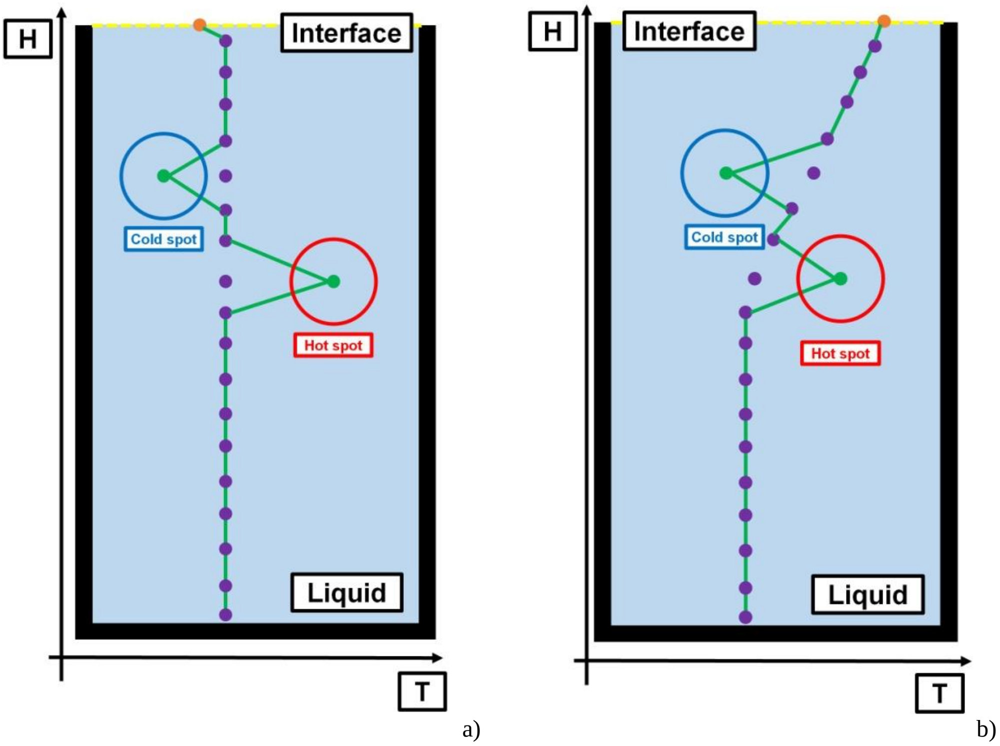

a) b)

Figure 126. Hot and cold spots in the liquid temperature profile: a) steady state; b) self-pressurisation.

During the steady state, the liquid is slightly overheated[1],[2] and the temperature is almost homogeneous. The interface temperature is lower than the liquid temperature in the bulk. Hence, the liquid bulk temperature in each sub-layer ($T_{n_L}^{B,L}$) is equal to the average liquid temperature (T^L), if a hot or cold spots are observed in the temperature profile. If this condiciont does noto occur, the values of the temperature $T_{n_L}^{B,L}$ are the ones of the ODE solver.

During the self-pressurisation, the liquid temperature monotonically increases from the core to the interface. The interface temperature is higher than the average liquid temperature. If there is a cold spot, the density of the sub-layer is higher than the one of the lower sub-layers. When there is a hot spot, the density of the sub-layer is lighter than the one of the upper sub-layer. In both cases, the liquid mixes in all the sub-layers below the cold spot and below the upper sub-layer of the cold spot. Hence, the liquid bulk temperature of the sub-layers below the cold spot and below the upper sub-layer of the cold spot is equal to the average liquid temperature of these sub-layers. The results of the approach to correct the temperature profile are reported in Figure 127. The colours in Figure 127 are the one used in Figure 126.

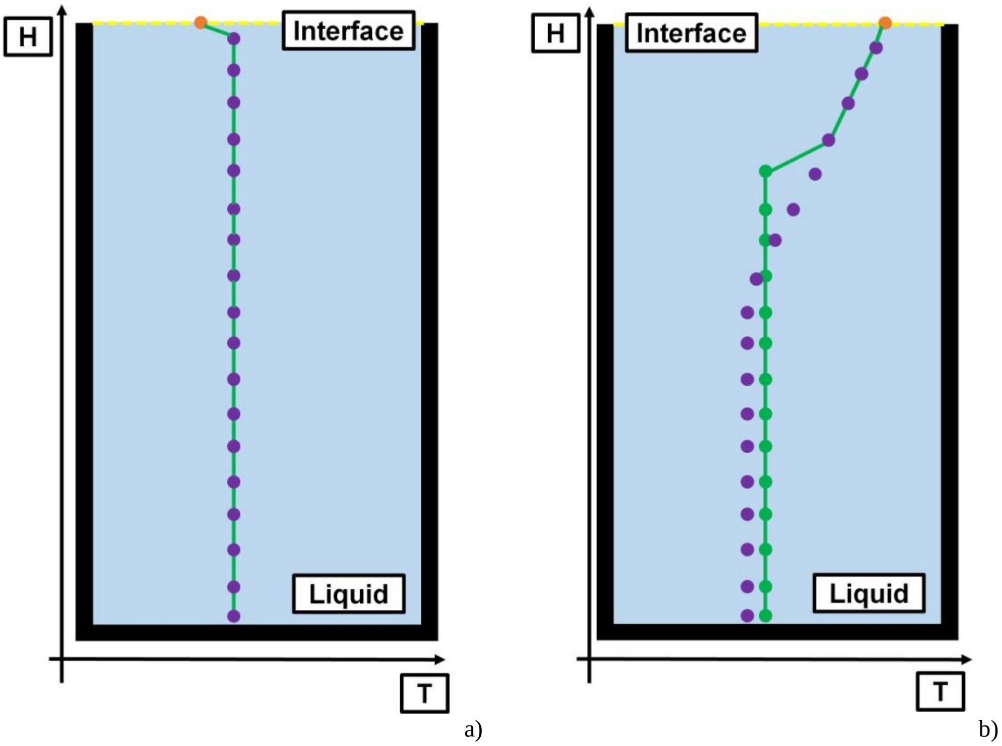

Figure 127. Corrected liquid temperature profile: (a) steady state; (b) self-pressurisation

As indicated in Figure 127, the corrected liquid temperature profile cannot be in agreement with the experimental data due to the proposed approach that respect the energy conservation laws.

To sum up, the bulk temperature can be computed with the equations of Table 117, in case of hot and cold spots:

Table 117. Equations to correct the liquid temperature profiles.

Name	Equation	Formula	Condition
Steady state formula	Equation 286	$T_{n_L}^{B,L} = T^L$	$T^L > T^I$
Self-pressurisation formula	Equation 287	$T_{n_L}^{B,L} = \bar{T}^L$	$T^L \leq T^I$

The average liquid temperature (T^L) is computed with Equation 285. The variable $\bar{T}^L$ is called the pseudo-average liquid temperature and it computed with Equation 285, applied to the sub-layers below the cold spot or to the sub-layer below the upper sub-layer of the cold spot. As it is indicated in Table

117, the steady state formula (Equation 286) can be used during the self-pressurization, if average liquid temperature is higher than the interface temperature.

1.6.Mathematical system

As for the previous models, the liquid stratification model (LS model) is developed for predicting the behaviour of a cryogenic liquid for the two storage modes: steady state (mode 1.b) and self-pressurisation (mode 4). The variables of the mathematical system are called target variables, and these can be divided into key and dipendent variables. As for the homogeneous model (H model), the mathematical system of the LS model is composed by the target equations, which are the formulas required for computing the time-evolution of the state variables. These equations are divided into algebraic and differential equations, which are deduced from the energy and mass conservation laws. The dipendent variables are computed with the algebraic equations from the independent one. Indipendent and dipendent variables, and differential and algebraic equations are reported in Table 118.

Table 118. Target equations and variables of mathematical systems of LS model.

Target variables		***Target equations***	
Type	**Symbol**	**Type**	**Name**
Indipendent	$\frac{\partial P^V}{\partial t}$	Differential	Pressure evolution (P-e) equations (Equation 483 and Equation 487)
	$\frac{\partial dxL}{\partial t}$	Differential	Thickness evolution (dxL-e) equations (Equation 484 and Equation 488)
	$\frac{\partial V^L}{\partial t}$	Differential	Liquid volume evolution (V^L-e) equations (Equation 329)
	$\frac{\partial V^L_{1,\ldots,n_L,\ldots N^L}}{\partial t}$	Differential	Sub-layer Liquid volume evolution (V^L_{nL}-e) equation (Equation 328)
	$\frac{\partial T_1^{B,L}}{\partial t}$	Differential	bottom sub-layer Liquid temperature evolution (T^L_1-e) equation (Equation 435)
	$\frac{\partial T_{n_L}^{B,L}}{\partial t}$	Differential	Core sub-layer Liquid temperature evolution (T^L_{nL}-e) equation (Equation 436)
	$\frac{\partial T_{N^L}^{B,L}}{\partial t}$	Differential	Interface sub-layer Liquid temperature evolution (T^L_{NL}-e) equation (Equation 437)
	$\frac{\partial T^V}{\partial t}$	Differential	Liquid temperature evolution (T^V-e) equation(Equation 438)
	$\dot{m}_2^{D,L}$	Algebraic	First descending flow (FDF) equation (Equation 459)
	$\dot{m}^{D,L}_{3,\ldots,(n_L+1),\ldots,N^L}$	Algebraic	Descending flow equation (CDF) (Equation 460)
	$\dot{m}_{BOG}$	Algebraic	Boil-off Gas (BOG) equations (Equation 485 and Equation 489)
	$\dot{m}^L_{IN}$	Algebraic	Inlet Liquid Flow (ILF) equations (Equation 486 and Equation 490)
Dependent	V^V	Algebraic	Volume conservation equation (Equation 654)
	P^L_{nL}	Algebraic	Hydrostatic pressure equation (Equation 1107)
	P^I	Algebraic	Pressure equality equation (see Section 1.4 of Chapter 4)
	T^I	Algebraic	Saturation pressure equation (Equation 738)

The P-e, dxL-e, V^L-e, V^L_{nL}-e, T^L_1-e, T^L_{nL}-e, T^L_{NL}-e and T^V-e, FDF, CDF, BOG and ILF equations are deduced from the mass and energy conservation laws, as it is explained in Section 2 of Chapter 6.

1.7. Algebraic Differential Equations systems

As it is reported in Table 118, the mathematical system of the liquid stratification model (LS model) is composed by the algebraic and differential equations. In the previous models, the algebraic equations can be separated from the differential equations, which form the Ordinary Differential Equation (ODEs) system. In the LS model, the differential equations cannot be separated from the equations of the descending flows (Equation 459 and Equation 460), which are algebraic equations because the liquid temperature equations (Equation 435, Equation 436, and Equation 437) directly depends on the values of the descending flows ($\dot{m}_2^{D,L}$ and $\dot{m}^{D,L}_{3,\dots,(n_L+1),\dots,N^L}$). As consequence, the mathematical system of the LS model is composed by the Differential Algebraic Equations (DAEs) system. Taking into account that the LS model can be applied in two operative modes (steady state and self-pressurisation), the DAEs system of the LS model is composed as it is described in Table 119.

Table 119. DAEs systems for LS model.

Storage modes	Self-pressurisation (4)	Steady state (1.b)
Equations	Equation 483	Equation 487
	Equation 484	Equation 488
	Equation 485	Equation 489
	Equation 486	Equation 490
	Equation 329	Equation 329
	Equation 328	Equation 328
	Equation 435	Equation 435
	Equation 436	Equation 436
	Equation 437	Equation 437
	Equation 438	Equation 438
	Equation 459	Equation 459
	Equation 460	Equation 460

The descending flows ($\dot{m}_2^{D,L}$ and $\dot{m}^{D,L}_{3,\dots,(n_L+1),\dots,N^L}$) are calculated as function of the time-derivates of the pressure and of the thickness of the sub-layer, which does not directly depend on these flows. These flows can be computed, after calculating these time-derivates. So, the equations of the descending flows (Equation 459 and Equation 460) can be removed from the DEAs systems and the remaining equations form the Ordinary Differential Equations (ODEs) system. This ODE can be solved using the lethod of Runge-Kutta-Fehlberg with Cash-Karp parameters (RKF-CKp) [131] (see Section 5 of Chapter 3).

2. Procedure to obtain the mathematical system

For reducing the computational time while maintaining a reasonable accuracy, the indipendent variables of the mathematical system can should be explicitly computed. So, the pressure-evolution (P-e), the thickness-evolution (dxL-e), liquid volume (V^L-e), sub-layer liquid volume (V^L_{nL}-e), bottom sub-layer liquid temperature (T^L_1-e), sub-layer liquid temperature evolution (T^L_{nL}-e), interface sub-layer liquid temperature evolution (T^L_{NL}-e) and ullage temperature evolution (T^V-e), first descending flow (FDF), core descending flow (CDF), boil-off gas (BOG) and inlet liquid flow (ILF) equations have to be rearranged to provide explicit expressions of the indipendent variables. These explicit equations can be deduced from the mass and energy conservation laws following the mathematical procedure described in Figure 128.

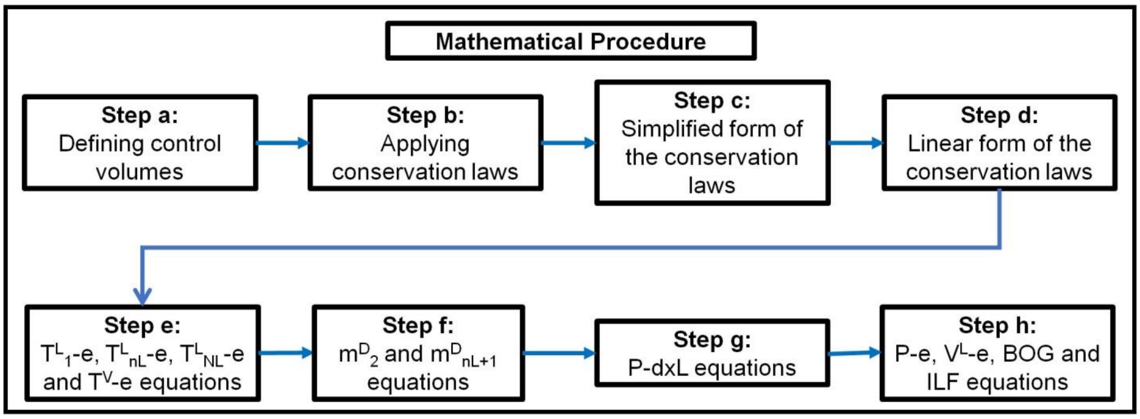

Figure 128. Mathematical procedure.

As it is illustrated in Figure 128, the method is composed by the following steps:

a) Defining the control volumes;
b) Applying the mass and energy conservation laws;
c) Deducing the simplified conservation laws (aka balance equations);
d) Obtaining linear form of the balance equations;
e) Deducing T^L_1-e, T^L_{nL}-e, T^L_{NL}-e and T^V-e equations;
f) Obtaining FDF and CDF equations;
g) Deducing the pressure-thickness (P-dxL) equations;
h) Obtaining the P-e, dxL-e, BOG and ILF equations;

Section 2.1, 2.2, 2.3, 2.4, 2.5, 2.6, 2.7 and 2.8 respectively describe steps a), b), c), d), e), f), g) and h).

2.1. Control volumes

The first step of the mathematical procedure step (step a) of Section 2 of Chapter 6) is the definition of the control volumes is the first step, as it is described in Figure 128. Due to the hypothesis of vapour virtual stratification (assumption a) of Section 1.2 of Chapter 6), the control volume of the vapour is the one reported in Section 2.2 of Chapter 5. Due to the hypothesis of liquid stratification (assumption b) of Section 1.2), the liquid is divided into sub-layers, and each sub-layer is decomposed into the bulk and the boundary layer, which is described in the Storage Boundary Layer (SBL) model. Hence, only the bulk of the sub-layers are considered as control volumes of the liquid.

Due to the heat inputs at the wet side wall, the liquid is pushed by bouyancy forces and it moves upward along this side wall. During this movement, mass is entrained from the bulk to the boundary layer. The liquid flow along the wet side wall can reduce when the temperature gradient in the bulk and mass flows from the boundary layer to the bulk. Uncer certains conditions, the liquid flow along the wet side wall can stop. At the interface, the mass flow of the wet side wall goes down, creating a descending mass flow in the core. So, the directions of descending flow and boundary-to-bulk flow can change with the variation of the mass flow in the boundary layer of the wet side wall. The heat inputs at the bottom create a rising flow that transport energy from the bottom to the core of the liquid. Due to the liquid temperature gradient, heat is transferred across the liquid from the interface to the bulk. As consequence, the liquid bulk of the sub-layer can be described with the control volumes of Figure 129. In Figure 129, the blue colour indicates the liquid. The green and black arrows are respectively the net mass flow and the inlet and outlet mass flows. The red arrows refer to the enthalpy flows. The white arrows with red border are the heat leakage rates. The yellow dashed line is the interface.

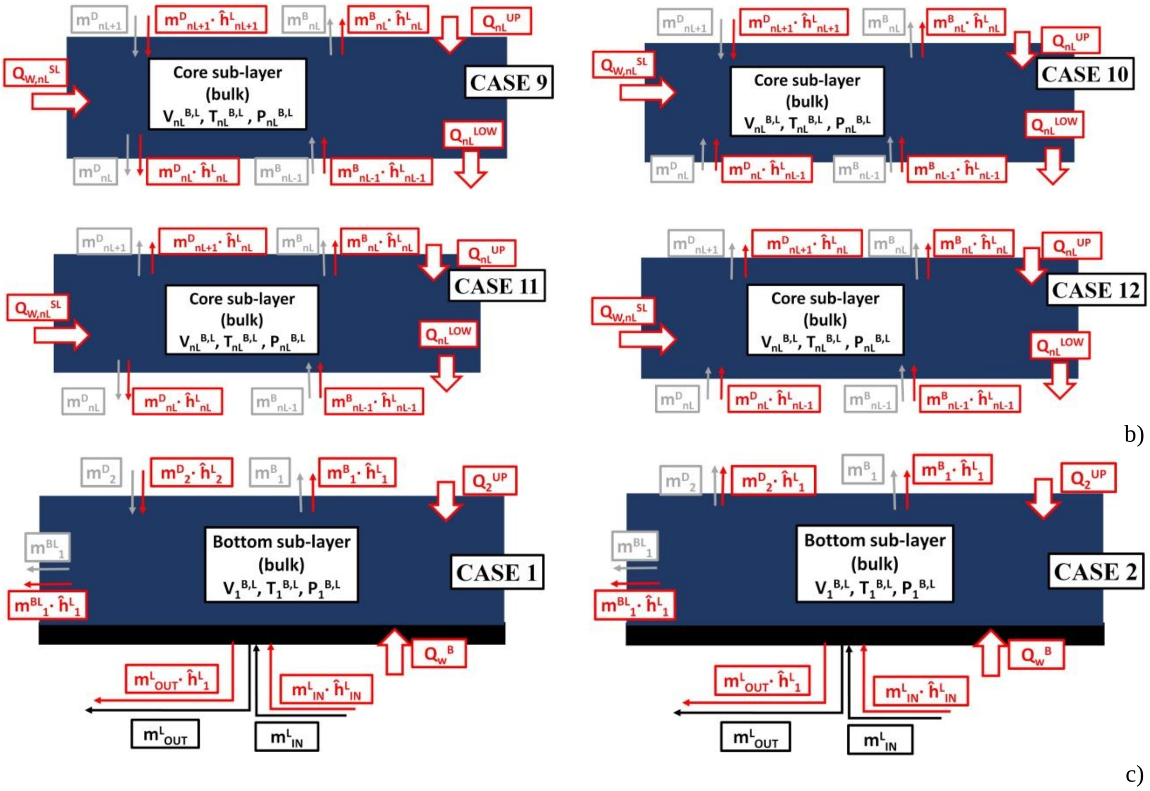

Figure 129. Control volumes of the LS model: a) interface-liquid; b) bulk-liquid; c) bottom-liquid.

As described by Figure 129, liquid stratification model (LS model) can be decomposed into three control volumes: *interface-liquid energy-mass*, *bulk-liquid energy-mass* and *bottom-liquid energy-mass*. These control volumes consider the descending mass flow ($\dot{m}_{n_L+1}^{D,L}$), the bottom rising mass flow ($\dot{m}_{n_L}^{B}$), the boundary layer-to-bulk mass flow ($\dot{m}_{n_L}^{BL}$), and the enthalpy flows accompanying each mass flow. The heat inputs are present at the bottom and these heat flows enter the bulk of the bottom sub-layer. The natural convection at the wet side wall can stop and the mass flow in the boundary layer can be equal to zero. Heat is, however, transferred from the wet wall to the bulk. So, the wet side wall-to-liquid heat flow is directly added to the control volume only when there is no mass flow in the boundary layer. As it is described in Figure 129, two intra-layer heat flows are considered: the upper and the lower heat flows ($\dot{Q}_{n_L}^{UP}$ and $\dot{Q}_{n_L}^{LOW}$). The upper heat flow is the heat enchanged between the upper sub-layer and the current one. The lower heat flow is the thermal energy transferred between the current sub-layer and the lower one. As reported in Figure 129, different cases of control volumes are present due to the direction of the descending flow and of the boundary layer-to-bulk flow. These cases are reported in Table 120.

Table 120. Cases of the control volumes.

	Liquid interface sub-layer
Case 1	$\dot{m}_{N^L}^{D,L}$ is directed downward. $\dot{m}_{n_L}^{BL,L}$ exits the boundary layer.
Case 2	$\dot{m}_{N^L}^{D,L}$ is directed upward. $\dot{m}_{n_L}^{BL,L}$ exits the boundary layer.
Case 3	$\dot{m}_{N^L}^{D,L}$ is directed downward. $\dot{m}_{n_L}^{BL,L}$ is equal to zero.
Case 4	$\dot{m}_{N^L}^{D,L}$ is directed upward. $\dot{m}_{n_L}^{BL,L}$ is equal to zero.
	Bottom liquid sub-layer
Case 1	$\dot{m}_2^{D,L}$ is directed downward.
Case 2	$\dot{m}_2^{D,L}$ is directed upward.
	Bulk-liquid sub-layer

Case 1	$\dot{m}_{n_L}^{BL,L}$ enters the boundary layer. $\dot{m}_{n_L+1}^{D,L}$ and $\dot{m}_{n_L}^{D,L}$ are directed downward.
Case 2	$\dot{m}_{n_L}^{BL,L}$ enters the boundary layer. $\dot{m}_{n_L+1}^{D,L}$ is directed downward and $\dot{m}_{n_L}^{D,L}$ is directed upward.
Case 3	$\dot{m}_{n_L}^{BL,L}$ enters the boundary layer. $\dot{m}_{n_L+1}^{D,L}$ is directed upward and $\dot{m}_{n_L}^{D,L}$ is directed downward.
Case 4	$\dot{m}_{n_L}^{BL,L}$ enters the boundary layer. $\dot{m}_{n_L+1}^{D,L}$ and $\dot{m}_{n_L}^{D,L}$ are directed upward.
Case 5	$\dot{m}_{n_L}^{BL,L}$ exits the boundary layer. $\dot{m}_{n_L+1}^{D,L}$ and $\dot{m}_{n_L}^{D,L}$ are directed downward.
Case 6	$\dot{m}_{n_L}^{BL,L}$ exits the boundary layer. $\dot{m}_{n_L+1}^{D,L}$ is directed upward and $\dot{m}_{n_L}^{D,L}$ is directed downward.
Case 7	$\dot{m}_{n_L}^{BL,L}$ exits the boundary layer. $\dot{m}_{n_L+1}^{D,L}$ is directed downward and $\dot{m}_{n_L}^{D,L}$ is directed upward.
Case 8	$\dot{m}_{n_L}^{BL,L}$ exits the boundary layer. $\dot{m}_{n_L+1}^{D,L}$ and $\dot{m}_{n_L}^{D,L}$ are directed upward.
Case 9	$\dot{m}_{n_L}^{BL,L}$ is equal to zero. $\dot{m}_{n_L+1}^{D,L}$ and $\dot{m}_{n_L}^{D,L}$ are directed downward.
Case 10	$\dot{m}_{n_L}^{BL,L}$ is equal to zero. $\dot{m}_{n_L+1}^{D,L}$ is directed downward and $\dot{m}_{n_L}^{D,L}$ is directed upward.
Case 11	$\dot{m}_{n_L}^{BL,L}$ is equal to zero. $\dot{m}_{n_L+1}^{D,L}$ is directed upward and $\dot{m}_{n_L}^{D,L}$ is directed downward.
Case 12	$\dot{m}_{n_L}^{BL,L}$ is equal to zero. $\dot{m}_{n_L+1}^{D,L}$ and $\dot{m}_{n_L}^{D,L}$ are directed upward.

For the bottom-liquid sub-layer, the mass flow rate in the boundary layer ($\dot{m}_1^{UP}$) is computed with the exact boundary layer (EBL) approach of SBL model (see Section 1 of Appendix P). So, $\dot{m}_1^{BL}$ always higher than zero and it enters the boundary layer. There is only one case for bottom-liquid sub-layer.

2.2. Conservation laws

The application of the energy and mass conservation laws is the second step (step b) of Section 2 of Chapter 6) of the mathematical procedure, as it is presented in Figure 128. Considering the heat flows and the enthalpy flows of Figure 129, the mass and energy conservation laws of the liquid stratification model (LS model) are the ones that are reported in Table 121.

Table 121. Energy and mass balance equations of the LS model.

		Volume
Volume balance	Equation 288	$\frac{\partial V^V}{\partial t} + \sum_{n_L=1}^{N^L} \frac{\partial V_{n_L}^L}{\partial t} = 0$
		Ullage
Vapour mass balance	Equation 289	$\frac{\partial m^V}{\partial t} = \dot{m}_{IN}^V + \dot{m}_N - \dot{m}_{BOG}$
Vapour energy balance	Equation 290	$\frac{\partial \widetilde{H}^V}{\partial t} = \dot{m}_N \cdot \tilde{h}_S^V - \dot{Q}_I^V - \dot{m}_{BOG} \cdot \tilde{h}_{N^V}^V + \dot{m}_{IN}^V \cdot \tilde{h}_{IN}^V + \dot{Q}_W^{SV}$
		Interface-liquid sub-layer
Case 1	Equation 291	$\frac{\partial \widetilde{H}_{N^L}^L}{\partial t} = -\dot{Q}_I^L - \dot{Q}_{N^L}^{LOW} - \dot{m}_{N^L}^{D,L} \cdot \tilde{h}_{N^L}^{B,L} + \dot{m}_{N^L}^{BL,L} \cdot \tilde{h}_{N^L}^{BL,L} - \dot{m}_N \cdot \tilde{h}_S^L + \dot{m}_{N^L-1}^B \cdot \tilde{h}_{N^L-1}^{B,L}$
	Equation 292	$\frac{\partial m_{N^L}^L}{\partial t} = -\dot{m}_{N^L}^{D,L} + \dot{m}_{N^L}^{BL,L} - \dot{m}_N + \dot{m}_{N^L-1}^B$
Case 2	Equation 293	$\frac{\partial \widetilde{H}_{N^L}^L}{\partial t} = -\dot{Q}_I^L - \dot{Q}_{N^L}^{LOW} + \dot{m}_{N^L}^{D,L} \cdot \tilde{h}_{N^L-1}^{B,L} + \dot{m}_{N^L}^{BL,L} \cdot \tilde{h}_{N^L}^{BL,L} - \dot{m}_N \cdot \tilde{h}_S^L + \dot{m}_{N^L-1}^B \cdot \tilde{h}_{N^L-1}^{B,L}$
	Equation 294	$\frac{\partial m_{N^L}^L}{\partial t} = \dot{m}_{N^L}^{D,L} + \dot{m}_{N^L}^{BL,L} - \dot{m}_N + \dot{m}_{N^L-1}^B$
Case 3	Equation 295	$\frac{\partial \widetilde{H}_{N^L}^L}{\partial t} = -\dot{Q}_I^L - \dot{Q}_{N^L}^{LOW} - \dot{m}_{N^L}^{D,L} \cdot \tilde{h}_{N^L}^{B,L} + \dot{Q}_{w,N^L}^{SL} - \dot{m}_N \cdot \tilde{h}_S^L + \dot{m}_{N^L-1}^B \cdot \tilde{h}_{N^L-1}^{B,L}$
	Equation 296	$\frac{\partial m_{N^L}^L}{\partial t} = -\dot{m}_{N^L}^{D,L} - \dot{m}_N + \dot{m}_{N^L-1}^B$
Case 4	Equation 297	$\frac{\partial \widetilde{H}_{N^L}^L}{\partial t} = -\dot{Q}_I^L - \dot{Q}_{N^L}^{LOW} + \dot{m}_{N^L}^{D,L} \cdot \tilde{h}_{N^L-1}^{B,L} + \dot{Q}_{w,N^L}^{SL} - \dot{m}_N \cdot \tilde{h}_S^L + \dot{m}_{N^L-1}^B \cdot \tilde{h}_{N^L-1}^{B,L}$
	Equation 298	$\frac{\partial m_{N^L}^L}{\partial t} = \dot{m}_{N^L}^{D,L} - \dot{m}_N + \dot{m}_{N^L-1}^B$
		Bottom-liquid sub-layer
Case 1	Equation 299	$\frac{\partial \widetilde{H}_1^L}{\partial t} = \dot{Q}_w^B + \dot{m}_2^{D,L} \cdot \tilde{h}_2^{B,L} - \dot{m}_1^B \cdot \tilde{h}_1^{B,L} - \dot{m}_1^{BL,L} \cdot \tilde{h}_1^{B,L} + \dot{Q}_1^{UP} + \dot{m}_{IN}^L \cdot \tilde{h}_{IN}^L - \dot{m}_{OUT}^L \cdot \tilde{h}_1^{B,L}$

Table 121. Energy and mass balance equations of the LS model.

	Equation 300	$\frac{\partial m_1^L}{\partial t} = \dot{m}_2^{D,L} - \dot{m}_1^{B} - \dot{m}_1^{BL,L} + \dot{m}_{IN}^{L} - \dot{m}_{OUT}^{L}$
Case 2	Equation 301	$\frac{\partial \widetilde{H}_1^L}{\partial t} = \dot{Q}_w^{B} - \dot{m}_2^{D,L} \cdot \tilde{h}_1^{B,L} - \dot{m}_1^{B} \cdot \tilde{h}_1^{B,L} - \dot{m}_1^{BL,L} \cdot \tilde{h}_1^{B,L} + \dot{Q}_1^{UP} + \dot{m}_{IN}^{L} \cdot \tilde{h}_{IN}^{L} - \dot{m}_{OUT}^{L} \cdot \tilde{h}_1^{B,L}$
	Equation 302	$\frac{\partial m_1^L}{\partial t} = -\dot{m}_2^{D,L} - \dot{m}_1^{B} - \dot{m}_1^{BL,L} + \dot{m}_{IN}^{L} - \dot{m}_{OUT}^{L}$
	Bulk-liquid sub-layer	
Case 1	Equation 303	$\frac{\partial \widetilde{H}_{n_L}^L}{\partial t} = \dot{Q}_{n_L}^{UP} - \dot{Q}_{n_L}^{LOW} - \dot{m}_{n_L}^{BL,L} \cdot \tilde{h}_{n_L}^{B,L} - \dot{m}_{n_L}^{D,L} \cdot \tilde{h}_{n_L}^{B,L} + \dot{m}_{n_L+1}^{D,L} \cdot \tilde{h}_{n_L+1}^{B,L} + \dot{m}_{n_L-1}^{B} \cdot \tilde{h}_{n_L-1}^{B,L} - \dot{m}_{n_L}^{B} \cdot \tilde{h}_{n_L}^{B,L}$
	Equation 304	$\frac{\partial m_{n_L}^L}{\partial t} = -\dot{m}_{n_L}^{BL,L} - \dot{m}_{n_L}^{D,L} + \dot{m}_{n_L+1}^{D,L} + \dot{m}_{n_L-1}^{B} - \dot{m}_{n_L}^{B}$
Case 2	Equation 305	$\frac{\partial \widetilde{H}_{n_L}^L}{\partial t} = \dot{Q}_{n_L}^{UP} - \dot{Q}_{n_L}^{LOW} - \dot{m}_{n_L}^{BL,L} \cdot \tilde{h}_{n_L}^{B,L} + \dot{m}_{n_L}^{D,L} \cdot \tilde{h}_{n_L-1}^{B,L} + \dot{m}_{n_L+1}^{D,L} \cdot \tilde{h}_{n_L+1}^{B,L} + \dot{m}_{n_L-1}^{B} \cdot \tilde{h}_{n_L-1}^{B,L} - \dot{m}_{n_L}^{B} \cdot \tilde{h}_{n_L}^{B,L}$
	Equation 306	$\frac{\partial m_{n_L}^L}{\partial t} = -\dot{m}_{n_L}^{BL,L} + \dot{m}_{n_L}^{D,L} + \dot{m}_{n_L+1}^{D,L} + \dot{m}_{n_L-1}^{B} - \dot{m}_{n_L}^{B}$
Case 3	Equation 307	$\frac{\partial \widetilde{H}_{n_L}^L}{\partial t} = \dot{Q}_{n_L}^{UP} - \dot{Q}_{n_L}^{LOW} - \dot{m}_{n_L}^{BL} \cdot \tilde{h}_{n_L}^{B,L} - \dot{m}_{n_L}^{D,L} \cdot \tilde{h}_{n_L}^{B,L} - \dot{m}_{n_L+1}^{D,L} \cdot \tilde{h}_{n_L}^{B,L} + \dot{m}_{n_L-1}^{B} \cdot \tilde{h}_{n_L-1}^{B,L} - \dot{m}_{n_L}^{B} \cdot \tilde{h}_{n_L}^{B,L}$
	Equation 308	$\frac{\partial m_{n_L}^L}{\partial t} = -\dot{m}_{n_L}^{BL} - \dot{m}_{n_L}^{D,L} - \dot{m}_{n_L+1}^{D,L} + \dot{m}_{n_L-1}^{B} - \dot{m}_{n_L}^{B}$
Case 4	Equation 309	$\frac{\partial \widetilde{H}_{n_L}^L}{\partial t} = \dot{Q}_{n_L}^{UP} - \dot{Q}_{n_L}^{LOW} - \dot{m}_{n_L}^{BL,L} \cdot \tilde{h}_{n_L}^{B,L} + \dot{m}_{n_L}^{D,L} \cdot \tilde{h}_{n_L-1}^{B,L} - \dot{m}_{n_L+1}^{D,L} \cdot \tilde{h}_{n_L}^{B,L} + \dot{m}_{n_L-1}^{B} \cdot \tilde{h}_{n_L-1}^{B,L} - \dot{m}_{n_L}^{B} \cdot \tilde{h}_{n_L}^{B,L}$
	Equation 310	$\frac{\partial m_{n_L}^L}{\partial t} = -\dot{m}_{n_L}^{BL,L} + \dot{m}_{n_L}^{D,L} - \dot{m}_{n_L+1}^{D,L} + \dot{m}_{n_L-1}^{B} - \dot{m}_{n_L}^{B}$
Case 5	Equation 311	$\frac{\partial \widetilde{H}_{n_L}^L}{\partial t} = \dot{Q}_{n_L}^{UP} - \dot{Q}_{n_L}^{LOW} + \dot{m}_{n_L}^{BL,L} \cdot \tilde{h}_{n_L}^{BL,L} - \dot{m}_{n_L}^{D,L} \cdot \tilde{h}_{n_L}^{B,L} + \dot{m}_{n_L+1}^{D,L} \cdot \tilde{h}_{n_L+1}^{B,L} + \dot{m}_{n_L-1}^{B} \cdot \tilde{h}_{n_L-1}^{B,L} - \dot{m}_{n_L}^{B} \cdot \tilde{h}_{n_L}^{B,L}$
	Equation 312	$\frac{\partial m_{n_L}^L}{\partial t} = \dot{m}_{n_L}^{BL,L} - \dot{m}_{n_L}^{D,L} + \dot{m}_{n_L+1}^{D,L} + \dot{m}_{n_L-1}^{B} - \dot{m}_{n_L}^{B}$
Case 6	Equation 313	$\frac{\partial \widetilde{H}_{n_L}^L}{\partial t} = \dot{Q}_{n_L}^{UP} - \dot{Q}_{n_L}^{LOW} + \dot{m}_{n_L}^{BL,L} \cdot \tilde{h}_{n_L}^{BL,L} + \dot{m}_{n_L}^{D,L} \cdot \tilde{h}_{n_L-1}^{B,L} + \dot{m}_{n_L+1}^{D,L} \cdot \tilde{h}_{n_L+1}^{B,L} + \dot{m}_{n_L-1}^{B} \cdot \tilde{h}_{n_L-1}^{B,L} - \dot{m}_{n_L}^{B} \cdot \tilde{h}_{n_L}^{B,L}$
	Equation 314	$\frac{\partial m_{n_L}^L}{\partial t} = \dot{m}_{n_L}^{BL,L} + \dot{m}_{n_L}^{D,L} + \dot{m}_{n_L+1}^{D,L} + \dot{m}_{n_L-1}^{B} - \dot{m}_{n_L}^{B}$
Case 7	Equation 315	$\frac{\partial \widetilde{H}_{n_L}^L}{\partial t} = \dot{Q}_{n_L}^{UP} - \dot{Q}_{n_L}^{LOW} + \dot{m}_{n_L}^{BL,L} \cdot \tilde{h}_{n_L}^{BL,L} - \dot{m}_{n_L}^{D,L} \cdot \tilde{h}_{n_L}^{B,L} - \dot{m}_{n_L+1}^{D,L} \cdot \tilde{h}_{n_L}^{B,L} + \dot{m}_{n_L-1}^{B} \cdot \tilde{h}_{n_L-1}^{B,L} - \dot{m}_{n_L}^{B} \cdot \tilde{h}_{n_L}^{B,L}$
	Equation 316	$\frac{\partial m_{n_L}^L}{\partial t} = \dot{m}_{n_L}^{BL,L} - \dot{m}_{n_L}^{D,L} - \dot{m}_{n_L+1}^{D,L} + \dot{m}_{n_L-1}^{B} - \dot{m}_{n_L}^{B}$
Case 8	Equation 317	$\frac{\partial \widetilde{H}_{n_L}^L}{\partial t} = \dot{Q}_{n_L}^{UP} - \dot{Q}_{n_L}^{LOW} + \dot{m}_{n_L}^{BL,L} \cdot \tilde{h}_{n_L}^{BL,L} + \dot{m}_{n_L}^{D,L} \cdot \tilde{h}_{n_L-1}^{B,L} - \dot{m}_{n_L+1}^{D,L} \cdot \tilde{h}_{n_L}^{B,L} + \dot{m}_{n_L-1}^{B} \cdot \tilde{h}_{n_L-1}^{B,L} - \dot{m}_{n_L}^{B} \cdot \tilde{h}_{n_L}^{B,L}$
	Equation 318	$\frac{\partial m_{n_L}^L}{\partial t} = \dot{m}_{n_L}^{BL,L} + \dot{m}_{n_L}^{D,L} - \dot{m}_{n_L+1}^{D,L} + \dot{m}_{n_L-1}^{B} - \dot{m}_{n_L}^{B}$
Case 9	Equation 319	$\frac{\partial \widetilde{H}_{n_L}^L}{\partial t} = \dot{Q}_{n_L}^{UP} - \dot{Q}_{n_L}^{LOW} + \dot{Q}_{w,n_L}^{SL} - \dot{m}_{n_L}^{D,L} \cdot \tilde{h}_{n_L}^{B,L} + \dot{m}_{n_L+1}^{D,L} \cdot \tilde{h}_{n_L+1}^{B,L} + \dot{m}_{n_L-1}^{B} \cdot \tilde{h}_{n_L-1}^{B,L} - \dot{m}_{n_L}^{B} \cdot \tilde{h}_{n_L}^{B,L}$
	Equation 320	$\frac{\partial m_{n_L}^L}{\partial t} = -\dot{m}_{n_L}^{D,L} + \dot{m}_{n_L+1}^{D,L} + \dot{m}_{n_L-1}^{B} - \dot{m}_{n_L}^{B}$
Case 10	Equation 321	$\frac{\partial \widetilde{H}_{n_L}^L}{\partial t} = \dot{Q}_{n_L}^{UP} - \dot{Q}_{n_L}^{LOW} + \dot{Q}_{w,n_L}^{SL} + \dot{m}_{n_L}^{D,L} \cdot \tilde{h}_{n_L-1}^{B,L} + \dot{m}_{n_L+1}^{D,L} \cdot \tilde{h}_{n_L+1}^{B,L} + \dot{m}_{n_L-1}^{B} \cdot \tilde{h}_{n_L-1}^{B,L} - \dot{m}_{n_L}^{B} \cdot \tilde{h}_{n_L}^{B,L}$
	Equation 322	$\frac{\partial m_{n_L}^L}{\partial t} = \dot{m}_{n_L}^{D,L} + \dot{m}_{n_L+1}^{D,L} + \dot{m}_{n_L-1}^{B} - \dot{m}_{n_L}^{B}$
Case 11	Equation 323	$\frac{\partial \widetilde{H}_{n_L}^L}{\partial t} = \dot{Q}_{n_L}^{UP} - \dot{Q}_{n_L}^{LOW} + \dot{Q}_{w,n_L}^{SL} - \dot{m}_{n_L}^{D,L} \cdot \tilde{h}_{n_L}^{B,L} - \dot{m}_{n_L+1}^{D,L} \cdot \tilde{h}_{n_L}^{B,L} + \dot{m}_{n_L-1}^{B} \cdot \tilde{h}_{n_L-1}^{B,L} - \dot{m}_{n_L}^{B} \cdot \tilde{h}_{n_L}^{B,L}$
	Equation 324	$\frac{\partial m_{n_L}^L}{\partial t} = -\dot{m}_{n_L}^{D,L} - \dot{m}_{n_L+1}^{D,L} + \dot{m}_{n_L-1}^{B} - \dot{m}_{n_L}^{B}$
Case 12	Equation 325	$\frac{\partial \widetilde{H}_{n_L}^L}{\partial t} = \dot{Q}_{n_L}^{SUP} - \dot{Q}_{n_L}^{INF} + \dot{Q}_{w,n_L}^{SL} + \dot{m}_{n_L}^{D,L} \cdot \tilde{h}_{n_L-1}^{B,L} - \dot{m}_{n_L+1}^{D,L} \cdot \tilde{h}_{n_L}^{B,L} + \dot{m}_{n_L-1}^{B} \cdot \tilde{h}_{n_L-1}^{B,L} - \dot{m}_{n_L}^{B} \cdot \tilde{h}_{n_L}^{B,L}$
	Equation 326	$\frac{\partial m_{n_L}^L}{\partial t} = \dot{m}_{n_L}^{D,L} - \dot{m}_{n_L+1}^{D,L} + \dot{m}_{n_L-1}^{B} - \dot{m}_{n_L}^{B}$

$\tilde{h}^{BL}$ is the specific enthalpy of the boundary layer and it is computed from the temperature of the boundary layer. $\dot{m}_{n_L}^{BL,L}$ is the mass entrained in the liquid boundary layer, which is the difference in flow rate between $\dot{m}^{UP}_{n_L}$ and $\dot{m}^{UP}_{n_L-1}$. These boundary variables are computed with the Storage Boundary Layer (SBL) model of the wet side wall.

2.3. Simplified form of the balance equations

The deduction of the simplified form of the balance equations is the third step (step c) of Section 2 of Chapter 6) of the mathematical produce, as it is presented in Figure 128. To obtain the explicit equations for computing the indipendent variables of the mathematical system, the number of the conservation equations of Table 121 must be reduced. The equations of Table 121 depend on the time-derivates of the ullage volume ($\frac{\partial V^V}{\partial t}$) and of the sub-layer liquid volume ($\frac{\partial V^{SL}_{n_L}}{\partial t}$). The time-derivates $\frac{\partial V^V}{\partial t}$ can be computed with the conservation law of the volume (Equation 288) and the time derivate $\frac{\partial V^{SL}_{n_L}}{\partial t}$ can be computed as function of the time-derivates of the thickness ($\frac{\partial dxL}{\partial t}$), as it is reported in Table 122.

Table 122. Equations to compute $\frac{\partial v^V}{\partial t}$ and $\frac{\partial v^L_{n_L}}{\partial t}$.

Variable	Equation	Formula
$\frac{\partial V^V}{\partial t}$	Equation 327	$\frac{\partial V^V}{\partial t} = -\frac{\partial V^L}{\partial t}$
$\frac{\partial V^L_{1,\ldots,n_L,\ldots N^L}}{\partial t}$	Equation 328	$\frac{\partial V^{SL}_{n_L}}{\partial t} = Z_{n_L} \cdot \frac{\partial dxL}{\partial t}$

The variable $\frac{\partial V^L}{\partial t}$ is the the time-derivate of the whole liquid and it can be computed as sum of the time-variation of the volume of each sub-layer, as it follows:

Equation 329
$$\frac{\partial V^L}{\partial t} = \left(\sum_{n_L=1}^{N^L} \frac{\partial V^{SL}_{n_L}}{\partial t} \right)$$

Using the equations of these time-derivates in the equations of Table 121 simplifies the system of the conservation laws. The simplified form of the conservation laws does not have the term $\frac{\partial V^V}{\partial t}$ and $\frac{\partial V^{SL}_{n_L}}{\partial t}$, and the enthalpy variation is expressed as function of temperature, pressure and mass. The simplified forms of the balance equations are reported in Table 123.

Table 123. Simplified form of the balance equations of LS model.

	Ullage	
Vapour mass balance	Equation 330	$-\rho^V \cdot \left[\sum_{n_L=1}^{N^L} Z_{n_L}\right] \cdot \frac{\partial dxL}{\partial t} + V^V \cdot \left[\left.\frac{\partial \rho^V}{\partial T^V}\right\|_{P^V} \cdot \frac{\partial T^V}{\partial t} + \left.\frac{\partial \rho^V}{\partial P^V}\right\|_{T^V} \cdot \frac{\partial P^V}{\partial t}\right] = \dot{m}^V_{IN} + \dot{m}_N - \dot{m}_{BOG}$
Vapour energy balance	Equation 331	$m^V \cdot \left[C^V_P \cdot \frac{\partial T^V}{\partial t} + \left.\frac{\partial \tilde{h}^V}{\partial P^V}\right\|_{T^V} \cdot \frac{\partial P^V}{\partial t}\right] = \dot{m}_N \cdot \left(\tilde{h}^V_S - \tilde{h}^V_1\right) - \dot{Q}^V_I + \dot{m}^V_{IN} \cdot \left(\tilde{h}^V_{IN} - \tilde{h}^V_{N^V}\right) + \dot{Q}^{SV}_w + \sum_{i=1}^{N^+}\left[\dot{m}^{BL,V}_i \cdot \tilde{h}^V_i\right] - \sum_{i=1}^{N^-}\left[\dot{m}^{BL,V}_i \cdot \tilde{h}^V_i\right] + \sum_{i=1}^{N^V}\left[F^{D,+}_{i+1} \cdot \dot{m}^{D,V}_{i+1} \cdot \left(\tilde{h}^V_{i+1} - \tilde{h}^V_i\right)\right] - \sum_{i=1}^{N^V}\left[F^{D,-}_{i+1} \cdot \dot{m}^{D,V}_{i+1} \cdot \left(\tilde{h}^V_i - \tilde{h}^V_{i+1}\right)\right]$
	Interface-liquid sub-layer	
Case 1	Equation 332	$m^{B,L}_{N^L} \cdot \left[C^L_P \cdot \frac{\partial T^{B,L}_{N^L}}{\partial t} + \left.\frac{\partial \tilde{h}^{B,L}}{\partial P^V}\right\|_{T^L} \cdot \frac{\partial P^V}{\partial t}\right] = -\dot{Q}^L_I - \dot{Q}^{LOW}_{N^L} + \dot{m}^{BL,L}_{N^L} \cdot \left(\tilde{h}^{BL,L}_{N^L} - \tilde{h}^{B,L}_{N^L}\right)$

Table 123. Simplified form of the balance equations of LS model.

		$-\dot{m}_N \cdot \left(\tilde{h}_S^{B,L} - \tilde{h}_{N^L}^{B,L}\right) + \dot{m}_{N^L-1}^B \cdot \left(\tilde{h}_{N^L-1}^{B,L} - \tilde{h}_{N^L}^{B,L}\right)$
	Equation 333	$\rho^L \cdot Z_{N^L} \cdot \frac{\partial dxL}{\partial t} + V_{N^L}^{B,L} \cdot \left[\frac{\partial \rho^L}{\partial T^L}\Big\vert_{P^V} \cdot \frac{\partial T_{N^L}^{B,L}}{\partial t} + \frac{\partial \rho^L}{\partial P^V}\Big\vert_{T^L} \cdot \frac{\partial P^L}{\partial t}\right] = -\dot{m}_{N^L}^{D,L} + \dot{m}_{N^L}^{BL,L} - \dot{m}_N + \dot{m}_{N^L-1}^B$
Case 2	Equation 334	$m_{N^L}^{B,L} \cdot \left[C_P^L \cdot \frac{\partial T_{N^L}^{B,L}}{\partial t} + \frac{\partial \tilde{h}^L}{\partial P^V}\Big\vert_{T^L} \cdot \frac{\partial P^V}{\partial t}\right] = -\dot{Q}_I^L - \dot{Q}_{N^L}^{LOW} + \dot{m}_{N^L}^{D,L} \cdot \left(\tilde{h}_{N^L-1}^{B,L} - \tilde{h}_{N^L}^{B,L}\right)$ $+\dot{m}_{N^L}^{BL,L} \cdot \left(\tilde{h}_{N^L}^{BL,L} - \tilde{h}_{N^L}^{B,L}\right) - \dot{m}_N \cdot \left(\tilde{h}_S^{B,L} - \tilde{h}_{N^L}^{B,L}\right) + \dot{m}_{N^L-1}^B \cdot \left(\tilde{h}_{N^L-1}^{B,L} - \tilde{h}_{N^L}^{B,L}\right)$
	Equation 335	$\rho^L \cdot Z_{N^L} \cdot \frac{\partial dxL}{\partial t} + V_{N^L}^{B,L} \cdot \left[\frac{\partial \rho^L}{\partial T^L}\Big\vert_{P^V} \cdot \frac{\partial T_{N^L}^{B,L}}{\partial t} + \frac{\partial \rho^L}{\partial P^V}\Big\vert_{T^L} \cdot \frac{\partial P^L}{\partial t}\right] = \dot{m}_{N^L}^{D,L} + \dot{m}_{N^L}^{BL,L} - \dot{m}_N + \dot{m}_{N^L-1}^B$
Case 3	Equation 336	$m_{N^L}^{L} \cdot \left[C_P^L \cdot \frac{\partial T_{N^L}^{B,L}}{\partial t} + \frac{\partial \tilde{h}^L}{\partial P^V}\Big\vert_{T^L} \cdot \frac{\partial P^V}{\partial t}\right] = -\dot{Q}_I^L - \dot{Q}_{N^L}^{LOW} + \dot{Q}_{w,N^L}^{SL}$ $-\dot{m}_N \cdot \left(\tilde{h}_S^{B,L} - \tilde{h}_{N^L}^{B,L}\right) + \dot{m}_{N^L-1}^B \cdot \left(\tilde{h}_{N^L-1}^{B,L} - \tilde{h}_{N^L}^{B,L}\right)$
	Equation 337	$\rho^L \cdot Z_{N^L} \cdot \frac{\partial dxL}{\partial t} + V_{N^L}^{B,L} \cdot \left[\frac{\partial \rho^L}{\partial T^L}\Big\vert_{P^V} \cdot \frac{\partial T_{N^L}^{B,L}}{\partial t} + \frac{\partial \rho^L}{\partial P^V}\Big\vert_{T^L} \cdot \frac{\partial P^L}{\partial t}\right] = -\dot{m}_{N^L}^{D,L} - \dot{m}_N + \dot{m}_{N^L-1}^B$
Case 4	Equation 338	$m_{N^L}^{B,L} \cdot \left[C_P^L \cdot \frac{\partial T_{N^L}^{B,L}}{\partial t} + \frac{\partial \tilde{h}^{B,L}}{\partial P^V}\Big\vert_{T^L} \cdot \frac{\partial P^V}{\partial t}\right] = -\dot{Q}_I^L - \dot{Q}_{N^L}^{LOW} + \dot{Q}_{w,N^L}^{SL}$ $+\dot{m}_{N^L}^{D,L} \cdot \left(\tilde{h}_{N^L-1}^{B,L} - \tilde{h}_{N^L}^{B,L}\right) - \dot{m}_N \cdot \left(\tilde{h}_S^{B,L} - \tilde{h}_{N^L}^{B,L}\right) + \dot{m}_{N^L-1}^B \cdot \left(\tilde{h}_{N^L-1}^{B,L} - \tilde{h}_{N^L}^{B,L}\right)$
	Equation 339	$\rho^L \cdot Z_{N^L} \cdot \frac{\partial dxL}{\partial t} + V_{N^L}^{B,L} \cdot \left[\frac{\partial \rho^L}{\partial T^L}\Big\vert_{P^V} \cdot \frac{\partial T_{N^L}^{B,L}}{\partial t} + \frac{\partial \rho^L}{\partial P^V}\Big\vert_{T^L} \cdot \frac{\partial P^L}{\partial t}\right] = \dot{m}_{N^L}^{D,L} - \dot{m}_N + \dot{m}_{N^L-1}^B$
		Bottom-liquid sub-layer
Case 1	Equation 340	$m_1^{B,L} \cdot \left[C_P^L \cdot \frac{\partial T_1^{B,L}}{\partial t} + \frac{\partial \tilde{h}^{B,L}}{\partial P^V}\Big\vert_{T^L} \cdot \frac{\partial P^V}{\partial t}\right] = \dot{Q}_w^B + \dot{m}_2^{D,L} \cdot \left(\tilde{h}_2^{B,L} - \tilde{h}_1^{B,L}\right) + \dot{Q}_1^{UP} + \dot{m}_{IN}^L \cdot \left(\tilde{h}_{IN}^{B,L} - \tilde{h}_1^{B,L}\right)$
	Equation 341	$\rho^L \cdot Z_1 \cdot \frac{\partial dxL}{\partial t} + V_1^{B,L} \cdot \left[\frac{\partial \rho^L}{\partial T^L}\Big\vert_{P^V} \cdot \frac{\partial T_1^{B,L}}{\partial t} + \frac{\partial \rho^L}{\partial P^V}\Big\vert_{T^L} \cdot \frac{\partial P^L}{\partial t}\right] = \dot{m}_2^{D,L} - \dot{m}_1^B - \dot{m}_1^{BL,L} + \dot{m}_{IN}^L - \dot{m}_{OUT}^L$
Case 2	Equation 342	$m_1^{B,L} \cdot \left[C_P^L \cdot \frac{\partial T_1^{B,L}}{\partial t} + \frac{\partial \tilde{h}^{B,L}}{\partial P^V}\Big\vert_{T^L} \cdot \frac{\partial P^V}{\partial t}\right] = \dot{Q}_w^B + \dot{Q}_1^{UP} + \dot{m}_{IN}^L \cdot \left(\tilde{h}_{IN}^{L} - \tilde{h}_1^{B,L}\right)$
	Equation 343	$\rho^L \cdot Z_1 \cdot \frac{\partial dxL}{\partial t} + V_1^{B,L} \cdot \left[\frac{\partial \rho^L}{\partial T^L}\Big\vert_{P^V} \cdot \frac{\partial T_1^{B,L}}{\partial t} + \frac{\partial \rho^L}{\partial P^V}\Big\vert_{T^L} \cdot \frac{\partial P^L}{\partial t}\right] = -\dot{m}_2^{D,L} - \dot{m}_1^B - \dot{m}_1^{BL,L} + \dot{m}_{IN}^L - \dot{m}_{OUT}^L$
		Bulk-liquid sub-layer
Case 1	Equation 344	$m_{n_L}^{B,L} \cdot \left[C_P^L \cdot \frac{\partial T_{n_L}^{B,L}}{\partial t} + \frac{\partial \tilde{h}^{B,L}}{\partial P^V}\Big\vert_{T^L} \cdot \frac{\partial P^V}{\partial t}\right] = \dot{Q}_{n_L}^{UP} - \dot{Q}_{n_L}^{LOW}$ $+\dot{m}_{n_L+1}^{D,L} \cdot \left(\tilde{h}_{n_L+1}^{B,L} - \tilde{h}_{n_L}^{B,L}\right) + \dot{m}_{n_L-1}^B \cdot \left(\tilde{h}_{n_L-1}^{B,L} - \tilde{h}_{n_L}^{B,L}\right)$
	Equation 345	$\rho^L \cdot Z_{n_L} \cdot \frac{\partial dxL}{\partial t} + V_{n_L}^{L} \cdot \left[\frac{\partial \rho^L}{\partial T^L}\Big\vert_{P^V} \cdot \frac{\partial T_{n_L}^{B,L}}{\partial t} + \frac{\partial \rho^L}{\partial P^V}\Big\vert_{T^L} \cdot \frac{\partial P^L}{\partial t}\right]$ $= -\dot{m}_{n_L}^{BL,L} - \dot{m}_{n_L}^{D,L} + \dot{m}_{n_L+1}^{D,L} + \dot{m}_{n_L-1}^B - \dot{m}_{n_L}^B$
Case 2	Equation 346	$m_{n_L}^{B,L} \cdot \left[C_P^L \cdot \frac{\partial T_{n_L}^{B,L}}{\partial t} + \frac{\partial \tilde{h}^{B,L}}{\partial P^V}\Big\vert_{T^L} \cdot \frac{\partial P^V}{\partial t}\right] = \dot{Q}_{n_L}^{UP} - \dot{Q}_{n_L}^{LOW} + \dot{m}_{n_L}^{D,L} \cdot \left(\tilde{h}_{n_L-1}^{B,L} - \tilde{h}_{n_L}^{B,L}\right)$ $+\dot{m}_{n_L+1}^{D,L} \cdot \left(\tilde{h}_{n_L+1}^{B,L} - \tilde{h}_{n_L}^{B,L}\right) + \dot{m}_{n_L-1}^B \cdot \left(\tilde{h}_{n_L-1}^{B,L} - \tilde{h}_{n_L}^{B,L}\right)$
	Equation 347	$\rho^L \cdot Z_{n_L} \cdot \frac{\partial dxL}{\partial t} + V_{n_L}^{B,L} \cdot \left[\frac{\partial \rho^L}{\partial T^L}\Big\vert_{P^V} \cdot \frac{\partial T_{n_L}^{B,L}}{\partial t} + \frac{\partial \rho^L}{\partial P^V}\Big\vert_{T^L} \cdot \frac{\partial P^L}{\partial t}\right]$ $= -\dot{m}_{n_L}^{BL,L} + \dot{m}_{n_L}^{D,L} + \dot{m}_{n_L+1}^{D,L} + \dot{m}_{n_L-1}^B - \dot{m}_{n_L}^B$
Case 3	Equation 348	$m_{n_L}^{B,L} \cdot \left[C_P^L \cdot \frac{\partial T_{n_L}^{B,L}}{\partial t} + \frac{\partial \tilde{h}^{L}}{\partial P^V}\Big\vert_{T^L} \cdot \frac{\partial P^V}{\partial t}\right] = \dot{Q}_{n_L}^{UP} - \dot{Q}_{n_L}^{LOW} + \dot{m}_{n_L-1}^B \cdot \left(\tilde{h}_{n_L-1}^{B,L} - \tilde{h}_{n_L}^{B,L}\right)$
	Equation 349	$\rho^L \cdot Z_{n_L} \cdot \frac{\partial dxL}{\partial t} + V_{n_L}^{B,L} \cdot \left[\frac{\partial \rho^L}{\partial T^L}\Big\vert_{P^V} \cdot \frac{\partial T_{n_L}^{B,L}}{\partial t} + \frac{\partial \rho^L}{\partial P^V}\Big\vert_{T^L} \cdot \frac{\partial P^L}{\partial t}\right]$ $= -\dot{m}_{n_L}^{BL,L} - \dot{m}_{n_L}^{D,L} - \dot{m}_{n_L+1}^{D,L} + \dot{m}_{n_L-1}^B - \dot{m}_{n_L}^B$
Case 4	Equation 350	$m_{n_L}^{B,L} \cdot \left[C_P^L \cdot \frac{\partial T_{n_L}^{B,L}}{\partial t} + \frac{\partial \tilde{h}^{L}}{\partial P^V}\Big\vert_{T^L} \cdot \frac{\partial P^V}{\partial t}\right] = \dot{Q}_{n_L}^{UP} - \dot{Q}_{n_L}^{LOW}$ $+\dot{m}_{n_L}^{D,L} \cdot \left(\tilde{h}_{n_L-1}^{B,L} - \tilde{h}_{n_L}^{B,L}\right) + \dot{m}_{n_L-1}^B \cdot \left(\tilde{h}_{n_L-1}^{B,L} - \tilde{h}_{n_L}^{B,L}\right)$

Table 123. Simplified form of the balance equations of LS model.

	Equation 351	$\rho^{L} \cdot Z_{n_L} \cdot \frac{\partial dxL}{\partial t} + V_{n_L}^{B,L} \cdot \left[\left.\frac{\partial \rho^{L}}{\partial T^{L}}\right\|_{P^{V}} \cdot \frac{\partial T_{n_L}^{B,L}}{\partial t} + \left.\frac{\partial \rho^{L}}{\partial P^{V}}\right\|_{T^{L}} \cdot \frac{\partial P^{L}}{\partial t} \right] = -\dot{m}_{n_L}^{BL,L} + \dot{m}_{n_L}^{D,L} - \dot{m}_{n_L+1}^{D,L} + \dot{m}_{n_L-1}^{B} - \dot{m}_{n_L}^{B}$
Case 5	Equation 352	$m_{n_L}^{B,L} \cdot \left[C_P^{L} \cdot \frac{\partial T_{n_L}^{B,L}}{\partial t} + \left.\frac{\partial \tilde{h}^{B,L}}{\partial P^{V}}\right\|_{T^{L}} \cdot \frac{\partial P^{V}}{\partial t} \right] = \dot{Q}_{n_L}^{UP} - \dot{Q}_{n_L}^{LOW} + \dot{m}_{n_L}^{BL,L} \cdot \left(\tilde{h}_{n_L}^{BL,L} - \tilde{h}_{n_L}^{B,L} \right) + \dot{m}_{n_L+1}^{D,L} \cdot \left(\tilde{h}_{n_L+1}^{B,L} - \tilde{h}_{n_L}^{B,L} \right) + \dot{m}_{n_L-1}^{B} \cdot \left(\tilde{h}_{n_L-1}^{B,L} - \tilde{h}_{n_L}^{B,L} \right)$
	Equation 353	$\rho^{L} \cdot Z_{n_L} \cdot \frac{\partial dxL}{\partial t} + V_{n_L}^{B,L} \cdot \left[\left.\frac{\partial \rho^{L}}{\partial T^{L}}\right\|_{P^{V}} \cdot \frac{\partial T_{n_L}^{B,L}}{\partial t} + \left.\frac{\partial \rho^{L}}{\partial P^{V}}\right\|_{T^{L}} \cdot \frac{\partial P^{L}}{\partial t} \right] = \dot{m}_{n_L}^{BL,L} - \dot{m}_{n_L}^{D,L} + \dot{m}_{n_L+1}^{D,L} + \dot{m}_{n_L-1}^{B} - \dot{m}_{n_L}^{B}$
Case 6	Equation 354	$m_{n_L}^{L} \cdot \left[C_P^{L} \cdot \frac{\partial T_{n_L}^{B,L}}{\partial t} + \left.\frac{\partial \tilde{h}^{B,L}}{\partial P^{V}}\right\|_{T^{L}} \cdot \frac{\partial P^{V}}{\partial t} \right] = \dot{Q}_{n_L}^{UP} - \dot{Q}_{n_L}^{LOW} + \dot{m}_{n_L}^{BL,L} \cdot \left(\tilde{h}_{n_L}^{BL,L} - \tilde{h}_{n_L}^{B,L} \right) + \dot{m}_{n_L}^{D,L} \cdot \left(\tilde{h}_{n_L-1}^{B,L} - \tilde{h}_{n_L}^{B,L} \right) + \dot{m}_{n_L+1}^{D,L} \cdot \left(\tilde{h}_{n_L+1}^{B,L} - \tilde{h}_{n_L}^{B,L} \right) + \dot{m}_{n_L-1}^{B} \cdot \left(\tilde{h}_{n_L-1}^{B,L} - \tilde{h}_{n_L}^{B,L} \right)$
	Equation 355	$\rho^{L} \cdot Z_{n_L} \cdot \frac{\partial dxL}{\partial t} + V_{n_L}^{B,L} \cdot \left[\left.\frac{\partial \rho^{L}}{\partial T^{L}}\right\|_{P^{V}} \cdot \frac{\partial T_{n_L}^{B,L}}{\partial t} + \left.\frac{\partial \rho^{L}}{\partial P^{V}}\right\|_{T^{L}} \cdot \frac{\partial P^{L}}{\partial t} \right] = \dot{m}_{n_L}^{BL,L} + \dot{m}_{n_L}^{D,L} + \dot{m}_{n_L+1}^{D,L} + \dot{m}_{n_L-1}^{B} - \dot{m}_{n_L}^{B}$
Case 7	Equation 356	$m_{n_L}^{L} \cdot \left[C_P^{L} \cdot \frac{\partial T_{n_L}^{B,L}}{\partial t} + \left.\frac{\partial \tilde{h}^{B,L}}{\partial P^{V}}\right\|_{T^{L}} \cdot \frac{\partial P^{V}}{\partial t} \right] = \dot{Q}_{n_L}^{UP} - \dot{Q}_{n_L}^{LOW} + \dot{m}_{n_L}^{BL,L} \cdot \left(\tilde{h}_{n_L}^{BL,L} - \tilde{h}_{n_L}^{B,L} \right) + \dot{m}_{n_L-1}^{B} \cdot \left(\tilde{h}_{n_L-1}^{B,L} - \tilde{h}_{n_L}^{B,L} \right)$
	Equation 357	$\rho^{L} \cdot Z_{n_L} \cdot \frac{\partial dxL}{\partial t} + V_{n_L}^{B,L} \cdot \left[\left.\frac{\partial \rho^{L}}{\partial T^{L}}\right\|_{P^{V}} \cdot \frac{\partial T_{n_L}^{B,L}}{\partial t} + \left.\frac{\partial \rho^{L}}{\partial P^{V}}\right\|_{T^{L}} \cdot \frac{\partial P^{L}}{\partial t} \right] = \dot{m}_{n_L}^{BL,L} - \dot{m}_{n_L}^{D,L} - \dot{m}_{n_L+1}^{D,L} + \dot{m}_{n_L-1}^{B} - \dot{m}_{n_L}^{B}$
Case 8	Equation 358	$m_{n_L}^{B,L} \cdot \left[C_P^{L} \cdot \frac{\partial T_{n_L}^{B,L}}{\partial t} + \left.\frac{\partial \tilde{h}^{B,L}}{\partial P^{V}}\right\|_{T^{L}} \cdot \frac{\partial P^{V}}{\partial t} \right] = \dot{Q}_{n_L}^{UP} - \dot{Q}_{n_L}^{LOW} + \dot{m}_{n_L}^{BL} \cdot \left(\tilde{h}_{n_L}^{BL,L} - \tilde{h}_{n_L}^{B,L} \right) + \dot{m}_{n_L}^{D,L} \cdot \left(\tilde{h}_{n_L-1}^{B,L} - \tilde{h}_{n_L}^{B,L} \right) + \dot{m}_{n_L-1}^{B} \cdot \left(\tilde{h}_{n_L-1}^{B,L} - \tilde{h}_{n_L}^{B,L} \right)$
	Equation 359	$\rho^{L} \cdot Z_{n_L} \cdot \frac{\partial dxL}{\partial t} + V_{n_L}^{B,L} \cdot \left[\left.\frac{\partial \rho^{L}}{\partial T^{L}}\right\|_{P^{V}} \cdot \frac{\partial T_{n_L}^{B,L}}{\partial t} + \left.\frac{\partial \rho^{L}}{\partial P^{V}}\right\|_{T^{L}} \cdot \frac{\partial P^{L}}{\partial t} \right] = \dot{m}_{n_L}^{BL,L} + \dot{m}_{n_L}^{D,L} - \dot{m}_{n_L+1}^{D,L} + \dot{m}_{n_L-1}^{B} - \dot{m}_{n_L}^{B}$
Case 9	Equation 360	$m_{n_L}^{B,L} \cdot \left[C_P^{L} \cdot \frac{\partial T_{n_L}^{B,L}}{\partial t} + \left.\frac{\partial \tilde{h}^{B,L}}{\partial P^{V}}\right\|_{T^{L}} \cdot \frac{\partial P^{V}}{\partial t} \right] = \dot{Q}_{n_L}^{UP} - \dot{Q}_{n_L}^{LOW} + \dot{Q}_{w,n_L}^{SL} + \dot{m}_{n_L+1}^{D,L} \cdot \left(\tilde{h}_{n_L+1}^{B,L} - \tilde{h}_{n_L}^{B,L} \right) + \dot{m}_{n_L-1}^{B} \cdot \left(\tilde{h}_{n_L-1}^{B,L} - \tilde{h}_{n_L}^{B,L} \right)$
	Equation 361	$\rho^{L} \cdot Z_{n_L} \cdot \frac{\partial dxL}{\partial t} + V_{n_L}^{B,L} \cdot \left[\left.\frac{\partial \rho^{L}}{\partial T^{L}}\right\|_{P^{V}} \cdot \frac{\partial T_{n_L}^{B,L}}{\partial t} + \left.\frac{\partial \rho^{L}}{\partial P^{V}}\right\|_{T^{L}} \cdot \frac{\partial P^{L}}{\partial t} \right] = -\dot{m}_{n_L}^{D,L} + \dot{m}_{n_L+1}^{D,L} + \dot{m}_{n_L-1}^{B} - \dot{m}_{n_L}^{B}$
Case 10	Equation 362	$m_{n_L}^{B,L} \cdot \left[C_P^{L} \cdot \frac{\partial T_{n_L}^{B,L}}{\partial t} + \left.\frac{\partial \tilde{h}^{B,L}}{\partial P^{V}}\right\|_{T^{L}} \cdot \frac{\partial P^{V}}{\partial t} \right] = \dot{Q}_{n_L}^{UP} - \dot{Q}_{n_L}^{LOW} + \dot{Q}_{w,n_L}^{SL} + \dot{m}_{n_L}^{D,L} \cdot \left(\tilde{h}_{n_L-1}^{B,L} - \tilde{h}_{n_L}^{B,L} \right) + \dot{m}_{n_L+1}^{D,L} \cdot \left(\tilde{h}_{n_L+1}^{B,L} - \tilde{h}_{n_L}^{B,L} \right) + \dot{m}_{n_L-1}^{B} \cdot \left(\tilde{h}_{n_L-1}^{B,L} - \tilde{h}_{n_L}^{B,L} \right)$
	Equation 363	$\rho^{L} \cdot Z_{n_L} \cdot \frac{\partial dxL}{\partial t} + V_{n_L}^{B,L} \cdot \left[\left.\frac{\partial \rho^{L}}{\partial T^{L}}\right\|_{P^{V}} \cdot \frac{\partial T_{n_L}^{B,L}}{\partial t} + \left.\frac{\partial \rho^{L}}{\partial P^{V}}\right\|_{T^{L}} \cdot \frac{\partial P^{L}}{\partial t} \right] = \dot{m}_{n_L}^{D,L} + \dot{m}_{n_L+1}^{D,L} + \dot{m}_{n_L-1}^{B} - \dot{m}_{n_L}^{B}$
Case 11	Equation 364	$m_{n_L}^{B,L} \cdot \left[C_P^{L} \cdot \frac{\partial T_{n_L}^{B,L}}{\partial t} + \left.\frac{\partial \tilde{h}^{B,L}}{\partial P^{V}}\right\|_{T^{L}} \cdot \frac{\partial P^{V}}{\partial t} \right] = \dot{Q}_{n_L}^{UP} - \dot{Q}_{n_L}^{LOW} + \dot{Q}_{w,n_L}^{SL} + \dot{m}_{n_L-1}^{B} \cdot \left(\tilde{h}_{n_L-1}^{B,L} - \tilde{h}_{n_L}^{B,L} \right)$
	Equation 365	$\rho^{L} \cdot Z_{n_L} \cdot \frac{\partial dxL}{\partial t} + V_{n_L}^{B,L} \cdot \left[\left.\frac{\partial \rho^{L}}{\partial T^{L}}\right\|_{P^{V}} \cdot \frac{\partial T_{n_L}^{B,L}}{\partial t} + \left.\frac{\partial \rho^{L}}{\partial P^{V}}\right\|_{T^{L}} \cdot \frac{\partial P^{L}}{\partial t} \right] = -\dot{m}_{n_L}^{D,L} - \dot{m}_{n_L+1}^{D,L} + \dot{m}_{n_L-1}^{B} - \dot{m}_{n_L}^{B}$
Case 12	Equation 366	$m_{n_L}^{B,L} \cdot \left[C_P^{L} \cdot \frac{\partial T_{n_L}^{B,L}}{\partial t} + \left.\frac{\partial \tilde{h}^{B,L}}{\partial P^{V}}\right\|_{T^{L}} \cdot \frac{\partial P^{V}}{\partial t} \right] = \dot{Q}_{n_L}^{UP} - \dot{Q}_{n_L}^{LOW} + \dot{Q}_{w,n_L}^{SL} + \dot{m}_{n_L}^{D,L} \cdot \left(\tilde{h}_{n_L-1}^{B,L} - \tilde{h}_{n_L}^{B,L} \right) + \dot{m}_{n_L-1}^{B} \cdot \left(\tilde{h}_{n_L-1}^{B,L} - \tilde{h}_{n_L}^{B,L} \right)$
	Equation 367	$\rho^{L} \cdot Z_{n_L} \cdot \frac{\partial dxL}{\partial t} + V_{n_L}^{B,L} \cdot \left[\left.\frac{\partial \rho^{L}}{\partial T^{L}}\right\|_{P^{V}} \cdot \frac{\partial T_{n_L}^{B,L}}{\partial t} + \left.\frac{\partial \rho^{L}}{\partial P^{V}}\right\|_{T^{L}} \cdot \frac{\partial P^{L}}{\partial t} \right] = \dot{m}_{n_L}^{D,L} - \dot{m}_{n_L+1}^{D,L} + \dot{m}_{n_L-1}^{B} - \dot{m}_{n_L}^{B}$

Z_{n_L} is a geometrical coefficient and it is computed as described in Appendix AA. $V_{n_L}^{B,L}$ is described in Table 114 and $m_{n_L}^{B,L}$ is the mass of the bulk of the liquid sub-layer. In Equation 331, $F_{i+1}^{D,+}$ is equal to 1 when $\dot{m}_{i+1}^{D,V}$ is downward and it is equal to 0 if $\dot{m}_{i+1}^{D,V}$ is upward. $F_{i+1}^{D,-}$ is equal to 0 when $\dot{m}_{i+1}^{D,V}$ is downward and it is equal to 1 if $\dot{m}_{i+1}^{D,V}$ is upward. The equations of Table 123 are obtained with a mathematical procedure that is reported in Section 1of Appendix AC. The procedure to obtain the simplified form of vapour balance equation (Equation 331) is described in Section 2 of Chapter 5.

2.4.Linear form of the simplified balance equations

The deduction of the linear form of the simplified balance equations is the fourth step (step d) of Section 2 of Chapter 6) of the mathematical produce, as it is presented in Figure 128.

In order to reduce the computational time, the dependent variables of the simplified conservation laws have been replaced by coefficients to obtain linear form of the simplified conservation laws. These equations are reported in Table 124.

Table 124. Linear form of the simplified conservation laws of LS model.

		Ullage
Mass	Equation 368	$A^P \cdot \frac{\partial P^V}{\partial t} + B^P \cdot \frac{\partial T^V}{\partial t} + C^P \cdot \frac{\partial dxL}{\partial t} + D^P \cdot \dot{m}_{IN}^V + E^P \cdot \dot{m}_{BOG} + F^P = 0$
Energy	Equation 369	$A^{TV} \cdot \frac{\partial P^V}{\partial t} + B^{TV} \cdot \frac{\partial T^V}{\partial t} + C^{TV} \cdot \frac{\partial dxL}{\partial t} + D^{TV} \cdot \dot{m}_{IN}^V + E^{TV} \cdot \dot{m}_{BOG} + F^{TV} = 0$
		Interface-liquid sub-layer
Energy	Equation 370	$A_{N^L}^{TL} \cdot \frac{\partial P^V}{\partial t} + B_{N^L}^{TL} \cdot \frac{\partial T_{N^L}^{B,L}}{\partial t} + C_{N^L}^{TL} \cdot \frac{\partial dxL}{\partial t} + E_{N^L}^{TL} \cdot \dot{m}_{N^L}^{D,L} + F_{N^L}^{TL} = 0$
Mass	Equation 371	$A_{N^L}^{HL} \cdot \frac{\partial P^V}{\partial t} + B_{N^L}^{HL} \cdot \frac{\partial T_{N^L}^{B,L}}{\partial t} + C_{N^L}^{HL} \cdot \frac{\partial dxL}{\partial t} + E_{N^L}^{HL} \cdot \dot{m}_{N^L}^{D,L} + F_{N^L}^{HL} = 0$
		Bottom-liquid sub-layer
Energy	Equation 372	$A_1^{TL} \cdot \frac{\partial P^V}{\partial t} + B_1^{TL} \cdot \frac{\partial T_1^{B,L}}{\partial t} + C_1^{TL} \cdot \frac{\partial dxL}{\partial t} + D_1^{TL} \cdot \dot{m}_2^{D,L} + F_1^{TL} + G_1^{TL} \cdot \dot{m}_{IN}^L + H_1^{TL} \cdot \dot{m}_{OUT}^L = 0$
Mass	Equation 373	$A_1^{HL} \cdot \frac{\partial P^V}{\partial t} + B_1^{HL} \cdot \frac{\partial T_1^{B,L}}{\partial t} + C_1^{HL} \cdot \frac{\partial dxL}{\partial t} + D_1^{HL} \cdot \dot{m}_2^{D,L} + F_1^{HL} + G_1^{HL} \cdot \dot{m}_{IN}^L + H_1^{HL} \cdot \dot{m}_{OUT}^L = 0$
		Core-liquid sub-layer
Energy	Equation 374	$A_{n_L}^{TL} \cdot \frac{\partial P^V}{\partial t} + B_{n_L}^{TL} \cdot \frac{\partial T_{n_L}^{B,L}}{\partial t} + C_{n_L}^{TL} \cdot \frac{\partial dxL}{\partial t} + D_{n_L}^{TL} \cdot \dot{m}_{n_L+1}^{D,L} + E_{n_L}^{TL} \cdot \dot{m}_{n_L}^{D,L} + F_{n_L}^{TL} = 0$
Mass	Equation 375	$A_{n_L}^{HL} \cdot \frac{\partial P^V}{\partial t} + B_{n_L}^{HL} \cdot \frac{\partial T_{n_L}^{B,L}}{\partial t} + C_{n_L}^{HL} \cdot \frac{\partial dxL}{\partial t} + D_{n_L}^{HL} \cdot \dot{m}_{n_L+1}^{D,L} + E_{n_L}^{HL} \cdot \dot{m}_{n_L}^{D,L} + F_{n_L}^{HL} = 0$

The coefficients of the equations of Table 124 are defined in Table 125.

Table 125. Coefficients of the mass and energy balance equations.

Coefficients	**Equations**	**Formulas**
		Ullage mass conservation law
A^P	Equation 376	$A^P = V^V \cdot \left.\frac{\partial \rho^V(T^V, P^V)}{\partial P^V}\right\|_{T^V}$
B^P	Equation 377	$B^P = V^V \cdot \left.\frac{\partial \rho^V(T^V, P^V)}{\partial T^V}\right\|_{P^V}$
C^P	Equation 378	$C^P = -\rho^V \cdot \left[\sum_{n_L=1}^{N^L} Z_{n_L}\right]$
D^P	Equation 379	$D^P = -1$
E^P	Equation 380	$E^P = 1$

Table 125. Coefficients of the mass and energy balance equations.

F^P	Equation 381	$F^P = -[\dot{m}_N]$
Ullage energy conservation law		
A^{TV}	Equation 382	$A^{TV} = m^V \cdot \left.\frac{\partial \tilde{h}^V(T^V, P^V)}{\partial P^V}\right\|_{T^V}$
B^{TV}	Equation 383	$B^{TV} = m^V \cdot C_P^V(T^V, P^V)$
C^{TV}	Equation 384	$C^{TV} = 0$
D^{TV}	Equation 385	$D^{TV} = -\left[\tilde{h}_{IN}^V(T_{IN}^V, P_{IN}^V) - \tilde{h}^V(T_{N^V}^V, P^V)\right]$
E^{TV}	Equation 386	$E^{TV} = 0$
F^{TV}	Equation 387	$F^{TV} = -\left\{\dot{Q}_w^{SV} - \dot{Q}_I^V + \dot{m}_N \cdot \left(\tilde{h}_S^V - \tilde{h}_1^V\right) + \sum_{i=1}^{N^+}\left[\dot{m}_i^{BL} \cdot \tilde{h}_i^V\right] - \sum_{i=1}^{N^-}\left[\dot{m}_i^{BL} \cdot \tilde{h}_i^V\right] + \sum_{i=1}^{M^+}\left[\dot{m}_i^D \cdot \left(\tilde{h}_{i+1}^V - \tilde{h}_i^V\right)\right] - \sum_{i=1}^{M^-}\left[\dot{m}_i^D \cdot \left(\tilde{h}_{i+1}^V - \tilde{h}_i^V\right)\right]\right\}$
Interface-liquid sub-layer mass conservation law		
$A_{N^L}^{HL}$	Equation 388	$A_{N^L}^{HL} = V_{N^L}^{B,L} \cdot \left.\frac{\partial \rho^L}{\partial P^V}\right\|_{T^L}$
$B_{N^L}^{HL}$	Equation 389	$B_{N^L}^{HL} = V_{N^L}^{B,L} \cdot \left.\frac{\partial \rho^L}{\partial T^L}\right\|_{P^V}$
$C_{N^L}^{HL}$	Equation 390	$C_{N^L}^{HL} = \rho^L \cdot Z_{N^L}$
$E_{N^L}^{HL}$ (Case 1 and 3)	Equation 391	$E_{N^L}^{HL} = 1$
$E_{N^L}^{HL}$ (Case 2 and 4)	Equation 392	$E_{N^L}^{HL} = -1$
$F_{N^L}^{HL}$	Equation 393	$F_{N^L}^{HL} = -[\dot{m}_{N^L}^{BL,L} - \dot{m}_N + \dot{m}_{N^L-1}^B]$
Interface-liquid sub-layer energy conservation law		
$A_{N^L}^{TL}$	Equation 394	$A_{N^L}^{TL} = m_{N^L}^{B,L} \cdot \left.\frac{\partial \tilde{h}^L}{\partial P^V}\right\|_{T^L}$
$B_{N^L}^{TL}$	Equation 395	$B_{N^L}^{TL} = m_{N^L}^{B,L} \cdot C_P^L$
$C_{N^L}^{TL}$	Equation 396	$C_{N^L}^{TL} = 0$
$E_{N^L}^{TL}$ (Case 1 and 3)	Equation 397	$E_{N^L}^{TL} = 0$
$E_{N^L}^{TL}$ (Case 2 and 4)	Equation 398	$E_{N^L}^{TL} = -\left(\tilde{h}_{N^L-1}^{B,L} - \tilde{h}_{N^L}^{B,L}\right)$
$A_{N^L}^{TL}$ (Case 1 and 2)	Equation 399	$F_{N^L}^{HL} = -\left[-\dot{Q}_I^L - \dot{Q}_{N^L}^{LOW} + \dot{m}_{N^L}^{BL,L} \cdot \left(\tilde{h}_{N^L}^{BL,L} - \tilde{h}_{N^L}^{B,L}\right) - \dot{m}_N \cdot \left(\tilde{h}_S^L - \tilde{h}_{N^L}^{B,L}\right) + \dot{m}_{N^L-1}^B \cdot \left(\tilde{h}_{N^L-1}^{B,L} - \tilde{h}_{N^L}^{B,L}\right)\right]$
$A_{N^L}^{TL}$ (Case 3 and 4)	Equation 400	$F_{N^L}^{HL} = -\left[-\dot{Q}_I^L - \dot{Q}_{N^L}^{LOW} + \dot{m}_{N^L}^{BL,L} \cdot \left(\tilde{h}_{N^L}^{BL,L} - \tilde{h}_{N^L}^{B,L}\right) - \dot{m}_N \cdot \left(\tilde{h}_S^L - \tilde{h}_{N^L}^{B,L}\right) + \dot{m}_{N^L-1}^B \cdot \left(\tilde{h}_{N^L-1}^{B,L} - \tilde{h}_{N^L}^{B,L}\right)\right]$
Bottom-liquid sub-layer mass conservation law		

Table 125. Coefficients of the mass and energy balance equations.

A_1^{HL}	Equation 401	$A_1^{HL} = V_1^{B,L} \cdot \left.\frac{\partial \rho^L}{\partial P^V}\right\|_{T^L}$
$B_{N^1}^{HL}$	Equation 402	$B_{N^1}^{HL} = V_1^{B,L} \cdot \left.\frac{\partial \rho^L}{\partial T^L}\right\|_{P^V}$
C_1^{HL}	Equation 403	$C_1^{HL} = \rho^L \cdot Z_1$
D_1^{HL}	Equation 404	$D_1^{HL} = -1$
F_1^{HL} (Case 1)	Equation 405	$F_1^{HL} = -\left[\dot{m}_2^{D,L} - \dot{m}_1^B - \dot{m}_1^{BL,L}\right]$
F_1^{HL} (Case 2)	Equation 406	$F_1^{HL} = -\left[-\dot{m}_2^{D,L} - \dot{m}_1^B - \dot{m}_1^{BL,L}\right]$
G_1^{HL}	Equation 407	$G_1^{HL} = -1$
H_1^{HL}	Equation 408	$H_1^{HL} = 1$
Bottom-liquid sub-layer energy conservation law		
A_1^{TL}	Equation 409	$A_1^{TL} = m_1^{B,L} \cdot \left.\frac{\partial \tilde{h}^L}{\partial P^V}\right\|_{T^L}$
B_1^{TL}	Equation 410	$B_1^{TL} = m_1^{B,L} \cdot C_P^L$
C_1^{TL}	Equation 411	$C_1^{TL} = 0$
D_1^{TL} (Case 1)	Equation 412	$D_1^{TL} = -\left(\tilde{h}_2^{B,L} - \tilde{h}_1^{B,L}\right)$
D_1^{TL} (Case 2)	Equation 413	$D_1^{TL} = 0$
F_1^{TL}	Equation 414	$F_1^{TL} = -\left[\dot{Q}_w^B + \dot{Q}_1^{UP}\right]$
G_1^{TL}	Equation 415	$G_1^{TL} = -\left(\tilde{h}_{IN}^L - \tilde{h}_1^{B,L}\right)$
H_1^{TL}	Equation 416	$H_1^{TL} = 0$
Bulk-liquid sub-layer mass conservation law		
$A_{n_L}^{HL}$	Equation 417	$A_{n_L}^{TL} = V_{n_L}^{B,L} \cdot \left.\frac{\partial \rho^L}{\partial P^V}\right\|_{T^L}$
$B_{n_L}^{HL}$	Equation 418	$B_{n_L}^{TL} = V_{n_L}^{B,L} \cdot \left.\frac{\partial \rho^L}{\partial T^L}\right\|_{P^V}$
$C_{n_L}^{HL}$	Equation 419	$C_{n_L}^{TL} = \rho^L \cdot Z_{n_L}$
$D_{n_L}^{HL}$ (Case 1, 2, 5, 6, 9 and 10)	Equation 420	$D_{n_L}^{HL} = -1$
$D_{n_L}^{HL}$ (Case 3, 4, 7, 8, 11 and 12)	Equation 421	$D_{n_L}^{HL} = 1$
$E_{n_L}^{HL}$ (Case 1, 3, 5, 7, 9 and 11)	Equation 422	$E_{n_L}^{HL} = 1$
$E_{n_L}^{HL}$ (Case 2, 4, 6, 8,	Equation 423	$E_{n_L}^{HL} = -1$

Table 125. Coefficients of the mass and energy balance equations.

10 and 12)		
$F^{HL}_{n_L}$	Equation 424	$F^{HL}_{n_L} = -\left[-\dot{m}^{BL,L}_{n_L} + \dot{m}^{B}_{n_L-1} - \dot{m}^{B}_{n_L}\right]$
Bulk-liquid sub-layer energy conservation law		
$A^{TL}_{n_L}$	Equation 425	$A^{TL}_{n_L} = m^{B,L}_{n_L} \cdot \left.\frac{\partial \tilde{h}^L}{\partial P^V}\right\vert_{T^L}$
$B^{TL}_{n_L}$	Equation 426	$B^{TL}_{n_L} = m^{B,L}_{n_L} \cdot C^L_P$
$C^{TL}_{n_L}$	Equation 427	$C^{TL}_{n_L} = 0$
$D^{TL}_{n_L}$ (Case 1, 2, 5, 6, 9 and 10)	Equation 428	$D^{TL}_{n_L} = -\left(\tilde{h}^{B,L}_{n_L+1} - \tilde{h}^{B,L}_{n_L}\right)$
$D^{TL}_{n_L}$ (Case 3, 4, 7, 8, 11 and 12)	Equation 429	$D^{TL}_{n_L} = 0$
$E^{TL}_{n_L}$ (Case 1, 3, 5, 7, 9 and 11)	Equation 430	$E^{TL}_{n_L} = 0$
$E^{TL}_{n_L}$ (Case 2, 4, 6, 8, 10 and 12)	Equation 431	$E^{TL}_{n_L} = -\left(\tilde{h}^{B,L}_{n_L-1} - \tilde{h}^{B,L}_{n_L}\right)$
$F^{TL}_{n_L}$ (case 1, 2, 3 and 4)	Equation 432	$F^{TL}_{n_L} = -\left[\dot{Q}^{UP}_{n_L} - \dot{Q}^{LOW}_{n_L} + \dot{m}^{B}_{n_L-1} \cdot \left(\tilde{h}^{B,L}_{n_L-1} - \tilde{h}^{B,L}_{n_L}\right)\right]$
$F^{TL}_{n_L}$ (case 5, 6, 7 and 8)	Equation 433	$F^{TL}_{n_L} = -\left[\dot{Q}^{UP}_{n_L} - \dot{Q}^{LOW}_{n_L} + \dot{m}^{BL,L}_{n_L} \cdot \left(\tilde{h}^{BL,L}_{n_L} - \tilde{h}^{B,L}_{n_L}\right) + \dot{m}^{B}_{n_L-1} \cdot \left(\tilde{h}^{B,L}_{n_L-1} - \tilde{h}^{B,L}_{n_L}\right)\right]$
$F^{TL}_{n_L}$ (case 9, 10, 11 and 12)	Equation 434	$F^{TL}_{n_L} = -\left[\dot{Q}^{UP}_{n_L} - \dot{Q}^{LOW}_{n_L} + \dot{Q}^{SL}_{w,n_L} + \dot{m}^{B}_{n_L-1} \cdot \left(\tilde{h}^{B,L}_{n_L-1} - \tilde{h}^{B,L}_{n_L}\right)\right]$

The equations of Table 124 are obtained by substituting the non-key variables with the coefficient of Table 125.

2.5.Temperatures equations

The deduction of the temperatures equations is the fifth step (step e) of Section 2 of Chapter 6) of the mathematical produce, as it is presented in Figure 128. As it is indicated by the equations of Table 124, the bottom sub-layer liquid temperature (T^L_1-e), core sub-layer liquid temperature evolution (T^L_{nL}-e), interface sub-layer liquid temperature evolution (T^L_{NL}-e) and ullage temperature evolution (T^V-e) equations can be deduced from the linear form of the conservation laws (see Table 124), and the time-derivates of the bottom, core and interface bulk liquid sub-layer temperatures and the ullage temperature can be explicitly computed. These explicit equations, called temperature equations, are reported in Table 126.

Table 126. Temperature equations of LS model.

Name	Equation	Formula
T^L_1-e equation	Equation 435	$\frac{\partial T^{B,L}_1}{\partial t} = A''^{TL}_1 \cdot \frac{\partial P^V}{\partial t} + C''^{TL}_1 \cdot \frac{\partial dxL}{\partial t} + D''^{TL}_1 \cdot \dot{m}^{D,L}_2 + F''^{TL}_1 + G''^{TL}_1 \cdot \dot{m}^{L}_{IN} + H''^{TL}_1 \cdot \dot{m}^{L}_{OUT}$

Table 126. Temperature equations of LS model.

T^L_{nL}-e equation	Equation 436	$\frac{\partial T^{B,L}_{n_L}}{\partial t} = A''^{TL}_{n_L} \cdot \frac{\partial P^V}{\partial t} + C''^{TL}_{n_L} \cdot \frac{\partial dxL}{\partial t} + D''^{TL}_{n_L} \cdot \dot{m}^{D,L}_{n_L+1} + E''^{TL}_{n_L} \cdot \dot{m}^{D,L}_{n_L} + F''^{TL}_{n_L}$
T^L_{NL}-e equation	Equation 437	$\frac{\partial T^{B,L}_{N^L}}{\partial t} = A''^{TL}_{N^L} \cdot \frac{\partial P^V}{\partial t} + C''^{TL}_{N^L} \cdot \frac{\partial dxL}{\partial t} + E''^{TL}_{N^L} \cdot \dot{m}^{D,L}_{N^L} + F''^{TL}_{N^L}$
T^V-e equation	Equation 438	$\frac{\partial T^V}{\partial t} = \left[A''^{TV} \cdot \frac{\partial P^V}{\partial t} + C''^{TV} \cdot \frac{\partial dxL}{\partial t} + D''^{TV} \cdot \dot{m}^V_{IN} + E''^{TL} \cdot \dot{m}_{BOG} + F''^{TV}\right]$

The coefficients of Equation 435, Equation 436 and Equation 437 are reported in Table 127.

Table 127. Coefficients of T^L_{NL}-e equation (Equation 437), T^L_{nL}-e equation (Equation 436) and T^L_1-e equation (Equation 435).

Coefficient	**Equation**	**Formula**
T^L_{NL}-e equation (Equation 437)		
$A''^{TL}_{N^L}$	Equation 439	$A''^{TL}_{N^L} = -\frac{A^{TL}_{N^L}}{B^{TL}_{N^L}}$
$C''^{TL}_{N^L}$	Equation 440	$C''^{TL}_{N^L} = -\frac{C^{TL}_{N^L}}{B^{TL}_{N^L}}$
$E''^{TL}_{N^L}$	Equation 441	$E''^{TL}_{N^L} = -\frac{E^{TL}_{N^L}}{B^{TL}_{N^L}}$
$F''^{TL}_{N^L}$	Equation 442	$F''^{TL}_{N^L} = -\frac{F^{TL}_{N^L}}{B^{TL}_{N^L}}$
T^L_{nL}-e equation (Equation 436)		
$A''^{TL}_{n_L}$	Equation 443	$A''^{TL}_{n_L} = -\frac{A^{TL}_{n_L}}{B^{TL}_{n_L}}$
$C''^{TL}_{n_L}$	Equation 444	$C''^{TL}_{n_L} = -\frac{C^{TL}_{n_L}}{B^{TL}_{n_L}}$
$D''^{TL}_{n_L}$	Equation 445	$D''^{TL}_{n_L} = -\frac{D^{TL}_{n_L}}{B^{TL}_{n_L}}$
$E''^{TL}_{n_L}$	Equation 446	$E''^{TL}_{n_L} = -\frac{E^{TL}_{n_L}}{B^{TL}_{n_L}}$
$F''^{TL}_{n_L}$	Equation 447	$F''^{TL}_{n_L} = -\frac{F^{TL}_{n_L}}{B^{TL}_{n_L}}$
T^L_1-e equation (Equation 435)		
A''^{TL}_1	Equation 448	$A''^{TL}_1 = -\frac{A^{TL}_1}{B^{TL}_1}$
C''^{TL}_1	Equation 449	$C''^{TL}_1 = -\frac{C^{TL}_1}{B^{TL}_1}$
D''^{TL}_1	Equation 450	$D''^{TL}_1 = -\frac{D^{TL}_1}{B^{TL}_1}$
F''^{TL}_1	Equation 451	$F''^{TL}_1 = -\frac{F^{TL}_1}{B^{TL}_1}$
H''^{TL}_1	Equation 452	$H''^{TL}_1 = -\frac{H^{TL}_1}{B^{TL}_1}$

Table 127. Coefficients of T^{L}_{NL}-e equation (Equation 437), T^{L}_{nL}-e equation (Equation 436) and T^{L}_{1}-e equation (Equation 435).

G''^{TL}_{1}	Equation 453	$G''^{TL}_{1} = -\frac{G^{TL}_{1}}{B^{TL}_{1}}$

The coefficients of Equation 438 are reported in Table 128.

Table 128. Coefficients of T^{V}-e equation (Equation 438).

Coefficients	Equations	Formulas
A''^{TV}	Equation 454	$A''^{TV} = -\frac{A^{TV}}{B^{TV}}$
C''^{TV}	Equation 455	$C''^{TV} = -\frac{C^{TV}}{B^{TV}}$
D''^{TV}	Equation 456	$D''^{TV} = -\frac{D^{TV}}{B^{TV}}$
E''^{TV}	Equation 457	$E''^{TV} = -\frac{E^{TV}}{B^{TV}}$
F''^{TV}	Equation 458	$F''^{TV} = -\frac{F^{TV}}{B^{TV}}$

The coefficients of Equation 435, Equation 436, Equation 437 and Equation 438 are obtained by moving the variables $B^{TL}_{1} \cdot \frac{\partial T^{L}_{1}}{\partial t}$, $B^{TL}_{n_L} \cdot \frac{\partial T^{L}_{n_L}}{\partial t}$, $B^{TL}_{N^L} \cdot \frac{\partial T^{L}_{N^L}}{\partial t}$ and $B^{TV} \cdot \frac{\partial T^{V}}{\partial t}$ to the left part of the Equation 371, Equation 373, Equation 375 and Equation 369, respectively, and dividing these left parts by B^{TL}_{1}, $B^{TL}_{n_L}$, $B^{TL}_{N^L}$ and B^{TV}.

2.6. Equations of the descending flow

The deduction of the first descending flow (FDF) and core descending flow (CDF) equations is the sixth step (step f) of Section 2 of Chapter 6) of the mathematical produce, as it is presented in Figure 128. The conservation laws of energy of the bulk of the sub-layer of Table 121 depends on the descending flows $\dot{m}^{D,L}_{2}$ and $\dot{m}^{D,L}_{3,\ldots,n_L,\ldots,N^L}$. As a consequence, the equations that compute the indipendent variables are functions of these flows. The equation of the descending flows can be deduced from the linear form of the conservation laws (see Table 123) and from the temperature equations of the liquid (Equation 435, Equation 436 and Equation 437). The equations of the descending flow ($\dot{m}^{D,L}_{2}$, $\dot{m}^{D,L}_{n_L}$ and $\dot{m}^{D,L}_{N^L}$) are reported in Table 129.

Table 129. Equations of the descending flow.

Sub-layer	Equation	Formulas
Bottom	Equation 459	$\dot{m}^{D,L}_{2} = \left[A''^{HL}_{1} \cdot \frac{\partial P^{V}}{\partial t} + C''^{HL}_{1} \cdot \frac{\partial dxL}{\partial t} + F''^{HL}_{1} + G''^{HL}_{1} \cdot \dot{m}^{L}_{IN} + H^{HL}_{1} \cdot \dot{m}^{L}_{OUT}\right]$
Core and interface	Equation 460	$\dot{m}^{D,L}_{n_L+1} = \left[A''^{HL}_{n_L} \cdot \frac{\partial P^{V}}{\partial t} + C''^{HL}_{n_L} \cdot \frac{\partial dxL}{\partial t} + E''^{TL}_{n_L} \cdot \dot{m}^{D}_{n_L} + F''^{HL}_{n_L}\right]$

The coefficients of equations of Table 129 are given in Table 130.

Table 130. Coefficients of equations of the descending flow.

Coefficients	Equations	Formulas
$A''^{HL}_{1,\ldots,n_L,\ldots,(N^L-1)}$	Equation 461	$A''^{HL}_{1,\ldots,n_L,\ldots,(N^L-1)} = -\frac{A^{HL}_{1,\ldots,n_L,\ldots,(N^L-1)} - A''^{TL}_{1,\ldots,n_L,\ldots,(N^L-1)} \cdot B^{HL}_{1,\ldots,n_L,\ldots,(N^L-1)}}{D^{HL}_{1,\ldots,n_L,\ldots,(N^L-1)} - D''^{TL}_{1,\ldots,n_L,\ldots,(N^L-1)} \cdot B^{HL}_{1,\ldots,n_L,\ldots,(N^L-1)}}$

$C''^{HL}_{1,\dots,n_L,\dots,(N^L-1)}$	Equation 462	$C''^{HL}_{1,\dots,n_L,\dots,(N^L-1)} = -\frac{C^{HL}_{1,\dots,n_L,\dots,(N^L-1)} - C''^{TL}_{1,\dots,n_L,\dots,(N^L-1)} \cdot B^{HL}_{1,\dots,n_L,\dots,(N^L-1)}}{D^{HL}_{1,\dots,n_L,\dots,(N^L-1)} - D''^{TL}_{1,\dots,n_L,\dots,(N^L-1)} \cdot B^{HL}_{1,\dots,n_L,\dots,(N^L-1)}}$
$E''^{HL}_{1,\dots,n_L,\dots,(N^L-1)}$	Equation 463	$E''^{HL}_{1,\dots,n_L,\dots,(N^L-1)} = -\frac{E^{HL}_{1,\dots,n_L,\dots,(N^L-1)} - E''^{TL}_{1,\dots,n_L,\dots,(N^L-1)} \cdot B^{HL}_{1,\dots,n_L,\dots,(N^L-1)}}{D^{HL}_{1,\dots,n_L,\dots,(N^L-1)} - D''^{TL}_{1,\dots,n_L,\dots,(N^L-1)} \cdot B^{HL}_{1,\dots,n_L,\dots,(N^L-1)}}$
$F''^{HL}_{1,\dots,n_L,\dots,(N^L-1)}$	Equation 464	$F''^{HL}_{1,\dots,n_L,\dots,(N^L-1)} = -\frac{F^{HL}_{1,\dots,n_L,\dots,(N^L-1)} - F''^{TL}_{1,\dots,n_L,\dots,(N^L-1)} \cdot B^{HL}_{1,\dots,n_L,\dots,(N^L-1)}}{D^{HL}_{1,\dots,n_L,\dots,(N^L-1)} - D''^{TL}_{1,\dots,n_L,\dots,(N^L-1)} \cdot B^{HL}_{1,\dots,n_L,\dots,(N^L-1)}}$
G''^{HL}_{1}	Equation 465	$G''^{HL}_{1} = -\frac{G^{HL}_1 - G''^{TL}_1 \cdot B^{HL}_1}{D^{HL}_1 - D''^{TL}_1 \cdot B^{HL}_1}$
H''^{HL}_{1}	Equation 466	$H''^{HL}_{1} = -\frac{H^{HL}_1 - H''^{TL}_1 \cdot \frac{B^{HL}_1}{B^{HL}_1}}{D^{HL}_1 - D''^{TL}_1 \cdot B^{HL}_1}$

The mathematical steps to compute the equations of Table 129 are reported in Section 2 of Appendix AC. As it is reported in Table 129 and in Table 126, the temperature and the descending flow equations depend on the time-derivates of the pressure ($\frac{\partial P^V}{\partial t}$) and of the thickness of the sub-layer ($\frac{\partial dxL}{\partial t}$). So, equations to calculate $\frac{\partial P^V}{\partial t}$ and $\frac{\partial dxL}{\partial t}$ are required and these equations are deduced in Section 2.7 of Chapter 6.

2.7. Pressure-thickness equations

The deduction of the pressure-thickness equations is the seventh step (step g) of Section 2 of Chapter 6) of the mathematical produce, as it is presented in Figure 128. The time-derivates of the liquid temperature of the bulk of the sub-layers and of the ullage temperature are computed with the temperature equations (see Table 126), which are obtained from the linear form of the energy balance equations (see Table 124). The descending flows can be computed with the descending flow equations (see Table 129), which are deduced from the linear form of the liquid mass conservation law (see Table 124). So, the number of the equations of the linear form of the balance equations (see Table 124), which can be used to compute the time-derivates of the pressure ($\frac{\partial P^V}{\partial t}$) and of the thickness ($\frac{\partial dxL}{\partial t}$), decreases because linear form of the energy and mass balance equations are used to respectively compute time-derivates of the liquid temperature and the descending flows. The remaining usable equations are the linear form of the ullage mass conservation law (Equation 368) and the linear form of the interface liquid mass conservation law (Equation 371). Hence, the formulas to compute $\frac{\partial P^V}{\partial t}$ and $\frac{\partial dxL}{\partial t}$ can be deduced from these mathematical expressions, using the pressure-thickness (P-dxL) equations. These equations depend on $\frac{\partial P^V}{\partial t}$ and $\frac{\partial dxL}{\partial t}$ and they are reported in Table 131.

Table 131. Pressure-thickness equations.

Phase	Equation	Formulas
Vapour	Equation 467	$A''^{P} \cdot \frac{\partial P^V}{\partial t} + C''^{P} \cdot \frac{\partial dxL}{\partial t} + D''^{P} \cdot \dot{m}^V_{IN} + E''^{P} \cdot \dot{m}_{BOG} + F''^{P} = 0$
Liquid	Equation 468	$A''^{HL} \cdot \frac{\partial P^V}{\partial t} + C''^{HL} \cdot \frac{\partial dxL}{\partial t} + F''^{HL} + G''^{HL} \cdot \dot{m}^L_{IN} + H''^{HL} \cdot \dot{m}^L_{OUT} = 0$

The coefficients of the pressure-thickness equations are reported in Table 132.

Table 132. Coefficients of pressure-thickness equations.

Table 132. Coefficients of pressure-thickness equations.

Coefficients	Equations	Formulas
Vapour pressure-thickness equation		
A''^{P}	Equation 469	$A''^{P} = A^{P} + A''^{TV} \cdot B^{P}$
C''^{P}	Equation 470	$C''^{P} = C^{P} + C''^{TV} \cdot B^{P}$
D''^{P}	Equation 471	$D''^{P} = D^{P} + D''^{TV} \cdot B^{P}$
E''^{P}	Equation 472	$E''^{P} = E^{P} + E''^{TV} \cdot B^{P}$
F''^{P}	Equation 473	$F''^{P} = F^{P} + F''^{TV} \cdot B^{P}$
Liquid pressure-thickness equation		
A''^{HL}	Equation 474	$A''^{HL} = A''^{HL}_{N^L} + E''^{HL}_{N^L} \cdot \left[\sum_{n_L=1}^{N^L-1} A''^{HL}_{n_L} \cdot \left(\prod_{j=n_L+1}^{N^L-1} E''^{HL}_{j}\right)\right]$
C''^{HL}	Equation 475	$C''^{HL} = C''^{HL}_{N^L} + E''^{HL}_{N^L} \cdot \left[\sum_{n_L=1}^{N^L-1} C''^{HL}_{n_L} \cdot \left(\prod_{j=n_L+1}^{N^L-1} E''^{HL}_{j}\right)\right]$
F''^{HL}	Equation 476	$F''^{HL} = F''^{HL}_{N^L} + E''^{HL}_{N^L} \cdot \left[\sum_{n_L=1}^{N^L-1} F''^{HL}_{n_L} \cdot \left(\prod_{j=n_L+1}^{N^L-1} E''^{HL}_{j}\right)\right]$
G''^{HL}	Equation 477	$G''^{HL} = G''^{HL}_{1} \cdot \left(\prod_{n_L=2}^{N^L} E''^{HL}_{n_L}\right)$
H''^{HL}	Equation 478	$H''^{HL} = H''^{HL}_{1} \cdot \left(\prod_{n_L=2}^{N^L} E''^{HL}_{n_L}\right)$
$A''^{HL}_{N^L}$	Equation 479	$A''^{HL}_{N^L} = A^{HL}_{N^L} - A^{TL}_{N^L} \cdot \frac{B^{HL}_{N^L}}{B^{TL}_{N^L}}$
$C''^{HL}_{N^L}$	Equation 480	$C''^{HL}_{N^L} = C^{HL}_{N^L} - C^{TL}_{N^L} \cdot \frac{B^{HL}_{N^L}}{B^{TL}_{N^L}}$
$E''^{HL}_{N^L}$	Equation 481	$E''^{HL}_{N^L} = E^{HL}_{N^L} - E^{TL}_{N^L} \cdot \frac{B^{HL}_{N^L}}{B^{TL}_{N^L}}$
$F''^{HL}_{N^L}$	Equation 482	$F''^{HL}_{N^L} = F^{HL}_{N^L} - F^{TL}_{N^L} \cdot \frac{B^{HL}_{N^L}}{B^{TL}_{N^L}}$

As it is described in Table 131, the pressure-thickness equations relate the derivates of the pressure to the derivate of the thickness. The mathematical procedure to obtian these equations is reported in Section 3 of Appendix AC.

2.8. Pressure-evolution, thickness-evolution, inlet liquid flow and boil-off gas equations

The deduction of the pressure-evolution (P-e), thickness-evolution (dxL-e), inlet liquid flow (ILF) and boil-off gas (BOG) equations is the eighth step (step h) of Section 2 of Chapter 6) of the mathematical produce, as it is presented in Figure 128. The time-derivates of the ullage temperature and of the liquid temperatures in the sub-layer can be computed with the liquid temperature equations (see Table 126). The descending flows in the liquid bulk are computed with the descending flow equations (see Table 129). So, the time-derivates of the ullage pressure ($\frac{\partial P^V}{\partial t}$) and of the thickness ($\frac{\partial dxL}{\partial t}$), the inlet liquid flow ($\dot{m}^L_{IN}$) and the boil-off gas (BOG) flow ($\dot{m}_{BOG}$) are not computed yet. As said in Section 2.7 of Chapter 6, the pressure-thickness equations (see Table 131) can only be used to compute these variables. So, P-e, dxL-e, ILF and BOG equations can be deduced from the pressure-thickness equations. In the steady state mode (mode 1.b), the liquid volume and the ullage pressure remain constant because the storage container is filled with liquid and the BOG is evacuated. So, the thickness of the sub-layers remains constant. In the self-pressurisation mode (mode 4), the pressure increases in time and the thickness of the sub-layer can increase or decrease because the liquid volume can change in time. So, the mathematical expressions of P-e, dxL-e, ILF and BOG at the steady state are different from the ones of the self-pressurisation. These equations are the ones reported in Table 133 for the storage modes of hte steady strate and of the self-pressurisation.

Table 133. Equations and target variables of mathematical systems of LS model.

Indipendent variable	Equation	Differential formula
		Self-pressurisation
$\frac{\partial P^V}{\partial t}$	Equation 483	$\frac{\partial P^V}{\partial t} = -\frac{D''^{P} \cdot \dot{m}^V_{IN} - \frac{C''^{P}}{C''^{HL}} \cdot G''^{HL} \cdot \dot{m}^L_{IN} - \frac{C''^{P}}{C''^{HL}} \cdot H''^{HL} \cdot \dot{m}^L_{OUT}}{\left(A''^{P} - \frac{C''^{P}}{C''^{HL}} \cdot A''^{HL}\right)} - \frac{E''^{P} \cdot \dot{m}_{BOG} + F''^{P} - \frac{C''^{P}}{C''^{HL}} \cdot F''^{HL}}{\left(A''^{P} - \frac{C''^{P}}{C''^{HL}} \cdot A''^{HL}\right)}$
$\frac{\partial dxL}{\partial t}$	Equation 484	$\frac{\partial dxL}{\partial t} = -\frac{1}{C''^{HL}} \cdot \left[A''^{HL} \cdot \frac{\partial P^V}{\partial t} + F''^{HL} + G''^{HL} \cdot \dot{m}^L_{IN} + H''^{HL} \cdot \dot{m}^L_{OUT}\right]$
$\dot{m}_{BOG}$	Equation 485	$\dot{m}_{BOG} = 0$
$\dot{m}^L_{IN}$	Equation 486	$\dot{m}^L_{IN} = 0$
		Steady state
$\frac{\partial P^V}{\partial t}$	Equation 487	$\frac{\partial P^V}{\partial t} = 0$
$\frac{\partial dxL}{\partial t}$	Equation 488	$\frac{\partial dxL}{\partial t} = 0$
$\dot{m}_{BOG}$	Equation 489	$\dot{m}_{BOG} = -\frac{A''^{P} \cdot \frac{\partial P^V}{\partial t} + C''^{P} \cdot \frac{\partial dxL}{\partial t} + D''^{P} \cdot \dot{m}^V_{IN} + F''^{P}}{E''^{P}}$
$\dot{m}^L_{IN}$	Equation 490	$\dot{m}^L_{IN} = -\frac{A''^{HL} \cdot \frac{\partial P^V}{\partial t} + C''^{HL} \cdot \frac{\partial dxL}{\partial t} + F''^{HL} + H''^{HL} \cdot \dot{m}^L_{OUT}}{G''^{HL}}$

The mathematical steps to obtain these equations are reported in Section 4 of Appendix AC.

3. Distribution of the convective flows in the liquid

As it is presented in Section 2 of Chapter 6, the mass and energy conservation laws of the liquid stratification model (LS model) depend on the distribution of the convective flows in the liquid, in particular on the direction of the descending flow ($\dot{m}_{n_L+1}^{D,L}$) and on the values of the bulk rising flow of the bottom ($\dot{m}_{n_L}^{B}$). The descending flow usually goes from an upper sub-layer to a lower one. It can happen that this flow goes from a lower sub-layer to an upper one. These flows are respectively computed in Block 12 and 11 of the LS model, as shown in Figure 125.

Section 3.1 explains how the values of the bulk rising flow of the bottom are computed. Section 3.2 presents the calculation of the direction of the descending flow.

3.1.Bulk rising flow of the bottom

As reported by Anderson and Kolar [31], a confined fluid develops a stratified and an uniform region when it is heated at the side wall and at the bottom. The volume occupied by each region depends on the heat flows at each surface of the confined space, as illustrated in Figure 130. In Figure 130, the stratified region is described by the rectangles of light blue and the homogenous zone is illustrated by the dark blue colour. The white arrow with red boarder is the heat flows in the liquid and the green arrow is the net mass flow. The dashed yellow line is the interface. The white arrows with grey, orange, purple and blue boarders are respectively the mass flow rate of the wet side wall boundary layer, the descending flow, the boundary layer-to-bulk flow and the bulk rising flow rate of the bottom. the white dashed lines are the sub-layers with the same temperature.

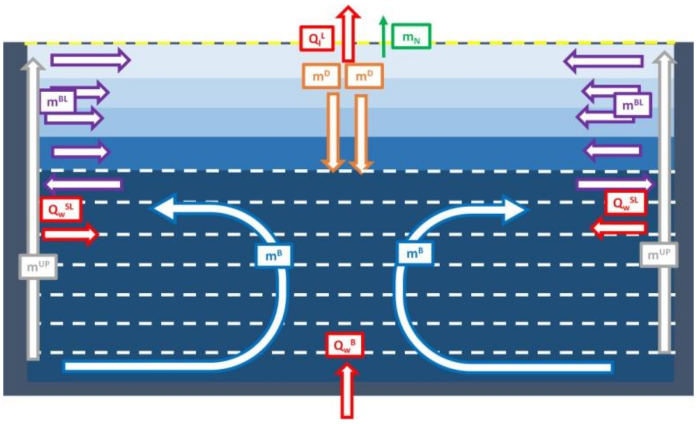

Figure 130. Fluid-dynamics of the liquid of the LS model.

As illustrated in Figure 130, the heat inputs at the bottom produces a rising flow in the bulk of the liquid, as observed by Anderson and Kolar [31]. This mass flow moves upward if the temperature of the upper liquid is lower than the temperature at the bottom. When the upper liquid is warmer than the lower part, this mass flow rate reduces because the buoyancy forces of the bulk are opposite to the fluid movement. The mass flow rate of the boundary layer can contribute stopping this flow rate. When the boundary layer mass flow is higher than the bulk rising flow of the bottom, the latter decreases because it is pushed downward by the descending bulk flow rate. The same behaviour presented above takes place in a cryogenic storage container with side wall and bottom heating such as the vertical cylinder of Seo and Jeong [24], Perez et al. [26] and Kang et al. [25]. Considering the physical described above, it is assumed that:

a) The bulk rising flow of the bottom is equal to the natural convective flow rate of the bottom, in every sub-layer;

b) If the temperature of the upper sub-layer is higher than the temperature of the lower sub-layer, the bulk rising flow is equal to zero because it is blocked by the adverse bulk buoyancy forces;
c) This rising flow is equal to zero, when it is lower than the mass flow rate of the side wall boundary layer;

So, the bulk rising flow rate of the bottom ($\dot{m}_{n_L}^{B}$) is estimated as described in Table 134.

Table 134. Equations to compute $\dot{\boldsymbol{m}}_{\boldsymbol{n_L}}^{\boldsymbol{B}}$.

Condition	Equation	Formulas
$T_{n_L+1}^{B,L} > T_{n_L}^{B,L}$	Equation 491	$\dot{m}_{n_L}^{B} = 0$
$T_{n_L+1}^{B,L} \leq T_{n_L}^{B,L}$ & $\dot{m}_{n_L}^{UP} > \dot{m}^{B}$	Equation 492	$\dot{m}_{n_L}^{B} = 0$
$T_{n_L+1}^{B,L} \leq T_{n_L}^{B,L}$ & $\dot{m}_{n_L}^{UP} \leq \dot{m}^{B}$	Equation 493	$\dot{m}_{n_L}^{B} = \dot{m}^{B}$

$\dot{m}^{B}$ is estimated with the exact boundary layer (EBL) approach of the Storage Boundary Layer (SBL) model (see Section 1 of Appendix P) and it is computed at the bottom of the storage container. In this approach, the bottom-to-liquid heat flow and the diameter are respectively used as input parameters. In sphere and oblate ellipsoid, the rising flow of the bottom is always equal to zero because, by hypothesis, the mass flow in the boundary layer is not detached form the side wall by the buoyancy forces and the bottom is nelgected.

3.2. Direction of the descending flow

The descending flows ($\dot{m}_{n_L+1}^{D,L}$) can be computed with the descending flow equations (see Table 129), as function of the coefficients of Table 130, of the time derivates of the ullage pressure and of the thickness of the sub-layer. These coefficients are function of the enthalpy flows at each sub-layer, which depends on the direction of the descending flows. The descending flow goes downward if the value of $\dot{m}_{n_L+1}^{D,L}$ is positive and the descending flow goes upward if the value of $\dot{m}_{n_L+1}^{D,L}$ is negative. As a consequence, the calculation of the descending flow and of the remaining indipendent variables is an iterative procedure because the direction of these flows should be known before computing their values and these can only be computed if the direction is known. So, the direction of the descending flow must be guessed as first, using the conservation laws of liquid mass in each sub-layer (see Table 121).

The conservation law of mass in the bulk of the liquid sub-layer (see Table 121) computes the variation of the mass ($\frac{\partial m_{n_L}^{L}}{\partial t}$), as function of the mass flow exchanged between the boundary layer and the bulk ($\dot{m}_{n_L}^{BL,L}$), on the descending flows ($\dot{m}_{n_L+1}^{D,L}$ and $\dot{m}_{n_L}^{D,L}$) and on the rising flows of the bottom ($\dot{m}_{n_L}^{B}$ and $\dot{m}_{n_L-1}^{B}$), which are computed as explained in Section 3.1 of Chapter 6. The values of the mass flow $\dot{m}_{n_L}^{BL}$ can be computed from the values of the rising mass flow of the wet side wall boundary layer, as it is explained in Section 2.1 of Appendix O. So, the mass flows $\dot{m}_{n_L}^{BL,L}$, $\dot{m}_{n_L}^{B}$ and $\dot{m}_{n_L-1}^{B}$ do not depend on the direction of the descending flows. The variation of the mass during steady state and self-pressurisation is low due to the thermal insulation of the storage container. So, the time-derivate of the bulk mass of the sub-layer ($\frac{\partial m_{n_L}^{L}}{\partial t}$) is lower than the descending flows and it can be neglected in conservation laws of liquid mass of the core and bottom sub-layers (see Table 121). These equations without $\frac{\partial m_{n_L}^{L}}{\partial t}$ can be described as the ones reported in Table 135.

Table 135. Conservation laws of core and bottom sub-layers without $\frac{\partial m_{n_L}^{L}}{\partial t}$.

Bottom-liquid sub-layer

Table 135. Conservation laws of core and bottom sub-layers without $\frac{\partial m^L_{n_L}}{\partial t}$.

Case 1	Equation 494	$\dot{m}_2^{D,L} - \dot{m}_1^B - \dot{m}_1^{BL} + \dot{m}_{IN}^L - \dot{m}_{OUT}^L = 0$
Core-liquid sub-layer		
Case 1	Equation 495	$-\dot{m}_{n_L}^{BL,L} - \dot{m}_{n_L}^{D,L} + \dot{m}_{n_L+1}^{D,L} + \dot{m}_{n_L-1}^B - \dot{m}_{n_L}^B = 0$
Case 2	Equation 496	$-\dot{m}_{n_L}^{BL,L} + \dot{m}_{n_L}^{D,L} + \dot{m}_{n_L+1}^{D,L} + \dot{m}_{n_L-1}^B - \dot{m}_{n_L}^B = 0$
Case 3	Equation 497	$-\dot{m}_{n_L}^{BL} - \dot{m}_{n_L}^{D,L} - \dot{m}_{n_L+1}^{D,L} + \dot{m}_{n_L-1}^B - \dot{m}_{n_L}^B$
Case 4	Equation 498	$-\dot{m}_{n_L}^{BL,L} + \dot{m}_{n_L}^{D,L} - \dot{m}_{n_L+1}^{D,L} + \dot{m}_{n_L-1}^B - \dot{m}_{n_L}^B = 0$
Case 5	Equation 499	$\dot{m}_{n_L}^{BL} - \dot{m}_{n_L}^{D,L} + \dot{m}_{n_L+1}^{D,L} + \dot{m}_{n_L-1}^B - \dot{m}_{n_L}^B = 0$
Case 6	Equation 500	$\dot{m}_{n_L}^{BL,L} + \dot{m}_{n_L}^{D} + \dot{m}_{n_L+1}^{D} + \dot{m}_{n_L-1}^B - \dot{m}_{n_L}^B = 0$
Case 7	Equation 501	$\dot{m}_{n_L}^{BL,L} - \dot{m}_{n_L}^{D,L} - \dot{m}_{n_L+1}^{D,L} + \dot{m}_{n_L-1}^B - \dot{m}_{n_L}^B = 0$
Case 8	Equation 502	$\dot{m}_{n_L}^{BL,L} + \dot{m}_{n_L}^{D,L} - \dot{m}_{n_L+1}^{D,L} + \dot{m}_{n_L-1}^B - \dot{m}_{n_L}^B = 0$
Case 9	Equation 503	$-\dot{m}_{n_L}^{D,L} + \dot{m}_{n_L+1}^{D,L} + \dot{m}_{n_L-1}^B - \dot{m}_{n_L}^B = 0$
Case 10	Equation 504	$\dot{m}_{n_L}^{D,L} + \dot{m}_{n_L+1}^{D,L} + \dot{m}_{n_L-1}^B - \dot{m}_{n_L}^B = 0$
Case 11	Equation 505	$-\dot{m}_{n_L}^{D,L} - \dot{m}_{n_L+1}^{D,L} + \dot{m}_{n_L-1}^B - \dot{m}_{n_L}^B = 0$
Case 12	Equation 506	$\dot{m}_{n_L}^{D,L} - \dot{m}_{n_L+1}^{D,L} + \dot{m}_{n_L-1}^B - \dot{m}_{n_L}^B = 0$

As it is indicated in Table 135, the descending flows $\dot{m}_2^{D,L}$, $\dot{m}_{n_L}^{D,L}$, $\dot{m}_{n_L+1}^{D,L}$ and $\dot{m}_{N^L}^{D,L}$ are the only unknowns because the time-derivate of the bulk mass of the liquid sub-layer is removed. Hence, the formulas to compute the the first guess of the descending flows can be deduced from the equations of Table 135. These formulas are reported in Table 136.

Table 136. Equations to compute the first guess value of the descending flow.

Bottom-liquid sub-layer		
Case 1	Equation 507	$\dot{m}_{2,0}^{D,L} = \dot{m}_1^B + \dot{m}_1^{BL} - \dot{m}_{IN}^L + \dot{m}_{OUT}^L$
Core-liquid sub-layer		
Case 1	Equation 508	$\dot{m}_{n_L+1,0}^{D,L} = \dot{m}_{n_L}^{BL,L} + \dot{m}_{n_L,0}^{D,L} - \dot{m}_{n_L-1}^B + \dot{m}_{n_L}^B$
Case 2	Equation 509	$\dot{m}_{n_L+1,0}^{D,L} = -\dot{m}_{n_L-1}^B + \dot{m}_{n_L}^B + \dot{m}_{n_L}^{BL,L} - \dot{m}_{n_L,0}^{D,L}$
Case 3	Equation 510	$\dot{m}_{n_L+1,0}^{D,L} = -\dot{m}_{n_L}^{BL} - \dot{m}_{n_L,0}^{D,L} + \dot{m}_{n_L-1}^B - \dot{m}_{n_L}^B$
Case 4	Equation 511	$\dot{m}_{n_L+1,0}^{D,L}=-\dot{m}_{n_L}^{BL,L} + \dot{m}_{n_L,0}^{D,L} + \dot{m}_{n_L-1}^B - \dot{m}_{n_L}^B$
Case 5	Equation 512	$\dot{m}_{n_L+1,0}^{D,L} = -\dot{m}_{n_L-1}^B + \dot{m}_{n_L}^B - \dot{m}_{n_L}^{BL} + \dot{m}_{n_L,0}^{D,L}$
Case 6	Equation 513	$\dot{m}_{n_L+1,0}^{D} = \dot{m}_{n_L}^B - \dot{m}_{n_L-1}^B - \dot{m}_{n_L}^{BL,L} - \dot{m}_{n_L,0}^{D,L}$
Case 7	Equation 514	$\dot{m}_{n_L+1,0}^{D,L} = \dot{m}_{n_L}^{BL,L} - \dot{m}_{n_L,0}^{D,L} + \dot{m}_{n_L-1}^B - \dot{m}_{n_L}^B$
Case 8	Equation 515	$\dot{m}_{n_L+1,0}^{D,L} = \dot{m}_{n_L}^{BL,L} + \dot{m}_{n_L,0}^{D,L} + \dot{m}_{n_L-1}^B - \dot{m}_{n_L}^B$
Case 9	Equation 516	$\dot{m}_{n_L+1,0}^{D,L} = -\dot{m}_{n_L-1}^B + \dot{m}_{n_L}^B + \dot{m}_{n_L,0}^{D,L}$
Case 10	Equation 517	$\dot{m}_{n_L+1,0}^{D,L} = -\dot{m}_{n_L,0}^{D,L} - \dot{m}_{n_L-1}^B + \dot{m}_{n_L}^B$
Case 11	Equation 518	$\dot{m}_{n_L+1,0}^{D,L} = -\dot{m}_{n_L,0}^{D,L} + \dot{m}_{n_L-1}^B - \dot{m}_{n_L}^B$
Case 12	Equation 519	$\dot{m}_{n_L+1,0}^{D,L} = \dot{m}_{n_L,0}^{D,L} + \dot{m}_{n_L-1}^B - \dot{m}_{n_L}^B$

$\dot{m}_{n_L+1,0}^{D,L}$, $\dot{m}_{n_L,0}^{D,L}$ and $\dot{m}_2^{D,L}$ are the first guess value of the descending flows. The algorithm to compute the direction of the descending flow, thus the indipendent variable, is reported in Appendix AD. The mass flow $\dot{m}_{N^L,0}^{D,L}$, which is the first guess value of the descending flow of hte interface sub-layer, can be computed with the core equations of Table 136, applied at the second-last sub-layers.

4. Intra-layer heat transfer model

During the self-pressurisation, a temperature gradient is developed in the liquid and the temperature increases moving from the interface to the bulk. The fluid-dynamic changes from the zone where the liquid is isothermal to the region of thermal stratification. In the stratified region, the natural convection in the boundary layer of wet side wall cannot be developed due to the adverse temperature gradient. As indicated by the experimental data [24]–[30], the thermal stratification expands in time. Hence, heat must be transferred across the thermal stratification region. These heat flows are considered in the conservation laws of energy of the sub-layers (see Table 121). These heat flows are calculated with the Intra-Layer Heat Transfer (ILHT) model, which is the Block 10 of the LS model, as it is shown in Figure 125.

Section 4.1 presents the hypotheses of the ILHT model. Section 4.2 describes the different heat transfer mechanism. Section 4.3 explains the equations to compute the intra-layer heat flows.

4.1. Hypothesis

Due to the liquid temperature gradient, heat is transferred across the liquid from the bottom to the core. The descending flows, which are function of the boundary layer mass flow, transport the thermal energy from the interface to the bottom, blocking any local convective flow in the core of the sub-layer. When mass flow in the boundary layer is equal to zero, the descending flows are absent and local convective flows can be present. As consequence, the Intra-Layer Heat Transfer (ILHT) model is based on the following assumptions:

a) *pure conduction*: the heat can be transferred only by conduction if the mass flow rate of the wet side wall boundary layer is not equal to zero;
b) *competitive heat transfer mechanism:* convective and conductive heat transfer mechanism competes when the boundary layer flow rate is equal to zero in the sub-layer;
c) *rigid surface:* each interface of the sub-layer is a rigid horizontal flat surface;

Due to the hypothesisi of rigid surface, the convective heat transfer can be described with the free-covnection heat transfer of horizontal surfaces.

4.2. Intra-layer heat transfer mechanism

Due to the hypotheses of pure conduction and of competitive heat transfer mechanism (assumption a) and b) of Section 4.1 of Chapter 6), three cases of heat transfer exist and they are described in Figure 131. In Figure 131, the blue, light blue and black rectangles are respectively the bulk and the boundary layer of the sub-layer, and the bottom wall. The yellow dashed line is the interface. The grey arrow is the rising flow rate in the boundary layer of the wet side wall. The purple lines with the circle are the thickness of the sub-layer. The white arrows with red border are the intra-layer heat flows. The dotted orange line is the interface between the sub-layer. The yellow arrows are the heat transfer coefficients. The green colour indicates the heat transfer mechanism.

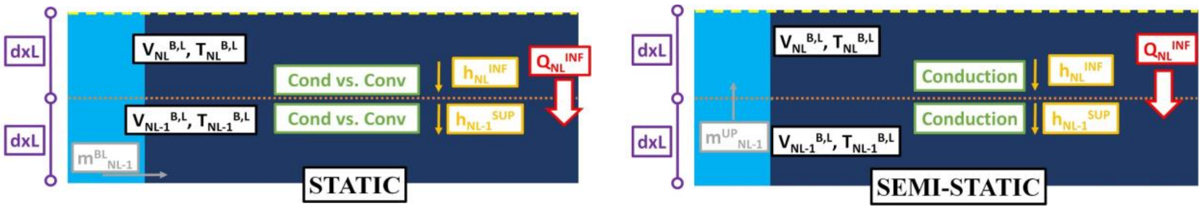

a)

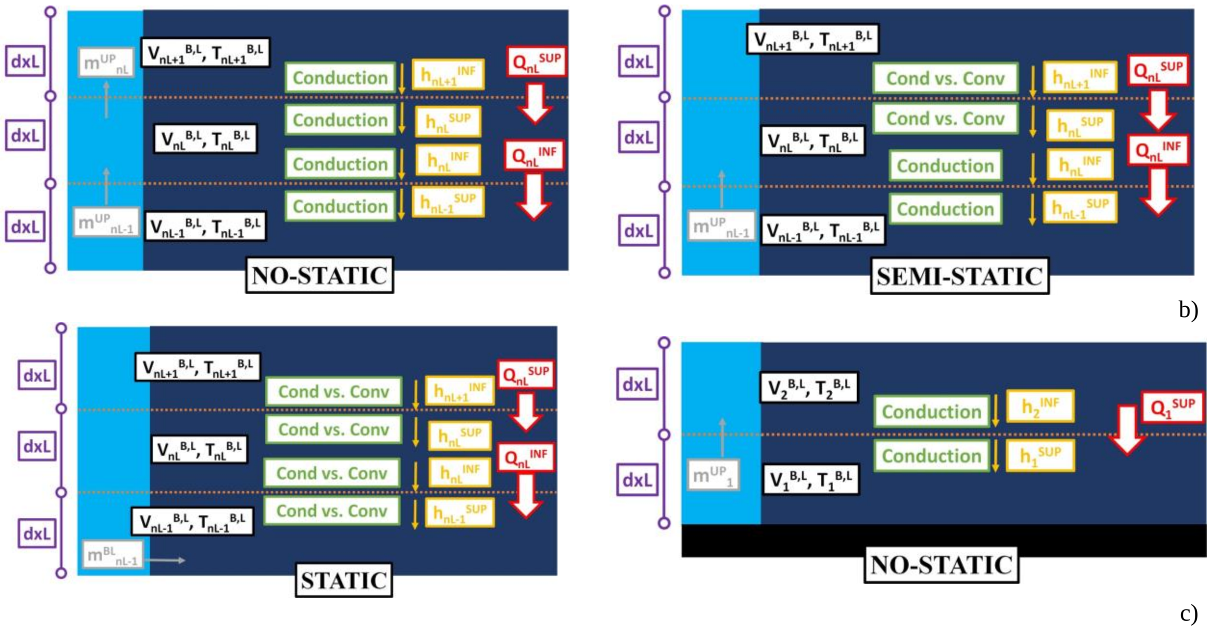

Figure 131. Three cases (no-static, semi-static and static) of ILHT model for the interface sub-layer (a), core sub-layer (b) and bottom sub-layer (c).

As illustrated in Figure 131, these cases are respectively called *no-static*, *semi-static* and *static*. In the sub-layer "n_L", the cases "no-static" occurs when the boundary layer mass flow of this sub-layer ($\dot{m}_{n_L}^{UP}$) and that of the lower ($\dot{m}_{n_L-1}^{UP}$) one are higher than zero. In the "semi-static" case, the boundary layer mass flow of the sub-layer ($\dot{m}_{n_L}^{UP}$) is equal to zero. In the sub-layer "n_L", the heat transfer mechanism is defined as "static" if the boundary layer mass flows of this sub-layer ($\dot{m}_{n_L}^{UP}$) and of the lower one ($\dot{m}_{n_L-1}^{UP}$) are equal to zero. The three cases are only presented for the core sub-layer of the liquid. For the liquid-interface sub-layer, only the semi-static and the static cases are considered because the boundary layer mass flow in this sub-layer ($\dot{m}_{N^L}^{UP}$) is always equal to zero. In the bottom-liquid sub-layer, only the no-static case is taken into account because the flow rate $\dot{m}_1^{UP}$ is computed with the exact boundary layer approach of the SBL model (see Section 1 of Appendix P).

4.3. Intra-layer heat flows

A heat flow can be computed as the ratio between the difference in temperatures between two zones and the thermal resistance of transferring this thermal energy between these zones. So, the intra-layer heat flows (upper and lower) of each case of Figure 131 can be respectively computed as follows:

Equation 520
$$\dot{Q}_{n_L}^{UP} = A_{n_L}^{I} \cdot \frac{T_{n_L+1}^{B,L} - T_{n_L}^{B,L}}{R_{n_L}^{UP}}$$

Equation 521
$$\dot{Q}_{n_L}^{LOW} = A_{n_L}^{I} \cdot \frac{T_{n_L}^{B,L} - T_{n_L-1}^{B,L}}{R_{n_L}^{LOW}}$$

$\dot{Q}_{n_L}^{UP}$ is the upper heat flow and $\dot{Q}_{n_L}^{LOW}$ is the lower heat flow. A^I is the intra-layer surface area, which is equal to the surface area of the section of the storage tank at the liquid height of the sub-layer considered. R is the pseudo-thermal resistance of the intra-layer heat transfer. Equation 520 can be applied at the core and bottom sub-layers. Equation 521 can be used in the interface and core sub-layers. The pseudo-thermal resistaces of the upper and lower heat flows ($R_{n_L}^{UP}$ and $R_{n_L}^{LOW}$) cna be respectively calculated as follows:

Equation 522 $$R_{n_L}^{UP}=\frac{1}{h_{n_L}^{UP}}+\frac{1}{h_{n_L+1}^{LOW}}$$

Equation 523 $$R_{n_L}^{LOW}=\frac{1}{h_{n_L}^{LOW}}+\frac{1}{h_{n_L-1}^{UP}}$$

h is the heat transfer coefficient of the intra-layer heat transfer. As it is indicated in Equation 522 and Equation 523, the thermal resistance is computed with the same type of the equation for all the sub-layer. So, the heat transfer coefficients h^{LOW} and h^{UP} have to be calculated as function of the heat transfer mechanism of the cases of Figure 131. As consequence, these heat transfer coefficients are computed as reported in Table 137.

Table 137. Equations to compute the heat transfer coefficient.

Sub-layer	Equation	Formula	Heat transfer mechanism
		No-static	
Interface, core and bottom	Equation 524	$h_{n_L}^{UP}=h_{n_L+1}^{LOW}=h_{n_L}^{LOW}=h_{n_L-1}^{UP}=\frac{2\cdot k_L}{dxL}$	Conduction
		Semi-static	
Interface	/	Use Equation 524 to compute $h_{N^L}^{LOW}$ and $h_{N^L-1}^{UP}$ (see Figure 131)	Conduction
Core	Equation 525	$h_{n_L}^{UP}=\begin{cases}\frac{2\cdot k_L}{dxL}, & \frac{2\cdot k_L}{dxL}>\hat{h}_{n_L}^{UP}\\ 0.5\cdot\left[\frac{\hat{h}_{n_L}^{UP}}{2}+\frac{2\cdot k_L}{dxL}\right], & \frac{2\cdot k_L}{dxL}\leq\hat{h}_{n_L}^{UP}\end{cases}$	Conduction vs. Convection
	Equation 526	$h_{n_L+1}^{LOW}=\begin{cases}\frac{2\cdot k_L}{dxL}, & \frac{2\cdot k_L}{dxL}>\hat{h}_{n_L+1}^{LOW}\\ 0.5\cdot\left[\frac{\hat{h}_{n_L+1}^{LOW}}{2}+\frac{2\cdot k_L}{dxL}\right], & \frac{2\cdot k_L}{dxL}\leq\hat{h}_{n_L+1}^{LOW}\end{cases}$	Conduction vs. convection
	/	Use Equation 524 to compute $h_{n_L}^{LOW}$ and $h_{n_L+1}^{LOW}$ (see Figure 131)	Conduction
Bottom-liquid	/	Use Equation 524 to compute h_{2}^{LOW} and h_{1}^{UP} (see Figure 131)	Conduction
		Static	
Interface-liquid	Equation 527	$h_{N^L}^{LOW}=\begin{cases}\frac{2\cdot k_L}{dxL}, & \frac{2\cdot k_L}{dxL}>\hat{h}_{N^L}^{LOW}\\ 0.5\cdot\left[\frac{\hat{h}_{N^L}^{LOW}}{2}+\frac{2\cdot k_L}{dxL}\right], & \frac{2\cdot k_L}{dxL}\leq\hat{h}_{N^L}^{LOW}\end{cases}$	Conduction vs. Convection
	Equation 528	$h_{N^L-1}^{SUP}=\begin{cases}\frac{2\cdot k_L}{dxL}, & \frac{2\cdot k_L}{dxL}>\hat{h}_{N^L-1}^{UP}\\ 0.5\cdot\left[\frac{\hat{h}_{N^L-1}^{SUP}}{2}+\frac{2\cdot k_L}{dxL}\right], & \frac{2\cdot k_L}{dxL}\leq\hat{h}_{N^L-1}^{UP}\end{cases}$	Conduction vs. convection
Bulk-liquid	/	Use Equation 525	Conduction vs. Convection
	/	Use Equation 526	Conduction vs. convection
	Equation 529	$h_{n_L}^{LOW}=\begin{cases}\frac{2\cdot k_L}{dxL}, & \frac{2\cdot k_L}{dxL}>\hat{h}_{n_L}^{LOW}\\ 0.5\cdot\left[\frac{\hat{h}_{n_L}^{LOW}}{2}+\frac{2\cdot k_L}{dxL}\right], & \frac{2\cdot k_L}{dxL}\leq\hat{h}_{n_L}^{LOW}\end{cases}$	Conduction vs. Convection
	Equation 530	$h_{n_L-1}^{UP}=\begin{cases}\frac{2\cdot k_L}{dxL}, & \frac{2\cdot k_L}{dxL}>\hat{h}_{n_L-1}^{UP}\\ 0.5\cdot\left[\frac{\hat{h}_{n_L-1}^{UP}}{2}+\frac{2\cdot k_L}{dxL}\right], & \frac{2\cdot k_L}{dxL}\leq\hat{h}_{n_L-1}^{U}\end{cases}$	Conduction vs. convection
Bottom-liquid	/	Use Equation 524 to compute h_{2}^{LOW} and h_{1}^{UP} (see Figure 131)	Conduction

As reported in Table 137, the values of this variable are determined considering the convection and the conduction heat transfer mechanism. The conduction mechanism is used when the convective heat transfer coefficient ($\hat{h}$) is lower than the conductive one ($\frac{2 \cdot k_L}{dxL}$), due to the hypothesis of the competitive heat transfer mechanism (assumption b) of Section 4.1 of Chapter 6). The convection mechanism is used if the conductive heat transfer coefficient ($\frac{2 \cdot k_L}{dxL}$) is lower than the convective one ($\hat{h}$). In Table 137, $\hat{h}$ is the convective heat transfer coefficient of horizontal flat surface, due to the hypothesis of rigid surfaces (assumption c) of Section 4.1 of Chapter 6). The values of this coefficient are computed with the semi-empirical approach of the heat transfer coefficient (see Section 4.6 of Chapter 4). The internal diameter of the storage container at the liquid height of the sub-layer and the difference in temperatures between the sub-layers are used to compute this coefficient. The semi-empirical formulas of warm horizontal flat surfaces facing upward and downward [138] are applied. The conditions to define if the surface is facing upward or downward are reported in Table 138.

Table 138. Orientation of the surface for the heat transfer coefficient.

Heat transfer coefficient	**Difference in temperature**	**Facing surface**
$\hat{h}_{n_L}^{UP}$, $\hat{h}_{n_L+1}^{LOW}$,	$T_{n_L+1}^{L} - T_{n_L}^{L} > 0$	downward
$\hat{h}_{n_L}^{LOW}$ and $\hat{h}_{n_L-1}^{UP}$	$T_{n_L+1}^{L} - T_{n_L}^{L} < 0$	upward

5. Storage Heat Transfer model

The heat inputs in the storage containers are the main cause of the behaviour of the cryogenic liquids in small scale tanks. The distribution of the heat flows in the storage container can be roughly described as in Figure 132. In Figure 132, the white arrows with red boarder are the heat flows. The white circles with purple boarder are the wall temperatures. The yellow dashed line is the interface.

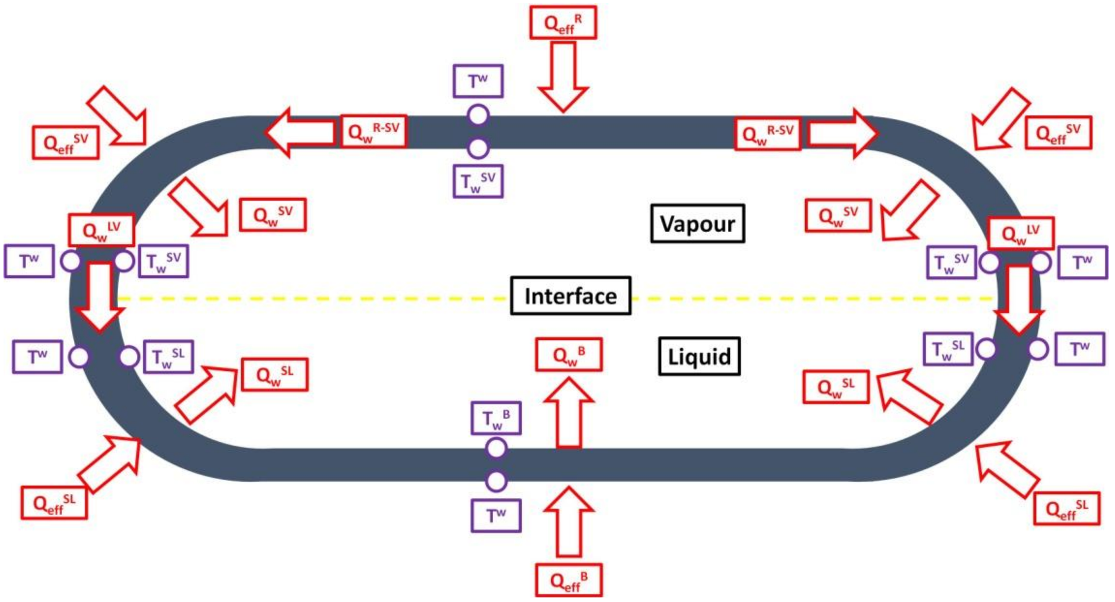

Figure 132. Rough distribution of the heat flows.

The energy energy conservation law (see Table 121) strongly depends on the heat flows at each surface of the storage containers. These heat flows are calculated with the Storage Heat Transfer (SHT) model, which is Block 8 of the liquid stratification model (LS model), as it shown in Figure 125. The SHT model of LS model is composed by the model of bottom heat transfer, the one of the wet side wall heat transfer and the one of dry side wall heat transfer. The bottom-to-liquid heat flow ($\dot{Q}_{w}^{B}$) is computed as done in the homogeneous model (H model) (see Section 4 of Chapter 4). Unlike the H model, the difference in temperatures between the wall and the liquid temperature of the bulk of the bottom sub-layer ($T_{1}^{B,L}$) is used. The dry side wall heat transfer is computed using the equations and the algorithms of the homogeneous model 2.0 (H 2.0 model) (see Section 3.2 of Chapter 5 and Appendix U) because the vapour is virtually stratified due to the hypothesis of the vapour virtual stratification (assumption a) of Section 1.2 of Chapter 6). It means that the only difference between the LS and H 2.0 model is the model used for the wet side wall heat transfer due to the hypothesis of liquid stratification (assumption b) of Section 1.2 of Chapter 6).

The model of the wet side wall heat transfer of the LS model is described in Section 5.1.

5.1. Wet side wall heat transfer

Section 5.1.1 describes the hypothesis of the model of the wet side wall heat transfer. Section 5.1.2 explains the conservation laws of energy of the wet side wall. Section 5.1.3 presents the equation to compute the wet side wall temperatures and the wet side wall-to-liquid heat flows.

5.1.1. Hypotheses

The thermal energy entering in the storage tank arrives to the dry and wet side walls. Part of this incoming energy is transferred by conduction from the dry side wall to the wet side wall (then exchanged with the liquid) because of the temperature difference between these two side walls Since the liquid is discretized in sub-layers in the liquid stratification model (LS model), then the following assumptions are applied:

a) *hypothesis of the discretized wet side wall:* the wet side wall can be discrestized into same number of sub-layers of the liquid;
b) *hypothesis of the intra side wall heat flow:* the dry side wall-to-interface heat flow enters the interface of the interface sub-layer of the wet side wall, but this sub-layer does not transfer heat flow to the lower sub-layers;
c) *hypothesis of no conduction:* the conduction heat flow between each sub-layer of the wet side wall is neglected and all the heat coming from the dry side wall is transferred to the liquid bulk o the interface sub-layer;
d) *hypothesis of steady state wet side wall:* the thermal inertia of the side wall can be ignored.

Due to these hypotheses, the wet side wall can be described as in Figure 133 in the LS model. In Figure 133, the white arrows with the red boarders are the heat flows. The white circles with the purple boarder are the wall temperatures. In Figure 133 (a), the vertical black rectangle is the wet side wall. In Figure 133 (b), the black squares with orange boarder are the sub-layers of the wet side wall.

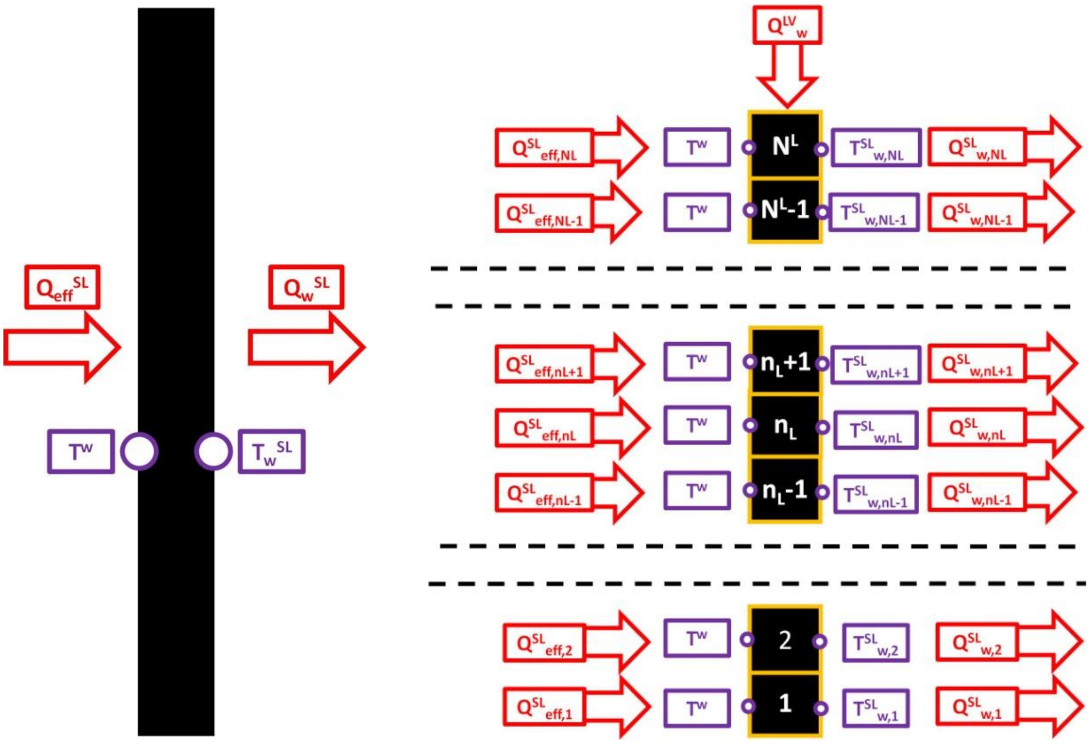

a) b)

Figure 133. Wet side wall: a) H and H 2.0 models; b) LS model.

As it is shown in Figure 133, the environment-to-wet side wall and the wet wall-to-liquid heat flows has to be considered in each sub-layer of the wet side wall, instead of using the overall heat flows as done in the homogeneous model (H model) and homogeneous 2.0 (H 2.0) model. The sub-layer “NL” and the sub-layer “1” are called interface and bottom sub-layer of the wet side wall, respectively. The remaining sub-layers are called core sub-layer of the wet side wall.

5.1.2. Energy conservation laws at the wet side wall

In the homogeneous model (H model) and homogeneous 2.0 (H 2.0) model, the environment-to-wet side wall heat flow ($\dot{Q}^{SL}_{eff}$) is uniformly distributed and equal to the wet side wall-to-liquid heat flow ($\dot{Q}^{SL}_{w}$) (see Figure 133 (a)). In the liquid stratificiaotn (LS) model, the environment-to-wet side wall heat flow is divided into each sub-layer of the wet side wall (see Figure 133 (b)). This heat flow depends on the difference in temperatures between the external wall (T^{w}) and the sub-layer of the wet side wall (T^{SL}_{w,n_L}). In each sub-layer of the wet side wall, thermal energy is transferred to the liquid according to the corresponding heat transfer coefficient (h^{SL}_{w,n_L}) and the difference in temperatures between the wet wall and the bulk of the liquid. Due to the adopted hypotheses in the wet side wall heat transfer model of LS model (see Section 5.1.1 of Chapter 6), the energy conservation law of the sub-layers of the discretized liquid can be described from the equations given in Table 139.

Table 139. Energy conservation laws at the wet side wall.

Wall Sub-layer	Equation	Formula
Interface-liquid	Equation 531	$h_{eff} \cdot dA^{SL}_{N^L} \cdot \left(T^{w} - T^{SL}_{w,N^L}\right) + \dot{Q}^{LV}_{w} = dA^{SL}_{N^L} \cdot h^{SL}_{w,N^L} \cdot (T^{SL}_{w,N^L} - T^{B,L}_{N^L})$
Core and bottom	Equation 532	$h_{eff} \cdot dA^{SL}_{n_L} \cdot (T^{w} - T^{SL}_{w,n_L}) = dA^{SL}_{n_L} \cdot h^{SL}_{w,n_L} \cdot (T^{SL}_{w,n_L} - T^{B,L}_{n_L})$

In Table 139, $dA^{SL}_{n_L}$ is the wet side wall surface area of the sub-layer of the wet side wall. $\dot{Q}^{LV}_{w}$ is calculated the dry side wall-to-interface model of the H model.

5.1.3. Wet side wall temperature

As it is reported in Table 139, the energy conservation law of each sub-layer depends on the temperature the corresponding wet side wall (T^{SL}_{w,n_L}). Considering the definition of heat flow[91], the temperature of each sub-layer of the wet side wall is calculated as follows:

Equation 533
$$T^{SL}_{w,n_L} = T^{B,L}_{n_L} + \frac{\dot{Q}^{SL}_{w,n_L}}{A^{SL}_{n_L} \cdot h^{SL}_{w,n_L}}$$

In Equation 533, h^{SL}_{w,n_L} is the local heat transfer coefficient is used because the average value of this heat transfer coefficient cannot be used due to the hypothesis of liquid discretisation. This local heat transfer coefficient is calculated with the boundary layer approach of the heat transfer coefficient of the homogeneous model (H model) (see Section 4.6 of Chapter 4). So, the value of this coefficient is computed using the boundary layer variables, which are calculated with the Integral Boundary Layer (IBL) approach of the Storage Boundary Layer (SBL) model.

As a results, a guess value of the heat flow $\dot{Q}^{SL}_{w,n_L}$ is used as input parameter, and the final values of the heat flow $\dot{Q}^{SL}_{w,n_L}$and of the temperature T^{L}_{w,n_L} are obtained by means of an iterative procedure as described in Appendix AE.

6. Storage Boundary Layer model

At steady state, the liquid near the wall becomes lighter than the bulk liquid and it starts to flow in the boundary layer of the wet side wall. So, the upward liquid flow carries thermal energy to the interface, where it is totally absorbed by the evaporation. The liquid bulk temperature gradient which develops during self-pressurisation reduces the amount of that reaches the interface by deviating part of the rising liquid flowtoward the liquid bulk. The rising mass flow developing at the bottom of the tank interacts with the convective flows at the wet side wall. Also at the dry side wall, the heat flow results in a rising vapourflows. This rising flows carry the thermal energy in the ullage and the overall convective motion generating in the ullage includes descending flows transporting heat from the ullage to the interface.

As consequence, the magnitude of the flows generating in the boundary layers at wet and dry side walls, and at the bottom determine the behaviour of the cryogenic liquid in the storage container because the fluid-dynamics at these surfaces affect the heat transfer mechanisms and the distribution of the heat in the liquid and in the ullage. So, the energy and mass conservation laws of (see Table 121) are written as function of rising flow of the bottom, mass flow of the wet side wall, and heat transfer coefficients at the dry and wet side walls. These coefficients are computed as function of the boundary layer variables such as the velocity outside boundary layer of comparable forced-convection flow (U) and momentum thickness of the boundary layer (δ_M). The boundary layer variables at the wet and dry side walls, and at the bottom are computed with the Storage Boundary Layer (SBL) model (see Section 3 of Chapter 4), which is Block 8 of liquid stratification model (LS model), as it shown in Figure 125.

The SBL model computes these variables with two approaches: the Exact Boundary Layer (EBL) and the Integral Boundary Layer (IBL), which are illustrated in Figure 134. In Figure 134 (a) (EBL approach), the black rectangle with yellow boarders is the whole wall. The white rectangle with green boarders is the boundary layer; the white circle with purple boarders and the white arrow with red boarders are respectively the wall temperature and the wall-to-fluid heat flow. In Figure 134 (b) (IBL approach), the black squares with yellow boarders is the discretized wall. The white rectangle with green boarders and the white square with green boarders is the discretized boundary layer; the white circles with purple boarders are the wall temperature of each part of the discretized wall; the white arrows with red boarders are the wall-to-fluid heat flows; the orange points are the point of the discretized wall where the boundary layer variables (U and δ_M) are computed.

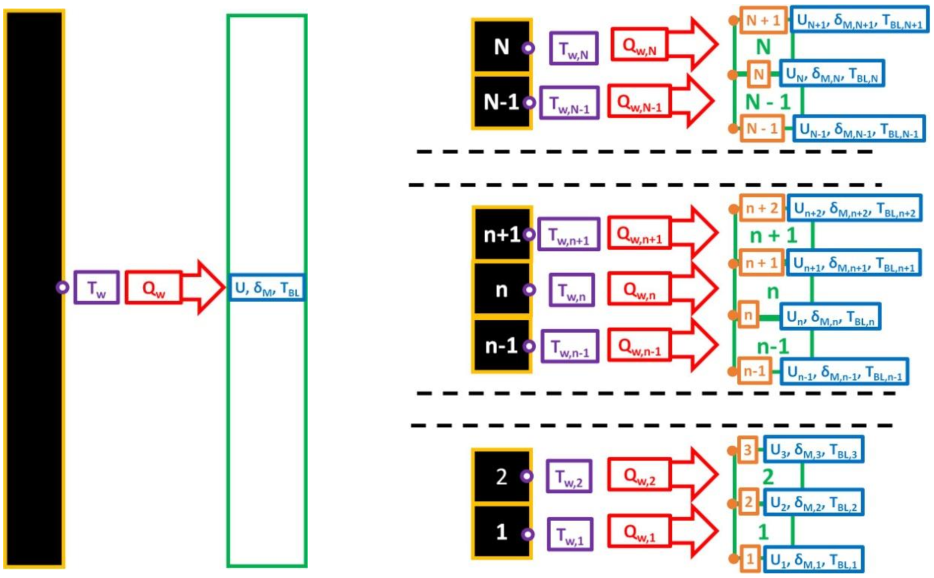

a) b)

Figure 134. a) EBL approach and b) IBL approach.

The rising flows of the bottom of the storage container are calculated with the EBL approach, using the bottom-to-liquid heat flow as input parameter. The IBL approach is used for the dry and wet side walls. Considering that in the liquid stratification model (LS model) the vapor is treated like in the homogeneous model 2.0 (H 2.0 model) (hypothesis of vapour virtual stratification - assumption a) of Section 1.2 of Chapter 6), the IBL approach used in the H 2.0 model (see Section 3.1 of Chapter 5) is applied for the dry side wall of the LS model. In the LS model, the liquid is discretized (hypothesis of liquid discretisation - assumption b) of Section 1.2 of Chapter 6) and the liquid bulk temperature gradient of the liquid is computed in each sub-layer (see Section 1.5.2 of Chapter 6). As a consequence, the IBL approach of the wet side wall of the LS model does not correspond to the ones used in the homogeneous model (H model) and in the homogeneous model 2.0 (H 2.0 model) because this temperature gradient creates instability in the numerical integrations of the energy and momentum conservation laws of the boundary layer in laminar regime and in computing the number of sub-space-points of the numerical integrations.

Section 6.1 and 6.2 respectively describe the modifications done on the fluid-dynamic regime and on the number of sub-space-points, respectively.

6.1.Fluid-dynamics regime at the wet side wall

At the side wall, the boundary layer variables such as U and δ_M are calculated with the Integral Boundary Layer (IBL) approach, which numerically integrates the momentum and energy conservation laws of the boundary layer (Equation 178 and Equation 179). The momentum conservation law (Equation 178) is a function of the viscous forces (τ_w), which can be computed as function of the fluid-dynamic regime with the equations of Table 78. The energy conservation law (Equation 179) is a function of the bulk temperature gradient, which reduces the numerator of this equation.

In the formula of the turbulent viscous forces (Equation 180), the variable τ_w depend on the quantity $U^2 \cdot \left(\frac{1}{U\cdot\delta_M}\right)^{0.25}$. So, the viscous forces become zero when the values of U and δ_M decrease. In In the formula of the laminar viscous forces (Equation 184), the viscous forces are functions of the ratio $\frac{U}{\delta_M}$.

As consequence, the viscous forces cannot be computed when the values of U and δ_M are close to zero, because the ratio $\frac{U}{\delta_M}$ goes to the undefined value 0/0.

In the liquid stratification model (LS model), the bulk temperature gradient of the liquid is calculated and it is considered in the energy conservation law of the boundary layer (Equation 179). So, the variable $\dot{q}_\infty$ is not equal to zero by default and the values of U and δ_M decrease when the bulk temperature gradient is higher than 0. Hence, the numerical integration becomes instable when the ullage bulk temperature is considered due to Equation 184. As a consequence, it is reasonable to consider that the fluid-dynamics regime at the dry side wall is turbulent. Using this assumption, the numerical integration is stable because Equation 180 goes to zero as the variable U and δ_M decrease, instead of going to an undefined value as done by Equation 184. The assumption of turbulent boundary layer was used by Vliet et al. [1], who used a numerical method to integrate the conservation laws of the boundary layer to compute the variables U and δ_M. This assumption is robust for storage containers with high filling ratio or medium-high heat fluxes because the values of these variables create turbulence in the boundary layer of the wet side wall.

6.2.Number of the sub-space-points

Analysis of theresults of the homogeneous model 2.0 (H 2.0 model) reveals a numerical instability of the Integration Boundary Layer (IBL) approach of the dry side wall. So, the number of sub-space-points (N_{SSP}) of the dry side walls was incremented from 10 (H 2.0 model) to 25

The conservation laws of the boundary layer (Equation 178 and Equation 179) are numerically solved by the IBL approach. In the IBL approach, the side wall is divided into sub-layers and these equations are numerically integrated in each sub-layer. To increases the stability, each sub-layer is spatially divided into sub-space-points, similarly to the homogeneous model (H model). The number of sub-space-points of each sub-layer is calculated as function of the ratio between the derivates and the critical derivates[89] of the pseudo-boundary layer variables[90], called E and M. These variables are used to stabilize the numerical integration of IBL approach and they are computed from the variables U and δ_M (see Section 2.1 of Appendix P). When this ratio is high, the number of sub-space-points is high to improve the accuracy. The number of sub-space-points decreases if this ratio is low. The bulk temperature gradient of liquid is added in the energy conservation law (Equation 179), reducing the derivates of the pseudo-boundary layer variables. As consequence, the ratio between these derivates and the critical derivates is close to 1 and the number of sub-space-points, which affects the accuracy, increases. Considering that the IBL approach is used to compute the heat transfer coefficient at the side wall with an iterative procedure, the number of sub-space-points can vary at each iteration, modifying the values of these coefficients. So, the liquid bulk temperature gradient varies the number of sub-space-points at each iteration, creating instability in the calculation of the heat transfer coefficient. Hence, the number of sub-step is fixed at 25, when the IBL approach is used for the wet side wall

7. Interface Heat Transfer model

During the storage of cryogenic liquids, a difference in temperature between the ullage and the interface forms. At the same time, a temperature difference exits between the interface and the liquid. So, thermal energy is transferred from the ullage to the interface, and between the interface and the liquid. If the storage container is at steady state, the interface is colder than the liquid and, as a result, the energy flows from the liquid to the interface. During the self-pressurisation, the liquid is colder than the interface and the thermal energy flows then from the interface to the liquid. The vapour-to-interface and the liquid-to-interface heat flows affect the mass transfer at the interface, thus the evaporation and the condensing mass flows. The difference in these mass flows is called net mass flow. The vapour-to-interface, the liquid-to-interface heat flows, and the net mass flow can be calculated with the Interface Heat Transfer (IHT) model, which is Block 9 of the liquid stratification model (LS model), as it shown in Figure 125. Again, the same vapour-to-interface heat flow of the homogeneous model 2.0 (H 2.0 model) can be used in the LS model since the hypothesis of vapour virtual stratification (assumption a) of Section 1.2 of Chapter 6) is used.

Section 7.1 and 7.2 describe the liquid-to-interface heat transfer and the new energy balance equation of the interface, respectively.

7.1. Liquid-to-Interface heat transfer

At the steady state, the liquid rising from the boundary layer of the wet side wall exchanges thermal energy with the interface. The transfer of this heat occurs as a sequence of four mechanisms (molecular evaporation, conduction, intermitted convection and bulk convection) [20], [21], [139]. Each of these mechanisms occurs in a specific region of the liquid that is near the interface: liquid interface, conduction layer, intermitted convection layer, and the bulk of the liquid (see Section 4.3.1 of Chapter 1). Due to the lack of experimental values for validating a heat transfer model in these regions, the overall heat flow through them can be computed as a function of the mass flow in the boundary layer of the wet side wall (see Section 5.3 of Chapter 4). During the self-pressurisation, the rising flow of the boundary layer of the wet side wall reduces, and it may not reach the interface due to the liquid bulk temperature gradient which reduces the buoyancy forces in this layer. As consequence, natural convection or conduction can locally occur in the liquid near the interface, exchanging thermal energy with the free-surface[101]. The four-region mechanism, the local convection mechanism and the conduction compete for transferring heat to the interface. In absence of experimental evidences, it can be assumed that the dominating heat transfer mechanism is the one with the highest rate, as done by Daigle et al. [2]. The liquid-to-interface heat flow can then be computed as follows:

Equation 534
$$\dot{Q}_I^L = \max\{abs(\dot{Q}_{I,1}^L); abs(\dot{Q}_{I,2}^L); abs(\dot{Q}_{I,3}^L)\}$$

In Equation 534, $\dot{Q}_{I,1}^L$is the heat flow of the four-region mechanism and it is called liquid-to-interface heat flow of the boundary layer convection; $\dot{Q}_{I,2}^L$ is the liquid-to-interface heat flow of local natural convection; $\dot{Q}_{I,3}^L$ is the liquid-to-interface heat flow of local conduction.

Section 7.1.1, 7.1.2 and 7.1.3 respectivey describe the models to compute $\dot{Q}_{I,1}^L$, $\dot{Q}_{I,2}^L$ and $\dot{Q}_{I,3}^L$.

---

[101] Here, the free-surface is considered as synonyms of interface.

7.1.1. Boundary layer convection

In the homogeneous model (H model) and in the homogeneous model 2.0 (H 2.0 model), the four-region mechanism is simplified in a one-step-mechanism, which is modelled with the boundary layer convection model (see Section 5.3 of Chapter 4 and Section 4.1 of Chapter 5). In this model, the liquid-to-interface heat flow is proportional to mass flow rate of the boundary layer and the difference in temperature between the boundary layer and the interface. In the liquid stratification model (LS model), the liquid is divided into sub-layers and the boundary layer convection model can be described as in Figure 135. In Figure 135, the orange rectangle is the vapour and the dashed yellow line is the interface; the blue rectangles are the liquid sub-layers; the white arrows with blue boarders are the mass flow and the white arrows with red boarders are enthalpy flows and heat flows.

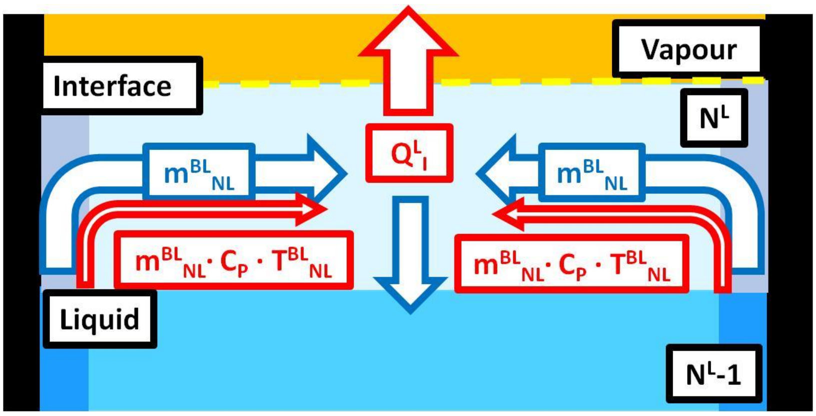

Figure 135. Boundary layer convection model of LS model.

As it is can be inferred from Figure 135, the liquid-to-interface heat flow ($\dot{Q}^L_{I,1}$) of the convection boundary layer can be computed as follows:

Equation 535
$$\dot{Q}^L_{I,1} = \dot{m}^{BL}_{N^L} \cdot C^L_P \cdot \left(T^{BL,L}_{N^L} - T^I\right)$$

In Equation 535, $\dot{m}^{BL}_{N^L}$ is the mass flow exchanged between the boundary layer and the bulk of the wet side wall at the interface sub-layer (this mass flow is equal to the mass flow of the boundary layer of the wet side wall at the second-last sub-layer, due to the Integral Boundary layer (IBL) approach); $T^{BL}_{N^L}$ is the temperature of the boundary layer of the wet side wall at the interface sub-layer. As it is indicated in Equation 535, the value of the heat flow $\dot{Q}^L_{I,1}$ is equal to zero when the mass flow $\dot{m}^{BL}_{N^L}$ is equal to zero. The value of the liquid-to-interface heat flow is negative when the interface is hotter than the temperature $T^{BL}_{N^L}$.

7.1.2. Local natural convection

As said, natural convective flows can be generated near the interface when the mass flow rate of the boundary layer of the wet side cannot reach the interface. Considering that the interface is a flat surface, these convective flows are similar to the one developed over and below a warm flat horizontal surface, as it is described in Figure 136. In Figure 136, the orange rectangle is the vapour and the blue rectangle is the interface-sub-layer. The yellow dashed line is the interface. The white arrow with the red boarder is the heat flow. The white arrows with blue boarders are the convective flows.

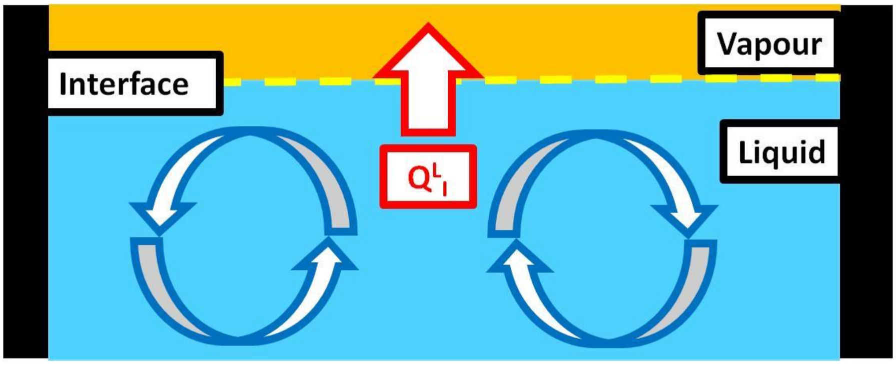

Figure 136. Natural convection in LS model.

As a consequence, the liquid-to-interface heat flow of the local natural convection can be calculated as follows:

Equation 536
$$\dot{Q}^L_{I,2} = A^I \cdot h^L_I \cdot \left(T^{B,L}_{N^L} - T^I\right)$$

In Equation 536, h^L_I is the liquid-to-interface heat transfer coefficient, and this variable is calculated with the semi-empirical approach (see Section 4.6 of Chapter 4), using the formulas of the Nusselt's number of horizontal flat surface facing upward and downward [138]. The upward formula is applied when the interface is colder than the temperature of the bulk of interface sub-layer ($T^{B,L}_{N^L}$). The downward formula is used if the temperature $T^{B,L}_{N^L}$ is higher than the interface temperature (T^I).

7.1.3. Conduction

The local natural convective flows (see Section 7.1.2 of Chapter 6) are developed when the difference in temperature in temperatures between the interface and the bulk of the interface sub-layer is enough to produce buoyancy forces that overcome the viscous forces. If this difference in temperature is low, these convective flows are absents and the liquid remains immobile. So, the thermal energy is exchanged between the liquid and the interface by conduction. In the liquid stratification model (LS model), the liquid is divided into sub-layers. So, the 1 dimensional (1D) Fourier's law[102] can be applied and the liquid-to-interface heat flow of conduction can be computed as follows:

Equation 537
$$\dot{Q}^L_{I,3} = -A^I \cdot k_L \cdot \left.\frac{\partial T^L}{\partial x}\right|_{x=H^L}$$

$\left.\frac{\partial T^L}{\partial x}\right|_{x=H^L}$ is the bulk temperature gradient at the interface. Due to the hypothesis of liquid discretisation , this gradient can be computed with finite difference approach[103] as follows:

Equation 538
$$\left.\frac{\partial T^L}{\partial x}\right|_{x=H^L} = -\frac{T^{B,L}_{N^L} - T^I}{dxL}$$

So, the liquid-to-interface heat flow of conduction can be computed is given by:

Equation 539
$$\dot{Q}^L_{I,3} = A^I \cdot k_L \cdot \frac{T^{B,L}_{N^L} - T^I}{dxL}$$

A^I is the interface surface area and it is computed with the geometrical formulas of Appendix AA.

---

[102] Fourier's law : $\dot{Q} = -A \cdot k \cdot \nabla T$

[103] Finite difference approach : $\frac{\partial y}{\partial x} = \frac{y_2 - y_1}{x_2 - x_1}$

7.2. Energy conservation law of the interface

Due to the hypothesis of actual thermodynamic state (assumption c) of Section 1.2 of Chapter 6), the difference in temperatures between the vapour and the interface, and between the liquid and the interface exist. As consequence, the vapour and the liquid transfer thermal energy to the interface. At the interface, some molecules of the liquid evaporate and some of the vapour condense, resulting in a net mass flow ($\dot{m}_N$) across the interface. So, the interface of the liquid stratification model (LS model) can be described as in Figure 137. In Figure 137, the light orange and the light blue are respectively the vapour and the liquid; the yellow dashed line is the interface; the white arrows with red borders are the heat transfer; the green and the bourdon dashed arrows are the mass and enthalpy flows, respectively; the continuous-line arrow is the net mass flow.

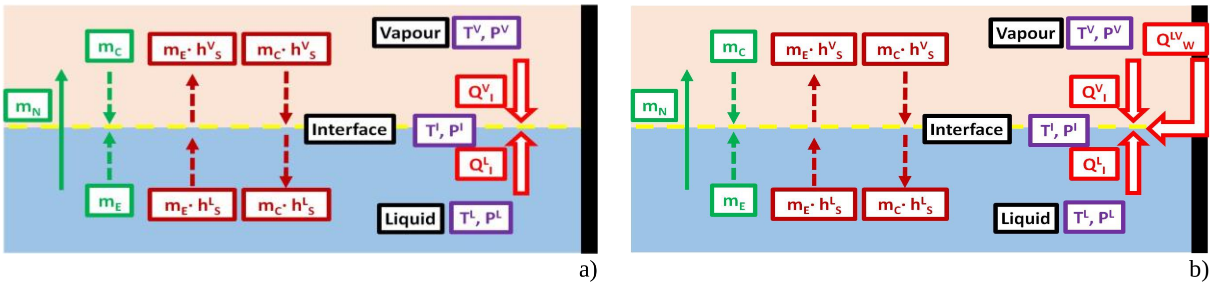

a) b)

Figure 137. Interface in IHT model of in LS model (a) anf H model (b).

As indicated in Figure 137, the interface is a rigid mass-less surface and it is at equilibrium due to the hypothesis of local thermodynamic equilibrium (assumption d) of Section 1.2 of Chapter 6). This hypothesis is the one used in the homogeneous model (H model). So, the interface is conceptually described as the one of the H model, but the dry side wall-to-interface heat flow ($\dot{Q}_W^{LV}$) is absent. So, the energy conservation law at the interface is described as follows:

Equation 540
$$\dot{m}_N \cdot \Delta\widetilde{H}_{EV} - \left(\dot{Q}_I^L + \dot{Q}_I^V\right) = 0$$

In Equation 540, the vapour-to-interface heat flow ($\dot{Q}_I^V$) is computed as in the homogeneous model 2.0 (H 2.0 model) (see Section 4.2 of Chapter 5). This model uses the convective flows of the ullage ($\dot{m}_{i+1}^{D,V}$) to calculate the heat flow $\dot{Q}_I^V$. These convective flows are computed in each virtual sub-layer of the ullage, from the interface to the roof. The value of the convective flow depends on the values of the convective flow of the lower virtual sub-layer. So, the convective flow at the interface of the virtual sub-layer of the ullage (sub-layer 1 of Figure 99) is computed as a function of the net mass flow. As a consequence, the remaining convective flow of the virtual sub-layer of the ullage depends on the mass flow $\dot{m}_N$. Hence, an iterative procedure is required to compute the net mass flow. The LS and H 2.0 models have the same vapour-to-interface heat flow model and the same energy conservation law (Equation 540), except for the dry side wall-to-interface heat flow ($\dot{Q}_W^{LV}$), which is absent in the LS model. So, the algorithm of the net mass flow of the H 2.0 model is used in the LS model to calculate this variable, by imposing that $\dot{Q}_W^{LV}$ is equal to zero (see Appendix V).

8. Comparison with experimental data

The liquid stratification model (LS model) is compared with the experimental data dealing with the storage of liquid nitrogen (LN_2) and liquid hydrogen (LH_2) in small scale tanks exposed to different overall heat fluxes. LN_2 data are measured in vertical cylinders with flat ends under low [24], [26] and medium [25] heat fluxes. LH_2 data are measured in oblate-ellipsoidal storage containers under low heat fluxes [27], [28] and in spherical storage tank under medium[30] and high[29] heat fluxes. The LS model describes the behaviour of the ullage with the same approach of the homogeneous model 2.0 (H 2.0 model). So, the fluid-dynamics and the heat transfer at the dry side wall are not analyzed, and the ullage temperature is not compared with the experimental data. The results of the average liquid temperature of LS model are quite similar to the ones of the homogenous (H) model. The fluid-dynamics and the heat transfer at the side wall determine the heat transfer at the interface and the thermal distribution in the liquid, which affect the behaviour of cryogenic liquids in small scale storage containers. As a consequence, the pressure, fluid-dynamics and heat transfer at wet side wall, the fluid-dynamics in the liquid, interfacial heat transfer and net mass flow calculated by the LS model are considered in this analysis. The computed values of the pressure are compared to experimental data. The results of the fluid-dynamics and heat transfer at wet side wall, the fluid-dynamics in the liquid, interfacial heat transfer and net mass flow are only presented because experimental data of these phenomena are not available.

The initial conditions of ullage temperature, liquid temperaurtre, filling ratio, pressure and heat inputs were compared to the experimental data for the equilibrium (EQ), homogeneous (H) and homogeneous 2.0 (H 2.0) models. The boil-off rate (BOR) of the LS model is based on the same theory and algorithm of the one of H 2.0 models, except for the Storage Boundary Layer (SBL) model of the wet side wall. The SBL model of this side wall does not significantly changes the values of the initial conditions. Hence, the initial conditions computed with the LS model are not compared with the experimental data.

Section 8.1, 8.2 and 8.3 presents the comparison between the results and the experimental data for Study cases at low, medium and high heat fluxes, respectively.

8.1. Study cases: low heat fluxes

The study cases at low heat fluxes are reported in Table 140 (more details of the study cases are given in Section 4 of Chapter 2).

Table 140. Study cases at low heat fluxes.

Authors	Seo and Jeong [24]	Perez et al. [26]	Hasan et al. [27]	Dresar et al. [28]
Study case	1	2	3	4
Geometry	Vertical cylinder with flat ends	Vertical cylinder with flat ends	Oblate ellipsoid	Oblate ellipsoid
Working fluid	Liquid nitrogen	Liquid nitrogen	Liquid hydrogen	Liquid hydrogen

Section 8.1.1 presents the fluid-dynamics at wet side wall. Section 8.1.2 describes the fluid-dynamics in the liquid. Section 8.1.3 explains the heat transfer at the wet side wall. Section 8.1.4 presents the heat transfer across the sub-layer of the liquid. Section 8.1.5 describes the interfacial heat transfer. Section 8.1.6 explains the net mass flow. Section 8.1.7 presents the comparison between the calculated value of the pressure and the measured one. Section 8.1.8 explains the comparison between the computed values of the liquid temperature profiles and the experimental ones.

8.1.1. Presentation of the results: fluid-dynamics at the wet side wall

Figure 138 shows the values of the boundary layer mass flow of the wet side wall ($\dot{m}^{SW}$), and the values of the bulk temperature gradient in each sub-layer ($\frac{\partial T^L}{\partial x}$), at different time-points, for Study case 1. In the caption of each graph in Figure 138, the time at which these variables are computed is reported near $\dot{m}^{SW}$ and $\frac{\partial T^L}{\partial x}$. These time-points correspond to the time-points at which the temperature is measured.

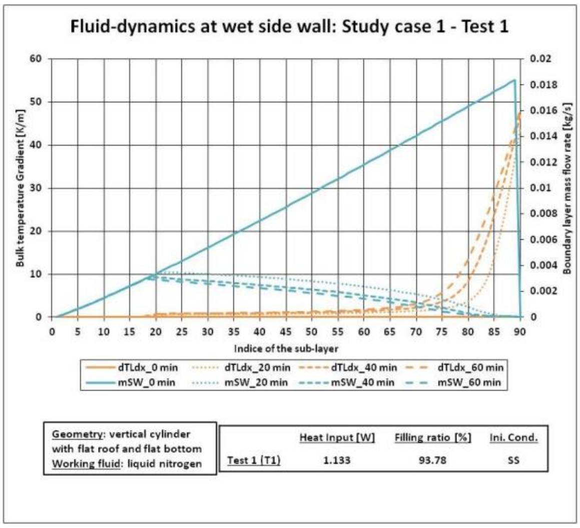

a)

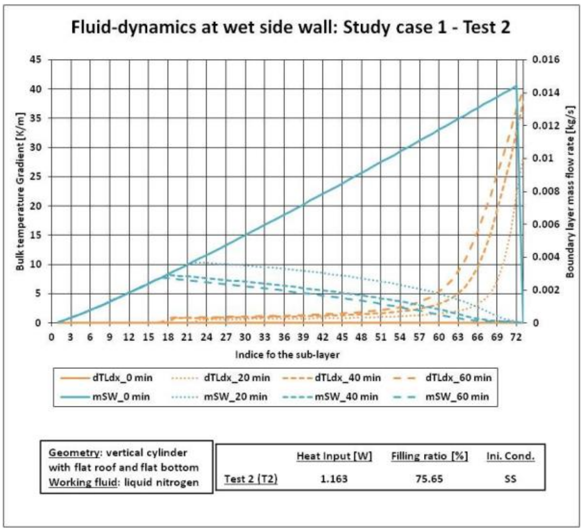

b)

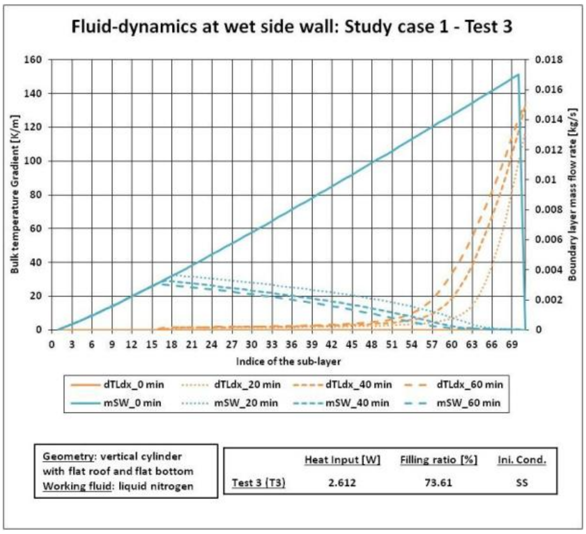

c)

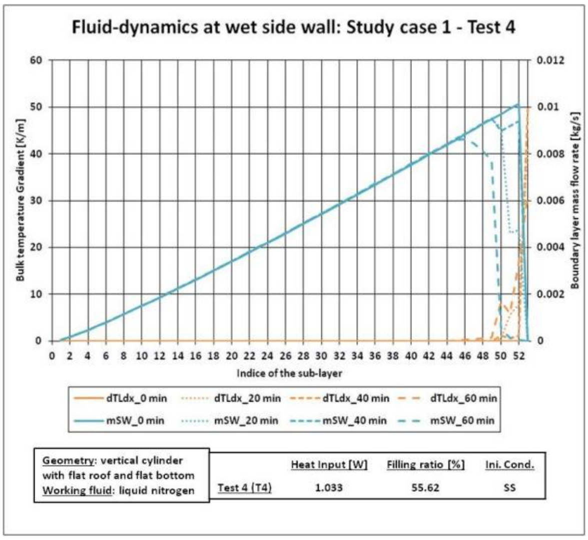

d)

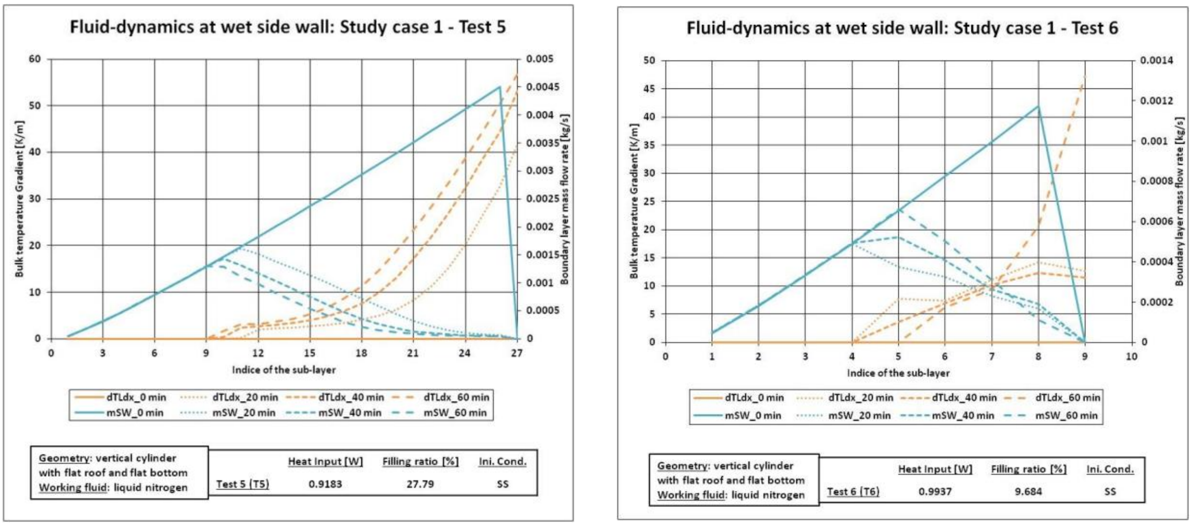

e) f)

Figure 138. Fluid-dynamics at the wet side wall of Study case 1: a) Test 1; b) Test 2; c) Test 3; d) Test 4; e) Test 5; f) Test 6.

As it is illustrated in Figure 138, $\frac{\partial T^L}{\partial x}$ is equal to zero in all sub-layers at the beginning of the self-pressurisation, thus at the end of the steady state. As the time passes, $\frac{\partial T^L}{\partial x}$ increases in the sub-layers near the interface. In the lowest part of the liquid, $\frac{\partial T^L}{\partial x}$ is similar to the one at the end of the steady state, thus is equal to zero. So, the temperature gradient drops down in the sub-layer near the interface and it slightly decreases after this initial drop.

As it is illustrated in Figure 138, the mass flow rate in the boundary layer of the wet side linearly increases from the bottom to the second-last sub-layer, at the beginning of the self-pressurisation. At this sub-layer, the value of this mass flow decreases to zero. As the self-pressurisation time passes, the mass flow in the boundary layer increases from the bottom sub-layer up to the sub-layer where the value of the liquid temperature gradient is higher than 0. From this sub-layer, this mass flow monotonically decreases. For Test 1 and 3, the values of the mass flow rate in the boundary layer are equal to zero before reaching the interface sub-layer.

Figure 139 shows the values of the boundary layer mass flow of the wet side wall ($\dot{m}^{SW}$) and the values of the bulk temperature gradient in each sub-layer ($\frac{\partial T^L}{\partial x}$), at different time-points, for Study case 2. In the caption of Figure 139, time at which these variables are computed is reported near the name of the property. These time-points correspond to the time-points at which the temperature is measured in the experimental works.

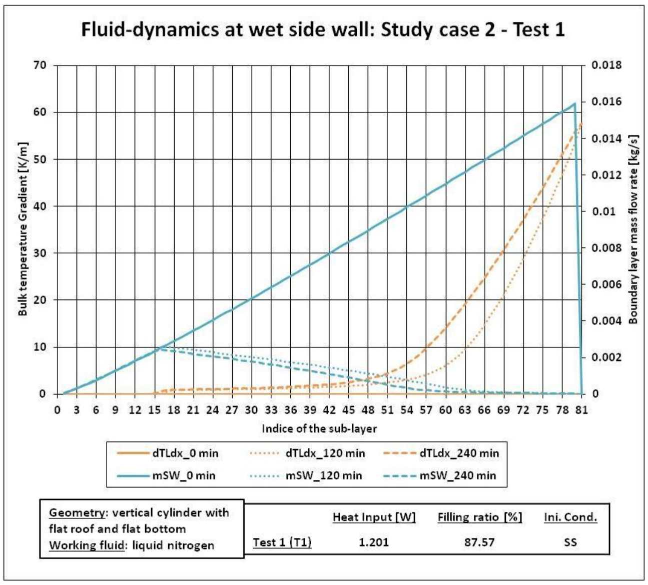

Figure 139. Fluid-dynamics at the wet side wall of Study case 2.

As it can be seen in Figure 139, $\frac{\partial T^L}{\partial x}$ is equal to zero at the beginning of the self-pressurisation, thus at the end of the steady state. During the self-pressurisation, this gradient is equal to zero in the first 15 sub-layer and it gently increases from the 16th to the 48th sub-layer. After this sub-layer, $\frac{\partial T^L}{\partial x}$ rapidly increases. $\dot{m}^{SW}$ constantly increases from the bottom to the second-last sub-layer and it becomes zero in the interface sub-layer. As the time passes, this mass flow linearly increases up to the 15th sub-layer. Then, it monotonically decreases and the value of this mass flow becomes equal to zero at 66th sub-layer.

Figure 140 shows the values of same properties (boundary layer mass flow of the wet side wall, $\dot{m}^{SW}$, and bulk temperature gradient in each sub-layer, $\frac{\partial T^L}{\partial x}$, at different time-points, for Study case 4); the time at which these variables are computed is reported as in previous Figures. These time-points correspond to the time-points at which the experimental temperature is measured.

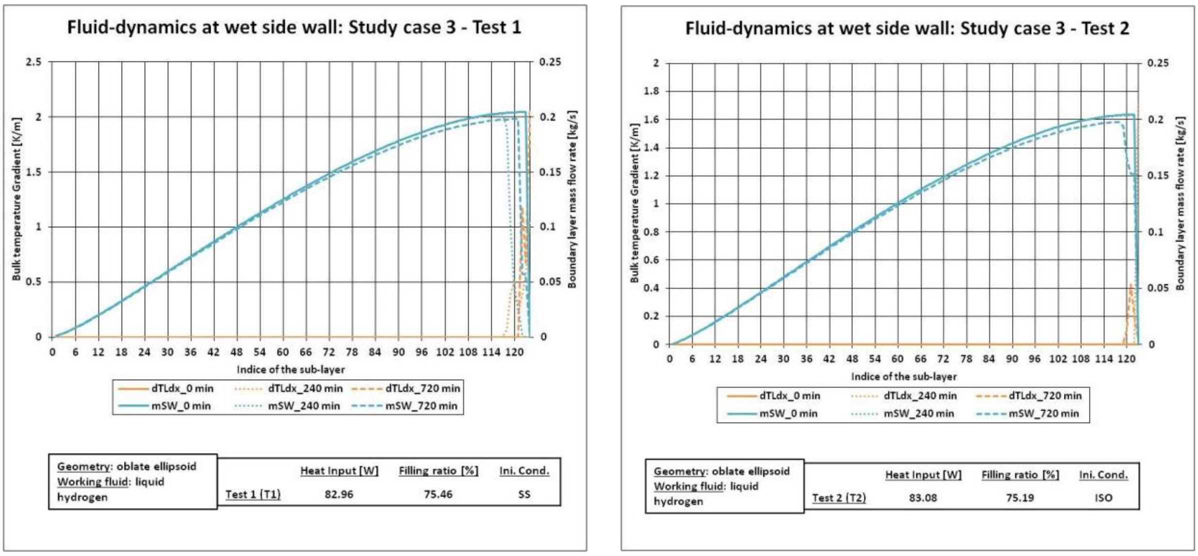

a) b)

Figure 140. Fluid-dynamics at the wet side wall of Study case 3: a) Test 1; b) Test 2.

In Study case 3, $\frac{\partial T^L}{\partial x}$ is equal to zero at the end of the self-pressurisation because the liquid is isothermal. In Test 1 (steady state initial condition), $\frac{\partial T^L}{\partial x}$ increases near the interface, forming peaks and nadirs. At 240 minutes, $\frac{\partial T^L}{\partial x}$ has peaks in the 120th sub-layer and a nadir in 121th sub-layer. after this nadir, $\frac{\partial T^L}{\partial x}$ increases up to the interface sub-layer (124th sub-layer). At 720 minutes, $\frac{\partial T^L}{\partial x}$ has a pick in the 122th sub-layer and a nadir in 123th sub-layer. the values of $\frac{\partial T^L}{\partial x}$ at 720 minutes are higher than the one at 240 minutes. In Test 2 (isothermal initial conditions), $\frac{\partial T^L}{\partial x}$ weakly increases near the interace and the value of this gradient is lower than the one of Test 1 at 240 minutes. At 720 minutes, $\frac{\partial T^L}{\partial x}$ produces a peak in the 122th sub-layer. this peak is lower than the one of Test 1. So, isothermal initial condition generates a bulk temperature gradient that is lower than the one of the steady state initial conditions.

In Study case 3, $\dot{m}^{SW}$ increases from the bottom to the interface, producing a flex point around 48th sub-layer for Test 1 (steady state initial conditions) and for Test 2 (isothermal initial conditions), at the end of the steady state. As time passes, $\dot{m}^{SW}$ is slightly lower than the one at the end of the steady state. $\dot{m}^{SW}$ rapidfly decreases near the interface. In Test 1, $\dot{m}^{SW}$ drops in 117th sub-layer and in 121th sub-layer at 240 minutes and at 720 minutes, respectively. these sub-layers are the sub-layer where $\frac{\partial T^L}{\partial x}$ significantly increases. In Test 2, the curve of 240 minutes is superposed to the curve of the end of the steady state. the value of $\dot{m}^{SW}$ at 720 minutes are lower than the one of the en of the steady state. $\dot{m}^{SW}$ quickly decreases in the 118th sub-layer (where $\frac{\partial T^L}{\partial x}$ increases) at 720 minutes.

Figure 141 shows the values of same properties (boundary layer mass flow of the wet side wall, $\dot{m}^{SW}$, and bulk temperature gradient in each sub-layer, $\frac{\partial T^L}{\partial x}$, at different time-points), for Study case 4; the time at which these variables are computed is reported as in previous Figures. These time-points correspond to the time-points at which the experimental temperature is measured.

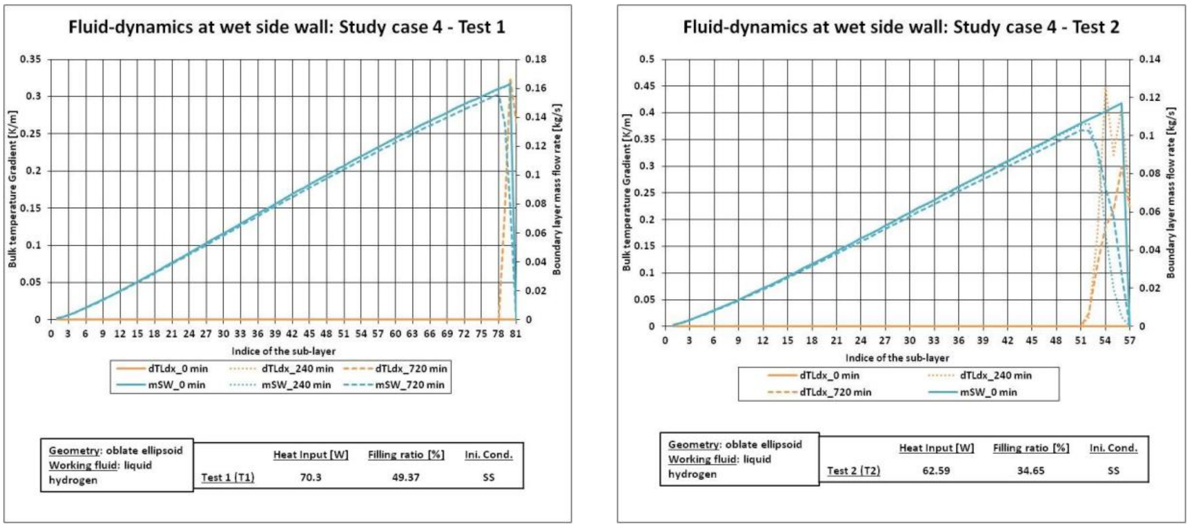

a) b)

Figure 141. Fluid-dynamics at the wet side wall of Study case 4: a) Test 1; b) Test 2.

As it is shown in Figure 141, the values of $\frac{\partial T^L}{\partial x}$ are equal to zero in all the sub-layers at the end of the steady state. In Test 1 (medium filling ratio), the liquid bulk temperature gradient at 720 minutes increases from the 78th sub-layer to the interface, creating a peak. At 240 minutes, the temperature gradient is flat. In Test 2 (low filling ratio), the liquid bulk temperature gradient increases from the 51th sub-layer to the interface. At 240 minutes, this increment produces two peaks and, at 720 minutes, there is one peaks.

As it is illustrated in Figure 141, the mass flow in the boundary layer of the wet side wall increases from the bottom to the second-last boundary layer. In the first 6 sub-layer, rate of the increment slightly increases. In Test 1, the space-distribution of this mass flow at 240 minutes is similar to the one at the end-of the self-pressurisation. At 720 minutes, the mass flow in the boundary layer of the wet side wall rapidly decreases from the 78th sub-layer. In Test 2, this mass flow rapidly decreases from the 51th sub-layer and this variable does not monotonically decrease.

To sum up, time-evolution and the space-distribution of $\frac{\partial T^L}{\partial x}$ and of the mass flow in the boundary layer of the wet side wall of Study case 1 are qualitatively similar to the one of Study case 2. At the end of the steady state (beginning of the self-pressurisation), the liquid bulk temperature gradient in equal to zero in all the sub-layer and the mass flow in the boundary layer linearly increases from the bottom to the second-last sub-layer. As time passes, the mass boundary layer increases where $\frac{\partial T^L}{\partial x}$ is equal to zero, thus in the lower part of the liquid. Then, this mass flow decreases and the liquid temperature gradient increases. Isothermal initial conditions tend to create isothermal liquid during the self-pressurisation, instead of the steady state inital conditions which form a bulk temperature gradient.

8.1.2. Presentation of the results: fluid-dynamics in the liquid

Figure 142 shows the values of the descending flow ($\dot{m}^D$) and the values of the rising flow of the bottom ($\dot{m}^B$), at different time-points, for Study case 1. These time-points are equal to the time-points at which the temperature is measured.

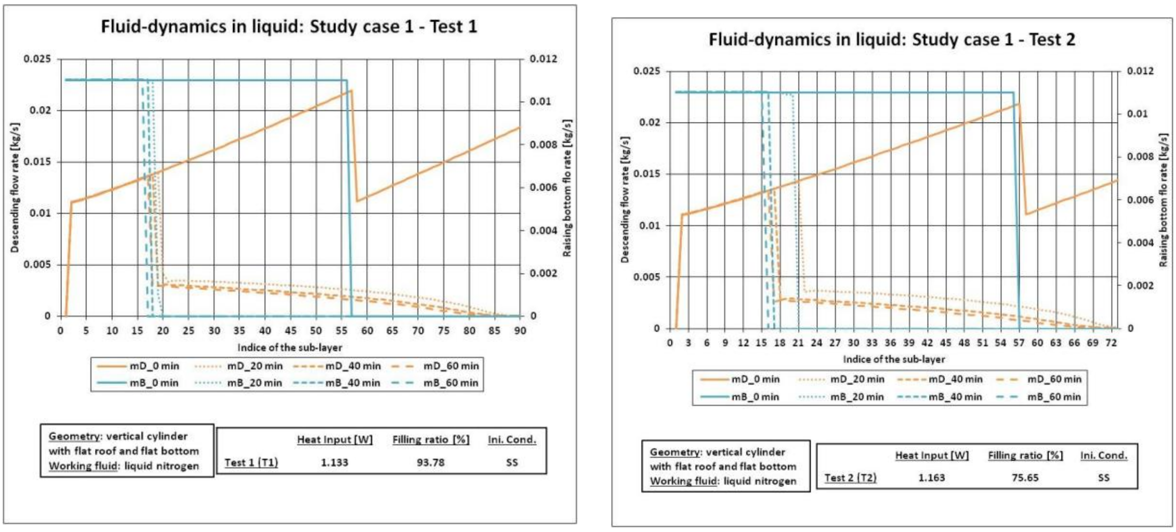

a)

b)

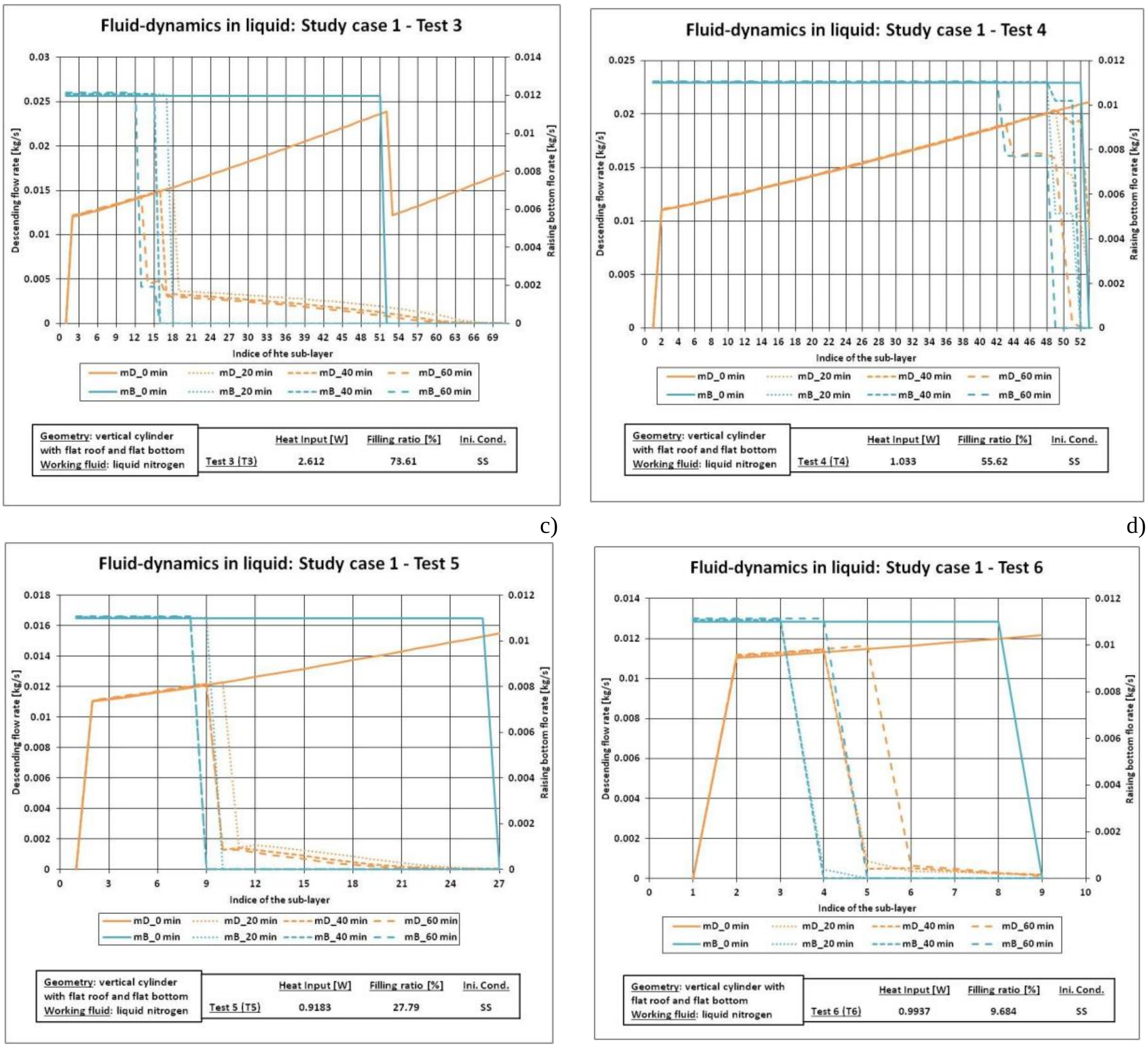

c) d) e) f)

Figure 142. Fluid-dynamics in the liquid of Study case 1: a) Test 1; b) Test 2; c) Test 3; d) Test 4; e) Test 5; f) Test 6.

As it is indicated in Figure 142, the value of the descending flow is equal to zero at the bottom sub-layer at any time-point. At the end of the steady state, thus at the beginning of the self-pressurisation, the descending mass flow linearly increases up to the interface bottom, except for Test 1, 2 and 3. For these tests, the value of this mass flow drops in the 54th, 57th and 52th sub-layers. After this drop, the descending mass flow increases up to the interface sub-layer. As time passes, this mass flow increases in the lower sub-layers, as similarly happens at the end of the self-pressurisation. After this increment, the descending flow drops and, after this drop, this mass flow constantly decreases, except for Test 4. In Test 1 and 3, the descending mass flow is equal to zero in the upper sub-layers. For Test 4, the descending mass flow does not monotonically decrease.

As it is illustrated in Figure 142, the rising flow at the bottom is constant for Test 4, 5 and 6 at the beginning of the self-pressurisation, thus at the end of the steady state, and it drops in the interface sub-layer because the interface is a rigid surface. For Test 1, 2 and 3, this drop respectively occurs at 54th, 57th and 52th sub-layer as it happens for the descending mass flow. After this drop, the rising flow of the bottom remains equal to zero. As time passes, the drop of the rising flow of the bottom occurs at sub-layers that are closer to the bottom sub-layer. This occurs for all the tests, except for Test 4. In this test, the rising flow of the bottom entails/provides/causes two consecutive drops, instead of one as in the other tests.

Figure 143 shows the values of descending flow ($\dot{m}^D$) and rising flow of the bottom ($\dot{m}^B$), at different time-points, for Study case 2. These time-points are equal to the time-points at which the temperature is measured..

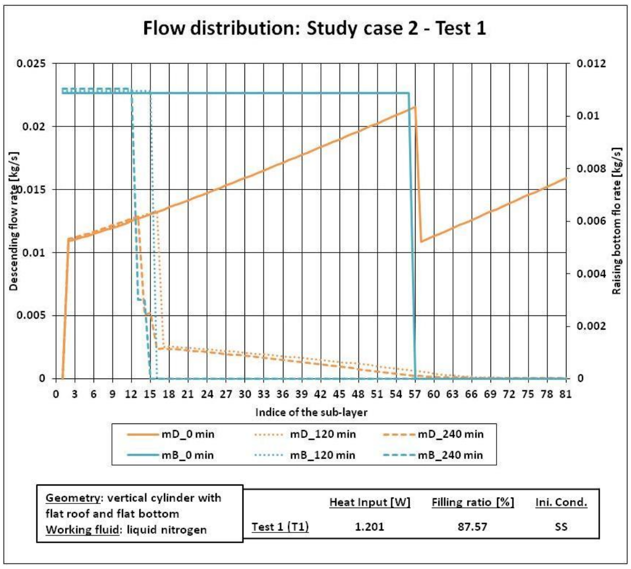

Figure 143. Fluid-dynamics in the liquid of Study case 2.

As it is shown in Figure 143, $\dot{m}^D$ increases from the first to the 55th sub-layer, at the beginning of the self-pressurisation, thus at the end of the steady state. At this sub-layer, the value of the descending mass flow drops at 57th sub-layer. After this drop, it linearly increases. As the time passes, this drop moves to the lower sub-layer and the descending mass flow constantly decreases. After the 66th sub-layer, the value of the descending mass flow is equal to zero.

As it is illustrated by Figure 143, $\dot{m}^B$ is constant from the bottom sub-layer to the 56th sub-layer. Then, the value of this mass flow drops and it is equal to zero in the remaining sub-layers. As the time passes, this drop occurs in the lower sub-layer.

Figure 144 shows the values of $\dot{m}^D$ and $\dot{m}^B$ at different time-points, for Study case 3. These time-points are equal to the time-points at which the temperature is measured.

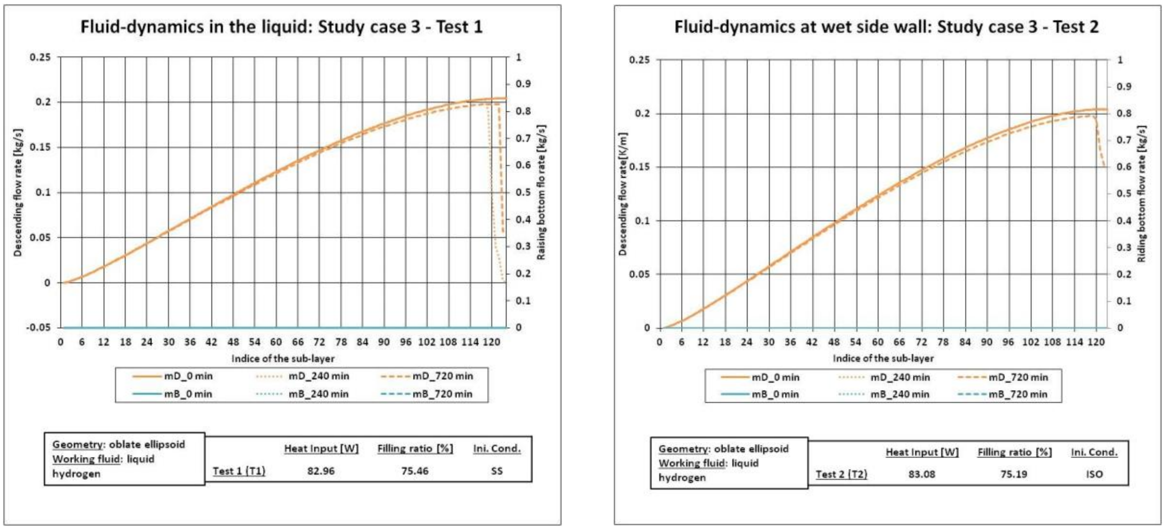

a) b)

Figure 144. Fluid-dynamics in the liquid of Study case 3: a) Test 1; b) Test 2.

In Study case 3, $\dot{m}^D$ increases from the bottom to the interface, forming a flex in the 48th sub-layer for Test 1 (steady state initial condition) and for Test 2 (isothermal initial condition), as it happens for

$\dot{m}^{SW}$ at the end of the steady state (see Section 8.1.1 of Chapter 6). The position of this flex-point does not move during the self-pressurisation. In Test 1, as time passes, $\dot{m}^{D}$ decreases near the itnerafce and this mass flow is slightly lower than the one of the end of the self-pressurisation. At 240 minutes, $\dot{m}^{D}$ rapidly decreases in the 117th sub-layer, as it occurs for $\dot{m}^{SW}$. At 720 minutes, $\dot{m}^{D}$ drops in the 121th sub-layer, similarly to $\dot{m}^{SW}$. These drops are similar to the ones of $\dot{m}^{SW}$ (see Section 8.1.1 of Chapter 6).

In Study case 3, $\dot{m}^{B}$ is equal to zero at the end of the steady state and during the self-pressurisation for both tests.

Figure 145 shows the values of $\dot{m}^{D}$ and $\dot{m}^{B}$ at different time-points, for Study case 4. These time-points are equal to the time-points at which the temperature is measured.

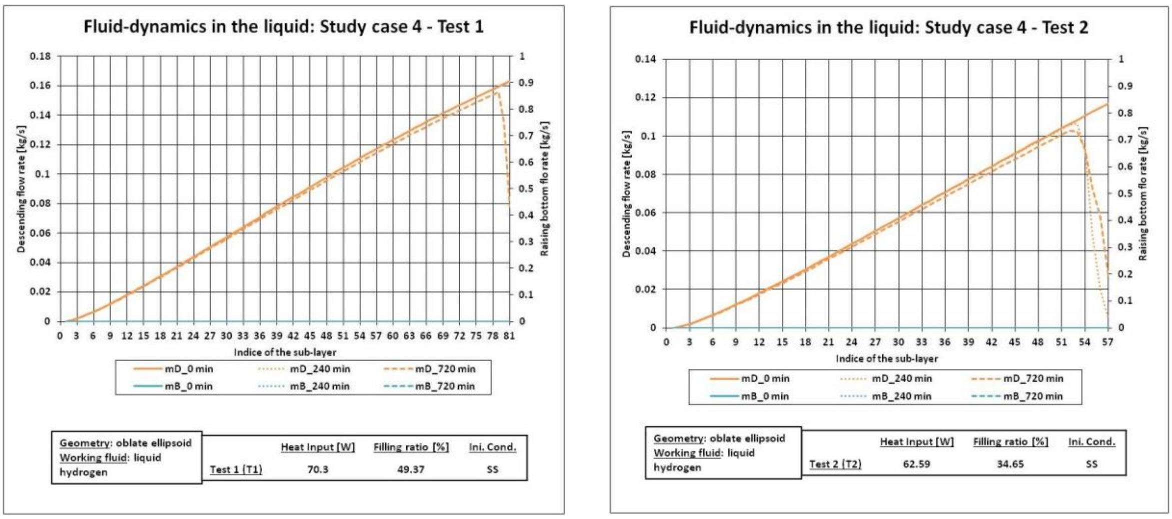

a) b)

Figure 145. Fluid-dynamics in the liquid of Study case 4: a) Test 1; b) Test 2.

As it is described in Figure 145, the space-distribution of $\dot{m}^{D}$ is similar to the one of mass flow in the boundary layer of the wet side wall at any time. $\dot{m}^{B}$ is equal to zero in all the sub-layer and at any time.

To sum up, the time-evolution and the space-distribution of $\dot{m}^{D}$ and of $\dot{m}^{B}$ of Study case 2 are quite similar to the ones of Test 1, 2 and 3 of Study case 3. For all the Study cases, the drops of the descending mass flow and of the rising flow of the bottom occur during the self-pressurisation. The drop of the rising flow of the bottom occurs in the sub-layer before the drop of the descending mass flow.

8.1.3. Presentation of the results: heat transfer at the wet side wall

Figure 146 shows the values of the wet side wall heat transfer coefficient (h_{w}^{SL}) and the values of the wet wall temperatures (T_{w}^{SL}), at different time-points, for Study case 1. These time-points are equal to the time-points at which the temperature is measured.

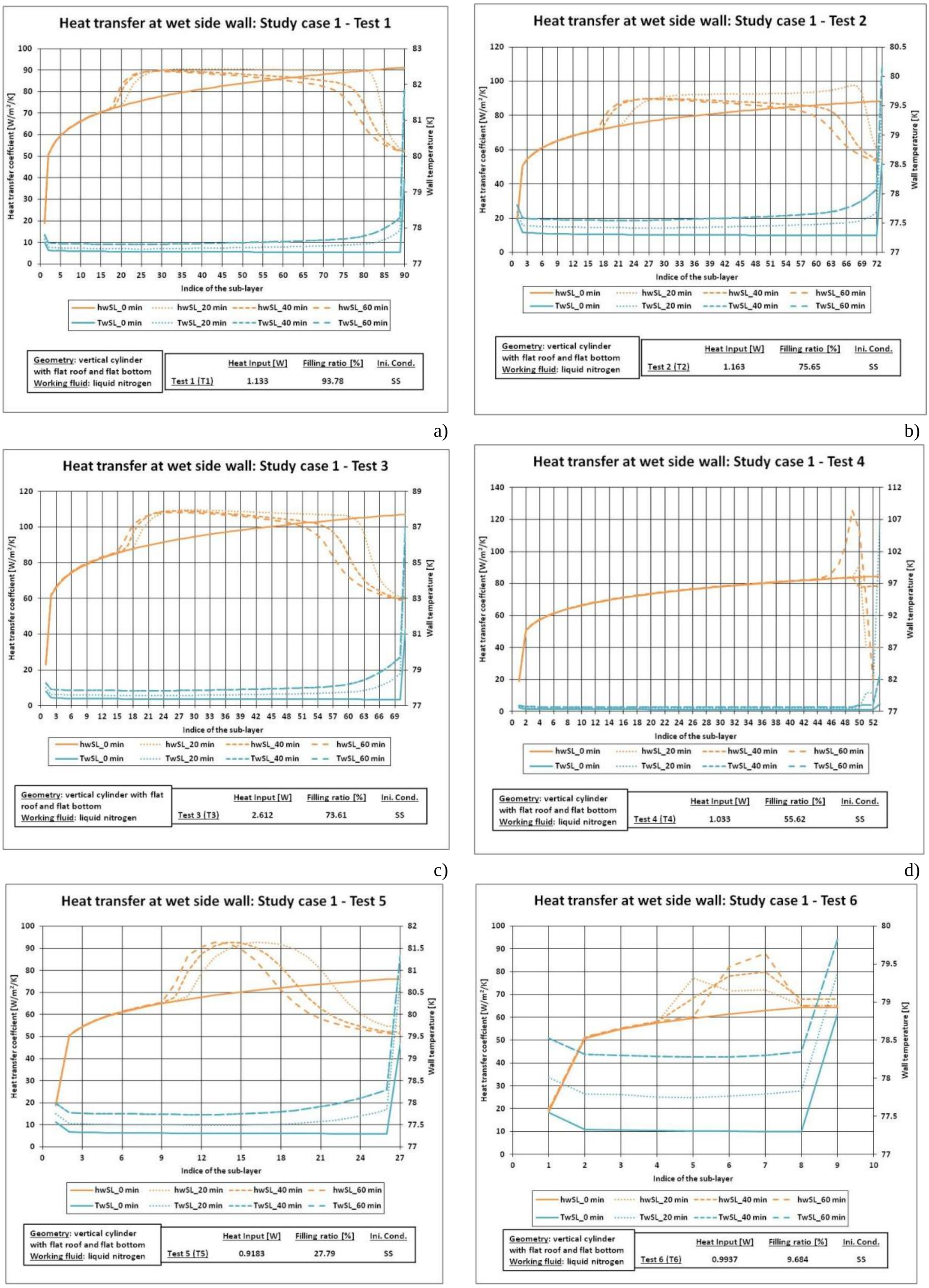

a) b) c) d) e) f)

Figure 146. Heat transfer at wet side wall of Study case 1: a) Test 1; b) Test 2; c) Test 3; d) Test 4; e) Test 5; f) Test 6.

As it is illustrated in Figure 146, the heat transfer coefficient of the wet side wall monotonically increases from the bottom to the interface sub-layer at the beginning of the steady-state, thus at the end of the self-pressurisation. The rate of the increment of the heat transfer coefficient smoothly decreases.

As the time passes, this rate rapidly increases in the lower sub-layer. For test 1, 2 and 3, the heat transfer coefficient gently decreases after this fast increment, creating a plateau. After the plateau, the heat transfer coefficient decreases. For test 4, this coefficient creates peaks in the upper sub-layer, followed by a decrement. This peak increases as time passes. For Test 5 and 6, the heat transfer coefficient is quite similar to the one of Test 1, 2 and 3, but the "hump of a camel" is present instead of the "plateau".

The wet side wall temperature decreases a little at the bottom of the storage container. This temperature remains constant up to the upper sub-layers. At the end of the self-pressurisation, the wet side wall temperature rapidly increases at the interface sub-layer. As the time passes, this increment starts before the interface sub-layer and it is smooth. This increment occurs when the heat transfer coefficient decreases. For Test 4, the increment of the wet side wall temperature is as steep as the one at the end of the self-pressurisation.

Figure 147 shows the values of h_w^{SL} and T_w^{SL}, at different time-points, for Study case 2. These time-points are equal to the time-points at which the temperature is measured.

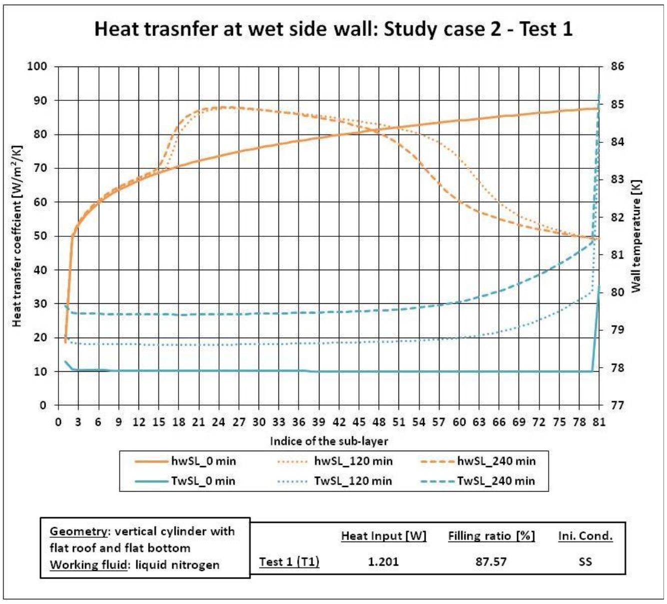

Figure 147. Heat transfer at the wet side wall of Study case 2.

As it is illustrated in Figure 147, the heat transfer coefficient of the wet side wall monotonically increases from the bottom to the interface sub-layer, at the beginning of the self-pressurisation, thus at the end of the steady state. At this time-point, the rate of the increment of this coefficient slowly decreases. As the time passes, the heat transfer coefficient increases in the lower sub-layer. Then, this coefficient rapidly grows and then it slowly decreases, creating a "plateau". After this plateau, the heat transfer coefficient decreases. The rate of this decrement reduces near the interface.

The wet side wall temperature is constant at the end of the self-pressurisation except at the bottom and the interface. At the bottom, this temperature decreases a little and, at the interface, this temperature instantaneously increases. As time passes, the wet side wall temperature increases for the same sub-layer and it remains constant from the bottom up to the upper sub-layers. In the upper sub-layer, the temperature rapidly then smoothly increases and, at the interface, it instantaneously grows.

Figure 148 shows the values h_w^{SL} and T_w^{SL}, at different time-points, for Study case 3.

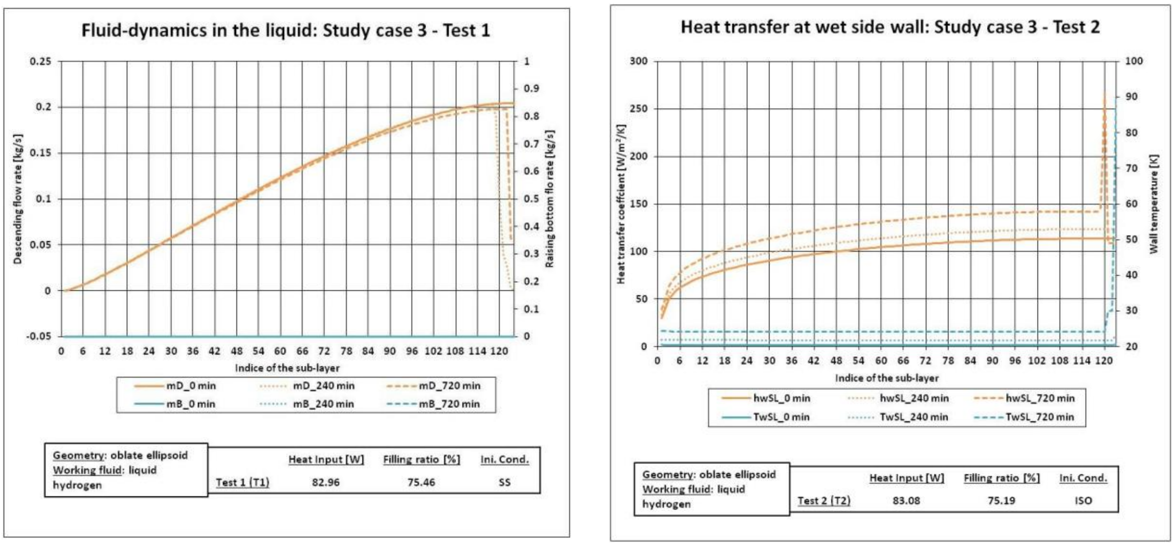

a) b)

Figure 148. Heat transfer at wet side wall of Study case 3: a) Test 1; b) Test 2.

In Study case 3, h_w^{SL} increases from the bottom to the interface at the end of the steady state, for Test 1 (steady state initial conditions) and for Test 2 (isothermal initial conditions). the rate of this increment decreases with the increment of hte index of the sub-layers for both tests. In Test 1, h_w^{SL} has two peaks in the 118th and in the 122th sub-layer, at 240 minutes. h_w^{SL} quickly decreases at the 121th sub-layer at 720 minutes. h_w^{SL} at 720 minutes is higher than the one at 240 minutes than the one at the end of the steady state. In Test 2, h_w^{SL} at 240 minutes is higher than the one at the end of the steady state. At 720 minutes, h_w^{SL} is higher than the one of the previous time-point and it produces a peak in the 120th sub-layer.

In Study case 3, T_w^{SL} is flat at the end of the steady state for Test 1 (steady state initial conditions) and for Test 2 (isothermal initial conditions). In Test 1, T_w^{SL} produces a small pick at 20 minutes, near the interface. T_w^{SL} rapidly increases in the 121th sub-layer at 720 minutes. In Test 2, the curve of T_w^{SL} at 240 minutes is qualitatively similar to the one of the end of the steady state, except for the small increment near the interface. the values of T_w^{SL} at 240 minutes are higher than the one of the end of the steady state. At 720 minutes, T_w^{SL} rapidly increases in the 120th sub-layer, reaching a value of around 90 K.

Figure 149 shows the values h_w^{SL} and T_w^{SL}, at different time-points, for Study case 4.

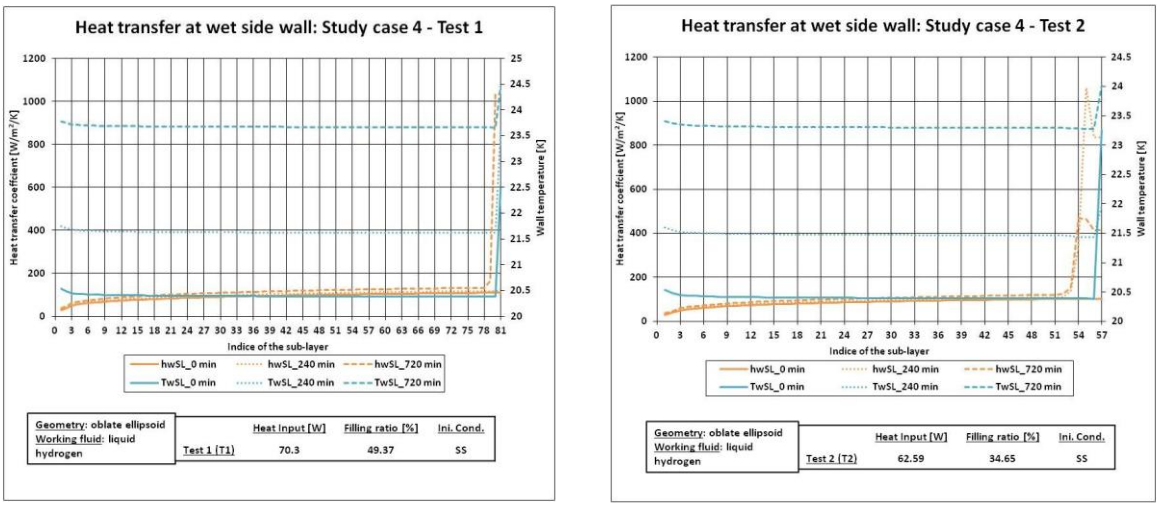

a) b)

Figure 149. Heat transfer at wet side wall of Study case 4: a) Test 1; b) Test 2.

As it is described in Figure 149, the heat transfer coefficient monotonically increases from the bottom the interface at the end of the steady state. The rate of the increment decreases from the bottom to the interface. In Test 1 (medium filling ratio), the space-distribution of this heat transfer coefficient is similar to the one at the end of the steady state. At 720 minutes, the heat transfer coefficient of the wet side wall rapidly increases from the 78th sub-layer. In Test 2 (low filling ratio), the heat transfer coefficient of the wet side wall increases at 52th sub-layer at 240 and 720 minutes. The increment of 240 minutes is higher than the one at 720 minutes and both increments have peaks.

As it is illustrated in Figure 149, the wet side wall temperature slightly reduces between the bottom and the 6th sub-layer, and it remains constant in the core of the liquid at the end of the steady state. At the interface, this wall temperature rapidly increases. In Test 1 (medium filling ratio), the space-distribution the wet side wall temperature at 240 minutes is similar to the initial one. At 720 minutes, the increment at the interface is lower than the one of the previous time-points. The wet wall temperature increases in time. In Test 2 (low filling ratio), the space-distribution of the wet side wall temperature is similar to the initial one, except near at the interface. At the interface, the increment of this wall temperature at time 240 and 720 minutes is lower than the initial one.

To sum up, the time-evolution and the space-distribution of the neat transfer coefficient and of the wet side wall temperature of Study case 1 are similar to the one of study case 2. The heat transfer coefficient increases in the lower sub-layer, it can form a plateau or a hump in the intermediate sub-layer and it decreases in the upper sub-layers. The wet side wall temperature increases as time passes and it remains constant, except in the upper sub-layers, where it increases.

8.1.4. Presentation of the results: intra-layer heat transfer

Figure 150 shows the spatial-evolution of the upper ($\dot{Q}^{UP}$) and lower ($\dot{Q}^{INF}$) heat flows across the sub-layers, at different time-points, for Study case 1. The upper heat flow is the heat flow between the sub-layer "nL+1" and the sub-layer "nL", and is equal to the liquid-to-interface heat flow ($\dot{Q}_I^L$) with the opposite sign ($-\dot{Q}_I^L$) at the interface sub-layer. The lower heat flow is the heat flow between the sub-layer "nL" and the sub-layer "nL-1", and is equal to the bottom-to-liquid heat flow with the opposite sign at the bottom ($-\dot{Q}_w^B$), as explained in Intra-Layer Heat Transfer (ILHT) model.

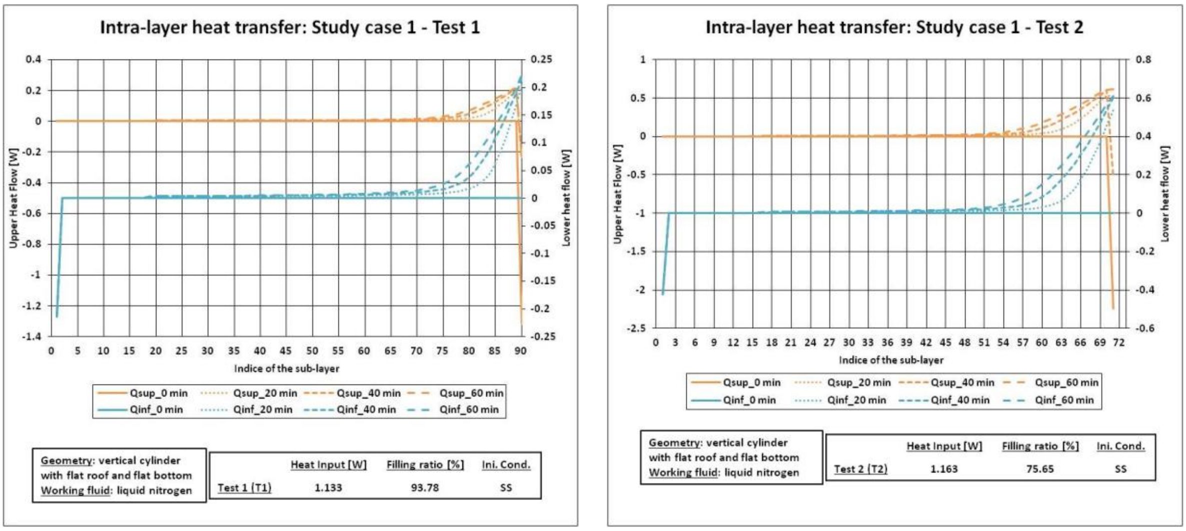

a) b)

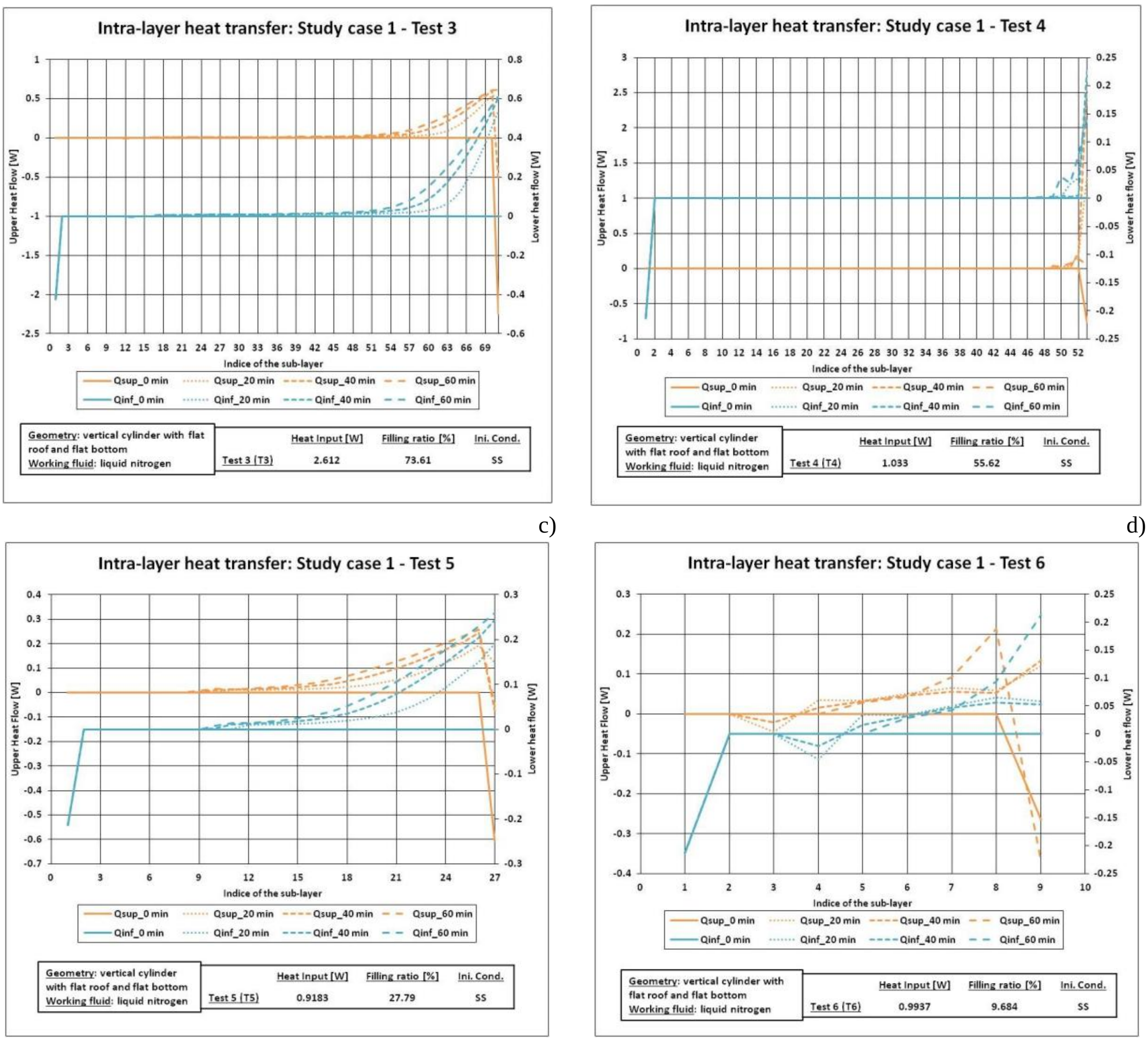

c) d)

e) f)

Figure 150. Intra-layer heat transfer of Study case 1: a) Test 1; b) Test 2; c) Test 3; d) Test 4; e) Test 5; f) Test 6.

As it is illustrated in Figure 150, the upper heat flow is equal to zero for all the sub-layer, except the interface sub-layer, at the end of the steady state. At the interface sub-layer, the upper heat flow drops to the value of the liquid-to-interface heat flow with the opposite sign ($-\dot{Q}_I^L$). As the time passes, the upper heat flow is equal to zero, except at in the upper sub-layers. Here, this heat flow monotonically increases up to the second last sub-layer. At the interface sub-layer, this heat flow drops to the value of the liquid-to-interface heat flow with the opposite sign ($-\dot{Q}_I^L$). In Test 6, the upper heat flow decreases in the sub-layer 3. After this decrement, it increases, similarly to the other tests. In Test 4, the upper heat flow discontinuously increases in the upper sub-layers because small peaks are present.

The lower heat flow increases from the bottom sub-layer, where it is equal to the one of the bottom-to-liquid heat flow with opposite sign ($-\dot{Q}_W^B$), and it remains equal to zero at the beginning of the self-pressurisation. In the upper sub-layer, the spatial evolution of the lower heat flow is similar to the one at the beginning of the self-pressurisation, as time passes. In the upper sub-layers, the lower heat flow regularly and rapidly increases. In Test 6, the lower heat flow decreases in the sub-layer 3. After this decrement, it increases , similarly tothe other tests. In test 4, the lower heat flow discontinuously increases in the upper sub-layers because small peaks are present.

Figure 151 shows the spatial-evolution of $\dot{Q}^{UP}$ and $\dot{Q}^{INF}$ across the sub-layers, at different time-points, for Study case 2.

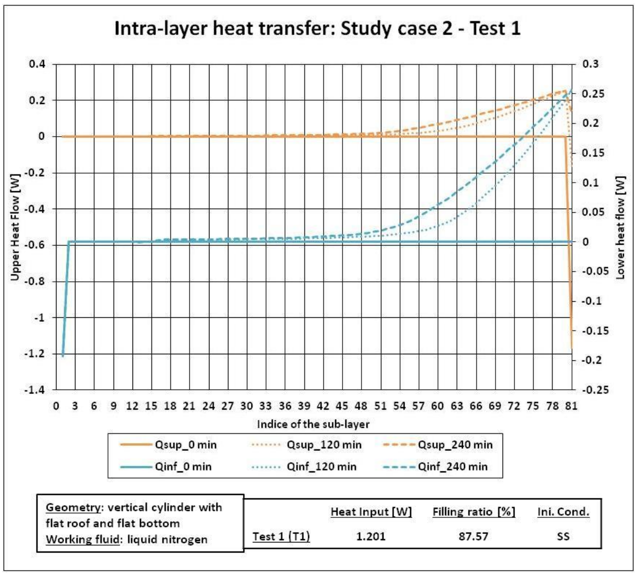

Figure 151. Intra-layer heat transfer of Study case 2.

As it is shown in Figure 151, at the end of the steady state the upper heat flow is equal to zero for all the sub-layer, except for the interface sub-layer. In this sub-layer, the upper heat flow is equal to the liquid-to-interface heat flow with opposite sign. As time passes, the upper heat flow becomes zero in the lower and intermediate sub-layers, as for the initial time-point (beginning of the self-pressurisation). In the upper sub-layer, this heat flow regularly increases and it drops in the interface sub-layer, as for the initial time-point.

At the end of the steady state, the lower heat flow is equal to zero, except at the bottom sub-layer. The lower heat flow increases between the bottom sub-layer and the second sub-layer because this heat flow is equal to the bottom-to-liquid heat flow with opposite sign. As the time passes, the space-distribution of the heat flow is similar to the one at the initial time-point in the lower sub-layer. In the intermediate sub-layers, the lower heat flow is slightly higher than zero and it is constant. In the upper sub-layer, the lower heat flow increases up to the interface.

Figure 152 shows the spatial-evolution of $\dot{Q}^{UP}$ and $\dot{Q}^{INF}$ for Study case 3.

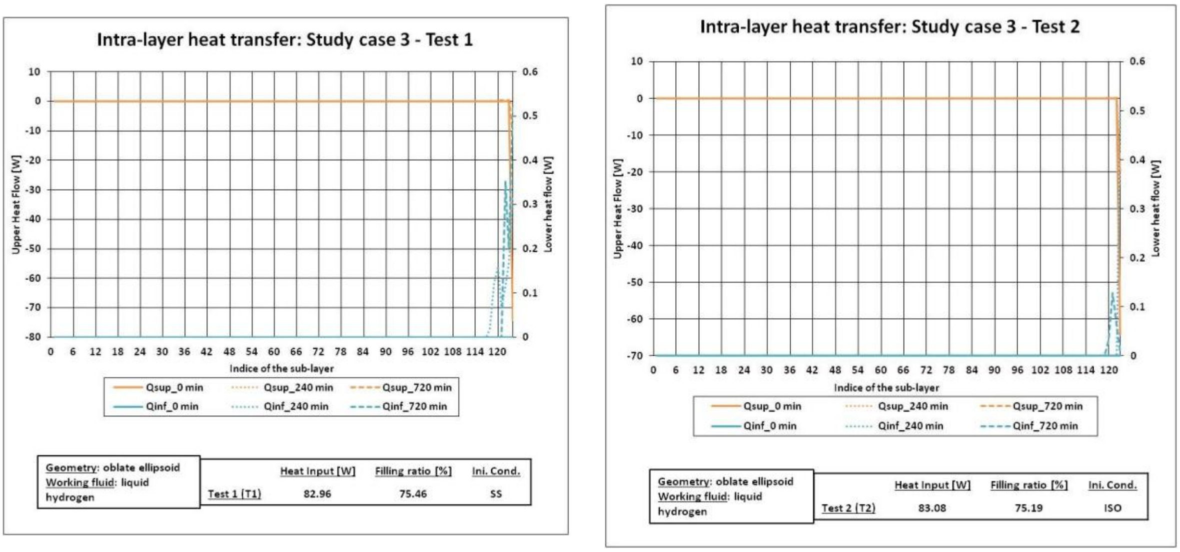

a) b)

Figure 152. Intra-layer heat transfer of Study case 3: a) Test 1; b) Test 2.

In Study case 3, $\dot{Q}^{UP}$ is equal to zero at the end of the steady state for Test 1 (steady state initial condition) and for Test 2 (isothermal initial conditions). For these tests, $\dot{Q}^{UP}$ rapidly decreases near the interace. The space-distribution of this variables does not change during the self-pressurisation.

In Study case 3, $\dot{Q}^{INF}$ is equal to zero at the end of the steady state Test 1 (steady state initial condition) and for Test 2 (isothermal initial conditions). In Test 1, $\dot{Q}^{INF}$ produces a peak in the 120th sub-layer and a nadir in 121th sub-layer at 240 minutes, as it occurs for bulk liquid temperature gradient ($\frac{\partial T^L}{\partial x}$) (see Section 8.1.1 of Chapter 6). $\dot{Q}^{INF}$ generates a peak at 122th sub-layer and a nadir in the 123th sub-layer, at 720 minutes, as it happens for $\frac{\partial T^L}{\partial x}$ (see Section 8.1.1 of Chapter 6). In Test 2, $\dot{Q}^{INF}$ increases near the interface at 240 minutes. This heat flow produces a peak in the 121th sub-layer, at 720 minutes, as it happens for $\frac{\partial T^L}{\partial x}$ (see Section 8.1.1 of Chapter 6). So, the space-distributions of $\dot{Q}^{UP}$ and of $\dot{Q}^{INF}$ are similar to the one of the $\frac{\partial T^L}{\partial x}$.

Figure 153 shows the spatial-evolution of $\dot{Q}^{UP}$ and $\dot{Q}^{INF}$ for Study case 4.

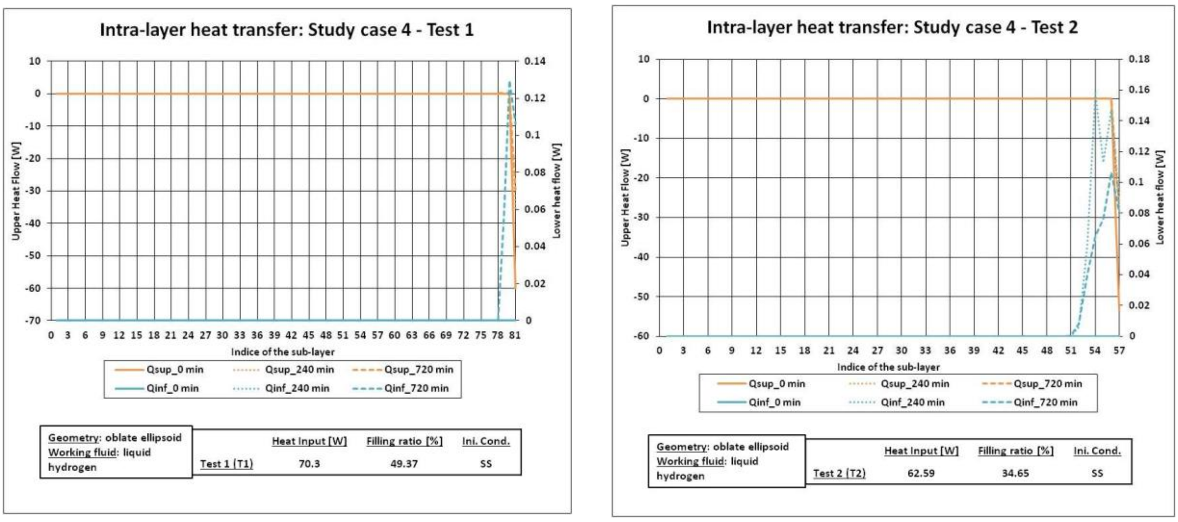

a) b)

Figure 153. Intra-layer heat transfer of Study case 4: a) Test 1; b) Test 2.

As it is described in Figure 153, the upper heat flow is equal to zero in all the sub-layer, except at the interface, at the end of the steady state. At the interface, the value of this heat flow is negative because the thermal energy is removed from the liquid. In Test 1 (medium filling ratio), the space-distribution of the upper heat flow is similar to the initial one, except at the interface; here, the value of this heat flow is negative, but it is higher than the initial one. In Test 2 (low filling ratio), the space-distribution of the upper heat flow at 240 minutes and at 720 minutes is similar to initial one. At the interface, the values of this heat flow are higher than the initial one.

As it is illustrated in Figure 153, the lower heat flow is equal to zero in all the sub-layers at end of the self-pressurisation. In Test 1, the space-distribution of this heat flow at 240 minutes is similar to the initial one. At 720 minutes, this heat flow only increases near the interface, creating a peak, as similarly done by liquid bulk temperature gradient ($\frac{\partial T^L}{\partial x}$). In Test 2, the lower heat flows at 240 minutes and at 720 minutes increases from 51th sub-layer and this increment is not regular. At 240 minutes, this heat flow increases creating a peak, as done by the liquid bulk temperature gradient (see Section 8.1.1 of Chapter 6). At 720 minutes, the lower heat flow produces two peaks as for $\frac{\partial T^L}{\partial x}$ gradient (see Section 8.1.1 of Chapter 6).

To sum up, the upper and lower heat flows are equal to zero in the lower sub-layers and they increase in the upper sub-layers, during the self-pressurisation. The values of the upper and lower heat flows are always positive, except at the interface and at the bottom, indicating that the thermal energy flows from the interface to the core.

8.1.5. Presentation of the results: heat transfer at interface

Figure 154 shows the time-evolution of the liquid-to-interface ($\dot{Q}_I^L$) and vapour-to-interface ($\dot{Q}_I^V$) heat flows. The solid and the dotted respectively indicate the liquid-to-interface and the vapour-to-interface heat flows. These heat inputs at the interface are noted as "QLI" and "QVI", respectively.

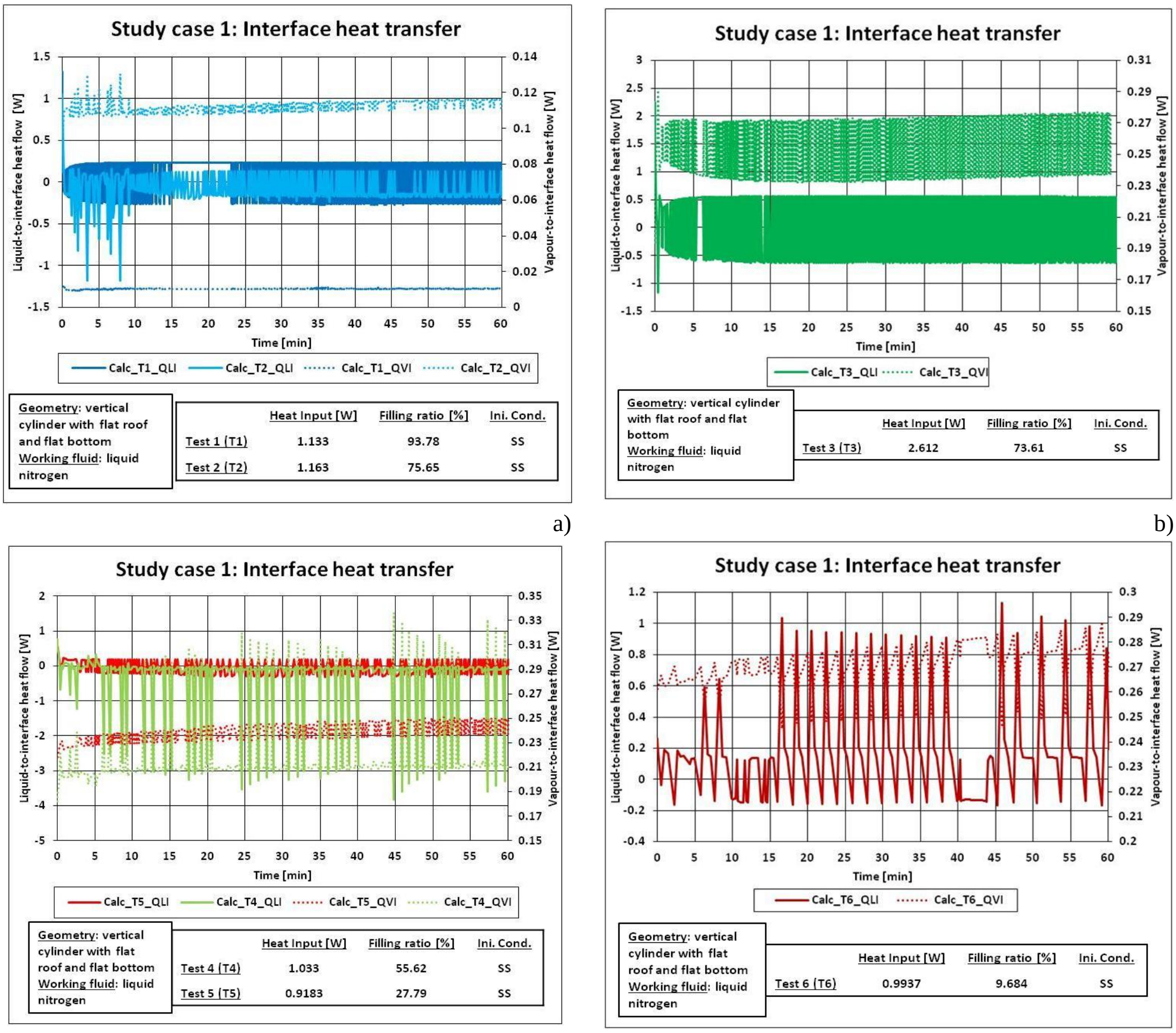

a)

Geometry: vertical cylinder with flat roof and flat bottom
Working fluid: liquid nitrogen

	Heat Input [W]	Filling ratio [%]	Ini. Cond.
Test 1 (T1)	1.133	93.78	SS
Test 2 (T2)	1.163	75.65	SS

b)

Geometry: vertical cylinder with flat roof and flat bottom
Working fluid: liquid nitrogen

	Heat Input [W]	Filling ratio [%]	Ini. Cond.
Test 3 (T3)	2.612	73.61	SS

c)

Geometry: vertical cylinder with flat roof and flat bottom
Working fluid: liquid nitrogen

	Heat Input [W]	Filling ratio [%]	Ini. Cond.
Test 4 (T4)	1.033	55.62	SS
Test 5 (T5)	0.9183	27.79	SS

d)

Geometry: vertical cylinder with flat roof and flat bottom
Working fluid: liquid nitrogen

	Heat Input [W]	Filling ratio [%]	Ini. Cond.
Test 6 (T6)	0.9937	9.684	SS

Figure 154. Heat transfer at the interface for the Study cases at low heat fluxes: a) Study case 1 (Test 1 and Test 2); b) Study case 1 (Test 3); c) Study case 1 (Test 4 and 5); d) Study case 1 (Test 6).

In Study case 1, $\dot{Q}_I^L$ immediately drops to the negative values as the self-pressurisation starts/ This initial drop is significant in Test 1 (high filling ratio), 2 (high-medium filling ratio) and 3 (high heat input), whereas it is less noticeable in Tests 4 (medium filling ratio), 5 (medium-low filling ratio) and 6 (low filling ratio). So, the initial drops increases with the increment of the filling ratio and of the heat inputs. After this initial drop, $\dot{Q}_I^L$ oscillates between negative and positive values during all the self-pressurisation. Except for Tests 1 and 3, the average values of these fluctuations are negative. So, the thermal energy flows from the interface to the liquid instead of being transferred from the liquid to the interface as occurs in the steady state. For Tests 5 and 6, these average values are respectively close to zero and positive. So, the heat flows from the liquid to the interface in Test 6, contrarily to the other tests and the results of the previous models. The value of $\dot{Q}_I^V$ during the self-pressurisation is similar to the one of the steady state. So, $\dot{Q}_I^V$ is not affected by the transition between the steady state and the self-pressurisation. The vapour-to-interface heat flow oscillates during the self-pressurisation, as the $\dot{Q}_I^L$. The amplitude of these oscillations is lower than the one of the $\dot{Q}_I^L$.

Figure 155 shows the time-evolution of the liquid-to-interface ($\dot{Q}_I^L$) and vapour-to-interface ($\dot{Q}_I^V$) heat flows. The solid and the dotted respectively indicate the liquid-to-interface and the vapour-to-interface heat flows.

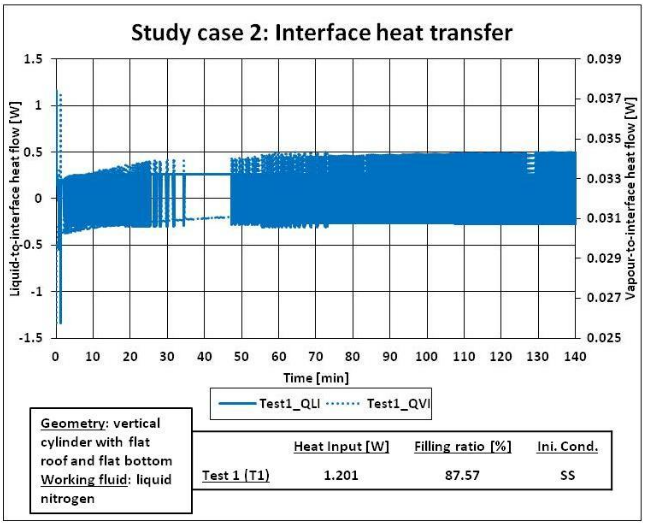

Geometry: vertical cylinder with flat roof and flat bottom
Working fluid: liquid nitrogen

	Heat Input [W]	Filling ratio [%]	Ini. Cond.
Test 1 (T1)	1.201	87.57	SS

Figure 155. Heat transfer at the interface for the Study cases of Study case 2 (low heat fluxes).

In Study case 2, $\dot{Q}_I^L$ initially drops as the storage container is close after the steady state. After this drop, this heat flow oscillates during the self-pressurisation. $\dot{Q}_I^V$ has an initial peak, which occurs when $\dot{Q}_I^L$ drops. After this, $\dot{Q}_I^V$ remains almost constant, but peaks are observed when $\dot{Q}_I^L$ drops to negative values.

Figure 156 shows the time-evolution of the liquid-to-interface ($\dot{Q}_I^L$) and vapour-to-interface ($\dot{Q}_I^V$) heat flows. The solid and the dotted stilll indicate the liquid-to-interface and the vapour-to-interface heat flows, respectively.

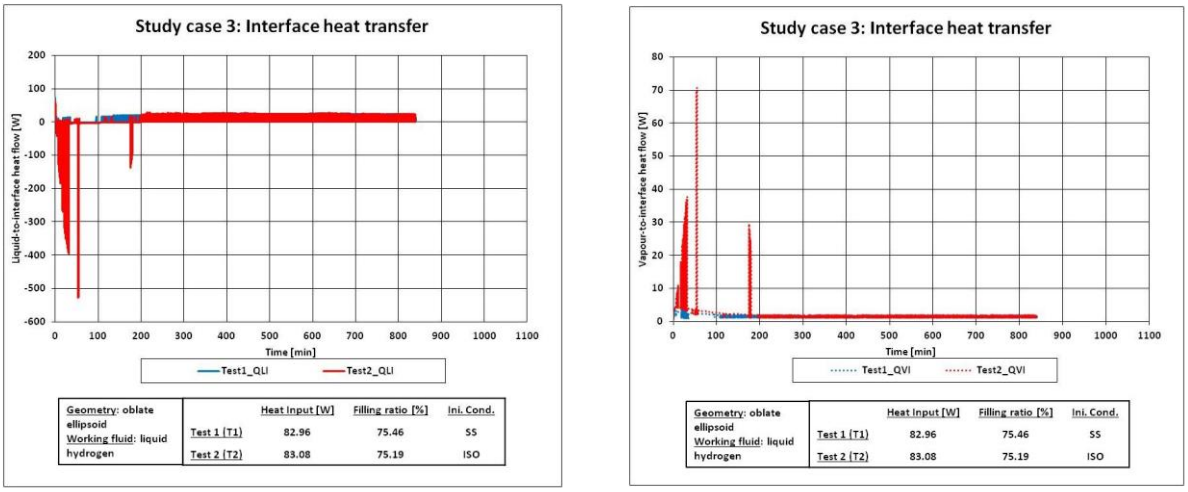

Geometry: oblate ellipsoid
Working fluid: liquid hydrogen

	Heat Input [W]	Filling ratio [%]	Ini. Cond.
Test 1 (T1)	82.96	75.46	SS
Test 2 (T2)	83.08	75.19	ISO

Geometry: oblate ellipsoid
Working fluid: liquid hydrogen

	Heat Input [W]	Filling ratio [%]	Ini. Cond.
Test 1 (T1)	82.96	75.46	SS
Test 2 (T2)	83.08	75.19	ISO

a) b)

Figure 156. Heat transfer at the interface for the Study cases of Study case 3 (low heat fluxes): a) liquid-to-interface heat flow; b) vapour-to-interface heat flow.

In Study case 3, the QLI decreases at the end of the steady state for both tests. In Test 1 (steady state initial conditions), QLI fluctuates during all the sel-pressurisation. After this initial decrement, the time-evolution of QLI of Test 2 (isothermal initial condition)has several negative peaks, whose minimum value is -520 W. After this peak, the value of QLI is close to zero and it is weakly fluctuates. At around 180 minutes, QLI produce a negative peak of -120 W. After this peak, QLI fluctuates. The absolute values of the peaks of QLI of Test 2 are much higher than the overall heat input in the storage container.

QVI of Test 1 fluctuates during all the self-pressurisation as it occurs for QLI. For Test 2, QVI initially increases and produces positive peaks, whose maximum value is around 70 W. Atter this peak, the time-evolution of QVI is regular up to 180 minutes. here, this heat flow produces a peak of around 30 W. After this peak, QVI quickly fluctuates for all the self-pressurisation. the time-evolution of QVI is qualitatively similar to the one of QLI. The values of the peak of QVI are always lower than the value of the overall heat input of the storage container.

Figure 157 shows the time-evolution of the liquid-to-interface (QLI) and vapour-to-interface (QVI) heat flows. The solid and the dotted stilll indicate the liquid-to-interface and the vapour-to-interface heat flows, respectively.

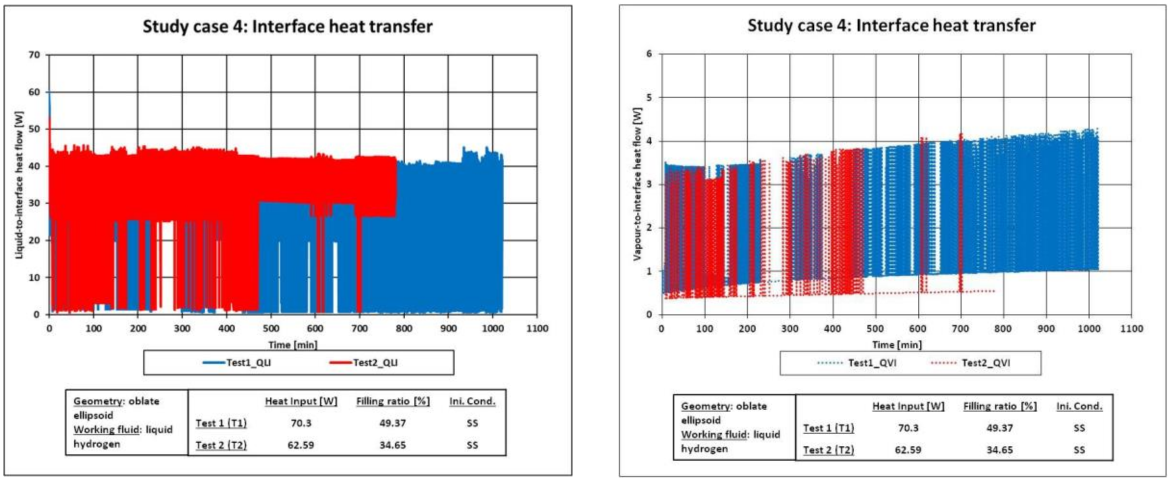

a) b)

Figure 157. Heat transfer at the interface for the Study cases of Study case 4 (low heat fluxes): a) liquid-to-interface heat flow; b) vapour-to-interface heat flow.

As it is described in Figure 157 (a), $\dot{Q}_I^L$ decreases at the end of the self-pressurisation. This decrement is lower than the one of the H 2.0 model. After this initial decrement, $\dot{Q}_I^L$ fluctuates during all the self-pressurisation. The average value of these fluctuations is constant during the self-pressurisation. $\dot{Q}_I^L$ of Test 2 (low filling ratio) is higher than the one of Test 1 (medium filling ratio).

As it is illustrated in Figure 157 (b), $\dot{Q}_I^V$ fluctuates during the whole self-pressurisation. The positive oscillations occur when the fluctuations of $\dot{Q}_I^L$ are negative and the negative oscillation of $\dot{Q}_I^V$ happens if the fluctuations of $\dot{Q}_I^L$ are positive. The average value of the fluctuation of $\dot{Q}_I^V$ slightly increases during the self-pressurisation. The values of $\dot{Q}_I^V$ of Test 1 are higher than the ones of Test 2.

To sum up, the interface transfer heats the liquid because the values of $\dot{Q}_I^L$ are negative. This heat flow oscillates during the whole self-pressurisation, producing peak. These peaks can be sometime higher than the overall heat input of the storage container. $\dot{Q}_I^V$ is not affected by the shift from the steady state to the self-pressurisation. This heat flow oscillates less than the liquid-to-interface, and the peak of $\dot{Q}_I^V$ usually occurs at the same time-point of the drops of $\dot{Q}_I^L$. Contrarily to the results of the previous models, the value of the liquid-to-interface can be positive during the self-pressurisation, indicating that the thermal energy flows from the liquid to the interface.

8.1.6. Presentation of the results: net mass flow

Figure 158 describes the time-evolution of the net mass flow ($\dot{m}_N$) during the self-pressurisation of Study case 1.

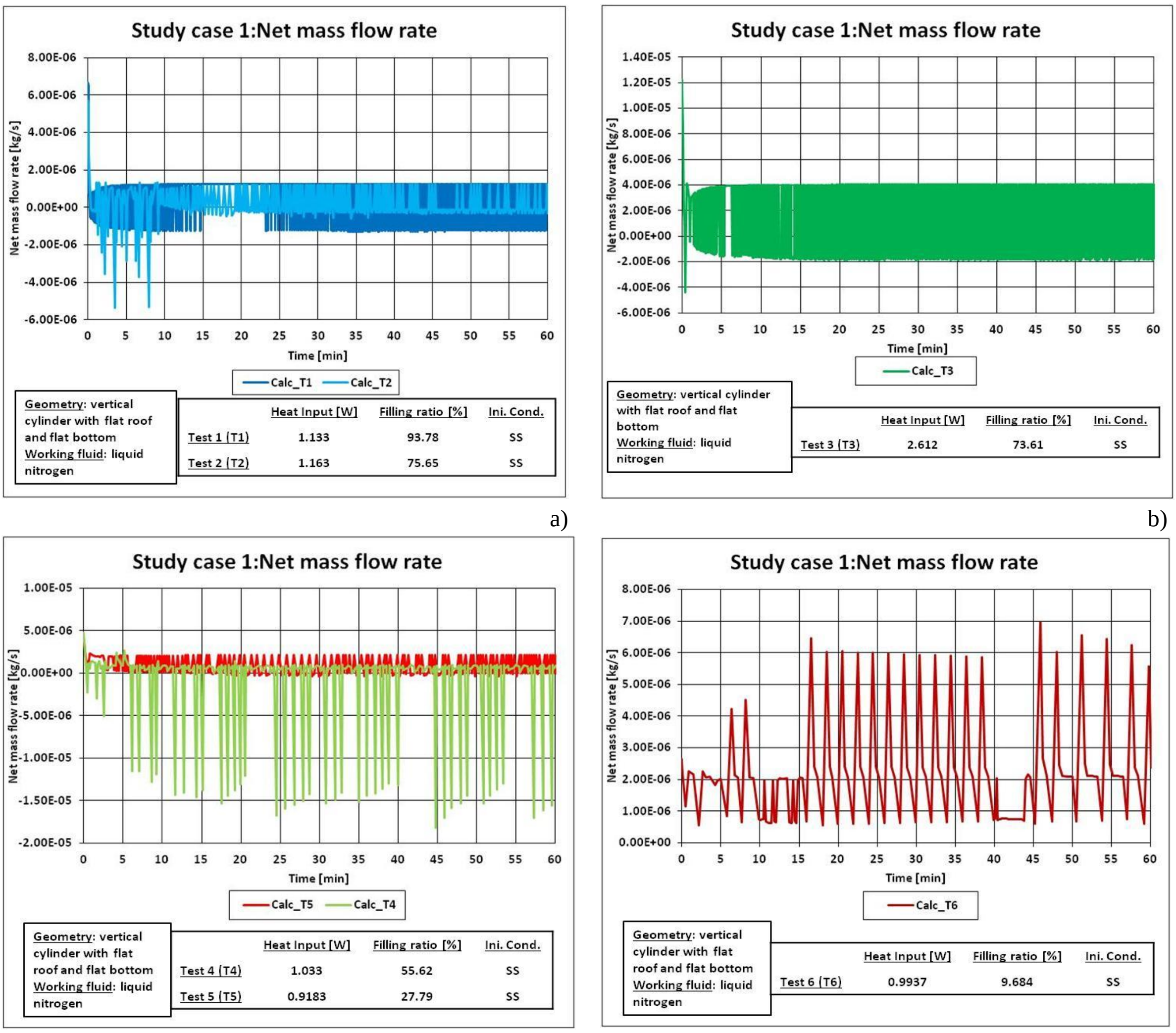

a) b)

c) d)

Figure 158. Net mass flow for the Study cases at low heat fluxes: a) Study case 1 (Test 1 and Test 2); b) Study case 1 (Test 3); c) Study case 1 (Test 4 and 5); d) Study case 1 (Test 6);

In Study case 1, $\dot{m}_N$ drops down at the beginning of the self-pressurisation, thus when the steady state ends, indicating that the condensation rate increases. During the self-pressurisation, this mass flow oscillates, and this oscillation is qualitatively similar to the one of the liquid-to-interface heat flow ($\dot{Q}_I^L$). $\dot{m}_N$ fluctuates around an average value. This average value of Test 6 (low filling ratio) is higher than the one of Test 1 (high filling ratio), except for Test 4 (medium filling ratio) and for Test 3 (high filling ratio). So, the average value of $\dot{m}_N$ increases with the reduction of the filling ratio and with the increment of the heat inputs.

Figure 159 describes the time-evolution of the net mass flow ($\dot{m}_N$) during the self-pressurisation of Study case 2.

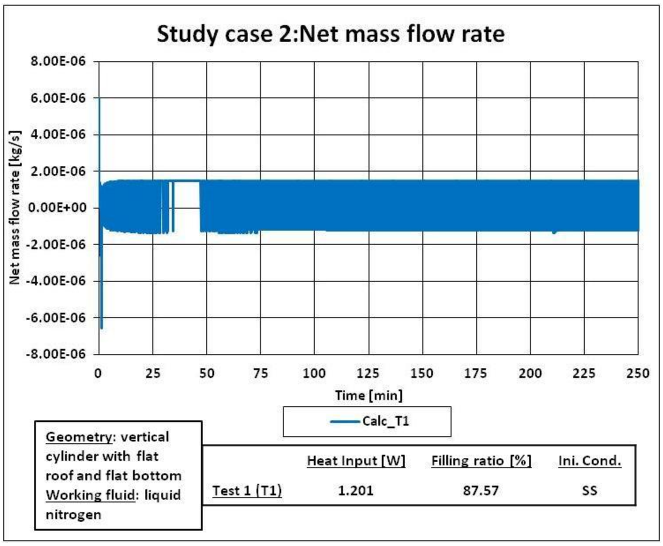

Figure 159. Net mass flow for the Study cases of Study case 2 (low heat fluxes).

In Study case 2, $\dot{m}_N$ immediately and quickly falls as the storage container is closed after the steady state. After this initial drop, $\dot{m}_N$ oscillates around an average value, which remains almost constant during the whole pressurisation. The oscillations of this variable occur at the same time-point of the oscillations of $\dot{Q}_I^L$.

Figure 160 describes the time-evolution of the net mass flow ($\dot{m}_N$) during the self-pressurisation of Study case 3.

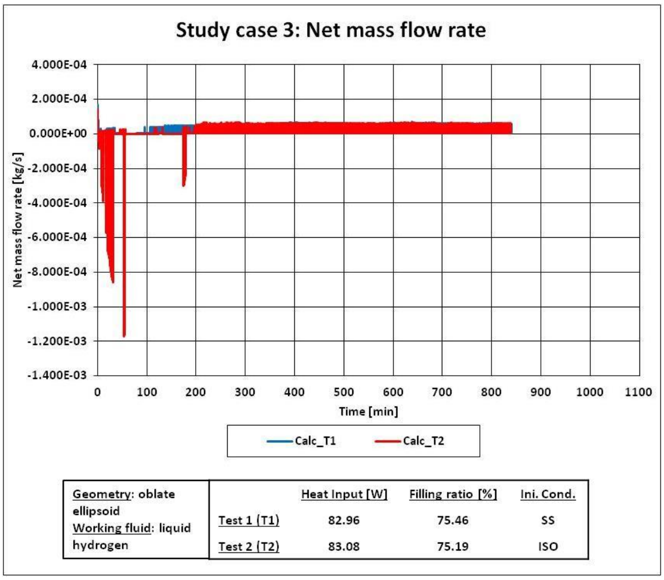

Figure 160. Net mass flow for the Study cases of Study case 3 (low heat fluxes).

In Study case 3, $\dot{m}_N$ decreases at the end of the steadys state for both tests. For Test 1 (steady state initial condition), this mass flow fluctuates during all the self-pressurisation. For Test 2 (isothermal initial condition), the time-evolution of this mass flow has negative peaks, whose minimum value is around -1.2·10^{-3} kg/s. After this peak, $\dot{m}_N$ remains almost constant. At around 180 minutes, there is a negative peak. After this peak, $\dot{m}_N$ fluctuates up to the end of the self-pressurisation. the time-evolutions of $\dot{m}_N$ of both tests are qualitatively similar to the one of $\dot{Q}_I^L$.

Figure 161 describes the time-evolution of the net mass flow ($\dot{m}_N$) during the self-pressurisation of Study case 4.

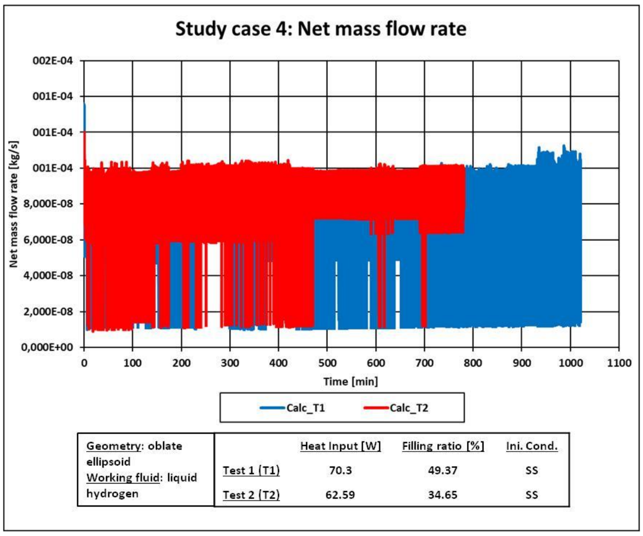

Figure 161. Net mass flow for the Study cases of Study case 4 (low heat fluxes).

In Study case 4, $\dot{m}_N$ rapidly decreases at the end of the steady state, similarly to the previous models. This increment reduces from Test 1 (medium filling ratio) to Test 2 (low filling ratio), thus it decreases with the reduction of the filling ratio. During the whole self-pressurisation, $\dot{m}_N$ fluctuations and these fluctuations are in qualitative agreement with the ones of $\dot{Q}_I^L$. The average value of these fluctuations is almost constant during the self-pressurisation and it is higher than the value of the homogeneous model 2.0 (H 2.0 model).

To sum up, the time-evolution of $\dot{m}_N$ is qualitatively similar to the one of the $\dot{Q}_I^L$. The average value of the net mass flow remains almost constant during the self-pressurisation and it increases with the reduction of the filling ratio and with the increment of the heat inputs.

8.1.7. Presentation of the results: pressure

Figure 162 shows the calculated time-evolution of the pressure against the experimental data, during the self-pressurisation of Study case 1 (low heat fluxes). The dots are the experimental data and the continuous lines are the computed values of the pressure.

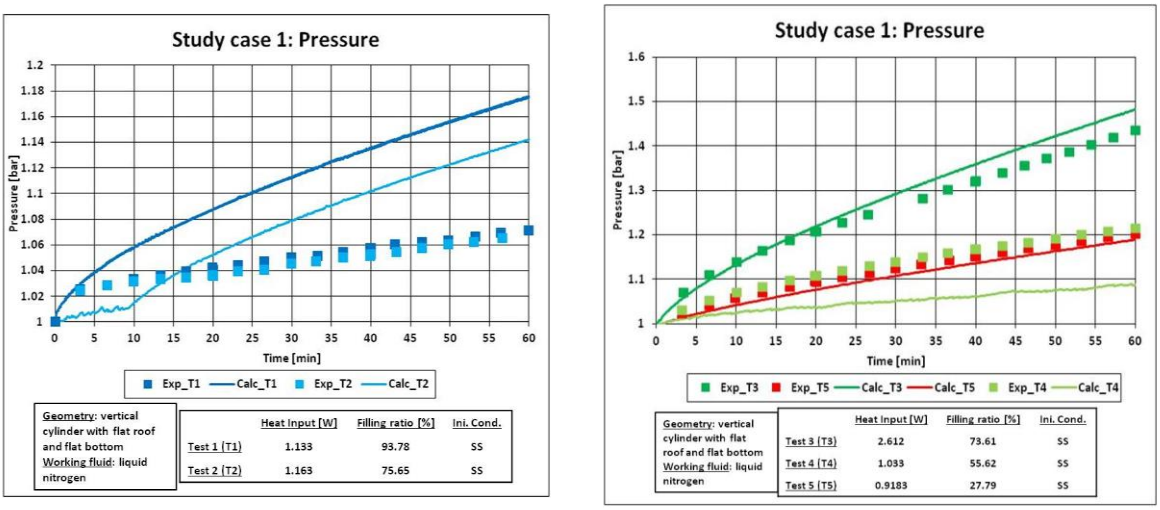

a)

b)

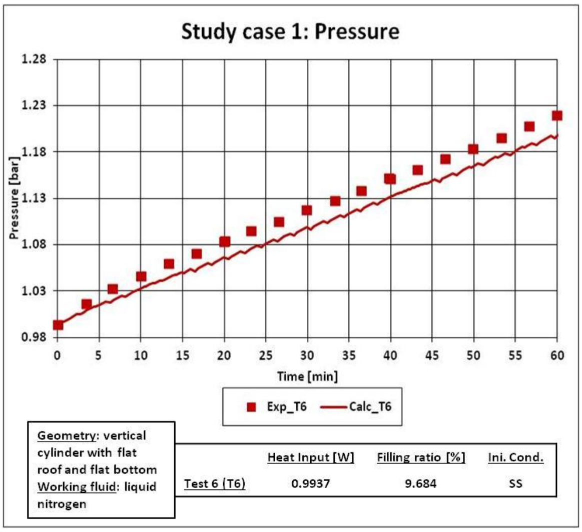

c)

Figure 162. Comparison between the computed and experimental values of the pressure for the Study case 1 (low heat fluxes): a) Test 1 and Test 2; b) Test 3, 4 and 5; c) Test 6.

In Study case 1, the computed pressure of Test 1 (high filling ratio) is close to the experimental data in the first 5 minutes of the self-pressurisation, where the initial transient is located. After this time-point, the computed rate of the self-pressurisation is higher than the measured one and the computed pressure is higher than the experimental one. In Test 2 (high-medium filling ratio), the computed pressure slowly increases in the first 10 minutes, thus during the initial transient, and the calculated values are lower than the experimental ones. After this time-point, the calculated pressure increases faster than the one of the experimental data and the computed values are higher than the measured ones. In Test 3 (high heat input) and in Test 5 (medium-low filling ratio), the calculated pressure is close to the experimental data during all the self-pressurisation. In Test 4 (medium filling ratio), the computed pressure is lower than the measured one and the calculated pressure does not monotonically increase, as shown in the experiment. In Test 6 (low filling ratio), the computed pressure is a little bit lower than the experimental one. The computed pressure does not monotonically increase because small increment and decrement of this variable can be observed.

Figure 163 shows the calculated time-evolution of the pressure respect to the experimental data, during the self-pressurisation of Study case 2 (low heat fluxes). The dots are the experimental data and the continuous line is the computed pressures.

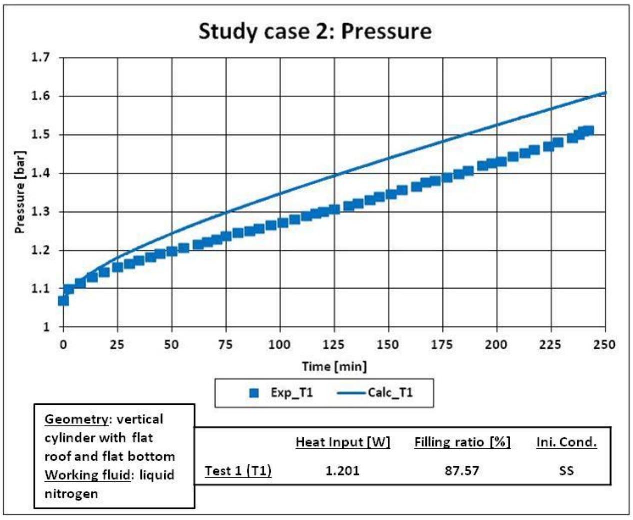

Figure 163. Comparison between the computed and experimental values of the pressure for the Study case 2 (low heat fluxes).

In Study case 2, the computed rate of the pressure increase is similar to that of the experimental ones in the first 10 minutes of the self-pressurisation, indicating that the computed initial transient is similar to the experimental one. After this time point, the computed rate of self-pressurisation increases slightly faster than the measured one and the calculated pressure is higher than the experimental one.

Figure 164 shows the calculated time-evolution of the pressure respect to the experimental data, during the self-pressurisation of Study case 3 (low heat fluxes). The dots are the experimental data and the continuous lines are the computed values of the pressure.

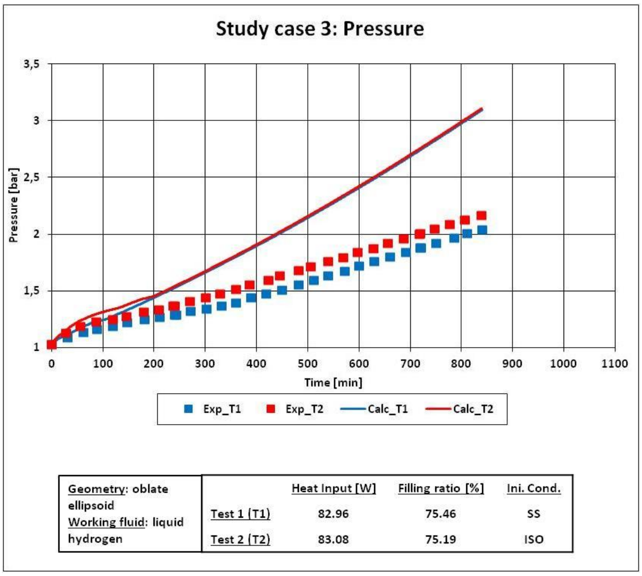

Geometry: oblate ellipsoid Working fluid: liquid hydrogen		Heat Input [W]	Filling ratio [%]	Ini. Cond.
	Test 1 (T1)	82.96	75.46	SS
	Test 2 (T2)	83.08	75.19	ISO

Figure 164. Comparison between the computed and experimental values of the pressure for the Study case 3 (low heat fluxes).

In Study case 3, the calculated pressure of both test is higher than the experimental one. Except for the first 200 minutes, the calculated curve of Test 1 (steady state initial condition) is almost superposed to the one of Test 2 (isothermal initial condition). In the first120 minutes, the calculate self-pressurisation rate of Test 1 is in line with the experimental data. in the same period, the calculated pressure of Test 2 is higher than the one of Test 1, as experimentally observed.

Figure 165 shows the calculated time-evolution of the pressure respect to the experimental data, during the self-pressurisation of Study case 4 (low heat fluxes). The dots are the experimental data and the continuous lines are the computed values of the pressure.

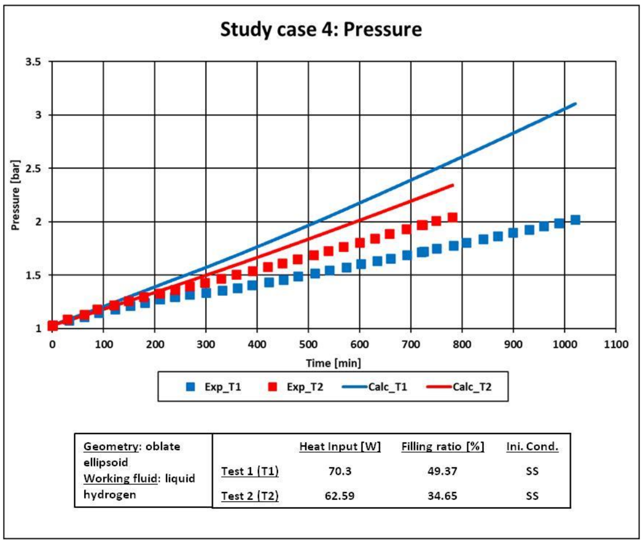

Geometry: oblate ellipsoid Working fluid: liquid hydrogen		Heat Input [W]	Filling ratio [%]	Ini. Cond.
	Test 1 (T1)	70.3	49.37	SS
	Test 2 (T2)	62.59	34.65	SS

Figure 165. Comparison between the computed and experimental

values of the pressure for the Study case 4 (low heat fluxes).

In Study case 4, the calculated pressure linearly increases in time, but the rate of this increment is higher than the experimental one. So, the computed pressure is higher than the experimental one. The computed pressure increases from Test 2 (low filling ratio) to Test 1 (medium filling). Thus, the computed pressure increases with the increment of the filling ratio, contrarily to the experiments.

To sum-up, the calculated pressure is close to the experimental one at high heat input and at low-medium and low filling ratios. The pressure is under-estimated at medium filling ratio and this variable is over-estimated at high filling ratio.

8.1.8. Presentation of the results: temperature profile in liquid

Figure 166 shows the space-distribution of the computed liquid temperature profile at different time-point against the experimental values, during the self-pressurisation at low heat fluxes, for Study case 1. The time-points considered are respectively called “t_0”, “t_{20}”, “t_{40}” and “t_{60}”, which correspond to 0, 20, 40 and 60 minutes of the self-pressurisation time, respectively. The symbols are the experimental data and the lines are the computed temperatures.

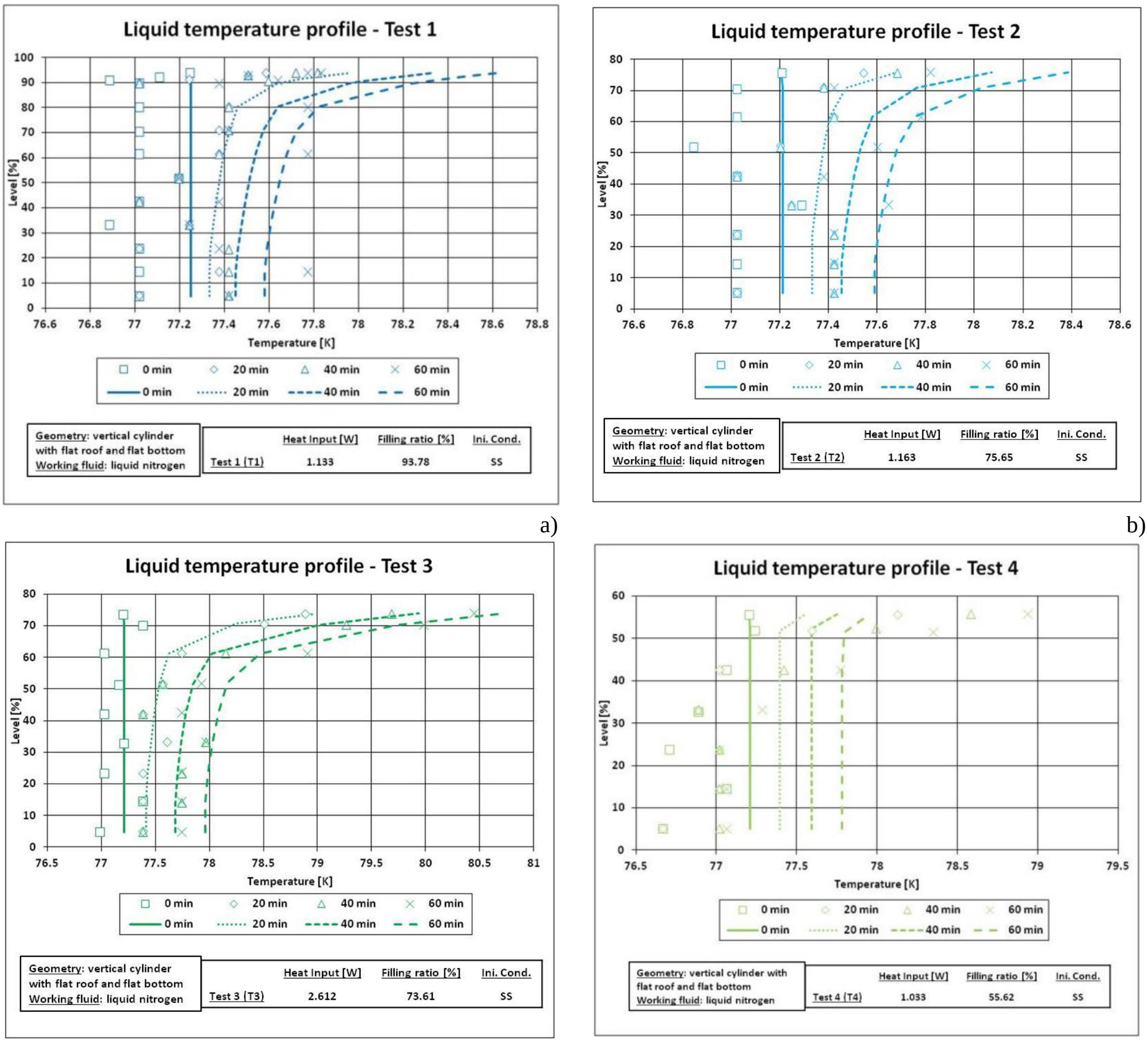

a) b)

c) d)

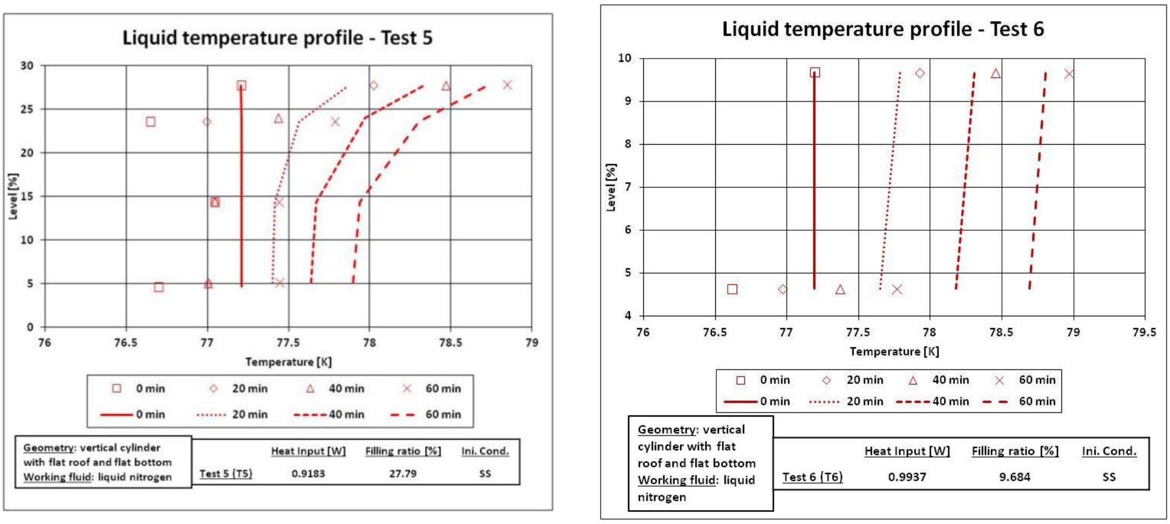

e) f)

Figure 166. Comparison between the computed and experimental liquid temperature profile of Study case 1: a) Test 1; b) Test 2; c) Test 3; d) Test 4; e) Test 5; f) Test 6.

In Test 1 (high filling ratio), the computed liquid temperature profile is flat at time-point “t_0” when the storage container is closed after the steady state. This temperature profile is shifted to the right respect the experimental one, indicating that the computed liquid temperature is higher than the experimental one. At “t_{20}”, “t_{40}”and “t_{60}”, the liquid temperature profile is flat near the bottom and the liquid temperature linearly increases with the level. The flat part of the liquid temperature profile, which describes the homogeneous region, decreases as the times passes. The slope of this line increases with the level and the profile becomes steeper near the interface than in the core. The temperature profiles of the liquid are shifted to the right as time passes because the liquid warms up. The calculated temperature profile at “t_{20}”, “t_{40}” and “t_{60}” do not agree with the experimental data, which are scattered.

In Test 2 (high-medium filling ratio), the liquid temperature profile is flat at “t_0” and this temperature profile is shifted to the right. As time passes, thus at “t_{20}”, “t_{40}”and “t_{60}”, the liquid temperature linearly increases from the bottom to the interface and the slope of this line increases with the level. The temperature of the liquid at “t_{60}” is higher than the one at “t_0” and the computed temperature profile of the liquid do not agree with the experimental data.

In Test 3 (high filling ratio), the liquid temperature profile is flat and agrees with the experimental data at “t_0”. The liquid temperature profile of “t_{20}” is flat near the bottom and the values of the temperature of “t_{20}” increases with the level, with a rate that is lower than the one of the previous tests. Near the interface, after 60 % of the level, the computed liquid temperature increases faster than the one of the previous tests. The space-distribution of the liquid temperature at “t_{60}” and at “t_{40}” is qualitatively similar to the one of “t_{20}”, but the slope of these evolutions is steeper than the one of “t_{20}”. The liquid temperature profile of “t_{20}”, “t_{40}” and “t_{60}” agrees with the experimental data.

In Test 4 (medium filling ratio), the liquid temperature profile at “t_0” is flat and it is shifted to the right, indicating that the computed values are higher than the experimental one. At “t_{20}”, “t_{40}” and “t_{60}”, the liquid temperature is flat from the bottom up to the value of the level of 50 %. After this point, it linearly increases. As indicated by the experimental data, the increment of the liquid temperature occurs around the values of the level of 30 %. So, the computed temperature profiles do not agree with the experimental data. The computed values of the temperature of “t_{60}” are higher than the one of “t_{40}”, which are higher than the one of “t_{20}”, due to the warming of the liquid.

In Test 5 (medium-low filling ratio), the liquid temperature profile at “t_0” is flat and, except for the point at the interface, the values of this profile are shifted to the right. At “t_{20}”, “t_{40}” and “t_{60}”, the temperature increases from the bottom to the interface, with a slope that increases with the level. In the core of the liquid, below 22 % of the level, the value of the liquid temperature is higher than the experimental one. Near the interface, above the 22 % of the level, the values of the temperature are lower than the experimental one. So, the temperature profiles at “t_{20}”, “t_{40}” and “t_{60}” are more in agreement with the experimental data than the ones of Test 4.

In Test 6 (low filling ratio), the temperature profiles at “t_0”, “t_{20}”, “t_{40}” and “t_{60}” are shifted to the right. The computed values of these profiles at the bottom are higher than the experimental one and the calculated values of these profiles at the interface are lower than the experimental data. So, the computed temperature profiles are less steep than the experimental ones.

Figure 167 show the space-distribution of the computed liquid temperature profile at different time-point against the experimental values, during the self-pressurisation at low heat fluxes, for Study case 2. The time-points considered are respectively called “t_0”, “t_{120}” and “t_{240}”, which correspond to 0 minutes, 120 minutes and 240 minutes of the self-pressurisation time, respectively. The markers are the experimental data and the lines are the computed values of the pressure.

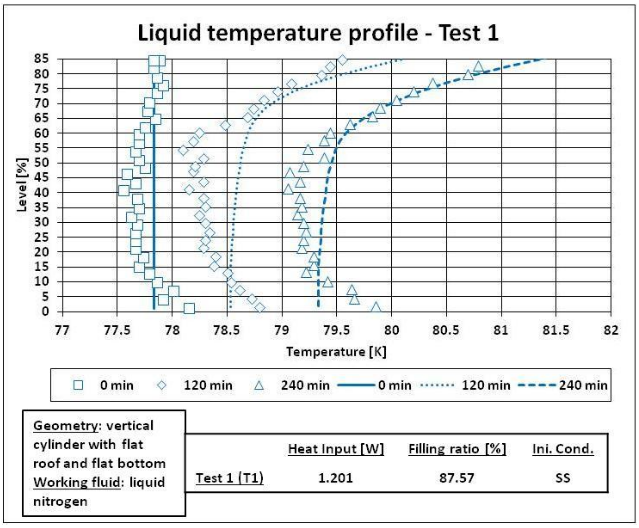

Figure 167. Comparison between the computed and experimental liquid temperature profile of Study case 2.

In Study case 2, the calculated temperature profile of “t_0” is flat and it is placed in the middle of the experimental data, whose values of temperature decrease from 0 to 15 % of level, are constant between 15 % and 60 %, and increase after 60 %. At “t_{120}”, the computed value of the temperature slightly increases from the bottom up to 65 % and the slope of this increment grows up after 65 %. This slope agrees with the measured one (the change of the slope occurs at 60 % of the level in the experiment). In the core and bottom part of the liquid, the computed temperature profile does not agree with the experimental data. At “t_{240}”, the computed temperature profile is almost flat between 0 and 55 %. After this point, the liquid temperature increases as fast as done by the experimental data. So, only the bottom and the core parts of the computed liquid temperature profile are not in agreement with the experimental ones.

Figure 168 show the space-distribution of the computed liquid temperature profile at different time-point against the experimental values, during the self-pressurisation at low heat fluxes, for Study case 3. The time-points considered are respectively called “t_0”, “t_{240}” and “t_{720}”, which correspond to 0 minutes, 240 minutes and 720 minutes of the self-pressurisation time, respectively. The markers are the experimental data and the lines are the computed values of the pressure.

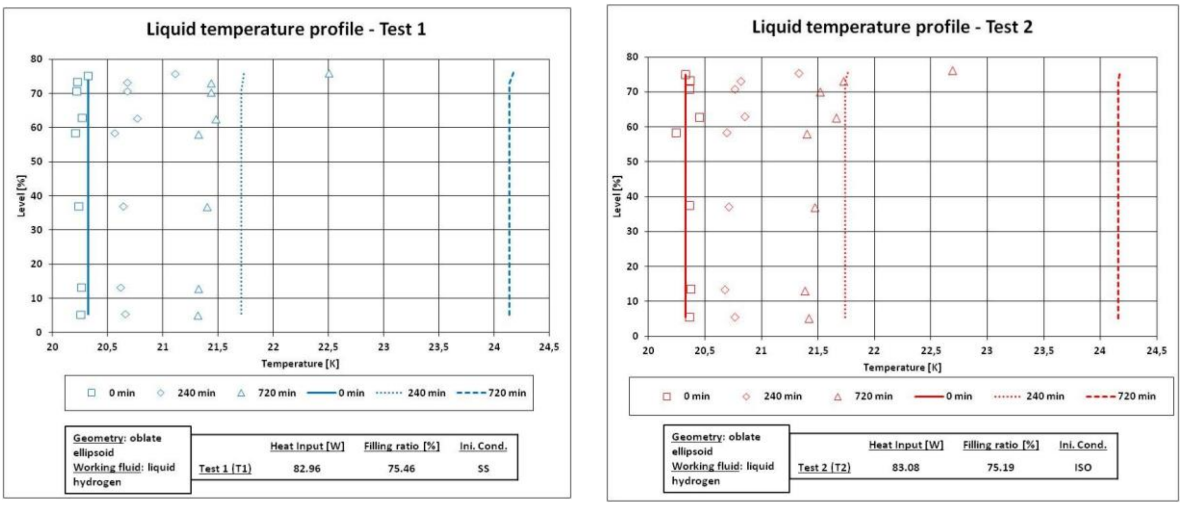

a) b)

Figure 168. Comparison between the computed and experimental liquid temperature profile of Study case 3 (low heat fluxes): a) Test 1; b) Test 2.

In Study case 3, the computed initial temperature of both test is flat and is close to the experimental values. In Test 1 (steady state initial condition) and in Test 2 (isothermal initial condition), the calculated temperature profiles at "t_{240}" and "t_{720}" are almost flat, except near the interface. the values of the calculated temperatures of both tests are higher than the experimental one. The slope of the temperature profile near the interface is lower than the experimental one, suggesting that the model computes a stratified region that is lower than the observed one.

Figure 169 show the space-distribution of the computed liquid temperature profile at different time-point against the experimental values, during the self-pressurisation at low heat fluxes, for Study case 4. The time-points considered are respectively called "t_0", "t_{240}" and "t_{720}", which correspond to 0 minutes, 240 minutes and 720 minutes of the self-pressurisation time, respectively. The markers are the experimental data and the lines are the computed values of the pressure.

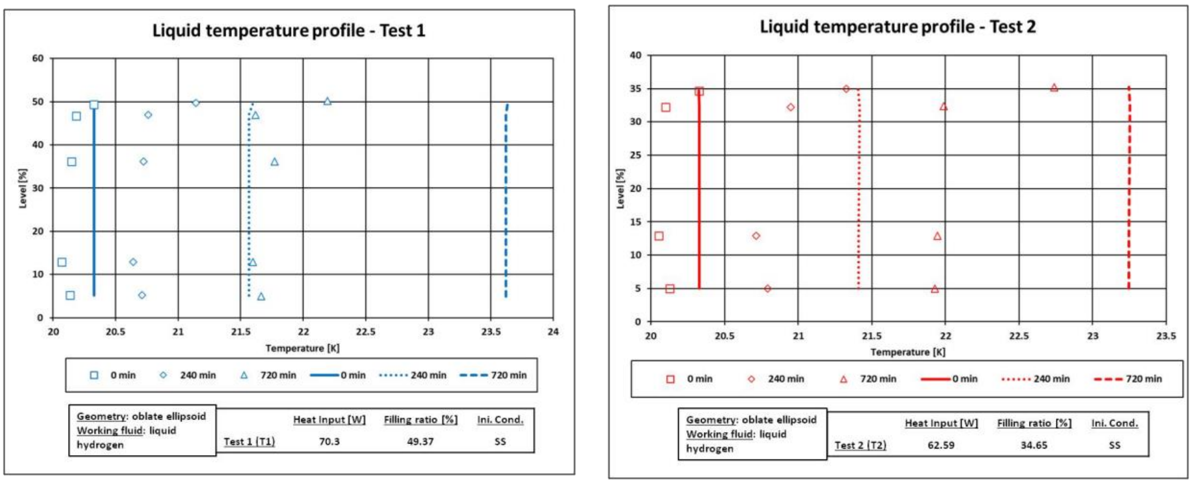

a) b)

Figure 169. Comparison between the computed and experimental liquid temperature profile of Study case 4 (low heat fluxes): a) Test 1; b) Test 2.

As it is described in Figure 169, the values of the liquid temperature profile are close to the experimental values and the computed profiles are flat. At the time-points "t_{240}" and "t_{720}", the computed temperature profiles are flat, except near the interface. In test 1 (medium filling ratio), the computed liquid temperature slightly increases near the interface. In test 2 (low filling ratio), the computed liquid temperature slightly decreases near the interface. Both space-distributions are not in agreement with the experimental data.

To sum up, the computed temperature profiles are flat at the beginning of the self-pressurisation, thus at the end of the steady state. After the initial time-point, the computed liquid temperature increases from the bottom to the interface, with a rate that grows up with the level. The computed temperature profiles are qualitatively similar to the experimental ones, except for the core and bottom part of the profiles of Study case 2. Only for Test 3 and 5 of Study case 1 and for Study case 2, the calculated values of the profiles are close to the experimental data. For Study case 3 and 4, the computed temperature profiles of the liquid are not in agreement with the experimental data.

8.2. Study cases: medium heat fluxes

The study cases at medium heat fluxes (see Section 4 of Chapter 2) are reported in Table 141.

Table 141. Study cases at medium heat fluxes.

Authors	Kang et al. [25]	Aydelott and Spuckler [30]
Study case	5	6
Geometry	Vertical cylinder with flat ends	Sphere
Working fluid	Liquid nitrogen	Liquid hydrogen

Section 8.2.1 presents the fluid-dynamics at wet side wall. Section 8.2.2 describes the fluid-dynamics in the liquid. Section 8.2.3 explains the heat transfer at the wet side wall. Section 8.2.4 presents the heat transfer across the sub-layer of the liquid. Section 8.2.5 describes the interfacial heat transfer. Section 8.2.6 explains the net mass flow. Section 8.2.7 presents the comparison between the calculated value of the pressure and the measured one. Section 8.2.8 explains the comparison between the computed values of the liquid temperature profiles and the experimental one.

8.2.1. Presentation of the results: fluid-dynamics at the wet side wall

Figure 170 shows the values of the boundary layer mass flow of the wet side wall ($\dot{m}^{SW}$) and the values of the bulk temperature gradient in each sub-layer ($\frac{\partial T^L}{\partial x}$), at different time-points, for Study case 5. These time-points are equal to the time-points at which the temperature is measured.

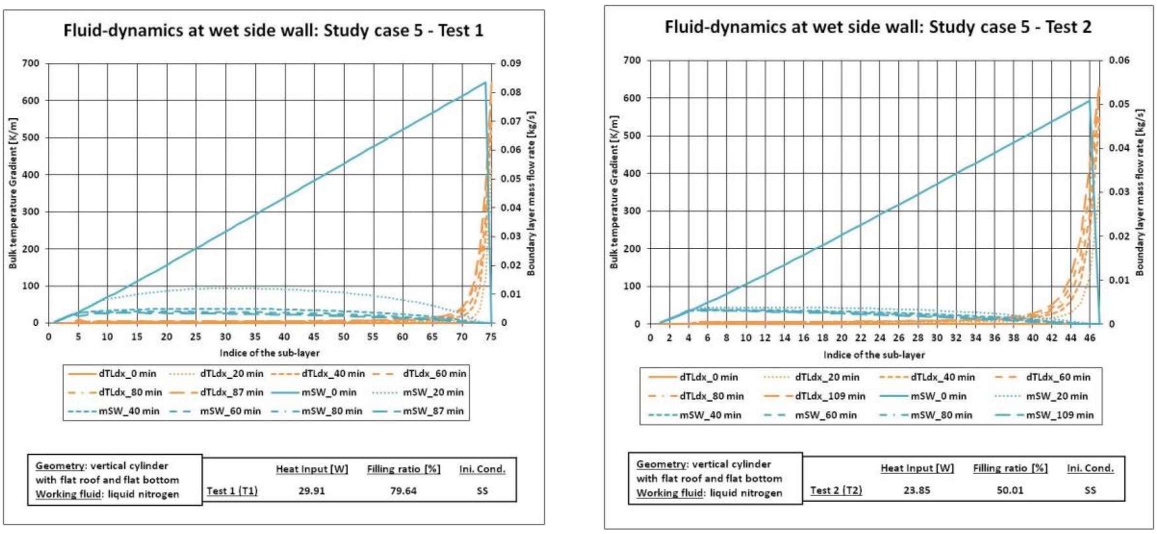

a) b)

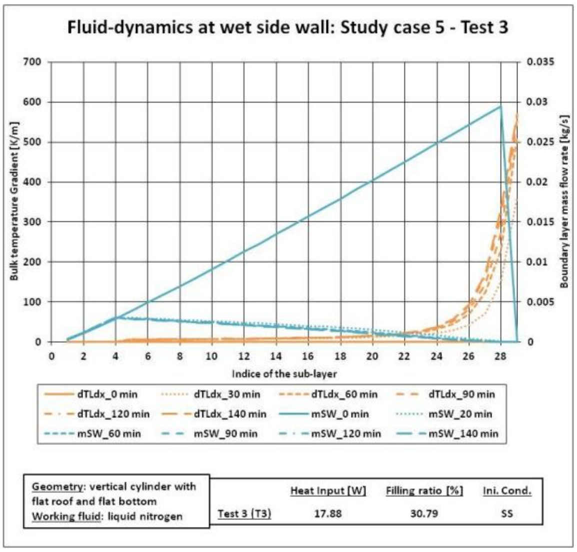

c)

Figure 170. Fluid-dynamics at the wet side wall of Study case 5 (medium heat fluxes): a) Test 1; b) Test 2; c) Test 3.

In Test 1 (high filling ratio), $\frac{\partial T^L}{\partial x}$ is equal to zero in all the sub-layers at the end of the steady state. As time passes, the values of $\frac{\partial T^L}{\partial x}$ are equal to zero in the first 5 sub-layers. Then, these values slightly increase between the 5th and 65th sub-layers. After the 65th sub-layer, the liquid bulk temperature gradient rapidly increases, reaching the maximum value of around 650 K/m at the interface sub-layer. $\frac{\partial T^L}{\partial x}$ increases as time passes. At the beginning of the self-pressurisation, $\dot{m}^{SW}$ linearly increases from the bottom to the second-last sub-layer and goes to zero in the interface sub-layer because the interface is a rigid surface. As time passes, the boundary layer mass flow in the wet side wall linearly increases in the first 5 sub-layers, where the liquid bulk temperature gradient is equal to zero. The slope of this increment reduces from the 6th sub-layer, creating a “dump”, and the $\dot{m}^{SW}$ in the boundary layer of the wet side wall decreases after the 35th sub-layer. $\dot{m}^{SW}$ becomes zero after the 70th sub-layer.

In Test 2 (medium filling ratio), $\frac{\partial T^L}{\partial x}$ is equal to zero in all the sub-layers at the beginning of the self-pressurisation. $\frac{\partial T^L}{\partial x}$ is equal to zero in the first 5 sub-layer and slightly higher than 0 between 6th sub-layer and 38th sub-layer. Then, $\frac{\partial T^L}{\partial x}$ rapidly increases, reaching the maximum value of around 650 K/m. $\dot{m}^{SW}$ linearly increases from the bottom to the second-last sub-layer, at the end of the steady state, and it goes to zero in the interface sub-layer because the interface is a rigid surface. As time passes, $\dot{m}^{SW}$ linearly increases only in the first 5 sub-layers, where $\frac{\partial T^L}{\partial x}$ is equal to zero. From the 6th sub-layer, $\dot{m}^{SW}$ monotonically decreases, without forming the “dump” , similarly toTest 1. $\dot{m}^{SW}$ is equal to zero after the 45th sub-layer.

In Test 3 (low filling ratio), $\frac{\partial T^L}{\partial x}$ is equal to zero everywhere at the beginning of the self-pressurisation. As time passes, $\frac{\partial T^L}{\partial x}$ remains zero in the first 5 sub-layers and slightly increases from the 6th sub-layer to the 24th sub-layer. After this sub-layer, $\frac{\partial T^L}{\partial x}$ rapidly increases and it reaches the value of 550 K/m, which is lower than the one of the previous tests. $\dot{m}^{SW}$ linearly increases at the end of the steady state and in the first 5 sub-layers during the self-pressurisation. After these sub-layers, $\dot{m}^{SW}$ linearly decreases and becomes equal to zero at the 28th sub-layer.

Figure 171 shows the values $\dot{m}^{SW}$ and $\frac{\partial T^L}{\partial x}$, at different time-points, for Study case 6. These time-points are equal to the time-points at which the temperature is measured.

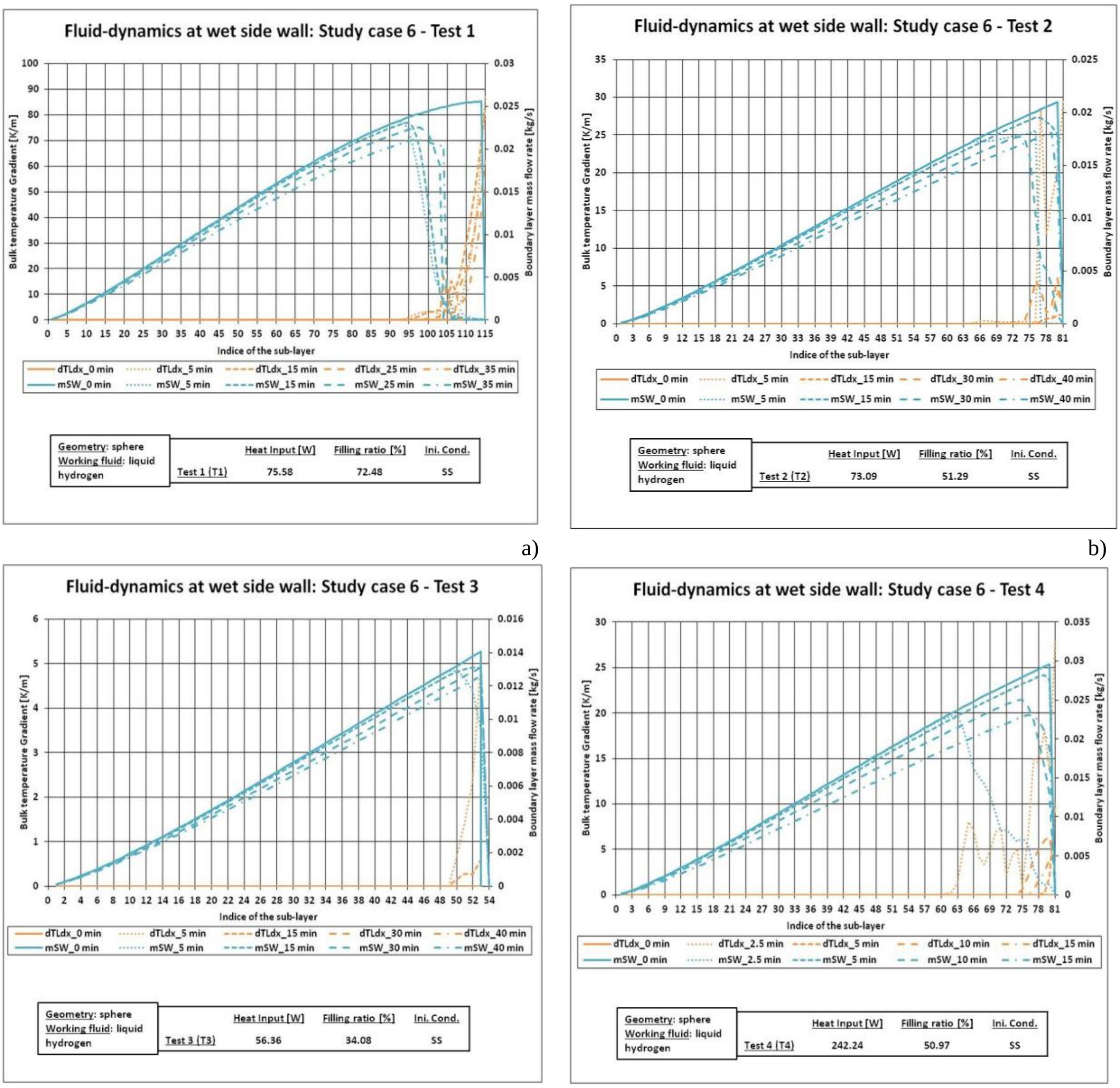

a) b)

c) d)

Figure 171. Fluid-dynamics at the wet side wall of Study case 6 (medium heat fluxes): a) Test 1; b) Test 2; c) Test 3; d) Test 4.

In Test 1 (high filling ratio), $\frac{\partial T^L}{\partial x}$ increases from the 95th sub-layer during the self-pressurisation, instead of being equal to zero as done in the steady state. below the 95th sub-layer, the liquid is homogeneous because $\frac{\partial T^L}{\partial x}$ is equal to zero. The increment of $\frac{\partial T^L}{\partial x}$ is not monotonic between the 95th and the 108th sub-layer because picks are present in the 105th sub-layer. After these picks, the increment is monotonic. $\frac{\partial T^L}{\partial x}$ at 5 minutes is higher than the ones at 15, 25 and 35 minutes, indicating a reduction of this variable during the self-pressurisation. at the end of the seteady state, $\dot{m}^{SW}$ increases in the sub-layers with a rate that changes in the bottom and near the interface. At the bottom, this rate slightly increases with the sub-layer and, at the interface, this rate slightly decreases. As time passes, $\dot{m}^{SW}$ quickly decreases from 95th sub-layer and this decrement is monotonic. This decrement is faster at 5 minutes than the ones at 15, 25 and 35 minutes. After the 105th sub-layer, $\dot{m}^{SW}$ is equal to zero during the self-pressurisation.

In Test 2 (medium filling ratio), the space-distibutions of $\frac{\partial T^L}{\partial x}$ and of $\dot{m}^{SW}$ are quite similar to the ones at high filling ratio. At the end of the steady state, the slow decrement of the rate of the increment of $\dot{m}^{SW}$near the interface is not present. During the self-pressurisation, $\frac{\partial T^L}{\partial x}$ has picks at 77th sub-layer at 5 minutes and at 76th sub-layer at 15 minutes. after these picks, this variable monotonically increases. At 30 and 40 minutes, the increment of $\frac{\partial T^L}{\partial x}$ is much lower than the ones at 5 minutes, indicating a reduction of this variable during the self-pressurisation. During the self-pressuirsation, $\dot{m}^{SW}$ quickly reduces near the interface and this rate of decrement increases with the magnitibude of $\frac{\partial T^L}{\partial x}$. At 5 minutes, $\dot{m}^{SW}$ is equal to zero after the 78th sub-layer. At the other time-point, this variable is equal to zero only at the interface.

In Test 3 (low filling ratio), the initial space-distributions of $\frac{\partial T^L}{\partial x}$ and of $\dot{m}^{SW}$ are similar to the ones of Test 2. At 5 minutes, $\frac{\partial T^L}{\partial x}$ increases from the 49th sub-layer. At 15 minutes, this increment has a pick at 51th sub-layer. Then, $\frac{\partial T^L}{\partial x}$ is equal to zero as time passes, indicating a reduction of the bulk temperature gradient during the mid and long part of the self-pressurisation. $\dot{m}^{SW}$ reduces near the interface, as $\frac{\partial T^L}{\partial x}$ increases. This reduction is, however, lower than the ones of Tests 1 and 2. $\dot{m}^{SW}$ reduces during the self-pressurisation.

In Test 4 (high heat input), the initial space-distributions of $\frac{\partial T^L}{\partial x}$ and of $\dot{m}^{SW}$ are similar to the ones of Test 2 and Test 3. At 2.5 minutes, $\frac{\partial T^L}{\partial x}$ increases from 60th sub-layer up to the inteface, producing picks. As time passes, the increment of $\frac{\partial T^L}{\partial x}$ reduces near the interface and the maiximum value of this variable is 10 K/m, instead of 30 K/m as done at 2.5 minutes. The increment of $\frac{\partial T^L}{\partial x}$ becomes more regular than the one at 2.5 minutes. $\dot{m}^{SW}$ decreases near the interface, as $\frac{\partial T^L}{\partial x}$ increases. The rate ofthis increment is higher at 2.5 minutes than in the other time-points. The values of $\dot{m}^{SW}$are only equal to zero at the interface.

To sum up, $\frac{\partial T^L}{\partial x}$ is equal to zero at the end of the steady state and in the bottom and core of the storage container. In the core of the liquid, $\frac{\partial T^L}{\partial x}$ slightly increase. Near the interface, $\frac{\partial T^L}{\partial x}$ rapidly increases and the maximum value reached decreases with the reduction of the filling ratio. For Study case 6, $\frac{\partial T^L}{\partial x}$ can reduce during the self-pressurisation, in particular at low filling ratio. $\dot{m}^{SW}$ always increases with the vertical height of the liquid and, in vertical cylinder, this increment is linear. In the core of the liquid, $\dot{m}^{SW}$ linearly decreases, (i) except at high filling ratio where a dump can be present and (ii) in spherical storage container. $\dot{m}^{SW}$ can be equal to zero near the interface, in particular at high filling ratio. The region where this occurs reduces as the filling ratio decreases. The space-distributions and time-evolutions of variables are qualitatively similar to the one of the Study cases at low heat fluxes (see Section 8.1.1 of Chapter 6).

8.2.2. Presentation of the results: fluid-dynamics in the liquid

Figure 172 shows the values of descending flow ($\dot{m}^D$) and rising flow of the bottom ($\dot{m}^B$) , at different time-points, for Study case 5. These time-points are equal to the time-points at which the temperature is measured.

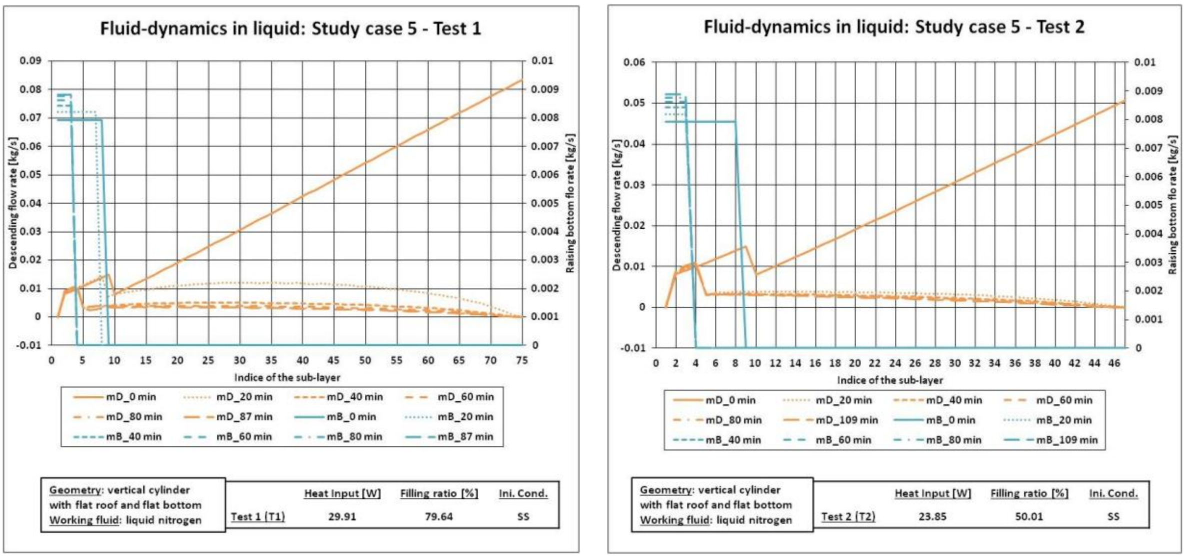

a) b)

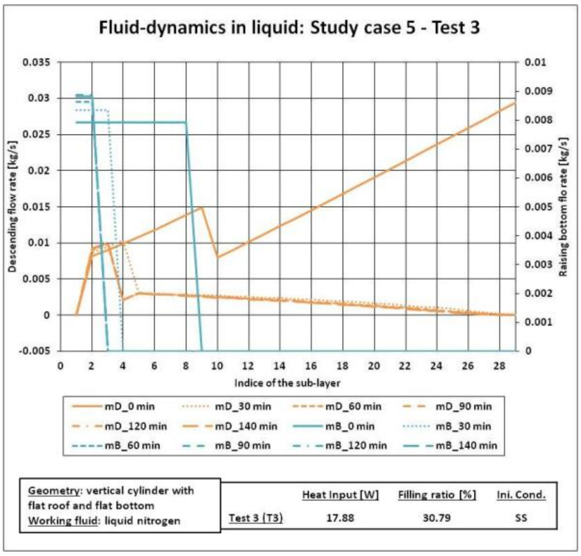

c)

Figure 172. Fluid-dynamics in the liquid of Study case 5 (medium heat fluxes): a) Test 1; b) Test 2; c) Test 3.

In Test 1 (high filling ratio), $\dot{m}^D$ linearly increases from the 2nd sub-layer to the 9th sub-layer and from the 10th sub-layer to the interface sub-layer, at the beginning of the self-pressurisation. mD drops between the 9th and 10th sub-layer. As time passes, $\dot{m}^D$ increases from the 2nd sub-layer to the 4th sub-layer, where it drops down after this drops, the space-distribution of $\dot{m}^D$ is qualitatively similar to the one of the $\dot{m}^{SW}$ (see Section 8.2.1). $\dot{m}^B$ is constant between the bottom and the 8th sub-layer at the beginning of the self-pressurisation. After this sub-layer, $\dot{m}^B$ goes to zero. After 20 minutes, $\dot{m}^B$ is constant between the first sub-layer and the 7th sub-layer. After this time-point, $\dot{m}^B$ is constant between bottom and the 3rd sub-layer. After this constant period, $\dot{m}^B$ is equal to zero.

In Test 2 (medium filling ratio), $\dot{m}^D$ increases from the 2nd sub-layer to the 9th sub-layer at the beginning of the self-pressurisation and it drops down. After this drop, $\dot{m}^D$ linearly increases, similarly toTest 1. During the self-pressurisation, $\dot{m}^D$ linearly increases between the 2nd and the 4th sub-layer, and it drops down after this sub-layer. After the drops, $\dot{m}^D$ decreases as done by $\dot{m}^{SW}$. $\dot{m}^B$ at the end of the steady state is similar to the one of Test 1 because the value of this mass flow goes to zero, after the constant value region between the bottom and the 8th sub-layer. For all the other time-points of the self-pressurisation, $\dot{m}^B$ is constant between the bottom and the 3rd sub-layer and the values of this variable is equal to zero for the remaining sub-layers.

In Test 3 (low filling ratio), the space-distribution of $\dot{m}^D$ at the end of the steady state is similar to the one of Test 1 and 2 because this evolution is composed by an increment between the 2nd and the 9th sub-layer, a drops and an increment between the 10th sub-layer up to the interface sub-layer. After 30 minutes, $\dot{m}^D$ increases up to the 4th sub-layer, where it drops down. From the 5th sub-layer, $\dot{m}^D$ constantly and similarly decreases as done by $\dot{m}^{SW}$. After 60 minutes, $\dot{m}^D$ increases between 2nd and 3rd sub-layer, where it drops. At 4th sub-layer, $\dot{m}^D$ slightly increases and constantly decreases at 5th sub-layer. $\dot{m}^B$ is constant between the first and the 8th sub-layer at the end steady state, similarly to Test 1 and 2. After 30 minutes, this constant part lasts up to the 5th sub-layer and, for the remaining time-points, this constant part is limited to the 2nd sub-layer.

Figure 173 shows the values of $\dot{m}^D$ and rising flow of $\dot{m}^B$, at different time-points, for Study case 6. These time-points are equal to the time-points at which the temperature is measured.

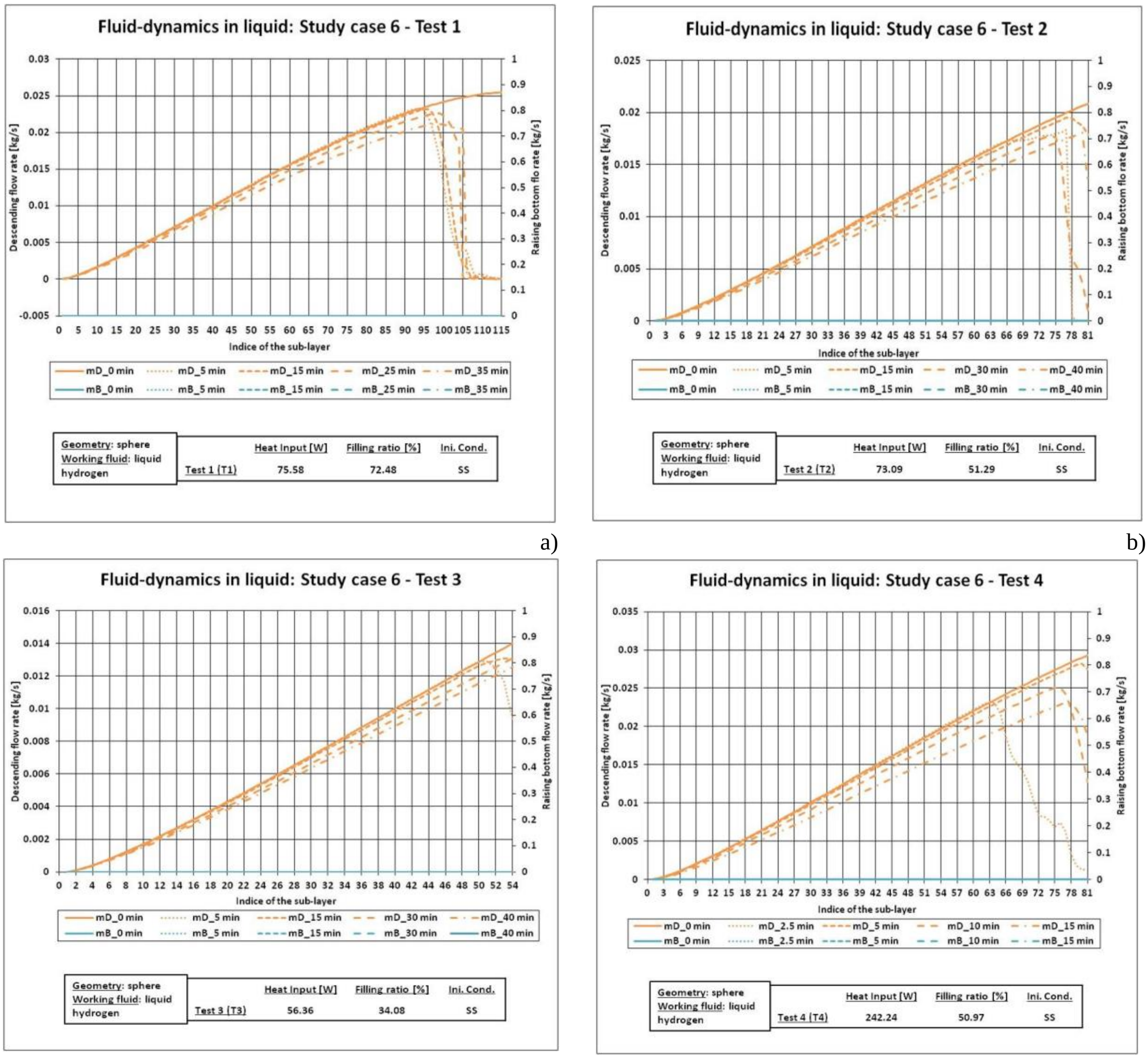

a) b)

c) d)

Figure 173. Fluid-dynamics in the liquid of Study case 6 (medium heat fluxes): a) Test 1; b) Test 2; c) Test 3; d) Test 4.

For Study case 6, $\dot{m}^B$ is equal to zero because the bottom is neglected in spherical storage container. the space-evolution of $\dot{m}^D$ is similar to the one of $\dot{m}^{SW}$ (see Figure 170) because $\dot{m}^B$ is equal to zero.

To sum up, $\dot{m}^D$ constantly increases at the end of the steady state, except for the discontinuity caused by the drop. This discontinuity occurs after the drop of $\dot{m}^B$, which is constant near the bottom. The space-distribution of $\dot{m}^D$ is similar to the one of the mass flow in the boundary layer of the wet side wall. The region where the rising mass flow of the bottom is constant decreases during the self-pressurisation. The space evolutions of $\dot{m}^D$ and $\dot{m}^B$ at medium heat fluxes are qualitatively similar to the ones at low heat fluxes (see Section 8.1.2 of Chapter 6).

8.2.3. Presentation of the results: heat transfer at the wet side wall

Figure 174 shows the values of the wet side wall heat transfer coefficient (h_w^{SL}) and the values of the wet wall temperatures (T_w^{SL}), at different time-points, for Study case 5. These time-points are equal to the time-points at which the temperature is measured.

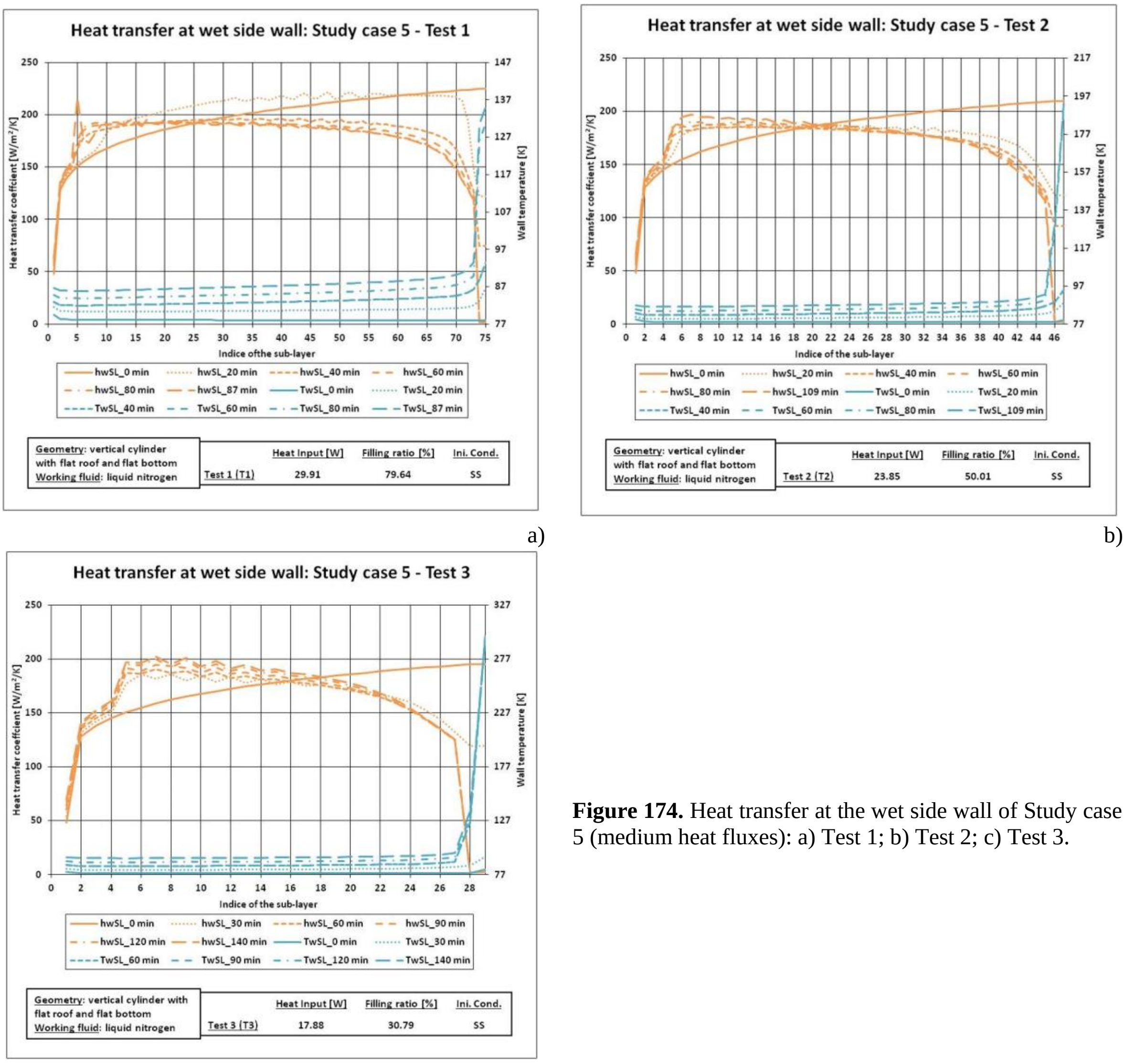

a)

b)

c)

Figure 174. Heat transfer at the wet side wall of Study case 5 (medium heat fluxes): a) Test 1; b) Test 2; c) Test 3.

In Test 1 (high filling ratio), h_w^{SL} increases from the bottom to the interface at the end of the steady state, and the rate of this increment decreases from the bottom to the interface sub-layer. After 20 minutes, the time-evolution of h_w^{SL} is similar to the one of the end of steady state, except for some oscillations between the 35th and 55th sub-layer and for the drop near the interface. As time passes, the space-distribution of h_w^{SL} of the wet side wall in the bottom and core of the liquid is qualitatively the same of the remaining time-points, except for the peak at 5th sub-layer. The drop of h_w^{SL} near the interface occurs in sub-layers that are placed below the one in which the drop occured at 20 minutes. Except for the small initial decrement, the profile of the space-distribution of the wet side wall temperature is flat at the beginning of the self-pressurisation. As the time passes, the space-distribution of T_w^{SL} is qualitatively similar to the initial one in the bottom and core part of the liquid. T_w^{SL} increases near the interface and the value of around 136 K are reached at the end of the self-pressurisation. For the same sub-layer, T_w^{SL} increases in time.

In Test 2 (medium filling ratio), at the end of the steady state, the space-distribution of h_w^{SL} is qualitatively similar to the one of the Test 1 because this variable rapidly increases in the bottom, and this increment becomes smooth in the core of the liquid. During the self-pressurisation, h_w^{SL} rapidly increases in the bottom of the liquid, but the rate of this increment reduces after the 2nd sub layer and it increases again after the 5th sub-layer. After the 6th sub-layer, h_w^{SL} decreases, and the rate of this decrement increases near the interface. The space-distribution of T_w^{SL} is similar to the one of Test 1, because the profile of this evolution is flat in the bottom and in the core of the liquid and it rapidly increases near the interface. This final increment grows up with the time and the maximum value of around 196 K is reached.

In Test 3 (low filling ratio), the space-distribution of h_w^{SL} is qualitatively similar to the one of Test 1 and 2, at the end of the steady state. During the self-pressurisation, the space-distribution of h_w^{SL} is qualitatively similar to the one of the Test 2, except between the 6th and the 14th sub-layer. In this part of the liquid, h_w^{SL} oscillates. Near the interface, h_w^{SL} rapidly decreases up to values that are close to zero. The space-distribution of T_w^{SL} is qualitatively similar to the one of Test 1 and Test 2, at the end of the steady state and during the self-pressurisation. Near the interface, T_w^{SL} increases more than the one of the previous testes and the maximum value of around 295 K is reached.

Figure 175 shows the values of h_w^{SL} and the values of T_w^{SL}, at different time-points, for Study case 6. These time-points are equal to the time-points at which the temperature is measured.

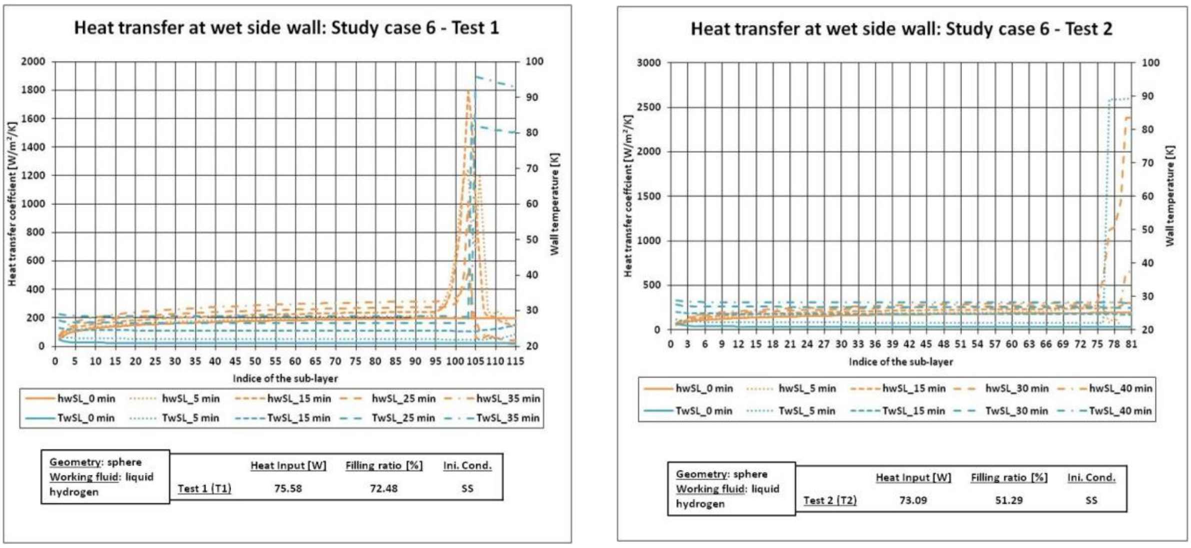

a) b)

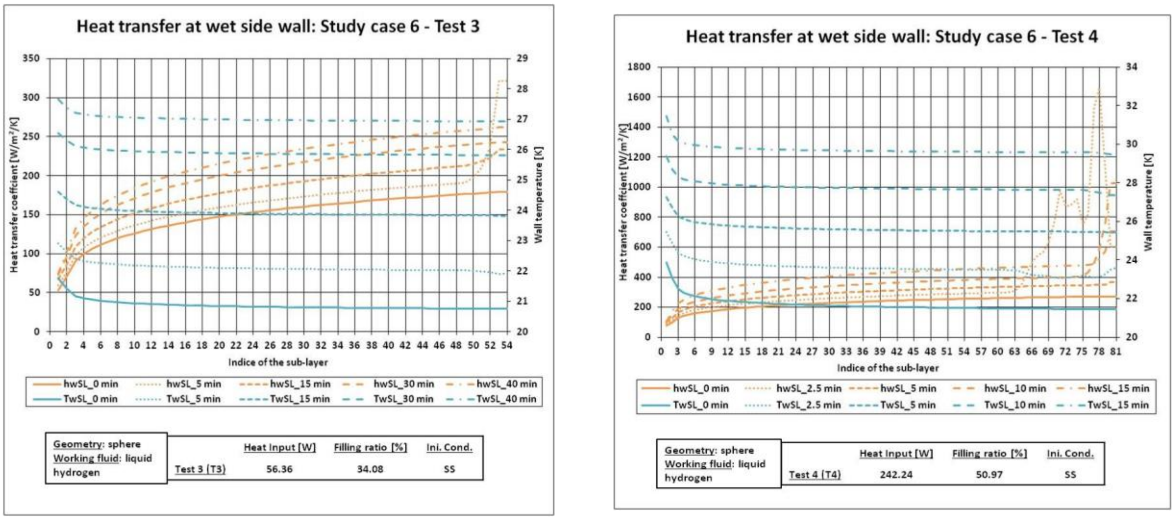

c) d)

Figure 175. Heat transfer at the wet side wall of Study case 6 (medium heat fluxes): a) Test 1; b) Test 2; c) Test 3; d) Test 4.

In Test 1 (high filling ratio), h_w^{SL} monotonically increases along the weside wall at the end of the steady state. The rate of this increment reduces as moving away from the bottom sub-layer. During the self-pressurisation, h_w^{SL} has picks after the 95th sub-layer. these picks occurs just before the values of $\dot{m}^{SW}$becomes zero (see Figure 171). As time passes, h_w^{SL} increases in the core of the wet side wall and the magnitude of the picks reduces. T_w^{SL} is constant at the end of the steady state, except near the bottom. During the self-pressurisation, T_w^{SL} quickly increases at 25 and 35 minutes, reaching the values of 80 K and 92 K, respectively. At these time-points, $\dot{m}^{SW}$ is equal to zero in the sub-layer near the interface. At 5 and 15 minutes, the increment of T_w^{SL} near the interface is much lower than the ones at 25 and 35 minutes.

In Test 2 (medium filling ratio), the space-distributions of h_w^{SL} and of T_w^{SL} at the end of the steady state are similar to the ones of Test 1. At 5 minutes, h_w^{SL} decreases after the 75th sub-layer, becoming almost zero. At 30 and 40 minutes, h_w^{SL} quickly increases near the interface as $\dot{m}^{SW}$ decreases (see Figure 171), passing from 302 W/m²/K to 653 W/m²/K, and from 273 W/m²/K to 2382 W/m²/K, respectively. The rate of this increment is higher than the one of the other time-points. At 5 minutes, T_w^{SL}increases near the interface when h_w^{SL} decreases. During this increment, the value of T_w^{SL} passes from 22 K to 89 K. During the self-pressurisation, T_w^{SL} increases passing from 20.8 K to 28.15 K in the core.

In Test 3 (low filling ratio), the space-distributions of h_w^{SL} and of T_w^{SL} at the end of the steady state are similar to the ones of Test 1 and 2. During the self-pressurisaiton, h_w^{SL}increases, passing from 178 W/m²/K at 0 minutes to 261 W/m²/K at 40 minutes in the interface sub-layer (54th sub-layer). At 5 minutes and at 15 minutes, h_w^{SL} increases faster near the interface than in the core, opposite to the space-distribution of $\dot{m}^{SW}$near the interface (see Figure 171). T_w^{SL} slowly decreases with the length of the wet side wall, during the self-pressurisation. This decrement is faster at the bottom than in the core and the value of T_w^{SL} reduces from 21.7 K to 20.7 K at the end of the self-pressurisation. The space-distribution of the remaning time-points is similar to the initial one, but it is shifted upward.

In Test 4 (high heat input), the space-distributions of h_w^{SL} and of T_w^{SL} at the end of the steady state are similar to the ones of Test 1, 2 and 3. At 2.5 minutes, h_w^{SL}increases faster from 63th sub-layer in the core, producing several picks. The maximum value of these picks is around 1662 W/m²/K and it is reached when $\dot{m}^{SW}$ strongly decreases (see Figure 171). At 10 minutes, h_w^{SL}strongly increases near the interface, but the maximum value is lower than the one of 2.5 minutes. At 15 minutes, h_w^{SL}increases faster in the interface than in the core, but this increment is lower than the one at 10 minutes. the space-evolution of T_w^{SL} during the self-pressurisation is smilar to the initial one, except at 5 minutes. at this time-point, T_w^{SL} decreases after the 63th sub-layer. then, this variable reamin constant and it increases from 78th sub-layer, when h_w^{SL} decreases. During the self-pressurisation, T_w^{SL} increases, passing from 21.45 K at 0 minutes to 29.48 K at 15 minutes in the interface sub-layer (81th sub-layer).

To sum up, h_w^{SL} monotonically increases at the end of the steady state. During the self-pressurisation, this increment occurs only in the lower part of the liquid and it does not occur monotonically. Near the interface, h_w^{SL} rapidly decreases approaching zero, but this decrement can produce som picks. T_w^{SL} is constant in the core of the liquid at the steady state, and during the self-pressurisation a small decrement of this temperature is observed at the bottom. Near the interface, T_w^{SL} increases with time. The maximum value increases with the reduction of the filling ratio. The space-distributions of h_w^{SL} are qualitatively independent from the filling ratio. The space-distributions and time-evolutions of variables are qualitatively similar to the one of the Study cases at low heat fluxes (see Section 8.1.3 of Chapter 6).

8.2.4. Presentation of the results: intra-layer heat transfer

Figure 176 shows the spatial-evolution of the upper ($\dot{Q}^{SUP}$) and lower ($\dot{Q}^{INF}$) heat flows across the sub-layers, at different time-points, for Study case 5. The upper heat flow is the heat flow between the sub-layer “nL+1” and the sub-layer “nL” and is equal to the liquid-to-interface heat flow ($\dot{Q}_I^L$) with the opposite sign ($-\dot{Q}_I^L$) at the interface sub-layerThe lower heat flow is the heat flow between the sub-layer “nL” and the sub-layer “nL-1” and is equal to the bottom-to-liquid heat flow with the opposite sign at the bottom ($-\dot{Q}_W^B$), as explained in Intra-Layer Heat Transfer (ILHT) model.

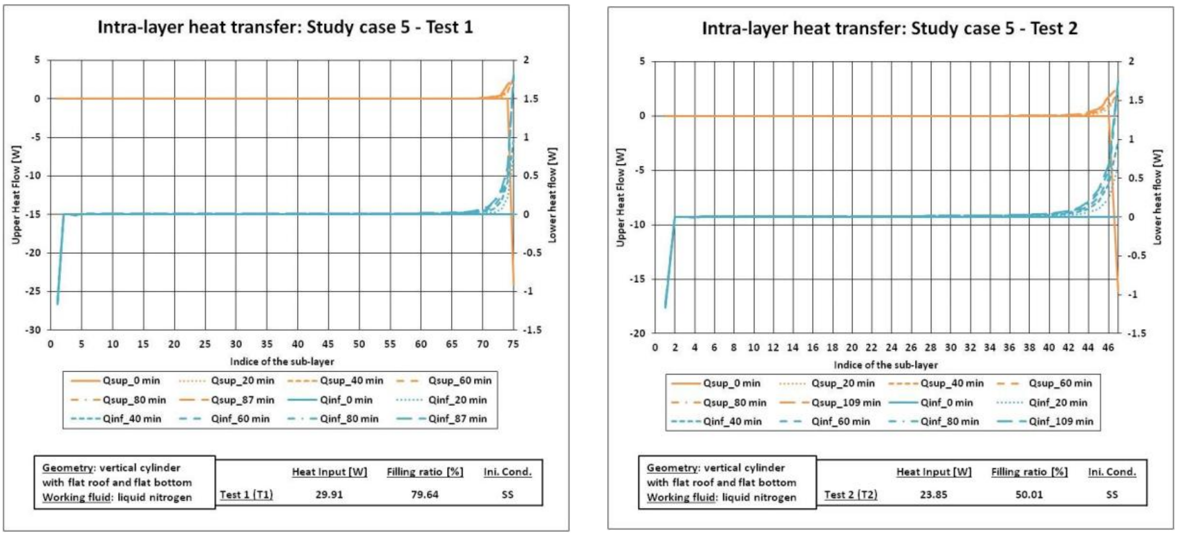

a) b)

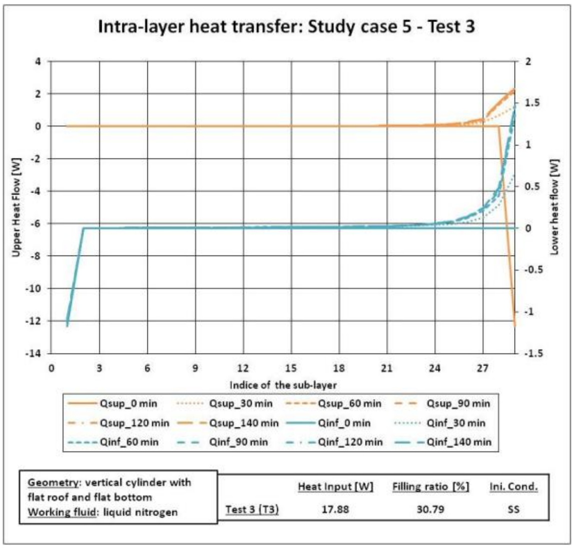

c)

Figure 176. Intra-layer heat transfer of Study case 5 (medium heat fluxes): a) Test 1; b) Test 2; c) Test 3.

In Test 1 (high filling ratio), $\dot{Q}^{SUP}$ is equal to zero at the end of the steady state, in the all the sub-layers, except the interface sub-layer, where $\dot{Q}^{SUP}$ is equal to the opposite of $\dot{Q}_I^L$. During the self-pressurisation, $\dot{Q}^{SUP}$ is equal to zero in the lower and in the core part of the liquid. Near the interface, $\dot{Q}^{SUP}$ increases up to the value of the opposite sign of $\dot{Q}_I^L$. The space-distribution of $\dot{Q}^{UP}$ is qualitatively similar to the one of the liquid bulk temperature gradient ($\frac{\partial T^L}{\partial x}$) (see Section 8.2.1 of Chapter 6). At the beginning of the self-pressurisation, $\dot{Q}^{INF}$ is equal to zero, except for the bottom sub-layer, where it is equal to the opposite sign value of the bottom-to-liquid heat flow. During the self-pressurisation, the space-distribution profile of $\dot{Q}^{INF}$ is flat in the core and near the bottom. In the sub-layers that are close to the interface, $\dot{Q}^{INF}$ increases and its evolution in this region are quite similar to the one of $\dot{Q}^{SUP}$.

In Test 2 (medium filling ratio), the space-distribution of $\dot{Q}^{SUP}$ is flat equal to zero, except for the interface sub-layer, at the beginning of the self-pressurisation. During the self-pressurisation, $\dot{Q}^{SUP}$ of the sub-layers that are near the interface are higher than zero and it increases approaching the interface, at the end of the steady state. The space-distribution of $\dot{Q}^{INF}$ is similar to that of $\dot{Q}^{SUP}$, except for the bottom sub-layer. During the self-pressurisation, $\dot{Q}^{INF}$ increases in the upper part of the liquid, as the interface is approached.

In Test 3 (low filling ratio), $\dot{Q}^{SUP}$ is equal to zero in the all the sub-layers, except the interface sub-layer, at the end of the steady sate. During the self-pressurisation, $\dot{Q}^{SUP}$ increases in the upper part of the liquid, approaching the interface. The space-distribution of lower heat flow is flat at the beginning of the self-pressurisation, except at the bottom. $\dot{Q}^{INF}$ increases near the interface, during the self-pressurisation.

Figure 177 shows the spatial-evolution of the $\dot{Q}^{SUP}$ and $\dot{Q}^{INF}$ heat flows across the sub-layers, at different time-points, for Study case 6.

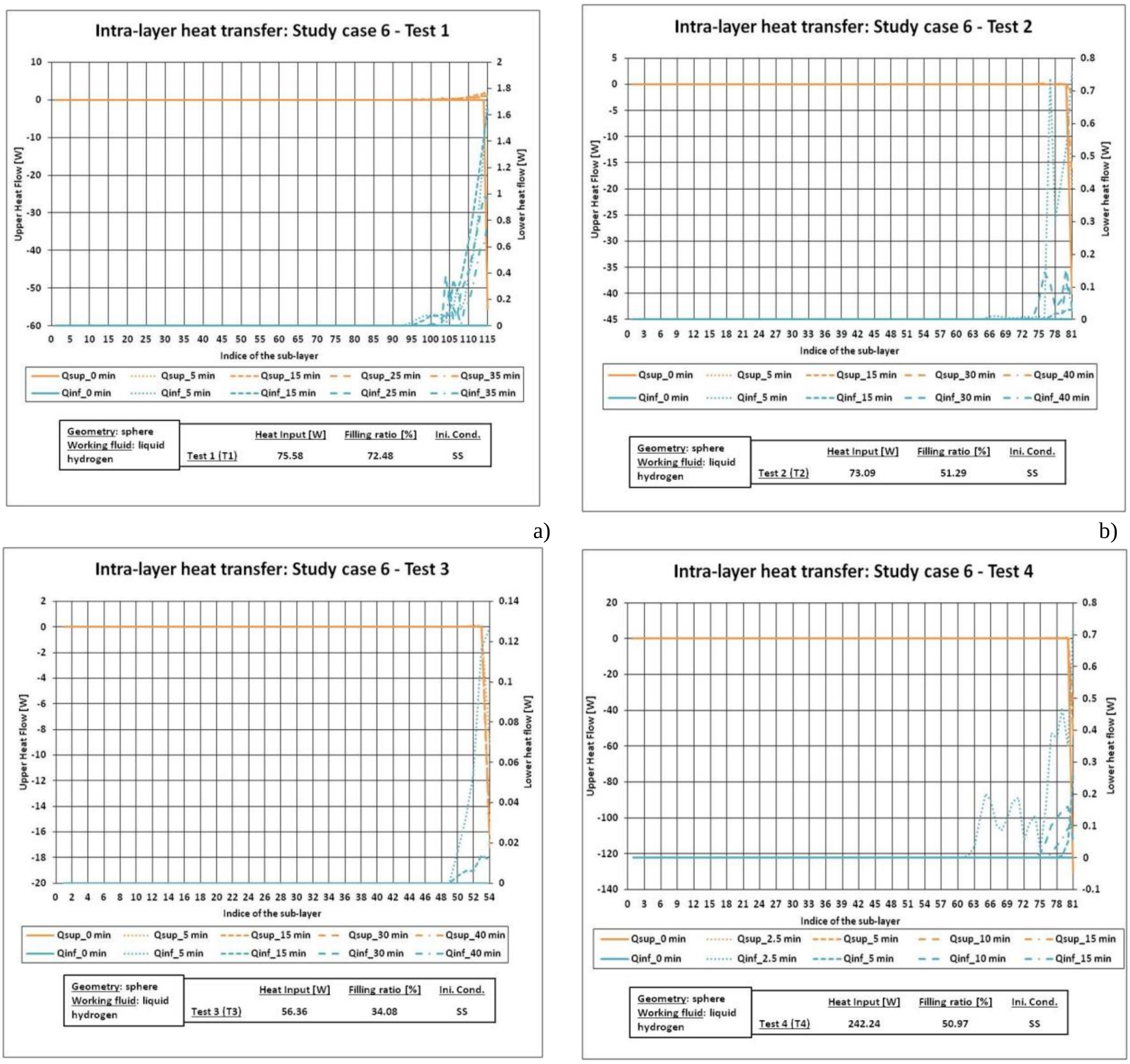

a) b)

c) d)

Figure 177. Intra-layer heat transfer of Study case 6 (medium heat fluxes): a) Test 1; b) Test 2; c) Test 3; d) Test 4.

In Test 1 (high filling ratio), $\dot{Q}^{SUP}$ is equal to zero in all the sub-layers, except at the interface, at the end of the steady state. During the self-pressurisation, $\dot{Q}^{SUP}$ increases near the interface. $\dot{Q}^{INF}$ is equal to zero at the end of the steady state. As time passes, this variable increases after the 95th sub-layer up to the interface. The increment of $\dot{Q}^{INF}$ procudes some picks between the 102th and the 108th sub-layer, as done by $\frac{\partial T^L}{\partial x}$ during the self-presurisation (see Figure 171).

In Test 2 (medium filling ratio), the space-distributions of $\dot{Q}^{SUP}$ and $\dot{Q}^{INF}$ at the end of the steady state is similar to the ones of Test 1. During the self-pressurisation, $\dot{Q}^{SUP}$ increases due to the increment of $\frac{\partial T^L}{\partial x}$ and it strongly decreases near the interface, reaching negative values, because the heat flows from the liquid to the interface at the interface sub-layer (81th sub-layer), instead of flowing in the opposite direction as done in Study case 5. $\dot{Q}^{INF}$ slightly increases after the 65th sub-layer and the rate of this increment augments after the 73th sub-layer. This increament produces picks at 5 and 15 minutes as done for $\frac{\partial T^L}{\partial x}$ during the self-presurisation (see Figure 171).

In Test 3 (low filling ratio), the space distribution of $\dot{Q}^{SUP}$ is similar to the one of Test 2 because the heat flows from the liquid to the interface at the interface sub-layer (54th sub-layer). $\dot{Q}^{INF}$ increases during the self-pressurisation. At 5 minutes, $\dot{Q}^{INF}$ is higher than the one at 15 minutes and, in the remaining time-points, $\dot{Q}^{INF}$ is equal to zero. The space-evolution of $\dot{Q}^{INF}$ is similar to the one of $\frac{\partial T^L}{\partial x}$.

In Test 4 (high heat inputs), the space distribution of $\dot{Q}^{SUP}$ is similar to the one of Test 2 and 3, due to the direction of the liquid-to-intarface heat flow. $\dot{Q}^{INF}$ increases near the interface during the self-pressurisation. At 2.5 minutes, this variable increases from the 62th sub-layer, creating picks. After 75th sub-layer, $\dot{Q}^{INF}$ strongly increases. The form and the position of these picks are similar to the ones of $\frac{\partial T^L}{\partial x}$ (see Figure 171). In the remainig time-points, the increment of this variable is more regular than the one at 2.5 minutes.

To sum up, the time-evolutions of the upper and lower heat flows are flat at the end of the steady state, except for the bottom and interface sub-layers. During the self-pressurisation, $\dot{Q}^{UP}$ and $\dot{Q}^{INF}$ increase near the interface, and their profiles are qualitatively similar to the ones of the liquid bulk temperature gradient (see Section 8.2.1 of Chapter 6). The values $\dot{Q}^{UP}$ and $\dot{Q}^{INF}$ are always positive, except at the interface and at the bottom, indicating that the thermal energy flows from the interface to the core. The space-distributions and time-evolutions of these heat flows are qualitatively similar to the one of the Study cases at low heat fluxes (see Section 8.1.4 of Chapter 6). The space distributions of $\dot{Q}^{UP}$ and $\dot{Q}^{INF}$ is similar to the one of $\frac{\partial T^L}{\partial x}$ (see Figure 171).

8.2.5. Presentation of the results: heat transfer at interface

Figure 178 shows the time-evolution in time of the liquid-to-interface heat flow ($\dot{Q}_I^L$) and vapour-to-interface heat flow ($\dot{Q}_I^V$) for Study case 5. The solid and the dotted curves respectively indicate the liquid-to-interface and the vapour-to-interface heat flows.

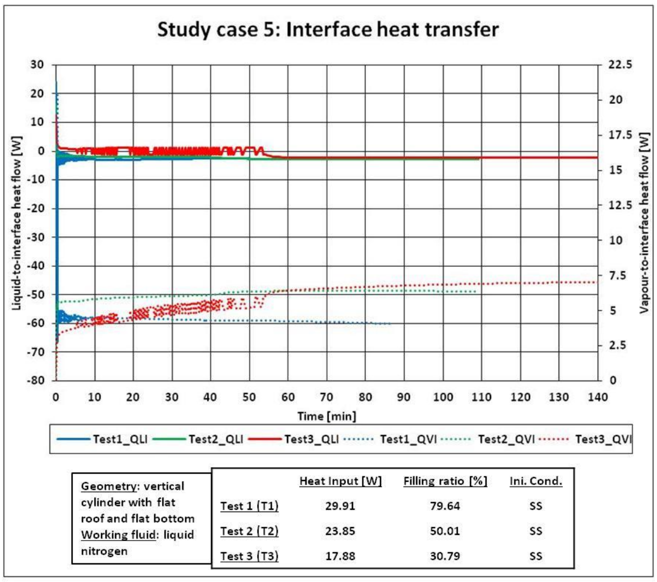

Geometry: vertical cylinder with flat roof and flat bottom
Working fluid: liquid nitrogen

	Heat Input [W]	Filling ratio [%]	Ini. Cond.
Test 1 (T1)	29.91	79.64	SS
Test 2 (T2)	23.85	50.01	SS
Test 3 (T3)	17.88	30.79	SS

Figure 178. Heat transfer at the interface for Study case 5 (medium heat fluxes).

In Test 1 (high filling ratio), $\dot{Q}_I^L$ produces a negative peak at the end of the steady state and its value is around -65 W. After this peak, $\dot{Q}_I^L$ oscillates around the average value of – 2.6 W in the first 10 minutes of the self-pressurisation. After this period of time, $\dot{Q}_I^L$ is constant and negative, indicating that the thermal energy flows from the interface to the bulk. $\dot{Q}_I^V$ generates a positive peaks at the beginning of the self-pressurisation, reaching the value of around 20 W. After this peak, $\dot{Q}_I^V$ fluctuates in the first 10 minutes and, after this period, this heat flow is constant at the value of around 4W. So, the time-evolution of $\dot{Q}_I^V$ is qualitatively symmetrical to the one of $\dot{Q}_I^L$.

In Test 2 (medium filling ratio), $\dot{Q}_I^L$ drops from the value of around 15 W to the value of around -1.6 W, at the end of the steady state, when the storage container is closed. So, the thermal energy flows from the interface to the liquid. After this drop, this heat flow remains constant during the self-pressurisation. $\dot{Q}_I^V$ jumps from the value of around 0.25 W to the value of around 5 W at the beginning of the self-pressurisation. After this jump, this heat flow remains constant. So, the time-evolution of $\dot{Q}_I^V$ is qualitatively symmetrical to the one of $\dot{Q}_I^L$.

In Test 3 (low filling ratio), $\dot{Q}_I^L$ drops from the value of around 12 W to the value of around 0.7 W at the beginning of the self-pressurisation. So, the thermal energy flows from the liquid to the interface as during the steady state, contrarily to Test 1 and 2, and to the results of the previous model. After this drops, $\dot{Q}_I^L$ fluctuates between negative and positive values between 5th and 55th minutes of the self-pressurisation. After this fluctuation, $\dot{Q}_I^L$ decreases to the value of around -2.3 W and it remains constant up to the end of the self-pressurisation. The thermal energy is transferred from the interface to the liquid, contrarily to the first part of the self-pressurisation. $\dot{Q}_I^V$ jumps from the value of 0.1 W to the value of 3.5 W at the end of the steady state. After this jump, this heat flow oscillates between 5th and 55th minutes of the self-pressurisation, but the average value of this oscillation increases. After these oscillations, $\dot{Q}_I^V$ monotonically increases, but the rate of this increment is lower than the one of the average value of the oscillations. So, the time-evolution of $\dot{Q}_I^V$ is qualitatively symmetrical to the one of $\dot{Q}_I^L$.

Figure 179 shows the time-evolution in time of $\dot{Q}_I^L$ and $\dot{Q}_I^V$ for Study case 6. The solid and the dotted curves respectively indicate the liquid-to-interface and the vapour-to-interface heat flows.

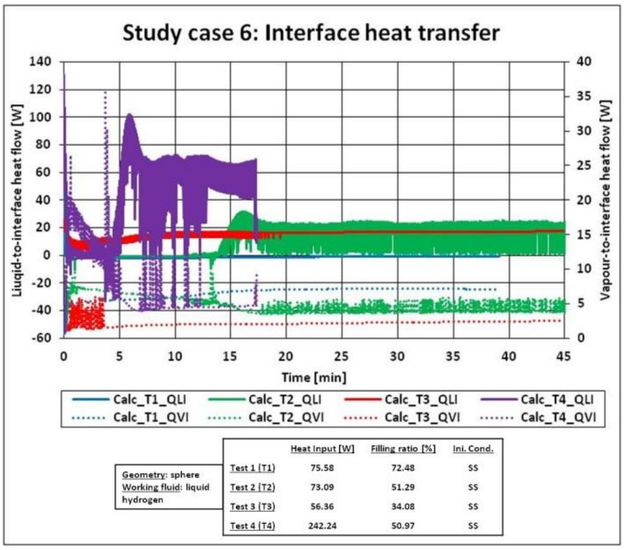

Figure 179. Heat transfer at the interface for Study case 6 (medium heat fluxes).

In Test 1 (high filling ratio), $\dot{Q}_I^L$ decreases at the end of the steady state, passing from positive to negative values. These negative values are close to zero and they remain almost constant at the value of -1.07 W during all the self-pressurisation. $\dot{Q}_I^V$ is constant at the value of 7.09 W during the self-pressurisation.

In Test 2 (medium filling ratio), the time-evolution of $\dot{Q}_I^L$ at the end of the steady stae is quite similar to the one of Test 1. $\dot{Q}_I^L$ remains constant and negative between 2 and 11 minutes. after this time-point, $\dot{Q}_I^L$ oscillates and it average value increases, creating a picks at 16.5 minutes. Then, the average value decreases, remaining constant and positive, and $\dot{Q}_I^L$ continues oscillating. $\dot{Q}_I^V$ oscillates after 11 minutes, with a frequence that is opposite to the one of $\dot{Q}_I^L$.

In Test 3 (low filling ratio), $\dot{Q}_I^L$ oscillates at the end o fhte steady state and its average value decreases, but it remains positive. This decrement is slower than the one of Tests 1 and 2 and the average value of $\dot{Q}_I^L$ increases after 5 minutes, remaining constant. After 19 minutes, $\dot{Q}_I^L$ remains constant and positive. $\dot{Q}_I^V$ oscillates in the first 4 minutes of the self-pressurisation. Then, it remains constant aroud 2.5 W.

In Test 4 (high heat inputs), $\dot{Q}_I^L$ strongly oscillates at the end of the steady state, passing from 130 W to -0.3 W. The oscillations of this variables decreases in amplitude between 1 and 5 minutes. then, the average value of $\dot{Q}_I^L$ increases creating a positive picks at 6 minutes. after this pick, the values of $\dot{Q}_I^L$ are positive, but they strongly oscillates. $\dot{Q}_I^V$ strongly oscillates at the end of the steady state. then, it decreases, creating a pick at 4 minutes, whose maximum value is around 35 W. Then, the average value of $\dot{Q}_I^V$ remain constant at the value of 4.6 W, but picks are present when there is a negative oscillation of $\dot{Q}_I^L$.

To sum up, $\dot{Q}_I^L$ drops at the end of the self-pressurisation as occurs at low heat fluxes (see Section 8.1.5 of Chapter 6) and in the results of the previous model. This heat flow fluctuates in the first part of the self-pressurisation, contrarily to the results of low heat fluxes (see Section 8.1.5 of Chapter 6). As the initial filling ratio reduces, $\dot{Q}_I^L$ increases and its value can be positive during the self-pressurisation, contrarily to the result of the previous models. The time-evolution of $\dot{Q}_I^V$ is qualitatively symmetrical to that of $\dot{Q}_I^L$. $\dot{Q}_I^V$ is always positive, indicating that the heat flows from the vapour to the interface.

8.2.6. Presentation of the results: net mass flow

The time-evolution of the net mass flow ($\dot{m}_N$) is described in Figure 180 for Study case 5.

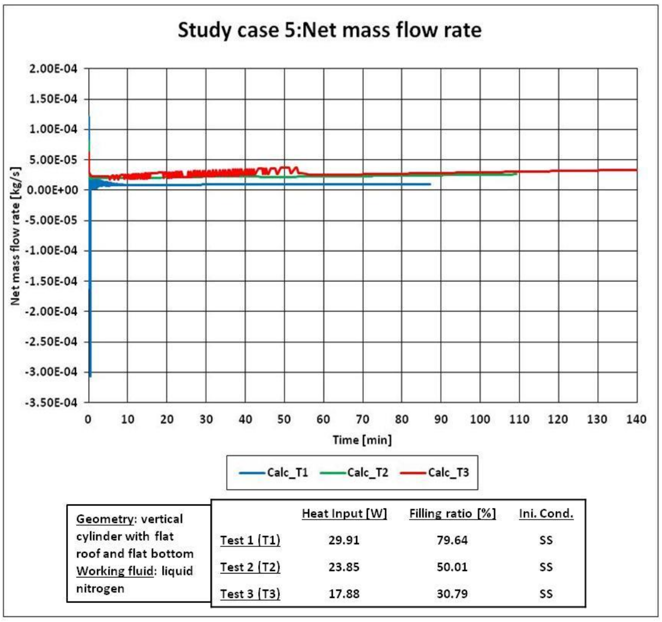

Geometry: vertical cylinder with flat roof and flat bottom
Working fluid: liquid nitrogen

	Heat Input [W]	Filling ratio [%]	Ini. Cond.
Test 1 (T1)	29.91	79.64	SS
Test 2 (T2)	23.85	50.01	SS
Test 3 (T3)	17.88	30.79	SS

Figure 180. Net mass flow for the Study cases 5 (medium heat fluxes).

In Test 1 (high filling ratio), $\dot{m}_N$ generates a negative peak at the end of the steady state, when the storage container is close to start the self-pressurisation. The value of this mass flow drops from $1.2\cdot10^{-4}$ kg/s to the value of $-5.5\cdot10^{-7}$ kg/s, indicating the net condensation[104] occurs. After this peak, $\dot{m}_N$ oscillates between positive and negative values in the first 10 minutes of the self-pressurisation, ad done by $\dot{Q}_I^L$ (see Section 8.2.5 of Chapter 6). After this oscillation, this mass flow remains constant at the value of $9.9\cdot10^{-6}$ kg/s and the net evaporation[105] occurs.

In Test 2 (medium filling ratio), the neat mass flow drops form the value of $8.2\cdot10^{-5}$ kg/s to the value of $1.9\cdot10^{-5}$ kg/s at the beginning of the self-pressurisation. After this drop, this mass flow remains constant. Contrarily to $\dot{m}_N$ of Test 1, the values obtained for Test are positive during the whole self-pressurisation, indicating that only net evaporation can occurs.

In Test 3 (low filling ratio), the net mass flow drops from the value of $6.2\cdot10^{-5}$ kg/s to the value of $2.6\cdot10^{-5}$ kg/s at the end of the steady state. After this drop, this mass flow fluctuates between the 5th and the 55th minutes of the self-pressurisation, as done by $\dot{Q}_I^L$ (see Section 8.2.5 of Chapter 6). During these oscillations, the average value of $\dot{m}_N$ slightly increases. After the oscillation, $\dot{m}_N$ remains almost constant. The values of $\dot{m}_N$ are always positive, indicating that net evaporation occurs.

Figure 181 describes the time-evolution of $\dot{m}_N$ during the self-pressurisation for Study case 6.

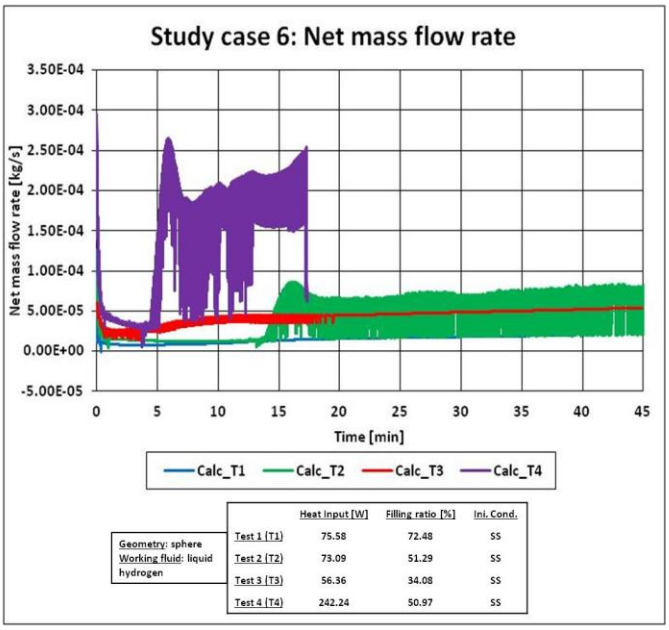

Figure 181. Net mass flow for the Study cases 6 (medium heat fluxes).

In Test 1 (high filling ratio), $\dot{m}_N$ strongly decreases at the end of the steady state, passing from $1.2\cdot10^{-4}$ kg/s to $1.04\cdot10^{-5}$ kg/s. After this initial decrement, this variable remains almost constant at the value of $1.9\cdot10^{-5}$ kg/s. The time-evolution of $\dot{m}_N$ is qualitatively similar to the one of $\dot{Q}_I^L$, but $\dot{m}_N$ does not oscillate.

In Test 2 (medium filing ratio), $\dot{m}_N$ strongly decreases at the end of the steady state, as done in Test 1. This variable is constant around the value of $1.2\cdot10^{-5}$ kg/s between 1 and 12 minutes, which is slightly higher than the one of Test 1 in the same period. Then, $\dot{m}_N$ oscillates and its average value increases, producing a pick at 16.5 minutes. Then, the average value decreases and remains constant. $\dot{m}_N$

---

[104] Net condensation occurs when the condensation rate is higher than the evaporation rate.

[105] Net evaporation occurs when the evaporation rate is higher than the condensation rate.

oscillates up to the end of the self-pressurisation. The time-evolution of $\dot{m}_N$ is qualitatively similar to the one of $\dot{Q}_I^L$.

In Test 3 (low filling ratio), $\dot{m}_N$ decreases lower than the one of Tests 1 and 2 at the end of the steady state and the minimum reached value is around $2.7 \cdot 10^{-5}$ kg/s. As the steady state ends, $\dot{m}_N$ oscillates with an amplitude that is lower than the one of Test 2. After 17 minutes, these oscillations stop and $\dot{m}_N$ remain constant at the value of $5.4 \cdot 10^{-5}$ kg/s.

In Test 4 (high filling ratio), $\dot{m}_N$ decreases stronger than the one of Test 1, passing from $2.9 \cdot 10^{-4}$ kg/s to $7.09 \cdot 10^{-5}$ kg/s. $\dot{m}_N$ oscillates and its average value decreases between 1 and 4 minutes. Then, its average value increases, creating a picks, as done by $\dot{Q}_I^L$ (see Figure 179). Then, the average value of $\dot{m}_N$ decreases, with strong oscillations. These oscillations are present up to the end of the self-pressurisation.

To sum up, the time-evolution of the net mass flow is qualitatively similar to the one of $\dot{Q}_I^L$ (see Section 8.2.5 of Chapter 6), as occurs in the previous models. The steady state values of this mass flow decrease with the reduction of the filling ratio, but the values of this variables increase with the reduction of the initial liquid level during the self-pressurisation. Except for the initial negative peak in Test 1, $\dot{m}_N$ is positive, suggesting the net evaporation is dominant during the self-pressurisation.

8.2.7. Presentation of the results: pressure

Figure 182 shows the calculated time-evolution of the pressure against the the experimental data, during the self-pressurisation of Study case 5. The dots are the experimental data and the continuous lines are the computed values of the pressure.

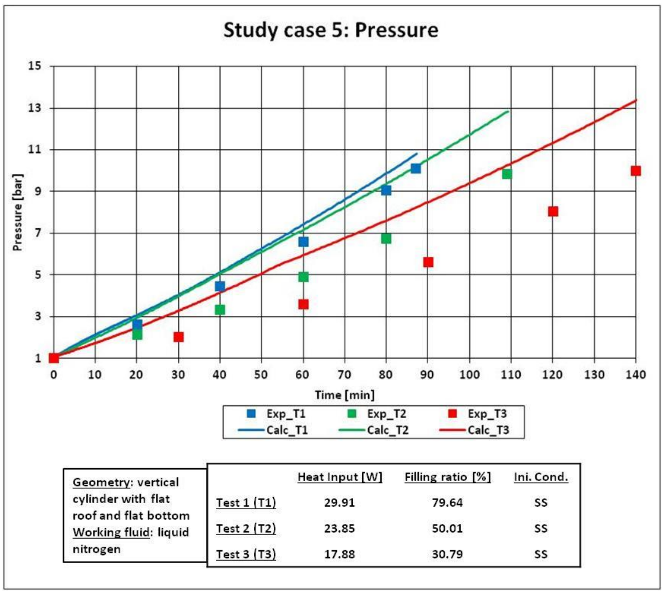

Geometry: vertical cylinder with flat roof and flat bottom
Working fluid: liquid nitrogen

	Heat Input [W]	Filling ratio [%]	Ini. Cond.
Test 1 (T1)	29.91	79.64	SS
Test 2 (T2)	23.85	50.01	SS
Test 3 (T3)	17.88	30.79	SS

Figure 182. Computed and experimental pressure for the Study case 5 (medium heat fluxes).

In Test 1 (high filling ratio), the calculated pressure almost linearly increases in time. The rate of this increment is slightly higher than the experimental one and the computed values of the pressure are higher than the measured ones. At the end of the self-pressurisation, the pressure difference between the calculated and the measured is around 0.6 bar.

In Test 2 (medium filling ratio), the calculated pressure linearly increases in time, similarly to Test 1, but the rate of this increment is slightly lower than the one of Test 1. The computed values of the pressure are higher than the experimental ones and the difference between the pressure calculated for Test 2 and the measured pressure is higher than the one obtained for Test 1. At the end of the self-pressurisation, the difference in pressure between the calculated and the measured is around 2.9 bar.

In Test 3 (low filling ratio), the calculated pressure linearly increases in time, similarly to the previous tests. The computed values of the pressure are higher than the experimental ones. The difference between the pressure calculated for Test 2 and the measured values is similar to the one obtained for Test 2. At the end of the self-pressurisation, the difference in pressure between the calculated and the measured is around 3.5 bar.

Figure 183 shows the comparision of the calculated values of the pressure against the measured one, during the self-pressurisation of Study case 6. The dots are the experimental data and the continuous lines are the computed values of the pressure.

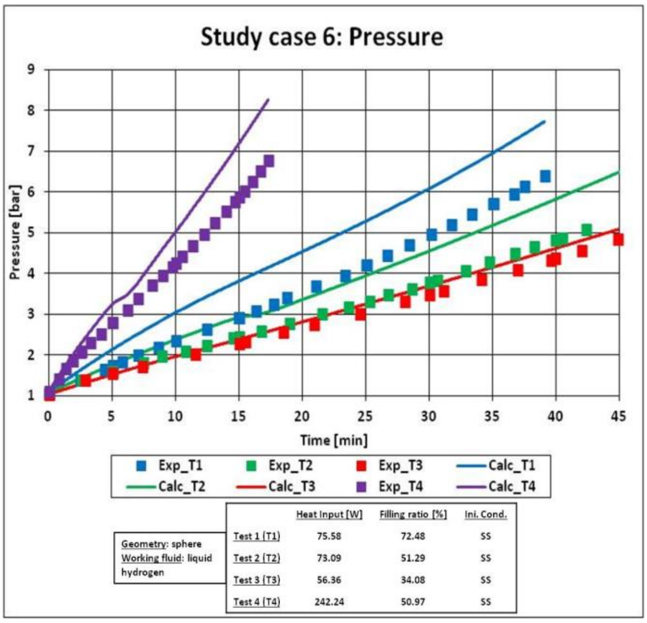

	Heat Input [W]	Filling ratio [%]	Ini. Cond.
Test 1 (T1)	75.58	72.48	SS
Test 2 (T2)	73.09	51.29	SS
Test 3 (T3)	56.36	34.08	SS
Test 4 (T4)	242.24	50.97	SS

Figure 183. Computed and experimental pressure for the Study case 6 (medium heat fluxes).

In Test 1 (high filling ratio), the calculated pressure almost linearly increases. The rate of this increment slightly changes during the self-pressurisation, as done by $\dot{m}_N$. The calculated values are always higher than the experimental one during the self-pressurisation. at the end of the self-pressurisation, the difference in pressure between the calculated and the measured values is around 1.3 bar.

In Test 2 (medium filling ratio), the time-evolution of the pressure is quite similar to the one of Test 1. The difference in pressure between the calculated and the measured values is slightly lower than the one of Test 1. The value of this differnce is around 1.1 bar at the end of the self-pressurisation.

In Test 3 (low filling ratio), the calculated pressure linearly increases during the self-pressurisation. the calculated value are close to the measured one and the difference in pressure between the calculated and the measured values is around 0.23 bar at the end of the self-pressurisation.

In Test 4 (high heat inputs), the computed pressure increases faster than the measured one in the first 5 minutes, but hte difference in lower than the one of Test 1. After 5 minutes, the slope of the pressure increment reduces, but the increases. After 6 minutes, the pressure increases with the rate observed in the first part of the self-pressurisation. the difference in pressure between the calculated and the measured values is higher than the initial one and its value is around 1.5 bar at the end of the self-pressurisation.

To sum up, the calculated pressure is close to the experimental data at high filling ratio. As the initial filling ratio is reduced, the pressure difference between the calculated and measured values increases. At the same time-point, the calculated pressure decreases with the reduction of the filling ratio, as qualitatively obtained in the experimental done. So, the pressure-filling ratio relation of LS model agrees with the experimental data more than in the previous model.

8.2.8. Presentation of the results: temperature profile in liquid

Figure 184 shows the computed liquid temperature profile at different time-points against the experimental values, during the self-pressurisation at medium heat fluxes (for Study case 5). In Test 1, the time-points considered are respectively called "t_0", "t_{20}", "t_{40}", "t_{60}", "t_{80}" and "t_{87}", which correspond to 0, 20, 40, 60, 80 and 87 minutes of the self-pressurisation time, respectively. In Test 2, the time-points of the Test 1 are considered, except for "t_{87}". This time-point is substituted by time-point "t_{109}", which corresponds to 109 minutes. In Test 3, the time-points considered are respectively called "t_0", "t_{30}", "t_{60}", "t_{90}", "t_{120}" and "t_{140}", which correspond to 0, 30, 60, 90, 120 and 140 minutes of the self-pressurisation time, respectively. The symbols are the experimental data and the lines are the computed temperaturess.

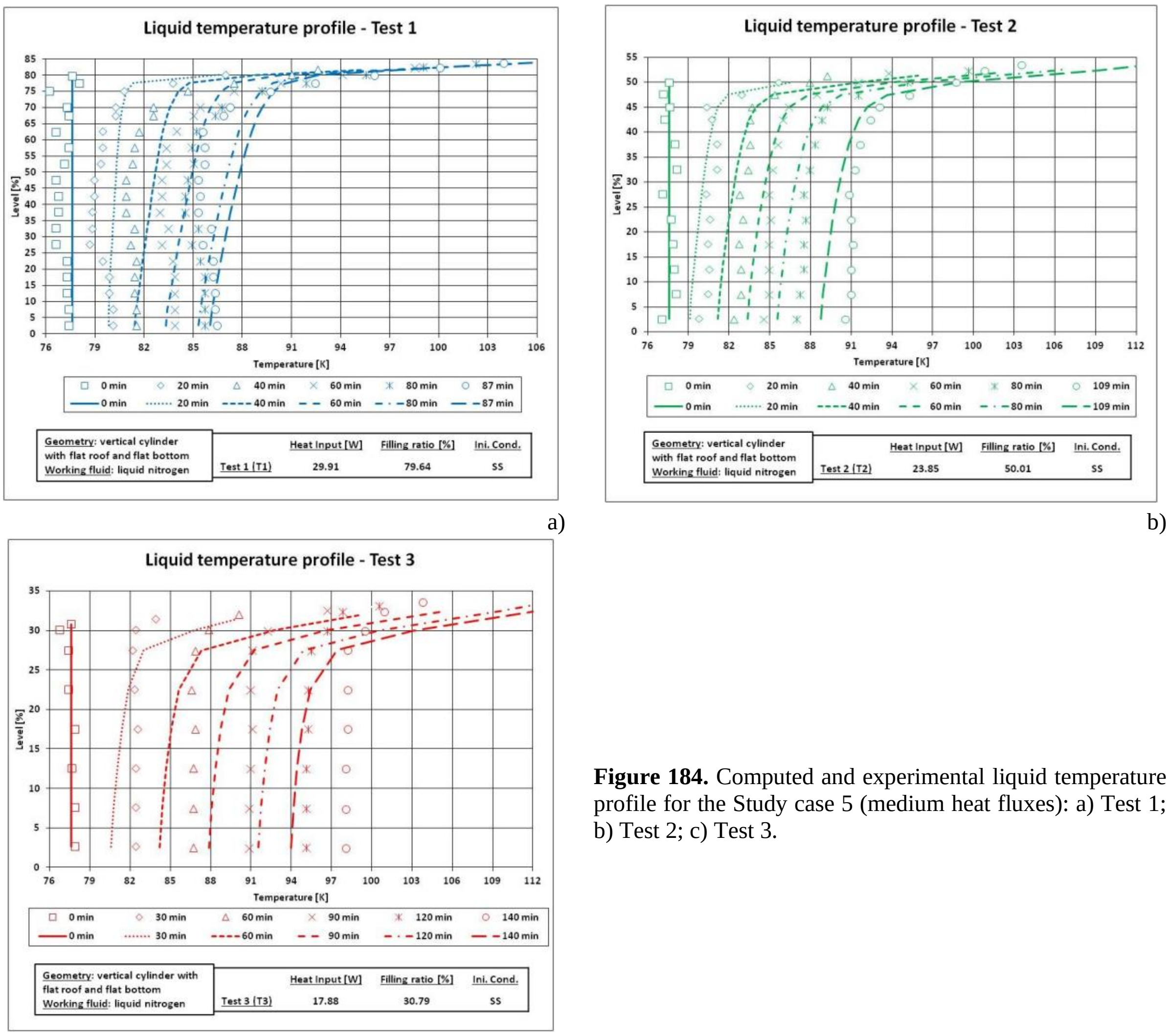

a)

b)

c)

Figure 184. Computed and experimental liquid temperature profile for the Study case 5 (medium heat fluxes): a) Test 1; b) Test 2; c) Test 3.

In Test 1 (high filling ratio), the liquid temperature profile is flat at “t_0” and the liquid temperatures are close to the experimental ones. At “t_{20}”, the liquid temperature slightly increases with a constant rate from the bottom to 77 % of the level. After this level, the liquid temperature strongly increases. The computed liquid temperatures agree with the experimental ones. The temperature profile of the liquid at “t_{40}”, “t_{60}”, “t_{80}” and “t_{87}” are qualitatively similar to the one of “t_{20}”. The increment of the liquid temperature in the core is steeper than the one of “t_{20}” and this increment grows up as time passes. Near the interface, the increment of the liquid temperature of t_{40}”, “t_{60}”, “t_{80}” and “t_{87}” is faster than the one at “t_{20}”. The temperature profiles of the liquid at “t_{40}”, “t_{60}”, “t_{80}” and “t_{87}” do not agree with the experimental data because the measured profile is almost flat in the core, and the measured temperature increment near the interface is smother than the calculated one.

In Test 2 (medium filling ratio), the liquid temperature profile is flat at “t_0” and the liquid temperatures are close to the experimental ones. At “t_{20}”, “t_{40}”, “t_{60}”, “t_{80}” and “t_{109}”, the calculated liquid temperature increases with a constant from the bottom to around 47 % of the filling ratio. The rate of this increment is almost constant with the self-pressurisation time, contrarily to Test 1. After this point, which decreases as time passes, the liquid temperature increases faster than in the core. The calculated temperature profiles agree more with the experimental data than for Test 1, but the computed liquid temperatures at the interface are higher than the experimental ones. The calculated liquid temperature is slightly lower that the experimental one in the core.

In Test 3 (low filling ratio), the liquid temperature profile is flat at “t_0” and the liquid temperatures are close to the experimental ones. At “t_{30}”, “t_{60}”, “t_{90}”, “t_{120}” and “t_{140}”, the calculated liquid temperature linearly increases in the core up to 27 % of the level, with a rate that remains constant in time. The calculated temperatures are lower than the experimental data, whose profiles are flat. After this point, the calculated liquid temperature increases faster than done in the core. This increment is higher than the experimental one and, for the same level, the calculated temperature is higher than the measured one. So, the calculated temperature at the interface is higher than the experimental one.

Figure 185 shows the comparison of computed liquid temperature profile at different time-points against the experimental values, during the self-pressurisation at medium heat fluxes (for Study case 6). In Test 1, the time-points considered are respectively called “t_0”, “t_5”, “t_{15}”, “t_{25}” and “t_{35}”, which correspond to 0, 5, 15, 25 and 35 minutes of the self-pressurisation time, respectively. In Test 2 and 3, the time-points considered are respectively called “t_0”, “t_5”, “t_{15}”, “t_{30}” and “t_{40}”, which correspond to 0, 5, 15, 30 and 40 minutes of the self-pressurisation time, respectively. In Test 4, the time-points considered are respectively called “t_0”, “$t_{2.5}$”, “t_5”, “t_{10}” and “t_{15}”, which correspond to 0, 2.5, 5, 10 and 15 minutes of the self-pressurisation time, respectively. The symbols are the experimental data and the lines are the computed temperaturess.

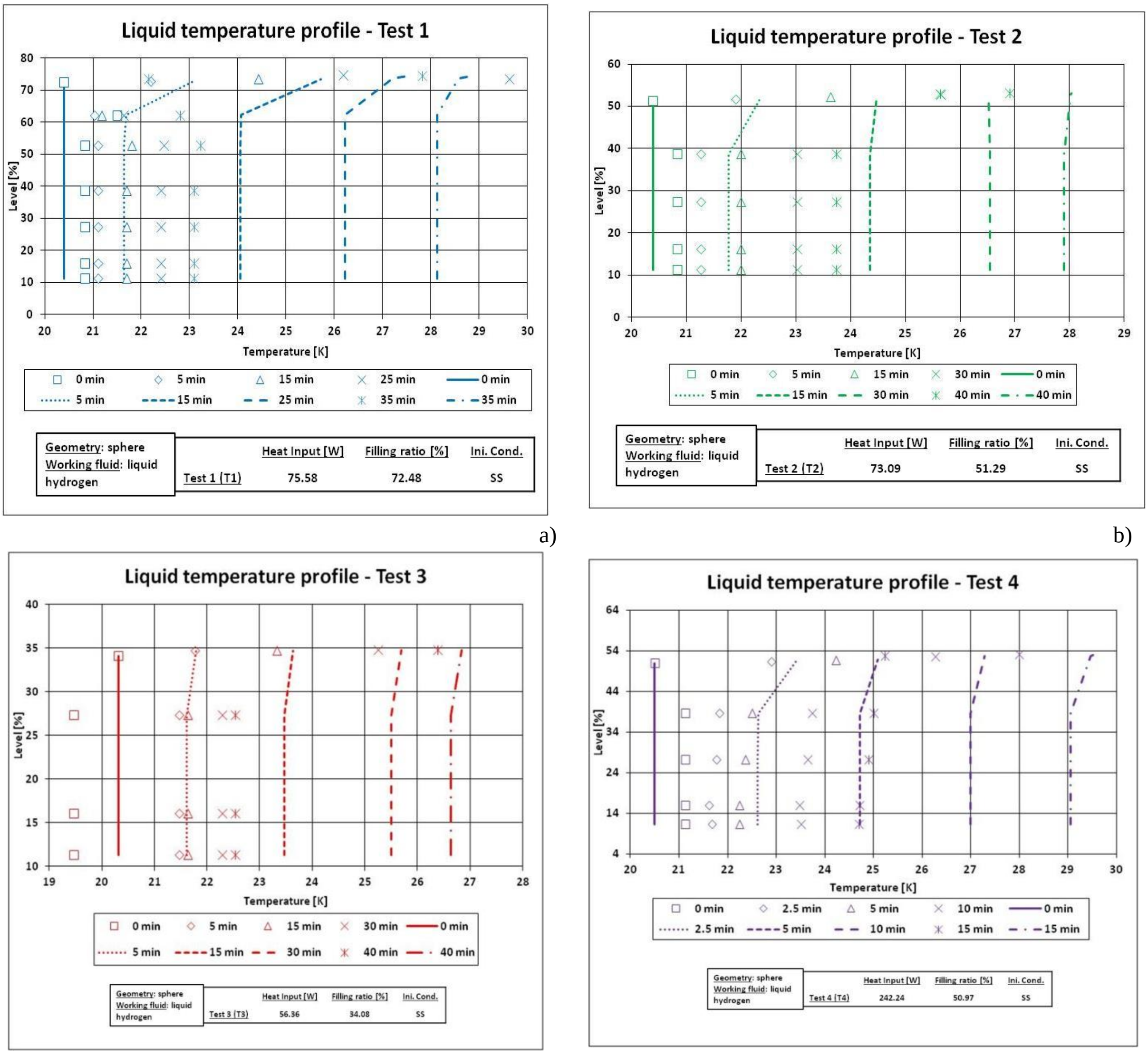

a) b) c) d)

Figure 185. Computed and experimental liquid temperature profile for the Study case 5 (medium heat fluxes): a) Test 1; b) Test 2; c) Test 3; d) Test 4.

In Test 1 (high filling ratio), the calculated liquid temperature profile is shifted to the left respect the measured profile at the end of the self-pressurisation. during the self-pressurisation, the computed temperature profile is flat below 62 % of the liquid height and, above this value, this profile linearly increases. In the flat zone, the computed values of temperature are higher than the measured ones. The slope of this increment decreases in time. The computed slope is lower than the experimental one. At “t_{25}” and “t_{35}”, there is a change in slope of the computed temperature profile near the interface.

In Test 2 (medium filling ratio), the space-distribution of the computed liquid temperature at the end of the steady state is similar to the one of Test 1. At “t_5”, the compute temperature profile is flat below 38 % of the liquid height and, above this value, the computed temperature linearly increases. The slope of this increment reduces in the remaining time-points and the computed temperature profile is almost flat at the end of the self-pressurisation. this behaviour is not in agreement with the experimental data, which indicate the thermal stratification of the liquid above 38 % of the liquid height.

In Test 3 (low filling ratio), the computed temperature profile at the end of the steady state is shifted to the right respect the experimental data. during the self-pressurisation, the computed temperatures increase above the 27.5% of the liquid height. After “t_5”, the bulk liquid temperature increases faster then the measured one, but the temperature near the interface is in agreement with th experimental data.

In Test 4 (high heat inputs), the initial computed temperature profile is similar to the one of Tests 1 and 2. At “$t_{2.5}$”, the computed liquid temperature increases above the 40 % of the liquid height and the calculated value are closer to the experimental data than the one at the other time-points. as time passes, the slope of this computed increment decreases and the bulk temperature increases faster than the experimental one.

To sum up, the calculated liquid temperature profile increases in the core of the liquid, contrarily to the experimental data, where the measure profile is flat. Near the interface, the calculated temperature increases faster than the measured one. The calculated temperature profiles are qualitatively constant with the filling ratio, but the core temperature is colder than the experimental one when the initial liquid level is reduced.

8.3. Study cases: high heat fluxes

The study cases at medium heat fluxes are reported in Table 142 (see more details in Section 4 of Chapter 2).

Table 142. Study cases at high heat fluxes.

Authors	Aydelott[29]
Study case	7
Geometry	Spherical tank
Working fluid	Liquid hydrogen

Section 8.3.1 presents the fluid-dynamics at wet side wall. Section 8.3.2 describes the fluid-dynamics in the liquid. Section explains the heat transfer at the wet side wall. Section 8.3.4 presents the heat transfer across the sub-layer of the liquid. Section 8.3.5 describes the interfacial heat transfer. Section 8.3.6 explains the net mass flow. Section 8.3.7 presents the comparison between the calculated value of the pressure and the measured one. Section 8.3.8 explains the comparison between the computed values of the liquid temperature profiles and the experimental one.

8.3.1. Presentation of the results: fluid-dynamics at the wet side wall

Figure 186 shows the values of the boundary layer mass flow of the wet side wall ($\dot{m}^{SW}$) and the values of the bulk temperature gradient ($\frac{\partial T^L}{\partial x}$) in each sub-layer, at different time-points, for Study case 7. In the caption of Figure 186, the time at which these variables are computed is reported right after each variable. These time-points correspond to the time -points at which the temperature is measured.

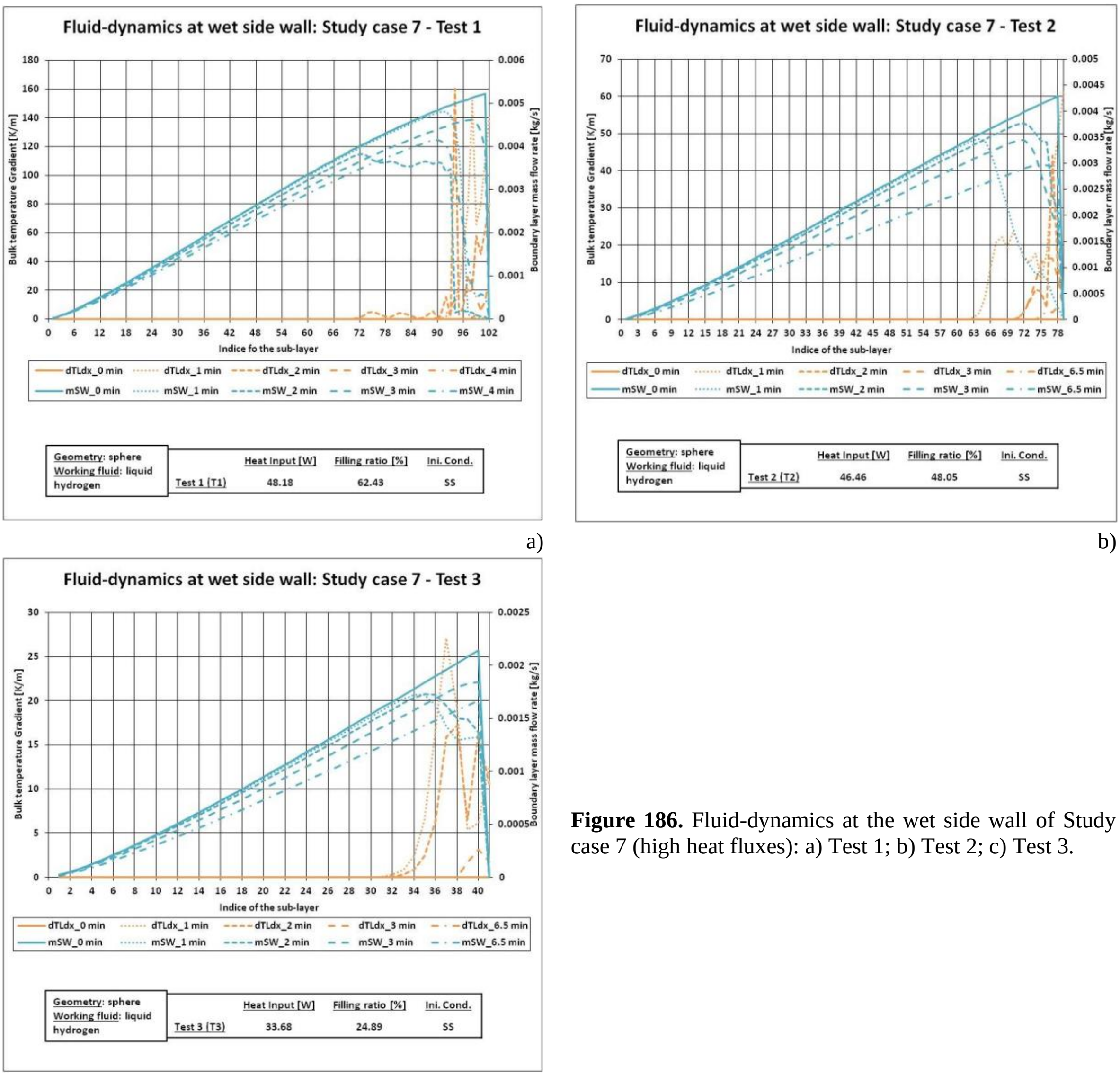

a)

b)

c)

Figure 186. Fluid-dynamics at the wet side wall of Study case 7 (high heat fluxes): a) Test 1; b) Test 2; c) Test 3.

In Test 1 (high filling ratio), the dLTdx is equal to zero in all the sub-layers at the beginning of the self-pressurisation. During the self-pressurisation, this gradient produces peaks near the sub-layers near the interface, contrarily to the Study cases at low and medium heat fluxes (see Section 8.1.1 and 8.2.1 of Chapter 6), where dLTdx monotonically increases. The maximum value reached is around 160 K/m, which is lower than the ones of Study case at medium heat fluxes (see Section 8.2.1). The $\dot{m}^{SW}$ monotonically increases at the end of the steady state, thus at beginning at the self-pressurisation. At the interface sub-layer, the value of this mass flow is equal to zero because the interface is rigid surface. The rate of this increment slightly increases and decreases near the bottom and the interface, respectively. During the self-pressurisation, $\dot{m}^{SW}$ increases from the bottom sub-layer up to the sub-layers near the interface. This increment is qualitatively similar to the one of the end of the steady state, only with lower values. Near the interface, this mass flow rapidly decreases and it goes to zero. The decrement of $\dot{m}^{SW}$ at 2 minutes occurs at the 72th sub-layer. At the other time-points, this decrement occurs after this sub-layer. At 3 minutes, the decrement of $\dot{m}^{SW}$ occurs at the 98th sub-layer, which is close to the interface, contrarily to the one of the other time-points.

In Test 2 (medium filling ratio), $\frac{\partial T^L}{\partial x}$ is equal to zero at the end of the steady state. During the self-pressurisation, this gradient produces peaks, which are not observed at low and medium heat fluxes (see Section 8.1.1 and 8.2.1 of Chapter 6). The maximum value of these peaks is around 60 K/m, which is lower than the one of Test 1 and lower than the ones of Study case at medium heat fluxes (see Section 8.2.1 of Chapter 6). $\dot{m}^{SW}$ linearly increases in the core and near the interface and, at the bottom, the rate of this increment is slightly lower than the one of other part of the liquid. During the self-pressurisation, the space-distribution of $\dot{m}^{SW}$ is qualitatively similar to the initial one, but it decreases as time passes. Near the interface, this mass flow rapidly decreases. At 1, 2, 3 and 6.5 minutes of the self-pressurisation, this decrement occurs after the 63th, 72th, 72th and 78th sub-layers, respectively. So, the position of the sub-layer, where this reduction occurs, does not decrease as done at the low and medium heat fluxes (see Section 8.1.1 and 8.2.1 of Chapter 6).

In Test 3 (low filling ratio), $\frac{\partial T^L}{\partial x}$ is equal to zero in the all sub-layers at the beginning of the self-pressurisation. During the self-pressurisation, this gradient creates peaks in the sub-layers near the interface. The maximum value of these peaks is around 26 K/m, which is lower than the ones of Study cases at medium heat fluxes (see Section 8.2.1 of Chapter 6) and of the ones of the previous tests. The $\dot{m}^{SW}$ linearly increases at the steady state in all the sub-layers and it only grows up in the bottom and in the core during the self-pressurisation. During the self-pressurisation, this increment is lower than the initial one. Near the interface, $\dot{m}^{SW}$ decreases. This decrement occurs at the 34th sub-layer after 1 minute, at the 40th sub-layer after 2 minutes, at 36th sub-layer after 3 minutes and 40th sub-layer at 6.5 minutes.

To sum up, the space-distribution of the bulk temperature gradient is different from the one of the Study cases at low and medium heat fluxes (see Section 8.1.1 and 8.2.1 of Chapter 6) because this gradient produces peaks in the sub-layer near the interface at high heat fluxes. The values of these peaks decrease with the reduction of the initial filling ratio. The maximum values of $\frac{\partial T^L}{\partial x}$ of high heat fluxes are lower than the one at medium heat fluxes (see Section 8.2.1 of Chapter 6). The space-distributions of the mass flow in the boundary layer of the wet side wall is qualitatively similar to the one of the Study cases at low and medium heat fluxes (see Section 8.1.1 and 8.2.1 of Chapter 6) because $\dot{m}^{SW}$ increases at the bottom and in the core of the liquid, and it decreases near the interface. Contrarily to the previous cases, this decrement occurs at a distance from the interface that can increase and decrease during the self-pressurisation.

8.3.2. Presentation of the results: fluid-dynamics in the liquid

Figure 187 shows the values of the descending flow ($\dot{m}^D$) and the values of the rising flow of the bottom ($\dot{m}^B$), at different time-points, for Study case 7. These time-points are equal to the time-points at which the temperature is measured.

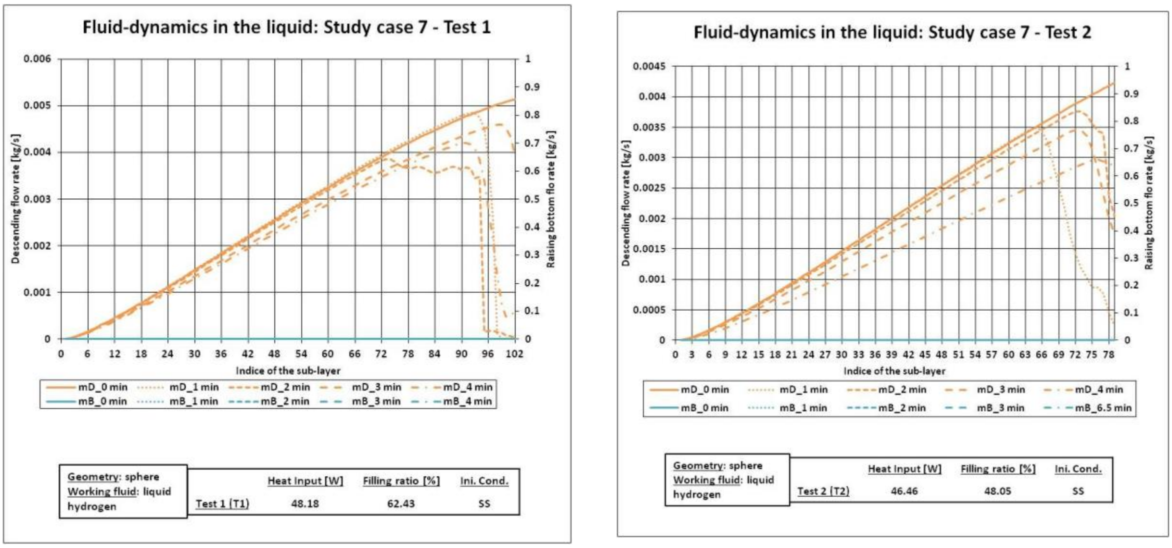

a) b)

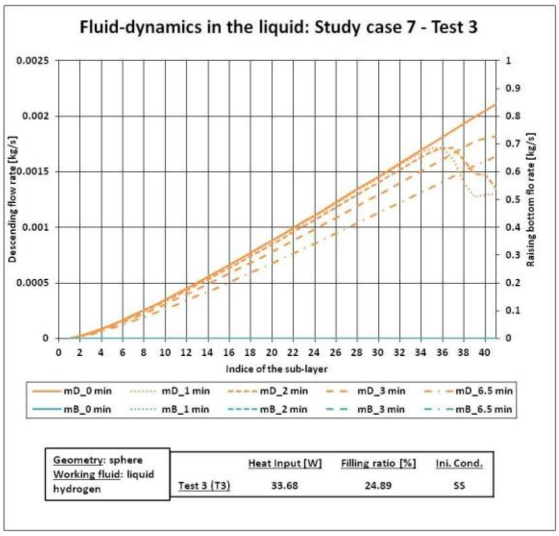

b)

Figure 187. Fluid-dynamics in the liquid of Study case 7 (high heat fluxes): a) Test 1; b) Test 2; c) Test 3.

In Test 1 (high filling ratio), Test 2 (medium filling ratio) and Test 3 (low filling ratio), $\dot{m}^B$ is equal to zero because spherical tanks do not have a bottom in the LS model. Space-distribution of $\dot{m}^D$ of each test is similar to the one of the $\dot{m}^{SW}$ of the corresponding test, due to the null values of the rising mass flow of the bottom.

8.3.3. Presentation of the results: heart transfer at the wet side wall

Figure 188 shows the values of the wet side wall heat transfer coefficient (h_W^{SL}) and the values of the wet wall temperatures (T_W^{SL}), at different time-points, for Study case 7. These time-points are equal to the time-points at which the temperature is measured.

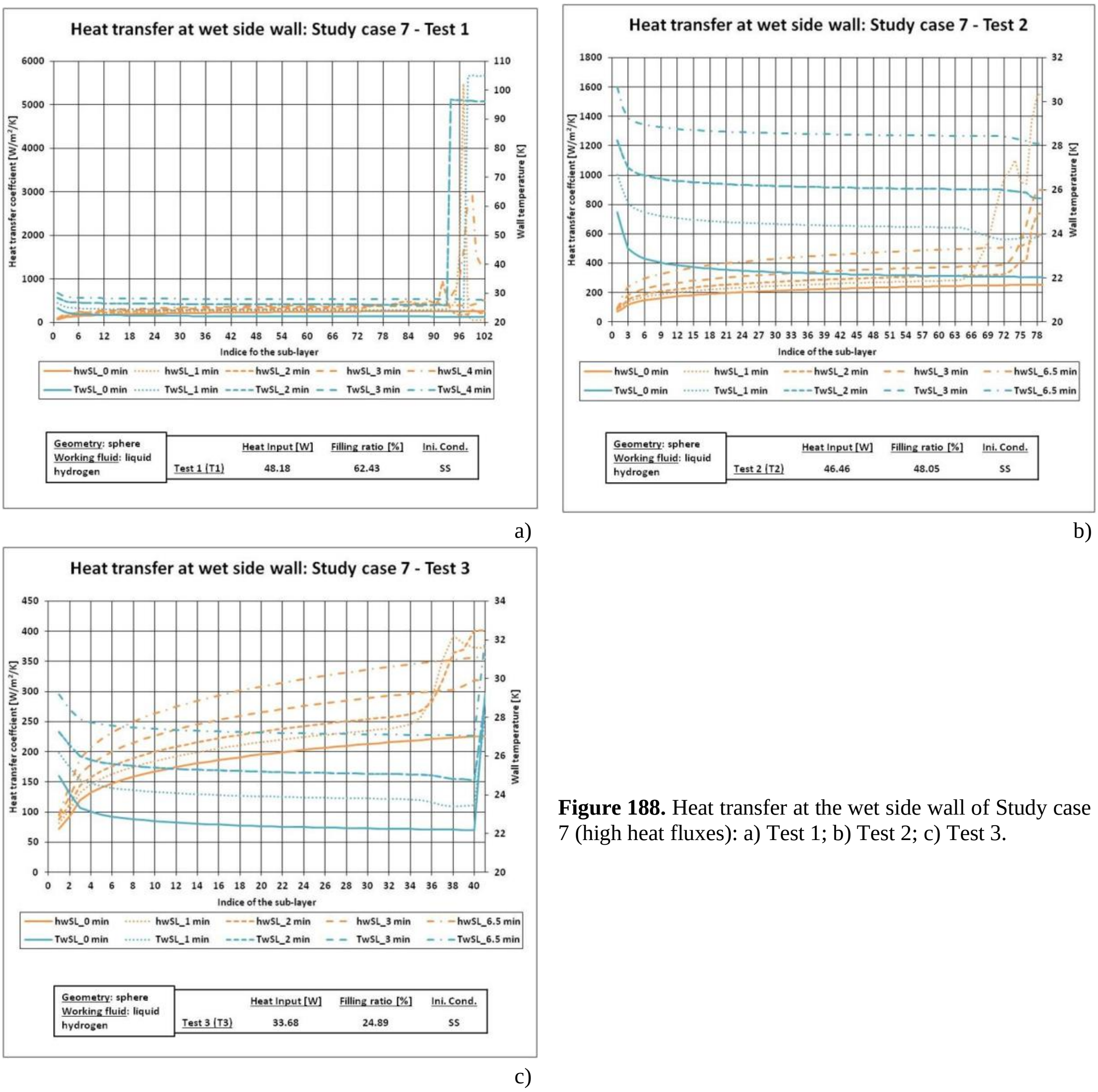

Figure 188. Heat transfer at the wet side wall of Study case 7 (high heat fluxes): a) Test 1; b) Test 2; c) Test 3.

In Test 1 (high filling ratio), h_w^{SL} monotonically increases from the bottom to the interface at the end of the steady state and the rate of this increment constantly decreases. During the self-pressurisation, the space-distribution of h_w^{SL} is qualitatively similarbut quantitatively higher than the initial ones. Near the interface, h_w^{SL} produces peaks, whose maximum value is around 5500 W/m^2/K and it is reached after 1 minute. The T_w^{SL} slightly decreases between the bottom and the 6th sub-layer and it remains constant in all the remaining sub-layers at the end of the steady state. During the self-pressurisation, the space-distribution of T_w^{SL} is qualitatively similar to the initial one. The T_w^{SL} in the core and at the bottom increases as time passes. Near the interface, this temperature jumps from the value of around 23 K to the value of 105 K after 1 minute and from the value of 26 K to the value of 96 K after 2 minutes.

In Test 2 (medium filling ratio), the initial space-distribution of h_w^{SL} is qualitatively similar to the one of Test 1. During the self-pressurisation, the space-distribution of h_w^{SL} is qualitatively similar to the initial one at the bottom and in the core. At 1 minute, h_w^{SL} rapidly increases creating a peak, whose value is around 1100 W/m^2/K and it occurs at the 74th sub-layer. After, h_w^{SL} rapidly decreases to the value of 950 W/m^2/K at 76th sub-layer and it rapidly increases up to the value of 1550 W/m^2/K at the interface. At 2 and 3 minutes of the self-pressurisation, the increment of h_w^{SL} near the interface is lower than the one at 1 minutes. At 6.5 minutes, this increment is almost negligible. T_w^{SL} decreases from the bottom sub-layer up to the interface sub-layer at the end of the self-pressurisation, but the rate of this decrement reduces as the interface is approached. As time passes, T_w^{SL} increases at the same sub-layer. During the self-pressurisation, the space-distribution of T_w^{SL} is qualitatively similar to the initial one in the core and in the bottom. Near the interface, T_w^{SL} decreases faster than at the core.

In Test 3 (low filling ratio), the space-distribution of h_w^{SL} is qualitatively similar to the ones of Test 1 and 2 at the end of the steady state. At 1 minute and at 2 minutes of the self-pressurisation, h_w^{SL} rapidly increases near the interface. This fast increment is less significant at 3 minutes and it is absent at 6.5 minutes. At 1 minute, this increment creates a peak in the 36th sub-layer, whose value is 380 W/m²/K, and, at 2 minutes, this increment produces two “steps of a staircase”. The space-distribution of T_w^{SL} is similar to the ones of Test 1 and 2 in the core and at the bottom, at the beginning of the self-pressurisation. Near the interface, T_w^{SL} rapidly increases from 22 K to 29 K. The space-distribution of this temperature during the self-pressurisation is qualitatively similar to the initial one. As time passes, the space-distribution of T_w^{SL} moves upward, indicating that this temperature increases.

To sum up, the heat transfer coefficient at the wet side wall increases in time and in space at the bottom and in the core of the liquid. At high, medium and low filling ratio, h_w^{SL} increases near the interface and it can create peaks in this zone. Wet side wall temperature decreases from the bottom sub-layer to the core, whereas it increases during the self-pressurisation. At high filling ratio, T_w^{SL} can jump near the interface. At medium filling ratio, this temperature remains almost constant near the interface and, at low filling ratio, T_w^{SL} increases near the interface.

8.3.4. Presentation of the results: intra-layer heat transfer

Figure 189 shows the spatial-evolution of the upper and lower heat flows ($\dot{Q}^{UP}$ and $\dot{Q}^{INF}$) across the sub-layers, at different time-points, for Study case 7. The upper heat flow is the heat flow between the sub-layer “nL+1” and the sub-layer “nL” and is equal to the liquid-to-interface heat flow ($\dot{Q}_I^L$) with the opposite sign ($-\dot{Q}_I^L$) at the interface sub-layer. The lower heat flow is the heat flow between the sub-layer “nL” and the sub-layer “nL-1” and is equal to the bottom-to-liquid heat flow with the opposite sign at the bottom ($-\dot{Q}_W^B$), as explained in Intra-Layer Heat Transfer (ILHT) model. The bottom-to-liquid heat flow is equal to zero because the bottom is neglected in spherical storage container as the one of Study case 7.

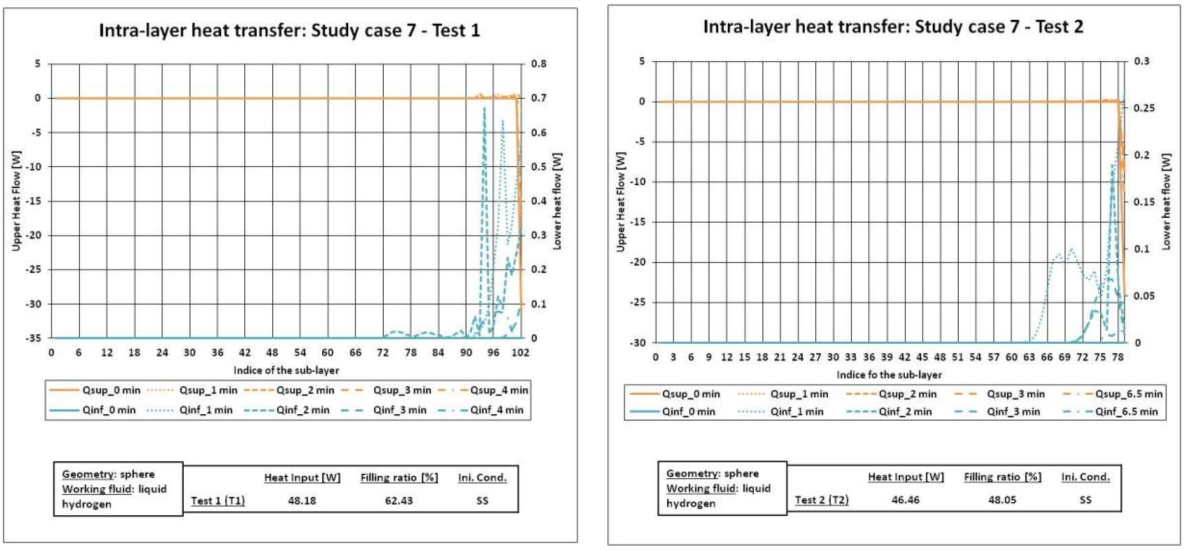

a) b)

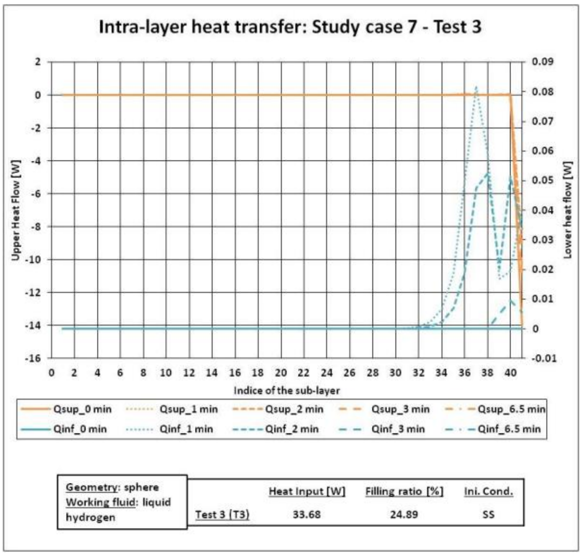

c)

Figure 189. Intra-layer heat transfer of Study case 7 (high heat fluxes): a) Test 1; b) Test 2; c) Test 3.

In Test 1 (high filling ratio), $\dot{Q}^{UP}$ and $\dot{Q}^{INF}$ are equal to zero in all sub-layers at the end of the steady state. Near the interface, $\dot{Q}^{UP}$ goes to the negative value of -32 W, which is the opposite sign value of the $\dot{Q}_I^L$ at steady state. During the self-pressurisation, the values of $\dot{Q}^{UP}$ and $\dot{Q}^{INF}$ remain equal to zero in the core and at the bottom. Near the interface, $\dot{Q}^{UP}$ and $\dot{Q}^{INF}$ produce peaks, whose maximum value is around 0.68 W for $\dot{Q}^{INF}$. At the interface, $\dot{Q}^{UP}$ is negative, contrarily to the Study cases at low and medium heat fluxes (see Section 8.1.4 and 8.2.5 of Chapter 6) where this heat flow is positive during the self-pressurisation. The space-distributions of these heat flows are qualitatively similar to the one of liquid bulk temperature gradient ($\frac{\partial T^L}{\partial x}$) (see Section 8.3.1 of Chapter 6).

In Test 2 (medium filling ratio), the space-distributions of $\dot{Q}^{UP}$ and $\dot{Q}^{INF}$ are qualitatively similar to those of Test 1 at the end of the steady state. As time passes, $\dot{Q}^{INF}$ creates peaks near the interface and these peaks are different at each time-point of the self-pressurisation. $\dot{Q}^{UP}$ produces peaks that are similar to the ones of $\dot{Q}^{INF}$, but they are not observable due to the scale of the axis. At the interface, $\dot{Q}^{UP}$ is negative, contrarily to the Study case at low and medium heat fluxes (see Section 8.1.4 and 8.2.5 of Chapter 6). The space-distributions of $\dot{Q}^{UP}$and $\dot{Q}^{INF}$ are similar to the ones of $\frac{\partial T^L}{\partial x}$ (see Section 8.3.1 of Chapter 6).

In Test 3 (low filling ratio), the initial space-distribution of $\dot{Q}^{UP}$ and $\dot{Q}^{INF}$ are similar to the ones of Tests 1 and 2. During the self-pressurisation, $\dot{Q}^{UP}$ increases approaching the interface and, at the interface sub-layer, it goes to negative values. In the same period of time, $\dot{Q}^{INF}$ increases near the interface, creating peaks whose maximum value is 0.082 W. The space-distribution of $\dot{Q}^{UP}$ and $\dot{Q}^{INF}$ are similar to the ones of the liquid bulk temperature gradient.

To sum up, the lower and the upper heat flows create peaks near the interface during the self-pressurisation, contrarily to the space-distribution of these heat flows of Study cases at low and medium heat fluxes (see Section 8.1.4 and 8.2.5 of Chapter 6). $\dot{Q}^{UP}$ is negative at the interface at medium and low filling ratio and it can be negative at high filling ratio. The space-distributions of $\dot{Q}^{UP}$ and $\dot{Q}^{INF}$ are similar to the one of the liquid bulk temperature as it occurs at low and medium heat fluxes (see Section 8.1.4 and 8.2.5 of Chapter 6).

8.3.5. Presentation of the results: heat transfer at the interface

Figure 190 shows the time-evolution of the liquid-to-interface ($\dot{Q}_I^L$) and vapour-to-interface ($\dot{Q}_I^V$) heat flows. The solid and the dotted lines respectively indicate $\dot{Q}_I^L$ and $\dot{Q}_I^V$ heat flows.

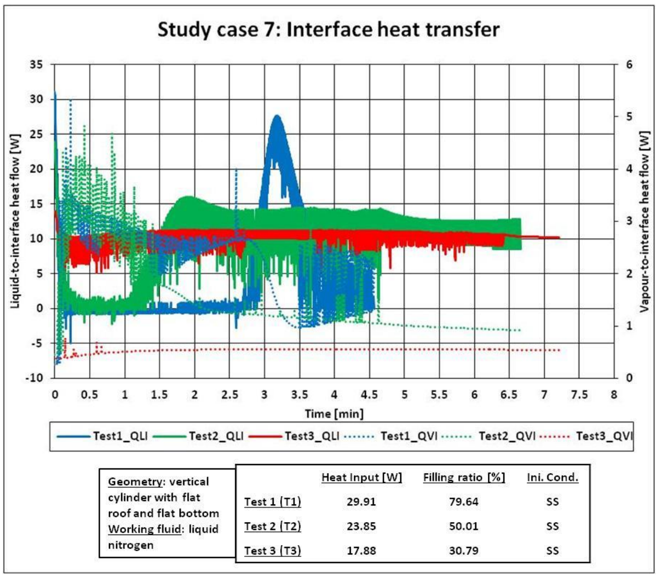

Geometry: vertical cylinder with flat roof and flat bottom
Working fluid: liquid nitrogen

	Heat Input [W]	Filling ratio [%]	Ini. Cond.
Test 1 (T1)	29.91	79.64	SS
Test 2 (T2)	23.85	50.01	SS
Test 3 (T3)	17.88	30.79	SS

Figure 190. Heat transfer at the interface for the Study cases 7 (high heat fluxes).

In Test 1 (high filling ratio), $\dot{Q}_I^L$ drops from the value of 31 W to the value of -2.3 W when the storage container is closed, after the steady state. After these initial drops, $\dot{Q}_I^L$ increases and it fluctuates around the average value of 0 W in the period of time between 0.4 to 2.6 minutes. After this period, $\dot{Q}_I^L$ keeps fluctuating, but the average value increases, creating a peak at 3.25 minutes, whose value is around 2.7 W. After these peaks, $\dot{Q}_I^L$ fluctuates and the average value of these fluctuations is around 3 W. $\dot{Q}_I^V$ increases from the value of 0.25 W to the value of 3.4 W at the beginning of the self-pressurisation. After this increment, $\dot{Q}_I^V$ creates two peaks, whose maximum value is around 5.3 W. After these peaks, $\dot{Q}_I^V$ fluctuates and the average value decreases until 2.5 minutes are reached. Then, $\dot{Q}_I^V$ creates a peack and, at 2.7 minutes, it decreases without fluctuations. After 3.5 minutes, $\dot{Q}_I^V$ fluctuates. So, the time-evolution of $\dot{Q}_I^V$ is often qualitatively symmetrical to the one of $\dot{Q}_I^L$.

In Test 2 (medium filling ratio), $\dot{Q}_I^L$ drops from the steady state value of 23 W to the value of -0.09 W, at the end of the steady state. After this initial drop, $\dot{Q}_I^L$ fluctuates, but the average value remains constant between 0.2 and 1.2 minutes. After this period, $\dot{Q}_I^L$ fluctuates and the average value increases creating a peak at 1.8 minutes. After this peak, the average value of the fluctuations of $\dot{Q}_I^L$ decreases and it remains constant. $\dot{Q}_I^V$ increases from the value of 0.4 W to the value of 1.3 W at the end of the steady state. After this increment, this heat flow fluctuates 0.5 and 1.5 minutes and the average value of these fluctuations decreases. After 2 minutes, the fluctuations of $\dot{Q}_I^V$ stop, except for some local peaks, and the value of this heat flow decreases in time.

In Test 3 (low filling ratio), $\dot{Q}_I^L$ decreases from the value of 14 W to the value of 9 W. After this decrement, this heat flow fluctuates for all the self-pressurisation, except for the last minute of the self-pressurisation. The average value of the fluctuations of $\dot{Q}_I^L$ remains constant during the self-pressurisation and it is always positive. $\dot{Q}_I^V$ slightly increases in the first minute of the self-pressurisation. Except for some small peaks, $\dot{Q}_I^V$ is constant during the self-pressurisation.

To sum-up, $\dot{Q}_I^L$ and $\dot{Q}_I^V$ fluctuate during the self-pressurisation at high and medium filling ratios. At high and medium filling ratios, the average value of these fluctuations creates a peak. At low filling ratio, this average value is more or less constant. At the same time-point of the self-pressurisation, $\dot{Q}_I^L$ increases with the reduction of the filling ratio and the values of this heat flux at low filing ratio are positive, indicating the heat flows from the liquid to the interface, contrarily to the previous model. $\dot{Q}_I^V$ increases with the increment of the filling ratio, contrarilyto the case at medium heat fluxes (see Section 8.2.5 of Chapter 6).

8.3.6. Presentation of the results: net mass flow

Figure 191 presents the time-evolution of the net mass flow ($\dot{m}_N$).

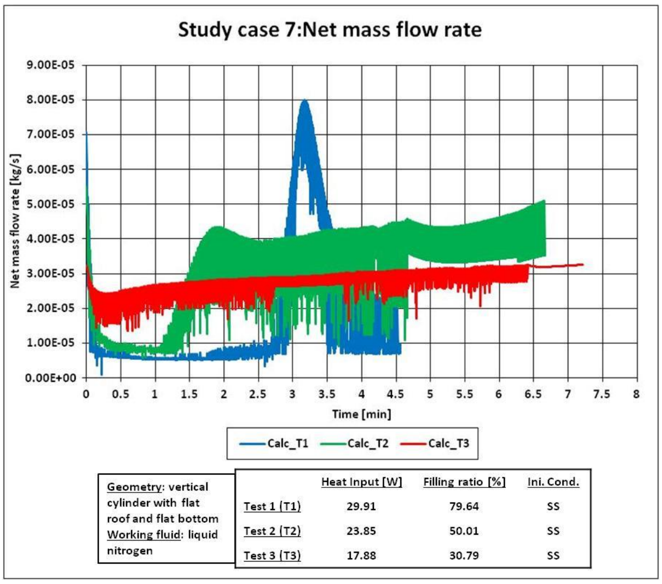

Figure 191. Net mass flow for the Study cases 7 (high heat fluxes).

In Test 1 (high filling ratio), $\dot{m}_N$ rapidly decreases at the beginning of the self-pressurisation and the value of this mass flow drops from $7.0 \cdot 10^{-5}$ kg/s to $9.1 \cdot 10^{-6}$ kg/s. After this drop, $\dot{m}_N$ slightly fluctuates between 0.2 and 1.7 minutes and the average value of these fluctuations is more or less constant in this period of time. After 1.7 minutes, the fluctuations of $\dot{m}_N$ increases and, after 1.6 minutes, the average value of these fluctuations increases, creating a peaks at 3.2 minutes, as done by QLI (see Section 8.3.5 of Chapter 6). After 3.5 minutes, the fluctuation of $\dot{m}_N$ increases in amplitude, but their average value is constant.

In Test 2 (medium filling ratio), the value of $\dot{m}_N$ drops from the value of $5.5 \cdot 10^{-5}$ kg/s to the value of $1.7 \cdot 10^{-5}$ kg/s, at the end of the steady state. After the initial drop, $\dot{m}_N$ fluctuates and their average value is more or less constant between 0.5 and 1.1 minutes. After this period, the oscillations increase in amplitude and their average value increases creating a peak at 1.9 minutes, as done by QLI (see Section 8.3.5 of Chapter 6). After this peak, the amplitude of the oscillations of $\dot{m}_N$ increases and their average value slightly increases.

In Test 3 (low filling ratio), $\dot{m}_N$ decreases from the value of $3.2 \cdot 10^{-5}$ kg/s to $1.8 \cdot 10^{-5}$ kg/s, contrarily to the previous tests where the initial decrement is much higher than the one observed for this test. After the initial decrement, $\dot{m}_N$ fluctuates and their average value slightly increases. The amplitude of these fluctuations is lower than the one of Tests 1 and 2. After 6.5 minutes, $\dot{m}_N$ does not fluctuate.

To sum up, $\dot{m}_N$ fluctuates at any filing ratio, but the amplitude of these oscillations is the highest at medium filing ratio but the lowest at low filling ratio. The initial decrement of $\dot{m}_N$ reduces with the reduction of the initial filling ratio. At high and medium filling ratios, $\dot{m}_N$ produces peak, whose size increases with the increment of the filling ratio. The time-evolution of the net mass flow is qualitatively similar to the one of $\dot{Q}_I^L$. Except for some negative peaks at high filling ratio, $\dot{m}_N$ is always positive, indicating the net evaporation occurs during the self-pressurisation at any filling ratio.

8.3.7. Presentation of the results: pressure

Figure 192 shows the calculated time-evolution of the pressure against the experimental data, during the self-pressurisation at high heat fluxes. The dots are the experimental data and the continuous lines are the computed values of the pressure.

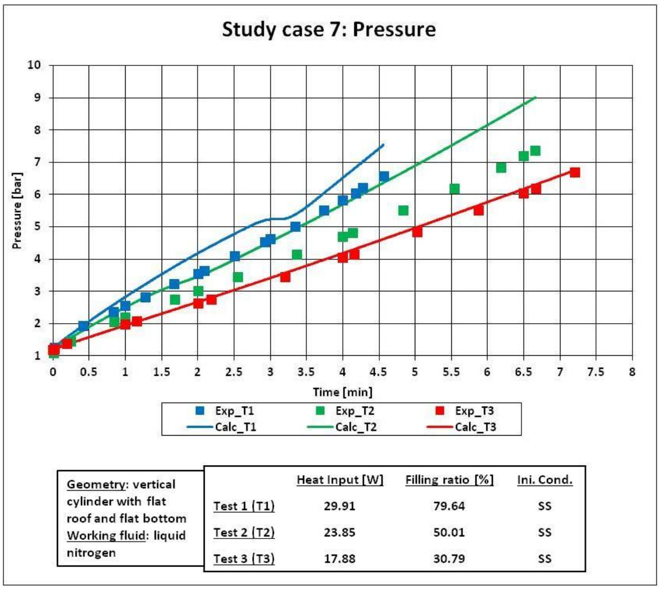

Geometry: vertical cylinder with flat roof and flat bottom
Working fluid: liquid nitrogen

	Heat Input [W]	Filling ratio [%]	Ini. Cond.
Test 1 (T1)	29.91	79.64	SS
Test 2 (T2)	23.85	50.01	SS
Test 3 (T3)	17.88	30.79	SS

Figure 192. Computed and experimental pressure for the Study case 7 (high heat fluxes).

In Test 1 (high filling ratio), the increment of the calculated pressure agrees with the experimental data in the first 0.5 minutes of the self-pressurisation. After this time, the calculated pressure is higher than the experimental one. At 3 minutes, the calculated increment of pressure becomes zero and, at 3.1 minutes, the calculated pressure increases with a rate that is higher than the previous one. The time-evolution of the calculated pressure does not agree with the experimental data.

In Test 2 (medium filling ratio), the calculated pressure is higher than the experimental one during all the self-pressurisation phase. At 1.7 minutes, the calculated pressure increment first slightly decreases then slightly increases with a rate that is higher than that between 0 and 1.5 minutes. The calculated pressure is qualitatively in agreement with experimental data, but the calculated pressure is higher than the measured one. The difference between the calculated and the measured pressure is of 1.6 bar at the end of the self-pressurisation.

In Test 3 (low filling ratio), the calculated pressure agrees with the experimental data during the whole self-pressurisation.

To sum up, the calculated pressure does not agree with the experimental data at high and medium filling ratios because the calculated pressure increment rate is higher than the experimental one. At high filling ratio, the calculated time-evolution of the pressure has a flex point with horizontal tangent, which is not experimentally observed. The same flex point occurs at medium filling ratio, but it is almost negligible.

8.3.8. Presentation of the results: temperature profile in liquid

Figure 193 show the space-evolution of the computed liquid temperature profile at different time-point against the experimental values, during the self-pressurisation at high heat fluxes, for Study case 7. In Test 1, the time-points considered are respectively called “t_0”, “t_1”, “t_2”, “t_3” and “t_4”, which correspond to 0 minutes, 1 minutes, 2 minutes, 3 minutes and 4 minutes of the self-pressurisation time, respectively. In Test 2 and 3, the time-points of the Test 1 are considered, except for “t_4”. This time-point is substituted by time-point “$t_{6.5}$”, which corresponds to 6.5 minutes. The markers are the experimental data and the lines are the computed values of the pressure.

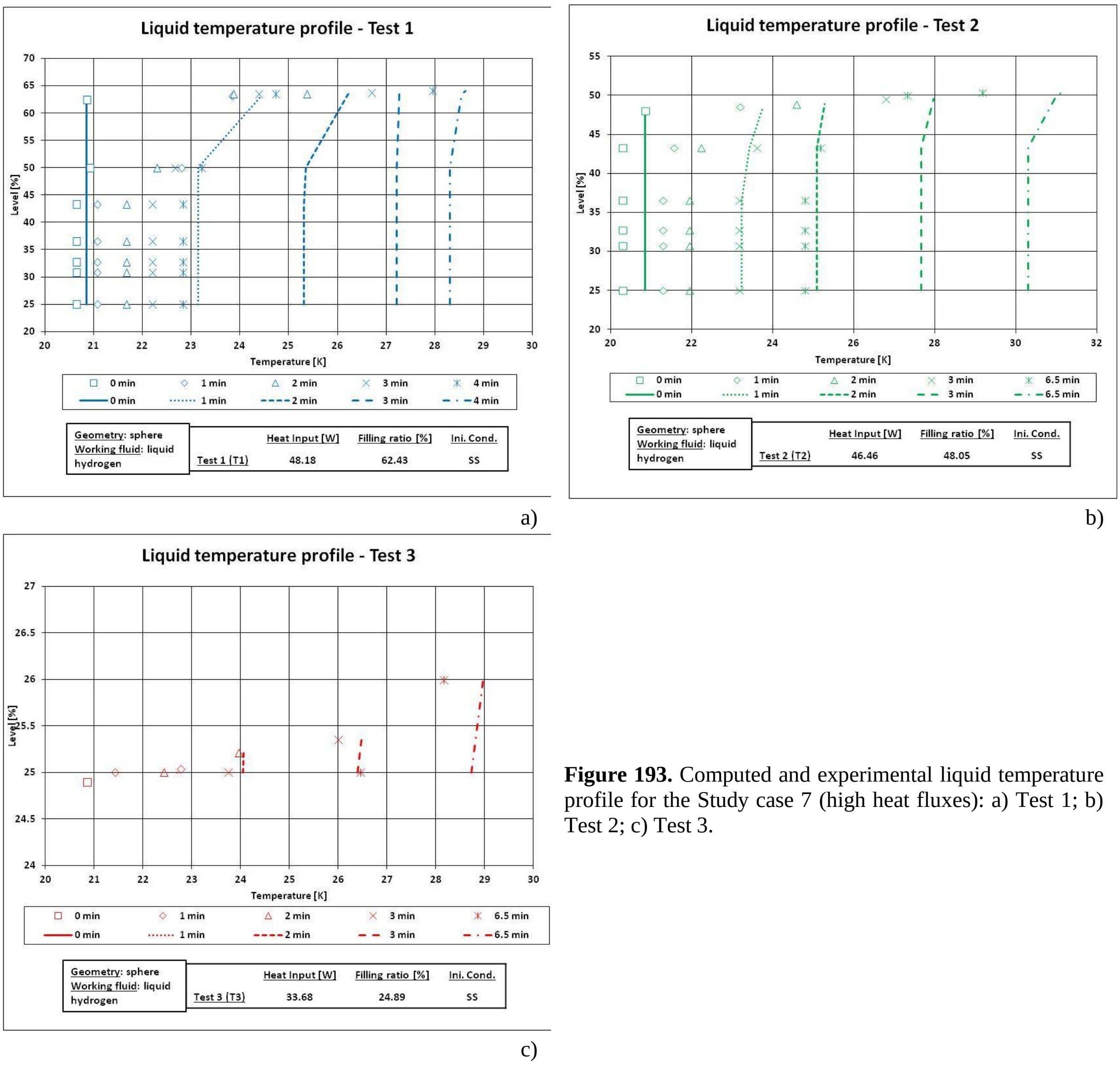

Figure 193. Computed and experimental liquid temperature profile for the Study case 7 (high heat fluxes): a) Test 1; b) Test 2; c) Test 3.

In Test 1 (high filling ratio), the calculated liquid temperature profile at “t_0” is flat and agrees with the experimental data. At “t_1”, the calculated temperature profile is flat between 0 and 50 % of the level. After this point, the liquid calculated temperature linearly increases. The calculated values of the temperature of the core are higher than the experimental one, and the increment near the interface is lower than the experimental one. At “t_2”, “t_3” and “t_4”, the space evolution of the calculated temperature profile is qualitatively similar to the one at “t_1”, but the rate of the increment of the liquid temperature near the interface reduces as time passes. So, the LS model predicts the thermal de-stratification, contrarily to the experimental data.

In Test 2 (medium filling ratio), the calculated initial temperature profile is flat and close to the experimental data. At "t_1", "t_2", "t_3" and "t_4", the calculated liquid temperature profile is flat in the core, and it increases near the interface. The calculated rate of this increment at "t_4" is higher than the one at "t_1", "t_2" and "t_3", whose rate of increment is similar. The calculated temperature profiles are not in agreement with the experimental data.

The experimental points at "t_0" and "t_1" related to Test 3 (low filling ratio) are not enough to infer a particular trend for the temperature profile. At "t_2", "t_3" and "$t_{6.5}$", the calculated temperature profile are not in agreement with the experimental data seeing that the rate of temperature increment is lower than the experimental one.

To sum up, the calculated temperature profiles do not agree with the experimental data because the computed values of the liquid temperature in the core are higher than the experimental ones, and the calculated rate of the increment near the interface is lower than the measured one.

9. Discussion

The results shown in previous sections are discussed to underline the reasons of the observed behaviour and deviations.

Section 9.1 discusses the results of the fluid-dynamics at the wet side wall. Section 9.2 examines the space and time-evolution of the fluid-dynamics in the liquid. Section 9.3 studies the heat transfer at the wet side wall. Section 9.4 examines the intra-layer heat transfer. Section 9.5 and 9.6 discuss the interface heat transfer and the net mass flow, respectively. Section 9.7 and 9.8 studies the pressure and the liquid temperature profile. Section 9.9 explains the conclusions and Section 9.10 presents the perspectives.

9.1.Fluid-dynamics at the wet side wall

As it is described in Section 8.1.1, 8.2.1 and 8.3.1 of Chapter 6, the mass flow in the boundary layer of the wet side wall ($\dot{m}^{SW}$) is affected by the liquid bulk temperature gradient ($\frac{\partial T^L}{\partial x}$). So the results of $\frac{\partial T^L}{\partial x}$ in the liquid stratification model (LS model) are discussed before the ones related to $\dot{m}^{SW}$.

Section 9.1.1 discuss the space-distribution and the time-evoltuion of $\frac{\partial T^L}{\partial x}$. Seciton 9.1.2 analyses how $\dot{m}^{SW}$ evolves in time and how it is distributed in the sub-layers.

9.1.1. Liquid bulk temperature gradient

The liquid bulk temperature gradient ($\frac{\partial T^L}{\partial x}$) is calculated with the finite differences approach, as it is explained in Section 1.5.2 of Chapter 6. In this method, Equation 284 compute $\frac{\partial T^L}{\partial x}$ for the core and interface sub-layers and Equation 285 calcualte $\frac{\partial T^L}{\partial x}$ for the bottom sub-layer. These equations calculate $\frac{\partial T^L}{\partial x}$ as the ratio between the difference in bulk temperatures between two adjacent sub-layers and the thickness of the sub-layer.

As it is described in Section 8.1.1, 8.2.1 and 8.3.1 of Chapter 6, the bulk liquid temperature gradient is equal to zero in the bottom of the liquid, and it slightly increases in the core of the liquid. Near the interface, this gradient monotonically increases at low and medium heat fluxes. So, the increment of $\frac{\partial T^L}{\partial x}$ is caused by the increment of the liquid temperature near the interface. The liquid temperature increases at the interface due to the accumulation of sensible heat, which comes from the side wall and from the interface. At high heat fluxes, the $\frac{\partial T^L}{\partial x}$ grows up creating peaks. Hence, the liquid temperature does not monotonically increase near the interface as occuring at low and medium heat fluxes, due to the strong fluctuations of the interface heat flows. This variable fluctuates due to the accumulation of the sensible heat at the interface sub-layer, which produces a high variation of the time-derivate of the liquid bulk temperature of this sub-layer. This variation produces cold and hot spots. So, the computed temperature becomes uniform due to the calculation prodeceure of Section 1.5.3 of Chapter 6. The values of $\frac{\partial T^L}{\partial x}$ at medium heat fluxes are higher than the one at low and high heat fluxes because the increment of the liquid temperature near the interface is the highest at medium heat fluxes. In fact, the computed pressure at medium heat fluxes (Study case 5) is higher than the one at high heat fluxes.

Due to the lack of experimental data of liquid bulk temperature gradient, the capacity of LS in computed this gradient cannot be evaluated.

9.1.2. Mass flow in the boundary layer of the wet side wall

The mass flow in the boundary layer of the wet side wall ($\dot{m}^{SW}$) is calculated with the Storage Boundary Layer (SBL) model (see Section 6 of Chapter 6). The SBL model of liquid stratification model (LS model) is mainly based on the theory of the SBL model of the homogenous (H) model, except for the fluid-dynamics regime and the calculation of the number of the sub-space-points of the numerical integration. So, the mass flow in the boundary layer is calculated as product of the boundary layer variables U and δ_M, which are affected by the liquid bulk temperature gradient ($\frac{\partial T^L}{\partial x}$).

$\dot{m}^{SW}$ linearly increases at the end of the steady state because $\frac{\partial T^L}{\partial x}$ is equal to zero. During the self-pressurisation, $\dot{m}^{SW}$ only increases at the bottom, where $\frac{\partial T^L}{\partial x}$ is equal to zero. As $\frac{\partial T^L}{\partial x}$ increases in the core of the liquid, $\dot{m}^{SW}$ decreases because $\frac{\partial T^L}{\partial x}$ reduces the values of U and δ_M, extracting mass, thus momentum and energy from the boundary layer. Near the interface, $\frac{\partial T^L}{\partial x}$ faster than in the core and $\dot{m}^{SW}$ rapidly decreases as it is observed in Section 8.1.1, 8.2.1 and 8.3.1 of Chapter 6. At high filling ratio, $\dot{m}^{SW}$ in the boundary layer of the wet side wall goes to zero because $\frac{\partial T^L}{\partial x}$ is high to reduce the boundary layer variables U and δ_M to zero. At high heat fluxes, $\dot{m}^{SW}$ does not monotonically reduce due to the peaks of $\frac{\partial T^L}{\partial x}$. The reduction of $\dot{m}^{SW}$ with the increment of $\frac{\partial T^L}{\partial x}$ is theoretically correct because this gradient reduce the energy in the boundary layer. Experimental values of thickness and velocity in the boundary layer of the wet (and dry) side wall of storage container with cryogenic liquid at steady state and during self-pressurisation do not exist. So, it cannot be stated that the fluid-dynamics of the LS model agrees or not with the experimental data.

9.2. Fluid-dynamics in the liquid

The fluid-dynamics in the liquid is characterized by two variables: the descending mass flow in the bulk of the liquid ($\dot{m}^D$) and the rising mass flow of the bottom ($\dot{m}^B$). $\dot{m}^D$ is affected by the mass flow in the boundary layer of the wet side wall ($\dot{m}^{SW}$) and by $\dot{m}^B$. So, the fluid-dynamics in the liquid is presented after the discussion of $\dot{m}^{SW}$ and $\dot{m}^B$ is discussed before $\dot{m}^D$. The space-distributions of $\dot{m}^D$ and $\dot{m}^B$ cannot be compared to data because of the lack of experimental data. Hence, the model to compute the flow distribution in the liquid cannot be validated.

Section 9.2.1 discusses the rising flow of the bottom. Section 9.2.2 analyses the descending flow.

9.2.1. Rising flow of the bottom

Due to the heat inputs at the bottom, the liquid flows upward due to the natural convection. rising mass flow of the bottom ($\dot{m}^B$) is calculated using the Exact Boundary Layer (EBL) approach of Storage Boundary Layer (SBL) model applied at the flat ends (see Section 1 of Appendix P). $\dot{m}^B$ is constant in each sub-layer and it goes to zero when the bulk temperature of the sub-layer is lower than the one of the upper sub-layer, or when the mass flow in the boundary layer is higher than mB at the bottom.

As it described in Section 8.3.2 of Chapter 6, $\dot{m}^B$ is equal to zero during the self-pressurisation and the beginning of the self-pressurisation when the storage container does not have flat ends, due to the theory of the SBL model. As it is described in Section 8.1.2 and 8.2.2 of Chapter 6, $\dot{m}^{B}$ is constant in the bottom of the liquid due to the theory used to compute this variable. At the end of the steady state, $\dot{m}^{B}$ is not present in all sub-layers because it becomes lower than The mass flow in the boundary layer of the wet side wall ($\dot{m}^{SW}$). As time passes, the liquid temperature increases in the core and the stratified region expands to the bottom. The upper sub-layer becomes hotter than the lower sub-layer, and the buoyancy forces are adverse to the motion of $\dot{m}^{B}$. As consequence, the zone where $\dot{m}^{B}$ is present reduces during the self-pressurisation, as it is observed in Section 8.1.2 and 8.2.2 of Chapter 6 for vertical storage container with flat ends.

9.2.2. Descending mass flow in the bulk of the liquid

The natural convection at the wet side wall produces the mass flow in the boundary layer of this side wall ($\dot{m}^{SW}$). The heat inputs at the bottom generates the rising flow of the bottom ($\dot{m}^{B}$). The direction and the value, of the descending flow ($\dot{m}^{D}$) are mainly affected by these mass flows, as it is reported in Section 2.6 of Chapter 6. So, The increments of $\dot{m}^{SW}$ and $\dot{m}^{B}$ increase $\dot{m}^{D}$. $\dot{m}^{D}$ is computed an iterative procedure, which is described in Section 3 of Chapter 6.

As it described in Section 8.3.2 of Chapter 6, the space-distribution of $\dot{m}^{D}$ is equal to the $\dot{m}^{SW}$, because mB is equal to zero in spherical storage container. As it is described in Section 8.1.2 and 8.2.2 of Chapter 6, $\dot{m}^{D}$ increases from the bottom to the core, but this mass flow drops down in the sub-layer where $\dot{m}^{B}$ goes to zero. So, the space-distribution of $\dot{m}^{D}$ is only affected by $\dot{m}^{SW}$ in ellipsoid and spherical storage tanks. In vertical storage tanks with flat ends, $\dot{m}^{D}$ is affected by this boundary layer mass flow and by $\dot{m}^{B}$.

9.3. Heat transfer at the wet side wall

The heat transfer at the wet side wall affects the thermal distribution of the liquid. This heat transfer can be analyzed with the results of the wet side wall heat transfer coefficient (h_{W}^{SL}) and the wet side wall temperature (T_{W}^{SL}).

Section 9.3.1 discusses the heat transfer coefficient at the wet side wall. Section 9.3.2 analyses the wet side wall temperature.

9.3.1. Heat transfer coefficient

The wet side wall heat transfer coefficient (h_{W}^{SL}) is calculated with the boundary layer approach (see Section 4.6 of Chapter 4). In this approach, h_{W}^{SL} is directly calculated (i) from the boundary layer variables U and δ_M (Equation 204, Equation 205 and Equation 206), if these variables are both higher than zero, or (ii) from the conduction equation (Equation 207), if one of the boundary layer variables is equal to zero.

As it is described in Section 8.1.3, 8.2.3 and 8.3.3 of Chapter 6, h_{W}^{SL} increases from the bottom to the interface sub-layer at the end of the steady state. This increment occurs when the mass flow rate in the boundary layer of the wet side wall ($\dot{m}^{SW}$) increases because the bulk temperature gradient ($\frac{\partial T^{L}}{\partial x}$) is equal to zero. So, hwSL increases because of $\dot{m}^{SW}$, thus the boundary layer variables U and δ_M increase. During the self-pressurisation, h_{W}^{SL} decreases approaching the interface, as it is described in Section 8.1.3, 8.2.3 and 8.3.3 of Chapter 6. This decrement occurs when $\dot{m}^{SW}$ decreases, due to the increment of $\frac{\partial T^{L}}{\partial x}$. So, $\frac{\partial T^{L}}{\partial x}$ reduces the boundary layer variables U and δ_M, and it decreases h_{W}^{SL}. The decrement of h_w^{SL} with the increment of $\frac{\partial T^L}{\partial x}$ does not always occurs as it is indicated by the Study cases at high heat fluxes (see Section 8.3.3 of Chapter 6). At these conditions, h_w^{SL} can form some picks when the bulk temperature gradient increases. The formula of the turbulent heat transfer coefficient (Equation 206) is used and hwSL is calculated as function of $U^{5/4}$ and of $\delta_M^{-\frac{1}{4}}$. $\frac{\partial T^L}{\partial x}$ reduces the momentum thickness of the boundary layer (δ_M), as it is explained in Equation 179. The reduction of δ_M can increase U, producing the peaks of hwSL at high heat fluxes. At high filling ratio and high heat inputs of low heat fluxes storage container, and at high filling ratio of medium heat fluxes storage tank, the value of hwSL drops because the value of the boundary layer variables U and δ_M are equal to zero and h_w^{SL} is calculated with the conductive equation. Due to the lack of the experimental data, the computed value of h_w^{SL} cannot be compared with measured value and the model of the heat transfer cannot be validated.

9.3.2. Wet side wall temperature

The weet side wall temperature (T_w^{SL}) is calculated with Equation 533, as the ratio between the wet wall-to-liquid heat flow and the heat transfer coefficient at the wet side wall (h_w^{SL}), as explained in Section 3.2.1 of Chapter 6. So, this temperature increases if the wet wall-to-liquid heat flow increases and if the heat transfer coefficient reduces. The wet wall-to-liquid heat flow is iteratively computed as it is explained in Appendix AE, using the hypotheses of intra side wall heat flow and of no conduction (assumption b) and c) of Section 5.1.1 of Chapter 6).

As it is observed in Section 8.1.3, 8.2.3 and 8.3.3 of Chapter 6, h_w^{SL} decreases in the first sub-layers, which are close to the bulk, and it is almost constant during the self-pressurisation. In the first sub-layer, h_w^{SL} rapidly increases. So, the reduction of T_w^{SL} is caused by such increment of h_w^{SL}. In the core, h_w^{SL} slightly decreases, causing the slight increment of T_w^{SL}. As the interface is approached, h_w^{SL} rapidly reduces and T_w^{SL} increases as indicated by Equation 533. So, T_w^{SL} increases as it is observed in Section 8.1.3, 8.2.3 and 8.3.3 of Chapter 6. At high filling ratio and medium heat flux, T_w^{SL} is as warm as the ullage at the interface sub-layer because h_w^{SL} is almost equal to zero and the heat coming from the dry side wall is not transfer along the side wall. So, this situation is not physical. Due to the lack of the experimental data, the computed value of T_w^{SL} cannot be compared with measured value and the model of the heat transfer cannot be validated.

9.4. Intra-layer heat transfer

The temperature increases near the interface and the heat can be transferred across the stratified region, as function of the fluid-dynamics in the liquid. The intra-layer heat transfer is characterized by the upper and lower heat flows ($\dot{Q}^{UP}$ and $\dot{Q}^{INF}$), which are calculated with the Intra-Layer Heat Transfer (ILHT) model (see Section 4 of Chapter 6), as function of (i) the fluid-dynamics condition and (ii) of the difference in temperature across the sub-layer , thus the liquid bulk temperature gradient ($\frac{\partial T^L}{\partial x}$).

As it is described in Section 8.1.4, 8.2.4 and 8.3.4 of Chapter 6, these heat flows are almost equal to zero in the bottom and in the core of the liquid because the temperature gradient of the bulk liquid is negligible. As the interface is approached, the bulk temperature gradient increases, and the space-distributions of $\dot{Q}^{UP}$ and $\dot{Q}^{INF}$ increases. Hence, the intra-layer heat flows are directly affected by $\frac{\partial T^L}{\partial x}$.

9.5.Heat transfer at the interface

The interface heat transfer is composed by the vapour-to-interface and the liquid-to-interface heat flows ($\dot{Q}_I^V$ and $\dot{Q}_I^L$), which are calculated with the Interface Heat Transfer (IHT) model (see Section 7 of Chapter 6). In this model, $\dot{Q}_I^V$ is affected by net mass flow ($\dot{m}_N$), thus $\dot{Q}_I^L$ is discussed before $\dot{Q}_I^V$.

Section 9.5.1 discusses the liquid-to-interface heat flow. Section 9.5.2 analyses the vapour-to-interface heat flow.

9.5.1. Liquid-to-interface heat flow

The liquid-to-inteface heat flow ($\dot{Q}_I^L$) is calculated with Equation 534, using the dominant heat transfer mechanism approach. This approach states that the mechanism of the liquid-to-interface heat transfer, thus the formula to compute $\dot{Q}_I^L$, is the one with the highest absolute value between the boundary layer (Equation 535), local convection (Equation 536) and conduction (Equation 539) mechanisms. The boundary layer mechanism is a function of the difference in temperature between the temperature of the interface sub-layer of the boundary layer and the interface. This boundary layer temperature is affected by the dry side wall-to-interface heat flow, which enters the interface sub-layer of the wet side wall. The local convection and conduction mechanisms depend on the difference between the liquid and the interface temperatures. This difference frequently varies during the self-pressurisation because the excessive accumulation of the sensible heat at the interface sub-layer produces large variations of the time-derivate of the liquid temperature in this sub-layer. These variations can produce values of temperature of the interface sub-layer than are higher than the interface. This condition is rarely in line with the experimental data of temperature profile.

At the end of the steady state, the boundary layer mechanism is the dominant one because the difference in temperature between the interface and the average liquid is almost negligible. As it is described in Section 8.1.5, 8.2.5 and 8.3.5 of Chapter 6, $\dot{Q}_I^L$ decreases when the self-pressurisation starts because the difference between the temperature of the interface sub-layer of the boundary layer and that of the interface reduces. This reduction is, however, lower than the one of the previous models because the bulk liquid temperature near the interface, thus boundary layer temperature, increases due to the accumulation of sensible heat, which produces large variation of the time-derivate of the liqud temperature of the interface sub-layer. As a consequence, $\dot{Q}_I^L$ is higher than the one of the previous models and the thermal energy can be transferred from the liquid to the interface during the self-pressurisation, as it is described in Section 8.1.5, 8.2.5 and 8.3.5 of Chapter 6. As the heat flow of the boundary layer mechanism decreases, this mechanism cannot be anymore the dominant one and the local convection mechanism often takes the lead role in the transfer of heat at the interface. As a consequence, $\dot{Q}_I^L$ fluctuates during the self-pressurisation, as it is observed in Section 8.1.5, 8.2.5 and 8.3.5 of Chapter 6, because the condition of using one of these mechanisms cannot be calculated by the model. Finally, $\dot{Q}_I^L$ usually increases with the reduction of the initial filling ratio.

9.5.2. Vapour-to-interface heat flow

The vapour-to-interface heat flow ($\dot{Q}_I^V$) is calculated with Equation 270, using the model reported in Section 4.2 of Chapter 5. This approach calculates $\dot{Q}_I^V$ as sum of three contributions: the local natural convection (Equation 271), the heat transfer across the virtual sub-layer (Equation 277) and the heat flow due to the descending flow in the ullage bulk (Equation 275). The last contribution is a function of the net mass flow ($\dot{m}_N$), which is calculated with the liquid-to interface heat flow.

As it is described in Section 8.1.5, 8.2.5 and 8.3.5 of Chapter 6, $\dot{Q}_I^V$ often oscillates during the self-pressurisation and it can produce negative and positive peaks. These fluctuations and these peaks usually occur when $\dot{Q}_I^L$ oscillates. As a consequence, time-evolution of $\dot{Q}_I^V$ is affected by $\dot{Q}_I^L$ because the model of the vapour-to-interface heat transfer depends on $\dot{m}_N$. $\dot{Q}_I^V$ increases with the increment of the heat fluxes. At high heat fluxes, the reduction of filling ratio reduces $\dot{Q}_I^V$. At medium and low filing ratio, $\dot{Q}_I^V$ increases with the reduction of the initial liquid level.

9.6.Net mass flow

The net mass flow ($\dot{m}_N$) is calculated with an iterative procedure (see Appendix V) because the vapour-to-interface heat flow ($\dot{Q}_I^V$) is a function of this mass flow. The liquid stratification model (LS model) uses the same algorithm of Appendix V, which is developed in homogenous (H 2.0) model 2.0. The interfacial conservation law of the energy of the LS model (Equation 540) is different from the one of the H 2.0 model, which is equal to the one of the homogeneous model (H model) (Equation 215). In the LS model, the dry side wall-to-interface heat flow is neglected, and only the vapour-to-interface ($\dot{Q}_I^V$) and the liquid-to-interface ($\dot{Q}_I^L$) heat flows are considered.

$\dot{m}_N$ decreases at the end of the steady state due to the reduction of $\dot{Q}_I^L$, as it is described in Section 8.1.6, 8.2.6 and 8.3.6 of Chapter 6. This decrement reduces with the reduction of the initial filing ratio and it is lower than one of the previous model. As time passes, $\dot{m}_N$ fluctuates as done by $\dot{Q}_I^L$. So, this mass flow is mainly affected by the time-evolution of $\dot{Q}_I^L$. The value of $\dot{m}_N$ is usually positive, even during the initial transient, indicating that the net evaporation can occurs during the self-pressurisation. The values of $\dot{m}_N$ increase with the reduction of the initial liquid level.

9.7.Pressure

The pressure is calculated from the pressure-evolution equation (Equation 483), with the solver of the Ordinary Differential Equations (ODEs) system, which is the method of Runge-Kutta-Fehlberg with Cash-Karp parameters [131] (RKF-CKp) (see Section 5 of Chapter 3). Considering that the storage container is close during the self-pressurisation, the time-derivate of the pressure depends on the coefficient F''^P, F''^{HL}, A''^P, A''^{HL}, C''^P and C''^{HL}. The coefficients F''^P and A''^P affect more the time-derivate of the pressure than the other coefficients and these coefficients mainly depend on the net mass flow ($\dot{m}_N$), the ullage volume, the derivate of the density respect to the temperature and the accumulation of sensible heat in the ullage. In storage container with liquid nitrogen (LN_2), $\dot{m}_N$ is much more important on the temperature evolution than the derivate of the density respect to the temperature. This derivate can be as significant as $\dot{m}_N$ in affecting the evolution of pressure in storage container with liquid hydrogen (LH_2). $\dot{m}_N$ is mainly affected by liquid-to-interface heat flow ($\dot{Q}_I^L$). So the time-derivate is directly affected by this heat flow.

At low heat fluxes (Study case 1 and 2), the calculated pressure agrees with the experimental data at high heat input, and at medium-low and low filling ratios. So, $\dot{m}_N$, thus $\dot{Q}_I^L$, is calculated as quantitatively close as possible to the data. At high, high-medium and medium filling ratios, the calculated pressure is over-estimated. Hence, $\dot{Q}_I^L$ is over-estimated, indicating that liquid is warmer than it should be at the interface. This excess of thermal energy at the interface can be caused by the turbulent fluid-dynamics regime, which is assumed occuring at any value of the heat fluxes. At high and medium heat fluxes (Study case 5 and 7), the calculated pressure is higher than the experimental one, except for Test 3 of Study case 7, because $\dot{Q}_I^L$, thus $\dot{m}_N$ is overestimated. At medium and high heat fluxes, the fluid-dynamics regime at the wet side wall is turbulent, and the dry side wall-to-interface heat flow is higher than the one at low heat fluxes. So, the accumulation of sensible heat at the interface, which increases $\dot{Q}_I^L$, is caused by the hypothesis of no conduction, which neglect the heat transferred along the wet side wall, and which removes part of the heat coming from the dry side wall.

9.8. Liquid temperature profile

The temperature profiles are deduced from the values of the bulk liquid temperature in each sub-layer. These bulk temperatures are calculated from the liquid temperature evolution equations (see Table 126), with the method of method of Runge-Kutta-Fehlberg with Cash-Karp parameters [131] (RKF-CKpfor solving the Ordinary Differential Equations (ODEs) system. So, the time-derivates of the bulk liquid temperature are mainly affected by the coefficient $F''^{TL}_{n_L}$, which depends on the upper and lower heat flows ($\dot{Q}^{UP}$ and $\dot{Q}^{INF}$), the enthalpy flow of the descending flows ($\dot{m}^D$), the enthalpy flow of boundary layer-bulk mass flow and the enthalpy flow of the rising flow of the bottom ($\dot{m}^B$). This latter is more important than $\dot{Q}^{UP}$, $\dot{Q}^{INF}$, $\dot{m}^D$, $\dot{m}^B$ and the other enthalpy flows..

As it is observed in Section 8.1.8, 8.2.8 and 8.3.8 of Chapter 6, the liquid temperature increases from the core to the interface, as done by the bulk temperature gradient. The mass boundary layer reduces in this part of the liquid and the boundary layer-bulk mass flow increases. As a consequence, the enthalpy flow of $\dot{m}^D$ increases and sensible heat is accumulated in the liquid, increasing the temperature near the interface. As time passes, this sensible heat is transferred to the lower sub-layer, but the rate of this transfer is lower than the measured one. The thermal energy exessively accumulates near the interface and this accumulation increases when the mass flow in the boundary layer of the wet side wall ($\dot{m}^{SW}$) is equal to zero, as occurs at high filling ratio and medium heat fluxes. The accumulation of sensible heat produces large variations of the time-derivate of the liquid temperature of the interface sub-layer. The temperature of this sub-layer can be lower than the one of the second-last sub-layer. So, the temperature profile is calculated as explained in Block 16 (see Section 1.5.3 of Chapter 6) and the temperature profile becomes flat, as occurs for the study cases with liquid hydrogen (LH$_2$) (Study case 4 and 6). The wet side wall must contribute to transfer heat from the sub-layer near the interface to the sub-layer of the core. In the core and in the bottom, the calculated liquid temperature often increases, contrarily to the experimental data, because the the space-distribution of $\dot{m}^B$, which affect the homogeneous region, is not correctly computed. The homogeneous region is calculated as the part of the liquid where $\dot{m}^B$ is higher than zero. So, the conditions used to set this mass flow equal to zero are often not physically correct.

9.9. Conclusion

The results of the fluid-dynamics and heat transfer at the wet side wall, fluid-dynamics in the liquid, intra-layer heat transfer, interface heat transfer, net mass, pressure and liquid temperature profiles have been analyzed.

This analysis proves the presence of a significant relation between the bulk temperature gradient and the fluid-dynamics at the side wall, which reduces with the increment of this gradient. At high filling ratio and low-medium heat fluxes, the liquid bulk temperature gradient ($\frac{\partial T^L}{\partial x}$) can block the mass flow in the boundary layer of the wet side wall ($\dot{m}^{SW}$) near the interface. The analysis of the results of the heat transfer at the wet side wall underlined the fundamental link with the fluid-dynamics, thus with $\frac{\partial T^L}{\partial x}$. The heat transfer coefficient of the wet side wall decreases near the interface because the natural convection is reduced by the bulk temperature gradient. As consequence, the wet side wall temperature increases at the interface. This temperature can become as hot as the ullage (i) at medium heat fluxes and (ii) when the mass flow in the boundary layer is equal to zero. So, the model of the heat transfer coefficient is not physically accurate in these conditions due to the hypothesis of no conduction (assumption c) of Section 5.1.1 of Chapter 6). As discussed in Section 9.4 of Chapter 6, the intra-layer heat flows are affected by $\frac{\partial T^L}{\partial x}$ because the space-distributions of the upper and of lower heat flows ($\dot{Q}^{UP}$ and $\dot{Q}^{INF}$) are equal to the one of $\frac{\partial T^L}{\partial x}$.

The liquid-to-interface heat flow ($\dot{Q}_I^L$) fluctuates during the self-pressurisation because of the approach of the dominant heat transfer mechanism. This approach is unsuitable because the difference in temperature at the interface is not stable, due to the accumulation of sensible heat at the interface. The fluctuations of $\dot{Q}_I^L$ affect the time-evolution of vapour-to-interface heat flow ($\dot{Q}_I^V$) and of the net mass flow ($\dot{m}_N$). As consequence, this heat flow and this mass flow oscillate during the self-pressurisation.

The calculated pressure is compared with the experimental data and the liquid stratification model (LS model) can compute the self-pressurisation in the following cases: high heat input; medium-low and low filling ratios at low heat fluxes; at high filling ratio and medium heat fluxes; low filling ratio at high heat fluxes. In other conditions, the calculated temperature is usually over-estimated because $\dot{m}_N$ higher than the one that it should be. So, the accumulation of heat at the interface is overestimated. This accumulation is caused by the hypothesis of turbulent fluid-dynamics regime at low heat fluxes and by the hypothesis of no conduction (assumption c) of Section 5.1.1 of Chapter 6) at medium and high heat fluxes. Respect to the previous models, the relation between the initial filling ratio and the pressure agrees with the experimental data because the pressure increases with the increment of the initial filling ratio at the medium and high heat fluxes. So, the hypothesis of discretized liquid (assumption b) of Section 1.2 of Chapter 6) qualitatively improved the calculation of the time-evolution of the pressure. The temperature profiles of the liquid are also compared with the experimental data. The shape of the temperature profile is affected by the fluid-dynamics in the bulk, in particular (i) by $\dot{m}^B$ and (ii) by the enthalpy flow of the boundary layer-to-bulk mass flow. In the core, the calculated temperature slightly increases and the calculated temperature profile are not in agreement with the experimental data in this zone. So, the space-distribution of $\dot{m}^B$ is not correctly computed because the conditions to set this mass flow to zero are not completely correct physically. The liquid temperature increases near the interface due to the enthalpy flow of the boundary-to-bulk mass flow, which increases with the increment of $\frac{\partial T^L}{\partial x}$. Near the interface, the calculated liquid temperature is usually higher than the experimental one, indicating that the sensible heat is accumulated with a rate that is higher than the one that can be deduced from the experimental data.

9.10. Summary and perspective

The homogeneous model 2.0 (H 2.0 model) (see Chapter 5) cannot calculate accurately the rate of self-pressurisation, as measured experimentaly, because of the liquid isothermal hypothesis. The virtual stratification of the ullage of H 2.0 model qualitatively and, often, quantitatively computes accurately the vapour temperature. So, the liquid stratification model (LS model) is developed under the hypothesis of the liquid discretisation (assumption b) of Section 1.2 of Chapter 6) and the hypothesis of vapour virtual discretisation (assumption a) of Section 1.2 of Chapter 6). As a consequence of this assumption, the number of the variables of the LS model is higher than the one of the H 2.0 model and the number of equations to compute these variable also increases. These equations are deduced from the mass and energy conservation laws of the ullage and of each sub-layer of the liquid. These equations are analytically solved to explicitly compute the time-derivate of the pressure, of the thickness of the sub-layer, of the bulk liquid temperature of each sub-layer, and of the vapour temperature. To compute these time-derivates, the heat flows at the internal surfaces of the storage container, the interface heat and mass flow, the intra-layer heat flows, the descending flow and the rising flow of the bottom have to be computed. The wet side wall-to-liquid heat flow is calculated at each sub-layer, (i) under the hypotheses of intra side wall heat transfer and of no conduction (assumptions b) and c) of Section 5.1.1 of Chapter 6), and (ii) using the heat transfer coefficient of the boundary layer approach. The dry side wall-to-vapour heat flow and the bottom-to-liquid heat flows are calculated as done in H 2.0 model. Vapour-to-interface heat flow ($\dot{Q}_I^V$) is calculated with the method of the H 2.0 model, which depends on the net mass flow ($\dot{m}_N$). the liquid-to-interface heat flow ($\dot{Q}_I^L$) is computed with the approach of dominant heat transfer mechanism. $\dot{m}_N$ is calculated with an iterative procedure as done in H 2.0 model, but the dry side wall-to-interface heat flow is only neglected in the interface energy conservation law. This heat flow is added to the interface sub-layer of the wet side wall (see Figure 133). The descending flow ($\dot{m}^D$) is calculated with equations deduced from the mass conservation law in each sub-layer, as function of the mass flow rate in the boundary layer of the wet side wall ($\dot{m}^{SW}$). $\dot{m}^{SW}$ is calculated from the boundary layer variables U and δ_M, which are calculated with the Storage Boundary Layer (SBL) model (see Section 6 of Chapter 6). In this model, only the turbulent regime is considered to compute the terms of the momentum and energy conservation laws of the boundary layer (Equation 178 and Equation 179), which are numerically integrated to calculate the boundary layer variables U and δ_M, to improve the stability of the calculations. The number of sub-space-points of the integration in each sub-layer is fixed. The rising flow of the bottom ($\dot{m}^B$) is calculated at the bottom sub-layer with the SBL model applied at the flat ends. $\dot{m}^B$ is equal to the one of the bottom sub-layer, (i) if it is higher than $\dot{m}^{SW}$, and (ii) if its temperature is higher than the adjacent upper sub-layer. Otherwise, $\dot{m}^B$ is equal to zero. The intra-layer heat flows, which is composed by upper and lower heat flows ($\dot{Q}^{UP}$ and $\dot{Q}^{INF}$), is calculated with the Intra-Layer Heat Transfer (ILHT) model. This model is based on the hypotheses of pure conduction, of the competitive heat transfer mechanism and of the rigid surface (assumptions a), b) and c) of Section 4.1 of Chapter 6).

The results of the fluid-dynamics at the wet side wall, the fluid-dynamics in the liquid, the heat transfer at the interface, intra-layer heat transfer, and interface heat-mass transfer are analyzed. $\dot{m}^{SW}$ decreases with the increment of the bulk temperature gradient ($\frac{\partial T^L}{\partial x}$). This decrement grows up near the interface. The heat transfer coefficient of the wet side wall (hwS) increases with the increment of $\dot{m}^{SW}$. So, h_w^{SL} decreases near the interface due to the increment of $\frac{\partial T^L}{\partial x}$, which reduces $\dot{m}^{SW}$. It can happen that h_w^{SL} increases with the reduction of $\dot{m}^{SW}$ due to the increment of the boundary layer variable U. The wet side wall temperature (T_w^{SL}) increases near the interface due to the reduction of the heat transfer coefficient. This increment leads to unphysical values at medium heat fluxes, when $\dot{m}^{SW}$ is equal to zero. Besides this case, the LS model can calculate (i) the influence of $\frac{\partial T^L}{\partial x}$ on the fluid-dynamics, and (ii) the relation between the fluid-dynamics and h_w^{SL}. The conductive formula of the heat transfer coefficient (Equation 207) has, however, to be modified because it overestimates the T_w^{SL}. The liquid-to-interface heat flow ($\dot{Q}_I^L$), which is negative in the H 2.0 model, is higher than the ones obtained with the previous models because the difference in temperatures at the interface is lower than the one of the H 2.0 model, due to the hypothesis of the liquid discretisation (assumption b) of Section 1.2 of Chapter 6). This heat flow fluctuates because the approach of dominant heat transfer mechanism cannot calculate the fluid-dynamics conditions of using the local convection formula (Equation 536) or the boundary layer formula (Equation 535).

The calculated values of pressure and of the liquid temperature profiles are compared with the experimental ones. The calculated pressure agrees more with the experimental data than in the H 2.0 model, due to the hypothesis of the liquid discretisation (assumption b) of Section 1.2 of Chapter 6) that allows computing the liquid-to-interface more accurately with respect to the measured data. The calculated pressure is often higher than the experimental one, due to the higher liquid temperature near the interface than the measured one. High temperature near the interface is caused by the liquid temperature profiles, which increase faster than the experimental ones near the interface. This excessive accumulation of heat is caused by the hypothesis of no conduction (assumption c) of Section 5.1.1 of Chapter 6). In the core, the calculated temperature slightly increases, in contradiction with the experimental one, due to the conditions that set the rising mass flow equal to zero. These conditions do not completely respect the experimental observations.

As consequence, the liquid stratification model has to be improved in computing the:

a) The space-distribution of $\dot{m}^{B}$;
b) The accumulation of sensible heat near the interface;
c) h_{W}^{SL} in absence of mass flow;
d) The fluid-dynamics conditions of the dominant heat transfer mechanism;

The value of $\dot{m}^{B}$ is equal to zero when the temperature increment in the liquid is adverse to the motion of this mass flow, or when it is lower than the $\dot{m}^{SW}$. If $\dot{m}^{B}$ enters in a zone of adverse temperature increment, or if is lower than $\dot{m}^{SW}$, it progressively looses momentum, instead of immediately vanishing as done in the LS model. So, the condition that set $\dot{m}^{B}$ equal to zero should be removed and substituted by a progressive block of $\dot{m}^{B}$.

As said, the hypothesis of no conduction (assumption c) of Section 5.1.1 of Chapter 6) accumulates the dry side wall-to-interface heat flow in the interface sub-layer of the wet side wall. This thermal energy is transferred to the bulk of the interface sub-layer. So, the description of the accumulation of sensible heat near the interface can be improved (i) by removing the hypothesis of no conduction (assumption c) of Section 5.1.1 of Chapter 6) and (ii) by considering that the dry side wall-to-interface heat flow is transferred by conduction along the wet side wall.

When the boundary layer variables U and δ_M are equal to zero in a sub-layer, the heat transfer coefficient is computed with the conductive formula, which is a function of the conductive heat transfer coefficient and the radius of the storage container (Equation 207). So, the hypothesis of conduction in case of absence of convection at the wet side wall can be substituted with the hypothesis of local natural convection. In this hypothesis, micro circulations of liquid can occur near the wet side wall if the free-convection at the side wall is absent.

The liquid-to-interface heat flow is calculated with the approach of the dominant heat transfer mechanism. So, this approach can be substituted by a method that is based on the fluid-dynamics conditions. These conditions can be defined with the values of boundary layer variables U and δ_M at the second-last sub-layer. If the boundary layer variables U and δ_M are positive in the second-last sub-layer, $\dot{m}^{SW}$ passes along the interface stops the local natural convection. So, the latter can be developed only when there is no natural convection in the second-last sub-layer and the boundary layer variables U and δ_M are equal to zero.

10.Comparison with the previous model

The liquid stratification model (LS model) is developed to improve the prediction of the self-pressurisation. The LS model can qualitatively and, often, quantitatively calculate a self-pressurisation in agreement with the experimental data. This model is compared with the results of the homogeneous (H 2.0) model:

- in terms of statistical errors affecting storage pressure (Average Absolute Deviation, AAD, Bias, Maximum Absolute Deviation, MAD, see Section 1 of Appendix S). Pressure is the only value that has been considered since the ullage of the LS model is described as the one of H 2.0 model;
- in terms of calculation time to evaluate the impact of the liquid discretisation of the LS model with respect to a less complex model (the H 2.0 model).

Section 10.1 describes the comparison in the computational time between the LS model and the H 2.0 model. Section 10.2 compares the accuracy of the LS model with the one of the H 2.0 model in describing the system pressure.

10.1. Computational time

According to the objectives of the thesis (see Section 6 of Chapter 1), the computational time of the liquid stratificiaont (LS) model is analyzed. The values of the difference ($\Delta t_C^{LS-H2.0}$) between the computational time of the LS model (t_C^{LS}) and that of the H 2.0 model ($t_C^{H2.0}$) are reported in Table 143.

Table 143. Values of $\Delta \boldsymbol{t}_{\boldsymbol{C}}^{\boldsymbol{H2.0-LS}}$ and $\boldsymbol{t}_{\boldsymbol{C}}^{\boldsymbol{LS}}$.

<table>
<tr><td colspan="13">Study case 1</td></tr>
<tr><td></td><td colspan="2">Test 1</td><td colspan="2">Test 2</td><td colspan="2">Test 3</td><td colspan="2">Test 4</td><td colspan="2">Test 5</td><td colspan="2">Test 6</td></tr>
<tr><td>$\Delta t_C^{LS-H\,2.0}\ [h]$</td><td colspan="2">43.924</td><td colspan="2">7.3917</td><td colspan="2">12.370</td><td colspan="2">9.7741</td><td colspan="2">5.6809</td><td colspan="2">6.0688</td></tr>
<tr><td>$t_C^{LS}\ [h]$</td><td colspan="2">44.557</td><td colspan="2">7.7230</td><td colspan="2">12.847</td><td colspan="2">10.134</td><td colspan="2">6.1503</td><td colspan="2">6.6714</td></tr>
<tr><td colspan="13">Study case 2</td></tr>
<tr><td></td><td colspan="12">Test 1</td></tr>
<tr><td>$\Delta t_C^{LS-H\,2.0}\ [h]$</td><td colspan="12">94.591</td></tr>
<tr><td>$t_C^{LS}\ [h]$</td><td colspan="12">94.916</td></tr>
<tr><td colspan="13">Study case 3</td></tr>
<tr><td></td><td colspan="6">Test 1</td><td colspan="6">Test 2</td></tr>
<tr><td>$\Delta t_C^{LS-H\,2.0}\ [h]$</td><td colspan="6">518.80</td><td colspan="6">551.32</td></tr>
<tr><td>$t_C^{LS}\ [h]$</td><td colspan="6">521.52</td><td colspan="6">553.32</td></tr>
<tr><td colspan="13">Study case 4</td></tr>
<tr><td></td><td colspan="6">Test 1</td><td colspan="6">Test 2</td></tr>
<tr><td>$\Delta t_C^{LS-H\,2.0}\ [h]$</td><td colspan="6">288.60</td><td colspan="6">226.42</td></tr>
<tr><td>$t_C^{LS}\ [h]$</td><td colspan="6">289.94</td><td colspan="6">227.07</td></tr>
<tr><td colspan="13">Study case 5</td></tr>
<tr><td></td><td colspan="4">Test 1</td><td colspan="4">Test 2</td><td colspan="4">Test 3</td></tr>
<tr><td>$\Delta t_C^{LS-H\,2.0}\ [h]$</td><td colspan="4">43.346</td><td colspan="4">5.5309</td><td colspan="4">8.3550</td></tr>
<tr><td>$t_C^{LS}\ [h]$</td><td colspan="4">44.457</td><td colspan="4">6.6137</td><td colspan="4">9.6988</td></tr>
<tr><td colspan="13">Study case 6</td></tr>
<tr><td></td><td colspan="3">Test 1</td><td colspan="3">Test 2</td><td colspan="3">Test 3</td><td colspan="3">Test 4</td></tr>
<tr><td>$\Delta t_C^{LS-H\,2.0}\ [h]$</td><td colspan="3">294.68</td><td colspan="3">152.95</td><td colspan="3">41.514</td><td colspan="3">102.55</td></tr>
<tr><td>$t_C^{LS}\ [h]$</td><td colspan="3">298.44</td><td colspan="3">153.92</td><td colspan="3">41.909</td><td colspan="3">103.25</td></tr>
<tr><td colspan="13">Study case 7</td></tr>
<tr><td></td><td colspan="4">Test 1</td><td colspan="4">Test 2</td><td colspan="4">Test 3</td></tr>
<tr><td>$\Delta t_C^{LS-H\,2.0}\ [h]$</td><td colspan="4">143.70</td><td colspan="4">104.97</td><td colspan="4">43.681</td></tr>
<tr><td>$t_C^{LS}\ [h]$</td><td colspan="4">144.70</td><td colspan="4">105.42</td><td colspan="4">44.294</td></tr>
</table>

As it is indicated in Table 143, the calculation time increases with the increment of the filling ratio because the number of sub-layers grows up when the initial filling ratio augments. The order of magnitude of the difference in computation time between the LS and H 2.0 models is quite similar to the one of the computational time of the LS model. So, the computational time hugely increases from the H 2.0 to the LS model. This increment is caused by two factors: the method of computing the number of sub-space-points in Storage Boundary Layer (SBL) model (see Section 3.1.2 of Chapter 6) and by the Storage Heat Transfer (SHT) model at the wet side wall (see Section 5.1 of Chapter 6). The number of sub-space-points in the SBL model is fixed, instead of being decreased if the derivate of the boundary layer variables U and δ_M are low, similarly to the H 2.0 model. As a consequence, the computational time of the numerical integration in the SBL increases in the LS model. In the H 2.0 model, the wet side wall-to-liquid heat flow is calculated over the whole surface, with an iterative procedure. In the LS model, this heat flow is computed in each sub-layer with an iterative procedure. As consequence, the computational time of computing the liquid-to-interface heat increases in the LS model.

10.2. Accuracy in computing the pressure

The Average Absolute Deviation (AAD), BIAS and Maximum Absolute Deviation (MAD) are related to the deviation between experimental pressures and pressures calculated by LS and H 2.0 models are reported in Figure 194.

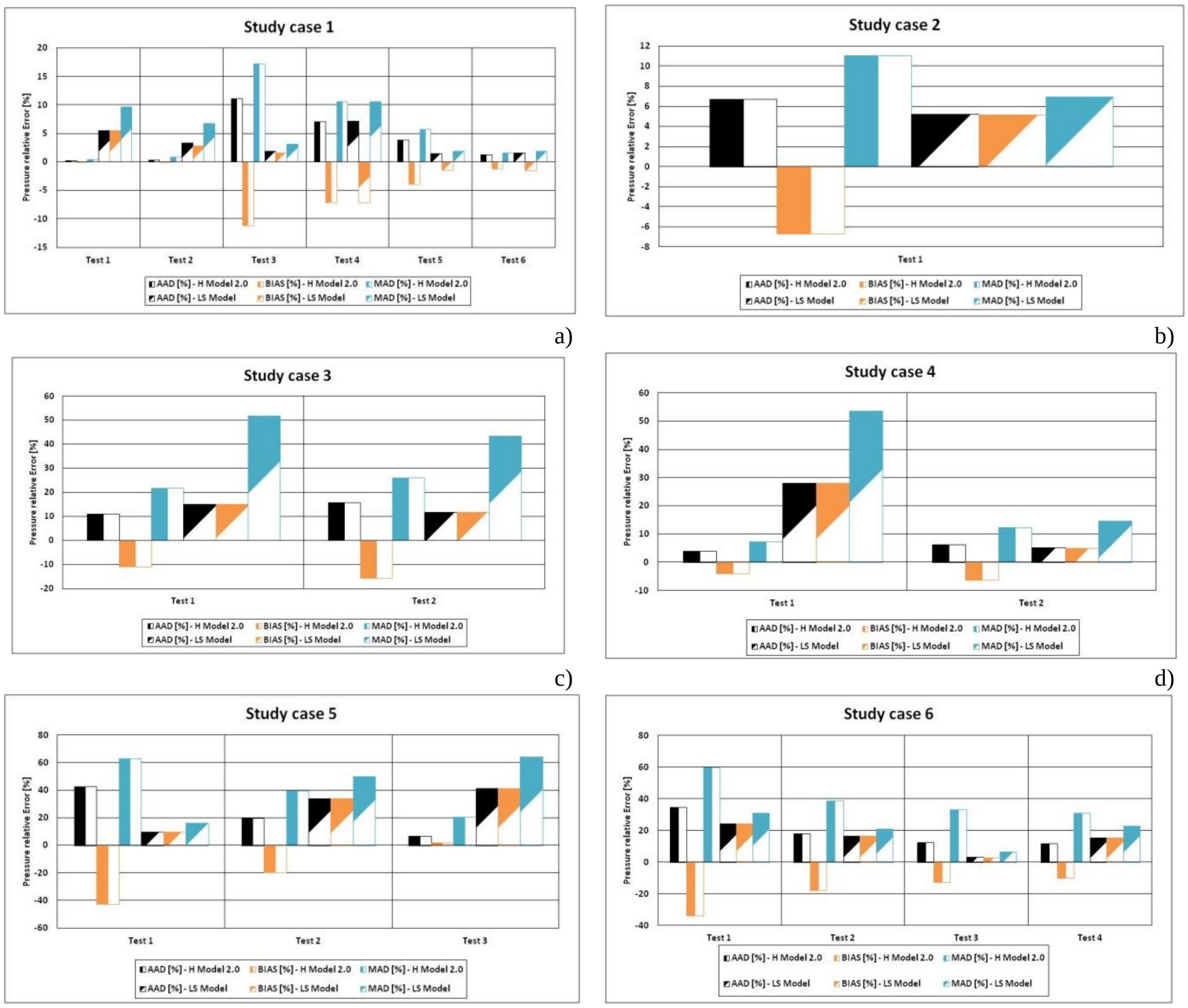

a)

b)

c)

d)

e)

f)

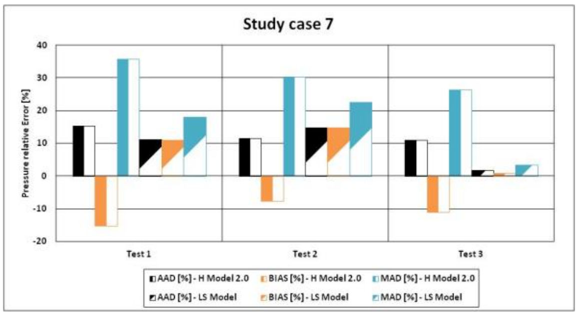

g)

Figure 194. The values of AAD, BIAS and MAD in terms of pressure between the H 2.0 and LS models for Study case 1 (a), 2 (b), 3, (c) 4 (d), 5 (e), 6 (f) and 7 (g).

In Study case 1, the AAD, BIAS and MAS of LS model are (i) lower than those of H 2.0 model for Test 3 (high heat input) and Test 5 (medium-low filling ratio), (ii) similar to the ones of H 2.0 model for Test 4 (medium filling ratio) and for Test 6 (low filling ratio) and (iii) higher than the ones H 2.0 model for Test 1 (high filling ratio) and Test 2 (high-medium filling ratio). The relative variation[106] of these statistical errors is reported in Table 144.

Table 144. Relative variation of AAD, BIAS and MAD between LS and H 2.0 model for ullage pressure of Study case 1.

Test	1	2	3	4	5	6
AAD [%]	2772.0	959.63	-82.735	0.86588	-63.007	25.120
BIAS [%]	-13683	-5550.9	-114.41	0.86588	-63.007	25.120
MAD [%]	1862.6	692.02	-81.722	-0.42620	-67.021	21.699

The average relative variations of AAD, the BIAS and the MAD are respectively 602 %, -3230 % and 404 %, indicating the accuracy of LS model reduces

In Study case 2, the AAD, BIAS and MAD of LS model are lower than the ones of the H 2.0 model. The relative variation of these statistical errors is reported in Table 145.

Table 145. Relative variation of AAD, BIAS and MAD between LS and H 2.0 model for ullage pressure of Study case 2.

Test	1
AAD [%]	-22.154
BIAS [%]	-177.212
MAD [%]	-37.269

The accuracy of LS model increases because the values of these relative variations are negative, as it is indicated by the formula to compute this value[106].

In Study case 3, the absolutes values of the AAD, BIAS and MAD of LS model are higher than the ones of H 2.0 model for Test 1 (steady state initial conditions). For Test 2 (isothermal initial conditions), the absolute values of AAD and BIAS of LS model are lower than the ones of H 2.0 model. the MAD of LS model is higher than the one of H 2.0 model. The relative variation of these AAD, BIAS and MAD is reported in Table 146.

Table 146. Relative variation of AAD, BIAS and MAD between LS and H 2.0 model for ullage pressure of Study case 3.

Test	1	2
AAD [%]	38.024	-25.805
BIAS [%]	-239.88	-174.19
MAD [%]	138.050	66.958

The average relative variations of AAD, the BIAS and the MAD are respectively 6.1 %, -207 % and 102 %, indicating the LS is slightly les accurate than H 2.0 model.

In Study case 4, the values of the AAD, BIAS and MAD of LS model are (i) higher than those of the H 2.0 model for Test 1 and (ii) quite similar to those of H 2.0 model for Test 2, except for the BIAS.

---

[106] The relative decrement is computed as: $\frac{y_{LS}-y_{H\ 2.0}}{y_{H\ 2.0}} \cdot 100$. y can be ADD, BIAS and MAD.

This value of the LS model is positive indicating that, on average, the pressure is overestimated, instead of being under-estimated as in the H 2.0 model. The relative variation of these AAD, BIAS and MAD is reported in Table 147.

Table 147. Relative variation of AAD, BIAS and MAD between LS and H 2.0 model for ullage pressure of Study case 4.

Test	1	2
AAD [%]	591.34	-16.711
BIAS [%]	-791.39	-178.76
MAD [%]	629.84	17.948

The average relative variations of AAD, the BIAS and the MAD are respectively 287%, -486 % and 323 %, indicating LS model is less accurate than the H 2.0 model for low heat fluxes in liquid hydrogen storage tanks.

In Study case 5, the values of the AAD, BIAS and MAD of LS model increases from Test 1 (high filling ratio) to Test 2 (medium filling ratio), and from Test 2 to Test 3 (low filling ratio). The values of these statistical errors of LS model are (i) lower than the one of H 2.0 model at Test 1 and (ii) higher than the one of H 2.0 model for Test 2 (medium filling ratio) and Test 3 (low filling ratio). The relative variation of these statistical errors is reported in Table 148.

Table 148. Relative variation of AAD, BIAS and MAD between LS and H 2.0 model for ullage pressure of Study case 5.

Test	1	2	3
AAD [%]	-77.084	69.788	515.18
BIAS [%]	-122.92	-271.09	1854.1
MAD [%]	-74.094	25.560	209.034

The average relative variations of AAD, the BIAS and the MAD are respectively 169%, 486 % and 53 %, indicating that the accuracy of the LS model is lower than the one of H 2.0 model for medium heat fluxes.

In Study case 6, the values of AAD, BIAS and MAD of LS model are lower than the one of H 2.0 model, except for Test 4. In this test, the ADD and the the absolute value of BIAS of H 2.0 model are slightly lower than the ones of LS model. the values of AAD, BIAS and MAD of LS model are lower at Test 3 than at Test 1 and 2. The values of these statistical errors at Test 2 are similar to the ones at Test 4. The relative variation of these statistical errors is reported in Table 150.

Table 149. Relative variation of AAD, BIAS and MAD between LS and H 2.0 model for ullage pressure of Study case 6.

Test	1	2	3	4
AAD [%]	-29.700	-7.1883	-73.900	28.535
BIAS [%]	-172.31	-194.43	-122.27	-249.36
MAD [%]	-48.159	-46.046	-79.908	-26.275

The average relative variations of AAD, the BIAS and the MAD are respectively -21 %, -185 % and -50 %, suggesting that the accuracy of the LS model is higher than the one of the H 2.0 model at high heat fluxes.

In Study case 7, the highest values of the AAD, BIAS and MAD of LS model are calculated at Test 2 (medium filling ratio). The lowest values of these statistical errors are computed at Test 3 (flow filling ratio). The values of the AAD, BIAS and MAD of LS model are lower than the ones of H 2.0 model. The relative variation of these statistical errors is reported in Table 150.

Table 150. Relative variation of AAD, BIAS and MAD between LS and H 2.0 model for ullage pressure of Study case 7.

Test	1	2	3
AAD [%]	-27.370	28.475	-84.523
BIAS [%]	-172.18	-293.09	-108.21
MAD [%]	-49.426	-25.875	-87.259

The average relative variations of AAD, the BIAS and the MAD are respectively -27 %, -191 % and -54 %, suggesting that the accuracy of the LS model is higher than the one of the H 2.0 model at high heat fluxes.

10.3. Discussion and conclusions

The computational time of the liquid stratification model (LS model) is much higher than the one of the homogeneous model 2.0 (H 2.0 model). This increment is produced by the integration method of the Storage Boundary Layer (SBL), which numerically compute the boundary layer variables such as U and δ_M form the conservation laws of energy and momentum. This increment of the computational time does not worth the increment of the complexity in certain conditions.

The LS model is compared with the H 2.0 model in terms of Average Absolute Deviation (AAD), Bias and Maximum Absolute Deviation (MAD) in the variable pressure, since this last is the main variable impacted by the hypotheses done while setting up the LS model:

- In Study case 1, the LS model is globally less accurate than the H 2.0, even if the values of AAD, BIAS and MAD at high heat input and medium-low filling ratio are lower than one of the H 2.0 model. The loss of accuracy is caused by the over-estimation of the pressure at high and medium filling ratios due to the accumulation of sensible heat at the interface.
- In Study case 2, the LS model is more accurate than the H 2.0 in computing the pressure.
- At medium heat fluxes (Study case 5), the LS model is more accurate in computing the pressure than the H 2.0 model at high filling ratio.
- As the filling ratio decreases, the accuracy of the LS model becomes lower than the one of the H 2.0 model. So, the LS model is globally less accurate than the H 2.0 model.
- At high heat fluxes (Study case 7), the LS model is more accurate than the H 2.0.

To sum up, the LS model improved the calculation of the ullage pressure at high heat fluxes. At medium and low heat fluxes, LS model is quantitatively better than the H 2.0 model due to the excessive accumulation of the sensible at the interface. At medium heat fluxes, the LS model is less accurate at low filling ratio than at high filling ratio. At low heat fluxes, this model is often less accurate at high liquid level than at low liquid level. Qualitatively speaking, the LS model can predict the decrement of the pressure with the reduction of the filling ratio, as experimentally occurs, contrarily to the H 2.0 model. So, the discritisation method proves its utility.

Further efforts should be addressed to timprove the quantitative prediction of the pressure by properly computing the accumulation of sensible heat near the interface, and to reduce the computational time by using a new method to integrate the conservertiona laws of the energy and momentum in the boundary layer. To sum up, some developments should be done on the LS model to:

a) Reduce the computational time by using a new method for integrating the conservation laws of energy and of momentum in the boundary layer;
b) Consider the conductive heat flow along the wet side wall, whose neglect produces the over-estimation of the accumulation of the sensible heat near the interface;
c) Compute the laminar mass flow in the boundary layer of the wet side wall, which is one of the causes of the excessive accumulation of sensible heat at the interface.;

A new model forthe liquid-to-interface heat flow could then be developed, as suggested in Section 9.10. In addition to that, the description of the vapour phase could also be improved.

Chapter 7

Résumé et perspective

Quatre modèles (équilibre, homogène, homogène 2.0 et stratification liquide) ont été proposés pour développer un modèle capable de décrire les phénomènes qui se produisent dans les cuves de stockage cryogéniques à petite échelle (PE).

Le modèle d'équilibre a été développé avec l'hypothèse que le liquide et la vapeur soient homogènes et à l'équilibre thermodynamique instantané.La pression et la température gazeuse de ce modèle n'étant pas en accord avec les données de référence, le modèle homogène a été développé, en enlevant la condition d'équilibre thermodynamique. La pression calculée avec ce modèle sont inférieures aux données expérimentales en raison de la faible valeur du flux thermique liquide-vers-interface. De plus, ce modèle calcule des pics de température gazeuse pour des flux de chaleur moyens et élevés qui ne sont pas observés expérimentalement, en raison du flux d'enthalpie accompagnant le débit massique net à travers l'interface liquide-vapeur (le débit massique net est la différence entre la condensation et taux d'évaporation).

Le modèle homogène 2.0 a été développé avec l'hypothèse de la discrétisation virtuelle de la vapeur. Le gradient de température global dans la vapeur est calculé, le débit d'enthalpie du débit massique net est calculé en fonction de la différence de température à l'interface. Ce modèle calcule l'incrément de la température de la vapeur qui est qualitativement et, souvent, quantitativement en accord avec les données expérimentales.

Le modèle de stratification liquide a été développé pour améliorer la prédiction d'auto-pressurisation et implémente les hypothèses de discrétisation du liquide et de discrétisation virtuelle de la vapeur. Le gradient de température global dans le liquide est pris en compte dans la dynamique des fluides et le transfert de chaleur au niveau de la paroi latérale humide est calculé en fonction de la dynamique des fluides. La pression calculée par ce modèle est généralement supérieure aux données expérimentales car le flux thermique liquide-vers-interface est surestimé. Cette surestimation est causée par (i) l'hypothèse d'absence de conduction dans le modèle Storage Heat Transfer de la paroi latérale humide et (ii) l'hypothèse d'un régime dynamique des fluides turbulent dans le modèle Storage Boundary Layer de la paroi latérale humide. (i) Surestimation de ce flux thermique à l'interface et utilisation des coefficients correcteurs alpha et bêta, (ii) temps de calcul élevé et (iii) manque de données expérimentales de dynamique des fluides et de transfert de chaleur couplées aux données mesurées de pression et de température sont les principaux enjeux critiques de ce modèle. En conséquence, un nouveau modèle de transfert de chaleur de la paroi latérale humide est proposé, considérant la chaleur transférée par conduction le long de la paroi latérale humide. L'utilisation du coefficient correcteur est supprimée en discrétisant la vapeur en sous-couches, qui sont divisées en cœur et couche limite. Le nombre de sous-couches, qui détermine le temps de calcul, peut être réduit avec (i) une nouvelle approche d'intégration qui augmente la précision et (ii) en remplaçant la sous-couche liquide présentant les mêmes températures par la région isotherme. Ainsi, le liquide est décomposé dans la région stratifiée, qui est discrétisée en sous-couches, et dans la région isotherme, qui est décrite comme pour le modèle homogène.

Les données expérimentales de dynamique des fluides et de transfert de chaleur couplées aux données mesurées de pression et de températures peuvent être obtenues avec un dispositif expérimental qui mesure (i) la pression, (ii) les profils de température au niveau de la paroi externe, au niveau de la paroi interne, à proximité de la paroi et le long de la paroi et sur l'axe vertical du réservoir de stockage, et (iii) qui prend des photos des mouvements du fluide dans le liquide et dans la vapeur.

Summary and perspective

Four models (equilibrium, homogneoeus, homogneous 2.0 and liquid stratification) have been proposed for developing a model that can describes the phenomena occurring in the small scale (SS) cryogenic storage containers. The equilibrium model (EQ model) has been developed under the hypothesis of the instantaneous thermodynamic equilibrium. In this model, the liquid and the vapour are at thermodynamic equilibrium and they are homogeneous. Being pressure and ullage temperature from EQ Model not in agreement with reference data, the homogeneous model (H model) has been developed, applying the hypothesis of actual thermodynamic state instead. The pressure calculated with H model are lower than the experimental data due to the low value of the liquid-to-interface heat flow. In addition, the H model computes peaks of the ullage temperature for medium and high heat fluxes which are not experimentally observed, due to the enthalpy flow accompanying the net mass flow across the liquid-vapour interface (the net mass flow is the difference between condensation and evaporation rates). Consequently, the homogeneous model 2.0 (H 2.0 model) has been developed with the hypothesis of the vapour virtual discretisation. The bulk temperature gradient in the ullage is computed. The enthalpy flow of the net mass flow is calculated as function of the difference in temperature near the interface. The H 2.0 model computes the increment of the ullage temperature that is qualitatively and, often, quantitatively in agreement with the reference experimental data. Finally, the liquid stratification model (LS model) was developed to improve the self-pressurization prediction, with the liquid discretization hypothesis and the vapor virtual discretization hypothesis. The liquid region is discretized into sub-layers of equal size. The bulk temperature gradient is considered in the fluid-dynamics and the heat transfer at the wet side wall is computed as function of the fluid-dynamics. The pressure computed by this model is usually higher than the experimental data because the liquid-to-interface heat flow is overestimated. (i) Over-estimation of this heat flow at the interface and the use of the corrective coefficients alpha and beta, (ii) the high computational time, and (iii) the lack of experimental data of fluid-dynamics and heat transfer coupled with the measured data of pressure and of temperatures are the main critical issues of the LS model. This over-estimation is caused (i) by the hypothesis of no conduction in the storage heat transfer (SHT) model of the wet side wall and (ii) by the hypothesis of turbulent fluid-dynamic regime in the storage boundary layer (SBL) model of the wet side wall. As consequence, a new heat transfer model of the wet side wall is proposed, considering the heat transferred by conduction along the wet side wall. The use of the corrective coefficient is removed by discretizing the ullage in sub-layers, which can be divided into bulk and boundary layer. The high computational time is caused by integration approach of the SBL model for the side wall and by the number of the liquid sub-layer. As consequence, a new integration approach is proposed to increase the accuracy and reducing the number of sub-layers. The number of the sub-layer can be further reduced by substituting the liquid sub-layer with the same temperatures with the isothermal region. So, the liquid is decomposed in the stratified region, which is discretized in sub-layers, and in the isothermal region, which is described as done for the H model. The experimental data of fluid-dynamics and heat transfer coupled with the measured data of pressure and of temperatures can be obtained with an experimental device that measures (i) the pressure, (ii) the temperature profiles at the external wall, at the internal wall, near the wall and along the vertical axis of the storage tank, and (iii) that takes pictures of the fluid motions in the liquid and in the vapour.

Section 1 presents the summary of the thesis. Section 2 describes the conclusions. Section 3 explains the perspective of this work, which can improves the critical issues of the LS model.

1. Summary of the thesis

Section 1.1 summarizes Chapter 1, which explains the context, phenomena, the state of the art and objectives. Section 1.2 recaps Chapter 2, which presents the experimental data and the preliminary analysis. Section 1.3 recapitulates Chapter 3, which describes the equilibrium model (EQ model). Section 1.4 sums up Chapter 4, which presents the homogeneous model (H model). Section 1.5 summarizes Chapter 5, which explains the homogeneous model 2.0 (H 2.0 model). Section 1.6 recapitulates the Chapter X, which describes the liquid stratification model (LS model).

1.1.Chapter 1: context, phenomena, state of art and objectives

Chapter 1 describes the role of the cryogenic fuels in the energy transition, the storage of the small scale (SS) cryogenic liquids storage, the challenges of this storage, the phenomena occurring in SS cryogenic storage containers, the analyses of the scientific literature and the objectives of the thesis. The role, the SS storage and the challenges are the context of this thesis.

Section 1.1.1 resumes the contect of the thesis. Section 1.1.2 sums up the phenomena. Section 1.1.3 recaps the state of the art and the objectives.

1.1.1. Context of the thesis

To reduce the emissions of anthropogenic carbon dioxide (CO_2), energy and transport sectors are progressively de-carbonised by substituting fuel-oils with low-carbon fuels such as hydrogen, bio-methane and with Natural Gas (NG). These gases are respectively liquefied into Liquid Hydrogen (LH2), bio-liquefied natural gas (bio-LNG) and Liquefied Natural Gas (LNG), which are cryogenic liquids, to be easily transported over long distance and to be compactly stored. In the large scale supply chain, these cryogenic liquids are usually stored in large scale tanks, which operate at constant and almost atmospheric pressure, under near-by stationary conditions. The size of these large scale storage tanks is around 160 000 m^3 in on ground terminals of Liquefied Natural Gas (LNG), and it is almost 4 000 m^3 for on ground LH_2 storage site for aerospace applications. During the storage, the cryogenic liquid evaporates producing the Boil-Off Gas (BOG), which is treated in dedicated plants, where it can be re-liquefied or directly used as gas. In small scale applications such as fuelling for heavy duty and marine, and for power production in off-grid sites, these cryogenic fluids are stored in small scale tanks, whose volume can change as function of the end users. In refuelling station, the size for these storage containers can be around 60 m^3 and it can be lower than 1 m^3 for trucks. In small scale applications, the BOG treatment unit cannot be installed, and the storage container is kept close as much as possible to avoid realising of BOG. As consequence, the small scale storage containers can work at pressure, whose value can range between 5 and 17 barg.

Considering the use of cryogenic liquids as fuel vector and the operating conditions of their storage tanks, the storage variable such as Holding-Up Time (HUT), the Net Suction Positive Head (NSPH), the Methane Number (MN) and the Gross Heating Value (GHV) are calculated during the storage of these cryogenic fluids to assure that the fuel matches the specification required by the thermal machine[107]. The **HUT** is the time required to reach the maximum operating pressure, conditions at which the storage container is open and the BOG is released. The free-release of BOG is highly undesired because the stored product is lost, and the greenhouse gases can be released, for example if LNG is stored. The **NSPH** is the difference in pressure between the saturation one and the one of the

---

[107] Thermal machine can be a sparkling engine, a gas turbine, a burner or any other device that burns fuel.

inlet flow of the cryogenic pump. As this difference reduces, the cryogenic liquid can easily form bubbles in the pump, causing cavitations, which can damage this equipment. The **MN** quantifies the anti-knocking properties of the natural gas-air mixture that enters the sparkling engine. If the value of the MN is not inside the specific range of the sparkling engine, engine knocking can occur and the machine can break. The **GHV** is the amount of energy released during the free-combustion with stoichiometric oxygen. The increment of this variable can produce the overheating of the thermal machine.

The time-evolutions of the storage variables are affected by the evolution of the physical variables such as pressure, (liquid and vapour) temperature profile, and filling ratio.

1.1.2. Phenomena occurring in cryogenic storage containers

The physical variables depend on the storage phenomena occurring in cryogenic storage containers of small scale.The main phenomena are the thermal stratification in liquid and in the ullage[108], the self-pressurisation and the ageing for cryogenic mixture such as liqueified natural gas (LNG).

The **thermal stratification** is the development of a temperature gradient in the core, due to the natural convection at the side wall. In the liquid, this phenomenon develops from the accumulation of the sensible heat near the interface, when the storage container is closed. Closing the storage container, leads to an accumulation of mass in the ullage, increasing the interface temperature. The sensible heat carried by the natural convection at the wet side wall is not totally exchanged at the interface, instead of being completely transferred in open storage tank, and part of this thermal energy accumulates near the interface. As time passes, the sensible heat is progressively transferred from the interface to the core of the liquid, forming a temperature gradient that is adverse[109] to the natural convection at the wet side wall. The mass flow reduces in the zone of the liquid where this gradient is high, and mass exits the boundary layer, carrying sensible heat in the core and potentially blocking the free-convection in this part of the liquid. As consequence, the stratified region moves downward and this expansion is blocked by the rising flows of the bottom, which are caused by the natural convection at this surface. So, the thermal stratification influences temperature of the liquid that is withdrawn by the cryogenic pump, thus it affects the NPSH. In the vapour, thermal stratification occurs in the whole vapour volume; this can be divided in different regions characterized by a specific fluid-dynamics and values of the temperature gradient. These regions are (from the interface to the tank roof): (i) *the turbulent region* near the interface, where the vapour chaotically moves; (ii) *the cold and mixing region*, where the vapour moves from the boundary layer to the bulk and the descending flow meets the chaotic flow of the turbulent region; (iii) *the high gradient region*, in which, because of the high value of the temperature gradient (around 6 to 10 K/cm), part of the boundary layer mass flow reveres its direction, and moves downward between the boundary layer and the bulk; (iv) *the transition region*, where the temperature gradient decreases; (v) *the low gradient region*, where the thermal stratification is unstable because the low value of the gradient partially reduces the mass flow in the boundary layer; and (vi) *the warm mixing end*, where the temperature is almost homogeneous.

The **self-pressurisation** is the natural increment of the pressure in cryogenic storage container due to the accumulation of mass and of the increment of ullage temperature. As the storage container is closed, the difference in temperature between the interface and the liquid reduces due to the thermal stratification. The liquid-to-interface heat flow decreases and the evaporation rate decreases as well. So, the mass is accumulated in the ullage with a rate that is lower than the initial one. As a matter of

---

[108] The ullage is the empty space of the storage container, thus it is synonym of vapour phase.
[109] Adverse temperature gradient means that the gradient reduces the buoyancy forces in the boundary layer.

fact, the self-pressurisation is related to the liquid thermal stratification, and the increment of the pressure affects the HUT.

The **ageing** is the selective evaporation of the most volatile species of a cryogenic mixture. In LNG, nitrogen is the most volatile component, followed by methane. Nitrogen rapidly vanishes in the liquid and the ullage is mainly pure methane. After some time, medium-light species such as ethane and propane are present in the ullage. As the storage container is closed, the evaporation rate reduces. Thus, the concentrations of the species in the ullage and in the liquid do not significantly change during the self-pressurisation. The MN and the GHV, which depend on the composition, are affected by the ageing. Specifically for LNG, the MN can decrease and the GHV always increases during the storage.

These phenomena can be predicted with a physical model that considers the relation between storage conditions, fluid-dynamics, heat transfer and interfacial phenomena.

1.1.3. State of the art and objectives

In this literature, such storage phenomena have been modelled with Computational Fluid-Dynamic (CFD) and Lumped Parameter (LP) models. Among the LP models, equilibrium with evaporative rate (E-ER), equilibrium with heat flow (E-FL), non-equilibrium and homogeneous (nE-H), energy distribution function (EDF), and discretized (D) approach are usually adopted.

LP modelling with E-ER approach considers that the liquid and the vapour are at equilibrium and the evaporation rate, thus the BOG production, is given as input parameter. In the LP model with E-FL approach, the BOG production is calculated from the heat inputs of the storage container, which are given as input parameter. LP models with E-ER and E-FL approaches are unsuitable to be applied in real situations since the equilibrium conditions are rarely reached. The LP model with nE-H approach assumes that liquid and vapour are homogeneous, but the vapour is overheated. Thus, a heat flow between the vapour and the liquid exists and it is usually computed with convective and conductive models. The heat inputs are usually computed as function of the difference in temperature between the environment and the internal fluid (vapour and liquid), assuming that the heat transfer is composed by three steps: environment-to-external surface, external surface-to-internal surface, and internal surface-to-fluid (liquid and vapour). LP model with nE-H approach is suitable when the heat inputs rate is low because thermal stratification is weak. These models do not describe well this transfer because they are not based on the fluid-dynamics near the interface. The LP models with EDF approach are similar to LP model with nE-H approach, but the temperature profile in the liquid is considered and calculated with the energy distribution function. This function is obtained by regressing the coefficients with experimental data. LP models with EDF approach can be applied only if the storage conditions are similar to the experimental ones. The LP models with D approach consider that the vapour and the liquid can be discretized in sub-layers, which are divided into bulk and boundary layers. The heat transfer is rarely coupled with the fluid-dynamics, the bulk temperature gradient is often neglected in the conservation law of the boundary layer, and the intra-layer heat transfer is calculated as function of the thickness of the sub-layer.

The models found in literature have been evaluated with the score-table method, which assigns a value to each model as function of the capacity in predicting the phenomena. The LP model with D approach have usually the highest score, indicating that this approach is theoretically suitable for predicting the behaviour of cryogenic liquid in small scale tanks.

The commercial software LNGMaster$^{(R)}$, developed by Engie Lab Crigen for the large scale storage, cannot predict the behaviour of LNG in small scale tank because the heat transfer model, the interface mass and heat transfer and the conservation laws are not developed for the storage phenomena of the small scale. The literature models do not consider (i) the relation between fluid-dynamics and heat transfer at the side walls, and (ii) the effect of the bulk temperature gradient on the fluid-dynamics at the side wall.

As consequence, a model is required to predict the behaviour of pure cryogenic liquids in small scale tanks, which can be used in industrial applications. This model must considers the heat transfer-fluid-dynamics relation and the bulk temperature gradient, and it must be validated with the largest set of experimental data, contrarily of what has been done in literature. the objective of the thesis is the development of a thesis for pure cryogenic liquids in static SS storage containers, which can be extended to cryogenic mixture such as LNG.

1.2. Chapter 2: experimental data and thermal distribution analysis

Chapter 2 describes the measured variables that are required for validating the physical model, the review of the experimental work, the table-score method for selecting the experimental works for validating the model, the selected experimental work, the method for computing the interface temperature, the boil-off gas (BOG) temperature and the filling raito, the heat input, the analysis of the thermal distribution and the role of the dry side wall-to-wet side wall heat flow.

Section 1.2.1 recaps the measured variables, the review and the selected experiments. Section 1.2.2 sums up the the analysis of the thermal distribution and the role of the dry side wall-to-wet side wall heat flow.

1.2.1. Experimental data: variables, review and selected experiments

Liquid temperature increase from the interface to the bottom due to the liquid thermal stratification. The ullage temperature increases from the interface to the roof, due to the vapour thermal stratification. the self-pressurisation increases the pressure in the ullage. The vapour and liquid compositions change in time due to the ageing. Hence, a robust and reliable storage model must be developed and validated with respect to experimental values of liquid and vapour temperature profiles, pressure, and composition of the fluid phases within the tank. Furthermore, experimental values of boundary layers velocity, boundary layer thickness, boundary layer temperatures and wall temperatures are highly recommended because the storage phenomena are affected by the fluid-dynamics and the heat transfer with the walls of the storage containers.

According to the bibliographic research, thermal stratification has been experimentally investigated using non-cryogenic and cryogenic liquids for different values of the bottom-to-side wall heating ratio. Self-pressurisation and thermal stratification have been experimentally studied using liquid nitrogen (LN_2), liquid hydrogen (LH_2) and liquefied natural ges (LNG), for different heat fluxes and geometry of the storage containers. Experiments of ageing using LNG-like mixtures have also been found. To the contrary, no traces of experimental data of temperatures and pressure with their relative leasured data of the fluid-dynamics and heat transfer have been found in literature.

Due to the high number of experiments, a score-table method has been proposed in this work to evaluate the experimental works and select the most suitable one, called “Study cases”, to be used for the model validation. This method assigns a value to each studied phenomena, type of working fluid, geometry of the tank, and kind/availability of the experimental results. 9 experimental works have been found to be suitable for model validation and 3 of these works deal with LN_2 ([24]–[26]), 4 with

LH_2 ([27]–[30]), 2 with LNG-like mixtures [8] and [9], which have not been considered because they are out of the scope of the thesis.

Seo and Jeong [24], “**Study case 1**”, investigated the thermal stratification and self-pressurisation of LN_2 at low heat fluxes (6.1-5.2 W/m²) in a vertical storage container with flat ends (bottom and roof). The experimental tests were done at 90%, 70%, 50%, 30% and 10% of filling ratios, and a test at high heat inputs (13 W/m²) was also carried out in the same work. Perez et al. [26], “**Study case 2**”, measured the storage phenomena, the de-stratification and the Boil-Off Gas production at low heat fluxes (6 W/m²) in a vertical cylinder with flat ends containing LN_2. Hasan et al. [27], “**Study case 3**”, studied the self-pressurisation and the thermal stratification of LH_2 at low heat fluxes (6.1 W/m²) in oblate ellipsoid. The effect of the initial steady state and of the isothermal steady state conditions on the evolution of the storage phenomena are also studied. These tests are conducted at high filling ratio (75 %). Dresar et al. [28], “**Study case 4**”, experimentally investigated the storage phenomena at low heat fluxes (5.2-4.6 W/m²) at medium (49%) and low (34%) filling ratio in oblate ellipsoid containing LH_2. Kang et al. [25], “**Study case 5**”, studied the thermal stratification and the self-pressurisation at medium heat fluxes (84-50 W/m²) in vertical cylinder with flat ends. Three tests were done at high (80%), medium (50%) and low (30%) filling ratios of LN_2. Aydelott and Spuckler [30], “**Study case 6**”, did four tests of self-pressurisation and thermal stratification in spherical storage tank containing LH_2. Three tests were done at medium heat fluxes (76-57 W/m²), and at high (72%), medium (51%) and low (34%) initial filling ratios. One test was done with high heat inputs (245W/m²). Aydelott [29], “**Study case 7**”, experimentally investigated the self-pressurisation and thermal stratification at high heat fluxes (289-202 W/m²), in spherical storage container filled with LH_2. Three tests were done, at high (62%), medium (48%), and low (25%) filling ratios.

Some experimental data such as filling ratio, interface temperature, and average liquid and vapour temperatures are useful for the comparison of the result with the measured values of temperature and pressure. Unluckily, these values have not been measured in these experiments, thus they have been deduced in this work from the experimental values of pressure and temperatures.

1.2.2. Thermal distribution analysis and dry side wall-to-wet side wall heat flow

Wang et al. [122] developed a discretized model, which was compared with the experimental data of Perez et al. [26]. They discovered that the heat input in the storage container declared by Perez et al. [26] were higher than the one calculated by their model. As consequence, the heat inputs of each experimental test of each Study case have been calculated in this thesis, using the overall enthalpy variation approach. This method uses the first principle of thermodynamics to compute the average heat inputs during the self-pressurisation from the variation of the overall enthalpy. This variation is calculated as the difference in enthalpy between the beginning and the end of the self-pressurisation. The enthalpy is calculated as the product of mass and of specific enthalpy, which can be deduced from the values of filling ratio and average temperatures. The computed values of the heat inputs often are different from the declared one.

The behaviour of cryogenic liquids depends on the heat input in the storage container and on the thermal distribution of this heat intake between the liquid and the vapour. This distribution can be affected by the heat transferred from the vapour to the interface, and the heat transferred from the dry side to the wet side of the wall. A theoretical analysis [123] was done to study the thermal distribution, but it was not based on experimental data. So, the experimental approach of the thermal analysis has been developed in this work. This approach uses the overall mass and energy conservation laws to compute the heat entering the liquid and the vapour. The heat entering the liquid during the self-pressurisation is higher than the one at the steady state. The vapour receives less heat during the self-pressurisation than at the steady state. Hence, the heat transferred at the interface affects the thermal distribution.

The previous analysis could not determine if the heat transferred between the dry and the wet side of the wall plays a role in the distribution of the heat in the storage container. So, the dry side wall-to-dry side wall heat transfer has been studied. This heat flow is calculated with the one-dimensional Fourier's law. The temperature gradient is calculated with the experimental data of the temperature profile in the ullage at the steady state and during the self-pressurisation. The temperature gradient often increases during the self-pressurisation. The rate of heat transferring between the dry side wall and the wet side wall increases. Thus, the dry side wall-to-wet side wall cannot be ignored in modelling the behaviour of cryogenic liquid as well as the liquid-to-vapour heat flow.

1.3. Chapter 3: Equilibrium model

Chapter 3 describes the theory of the equilibrium model (EQ model), presenting the hypothesis, the variables, the mathamtical system and strucutues. Chapter 3 explains the sub-models of the EQ model such as the Boil-off rate (BOR), the storage heat transfer (SHT) model, the thermodynamic model and the Ordinary Differential Equation (Ode) solver. Chapter 3 presents the comparison of the results of the EQ model with the experimental data and the discussion of the results.

Section 1.3.1 recaps the theory of the EQ model. Section 1.3.2 brefely presents the sub-models. Section 1.3.3 sums up the comparison and the discussion.

1.3.1. Theory of the equilibrium model

Lumped Parameter (LP) models with the hypothesis of thermodynamic equilibrium conditions are used for modelling cryogenic liquids in large scale (LS) storage containers. This type of model is rarely used for small scale storage tanks, suggesting that efforts should be put to understand their reliability in predicting the behaviour of cryogenic liquids. As consequence, **the equilibrium model (EQ model) has been developed, under the hypothesis of instantaneous thermodynamic equilibrium.** This assumption states that the liquid and vapour are always at thermodynamic equilibrium during the entire storage period. The main variables of the EQ model are the ullage pressure and the liquid volume, and the values of these variables change during the self-pressurisation. These variables can be calculated by solving the Ordinary Differential Equation (ODEs) system, which is composed by the pressure-evolution (P^V-e) and liquid volume-evolution (V^L-e) equations. These equations are explicit formulas[110] of the time-derivates of the pressure and of the liquid volume. The P^V-e and V^L-e equations are deduced from the overall mass and energy conservation laws, using a 8-steps mathematical procedure.

1.3.2. Sub-models of the equilibrium model

The conservation laws of the equilibrium model (EQ model), thus the P^V-e and V^L-e equations, depend on the heat input in the storage container. This heat intake has been calculated with the Storage Heat Transfer (SHT) model developed under the the hypothesis of negligible thermal resistance. This assumption states that the heat transfer coefficients at the internal walls of the storage container are so high that the heat is transferred without any thermal resistance[111]. The value of the heat input is, then, computed as product of the overall internal surface, the effective heat transfer coefficient (h_{eff}) and

---

[110] Explicit formulas can reduce the computational time because they do not iterative procedure

[111] The thermal resistance is the struggle of transferring heat from a hot to a cold surface.

the difference in temperatures between the external wall (T^{w}) and the fluid. The effective heat transfer coefficient is a parameter of the storage container that reflects the insulating properties. This coefficient is calculated with the Boil-Off Rate (BOR) model, from the experimental value of BOR or of the heat input. This model is based on the hypothesis of the overall thermal insulation, which states the whole thermal insulation of the storage container can be simplified to a single layer having a uniform and single thermal resistance. So, the effective heat transfer coefficient is computed as the ratio between the measured heat input and the product of the overall internal surface and the difference in temperatures between the external wall and the fluid.

To compute the time-derivates of liquid volume and pressure using the P^{V}-e and V^{L}-e equations, the thermo-physical properties of the liquid and of the vapour must be computed. For nitrogen and hydrogen, these properties are calculated by means of the reference equation of state ([12] and [13]) as implemented in the REFPROP V 9.0 library. With respect to the main transport properties, viscosity and thermal conductivity are both computed with the model of Lemmon and Jacobsen[128] for nitrogen, and respectively computed with the models of Muzny et al.[129] and Assael et al.[130] for para-hydrogen.

The P^{V}-e and V^{L}-e equations compose the ODE system of the EQ model. To be applied to industrial applications, the ODE system must be solved as fast as possible, maintaining a reasonable accuracy. As a consequence, the adaptive step approach of the method of Runge-Kutta-Fehlberg with Cash-Karp parameters (RKF-CKp) [131] is used. This method increases the time-step when the values of the time-derivates are almost stable and the risk of losing accuracy is low. The time-step is reduced if the values of the time-derivate frequently change because calculations can be highly imprecise. The RKF-CKp method discretises the simulation in time-points and the time-step is the distance between these points. Each time step is further divided in the sub time-point, where the sub time-step is the distance between each sub time-point. The time-step is calculated with an iterative procedure, where the first guess value of the time-step is progressively reduced until the value of the numerical error is lower than the desired one.

1.3.3. Comparison, discussion and conclusions

The results of the EQ model are compared with the reference experimental data of liquid nitrogen (LN_2) and of liquid hydrogen (LH_2) of Chapter 2 at low medium and high fluxes and in storage container of different geometries. These data are obtained for close storage container, where the self-pressurisation occurs after the steady state period. As consequence, the simulations are done at first with a steady state period, where the storage container is open at constant pressure, and then followed by a self-pressurisation period. The effective heat transfer coefficient at each experiment is computed with the BOR model, using the measured values of the heat input. Main outcomes of the EQ model are the following:

- The computed values of the effective heat transfer coefficient decrease with the reduction of the filling ratio, which is not physically true.
- During the self-pressurisation, the value of the heat input decreases in time due to the increment of the internal temperature.
- The net mass flow drops when the storage container is closed. This drop increases with the increment of the initial filling ratio and of the heat input.
- The calculated pressure is lower than the experimental one, and the difference in pressure between the calculated and measured values increases with the increment of the heat fluxes and initial filling ratio.

- The vapour temperature of the EQ model is lower than the experimental one.
- The computed values of the liquid temperature and the filling ratio are similar to the experimental ones.
- The assumption of instantaneous thermodynamic equilibrium under-estimates the values of the pressure and the ullage temperature.
- The hypothesis of negligible thermal resistance does not compute valus of the effective heat transfer coefficient that are physically acceptable.

As consequence, the hypotheses of instantaneous thermodynamic equilibrium and of negligible thermal resistance are not suitable in predicting the behaviour of the cryogenic liquids in small scale tanks.

1.4. Chapter 4: Homogeneous model

Chapter 4 describes the theory of the homogeneous model (H model), presenting the hypothesis, the variables, the mathematical system and the algortimh. Chapter 4 explains the sub-models of the H model such as the boil-off rate (BOR) model, the storage heat transfer (SHT) model, the storage boundary layer (SBL) model, the interface heat transfer (IHT) model. Chapter 4 presents the comparison of the results of the H model with the experimental data and with the results of the equilibrium model, and the discussion of the results of the H model.

Section 1.4.1 recaps the theory of the H model. Section 1.4.2 presents the sub-models of the H model. Section 1.4.3 sums up the comparions and the discussions.

1.4.1. Theory of the homogeneous model

The homogeneous model (H model) is developed because the equilibrium model (EQ model) cannot predict the storage of cryogenic liquids in small scale storage containers due to the the hypothesis of the instantaneous thermodynamic equilibrium. As consequence, **in H model,** this hypothesis is substituted **by the hypotheses of local thermodynamic equilibrium, total homogeneity, and of actual thermodynamic state**:

- The first assumption states that only the interface is at thermodynamic equilibrium at the pressure of the ullage.
- The second and the third assumptions consider the liquid and the vapour as homogeneous and isothermal, at the “actual” thermodynamic state, which can be sub-cooled, overheated and saturated.

It turns out that pressure, liquid volume, liquid and vapour temperatures must be considered as additional variables in the H model. In the H model, the Ordinary Differential Equations (ODE) system is thus composed by the pressure-evolution (P^V-e), liquid volume-evolution (V^L-e), liquid temperature-evolution (T^L-e) and vapour temperature-evolution (T^V-e) equations. P^V-e, V^L-e, T^L-e, and T^V-e equations can be deduced from the energy and mass conservation laws with a procedure composed of 7 steps.

1.4.2. Sub-models of the homogeneous model

The equations of the ODE system of the homogeneous model (H model) are functions of the heat flows at each internal surface of the storage containers. These heat flows are calculated with the Storage Heat Transfer (SHT) model. In this sub-model, the temperature at each wall is homogeneous and the thermal inertia of the walls can be ignored. The environment-to-fluid heat transfer is composed of two steps, from the external wall to the internal wall, and from the internal wall to the fluid:

- At the bottom, the heat flow from the external wall must be equal to the bottom-to-liquid heat flow.
- At the wet side wall, the thermal energy flows from the external wall to the wet side wall, and this heat flow must be equal to the wet side wall-to-liquid heat flow.
- At the dry side wall, the heat flows from the external wall and from the wall of the roof. These 2 heat flows are balanced by dry side wall-to-interface heat flow and by the dry side wall-to-vapour heat flow.
- At the roof, the thermal energy transferred from the external wall is completely given to the dry side wall.

The temperatures of all these walls can be calculated from the heat flows and the heat transfer coefficients, which can be computed with the boundary layer and the semi-empirical approaches.

- At the bottom, the heat transfer coefficient is computed with the semi-empirical approach as function of the bottom-to-liquid heat flow.
- At the wet side wall, the heat transfer coefficient is computed with the boundary layer approach as function of the boundary layer variables, which are calculated with the Storage Boundary Layer (SBL) model as function of the difference in temperature between the wet side wall and the liquid.
- At the dry side wall, the heat transfer coefficient is computed with the boundary layer approach, where the boundary layer variables are computed as function of the difference in temperature between the dry side wall and the vapour.

As consequence, the calculation of the heat flow at each surface requires an iterative procedure. The bottom-to-liquid heat flow is computed with the Newton-Raphson method with finite difference[112]. The dry side wall-to-vapour heat flow and the wet side wall-to-liquid heat flows are calculated using the direct substitution method[113]. The dry side wall-to-interface heat flow is calculated with the 1 dimensional Fourier's law, where the temperature gradient in the dry side wall is computed as the ratio between the difference in temperature between the dry side wall and the interface and the distance between the middle point of the dry side wall and the interface.

To compute the heat flows at the internal surfaces of the storage container, the effective heat transfer coefficient is required and it is computed with the Boil-Off Rate (BOR) model. In the storage container, the ullage is thermally stratified and this stratification reduces the dry side wall-to-vapour heat transfer coefficient. So, the coefficient alpha (α) is added to correct this heat transfer coefficient that is calculated for the isothermal ullage. Due to the vapour thermal stratification, there is a temperature gradient in the dry side wall. The thickness of the side wall, which affects the dry side wall-to-interface heat flow, is not known and it is computed with ASME code. As consequence, the coefficient beta (β) is added to correct the calculation of the dry side wall-to-interface heat flow. To compute the effective heat transfer coefficient, and the corrective coefficients alpha and beta, the values of BOR, ullage temperature, pressure and filling ratio must be measured for two tests: one at high filling ratio and the other at low filling ratio. These values of the first test are used to compute the values of the effective heat transfer coefficient and of the coefficient beta. The values of BOR, ullage temperature, pressure and filling ratio of the second test are applied to compute the alpha and the beta

---

[112] Netwton-Raphson method with finite difference : $x = x_0 - f_1 \frac{x_2 - x_1}{f_2 - f_1}$

[113] Direct substituting method : $x = f^{-1}(g(x_0))$

coefficients. The effective heat transfer coefficient and the alpha coefficient are calculated with algorithms that uses the overall conservation laws of energy at the storage containers. The beta coefficient is computed with an algorithm that uses the steady state conservation laws of the ullage.

The equations of the ODE system of the H model are functions of the vapour-to-interface and the liquid-to-interface heat flows, and on the net mass flow. These variables are calculated with the Interface Heat Transfer (IHT) model, which is based on the hypothesis of rigid mass-less surface. This assumption states that the interface is a rigid surface that does not have mass:

- During the self-pressurisation, the interface is colder than the ullage, and it is assumed as a cold surface over a warm fluid. So, the vapour-to-interface heat flow can be computed as product between the heat transfer coefficient and the difference in temperatures between the vapour and the interface.
- At steady state, the liquid rises along the wet side wall, carrying sensible heat to the interface. So, the liquid-to-interface heat flow can be computed as function of the difference in temperatures between the boundary layer and the interface, and of the mass flow in the boundary layer. the temperature and the mass flwo in theobundary layer are computed with the SBL model;
- If the interface is at saturation as indicated by the hypothesis of the local thermodynamic equilibrium, the net mass flow can be computed from the interface energy conservation law.

In the IHT, the temperature and the mass flow in the boundary layer are computed with the SBL model. the temperature is obtained from the balance equations of enrgy and of mass of the sub-layer of the boundary layer. the mass flow is computed from the boundary layer variables such as the momentum thickness of the boundary layer (δ_M) and the velocity outside boundary layer of comparable forced-convection flow (U). In the SHT model, the heat transfer coefficients at the side walls are calculated from the boundary layer variables δ_M and U. These boundary layer variables are calculated with the Storage Boundary Layer (SBL) model, under the hypotheses of Boussinesq approximation[114], Newton's law of shear tensor[115], and the equality between the thermal and momentum thickness of the boundary layer. The SBL model is composed by the Exact Boundary Layer (EBL) and the Integral Boundary Layer (IBL) approaches. In the EBL approach, the boundary layer variables are calculated with the formulas of Squire [98] and of Eckert and Jackson [99], which are obtained by analytically integration of the conservation laws of energy and of momentum of the boundary layer of a isothermal vertical flat surface. So, the EBL approach is applied to the flat ends such as roof and bottom, and the IBL approach is used for the dry and wet side wall. In the IBL approach, the boundary layers at the wet and dry side walls are divided into sub-layers, along the vertical axis of the side wall. The conservation laws of energy and of momentum are numerically integrated in each sub-layer. The number of sub-layers is calculated for the wet and dry side walls, by increasing the number of these sub-layers until the numerical error of the integration is lower than the desired value. To increase the accuracy, the boundary layer variables δ_M and U are substituted by the momentum and energy pseudo-variables[116], which are respectively called M and E, and each sub-layer is divided into sub-space-points, whose number is calculated as function of the derivates of the pseudo-variables. In each sub-space-point, the conservation laws are numerically integrated with the Eulero forward method[117]. So, the relation between the fluid-dynamics and heat transfer is considered,

---

[114] The Boussinesq approximation states that the density variation only affects the buoyancy forces. This approximation is usually applied in fluid-dynamics of incompressible fluids.

[115] The Newton's law states the stresses are proportional to the rate of change of the fluid's velocity vector.

[116] Momentum pseudo-variable : $M = U^2 \cdot \delta_M$; energy pseudo-variable: $E = U \cdot \delta_M$

[117] Eulero forward method : $y = y_0 + \left.\frac{\partial y}{\partial x}\right|_0$

and the H model can be easily adapted to different geometries due to the discretisation of the side walls.

1.4.3. Comparison, discussion and conclusions

The results of the homogeneous model (H model) are compared with the experimental data of liquid nitrogen (LN_2) and of liquid hydrogen (LH_2) of Chapter 2. The interface heat transfer, the net mass flow, the pressure, the ullage and the liquid temperatures results are analysed. Main outcomes of the H model are the following:

- The values of the effective heat transfer coefficient remain constant with the filling ratio. These values increase with the increment of the heat input.
- The values of the alpha coefficient decrease with the reduction of the initial filling ratio, because the ullage thermal stratification reduces the value of the heat transfer coefficient.
- The values of beta are often equal to zero, indicating that the vapour-to-interface heat flow is over-estimated at steady state. So, **a new model of the vapour-to-interface heat flow should be proposed.**
- The computed initial values of the ullage temperature are lower than the experimental one due to the null values of the beta coefficient.
- The liquid-to-interface heat flow drops at the beginning of the self-pressurisation, due to the reduction of the difference in temperature between the boundary layer and the interface. After this drop, this heat flow is usually negative and the thermal energy flows from the interface to the liquid.
- The value of the liquid-to-interface heat flow increases with the reduction of the initial filling ratio because the convective flow of the boundary layer of the wet side wall reduces.
- The increment of heat fluxes at the storage container increases this convective flow, decreasing the value of liquid-to-interface heat flow.
- The vapour-to-interface and the dry side wall-to-interface heat flows remain almost constant during the self-pressurisation.
- The time-evolution of the net mass flow is qualitatively similar to the one of the liquid-to-interface heat flow.
- The calculated pressure is lower than the experimental one, and the difference increases with the increment of the heat fluxes. At low filling ratio, the value of this difference is lower than the one at high filling ratio.
- The low values of the calculated self-pressurisation rate are caused by the low values of the net mass flow.
- The low rate of ullage temperature increment is responsible for the low self-pressurisation rate for LH_2. So, **a new model of the liquid-to-interface heat flow is required.**
- At low heat fluxes, the computed vapour temperature is qualitatively similar to the experimental data.
- At medium and high heat fluxes, the computed curve of ullage temperature produces peaks, which are not experimentally observed. These peaks are caused by the reduction of the enthalpy flow of the net mass flow, when this mass flow decreases at the beginning of the self-pressurisation. As consequence, **the temperature profile should be considered for compute the enthalpy difference at the interface in the energy balance equation of the ullage**.
- The calculated liquid temperature agrees with the experimental data, except at high heat fluxes for liquid hydrogen.

The comparison with the experimental data indicates that a new model of the vapour-to-interface heat flow, and a new energy conservation law of the ullage are required due to the null value of the beta coefficient, and due to the peaks of temperature in the ullage.

The results of the H model are compared with the results of the equilibrium model (EQ model) to understand if the increment of the complexity increases the accuracy in computing the behaviour of cryogenic liquids in small scale tanks. Hence, the Average Absolute Deviation (AAD)[118], the BIAS[119] and the Maximum Absolute Deviation (MAD)[120] are calculated for the results of H and EQ models. The increment of the complexity increases the computational time of the H model, which is compared with the one of the EQ model. The computational time of the H model is higher than the one of the EQ model, but it remains lower than the physical time of the self-pressurisation period. Hence, the EQ model is enough fast for industrial applications. The AAD, the BIAS and the MAD of the pressure and of the ullage pressure of the H model are usually lower than the one of the EQ model. The values of the statistical errors of the filling ratio and of the liquid temperature of the H model are quite similar to the one of the EQ model. So, the hypothesis of the H model improves the calculation of the pressure and of the vapour temperature.

1.5.Chapter 5: Homogeneous model 2.0

Chapter 5 describes the theory of the homogeneous model 2.0 (H 2.0 model), presenting the hypothesis and the new energy balance equation of the ullage. Chapter 5 explains the sub-models of the H 2.0 model such as the boil-off rate (BOR) model, the storage heat transfer (SHT) model, the storage boundary layer (SBL) model, the interface heat transfer (IHT) model. Chapter 5 presents the comparison of the results of the H 2.0 model with the experimental data and with the results of the homogeneous model (H model), and the discussion of the results of the H 2.0 model.

Section 1.5.1 recaps the theory of the H 2.0 model. Section 1.5.2 presents the sub-models of the H 2.0 model. Section 1.5.3 sums up the comparions and the discussions.

1.5.1. Recap of the theory of the homogeneous model 2.0

The homogeneous model 2.0 (H 2.0 model) is developed to improve the prediction of the ullage temperature and the vapour-to-interface heat flow. These parameters respectively depend on the accumulation of the sensible heat and on the fluid-dynamics of the ullage. **The H 2.0 model is based on the hypothesis of the vapour virtual discretisatio, which states that the vapour is virtually discretized in sub-layer**. So, the ullage can be mathematically described with the overall ullage conservation laws of energy and of mass. The number of variables of the H 2.0 model is equal to the one of the H model. The vapour bulk temperature gradient, which is required to describe the fluid-dynamics in the ullage, is calculated with as ratio of the difference in temperatures between the vapour and the interface and of the distance between the middle point of the vapour and the interface. The overall energy conservation law of the ullage is deduced from the energy and mass conservation laws of each virtual vapour sub-layer. The vapour temperature-evolution (T^V-e) equation, which is deduced from the vapour energy conservation law, is quite similar to the one of the H model. The main difference is the coefficient F^{TV}, which describes the accumulation of sensible heat in the ullage. This coefficient is calculated as function of the dry side wall-to-interface heat flow, the vapour-to-interface

---

[118] Average absolute deviation : $ADD = \frac{1}{N_{EXP}} \cdot \sum_{i=1}^{N_{EXP}} |\xi_i|$

[119] BIAS : $BIAS = \frac{1}{N_{EXP}} \cdot \sum_{i=1}^{N_{EXP}} \xi_i$

[120] MAD : $MAD = \max[|\xi_i|]$

heat flow, the enthalpy flow of the net mass flow, the enthalpy flow of the mass flow entering and exiting the dry side wall boundary layer, and of the enthalpy flows of the descending mass flow. The enthalpy flow of the net mass flow is calculated as function of the difference in specific enthalpies between the first virtual sub-layer and the interface, instead of being computed as function of the difference in the specific enthalpy between the vapour and the interface. These descending flows are deduced from the steady state conservation laws of mass of the virtual sub-layers.

1.5.2. Sub-models of the homogenenous model 2.0

The T^V-e equation depends on the vapour-to-interface heat flow, and on the enthalpy flow of the net mass flow, as function of the liquid-to-interface heat flow. These heat and mass flows are calculated with the Interface Heat Transfer (IHT) model, which is based on the hypothesis of rigid mass-less interface as done in the homogeneous model (H model). The liquid-to-interface heat flow is calculated with two approaches, thus two equations, respectively called the boundary layer approach and the local natural convection approach, to consider the liquid fluid-dynamics near the interface, produced by the thermal stratification. So, the boundary layer approach is used when boundary layer temperature is higher than the interface one. The local natural convection approach is applied if the interface is warmer than the boundary layer. The vapour-to-interface heat flow is calculated as sum of the three contributions, which are the local natural convection, the descending flows of the ullage and the heat transfer across the virtual sub-layer, to consider the fluid-dynamics in the ullage. The descending flows in the ullage are computed as function of the net mass flow. As consequence, the net mass flow is computed with an iterative procedure, based on the Newton-Raphson with finite difference[112] method. In this method, the energy conservation law at the interface, which computes this mass flow, is used in this numerical method. This conservation law is similar to the one of the H model.

The T^V-e equation is a function of the dry side wall-to-interface heat flow, which can be computed with the Storage Heat Transfer (SHT) model. The energy conservation law of the dry side wall is the one of the H model, and the vapour-to-interface heat transfer coefficient is computed with the boundary layer approach, as done in the H model. The boundary layer variables are computed as function of the vapour bulk temperature gradient, which is considered in the H 2.0 model due to the hypothesis of the vapour virtual discretisation. This gradient reduces the stability of the direct substitution method[113], which is used for computing the dry side wall-to-liquid heat flow in the H model. So, this method is substituted by the Newton-Raphson with finite difference method[112]. The heat transfer coefficient is computed as function of the dry side wall-to-liquid heat flow. The bottom-to-liquid and the wet side wall-to-liquid heat flows are computed with the same algorithms and theories of H model.

The coefficient F^{TV} of the T^V-e equation is a direct function of the descending flows and of the mass flows that enter and exit the boundary layer. The vapour-to-interface heat flow depends on the descending flows, and the dry side wall-to-interface heat transfer coefficient is computed from the boundary layer variables. Hence, the time-evolution of the ullage temperature is connected to the fluid-dynamics, which is affected by the vapour bulk temperature gradient. The fluid-dynamics of the ullage is calculated with the Storage Boundary Layer (SBL) model. At the dry side wall, the boundary layer variables are computed by numerically integrating the momentum and energy conservation laws. The ullage bulk temperature gradient reduces the energy content in the boundary layer, causing the reduction of the boundary layer variables U and δ_M. When these variables decrease, the laminar viscous forces make the numerical integration unstable because these forces are functions of the ratio U/δ_M. So, only the turbulent regime is considered in the SBL model for the dry side wall. To stabilise the numerical integration, the number of the sub-space-points of this calculation is fixed at 10 because the method of the H model is not suitable when the bulk temperature gradient is added.

The heat flows at the internal walls of the storage container depend on the effective heat transfer coefficient (h_{eff}). The dry side wall-to-interface and the dry side wall-to-vapour heat flows are respectively function of the beta (β) and alpha (α) coefficients. The effective heat transfer coefficient and the coefficients alpha and beta are calculated with the Boil-Off Rate (BOR) model. As done in the H model, the test at high filling ratio is used to compute the effective heat transfer coefficient. The test at low filing ratio is used to calculate the alpha coefficient. The beta coefficient is computed with two algorithms, which are respectively called h_{eff}-β algorithm and α-β algorithm. The h_{eff}-β algorithm is similar to the one of the H model. h_{eff}-α algorithm is developed for the H 2.0 model because the formula used in the H model does not physically agree with the hypothesis of the H 2.0 model. The α-β algorithm is based on the energy conservation law of steady-state vapour. The Newton-Raphson with finite difference method[112] is used to compute the value of the β coefficient.

1.5.3. Comparison, discussion and conclusions

The results of the homogeneous model 2.0 (H 2.0 model) of fluid-dynamics/heat transfer at the dry side wall are analyzed and the results of pressure and ullage temperature are compared with the selected experimental data of. The values of the beta coefficient are sometime equal to zero at high and medium heat fluxes, due to the overestimation of the vapour-to-interface heat flow at steady state. The initial values of the ullage temperature, which depend on the value of the beta coefficient, are closer to the experimental data than the one of the H model. So, the description of the vapour-to-interface heat flow is better than the one of the homogeneous model (H model). The calculation of this heat flow at the steady state should be further improved. The values of alpha coefficient are usually closer to 1 than the ones of the H model. So, H 2.0 model agrees more with the physics in describing the effect of the fluid-dynamics on the heat transfer at the dry side wall than the H model.

At low heat inputs, the vapour bulk temperature gradient is almost constant during the self-pressurisation. At medium and high heat fluxes, this gradient increases in time and it increases with the increment of the initial filling ratio. The values of the mass flow in the boundary layer of the dry side wall decreases during the self-pressurisation because the bulk temperature gradient increases in time. At low heat fluxes, this mass flow increases with the reduction of the initial filling ratio because the length of the dry side wall increases. At medium and high heat fluxes, the mass flow in the boundary layer of the dry side wall decreases with the increment of the initial filling ratio and heat input, because the vapour bulk temperature gradient decreases.

The dry side wall-to-interface heat transfer coefficient decreases during the self-pressurisation at high heat fluxes. The time-evolution of this heat transfer coefficient is different at each test of the study cases at low and medium heat fluxes. The decrement of the heat transfer coefficient is caused by the reduction of the mass flow rate in the boundary layer, which is produced by the increment of the vapour bulk temperature gradient. At low heat fluxes, the dry side wall-to-vapour heat flow increases with the reduction of the filling ratio because the surface area increases. At medium and high heat fluxes, the values of this heat flow at medium filling ratio are usually higher than the one at the other filling ratios, because the dry side wall heat transfer coefficient decreases with the liquid level.

The liquid-to-interface heat flow drops at the beginning of the self-pressurisation as in the H model. This drop is lower than the one of the H model and the values of this heat flow are higher than the one of the H model. Hence, the local convection approach, which is used during the self-pressurisation, computes values of the absolute liquid-to-interface heat flow that are lower than the one of the boundary layer approach. The time-evolution of the dry side wall-to-interface heat flow is similar to the one of the H model. The time-evolution of the vapour-to-interface heat flow is quite similar to the one of the H model. The time-evolution of the net mass flow is similar to the one of the H model. The values of this mass flow are higher than the one of the previous model due to the local convection approach of the liquid-to-interface heat flow.

At low heat fluxes, the calculated pressure is often close to the experimental data. **At medium and high heat fluxes, the calculated pressure is lower than the experimental data**. This computed variable is slightly higher than the one of the H model because the net mass flow is higher than the one of the previous mode, due to the local natural convection approach of the liquid-to-interface heat flow. The computed ullage temperature monotonically increases during the self-pressurisation at low, medium and high heat fluxes. The computed values are often in agreement with the experimental data. So, the energy conservation law of the ullage is coherent with the physics.

The results of the H 2.0 model are compared with the one of the H model, by computing the Average Absolute Deviation (AAD), the BIAS and the Maximum Absolute Deviation (MAD). The computational time of the H 2.0 is sometime higher than the one of the H model. The difference in computational time between these models is low. Hence, the increment of the complexity of the ullage has not significantly changed the computational time. The AAD of the pressure is usually lower than the one of the H model, because the pressurisation rate is higher than the one of the H model, due to the local natural convection approach of the liquid-to-interface heat flow. The AAD of the ullage temperature is lower than the one of the H model due to the conservation law of the energy of the ullage, which is deduced from the hypothesis of vapour virtual discretisation**. As consequence, the prediction of the time-evolution of the pressure must be improved**, because the computed values are far away from the experimental data, in particular at high and medium heat fluxes. So, **a new storage model is required**.

1.6.Chapter 6: liquid stratification model

Chapter X describes the theory of the liquid stratification model (LS model), presenting the hypotheses, the variables, the mathematical system and the algortimh. Chapter X explains the sub-models of the LS model such as the intra-laer heat transfer (ILHT) model, the storage heat transfer (SHT) model, the storage boundary layer (SBL) model and the interface heat transfer (IHT) model. Chapter X presents the comparison of the results of the LSS model with the experimental data and with the results of the homogeneous model 2.0 (H 2.0 model), and the discussion of the results of the LS model.

Section recaps the theory of the LS model. Section presents the sub-models of the LS model. Section sums up the comparions and the discussions.

1.6.1. Theory of the liquid stratification model

The pressure is under-estimated in the previous models because the liquid-to-interface heat flow excessively decreases during the self-pressurisation, due to the hypothesis of homogenous liquid. So, to improve the prediction of the pressure, the liquid bulk temperature gradient has been considered in the liquid stratification model (LS model) under the hypothesis of liquid discretisation. This assumption states that the liquid can be discretized in sub-layer of equal thickness, and each sub-layer is divided into the bulk and the boundary layer. The boundary layer volume is much lower than the one of the bulk of the sub-layer, thus the boundary layer of the sub-layer can be considered at steady state. The first sub-layer is called bottom sub-layer, and the last sub-layer is called interface sub-layer.

The remaining sub-layers are called each the core sub-layer. The number of the sub-layers of the liquid is calculated as done in the homogeneous model (H model) for the sub-layer of the wet side wall. Due to the hypothesis of the liquid discretisation, the new variables of the LS model are the bulk liquid temperature, the thickness, the liquid descending mass flow, the bulk liquid volume and the liquid pressure in each sub-layer. These new variables, the pressure and the ullage temperature are calculated by solving the Ordinary Differential Equations (ODEs) of the LS model. This system is composed of the (P^V-e) evolution, thickness-evolution (dxL-e), liquid bottom, liquid core and liquid interface temperature-evolution ($T^L{}_1$-e, $T^L{}_{nL}$-e and $T^L{}_{NL}$-e), and vapour temperature-evolution (T^V-e) equations. This system is coupled with the algebraic equations of the first and core descending flows (FDF and CDF) to compute the descending mass flows. In the ODE solver, the computed values of the liquid temperatures can be unphysical, and cold and hot spots can be computed. To avoid this, the temperatures in all sub-layers are equal to the average liquid temperature when the interface is cooler than the interfacial temperature. If the interface is warmer than the average liquid temperature, the liquid temperature is equal to the reduced average liquid temperature in the sub-layers that are below the hot/cold spot. This reduced temperature is computed as average value in sub-layer below the hot/cold spots. The P^V-e, dxL-e, $T^L{}_1$, $T^L{}_{nL}$, $T^L{}_{NL}$-e, T^V-e, FDF and CDF equations can be deduced with a mathematical procedure, which is composed of 8 steps.

The energy and mass conservation laws of each sub-layer depends on the convective flows of the liquid, which are the rising flow of the bottom and the liquid descending flow. Due to the heat input at the bottom, the convective flow is produced and the mass flow rises from the bottom to the core of the liquid. This mass flow cannot rise if the temperature of the liquid increases along the vertical axis, and if the mass flow of the wet side wall boundary layer is higher than the rising flow of the bottom. The rising flow of the bottom is computed with the Exact Boundary Layer (EBL) approach of the Storage Boundary Layer (SBL) model. The descending flows are calculated with the FDF and the CDF equations. The coefficients of these equations are functions of the direction of these mass flows. As consequence, the descending mass flow, thus the time-derivates of the variables of the LS model, are obtained with an iterative procedure.

1.6.2. Sub-models of the liquid stratification model

The mass and energy conservation laws of each sub-layer are functions of the heat transferred across the sub-layer. This heat transfer is calculated with the Inter-Layer Heat Transfer (ILHT) model, which is based on the hypothesis of competitive heat transfer mechanism and of the hypothesis of the rigid surface. In this model, this heat transfer is composed by the upper and the lower heat flows, which are computed as function of three fluid-dynamics condition: no-static, the semi-static and the static. The upper and the lower heat flows are calculated as function of the difference in temperatures between the sub-layer and the thermal resistance. This resistance is computed as function of the different fluid-dynamics conditions, using the heat transfer coefficient of the semi-empirical approach of the Storage Heat transfer (SHT) model for flat horizontal surfaces facing downward and upward.

The heat flows at each surface of the storage container are present in the energy and mass conservation laws of the ullage and of each sub-layer. Thus they affect the P^V-e, dxL-e, $T^L{}_1$, $T^L{}_{nL}$, $T^L{}_{NL}$-e, T^V-e, FDF and CDF equations. These heat flows are the bottom-to-liquid, the wet side wall-to-liquid, the dry side wall-to-liquid and the dry side wall-to-interface. The bottom-to-liquid is calculated as done in the homogeneous model (H model), but the temperature of the bulk bottom sub-layer is used instead of the average liquid temperature. The dry side wall-to-interface and dry side wall-to-vapour heat flows are calculated as done in the H 2.0 model. Due to the hypothesis of liquid discretisation, the wet side wall-to-liquid heat flow is computed in each sub-layer. The wet side wall is discretized in the same number of sub-layers of the liquid. The steady state energy conservation law is applied to each of those sub-layers, neglecting the conductive heat flow between each sub-layer of the wall. Except for the interface sub-layer of the wet side wall, the environment-to-wet side wall heat flow is equal to the wet side wall-to-liquid heat flow. At the interface sub-layer of the wet side wall, the wet side wall-to-liquid heat flow is equal to the sum of the environment-to-wet side wall heat flow and of the dry side wall-to-interface heat flow. The heat transfer coefficients at the wet side wall are calculated with the boundary layer approach, where the boundary layer variables are calculated considering the liquid bulk temperature gradient. These variables are calculated as function of the wet side wall-to-liquid heat flow. As consequence, this heat flow is calculated with an iterative procedure, which is applied at each sub-layer.

The descending flows, the rising flows of the bottom and the heat transfer coefficients at the side walls, depend on the boundary layer variables, which are calculated with the Storage Boundary Layer (SBL) model. The boundary layer variables and the mass flow at the bottom and at the dry side wall are computed respectively with the Exact Boundary Layer (EBL) approach and the Integrated Boundary Layer (IBL) approach, as it is done in the homogeneous model 2.0 (H 2.0 model). The number of the sub-space-points of the sub-layer of the dry side wall is set to 25 to increase the precision of the numerical integration. At the wet side wall, the IBL approach considers the liquid bulk temperature gradient. So, only the turbulent regime is considered because the laminar viscous forces equation creates instabilities during the numerical integration when this gradient is added. In the numerical integration, the number of the sub-space-points is fixed to 10.

The mass and energy conservation laws of the ullage and of the sub-layer depend on the liquid-to-interface and vapour-to-interface heat flows, and on the net mass flow. The vapour-to-interface heat flow is calculated with the approach of the H 2.0 model. The net mass flow is computed with the iterative procedure of the H 2.0 model. In this procedure, the energy conservation law at the interface neglects the dry side wall-to-interface heat flow. The liquid-to-interface heat flow is computed with the approach of the dominant heat transfer mechanism, due to the lack of experiments on the fluid-dynamics of the liquid near the interface. In this approach, the boundary layer, the local convection and the conduction heat transfer mechanisms are considered. The maximum absolute value of the heat flow of these approaches is the heat transfer mechanism that computes the liquid-to-interface heat flow.

1.6.3. Comparison, discussion and conclusions

The results of the LS model are compared with Study cases 1, 2, 5, and 7. The fluid-dynamics and the heat transfer at the wet side wall, the fluid-dynamics in the liquid, the intra-layer heat transfer, the interface heat transfer and the net mass flow are discussed. The computed pressure and the liquid temperature profile are compared with the experimental data. The ullage temperature, the average liquid temperature and the filling ratio are not compared because they are not significantly affected by the hypothesis of the liquid discretisation.

The fluid-dynamics at the wet side wall is analyzed with the liquid bulk temperature gradient and with the mass flow rate in the boundary layer of the wet side wall. This gradient is equal to zero near the bottom, and it is slightly above zero in the core of the liquid. As the interface is approached, the liquid bulk temperature gradient rapidly increases due to the accumulation of sensible heat. The liquid bulk temperature gradient usually increases in time. This gradient can reduce during the self-pressurisation due to the method of controlling the temperature profile, contrarily to the experimental data. The mass flow in the boundary layer of the wet side wall linearly increases at the end of the steady state[121] because the liquid bulk temperature gradient is equal to zero. During the self-pressurisation, this mass flow rapidly decreases near the interface, and it is sometime equal to zero due to the increment of the liquid bulk temperature gradient.

The heat transfer at the wet side wall is analyzed with the heat transfer coefficient at the wet side wall and with the wet side wall temperature. This heat transfer coefficient monotonically increases at the end of the steady state because the liquid bulk temperature gradient is equal to zero. During the self-pressurisation, the wet side wall heat transfer coefficient increases in the bottom and in the core, where this temperature gradient is low. As the interface is approached, this heat transfer coefficient usually decreases due to the reduction of the boundary layer variables. The wet side wall temperature, which is computed with the heat transfer coefficient, is usually constant in the core of the liquid. During the self-pressurisation, this wall temperature increases near the interface due to the reduction of the heat transfer coefficient. The value of the wall temperature can be as high as the one of the ullage, which is unrealistic.

The descending mass flow and the rising flow of the bottom describe the fluid-dynamics in the liquids. The rising mass flow is constant in the sub-layers near the bottom. This mass flow is equal to zero in the core and at the interface, because this mass flow is lower than the boundary layer mass flow of the wet side wall. During the self-pressurisation, the zone in which the mass rising flow is above zero reduces, due to the bulk temperature gradient. The descending mass flow increases from the bottom to the interface. During this increment, this mass flow drops due to the reduction of the rising flow of the bottom. The descending mass flow decreases during the self-pressurisation due to the reduction of the mass flow in the boundary layer of the wet side wall.

The upper and the lower heat flows increase near the interface due to the increment of the liquid bulk temperature gradient. The liquid-to-interface heat flow decreases at the end of the steady state. The values of this heat flow are higher than the one of the previous model. The liquid-to-interface heat flow fluctuates during the self-pressurisation. At high heat fluxes, peaks of these heat flows are observed due to the reduction of the bulk temperature gradient, which is caused by the method of controlling the temperature profile. The vapour-to-interface heat flow fluctuates due to the fluctuations of the liquid-to-interface heat flow. The time-evolution of the net mass flow is similar to the one of the liquid-to-interface heat flow.

The calculated pressure is close to the experimental data for three conditions: at high heat input in low heat fluxes storage container; at high filling ratio and medium heat fluxes; at high heat fluxes. In the other storage conditions, **this variable is higher than the experimental one because the accumulation of the sensible heat at the interface is higher than what it should be.** This excessive accumulation is caused by the assumption of the turbulent regime in the SBL model of the wet side wall, and by the hypothesis of no conduction, which does not consider the conduction in the wet side wall. **So, a new heat transfer model of the wet side wall is required. The computed relation between the pressure and the initial filling ratio is in line the experimental one** because the computed pressure reduces with the reduction of the initial filling ratio, as experimentally observed.

The results of the LS model are compared with the one of the H 2.0 model. The Average Absolute Deviation (AAD), the BIAS and the Maximum Absolute Deviation (MAD) of the LS model are computed for the pressure. The average AAD values of the tests of the LS model are 3.7 %, 28 % and 9.2 % at low, medium and high heat fluxes, respectively. **Except at medium heat fluxes, these values**

---

[121] Except for Test 2 of Study case 3, each simulation is composed by a steady state period and by the self-pressurisation period, as done in the experiments.

are lower than the of the H 2.0 model. Thus, the hypothesis of the liquid discretisation has improved the prediction of the pressure. The computational time of the LS model is at least 2 orders of magnitude higher than the one of the H 2.0. So, the computational time of the LS model is much higher than the one of the H 2.0 model. The increment of this variable is caused by the two sub-models: the SHT and the SBL models. The SHT computes the wet side wall-to-liquid heat flow with an iterative procedure at each sub-layer, instead of the overall value as done in the H 2.0 model. At each iteration, the SBL model is used for computing the boundary layer variables to calculate the heat transfer coefficient, increasing the computational time. **Hence, a new method of integrating the conservation laws of momentum and of energy of the boundary layer is required.**

2. Conclusions

Despite many models are available in the literature for taking into account storage phenomena, these models were not validated with respect to a large set of data, do not describe the impact of the bulk temperature gradient on the fluid-dynamics, and do not relate the heat transfer at the side walls with the fluid-dynamics. So, the objective of this thesis was the development of a physical model capable of taking into account these aspects and of predicting the behaviour of cryogenic pure liquids in small scale tanks used in industrial applications. The equilibrium model (EQ model) has been developed under the hypothesis of instantaneous thermodynamic equilibrium. This hypothesis is unsuitable for computing the time-evolutions of pressure, ullage temperature and liquid temperature. So, the homogeneous model (H model) is developed under the hypothesis of total homogeneity. The computed pressure is lower than the experimental one due to the neglect of the temperature gradient in the liquid. The calculated vapour temperature produces peaks, which are not experimentally observed, due to the isothermal state of the ullage. So, the homogeneous model 2.0 (H 2.0 model) is developed to qualitatively correct the increment of the ullage temperature. The hypothesis of the vapour virtual stratification is used and this hypothesis succeeds in computing accurately the time-evolution of the ullage temperature. Then, the liquid stratification model (LS model) is developed to enhance the prediction of the increment of the pressure in the storage containers during self-pressurization. The hypotheses of vapour virtual discretisation and of liquid discretisation are applied. The time-evolution of the computed pressure qualitatively agrees with the experimental data, and it is often quantitatively close to the measured values. Hence, it can be concluded that:

a) The hypothesis of instantaneous thermodynamic equilibrium) and of thetotal homogeneity are unsuitable for computing the behaviour of the cryogenic liquid in small scale tank;
b) The hypothesis of vapour virtual discretisation is suitable for qualitatively predicting the heat accumulation in the ullage and the vapour-to-interface heat flow;
c) The hypothesis of the liquid discretisation can qualitatively and often quantitatively predict the self-pressurisation rate in close storage containers;
d) The fluid-dynamics model considers the effect of the bulk temperature gradient. This can be flexibly adapted to the geometry of the storage containers, due to the discretisation of the boundary layer. The laminar turbulent regime should be considered in the conservation laws of momentum and of energy in the boundary layer. A new algorithm is required for integrating these conservation laws;
e) The heat transfer model is directly related to the fluid-dynamics, as it is deduced from the experimental observations;
f) The heat transfer between the liquid sub-layers is considered, and the heat flow does not depend on the thickness of the sub-layer, as considered in the models in the literature [122].
g) The Boil-Off Rate (BOR) model can compute the lumped effective thermal resistance of the storage container, from the key information such as the geometry and the nominal rate of evaporation;
h) The dry side wall heat flow, and the dry side wall-to-vapour heat transfer coefficient, which are obtained by unphysical hypothesis, are corrected with parameters deduced from the experimental data of heat inputs;
i) The computational time of the LS model is too high for industrial applications due to the numerical integration of the conservation laws of momentum and of energy;

As consequence, the development of the physical model to compute the behaviour of the cryogenic liquids is not yet completed. Nevertheless, an important step forward in the modelling of complex phenomena occurring in small scale tanks has been achieved during this work.

3. Perspectives

As it is reported in Section 2, the liquid stratification model (LS model) has some critical issues:

a) Lack of useful experimental data hinders the validation of the results related to fluid-dynamics and heat transfer;
b) Fluctuations of the liquid-to-interface heat flow;
c) Excessive accumulation of the sensible heat near the interface due to the hypotheses of no conduction and turbulent regime;
d) High computational time due to the method of integrating the momentum and energy conservation laws of the boundary layer;
e) Null values of beta coefficients are not consistent in the model of computing the vapour-to-interface heat flow at the steady state;
f) The use of the beta and alpha coefficients because the vapour and the dry side wall are isothermal;

Due to the high computational time, further simulations will be needed in the future to pursue the development and improve the prediction of the behaviour of cryogenic liquid can be tested; in addition, the model could be considerably improved if fluid-dynamic and heat transfer experimental data will be produced.

Because of the fluctuations of the liquid-to-interface heat flow, the values of the heat flow-depending differential equations frequently changes in time. So, the numerical method used for solving the Ordinary Differential Equation (ODEs), which is the Runge-Kutta-Fehlberg method with Cash-Karp parameters [131] (RKF-CKp), computes a small time-step to reduce as possible the numerical error of the time-integration. As a consequence, the computational time can increase. If the accumulation of sensible heat is not properly computed, the computed pressure will be higher than the experimental one. The physical model will therefore be not enough accurate. Without comparing variables related to the fluid-dynamics and the heat transfer with the experimental data, the heat transfer mechanism at the wet side wall and near the interface cannot be determined. Moreover, the accuracy of computing the boundary layer variables (in particular the thickness) cannot be evaluated.

If the value of the beta coefficient is equal to zero, the behaviour of the ullage cannot be quantitatively computed because the ullage temperature at the steady state will be lower than the observed one. The use of the beta and alpha coefficient limits the industrial application of the physical model because experimental data of the heat input of the storage container are required to compute the values of these coefficients. So, these critical issues have different level of importance for developing the physical model, thus they are addressed with a specific chronological order. The level of importance and the chronological order are reported in Table 151.

Table 151. Level of importance and chronological order.

Critical issue	Level of importance	Chronological order
Lack of useful experimental data (a))	Medium-high	After solving the critical issue c)
Fluctuations of liquid-to-interface heat flow (b))	High	To do as soon as possible
Excessive accumulation (c))	Medium-high	After solving the critical issue d)
High computation time (d))	High	To do as soon as possible
Vapour-to-interface heat flow (e))	Medium	After solving the critical issue a)
Beta and alpha coefficients (f))	Medium	Last critical issue to be solved

As it is reported in Table 151, the critical issue a) and b) are the subjects that have to be firstly solved because these issues significantly increases the computational time, slowing down the development of the physical model, which requires a lot of tests. Then, the critical issues c) and a) can be solved to improve the accuracy in computing the pressure, which is the most important variable. At the end, the critical issues e) and f) can be solved to increases the applicability range of the physical model.

Section 3.1 explains how the computational time can be reduced. Section 3.2 describes how the fluctuations of the liquid-to-interface can be removed. Section 3.3 presents the method for increasing the prediction of the accumulation of the sensible heat. Section 3.4 explains the discretisation of the ullage, which can be used for removing the beta and alpha coefficients, and for computing the vapour-to-interface heat flow. Section 3.5 explains the two regions liquid model, as alternative to reduce the computational time. Section 3.6 presents the possible experimental champaign.

3.1. Reducing the computational time: Runge-Kutta-Felberg for the numerical integration in the Storage Boundary Layer model

As it is experimentally observed, the (vapour or liquid) bulk temperature gradient determines the fluid-dynamics at the (wet and dry) side walls. The heat transfer at the side walls of the storage container is related to the free-convective flows at these surfaces. In the liquid stratification model (LS model), this relation is considered by computing the heat transfer coefficients at the dry and wet side walls as function of the boundary layer variables U and δ_M. The (wet and dry) side wall is discretized in sub-layers, whose number is computed with an iterative procedure (see Section 1 of Appendix L). This procedure increases the number of the sub-layer until the numerical error of computing the mass flow in the boundary layer is lower than the desired value of the error. Each sub-layer is divided into sub-space-points (see Section 2.1.4.1 of Appendix P). The boundary layer variables U and $\delta_M$are calculated by numerically integrating the conservation laws of momentum and of energy in these sub-space-points (see Section 2.1.4.2 of Appendix P). The Eulero forward method^{117} is used to do this calculation. This method is less accurate than Runge-Kutta method or other high orders integration methods. If the accuracy of the calculation increases, the number of the sub-layer can be reduced and the division in sub-layers can be removed. So, to reduce the computational time, it is mandatory to use a numerical integration method that is accurate. Hence, the number of sub-layer can be reduced without losing accuracy.

Runge-Kutta-Feldberg (RKF) method, which is an explicit fourth-order method, can substituted the Eulero forward method because it has high accuracy and it does not require a starting method, as indicated by Perry [140]. This method computes the approximated solution ($\tilde{y}_{x_0+\Delta x}$) of the differential system as follows:

Equation 541 $$\tilde{y}_{x_0+\Delta x} = \tilde{y}_{x_0} + \frac{25}{216}\cdot k_1 + \frac{1408}{2565}\cdot k_3 + \frac{2197}{4104}\cdot k_4 - \frac{1}{5}\cdot k_5$$

k_1, k_3 and k_5 are the increments of the variable and they are computed as follows:

Equation 542 $$k_1 = \Delta x \cdot f(x_0, \tilde{y}_{x_0})$$

Equation 543 $$k_3 = \Delta x \cdot f(x_0 + \frac{3}{8}\cdot \Delta x, \tilde{y}_{x_0} + \frac{3}{32}\cdot k_1 + \frac{9}{32}\cdot k_2)$$

Equation 544 $$k_5 = \Delta x \cdot f(x_0 + \Delta x, \tilde{y}_{x_0} + \frac{439}{216}\cdot k_1 - 8\cdot k_2 + \frac{3680}{513}\cdot k_3 - \frac{845}{4104}\cdot k_4)$$

k_2 and k_4 can be calculated as follows:

Equation 545 $$k_2 = \Delta x \cdot f(x_0 + \frac{1}{4}\cdot \Delta x, \tilde{y}_{x_0} + \frac{k_1}{4})$$

Equation 546 $$k_4 = \Delta x \cdot f(x_0 + \frac{12}{13}\cdot \Delta x, \tilde{y}_{x_0} + \frac{1932}{2197}\cdot k_1 - \frac{7200}{2197}\cdot k_2 + \frac{7296}{2197}\cdot k_3)$$

The main drawback of this method is the time for computing the derivates for the increments k_1, k_2, k_3, k_4 and k_5. The conservation laws of momentum and of energy (Equation 178 and Equation 179) are quickly computed because they can be computed with simple formulas (see Table 78) from the boundary layer variables. So, the increment of the time for computing k_1, k_2, k_3, k_4 and k_5 should not increase the computational time of the SBL model. Considering that RKF method uses 5 intermediates points, the number of the sub-space-points can be potentially reduced to 1, further reducing the computational time.

3.2. Fluctuations of the liquid-to-interface heat flow: fluid-dynamics-dominant heat transfer mechanism

To reduce the fluctuations ofthe liquid-to-interface heat flow, this heat flow is computed with the fluid-dynamics-dominant heat transfer mechanism, which is combination of the fluid-dynamics and of dominant heat transfer mechanism.

The liquid-to-interface heat flow ($\dot{Q}_L^I$) is computed with the method of the dominant heat transfer mechanism in the liquid stratification model (LS model) (see Section of Chapter X). This method considers that the thermal energy can be exchanged at the interface with three heat transfer approaches. The only approach among them that is considered in the calculations is the one with the highest absolute value (equation). These heat transfer approaches are the boundary layer, the local natural convection, and the conduction. The boundary layer mechanism depends on the mass flow in the second-last sub-layer of the wet side wall ($\dot{m}_{N^L}^{BL} = \dot{m}_{N^L-1}^{UP}$), and on the difference in temperatures between the boundary layer of the interface sub-layer ($T_{N^L}^{BL}$) and the interface (T^I) (equation). The local natural convection and the conduction heat transfer are functions of the difference in temperature between the bulk of the interface sub-layer ($T_{N^L}^{B,L}$) and the interface (equation). During the self-pressurisation, the temperature difference ($T_{N^L}^{BL} - T^I$) between the boundary layer of the interface sub-layer and the interface reduces. The absolute value of this heat transfer mechanism is similar to the one of the local natural convection. Hence, the liquid-to-interface heat flow fluctuates between the values of the boundary layer mechanism and the one of the local natural convection mechanism.

During the self-pressurisation, the mass flow in the boundary layer can continue its flow above the interface, as experimentally observed [20], [21], [139]. This motion of fluid suppresses the development of the local natural convection near the interface, which is composed by small recirculation of fluid. So, the fluid-dynamic conditions to select the heat transfer mechanism should be defined as described in Figure 195. In Figure 195, the orange rectangle is the vapour, and the black rectangles are the side walls. The blue rectangles are the liquid sub-layers (bulk and boundary layer). The white arrows with blue boarders are the mass flows, and the white arrows with red boarder are the enthalpy and heat flows. The red vertical arrows are the conduction heat flows.

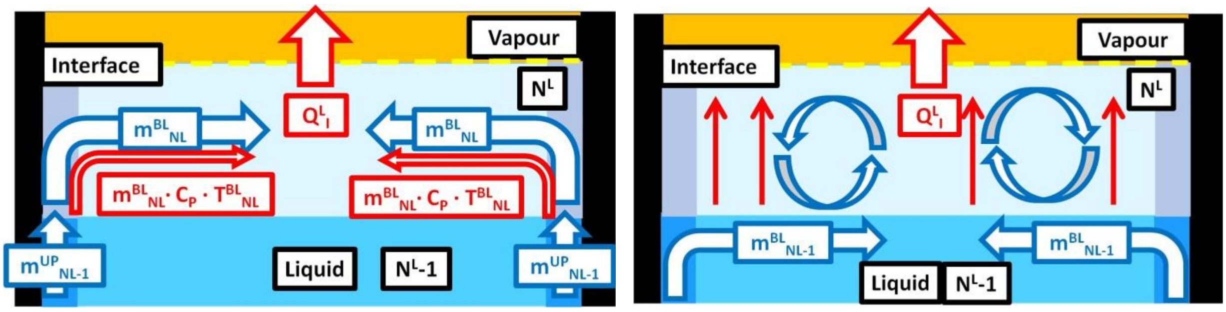

a)

b)

Figure 195. Fluid-dynamics-dominant heat transfer mechanism: a) boundary layer mechanism; b) dominant heat transfer mechanism between convection and conduction.

As it is described in Figure 195, the boundary layer mechanism is considered until the mass flow in the boundary layer of the second-last sub-layer is higher than 0. Once this condition is not respected, the dominant heat transfer approach is applied only for conduction and local natural convection. So, the fluid-dynamics conditions and the dominant heat transfer approach determine the type of heat transfer mechanism for computing the liquid-to-interface heat flow. This heat flow can be computed from the equations in Table 152.

Table 152. Equations of the fluid-dynamics-dominant heat transfer.

Approach	Equation	Formula	Condition
Boundary layer	Equation 547	$\dot{Q}_L^I = \dot{m}_{N^L}^{BL} \cdot C_L^P \cdot \left(T_{N^L}^{BL} - T^I\right)$	$\dot{m}_{N^L}^{BL} > 0$
Dominant	Equation 548	$\dot{Q}_L^I = \max\left[\dot{Q}_{L,CV}^I, \dot{Q}_{L,CD}^I\right]$	$\dot{m}_{N^L}^{BL} = 0$

$T_{N^L}^{BL}$ and $\dot{m}_{N^L}^{BL}$ are computed with the Storage Boundary Layer (SBL) model of the wet side wall. C_L^P is the specific heat at constant pressure. $\dot{Q}_{L,CV}^I$ and $\dot{Q}_{L,CD}^I$ are respectively the convection and the conduction liquid-to-interface heat flows. These heat flows can be computed with the equations of Table 153.

Table 153. Equations of convection and conduction liquid-to-interface heat flows.

Approach	Equation	Formula
Convection	Equation 549	$\dot{Q}_{L,CV}^I = h_L^I \cdot A^I \cdot \left(T_{N^L}^{SBL} - T^I\right)$
Dominant	Equation 550	$\dot{Q}_{L,CD}^I = \frac{k_L}{dxL} \cdot A^I \cdot \left(T_{N^L}^{SBL} - T^I\right)$

h_L^I is heat transfer coefficient of the convective heat flow and it is computed with the semi-empirical approach (see Section 4.6 of Chapter 4), using the formulas of the downward and upward flat warm horizontal surfaces [138] (see Section 2 of Appendix N).

3.3. Accumulation of the sensible heat: conductive approach of the wet side wall heat transfer and laminar-turbulent fluid-dynamics regime

The computed pressure of the liquid stratification model (LS model) is higher than the experimental data because the liquid temperature at the interface is higher than the experimental one. This condition of high liquid temperature is caused by the excessive accumulation of the sensible heat, due to the hypotheses of no conduction (assumption c) of Section 5.1.1 of Chapter 6) and turbulent fluid-dynamic regime (see Section 6.1 of Chapter 6). This critical issue can be solved with: the conductive approach of the wet side wall heat transfer and with the laminar-turbulent fluid-dynamic regime.

Section 3.3.1 explains the conductive approach. Section 3.3.2 describes the laminar-turbulent fluid-dynamic regime.

3.3.1. Conductive approach of the wet side wall heat transfer

In the liquid stratification model (LS model) (see Section 5.1.1 of Chapter 6), the wet side wall is divided into sub-layers, as done for the liquid. The environment-to-wet wall heat flow ($\dot{Q}_{eff,n_L}^{SL}$) is immediately transferred to the liquid for all the sub-layers, except in the interface sub-layer of the wet side wall. So, $\dot{Q}_{eff,n_L}^{SL}$ is equal to the wet side wall-to-liquid heat flow ($\dot{Q}_{w,n_L}^{SL}$). In the interface sub-layer, the wet side wall-to-liquid heat flow is equal to the sum of the environment-to-wet wall heat flow and the dry side wall-to-interface heat flow ($\dot{Q}_w^{LV}$). Due to the hypothesis of no conduction, the thermal energy is not transferred by conduction between each sub-layer of the wet side wall.

The conductive approach of the wet side wall heat transfer can be illustrated with Figure 196. In Figure 196, the white arrows with the red boarder are the environment-to-wet wall, wet side wall-to-liquid, dry side wall-to-interface and conductive ($\dot{Q}^{CD}_{n_L}$) heat flows. The white circles with the purple boarder are the wall temperatures. The black squares with orange boarder are the sub-layers of the wet side wall. The horizontal dashed lines indicate that some sub-layers are omitted and these sub-layers are located between these lines.

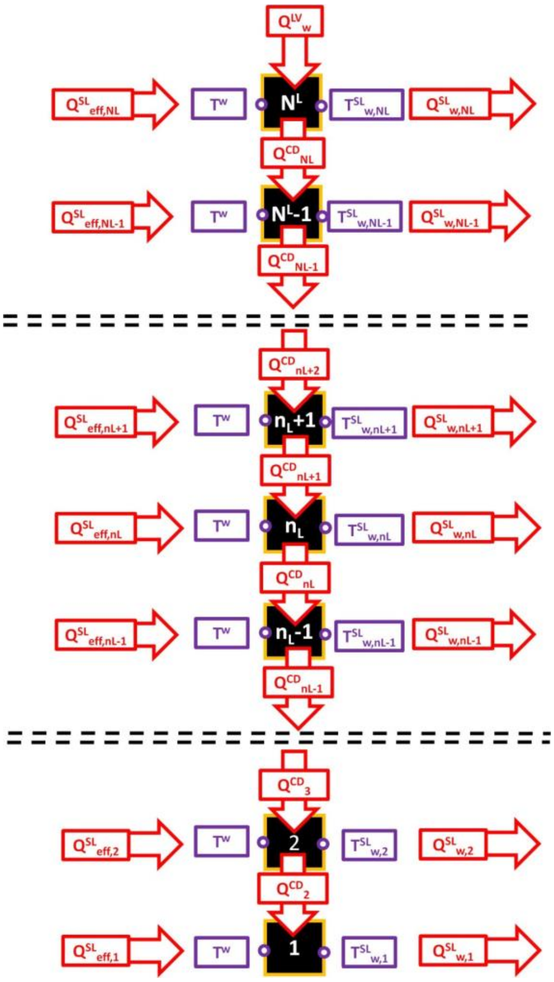

Figure 196. Conductive approach of the wet side wall heat transfer.

As it is described in Figure 196, the wet side wall is discretized in sub-layers, as many as the one of the liquid. The first sub-layer is called bottom sub-layer and the last sub-layer is called interface sub-layer. The remaining sub-layers are called core sub-layer. The thermal energy is transferred along the wet side wall by conduction. So, the energy conservation law at the wet side wall can be described with the equations of Table 154.

Table 154. Conservation laws of energy at the sub-layer of the wet side walls of the conductive approach.

Sub-layer	Equation	Formula
Bottom	Equation 551	$\left[h_{eff} \cdot dA^{SL}_{1} \cdot \left(T^{w} - T^{SL}_{w,1}\right) + \dot{Q}^{CD}_{2}\right] - h^{SL}_{w,1} \cdot dA^{SL}_{1} \cdot \left(T^{SL}_{w,1} - T^{B,L}_{1}\right) = 0$
Core	Equation 552	$\left[h_{eff} \cdot dA^{SL}_{n_L} \cdot \left(T^{w} - T^{SL}_{w,n_L}\right) + \dot{Q}^{CD}_{n_L+1}\right] - h^{SL}_{w,n_L} \cdot dA^{SL}_{n_L} \cdot \left(T^{SL}_{w,n_L} - T^{B,L}_{n_L}\right) - \dot{Q}^{CD}_{n_L} = 0$
Interface	Equation 553	$\left[h_{eff} \cdot dA^{SL}_{N^L} \cdot \left(T^{w} - T^{SL}_{w,N^L}\right) + \dot{Q}^{LV}_{w}\right] - h^{SL}_{w,N^L} \cdot dA^{SL}_{N^L} \cdot \left(T^{SL}_{w,N^L} - T^{B,L}_{N^L}\right) - \dot{Q}^{CD}_{N^L} = 0$

$T^{B,L}$ is the temperature of the bulk of the liquid sub-layer. $dA^{SL}_{n_L}$ is the surface area of the sub-layer of the wet side wall. h^{SL}_{w,n_L} is the heat transfer coefficient at the wet side wall and it is computed with the boundary layer approach, using the values of the boundary layer variables, which are computed with the Storage Boundary Layer (SBL) model. $\dot{Q}_{W}^{LV}$ can be computed with the model of the LS model or with other models. The conductive heat flows ($\dot{Q}_{N^L}^{CD}$, $\dot{Q}_{n_L}^{CD}$ and $\dot{Q}_{2}^{CD}$) can be computed with the 1 dimensional Fourier's law, as function of the wet side wall temperature gradient. This gradient can be computed with the finite difference approach. So, the conductive heat flow can be computed as follows:

Equation 554 $$\dot{Q}_{n_L}^{CD} = k_w \cdot A_{n_L}^{R} \cdot \frac{\left(T_{w,n_L}^{SL} - T_{w,n_L-1}^{SL}\right)}{dLc_{n_L}}$$

Equation 554 can be applied to all the sub-layers of the wet side wall. A^R is the ring surface area of the wet side wall, and dLc is the distance between the center of each sub-layer of the wet side wall. k_w is the thermal conductivity of the side wall. The wet side wall temperatures (T_{w,n_L}^{SL}) are computed as done in Chapter X, as function of the heat transfer coefficient of the wet side wall and of the wet side wall-to-liquid heat flow. Hence, the calculation of the wet side wall-to-liquid heat flow is an iterative procedure. Due to the presence of the conductive heat flows, the computational time increases because these heat flows make the Newton-Raphson with finite difference approach less stable than the one used in the LS model without the conductive heat flows (see Section 2 of Appendix I). So, a new method of solving the equations of Table 154 is required. If a new method cannot be found, the stability and the convergence speed of the Newton-Raphson with finite difference approach[112] can be increased by computing a first guess value of the wet side wall-to-liquid heat flows that are close to the solution.

3.3.2. Laminar-turbulent fluid-dynamic regime

One of the reasons of the excessive accumulation of the sensible heat near the interface is the hypothesis of the turbulent fluid-dynamic regime (see Section 6.1 of Chapter 6). This hypothesis over-estimates the mass flow in the boundary layer of the wet side wall, which carries sensible heat to the interface. This hypothesis is used in the Integral Boundary Layer (IBL) approach, because laminar viscous forces make the numerical algorithm unstable when the liquid bulk temperature gradient is added.

The laminar-turbulent fluid-dynamic regime is proposed, and the laminar, thus the transition regime, is considered as done in the homogeneous model (H model). The potential instability of the laminar viscous force can be solved as done for reducing the computational time of the Storage Boundary Layer (SBL) model.

3.4. Discretisation of the ullage

The critical issues of the vapour-to-interface heat flow (issue e) of Section3) and of the use of beta and alpha (issue f) of Section 3) are related to the hypothesis of the vapour virtual discretisation, because this assumption considers the ullage (thus the dry side wall) as isothermal, contrarily the experimental observations. These observations show that the vapour is thermally stratified. As a consequence, the ullage temperature gradient, which affects the fluid-dynamics and the dry side wall-to-vapour heat transfer, cannot be qualitatively calculated in agreement with the experimental observations. So, the alpha and beta coefficients were introduced, and they were calculated from the experimental data of heat input and ullage temperature as done in Chapter 5. The ullage temperature is rarely measured in the Boil-Off Rate (BOR) test, which is used to measure the BOR of the storage tank. As consequence, the physical model of the storage behaviour cannot be extended to study cases where the experimental value of the ullage temperature is not available. Hence, the applicability of the physical model is quite limited.

To overcome this critical issue, the hypothesis of the vapour discretisation must be added. The ullage can be described with Figure 197. In Figure 197, the light blue rectangle is the liquid and the yellow dashed line is the interface. The orange and the yellow rectangles are respectively the bulk and the boundary layer of each sub-layer. The dark and light colours indicate the low and the high temperatures. The peak rectangles are the sub-layer of the dry side wall.

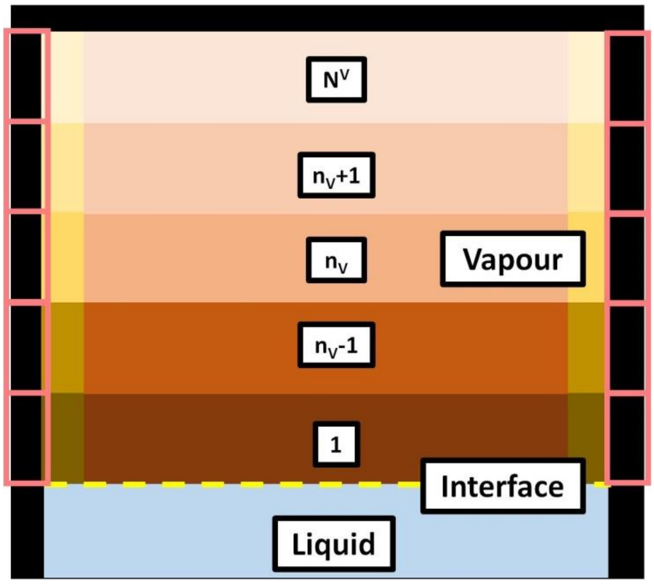

Figure 197. Discretized ullage.

This hypothesis states that the ullage can be discretized in sub-layer of equal thickness, and each sub-layer can be divided into the bulk and the boundary layer. As consequence, the dry side wall can be discretized in sub-layers that are similar to the ones of the ullage, as it is illustrated in Figure 198.

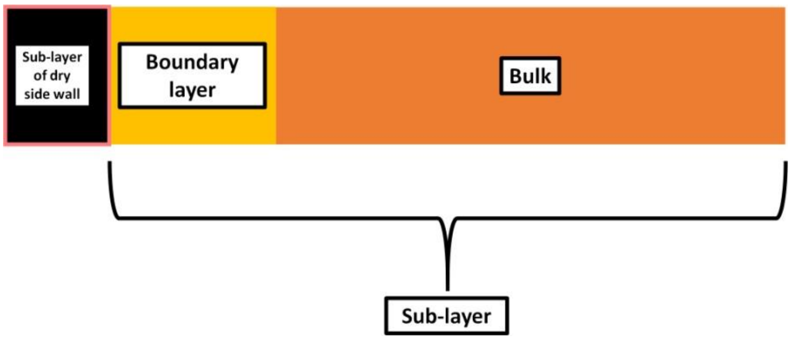

Figure 198. Dry side wall sub-layer and vapour sub-layer (bulk and boundary layer).

The volume of the boundary layer is much lower than the one of the bulk. So, the mass and energy transient are only considered in the bulk and the boundary layer is always at steady state. The first sub-layer is called interface sub-layer and the last is called roof-sub-layer. The remaining sub-layers are called core sub-layers. The dry side wall-to-interface heat transfer model, the conservation laws, the vapour-to-interface heat flow. The equations to compute the dry side wall and vapour bulk temperature gradients are affected by this hypothesis.

3.4.1. Bulk vapour and dry side wall temperature

Due to the hypothesis of vapour discretisation, the temperature distribution in the liquid and in the vapour can be described with Figure 199. In Figure 199, the red points are the bulk vapour and dry side wall temperatures, and the interface temperature. The green "{" indicates the distance between each temperature point.

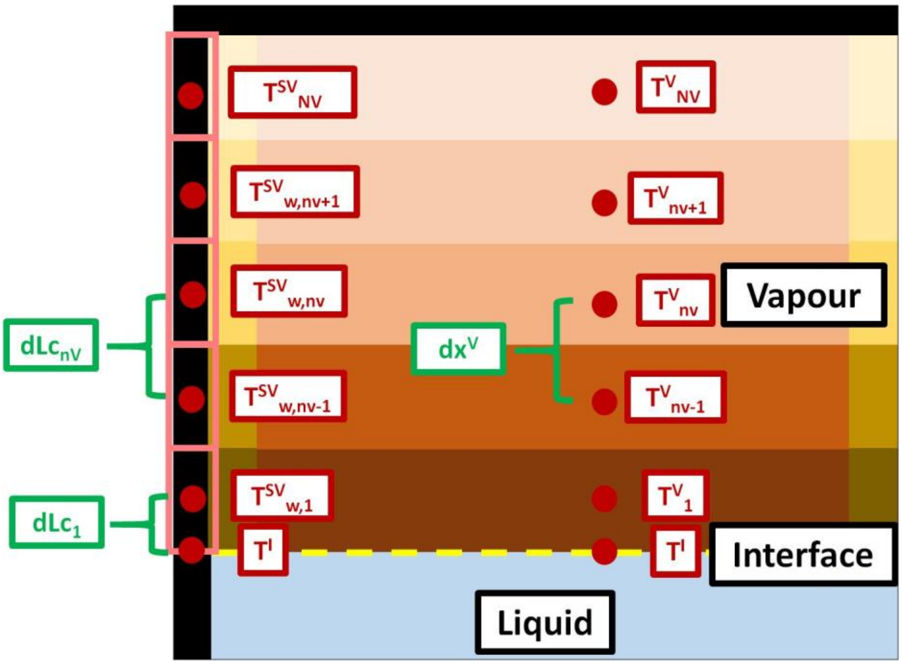

Figure 199. Temperature distribution in the dry side wall and in the ullage.

As a consequence of the temperature distribution in Figure 199, the vapour bulk temperature gradient and the dry side wall temperature gradient can be computed with finite difference approach. So, the equations that are reported in Table 155 can be applied.

Table 155. Equations of the dry side wall and bulk vapour temperature gradient.

Sub-layer	Equation	Formula
	Vapour	
Interface	Equation 555	$\frac{\partial T_1^V}{\partial x} = \frac{T_2^V - T_1^V}{dxV}$
Core	Equation 556	$\frac{\partial T_{n_V}^V}{\partial x} = \frac{T_{n_V}^V - T_{n_V-1}^V}{dxV}$
Roof	Equation 557	$\frac{\partial T_{N^V}^V}{\partial x} = \frac{T_{N^V}^V - T_{N^V-1}^V}{dxV}$
	Dry side wall	
Interface	Equation 558	$\frac{\partial T_{w,1}^{SV}}{\partial x} = \frac{T_{w,2}^{SV} - T_{w,1}^{SV}}{dLc_1}$
Core	Equation 559	$\frac{\partial T_{w,n_V}^{SV}}{\partial x} = \frac{T_{w,n_V}^{SV} - T_{w,n_V-1}^{SV}}{dLc_{n_V}}$
Roof	Equation 560	$\frac{\partial T_{w,N^V}^{SV}}{\partial x} = \frac{T_{w,N^V}^{SV} - T_{w,N^V-1}^{SV}}{dLc_{N^V}}$

dxV is the thickness of the vapour sub-layer. dLc_1 is the distance between center of the interface sub-layer of the dry side wall and the interface. dLc_{n_V} is the distance between middle point of the "n_V" sub-layer of vapour and the middle point of the "$n_V - 1$" sub-layer of vapour.

3.4.2. Conservation laws of the ullage

Heat input at the dry side wall produces the natural convection of the vapour at this surface. This fluid motion generates a descending mass flow, which affects the thermal distribution. This flow is usually directed downward, but it can be directed upward if the mass flow reduces in the boundary layer of the dry side wall, instead of increasing. The mass flow in the boundary layer of the dry side wall can decrease and vanish if the value of the ullage bulk temperature gradient is high. Due to this gradient, the heat is transferred from the roof to the interface across the ullage. Due to the hypothesis of the vapour stratification, the heat flows, the enthalpy flows and the mass flows of the bulk of the sub-layer can be described with Figure 200. In Figure 200, the orange colour indicates the vapour. The green and black arrows are respectively the net mass flow and the inlet and outlet mass flows. The red arrows refer to the enthalpy flows. The white arrows with red border are the heat leakage rates. The yellow dashed line is the interface.

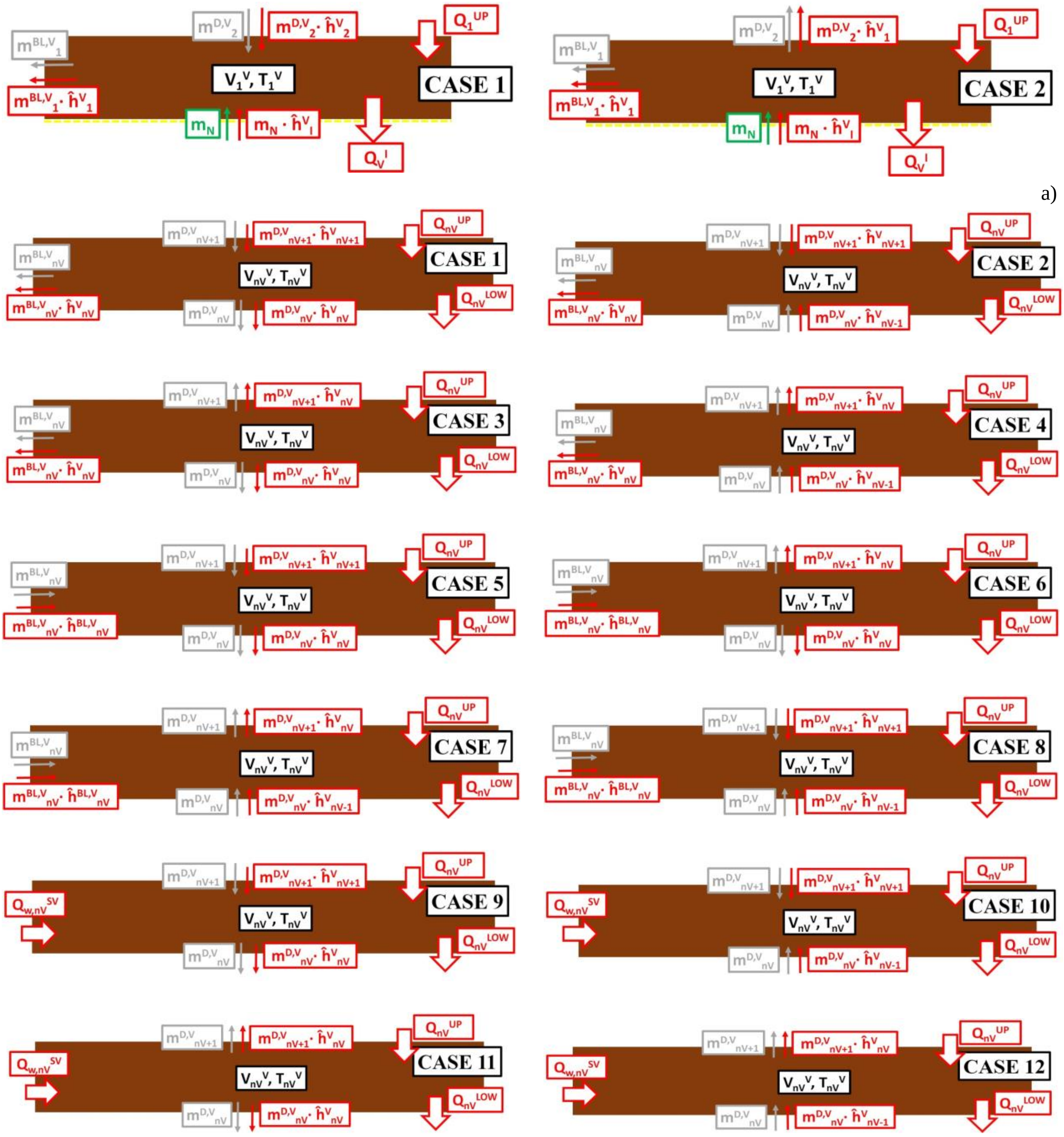

b)

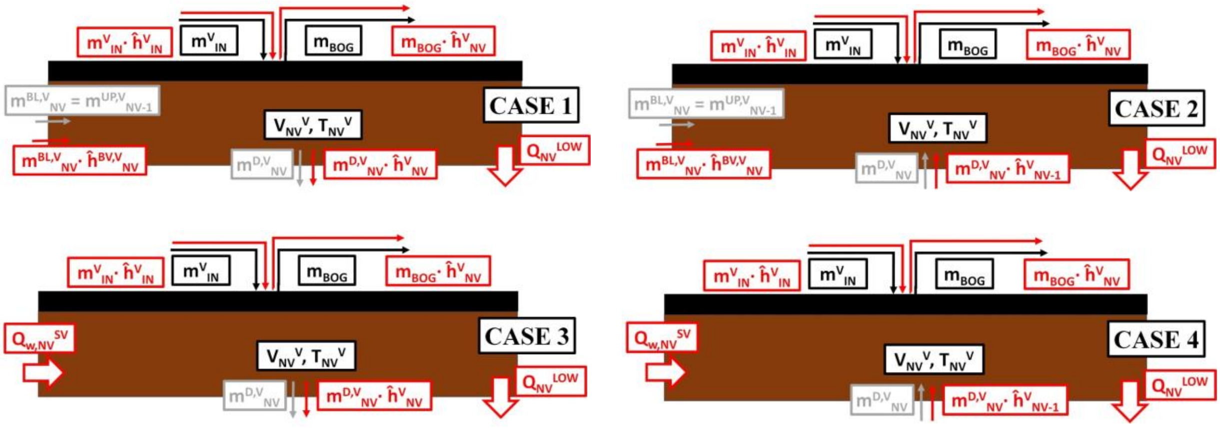

c)

Figure 200. Control volumes of the stratified ullage: a) interface bulk sub-layer; b) core bulk sub-layer; c) roof bulk sub-layer.

As described in Figure 200, upper heat flow ($\dot{Q}_{n_V}^{UP}$) and lower heat flow ($\dot{Q}_{n_V}^{LOW}$) respectively enters and exits the sub-layer. These heat flows are always directed downward because the ullage temperature monotonically increases from the interface to the roof. In the core sub-layer, the descending mass flows ($\dot{m}_{n_V+1}^{D,V}$ and $\dot{m}_{n_V}^{D,V}$) can be upward or downward directed. The boundary layer-to-bulk mass flow ($\dot{m}_{n_V}^{BL,V}$) can be directed toward the boundary layer, or toward the bulk or be equal to 0. If this happens, the dry side wall-to-vapour heat flow directly enters the bulk of the sub-layer. In the roof sub-layer, the descending mass flow ($\dot{m}_{N^V}^{D,V}$) can be downward or upward and the boundary layer-to-bulk mass flow ($\dot{m}_{N^V}^{BL,V}$), which is always directed to the bulk, can be equal to zero 0. As consequence, different cases are present in the core sub-layers and in the roof sub-layer due to the fluid-dynamics at the side wall. These cases are described in Table 156.

Table 156. Fluid-dynamics cases of the discretized vapour.

	Roof sub-layer (Figure 200 (c))
Case 1	$\dot{m}_{N^V}^{D,V}$ is directed downward. $\dot{m}_{N^V}^{BL,V}$ exits the boundary layer.
Case 2	$\dot{m}_{N^V}^{D,V}$ is directed upward. $\dot{m}_{N^V}^{BL,V}$ exits the boundary layer.
Case 3	$\dot{m}_{N^V}^{D,V}$ is directed downward. $\dot{m}_{N^V}^{BL,V}$ is equal to zero.
Case 4	$\dot{m}_{N^V}^{D,V}$ is directed upward. $\dot{m}_{N^V}^{BL,V}$ is equal to zero.
	Interface sub-layer (Figure 200 (a))
Case 1	$\dot{m}_{2}^{D,V}$ is directed downward. $\dot{m}_{1}^{BL,V}$ enters the boundary layer.
Case 2	$\dot{m}_{2}^{D,V}$ is directed upward. $\dot{m}_{1}^{BL,V}$ enters the boundary layer.
	Core-bulk sub-layer (Figure 200 (b))
Case 1	$\dot{m}_{n_V}^{BL,V}$ enters the boundary layer. $\dot{m}_{n_V+1}^{D,V}$ and $\dot{m}_{n_V}^{D,V}$ are directed downward.
Case 2	$\dot{m}_{n_V}^{BL,V}$ enters the boundary layer. $\dot{m}_{n_V+1}^{D,V}$ is directed downward and $\dot{m}_{n_V}^{D,V}$ is directed upward.
Case 3	$\dot{m}_{n_V}^{BL,V}$ enters the boundary layer. $\dot{m}_{n_V+1}^{D,V}$ is directed upward and $\dot{m}_{n_V}^{D,V}$ is directed downward.
Case 4	$\dot{m}_{n_V}^{BL,V}$ enters the boundary layer. $\dot{m}_{n_V+1}^{D,V}$ and $\dot{m}_{n_V}^{D,V}$ are directed upward.
Case 5	$\dot{m}_{n_V}^{BL,V}$ exits the boundary layer. $\dot{m}_{n_V+1}^{D,V}$ and $\dot{m}_{n_V}^{D,V}$ are directed downward.
Case 6	$\dot{m}_{n_V}^{BL,V}$ exits the boundary layer. $\dot{m}_{n_V+1}^{D,V}$ is directed upward and $\dot{m}_{n_V}^{D,V}$ is directed downward.
Case 7	$\dot{m}_{n_V}^{BL,V}$ exits the boundary layer. $\dot{m}_{n_V+1}^{D,V}$ is directed downward and $\dot{m}_{n_V}^{D,V}$ is directed upward.
Case 8	$\dot{m}_{n_V}^{BL,V}$ exits the boundary layer. $\dot{m}_{n_V+1}^{D,V}$ and $\dot{m}_{n_V}^{D,V}$ are directed upward.
Case 9	$\dot{m}_{n_V}^{BL,V}$ is equal to zero. $\dot{m}_{n_V+1}^{D,V}$ and $\dot{m}_{n_V}^{D,V}$ are directed downward.
Case 10	$\dot{m}_{n_V}^{BL,V}$ is equal to zero. $\dot{m}_{n_V+1}^{D,V}$ is directed downward and $\dot{m}_{n_V}^{D,V}$ is directed upward.
Case 11	$\dot{m}_{n_V}^{BL,V}$ is equal to zero. $\dot{m}_{n_V+1}^{D,V}$ is directed upward and $\dot{m}_{n_V}^{D,V}$ is directed downward.

Table 156. Fluid-dynamics cases of the discretized vapour.

Case 12	$\dot{m}_{n_V}^{BL,V}$ is equal to zero. $\dot{m}_{n_V+1}^{D,V}$ and $\dot{m}_{n_V}^{D,V}$ are directed upward.

For the interface sub-layer, the net mass flow ($\dot{m}_N$) can be directed downward and upward. Only the sign of the enthalpy flow of this mass flow ($\dot{m}_N \cdot \tilde{h}_S^V$) only changes in both situations. Considering the cases of Table 156, the conservation laws of mass and of energy can be written as it is reported in Table 157.

Table 157. Energy and mass conservation laws of the discretized vapour.

Case	Equation	Formula
		Roof-vapour sub-layer
1	Equation 561	$\frac{\partial \widetilde{H}_{N^V}^V}{\partial t} = -\dot{Q}_{N^V}^{LOW} - \dot{m}_{N^V}^{D,V} \cdot \tilde{h}_{N^V}^V + \dot{m}_{N^V}^{BL,V} \cdot \tilde{h}_{N^V}^{BL,V} - \dot{m}_{BOG} \cdot \tilde{h}_{N^V}^V + \dot{m}_{IN}^V \cdot \tilde{h}_{IN}^V$
	Equation 562	$\frac{\partial m_{N^V}^V}{\partial t} = -\dot{m}_{N^V}^{D,V} + \dot{m}_{N^V}^{BL,V} - \dot{m}_{BOG} + \dot{m}_{IN}^V$
2	Equation 563	$\frac{\partial \widetilde{H}_{N^V}^V}{\partial t} = -\dot{Q}_{N^V}^{LOW} + \dot{m}_{N^V}^{D,V} \cdot \tilde{h}_{N^V-1}^V + \dot{m}_{N^V}^{BL,V} \cdot \tilde{h}_{N^V}^{BL,V} - \dot{m}_{BOG} \cdot \tilde{h}_{N^V}^V + \dot{m}_{IN}^V \cdot \tilde{h}_{IN}^V$
	Equation 564	$\frac{\partial m_{N^V}^V}{\partial t} = \dot{m}_{N^V}^{D,V} + \dot{m}_{N^V}^{BL,V} - \dot{m}_{BOG} + \dot{m}_{IN}^V$
3	Equation 565	$\frac{\partial \widetilde{H}_{N^V}^V}{\partial t} = -\dot{Q}_{N^V}^{LOW} + \dot{Q}_{w,N^V}^{SV} - \dot{m}_{N^V}^{D,V} \cdot \tilde{h}_{N^V}^V + \dot{m}_{N^V}^{BL,V} \cdot \tilde{h}_{N^V}^{BL,V} - \dot{m}_{BOG} \cdot \tilde{h}_{N^V}^V + \dot{m}_{IN}^V \cdot \tilde{h}_{IN}^V$
	Equation 566	$\frac{\partial m_{N^V}^V}{\partial t} = -\dot{m}_{N^V}^{D,V} - \dot{m}_{BOG} + \dot{m}_{IN}^V$
4	Equation 567	$\frac{\partial \widetilde{H}_{N^V}^V}{\partial t} = -\dot{Q}_{N^V}^{LOW} + \dot{Q}_{w,N^V}^{SV} + \dot{m}_{N^V}^{D,V} \cdot \tilde{h}_{N^V-1}^V - \dot{m}_{BOG} \cdot \tilde{h}_{N^V}^V + \dot{m}_{IN}^V \cdot \tilde{h}_{IN}^V$
	Equation 568	$\frac{\partial m_{N^V}^V}{\partial t} = \dot{m}_{N^V}^{D,V} - \dot{m}_{BOG} + \dot{m}_{IN}^V$
		Interface sub-layer
1	Equation 569	$\frac{\partial \widetilde{H}_1^V}{\partial t} = -\dot{Q}_I^V + \dot{m}_2^{D,V} \cdot \tilde{h}_2^V - \dot{m}_1^{BL,V} \cdot \tilde{h}_1^V + \dot{Q}_1^{UP} - \dot{m}_N \cdot \tilde{h}_S^V$
	Equation 570	$\frac{\partial m_1^V}{\partial t} = \dot{m}_2^{D,V} - \dot{m}_1^{BL,V} - \dot{m}_N$
2	Equation 571	$\frac{\partial \widetilde{H}_1^V}{\partial t} = -\dot{Q}_I^V - \dot{m}_2^{D,V} \cdot \tilde{h}_1^V - \dot{m}_1^{BL,V} \cdot \tilde{h}_1^V + \dot{Q}_1^{UP} - \dot{m}_N \cdot \tilde{h}_S^V$
	Equation 572	$\frac{\partial m_1^V}{\partial t} = -\dot{m}_2^{D,V} - \dot{m}_1^{BL,V} - \dot{m}_N$
		Core sub-layer
1	Equation 573	$\frac{\partial \widetilde{H}_{n_V}^V}{\partial t} = \dot{Q}_{n_V}^{UP} - \dot{Q}_{n_V}^{LOW} - \dot{m}_{n_V}^{BL,V} \cdot \tilde{h}_{n_V}^V - \dot{m}_{n_V}^{D,V} \cdot \tilde{h}_{n_V}^V + \dot{m}_{n_V+1}^{D,V} \cdot \tilde{h}_{n_V+1}^V$
	Equation 574	$\frac{\partial m_{n_V}^V}{\partial t} = -\dot{m}_{n_V}^{BL,V} - \dot{m}_{n_V}^{D,V} + \dot{m}_{n_V+1}^{D,V}$
2	Equation 575	$\frac{\partial \widetilde{H}_{n_V}^V}{\partial t} = \dot{Q}_{n_V}^{UP} - \dot{Q}_{n_V}^{LOW} - \dot{m}_{n_V}^{BL,V} \cdot \tilde{h}_{n_V}^V + \dot{m}_{n_V}^{D,V} \cdot \tilde{h}_{n_V-1}^V + \dot{m}_{n_V+1}^{D,V} \cdot \tilde{h}_{n_V+1}^V$
	Equation 576	$\frac{\partial m_{n_V}^V}{\partial t} = -\dot{m}_{n_V}^{BL,V} + \dot{m}_{n_V}^{D,V} + \dot{m}_{n_V+1}^{D,V}$
3	Equation 577	$\frac{\partial \widetilde{H}_{n_V}^V}{\partial t} = \dot{Q}_{n_V}^{UP} - \dot{Q}_{n_V}^{LOW} - \dot{m}_{n_V}^{BL,V} \cdot \tilde{h}_{n_V}^V - \dot{m}_{n_V}^{D,V} \cdot \tilde{h}_{n_V}^V - \dot{m}_{n_V+1}^{D,V} \cdot \tilde{h}_{n_V}^V$
	Equation 578	$\frac{\partial m_{n_V}^V}{\partial t} = -\dot{m}_{n_V}^{BL,V} - \dot{m}_{n_V}^{D,V} - \dot{m}_{n_V+1}^{D,V}$
4	Equation 579	$\frac{\partial \widetilde{H}_{n_V}^V}{\partial t} = \dot{Q}_{n_V}^{UP} - \dot{Q}_{n_V}^{LOW} - \dot{m}_{n_V}^{BL,V} \cdot \tilde{h}_{n_V}^V + \dot{m}_{n_V}^{D,V} \cdot \tilde{h}_{n_V-1}^V - \dot{m}_{n_V+1}^{D,V} \cdot \tilde{h}_{n_V}^V$
	Equation 580	$\frac{\partial m_{n_V}^V}{\partial t} = -\dot{m}_{n_V}^{BL,V} + \dot{m}_{n_V}^{D,V} - \dot{m}_{n_V+1}^{D,V}$
5	Equation 581	$\frac{\partial \widetilde{H}_{n_V}^V}{\partial t} = \dot{Q}_{n_V}^{UP} - \dot{Q}_{n_V}^{LOW} + \dot{m}_{n_V}^{BL,V} \cdot \tilde{h}_{n_V}^{BL,V} - \dot{m}_{n_V}^{D,V} \cdot \tilde{h}_{n_V}^V + \dot{m}_{n_V+1}^{D,V} \cdot \tilde{h}_{n_V+1}^V$
	Equation 582	$\frac{\partial m_{n_V}^V}{\partial t} = \dot{m}_{n_V}^{BL,V} - \dot{m}_{n_V}^{D,V} + \dot{m}_{n_V+1}^{D,V}$

Table 157. Energy and mass conservation laws of the discretized vapour.

6	Equation 583	$\frac{\partial \tilde{H}^{V}_{n_V}}{\partial t} = \dot{Q}^{UP}_{n_V} - \dot{Q}^{LOW}_{n_V} + \dot{m}^{BL,V}_{n_V} \cdot \tilde{h}^{BL,V}_{n_V} + \dot{m}^{D,V}_{n_V} \cdot \tilde{h}^{V}_{n_V-1} + \dot{m}^{D,V}_{n_V+1} \cdot \tilde{h}^{V}_{n_V+1}$
	Equation 584	$\frac{\partial m^{V}_{n_V}}{\partial t} = \dot{m}^{BL,V}_{n_V} + \dot{m}^{D,V}_{n_V} + \dot{m}^{D,V}_{n_V+1}$
7	Equation 585	$\frac{\partial \tilde{H}^{V}_{n_V}}{\partial t} = \dot{Q}^{UP}_{n_V} - \dot{Q}^{LOW}_{n_V} + \dot{m}^{BL,V}_{n_V} \cdot \tilde{h}^{BL,V}_{n_V} - \dot{m}^{D,V}_{n_V} \cdot \tilde{h}^{V}_{n_V} - \dot{m}^{D,V}_{n_V+1} \cdot \tilde{h}^{V}_{n_V}$
	Equation 586	$\frac{\partial m^{V}_{n_V}}{\partial t} = \dot{m}^{BL,V}_{n_V} - \dot{m}^{D,V}_{n_V} - \dot{m}^{D,V}_{n_V+1}$
8	Equation 587	$\frac{\partial \tilde{H}^{V}_{n_V}}{\partial t} = \dot{Q}^{SV}_{w,n_V} + \dot{Q}^{UP}_{n_V} - \dot{Q}^{LOW}_{n_V} + \dot{m}^{D,V}_{n_V} \cdot \tilde{h}^{V}_{n_V-1} - \dot{m}^{D,V}_{n_V+1} \cdot \tilde{h}^{V}_{n_V}$
	Equation 588	$\frac{\partial m^{V}_{n_V}}{\partial t} = \dot{m}^{D,V}_{n_V} - \dot{m}^{D,V}_{n_V+1}$
9	Equation 589	$\frac{\partial \tilde{H}^{V}_{n_V}}{\partial t} = \dot{Q}^{SV}_{w,n_V} + \dot{Q}^{UP}_{n_V} - \dot{Q}^{LOW}_{n_V} - \dot{m}^{D,V}_{n_V} \cdot \tilde{h}^{V}_{n_V} + \dot{m}^{D,V}_{n_V+1} \cdot \tilde{h}^{V}_{n_V+1}$
	Equation 590	$\frac{\partial m^{V}_{n_V}}{\partial t} = -\dot{m}^{D,V}_{n_V} + \dot{m}^{D,V}_{n_V+1}$
10	Equation 591	$\frac{\partial \tilde{H}^{V}_{n_V}}{\partial t} = \dot{Q}^{SV}_{w,n_V} + \dot{Q}^{UP}_{n_V} - \dot{Q}^{LOW}_{n_V} + \dot{m}^{D,V}_{n_V} \cdot \tilde{h}^{V}_{n_V-1} + \dot{m}^{D,V}_{n_V+1} \cdot \tilde{h}^{V}_{n_V+1}$
	Equation 592	$\frac{\partial m^{V}_{n_V}}{\partial t} = \dot{m}^{D,V}_{n_V} + \dot{m}^{D,V}_{n_V+1}$
11	Equation 593	$\frac{\partial \tilde{H}^{V}_{n_V}}{\partial t} = \dot{Q}^{UP}_{n_V} - \dot{Q}^{LOW}_{n_V} - \dot{m}^{D,V}_{n_V} \cdot \tilde{h}^{V}_{n_V} - \dot{m}^{D,V}_{n_V+1} \cdot \tilde{h}^{V}_{n_V}$
	Equation 594	$\frac{\partial m^{V}_{n_V}}{\partial t} = -\dot{m}^{D,V}_{n_V} - \dot{m}^{D,V}_{n_V+1}$
12	Equation 595	$\frac{\partial \tilde{H}^{V}_{n_V}}{\partial t} = \dot{Q}^{SV}_{w,n_V} + \dot{Q}^{UP}_{n_V} - \dot{Q}^{LOW}_{n_V} + \dot{m}^{D,V}_{n_V} \cdot \tilde{h}^{V}_{n_V-1} - \dot{m}^{D,V}_{n_V+1} \cdot \tilde{h}^{V}_{n_V}$
	Equation 596	$\frac{\partial m^{V}_{n_V}}{\partial t} = \dot{m}^{D,V}_{n_V} - \dot{m}^{D,V}_{n_V+1}$

$\tilde{h}^{BL,V}$ is the specific enthalpy of the boundary layer and it is computed from the temperature of the boundary layer ($T^{BL,V}$). $\dot{m}^{BL,L}_{n_L}$ ca be computed as difference in mass flow between $\dot{m}^{UP,V}_{n_V}$ and $\dot{m}^{UP,V}_{n_V-1}$. These boundary variables are computed with the Storage Boundary Layer (SBL) model of the dry side wall.

3.4.3. Dry side wall heat transfer

Due to the hypothesis of vapour discretisation, the dry side wall can be described as in Figure 201. In Figure 201, the white arrows with the red boarder are the environment-to-dry wall ($\dot{Q}^{SV}_{eff,n_V}$), dry side wall-to-vapour ($\dot{Q}^{SV}_{w,n_V}$), dry side wall-to-interface ($\dot{Q}^{LV}_{w}$) and conductive ($\dot{Q}^{CD}_{n_V}$) heat flows. The white circles with the purple boarder are the wall temperatures. The black squares with orange boarder are the sub-layers of the wet side wall.

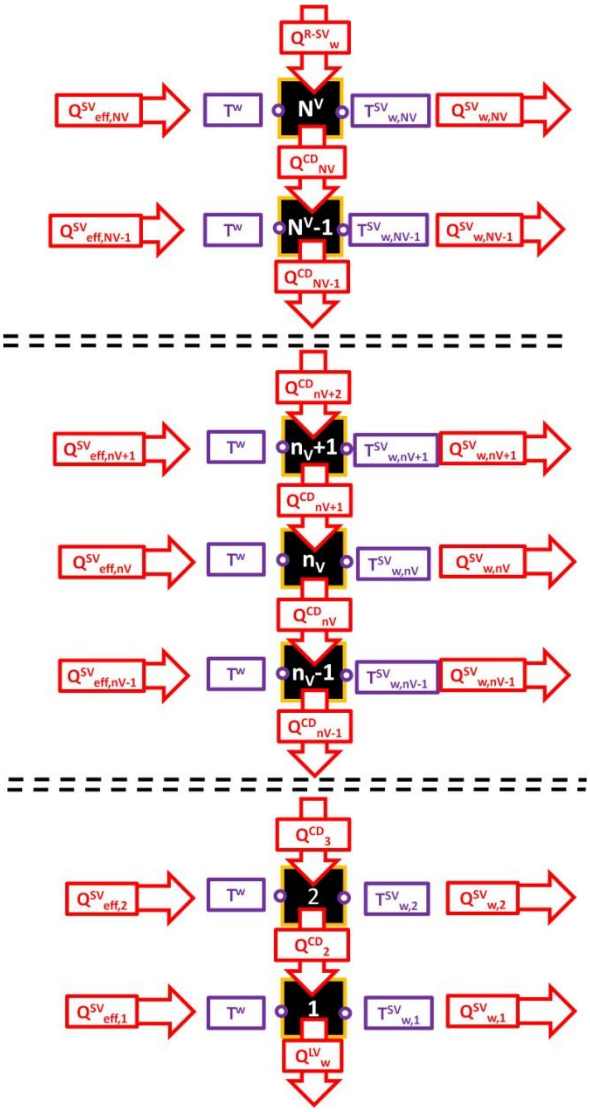

Figure 201. Heat transfer model at the dry side wall with vapour discretisation.

As it is reported in Figure 201, the thermal energy is transferred by conduction from the roof to the interface sub-layer of the dry side wall. At the same time, the heat comes from the environment in each sub-layer. Thermal energy is transferred from each sub-layer to the vapour. At the interface sub-layer, heat is transferred to the wet side wall. At the roof sub-layer, thermal energy comes from the wall of the roof. Since the dry side wall is at steady state, the energy conservation laws of the dry side wall can be described with the equations of Table 158.

Table 158. Conservation laws of energy at the sub-layer of the dry side walls.

Mechanism	Equation	Formula
Interface sub-layer	Equation 597	$\left[h_{eff}\cdot dA_{1}^{SV}\cdot\left(T^{w}-T_{w,1}^{SV}\right)+\dot{Q}_{2}^{CD}\right]-\left[h_{w,1}^{SV}\cdot dA_{1}^{SV}\cdot\left(T_{w,1}^{SV}-T_{1}^{B,V}\right)+\dot{Q}_{w}^{LV}\right]=0$
Core sub-layer	Equation 598	$\left[h_{eff}\cdot dA_{n_V}^{SV}\cdot\left(T^{w}-T_{w,n_V}^{SV}\right)+\dot{Q}_{n_V+1}^{CD}\right]-\left[h_{w,n_V}^{SV}\cdot dA_{n_V}^{SV}\cdot\left(T_{w,n_V}^{SV}-T_{n_V}^{B,V}\right)+\dot{Q}_{n_V}^{CD}\right]=0$
Roof sub-layer	Equation 599	$\left[h_{eff}\cdot dA_{N^V}^{SV}\cdot\left(T^{w}-T_{w,N^V}^{SV}\right)+\dot{Q}_{w}^{R-SV}\right]-\left[h_{w,N^V}^{SV}\cdot dA_{N^V}^{SV}\cdot\left(T_{w,N^V}^{SV}-T_{N^V}^{B,V}\right)+\dot{Q}_{N^V}^{CD}\right]=0$

$T^{B,V}$ is the bulk temperature of the vapour-sub-layers. $dA_{n_V}^{SV}$ is the surface area of the sub-layer of the dry side wall. h_{w,n_V}^{SV} is the heat transfer coefficient at the dry side wall, and it is computed with the boundary layer approach, using the values of the boundary layer variables, which are computed with the storage boundary layer (SBL) model. $\dot{Q}_{w}^{LV}$ can be computed as function of the dry side wall temperature gradient at the interface ($\frac{\partial T^{SV}_{w,1}}{\partial x}$), which is calculated with Equation 558. The conductive heat flows ($\dot{Q}^{CD}_{N^V}$, $\dot{Q}^{CD}_{n_V}$ and $\dot{Q}^{CD}_{V}$) can be computed with the 1 dimensional Fourier's law, as function of the dry side wall temperature gradient (see Table 155). So, the conductive heat flow can be computed as follows:

Equation 600
$$\dot{Q}^{CD}_{n_V} = k_w \cdot A^R_{n_L - 1} \cdot \frac{\partial T^{SV}_{w,n_V}}{\partial x}$$

Equation 600 can be applied to all the sub-layers. A^R is the ring surface area of the wet side wall, and dLc is the distance between the middle point of each sub-layer of the wet side wall. The dry side wall-to-interface heat flow can be computed as follows:

Equation 601
$$\dot{Q}^{LV}_{w} = k_w \cdot A^R_I \cdot \frac{T^{SV}_{w,1} - T^I}{dLc_I}$$

dLc_I is the distance between the centre of the interface sub-layer and the point of the wall in contact with the interface.

The dry side wall temperature (T^{SV}_{w,n_V}) can be computed as follows:

Equation 602
$$T^{SV}_{n_V} = T^{B,V}_{n_V} + \frac{\dot{Q}^{SV}_{w,n_V}}{h^{SV}_{w,n_V} \cdot dA^{SV}_{n_V}}$$

$\dot{Q}^{SV}_{w,n_V}$ is the dry side wall-to-vapour heat flow and h^{SV}_{w,n_V} is the dry side wall-to-vapour heat transfer coefficient. This coefficient is calculated with the boundary layer approach, using the values of the boundary layer variables. These variables are computed with the IBL approach of the SBL model. In this approach, the dry side wall-to-vapour heat flow is used as input parameter, and laminar, transition and turbulent regime are considered. Hence, the calculation of the dry side wall-to-vapour heat flow is an iterative procedure.

3.4.4. Vapour-to-interface heat flow

Due to the natural convection at the dry side wall, the vapour rises from the interface to the roof. Once the vapour at the roof, it goes down, and it can reach the interface. So, this mass flow releases thermal heat at the interface. As consequence, the vapour-to-interface heat flow can be computed as follows:

Equation 603
$$\dot{Q}^{V}_{I} = \dot{m}^{D,V}_{2} \cdot \left(\tilde{h}^{B,V}_{2} - \tilde{h}^{V}_{S}\right)$$

$\dot{m}^{D,V}_{2}$ is calculated from the conservation law of the mass at the interface sub-layer. If the mass flow $\dot{m}^{D,V}_{2}$ is directed upward, the vapour-to-interface heat flow is equal to zero.

3.5. Two liquid regions model: a solution to thfurther reduce the computational time

As said, one of the drawbacks of the LS model is the high computational time. This last is produced by the numerical integration of the momentum and energy conservation laws of the boundary layer at the wet and dry side walls, and by algorithms to compute the wet side wall-to-liquid and the dry side wall-to-vapour heat flows. These algorithms involve iterative procedures where the heat transfer coefficients at the side walls are computed from the values of the boundary layer variables, which in turn are computed by numerical integration. As a consequence, the computational time increases with the number of the liquid sub-layers. So, the computational time can be reduced by decreasing the number of the sub-layers. The suggestions of Section 3.1, 3.2, 3.3 and 3.4 of Chapter 7 should be done before doing this decrement. In particular, the new numerical method, the new model of the liquid-to-interface heat flow and the conductive approach of the wet side wall must be implemented because they significantly affect the performance of the LS model, even if the number of the sub-layer is low.

The number of the sub-layer is computed with an iterative procedure. In this procedure, the mass flow in the boundary layer of the side wall is calculated from the values of the boundary layer variables, which are computed by the numerical integration. The number of the sub-layer is increased until the numerical error in computing this mass flow is lower than the desired value. So, one of the solutions to reduce the computational time is to increase the numerical error, leading to a decrease of the accuracy. To avoid this, the liquid bulk can only be discretized in the region where the stratification occurs. The non-stratified region is described as done in the homogeneous model (H model). Hence, the number of the sub-layers is reduced and the accuracy in the stratified region can be maintained. This type of approach is called *two liquid regions (TLR) model*. To the author knowledge, this type of approach does not exist in literature. Only the approach of Wang et al. [122] is quite similar to the TLR model. In the model of Wang et al. [122], the whole domain of the liquid is discretized and divided into two domains: the condition layer and the convective region. The thickness of the condition layer is computed with the layer growth equation.

Section 3.5.1describes the hypothesis of the TLR model. Section 3.5.2 explains the convective flows and the heat flows in the liquid. Section 3.5.3 presents the new conservation laws of the TLR model.

3.5.1. Hypothesis of two liquid regions model

The thermal energy of the environment flows to the liquid from the wet side wall and from the bottom. At the wet side wall, this energy warms the liquid, which becomes lighter. The liquid moves along the side wall carrying sensible heat to the interface. The liquid exchanges heat with the interface and it goes down along the central axes of the storage container, producing a descending flow. This flow carries thermal energy in the core of the liquid, developing the stratified region if the storage container is close. The heat flow at the bottom warms the liquid, which moves upward. This rising flow progressively vanishes as it enters the stratified region. The lower part of the liquid remains isothermal. So, it can be assumed that:

a) The liquid domain can be decomposed into the stratified and isothermal regions;
b) The liquid bulk is discretized only in the stratified region;
c) The ullage is entirely discretized;
d) The interface is at thermodynamic equilibrium

The assumption a) is called the *hypothesis of the two liquid regions*. The assumption b) is named *the hypothesis of liquid partial discretisation*. The hypothesis c) comes from the discretisation of the ullage (see Section 3.4 of Chapter 7). The assumption d) is the one of the LS model.

As consequence, the storage container of the two liquid regions (TLR) model can be described with Figure 202. In Figure 202, the black arrows are in the inlet and outlet streams, and the green arrow is the net mass flow. The white arrows with red boarder are the heat flows. The light blue and yellow arrows are the convective flows in the liquid and in the ullage respectively. The ullage and the liquid are respectively indicated with the red and the blue colours. The light colours in these phases indicate the high temperatures. The yellow dashed line is the interface, and the underneath purple dashed line is the interface that separates the isothermal region from the stratified region.

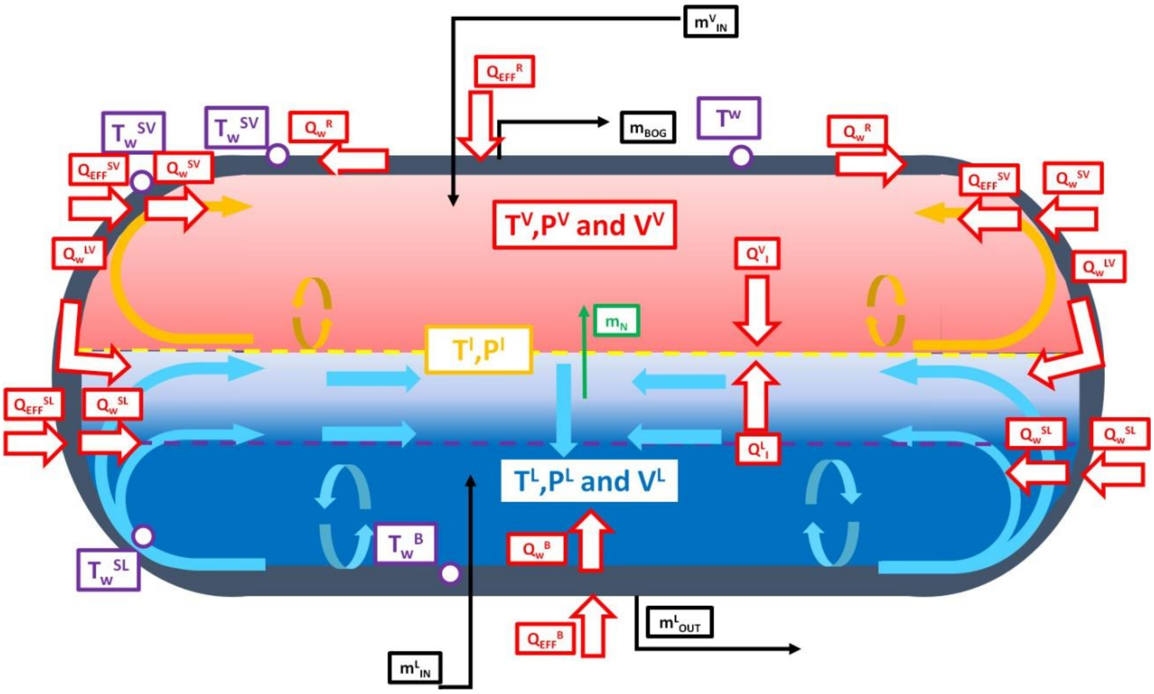

Figure 202. TLR model.

Due to the hypothesis of the liquid partial discretisation (b)), the stratified region is divided into sub-layers of equal thickness. Each sub-layer is composed by the bulk and the boundary layer. These sub-layers can be described as done in the LS model. So, the liquid-to-interface heat flow can be computed as explained in Section 3.2 of Chapter 7. The isothermal region can be considered as the liquid of the homogeneous model (H model). Due to assumption c) of Section 3.5.1 of Chapter 7, the ullage can be described with the model proposed in Section 3.4 of Chapter 7 and the vapour-to-interface heat flow can be computed with Equation 603.

3.5.2. Description of the liquid

Due to the hypotheses a) and b) of Section 3.5.1 of Chapter 7, the fluid-dynamics and the heat transfers in the liquid phase can be described as it is illustrated in Figure 203. In Figure 203, the light colours indicate the zone of the liquid at high temperature. The dark colours describe the regions at low temperature. The black rectangles are the wet walls (bottom and wet side wall). The yellow dashed line is the interface, and the purple dashed line is the interface between the isothermal and the stratified region. The grey arrows are the convective flows, which are the mass flow in the boundary layer of the wet side wall ($\dot{m}^{UP}$), the boundary layer-to-bulk mass flow ($\dot{m}^{BL}$) and the descending flow ($\dot{m}^{D}$). The green arrow is the net mass flow ($\dot{m}^{N}$). The white arrows with red boarders are the heat flows. The white circles with purple boarder are the wet walls temperatures. The pink rectangles are the sub-layers of the wet side wall, the isothermal region of the wet side wall and the bottom wall. The red arrows are the conductive heat flows between each sub-layer of the wet side wall.

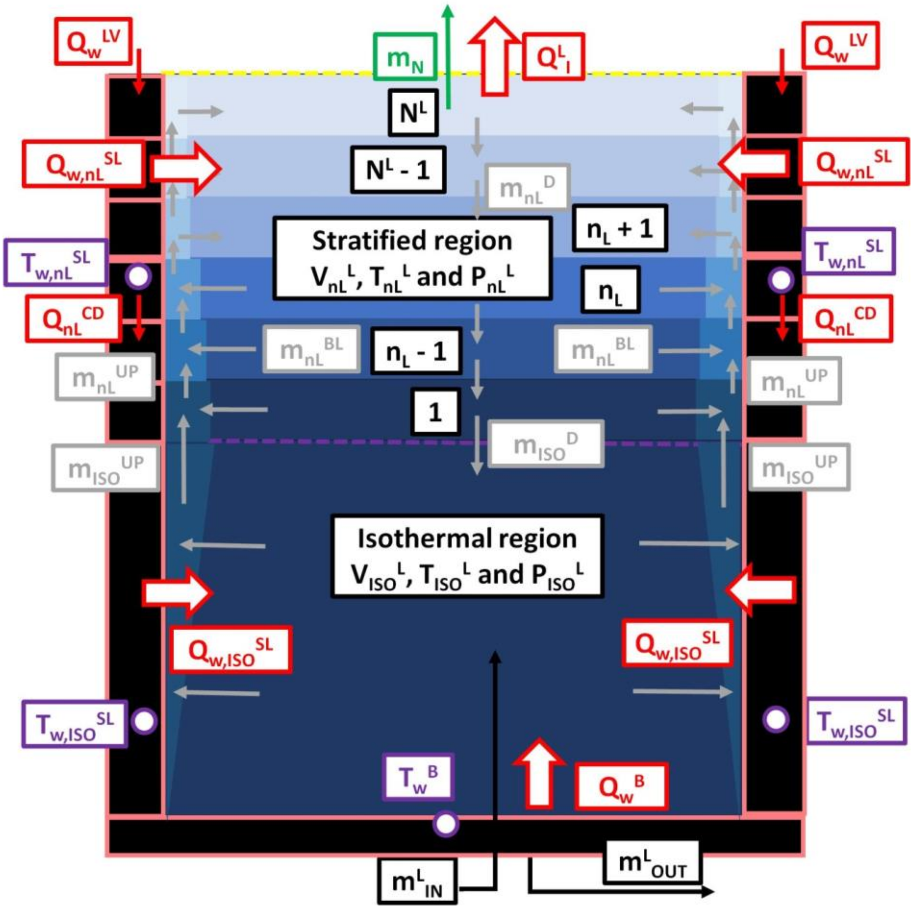

Figure 203. Description of the liquid in the TLR model.

As it is illustrated by Figure 203, the descending flow of the sub-layer in contact with the isothermal region ($\dot{m}_{ISO}^{D}$) and the volume of the stratified region are the new variables to consider in the TLR model. The remaining variables (wall temperature, mass flow in the boundary layer, descending flow, boundary layer-to-bulk flow, heat flow and net mass flow) can be calculated as done in the liquid stratification model (LS model) with the modifications proposed in Section 3.1, 3.2 and 3.3 of Chapter 7. As consequence, the new integration method of the SBL model (see Section 3.1 of Chapter 7) computes the boundary layer variables, thus the mass flow, in the sub-layer of the boundary layer of the isothermal and of the stratified region. The new heat transfer model of the wet side wall (see Section 3.2 of Chapter 7) calculates the wall temperature, the wet side wall-to-liquid heat flows in each sub-layer of the wet side wall, the conductive heat flows along the wet side wall and the heat transfer coefficients. These coefficients are computed from the boundary layer variables as done in the LS model. At the isothermal wet side wall, the wet side wall-to-liquid is computed with the model of the homogeneous model (H model). The heat transfer coefficient is computed as average values of the local heat transfer coefficient, which are computed from the values of the boundary layer variables. In the sub-layer of the wet side wall in contact with the isothermal region, the conductive heat flow of this sub-layer ($\dot{Q}_{1}^{CD}$) is equal to zero. The intra-layer heat flows ($\dot{Q}_{n_L}^{UP}$ and $\dot{Q}_{n_L}^{LOW}$) are computed with the Intra-Layer Heat Transfer (ILHT) of the LS model. At the sub-layer in contact with the isothermal region, the lower heat flow ($\dot{Q}_{1}^{LOW}$) is equal to zero. As it is illustrated by Figure 203, the rising flow of the bottom ($\dot{m}_{n_L}^{B}$) is not considered because these convective flows are inside the isothermal region, which is described by the H model.

3.5.3. Conservation laws

As it is illustrated by Figure 203, the convective flows of the stratified region can change in direction as it is described in the liquid stratificiaton (LS) model. The heat flows in the stratified regions are similar to the one of the LS model. So, the conservation laws of the LS model can be applied to the all the sub-layers of the stratified region, except for the sub-layer in contact for the isothermal region (sub-layer 1), by removing the rising mass flow of the bottom and its enthalpy flow.

As it is illustrated by Figure 203, the isothermal region and the sub-layer 1 cannot be described with the conservation laws of the LS model, due to the descending mass flow of the isothermal region ($\dot{m}^D_{ISO}$). This mass flow can be directed upward or downward, due to the convective flows of the wet side wall, and due to the inlet and outlet liquid flows ($\dot{m}^L_{IN}$ and $\dot{m}^L_{OUT}$). So, the combination of the possible direction of the descending flow $\dot{m}^D_{ISO}$ produces different fluid-dynamics cases, which are reported in Figure 204. In Figure 204, the blue colour indicates the liquid bulk. The black arrows are the inlet and outlet mass flows. The red arrows refer to the enthalpy flows. The white arrows with red border are the upper heat flow. the gry arrows are the descending flows and the boundary layer-to-bulk mass flows.

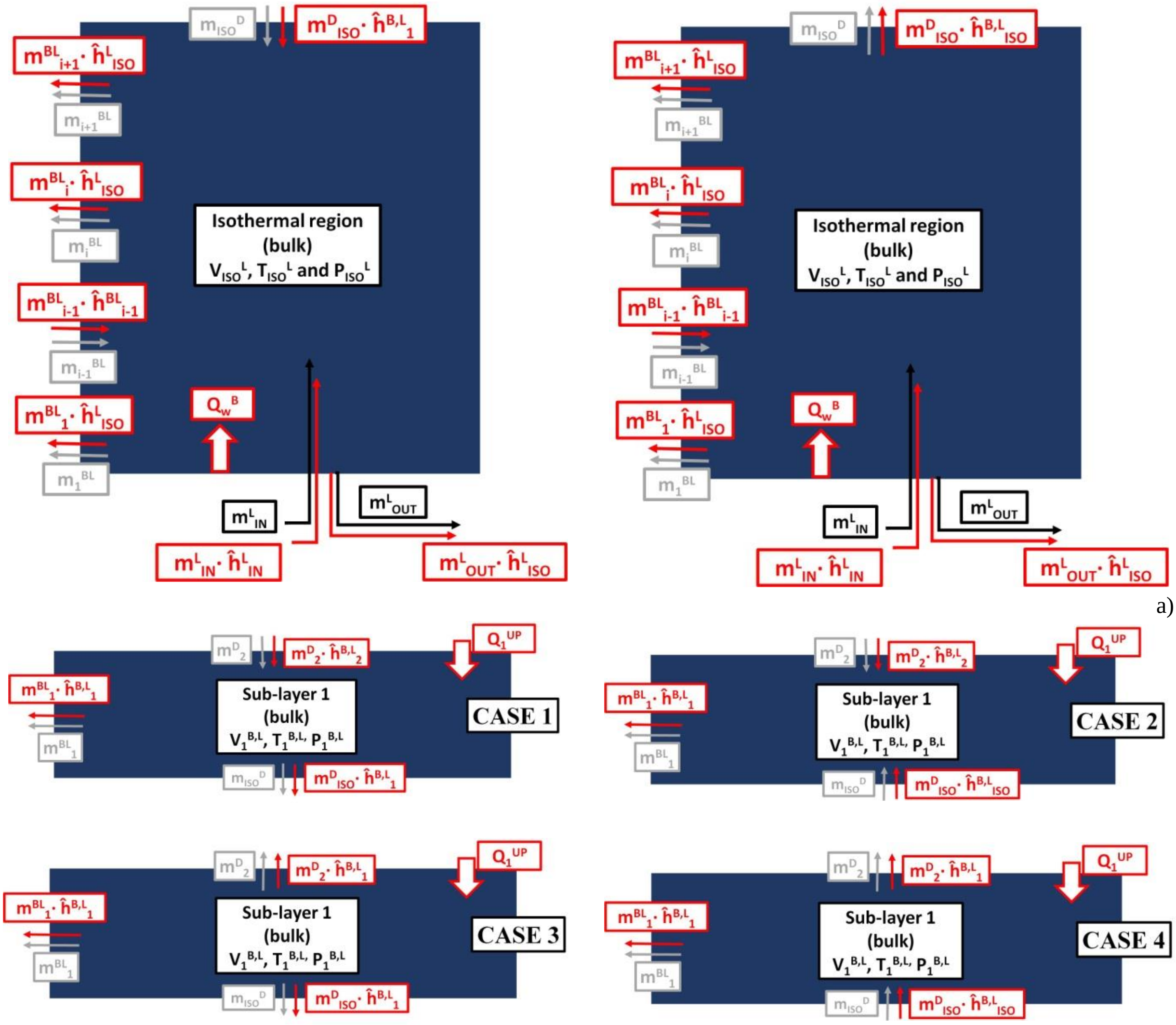

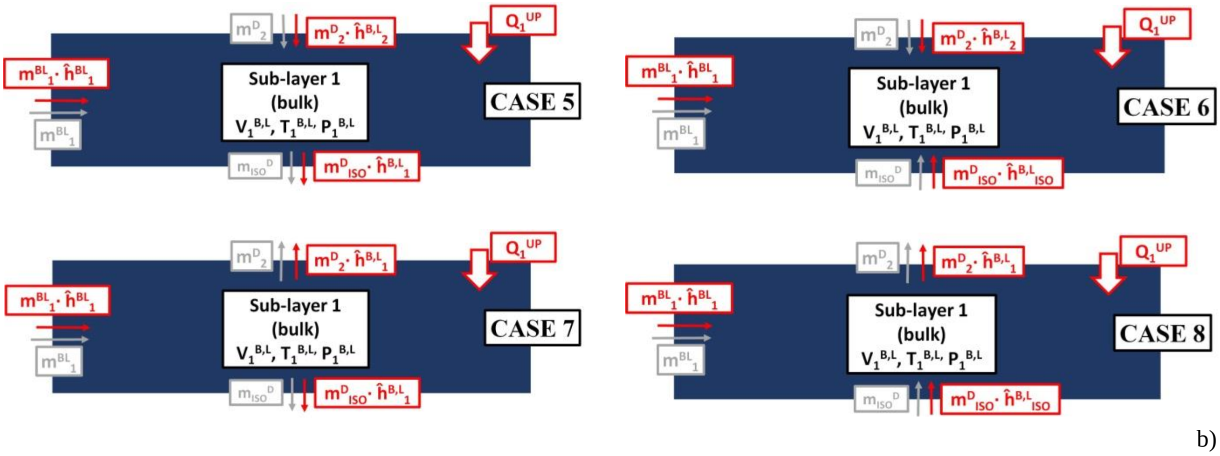

Figure 204. Control volumes of the TLR models: a) isothermal region; b) sub-layer 1.

These fluid-dynamic cases are reported in Table 159.

Table 159. Fluid-dynamics cases of the isothermal region and of the sub-layer 1.

	Isothermal region
Case 1	$\dot{m}_{ISO}^{D}$ is directed downward.
Case 2	$\dot{m}_{ISO}^{D}$ is directed upward.
	Sub-layer 1
Case 1	$\dot{m}_{ISO}^{D}$ is directed downward. $\dot{m}_{2}^{D}$ is directed downward. $\dot{m}_{1}^{BL}$ enters the sub-layer.
Case 2	$\dot{m}_{ISO}^{D}$ is directed upward. $\dot{m}_{2}^{D}$ is directed downward. $\dot{m}_{1}^{BL}$ enters the sub-layer.
Case 3	$\dot{m}_{ISO}^{D}$ is directed downward. $\dot{m}_{2}^{D}$ is directed upward. $\dot{m}_{1}^{BL}$ enters the sub-layer.
Case 4	$\dot{m}_{ISO}^{D}$ is directed upward. $\dot{m}_{2}^{D}$ is directed upward. $\dot{m}_{1}^{BL}$ enters the sub-layer.
Case 5	$\dot{m}_{ISO}^{D}$ is directed downward. $\dot{m}_{2}^{D}$ is directed downward. $\dot{m}_{1}^{BL}$ exits the sub-layer.
Case 6	$\dot{m}_{ISO}^{D}$ is directed upward. $\dot{m}_{2}^{D}$ is directed downward. $\dot{m}_{1}^{BL}$ exits the sub-layer.
Case 7	$\dot{m}_{ISO}^{D}$ is directed downward. $\dot{m}_{2}^{D}$ is directed upward. $\dot{m}_{1}^{BL}$ exits the sub-layer.
Case 8	$\dot{m}_{ISO}^{D}$ is directed upward. $\dot{m}_{2}^{D}$ is directed upward. $\dot{m}_{1}^{BL}$ exits the sub-layer.

The conservation laws of the isothermal region and of the sub-layer 1 are reported in Table 160, for each of the cases of Table 159.

Table 160. Energy and mass conservation laws of the isothermal region and of the sub-layer 1.

Case	Equation	Formula
		Isothermal region
1	Equation 604	$\frac{\partial \widetilde{H}_{ISO}^{B,L}}{\partial t} = \dot{m}_{ISO}^{D} \cdot \tilde{h}_{1}^{B,L} + \sum_{i=1}^{N_{ISO}^{L,-}} \dot{m}_{i}^{BL} \cdot \tilde{h}_{i}^{B,L} - \sum_{i=1}^{N_{ISO}^{L,+}} \dot{m}_{i}^{BL} \cdot \tilde{h}_{ISO}^{B,L} + \dot{Q}_{w}^{B} + \dot{m}_{IN}^{L} \cdot \tilde{h}_{IN}^{L} - \dot{m}_{OUT}^{L} \cdot \tilde{h}_{ISO}^{B,L}$
	Equation 605	$\frac{\partial m_{ISO}^{L}}{\partial t} = \dot{m}_{ISO}^{D} + \sum_{i=1}^{N_{ISO}^{L,-}} \dot{m}_{i}^{BL} - \sum_{i=1}^{N_{ISO}^{L,+}} \dot{m}_{i}^{BL} + \dot{m}_{IN}^{L} - \dot{m}_{OUT}^{L}$
2	Equation 606	$\frac{\partial \widetilde{H}_{ISO}^{B,L}}{\partial t} = -\dot{m}_{ISO}^{D} \cdot \tilde{h}_{ISO}^{B,L} + \sum_{i=1}^{N_{ISO}^{L,-}} \dot{m}_{i}^{BL} \cdot \tilde{h}_{i}^{BL} - \sum_{i=1}^{N_{ISO}^{L,+}} \dot{m}_{i}^{BL} \cdot \tilde{h}_{ISO}^{B,L} + \dot{Q}_{w}^{B} + \dot{m}_{IN}^{L} \cdot \tilde{h}_{IN}^{L} - \dot{m}_{OUT}^{L} \cdot \tilde{h}_{ISO}^{B,L}$
	Equation 607	$\frac{\partial m_{ISO}^{L}}{\partial t} = -\dot{m}_{ISO}^{D} + \sum_{i=1}^{N_{ISO}^{L,-}} \dot{m}_{i}^{BL} - \sum_{i=1}^{N_{ISO}^{L,+}} \dot{m}_{i}^{BL} + \dot{m}_{IN}^{L} - \dot{m}_{OUT}^{L}$
		Sub-layer 1
1	Equation 608	$\frac{\partial \widetilde{H}_{1}^{B,L}}{\partial t} = -\dot{m}_{ISO}^{D} \cdot \tilde{h}_{1}^{B,L} + \dot{m}_{2}^{D} \cdot \tilde{h}_{2}^{B,L} - \dot{m}_{1}^{BL} \cdot \tilde{h}_{1}^{B,L} + \dot{Q}_{1}^{UP}$
	Equation 609	$\frac{\partial m_{1}^{B,L}}{\partial t} = -\dot{m}_{ISO}^{D} + \dot{m}_{2}^{D} - \dot{m}_{1}^{BL}$

Table 160. Energy and mass conservation laws of the isothermal region and of the sub-layer 1.

2	Equation 610	$\frac{\partial \widetilde{H}_1^{B,L}}{\partial t} = \dot{m}_{ISO}^D \cdot \tilde{h}_{ISO}^{B,L} + \dot{m}_2^D \cdot \tilde{h}_2^{B,L} - \dot{m}_1^{BL} \cdot \tilde{h}_1^{B,L} + \dot{Q}_1^{UP}$
	Equation 611	$\frac{\partial m_1^{B,L}}{\partial t} = \dot{m}_{ISO}^D + \dot{m}_2^D - \dot{m}_1^{BL}$
3	Equation 612	$\frac{\partial \widetilde{H}_1^{B,L}}{\partial t} = -\dot{m}_{ISO}^D \cdot \tilde{h}_1^{B,L} - \dot{m}_2^D \cdot \tilde{h}_1^{B,L} - \dot{m}_1^{BL} \cdot \tilde{h}_1^{B,L} + \dot{Q}_1^{UP}$
	Equation 613	$\frac{\partial m_1^{B,L}}{\partial t} = -\dot{m}_{ISO}^D - \dot{m}_2^D - \dot{m}_1^{BL}$
4	Equation 614	$\frac{\partial \widetilde{H}_1^{B,L}}{\partial t} = \dot{m}_{ISO}^D \cdot \tilde{h}_{ISO}^{B,L} - \dot{m}_2^D \cdot \tilde{h}_1^{B,L} - \dot{m}_1^{BL} \cdot \tilde{h}_1^{B,L} + \dot{Q}_1^{UP}$
	Equation 615	$\frac{\partial m_1^{B,L}}{\partial t} = \dot{m}_{ISO}^D - \dot{m}_2^D - \dot{m}_1^{BL}$
5	Equation 616	$\frac{\partial \widetilde{H}_1^{B,L}}{\partial t} = -\dot{m}_{ISO}^D \cdot \tilde{h}_1^{B,L} + \dot{m}_2^D \cdot \tilde{h}_2^{B,L} + \dot{m}_1^{BL} \cdot \tilde{h}_1^{BL} + \dot{Q}_1^{UP}$
	Equation 617	$\frac{\partial m_1^{B,L}}{\partial t} = -\dot{m}_{ISO}^D + \dot{m}_2^D + \dot{m}_1^{BL}$
6	Equation 618	$\frac{\partial \widetilde{H}_1^{B,L}}{\partial t} = \dot{m}_{ISO}^D \cdot \tilde{h}_{ISO}^{B,L} + \dot{m}_2^D \cdot \tilde{h}_2^{B,L} + \dot{m}_1^{BL} \cdot \tilde{h}_1^{BL} + \dot{Q}_1^{UP}$
	Equation 619	$\frac{\partial m_1^{B,L}}{\partial t} = \dot{m}_{ISO}^D + \dot{m}_2^D + \dot{m}_1^{BL}$
7	Equation 620	$\frac{\partial \widetilde{H}_1^{B,L}}{\partial t} = -\dot{m}_{ISO}^D \cdot \tilde{h}_1^{B,L} - \dot{m}_2^D \cdot \tilde{h}_1^{B,L} + \dot{m}_1^{BL} \cdot \tilde{h}_1^{BL} + \dot{Q}_1^{UP}$
	Equation 621	$\frac{\partial m_1^{B,L}}{\partial t} = -\dot{m}_{ISO}^D - \dot{m}_2^D + \dot{m}_1^{BL}$
8	Equation 622	$\frac{\partial \widetilde{H}_1^{B,L}}{\partial t} = \dot{m}_{ISO}^D \cdot \tilde{h}_{ISO}^{B,L} - \dot{m}_2^D \cdot \tilde{h}_1^{B,L} + \dot{m}_1^{BL} \cdot \tilde{h}_1^{BL} + \dot{Q}_1^{UP}$
	Equation 623	$\frac{\partial m_1^{B,L}}{\partial t} = \dot{m}_{ISO}^D - \dot{m}_2^D + \dot{m}_1^{BL}$

The number of equations for describing the liquid phase is equal to $N^L + 3$, where N^L is the number of the liquid sub-layer of the stratified region. The variables of these equations are the time-derivate of the liquid volume ($\frac{\partial V^L}{\partial t}$), the time-derivate of the thickness ($\frac{\partial dxL}{\partial t}$), the time-derivate of the volume of the isothermal region ($\frac{\partial V_{ISO}^L}{\partial t}$), the time-derivates of the bulk liquid temperature of the sub-layer ($\frac{\partial T_{n_L}^L}{\partial t}$), the time-derivate of the temperature of the isothermal region ($\frac{\partial T_{ISO}^L}{\partial t}$), the descending flows ($\dot{m}_{n_L}^D$) and the descending flow of the isothermal region ($\dot{m}_{ISO}^D$). So, the number of the variables is $N^L + 4$, which is higher than the one of the equations. As consequence, the mathematical system is under-estimated because the mass flow $\dot{m}_{ISO}^D$ cannot be computed with the conservation laws.

During the self-pressurisation, the liquid coming from the side wall accumulates in the stratified region because it is warmer than the isothermal region. As time passes, this region expands due to the mass accumulation and the isothermal region reduces in volume. This reduction increases the rate of warming of the isothermal region. So, the temperature of the isothermal region becomes higher than the one of the stratified liquid in contact with this region. Hence, the mass flows from the stratified to the isothermal region because the lower part of the stratified liquid is heavier than the isothermal liquid. As results, the expansion of the stratification region stops. So, the mass flow $\dot{m}_{ISO}^D$ is equal to zero if the temperature of the isothermal region ($T_{ISO}^{B,L}$) is lower than the one of the sub-layer 1 ($T_1^{B,L}$). This mass flow can be computed with the conservation law of the mass of the sub-layer 1 when $T_{ISO}^{B,L}$ is higher than $T_1^{B,L}$, under the hypothesis that the time-derivate of the thickness is constant.

3.6. Lack of useful experimental data: design of the experimental campaign

The results of the fluid-dynamics and of the heat transfer of the liquid stratification model (LS model) cannot be validated because of the lack of experimental data (of boundary layer thickness, average velocity, wall temperature and heat input at the dry and wet side wall) that are done during the measremetns of pressure and temperatures, for a cryogenic storage container during the self-pressurisation. As a consequence, experimental campaigns are mandatory to measure these fluid-dynamics and heat transfer variables, as well as other storage variables such as pressure, temperature, and filing ratio.

The works of Aktinson-Barr [22], of Boardman [36], and of Beresford [37] should be deeply studied for designing this campaign because they qualitatively and quantitatively measured flow patterns, boundary layer velocity and thickness, and temperature distribution. Flow patterns can be visualized using the Schlieren technique [22]. Velocities in liquid can be measured with Laser Droplets anemometry (LDA) [22]. Heat inputs can be deduced from the steady state values of Boil-off gas (BOG) measured with a flow-meter. Boundary layer thickness and velocity can be deduced from photographs [36], [37] that are taken using a suitable tracing fluid. Wall and bulk temperatures can be measured with thermocouples. Pressure and filling ratio can be measured with sensors. For safety reason, liquid nitrogen should be used as working fluid.

The variables of interest can be measured with the experimental device that is described in Figure 205. In Figure 205, the liquid is described by the light blue colour. The light red colour is the ullage and the dashed yellow line is the interface. BOG FM is the BOG mass flow meter and LN_2 FM is the flow meter of the liquid, T means thermocouple, P is the pressure sensor and the LF is the transistor of the liquid level.

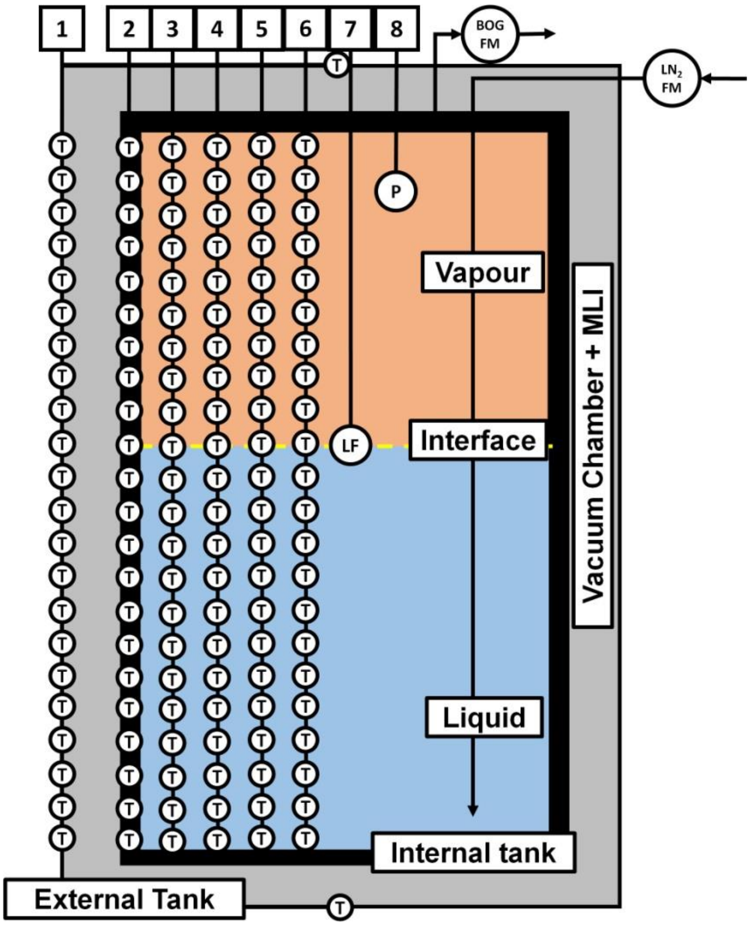

Figure 205. Heat Experimental device.

As it is reported in Figure 205, the storage container of the experimental campaign is composed by an external tank and an internal tank. The geometry of both tanks is a vertical cylinder with flat ends, as done in many experiments [3], [24]–[26], [34]. The volume of the internal tank should be at least of 1 m^3, tobe representative of the size of the small scale storage container. Between these tanks, a vacuum chamber is placed and multi-layer insulation covers the internal tank to simulate the thermal insulation of a typical small scale storage containers. Heaters are not installed, and the thermal energy naturally flows from the environment to the fluid (liquid and vapour), as mainly occurs in small scale storage containers. The environment should be, and remain at standard conditions, thus at 25°C and 1 atm. As it is reported in Figure 205, there are 8 probes, and the probes from 1 to 6 are used to locate the thermocouples. The first probes are used for measuring the external wall temperature along the side wall, at the roof and at the bottom. Along the side wall, the thermocouples are spaced 2 cm apart. This value of the distance between the thermocouples is used for the probes 2 to 6. The second probe is used for measuring the internal wall temperatures. The sixth probe is placed along the vertical axis of the storage container for measuring the temperatures in the core. The third, fourth and fifth probes should be placed as close as possible to the side wall to measure the temperature near the boundary layer of the side wall. The distance at which these probes should be placed is not found in literature. The values of the boundary layer thickness and velocity should be deduced from the pictures of flow patterns and from measured data of LDA, at any vertical and radial points where are placed the thermocouples of the probes 3, 4, 5 and 6.

The experimental tests should be done at different values of the filling ratio, at different heat fluxes and at different initial conditions. The heat fluxes can be increased by increasing the pressure in the vacuum chamber or they can be reduced by decreasing the pressure in this chamber. These values are

95%, 90%, 80%, 70%, 60%, 50%, 40%, 30%, 20%, 10% and 5%. 95% and 5 % are used to simulate the conditions of full and empty storage container, which can occur in storage containers used for the mobility. At each filling ratio, tests at isothermal and steady state initial conditions, which can occur in storage containers used for the mobility, should be done. The procedures of Hasan et al. [27] and of Dresar et al. [28] should be used for the isothermal initial conditions. In this procedure, the cryogenic liquid is quickly withdrawn after the refrigeration of the tank and the storage is immediately closed after this operation. Steady state conditions can be reached by evaporating the cryogenic liquid at constant pressure. The end of the steady state test is reached when the BOG is stable [24]–[26]. During this period, liquid nitrogen can be injected to maintain the filling ratio constant. This liquid should be injected at the thermodynamic condition of the liquid stored during the steady state, thus close to saturation, to not thermally perturb the system. For each filling ratio and for each initial condition, tests at low, medium and high heat fluxes should be done. Low, medium and high heat fluxes respectively correspond to the values of 6 W/m² [24], [26]–[28], 84-77 W/m² [25], [30] and 289 W/m² [29]. As done by Kang et al. [25], the self-pressurisation test should last until the critical value is reached. This critical value should be computed by considering the mechanical stresses on the experimental device and the industrial operating conditions, where the pressure can be higher than 17 bar. The sample of temperatures (wall and bulk), pressure, filling ratio, pictures and LDA data should be taken every 1 minute,[2] and at the end of the steady state. The BOG should be measured during all the steady state period, except for the isothermal tests.

Conclusions

La transition énergétique dans les applications à petite échelle des secteurs de l'énergie et des transports nécessite des modèles mathématiques pour prédire l'évolution temporelle des variables de stockage telles que (i) le temps de rétention, (ii) la hauteur d'aspiration positive nette, (iii) l'indice de méthane et (iv) le pouvoir calorifique supérieur du liquide cryogénique. L'évolution temporelle de ces variables est étroitement liée aux phénomènes de stockage tels que (i) la stratification thermique des liquides et des vapeurs, (ii) l'auto-pressurisation et (iii) le vieillissement, qui sont produits par le flux thermique permanent entrant dans les cuves en raison de la différence de température avec l'environnement.

La littérature scientifique a été examinée à l'aide d'une méthode de table-score pour trouver (i) les approches de modélisation les plus appropriées et (ii) les données expérimentales utiles à la comparaison. Même s'il existe un grand nombre d'approches de modélisation et de travaux expérimentaux, selon les critères de la méthode table-score : (i) les données expérimentales de l'azote liquide et de l'hydrogène liquide sont les plus utiles et (ii) les modèle à paramètres groupés (LP) avec approche discrétisée sont les plus adaptés pour prédire les phénomènes de stockage. Ce type de modèles présente certains inconvénients dus à (i) la négligence du gradient de température globale dans le modèle de dynamique des fluides, (ii) la négligence entre le transfert de chaleur et la dynamique des fluides au niveau des parois latérales, (iii) l'absence de validation des modèles avec des données expérimentales et (iv) l'utilisation des données expérimentales pour fixer les coefficients du modèle de transfert de masse à l'interface.

En conséquence, l'objectif de la thèse est le développement d'un modèle physique qui prédit les phénomènes de stockage de liquides cryogéniques purs dans des réservoirs de stockage de petite taille pour (i) surmonter les problèmes critiques du modèle LP avec une approche discrétisée et (ii) être utilisé comme base pour les logiciels commerciaux. Pour atteindre cet objectif, quatre modèles avec différents degrés de complexité ont été développés selon une approche de complexité croissante. Dans cette approche, chaque modèle a été comparé aux données expérimentales et les améliorations sont proposées et mises en œuvre en fonction des criticité des modèles précédentes.

Le premier modèle (modèle d'équilibre ou EQ) repose sur les hypothèses (i) d'équilibre thermodynamique instantané et (ii) d'homogénéité totale de chaque phase. L'évolution temporelle de la pression et du volume du liquide est calculée lors de l'auto-pressurisation avec des formules explicites déduites des lois de conservation de l'énergie et de la masse. Les entrées thermiques sont calculées en fonction de la température de la paroi extérieure et de la propriété isolante de la cuve de stockage. Même si l'évolution temporelle du taux de remplissage et de la température du liquide est proche des données expérimentales, la température de la vapeur et la pression ne sont pas en accord avec les valeurs mesurées. L'hypothèse d'équilibre thermodynamique instantané ne convient donc pas pour prédire le comportement des liquides cryogéniques dans des réservoirs à petite échelle.

Le deuxième modèle (modèle homogène ou H) a été proposé en prenant en compte de l'état thermodynamique réel de chaque phase. Cette nouvelle hypothèse fait augmenter le nombre de variables et d'équations indépendantes, déduites des lois de conservation de l'énergie et de la masse. Le transfert matière/énergie à l'interface, la dynamique des fluides au niveau des parois et le transfert thermique au niveau des parois sont pris en compte et calculés avec des sous-modèles dédiés. Les apports thermiques sont calculés à partir du coefficient d'isolation globale de la cuve de stockage et des coefficients correcteurs des flux thermiques paroi latérale sèche-interface et paroi latérale sèche-vapeur. Aux faibles flux de chaleur, l'évolution temporelle de la température de la vapeur est souvent en accord avec les données expérimentales. À moyenne et haute température, le modèle n’est pas en mesure d’être qualitativement en accord avec l'augmentation de la température de la vapeur observée expérimentalement et la pression est sous-estimée à tous les flux de chaleur. Donc, (i) l’hypothèse de vapeur homogène n’est pas adaptée lorsque le ciel gazeux est fortement stratifié comme cela se produit pour des flux de chaleur moyens et élevés et (ii) l’utilisation du coefficient correcteur limite l’applicabilité de ce modèle.

Dans le troisième modèle (modèle homogène 2.0 ou H 2.0) proposé le ciel gazeux est virtuellement discrétisé. La température de la vapeur dans chaque sous-couche est calculée avec le profil de température virtuel et les lois de conservation de la masse et de l'énergie de chaque sous-couche sont utilisées pour déduire la formule explicite qui calcule l'évolution temporelle de la température de la vapeur. Les sous-modèles du modèle H sont modifiés en raison de cette hypothèse. Même si la pression calculée est inférieure aux données expérimentales aux flux thermiques moyens et élevés, la température de la vapeur est souvent en accord avec les données expérimentales et l'évolution temporelle calculée est qualitativement correcte.

Pour améliorer la prédiction de la pression, un quatrième modèle (modèle de stratification liquide ou LS) est proposé et le liquide est discrétisé en sous-couches horizontales d'égale épaisseur. Le flux de chaleur entre la sous-couche du liquide est pris en compte et il est calculé en fonction des conditions dynamiques des fluides. La paroi latérale humide est discrétisée en sous-parois pour prendre en compte le profil de température produit par la stratification thermique, mais le flux de chaleur conducteur dans la paroi n'est pas pris en compte. Le modèle du flux de chaleur liquide-interface est modifié pour prendre en compte le changement des conditions dynamiques des fluides dû à la stratification thermique. La pression calculée est généralement supérieure à celle calculée et la différence pour des flux thermiques moyens est inférieure à celle des flux faibles. Les profils de température du liquide sont souvent proches de ceux expérimentaux à taux de remplissage et apport thermique élevés. La comparaison indique cependant que (i) la chaleur sensible s'accumule de manière excessive à proximité de l'interface et (ii) le temps de calcul est élevé en raison de l'algorithme d'intégration de l'approche Integrated Boundary Layer (IBL). Le temps de calcul peut être réduit grâce à un nouvel algorithme d'intégration de l'approche IBL et l'accumulation de chaleur sensible peut être réduite en ajoutant le flux de chaleur conducteur dans la paroi latérale humide.

Même si l'approche de discrétisation nécessite un énorme effort informatique, elle donne des résultats qui sont souvent qualitativement et quantitativement en accord avec les données expérimentales. Ainsi, (i) la méthode de complexité croissante fonctionne parce que le principal problème critique de chaque modèle a été surmonté et (ii) la méthode de discrétisation devrait être étendue à la vapeur, après avoir surmonté les problèmes critiques du modèle LS, pour supprimer l'utilisation du coefficient correcteur du modèle H, qui sont calculés dans le modèle LS. En raison du manque de données expérimentales sur la dynamique des fluides et les phénomènes de stockage, une campagne expérimentale de mesure des profils de mouvements, de pression et de température des fluides est fortement recommandée.

Conclusions

The implementation of the energy transition in small scale (SS) applications of energy and transport sectors relies on reliable mathematical models for predicting the time-evolution of storage variables such as (i) hold-up time, (ii) net pressure suction head, (iii) methane number and (iv) gross heating value of storage tank filled with cryogenic liquids. The time-evolution of these variables is strictly related to storage phenomena such as (i) liquid and vapour thermal stratification, (ii) self-pressurisation and (iii) ageing, which are produced by the permanent heat flow from the environment.

The scientific literature has been reviewed with a table-score method to find the most suitable (i) modelling approaches and (ii) experimental data. Even if a large number of modelling approach and few experimental works exist, according to the criteria of the table-score method: (i) experimental data of liquid nitrogen and liquid hydrogen are the most useful for the model design and validation and (ii) lumped parameter (LP) model with discretised approach are the most suitable for predicting the storage phenomena. This type of models has some drawbacks such as (i) the neglect of the bulk temperature gradient in the fluid-dynamics model, (ii) the neglect of the link between the heat transfer and the fluid-dynamics at the side walls, (iii) the absence of validation of models with respect to experimental data, and (iv) the fitting of coefficients of the interfacial mass transfer model with experimental data.

So, the objective of the thesis is the development of a physical model that predicts the storage phenomena of pure cryogenic liquids in SS storage tanks to (i) overcome the critical issues of the LP model with discretized approach and (ii) be used as base for commercial software. To achieve this objective, four models of increasing complexity have been developed: each model has been compared with experimental data and further improvements are proposed and implemented to overcome the main critical issues.

The first model (equilibrium or EQ model), is based on the hypotheses of (1) instantaneous thermodynamic equilibrium and (ii) total homogeneity of the liquid and the vapor. The time-evolution of the pressure and liquid volume are calculated during the self-pressurisation with explicit formulas that are deduced from the energy and mass conservation laws. The heat inputs are computed as function of the external wall temperature and of the insulating property of the storage tank. Even if the time-evolution of filling ratio and liquid temperature are close to the experimental data, the calculated vapour temperature and the pressure are not in agreement with measured values. So, the hypothesis of instantaneous thermodynamic equilibrium is not suitable for predicting the behaviour of cryogenic liquids in small scale tanks.

The second model (homogeneous or H model) has been proposed by assuming the actual thermodynamic state of the liquid and of the vapour. This new hypothesis increases the number of independent variables and equations which are deduced from the energy and mass conservation laws. The mass-interface heat transfer, the fluid-dynamics and heat transfer at the walls are considered and computed with dedicated sub-models. The heat inputs are computed from the overall insulation property of the storage container and from the corrective coefficients of the dry side wall-to-interface and dry side wall-to-vapour heat flows. At low heat fluxes, the time-evolution of the ullage temperature is often in agreement with the experimental data. At medium and high fluxes, the model cannot qualitatively compute the rise of the ullage temperature and the pressure is under-estimated at any heat fluxes. So, (i) the hypothesis of homogenous vapour is unsuitable when the ullage is strongly stratified as it occurs at medium and high heat fluxes and (ii) the use of the corrective coefficient limits the applicability of this model.

The ullage is virtually discretized in the third model (homogeneous model 2.0 or H 2.0 model). The ullage temperature in each sub-layer is computed with the virtual temperature profile and the mass and energy conservation laws of the sub-layer are used for deducing the explicit formula that compute the time-evolution of the vapour temperature. The sub-models of the H model are modified due to this hypothesis. Even if the calculated pressure is lower than the experimental data at medium and high heat fluxes, the ullage temperature is often in agreement with the experimental data and the computed time evolution is qualitatively correct.

To improve the prediction of the pressure, a fourth model (liquid stratification or LS model) is proposed and the liquid is discretized in horizontal sub-layers of equal thickness. The heat flow between the sub-layer of the liquid is considered and it is calculated as a function of the fluid-dynamic conditions. The wet side wall is discretized in sub-walls to consider the temperature profile produced by the thermal stratification, but the conductive heat flow in the wall is not considered. The model of the liquid-to-interface heat flow is modified to consider the change of the fluid-dynamic conditions due to the thermal stratification. The calculated pressure is usually higher than the computed one and the difference is lower at medium-high heat fluxes than at low heat fluxes. The liquid temperature profiles are often close to the experimental ones at high filling ratio and high heat input. The comparison, however, indicates that (i) the sensible heat excessively accumulated in the near the interface and (ii) the computational time is high due to the integration algorithm of the Integrated Boundary Layer (IBL) approach. The computational time can be reduced with a new integration algorithm of the IBL approach and the accumulation of sensible heat can be reduced by adding the conductive heat flow in the wet side wall.

Even if the discretisation approach implies a huge computational effort, it gives results that are qualitatively and often quantitatively in agreement with experimental data. So, (i) the method of increasing complexity works because the main critical issues of each model have been overcome and (ii) the discretisation method should be extended to the vapour, after overcoming the critical issues of the LS model, to remove the use of the corrective coefficient of the H model, which are calculated in the LS model. Due to the lack of experimental data of fluid-dynamics and storage phenomena, an experimental campaign for measuring fluid-motions, pressure and temperature profiles is highly recommended.

Appendix A

Experimental data of the study cases

The experimental data of pressure and of the temperature profile are reported for seven of the selected works. The pressure measurement of Seo and Jeong [24] at Test 3 and at Test 6 are incomplete. Kang et al. [25] reported the temperature profile in a part of the ullage volume. Aydelott [29] and Aydelott and Spuckler [30] did not given the evolution of the temperature profiles, but they limited their studies to the time-variation of the temperature. Hence, some experimental data are missing and, here, it is described how these missing data were obtained. The raw data were visually extracted by the figures reported in each paper using the software GetDataGraphDigitizer®.

Section 1, 2, 3, 4, 5, 6 and 7 respectively report the experimental data of pressure and of temperature profile for Seo and Jeong [24], Kang et al. [25], Perez et al. [26], Hasan et al. [27], Dresar et al. [28], Aydelott [29] and Aydelott and Spuckler [30].

1. Experimental data of Seo and Jeong – 2010

The experimental data of pressure are described in Section 1.1. The temperature profiles are reported in Section 1.2.

1.1. Experimental data of pressure

Table 161 reports the raw values of the measured pressure for Test 1, 2, 3, 4, 5 and 6. The values underlined are computed by the author since Seo and Jeong[24] did not reported them.

Table 161. Values of the experimental data of pressure of Seo and Jeong**[24]**.

Test 1		**Test 2**		**Test 3**	
Time [min]	**P [bar]**	**Time [min]**	**P [bar]**	**Time [min]**	**P [bar]**
0	1	0	0.995455	0	0.995408
3.19749	1.02576	3.19749	1.02424	3.40694	1.07194
6.58307	1.02879	6.58307	1.02879	6.62461	1.1102
9.96865	1.03333	9.96865	1.03182	10.0315	1.14082
13.3542	1.03636	13.3542	1.03333	13.2492	1.16531
16.5517	1.03939	16.5517	1.03485	16.6562	1.18827
19.9373	1.04242	19.9373	1.03636	19.8738	1.20816
20	1.040852444	20	1.035703013	20	1.208802767
23.1348	1.04394	23.1348	1.03939	23.2808	1.22806
26.5204	1.04697	26.5204	1.04091	26.4984	1.24643
29.906	1.05	29.906	1.04545	33.3123	1.28316
33.2915	1.05152	33.1034	1.04697	36.53	1.30306
36.489	1.05455	36.489	1.05	39.9369	1.3199
39.8746	1.05758	39.8746	1.05152	43.3438	1.3398
40	1.057521962	40	1.052657399	43.3438	1.3398
43.0721	1.06061	43.2602	1.05455	46.1198333	1.35601505
46.4577	1.06212	46.4577	1.05758	48.8958667	1.37223011
49.8433	1.06364	49.8433	1.06061	51.6719	1.38844516
53.2288	1.06667	53.0408	1.06212	54.4479333	1.40466021
56.4263	1.0697	56.6144	1.06515	57.2239667	1.42087526

Table 161. Values of the experimental data of pressure of Seo and Jeong**[24]**.

60	1.07121	60	1.0697	60	1.43709032

Test 4		Test 5		Test 6	
Time [min]	**P [bar]**	**Time [min]**	**P [bar]**	**Time [min]**	**P [bar]**
0	0.995408	0	0.995408	0	0.99397
3.21767	1.03214	3.21767	1.02449	3.47015	1.01658
6.62461	1.05357	6.62461	1.04286	6.64179	1.03317
10.0315	1.07041	9.84227	1.05816	10	1.04673
13.2492	1.08418	13.2492	1.07194	13.3582	1.0603
16.6562	1.09796	16.6562	1.08418	16.7164	1.07085
19.8738	1.10867	19.8738	1.09643	20	1.083289198
20	1.108728116	20	1.095156436	20.0746	1.08442
23.2808	1.12092	23.2808	1.10561	23.2463	1.09497
26.6877	1.1301	26.6877	1.1148	26.6045	1.10553
29.9054	1.14082	29.9054	1.12551	29.9627	1.11759
33.3123	1.15	33.123	1.13469	33.3209	1.12814
36.53	1.15918	36.7192	1.14388	36.4925	1.13869
39.9369	1.16837	39.9369	1.15306	39.8507	1.15226
40	1.168017981	40	1.152969261	40	1.151207412
43.3438	1.17602	43.3438	1.16224	43.209	1.16131
46.5615	1.18367	46.5615	1.1699	46.5672	1.17337
49.9685	1.19286	49.9685	1.17755	49.9254	1.18392
53.1861	1.20051	53.1861	1.18673	53.2836	1.19598
56.5931	1.20816	56.5931	1.19592	56.6418	1.20804
60	1.21582	60	1.20357	60	1.2201

The values of pressure at 20 and at 40 minutes for each test of Seo and Jeong[24] are computed with an interpolating function. This function is a sixth-order polynomial and it is described by Equation 624.

Equation 624
$$P = \sum_{i=1}^{7} a_i \cdot t^{7-i}$$

P is the pressure and t is the time. The index i indicates the terms of the sum. a_i are the coefficients of this polynomial and they are given in Table 162.

Table 162. Values of the coefficients $\boldsymbol{a_i}$ of Equation 624 at different filling ratio.

LFi \ a	1	2	3	4	5	6	7
Test 1	-7.20E-11	1.45E-08	-1.13E-06	4.35E-05	-0.0008461	0.00844917	1.00163047
Test 2	-9.12E-11	1.86E-08	-1.48E-06	5.73E-05	-0.0011051	0.01027837	0.99697699
Test 3	-5.69E-10	8.52E-08	-5.06E-06	1.53E-04	-0.002542	0.02891737	0.99585091
Test 4	-5.94E-11	1.20E-08	-9.57E-07	3.82E-05	-0.0008287	0.01282993	0.99620627
Test 5	-3.01E-11	6.28E-09	-5.21E-07	2.21E-05	-0.0005222	0.00982796	0.99598108
Test 6	-1.36E-11	3.09E-09	-2.78E-07	1.27E-05	-0.000314	0.00743427	0.99403794

The values reported in Table 165 are determined with function Polyfit of MATLAB®.

Seo and Jeong [24] stated that the pressurisation rate is constant after the initial transient. The values of the pressure up to 60 minutes can be computed with a liner extrapolation for the case 70 % (2.5 W) and for the case 10 %. The last two measured values of pressure compute the slope and intercept of the extrapolation line. Equation 625 describes the liner extrapolation formula used by the author.

Equation 625
$$P = \frac{P_N - P_{N-1}}{t_N - t_{N-1}} \cdot (t - t_N) + P_N$$

P and t are respectively the pressure and the time. The indexes N and $N-1$ respectively describes the last and the second-last experimental values.

1.2. Experimental data of temperature profiles

Table 163 reports the measured values of the temperature profile along a vertical axis of the pressurized tank of Seo and Jeong[24] at different liquid levels and heat input rates. Seo and Jeong[24] gives these values as function of the height in the tank. The level positions of each sensor are computed and the temperature profile as function of this variable are reported at the different time step.

Table 163. Values of the experimental temperature profiles of Seo and Jeong**[24]**.

Test 1							
0 min		**20 min**		**40 min**		**60 min**	
T [K]	**H [%]**	**T [K]**	**H [%]**	**T [K]**	**H [%]**	**T [K]**	**H [%]**
77.019	4.67359155	77.019	5.0984507	77.4177	5.0984507	77.4177	5.0984507
77.019	14.4456338	77.3734	14.4456338	77.4177	14.4456338	77.7722	14.4456338
77.019	23.7928169	77.019	23.7928169	77.4177	23.3679812	77.3734	23.7928169
76.8861	33.14	77.2405	33.14	77.2405	33.14	77.2405	33.14
77.019	42.4871831	77.019	42.4871831	77.019	42.4871831	77.3734	42.4871831
77.1962	51.8342723	77.1962	52.2591549	77.1962	51.8342723	77.1962	51.8342723
77.019	61.6065728	77.3734	61.6065728	77.3734	61.6065728	77.7722	61.6065728
77.019	70.5286385	77.3734	70.9535211	77.4177	70.9535211	77.4177	70.9535211
77.019	80.300939	77.4177	80.300939	77.4177	80.300939	77.7722	80.300939
77.019	89.6478873	77.019	89.6478873	77.019	89.6478873	77.3734	89.6478873
76.8861	90.9225352	77.2405	91.3474178	77.5949	90.4976526	77.6392	90.9225352
77.1076	92.1971831	77.5063	92.6220657	77.5063	93.0469484	77.5063	92.6220657
77.019	93.8967136	77.3734	94.3215962	77.8165	93.8967136	77.7722	93.8967136
77.019	95.1713615	77.7722	95.5962441	78.1266	95.1713615	78.1709	94.7464789
77.3734	96.870892	78.1266	96.870892	78.1709	96.870892	78.5253	96.870892
Test 2							
0 min		**20 min**		**40 min**		**60 min**	
T [K]	**H [%]**	**T [K]**	**H [%]**	**T [K]**	**H [%]**	**T [K]**	**H [%]**
77.0222	5.0984507	77.0222	5.0984507	77.4222	5.0984507	77.4222	5.0984507
77.0222	14.4456338	77.4222	14.4456338	77.4222	14.4456338	77.4222	14.8705164
77.0222	23.7928169	77.0222	23.7928169	77.4222	23.7928169	77.4222	24.2176995
77.2889	33.14	77.2444	33.14	77.2444	33.14	77.6444	33.5648826
77.0222	42.4871831	77.0222	42.9120657	77.0222	42.4871831	77.3778	42.4871831
76.8444	51.8342723	77.2	52.2591549	77.2	51.8342723	77.6	51.8342723
77.0222	61.6065728	77.4222	61.6065728	77.4222	61.6065728	77.7778	61.6065728
77.0222	70.5286385	77.3778	70.9535211	77.3778	70.9535211	77.4222	70.9535211
77.4222	80.300939	77.7778	80.300939	78.1333	80.300939	78.1778	80.300939
78.8889	89.6478873	79.6444	89.6478873	80	89.6478873	80.4	89.6478873

Table 163. Values of the experimental temperature profiles of Seo and Jeong**[24]**.

79.5111	90.9225352	80.2667	91.3474178	80.6222	91.3474178	80.9778	91.3474178
79.7333	92.6220657	80.4889	92.6220657	80.8444	92.6220657	81.2	92.6220657
80.0444	93.8967136	80.7556	93.8967136	81.5111	94.3215962	81.8667	93.8967136
80.4	95.1713615	81.1111	95.5962441	81.5111	95.1713615	82.2222	95.1713615
80.8	96.870892	81.5111	96.870892	81.8667	96.870892	82.5778	96.870892
Test 3							
0 min		**20 min**		**40 min**		**60 min**	
T [K]	**H [%]**	**T [K]**	**H [%]**	**T [K]**	**H [%]**	**T [K]**	**H [%]**
76.984	4.70347418	77.3866	5.14056338	77.3866	4.71568075	77.7444	4.72652582
77.3866	14.4877465	77.3866	14.4877465	77.7444	14.0737089	77.7444	14.4985915
77.0288	23.3992019	77.3866	23.4100469	77.7444	23.420892	77.7444	23.8457746
77.2077	32.751784	77.6102	33.1888732	77.9681	33.1997653	77.9681	33.1997653
77.0288	42.0935681	77.3866	42.1044131	77.3866	42.1044131	77.7444	42.5401408
77.1629	51.4446009	77.5655	51.4568075	77.5655	51.4568075	77.9233	51.8929577
77.0288	61.2126761	77.7444	61.2347418	78.147	61.2469484	78.9073	61.2699531
77.3866	70.1460094	78.5048	70.6046948	79.2652	70.2028169	79.9808	70.2248826
78.147	79.5164319	79.2652	79.5502347	80.3834	80.0089202	81.1438	79.6070423
80.7859	89.3685446	82.2173	89.4117371	82.9329	89.4333333	83.6486	89.4553991
81.3674	90.6605634	82.7987	90.7042254	83.5144	90.7258216	84.23	90.7474178
81.9489	91.9530516	83.3802	92.4211268	84.0958	92.442723	84.8115	92.4647887
82.6198	93.67277	83.6933	94.1300469	84.4089	94.1521127	85.0799	93.7474178
82.9776	95.3830986	84.0511	95.415493	84.7668	95.4375587	85.4824	95.4591549
83.6933	96.6793427	84.7668	97.1370892	85.4377	96.7323944	86.1981	96.7553991
Test 4							
0 min		**20 min**		**40 min**		**60 min**	
T [K]	**H [%]**	**T [K]**	**H [%]**	**T [K]**	**H [%]**	**T [K]**	**H [%]**
76.6646	5.0984507	76.6646	5.0984507	77.019	5.0984507	77.0633	5.0984507
77.0633	14.4456338	77.019	14.4456338	77.019	14.4456338	77.0633	14.4456338
76.7089	23.7928169	77.019	23.7928169	77.019	23.7928169	77.019	23.7928169
76.8861	32.7151643	76.8861	33.14	76.8861	33.14	77.2848	33.14
77.0633	42.4871831	77.019	42.4871831	77.4177	42.4871831	77.7722	42.4871831
77.2405	51.8342723	77.5949	51.8342723	77.9937	52.2591549	78.3481	51.4093897
78.1709	61.1816901	78.9241	61.1816901	79.3228	61.1816901	79.6772	61.1816901
78.9241	70.5286385	79.6329	70.5286385	80.0759	70.9535211	80.4304	70.9535211
80.7848	79.8760563	81.1392	79.8760563	81.4937	79.8760563	82.2468	79.8760563
82.2468	89.6478873	82.6013	89.6478873	82.9557	89.2230047	83.6646	89.2230047
82.5127	90.9225352	82.8228	90.9225352	83.5759	90.9225352	83.9304	90.9225352
82.6899	92.1971831	83.0443	92.1971831	83.3987	92.6220657	84.1519	92.6220657
83	93.8967136	83.6646	94.3215962	84.0633	93.8967136	84.4177	93.8967136
83.3544	95.5962441	83.6646	95.1713615	84.0633	95.1713615	84.7722	95.5962441
83.7089	96.870892	84.019	96.870892	84.4177	96.870892	84.7722	97.2957746
Test 5							
0 min		**20 min**		**40 min**		**60 min**	
T [K]	**H [%]**	**T [K]**	**H [%]**	**T [K]**	**H [%]**	**T [K]**	**H [%]**
76.6978	4.65266667	77.0039	5.0829108	77.0039	5.0829108	77.4414	5.09610329
77.0433	14.3474648	77.0433	14.3474648	77.0433	14.3474648	77.4371	14.3592958

Table 163. Values of the experimental temperature profiles of Seo and Jeong**[24]**.

76.6453	23.5988732	76.9952	23.6093897	77.4325	24.0435681	77.7827	23.6330516
76.9032	33.2910329	77.647	33.3133803	77.997	33.3238967	78.3907	33.3357746
77.7739	42.5805634	78.5176	42.6029108	79.3049	43.0476526	79.6551	42.6371362
79.4756	52.3159624	80.1756	52.3370892	80.5694	52.3488263	80.9195	51.9384977
81.09	61.628169	81.8775	61.6516432	82.2275	61.6624413	82.5775	61.67277
81.8732	70.9150235	82.9669	70.9478873	83.3167	71.3793427	83.6669	70.9690141
83.2687	80.6413146	84.0124	80.6638498	84.3624	80.6741784	85.1062	80.6967136
84.3581	89.9375587	85.0581	89.9586854	85.4081	89.9690141	86.1518	89.9915493
84.62	91.2084507	85.3198	91.6507042	85.67	91.2399061	86.3698	91.6821596
84.838	92.8995305	85.1442	92.9084507	85.888	92.9309859	86.2379	92.9413146
85.0999	94.1704225	85.7561	94.1901408	86.1497	94.6230047	86.8498	94.2230047
85.4493	95.4441315	86.1053	95.8849765	86.4993	95.4755869	87.1991	95.9178404
85.7985	97.1389671	86.1485	97.1492958	86.4985	97.1600939	87.1985	97.1807512
Test 6							
0 min		**20 min**		**40 min**		**60 min**	
T [K]	**H [%]**	**T [K]**	**H [%]**	**T [K]**	**H [%]**	**T [K]**	**H [%]**
76.6183	4.63167606	76.9716	4.63167606	77.3691	4.63167606	77.7666	4.63167606
76.6183	14.3161033	77.4132	14.3161033	77.7224	14.3161033	78.2082	14.3161033
77.0158	24.0005164	77.7224	23.5794366	78.5174	23.5794366	78.8707	23.5794366
78.7382	32.8428169	79.489	33.2638498	80.2397	32.8428169	80.5931	33.2638498
80.3722	42.52723	81.123	42.52723	81.8738	42.52723	82.2271	42.52723
81.2997	51.7906103	82.4038	51.7906103	83.1546	51.7906103	83.4637	51.7906103
82.5804	61.4751174	83.6845	61.4751174	84.3912	61.4751174	84.7445	61.0539906
83.6845	70.3173709	84.7445	70.7384977	85.0978	70.7384977	85.4511	70.7384977
85.0978	80.0018779	85.8044	80.0018779	86.511	80.0018779	86.8644	80.0018779
85.8486	89.6859155	86.511	89.6859155	87.2177	89.6859155	87.5268	89.6859155
86.3785	90.9492958	87.0852	90.9492958	87.7918	90.9492958	88.1451	90.9492958
86.2461	92.2126761	86.9527	92.6333333	87.6151	92.2126761	87.9685	92.6333333
86.9085	93.8967136	87.571	93.8967136	87.9243	93.8967136	88.2776	93.8967136
87.2618	95.1600939	87.571	95.1600939	88.2776	95.1600939	88.6309	95.1600939
87.2618	96.4230047	87.9243	96.4230047	88.2776	96.4230047	88.9401	96.8441315

The values of the temperature profiles are complete.

2. Experimental data of Kang et al. – 2018

The experimental data of pressure are described in Section 2.1. The temperature profiles are reported in Section 2.2.

2.1. Experimental data of pressure

The experimental data of the pressure of Kang et al.[25] are reported in Table 164 for the different filling ratio. These data are not the original values that are graphically obtained from the paper of Kang et al.[25]. The values reported in Table 164 are used for the comparing with the storage model.

Table 164. Values of the experimental pressure of Kang et al. **[25]**.

Test 1		**Test 2**		**Test 3**	
Time [min]	**P [bar]**	**Time [min]**	**P [bar]**	**Time [min]**	**P [bar]**

Table 164. Values of the experimental pressure of Kang et al. **[25]**.

0	1.04296	0	1.04296	0	1.04296
20	2.644881659	20	2.140724582	30	2.054594684
40	4.474610889	40	3.370208774	60	3.628587631
60	6.591113238	60	4.916220037	90	5.644295812
80	9.059814504	80	6.748042021	120	8.084419733
87	10.12990759	109	9.875230729	140	10.01163834

The raw experimental data of pressure are obtained with GetDataGraphDigitizer®. The extracted data are not perfectly located at the time the temperature data was experimentally measured by Kang et al.[25]. The interpolation functions of the raw experimental data of pressure are determined at different liquid level. This interpolation function computes the values of the experimental pressure at the exact time the data was experimentally measured by Kang et al.[25]. This interpolation function is sixth order polynomial and it is described by Equation 624. Table 165 reports the values of the coefficient a_i used for the interpolation function for the experiment of Kang et al. [25].

Table 165. Values of the coefficients $\boldsymbol{a_i}$ of Equation 624 at different filling ratio for Kang et al.**[25]**.

LFi \ a	1	2	3	4	5	6	7
80 %	2.50E-10	-6.96E-08	7.42E-06	-0.0003734	0.0090216	0	1.04296
50 %	1.42E-10	-4.33E-08	4.92E-06	-0.0002554	0.0062081	0	1.04296
30 %	8.29E-12	-3.63E-09	6.08E-07	-4.88E-05	0.00213122	0	1.04296

The values reported in Table 165 are determined with function Polyfit of MATLAB®.

2.2. Experimental data of temperature profiles

The values of the temperature profiles are reported in Table 166 for the experiment of Kang et al. [25]. These data are reported for the three filling ratio 80 %, 50 % and 30 % at different time steps. The underlined values are computed with this approach that is reported after Table 166.

Table 166. Values of the experimental temperature profiles of Kang et al. **[25]** at different liquid levels.

Test 1											
0 min		**20 min**		**40 min**		**60 min**		**80 min**		**109 min**	
T [K]	**H [%]**	**T [K]**	**H [%]**	**T [K]**	**H [%]**	**T [K]**	**H [%]**	**T [K]**	**H [%]**	**T [K]**	**H [%]**
77.3889	2.60304	80.1111	2.60304	81.537	2.60304	83.8704	2.49458	85.6852	2.60304	86.463	2.60304
77.3889	7.59219	80.1111	7.59219	81.537	7.48373	83.8704	7.48373	85.6852	7.59219	86.3333	7.59219
77.2593	12.5813	79.8519	12.5813	81.4074	12.5813	83.8704	12.4729	85.6852	12.5813	86.3333	12.5813
77.2593	17.5705	79.8519	17.5705	81.4074	17.5705	83.8704	17.5705	85.6852	17.5705	86.2037	17.5705
77.2593	22.5597	79.463	22.5597	81.537	22.5597	83.7407	22.4512	85.4259	22.5597	86.2037	22.4512
76.6111	27.6573	78.6852	27.6573	81.1481	27.5488	83.0926	27.5488	84.9074	27.5488	85.5556	27.4403
76.6111	32.6464	78.8148	32.538	81.4074	32.538	83.4815	32.538	85.2963	32.538	86.0741	32.4295
76.7407	37.6356	78.8148	37.6356	80.8889	37.5271	82.963	37.5271	84.5185	37.5271	85.2963	37.5271
76.7407	42.6247	78.9444	42.6247	80.8889	42.6247	83.0926	42.5163	84.5185	42.6247	85.4259	42.5163
76.6111	47.6139	78.9444	47.6139	80.8889	47.6139	83.0926	47.5054	84.6481	47.5054	85.2963	47.5054
77.1296	52.603	79.3333	52.603	81.2778	52.603	83.3519	52.4946	85.037	52.603	85.6852	52.4946
77.3889	57.5922	79.463	57.5922	81.4074	57.5922	83.3519	57.4837	84.9074	57.5922	85.6852	57.5922
76.6111	62.4729	79.463	62.5813	81.6667	62.4729	84	62.5813	85.1667	62.5813	85.5556	62.4729
77.3889	67.5705	80.2407	67.5705	82.5741	67.5705	85.037	67.462	86.3333	67.5705	86.8519	67.462
77.2593	70.1735	80.2407	70.0651	82.5741	70.0651	85.4259	70.0651	86.7222	70.0651	87.2407	70.0651
76.2222	75.0542	80.7593	75.0542	84.6481	75.0542	87.5	75.0542	89.1852	75.0542	89.7037	74.9458

Table 166. Values of the experimental temperature profiles of Kang et al. **[25]** at different liquid levels.

78.037	77.5488	83.7407	77.5488	87.5	77.5488	90.3519	77.5488	91.9074	77.5488	92.4259	77.4403
77.7778	80.1518	86.9815	80.1518	91	80.0434	94.1111	80.0434	95.537	80.0434	96.0556	79.9349
86.7222	82.538	94.7593	82.538	98.1296	82.538	98.5185	82.321	99.037	82.538	100.074	82.4295
91.1296	85.0325	100.981	85.0325	104.87	85.0325	106.685	85.0325	107.204	84.9241	107.593	85.0325
100.333	90.1302	110.574	90.1302	114.333	90.0217	116.407	90.0217	117.444	90.0217	117.833	90.0217
107.463	92.6247	116.667	92.6247	120.296	92.5163	122.241	92.5163	123.278	92.6247	123.796	92.6247
112.13	95.1193	120.815	95.1193	123.926	95.1193	125.87	95.0108	127.037	95.1193	127.685	95.0108
Test 2											
0 min		**20 min**		**40 min**		**60 min**		**80 min**		**109 min**	
T [K]	**H [%]**	**T [K]**	**H [%]**	**T [K]**	**H [%]**	**T [K]**	**H [%]**	**T [K]**	**H [%]**	**T [K]**	**H [%]**
77.0806	2.60053	79.7829	2.70514	82.3563	2.59233	84.5438	2.58893	86.9886	2.58513	90.5916	2.57953
78.1164	7.60436	80.4326	7.60076	82.8774	7.59696	84.9362	7.59376	87.2524	7.59016	90.984	7.58436
77.9942	12.61	80.5677	12.606	82.8839	12.6024	84.9425	12.4904	87.5162	12.5952	90.9903	12.481
77.8719	17.6156	80.4455	17.6116	82.7616	17.608	84.949	17.4958	87.5225	17.4918	91.1256	17.595
77.7497	22.6213	80.5806	22.6168	83.0254	22.613	85.0841	22.501	87.6576	22.497	91.0032	22.4918
77.1128	27.6277	80.3297	27.6227	82.7744	27.5101	84.9619	27.5067	87.5354	27.5027	90.881	27.4975
78.1486	32.6315	81.1082	32.6269	83.4242	32.5145	85.2257	32.5117	87.9279	32.5075	91.2734	32.5023
78.0264	37.6371	81.1146	37.6323	83.5593	37.5197	85.6181	37.5165	88.3203	37.5123	91.6659	37.5071
77.2608	42.6438	80.735	42.6384	83.5657	42.5252	86.0106	42.5214	88.8413	42.4081	92.4444	42.5114
77.6499	45.0371	80.3521	45.0329	83.6976	45.0277	86.3998	45.0235	89.2307	45.0191	93.091	45.0131
77.1385	47.6494	82.9288	47.5316	85.3737	47.5278	88.4619	47.523	91.55	47.4094	95.2816	47.4036
77.785	50.0423	85.6342	50.0301	87.9504	50.0265	91.5533	50.0209	95.1563	50.0153	98.7592	50.0097
84.222	52.535	90.7845	52.5248	94.6446	52.41	97.4757	52.5144	99.663	52.4022	100.821	52.4004
87.8282	55.0321	95.034	55.0209	99.6662	54.9049	102.754	54.9001	105.457	55.0047	107.387	55.0017
91.177	57.5296	99.4122	57.5168	104.688	57.3998	108.162	57.3944	111.122	57.3898	113.953	57.3854
99.29	62.5225	107.654	62.5095	113.83	62.3911	118.205	62.4931	121.937	62.3785	125.54	62.3729
107.532	67.5151	115.896	67.3933	122.715	67.3827	127.605	67.3751	131.723	67.3687	135.84	67.3623
115.387	72.5083	123.494	72.4957	130.314	72.3763	135.718	72.3679	139.707	72.3617	147.022634	72.3617
124.015	77.5004	131.864	77.3793	138.555	77.3689	144.828951	77.3689	148.920763	77.3689	158.007226	77.3689
133.672	82.382	139.668362	82.382	146.399438	82.382	153.716889	82.382	157.843948	82.382	169.004762	82.382
138.371299	85.0325	143.90444	85.0325	150.603626	85.0325	158.416073	85.0325	162.561767	85.0325	174.819321	85.0325
147.8093	90.1302	152.051677	90.1302	158.68953	90.1302	167.454001	90.1302	171.635538	90.1302	186.002448	90.1302
152.427675	92.6247	156.038432	92.6247	162.646273	92.6247	171.876606	92.6247	176.075682	92.6247	191.474781	92.6247
157.046236	95.1193	160.025348	95.1193	166.603175	95.1193	176.299388	95.1193	180.516004	95.1193	196.947333	95.1193
Test 3											
0 min		**30 min**		**60 min**		**90 min**		**120 min**		**140 min**	
T [K]	**H [%]**	**T [K]**	**H [%]**	**T [K]**	**H [%]**	**T [K]**	**H [%]**	**T [K]**	**H [%]**	**T [K]**	**H [%]**
77.8928	2.64317	82.4214	2.64317	86.6913	2.53304	90.8318	2.42291	95.1017	2.53304	98.0776	2.42291
77.8928	7.59912	82.4214	7.59912	86.6913	7.48899	90.8318	7.48899	95.1017	7.48899	98.0776	7.37885
77.634	12.5551	82.4214	12.5551	86.6913	12.5551	90.9612	12.4449	95.1017	12.4449	98.0776	12.4449
77.8928	17.511	82.5508	17.511	86.8207	17.511	91.0906	17.511	95.2311	17.511	98.207	17.511
77.3752	22.5771	82.2921	22.5771	86.5619	22.467	90.9612	22.467	95.2311	22.467	98.207	22.467
77.3752	27.533	82.1627	27.533	86.8207	27.4229	91.0906	27.533	95.4898	27.4229	98.207	27.533
76.7283	30.0661	82.4214	30.0661	87.8558	30.0661	92.2551	29.9559	96.6543	29.9559	99.5009	29.9559
83.1978	32.489	89.1497	32.489	93.4196	32.489	96.6543	32.489	97.8189	32.3789	100.924	32.3789
85.7856	35.022	92.6433	35.022	97.9482	34.9119	101.83	35.022	105.065	35.022	107.135	35.022

Table 166. Values of the experimental temperature profiles of Kang et al. **[25]** at different liquid levels.

88.8909	37.5551	96.525	37.5551	102.477	37.5551	106.617	37.4449	110.24	37.4449	112.44	37.4449
91.0906	40.0881	99.5009	40.0881	105.841	39.978	110.758	39.978	114.898	39.978	117.357	39.978
93.6784	42.511	102.477	42.511	109.205	42.511	114.64	42.511	119.039	42.511	121.497	42.511
98.0776	47.5771	107.523	47.5771	115.545	47.467	121.756	47.467	126.673	47.467	129.519	47.467
102.865	52.533	112.699	52.533	121.497	52.533	128.355	52.533	133.789	52.4229	137.024	52.4229
107.006	57.489	117.486	57.5991	126.673	57.489	134.177	57.489	139.871	57.489	145.046192	57.489
111.664	62.5551	122.662	62.5551	132.237	62.4449	139.612	62.4449	146.589653	62.4449	152.809615	62.4449
116.839	67.511	128.096	67.511	137.8	67.511	145.43008	67.511	153.25903	67.511	160.745666	67.511
121.756	72.5771	133.272	72.5771	143.444778	72.5771	151.183679	72.5771	159.928407	72.5771	168.681717	72.5771
135.083	82.5991	143.942382	82.5991	154.571326	82.5991	162.565721	82.5991	173.122085	82.5991	184.38119	82.5991
137.805408	85.0325	146.518218	85.0325	157.272917	85.0325	165.329348	85.0325	176.325587	85.0325	188.193114	85.0325
144.055691	90.1302	151.914307	90.1302	162.932446	90.1302	171.118835	90.1302	183.036564	90.1302	196.178666	90.1302
147.114194	92.6247	154.554819	92.6247	165.701871	92.6247	173.951853	92.6247	186.320503	92.6247	200.086303	92.6247
150.17282	95.1193	157.195438	95.1193	168.471406	95.1193	176.784984	95.1193	189.604573	95.1193	203.994097	95.1193

Kang et al.[25] reported the values of the vapour temperature up to 95 % filling ratio for the Test 1, and up to 82 % for the Test 2 and 3. For the last two tests, these values of the filling ratio are reduced in time. At the end of the pressurisation, the temperature profile in the vapour is reported up to 67 % in Test 2 and up to 52 % in Test 3. The values of the vapour temperature up to 95% for these two tests are calculated. By looking at the graphs, it seems that the temperature profile is linear in the vapour. A linear interpolation function is applied, using the last three measured values of vapour temperature. The interpolation function is described by Equation 626.

Equation 626 $$T = a_1 \cdot H + a_2$$

T is the temperature in the vapour and H is the level. a_1 and a_2 are parameters that are obtained by fitting the last three values of the measured vapour temperature. The values of these parameters are reported in Table 167.

Table 167. Values of the coefficients $\boldsymbol{a_1}$ and $\boldsymbol{a_2}$ of Equation 626 at different filling ratio for Kang et al. **[25]**.

Test 1			**Test 2**			**Test 3**		
Time \ a	**1**	**2**	**Time \ a**	**1**	**2**	**Time \ a**	**1**	**2**
0 min	0	0	**0 min**	1.85142329	-19.059852	**0 min**	1.22609864	33.5471757
20 min	0	0	**20 min**	1.59821827	8.00394429	**30 min**	1.05853391	56.508434
40 min	0	0	**40 min**	1.58618679	15.7261978	**60 min**	1.11021232	62.8687873
60 min	0	0	**60 min**	1.77294241	7.6583473	**90 min**	1.1357057	68.757453
80 min	0	0	**80 min**	1.77997346	11.2061739	**120 min**	1.3164716	64.3827159
87 min	0	0	**109 min**	2.19375939	-11.721524	**140 min**	1.56650105	54.9896136

The values reported in Table 167 are determined with function Polyfit of MATLAB®. The values of vapour temperature of Test 1 are reported up to 95 %. So, the values of a_1 and of a_2 are zero because the interpolation function is not required.

3. Experimental data of Perez et al. – 2021

The experimental data of pressure are described in Section 3.1. The temperature profiles are reported in Section 2.2.

3.1. Experimental data of pressure

Test 1 is done with an initial filling ratio of 88 % and a heat input rate of 2.2 W. The self-pressurisation stage is ended at around 4 hours, when the pressure reached the values of 150 kPa. The measured values of the pressure measured in the self-pressurisation stage of Test 1 are reported in Table 168.

Table 168. Measured values of the pressure for the self-pressurisation stage of Test 1 of Perez et al. **[26]**.

Part 1		Part 2	
Time [min]	**P [bar]**	**Time [min]**	**P [bar]**
0	1.07111	135.7464	1.32296
2.171946	1.10074	141.1764	1.33185
7.60182	1.11556	145.5204	1.34074
13.0317	1.13037	150.9504	1.34667
18.46152	1.14519	156.3798	1.35852
24.9774	1.15704	162.8958	1.36741
30.40722	1.16593	167.2398	1.3763
34.75116	1.17481	171.5838	1.38222
40.18098	1.1837	177.0138	1.39111
44.52486	1.19259	182.4432	1.4
49.95474	1.19852	186.7872	1.40889
55.38462	1.20741	193.3032	1.42074
61.9002	1.2163	197.6472	1.42667
66.2442	1.22222	201.9912	1.43259
70.5882	1.22815	207.4206	1.44444
74.9322	1.23704	212.8506	1.45333
80.3622	1.24593	217.1946	1.46222
85.7916	1.25185	223.7106	1.47111
90.1356	1.25778	228.054	1.48296
95.5656	1.26667	234.57	1.49185
100.9956	1.27259	237.828	1.50074
106.4256	1.28148	242.172	1.51259
111.855	1.29037	240	1.5108119
116.199	1.2963	253.0314	1.52148
120	1.30148438	258.4614	1.52148
124.887	1.30815	262.8054	1.52148
131.403	1.31704	269.3214	1.52148

The values underlined in Table 168 are the computed because the pressure is not recorded at the same time of the temperature profile. These computed values of the pressure are obtained with a linear interpolation between the previous experimental point and next experimental point. Equation 625 is used for this interpolating function and the indexes N and $N-1$ respectively indicates the next experimental point and the previous experimental point.

3.2. Experimental data of temperature profiles

Table 169 reports the values of the temperature profile measured by Perez et al.[26]. The values reported in Table 169 refer to the self-pressurisation stage of Test 1 and they were collected at the beginning of the self-pressurisation stage, at 120 minutes and at the end of the self-pressurisation stage. The latter stage is ended after 240 minutes.

Table 169. Measured values of the temperature profile at three different time steps for the self-pressurisation stage of Test 1 of Perez et al.**[26]**.

0 min		**120 min**		**240 min**	
T [K]	**H [%]**	**T [K]**	**H [%]**	**T [K]**	**H [%]**
78.155	1.04956	78.795	1.57434	79.855	1.83673
77.918	3.93586	78.722	4.46064	79.654	4.46064
78.009	7.08455	78.612	7.34694	79.636	7.60933
77.863	9.70845	78.539	9.97085	79.416	10.2332
77.79	12.5948	78.502	13.1195	79.215	13.3819
77.698	14.9563	78.375	15.481	79.288	15.7434
77.735	18.105	78.393	18.6297	79.288	18.6297
77.662	20.9913	78.283	21.516	79.179	21.516
77.662	23.6152	78.301	24.1399	79.197	24.1399
77.662	26.2391	78.338	26.7638	79.215	27.0262
77.68	29.1254	78.301	29.9125	79.197	29.9125
77.625	31.7493	78.247	32.5364	79.142	32.7988
77.698	34.6356	78.301	35.4227	79.179	35.4227
77.68	37.7843	78.283	38.309	79.16	38.309
77.552	40.9329	78.155	41.1953	79.051	41.4577
77.662	43.0321	78.283	43.8192	79.16	43.8192
77.589	46.4431	78.192	47.2303	79.069	46.9679
77.753	48.2799	78.21	48.8047	79.197	48.8047
77.698	50.9038	78.283	51.4286	79.38	51.691
77.662	53.7901	78.1	54.3149	79.234	54.5773
77.698	56.6764	78.192	57.2012	79.38	57.4636
77.698	59.5627	78.247	60.0875	79.435	60.0875
77.753	61.9242	78.484	62.7114	79.617	62.9738
77.845	64.8105	78.685	65.3353	79.818	65.5977
77.771	67.4344	78.74	68.2216	79.892	68.484
77.79	70.3207	78.831	71.1079	80.038	71.1079
77.863	73.4694	78.959	73.9942	80.202	73.9942
77.918	76.0933	79.087	76.6181	80.367	76.8805
77.863	78.7172	79.361	79.5044	80.696	79.7668
77.826	81.8659	79.435	82.3907	80.787	82.6531
77.881	84.4898	79.636	85.0146	80.897	85.277
77.936	87.1137	80.166	87.3761	81.153	87.6385
78.173	90.5248	80.385	90.7872	81.61	91.0496
78.283	93.4111	80.403	93.6735	81.646	93.9359
78.649	96.035	80.732	96.5598	82.048	96.5598

Perez et al.[26] measured the values of the temperature in Celsius degree. The temperatures are converted in Kelvin degree by assuming that the difference between Kelvin and Celsius is 273.15 K.

4. Experimental data of Hasan et al. - 1991

The experimental data of pressure are described in Section 4.1. The temperature profiles are reported in Section 4.2.

4.1. Experimental data of pressure

The experimental data of pressure and of temperature profile at 3.5 W/m² and at the two different initial conditions can be extracted from the paper of Hasan et al.[27]. For the other tests at 2.0 W/m² and at 0.3 W/m², there are not enough data for validating. These partial sets of data can be used for further testing the model, after the validation. Table 170 describes the values of pressure during the self-pressurisation test of Hasan et al. [27]. This test is done at two initial conditions (steady boil-off gas (BOG) and isothermal) and at 3.5 W/m² of overall heat fluxes.

Table 170. Measured values of the pressure for the experiments at different initial conditions at 3.5 W/m² of Hasan et al. **[27]**.

Test 1				Test 2			
Time [min]	**P [bar]**	**Time [min]**	**P [bar]**	**Time [min]**	**P [bar]**	**Time [min]**	**P [bar]**
0	1.03	449.271	1.51	0	1.03	444.555	1.633429
31.31868	1.0871429	482.3562	1.558	27.92484	1.1282857	481.2702	1.679143
62.568	1.132857	511.728	1.594571	55.64142	1.192286	505.1766	1.715714
88.2546	1.162571	539.3196	1.638	86.8212	1.226571	540.0558	1.759143
119.4066	1.192286	572.3496	1.676857	119.7534	1.249429	569.4276	1.795714
146.901	1.219714	599.9412	1.720286	145.4262	1.276857	597.033	1.841429
181.683	1.247143	629.34	1.761429	180.2778	1.315714	628.224	1.878
210.9714	1.27	660.564	1.802571	209.5524	1.336286	655.806	1.919143
240	1.290396862	691.77	1.841429	237.0744	1.368286	687.024	1.960286
243.8904	1.290571	720	1.878754885	240	1.36899789	718.248	2.001429
271.3986	1.320286	721.158	1.880286	270.1182	1.409429	720	2.006309058
302.5092	1.343143	750.558	1.921429	301.284	1.441429	747.66	2.04486
331.8252	1.370571	785.448	1.967143	328.8204	1.475714	777.072	2.08829
359.3196	1.398	811.188	2.006	360.0276	1.514571	806.46	2.12714
388.7196	1.439143	840.546	2.04029	385.77	1.553429	839.49	2.166
418.0776	1.473429	/	/	422.4708	1.596857	/	/

The pressure was measured at the same time of the temperature profile. These values were computed with Equation 624 and they are reported in Table 170 with an underline. The coefficients of Equation 624 are given in Table 171.

Table 171. Values of the coefficients $\boldsymbol{a_i}$ of Equation 624 at different initial conditions.

a	1	2	3	4	5	6	7
Test 1	-1.47E-19	1.11E-14	-2.70E-11	2.39E-08	-8.61E-06	0.00211358	1.02920295
Test 2	-5.72E-17	1.60E-13	-1.74E-10	9.16E-08	-2.33E-05	0.00360952	1.03743917

Polyfit function of MATLAB® determined the values of the coefficients in Table 171.

The value of pressure at 720 minutes at steady BOG initial condition is calculated with Equation 628.

Equation 627
$$P = m \cdot (t - t_0) + q$$

m, t_0 and q are the coefficients, whose values are $0.001322\,bar/min$, $691.77\,min$ and $1.841429\,bar$.

4.2. Experimental data of temperature profiles

Temperature profiles were measured under heat fluxes of 3.5 W/m² for the two initial conditions (steady BOG and isothermal). The values of the temperature are given in Table 172.

Table 172. Measured values of temperature profiles of Hasan et al.**[27]**.

Test 1					
0 min		**240 min**		**720 min**	
T [K]	**H [%]**	**T [K]**	**H [%]**	**T [K]**	**H [%]**
20.258	5.34605455	20.6623	5.54236364	21.3184	5.13803455
20.2662	13.3282364	20.6198	13.3254545	21.3264	12.9206727
20.2402	37.0756909	20.6442	37.0724727	21.4016	36.8668364
20.2116	58.4285455	20.5652	58.4258182	21.3223	58.0205455
20.2669	63.018	20.7717	62.814	21.4786	62.6089091
20.2244	70.8010909	20.6789	70.7972727	21.4361	70.392
20.227	73.3952727	20.6814	73.1918182	21.4387	72.9861818
20.2806	76.3881818	20.9372	76.3827273	22.5024	75.9709091
20.4329	77.1850909	21.2911	76.7792727	22.5537	76.7689091
20.4338	77.9830909	22.0495	77.5712727	22.8067	77.166
20.4344	78.582	22.6057	78.1652727	23.1101	77.5625455
20.6877	79.3783636	24.1225	79.7498182	24.8289	79.1454545
23.1725	89.1365455	35.3443	89.2390909	36.2025	88.8327273

Test 2					
0 min		**240 min**		**720 min**	
T [K]	**H [%]**	**T [K]**	**H [%]**	**T [K]**	**H [%]**
20.3621	5.55605455	20.7661	5.55283636	21.4221	5.14767273
20.3745	13.5544909	20.6772	13.3521273	21.3836	12.9465273
20.361	37.5501818	20.7139	37.1474182	21.4711	36.9414
20.2416	58.3472727	20.6961	58.3434545	21.4025	57.9381818
20.4504	62.7447273	20.8547	62.9416364	21.6622	62.5352727
20.3617	70.7438182	20.7657	70.7405455	21.5224	70.1350909
20.3657	73.3434545	20.8199	73.14	21.729	73.1323636
20.3198	76.3434545	21.4309	76.3341818	22.6932	76.1241818
20.2706	77.1436364	21.9372	77.13	22.9972	76.722
20.2718	77.9432727	22.3924	77.5265455	23.5534	77.1174545
20.273	78.7434545	22.8983	78.1221818	23.6054	78.1167273
20.2746	79.7432727	24.6176	79.5081818	25.1224	79.3041818
20.2386	89.1414545	35.3902	89.2205455	35.5417	89.2189091

The temperature profiles in Table 172 were originally given as function of the height in cm. The height is transformed into level.

5. Experimental data of Dresar et al. – 1992

The experimental data of pressure are described in Section 5.1. The temperature profiles are reported in Section 5.2.

5.1.Experimental data of pressure

Dresar et al.[28] experimentally investigated the behaviour of liquid hydrogen at 29 % and 49 % filling ratios, at 2.0 W/m² and at 3.5 W/m² overall heat fluxes, and for the two initial conditions (steady boil-off gas (BOG) and isothermal). The experimental data at 3.5 W/m² overall heat fluxes and for the initial condition of steady BOG can be used for validating the model because the values of pressure and of temperature profiles are reported. The other experimental data, reported in the paper of Dresar et al.[28], could be used for challenging the model.

Table 173. Measured values of pressure of Dresar et al.**[28]**.

Test 1				**Test 2**			
Time [min]	**P [bar]**	**Time [min]**	**P [bar]**	**Time [min]**	**P [bar]**	**Time [min]**	**P [bar]**
0	1.03	512.1168	1.51827	0	1.03	510.015	1.68981
0.2278236	1.0356	541.1022	1.54724	0.2278236	1.0356	539.0832	1.73172
32.49594	1.07749	573.2874	1.5762	29.37894	1.09046	568.11	1.76716
61.5228	1.11294	602.274	1.60517	61.647	1.13235	600.378	1.80906
90.5706	1.15162	634.458	1.63412	87.5568	1.18076	629.424	1.84774
122.7762	1.1838	660.222	1.65987	119.8248	1.22265	658.494	1.88965
151.7616	1.21277	692.406	1.68882	148.8726	1.26133	690.762	1.93155
180.747	1.24174	720	1.719283412	177.8994	1.29678	720	1.969732015
209.7534	1.27395	724.614	1.72101	210.126	1.3322	723.012	1.97021
238.7178	1.29968	750.402	1.75	239.1324	1.36441	748.878	2.01214
240	1.300676735	782.586	1.77895	240	1.366802035	781.086	2.04433
267.6618	1.32218	808.368	1.80794	268.1382	1.39661	/	/
299.7642	1.33819	840.576	1.84013	297.165	1.43205	/	/
331.8876	1.35743	869.562	1.8691	329.4126	1.47072	/	/
360.852	1.38317	898.548	1.89807	358.4394	1.50616	/	/
389.817	1.4089	930.732	1.92702	390.666	1.54158	/	/
422.0022	1.43785	959.742	1.95922	419.7138	1.58026	/	/
450.9462	1.46035	988.722	1.98819	448.7406	1.6157	/	/
479.9526	1.49256	1020.93	2.02038	477.7878	1.65438	/	/

The values underlined are computed with Equation 624 at the same time of the measurement of temperature profiles. The coefficients of Equation 624 are reported in Table 174.

Table 174. Values of the coefficients $\boldsymbol{a_i}$ of Equation 624 at different filling ratio for Dresar et al.**[28]**.

a	**1**	**2**	**3**	**4**	**5**	**6**	**7**
Test 1	1.94909E-18	-4.30973E-15	1.4138E-12	2.9724E-09	-2.592E-06	0.00153416	1.03127268
Test 2	-7.3166E-18	1.96666E-14	-2.268E-11	1.43464E-08	-4.92E-06	0.00200158	1.03247567

Polyfit function of MATLAB® determined the values of the coefficients in Table 174.

The value of pressure at 240 minutes at 49 % of liquid level is calculated with Equation 628. In this case, $m = 0.00077736\ bar/min$, $t_0 = 238.7178\ min$ and $q = 1.29968\ bar$ are used.

5.2.Temperature profiles

Temperature profiles were reported in the paper under heat fluxes of 3.5 W/m² for the 49 % and for 29 % filling ratios, and for the steady boil-off gas (BOG) initial conditions. The values of the temperature are given in Table 175 for these experiments. Dresar et al.[28] reported these values of the temperature as function of the height in meters. The height in meters was converted in level by the author.

Table 175. Measured values of temperature profiles of Dresar et al.**[28]**.

Test 1					
0 min		**240 min**		**720 min**	
T [K]	**H [%]**	**T [K]**	**H [%]**	**T [K]**	**H [%]**
20.1375	5.19504	20.7103	5.18870727	21.6641	4.95703091

Table 175. Measured values of temperature profiles of Dresar et al.**[28]**.

20.0691	12.9353455	20.6419	12.9290182	21.5965	12.9184909
20.1504	36.1531091	20.7232	36.1467818	21.7733	36.1351636
20.1876	46.7669455	20.7611	46.9817455	21.6203	46.9722545
20.2962	50.5249636	21.0599	50.5165636	22.2046	50.2827273
21.274	57.1478182	24.7106	57.1101818	26.429	57.0910909
22.0633	64.4367273	27.8864	64.3723636	30.5594	64.3429091
22.8649	75.2629091	31.2655	75.1701818	34.7029	75.3534545
23.1621	78.3556364	33.0909	78.4669091	36.7184	78.4270909
25.391	87.8394545	40.6657	87.8918182	44.5796	87.8487273
Test 2					
0 min		**240 min**		**720 min**	
T [K]	**H [%]**	**T [K]**	**H [%]**	**T [K]**	**H [%]**
20.1297	4.98954	20.7917	4.98590727	21.9264	4.97968909
20.0534	12.8866364	20.7154	12.8829818	21.9447	12.8762727
20.098	32.1893455	20.9491	32.1846545	21.9898	32.3983091
20.3919	36.5747455	21.6207	36.3486545	23.0391	36.3408545
22.8981	57.18	29.3288	57.3643636	34.8129	57.1145455
23.3872	64.1967273	31.6145	64.3707273	38.1393	64.3352727
23.6967	75.3818182	33.5306	75.1085455	40.9064	75.0681818
23.987	78.2318182	35.0517	78.6098182	42.427	78.3501818
25.8055	87.654	41.4086	87.7876364	48.974	87.9654545

Further manipulations of the experimental data were not done.

6. Experimental data of Aydelott - 1967

The experimental data of pressure are described in Section 6.1. The temperature profiles are reported in Section 6.2.

6.1. Experimental data of pressure

The experimental data of pressure and of temperatures evolution are extracted for three tests of Aydelott[29]. These three tests were done with uniform heating at liquid levels of 34.9 %, of 48.9 % and of 76.5 %. For these filling ratios, the overall heat fluxes were respectively 189 W/m², 204 W/m² and 229 W/m². Table 176 reports the measured values of the pressure for these three tests of Aydelott[29]. The experimental data of this variable were given in psia, as function of the time in second. The pressure in psia is transformed in bar, considering that 1 psia = 0.0689476 bar.

Table 176. Measured values of pressure Aydelott**[29]**, at different filling ratio and heat inputs rates.

Test 1		**Test 2**		**Test 3**	
Time [min]	**P [bar]**	**Time [min]**	**P [bar]**	**Time [min]**	**P [bar]**
0	1.199998504	0	1.199998504	0	1.199998504
0.018181833	1.253591474	0.0124889	1.09167493	0.022626	1.226894963
0.418181667	1.943067474	0.248803333	1.457110999	0.191305	1.386874079
0.836363333	2.381829316	0.847841667	2.063911932	1	1.987611334
1	2.556726942	1	2.199372766	1.158811667	2.089015753
1.272726667	2.820584263	1.680433333	2.754008461	2	2.630705783
1.672733333	3.228002526	2	3.013480689	2.1883	2.754532462

Table 176. Measured values of pressure Aydelott**[29]**, at different filling ratio and heat inputs rates.

2	3.553232569	2.550666667	3.455957081	3.2021	3.456805137
2.090916667	3.635420789	3.36075	4.146301821	4	4.044203697
2.509083333	4.105519316	4	4.707581507	4.154166667	4.158905442
2.927266667	4.544274263	4.14055	4.812445953	5.02925	4.836232875
3	4.630580643	4.838133333	5.516304423	5.873383333	5.525743349
3.34545	5.014372789	5.542983333	6.195541704	6.5	6.055271765
3.74545	5.515808	6.18755	6.850916221	6.671316667	6.202843255
4	5.827605094	6.5	7.194005912	7.208133333	6.695156698
4.181816667	6.048586789	6.658133333	7.373256344	/	/
4.272733333	6.205284	/	/	/	/
4.563633333	6.581358684	/	/	/	/

The underlined values of pressure were computed with Equation 624. Doing this, there are the values of pressure at the same time of the temperature profile. The coefficients of Equation 624 are given in Table 177.

Table 177. Values of the coefficients a_i of Equation 624 at different filling ratios for Aydelott**[29]**.

a	1	2	3	4	5	6	7
Test 1	-0.00408	0.063261	-0.38411	1.162317	-1.79732	2.309562	1.207092
Test 2	2.57E-06	0.000601	-0.01294	0.102391	-0.34774	1.315877	1.141178
Test 3	-8.24E-05	0.002229	-0.02347	0.121975	-0.30277	0.985808	1.203928

The values in Table 177 are determined with the function Polyfit of MATLAB®.

6.2.Experimental data of temperature profiles

The values of the temperature profiles are described in Table 178.

Table 178. Vales of the temperature profiled for the three of experimental tests of Aydelott**[29]**.

Test 1									
0 min		**1 min**		**2 min**		**3 min**		**4 min**	
T [K]	**H [%]**	**T [K]**	**H [%]**	**T [K]**	**H [%]**	**T [K]**	**H [%]**	**T [K]**	**H [%]**
20.643961	25	21.0761756	25	21.6758458	25	22.2083095	25	22.8347752	25
20.643961	30.7690289	21.0761756	30.7690289	21.6758458	30.7690289	22.2083095	30.7690289	22.8347752	30.7690289
20.643961	32.6924759	21.0761756	32.6924759	21.6758458	32.6924759	22.2083095	32.6924759	22.8347752	32.6924759
20.643961	36.5384952	21.0761756	36.5384952	21.6758458	36.5384952	22.2083095	36.5384952	22.8347752	36.5384952
20.643961	43.2690289	21.0761756	43.2690289	21.6758458	43.2690289	22.2083095	43.2690289	22.8347752	43.2690289
20.9284612	50	22.7956735	50	22.3019956	50	22.6621844	50	23.2126894	50
20.9284612	63.4615048	23.2968181	63.4615048	25.4882253	63.4615048	24.3858701	63.4615048	24.7258847	63.4615048
21.5626839	71.1539808	49.2949251	71.1539808	59.1451607	71.1539808	62.2531731	71.1539808	63.8513609	71.1539808
21.5626839	77.8845144	54.7834703	77.8845144	66.7192201	77.8845144	70.2192436	77.8845144	73.7827806	77.8845144
31.075636	83.6539808	73.11762	83.6539808	93.0466857	83.6539808	104.990174	83.6539808	113.137474	83.6539808
Test 2									
0 min		**1 min**		**2 min**		**4 min**		**6.5 min**	
T [K]	**H [%]**	**T [K]**	**H [%]**	**T [K]**	**H [%]**	**T [K]**	**H [%]**	**T [K]**	**H [%]**
20.2938496	25	21.2947941	25	21.9538657	25	23.1722925	25	24.7882456	25
20.2938496	30.7690289	21.2947941	30.7690289	21.9538657	30.7690289	23.1722925	30.7690289	24.7882456	30.7690289
20.2938496	32.6924759	21.2947941	32.6924759	21.9538657	32.6924759	23.1722925	32.6924759	24.7882456	32.6924759
20.2938496	36.5384952	21.2947941	36.5384952	21.9538657	36.5384952	23.1722925	36.5384952	24.7882456	36.5384952
20.2938496	43.2690289	21.5623067	43.2690289	22.2311446	43.2690289	23.6142726	43.2690289	25.1711874	43.2690289
21.2503503	50	22.7494529	50	24.0048964	50	25.7621037	50	27.323677	50

Table 178. Vales of the temperature profiled for the three of experimental tests of Aydelott**[29]**.

38.2802528	63.4615048	63.8562955	63.4615048	79.7393124	63.4615048	96.0172628	63.4615048	104.718988	63.4615048
45.5754253	71.1539808	74.4340294	71.1539808	93.1388637	71.1539808	116.164573	71.1539808	130.156785	71.1539808
48.0116495	77.8845144	76.650841	77.8845144	95.7839277	77.8845144	120.047166	77.8845144	135.168527	77.8845144
58.9594916	83.6539808	86.9555609	83.6539808	105.961292	83.6539808	135.334821	83.6539808	156.326119	83.6539808
Test 3									
0 min		**1 min**		**2 min**		**4 min**		**6.5 min**	
T [K]	**H [%]**	**T [K]**	**H [%]**	**T [K]**	**H [%]**	**T [K]**	**H [%]**	**T [K]**	**H [%]**
20.5857942	25	21.434185	25	22.4364371	25	23.7570811	25	26.4635025	25
21.0822946	30.7690289	32.4875838	30.7690289	35.7405244	30.7690289	36.6217082	30.7690289	36.3990854	30.7690289
24.5535752	32.6924759	41.4168405	32.6924759	48.3925105	32.6924759	52.8571951	32.6924759	55.1949376	32.6924759
25.0496312	36.5384952	43.7542296	36.5384952	51.7169363	36.5384952	58.3506392	36.5384952	61.6933231	36.5384952
29.0183565	43.2690289	47.6341626	43.2690289	56.2566075	43.2690289	64.4183995	43.2690289	69.578589	43.2690289
31.2603583	50	55.6195734	50	67.0448219	50	79.1033295	50	85.9257274	50
48.1761497	63.4615048	79.2504385	63.4615048	97.7709971	63.4615048	120.451687	63.4615048	136.234766	63.4615048
53.8979876	71.1539808	87.2933547	71.1539808	107.389562	71.1539808	133.695438	71.1539808	153.929389	71.1539808
57.8778241	77.8845144	90.6094081	77.8845144	109.569912	77.8845144	137.229161	77.8845144	158.135395	77.8845144
68.3256102	83.6539808	99.7871461	83.6539808	118.361114	83.6539808	148.321136	83.6539808	173.786393	83.6539808

The values reported in Table 178 are computed because Aydelott [29] reported the evolution in time of the temperature. For each temperature curve, the author uses Equation 628 to interpolate the measured values of the temperature.

Equation 628

$$T = \sum_{i=1}^{7} b_i \cdot t^{7-i}$$

The values of the coefficients b_i are reported in Table 179 for the different inner thermocouples.

Table 179. Values of the coefficients $\boldsymbol{b_i}$ of Equation 628 at different filling ratios for Aydelott [29].

Test 1							
b	**1**	**2**	**3**	**4**	**5**	**6**	**7**
R - 10	-0.0090643	0.12315923	-0.6258578	1.45259557	-1.4587121	0.94861909	20.6454359
R - 8	-0.0090643	0.12315923	-0.6258578	1.45259557	-1.4587121	0.94861909	20.6454359
R - 9	-0.0090643	0.12315923	-0.6258578	1.45259557	-1.4587121	0.94861909	20.6454359
R - 7	-0.0090643	0.12315923	-0.6258578	1.45259557	-1.4587121	0.94861909	20.6454359
R - 6	-0.0090643	0.12315923	-0.6258578	1.45259557	-1.4587121	0.94861909	20.6454359
R - 1	0.03916124	-0.5141368	2.43520493	-4.750185	2.53269551	2.10253797	20.9503955
R - 2	0.00538553	-0.0619044	0.1882395	0.23213623	-2.1679701	4.19916231	20.9017691
R - 3	0.02897842	-0.4231448	2.10269861	-2.7929566	-9.8203118	38.6132357	21.5864255
R - 4	-0.0849452	1.13093318	-5.9702757	17.3394629	-35.213227	56.0459463	21.5355763
R - 5	-0.0043693	0.12896286	-1.4192219	8.03713727	-27.026548	62.314497	31.0871618
Test 2							
b	**1**	**2**	**3**	**4**	**5**	**6**	**7**
R - 10	-0.0005652	0.01129947	-0.0880288	0.34451003	-0.7306241	1.44513297	20.3130698
R - 8	-0.0005652	0.01129947	-0.0880288	0.34451003	-0.7306241	1.44513297	20.3130698
R - 9	-0.0005652	0.01129947	-0.0880288	0.34451003	-0.7306241	1.44513297	20.3130698
R - 7	-0.0005652	0.01129947	-0.0880288	0.34451003	-0.7306241	1.44513297	20.3130698
R - 6	-0.0010469	0.02271402	-0.1905227	0.77735723	-1.6047463	2.26123881	20.2973126
R - 1	0.0025501	-0.0476865	0.32334007	-0.928921	0.79122808	1.85173176	20.7572105

Table 179. Values of the coefficients b_i of Equation 628 at different filling ratios for Aydelott [29].

R - 2	-0.0048999	0.12287108	-1.2838486	7.19964191	-23.899325	52.940918	28.7809383
R - 3	-0.0175886	0.38967056	-3.4006673	15.0334924	-37.557203	66.1802986	33.8060268
R - 4	-0.0167894	0.3689654	-3.2204365	14.3621368	-36.413243	65.7642088	35.8059984
R - 5	-0.0322168	0.69962996	-5.8922651	24.3721551	-53.284991	76.9807235	44.1125255
Test 3							
b	**1**	**2**	**3**	**4**	**5**	**6**	**7**
R - 10	-0.0029461	0.05509781	-0.36864	1.05841718	-1.2427557	1.32877069	20.6062412
R - 8	0.001175	-0.01388	-0.0545944	1.47021949	-7.9316984	17.9316721	21.0846901
R - 9	0.00500762	-0.0927058	0.54226244	-0.477482	-6.1084835	23.0679574	24.4802844
R - 7	0.00041209	0.00272609	-0.2041624	2.2304743	-10.707066	27.4225516	25.0092942
R - 6	-0.0020051	0.05005841	-0.5339936	3.16858976	-11.457951	27.4005813	29.0088824
R - 1	-0.0097565	0.2167768	-1.8764472	8.21312417	-20.863785	38.5660225	31.3736386
R - 2	0.00025905	0.00658421	-0.2339435	2.33523294	-11.741207	40.6862706	48.1972422
R - 3	-0.0017634	0.05113672	-0.6089602	3.8406597	-14.663623	44.8627193	53.8131853
R - 4	-0.0101081	0.23479576	-2.1105525	9.39308176	-23.405512	48.4418973	58.0658064
R - 5	-0.0163007	0.36164539	-3.0742451	12.6669593	-27.711422	48.9691314	68.5913782

The values in Table 179 are determined with the function Polyfit of MATLAB®.

The value of the temperature is computed with Equation 628 at the time steps 1 minutes, 2 minutes, 4 minutes and 6.5 minutes for 48.9 % and 34.9 % filling ratios and at the time steps 1 minutes, 2 minutes, 3 minutes and 4 minutes for the liquid level of 76.5 %. These values of the time steps are chosen because they are close to the time the measurements of temperature were done. At each time step, the temperatures are computed with Equation 628 and they are organized as function of the level.

7. Experimental data of Aydelott and Spuckler - 1969

The experimental data of pressure are described in Section 7.1. The temperature profiles are reported in Section 7.2.

7.1.Experimental data of pressure

In the paper of Aydelott and Spuckler[30], the experimental data from four test of self-pressurisation cab be extracted. These tests were done at 79.8 %, 54.2 %, 48.9 % and 31.6 % of filling ratios and at 69 W/m², 203 W/m², 60 W/m², and 53 W/m².

The values of the measured pressure of Aydelott and Spuckler[30] are reported in four the four tests.

Table 180. Measured values of pressure Aydelott and Spuckler**[30]**.

Test 1		**Test 2**		**Test 3**		**Test 4**	
Time [min]	**P [bar]**	**Time [min]**	**P [bar]**	**Time [min]**	**P [bar]**	**Time [min]**	**P [bar]**
0	1.05174	0	1.050437	0	1.027457	0	1.083463
2.45614	1.378952	2.60223	1.363087	2.83019	1.378952	0.8	1.403573
4.38596	1.636044	5	1.59554	5	1.54431	1.30909	1.64982
5	1.722064	5.01859	1.596937	7.35849	1.703413	1.89091	1.84681
5.78947	1.823023	7.43494	1.804524	11.5094	2.000832	2.5	2.04679
7.01754	1.986629	8.92193	1.960559	15	2.267383	2.54545	2.068428
8.59649	2.173601	10.7807	2.089933	15.4717	2.325292	3.27273	2.290046
10	2.337206	12.4535	2.219506	18.4906	2.541595	4.07273	2.511665

Table 180. Measured values of pressure Aydelott and Spuckler**[30]**.

12.4561	2.617671	14.4981	2.401217	20.9434	2.730863	5	2.78057
14.9123	2.898137	15	2.437045	24.5283	3.001248	5.01818	2.782525
15	2.914821	16.7286	2.582736	28.1132	3.298667	6.18182	3.102642
16.3158	3.061742	18.9591	2.764254	30	3.470474	7.05455	3.37351
17.7193	3.225348	21.5613	2.997911	31.1321	3.569052	8.14545	3.693619
18.7719	3.388947	23.6059	3.153353	34.1509	3.839437	8.94545	3.939866
21.0526	3.669412	25.2788	3.309195	36.9811	4.08278	9.74545	4.161477
23.3333	3.949877	26.7658	3.465224	39.6226	4.326124	10	4.256129
25	4.19586	28.6245	3.620866	40	4.35938	10.4727	4.407724
25.0877	4.206969	30	3.769778	42.0755	4.542433	11.3455	4.678584
26.6667	4.440694	30.6691	3.828846	44.9057	4.839853	12.2182	4.949452
28.4211	4.697786	32.8996	4.062889	/	/	13.0909	5.24494
30.1754	4.954878	34.7584	4.271063	/	/	13.9636	5.515808
31.7544	5.188596	36.803	4.479043	/	/	14.6909	5.762047
33.3333	5.445695	38.29	4.635078	/	/	15	5.867287
35	5.696788	40	4.819349	/	/	15.4182	6.008294
35.0877	5.702787	40.5204	4.869121	/	/	16.0727	6.254533
36.6667	5.936506	42.3792	5.077294	/	/	16.6545	6.500773
37.5439	6.123485	45.539	5.441696	/	/	17.3091	6.77164
39.1228	6.380576	/	/	/	/	/	/

The underlined values are calculated with Equation 624 to have the values of pressure at the same time steps of the temperature profile. The values of the coefficients of Equation 624 are reported in Table 181.

Table 181. Values of the coefficients a_i of Equation 624 of Aydelott and Spuckler**[30]**.

a	1	2	3	4	5	6	7
Test 1	3.61E-09	-4.25E-07	1.76E-05	-0.00027	0.000424	0.137347	1.04831
Test 2	6.96E-11	5.55E-09	-2.05E-06	0.000148	-0.00393	0.124443	1.054354
Test 3	-1.94E-09	3.06E-07	-1.89E-05	0.000577	-0.00873	0.132944	1.036685
Test 4	1.23E-07	1.99E-06	-0.00027	0.005874	-0.05208	0.486621	1.074198

The values reported in Table 181 are computed with Polyfit of MATLAB®.

7.2. Experimental data of temperature profiles

The values of the temperature profile are computed from the experimental data of the temperature evolution in time of Aydelott and Spuckler[30]. The data of the temperature profiles are reported in Table 182.

Table 182. Vales of the temperature profiled for the four of experimental tests of Aydelott and Spuckler**[30]**.

Test 1									
0 min		**5 min**		**15 min**		**25 min**		**25 min**	
T [K]	**H [%]**	**T [K]**	**H [%]**	**T [K]**	**H [%]**	**T [K]**	**H [%]**	**T [K]**	**H [%]**
20.8447389	11.3207143	21.1099342	11.3207143	21.7003342	11.3207143	22.4160605	11.3207143	23.1028245	11.3207143
20.8447389	16.0376786	21.1099342	16.0376786	21.7003342	16.0376786	22.4160605	16.0376786	23.1028245	16.0376786
20.8447389	27.3585714	21.1099342	27.3585714	21.7003342	27.3585714	22.4160605	27.3585714	23.1028245	27.3585714
20.8447389	38.6792857	21.1099342	38.6792857	21.7003342	38.6792857	22.4160605	38.6792857	23.1028245	38.6792857
20.8449056	52.8301786	21.1172902	52.8301786	21.8027308	52.8301786	22.4720808	52.8301786	23.230268	52.8301786

Table 182. Vales of the temperature profiled for the four of experimental tests of Aydelott and Spuckler**[30]**.

21.5054061	62.2641071	21.0391661	62.2641071	21.1924142	62.2641071	21.635054	62.2641071	22.8096532	62.2641071
21.0589057	73.5848214	29.9254236	73.5848214	31.4969091	73.5848214	29.6289046	73.5848214	22.1540627	73.5848214
27.3312996	83.0189286	49.1029988	83.0189286	68.2809535	83.0189286	75.2900149	83.0189286	78.4189196	83.0189286
Test 2									
0 min		**5 min**		**15 min**		**30 min**		**40 min**	
T [K]	**H [%]**	**T [K]**	**H [%]**	**T [K]**	**H [%]**	**T [K]**	**H [%]**	**T [K]**	**H [%]**
20.8384611	11.3207143	21.2698291	11.3207143	21.9964511	11.3207143	23.0277521	11.3207143	23.73913	11.3207143
20.8384611	16.0376786	21.2698291	16.0376786	21.9964511	16.0376786	23.0277521	16.0376786	23.73913	16.0376786
20.8384611	27.3585714	21.2698291	27.3585714	21.9964511	27.3585714	23.0277521	27.3585714	23.73913	27.3585714
20.8384611	38.6792857	21.2698291	38.6792857	21.9964511	38.6792857	23.0277521	38.6792857	23.73913	38.6792857
21.2443503	52.8301786	25.5655552	52.8301786	25.4983113	52.8301786	26.8698791	52.8301786	25.6345441	52.8301786
28.2756893	62.2641071	46.9597186	62.2641071	63.9670589	62.2641071	73.9513639	62.2641071	76.4361778	62.2641071
39.3868093	73.5848214	59.7794313	73.5848214	82.4533298	73.5848214	100.962982	73.5848214	105.969791	73.5848214
46.4503705	83.0189286	66.7748459	83.0189286	91.6261888	83.0189286	114.043527	83.0189286	123.134912	83.0189286
Test 3									
0 min		**5 min**		**15 min**		**30 min**		**40 min**	
T [K]	**H [%]**	**T [K]**	**H [%]**	**T [K]**	**H [%]**	**T [K]**	**H [%]**	**T [K]**	**H [%]**
19.4704045	11.3207143	21.4804447	11.3207143	21.6406438	11.3207143	22.2983146	11.3207143	22.5437323	11.3207143
19.4704045	16.0376786	21.4804447	16.0376786	21.6406438	16.0376786	22.2983146	16.0376786	22.5437323	16.0376786
19.4704045	27.3585714	21.4804447	27.3585714	21.6406438	27.3585714	22.2983146	27.3585714	22.5437323	27.3585714
21.0280724	38.6792857	27.2278607	38.6792857	28.3139578	38.6792857	28.0673455	38.6792857	28.4023216	38.6792857
39.2004202	52.8301786	57.9451413	52.8301786	73.400163	52.8301786	83.9186905	52.8301786	88.3086119	52.8301786
51.3627078	62.2641071	67.5634435	62.2641071	88.9221864	62.2641071	106.118528	62.2641071	113.066982	62.2641071
61.3206046	73.5848214	76.7697859	73.5848214	98.789602	73.5848214	119.295565	73.5848214	128.930072	73.5848214
69.7067224	83.0189286	84.5567107	83.0189286	106.050597	83.0189286	128.951661	83.0189286	139.024162	83.0189286
Test 4									
0 min		**2.5 min**		**5 min**		**10 min**		**15 min**	
T [K]	**H [%]**	**T [K]**	**H [%]**	**T [K]**	**H [%]**	**T [K]**	**H [%]**	**T [K]**	**H [%]**
21.1307391	11.3207143	21.6666815	11.3207143	22.2453225	11.3207143	23.5045502	11.3207143	24.6900846	11.3207143
21.1307391	16.0376786	21.6176796	16.0376786	22.2340797	16.0376786	23.476231	16.0376786	24.7151623	16.0376786
21.1307391	27.3585714	21.763844	27.3585714	22.3561524	27.3585714	23.6457285	27.3585714	24.8964832	27.3585714
21.1310725	38.6792857	21.8333381	38.6792857	22.4982341	38.6792857	23.7296719	38.6792857	24.9968765	38.6792857
21.1789058	52.8301786	22.1540321	52.8301786	22.7726422	52.8301786	23.9899101	52.8301786	25.2255251	52.8301786
25.6477427	62.2641071	53.5855053	62.2641071	68.7258467	62.2641071	81.9446468	62.2641071	86.5377254	62.2641071
36.0874178	73.5848214	69.756293	73.5848214	91.4432942	73.5848214	118.958844	73.5848214	137.533253	73.5848214
45.584092	83.0189286	79.883985	83.0189286	102.482747	83.0189286	133.742387	83.0189286	157.191329	83.0189286

The time steps in Table 182 are defined. These values of time are chosen because they are close to the time at which the experimental data of temperature were measured. Aydelott and Spuckler[30] reported the evolution in time of the temperature for each thermocouple. Equation 628 interpolates these evolutions of the temperature. The coefficients of Equation 628 are reported in Table 183.

Table 183. Values of the coefficients b_i of Equation 628 of Aydelott and Spuckler**[30]**.

Test 1							
b	**1**	**2**	**3**	**4**	**5**	**6**	**7**
R - 9	-2.07E-09	2.92E-07	-1.55E-05	0.00036901	-0.0032324	0.06158932	20.8454838
R - 8	-2.07E-09	2.92E-07	-1.55E-05	0.00036901	-0.0032324	0.06158932	20.8454838

Table 183. Values of the coefficients $\boldsymbol{b_i}$ of Equation 628 of Aydelott and Spuckler**[30]**.

R - 7	-2.07E-09	2.92E-07	-1.55E-05	0.00036901	-0.0032324	0.06158932	20.8454838
R - 6	-2.07E-09	2.92E-07	-1.55E-05	0.00036901	-0.0032324	0.06158932	20.8454838
R - 1	-5.03E-09	5.18E-07	-1.83E-05	0.00024001	-7.84E-05	0.05036656	20.8473379
R - 2	1.86E-08	-3.35E-06	1.97E-04	-0.0049944	0.0579909	-0.2745837	21.4736118
R - 3	2.38E-07	-1.67E-05	2.14E-04	0.00835342	-0.2778051	2.91942652	21.1437014
R - 4	-3.96E-08	6.15E-06	-0.0004033	0.01503119	-0.3622674	5.87469282	27.1408138
				Test 2			
b	**1**	**2**	**3**	**4**	**5**	**6**	**7**
R - 9	-4.30E-09	5.31E-07	-2.49E-05	0.00055772	-0.0063241	0.1069855	20.8372393
R - 8	-4.30E-09	5.31E-07	-2.49E-05	0.00055772	-0.0063241	0.1069855	20.8372393
R - 7	-4.30E-09	5.31E-07	-2.49E-05	0.00055772	-0.0063241	0.1069855	20.8372393
R - 6	-4.30E-09	5.31E-07	-2.49E-05	0.00055772	-0.0063241	0.1069855	20.8372393
R - 1	1.54E-07	-1.79E-05	0.0007165	-0.0103699	-0.0035362	1.02999618	21.4059287
R - 2	4.93E-08	-4.72E-06	9.79E-05	0.00385487	-0.2228625	4.71667104	28.4188775
R - 3	1.61E-07	-1.74E-05	6.33E-04	-0.006899	-0.1135707	4.74839378	39.3954123
R - 4	-1.53E-07	2.16E-05	-0.0011629	0.03032492	-0.4383071	5.7504084	45.8515499
				Test 3			
b	**1**	**2**	**3**	**4**	**5**	**6**	**7**
R - 9	-6.04E-09	1.41E-06	-0.0001174	0.00454504	-0.0847573	0.72129759	19.4938108
R - 8	-6.04E-09	1.41E-06	-0.0001174	0.00454504	-0.0847573	0.72129759	19.4938108
R - 7	-6.04E-09	1.41E-06	-0.0001174	0.00454504	-0.0847573	0.72129759	19.4938108
R - 6	-1.41E-07	1.92E-05	-0.0010172	0.02645669	-0.3572816	2.44720428	21.1946028
R - 1	-1.11E-07	1.56E-05	-0.0008829	0.02595325	-0.4476771	5.42171158	39.2889871
R - 2	4.06E-08	-5.69E-06	0.00027641	-0.0046246	-0.0485938	3.61292816	51.1361193
R - 3	2.11E-08	-2.42E-06	9.33E-05	-0.0006023	-0.0682275	3.45496552	61.2248556
R - 4	9.68E-08	-1.20E-05	0.00053309	-0.0093911	0.00964593	3.14266837	69.4790013
				Test 4			
b	**1**	**2**	**3**	**4**	**5**	**6**	**7**
R - 9	-1.52E-06	7.88E-05	-1.51E-03	0.01289898	-0.0445913	0.26978074	21.1211072
R - 8	1.08E-07	-8.46E-06	2.38E-04	-0.0031986	0.02183167	0.176476	21.0815085
R - 7	7.12E-07	-2.75E-05	3.27E-04	-0.0007325	-0.0073084	0.27613653	21.1203726
R - 6	-2.37E-06	1.08E-04	-1.84E-03	0.01435493	-0.0535602	0.35421609	21.1201203
R - 1	-2.41E-06	1.31E-04	-2.75E-03	0.02845382	-1.52E-01	0.64433534	21.1441342
R - 2	-1.65E-05	9.17E-04	-2.06E-02	0.2583891	-2.2749798	15.6308158	25.4085891
R - 3	-2.38E-06	1.49E-04	-5.58E-03	0.12646469	-1.7163279	17.1560643	35.8211217
R - 4	6.56E-05	-3.12E-03	0.05256607	-0.3422082	0.00427715	15.0326212	45.8579577

The values in Table 183 are calculated with the function Polyfit of MATLAB®.

Appendix B

The thermal analysis requires geometrical formulas to compute the total volume, the internal surface and the filling ratio. These geometrical formulas are reported in Table 184.

Table 184. Geometrical formulas.

Geometrical Variables	Name	Equations	Formulas
Vertical cylinder with flat bottom and flat roof			
Total volume	V^{TOT}	Equation 629	$V^{TOT} = \frac{\pi \cdot D^2}{4} \cdot H$
Total surface	A^{TOT}	Equation 630	$A^{TOT} = \pi \cdot D \cdot H + 2 \cdot \left[\frac{\pi \cdot D^2}{4}\right]$
Liquid Volume	V^L	Equation 631	$V_L = V \cdot LF$
Wet surface	A^L	Equation 632	$A^L = \pi \cdot D \cdot H \cdot LF + 2 \cdot \left[\frac{\pi \cdot D^2}{4}\right]$
Wet side surface	A^{SL}	Equation 633	$A^{SL} = \pi \cdot D \cdot H \cdot LF$
Bottom	A^B	Equation 634	$A^B = \frac{\pi \cdot D^2}{4}$
Dry side surface	A^{SV}	Equation 635	$A^{SV} = \pi \cdot D \cdot H \cdot (1 - LF)$
Roof	A^R	Equation 636	$A^R = \frac{\pi \cdot D^2}{4}$
Interface section	A^I	Equation 637	$A^I = \frac{\pi \cdot D^2}{4}$
Filling ratio	LF	Equation 638	$LF = \frac{V_L}{V}$
Oblate ellipsoid with two equal semi axis			
Total volume	V^{TOT}	Equation 639	$V^{TOT} = \frac{\pi}{6} \cdot {D_{MAX}}^2 \cdot D_{MIN}$
Total surface	A^{TOT}	Equation 640	$A^{TOT} = 2 \cdot \pi \cdot a^2 \cdot \left[1 + \left(\frac{c}{a}\right)^2 \cdot \frac{1}{e} \cdot \operatorname{atanh}(e)\right]$
Liquid Volume	V^L	Equation 641	$V_L = 6 \cdot V \cdot LF^2 \cdot \left(\frac{1}{2} - \frac{LF}{3}\right)$
Wet surface	A^L	Equation 642	$A^L = \pi \cdot D \cdot H \cdot LF + 2 \cdot \left[\frac{\pi \cdot D^2}{4}\right]$
Interface section	A^I	Equation 643	$A^I = \pi \cdot {D_{MAX}}^2 \cdot LF \cdot (1 - LF)$
Filling ratio	LF	Equation 644	$\frac{LF^3}{3} - \frac{LF^2}{2} + \frac{V_L}{6 \cdot V} = 0$
Eccentricity	e	Equation 645	$e = \sqrt{1 - \left(\frac{c}{a}\right)^2}$
Horizontal semi-axis	a	Equation 646	$a = \frac{D_{MAX}}{2}$
Vertical semi-axis	c	Equation 647	$c = \frac{D_{MIN}}{2}$
Sphere			
Total volume	V^{TOT}	Equation 648	$V^{TOT} = \frac{\pi}{6} \cdot D^3$
Total surface	A^{TOT}	Equation 649	$A^{TOT} = \pi \cdot D^2$
Liquid Volume	V^L	Equation 650	$V_L = 6 \cdot V \cdot LF^2 \cdot \left(\frac{1}{2} - \frac{LF}{3}\right)$
Wet surface	A^L	Equation 651	$A_L = A_{TOT} \cdot LF$
Interface section	A^I	Equation 652	$A^I = \pi \cdot D^2 \cdot LF \cdot (1 - LF)$
Filling ratio	LF	Equation 653	$\frac{LF^3}{3} - \frac{LF^2}{2} + \frac{V_L}{6 \cdot V} = 0$
Ullage			
Ullage volume	V^V	Equation 654	$V^V = V^{TOT} - V^L$
Surface area of the dry walls	A^V	Equation 655	$A^V = A^{TOT} - A^L$
Ullage height	H^V	Equation 656	$H^V = H - H^L$
Empty level	ER	Equation 657	$ER = 1 - LF$

Appendix C

The dry side wall-to-interface heat transfer is calculated with Equation 27. Equation 27 requires the temperature gradient, the thermal conductivity and the surface area of the ring. The thermal conductivity and the surface area can be estimated with the equations reported in Table 185.

Table 185. Formulas for dry side wall-to-interface heat transfer.

Geometrical Variables	Name	Equations	Formulas
Wall thermal conductivity	k	Equation 658	$k = 10^{\{\sum_{i=0}^{8} a_i \cdot [\log_{10}(T)]^i\}}$
Ring area	A_R	Equation 659	$A_R = \pi \cdot e \cdot (D + e)$
Diameter of the ring	D	Equation 660	$D = D_{MAX} \cdot \sqrt{LF \cdot (1 - LF)}$
Wall thickness for vertical cylinder [141]	e	Equation 661	$e = \frac{P \cdot R}{S \cdot E - 0.6 \cdot P}$
Wall thickness for sphere and ellipsoid [141]	e	Equation 662	$e = \frac{P \cdot R}{2 \cdot S \cdot E - 0.2 \cdot P}$

P is the maximum pressure, whose value is assumed to be 10 MPa for Kang et al. [124], Aydelott and Spuckler [30] and Aydelott [29], and to be 1 MPa for Seo and Jeong [24], Perez et al. [26], Hansa et al. [27] and Dresar et al. [28]. R is the internal radius of the storage containers, S is the yield tensile[122], whose value is 226.3 MPa at 20 °C, as reported by Kweon et al. [142]. E is the welding efficiency[123] and it assumed to be 1. Equation 661 and Equation 662 are respectively applied for vertical cylindrical tanks and spherical/ellipsoidal tanks. Table 186 reports the values of the thickness of the side wall for the experimental works.

Table 186. Thickness in mm of the side wall.

Experimental work	Kang et al. [124]	Aydelott and Spuckler [30]		Aydelott [29]
Thickness	2.950522	6.269592		2.575011
Experimental work	Seo and Jeong [24]	Perez et al. [26]	Hasan et al. [27]	Dresar et al. [28]
Thickness	0. 44528	0. 44417	2.433628	2.433628

Except Kang et al. [25], the values of the thermal conductivity of the steel is not reported because the type of steel used is not specified. A values of 16.5 W/m/K of k is indicated by Kang et al. [25], for Type 304 Stainless Steel (S30400 – A312). Hence, it is assumed that this steel is used in all the experiments. So, the wall thermal conductivity is estimated with Equation 658, as suggested by the NIST [121] for Type 304 Stainless Steel (S30400 – A312). In Equation 658, T is the temperature in Kelvin and a_i is the coefficient, whose values are given in Table 187.

Table 187. Values of coefficient $\boldsymbol{a_i}$ of Equation 658.

$\boldsymbol{a_0}$	$\boldsymbol{a_1}$	$\boldsymbol{a_2}$	$\boldsymbol{a_3}$	$\boldsymbol{a_4}$	$\boldsymbol{a_5}$	$\boldsymbol{a_6}$	$\boldsymbol{a_7}$	$\boldsymbol{a_8}$
-1.4087	1.3982	0.2543	-0.6260	0.2334	0.4256	-0.4658	0.1650	-0.0199

The values given in Table 187 are obtained by fitting experimental data with a relative error of 2 % between 4 K and 300 K [121]. Equation 661 and Equation 662 are used to compute the wall thickness because the value of this variable is not report in any experimental works, except for Kang et al. [25]. The latter notified that the thickness is around 5.1 mm. This value is, however, not consistent with the one obtained from Equation 661, which is 2.95 mm.

---

[122] The yield tensile is the limit value of the elastic behaviour of a metal. Over this value, the stress plastically deforms the metal.

[123] The welding efficiency is the reliability of the joints.

Appendix D

The filling ratio is computed with an iterative procedure because the average temperatures, which affect the densities and the masses, depend on the filling ratio, as explained by Equation 3 and by Equation 4. The input variables in this algorithm are the experimental values of the pressure and of the temperature profiles, and the total volume of the storage containers. The method to compute the liquid level is described in Figure 206.

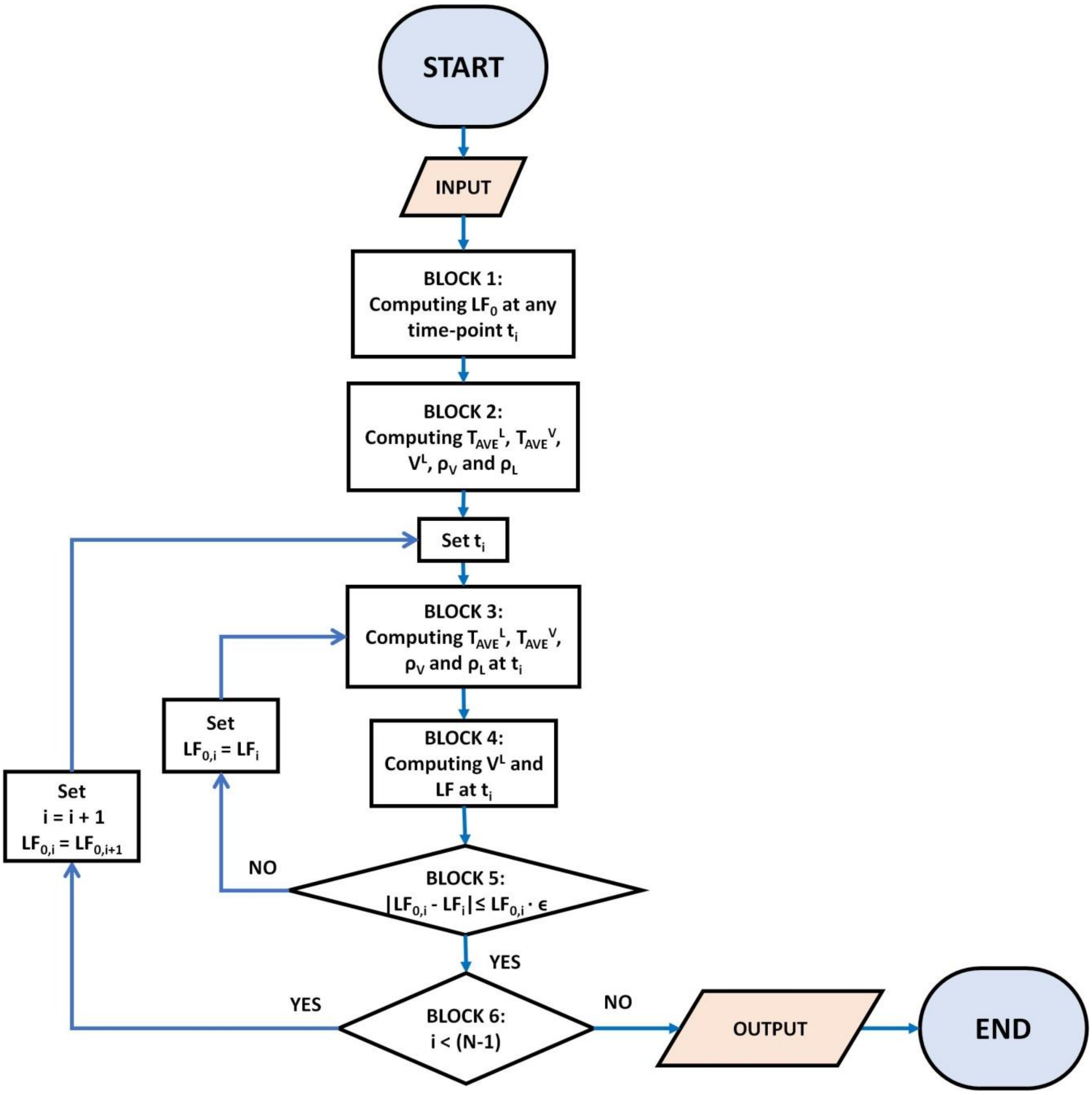

Figure 206. Algorithm to compute the filling ratio evolution.

As it can be seen by Figure 206, the algorithm is composed from seven steps.

a) BLOCK 1: The first guess of the liquid level (LF_0) at any time-point (t_i) can be computed by linear interpolation with Equation 663, except at the beginning.

Equation 663
$$LF_{0,i} = \left.\frac{H_j^L - H_{j-1}^L}{T_j - T_{j-1}}\right|_i \cdot (T_I - T_{j-1})\Big|_i + H_{j-1}^L\Big|_i$$

LF_i is the filling ratio at time step i, H^L is the level, T is the temperature and T_I is the interface temperature. The indexes j and $j-1$ respectively indicate the experimental point at which $T_I \leq$

T_j and the previous experimental point. Equation 663 does not compute the values of LF_0 at the end of the self-pressurisation (t_F), except for Test 5 and Test 6 of Seo and Jeong [21]. For these tests, Equation 663 does not compute the values of LF_0 at the beginning of the self-pressurisation (t_0).

b) BLOCK 2: The average temperatures in liquid and in vapour (T^L_{AVE} and T^V_{AVE}) are computed with Equation 3 and with Equation 4, respectively. The liquid and vapour densities (ρ_V and ρ_L) are calculated with these temperatures, using the thermodynamic model of Helmholtz free energy. The values of liquid volume (V^L) are computed using the geometrical formulas reported in Appendix B, with the filling ratio of Block 1 (Step a) of Appendix D). The values of T^L_{AVE}, T^V_{AVE}, ρ_V, ρ_L and V^L are computed at the time-point t_F, except for Test 5 and Test 6 of Seo and Jeong [21]. For these tests, the values of these variables are calculated at the time-point t_0.

c) BLOCK 3: The average temperatures in liquid and in vapour (T^L_{AVE} and T^V_{AVE}) are calculated with Equation 3 and with Equation 4, respectively. The vapour and liquid densities (ρ_V and ρ_L) are determined with these temperatures, using the thermodynamic model of Helmholtz free energy;

d) BLOCK 4: The liquid volume (V^L) at time step t_i is obtained with Equation 664.

Equation 664
$$V^L_{t_i} = \frac{[\rho_L \cdot V_L + \rho_V \cdot (V^{TOT} - V_L)]|_{t_F} - (\rho_V)|_{t_i} \cdot V^{TOT}}{(\rho_L - \rho_V)|_{t_i}}$$

V^{TOT} is the total volume. Equation 664 is obtained from the mass conservation law, which is described by Equation 5. The liquid level is, then, calculated with geometrical formulas reported in Appendix B;

e) BLOCK 5: The convergence criterion is defined with Equation 665.

Equation 665
$$\left|LF_0|_{t_i} - LF|_{t_i}\right| < LF_0|_{i-1} \cdot \varepsilon$$

ε is the relative tolerance, whose value is 10^{-5}. Two pathways exist:

- Pathway 1.5 (P 1.5): If Equation 665 is true, the algorithm moves to the Block 6 (step f) of Appendix D);
- Pathway 2.5 (P 2.5): If Equation 665 is false, the algorithm restarts from Block 3 (step c) of Appendix D) with this condition $LF_0|_{t_i} = LF|_{t_i}$.

f) BLOCK 6: Two pathways exist:

- Pathway 1.6 (P 1.6): If the current time-point (t_i) is below the second-last time step, called t_{N-1}, the loop is restarts Block 3 (step c) of Appendix D) taking the guess value at time step t_{i+1}.
- Pathway 2.6 (P 2.6): if t_i is above t_{N-1}, algorithm stops.

Appendix E

Matematical procedure of the mathematical system of the analysis of the thermal distribution

The mathematical system of the analysis of the thermal distribution (see Table 26) can be deduced from the conservation laws of mass and of energy, using the procedure that is reported in this appendix. This procedure is composed by three steps:

a) Deducing the conservation laws of energy and of mass;
b) Obtaining the solution for the steady state;
c) Deducing the solution laws for the self-pressurisation;

Section 1 explains the conservation laws of mass and of energy. Section 2 and 3 respectively describe the solution at the steady state and during the self-pressurisation, respectively.

1. Conservation laws

Considering the control volumes of Figure 30, the thermal analysis can be developed using the conservation laws that are reported in Table 188.

Table 188. Conservations laws of the thermal analysis.

Balance equation	**Equations**	**Formulas**
Liquid energy	Equation 666	$\frac{\partial \widetilde{H}^L}{\partial t} = \dot{Q}_L^W - \dot{Q}_L^I - \dot{m}_N \cdot \tilde{h}_L(P)$
Vapour energy	Equation 667	$\frac{\partial \widetilde{H}^V}{\partial t} = \dot{Q}_V^W - \dot{Q}_V^I + \dot{m}_N \cdot \tilde{h}_V(P) - \dot{m}_{BOG} \cdot \tilde{h}_V(T_{BOG}, P)$
Interface energy	Equation 668	$\dot{Q}_L^I + \dot{Q}_V^I + \dot{Q}_W^{LV} - \dot{m}_N \cdot \Delta\widetilde{H}_{ev}(P) = 0$
Mass liquid	Equation 669	$\frac{\partial m^L}{\partial t} = -\dot{m}_N$
Mass vapour	Equation 670	$\frac{\partial m^V}{\partial t} = \dot{m}_N - \dot{m}_{BOG}$

The conservation laws of Table 188 are developed for steady state and for the self-pressurisation.

2. Solution at steady state

At steady state, the temperatures and the pressure do not change. The filling ratio is slightly reduced. Hence, the liquid and vapour specific enthalpies and density do not vary and the conservation laws of the thermal distribution analysis can be computed as reported in Table 189.

Table 189. Conservations laws of the thermal analysis at steady state.

Balance equation	**Equations**	**Formulas**
Liquid energy	Equation 671	$m^L \cdot \frac{\partial V^L}{\partial t} \cdot \tilde{h}_L(P^L, T^L) = \dot{Q}_L^W - \dot{Q}_L^I - \dot{m}_N \cdot \tilde{h}_S^L(P^V)$
Vapour energy	Equation 672	$m^V \cdot \frac{\partial V^V}{\partial t} \cdot \tilde{h}_V(P^V, T^V) = \dot{Q}_V^W - \dot{Q}_V^I + \dot{m}_N \cdot \tilde{h}_S^V(P^V) - \dot{m}_{BOG} \cdot \tilde{h}_V(T_{BOG}, P^V)$
Mass liquid	Equation 673	$m^L \cdot \frac{\partial V^L}{\partial t} = -\dot{m}_N$
Mass vapour	Equation 674	$m^V \cdot \frac{\partial V^V}{\partial t} = \dot{m}_N - \dot{m}_{BOG} = 0$

The evaporation rate is low because the storage container is well insulated. Hence, it can be assumed that $\frac{\partial V^V}{\partial t}$ is equal to zero. As consequence, the net mass flow is equal to the boil-off gas (BOG) flow. The mass balance equation of the vapour (Equation 674) is added to the vapour energy conservation law (Equation 672). So, Equation 13 is obtained. The term $m^L \cdot \frac{\partial V^L}{\partial t}$ can be removed from Equation 671 by inserting Equation 673. The liquid energy balance can be written with Equation 675.

Equation 675 $$\dot{Q}_L^W - \dot{Q}_L^I = -\dot{m}_{BOG} \cdot \left\{\tilde{h}_L(P^L,T^L) - \tilde{h}_S^L(P^V)\right\}$$

The liquid-to-interface heat flow can be removed from Equation 675, by inserting Equation 668. As consequence, Equation 12 is obtained.

3. Self-pressurisation

During the self-pressurisation, the temperatures, the pressure and the filling ratio changes in time. Hence, the storage containers are described by Equation 666, Equation 667 and Equation 670. These equations can be integrated in time and this system of equation is obtained.

Table 190. Conservations laws of the thermal analysis during self-pressurisation.

Balance equation	Equations	Formulas
Liquid energy	Equation 676	$\int_{t_0}^{t_F} \frac{\partial \tilde{H}^L}{\partial t} \cdot dt = \int_{t_0}^{t_F} \left[\dot{Q}_L^W - \dot{Q}_L^I - \dot{m}_N \cdot \tilde{h}_L(P)\right] \cdot dt$
Vapour energy	Equation 677	$\int_{t_0}^{t_F} \frac{\partial \tilde{H}^V}{\partial t} \cdot dt = \int_{t_0}^{t_F} \left[\dot{Q}_V^W - \dot{Q}_V^I + \dot{m}_N \cdot \tilde{h}_V(P)\right] \cdot dt$
Mass vapour	Equation 678	$\int_{t_0}^{t_F} \frac{\partial m^V}{\partial t} \cdot dt = -\int_{t_0}^{t_F} \frac{\partial m^L}{\partial t} \cdot dt$

In the self-pressurisation, the storage container is closed. Hence, the overall mass is constant and the variation of liquid mass is opposite to the variation of vapour mass. The self-pressurisation time can be decomposed in time steps, called "t_i". So, the right and the left term of Equation 676 and Equation 677 can be computed with the equations of Table 191.

Table 191. Right and left part of Equation 676 and Equation 677.

Equations	Formulas
	Right
Equation 679	$\int_{t_0}^{t_F} \left[\dot{Q}_L^W - \dot{Q}_L^I - \dot{m}_N \cdot \tilde{h}_L(P)\right] \cdot dt = \int_{t_0}^{t_F} \left[\dot{Q}_L^W - \dot{Q}_L^I\right] \cdot dt - \sum_{i=1}^{N-1} \left[m_N \cdot \tilde{h}^L(P^V)\right]\Big\|_i$
Equation 680	$\int_{t_0}^{t_F} \left[\dot{Q}_V^W - \dot{Q}_V^I + \dot{m}_N \cdot \tilde{h}_V(P)\right] \cdot dt = \int_{t_0}^{t_F} \left[\dot{Q}_V^W - \dot{Q}_V^I\right] \cdot dt + \sum_{i=1}^{N-1} \left[m_N \cdot \tilde{h}^V(P^V)\right]\Big\|_i$
	Left
Equation 681	$\int_{t_0}^{t_F} \frac{\partial \tilde{H}^L}{\partial t} \cdot dt = \Delta t \cdot \left[\tilde{H}^L\big\|_{t_F} - \tilde{H}^L\big\|_{t_0}\right]$
Equation 682	$\int_{t_0}^{t_F} \frac{\partial \tilde{H}^V}{\partial t} \cdot dt = \Delta t \cdot \left[\tilde{H}^V\big\|_{t_F} - \tilde{H}^V\big\|_{t_0}\right]$

Equation 681 and Equation 679, and Equation 682 and Equation 680 are respectively inserted into Equation 676 and Equation 677. Equation 14 and Equation 15 are obtained.

Appendix F

Mathematical steps to deduce the pressure evolution, liquid volume evolution, inlet liquid flow and Boil-Off Gas equations of the equilibrium model

Section 1 describes the fundamental laws and other useful equations of the mathematical procedure. Section 2 and 3 respectively explains the mathematical steps to obtain the net mass flow (NMF) equation (Equation 37) and the linear form of the NMF equation (Equation 38). Section 3.1 and 3.2 present the mathematical steps of the simplified form of conservation laws (see Table 40 of Section 2.5) and their linear forms (see Table 41 of Section 2.6), respectively. Section 4 describes the mathematical steps to obtain the pressure-liquid volume (P-V^L) equations (see Table 43 of Section 2.7). Section 5 explains the mathematical steps to obtain the pressure evolution (P-e), liquid volume evolution (V^L-e), inlet liquid flow (ILF) and Boil-Off Gas (BOG) equations for the storage mode 1.b (steady state) and 4 (self-pressurisation) (see Table 45 of Section 2.8).

1. Fundamental laws of the mathematical procedure and other useful equations

The fundamental laws and the useful equations are required to deduce the equations of the mathematical system of the equilibrium model (EQ model).

Section 1.1 presents the fundamental laws. Section 1.2 describes the useful equations.

1.1. Fundamental laws of the mathematical procedure

The conservation laws of the equilibrium model are deduced from the fundamentals formulas, which are reported in Table 192.

Table 192. Fundamental formulas.

Name	Equation	Formulas
Definition of enthalpy	Equation 683	$\tilde{H} = \tilde{h} \cdot m$
Definition of mass	Equation 684	$m = \rho \cdot V$
First principle of thermodynamics	Equation 685	$\frac{\partial \tilde{U}}{\partial t} = \dot{Q}_N - \dot{W}_N - \sum_{i=1}^{N_{OUT}} \dot{U}_i + \sum_{i=1}^{N_{IN}} \dot{U}_i$
Conservation of mass	Equation 686	$\frac{\partial m}{\partial t} = -\sum_{i=1}^{N_{OUT}} \dot{m}_i + \sum_{i=1}^{N_{IN}} \dot{m}_i$

$\dot{Q}_N$ is the net heat input, $\dot{W}_N$ is the net work, $\dot{U}$ is the internal energy flow and $\dot{m}$ is the mass flow. N_{OUT} and N_{IN} are the number of inlet and outlet flows, respectively. Equation 685 and Equation 686 are used to determine the conservation laws of equilibrium model (EQ model) (see Table 38).

1.2. Useful equations

To deduce the mathematical system of the equilibrium model (EQ model), the time-derivate of the saturation temperature ($\frac{\partial T}{\partial t}$), the time-derivates of the liquid mass ($\frac{\partial m^L}{\partial t}$), the time-derivate of the overall enthalpy ($\frac{\partial \tilde{H}}{\partial t}$) and the time-derivate of the overall mass ($\frac{\partial m}{\partial t}$) should be computed from the values of the time-derivates of pressure and of liquid volume ($\frac{\partial P^V}{\partial t}$ and $\frac{\partial V^L}{\partial t}$). The time derivates $\frac{\partial T}{\partial t}$, $\frac{\partial m^L}{\partial t}$, $\frac{\partial \widetilde{H}}{\partial t}$ and $\frac{\partial m}{\partial t}$ can be respectively computed with the time-derivate of the saturation temperature (TD-ST) equation, with the time-derivate of the liquid mass equation (TD-LM) and with the time-derivate of the overall enthalpy (TD-OH) equation.

Section 1.2.1, 1.2.2, 1.2.3 and 1.2.4 respectively describe how TD-ST, the TD-LM, the TD-OH and the TD-OM equations are obtained.

1.2.1. Time-derivate of the saturation temperature equation

Due to the hypothesis of the instantaneous thermodynamic equilibrium (assumption a) of Section 1.1), the temperature is calculated from the saturation equation. So, the time-derivate of the temperature ($\frac{\partial T}{\partial t}$) can be computed from the time-derivate of the pressure. Using the chain rule[124], the time-derivate of the temperature can be calculated as follows:

Equation 687 $$\frac{\partial T}{\partial t} = \left.\frac{\partial T}{\partial P^V}\right|_S \cdot \frac{\partial P^V}{\partial t}$$

$\left.\frac{\partial T}{\partial P^V}\right|_S$ is determined with the thermodynamic model (see Section 4.1). Equation 687 is called *time-derivate of the saturation temperature (TD-ST) equation*.

1.2.2. Time-derivate of the liquid mass equation

Using the definition of the mass (Equation 684), the liquid mass can be computed as the product between the liquid density and the liquid volume. The liquid density can be computed as function of the pressure and of the temperature. So, the time-derivate of the liquid mass ($\frac{\partial m^L}{\partial t}$) can be calculated as function of the time-derivates of the temperature ($\frac{\partial T}{\partial t}$) and of the pressure ($\frac{\partial P^V}{\partial t}$). Using the product rule[125] and the chain rule, the time-derivate of the liquid mass can be computed as follows:

Equation 688 $$\frac{\partial m^L}{\partial t} = V^L \cdot \left(\frac{\partial P^V}{\partial t} \cdot \left.\frac{\partial \rho_S^L}{\partial P^V}\right|_T + \left.\frac{\partial \rho_S^L}{\partial T}\right|_{P^V} \cdot \frac{\partial T}{\partial t} \right) + \frac{\partial V^L}{\partial t} \cdot \rho_S^L$$

Equation 688 is called *time-derivate of the liquid mass (TD-LM) equation*. Equation 688 is required to determine the net mass flow (NMF) equation (Equation 37).

1.2.3. Time-derivate of the overall enthalpy equations

The overall enthalpy ($\widetilde{H}$) is the sum of the liquid enthalpy ($\widetilde{H}^L$) and the vapour enthalpy ($\widetilde{H}^V$). These enthalpies can be computed with the definition of the enthalpy (Equation 689). So, the liquid enthalpy is equal to the product of the liquid mass (m^L) and of the liquid specific enthalpy ($\tilde{h}^L$). The vapour enthalpy is the the product of the vapour mass (m^V) and of the vapour specific enthalpy ($\tilde{h}^V$). The vapour and liquid specific enthalpies are function of the pressure and of the internal temperature. As consequence, the time derivate of the overall enthalpy ($\frac{\partial \widetilde{H}}{\partial t}$) can be calculated as function of the time-

---

[124] Chain rule: $\frac{\partial\{f[g(x)]\}}{\partial x} = \frac{\partial f[g(x)]}{\partial g(x)} \cdot \frac{\partial g(x)}{\partial x}$

[125] Product rule: $\frac{\partial[f(x)\cdot g(x)]}{\partial x} = \frac{\partial f(x)}{\partial x} \cdot g(x) + f(x) \cdot \frac{\partial g(x)}{\partial x}$

derivates of the liquid and vapour mass ($\frac{\partial m^L}{\partial t}$ and $\frac{\partial m^V}{\partial t}$), of the time-derivate of the temperature ($\frac{\partial T}{\partial t}$) and of the time-derivate of the pressure ($\frac{\partial P^V}{\partial t}$). Using the sum[126], the product and the chain rules, the time derivate of the overall enthalpy can be computed as follows:

Equation 690
$$\frac{\partial \tilde{H}}{\partial t} = \frac{\partial \tilde{H}^L}{\partial t} + \frac{\partial \tilde{H}^V}{\partial t} = \sum_{i=L,V} \left\{ \tilde{h}_S^i \cdot \frac{\partial m^i}{\partial t} + m^i \cdot \left[\left.\frac{\partial \tilde{h}_S^i}{\partial T}\right|_{P^V} \cdot \frac{\partial T}{\partial t} + \left.\frac{\partial \tilde{h}_S^i}{\partial P^V}\right|_T \cdot \frac{\partial P^V}{\partial t} \right] \right\}$$

Equation 690 is called the *time-derivate of overall enthalpy (TD-OH) equation*.

1.2.4. Time-derivate of the overall mass equation

The overall mass is the sum of the liquid mass and of vapour mass. As indicated by the definition of the mass (Equation 684), the mass can be calculated as product of the density and of the volume. So, the liquid mass is the product of the liquid density and the liquid volume. The vapour mass is the product of the vapour density and of the vapour volume. The density is a function of the temperature and of the pressure. As consequence, the time-derivates of the overall mass ($\frac{\partial m}{\partial t}$) can be computed as function of time-derivates of the liquid and vapour volumes ($\frac{\partial V^L}{\partial t}$ and $\frac{\partial V^V}{\partial t}$), time-derivate of the temperature ($\frac{\partial T}{\partial t}$) and time-derivate of the pressure ($\frac{\partial P^V}{\partial t}$). Using the sum, the product and the chain rules, the time-derivate of the overall mass can be computed as follows:

Equation 691
$$\frac{\partial m}{\partial t} = \frac{\partial m^L}{\partial t} + \frac{\partial m^V}{\partial t} = \sum_{i=L,V} \left[V^i \cdot \left(\left.\frac{\partial \rho_S^i}{\partial T}\right|_{P^V} \cdot \frac{\partial T}{\partial t} + \left.\frac{\partial \rho_S^i}{\partial P^V}\right|_T \cdot \frac{\partial P^V}{\partial t} \right) + \frac{\partial V^i}{\partial t} \cdot \rho_S^i \right]$$

Equation 691 is called *time-derivate of overall (TD-OM) mass equation*.

2. Mathematical steps for net mass flow equation

The accumulation of the mass in the liquid can be described with the liquid mass balance equation (Equation 34). In this equation, the time-derivate of the liquid mass ($\frac{\partial m^L}{\partial t}$) can be substituted with the time-derivate of the liquid mass equation (Equation 688). So, liquid mass balance equation can be written as follows:

Equation 692
$$V^L \cdot \left(\frac{\partial P^V}{\partial t} \cdot \left.\frac{\partial \rho_S^L}{\partial P^V}\right|_T + \left.\frac{\partial \rho_S^L}{\partial T}\right|_{P^V} \cdot \frac{\partial T}{\partial t} \right) + \frac{\partial V^L}{\partial t} \cdot \rho_S^L = -\dot{m}_N + \dot{m}_{IN}^L - \dot{m}_{OUT}^L$$

In Equation 692, the time-derivate of the temperature ($\frac{\partial T}{\partial t}$) can be substituted with the time-derivate of the temperature (Equation 687). So, Equation 692 can be written as follows:

Equation 693
$$V^L \cdot \left(\left.\frac{\partial \rho_S^L}{\partial T}\right|_{P^V} \cdot \left.\frac{\partial T}{\partial P^V}\right|_S \cdot \frac{\partial P^V}{\partial t} + \left.\frac{\partial \rho_S^L}{\partial P^V}\right|_T \cdot \frac{\partial P^V}{\partial t} \right) + \frac{\partial V^L}{\partial t} \cdot \rho_S^L = -\dot{m}_N + \dot{m}_{IN}^L - \dot{m}_{OUT}^L$$

The time-derivate of the pressure ($\frac{\partial P^V}{\partial t}$) is grouped in the left part of Equation 693. Equation 693 can be written as follows:

---

[126] Sum rule: $\frac{\partial[f(x)+g(x)]}{\partial x} = \frac{\partial f(x)}{\partial x} + \frac{\partial g(x)}{\partial x}$

Equation 694
$$V^L \cdot \frac{\partial P^V}{\partial t} \cdot \left(\left.\frac{\partial \rho_S^L}{\partial T}\right|_{P^V} \cdot \left.\frac{\partial T}{\partial P^V}\right|_S + \left.\frac{\partial \rho_S^L}{\partial P^V}\right|_T \right) + \frac{\partial V^L}{\partial t} \cdot \rho_S^L = -\dot{m}_N + \dot{m}_{IN}^L - \dot{m}_{OUT}^L$$

The left and the right parts of Equation 694 can be multiplied by -1 and the mass flows $\dot{m}_{IN}^L$ and $\dot{m}_{OUT}^L$ can be moved to the left part of Equation 694. So, The NMF equation (Equation 37) is obtained.

3. Mathematical steps for the linear form of net mass flow equation

The net mass flow (NMF) equation (Equation 37) is composed by non-differential terms and differential terms. The non-differential terms are $V^L \cdot \left(\left.\frac{\partial \rho_S^L}{\partial T}\right|_{P^V} \cdot \left.\frac{\partial T}{\partial P^V}\right|_S + \left.\frac{\partial \rho_S^L}{\partial P^V}\right|_T \right)$, ρ_S^L, -1 and 1. These terms respectively multiply the time-derivate of the pressure ($\frac{\partial P^V}{\partial t}$), the time-derivate of the liquid volume ($\frac{\partial V^L}{\partial t}$), the inlet liquid mass flow ($\dot{m}_{IN}^L$) and the outlet liquid mass flow ($\dot{m}_{OUT}^L$). If the non-differential terms are substituted with the coefficients of Table 39, the linear form of net mass flow (NMF) equations (Equation 38) is obtained.

3.1.Mathematical step of simplified form of conservations laws

As this point of the mathematical procedure, the overall mass and energy conservation laws (Equation 658 and Equation 33) are the only equations that have not been used yet. These equations are applied for obtaining the simplified from of the conservation laws, which are the simplified forms of the overall mass and the overall energy conservation laws.

3.1.1. Mathematical step of simplified form of overall energy conservations law

The accumulation of enthalpy is described with the overall energy conservation law (Equation 658). In this equation, the time-derivate of the overall enthalpy ($\frac{\partial \tilde{H}}{\partial t}$) can be substituted with time-derivate of the overall enthalpy equation (Equation 690). So, Equation 658 can be computed as follows:

Equation 695
$$\sum_{i=L,V} \left\{ \tilde{h}_S^i \cdot \frac{\partial m^i}{\partial t} + m^i \cdot \left[\left.\frac{\partial \tilde{h}_S^i}{\partial T}\right|_{P^V} \cdot \frac{\partial T}{\partial t} + \left.\frac{\partial \tilde{h}_S^i}{\partial P^V}\right|_T \cdot \frac{\partial P^V}{\partial t} \right] \right\} = \dot{Q} + \dot{m}_{IN}^L \cdot \tilde{h}_{IN}^L - \dot{m}_{OUT}^L \cdot \tilde{h}_S^L + \dot{m}_{IN}^V \cdot \tilde{h}_{IN}^V - \dot{m}_{BOG} \cdot \tilde{h}_S^V$$

In Equation 695, the time-derivate of the temperature ($\frac{\partial T}{\partial t}$) can be substituted with the time-derivate of the saturation temperature equation (Equation 687).

Equation 696
$$\sum_{i=L,V} \left\{ \tilde{h}_S^i \cdot \frac{\partial m^i}{\partial t} + m^i \cdot \left[C_{P_S}^i \cdot \left.\frac{\partial T}{\partial P^V}\right|_S \cdot \frac{\partial P^V}{\partial t} + \left.\frac{\partial \tilde{h}_S^i}{\partial P^V}\right|_T \cdot \frac{\partial P^V}{\partial t} \right] \right\} = \dot{Q} + \dot{m}_{IN}^L \cdot \tilde{h}_{IN}^L - \dot{m}_{OUT}^L \cdot \tilde{h}_S^L + \dot{m}_{IN}^V \cdot \tilde{h}_{IN}^V - \dot{m}_{BOG} \cdot \tilde{h}_S^V$$

In Equation 696, the time-derivate of the pressure ($\frac{\partial P^V}{\partial t}$) is grouped. Equation 696 can be written as follows:

Equation 697
$$\sum_{i=L,V} \left\{ \tilde{h}_S^i \cdot \frac{\partial m^i}{\partial t} + m^i \cdot \frac{\partial P^V}{\partial t} \cdot \left[C_{P_S}^i \cdot \left.\frac{\partial T}{\partial P^V}\right|_S + \left.\frac{\partial \tilde{h}_S^i}{\partial P^V}\right|_T \right] \right\} = \dot{Q} + \dot{m}_{IN}^L \cdot \tilde{h}_{IN}^L - \dot{m}_{OUT}^L \cdot \tilde{h}_S^L + \dot{m}_{IN}^V \cdot \tilde{h}_{IN}^V - \dot{m}_{BOG} \cdot \tilde{h}_S^V$$

In Equation 697, the time-derivates of the liquid and vapour mass ($\frac{\partial m^L}{\partial t}$ and $\frac{\partial m^V}{\partial t}$) can be respectively substituted with Equation 34 and with Equation 35. Equation 697 can be written as follows:

Equation 698

$$\begin{gathered}\sum_{i=L,V}\left\{m^i\cdot\frac{\partial P^V}{\partial t}\cdot\left[C_{P_S}^i\cdot\left.\frac{\partial T}{\partial P^V}\right|_S+\left.\frac{\partial \tilde{h}_S^i}{\partial P^V}\right|_T\right]\right\}\\ +\tilde{h}_S^V\cdot(\dot{m}_N+\dot{m}_{IN}^V-\dot{m}_{BOG})+\tilde{h}_S^L\cdot(-\dot{m}_N+\dot{m}_{IN}^L-\dot{m}_{OUT}^L)\\ =\dot{Q}+\dot{m}_{IN}^L\cdot\tilde{h}_{IN}^L+\dot{m}_{IN}^V\cdot\tilde{h}_{IN}^V\end{gathered}$$

The terms $\tilde{h}_S^V\cdot(\dot{m}_N+\dot{m}_{IN}^V-\dot{m}_{BOG})$ and $\tilde{h}_S^L\cdot(-\dot{m}_N+\dot{m}_{IN}^L-\dot{m}_{OUT}^L)$ are moved to the right part of Equation 698. So, Equation 698 can be written as follows:

Equation 699

$$\begin{gathered}\sum_{i=L,V}\left\{m^i\cdot\frac{\partial P^V}{\partial t}\cdot\left[C_{P_S}^i\cdot\left.\frac{\partial T}{\partial P^V}\right|_S+\left.\frac{\partial \tilde{h}_S^i}{\partial P^V}\right|_T\right]\right\}\\ =\dot{Q}+\dot{m}_{IN}^L\cdot\tilde{h}_{IN}^L+\dot{m}_{IN}^V\cdot\tilde{h}_{IN}^V-\tilde{h}_S^V\cdot(\dot{m}_N+\dot{m}_{IN}^V-\dot{m}_{BOG})-\tilde{h}_S^L\\ \cdot(-\dot{m}_N+\dot{m}_{IN}^L-\dot{m}_{OUT}^L)\end{gathered}$$

The mass flows $\dot{m}_{IN}^L$, $\dot{m}_{IN}^V$, $\dot{m}_N$, $\dot{m}_{IN}^V$ and $\dot{m}_{BOG}$ are grouped in the right part of Equation 699. So, Equation 699 can be written as follows:

Equation 700

$$\begin{gathered}\sum_{i=L,V}\left\{m^i\cdot\frac{\partial P^V}{\partial t}\cdot\left[C_{P_S}^i\cdot\left.\frac{\partial T}{\partial P^V}\right|_S+\left.\frac{\partial \tilde{h}_S^i}{\partial P^V}\right|_T\right]\right\}\\ =\dot{Q}+\dot{m}_{IN}^L\cdot\left[\tilde{h}_{IN}^L-\tilde{h}_S^L\right]+\dot{m}_{IN}^V\cdot\left[\tilde{h}_{IN}^V-\tilde{h}_S^V\right]-\dot{m}_N\cdot\left[\tilde{h}_S^V-\tilde{h}_S^L\right]\end{gathered}$$

The term $\dot{m}_N\cdot\left[\tilde{h}_S^V-\tilde{h}_S^L\right]$ is moved to the left part of Equation 700. The difference $\left[\tilde{h}_S^V-\tilde{h}_S^L\right]$ is the latent heat of evaporation. So, the simplified form of the overall energy conservation law (Equation 43) is obtained.

3.1.2. Mathematical step of simplified form of overall mass conservations law

The accumulation of mass is calculated with the overall mass conservation law (Equation 33). In this equation, the time-derivate of the overall mass can be substituted with the time-derivate of the overall mass equation (Equation 691). So, the overall mass conservation law can be written as follows:

Equation 701

$$\begin{gathered}\sum_{i=L,V}\left[V^i\cdot\left(\left.\frac{\partial \rho_S^i}{\partial T}\right|_{P^V}\cdot\frac{\partial T}{\partial t}+\left.\frac{\partial \rho_S^i}{\partial P^V}\right|_T\cdot\frac{\partial P^V}{\partial t}\right)+\frac{\partial V^i}{\partial t}\cdot\rho_S^i\right]\\ =\dot{m}_{IN}^L-\dot{m}_{OUT}^L+\dot{m}_{IN}^V-\dot{m}_{BOG}\end{gathered}$$

The time-derivate of the temperature ($\frac{\partial T}{\partial t}$) can be substituted with the time-derivate of the saturation temperature equation (Equation 687). So, Equation 701 can be written as follows:

Equation 702

$$\begin{gathered}\sum_{i=L,V}\left[V^i\cdot\left(\left.\frac{\partial \rho_S^i}{\partial T}\right|_{P^V}\cdot\left.\frac{\partial T}{\partial P^V}\right|_S\cdot\frac{\partial P^V}{\partial t}+\left.\frac{\partial \rho_S^i}{\partial P^V}\right|_T\cdot\frac{\partial P^V}{\partial t}\right)+\frac{\partial V^i}{\partial t}\cdot\rho_S^i\right]\\ =\dot{m}_{IN}^L-\dot{m}_{OUT}^L+\dot{m}_{IN}^V-\dot{m}_{BOG}\end{gathered}$$

The time-derivate of the pressure ($\frac{\partial P^V}{\partial t}$) is grouped in Equation 702. Equation 702 can be written as follows:

Equation 703

$$\begin{gathered}\sum_{i=L,V}\left[V^i\cdot\frac{\partial P^V}{\partial t}\cdot\left(\left.\frac{\partial \rho_S^i}{\partial T}\right|_{P^V}\cdot\left.\frac{\partial T}{\partial P^V}\right|_S+\left.\frac{\partial \rho_S^i}{\partial P^V}\right|_T\right)+\frac{\partial V^i}{\partial t}\cdot\rho_S^i\right]\\ =\dot{m}_{IN}^L-\dot{m}_{OUT}^L+\dot{m}_{IN}^V-\dot{m}_{BOG}\end{gathered}$$

In Equation 703, the time-derivate of the ullage volume ($\frac{\partial V^V}{\partial t}$) can be substituted with the volume conservation law (Equation 36). Equation 703 can be written as follows:

Equation 704
$$\sum_{i=L,V}\left[V^i\cdot\frac{\partial P^V}{\partial t}\cdot\left(\left.\frac{\partial\rho_S^i}{\partial T}\right|_{P^V}\cdot\left.\frac{\partial T}{\partial P^V}\right|_S+\left.\frac{\partial\rho_S^i}{\partial P^V}\right|_T\right)\right]+\frac{\partial V^L}{\partial t}\cdot\rho_S^L-\frac{\partial V^L}{\partial t}\cdot\rho_S^V = \dot{m}_{IN}^L-\dot{m}_{OUT}^L+\dot{m}_{IN}^V-\dot{m}_{BOG}$$

The time-derivate of the liquid volume ($\frac{\partial V^L}{\partial t}$) is grouped in the left part of Equation 704. The simplified mass conservation law (Equation 44) is obtained.

3.2. Mathematical step of linear form of the simplified form of conservations laws

The linear form of the simplified form of the conservation laws are composed by the energy and mass linear forms (Equation 45 and Equation 46).

Section 3.2.1 and 3.2.2 respectively describes the mathematical step to obtain the linear form of the simplified for of the energy and mass conservation laws.

3.2.1. Mathematical step of linear form of the simplified form of energy conservations law

The simplified form of the overall energy conservation law (Equation 43) can be written as follows:

Equation 705
$$\sum_{i=L,V}\left\{m^i\cdot\frac{\partial P^V}{\partial t}\cdot\left[C_{P_S}^i\cdot\left.\frac{\partial T}{\partial P^V}\right|_S+\left.\frac{\partial\tilde{h}_S^i}{\partial P^V}\right|_T\right]\right\} +\dot{m}_N\cdot\Delta\widetilde{H}_{EV}-\dot{Q}-\dot{m}_{IN}^L\cdot\left[\tilde{h}_{IN}^L-\tilde{h}_S^L\right] -\dot{m}_{IN}^V\cdot\left[\tilde{h}_{IN}^V-\tilde{h}_S^V\right]=0$$

In Equation 705, the time-derivate of the liquid volume ($\frac{\partial V^L}{\partial t}$) can be added as follows:

Equation 706
$$\frac{\partial P^V}{\partial t}\cdot\sum_{i=L,V}\left\{m^i\cdot\left[C_{P_S}^i\cdot\left.\frac{\partial T}{\partial P^V}\right|_S+\left.\frac{\partial\tilde{h}_S^i}{\partial P^V}\right|_T\right]\right\}+\frac{\partial V^L}{\partial t}\cdot 0 +\dot{m}_N\cdot\Delta\widetilde{H}_{EV}-\dot{Q}-\dot{m}_{IN}^L\cdot\left[\tilde{h}_{IN}^L-\tilde{h}_S^L\right] -\dot{m}_{IN}^V\cdot\left[\tilde{h}_{IN}^V-\tilde{h}_S^V\right]=0$$

Equation 706 is composed by non-differential variables and differential variables. The non-differential variables are $\sum_{i=L,V}\left\{m^i\cdot\left[C_{P_S}^i\cdot\left.\frac{\partial T}{\partial P^V}\right|_S+\left.\frac{\partial\tilde{h}_S^i}{\partial P^V}\right|_T\right]\right\}$, $\Delta\widetilde{H}_{EV}$, $-\left[\tilde{h}_{IN}^L-\tilde{h}_S^L\right]$, $-\left[\tilde{h}_{IN}^V-\tilde{h}_S^V\right]$, 0 and $-\dot{Q}$. These variables can be substituted with the coefficients of Table 42. So, the linear form of the simplified form of the overall energy conservation law (Equation 45) is obtained.

3.2.2. Mathematical step of linear form of the simplified form of mass conservations law

The overall mass conservation law (Equation 44) can be written as follows:

Equation 707
$$\frac{\partial P^V}{\partial t}\cdot\left\{\sum_{i=L,V}\left[V^i\cdot\left(\left.\frac{\partial\rho_S^i}{\partial T}\right|_{P^V}\cdot\left.\frac{\partial T}{\partial P^V}\right|_S+\left.\frac{\partial\rho_S^i}{\partial P^V}\right|_T\right)\right]\right\}+\frac{\partial V^L}{\partial t}\cdot\left(\rho_S^L-\rho_S^V\right)$$

$$-\dot{m}_{IN}^{L}+\dot{m}_{OUT}^{L}-\dot{m}_{IN}^{V}+\dot{m}_{BOG}=0$$

In Equation 707, the net mass flow can be added as follows:

Equation 708
$$\frac{\partial P^{V}}{\partial t}\cdot\left\{\sum_{i=L,V}\left[V^{i}\cdot\left(\left.\frac{\partial\rho_{S}^{i}}{\partial T}\right|_{P^{V}}\cdot\left.\frac{\partial T}{\partial P^{V}}\right|_{S}+\left.\frac{\partial\rho_{S}^{i}}{\partial P^{V}}\right|_{T}\right)\right]\right\}+\frac{\partial V^{L}}{\partial t}\cdot\left(\rho_{S}^{L}-\rho_{S}^{V}\right)$$
$$+\dot{m}_{N}\cdot 0-\dot{m}_{IN}^{L}+\dot{m}_{OUT}^{L}-\dot{m}_{IN}^{V}+\dot{m}_{BOG}=0$$

Equation 708 is composed by differential and non-differential variables. The non-differential variables are $\sum_{i=L,V}\left[V^{i}\cdot\left(\left.\frac{\partial\rho_{S}^{i}}{\partial T}\right|_{P^{V}}\cdot\left.\frac{\partial T}{\partial P^{V}}\right|_{S}+\left.\frac{\partial\rho_{S}^{i}}{\partial P^{V}}\right|_{T}\right)\right]$, $\left(\rho_{S}^{L}-\rho_{S}^{V}\right)$, 0, -1, 1, -1 and 1. These variables respectively multiplies $\frac{\partial P^{V}}{\partial t}$, $\frac{\partial V^{L}}{\partial t}$, $\dot{m}_{N}$, $\dot{m}_{IN}^{L}$, $\dot{m}_{OUT}^{L}$, $\dot{m}_{IN}^{V}$ and $\dot{m}_{BOG}$. These non-differentia variables can be substituted with the coefficients of Table 42. So, linear form of the simplified form of the overall mass conservation law (Equation 46) is obtained.

4. Mathematical step of pressure-liquid volume equations

The pressure-liquid volume (P-V^{L}) equations are divided into energy P-V^{L} equation (Equation 45) and the mass P-V^{L} equation (Equation 64).

Section 4.1 and 4.2 respectively describe the mathematical steps to obtain the mass P-V^{L} equation and the energy P-V^{L} equation.

4.1. Mathematical step of mass pressure-liquid volume equations

The mass pressure-liquid volume (P-V^{L}) equation (Equation 64) is obtained by removing the term $\dot{m}_{N}\cdot B_{MB}$ from Equation 46 because the coefficient B_{MB} is equal to zero (see Table 42).

4.2. Mathematical step of pressure-liquid volume energy equations

In the linear form of the simplified form of the energy conservation law (Equation 45), the net mass flow can be computed with the linear form of the net mass flow (NMF) equation (Equation 38). Hence, Equation 45 can be written as follows:

Equation 709
$$\frac{\partial P^{V}}{\partial t}\cdot A_{EB}-\left\{\left[\frac{\partial P^{V}}{\partial t}\cdot A_{MB}^{L}+\frac{\partial V^{L}}{\partial t}\cdot C_{MB}^{L}+\dot{m}_{IN}^{L}\cdot D_{MB}^{L}+\dot{m}_{OUT}^{L}\cdot E_{MB}^{L}\right]\right\}\cdot B_{EB}$$
$$+\frac{\partial V^{L}}{\partial t}\cdot C_{EB}+\dot{m}_{IN}^{L}\cdot D_{EB}^{L}+\dot{m}_{IN}^{V}\cdot D_{EB}^{V}$$
$$+\dot{m}_{OUT}^{L}\cdot E_{EB}^{L}+\dot{m}_{BOG}\cdot E_{EB}^{V}+F_{EB}=0$$

In Equation 709, the time-derivates $\frac{\partial P^{V}}{\partial t}$ and $\frac{\partial V^{L}}{\partial t}$, and the mass flows $\dot{m}_{IN}^{L}$ and $\dot{m}_{OUT}^{L}$ are grouped. Equation 709 can be written as follows:

Equation 710
$$\frac{\partial P^{V}}{\partial t}\cdot\left(A_{EB}-A_{MB}^{L}\cdot B_{EB}\right)+\frac{\partial V^{L}}{\partial t}\cdot\left(C_{EB}-C_{MB}^{L}\cdot B_{EB}\right)$$
$$+\dot{m}_{IN}^{L}\cdot\left(D_{EB}^{L}-D_{MB}^{L}\cdot B_{EB}\right)+\dot{m}_{IN}^{V}D_{EB}^{V}$$
$$+\dot{m}_{OUT}^{L}\cdot\left(E_{EB}^{L}+E_{MB}^{L}\cdot B_{EB}\right)+\dot{m}_{BOG}\cdot E_{EB}^{V}+F_{EB}=0$$

Equation 710 is composed by non-differential variables such as$\left(A_{EB}-A_{MB}^{L}\cdot B_{EB}\right)$, $\left(C_{EB}-C_{MB}^{L}\cdot B_{EB}\right)$, $\left(D_{EB}^{L}-D_{MB}^{L}\cdot B_{EB}\right)$ and $\left(E_{EB}^{L}-E_{MB}^{L}\cdot B_{EB}\right)$. These variables can be substituted with the coefficients of Table 44 and the energy P-V^{L} equation (Equation 63) is obtained.

5. Mathematical steps of pressure-evolution, liquid volume-evolution, inlet liquid flow and boil-off gas equations

The pressure evolution (P-e), liquid volume evolution (V^L-e), inlet liquid flow (ILF) and boil-off gas (BOG) equations (see Table 45) respectively computes the time-derivate of the pressure, the time-derivate of the liquid volume, the inlet liquid mass flow and the BOG flow during the steady state and the self-pressurisation. At the steady state (storage mode 1.b), the values of these derivates are equal to zero, as it is reported in Table 45. So, the pressure-liquid volume (P-V^L) equations are used to deduce the ILF and the BOG equations of the steady state (Equation 76 and Equation 74). During the self-pressurisation (storage mode 4), the inlet liquid mass flow and the BOG flow are equal to zero 0 because the storage container is closed. So, the P-V^L equations are used to deduce the P-e and the V^L-e equations of the self-pressurisation.

Section 5.1 describes the mathematical steps to obtain the ILF equation of the steady state. Section 5.2 explains the mathematical steps to deduce the BOG equation of the steady state. Section 5.3 presents the mathematical steps to obtain the V^L-e equation. Section 5.4 describes the mathematical steps to deduce the P-e equation.

5.1. Inlet liquid flow equation of the steady state

In the mass P-V^L equation (Equation 64), the term $\left(\frac{\partial P^V}{\partial t} \cdot A_{MB} + B_{MB} + \frac{\partial V^L}{\partial t} \cdot C_{MB} + \dot{m}_{IN}^V \cdot D_{MB}^V + \dot{m}_{OUT}^L \cdot E_{MB}^L + F_{MB}\right)$ is substituted with the coefficient Z_{MB}, which is computed with Equation 86. The mass P-V^L equation can be written as follows:

Equation 711 $$\dot{m}_{IN}^L \cdot D_{MB}^L + \dot{m}_{BOG} \cdot E_{MB}^V + Z_{MB} = 0$$

The term $(\dot{m}_{BOG} \cdot E_{MB}^V + Z_{MB})$ is moved to the right part of Equation 711. Equation 711 can be written as follows:

Equation 712 $$\dot{m}_{IN}^L \cdot D_{MB}^L = -(\dot{m}_{BOG} \cdot E_{MB}^V + Z_{MB})$$

The left and the right part of Equation 712 are divided by D_{MB}^L. Equation 712 can be written as follows:

Equation 713 $$\dot{m}_{IN}^L = -\frac{1}{D_{MB}^L} \cdot [\dot{m}_{BOG} \cdot E_{MB}^V + Z_{MB}]$$

The term $-\frac{E_{MB}^V}{D_{MB}^L}$ and $-\frac{Z_{MB}}{D_{MB}^L}$ are respectively substituted by the coefficients D''_{MB} and Z''_{MB}. These coefficients can be respectively computed with Equation 81 and with Equation 83. Then, the Inlet liquid flow (ILF) equation (Equation 76) is obtained.

5.2. Boil-off gas equation of the steady state

In the energy P-V^L equation (Equation 63), The term $\left(\frac{\partial P^V}{\partial t} \cdot A'_{EB} + B_{EB} + \frac{\partial V^L}{\partial t} \cdot C'_{EB} + \dot{m}_{IN}^V \cdot D_{MB}^V + \dot{m}_{OUT}^L \cdot E'^L_{EB} + F_{EB}\right)$ of is substituted by the coefficients Z_{EB}, which is calculated with Equation 85. The energy P-V^L equation can be written as follows:

Equation 714 $$\dot{m}_{IN}^{L} \cdot D'^{L}_{EB} + \dot{m}_{BOG} \cdot E_{EB}^{V} + Z_{EB} = 0$$

In Equation 714, the inlet liquid mass flow ($\dot{m}_{IN}^{L}$) can be computed with the inlet liquid flow (ILF) equation (Equation 76). Equation 714 can be written as follows:

Equation 715 $$[\dot{m}_{BOG} \cdot D''_{MB} + Z''_{MB}] \cdot D'^{L}_{EB} + \dot{m}_{BOG} \cdot E_{EB}^{V} + Z_{EB} = 0$$

The mass flow $\dot{m}_{BOG}$ is grouped in the left term of Equation 715. Equation 715 can be written as follows:

Equation 716 $$Z''_{MB} \cdot D'^{L}_{EB} + \dot{m}_{BOG} \cdot (E_{EB}^{V} + D''_{MB} \cdot D'^{L}_{EB}) + Z_{EB} = 0$$

In Equation 716, the terms $(E_{EB}^{V} + D''_{MB} \cdot D'^{L}_{EB})$ and $(Z''_{MB} \cdot D'^{L}_{EB} + Z_{EB})$ are respectively substituted by the coefficients E''^{V}_{EB} and Z''^{L}_{EB}. These coefficients are respectively computed with Equation 77 and with Equation 79. Equation 716 can be written as follows:

Equation 717 $$\dot{m}_{BOG} \cdot E''^{V}_{EB} + Z''^{L}_{EB} = 0$$

The coefficient Z''^{L}_{EB} is moved to the right part of Equation 717 and the whole Equation 717 is divided by E''^{V}_{EB}. Then, the Boil-off Gas (BOG) equation (Equation 74) is obtained.

5.3. Liquid-volume evolution equation of the self-pressurisation

In the mass pressure-liquid volume (P-V^{L}) equation (Equation 64), The term $(\dot{m}_{IN}^{L} \cdot D_{MB}^{L} + \dot{m}_{IN}^{V} \cdot D_{MB}^{V} + \dot{m}_{OUT}^{L} \cdot E_{MB}^{L} + \dot{m}_{BOG} \cdot E_{MB}^{V} + F_{MB})$ can be substituted with the by the coefficients Z_{MB}. This coefficient is computed with Equation 88. The P-V^{L} equation can be written as follows:

Equation 718 $$\frac{\partial P^{V}}{\partial t} \cdot A_{MB} + \frac{\partial V^{L}}{\partial t} \cdot C_{MB} + Z_{MB} = 0$$

The term $(\frac{\partial P^{V}}{\partial t} \cdot A_{MB} + Z_{MB})$ is moved to the right part of Equation 718. Equation 718 can be written as follows:

Equation 719 $$\frac{\partial V^{L}}{\partial t} \cdot C_{MB} = -\left(\frac{\partial P^{V}}{\partial t} \cdot A_{MB} + Z_{MB}\right)$$

The right part of Equation 719 is divided by C_{MB}. Equation 719 can be written as follows:

Equation 720 $$\frac{\partial V^{L}}{\partial t} = -\frac{1}{C_{MB}} \cdot \left(\frac{\partial P^{V}}{\partial t} \cdot A_{MB} + Z_{MB}\right)$$

In Equation 720, the terms $-\frac{A_{MB}}{C_{MB}}$ and $-\frac{Z_{MB}}{C_{MB}}$ are respectively substituted by coefficients A''_{MB} and Z''_{MB}. These coefficients are respectively computed with Equation 82 and with Equation 84. Then, the liquid-volume evolution (V^{L}-e) equation (Equation 71) is obtained.

5.4. Pressure evolution equation of the self-pressurisation

In the energy pressure-liquid volume (P-V^{L}) equation (Equation 63), the term $(\dot{m}_{IN}^{L} \cdot D'^{L}_{EB} + \dot{m}_{IN}^{V} \cdot D_{EB}^{V} + \dot{m}_{OUT}^{L} \cdot E'^{L}_{EB} + \dot{m}_{BOG} \cdot E_{EB}^{V} + F_{EB})$ can be substituted by the coefficients Z_{EB}. This coefficient can be computed with Equation 87. The energy P-V^{L} equation can be computed as follows:

Equation 721

$$\frac{\partial P^V}{\partial t} \cdot A'_{EB} + \frac{\partial V^L}{\partial t} \cdot C'_{EB} + Z_{EB} = 0$$

In Equation 721, the time-derivate of the liquid volume ($\frac{\partial V^L}{\partial t}$) is substituted with the liquid-volume evolution (V^L-e) equation of the self-pressurisation (Equation 71). Equation 721 can be written as follows:

Equation 722

$$\frac{\partial P^V}{\partial t} \cdot A'_{EB} + \left(\frac{\partial P^V}{\partial t} \cdot A''_{MB} + Z''_{MB}\right) \cdot C'_{EB} + Z_{EB} = 0$$

The time-derivate of the pressure ($\frac{\partial P^V}{\partial t}$) is grouped in the left part of Equation 722. Equation 722 can be written as follows:

Equation 723

$$\frac{\partial P^V}{\partial t} \cdot (A'_{EB} + A''_{MB} \cdot C'_{EB}) + Z''_{MB} \cdot C'_{EB} + Z_{EB} = 0$$

In Equation 723, the terms $(A'_{EB} + A''_{MB} \cdot C'_{EB})$ and $(Z''_{MB} \cdot C'_{EB} + Z_{EB})$ are respectively substituted by the coefficients A''_{EB} and Z''_{EB}. These coefficients are respectively calculated with Equation 78 and with Equation 80. Equation 723 can be written as follows:

Equation 724

$$\frac{\partial P^V}{\partial t} \cdot A''_{EB} + Z''_{EB} = 0$$

In Equation 724, the coefficient Z''_{EB} is moved to the right and Equation 724 is divided by the coefficient A''_{EB}. Then, the pressure-evolution (P^V-e) equation (Equation 69) is obtained.

Appendix G

Reference models for thermo-physical properties

Section 1 describes the equations of thermodynamic models. Section 2 reports the coefficients of the equations of Section 1. Section 3 presents the equations to compute the transport properties. Section 4 reports the coefficients of equations of Section 3.

1. Equations of the thermodynamic models

The fundamental equations on Helmholtz free energy are based on the principles that:

a) The Helmholtz free energy is composed by an ideal gas part and a residual part, for pure fluid;
b) All the thermodynamic properties, in particular the ones of Table 49 of Section 4, can be obtained from the Helmholtz free energy with analytical formulas, as reported in Table 193.

The equation of Helmholtz free energy and the equations of the thermodynamic variables of Table 49 of Section 4 are reported in Table 193.

Table 193. Ideal gas isobaric heat capacity, ideal gas and residual Helmholtz free energy.

Properties	**Equations**	**Formulas**
Helmholtz free energy	Equation 725 [125]	$a(\rho,T) = a^o(\rho,T) + a^r(\rho,T)$
dimensionless form of Helmholtz free energy	Equation 726 [125]	$\alpha(\delta,\tau) = \alpha^o(\delta,\tau) + \alpha^r(\delta,\tau)$
	Nitrogen	
The ideal gas Helmholtz free energy	Equation 727 [126]	$\alpha^o = \ln(\delta) + a_1 \cdot \ln(\tau) + a_2 + a_3 \cdot \tau + \frac{a_4}{\tau} + \frac{a_5}{\tau^2} + \frac{a_6}{\tau^3} + a_7 \cdot \ln[1 - \exp(-a_8 \cdot \tau)]$
The residual of Helmholtz free energy	Equation 728 [126]	$\alpha^r(\delta,\tau) = \sum_{k=1}^{N} N_k \cdot \delta^{i_k} \cdot \tau^{j_k} + \sum_{k=7}^{N_2} N_k \cdot \delta^{i_k} \cdot \tau^{j_k} \cdot \exp(-\delta^{l_k}) + \sum_{k=33}^{N_3} N_k \cdot \delta^{i_k} \cdot \tau^{j_k} \cdot \exp[-\phi_k \cdot (\delta - 1)^2 - \beta_k \cdot (\tau - \gamma_k)^2]$
Ideal gas isobaric heat capacity	Equation 729 [126]	$\frac{C_P^0}{R} = a_0 + a_1 \cdot T + a_2 \cdot T^2 + a_3 \cdot T^3 + a_4 \cdot \frac{(u)^2 \cdot \exp(u)}{[\exp(u) - 1]^2}$
	Hydrogen (para, ortho and normal)	
The ideal gas Helmholtz free energy	Equation 730 [127]	$\alpha^o = \ln(\delta) + 1.5 \cdot \ln(\tau) + a_1 + a_2 \cdot \tau + \sum_{k=3}^{N} a_k \cdot \ln[1 - \exp(b_k \cdot \tau)]$
The residual of Helmholtz free energy	Equation 731 [127]	$\alpha^r(\delta,\tau) = \sum_{i=1}^{l} N_i \cdot \delta^{d_i} \cdot \tau^{t_i} + \sum_{i=l+7}^{m} N_i \cdot \delta^{d_i} \cdot \tau^{t_i} \cdot \exp(-\delta^{p_i}) + \sum_{i=m+1}^{n} N_i \cdot \delta^{d_i} \cdot \tau^{t_i} \cdot \exp[\varphi_i \cdot (\delta - D_i)^2 + \beta_i \cdot (\tau - \gamma_i)^2]$
Ideal gas isobaric heat capacity	Equation 732 [127]	$\frac{C_P^0}{R} = 2.5 + \sum_{k=1}^{7} u_k \cdot \left(\frac{v_k}{T}\right)^2 \cdot \frac{\exp\left(\frac{v_k}{T}\right)}{\left[\exp\left(\frac{v_k}{T}\right) - 1\right]^2}$

Table 193. Ideal gas isobaric heat capacity, ideal gas and residual Helmholtz free energy.

Thermodynamic properties of Table 49 of Section 4		
Specific enthalpy	Equation 733	$\frac{\tilde{h}(\delta,\tau)}{R\cdot T}=1+\tau\cdot\left(\left.\frac{\partial\alpha^{o}}{\partial\tau}\right\vert_{\delta}+\left.\frac{\partial\alpha^{r}}{\partial\tau}\right\vert_{\delta}\right)+\delta\cdot\left.\frac{\partial\alpha^{r}}{\partial\delta}\right\vert_{\tau}$
Latent heat of evaporation	Equation 734	$\Delta\tilde{H}_{EV}=\tilde{h}_S^V-\tilde{h}_S^L$
Isobaric heat capacity	Equation 735	$\frac{C_P(\delta,\tau)}{R}=-\tau^2\cdot\left(\left.\frac{\partial^2\alpha^0}{\partial\tau^2}\right\vert_{\delta}+\left.\frac{\partial^2\alpha^r}{\partial\tau^2}\right\vert_{\delta}\right)+\frac{\left(1+\delta\cdot\left.\frac{\partial\alpha^r}{\partial\delta}\right\vert_{\tau}-\delta\cdot\tau\cdot\left.\frac{\partial\left(\left.\frac{\partial\alpha^r}{\partial\delta}\right\vert_{\tau}\right)}{\partial\tau}\right\vert_{\delta}\right)^2}{1+2\cdot\delta\cdot\left.\frac{\partial\alpha^r}{\partial\delta}\right\vert_{\tau}+\delta^2\cdot\left.\frac{\partial^2\alpha^r}{\partial\delta^2}\right\vert_{\tau\tau}}$
Density	Equation 736	$\rho=\frac{P(\delta,\tau)}{R\cdot T\cdot\left[1+\delta\cdot\left.\frac{\partial\alpha^r}{\partial\delta}\right\vert_{\tau}\right]}$
Volume expansion coefficient	Equation 737	$\beta(\delta,\tau)=\frac{1}{T}\cdot\frac{1+\delta\cdot\left.\frac{\partial\alpha^r}{\partial\delta}\right\vert_{\tau}-\delta\cdot\tau\cdot\left.\frac{\partial\left(\left.\frac{\partial\alpha^r}{\partial\delta}\right\vert_{\tau}\right)}{\partial\tau}\right\vert_{\delta}}{1+2\cdot\delta\cdot\left.\frac{\partial\alpha^r}{\partial\delta}\right\vert_{\tau}+\delta^2\cdot\left.\frac{\partial^2\alpha^r}{\partial\delta^2}\right\vert_{\tau}}$
Saturation pressure	Equation 738	$\frac{P_S}{R\cdot T}\cdot\left(\frac{1}{\rho_S^V}-\frac{1}{\rho_S^L}\right)-\ln\left(\frac{\rho_S^L}{\rho_S^V}\right)=\alpha^r(\delta_S^L,\tau)-\alpha^r(\delta_S^V,\tau)$

The comments of equations of Table 193 are reported in Table 194.

Table 194. Comments of the equations of Table 193.

Equations	Comments
Equation 725	a, a^o and a^r are respectively the Helmholtz free energy, the Helmholtz free energy of ideal gas and the residual Helmholtz free energy of the fluid.
Equation 726	α, α^o and α^r are dimensionless form[127] of Helmholtz free energy, the Helmholtz free energy of ideal gas and the residual Helmholtz free energy of the fluid, respectively. δ and τ are respectively the reduced density[128] and inverse reduced temperature[129].
Equation 727	Equation 727 is obtained from the integration of Ideal gas isobaric heat capacity (Equation 729). The values of the coefficients $a_{i=1,\dots,8}$, in Equation 727 are reported in Table 197.
Equation 728	In Equation 728, N_k, i_k, j_k, l_k, ϕ_k, β_k and γ_k are the parameters and they obtained by interpolation with experimental data. The values of this are given Table 199.
Equation 729	u is equal to $\frac{3364.011}{T}$. T is the temperature. The values of the coefficients $a_{i=0,\dots,4}$ of Equation 729 are reported in Table 195.
Equation 730	Equation 730 is obtained from the integration of Ideal gas isobaric heat capacity (Equation 732). The coefficients $a_{k=1,\dots,N}$ and $b_{k=3,\dots,N}$ in Equation 730 and in Table 198.
Equation 731	In Equation 731, l, m, n are respectively 7, 9 and 14. N_i, d_i, t_i, p_i, φ_i, β_i, γ_i and D_i are experimentally regressed parameters that reported in Table 200.
Equation 732	The values of the parameters u_k and v_k of Equation 732 are reported Table 196.

---

[127] The dimensionless form is determined as $a/(R\cdot T)$

[128] The reduced density is computed as ρ/ρ_C, where ρ_C is the critical density.

[129] The inverse reduced temperature is calculated T_C/T, where T_C is the critical temperature.

Equation 729 and Equation 732 are obtained by regression of the experimental data. Equation 728 and Equation 731 are the residual form of the Helmholtz free energy. These residuals describe the deviation of the real behaviour of the fluid with respect to the ideal gas. The terms of the residual part of the equation are often empirical and loosely tied with theoretical models. The functional form of the residual is determined to yield the most accurate representation of the thermodynamic properties. An optimization procedure is often applied to obtain the residual form of Helmholtz free energy.

The three summation terms of Equation 728 and of Equation 731 individually are simple polynomial contribution, the combination of polynomials with exponential terms and the modified Gauss bell-shaped contribution. The latter is introduced to improve the description in the critical region. The Gaussian bell-shape of nitrogen and of normal hydrogen Helmholtz free energy residual are respectively described by the term $\exp[-\phi_k \cdot (\delta-1)^2 - \beta_k \cdot (\tau-\gamma_k)^2]$ and $\exp[\varphi_i \cdot (\delta-D_i)^2 + \beta_i \cdot (\tau-\gamma_i)^2]$.

The derivates of density and of the specific enthalpy can be deduced from Equation 736 and form Equation 733, respectively.

The tables are reported in Section 2.

2. Tables of thermodynamic model

The values of the parameters $a_{i=0,\dots,4}$ of Equation 729 are reported in Table 195.

Table 195. Values of coefficients Equation 729.

a_0	a_1	a_2	a_3	a_4
3.5	$3.066469 \cdot 10^{-6}$	$4.701240 \cdot 10^{-9}$	$-3.987984 \cdot 10^{-13}$	1.012941

Table 196 reports the values of the parameters u_k and v_k of Equation 732.

Table 196. Values of coefficients of Equation 732.

u_1	u_2	u_3	u_4	u_5
1.616	−0.4117	−0.792	0.758	1.217
v_1	v_2	v_3	v_4	v_5
531	751	1989	2484	6859

The values of the coefficients $a_{i=1,\dots,8}$, in Equation 727 are reported in Table 197.

Table 197. Values of coefficients of Equation 727.

a_1	a_2	a_3	a_4
2.5	-12.76952708	-0.00784163	$-1.934819 \cdot 10^{-4}$
a_5	a_6	a_7	a_8
$-1.247742 \cdot 10^{-5}$	$6.678326 \cdot 10^{-8}$	1.012941	26.65788

The coefficients $a_{k=1,\dots,N}$ and $b_{k=3,\dots,N}$ in Equation 730 and in Table 198.

Table 198. Values of coefficients of Equation 730.

a_1	a_2	a_3	a_4	a_5
-1.4485891134	1.884521239	4.30256	13.0289	-47.7365
a_6	a_7	a_8	a_9	/
50.0013	-18.6261	0.993973	0.536078	/
b_1	b_2	b_3	b_4	b_5
/	/	-15.1496751472	-25.0925982148	-294735563787
b_6	b_7	b_8	b_9	/
-35.4059141417	-40.724998482	-163.7925799988	-309.2173173842	/

In Equation 728, N_k, i_k, j_k, l_k, ϕ_k, β_k and γ_k are the parameters and they obtained by interpolation with experimental data and they are given Table 199.

Table 199. Values of coefficients of Equation 728.

Gaussian bell-shape of Equation 728.

k	ϕ_k	β_k	γ_k
33	20	325	1.16
34	20	325	1.16
35	15	300	1.13
36	25	275	1.25

First and second term of Equation 728

k	N_k	i_k	j_k	l_k
1	0.924803575275	1.0	0.25	0
2	-0.492448489428	1.0	0.875	0
3	0.66188336938	2.0	0.5	0
4	$-0.192902649201\cdot10^{1}$	2.0	0.875	0
5	$-0.622469309629\cdot10^{-1}$	3.0	0.375	0
6	0.349943957581	3.0	0.75	0
7	0.564857472498	1.0	0.5	1
8	$-0.161720005987\cdot10^{1}$	1.0	0.75	1
9	-0.481395031883	1.0	2.0	1
10	0.421150636384	3.0	1.25	1
11	$-0.161962230825\cdot10^{-1}$	3.0	3.5	1
12	0.172100994165	4.0	1.0	1
13	$0.735448924933\cdot10^{-2}$	6.0	0.5	1
14	$0.168077305479\cdot10^{-1}$	6.0	3.0	1
15	$-0.107626664179\cdot10^{-2}$	7.0	0.0	1
16	$-0.137318088513\cdot10^{-1}$	7.0	2.75	1
17	$0.635466899859\cdot10^{-3}$	8.0	0.75	1
18	$0.304432279419\cdot10^{-2}$	8.0	2.5	1
19	$-0.435762336045\cdot10^{-1}$	1.0	4.0	2
20	$-0.723174889316\cdot10^{-1}$	2.0	6.0	2
21	$0.389644315272\cdot10^{-1}$	3.0	6.0	2
22	$-0.212201363910\cdot10^{-1}$	4.0	3.0	2
23	$0.408822981509\cdot10^{-2}$	5.0	3.0	2
24	$-0.551990017984\cdot10^{-4}$	8.0	6.0	2
25	$-0.462016716479\cdot10^{-1}$	4.0	16.0	3
26	$-0.300311719011\cdot10^{-2}$	5.0	11.0	3
27	$0.368825891208\cdot10^{-1}$	5.0	15.0	3
28	$-0.255856846220\cdot10^{-2}$	8.0	12.0	3
29	$0.896915264558\cdot10^{-2}$	3.0	12.0	4
30	$-0.441513370350\cdot10^{-2}$	5.0	7.0	4
31	$0.133722294858\cdot10^{-2}$	6.0	4.0	4
32	$0.264832491957\cdot10^{-3}$	9.0	16.0	4
33	$0.193688194015\cdot10^{2}$	1.0	0.0	2
34	$-0.209115600730\cdot10^{2}$	1.0	1.0	2
35	$0.167788306989\cdot10^{-1}$	3.0	2.0	2
36	$0.262767566274\cdot10^{4}$	2.0	3.0	2

In Equation 731, l, m, n are respectively 7, 9 and 14. N_i, d_i, t_i, p_i, φ_i, β_i, γ_i and D_i are experimentally regressed parameters that reported in Table 200.

Table 200. Values of coefficients of Equation 731.

Gaussian bell-shape of Equation 731				
$\boldsymbol{i}$	$\boldsymbol{\phi_i}$	$\boldsymbol{\beta_i}$	$\boldsymbol{\gamma_i}$	$\boldsymbol{D_i}$
10	-1.7437	-0.194	0.8048	1.5487
11	-0.5516	-0.2019	1.5248	0.1785
12	-0.0634	-0.0301	0.06648	1.28
13	-2.1341	-0.2383	0.6832	0.6319
14	-1.777	-0.3253	1.493	1.7104
-1.777First and second terms of Equation 731				
$\boldsymbol{i}$	$\boldsymbol{N_i}$	$\boldsymbol{t_i}$	$\boldsymbol{d_i}$	$\boldsymbol{p_i}$
1	-7.33375	0.6855	1	0
2	0.01	1	4	0
3	2.60375	1	1	0
4	4.66279	0.489	1	0
5	0.682390	0.774	2	0
6	-1.47078	1.133	2	0
7	0.135801	1.386	3	0
8	-1.05327	1.619	1	1
9	0.328239	1.162	3	1
10	-0.00577833	3.96	2	/
11	0.0449743	5.276	1	/
12	0.0703464	0.99	3	/
13	-0.0401766	6.791	1	/
14	0.119510	3.19	1	/

The parameters reported in Table 195, Table 196, Table 199 and Table 200 are obtained from regression of experimental data. The coefficients in Table 197 and Table 198 are obtained from the integration of Equation 729 and Equation 732, respectively. Table 195, Table 197 and Table 199 are obtained from by Span et al. [126]. Table 196, Table 198 and Table 200 are taken form Leachman et al. [127].

3. Equations of transport properties

The transport properties of Table 49 of Section 4 are computed with the equations that are reported in Table 201.

Table 201. Equations to compute the transport properties.

Properties	**Equations**	**Formula**
Kinematic viscosity	Equation 739	$v = \frac{\eta}{\rho}$
Thermal diffusivity	Equation 740	$\alpha = \frac{k}{\rho \cdot C_P}$
LN_2-viscosity		
Dynamic viscosity	Equation 741 [128]	$\eta(\tau,\delta) = \eta^o(T) + \eta^r(\tau,\delta)$
Dilute gas viscosity	Equation 742 [128]	$\eta^o(T) = \frac{0.0266958 \cdot \sqrt{M \cdot T}}{\sigma^2 \cdot \Omega(T^*)}$
Collision integral	Equation 743 [128]	$\Omega(T^*) = \exp\left\{\sum_{i=0}^{4} b_i \cdot [\ln(T^*)]^i\right\}$
Residual of viscosity	Equation 744 [128]	$\eta^r(\tau,\delta) = \sum_{i=1}^{5} N_i \cdot \tau^{t_i} \cdot \delta^{d_i} \cdot \exp(-\gamma_i \cdot \delta^{l_i})$
LN_2-thermal conductivity		

Table 201. Equations to compute the transport properties.

Thermal conductivity	Equation 745 [128]	$\lambda(\tau,\delta) = \lambda^{o}(T) + \lambda^{r}(\tau,\delta) + \lambda^{c}(\tau,\delta)$
Dilute gas thermal conductivity	Equation 746 [128]	$\lambda^{o}(T) = N_1 \cdot \left[\frac{\eta^{o}(T)}{1\mu Pa \cdot s}\right] + N_2 \cdot \tau^{t_2} + N_3 \cdot \tau^{t_3}$
Residuals of thermal conductivity	Equation 747 [128]	$\lambda^{r}(\tau,\delta) = \sum_{i=4}^{n} N_i \cdot \tau^{t_i} \cdot \delta^{d_i} \cdot \exp(-\gamma_i \cdot \delta^{l_i})$
Critical enhancement of thermal conductivity	Equation 748 [143]	$\lambda^{c} = \rho \cdot C_P \cdot \frac{k \cdot R_0 \cdot T}{6 \cdot \pi \cdot \xi \cdot \eta(T,\rho)} \cdot (\tilde{\Omega} - \tilde{\Omega}_0)$
Parameter	Equation 749 [128]	$\tilde{\Omega} = \frac{2}{\pi} \cdot \left[\left(\frac{C_P - C_V}{C_P}\right) \cdot \tan^{-1}\left(\frac{\xi}{q_D}\right) + \frac{C_V}{C_p} \cdot \left(\frac{\xi}{q_D}\right)\right]$
Parameter	Equation 750 [128]	$\widetilde{\Omega_0} = \frac{2}{\pi} \cdot \left\{1 - \exp\left[-\frac{1}{\left(\frac{\xi}{q_D}\right)^{-1} + \frac{1}{3} \cdot \left(\frac{\xi}{q_D}\right)^{2} \cdot \left(\frac{\rho_C}{\rho}\right)^{2}}\right]\right\}$
Collision length	Equation 751 [128]	$\xi = \xi_0 \cdot \left[\frac{\tilde{\chi}(T,\rho) - \tilde{\chi}(T_{ref},\rho) \cdot \frac{T_{ref}}{T}}{\Gamma}\right]^{\frac{v}{\gamma}}$
Parameter	Equation 752 [128]	$\tilde{\chi}(T,\rho) = \frac{P_C \cdot \rho}{\rho_C^2} \cdot \frac{\partial \rho}{\partial P}\Big\vert_T$
LH$_2$-viscosity		
Viscosity	Equation 753 [129]	$\eta(T,\rho) = \eta_0(T) + \eta_1(T) \cdot \rho + c_1 \cdot \rho_r^2 \cdot \exp\left[c_2 \cdot T_r + \frac{c_3}{T_r} + \frac{c_4 \cdot \rho_r^2}{c_5 + T_r} + c_6 \cdot \rho_r^6\right]$
Zero-density limit	Equation 754 [129]	$\eta_0(T) = \frac{0.021357 \cdot (M \cdot T)^{0.5}}{\sigma^2 \cdot S(T^*)}$
Reduced effective cross section	Equation 755 [129]	$\ln[S(T^*)] = \sum_{i=0}^{4} a_i \cdot [\ln(T^*)]^{i}$
Excess contribution of the viscosity	Equation 756 [129]	$\eta_1(T) = \eta_0(T) \cdot \left[\sigma^3 \cdot \sum_{i=0}^{6} \frac{b_i}{T^*}\right]$
LH$_2$-thermal conductivity		
Thermal conductivity	Equation 757 [130]	$\lambda(T,\rho) = \lambda_0(T) + \Delta\lambda(T,\rho) + \Delta\lambda_c(T,\rho)$
Dilute gas limit of thermal conductivity	Equation 758 [130]	$\lambda_0(T) = \frac{\sum_{i=0}^{6} A_{1,i} \cdot \left(\frac{T}{T_c}\right)^{i}}{\sum_{i=0}^{3} A_{2,i} \cdot \left(\frac{T}{T_c}\right)^{i}}$
Excess thermal conductivity	Equation 759 [130]	$\Delta\lambda(T,\rho) = \sum_{i=0}^{5} \left\{\left[B_{1,i} + B_{2,i} \cdot \left(\frac{T}{T_c}\right)\right] \cdot \left(\frac{\rho}{\rho_c}\right)^{i}\right\}$
Critical enhancement of the thermal conductivity	Equation 760 [130]	$\Delta\lambda_c(T,\rho) = \frac{C_1}{C_2 + \left\lvert\frac{T}{T_c} - 1\right\rvert} \cdot \exp\left\{-\left[C_3 \cdot \left(\frac{\rho}{\rho_c} - 1\right)\right]^{2}\right\}$

Table 201. Equations to compute the transport properties.

Critical enhancement of the thermal conductivity	Equation 761 [130]	$\Delta\lambda_c(T,\rho) = \frac{\rho \cdot C_P \cdot R_D \cdot k_B \cdot T}{6 \cdot \pi \cdot \eta \cdot \xi} \cdot (\bar{\Omega} - \bar{\Omega}_0)$
Parameter	Equation 762 [130]	$\bar{\Omega} = \frac{2}{\pi} \cdot \left[\left(\frac{C_P - C_V}{C_P}\right) \cdot \arctan(\bar{q}_D \cdot \xi) + \frac{C_V}{C_P} \cdot \bar{q}_D \cdot \xi\right]$
Parameter	Equation 763 [130]	$\bar{\Omega}_0 = \frac{2}{\pi} \cdot \left\{1 - \exp\left[-\frac{1}{(\bar{q}_D \cdot \xi)^{-1} + \frac{\left(\bar{q}_D \cdot \xi \cdot \frac{\rho_c}{\rho}\right)^2}{3}}\right]\right\}$
Correlation length	Equation 764 [130]	$\xi = \xi_0 \cdot \left(\frac{P_c \cdot \rho}{\Gamma \cdot \rho_c^2}\right)^{\frac{v}{\gamma}} \cdot \left[\left.\frac{\partial\rho(T,\rho)}{\partial P}\right\|_T - \left(\frac{T_{ref}}{T}\right) \cdot \left.\frac{\partial\rho(T_{ref},\rho)}{\partial P}\right\|_T\right]^{\frac{v}{\gamma}}$

The comments of the equations of Table 201 are given in Table 202.

Table 202. Comments of the equations of Table 201.

Equations	**Comments**
Equation 743	$b_{1,\dots,4}$ are fitting parameters of Equation 743, whose values are reported in Table 203.
Equation 744	t_i, d_i, γ_i and l_i are parameters of Equation 744 and their values are reported in Table 204.
Equation 746 and Equation 747	N_1, N_2, N_3, t_2, t_3, t_i, d_i, γ_i and l_i are the parameters of Equation 746 and of Equation 747 and they are given in Table 208.
Equation 753	$c_{1,\dots,6}$ are the parameters of Equation 753 and they are reported in Table 205.
Equation 755	The coefficients a_i of Equation 755 are reported in Table 206.
Equation 756	The coefficients b_i of Equation 756 are reported in Table 207.
Equation 758	The values of the coefficients $A_{1,i}$ and $A_{2,i}$ of Equation 758 are given in Table 209.
Equation 759	The coefficients $B_{1,i}$ and $B_{2,i}$ of Equation 759 are reported in Table 210.
Equation 765 [128]	σ is the Lennard-Jones size parameter and it is equal to $0.3656\ nm$. M is the molecular weight and it is equal to $28.01348\ g/mol$.
Equation 766 [128]	T^* is the reduced temperature[130], which is computed with the Lennard-Jones energy parameter. This parameter is compute as $\frac{\varepsilon}{k}$ and its value is $98.94\ K$.
Equation 767 [143]	k is the Boltzmann's constant and it is equal to $1.380658 \cdot 10^{-23} J/K$. $R_0$is the theoretically based constant, whose value is 1.01. λ^c is zero when the terms in the brackets of Equation 751 is negative or zero
Equation 768 [128]	q_D is a fluid-specific term that is equal to $0.4\ nm$. This value is obtained by regression with experimental data.
Equation 769 [128]	ρ_C is the critical density of nitrogen, whose value is $11.1839\ mol/dm^3$.
Equation 770 [128]	v and γ are the theoretically based constants, whose values are 0.63 and 1.2415. $\xi_0$and Γ are the fluid-specific terms, whose values are $0.17\ nm$ and 0.055, respectively. These values are obtained by fitting the experimental data. T_{ref} is the reference temperature[131].

---

[130] The reduced temperature is determined as $\frac{k_B \cdot T}{\varepsilon}$.

[131] The reference temperature is calculated as $2 \cdot T_c$ In Equation 751, where T_C is the critical temperature, whose value is $126.192\ K$. In Equation 764, this variable is computed as $\frac{3}{2} \cdot T_c$ and T_c is equal to $49.407\ K$.

Table 202. Comments of the equations of Table 201.

Equation 771 [129]	T_r and ρ_r are respectively the scaled temperature[132] and the scaled density[133].
Equation 772 [129]	M is the molar mass, whose value is $2.01588\frac{g}{mol}$ for hydrogen. σ is the length scaling parameter and it is equal to $0.297\ nm$.
Equation 773 [129]	T^* is the reduced temperature, but it is computed with the value of $30.41\ K$ of the Lennard-Jones energy parameter.
Equation 774 [130]	Equation 760 is applied away the critical point. C_1, C_2 and C_3 are parameters, whose values are $3.57 \cdot 10^{-4}\frac{W}{m \cdot K}$, $-2.46 \cdot 10^{-2}\frac{W}{m \cdot K}$ and 0.2.
Equation 775 [130]	Equation 761 is used when the temperature is near to the critical point, around 5-10K
Equation 776 [130]	$\bar{q}_D^{-1}$ is the effective wave-number cut-off, whose values is $5.0 \cdot 10^{-10} m$. This parameter is obtained by fitting the experimental data of thermal conductivity in supercritical region.
Equation 777 [130]	ρ_c is the critical density of hydrogen, whose value is 31.323 kg/m^3.
Equation 778 [130]	ξ_0 and Γ are the system-dependent amplitudes, whose values are $1.5 \cdot 10^{-10} m$ and 0.052. P_c is the critical pressure, whose value is 1.2858 MPa

The tables are reported in Section 4.

4. Tables of transport property model

$b_{1,\ldots,4}$ are fitting parameters of Equation 743, whose values are reported in Table 203.

Table 203. Values of coefficients of Equation 743.

b_0	b_1	b_2	b_3	b_4
0.431	-0.4623	0.08406	0.005341	-0.00331

t_i, d_i, γ_i and l_i are parameters of Equation 744 and their values are reported in Table 204.

Table 204. Values of coefficients of Equation 744.

i	N_i	t_i	d_i	l_i	γ_i
1	10.72	0.1	2	0	0
2	0.03989	0.25	10	1	1
3	0.001208	3.2	12	1	1
4	−7.402	0.9	2	2	1
5	4.620	0.3	1	3	1

$c_{1,\ldots,6}$ are the parameters of Equation 753 and they are reported in Table 205.

Table 205. Values of coefficients of Equation 753.

c_1	c_2	c_3
6.43449673	$4.56334068 \cdot 10^{-02}$	$2.32797868 \cdot 10^{-01}$
c_4	c_5	c_6
$9.58326120 \cdot 10^{-01}$	$1.27941189 \cdot 10^{-01}$	$3.63576595 \cdot 10^{-01}$

The coefficients a_i of Equation 755 are reported in Table 206.

Table 206. Values of coefficients of Equation 755.

a_0	a_1	a_2	a_3	a_4
$2.09630 \cdot 10^{-1}$	$-4.55274 \cdot 10^{-1}$	$1.43602 \cdot 10^{-1}$	$-3.35325 \cdot 10^{-2}$	$2.76981 \cdot 10^{-3}$

The coefficients b_i of Equation 756 are reported in Table 207.

Table 207. Values of coefficients of Equation 756.

b_0	b_1	b_2	b_3	b_4	b_5	b_6

---

[132] The scaled temperature is defined as $^{T}/_{T_c}$, where T_c is the critical temperature whose value is $33.145\ K$.

[133] The scaled density is defined as $^{\rho}/_{\rho_c}$, where ρ_c is the critical temperature whose value is $90.5\frac{kg}{m^3}$.

−0.1870	2.4871	3.7151	−11.0972	9.0965	−3.8292	0.5166

N_1, N_2, N_3, t_2, t_3, t_i, d_i, γ_i and l_i are the parameters of Equation 746 and of Equation 747 and they are given in Table 208.

Table 208. Values of coefficients of Equation 746 and of Equation 747.

i	N_i	t_i	d_i	l_i	γ_i
1	1.511	/	/	/	/
2	2.117	-1.0	/	/	/
3	−3.332	-0.7	/	/	/
4	8.862	0.0	1	0	0
5	31.11	0.03	2	0	0
6	−73.13	0.2	3	1	1
7	20.03	0.8	4	2	1
8	−0.7096	0.6	8	2	1
9	0.2672	1.9	10	2	1

The values of the coefficients $A_{1,i}$ and $A_{2,i}$ of Equation 758 are given in Table 209.

Table 209. Values of coefficients of Equation 758.

i	$A_{1,i}$	$A_{2,i}$
0	$-3.409\ 76\cdot10^{-1}$	$1.384\ 97\cdot10^{2}$
1	$4.588\ 20\cdot10^{0}$	$-2.218\ 78\cdot10^{1}$
2	$-1.450\ 80\cdot10^{0}$	$4.571\ 51\cdot10^{0}$
3	$3.263\ 94\cdot10^{-1}$	$1.000\ 00\cdot10^{0}$
4	$3.169\ 39\cdot10^{-3}$	/
5	$1.905\ 92\cdot10^{-4}$	/
6	$-1.139\ 00\cdot10^{-6}$	/

The coefficients $B_{1,i}$ and $B_{2,i}$ of Equation 759 are reported in Table 210.

Table 210. Values of coefficients of Equation 759.

i	$B_{1,i}$	$B_{2,i}$
1	$3.630\ 81\cdot10^{-2}$	$1.833\ 70\cdot10^{-3}$
2	$-2.076\ 29\cdot10^{-2}$	$-8.867\ 16\cdot10^{-3}$
3	$3.148\ 10\cdot10^{-2}$	$1.582\ 60\cdot10^{-2}$
4	$-1.430\ 97\cdot10^{-2}$	$-1.062\ 83\cdot10^{-2}$
5	$1.749\ 80\cdot10^{-3}$	$2.806\ 73\cdot10^{-3}$

Table 203, Table 204, Table 205, Table 206, Table 207 Table 208, Table 209 and Table 210 are obtained by regression of the experimental data. Table 203, Table 204 and Table 208 are obtained from Lemmon and Jacobsen [128]. Table 205, Table 206 and Table 207 are taken from Muzny et al. [129]. Table 209 and Table 210 is obtained from Assael et al. [130].

Appendix H

Ordinary Differential Equations Solver

The mathematical system of the equilibrium model (EQ model) is composed by differential equations. Runge-Kutta-Fehlberg with Cash-Karp parameters[131] (RKF-CKp) method is used to solve the Ordinary Differential Equations (ODEs) system of the EQ model, as explained in Section 5. This method computes the approximate solution, the integration time-step and other variables. The equations used and the variables computed are reported in Table 211.

Table 211. Equations of the RKF-CKp method.

Variable	Symbol	Equation	Formula
approximate solution of variable “n” at time-point t_i	$\tilde{y}_{n,i}$	Equation 779 [131]	$\tilde{y}_{n,i} = \tilde{y}_{n,i-1} + dt_i \cdot \sum_{j=1}^{6} c_j \cdot \left.\frac{\partial y}{\partial t}\right\|_{j,n}$
derivates at each time-sub step “0”[134] of variable “n”	$\left.\frac{\partial y}{\partial t}\right\|_{0,n}$	Equation 780 [131]	$\left.\frac{\partial y}{\partial t}\right\|_{0,n} = \left.\frac{\partial y}{\partial t}\right\|_{i-1,n}$
derivates at each time-sub step “1” of variable “n”	$\left.\frac{\partial y}{\partial t}\right\|_{1,n}$	Equation 781 [131]	$\left.\frac{\partial y}{\partial t}\right\|_{1,n} = f\left(t_{i-1} + a_1 \cdot dt_i; y_{n,i-1} + dt_i \cdot b_{1,0} \cdot \left.\frac{\partial y}{\partial t}\right\|_{0,n}\right)$
derivates at each time-sub step “2” of variable “n”	$\left.\frac{\partial y}{\partial t}\right\|_{2,n}$	Equation 782 [131]	$\left.\frac{\partial y}{\partial t}\right\|_{2,n} = f\left(t_{i-1} + a_2 \cdot dt_i; y_{n,i-1} + dt_i \cdot \sum_{s=0}^{1} b_{2,s} \cdot \left.\frac{\partial y}{\partial t}\right\|_{s,n}\right)$
derivates at each time-sub step “3” of variable “n”	$\left.\frac{\partial y}{\partial t}\right\|_{3,n}$	Equation 783 [131]	$\left.\frac{\partial y}{\partial t}\right\|_{3,n} = f\left(t_{i-1} + a_3 \cdot dt_i; y_{n,i-1} + dt_i \cdot \sum_{s=0}^{2} b_{3,s} \cdot \left.\frac{\partial y}{\partial t}\right\|_{s,n}\right)$
derivates at each time-sub step “4” of variable “n”	$\left.\frac{\partial y}{\partial t}\right\|_{4,n}$	Equation 784 [131]	$\left.\frac{\partial y}{\partial t}\right\|_{4,n} = f\left(t_{i-1} + a_4 \cdot dt_i; y_{n,i-1} + dt_i \cdot \sum_{s=0}^{3} b_{4,s} \cdot \left.\frac{\partial y}{\partial t}\right\|_{s,n}\right)$
derivates at each time-sub step “5” of variable “n”	$\left.\frac{\partial y}{\partial t}\right\|_{5,n}$	Equation 785 [131]	$\left.\frac{\partial y}{\partial t}\right\|_{5,n} = f\left(t_{i-1} + a_5 \cdot dt_i; y_{n,i-1} + dt_i \cdot \sum_{s=0}^{4} b_{5,s} \cdot \left.\frac{\partial y}{\partial t}\right\|_{s,n}\right)$
Integration time-step	$\tilde{y}^*_{n,i}$	Equation 786 [131]	$dt_i = \max \begin{bmatrix} 0.9 \cdot dt_{0,i} \cdot [\Delta_{MAX}]^{-0.25} \\ 0.1 \cdot dt_{0,i} \end{bmatrix}$
the maximum allowable error	Δ_{MAX}	Equation 787 [131]	$\Delta_{MAX} = \max \left[\frac{\Delta_n}{\Delta_{MAX,n}}\right]$
numerical error of variable “n”	Δ_n	Equation 788 [131]	$\Delta_n = \tilde{y}_{n,i} - \tilde{y}^*_{n,i}$
embedded solution of the variable “n”	$\tilde{y}^*_{n,i}$	Equation 789 [131]	$\tilde{y}^*_{n,i} = \tilde{y}_{n,i-1} + dt_i \cdot \sum_{j=1}^{6} c^*_j \cdot \left.\frac{\partial y}{\partial t}\right\|_{j,n}$
the maximum allowable error of the variable “n”	$\Delta_{MAX,n}$	Equation 790 [131]	$\Delta_{MAX,n} = \varepsilon \cdot \tilde{y}_{n,i-1}$
Integration time-step for the next time-point	dt_{i+1}	Equation 791 [131]	$dt_{i+1} = \min \begin{bmatrix} 0.9 \cdot dt_i \cdot [\Delta_{MAX}]^{-0.2} \\ 5 \cdot dt_i \end{bmatrix}$
First guess value of integration time-step at the first time-point 1	$dt_{0,1}$	Equation 792	$dt_{0,1} = \min \left[\frac{\Delta_{MAX,n}}{\left.\frac{\partial y}{\partial t}\right\|_{0,n}}\right]$

Equation 792 is determined by the author of this thesis. The comments of equations of Table 211 are given in Table 212.

Table 212. Comments of equations of RKF-CKp method (Table 211).

Equation	Comments
Equation 779	$\tilde{y}_{n,i-1}$ is the approximated solutions of the “n” variable at the previous time-point “t_{i-1}”. dt_i is the current time step and c_i is the values of one of the ith Cash-Karp parameter. Cash-Karp parameters reported in Table 213.

---

[134] Time-sub-space-point “0” is the previous time-point t_{i-1}

Table 212. Comments of equations of RKF-CKp method (Table 211).

Equation 780, Equation 781, Equation 782, Equation 783, Equation 784 and Equation 785	$b_{j,s}$ and a_j the Cash-Karp parameters and they are given in Table 213.
Equation 786	$dt_{0,i}$ is the first guess value of the current time-step. 0.9 is a safety factor. The exponent 0.25 is used because the maximum error has an implicit scaling with dt_i. dt_i is taken as maximum value to avoid small increment of this variable when Δ_{MAX} becomes very big.
Equation 787	Δ_{MAX} is computed as maximum of all the maximum allowable error of the variable "n".
Equation 790	ε is the relative tolerance
Equation 791	dt_{next} is taken as minimum value to avoid large increment of this variable when Δ_{MAX} becomes very small.
Equation 792	$\left.\frac{\partial y}{\partial t}\right\|_{0,n}$ is the value of the derivate at the initial time-point

Cash-Karp parameters reported in Table 213.

Table 213. Cash-Karp parameters.

j	$\boldsymbol{a_j}$	$\boldsymbol{b_{j,s}}$					$\boldsymbol{c_j}$	$\boldsymbol{c_j^*}$
0	/	/	/	/	/	/	$\frac{37}{378}$	$\frac{2825}{27648}$
1	$\frac{1}{5}$	$\frac{1}{5}$	/	/	/	/	0	0
2	$\frac{3}{10}$	$\frac{3}{40}$	$\frac{9}{40}$	/	/	/	$\frac{250}{621}$	$\frac{18575}{48384}$
3	$\frac{3}{5}$	$\frac{3}{10}$	$-\frac{9}{10}$	$\frac{6}{5}$	/	/	$\frac{125}{594}$	$\frac{13525}{55296}$
4	1	$-\frac{11}{54}$	$\frac{5}{2}$	$-\frac{70}{27}$	$\frac{35}{27}$	/	0	$\frac{277}{14336}$
5	$\frac{7}{8}$	$\frac{1631}{55296}$	$\frac{175}{13824}$	$\frac{575}{13824}$	$\frac{44275}{110592}$	$\frac{253}{4096}$	$\frac{512}{1771}$	$\frac{1}{4}$

Appendix I

Algorithm of the numerical methods

This appendix describes the fundamental algorithms that are for the numerical procedure of the homogeneous model, and the numerical methods to compute the average value and the integration of the boundary layer.

Section 1 and 2 explains the numerical method of successive substation and of Newton-Raphson with finite difference, respectively. Section 3 discusses the trapezoidal rule for the numerical integration for computing the average value. Section 4 describes the Eulero method, which is used in the integration of the boundary layer.

1. Direct substitution method

The direct substitution method is a mathematical approach where the objective variable[135] is not obtained by analytically solving the objective function[136]. For this method, the objective function is implicit in the objective variable, as it is described in Equation 793.

Equation 793
$$f(x, g_{i=1,\dots,N}(x)) = 0$$

x is the objective variable, f is the objective function and $g_{i=1,\dots,N}$ are secondary functions that depends on the objective variable. Equation 793 indicates that the objective function directly depends on the objective variable and it is indirectly function of this variable through the secondary functions. The direct substitution method can be described by a general procedure. This procedure is described in Figure 207.

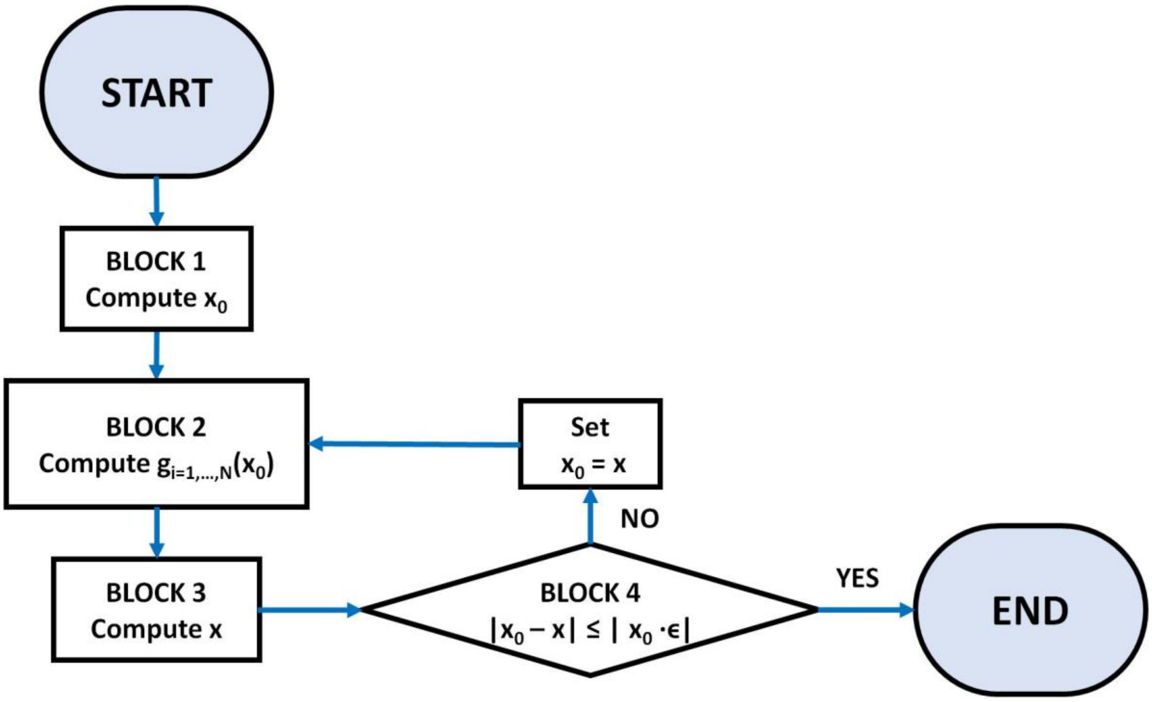

Figure 207. Algorithm of direct substitution method.

The algorithm is composed by the following steps:

---

[135] The objective variable is the variable that is wanted.
[136] The objective function is the equation that is solved.

a) BLOCK 1. The first guess value of the objective variable (x_0) is calculated. This calculation is done by simplifying Equation 793 as far as possible;
b) BLOCK 2. The secondary functions ($g_{i=1,\dots,N}(x)$) are computed with x_0;
c) BLOCK 3. The value of the objective variable is computed with Equation 794.

Equation 794 $$x = f^{-1}(g_{i=1,\dots,N}(x_0))$$

f^{-1} is the reversed objective function. Equation 794 is obtained by reversing Equation 793;
d) BLOCK 4. The convergence is defined with Equation 795.

Equation 795 $$|x_0 - x| \leq |x_0 \cdot \varepsilon|$$

ε is the value of the relative tolerance. Two pathways are present:
- Pathway 1.4 (P 1.4): If Equation 795 is true, there is converge and the algorithm stops;
- Pathway 2.4 (P 2.4): If Equation 795 is false and the algorithm starts from Block 2 (step b) of Section 1 of Appendix F), after setting that x_0 is equal to x;

This method is sometime unstable when the secondary functions strongly change with the objective variable. This method requires a good first guess value to reduce the iterations.

2. Netwon-Rhapson method with finite difference method

Newton-Raphson method is a mathematical iterative procedure to numerically find the objective variable of an objective function. This approach is based on the idea that the objective variable can be computed by approximating the function with a line. As consequence, the objective variable can be found with Equation 796.

Equation 796 $$x = x_0 - \frac{f(x_0)}{f'(x_0)}$$

x_0 is the first guess value, $f(x_0)$ is the value of the equation at x_0 and $f'(x_0)$ is the value of the derivate of f at x_0.

$f'(x_0)$ cannot be analytically found. Hence, $f'(x_0)$ can be numerically estimated using with the finite difference method. With this approach, the derivate is approximated with the incremental ratio. As consequence, $f'(x_0)$ is computed with Equation 797.

Equation 797 $$f'(x_0) = \frac{f(x_2) - f(x_1)}{x_2 - x_1}$$

x_2 and x_1 are the values of x near x_0, and they are called intermediate variables. $f(x_2)$ and $f(x_1)$ are respectively the values of f at x_2 and at x_1.

As consequence, the objective variable is determined with Equation 798.

Equation 798 $$x = x_1 - \frac{f(x_1)}{f(x_2) - f(x_1)} \cdot (x_2 - x_1)$$

Equation 798 is the key equation of the Newton-Raphson method with finite difference approach. The general procedure of this method is described in Figure 208.

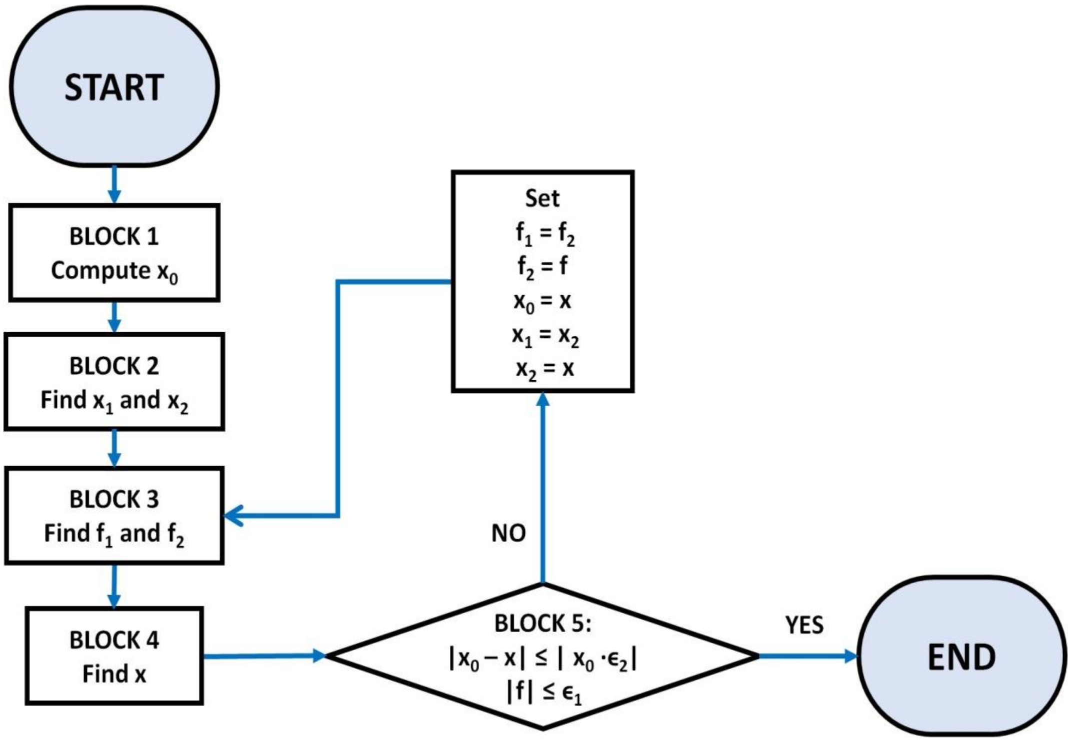

Figure 208. Algorithm of Newton-Raphson method with finite difference method.

The algorithm is composed by the following steps:

a) BLOCK 1. The first guess value (x_0) is calculated. This calculation is done by deducing a simplified formula from the objective function.
b) BLOCK 2. The intermediate variables x_2 and x_1 are computed;
c) BLOCK 3. The values of the objective function $f_2 = f(x_2)$ and $f_1 = f(x_1)$are determined;
d) BLOCK 4. The objective variable (x) is calculated with Equation 798;
e) BLOCK 5. The condition of convergence is calculated with Equation 799 and with Equation 800.

Equation 799 $$|f| \le \varepsilon_1$$

Equation 800 $$|x_0 - x| \le |x_0 \cdot \varepsilon_2|$$

Two pathways are present:

- Pathway 1.5 (P 1.5). Equation 799 and Equation 800 are true, the algorithm stops because convergence is reached;
- Pathway 2.5 (P 2.5). if Equation 799 is false or Equation 800 is false, the algorithm start from (step c) of Section 2 of Appendix F) because convergence is not reached. it is imposed that x_0, x_1, x_2, f_2 and f are respectively equal to x, x_2, x, f and f_1

This method quickly converges, but it often diverges. This divergence can be caused by the first guess value or by the approximation of the derivate with the finite difference method. The divergence is reduced when the first guess value is close to the value of the objective variable. When the derivate strongly change, this method diverges. Hence, constrains can be set to facilitate the convergence.

3. Trapezoidal rule

The trapezoidal rule is a numerical method to integrate an function, called $f(x)$, in the interval defined by x_2 and x_1. This method consists of discretizing this interval in steps and to approximate the integral in each step as the area of a trapezoid. Hence, the numerical integral is calculated with Equation 801.

Equation 801
$$F_2 - F_1 = \int_{x_1}^{x_2} f(x) \cdot dx = \sum_{i=1}^{N_S} (f_i + f_{i+1}) \cdot \frac{dx}{2}$$

dx is the size of the step and N_S is the number of the steps. f_i and f_{i+1} are respectively the values of the function f at point x_i and x_{i+1}. The point x_{i+1} is computed as $x_i + dx$.

4. Explicit Eulero method

The explicit Eulero method is a numerical method to integrate and Ordinary Differential Equations System. This method approximate the solution at the step "$i + 1$" with Equation 802.

Equation 802
$$y_{i+1} = y_i + dx \cdot \left.\frac{\partial y}{\partial x}\right|_i$$

y_{i+1} is the approximated solution at step "$i + 1$" and y_i is the solution at the previous step "i". dx is the length of the step. $\left.\frac{\partial y}{\partial x}\right|_i$ is the derivate of y respect to x, at the point (y_i, x_i),

Appendix L

Algorithms of the homogeneous model

The homogeneous model is composed by algorithms to initialize the simulation, to calculate the relative tolerance of the solver of the Ordinary Differential Equations (ODEs) system, to pass from the steady state to the self-pressurisation mode and to calculate the liquid pressure.

Section 1 describes the Block 2 of the H model, which computes the number of sub-layer for start the simulation. Section 2 explains the Block 8 to compute the relative tolerance of the solver of the ODEs system. Section 3 presents the Block 12, which computes the condition of steady state. Section 4 explains the algorithm to compute the liquid pressure.

1. Algorithm of Block 2: the calculation of the number of sub-layers

As said in Section 1.3.1, the numbers of liquid and vapour sub-layers (N^L and N^V) are calculated with an iterative procedure. This iterative procedure minimizes the numerical error of mass flow rate in the boundary layer respect the defined value of the relative tolerance. The numerical errors and these numbers can be computed with the equations of Table 214.

Table 214. Equation of the algorithm of Block 2.

Variable	Name	Equation	Formula
numbers of liquid sub-layers	N^L	Equation 803	$N^L = round[N^L_{MAX} \cdot LF_0]$
numbers of vapour sub-layers	N^V	Equation 804	$N^V = round[N^V_{MAX} \cdot (1 - LF_0)]$
numerical error of the estimation of the mass flow rate in the boundary layer	Δm	Equation 805	$\Delta m = \dot{m}^{ref}_{BL} \cdot \varepsilon$

$\dot{m}^{ref}_{BL}$ is the reference value of the mass flow in the boundary layer. ε is the relative tolerance of the numerical error and its value is 10^{-4}. LF_0 is the initial value of the filling ratio. N^L_{MAX} and N^V_{MAX} are the maximum number of the sub-layer of liquid and vapour.

Section 1.1 presents the hypothesis of this algorithm. Section 1.2 describes the output and input. Section 1.3 explains the target variables and function. Section 1.4 presents the block structure of this algorithm.

1.1. Hypothesis

The algorithm minimizes the numerical error that is computed with Equation 805. When the values of heat input and of the length of the side wall are the largest values possible, the value of this error is the highest. Hence, some assumptions should be done to reproduce these conditions and they are:

a) The value of the internal pressure is 1 bar;
b) The liquid and the vapour are at saturation at the value of the internal pressure;
c) Liquid and vapour are isothermal and homogeneous;
d) The filling ratio is equal to 1 when the number of the liquid sub-layer is computed;
e) The filling ratio is equal to 0, if the number of the vapour sub-layer is calculated;
f) The value of the heat input at the side wall is equal to the value of the overall heat input;

The assumptions a) and b) are used to define the thermodynamic state for the calculation of the thermo-physical properties with the reference models (see Section 4 of Chapter 3). Assumption c) is done simplifies the fluid-dynamics, neglecting the effect of the bulk temperature gradient. Assumption d) and e) are applied to maximize the length of the liquid and vapour side wall, respectively. Section f) is used to maximize the heat leakage at the side wall. This leads to a more robust estimations of N_S^L and N_S^V.

1.2. Input and output variables

The input and the output variables of the algorithm of block 2 of the homogeneous model (H model) are reported in Table 215.

Table 215. Input and output variables of the algorithm of Block 2 of H model.

Variable	**Description**
Input	Initial value of the filling ratio (LF_0), relative tolerance of the numerical error (ε), geometry, overall heat input ($\dot{Q}_{IN}$), phase of the fluid and initial number of the sub-layer ($N_{MAX,0}^{V,L}$)
Output	the numbers of liquid and vapour sub-layers (N^L and N^V)

The value of $N_{MAX,0}^{V,L}$ is set to 80. The initial value of the filling ratio is the one used in the simulation. The value of the overall heat input can be computed with the Boil-Off Rate (BOR) model (see Section 6) or it can be defined by the user. If the results of the homogenous (H) model is compared with the experimental data, LF_0 is equal to the experimental value of the initial filling ratio and $\dot{Q}_{IN}$ is the equal to the experimental heat leakage rate.

1.3. Target variable and target function

The algorithm of block 2 of the homogeneous model (H model) is an iterative procedure that minimizes the numerical error of the mass flow rate in the boundary layer by increasing the number of the sub-layer. The target variable and the target function are reported in Table 216.

Table 216. Target variable and function of the algorithm of Block 2 of H model.

Target variable	**Target equation**	
	Equation	**Formula**
$N_{MAX}^{V,L}$	Equation 806	$f_T = \left\|\dot{m}_{BL} - \dot{m}_{BL,0}\right\| - (\dot{m}_{BL}^{ref} \cdot \varepsilon)$

f_T is the value of the target function. The first guess value of the mass flow rate in the boundary layer is $\dot{m}_{BL,0}$. The mass flow rate in the boundary layer is $\dot{m}_{BL}$.

1.4. Structure of the algorithm

The algorithm of block 2 of the homogeneous model (H model) requires the Storage Boundary Layer (SBL) model. The Integral Boundary Layer (IBL) approach can be instable due to the equation of the viscous forces of the laminar regime (Equation 181). The value of the mass flow rate in the boundary layer can be negative or equal to zero if the number of the sub-layer is too high. Hence, the increment of the number of the sub-layer at each iteration is controlled to avoid instability, using the equation of Table 217.

Table 217. Supplementary equations of The algorithm of block 2 of the H model.

Scope	**Equation**	**Formula**
Increase the number of sub-layer	Equation 807	$N_{MAX}^{V,L} = N_{MAX,0}^{V,L} + 2$
Control to avoid instability	Equation 808	$N_{MAX}^{V,L} = N_{MAX,0}^{V,L}$

The algorithm of block 2 of the homogeneous model (H model) is described in Figure 209.

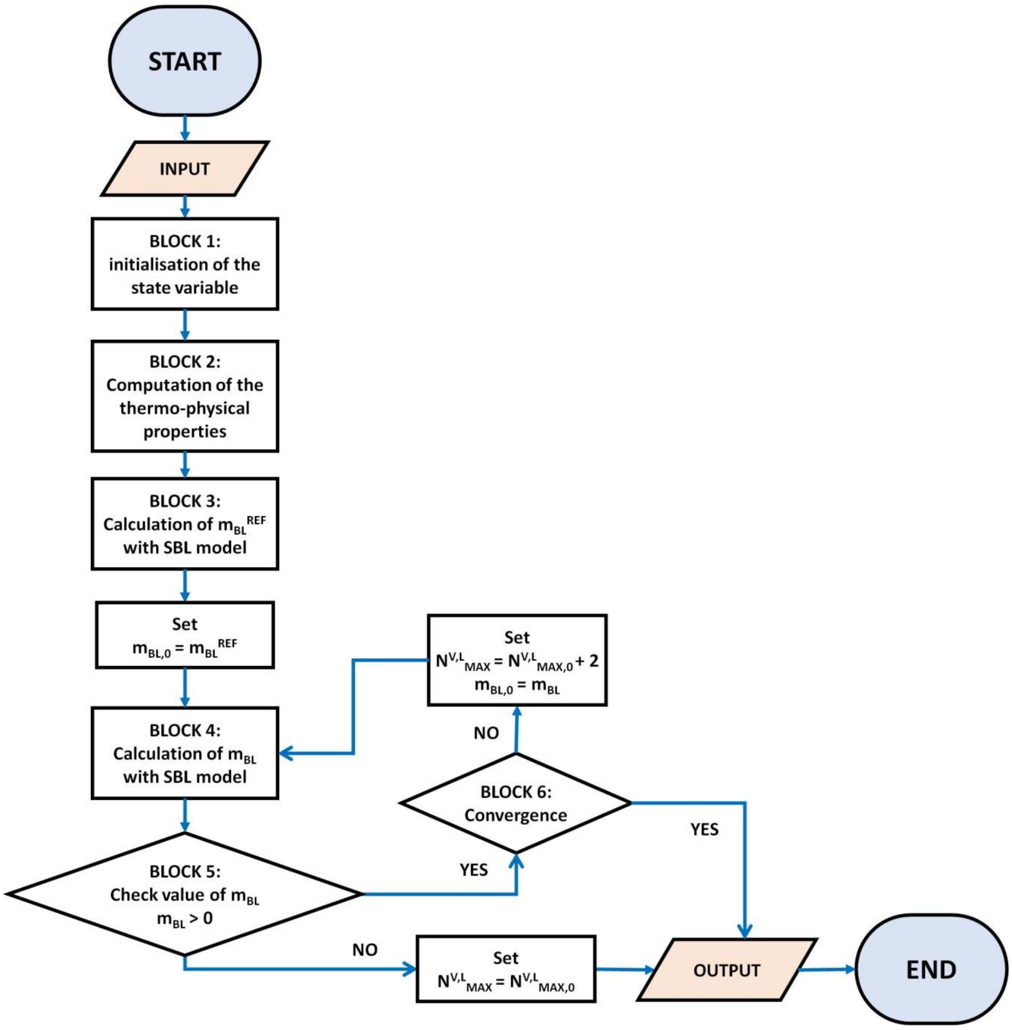

Figure 209. Algorithm of Block 2 of H model.

As it is illustrated in Figure 209, this algortimh is composed from the following steps:

a) BLOCK 1. The state variables (see Table 31) are initialized using hypotheses a), b), d) and e) of Section 1.1 of Appendix L;
b) Assumptions d) and e) are used when the phase of the fluid is liquid and vapour, respectively;
c) BLOCK 2. The thermo-physical variables are computed at the values of pressure and of temperatures that are defined in BLOCK 1 (step a) of Section 1.4). The reference models of Section 4 of Chapter 3 compute these variables;
d) BLOCK 3. The reference value of the mass flow rate in the boundary layer ($\dot{m}_{BL}^{ref}$) is computed with the Storage Boundary Layer (SBL) model (see Section 3). The Exact Boundary Layer (EBL) approach (see Section 3.3) is used and the value of the overall heat input is applied in this approach. Before moving to the next block, the first guess value of the mass flow rate in the boundary layer ($\dot{m}_{BL,0}$) is equal to $\dot{m}_{BL}^{ref}$;
e) BLOCK 4. The mass flow rate in the boundary layer ($\dot{m}_{BL}$) is computed with the SBL model with the Integral Boundary Layer (IBL) model (see Section 3.4). The value of the overall heat input is applied in this approach.
f) BLOCK 5. The stability control on the variable $\dot{m}_{BL}$ is done and two pathways are present:
    - Pathway 1.5 (P 1.5). If the value of mass flow rate in the boundary layer ($\dot{m}_{BL}$) is lower or equal to zero, the number of the sub-layer is equal to initial number of the sub-layer ($N_{MAX,0}^{V,L}$) (see Table 215). The algorithm stops;

  - Pathway 2.6 (P 2.5). When the value of $\dot{m}_{BL}$ is positive, the algorithm moves to Block 6 (step g) of Section 1.4);

g) BLOCK 6. The value of the target function (f_T) is computed with Equation 806. Two pathways are present as function of this value:
  - Pathway 1.6 (P 1.6). If f_T is negative or equal to zero, the algorithm stops because the minimisation of the target function is achieved;
  - Pathway 1.7 (P 1.7). If f_T is positive, the minimisation of the target function is not achieved. Hence, the number of the sub-layer is calculated with Equation 807 and first guess value of the mass flow rate in the boundary layer ($\dot{m}_{BL,0}$) is equal to the value of the mass flow rate in the boundary layer calculated in Block 4 (step e) of Section 1.4). Then, the algorithm moves to Block 4 (step e) of Section 1.4);

This algortimh requires 10 % of the overall computational time.

2. Algorithm of Block 8: calculation of the relative tolerance

The system of Ordinary Differential Equations (ODEs) of the homogeneous model (H model) (see Table 65) is numerically solved, in particular using the method of Runge-Kutta-Fehlberg with Cash-Karp parameters (RKF-CKp)[131], as done for the equilibrium model (EQ model) (see Section 5 of Chapter 3). Hence, the solution of this ODE system has a numerical error. This error can be reduced by decreasing the value of the relative tolerance. As this reduction is done, the computational time increases. In particular for the H model, this increment of the computational time is undesired because the computational of H model is potentially higher than the one of the EQ model, due to the due to the Storage Heat Transfer (SHT) and Storage Boundary Layer (SBL) models. So, the value of the relative tolerance should be increased when this numerical error is potentially lower and it should be reduced if this error is potentially higher. As consequence, a numerical procedure is developed using this compact of varying the value of the relative tolerance. This procedure is composed by two steps, respectively called *estimation of the maximum ratio* and the *selection of the relative tolerance*.

Section 2.1 explains the calculation of the maximum ratio. Section 2.2 presents the computation of the maximum known terms. Section 2.3 describes the criterion of selective the relative tolerance. Section 2.4 shows the algorithm.

2.1. Estimation of the maximum ratio

Low values of the relative tolerance are required when the values of time-derivate are high because the numerical error is potentially high. The value of the relative tolerance can be increased when the value of the time-derivates are low because the potential numerical error is low. Hence, a variable is required to estimate the condition at which the values of the derivates are high and low. This variable is the absolute maximum ratio of the time-derivates and it is estimated with the equations of Table 218.

Table 218. Equations to estimate the absolute maximum ratio of the time-derivates.

Variable	Name	Equation	Formula
Absolute maximum ratio of the time-derivates	Ω_{MAX}	Equation 809	$\Omega_{MAX} = \max[\Omega_n]$
Absolute maximum ratio of the time-derivate of variable "n"	Ω_n	Equation 810	$\Omega_n = \left\lvert \dfrac{\left.\frac{\partial y_n}{\partial t}\right\rvert_{t-1}}{\left.\frac{\partial y_n}{\partial t}\right\rvert_{MAX,t-1}} \right\rvert$

y_n is a general variable and it can be the pressure, the liquid volume, the liquid and the vapour temperature. $\left.\frac{\partial y}{\partial t}\right\rvert_{t-1}$ is the value of the time-derivate of the variable at the previous time-point ($t-1$)

and this value can be computed with the pressure-evolution, liquid volume-evolution, liquid temperature-evolution and vapour-temperature evolution equations (see Table 64), as function of the variable represented by y_n. $\left.\frac{\partial y_n}{\partial t}\right|_{MAX,t-1}$ is the maximum value of this time-derivate and it can be estimated with the equations of Table 219.

Table 219. Equations to compute $\left.\frac{\partial y_n}{\partial t}\right|_{MAX,t-1}$.

Variable	Name	Equation	Formula	Storage mode
maximum value of time-derivate of the pressure	$\left.\frac{\partial P^V}{\partial t}\right\|_{MAX,t-1}$	Equation 811	$\left.\frac{\partial P^V}{\partial t}\right\|_{MAX,t-1} = 0$	1.b
		Equation 812	$\left.\frac{\partial P^V}{\partial t}\right\|_{MAX,t-1} = -\frac{Z^P_{MAX} - Z^{HL}_{MAX} \cdot \frac{C'^P}{C'^{HL}}}{A'^P - A'^{HL} \cdot \frac{C'^P}{C'^{HL}}}$	4
maximum value of time-derivate of the liquid volume	$\left.\frac{\partial V^L}{\partial t}\right\|_{MAX,t-1}$	Equation 813	$\left.\frac{\partial V^L}{\partial t}\right\|_{MAX,t-1} = 0$	1.b
		Equation 814	$\left.\frac{\partial V^L}{\partial t}\right\|_{MAX,t-1} = -\frac{1}{C'^{HL}} \cdot \left[Z^{HL}_{MAX} + A'^{HL} \cdot \frac{\partial P^V}{\partial t}\right]$	4
time-derivate of the liquid temperature	$\left.\frac{\partial T^L}{\partial t}\right\|_{MAX,t-1}$	Equation 815	$\left.\frac{\partial T^L}{\partial t}\right\|_{MAX,t-1} = -\frac{1}{B^{TL}} \cdot \left[A^{TL} \cdot \left.\frac{\partial P^V}{\partial t}\right\|_{MAX,t-1} + C^{TL} \cdot \left.\frac{\partial V^L}{\partial t}\right\|_{MAX,t-1} + F^{TL}_{MAX}\right]$	1.b and 4
time-derivate of the vapour temperature	$\left.\frac{\partial T^V}{\partial t}\right\|_{MAX,t-1}$	Equation 816	$\left.\frac{\partial T^V}{\partial t}\right\|_{MAX,t-1} = -\frac{1}{B^{TV}} \cdot \left[A^{TV} \cdot \left.\frac{\partial P^V}{\partial t}\right\|_{MAX,t-1} + C^{TV} \cdot \left.\frac{\partial V^L}{\partial t}\right\|_{MAX,t-1} + F^{TV}_{MAX}\right]$	1.b and 4

The storage modes 1.b and 4 are respectively the steady state and the self-pressurisation. The coefficients B^{TL}, A^{TL}, C^{TL}, B^{TV}, A^{TV} and C^{TV}, and the coefficients C'^P, C'^{HL}, A'^P and A'^{HL} are reported in Table 42 and Table 72, respectively. The coefficients Z^{HL}_{MAX} and Z^P_{MAX} are computed as reported in Table 220.

Table 220. Equations for coefficients $\boldsymbol{Z^{HL}_{MAX}}$ and $\boldsymbol{Z^P_{MAX}}$.

Coefficients	Equation	Formula	Storage mode
Z^{HL}_{MAX}	Equation 817	$Z^{HL}_{MAX} = F'^{HL}_{MAX}$	4
Z^P_{MAX}	Equation 818	$Z^P_{MAX} = F'^P_{MAX}$	4

As reported in Table 220, the coefficients Z^{HL}_{MAX} and Z^P_{MAX} are calculated only for the storage mode 4 (self-pressurisation) because $\left.\frac{\partial P^V}{\partial t}\right|_{MAX,t-1}$ and $\left.\frac{\partial V^L}{\partial t}\right|_{MAX,t-1}$ are equal to zero for the storage mode 1.b (steady state), as respectively described by Equation 811 and by Equation 813. The coefficients F^{TV}_{MAX}, F^{TL}_{MAX}, F'^{HL}_{MAX} and F'^P_{MAX} are called the *maximum known terms*[137] and they calculated as described in Section 2.2 of Appendix L.

---

[137] The known term of an equation is the term that is not associated to any unknown.

2.2.Calculation of the maximum known terms

The pressure, the liquid volume, the liquid and vapour temperatures can increase or decreases during the storage of cryogenic liquids in small scale storage tanks. As consequence, the values of the time-derivates of these variables can be positive or negative. Hence, the maximum possible value of this derivate, thus the maximum known terms, should be computed with different equations if the value of the time-derivates increase or decrease. The increment and the decrement of the values of the time-derivates depends on the behaviour of the variables such as the interfacial heat transfer ($\dot{Q}_I^L$ and $\dot{Q}_I^V$), the net mass flow ($\dot{m}_N$), and the inlet and outlet flow rates ($\dot{m}_{IN}^L$, $\dot{m}_{OUT}^L$, $\dot{m}_{IN}^V$ and $\dot{m}_{BOG}$). So, the values of the coefficients F_{MAX}^{TV}, F_{MAX}^{TL}, ${F'}_{MAX}^{HL}$ and ${F'}_{MAX}^{P}$ are computed as function of the different conditions of the net mass flow, of interfacial heat transfers and of the outlet and inlet flow rates, as described by the equations of Table 221.

Table 221. Equations for coefficients $\boldsymbol{F_{MAX}^{TV}}$, $\boldsymbol{F_{MAX}^{TL}}$, $\boldsymbol{{F'}_{MAX}^{HL}}$ and $\boldsymbol{{F'}_{MAX}^{P}}$.

Coefficients	Equation	Formula	Condition
${F'}_{MAX}^{P}$	Equation 819	${F'}_{MAX}^{P} = F_1^P - [\dot{m}_{IN}^V]$	$\frac{\partial P^V}{\partial t} \geq 0$ $\dot{m}_{IN}^V \geq 0$ $\dot{m}_{BOG} \geq 0$
	Equation 820	${F'}_{MAX}^{P} = F_1^P - [\dot{m}_{IN}^V - \dot{m}_{BOG}]$	$\frac{\partial P^V}{\partial t} \geq 0$ $\dot{m}_{IN}^V \geq 0$ $\dot{m}_{BOG} < 0$
	Equation 821	${F'}_{MAX}^{P} = F_1^P$	$\frac{\partial P^V}{\partial t} \geq 0$ $\dot{m}_{IN}^V < 0$ $\dot{m}_{BOG} \geq 0$
	Equation 822	${F'}_{MAX}^{P} = F_1^P - [-\dot{m}_{BOG}]$	$\frac{\partial P^V}{\partial t} \geq 0$ $\dot{m}_{IN}^V < 0$ $\dot{m}_{BOG} < 0$
	Equation 823	${F'}_{MAX}^{P} = F_2^P - [-\dot{m}_{BOG}]$	$\frac{\partial P^V}{\partial t} < 0$ $\dot{m}_{IN}^V \geq 0$ $\dot{m}_{BOG} \geq 0$
	Equation 824	${F'}_{MAX}^{P} = F_2^P$	$\frac{\partial P^V}{\partial t} < 0$ $\dot{m}_{IN}^V \geq 0$ $\dot{m}_{BOG} < 0$
	Equation 825	${F'}_{MAX}^{P} = F_2^P - [\dot{m}_{IN}^V - \dot{m}_{BOG}]$	$\frac{\partial P^V}{\partial t} < 0$ $\dot{m}_{IN}^V < 0$ $\dot{m}_{BOG} \geq 0$
	Equation 826	${F'}_{MAX}^{P} = F_2^P - [\dot{m}_{IN}^V]$	$\frac{\partial P^V}{\partial t} < 0$ $\dot{m}_{IN}^V < 0$ $\dot{m}_{BOG} < 0$

Table 221. Equations for coefficients $\boldsymbol{F^{TV}_{MAX}}$, $\boldsymbol{F^{TL}_{MAX}}$, $\boldsymbol{F'^{HL}_{MAX}}$ and $\boldsymbol{F'^{P}_{MAX}}$.

F'^{HL}_{MAX}	Equation 827	$F'^{HL}_{MAX} = F^{HL}_1 - [\dot{m}^L_{IN}]$	$\frac{\partial V^L}{\partial t} \geq 0$ $\dot{m}^L_{IN} \geq 0$ $\dot{m}^L_{OUT} \geq 0$
	Equation 828	$F'^{HL}_{MAX} = F^{HL}_1 - [\dot{m}^L_{IN} - \dot{m}^L_{OUT}]$	$\frac{\partial V^L}{\partial t} \geq 0$ $\dot{m}^L_{IN} \geq 0$ $\dot{m}^L_{OUT} < 0$
	Equation 829	$F'^{HL}_{MAX} = F^{HL}_1$	$\frac{\partial V^L}{\partial t} \geq 0$ $\dot{m}^L_{IN} < 0$ $\dot{m}^L_{OUT} \geq 0$
	Equation 830	$F'^{HL}_{MAX} = F^{HL}_1 - [-\dot{m}^L_{OUT}]$	$\frac{\partial V^L}{\partial t} \geq 0$ $\dot{m}^L_{IN} < 0$ $\dot{m}^L_{OUT} < 0$
	Equation 831	$F'^{HL}_{MAX} = F^{HL}_2 - [-\dot{m}^L_{OUT}]$	$\frac{\partial V^L}{\partial t} < 0$ $\dot{m}^L_{IN} \geq 0$ $\dot{m}^L_{OUT} \geq 0$
	Equation 832	$F'^{HL}_{MAX} = F^{HL}_2$	$\frac{\partial V^L}{\partial t} < 0$ $\dot{m}^L_{IN} \geq 0$ $\dot{m}^L_{OUT} < 0$
	Equation 833	$F'^{HL}_{MAX} = F^{HL}_2 - [\dot{m}^L_{IN} - \dot{m}^L_{OUT}]$	$\frac{\partial V^L}{\partial t} < 0$ $\dot{m}^L_{IN} < 0$ $\dot{m}^L_{OUT} \geq 0$
	Equation 834	$F'^{HL}_{MAX} = F^{HL}_2 - [\dot{m}^L_{IN}]$	$\frac{\partial V^L}{\partial t} < 0$ $\dot{m}^L_{IN} < 0$ $\dot{m}^L_{OUT} < 0$
F^{TL}_{MAX}	Equation 835	$F^{TL}_{MAX} = F^{TL}_1 - [(-D^{TL}) \cdot \dot{m}^L_{IN}]$	$\frac{\partial T^L}{\partial t} \geq 0$ $(-D^{TL}) \cdot \dot{m}^L_{IN} \geq 0$ $(-E^{TL}) \cdot \dot{m}^L_{OUT} \geq 0$
	Equation 836	$F^{TL}_{MAX} = F^{TL}_1 - [(-D^{TL}) \cdot \dot{m}^L_{IN} - (-E^{TL}) \cdot \dot{m}^L_{OUT}]$	$\frac{\partial T^L}{\partial t} \geq 0$ $(-D^{TL}) \cdot \dot{m}^L_{IN} \geq 0$ $(-E^{TL}) \cdot \dot{m}^L_{OUT} < 0$
	Equation 837	$F^{TL}_{MAX} = F^{TL}_1$	$\frac{\partial T^L}{\partial t} \geq 0$ $(-D^{TL}) \cdot \dot{m}^L_{IN} < 0$ $(-E^{TL}) \cdot \dot{m}^L_{OUT} \geq 0$

Table 221. Equations for coefficients $\boldsymbol{F^{TV}_{MAX}}$, $\boldsymbol{F^{TL}_{MAX}}$, $\boldsymbol{F'^{\mathrm{HL}}_{MAX}}$ and $\boldsymbol{F'^{P}_{MAX}}$.

	Equation 838	$F^{TL}_{MAX} = F^{TL}_{2} - [-(-E^{TL}) \cdot \dot{m}^{L}_{OUT}]$	$\frac{\partial T^{L}}{\partial t} \geq 0$ $(-D^{TL}) \cdot \dot{m}^{L}_{IN} < 0$ $(-E^{TL}) \cdot \dot{m}^{L}_{OUT} < 0$
	Equation 839	$F^{TL}_{MAX} = F^{TL}_{2} - [-(-E^{TL}) \cdot \dot{m}^{L}_{OUT}]$	$\frac{\partial T^{L}}{\partial t} < 0$ $(-D^{TL}) \cdot \dot{m}^{L}_{IN} \geq 0$ $(-E^{TL}) \cdot \dot{m}^{L}_{OUT} \geq 0$
	Equation 840	$F^{TL}_{MAX} = F^{TL}_{2}$	$\frac{\partial T^{L}}{\partial t} < 0$ $(-D^{TL}) \cdot \dot{m}^{L}_{IN} \geq 0$ $(-E^{TL}) \cdot \dot{m}^{L}_{OUT} < 0$
	Equation 841	$F^{TL}_{MAX} = F^{TL}_{2}$ $-[(-D^{TL}) \cdot \dot{m}^{L}_{IN} - (-E^{TL}) \cdot \dot{m}^{L}_{OUT}]$	$\frac{\partial T^{L}}{\partial t} < 0$ $(-D^{TL}) \cdot \dot{m}^{L}_{IN} < 0$ $(-E^{TL}) \cdot \dot{m}^{L}_{OUT} \geq 0$
	Equation 842	$F^{TL}_{MAX} = F^{TL}_{2} - [(-D^{TL}) \cdot \dot{m}^{L}_{IN}]$	$\frac{\partial T^{L}}{\partial t} < 0$ $(-D^{TL}) \cdot \dot{m}^{L}_{IN} < 0$ $(-E^{TL}) \cdot \dot{m}^{L}_{OUT} < 0$
F^{TV}_{MAX}	Equation 843	$F^{TV}_{MAX} = F^{TV}_{1} - [(-D^{TV}) \cdot \dot{m}^{V}_{IN}]$	$\frac{\partial T^{V}}{\partial t} \geq 0$ $(-D^{TV}) \cdot \dot{m}^{V}_{IN} \geq 0$ $(-E^{TV}) \cdot \dot{m}_{BOG} \geq 0$
	Equation 844	$F^{TV}_{MAX} = F^{TV}_{1} - [(-D^{TV}) \cdot \dot{m}^{V}_{IN} - (-E^{TV})$ $\cdot \dot{m}_{BOG}]$	$\frac{\partial T^{V}}{\partial t} \geq 0$ $(-D^{TV}) \cdot \dot{m}^{V}_{IN} \geq 0$ $(-E^{TV}) \cdot \dot{m}_{BOG} < 0$
	Equation 845	$F^{TV}_{MAX} = F^{TV}_{1}$	$\frac{\partial T^{V}}{\partial t} \geq 0$ $(-D^{TV}) \cdot \dot{m}^{V}_{IN} < 0$ $(-E^{TV}) \cdot \dot{m}_{BOG} \geq 0$
	Equation 846	$F^{TV}_{MAX} = F^{TV}_{1} - [-(-E^{TV}) \cdot \dot{m}_{BOG}]$	$\frac{\partial T^{V}}{\partial t} \geq 0$ $(-D^{TV}) \cdot \dot{m}^{V}_{IN} < 0$ $(-E^{TV}) \cdot \dot{m}_{BOG} < 0$
	Equation 847	$F^{TV}_{MAX} = F^{TV}_{2} - [-(-E^{TV}) \cdot \dot{m}_{BOG}]$	$\frac{\partial T^{V}}{\partial t} < 0$ $(-D^{TV}) \cdot \dot{m}^{V}_{IN} \geq 0$ $(-E^{TV}) \cdot \dot{m}_{BOG} \geq 0$
	Equation 848	$F^{TV}_{MAX} = F^{TV}_{2}$	$\frac{\partial T^{V}}{\partial t} < 0$ $(-D^{TV}) \cdot \dot{m}^{V}_{IN} \geq 0$ $(-E^{TV}) \cdot \dot{m}_{BOG} < 0$
	Equation 849	$F^{TV}_{MAX} = F^{TV}_{2}$ $-[(-D^{TV}) \cdot \dot{m}^{V}_{IN} - (-E^{TV}) \cdot \dot{m}_{BOG}]$	$\frac{\partial T^{V}}{\partial t} < 0$ $(-D^{TV}) \cdot \dot{m}^{V}_{IN} < 0$ $(-E^{TV}) \cdot \dot{m}_{BOG} \geq 0$

Table 221. Equations for coefficients $\boldsymbol{F^{TV}_{MAX}}$, $\boldsymbol{F^{TL}_{MAX}}$, $\boldsymbol{F'^{HL}_{MAX}}$ and $\boldsymbol{F'^{P}_{MAX}}$.

Equation 850	$F^{TV}_{MAX} = F^{TV}_{2} - [(-D^{TV}) \cdot \dot{m}^{V}_{IN}]$	$\frac{\partial T^V}{\partial t} < 0$ $(-D^{TV}) \cdot \dot{m}^{V}_{IN} < 0$ $(-E^{TV}) \cdot \dot{m}_{BOG} < 0$

The coefficients D^P, E^P, D^{HL}, E^{HL}, D^{TL}, E^{TL}, $D^{TV}$and E^{TV} are reported in Table 42. The coefficients F^P_1, F^P_2, F^{HL}_1, F^{HL}_2, F^{TL}_1, F^{TL}_2, F^{TV}_1 and F^{TL}_2 are calculated with the equations of Table 222, as function of the interfacial heat transfer ($\dot{Q}^L_I$ and $\dot{Q}^V_I$), the net mass flow ($\dot{m}_N$), and the inlet and outlet flow rates ($\dot{m}^L_{IN}$, $\dot{m}^L_{OUT}$, $\dot{m}^V_{IN}$ and $\dot{m}_{BOG}$).

Table 222. Equations for coefficients $\boldsymbol{F^P_1}$, $\boldsymbol{F^P_2}$, $\boldsymbol{F^{HL}_1}$, $\boldsymbol{F^{HL}_2}$, $\boldsymbol{F^{TL}_1}$, $\boldsymbol{F^{TL}_2}$, $\boldsymbol{F^{TV}_1}$ and $\boldsymbol{F^{TL}_2}$.

Coefficient	Equation	Formula	Condition
F^P_1	Equation 851	$F^P_1 = -\dot{m}_N$	$\dot{m}_N \geq 0$
	Equation 852	$F^P_1 = 0$	$\dot{m}_N < 0$
F^P_2	Equation 853	$F^P_2 = 0$	$\dot{m}_N \geq 0$
	Equation 854	$F^P_2 = -\dot{m}_N$	$\dot{m}_N < 0$
F^{HL}_1	Equation 855	$F^{HL}_1 = 0$	$\dot{m}_N \geq 0$
	Equation 856	$F^{HL}_1 = -(-\dot{m}_N)$	$\dot{m}_N < 0$
F^{HL}_2	Equation 857	$F^{HL}_2 = -(-\dot{m}_N)$	$\dot{m}_N \geq 0$
	Equation 858	$F^{HL}_2 = 0$	$\dot{m}_N < 0$
F^{TL}_1	Equation 859	$F^{TL}_1 = -\left[\dot{Q}^B_w + \dot{Q}^{SL}_w\right]$	$\dot{Q}^L_I \geq 0$ $\dot{m}_N \cdot \left(\tilde{h}^L_S - \tilde{h}^L\right) \geq 0$
	Equation 860	$F^{TL}_1 = -\left[\dot{Q}^B_w + \dot{Q}^{SL}_w - \dot{m}_N \cdot \left(\tilde{h}^L_S - \tilde{h}^L\right)\right]$	$\dot{Q}^L_I \geq 0$ $\dot{m}_N \cdot \left(\tilde{h}^L_S - \tilde{h}^L\right) < 0$
	Equation 861	$F^{TL}_1 = -\left[\dot{Q}^B_w + \dot{Q}^{SL}_w - \dot{Q}^L_I\right]$	$\dot{Q}^L_I < 0$ $\dot{m}_N \cdot \left(\tilde{h}^L_S - \tilde{h}^L\right) \geq 0$
	Equation 862	$F^{TL}_1 = -\left[\dot{Q}^B_w + \dot{Q}^{SL}_w - \dot{Q}^L_I - \dot{m}_N \cdot \left(\tilde{h}^L_S - \tilde{h}^L\right)\right]$	$\dot{Q}^L_I < 0$ $\dot{m}_N \cdot \left(\tilde{h}^L_S - \tilde{h}^L\right) < 0$
F^{TL}_2	Equation 863	$F^{TL}_2 = -\left[\dot{Q}^B_w + \dot{Q}^{SL}_w - \dot{Q}^L_I - \dot{m}_N \cdot \left(\tilde{h}^L_S - \tilde{h}^L\right)\right]$	$\dot{Q}^L_I \geq 0$ $\dot{m}_N \cdot \left(\tilde{h}^L_S - \tilde{h}^L\right) \geq 0$
	Equation 864	$F^{TL}_2 = -\left[\dot{Q}^B_w + \dot{Q}^{SL}_w - \dot{Q}^L_I\right]$	$\dot{Q}^L_I \geq 0$ $\dot{m}_N \cdot \left(\tilde{h}^L_S - \tilde{h}^L\right) < 0$
	Equation 865	$F^{TL}_2 = -\left[\dot{Q}^B_w + \dot{Q}^{SL}_w - \dot{m}_N \cdot \left(\tilde{h}^L_S - \tilde{h}^L\right)\right]$	$\dot{Q}^L_I < 0$ $\dot{m}_N \cdot \left(\tilde{h}^L_S - \tilde{h}^L\right) \geq 0$
	Equation 866	$F^{TL}_2 = -\left[\dot{Q}^B_w + \dot{Q}^{SL}_w\right]$	$\dot{Q}^L_I < 0$ $\dot{m}_N \cdot \left(\tilde{h}^L_S - \tilde{h}^L\right) < 0$
F^{TV}_1	Equation 867	$F^{TV}_1 = -\left[\dot{Q}^{SV}_w + \dot{m}_N \cdot \left(\tilde{h}^V_S - \tilde{h}^V\right)\right]$	$\dot{Q}^V_I \geq 0$ $\dot{m}_N \cdot \left(\tilde{h}^V_S - \tilde{h}^V\right) \geq 0$
	Equation 868	$F^{TV}_1 = -\left[\dot{Q}^{SV}_w\right]$	$\dot{Q}^V_I \geq 0$ $\dot{m}_N \cdot \left(\tilde{h}^V_S - \tilde{h}^V\right) < 0$
	Equation 869	$F^{TV}_1 = -\left[\dot{Q}^{SV}_w - \dot{Q}^V_I + \dot{m}_N \cdot \left(\tilde{h}^V_S - \tilde{h}^V\right)\right]$	$\dot{Q}^V_I < 0$ $\dot{m}_N \cdot \left(\tilde{h}^V_S - \tilde{h}^V\right) \geq 0$
	Equation 870	$F^{TV}_1 = -\left[\dot{Q}^{SV}_w - \dot{Q}^V_I\right]$	$\dot{Q}^V_I < 0$ $\dot{m}_N \cdot \left(\tilde{h}^V_S - \tilde{h}^V\right) < 0$
F^{TV}_2	Equation 871	$F^{TV}_2 = -\left[\dot{Q}^{SV}_w - \dot{Q}^V_I\right]$	$\dot{Q}^V_I \geq 0$ $\dot{m}_N \cdot \left(\tilde{h}^V_S - \tilde{h}^V\right) \geq 0$
	Equation 872	$F^{TV}_2 = -\left[\dot{Q}^{SV}_w - \dot{Q}^V_I + \dot{m}_N \cdot \left(\tilde{h}^V_S - \tilde{h}^V\right)\right]$	$\dot{Q}^V_I \geq 0$ $\dot{m}_N \cdot \left(\tilde{h}^V_S - \tilde{h}^V\right) < 0$

Table 222. Equations for coefficients $\boldsymbol{F_1^P}$, $\boldsymbol{F_2^P}$, $\boldsymbol{F_1^{HL}}$, $\boldsymbol{F_2^{HL}}$, $\boldsymbol{F_1^{TL}}$, $\boldsymbol{F_2^{TL}}$, $\boldsymbol{F_1^{TV}}$ and $\boldsymbol{F_2^{TL}}$.

Equation 873	$F_2^{TV} = -\left[\dot{Q}_w^{SV}\right]$	$\dot{Q}_I^V < 0$ $\dot{m}_N \cdot \left(\tilde{h}_S^V - \tilde{h}^V\right) \geq 0$
Equation 874	$F_2^{TV} = -\left[\dot{Q}_w^{SV} + \dot{m}_N \cdot \left(\tilde{h}_S^V - \tilde{h}^V\right)\right]$	$\dot{Q}_I^V < 0$ $\dot{m}_N \cdot \left(\tilde{h}_S^V - \tilde{h}^V\right) < 0$

2.3. Selection of the relative tolerance

Once, the maximum ratio is computed, the relative tolerance can be determined. The choice of the value has to guarantee the accuracy and the reduction of the computational time. High accuracy is usually required when the values of the time-derivates frequently change or when these values are close to the maximum possible values. The computational time can be reduced and the accuracy can be low when the values of the time-derivates are regular or when they are far away from the maximum possible one. Hence, the value of the relative tolerance can be determined, as reported in Table 223.

Table 223. Values of the relative tolerance.

Condition	$\Omega_{MAX} \geq 10^{-1}$	$10^{-3} \leq \Omega_{MAX} < 10^{-1}$	$\Omega_{MAX} < 10^{-3}$
Tolerance	10^{-5}	10^{-4}	10^{-3}

As it is shown in Table 223, when Ω_{MAX} is higher than one, accuracy is preferred because the values of the time-derivates are close to the maximum possible one. As the value of this ratio decreases, the value of the relative tolerance progressively increases to reduce the computational time because the values of the time-derivates are far away from the maximum possible value.

2.4. Algorithm of the relative tolerance

The algorithm to determine the relative tolerance of the solver of the system of Ordinary Differential Equations (ODEs) is based on the equations of Table 223, Table 222, Table 221, Table 220, Table 219 and Table 218. The input and the output variables of this algorithm are reported in Table 224.

Table 224. Input and output of the algorithm of the relative tolerance.

Variables	**Description**
Input	Heat flows ($\dot{Q}_w^B$, $\dot{Q}_w^{SL}$ and $\dot{Q}_w^{SV}$), interfacial heat flows ($\dot{Q}_I^L$ and $\dot{Q}_I^V$), net mass flow ($\dot{m}_N$) and the coefficients D^P, E^P, D^{HL}, E^{HL}, D^{TL}, E^{TL}, D^{TV}, E^{TV}, B^{TL}, A^{TL}, C^{TL}, B^{TV}, A^{TV} and C^{TV} (see Table 42), the coefficients C'^P, C'^{HL}, A'^P and A'^{HL} (see Table 72), the values of the time-derivates of pressure, liquid volume, liquid and vapour temperatures at the previous time-point, the values of the inlet and outlet flow rates ($\dot{m}_{IN}^V$, $\dot{m}_{BOG}$, $\dot{m}_{IN}^L$ and $\dot{m}_{OUT}^L$) and the values of the specific enthalpies.
Output	The value of the relative tolerance to use in the ODE solver.

The structure of the algorithm to compute the relative tolerance is reported in Figure 210.

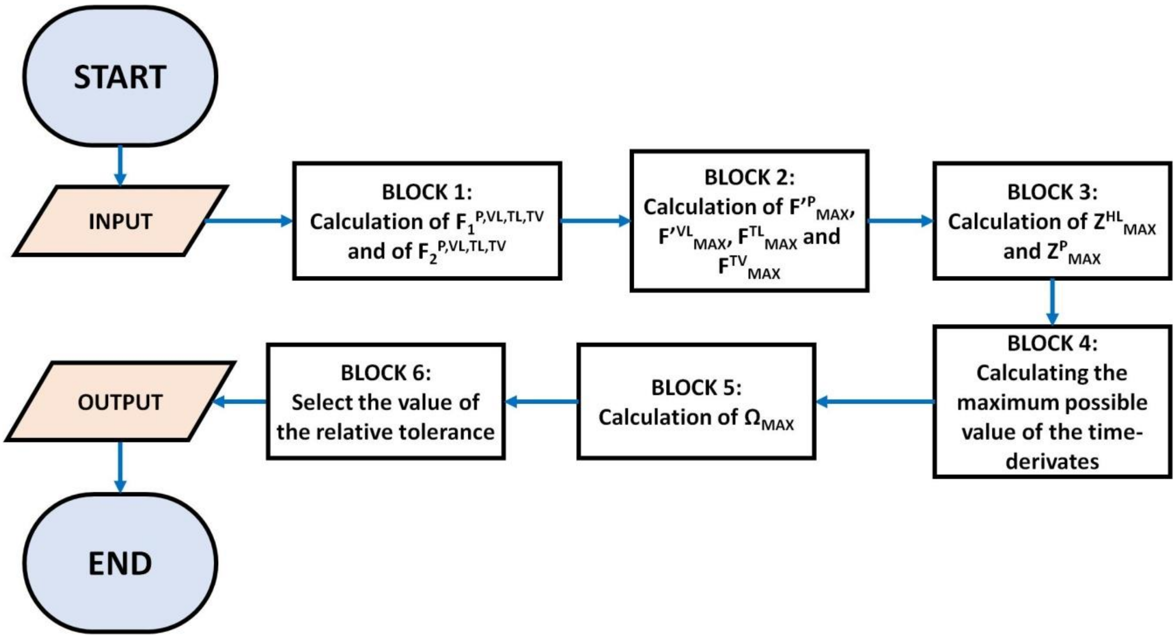

Figure 210. Algorithm of the relative tolerance.

As indicated in Figure 210, the algorithm is composed by the following steps:

a) BLOCK 1. The values of coefficients F_1^P, F_2^P, F_1^{HL}, F_2^{HL}, F_1^{TL}, F_2^{TL}, F_1^{TV} and F_2^{TL} are calculated with the equations of Table 222;
b) BLOCK 2. The values of the coefficients F_{MAX}^{TV}, F_{MAX}^{TL}, F'^{HL}_{MAX} and F'^{P}_{MAX} are computed with the equations of Table 221;
c) BLOCK 3. The coefficients Z_{MAX}^{HL} and Z_{MAX}^{P} are computed as reported in Table 220.
d) BLOCK 4. The maximum value of this time-derivate and it can be estimated with the equations of Table 219;
e) BLOCK 5. The value of the absolute maximum ratio of the time-derivates is calculated with the equations of Table 218.
f) BLOCK 6. The value of the relative tolerance is computed as reported in Table 223.

As it is indicated by Figure 210, the algorithm of the relative tolerance is not an iterative procedure.

3. Algorithm of Block 12: calculation of the steady state time

As it is explained in Section 1.3.3, the steady state time cannot be computed before starting the simulation. The value of this time can be calculated with the *steady state algorithm*. As it is described in Section 1.3.3, this algorithm is mainly composed by three steps: the calculation of average the time derivate at the current time-point, the comparison of these derivates with the one at the previous time-point and calculation of the steady state time.

Section 3.1 describes the calculation of the average value of the time-derivate. Section 3.2 presents the relative ratio and Section 3.3 explains the algorithm to compute the steady state time.

3.1. Average value of the time-derivate

The steady state is reached when the values of the time-derivates, computed by the homogeneous model (H model), are close to zero and they remains close to this value, as described in Section 1.3.3. Hence, the average value of the time-derivate over a certain time-interval should be computed to determine if the storage container is at steady state.

The time-evolution of the variables such as pressure, liquid volume, liquid and vapour temperature is calculated with the Ordinary Differential Equations (ODEs) solver (see Section 5 of Chapter 3). This solver temporally discretizes the simulation time is time-steps and time-point. Hence, the time-evolution of a generic variable y_n can be described as illustrated in Figure 211, in a period of time that goes from the current time-point (t_i) and the past reference time-point (t_{i-N_t}). In Figure 211, the blue lines are the integration time-step. The orange dashed lines connect the time-points with the values of the variable y_n. The green circles are the time-points. The orange are the values of the variable y_n at the time-points.

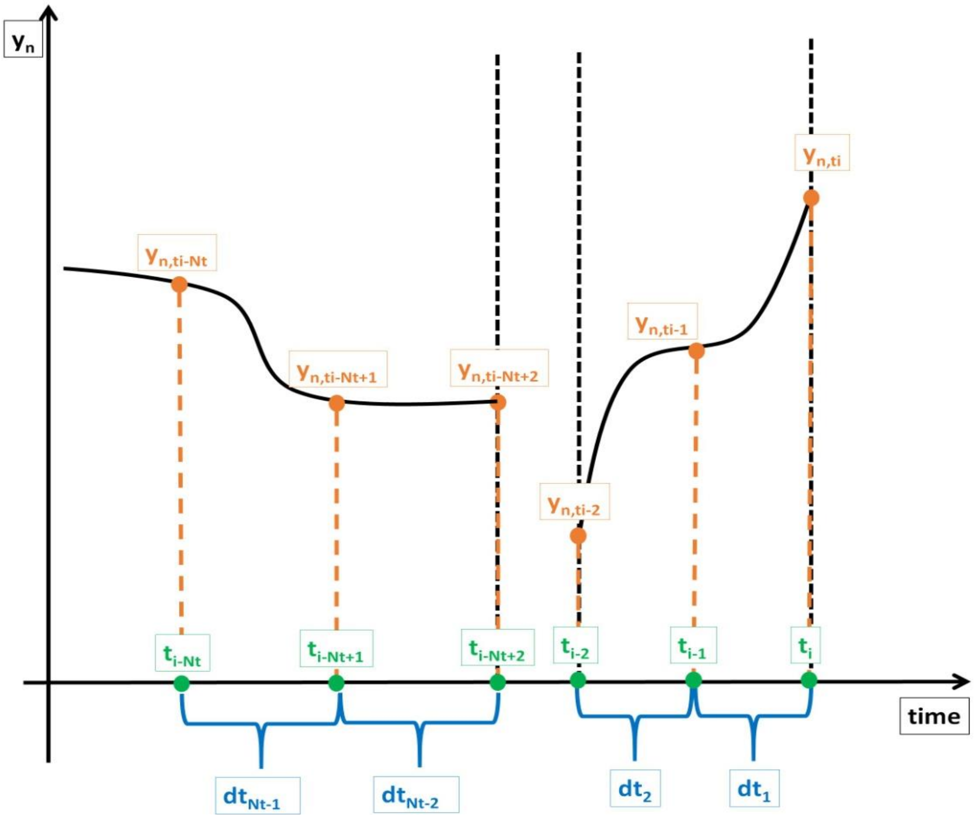

Figure 211. Time-evolution of $\boldsymbol{y_n}$ between $\boldsymbol{t_i}$ and $\boldsymbol{t_{i-N_t}}$.

So, the average value of the time derivate can be computed as time-integral over the time-interval between the time-points t_i and t_{i-N_t}. This average value can be computed with the trapezoidal rule (see Section 3 of Appendix F), using the equations of Table 225.

Table 225. Equations to compute the average value of the time-derivates.

Variables	Name	Equation	Formula
Average value of the time- derivate	$\overline{\frac{\partial y_n}{\partial t}}$	Equation 875	$\overline{\frac{\partial y_n}{\partial t}} = \frac{1}{\Delta t} \cdot \left\{ \sum_{j=N_t}^{2} \left[\frac{dt_{N_t+1-j}}{2} \cdot \left(\left.\frac{\partial y_n}{\partial t}\right\|_{t_{N_t+2-j}} + \left.\frac{\partial y_n}{\partial t}\right\|_{t_{N_t+1-j}} \right) \right] \right\}$
Time-interval	Δt	Equation 876	$\Delta t = t_i - t_{i-N_t}$
Integration time-step at time t_j	dt_j	Equation 877	$dt_j = t_{j+1} - t_j$

N_t is the number of time-points to compute the average value and the value of this variable is 10. $\left.\frac{\partial y_n}{\partial t}\right|_{t_j}$ is the value of the time-derivate at time t_j. y_n is a general variable and it can be the pressure, the liquid volume, the liquid and the vapour temperature.

3.2. Relative ratio of time derivates

The time-evolution of the variables of the homogenous (H) model is computed with the numerical method of the Ordinary Differential Equation (ODEs) system solver. Hence, the values of the time-derivates cannot be zero due to the numerical error that is intrinsic of this method. So, the steady state conditions are reached when all the values of the relative ratio of the time-derivates are lower than the defined value. This defined value is 10^{-4} and the relative ratio of the time-derivate of the variable y_n as can be computed as follows:

Equation 878
$$\Psi_n = \frac{abs\left(\overline{\frac{\partial y_n}{\partial t}}\right)}{abs\left(\left.\frac{\partial y_n}{\partial t}\right|_{MAX}\right)}$$

$\left.\frac{\partial y_n}{\partial t}\right|_{MAX}$ is the maximum value of the time-derivate of the variable y_n during the steady state.

3.3. Algorithm of the steady state

The algorithm computes the steady state time using the equations of Section 3.1 and 3.2 of Appendix L. Hence, the input and the output of this algorithm are reported in Table 226.

Table 226. Input and output variables of the steady state algorithm.

Variable	**Description**
Input	Values of the time-derivates at the current time-point ($\frac{\partial y_n}{\partial t}$), and between this point (t_i) and the past reference time-point (t_{i-N_t}), value of the defined value of the relative ratio (ϵ), the maximum values of the time-derivates ($\left.\frac{\partial y_n}{\partial t}\right|_{MAX}$), the value of the previous steady state time and the increment of the steady state time
Output	Value of the steady state time

The structure of the algorithm is described in Figure 212.

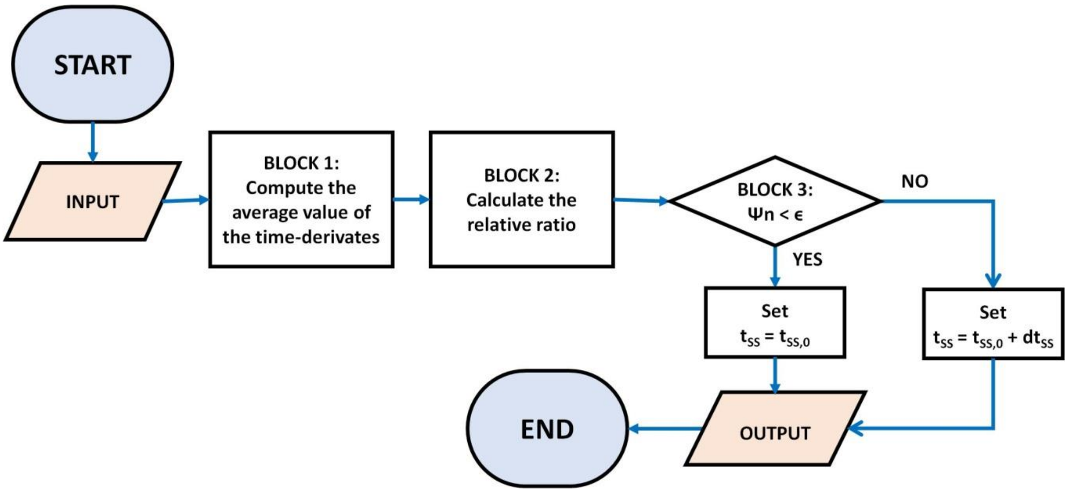

Figure 212. Structure of the steady state algorithm.

It is composed by the following steps:

a) BLOCK 1: the average values of the time-derivate of each variables are computed with the equations of Table 225;
b) BLOCK 2: the relative ratio is computed for each variable with Equation 878;

c) BLOCK 3: the value of the relative ratio is compared with the defined value and two pathways are present:
    - Patter 1.3 (P 1.3): if all the values of the relative ratio are lower or equal to the defined value, the value of the steady state time is equal to the value of the first guess value;
    - Patter 2.3 (P 2.3): if the one of the values of the relative ratio is higher than the defined value, the steady state time is computed with Equation 879.

Equation 879
$$t_{SS} = t_{SS,0} + dt_{SS}$$

dt_{SS} is the increment of the steady state time, whose value is 5 minutes. As consequence, the value maximum value of the simulating time (t_{MAX}) is increased of dt_{SS}.

In certain conditions, the value of the defined value of the relative ratio (ϵ) is lower than the one required to reach the steady state condition in the simulation. As consequence, the steady state period is as longer as the maxium steady state time.

4. Calculation of the liquid pressure

The pressure in the liquid increases from the interface to the bottom, if the liquid is stored in the tank. This increment is produced by the hydrostatic pressure law[138]. Hence, the liquid pressure increases with the distance between the interface and the bottom, thus with the liquid height. As consequence, the liquid pressure is not uniform because it changes with the liquid height. Since the liquid pressure is almost a liner function of the height, the liquid pressure in the core of the core of the liquid can be computed as follows:

Equation 880
$$P^L = P^V + \rho^L(T^L, P^L) \cdot \frac{H^L}{2} \cdot g$$

g is the gravity acceleration, whose value is 9.81 m/s².H^L is the liquid height and it is computed with the geometrical formulas of Appendix B. ρ^L is the liquid density at the liquid temperature and pressure, causing an interaction between the liquid density and the liquid pressure. Hence, the liquid pressure must be computed with an iterative procedure due to this interaction. The method of the direct substitution (see Section 1 of Appendix I) can be used to calculate the liquid pressure because Equation 880 is suitable for this type of numerical method. The proposed iterative procedure to compute the liquid pressure is called *liquid pressure (P^L) algorithm*.

The input and the output of this algorithm are reported in Table 227.

Table 227. Input and output of the P^L algorithm.

Variables	Description
Input	Liquid volume (V^L), liquid temperature (T^L), pressure (P^V), number of steps (N_S) and value of the relative tolerance (ε).
Output	The value of the liquid pressure.

The value of the number of step is 100 and the value of the relative tolerance is 10^{-5}. The P^L algorithm is described in Figure 213.

---

[138] Hydrostatic pressure law: $P - P_0 = \rho \cdot H \cdot g$

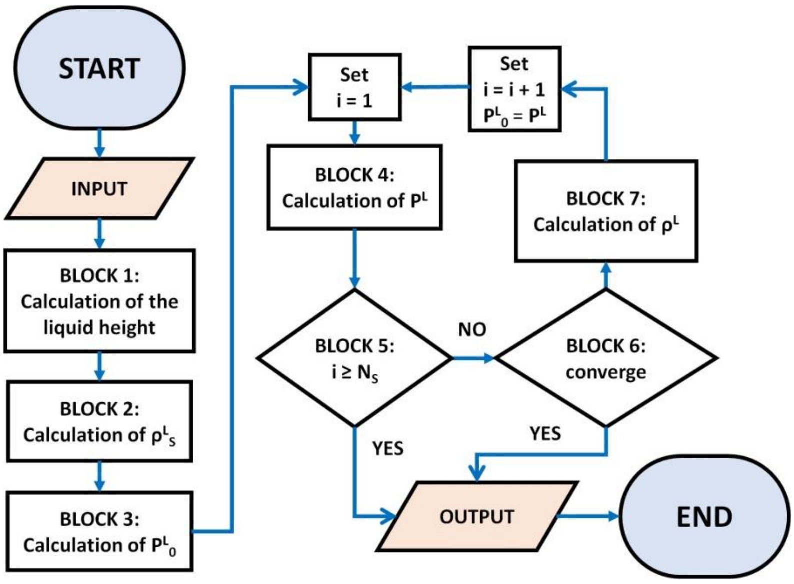

Figure 213. Algorithm to compute the pressure in the liquid.

This algorithm is composed by the following steps:

a) BLOCK 1. The liquid height is computed with the geometrical formulas of Appendix B;
b) BLOCK 2. The liquid density at saturation (ρ_S^L) at the ullage pressure is calculated with the thermodynamic model (see Section 4 of Chapter 3);
c) BLOCK 3. The first guess value of the liquid density is computed as follows:

Equation 881
$$P_0^L = P^V + \rho_S^L \cdot \frac{H^L}{2} \cdot g$$

The current number of iteration (i) is equal to 1.

d) BLOCK 4. The liquid pressure is calculated with Equation 880;
e) BLOCK 5. The current number of iteration is compared with the number of step. Two pathways are present;
    - Pathway 1.5 (P 1.5): the current number of the iteration is higher or equal to N_S. The algorithm stops;
    - Pathway 2.5 (P 2.5): i is lower than the number of steps. The algorithm moves to BLOCK 6 (step f) of Section 4 of Appendix L).
f) BLOCK 6. The criterion of convergence is defined with Equation 882.

Equation 882
$$\left|P^L - P_0^L\right| < (P_0^L \cdot \varepsilon)$$

Two patters are present, as function of Equation 882:
- Pathway 1.6 (P 1.6): Equation 882 is true. The algorithm stops;
- Pathway 2.6 (P 2.6): Equation 882 is false. The algorithm move to BLOCK 7 (step g) of Section 4) ;

g) BLOCK 7. The liquid density is computed with the thermodynamic model (see Section 4 of Chapter 3), using the value of liquid temperature and liquid pressure. The current number of iteration increases of 1 and the first guess value of the liquid pressure is equal to the liquid pressure. The algorithm continues from BLOCK 4 (step d) of Section 4 of Appendix L);

This algorithm quickly converges because the density of the liquid weakly depends on the liquid pressure.

Appendix M

Steps of the mathematical procedure to deduce the pressure evolution, liquid volume evolution, liquid and vapour temperature evolution, inlet liquid flow and Boil-Off Gas equations of the homogeneous model

The pressure-evolution (P-e), liquid volume-evolution (V^L-e), and liquid and temperatures-evolution (T^L-e and T^V-e), inlet liquid flow (ILF) and boil-off gas (BOG) equations (see Table 73 and Table 70) are obtained with a mathematical procedure. This mathematical procedure is composed by different mathematical steps to obtain the different intermediate equations of Section 2.

Section 2 explains the mathematical steps to obtain the simplified form of the conservations laws. Section 3 describes the mathematical steps to compute the temperatures-evolution equations (see Table 73). Section 4 presents the mathematical steps to deduce the pressure-liquid volume equations. Section 5 explains the mathematical steps to deduce the pressure-evolution, liquid volume-evolution, inlet liquid flow and boil-off gas equations (see Table 70).

1. General equations of the mathematical procedure

In the mathematical procedure to obtain the pressure-evolution, liquid volume-evolution, and liquid and temperatures-evolution, inlet liquid flow and boil-off gas equations (see Table 73 and Table 70), the time-derivates of the liquid mass ($\frac{\partial m^L}{\partial t}$), vapour mass ($\frac{\partial m^V}{\partial t}$), liquid enthalpy ($\frac{\partial \tilde{H}^L}{\partial t}$), and vapour enthalpy ($\frac{\partial \tilde{H}^V}{\partial t}$) should be computed as function of the time-derivates of the pressure ($\frac{\partial P^V}{\partial t}$), liquid volume ($\frac{\partial V^L}{\partial t}$), liquid temperature ($\frac{\partial T^L}{\partial t}$) and vapour temperature ($\frac{\partial T^V}{\partial t}$). To do that, the general equations of the mathematical procedure are required and these equations compute the variables $\frac{\partial m^L}{\partial t}$, $\frac{\partial m^V}{\partial t}$, $\frac{\partial \tilde{H}^L}{\partial t}$ and $\frac{\partial \tilde{H}^V}{\partial t}$ from the variables $\frac{\partial P^V}{\partial t}$, $\frac{\partial V^L}{\partial t}$, $\frac{\partial T^L}{\partial t}$ and $\frac{\partial T^V}{\partial t}$. The general equations that compute $\frac{\partial m^L}{\partial t}$ and $\frac{\partial m^V}{\partial t}$ are respectively called liquid and vapour mass general equations. The general equations that compute $\frac{\partial \tilde{H}^L}{\partial t}$ and $\frac{\partial \tilde{H}^V}{\partial t}$ are respectively called liquid and vapour energy general equations.

Section 1.1 explains how the liquid and vapour mass general equations are obtained. Section 1.2 describes the mathematical step to obtain the liquid and vapour energy general equations.

1.1. Liquid and vapour mass general equations

The mass can be computed as product between the volume and the density. The density is a function of the temperature (T) and of the pressure (P). So, the time-derivate of the mass is a function of the time-derivate of the volume, of the temperature and of the pressure. Using sum[126], the product[125] and the chain[124] rules, the time derivate of the mass can be computed as follows:

Equation 883
$$\frac{\partial m}{\partial t} = \rho \cdot \frac{\partial V}{\partial t} + V \cdot \left[\left.\frac{\partial \rho}{\partial T}\right|_P \cdot \frac{\partial T}{\partial t} + \left.\frac{\partial \rho}{\partial P}\right|_T \cdot \frac{\partial P}{\partial t} \right]$$

$\left.\frac{\partial \rho}{\partial T}\right|_P$ is the density-derivate respect to the temperature at constant pressure. $\left.\frac{\partial \rho}{\partial P}\right|_T$ is the density-derivate respect to the pressure at constant temperature. If Equation 883 is applied to liquid mass and to the vapour mass, the mass general equations can be obtained. These equations are reported in Table 228.

Table 228. Mass general equations.

Name	Equation	Formula
Liquid mass general equation	Equation 884	$\frac{\partial m^L}{\partial t} = \rho^L \cdot \frac{\partial V^L}{\partial t} + V^L \cdot \left[\left.\frac{\partial \rho^L}{\partial T^L}\right\|_{P^V} \cdot \frac{\partial T^L}{\partial t} + \left.\frac{\partial \rho^L}{\partial P^V}\right\|_{T^L} \cdot \frac{\partial P^V}{\partial t} \right]$
Vapour mass general equation	Equation 885	$\frac{\partial m^V}{\partial t} = \rho^V \cdot \frac{\partial V^V}{\partial t} + V^V \cdot \left[\left.\frac{\partial \rho^V}{\partial T^V}\right\|_{P^V} \cdot \frac{\partial T^V}{\partial t} + \left.\frac{\partial \rho^V}{\partial P^V}\right\|_{T^V} \cdot \frac{\partial P^V}{\partial t} \right]$

Equation 884 and Equation 885 are respectively called the liquid mass general equation and the vapour mass general equation.

1.2. Liquid and vapour energy general equations

The enthalpy is the product of the mass (m) and of the specific enthalpy ($\tilde{h}$). The specific enthalpy is a function of the temperature and of the pressure. So, the time-derivate of the enthalpy ($\frac{\partial \tilde{H}}{\partial t}$) can be computed as function of the time-derivates of mass ($\frac{\partial m}{\partial t}$), temperature ($\frac{\partial T}{\partial t}$) and pressure ($\frac{\partial P}{\partial t}$). Using the sum[126], the product[125] and the chain[124] rules, the time-derivate of the enthalpy can be computed as follows:

Equation 886
$$\frac{\partial \tilde{H}}{\partial t} = \tilde{h} \cdot \frac{\partial m}{\partial t} + m \cdot \left[C_P \cdot \frac{\partial T}{\partial t} + \left.\frac{\partial \tilde{h}}{\partial P}\right|_T \cdot \frac{\partial P}{\partial t} \right]$$

C_P is the specific heat at constant pressure. $\left.\frac{\partial \tilde{h}}{\partial P}\right|_T$ is the enthalpy-derivate respect to the pressure at constant temperature. If Equation 886 is applied to the liquid enthalpy and to the vapour enthalpy, the energy general equations can be deduced. These equations are reported in Table 229.

Table 229. Energy general equations.

Name	Equation	Formula
Liquid energy general equation	Equation 887	$\frac{\partial \tilde{H}^L}{\partial t} = \tilde{h}^L \cdot \frac{\partial m^L}{\partial t} + m^L \cdot \left[C_P^L \cdot \frac{\partial T^L}{\partial t} + \left.\frac{\partial \tilde{h}^L}{\partial P^V}\right\|_{T^L} \cdot \frac{\partial P^V}{\partial t} \right]$
Vapour energy general equation	Equation 888	$\frac{\partial \tilde{H}^V}{\partial t} = \tilde{h}^V \cdot \frac{\partial m^V}{\partial t} + m^V \cdot \left[C_P^V \cdot \frac{\partial T^V}{\partial t} + \left.\frac{\partial \tilde{h}^V}{\partial P^V}\right\|_{T^V} \cdot \frac{\partial P^V}{\partial t} \right]$

Equation 690 and Equation 888 are respectively called liquid energy general equation and vapour energy general equation.

2. Mathematical steps to obtain the simplified form of conservations equations

The simplified form of conservation laws (see Table 67) are equation obtained from the conservation laws, where only the time-derivates of pressure ($\frac{\partial P^V}{\partial t}$), liquid volume ($\frac{\partial V^L}{\partial t}$), liquid temperature ($\frac{\partial T^L}{\partial t}$) and vapour temperature ($\frac{\partial T^V}{\partial t}$). These simplified forms are composed by four equations: simplified form of liquid energy balance equation (Equation 101), simplified form of liquid mass balance equation (Equation 102), simplified form of vapour energy balance equation (Equation 103) and simplified form of vapour mass balance equation (Equation 104).

The mathematical steps to obtain the simplified form of liquid energy balance equation are described in Section 2.1. Section 2.2 presents the mathematical steps to obtain the vapour energy balance equation. Section 2.3 explains the mathematical steps to obtain the simplified form of liquid mass balance equation. Section 2.4 describes the mathematical steps to obtain the simplified form of vapour mass balance equation.

2.1. Simplified form of liquid energy balance equation

The accumulation of the liquid enthalpy is calculated with the liquid energy balance (Equation 96). In Equation 96, the time-derivate of the liquid enthalpy can be substituted with the liquid energy general equation (Equation 690). Liquid energy balance can be written as follows:

Equation 889

$$\tilde{h}^L \cdot \frac{\partial m^L}{\partial t} + m^L \cdot \left[C_P^L \cdot \frac{\partial T^L}{\partial t} + \left.\frac{\partial \tilde{h}^L}{\partial P^V}\right|_{T^L} \cdot \frac{\partial P^V}{\partial t} \right] = \dot{Q}_w^B + \dot{Q}_w^{SL} - \dot{Q}_I^L + \dot{m}_{IN}^L \cdot \tilde{h}_{IN}^L - \dot{m}_N \cdot \tilde{h}_S^L - \dot{m}_{OUT}^L \cdot \tilde{h}^L$$

The time-derivate of the liquid mass ($\frac{\partial m^L}{\partial t}$) can be substituted with the liquid mass balance equation (Equation 97). Equation 692 can be written as follows:

Equation 890

$$\tilde{h}^L \cdot (\dot{m}_{IN}^L - \dot{m}_N - \dot{m}_{OUT}^L) + m^L \cdot \left[C_P^L \cdot \frac{\partial T^L}{\partial t} + \left.\frac{\partial \tilde{h}^L}{\partial P^V}\right|_{T^L} \cdot \frac{\partial P^V}{\partial t} \right] = \dot{Q}_w^B + \dot{Q}_w^{SL} - \dot{Q}_I^L + \dot{m}_{IN}^L \cdot \tilde{h}_{IN}^L - \dot{m}_N \cdot \tilde{h}_S^L - \dot{m}_{OUT}^L \cdot \tilde{h}^L$$

The flow rates $\dot{m}_{IN}^L$, $\dot{m}_N$ and $\dot{m}_{OUT}^L$ are grouped in Equation 890. Then, the simplified form of the liquid energy balance equation (Equation 101) is obtained.

2.2. Simplified form of liquid mass balance equation

The accumulation of the liquid mass can be computed with the liquid mass balance equation (Equation 97). In Equation 97, the time-derivate of the liquid mass ($\frac{\partial m^L}{\partial t}$) can be substituted with liquid mass general equation (Equation 884). Then, the simplified form of liquid mass balance equation (Equation 102) is obtained.

2.3. Simplified form of vapour energy balance equation

The accumulation of the vapour enthalpy is computed with the vapour energy balance equation (Equation 98). In Equation 98, the time-derivate of the vapour enthalpy ($\frac{\partial \tilde{H}^V}{\partial t}$) can be substituted with the vapour energy general equation (Equation 888). Equation 98 can be computed as follows:

Equation 891

$$\tilde{h}^V \cdot \frac{\partial m^V}{\partial t} + m^V \cdot \left[C_P^V \cdot \frac{\partial T^V}{\partial t} + \left.\frac{\partial \tilde{h}^V}{\partial P^V}\right|_{T^V} \cdot \frac{\partial P^V}{\partial t} \right] = \dot{Q}_w^{SV} - \dot{Q}_I^V + \dot{m}_{IN}^V \cdot \tilde{h}_{IN}^V - \dot{m}_N \cdot \tilde{h}_S^V - \dot{m}_{BOG} \cdot \tilde{h}^V$$

The time-derivate of the ullage mass ($\frac{\partial m^V}{\partial t}$) can be substituted with the vapour mass balance equation (Equation 99). Equation 891 can be written as follows:

Equation 892

$$\tilde{h}^V \cdot (\dot{m}_{IN}^V + \dot{m}_N - \dot{m}_{BOG}) + m^V \cdot \left[C_P^V \cdot \frac{\partial T^V}{\partial t} + \left.\frac{\partial \tilde{h}^V}{\partial P^V}\right|_{T^V} \cdot \frac{\partial P^V}{\partial t} \right] = \dot{Q}_w^{SV} - \dot{Q}_I^V + \dot{m}_{IN}^V \cdot \tilde{h}_{IN}^V - \dot{m}_N \cdot \tilde{h}_S^V - \dot{m}_{BOG} \cdot \tilde{h}^V$$

The flow rates $\dot{m}_{IN}^{V}$, $\dot{m}_{N}$ and $\dot{m}_{BOG}$ are grouped in Equation 892. Then, the simplified form of the of vapour energy balance equation (Equation 103) are obtained.

2.4. Simplified form of vapour mass balance equation

The accumulation of the ullage mass is computed with the vapour mass balance equation (Equation 99). In Equation 99, the time-derivate of the vapour mass ($\frac{\partial m^V}{\partial t}$) can be substituted with the vapour mass general equation (Equation 885). The vapour mass balance equation can be computed as follows:

Equation 893
$$\rho^V \cdot \frac{\partial V^V}{\partial t} + V^V \cdot \left[\left.\frac{\partial \rho^V}{\partial T^V}\right|_{P^V} \cdot \frac{\partial T^V}{\partial t} + \left.\frac{\partial \rho^V}{\partial P^V}\right|_{T^V} \cdot \frac{\partial P^V}{\partial t} \right] = \dot{m}_{IN}^{V} - \dot{m}_{N} - \dot{m}_{BOG}$$

The time-derivate of the ullage volume ($\frac{\partial V^V}{\partial t}$) can be substituted with the volume conservation law (Equation 100). Then, the simplified form of vapour mass balance equation (Equation 104) is obtained.

3. Mathematical steps to obtain the liquid and vapour temperatures evolution equations

The liquid temperature-evolution (T^L-e) and the vapour temperature-evolution (T^V-e) equations (Equation 133 and Equation 134) are obtained from the linear form of the conservation laws (see Table 68). The mathematical steps to obtain Equation 133 are different from the ones of Equation 134.

Section 3.1 and 3.2 respectively describe the mathematical steps to obtain T^L-e and T^V-e equations.

3.1. Mathematical steps to obtain the liquid temperature evolution equation

In the linear form of the liquid energy balance equation (Equation 105), the term $B^{TL} \cdot \frac{\partial T^L}{\partial t}$ is moved to the left of Equation 105. The linear form of the liquid energy balance equation can be written as follows:

Equation 894
$$A^{TL} \cdot \frac{\partial P^V}{\partial t} + C^{TL} \cdot \frac{\partial V^L}{\partial t} + D^{TL} \cdot \dot{m}_{IN}^{L} + E^{TL} \cdot \dot{m}_{OUT}^{L} + F^{TL} = -B^{TL} \cdot \frac{\partial T^L}{\partial t}$$

The left and the right part of Equation 894 are multiplied by -1. Equation 894 can be written as follows:

Equation 895
$$-\left[A^{TL} \cdot \frac{\partial P^V}{\partial t} + C^{TL} \cdot \frac{\partial V^L}{\partial t} + D^{TL} \cdot \dot{m}_{IN}^{L} + E^{TL} \cdot \dot{m}_{OUT}^{L} + F^{TL} \right] = B^{TL} \cdot \frac{\partial T^L}{\partial t}$$

The right part of Equation 895 is divided by the coefficient B^{TL}. Then, the liquid temperature-evolution equation (Equation 133) is obtained.

3.2. Mathematical steps to obtain the vapour temperature evolution equation

In the linear form of the vapour energy balance equation (Equation 107), the term $B^{TV} \cdot \frac{\partial T^V}{\partial t}$ is moved to the left part of this equation. The linear form of the vapour energy balance equation can be written as follows:

Equation 896 $$A^{TV}\cdot\frac{\partial P^V}{\partial t}+C^{TV}\cdot\frac{\partial V^L}{\partial t}+D^{TV}\cdot\dot{m}_{IN}^V+E^{TL}\cdot\dot{m}_{BOG}+F^{TV}=-B^{TV}\cdot\frac{\partial T^V}{\partial t}$$

The left and the right part of Equation 896 are multiplied by -1. Equation 896 can be written as follows:

Equation 897 $$-\left[A^{TV}\cdot\frac{\partial P^V}{\partial t}+C^{TV}\cdot\frac{\partial V^L}{\partial t}+D^{TV}\cdot\dot{m}_{IN}^V+E^{TL}\cdot\dot{m}_{BOG}+F^{TV}\right]=B^{TV}\cdot\frac{\partial T^V}{\partial t}$$

The right part of Equation 896 is divided by the coefficient B^{TV}. Then, the vapour temperature-evolution equation (Equation 134) is obtained.

4. Mathematical steps to obtain the pressure-liquid volume equations

Pressure-liquid volume (P-V^L) equations (Equation 135 and Equation 136) are obtained from the linear form of the conservation laws (see Table 68), with mathematical steps that use the liquid temperature-evolution (T^L-e) and the vapour temperature-evolution (T^V-e) equations (Equation 133 and Equation 134).

Section 4.1 and 4.2 respectively describe the steps to obtain the vapour and liquid P-V^L equations.

4.1.Mathematical steps to obtain the vapour pressure-liquid volume equation

The linear form of the mass energy balance equation (Equation 108) is a function of the time-derivates of the pressure ($\frac{\partial P^V}{\partial t}$), ullage vapour ($\frac{\partial T^V}{\partial t}$) and liquid volume ($\frac{\partial V^L}{\partial t}$). The time-derivate of the ullage vapour ($\frac{\partial T^V}{\partial t}$) can be substituted with the vapour temperature-evolution (T^V-e) equation (Equation 134). So, the linear form of the mass energy balance equation can be written as follows:

Equation 898 $$\begin{gathered}-\frac{B^P}{B^{TV}}\cdot\left[A^{TV}\cdot\frac{\partial P^V}{\partial t}+C^{TV}\cdot\frac{\partial V^L}{\partial t}+D^{TV}\cdot\dot{m}_{IN}^V+E^{TL}\cdot\dot{m}_{BOG}+F^{TV}\right]\\+A^P\cdot\frac{\partial P^V}{\partial t}+C^P\cdot\frac{\partial V^L}{\partial t}+D^P\cdot\dot{m}_{IN}^V+E^P\cdot\dot{m}_{BOG}+F^P=0\end{gathered}$$

In Equation 898, the term $\frac{\partial P^V}{\partial t}$, $\frac{\partial V^L}{\partial t}$, $\dot{m}_{IN}^V$ and $\dot{m}_{BOG}$ are grouped in the left part. Equation 898 can be written as follows:

Equation 899 $$\begin{gathered}\left(A^P-\frac{B^P}{B^{TV}}\cdot A^{TV}\right)\cdot\frac{\partial P^V}{\partial t}+\left(C^P-\frac{B^P}{B^{TV}}\cdot C^{TV}\right)\cdot\frac{\partial V^L}{\partial t}\\+\left(D^P-\frac{B^P}{B^{TV}}\cdot D^{TV}\right)\cdot\dot{m}_{IN}^V+\left(E^P-\frac{B^P}{B^{TV}}\cdot E^{TV}\right)\cdot\dot{m}_{BOG}\\+F^P-\frac{B^P}{B^{TV}}\cdot F^{TV}=0\end{gathered}$$

In Equation 899, the term $\left(A^P-\frac{B^P}{B^{TV}}\cdot A^{TV}\right)$, $\left(C^P-\frac{B^P}{B^{TV}}\cdot C^{TV}\right)$, $\left(D^P-\frac{B^P}{B^{TV}}\cdot D^{TV}\right)$, $\left(E^P-\frac{B^P}{B^{TV}}\cdot E^{TV}\right)$ and $\left(F^P-\frac{B^P}{B^{TV}}\cdot F^{TV}\right)$ are substituted with the coefficients of Table 72. Then, the pressure-liquid volume (P-V^L) equation (Equation 135) is obtained.

4.2. Mathematical steps to obtain the liquid pressure-liquid volume equation

The linear form of the liquid mass balance equation (Equation 106) is a function of the time-derivates of the pressure ($\frac{\partial P^V}{\partial t}$), liquid vapour ($\frac{\partial T^L}{\partial t}$) and liquid volume ($\frac{\partial V^L}{\partial t}$). The time-derivate of the liquid temperature can be substituted with the liquid temperature-evolution (T^L-e) equation (Equation 133). linear form of the liquid mass balance equation can be written as follows:

Equation 900
$$-\frac{B^{HL}}{B^{TL}}\cdot\left[A^{TL}\cdot\frac{\partial P^V}{\partial t}+C^{TL}\cdot\frac{\partial V^L}{\partial t}+D^{TL}\cdot\dot{m}_{IN}^{L}+E^{TL}\cdot\dot{m}_{OUT}^{L}+F^{TL}\right]$$
$$+A^{HL}\cdot\frac{\partial P^V}{\partial t}+C^{HL}\cdot\frac{\partial V^L}{\partial t}+D^{HL}\cdot\dot{m}_{IN}^{L}+E^{HL}\cdot\dot{m}_{OUT}^{L}+F^{HL}=0$$

In Equation 900, the term $\frac{\partial P^V}{\partial t}$, $\frac{\partial V^L}{\partial t}$, $\dot{m}_{IN}^{L}$ and $\dot{m}_{OUT}^{L}$ are grouped in the left part of this equation. Equation 900 can be written as follows:

Equation 901
$$\left(A^{HL}-\frac{B^{HL}}{B^{TL}}\cdot A^{TL}\right)\cdot\frac{\partial P^V}{\partial t}+\left(C^{HL}-\frac{B^{HL}}{B^{TL}}\cdot C^{TL}\right)\cdot\frac{\partial V^L}{\partial t}$$
$$+\left(D^{HL}-\frac{B^{HL}}{B^{TL}}\cdot D^{TL}\right)\cdot\dot{m}_{IN}^{L}+\left(E^{HL}-\frac{B^{HL}}{B^{TL}}\cdot E^{TL}\right)\cdot\dot{m}_{OUT}^{L}$$
$$+F^{HL}-\frac{B^{HL}}{B^{TL}}\cdot F^{TL}=0$$

In Equation 901, the term $\left(A^{HL}-\frac{B^{HL}}{B^{TL}}\cdot A^{TL}\right)$, $\left(C^{HL}-\frac{B^{HL}}{B^{TL}}\cdot C^{TL}\right)$, $\left(D^{HL}-\frac{B^{HL}}{B^{TL}}\cdot D^{TL}\right)$, $\left(E^{HL}-\frac{B^{HL}}{B^{TL}}\cdot E^{TL}\right)$ and $\left(F^{HL}-\frac{B^{HL}}{B^{TL}}\cdot F^{TL}\right)$ are substituted with the coefficients of Table 72. The liquid pressure-liquid volume equation (Equation 136) is obtained.

5. Mathematical steps to obtain the pressure-evolution, liquid volume-evolution, boil-off gas and inlet flow rate equations.

The pressure evolution (P-e), liquid volume evolution (V^L-e), inlet liquid flow (ILF) and boil-off gas (BOG) equations (see Table 73) are obtained from the pressure-liquid volume (P-V^L) equations (see Table 71), for the steady state (storage mode 1.b) and for the self-pressurisation (storage mode 4). For the steady state, the pressure and the liquid volume are constant. Hence, the indipendent variables $\frac{\partial P^V}{\partial t}$ and $\frac{\partial V^L}{\partial t}$ are respectively computed with Equation 150 and Equation 152 (see Table 73). As consequence, the BOG flow ($\dot{m}_{BOG}$) and the inlet liquid mass flow ($\dot{m}_{IN}^{L}$) can be respectively computed with the BOG and ILF equations of the steady state. These equations are deduced from the pressure-liquid volume equations (see Table 71). In self-pressurisation, the mass flows $\dot{m}_{IN}^{L}$ and $\dot{m}_{BOG}$ are equals to zero because the storage container is closed. These flows are respectively computed with Equation 153 and Equation 155 (see Table 73). Hence, pressure time derivate ($\frac{\partial P^V}{\partial t}$) and the liquid volume time-derivate ($\frac{\partial V^L}{\partial t}$) can be respectively computed with the P-e and the V^L-e equations of the self-pressurisation, which are deduced from the pressure-liquid volume equations (see Table 71).

Section 5.1 and 5.2 respectively describe the mathematical steps to obtain the ILF and the BOG equations of the steady state. Section 5.3 and 5.4 respectively the mathematical steps to obtain the V^L-e and the P-e equations of the self-pressurisation.

5.1. Inlet liquid flow equation of the steady state

In the liquid pressure-liquid volume (P-V^L) equation (Equation 136), the term $\left(A'^{HL} \cdot \frac{\partial P^V}{\partial t} + C'^{HL} \cdot \frac{\partial V^L}{\partial t} + E'^{HL} \cdot \dot{m}_{OUT}^L + F'^{HL}\right)$ can be substituted with the coefficient Z^{HL}, which is computed with Equation 158. The liquid P-V^L equation can be written as follows:

Equation 902 $$\dot{m}_{IN}^L \cdot D'^{HL} + Z^{HL} = 0$$

In Equation 711, the coefficient Z^{HL} is moved to the right part of this equation. Equation 711 can be written as follows:

Equation 903 $$\dot{m}_{IN}^L \cdot D'^{HL} = -Z^{HL}$$

The left and the right part of Equation 903 are divided by the coefficient D'^{HL}. Then, the inlet liquid flow (ILF) of the steady state (Equation 156) is obtained.

5.2. Boil-off gas equation of the steady state

In the vapour pressure-liquid volume (P-V^L) equation (Equation 135), the term $\left(A'^{P} \cdot \frac{\partial P^V}{\partial t} + C'^{P} \cdot \frac{\partial V^L}{\partial t} + D'^{P} \cdot \dot{m}_{IN}^V + F'^{P}\right)$ can be substituted with the coefficient Z^P, which is computed with Equation 157. The vapour P-V^L equation can be written as follows:

Equation 904 $$\dot{m}_{BOG} \cdot E'^{P} + Z^P = 0$$

The coefficient Z^P is moved to the right part of Equation 904. Equation 904 can be written as follows:

Equation 905 $$\dot{m}_{BOG} \cdot E'^{P} = -Z^P$$

Equation 905 is divided by the coefficient E'^{P}. Then, the boil-off gas (BOG) equation of the steady state (Equation 154) is obtained.

5.3. Liquid volume-evolution equation of the self-pressurisation

In the liquid pressure-liquid volume (P-V^L) equation (Equation 136), the term $\left(D'^{HL} \cdot \dot{m}_{IN}^L + E'^{HL} \cdot \dot{m}_{OUT}^L + F'^{HL}\right)$ can be substituted with the coefficient Z^{HL}, which is computed with Equation 160. The liquid P-V^L equation can be written as follows:

Equation 906 $$A'^{HL} \cdot \frac{\partial P^V}{\partial t} + C'^{HL} \cdot \frac{\partial V^L}{\partial t} + Z^{HL} = 0$$

The term $(A'^{HL} \cdot \frac{\partial P^V}{\partial t} + Z^{HL})$ is moved to the right part of Equation 718. Equation 718 can be written as follows:

Equation 907 $$C'^{HL} \cdot \frac{\partial V^L}{\partial t} = -\left(Z^{HL} + A'^{HL} \cdot \frac{\partial P^V}{\partial t}\right)$$

Equation 907 is divided by the coefficient C'^{HL}. Then, the liquid volume (V^L-e) equation of self-pressurisation (Equation 151) is obtained.

5.4. Pressure-evolution equation of the self-pressurisation

In the vapour pressure-liquid volume (P-V^L) equation (Equation 135), the term $\left(D'^P \cdot \dot{m}_{IN}^V + E'^P \cdot \dot{m}_{BOG} + F'^P\right)$ can be substituted with the coefficient Z^P, which is computed with Equation 159. The vapour P-V^L equation can be written as follows:

Equation 908 $$A'^P \cdot \frac{\partial P^V}{\partial t} + C'^P \cdot \frac{\partial V^L}{\partial t} + Z^P = 0$$

The variable $\frac{\partial V^L}{\partial t}$ of Equation 721 is substituted with liquid volume-evolution (V^L-e) equation of the self-pressurisation (Equation 151). Equation 721 can be written as follows :

Equation 909 $$A'^P \cdot \frac{\partial P^V}{\partial t} - \frac{C'^P}{C'^{HL}} \cdot \left[Z^{HL} + A'^{HL} \cdot \frac{\partial P^V}{\partial t}\right] + Z^P = 0$$

The variable $\frac{\partial P^V}{\partial t}$ is grouped in the left part of Equation 722. Equation 722 can be written as follows :

Equation 910 $$\left(A'^P - A'^{HL} \cdot \frac{C'^P}{C'^{HL}}\right) \cdot \frac{\partial P^V}{\partial t} + Z^P - Z^{HL} \cdot \frac{C'^P}{C'^{HL}} = 0$$

The term $\left(Z^P - Z^{HL} \cdot \frac{C'^P}{C'^{HL}}\right)$ is moved to the right side of Equation 723. Equation 723 can be written as follows:

Equation 911 $$\left(A'^P - A'^{HL} \cdot \frac{C'^P}{C'^{HL}}\right) \cdot \frac{\partial P^V}{\partial t} = -\left(Z^P - Z^{HL} \cdot \frac{C'^P}{C'^{HL}}\right)$$

Equation 911 is divided by the term $\left(A'^P - A'^{HL} \cdot \frac{C'^P}{C'^{HL}}\right)$. Then, the pressure-evolution (P-e) equation of the self-pressurisation (Equation 149) is obtained.

Appendix N

Complementary information of Storage Heat Transfer model

The complementary information of the Storage Heat Transfer (SHT) model is given. This information is the definition of the dimensionless number, the equations to compute the Nusselt's number, the interpolation and extrapolation method to compute the Nusselt's number outside the applicability limits, and the method to use the heat fluxes and the difference in temperature Nusselt's number formulas.

Section 1 describes the dimensionless numbers that are required in the homogeneous model. Section 2 presents the equation to compute the Nusselt's number. Section 3 explains the applicability limits of these equations.

1. Dimensionless number

The dimensionless numbers are used in this thesis are the Prandtl's, Grashof's Raylegih and Nussel'ts number and they are reported in Table 230.

Table 230. Dimensionless number.

Variables	Name	Equation	Formula
Prandtl's number	Pr	Equation 912	$Pr = \frac{\nu}{\alpha} = \frac{\mu \cdot C_P}{k}$
Grashof's number (defined on difference in temperature)	$Gr_{\Delta T}$	Equation 913	$Gr_{\Delta T} = \frac{g_x \cdot \beta \cdot \theta_w \cdot x^3}{\nu^2}$
Grashof's number (defined on heat fluxes)	Gr_q	Equation 914	$Gr_q = Nu \cdot Gr_{\Delta T} = \frac{g_x \cdot \beta \cdot \dot{q}_w \cdot x^4}{k \cdot \nu^2}$
Grashof's number (discretized)	Gr_i	Equation 915	$Gr_i = Gr_{i-1} + \left.\frac{\partial Gr}{\partial Lc}\right\|_{i-1} \cdot dLc$
Derivate of Grashof's number (defined on difference in temperature)	$\frac{\partial Gr_{\Delta T}}{\partial Lc}$	Equation 916	$\frac{\partial Gr_{\Delta T}}{\partial Lc} = \frac{g_x \cdot \beta \cdot \theta_w \cdot 3 \cdot Lc^2}{\nu^2}$
Derivate of Grashof's number (defined on heat fluxes)	$\frac{\partial Gr_q}{\partial Lc}$	Equation 917	$\frac{\partial Gr_q}{\partial Lc} = \frac{g_x \cdot \beta \cdot \dot{q}_w \cdot 4 \cdot Lc^3}{k \cdot \nu^2}$
Pseudo-Grashof's number (defined on difference in temperature)	${Gr^S}_{\Delta T}$	Equation 918	${Gr^S}_{\Delta T} = \frac{g_x \cdot \beta \cdot \theta_w}{\nu^2}$
Pseudo-Grashof's number (defined on heat fluxes)	${Gr^S}_q$	Equation 919	${Gr^S}_q = \frac{g_x \cdot \beta \cdot \dot{q}_w}{k \cdot \nu^2}$
Rayleigh's number	Ra	Equation 920	$Ra = Gr \cdot Pr$
Nusselt's number (local)	Nu_x	Equation 921	$Nu_x = \frac{h \cdot x}{k}$
Nusselt's number (average)	$\overline{Nu}$	Equation 922	$\overline{Nu} = \frac{\bar{h} \cdot L_C}{k}$

The Prandtl number describes the ratio between the transferring of the momentum and the transferring of heat. The Grashof number is the ratio between the buoyancy forces and the viscous forces. The Nusselt number describes the ratio between the convective and conductive heat transfer processes.

2. Equations to compute the Nusselt's number for the semi-empirical approach

The heat transfer coefficient can be computed with the semi-empirical and with the boundary layer approaches, using the value of the heat fluxes ($\dot{q}_w$) or the value of the difference in temperatures (θ_w). In the semi-empirical approach, this coefficient is computed with Equation 193 as function of the average Nusselt's number ($\overline{Nu}$). This dimensionless number is calculated with semi-empirical formulas that are obtained from fitting the experimental data of heat transfer, for a defined characteristic length of the heat transfer. These formulas are reported in Table 231 for the heat fluxes mode (HF mode) and difference in temperatures mode (ΔT mode), specifying the characteristic length of each formula.

Table 231. Nusselt's number for the semi-empirical heat transfer coefficient.

L_C	Equation	Formula	Mode
		Bottom	
Diameter	Equation 923[138], [144]	$\overline{Nu} = 0.54 \cdot Ra_{\Delta T}^{\frac{1}{4}}$	ΔT mode
	Equation 924[138], [144]	$\overline{Nu} = 0.14 \cdot Ra_{\Delta T}^{\frac{1}{3}}$	
	Equation 925	$\overline{Nu} = 0.6108 \cdot Ra_q^{\frac{1}{5}}$	HF mode
	Equation 926	$\overline{Nu} = 0.2289 \cdot Ra_q^{\frac{1}{4}}$	
		Wet and dry side wall	
Liquid or vapour height in the tank	Equation 927[98], [145]	$\overline{Nu} = 0.68 \cdot Pr^{\frac{1}{4}} \cdot \left(Pr + \frac{20}{21}\right)^{-\frac{1}{4}} \cdot Ra_{\Delta T}^{\frac{1}{4}}$	ΔT mode
	Equation 928[99]	$\overline{Nu} = 0.0246 \cdot Pr^{\frac{7}{15}} \cdot \left[\left(0.494 \cdot Pr^{\frac{2}{3}} + 1\right) \cdot Pr\right]^{-\frac{2}{5}} \cdot Ra_{\Delta T}^{\frac{2}{5}}$	
	Equation 929	$\overline{Nu} = 0.7345 \cdot Pr^{\frac{1}{4}} \cdot \left(Pr + \frac{20}{21}\right)^{-\frac{1}{4}} \cdot Ra_q^{\frac{1}{5}}$	HF mode
	Equation 930	$\overline{Nu} = 0.0709 \cdot Pr^{\frac{7}{15}} \cdot \left[\left(0.494 \cdot Pr^{\frac{2}{3}} + 1\right) \cdot Pr\right]^{-\frac{2}{5}} \cdot Ra_q^{\frac{2}{7}}$	
		Roof	
Diameter	Equation 931[138], [144]	$\overline{Nu} = 0.27 \cdot Ra_{\Delta T}^{\frac{1}{4}}$	ΔT mode
	Equation 932	$\overline{Nu} = 0.3508 \cdot Ra_q^{\frac{1}{5}}$	HF mode

Equation 923, Equation 924, Equation 925 and Equation 926 are obtained for flat horizontal warm surface facing upward. Equation 931 and Equation 932 are deduced from the experimental data of flat horizontal cold surface facing upward. So, Equation 923, Equation 924, Equation 925 and Equation 926 are applied to the bottom because this surface is similar to the a flat horizontal warm surface facing upward; while Equation 931 and Equation 932 are used for the roof because this surface is like a flat horizontal cold surface facing upward. Equation 923, Equation 924, Equation 925, Equation 926, Equation 931 and Equation 932 compute the Nusselt's number in the heat transfer between the vapour and the interface. Equation 923, Equation 924, Equation 925 and Equation 926 are used when the interface the interface is hotter than the vapour, and Equation 931 and Equation 932 are applied if the interface is colder than the vapour.

Equation 925, Equation 926, Equation 929, Equation 930 and Equation 932 are obtained in this thesis, as it is described in Section 2.1.

2.1.Procedure to obtain the equations of heat fluxes model

Equation 923, Equation 924, Equation 927, Equation 928 and Equation 930 are obtained for isothermal surface. Hence, these formulas use the Rayleigh's number of Grashof's number that is defined on difference in temperature (Equation 913). In the Storage Heat Transfer, the heat fluxes can be used to compute the heat transfer coefficients and these equations has to be adapted to use the Rayleigh's number of Grashof's number that is defined on heat fluxes (Equation 914).

All the formulas of Table 231 can be generalized with Equation 933, which is reported below:

Equation 933 $$\overline{Nu} = A \cdot Ra_{\Delta T}^{B}$$

The Rayleigh number of Equation 933 can be computed with Equation 920. Hence, Equation 933 can be written as described below:

Equation 934 $$\overline{Nu} = A \cdot (Pr \cdot Gr_{\Delta T})^{B}$$

As it is indicated in Equation 914, $Gr_{\Delta T}$ can be computed as the ratio between Gr_q and $\overline{Nu}$. As consequence, Equation 934 can be written as:

Equation 935 $$\overline{Nu} = A \cdot \left(Pr \cdot \frac{Gr_q}{\overline{Nu}}\right)^{B}$$

The Nusselt's number can be deduced from Equation 935 and it can be computed as follows:

Equation 936 $$\overline{Nu} = A^{\frac{1}{1+B}} \cdot \left(Ra_q\right)^{\frac{B}{1+B}}$$

By properly replacing the coefficient A and the exponent B, Equation 925, Equation 926, Equation 929, Equation 930 and Equation 932 can be deduced from Equation 936.

3. Applicability limits

The equations reported in Table 80, Table 76, Table 78 and Table 231 are applied in certain applicability limits, which correspond to specific fluid-dynamic conditions. Table 232 reports the applicability limits for the equations of Table 80, Table 76, Table 78 and Table 231.

Table 232. Applicability limits.

Regime	**Limit value**	**Equations**
Laminar	$Ra_{\Delta T}^{LAM} = 10^8$	Equation 204, Equation 927[98], [145], Equation 161 [98], Equation 164 [98], Equation 180[99], Equation 181[98], Equation 186[132], Equation 187, Equation 192[98] and Equation 193[98]
	Ra_q^{LAM}	Equation 929, Equation 167 and Equation 170
Transition	$10^8 \leq Ra_{\Delta T} \leq 10^{10}$	Equation 205, Equation 162, Equation 165, Equation 168, Equation 171, Equation 182, Equation 183, Equation 188, Equation 189, Equation 194 and Equation 195
	$Ra_{\Delta T}^{LAM} \leq Ra_{\Delta T} \leq Ra_q^{TUR}$	Equation 168 and Equation 171
Turbulent	$Ra_{\Delta T}^{TUR} = 10^{10}$	Equation 206, Equation 928[99], Equation 163 [99], Equation 166 [99], Equation 184[98], Equation 185[99], Equation 190[132], Equation 191, Equation 196[99] and Equation 197[99]
	Ra_q^{TUR}	Equation 930, Equation 169 and Equation 172
Laminar	$Ra_{\Delta T}^{LAM} = 10^5 \leq Ra_{\Delta T} \leq Ra_{\Delta T}^{INT} = 2 \cdot 10^7$	Equation 923[138], [144]
	$Ra_q^{LAM} \leq Ra_q \leq Ra_q^{INT}$	Equation 925

Turbulent	$Ra_{\Delta T}^{INT} = 2 \cdot 10^7 \leq Ra_{\Delta T} \leq Ra_{\Delta T}^{TUR} = 3 \cdot 10^{10}$	Equation 924[138], [144]
	$Ra_q^{INT} \leq Ra_q \leq Ra_q^{TUR}$	Equation 926
Laminar	$Ra_{\Delta T}^{LAM} = 3 \cdot 10^5 \leq Ra_{\Delta T} \leq 3 \cdot 10^{10} = Ra_{\Delta T}^{INT}$	Equation 931[138], [144]
	$Ra_q^{LAM} \leq Ra_q \leq Ra_q^{INT}$	Equation 932

Ra_q^{LAM}, Ra_q^{INT} and Ra_q^{TUR} are respectively for laminar, transition and turbulent regimes, when the heat fluxes are used. The values of these limits are not reported. Hence, these values can be determined with Equation 937.

Equation 937
$$Ra_q = Ra_{\Delta T} \cdot Nu(Ra_{\Delta T})$$

$Ra_{\Delta T}$ is the limit Rayleigh's number on the difference in temperature and $Nu(Ra_{\Delta T})$ is Nusselt's number calculated at $Ra_{\Delta T}$. This dimensionless number is computed with the equations of Table 231.

Section 3.1 and 3.2 describes how the Nusselt's number is computed when equations of Table 231 are out of the applicability limits.

3.1.Linear interpolation of the Nusselt's number

The Nusselt's number can be computed with the semi-empirical formulas that are given in Table 80. Equation 923, Equation 924,Equation 924[138], [144] Equation 925, Equation 926, Equation 927, Equation 928, Equation 929, Equation 930, Equation 931 and Equation 932 can be applied in certain rages of the Rayleigh number. If the Rayleigh number is in one of the conditions described by Equation 938 and by Equation 939.

Equation 938
$$Ra_{low} < Ra < Ra_{up}$$

Equation 939
$$Ra < Ra_{low}$$

Ra_{low} is the lower applicability limit and Ra_{up} is the upper applicability limit. Under these circumstances, the Nusselt's number computed with Equation 940.

Equation 940
$$Nu = \exp\left[\frac{\ln\left(\frac{Nu_{up}}{Nu_{low}}\right)}{\ln\left(\frac{Ra_{up}}{Ra_{low}}\right)} \cdot \ln\left(\frac{Ra}{Ra_{low}}\right) + \ln\left(Nu_{low}\right)\right]$$

Nu_{up} and Nu_{low} are the Nusselt numbers that are respectively calculated at Ra_{up} and at Ra_{low}. The value of the exponential is the linear interpolation of the logarithm of the Nussel's number. As Indicated by the semi-empirical formulas of Table 80, the Nusselt's number is computed with a power-law equation of the Rayleigh's number. Hence, the logarithm of Nu is a linear equation. Equation 940 is modified when the condition of Equation 939 occurs. In this case, $Ra_{up} = Ra_{low}$, $Ra_{low} = 1$, $Nu_{up} = Nu(Ra_{low})$ and $Nu_{low} = 1$.

3.2.Extrapolation of Nusselt number

The extrapolation of Nusselt number is done when the value of the Rayleigh number is above the highest applicability limit. In these cases, it is assumed that the fluid-dynamic does not change. Hence, this dimensionless number can be estimated with the semi-empirical equations of Table 80.

Appendix O

Calculation of the boundary layer variables

The boundary layer variables (see Table 62) such as temperature (T_{BL}), mass flow ($\dot{m}_{BL}$), average speed ($\bar{u}$) and thermal thickness (δ_T) can be deduced from the momentum thickness (δ_M) and from the velocity outside boundary layer of comparable forced-convection flow (U) are computed with different equations, ad function of the boundary layer approach and heat mode used.

Section 1 and 2 present the equations to compute the boundary layer variables with the Exact Boundary Layer (EBL) and Integral Boundary Layer (IBL) approaches.

1. Equations to compute the temperature, the mass flow, the average velocity and the thermal thickness with the Exact Boundary Layer approach

In the Exact Boundary Layer (EBL) approach, the boundary layer variables (see Table 62) such as temperature (T_{BL}), mass flow ($\dot{m}_{BL}$), average speed ($\bar{u}$) and thermal thickness (δ_T) can be deduced from the momentum thickness (δ_M) and from the velocity outside boundary layer of comparable forced-convection flow (U). Table 233 reports equations to compute the T_{BL}, $\dot{m}_{BL}$, $\bar{u}$ and δ_T, and the thickness δ' from the values of δ_M and U.

Table 233. Equations to compute $\boldsymbol{T_{BL}}$, $\boldsymbol{\dot{m}_{BL}}$, $\boldsymbol{\bar{u}}$ and $\boldsymbol{\delta_T}$ in EBL approach.

Variables	Equation	Formula	Regime
$\bar{u}$	Equation 941 [2]	$\bar{u} = 0.0833 \cdot U$	Laminar
	Equation 942	$\bar{u} = \frac{\bar{u}^T - \bar{u}^L}{Ra^T - Ra^L} \cdot (Ra - Ra^L) + \bar{u}^L$	Transition
	Equation 943 [2]	$\bar{u} = 0.1464 \cdot U$	Turbulent
$\dot{m}_{BL}$	Equation 944 [2]	$\dot{m}_{BL}(x) = \bar{u} \cdot \rho \cdot \pi \cdot \delta_M \cdot D$	Laminar, transition and turbulent
δ_T	Equation 945 [2]	$\delta_T = \frac{\delta_M}{Pr^{\frac{1}{2}}}$	Laminar, transition and turbulent
δ'	Equation 946	$\delta' = \max\,[\delta_T; \delta_M]$	Laminar, transition and turbulent
T_{BL}	Equation 947 [2]	$T_{BL} = T + \frac{\theta_w}{3}$	Laminar
	Equation 948	$T_{BL} = \frac{{T_{BL}}^T - {T_{BL}}^L}{Ra^T - Ra^L} \cdot (Ra - Ra^L) + {T_{BL}}^L$	Transition
	Equation 949 [2]	$T_{BL} = T + \frac{\theta_w}{8}$	Turbulent

Equation 942, Equation 946 and Equation 948 are obtained in this thesis. Equation 942 and Equation 948 are obtained considering a linear interpolation between the laminar and turbulent regimes. Ra is the general Rayleigh number and it can be local, average, hear fluxes and difference in temperature. Ra^T and Ra^L are the general Rayleigh's number that defines the turbulent and laminar limits, respectively. $\bar{u}^T$ and $\bar{u}^L$ are computed with Equation 943 and with Equation 941, using Ra^T and Ra^L, respectively. θ_w is the difference in temperature between the wall and the bulk. It is computed as explained in Section 1.1

1.1. Calculation of the difference in temperature between the wall and the liquid in the Exact Boundary Layer approach

The Exact Boundary Layer (EBL) approach computes the boundary layer variables (see Table 62) as the formulas of Table 233. To use these formulas, the heat fluxes at the wall ($\dot{q}_w$) or the difference in temperatures between the wall and the fluid (θ_w) has to be given. In the difference in temperatures mode (ΔT mode), this value of the difference in given as input parameter and the temperature in the boundary layer (T_{BL}) can be computed with Equation 947, Equation 948 and Equation 949. In the heat fluxes mode (HF mode), T_{BL} can be estimated with Equation 947, Equation 948 and Equation 949. The θ_w must be computed from the heat fluxes for the difference fluid-dynamic regimes.

Section 1.1.1, 1.1.2 and 1.1.3 describes how the difference in temperatures is computed from the heat fluxes for the laminar, transient and turbulent regime, respectively.

1.1.1. Laminar regime

In laminar regime, the temperature profile of the boundary layer temperature along the perpendicular coordinate of the wall (y) can be computed as follows:

Equation 950 [145]
$$T^{BL}(x,y) = T(x) + \theta_w(x) \cdot \left(1 - \frac{y}{\delta_M(x)}\right)^2$$

T is the temperature of the bulk. x is the coordinate parallel to the surface. The heat fluxes at the wall can be computed as follows:

Equation 951 [145]
$$\dot{q}_w(x) = -k \cdot \left.\frac{\partial T_{BL}}{\partial x}\right|_{x=0}$$

$\left.\frac{\partial T_{BL}}{\partial x}\right|_{x=0}$ is the derivate of the temperature profile of the boundary layer temperature at the wall. This variable can be deduced from Equation 950. Hence, the heat flux is calculated as follows:

Equation 952 [145]
$$\dot{q}_w(x) = 2 \cdot k \cdot \frac{\theta_w(x)}{\delta_M(x)}$$

From Equation 952, the difference in temperature can be computed, as follows:

Equation 953
$$\theta_w(x) = \frac{\dot{q}_w(x) \cdot \delta_M(x)}{2 \cdot k}$$

Equation 953 computes the difference in temperatures as function of the boundary layer variable $\delta_M(x)$. The boundary layer variable $U(x)$ does not affect Equation 953.

1.1.2. Transition regime

In transition regime, the difference in temperature is calculated as linear interpolation between the laminar and the turbulent formulas. Hence, the difference in temperature is calculated as follows:

Equation 954
$$\theta_w(x) = \frac{\theta_w^T - \theta_w^L}{Ra^T - Ra^L} \cdot (Ra(x) - Ra^L) + \theta_w^L$$

θ_w^T and θ_w^L are respectively computed with Equation 956 and with Equation 953. Ra^T and Ra^L are the turbulent and laminar limits, as it is reported in Section 3 of Appendix N.

1.1.3. Turbulent regime

In turbulent regime, the heat flux at the wall $\dot{q}_w$is related to the difference in temperatures (θ_w) as follows:

Equation 955 [99]
$$\dot{q}_w(x) = 0.0225 \cdot \rho \cdot C_P \cdot U(x) \cdot \left(\frac{v}{U(x) \cdot \delta_M(x)}\right)^{0.25} \cdot \theta_w(x) \cdot Pr^{-\frac{2}{3}}$$

Equation 955 is experimentally deduced from the experimental data of heat transfer and forced-convection over isothermal vertical surface. From Equation 955, the difference in temperature can be deduced. Hence, θ_w is computed as follows:

Equation 956
$$\theta_w(x) = \frac{\dot{q}_w(x) \cdot Pr^{\frac{2}{3}}}{0.0225 \cdot \rho \cdot C_P \cdot U(x) \cdot \left(\frac{v}{U(x) \cdot \delta_M(x)}\right)^{0.25}}$$

Equation 956 depends on the boundary layer variables $U(x)$ and $\delta_M(x)$.

2. Equations to compute the temperature, the mass flow, the average velocity and the thermal thickness with the Integral Boundary Layer approach

In the Integrated Boundary Layer (IBL) approach, the boundary layer variables (see Table 62) such as average speed ($\bar{u}$) and thermal thickness (δ_T) can be deduced from the momentum thickness (δ_M) and from the velocity outside boundary layer of comparable forced-convection flow (U), as it is described in Table 233. The mass flow ($\dot{m}^{UP}$) is computed as follows:

Equation 957 [2]
$$\dot{m}^{UP}(x) = \bar{u}(x) \cdot \rho \cdot \pi \cdot \delta_M(x) \cdot (D - \delta_M(x))$$

Equation 957 [2] is applied for laminar, transition and turbulent regimes. D is the internal diameter of the storage container. The value of this variable is constant in vertically cylinder and it change with the vertical distance between the bottom and the sub-layer in spherical and oblate storage container.

The temperature in the boundary layer (T^{BL}) is computed as explained in Section 2.1 of Appendix O.

2.1. Temperature in the boundary layer of the Integral Boundary Layer approach

The temperature in the boundary layer (T^{BL}) cannot be computed as done for the Exact Boundary Layer (EBL) approach due to the hypothesis of discretized boundary layer (see Section 3.4). This variable can be, however, calculated with the mass and energy conservation laws. If the hypothesis of discretized boundary layer is applied, the mass flow and the enthalpy flow in the boundary layer can be illustrated with Figure 214. In Figure 214, the white arrows with red boarder are the heat inputs at the side wall. The black square with the yellow boarder and the white square with green boarder are the sub-layers of the wall and of the boundary layer, respectively. The white points with the purple boarder are the wall temperatures. The red and the blue arrows indicate the mass and the enthalpy flows, respectively.

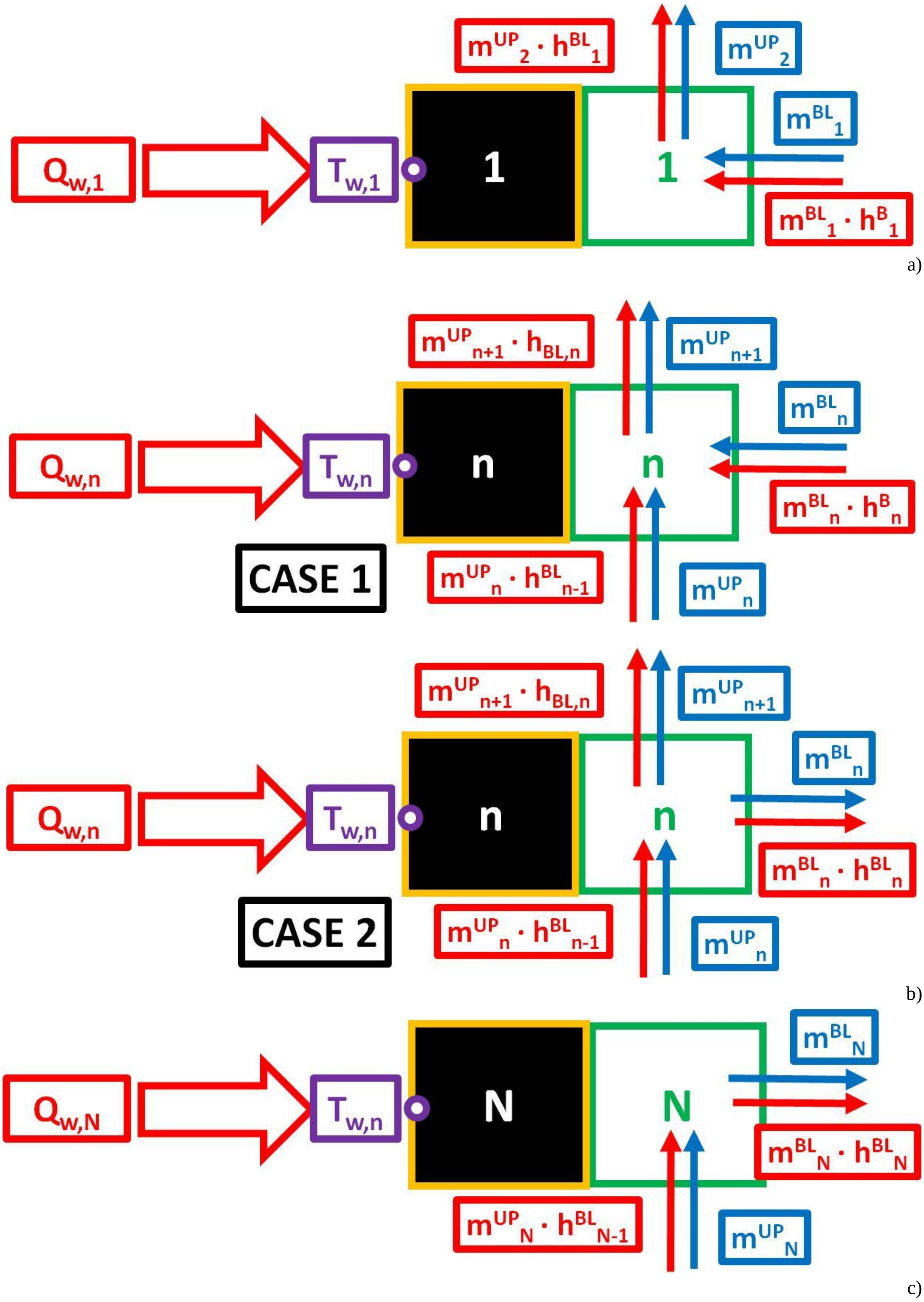

Figure 214. Mass and enthalpy flows in the boundary layer: a) first sub-layer, b) “n” sub-layer; c) last sub-layer.

As it is illustrated in Figure 214, there are two cases of the configuration of the enthalpy and mass flows in the “n” sub-layer, in particular due to the direction of the bulk-to-boundary layer mass flow ($\dot{m}_n^{UP}$). This variable can enter the sub-layer mass enters the boundary layer when the bulk temperature gradient is low. So, $\dot{m}_n^{UP}$ usually enters the boundary layer in homogeneous medium.

When this gradient increases, the buoyancy forces are lower than the viscuous forces and the mass exit the boundary layer. So, $\dot{m}_n^{UP}$ often exit the boundary layer in stratified medium. As it is illustrated in Figure 214, the mass flow rate in the boundary layer is equal to zero at the first and last sub-layers. The conservation laws of mass and of energy to describe the sub-layer of Figure 214 are reported in Table 234.

Table 234. Energy and mass conservation laws in sub-layers.

Conservation law	Equation	Formula
		First sub-layer
Mass	Equation 958	$\dot{m}_2^{UP} - \dot{m}_1^{BL} = 0$
Energy	Equation 959	$\dot{Q}_{W,1} + \dot{m}_2^{UP} \cdot \tilde{h}_1^{BL} - \dot{m}_1^{BL} \cdot \tilde{h}_1^{B} = 0$
		"n" sub-layer (Case 1)
Mass	Equation 960	$\dot{m}_n^{BL} - \dot{m}_{n+1}^{UP} + \dot{m}_n^{UP} = 0$
Energy	Equation 961	$\dot{Q}_{W,n} + \dot{m}_n^{BL} \cdot \tilde{h}_n^{B} - \dot{m}_{n+1}^{UP} \cdot \tilde{h}_n^{BL} + \dot{m}_n^{UP} \cdot \tilde{h}_{n-1}^{BL} = 0$
		"n" sub-layer (Case 2)
Mass	Equation 962	$-\dot{m}_n^{BL} - \dot{m}_{n+1}^{UP} + \dot{m}_n^{UP} = 0$
Energy	Equation 963	$\dot{Q}_{W,n} - \dot{m}_n^{BL} \cdot \tilde{h}_n^{BL} - \dot{m}_{n+1}^{UP} \cdot \tilde{h}_n^{BL} + \dot{m}_n^{UP} \cdot \tilde{h}_{n-1}^{BL} = 0$
		Last sub-layer
Mass	Equation 964	$-\dot{m}_N^{BL} + \dot{m}_N^{UP} = 0$
Energy	Equation 965	$\dot{Q}_{W,N} - \dot{m}_N^{BL} \cdot \tilde{h}_N^{BL} + \dot{m}_N^{UP} \cdot \tilde{h}_{N-1}^{BL} = 0$

$\tilde{h}^B$ is the specific enthalpy at the temperature of the bulk and $\tilde{h}^{BL}$ is the specific enthalpy at the temperature of the boundary layer. Due to the hypothesis of steady state of the boundary layer (assumption g) of Section 3.1), these equations do not have the transient.The mass flow $\dot{m}_1^{BL}$ can be substituted from the energy balance equation of the first sub-layer (Equation 959), using the mass balance equation of this sub-layer (Equation 958). The mass flow $\dot{m}_n^{BL}$ can be substituted in Equation 961 and Equation 963 (energy balance equations) with Equation 960 and with Equation 962, respectively. $\dot{m}_N^{BL}$ can be substituted from the energy balance equation of the last sub-layer (Equation 965), by applying the mass balance equation of this sub-layer (Equation 964). Hence, the conservation laws of the sub-layer of the boundary layer can described with the formulas of Table 235.

Table 235. Energy and mass conservation laws in sub-layers after removing $\boldsymbol{\dot{m}_1^{BL}}$, $\boldsymbol{\dot{m}_n^{BL}}$ and $\boldsymbol{\dot{m}_N^{BL}}$.

Conservation law	Equation	Formula
		First sub-layer
Mass	Equation 966	$\dot{m}_2^{UP} = \dot{m}_1^{BL}$
Energy	Equation 967	$\dot{Q}_{W,1} + \dot{m}_2^{UP} \cdot \tilde{h}_1^{BL} - \dot{m}_2^{UP} \cdot \tilde{h}_1^{B} = 0$
		"n" sub-layer (Case 1)
Mass	Equation 968	$\dot{m}_n^{BL} = \dot{m}_{n+1}^{UP} - \dot{m}_n^{UP}$
Energy	Equation 969	$\dot{Q}_{W,n} + (\dot{m}_{n+1}^{UP} - \dot{m}_n^{UP}) \cdot \tilde{h}_n^{B} - \dot{m}_{n+1}^{UP} \cdot \tilde{h}_n^{BL} + \dot{m}_n^{UP} \cdot \tilde{h}_{n-1}^{BL} = 0$
		"n" sub-layer (Case 2)
Mass	Equation 970	$\dot{m}_n^{BL} = \dot{m}_n^{UP} - \dot{m}_{n+1}^{UP}$
Energy	Equation 971	$\dot{Q}_{W,n} - (\dot{m}_n^{UP} - \dot{m}_{n+1}^{UP}) \cdot \tilde{h}_n^{BL} - \dot{m}_{n+1}^{UP} \cdot \tilde{h}_n^{BL} + \dot{m}_n^{UP} \cdot \tilde{h}_{n-1}^{BL} = 0$
		Last sub-layer
Mass	Equation 972	$\dot{m}_N^{BL} = \dot{m}_N^{UP}$
Energy	Equation 973	$\dot{Q}_{W,N} - \dot{m}_N^{UP} \cdot \tilde{h}_N^{BL} + \dot{m}_N^{UP} \cdot \tilde{h}_{N-1}^{BL} = 0$

The specific enthalpy of the bulk ($\tilde{h}^B$) can be calculated as product of the temperature of the bulk (T^B) and the specific heat at constant temperature (C_P). The specific enthalpy of the boundary layer ($\tilde{h}^{BL}$) can be computed as product of the temperature of the boundary layer (T^{BL}) and the specific heat at constant temperature. The mass flows $\dot{m}_2^{UP}$, $\dot{m}_{n+1}^{UP}$, $\dot{m}_n^{UP}$ and $\dot{m}_N^{UP}$ are grouped in Equation 967, Equation 969, Equation 971 and Equation 973. So, the energy balance equations of the boundary layer can be described with the formulas of Table 236.

Table 236. Energy and mass conservation laws in sub-layers after grouping $\dot{\boldsymbol{m}}_{\boldsymbol{2}}^{\boldsymbol{UP}}$, $\dot{\boldsymbol{m}}_{\boldsymbol{n+1}}^{\boldsymbol{UP}}$, $\dot{\boldsymbol{m}}_{\boldsymbol{n}}^{\boldsymbol{UP}}$ and $\dot{\boldsymbol{m}}_{\boldsymbol{N}}^{\boldsymbol{UP}}$.

Sub-layer	Equation	Formula
First	Equation 974	$\dot{Q}_{W,1} + \dot{m}_2^{UP} \cdot C_P \cdot (T_1^B - T_1^{BL}) = 0$
Core (Case 1)	Equation 975	$\dot{Q}_{W,n} + \dot{m}_{n+1}^{UP} \cdot (T_n^B - T_n^{BL}) + \dot{m}_n^{UP} \cdot (T_{n-1}^{BL} - T_n^{BL}) = 0$
Core (Case 2)	Equation 976	$\dot{Q}_{W,n} + \dot{m}_n^{UP} \cdot (T_{n-1}^{BL} - T_n^{BL}) = 0$
Last	Equation 977	$\dot{Q}_{W,N} - \dot{m}_N^{UP} \cdot (T_{N-1}^{BL} - T_N^{BL}) = 0$

From the formulas of Table 236, the boundary layer temperature can be deduced. So, this variable is computed with the formulas of Table 237 for each sub-layer of the boundary layer.

Table 237. Equations to compute the boundary layer temperatures.

Sub-layer	Equation	Formula
First	Equation 978	$T_1^{BL} = T_1^B + \dfrac{\dot{Q}_{W,1}}{\dot{m}_2^{UP} \cdot C_P}$
“n” case 1	Equation 979	$T_n^{BL} = T_n^B + \dfrac{\dot{Q}_{W,n} + \dot{m}_n^{UP} \cdot C_P \cdot (T_{BL,n-1} - T_{B,n})}{\dot{m}_{n+1}^{UP} \cdot C_P}$
“n” case 2	Equation 980	$T_n^{BL} = T_{n-1}^{BL} + \dfrac{\dot{Q}_{W,n}}{\dot{m}_n^{UP} \cdot C_P}$
Last	Equation 981	$T_N^{BL} = T_{N-1}^{BL} + \dfrac{\dot{Q}_{W,N}}{\dot{m}_N^{UP} \cdot C_P}$

Formulas of Table 237 can be applied for the dry and wet side walls.

Appendix P

Algorithm of Storage Boundary Layer model

The Storage Boundary Layer (SBL) uses Exact Boundary Layer (EBL) approach and for the Integral Boundary Layer (IBL) approach. These apporahces compute the boundary layer variables (see Table 62) at the flat ends of the storage container and at the side wall, respectively.

Section 1 and 2 describes the algorithms of SBL model for the EBL approach and for the IBL approach, respectively.

1. Algorithm of the Exact Boundary Layer approach

The Exact Boundary Layer (EBL) approach computes the boundary layer variables of Table 62 at the flat ends. The formulas to compute these variables are deduced from theory of free-convection over vertical surface in homogeneous medium [1],[2]. The input and the output of the EBL approach are reported in Table 238.

Table 238. Input and output of the EBL approach.

Variable	Description
Input	State variables and thermo-physical properties (see Table 62 and Table 49), heat flows at the surface or the surface wall temperature, gravity acceleration and characteristic length.
Output	boundary layer variables (see Table 62)

The value of the gravity acceleration is 9.81 m/s², and the characteristic length is half of the diameter for flat ends of vertical cylinder. The algorithm of the EBL approach is described in Figure 215.

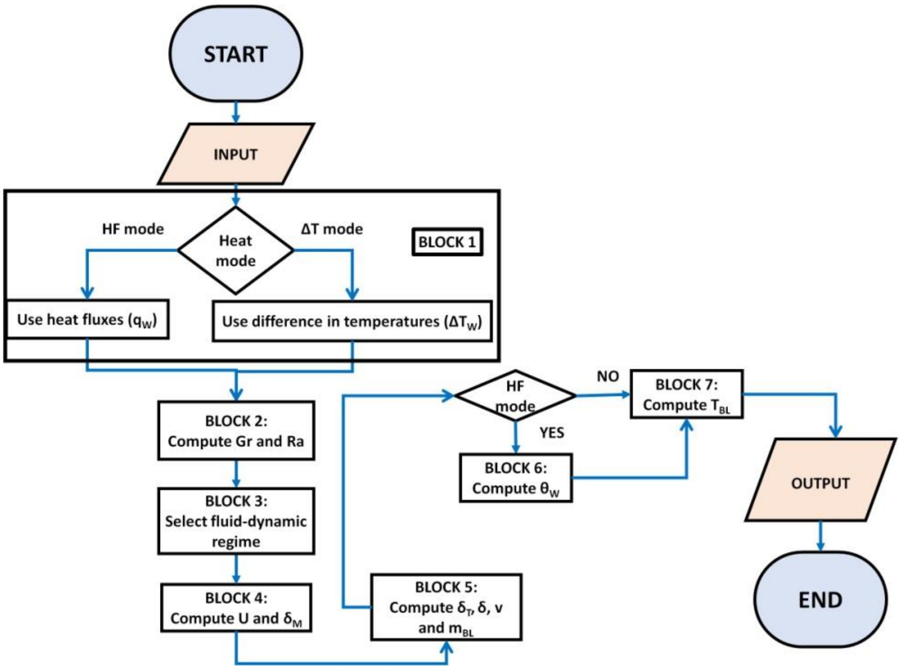

Figure 215. Algorithm of EBL approach.

This algortimh is composed by the following steps:

a) BLOCK 1: selection of the heat mode. If this difference in temperatures is given as input parameter, the ΔT mode is chosen. When the heat flow is used as input, the HF mode is applied;

b) BLOCK 2. The Grashof (Gr) and the Rayleigh (Ra) numbers are calculated with the equations of Table 230 ;
c) BLOCK 3. The fluid-dynamics regime is selected, as explained in Section 3 of Appendix N;
d) BLOCK 4. The momentum thickness (δ_M) and the velocity outside boundary layer of comparable forced-convection flow (U) are computed with the equations of Table 76.
e) BLOCK 5. The mass flow ($\dot{m}_{BL}$), average speed ($\bar{u}$), thermal thickness (δ_T) and the thickness (δ') are computed with the equations of Table 233.
f) BLOCK 6. The difference in temperature (θ_w) is calculated with the equations of Section 1.1 of Appendix O, if the HF mode is applied. If the ΔT mode is chosen, this block is not done and the algorithm goes to BLOCK 7 (step g) of Section 1 of Appendix P.
g) BLOCK 7. The temperature in the boundary layer is computed as indicated in Table 233.

As it is described in Figure 215, this algortimh does not have any iterative procedure.

2. Algorithm of the Integral Boundary Layer approach

In the Integral Boundary Layer (IBL) approach, the momentum thickness (δ_M) and the velocity outside boundary layer of comparable forced-convection flow (U) are computed by numerically integrate momentum and energy conservation laws of the boundary layer (Equation 178 and Equation 179) along the side walls. This integration requires the input variables that are reported in Table 239.

Table 239. Input and output of the IBL approach.

Variable	Description
Input	State variables and thermo-physical properties (see Table 62 and Table 49), heat flows at the surface or the surface wall temperature, gravity acceleration, length of the side wall (L_c), diameter at every sub-layer (a_n) and the discretized length of the side ($dL_{c,n}$)
Output	boundary layer variables (see Table 62)

a_n and $dL_{c,n}$ are determined with the equations of Table 77. The algorithm of the IBL approach is described in Figure 216.

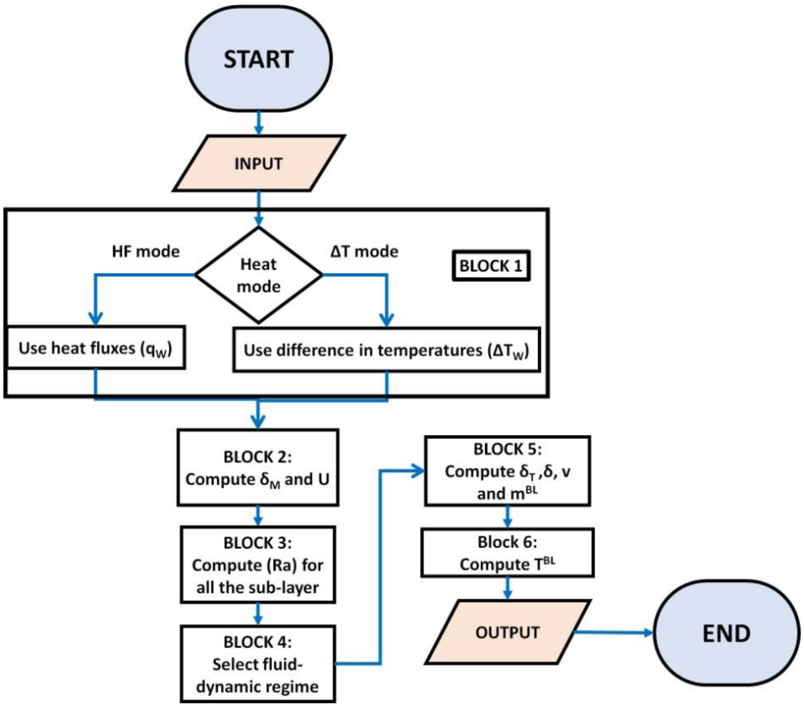

Figure 216. Algorithm of IBL model.

This is composed by the following steps:

a) BLOCK 1: selection of the heat mode. If this difference in temperatures is given as input parameter, the ΔT mode is chosen. When the heat flow is used as input, the HF mode is applied;
b) BLOCK 2. The momentum thickness (δ_M) and the velocity outside boundary layer of comparable forced-convection flow (U) are computed with the integration algorithm for all the sub-layers, as it is reported in Section 2 of Appendix P;
c) BLOCK 3. The Rayleigh (Ra) numbers are calculated with the equations of Table 230 for all the sub-layers;
d) BLOCK 4. The fluid-dynamics regime is selected, as explained in Section 3 of Appendix N for all the sub-layer ;
e) BLOCK 5. Average speed ($\bar{u}$), thermal thickness (δ_T) and the thickness (δ') are computed with the equations of Table 233, for all the sub-layers. The mass flow ($\dot{m}_{BL}$) is calculated in all the sub-layer with Equation 982.

Equation 982 $$\dot{m}_{BL}(x) = \bar{u} \cdot \rho \cdot \pi \cdot \delta_M \cdot (a_n - \delta_M)$$

Equation 982 can be applied in laminar, transition and turbulent regime.

f) BLOCK 6. The temperature in the boundary layer is computed as indicated in Section 2.1 of Appendix O. As it is showen in Figure 216, this algortimh is not an iterative procedure. Iterative calculations are present in Block 2 for computing the boundary layer variables δ_M and U. Block 2 described in Section 2.1.

2.1.BLOCK 2: Integration algorithm

The numerical integration is the Block 2 of the algorithm of the IBL approach (see Figure 216). This integration is the core of the algorithm of the Integral Boundary Layer (IBL) approach. The numerical integration computes the values of the momentum thickness (δ_M) and the velocity outside boundary layer of comparable forced-convection flow (U) in all the sub-layers, by integrating the momentum and energy conservation laws of the boundary layer (Equation 178 and Equation 179) along the side walls. This numerically integration requires some hypotheses. Pseudo-boundary layer variables are introduced to improve the stability of the numerical algorithm. These variables are respectively called of momentum boundary variable (M) and energy boundary variable (E).

Section 2.1.1 explains the hypotheses. Section 2.1.2 presents the pseudo-variables and Section 2.1.3 describes the structure of the integration algorithm.

2.1.1. Hypotheses

The liquid side wall is limited by the interface and by the bottom, respectively in the upper and in the lower parts of the wall. The interface and the bottom are rigid surface and the side wall mass flow rate cannot pass through these surfaces. The vapour side wall is confined by the interface and by the roof, respectively in the upper and in the lower parts of the wall. The interface and the roof are rigid surface and the boundary layer mass flow does not pass through these surfaces. Hence, it can be assumed:

a) The mass flow rate leaving the last sub-layer ($\dot{m}_{BL,N+1}$) is equal to zero;
b) The mass flow rate entering the first sub-layer ($\dot{m}_{BL,1}$) is equal to zero;
c) Hypotheses a) and b) of Section 2.1.1 are valid for liquid and vapour side wall.

Hence, the values of momentum thickness (δ_M) and the velocity outside boundary layer of comparable forced-convection flow (U) are equals to zero at the last and first sub-layers.

2.1.2. Pseudo-variables

Momentum and energy conservation laws of the boundary layer (Equation 178 and Equation 179) contains several term such as the viscous forces, the buoyancy forces, the bulk heat fluxes, the wall gradient heat fluxes and the wall heat fluxes, and the coefficients. These terms can be computed with the equations of Table 78, which change with the fluid-dynamic regime. These equations depends on momentum thickness (δ_M) and from the velocity outside boundary layer of comparable forced-convection flow (U). Hence, the numerical integration can be instable because the laminar equations changes from the transition equations, which are different from the turbulent equations.

To avoid this instability, the pseudo-boundary layer variables are introduced. These variables are respectively called computed the momentum and the energy boundary variables (M and E). These variables are computed as follows:

Equation 983 $$M = U^2 \cdot \delta_M$$

Equation 984 $$E = U \cdot \delta_M$$

As consequence, momentum and energy conservation laws of the boundary layer (Equation 178 and Equation 179) can be expressed as follows:

Equation 985 $$\frac{\partial M}{\partial x} = \frac{(F_B - \tau_w)}{\rho \cdot \Lambda}$$

Equation 986 $$\frac{\partial E}{\partial x} = \frac{\left(\dot{q}_w - \dot{q}_\infty - \dot{q}_{\theta_w}\right)}{C_P \cdot \rho \cdot \theta_w \cdot \Upsilon}$$

$F_{B,x}$, τ_w, Λ, $\dot{q}_w$, $\dot{q}_\infty$, $\dot{q}_{\theta_w}$ and Υ are calculated with the equations of Table 78. Hence, δ_M and U must be deduced from M and E, and they can be computed as follows:

Equation 987 $$U = \frac{M}{E}$$

Equation 988 $$\delta_M = \frac{E^2}{M}$$

The values of U, δ_M, M and E are computed for every sub-layers.

2.1.3. Structure of the algorithm

The input and the output variables of the integration algorithm (Block 2 of Integral Boundary Layer (IBL) algorithm, see Figure 216) are reported in Table 240.

Table 240. Input and output of the Block 2 of IBL approach.

Variable	Description
Input	State variables and thermo-physical properties (see Table 62 and Table 49), heat flows at the surface or the surface wall temperature, geometry, heat mode and number of sub-layer (N_s).
Output	momentum thickness (δ_M) and the velocity outside boundary layer of comparable forced-convection flow (U) in every sub-layer

N_s is determined with algorithm of Section 1 of Appendix L.

The numerical integration requires the values of δ_M and U at the first sub-layer. The values of these variables are computed with the Exact Boundary Layer (EBL) approach.

The algorithm of the numerical integration is described in Figure 217.

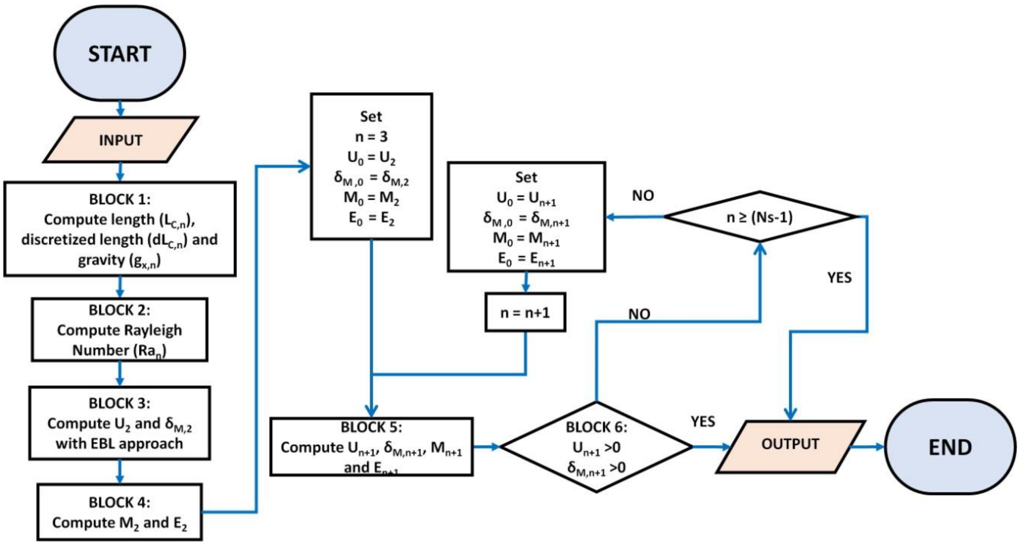

Figure 217. Integration algorithm (Block 2 of IBL approach).

This algorithm is composed by the following steps:

a) BLOCK 1. The length ($L_{C,n}$), the discretized length ($dL_{C,n}$) and the parallel to plane component of the gravity acceleration ($g_{x,n}$) are computed for every sub-layers, with equations of Table 77;

b) BLOCK 2. The Rayleigh (Ra_n) numbers are calculated with the equations of Table 230 for all the sub-layers;

c) BLOCK 3. The values of momentum thickness ($\delta_{M,2}$) and from the velocity outside boundary layer of comparable forced-convection flow (U_2) at the exit of the first sub-layers are computed with the Exact Boundary Layer (EBL) approach (see Section 1 of Appendix P);

d) BLOCK 4. The value of the momentum and energy boundary variables (M_2 and E_2) at the exit of the first sub-layer are computed with Equation 983 and with Equation 984, using $\delta_{M,2}$ and U_2. The input variables of of δ_M, U, M and E of integration algorithm of the sub-layer (see Section 2.1.4) are equal to $\delta_{M,2}$, U_2, M_2 and E_2, respectively. these variables are called which are called $\delta_{M,0}$, U_0, M_0 and E_0;

e) BLOCK 5. The values of $\delta_{M,n+1}$, U_{n+1}, M_{n+1} and E_{n+1} are computed with the integration algorithm of the sub-layer (see Section 2.1.4);

f) BLOCK 6. The values of $\delta_{M,n+1}$ and U_{n+1} must be positive and two pathways are present:
  - Pathway 1.6 (P 1.6): if $\delta_{M,n+1}$ is lower or equal to 0, or U_{n+1} is lower or equal to 0, the algorithm stops;
  - Pathway 2.6 (P 2.6): if $\delta_{M,n+1}$ and U_{n+1} are positive, $\delta_{M,0}$, U_0, M_0 and E_0 are equal to $\delta_{M,n+1}$, U_{n+1}, M_{n+1} and E_{n+1}, respectively. If the number of current step is below $N_S - 1$, the algorithm goes back to Block 5 (step e) of Section 2.1.3) to do the numerical integration at the next sub-layer.

One may note that step f) is present because E and M can be lower than zero. This situation indicates that there is not enough momentum or energy to sustain the free-convection. Hence, the numerical integration must stops too.

2.1.4. BLOCK 5: integration algorithm of sub-layer

The buoyancy forces ($F_{B,x}$) of the momentum conservation law (Equation 178) can be respectively computed with Equation 181, Equation 183 and Equation 185 for the laminar, transition and turbulent regime. In Equation 181, the force is computed with the ratio $\frac{U}{\delta_M}$ and, in Equation 185, $F_{B,x}$ is calculated with $U^2 \cdot \left(\frac{v}{U \cdot \delta_M}\right)^{0.25}$. When the value of U and of δ_M are low, the ratio $\frac{U}{\delta_M}$ is more instable than the term $U^2 \cdot \left(\frac{v}{U \cdot \delta_M}\right)^{0.25}$. Hence, the numerical integration of Equation 178 is more instable in the laminar regime than in the turbulent one. The stability is increased with the discretisation of the sub-layer and with a suitable algorithm.

Section 2.1.4.1 describes the discretisation of the sub-layer. Section 2.1.4.2 explains the structure of the integration algorithm of the sub-layer.

2.1.4.1. Discretisation of the sub-layer

To increase the stability and the precision of the integration algorithm (see Section 2.1 of Appendix P), the sub-layer of the boundary layer is further discretized into sub-space-points. The number of the sub-space-points increases the computational time. Hence, it must be chosen to optimize the computational time, maintaining a suitable accuracy. A high number of sub-space-points is required the values of the derivate are close to the critical value. The critical derivate is the derivate that computes the value zero of the pseudo-variable. The number of sub-space-points can be reduced when the derivate are far away from the critical ones. Since there are two pseudo-variables, two type of number of sub-space-point can be presented because the momentum and the energy conservation laws (Equation 178 and Equation 179) can have different instability. Hence, the number of the sub-space-points can be computed with the equations of Table 241.

Table 241. Equation to compute N_{SS}.

Variable	Symbol	Equation	Formula
the number of sub-space-points	N_{SS}	Equation 989	$N_{SS} = max[N_{SS}^M; N_{SS}^E; 10^3]$
number of sub-space-points for the momentum	N_{SS}^M	Equation 990	$N_{SS}^M = round\left[abs\left(\frac{\left.\frac{\partial M}{\partial L_C}\right\vert_0}{\left.\frac{\partial M}{\partial L_C}\right\vert_{MAX}}\right)\right]$
number of sub-space-points for the energy	N_{SS}^E	Equation 991	$N_{SS}^E = round\left[abs\left(\frac{\left.\frac{\partial E}{\partial L_C}\right\vert_0}{\left.\frac{\partial E}{\partial L_C}\right\vert_{MAX}}\right)\right]$
the critical derivate of momentum boundary variable	$\left.\frac{\partial M}{\partial L_C}\right\vert_{MAX}$	Equation 992	$\left.\frac{\partial M}{\partial L_C}\right\vert_{MAX} = \left\vert -\frac{M_0}{dL_C}\right\vert$
the critical derivate of energy boundary variable	$\left.\frac{\partial E}{\partial L_C}\right\vert_{MAX}$	Equation 993	$\left.\frac{\partial E}{\partial L_C}\right\vert_{MAX} = \left\vert -\frac{E_0}{dL_C}\right\vert$

$\left.\frac{\partial M}{\partial L_C}\right\vert_0$ and $\left.\frac{\partial E}{\partial L_C}\right\vert_0$ The values of the derivates at the previous numerical step, respectively for the momentum and the energy pseudo-boundary variables. M_0 and E_0 are the values at the previous numerical step. To avoid long computational time, the value of N_{SS} cannot be higher than 10^3, as described by Equation 989.

The round function of Equation 990 and Equation 991 return the order of magnitude of the ratio of $\frac{\left.\frac{\partial M}{\partial L_C}\right\vert_0}{\left.\frac{\partial M}{\partial L_C}\right\vert_{MAX}}$ and of $\frac{\left.\frac{\partial E}{\partial L_C}\right\vert_0}{\left.\frac{\partial E}{\partial L_C}\right\vert_{MAX}}$. Hence, the number of sub-layers for momentum and energy are equal to the order of magnitude. This can cause the under-estimation of N_{SS}^{M} and of N_{SS}^{E} when the ratios $\frac{\left.\frac{\partial M}{\partial L_C}\right|_0}{\left.\frac{\partial M}{\partial L_C}\right|_{MAX}}$ and $\frac{\left.\frac{\partial E}{\partial L_C}\right|_0}{\left.\frac{\partial E}{\partial L_C}\right|_{MAX}}$ are not close to the order of magnitude. So, the values of N_{SS}^{M} and of N_{SS}^{E} of Equation 990 and Equation 991 are adjusted with the equations reported in Table 242.

Table 242. Conditions for modifying $\boldsymbol{N_{SS}^{M}}$ and $\boldsymbol{N_{SS}^{E}}$.

Equation	Formula	Condition
Equation 994	$N_{SS}^{M} = 1$	$\frac{\left.\frac{\partial M}{\partial L_C}\right\|_0}{\left.\frac{\partial M}{\partial L_C}\right\|_{MAX}} < 0.5$
Equation 995	$N_{SS}^{M} = 10$	$0.5 \leq \frac{\left.\frac{\partial M}{\partial L_C}\right\|_0}{\left.\frac{\partial M}{\partial L_C}\right\|_{MAX}} < 1$
Equation 996	$N_{SS}^{M} = 10 \cdot N_{SS}^{M}$	$1 \leq \frac{\left.\frac{\partial M}{\partial L_C}\right\|_0}{\left.\frac{\partial M}{\partial L_C}\right\|_{MAX}} < 10$
Equation 997	$N_{SS}^{E} = 1$	$\frac{\left.\frac{\partial E}{\partial L_C}\right\|_0}{\left.\frac{\partial E}{\partial L_C}\right\|_{MAX}} < 0.5$
Equation 998	$N_{SS}^{E} = 10$	$0.5 \leq \frac{\left.\frac{\partial E}{\partial L_C}\right\|_0}{\left.\frac{\partial M}{\partial L_C}\right\|_{MAX}} < 1$
Equation 999	$N_{SS}^{E} = 10 \cdot N_{SS}^{E}$	$1 \leq \frac{\left.\frac{\partial E}{\partial L_C}\right\|_0}{\left.\frac{\partial E}{\partial L_C}\right\|_{MAX}} < 10$

In Equation 999 and Equation 996, N_{SS}^{M} and N_{SS}^{E} are computed with Equation 990 and Equation 991, respectively.

2.1.4.2. Structure of the algorithm

The inputs and the output variables of the integration algorithm of sub-layer are reported in Table 243.

Table 243. Input and output of the Block 2 of IBL approach.

Variable	Description
Input	$\delta_{M,0}$, U_0, M_0 and E_0 (see Section 2.1.3 of Appendix P), Rayleigh number (Ra_n) state variables and thermo-physical properties (see Table 49), heat flows at the surface or the surface wall temperature and heat mode
Output	momentum thickness ($\delta_{M,n+1}$), the velocity outside boundary layer of comparable forced-convection flow (U_{n+1}), and the pseudo-variables (E_{n+1} and M_{n+1}) at the exit of the sub sub-layer "n"

The integration algorithm of the sub-layer is presented in Figure 218.

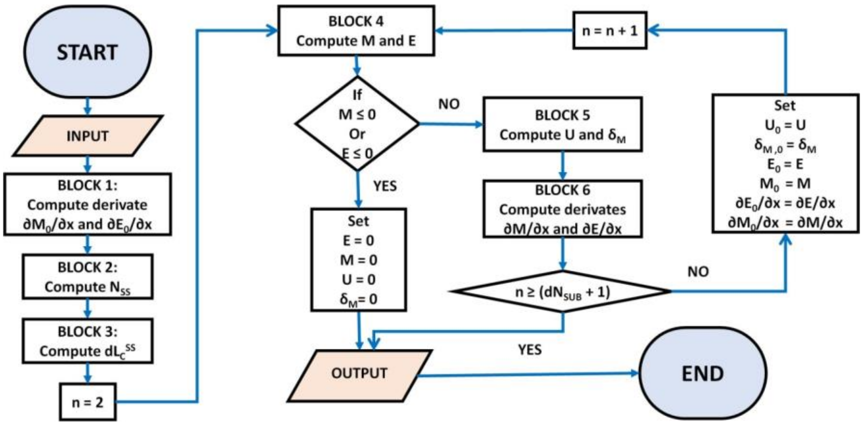

Figure 218. Integration algorithm of sub-layer.

This algortimh is composed by the following steps:

a) BLOCK 1. The derivates $\left.\frac{\partial M}{\partial L_C}\right|_0$ and $\left.\frac{\partial E}{\partial L_C}\right|_0$ are computed with the values of $\delta_{M,0}$, U_0, M_0 and E_0, using Equation 178 and Equation 179. The fluid-dynamic regime to calculate Equation 178 and Equation 179 is computed using Ra_n;

b) BLOCK 2. The number of sub-space-point (N_{SS}) is obtained as explained in Section 2.1.4.1 of Appendix P);

c) BLOCK 3. The length of each sub-space-point (dL_c^{SS}) is determined with Equation 1000.

Equation 1000
$$dL_c^{SS} = \frac{dL_{C,n}}{N_{SS}}$$

$dL_{C,n}$ is the length side of the sub-layer. This variable is computed with the equations of Table 77. The current number of the iteration is equal to 2;

d) BLOCK 4. The Eulero method computes the value of M and E. Hence, the values of these variables are computed with Equation 1001 and Equation 1002.

Equation 1001
$$M = M_0 + dL_c^{SS} \cdot \left.\frac{\partial M}{\partial L_C}\right|_0$$

Equation 1002
$$E = E_0 + dL_c^{SS} \cdot \left.\frac{\partial E}{\partial L_C}\right|_0$$

Two pathways are present:

- Pathway 1.4 (P 1.4): if M is lower or equal to 0, or if E is lower or equal to zero, the algorithm stops;
- Patter 2.4 (P 2.4): if M and E are positive, the algorithm moves to Block 5 (step e) of Section 2.1.4.2)

e) BLOCK 5. The variables U and $\delta_M$are computed with Equation 983 and Equation 984;

f) BLOCK 6. The derivates $\frac{\partial M}{\partial L_C}$ and $\frac{\partial E}{\partial L_C}$ are computed with the values of δ_M and U_0, using Equation 178 and Equation 179, respectively. The fluid-dynamic regime to calculate Equation 178 and Equation 179 is determined using Ra_n. Two pathways are present:

- Patter 1.6 (P 1.6): if the current number of the iteration is equal or higher than $N_{SS} + 1$, the algorithms stops;
- Patter 2.6 (P 2.6): if the current number of the iteration is lower than $N_{SS} + 1$, the values of $\left.\frac{\partial M}{\partial L_C}\right|_0$, $\left.\frac{\partial E}{\partial L_C}\right|_0$, $\delta_{M,0}$, U_0, M_0 and E_0 are equal to the value of $\frac{\partial M}{\partial L_C}$, $\frac{\partial E}{\partial L_C}$, δ_M, U, M and E. The algorithm moves to Block 4 (step d) of Section 2.1.4.2).

Appendix Q

Algorithm of Storage Heat Transfer model of homogeneous model

The Storage Heat Transfer (SHT) model is composed by different algorithms. Each algorithm is applied at each surface of the storage container to compute the heat input.

Section 1, 2 and 3 describe the algorithms at bottom, liquid side and vapour side, respectively.

1. Bottom heat input algorithm

The heat flow between the bottom wall and the liquid ($\dot{Q}_w^B$) is calculated with the energy balance equation at the bottom wall (Equation 198 of Table 79). This calculation is done with an iterative procedure, which is called $\dot{Q}_w^B$ algorithm. The variables and the equations of this algorithm are reported in Table 244.

Table 244. Variables and equations of $\dot{Q}_w^B$ algorithm.

Variables	Name	Equation	Formula
Heat flow between the bottom wall and the liquid	$\dot{Q}_w^B$	Equation 1003	$f_w^B = \bar{h}_w^B \cdot A^B \cdot (T_w^B - T^L) - h_{eff} \cdot A^B \cdot (T^w - T_w^B)$
heat transfer coefficient	$\bar{h}_w^B$	Equation 203 [135]	semi-empirical approach (Section 4.6), using the heat flow
wall bottom temperature	T_w^B	Equation 1004	$T_w^B = \frac{\dot{Q}_w^B}{\bar{h}_w^B \cdot A^B} + T^L$

Equation 1003 is obtained from the energy balance equation at the bottom wall (Equation 198 of Table 79). Equation 1004 is obtained from the definition of heat flow[139]. As reported in Table 244, the mathematical system of $\dot{Q}_w^B$ algorithm is determined because the number of equation is equal to the number of variable. The structure of Equation 1003 requires being solved with the Newton-Raphson with finite difference method (see Section 2 of Appendix I). Hence, $\dot{Q}_w^B$ is the objective variable and Equation 1003 is the objective function.

To assure stability of the $\dot{Q}_w^B$ algorithm, the value of the bottom-to-liquid heat flow cannot overcome a maximum value. This maximum value, which is called $\dot{Q}_{w,MAX}^B$, is calculated with Equation 995.

Equation 1005 $$\dot{Q}_{w,MAX}^B = h_{eff} \cdot A^B \cdot (T^w - T^L)$$

The Newton-Raphson with finite difference method (see Section 2 of Appendix I) requires the values of the intermediate variables and a first guess value of the objective variable. This first value is computed to assure stability and fast convergence. The first guess value of the heat flow and the intermediate variables are calculated with the equations of Table 246.

Table 245. First guess value and intermediate variables of $\dot{Q}_w^B$.

Variables	Name	Equation	Formula
first guess value of the heat flow	$\dot{Q}_w^{B,0}$	Equation 1006	$\dot{Q}_w^{B,0} = \frac{h_{eff} \cdot \bar{h}_w^B}{h_{eff} + \bar{h}_w^B} \cdot A^B \cdot (T^w - T^L)$
First intermediate variable of the heat flow	$\dot{Q}_w^{B,1}$	Equation 1007	$\dot{Q}_w^{B,1} = 0.999 \cdot \dot{Q}_w^{B,0}$
Second intermediate variable of the heat flow	$\dot{Q}_w^{B,2}$	Equation 1008	$\dot{Q}_w^{B,2} = 1.001 \cdot \dot{Q}_w^{B,0}$

---

[139] The heat flow is computed as follows: $\dot{Q} = h \cdot A \cdot \Delta T$

$\bar{h}_w^B$ of Equation 1006 is calculated with Equation 203 [135], using semi-empirical approach (Section 4.6) and using $\dot{Q}_{w,MAX}^B$ of Equation 995.

The input and the output variables of $\dot{Q}_w^B$ algorithm are reported in Table 246.

Table 246. Input and output variables of $\dot{\boldsymbol{Q}}_w^B$ algorithm.

Variables	Description
Input	Thermo-physical properties, effective heat transfer coefficient (h_{eff}), surface area of the bottom (A^B), eternal wall temperature (T^W), liquid temperature (T^L), number of iteration (N_I), the value of the absolute tolerance (ε_1) and the value of relative tolerance (ε_2).
Output	heat flow between the bottom wall and the liquid ($\dot{Q}_w^B$), wall bottom temperature (T_w^B) and heat transfer coefficient ($\bar{h}_w^B$)

The value of the absolute tolerance is 10^{-10}. The value of the relative tolerance is 10^{-5}. A^B is computed with the geometrical formulas of Appendix B). The effective heat transfer coefficient is computed with the Boil-off Rate (BOR) model.

$\dot{Q}_w^B$ algorithm is presented in Figure 219.

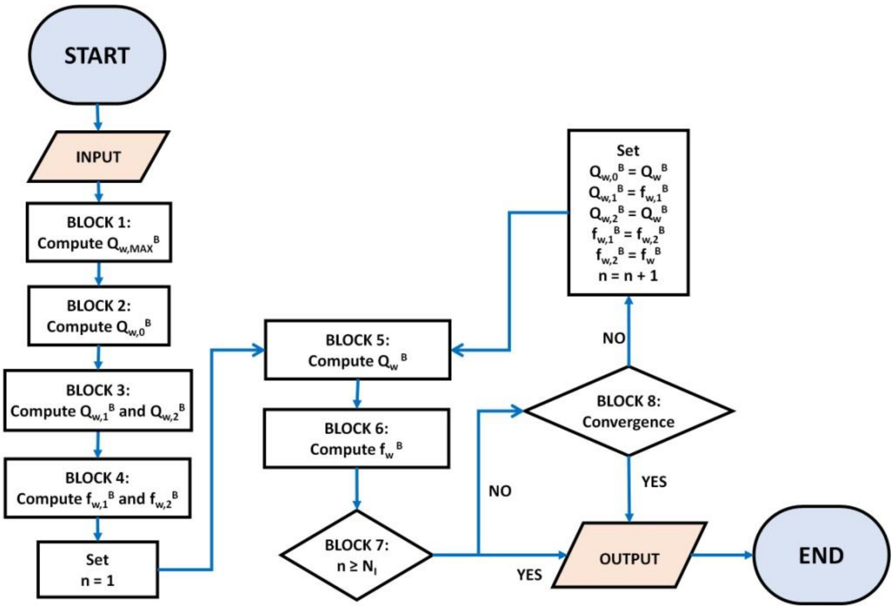

Figure 219. $\dot{\boldsymbol{Q}}_w^B$ algorithm.

The mathematical procedure is composed by the following steps:

a) BLOCK 1. The maximum heat input at the bottom ($\dot{Q}_{w,MAX}^B$) is calculated with Equation 995.

b) BLOCK 2. The first guess value ($\dot{Q}_w^{B,0}$) and, the intermediate variables of the heat input ($\dot{Q}_w^{B,1}$and $\dot{Q}_w^{B,2}$) are computed with the equations of Table 246.

c) BLOCK 3. The values of the objective function ($f_w^{B,1}$ and $f_w^{B,2}$) are computed at $\dot{Q}_w^{B,1}$ and $\dot{Q}_w^{B,2}$, with Equation 1003. The heat transfer coefficient $\bar{h}_w^B$ is calculated with Equation 203 (semi-empirical approach (Section 4.6)), using the heat flows $\dot{Q}_w^{B,1}$ and $\dot{Q}_w^{B,2}$. The wall bottom temperature is calculated with Equation 1004, with the values of $\dot{Q}_w^{B,1}$ and $\dot{Q}_w^{B,2}$. The value of the current iteration (n) is equal to 1.

d) BLOCK 4. The heat input is computed with Equation 1009.

Equation 1009
$$\dot{Q}_w^B = \dot{Q}_w^{B,1} - f_w^{B,1} \cdot \frac{\dot{Q}_w^{B,2} - \dot{Q}_w^{B,1}}{f_w^{B,2} - f_w^{B,1}}$$

e) BLOCK 6. The objective function (f_w^B) is computed with Equation 1003, The heat transfer coefficient is calculated with Equation 203 (semi-empirical approach (Section 4.6)), using $\dot{Q}_w^B$. The wall temperature is computed with Equation 1004;

f) BLOCK 7. Two pathways are present, according to the value of the current iteration:
    - Pathways 1.7 (P 1.7): if the current number of iteration is higher or equal to the number of iteration, the mathematical procedure stops.
    - Pathways 2.7 (P 2.7): when the current number is lower than the number of iteration, the algorithm moves to Block 8 (step o of Section 1 of Appendix Q);

g) BLOCK 8. The convergence criteria are defined by Equation 1010 and by Equation 1011.

Equation 1010
$$|f_w^B| \leq \varepsilon_1$$

Equation 1011
$$\left|\dot{Q}_w^{B,0} - \dot{Q}_w^B\right| \leq \left|\dot{Q}_w^{B,0} \cdot \varepsilon_2\right|$$

Two pathways are presents:

- Pathway 1.8 (P 1.8): If Equation 1010 and Equation 1011 hold true, the algorithm stops;
- Pathway 2.8 (P 2.8): If Equation 1010 is false or Equation 1011 is false, the algorithm starts at Block 4 (step d) of Section 1 of Appendix Q). $\dot{Q}_w^{B,0}$, $\dot{Q}_w^{B,1}$, $\dot{Q}_w^{B,2}$, $f_w^{B,1}$ and $f_w^{B,2}$are respectively equals to $\dot{Q}_w^B$, $\dot{Q}_w^{B,2}$, $\dot{Q}_w^B$, $f_w^{B,2}$ and f_w^B.

This algorithm quickly converges because the first guess value is well computed. Less than 3 iterations are usually required to reach convergence. For the oblate ellipsoid and sphere, this algorithm is neglected. Block 7 is required to avoid over-iterations[140], even if the convergence is not reached.

2. Wet side wall heat input algorithms

The heat flow between the wet side wall and the liquid ($\dot{Q}_w^{SL}$) is computed from the energy balance equation at the wet side wall (Equation 199 of Table 79), with an iterative procedure, which is called $\dot{Q}_w^{SL}$ algorithm. The variables and the equations of this algorithm are reported in Table 247.

Table 247. Variables and equations of $\dot{Q}_w^{SL}$ algorithm.

Variables	Name	Equation	Formula
Heat flow between the wet side wall and the liquid	$\dot{Q}_w^{SL}$	Equation 1012	$\dot{Q}_w^{SL} = \bar{h}_w^{SL} \cdot A^{SL} \cdot (T_w^{SL} - T^L)$
heat transfer coefficient	$\bar{h}_w^{SL}$	Equation 208	Boundary layer method (Section 4.6), using the difference in temperatures between the wall and the liquid.
Wet side wall temperature	T_w^{SL}	Equation 1013	$T_w^{SL} = \dfrac{h_{eff} \cdot A^{SL} \cdot T^w + \bar{h}_w^{SL} \cdot A^{SL} \cdot T^L}{h_{eff} \cdot A^{SL} + \bar{h}_w^{SL} \cdot A^{SL}}$

Equation 1012 is the definition of convective heat flow (see Section 1 of Appendix Q). Equation 1013 is deduced from the energy balance equation at the wet side wall (Equation 199 of Table 79). As indicated by the equations of Table 71, the method of the direct substitution (see Section 1 of Appendix I) can be used to compute the heat flow between the wet side wall and the liquid. As it is explained in Section 1 of Appendix I, the direct substitution method requires a first guess value of the objective variable. Hence, the first guess value of the wet side wall-to-liquid heat flow is calculated as follows:

---

[140] Over-iteration is defined as the condition when the algorithm continues to compute without limits of the number of iteration.

Equation 1014
$$\dot{Q}_w^{SL,0} = h_{eff} \cdot A^{SL} \cdot (T^w - T^L)$$

The input and the output variables of $\dot{Q}_w^{SL}$ algorithm are reported in Table 248.

Table 248. Input and output variables of $\dot{Q}_w^{SL}$ algorithm.

Variables	**Description**
Input	Thermo-physical properties, effective heat transfer coefficient (h_{eff}), surface area of the wet side wall (A^{SL}), eternal wall temperature (T^w), liquid temperature (T^L), number of iteration (N_I), the value of relative tolerance (ε).
Output	Wet side wall-to-liquid heat flow ($\dot{Q}_w^{SL}$), wet side wall temperature (T_w^{SL}) and heat transfer coefficient ($\bar{h}_w^{SL}$)

The value of the relative tolerance is 10^{-5}. A^{SL} is computed with the geometrical formulas of Appendix B. The effective heat transfer coefficient is computed with the Boil-off Rate (BOR) model.

$\dot{Q}_w^{SL}$ algorithm is described in Figure 220.

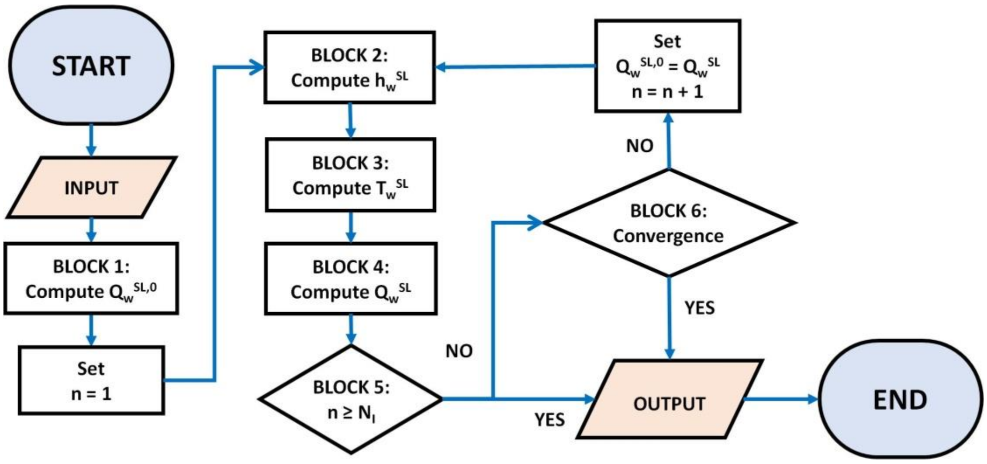

Figure 220. $\dot{Q}_w^{SL}$ algorithm.

This algortimh is composed by the following steps:

a) BLOCK 1. The first guess value of the heat inputs ($\dot{Q}_w^{SL,0}$) is computed with Equation 1014. The current number of iteration (n) is equal to 1;
b) BLOCK 2. The heat transfer coefficient $\bar{h}_w^{SL}$ is computed with Equation 208. The boundary layer method (Section 4.6) is applied. The heat flow $\dot{Q}_w^{SL,0}$ is used in this method if n is equal to 1. If the current iteration is not the first one, the difference in temperatures between the wet side wall and the liquid is used in the boundary layer method.
c) BLOCK 3. The wet side wall temperature is computed with Equation 1013;
d) BLOCK 4. The heat flow between the wet side wall and the liquid is calculated with Equation 1012;
e) BLOCK 5. Two pathways are present, according to the value of the current iteration:
    - Pathways 1.4 (P 1.4): if the current number of iteration is higher or equal to the number of iteration, the mathematical procedure stops;
    - Pathways 2.4 (P 2.4): when the current number is lower than the number of iteration, the algorithm moves to Block 6 (step f) of Section 2 of Appendix Q);
f) BLOCK 6. The convergence criterion is defined with Equation 1015.

Equation 1015
$$\left|\dot{Q}_w^{SL,0} - \dot{Q}_w^{SL}\right| \leq \left|\dot{Q}_w^{SL,0} \cdot \varepsilon\right|$$

Two pathways are present, according to the value of the current iteration:

- Pathways 1.6 (P 1.6): if Equation 1015 is true, the algorithm stops;
- Pathways 2.6 (P 2.6): if Equation 1015 is false, the algorithm starts at Block 2 (step b) Section 2 of Appendix Q). $\dot{Q}_w^{SL,0}$ is equal to $\dot{Q}_w^{SL}$ and the current number of iteration is increased of 1.

This algorithm converges in less than 5 iterations.

3. Dry side wall heat input algorithms

The heat flow between the dry side wall and the liquid ($\dot{Q}_w^{SV}$) is calculated from the energy balance equation at the wet side wall (Equation 200 of Table 79). This calculation is done with an iterative procedure, which is called $\dot{Q}_w^{SV}$ algorithm. The variables and the equations of this algorithm are reported in Table 249.

Table 249. Variables and equations of $\dot{Q}_w^{SV}$ algorithm.

Variables	Name	Equation	Formula
Heat flow between the dry side wall and the liquid	$\dot{Q}_w^{SV}$	Equation 1016	$\dot{Q}_w^{SV} = \bar{h}_w^{SV} \cdot A^{SV} \cdot (T_w^{SV} - T^V)$
heat transfer coefficient	$\bar{h}_w^{SV}$	Equation 208	Boundary layer method (Section 4.6), using the difference in temperatures between the wall and the vapour
Dry side wall temperature	T_w^{SV}	Equation 1017	$T_w^{SV} = \dfrac{h_{eff} \cdot (A^{SV} + A^R) \cdot T^w + \dfrac{\beta \cdot k_V \cdot T^I \cdot A_R}{L_c\left(H^{Liq} + \dfrac{H^{Vap}}{2}\right) - L_c(H^{Liq})} + \alpha \cdot h_w^{SV} \cdot A^{SV} \cdot T^V}{h_{eff} \cdot (A^{SV} + A^R) + \dfrac{\beta \cdot k_V \cdot A_R}{L_c\left(H^{Liq} + \dfrac{H^{Vap}}{2}\right) - L_c(H^{Liq})} + \alpha \cdot h_w^{SV} \cdot A^{SV}}$

Equation 1016 is the definition of convective heat flow (see Section 1 of Appendix Q). Equation 1017 is obtained from the energy balance equation at the dry side wall (Equation 200 of Table 79). $L_c\left(H^{Liq} + \frac{H^{Vap}}{2}\right)$ and $L_c(H^{Liq})$ are explained in Section 4.5 of Chapter 4. As indicated by the equations of Table 249, the method of the direct substitution (see Section 1 of Appendix I) can be applied for calculating the heat flow between the dry side wall and the vapour.

As it is explained in Section 1 of Appendix I, the direct substitution method requires a first guess value of the objective variable. Hence, the first guess value of the dry side wall-to-vapur heat flow and the vapour is calculated as follows:

Equation 1018
$$\dot{Q}_w^{SV,0} = h_{eff} \cdot (A^{SV} + A^R) \cdot \left(T^w - T_w^{SV,0}\right) - \beta \cdot \dot{Q}_w^{LV}$$

$T_w^{SV,0}$ is the first guess dry side wall vapour temperature. $\dot{Q}_w^{LV}$ is computed as described in Section 4.5 of Chapter 4.

The input and the output variables of $\dot{Q}_w^{SV}$ algorithm are reported in Table 250.

Table 250. Input and output variables of $\dot{Q}_w^{SV}$ algorithm.

Variables	Description
Input	Thermo-physical properties, effective heat transfer coefficient (h_{eff}), the corrective coefficients α and β, surface area of the dry side wall (A^{SV}), external wall temperature (T^w), vapour temperature (T^V), number of iteration (N_I), the value of relative tolerance (ε).

Output	dry side wall-to-vapour heat flow($\dot{Q}_w^{SV}$), dry side wall temperature (T_w^{SV}) and heat transfer coefficient ($\bar{h}_w^{SV}$)

The value of the relative tolerance is 10^{-5}. A^{SV} is computed with the geometrical formulas of Appendix B. The effective heat transfer coefficient and the corrective coefficients are computed with the Boil-off Rate (BOR) model.

$\dot{Q}_w^{SV}$ algorithm is described in Figure 221.

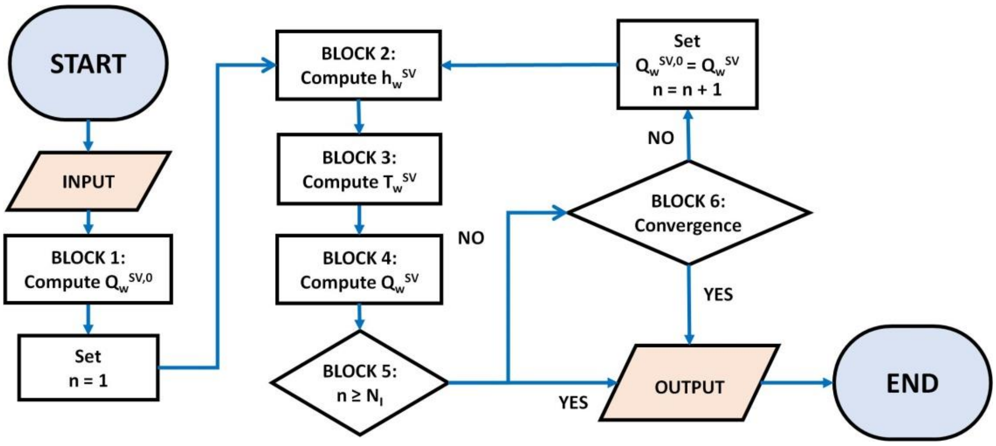

Figure 221. $\dot{Q}_w^{SV}$ algorithm.

This algortimh is composed by the following steps:

a) BLOCK 1. The first guess value of the heat inputs ($\dot{Q}_w^{SV,0}$) is computed with Equation 1018. $T_w^{SV,0}$ of Equation 1018 is equal to the vapour temperature at the initial time-point (t_0). For all the other time-points, $T_w^{SV,0}$ is equal to the dry side wall temperature at the previous time-point (t_{i-1}). The current number of iteration (n) is equal to 1;

b) BLOCK 2. The heat transfer coefficient $\bar{h}_w^{SV}$ is computed with Equation 208. The boundary layer method (Section 4.6) is applied. The heat flow $\dot{Q}_w^{SV,0}$ is used in this method if n is equal to 1. If the current iteration is not the first one, the difference in temperatures between the dry side wall and the vapour is used in the boundary layer method.

c) BLOCK 3. The dry side wall temperature is computed with Equation 1017;

d) BLOCK 4. The dry side wall-to-vapour heat flow is calculated with Equation 1016;

e) BLOCK 5. Two pathways are present, according to the value of the current iteration:
   - Pathways 1.4 (P 1.4): if the current number of iteration is higher or equal to the number of iteration, the mathematical procedure stops;
   - Pathways 2.4 (P 2.4): when the current number is lower than the number of iteration, the algorithm moves to Block 6 (step f) of Section 3 of Appendix Q);

f) BLOCK 6. The convergence criterion is defined with Equation 1019.

Equation 1019
$$\left|\dot{Q}_w^{SV,0} - \dot{Q}_w^{SV}\right| \leq \left|\dot{Q}_w^{SV,0} \cdot \varepsilon\right|$$

Two pathways are present, according to the value of the current iteration:
   - Pathways 1.6 (P 1.6): if Equation 1015 is true, the algorithm stops;
   - Pathways 2.6 (P 2.6): if Equation 1015 is false, the algorithm starts at Block 2 (step b) of Section 3 of Appendix Q). $\dot{Q}_w^{SV,0}$ is equal to $\dot{Q}_w^{SV}$ and the current number of iteration is increased of 1.

The number of iteration for convergence is quite similar to the one of the $\dot{Q}_w^{SL}$ algorithm (see Section 2 of Appendix Q).

Appendix R

Algorithm of the Boil-off Rate Model of homogeneous model

The Boil-off Rate (BOR) model is composed by several algorithms to compute the effective heat transfer coefficient, and the alpha and beta coefficients.

Section 1 and 2 respectively describe the algorithm to compute the effective heat transfer coefficient and the alpha coefficient.

1. Effective heat transfer algorithm

The effective heat transfer coefficient algorithm computes h_{eff}, the corrective coefficient β, the net mass flow ($\dot{m}_N$), the wet walls temperature (T_w^L) and the dry side wall temperature (T_w^{SV}), under the hypothesis of exact heat transfer coefficient (Assumption e) of Section 6.1) for the test at high filling ratio (Test 1). The variables β, $\dot{m}_N$, T_w^L and T_w^{SV} are required to compute h_{eff}. Hence, h_{eff} algorithm is composed by sub-algorithms to compute β, T_w^L and T_w^{SV} and formula to calculate $\dot{m}_N$. The objective variable of h_{eff} algorithm is the effective heat transfer coefficient. This coefficient can be computed using the overall wall energy balance equation (Equation 220) as follows:

Equation 1020
$$h_{eff} = \frac{\dot{Q}_{IN}}{(A^{SL} + A^B) \cdot (T^W - T_w^L) + (A^{SV} + A^R) \cdot (T^W - T_w^{SV})}$$

Equation 1020 is the objective function of the h_{eff} algorithm. Equation 1020 is deduced from the overall energy balance equation (Equation 220). The variables β, $\dot{m}_N$, T_w^L and T_w^{SV} are the secondary variables of this algorithm. These variables are computed using algorithms based on the equations of Table 82.

As it is suggested by Equation 1020, the input and the output variables of h_{eff} algorithm are described in Table 251.

Table 251. Input and output of $\boldsymbol{h_{eff}}$ algorithm.

Variables	Description
Inputs	Overall heat input ($\dot{Q}_{IN}$), dry side wall, wet side wall, bottom and roof surface areas (A^{SV}, A^{SL}, A^B and A^R), external wall temperature (T^W), thermo-physical properties and the values of pressure, vapour temperature, filling ratio, saturated liquid temperature, relative tolerance (ε) and number of iteration (N_I)
Output	Effective heat transfer coefficient (h_{eff}), corrective coefficient (β), wet walls temperature (T_w^L) and the dry side wall temperature (T_w^{SV})

The value of the relative tolerance (ε) is 10^{-5}. The h_{eff} algorithm is based on the direct substitution method (see Section 1 of Appendix I) because this method is suitable for Equation 1020. This method requires a first guess value of the objective variable. This value is computed as follows:

Equation 1021
$$h_{eff,0} = \frac{\dot{Q}_{IN}}{(A^{SL} + A^B) \cdot (T^w - T^L) + (A^{SV} + A^R) \cdot (T^w - T^V)}$$

Equation 1021 is deduced from Equation 1020, by considering that T_w^L and T_w^{SV} are equal to T^L and T^V, respectively.

The h_{eff} algorithm is described in Figure 222.

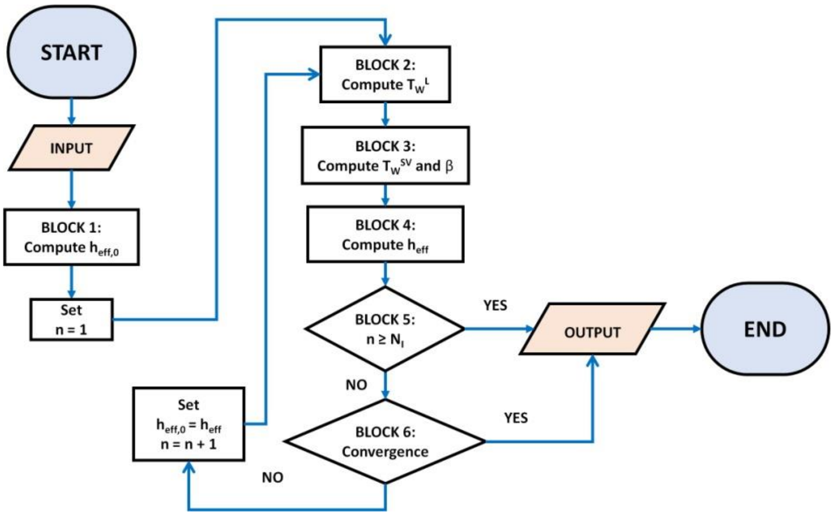

Figure 222. $\boldsymbol{h_{eff}}$ algorithm of BOR model.

The h_{eff} algorithm by the following steps:

a) BLOCK 1. The first guess value of the effective heat transfer coefficient ($h_{eff,0}$) is computed with Equation 1021. The current number of iteration (n) is equal to 1;

b) BLOCK 2. The wet walls temperature (T_w^L) is calculated with T_w^L algorithm, which is a sub-algorithm of h_{eff} algorithm. T_w^L algorithm is discussed in Section 1.1 of Appendix R;

c) BLOCK 3. The corrective coefficient β and the dry side wall temperature (T_w^{SV}) are calculated with β and T_w^{SV} algorithms, respectively. These algorithms are sub-algorithm of the h_{eff} algorithm and they are respectively discussed in Section 1.2 and 1.3 of Appendix R;

d) BLOCK 4. The effective heat transfer coefficient (h_{eff}) is calculated with Equation 1020 ;

e) BLOCK 5. Two pathways are present, as function of the value of the current number of iteration (n):
   - Pathway 1.5 (P 1.5): if n is higher or equal to the number of iteration (N_I), the algorithm stops;
   - Pathway 2.5 (P 2.5): when the current number of iteration is lower than N_I, the algorithms move to Block 6 (step f) of Section 1 of Appendix R);

f) BLOCK 6. The convergence criterion is defined with Equation 1022.

Equation 1022
$$\left|h_{eff} - h_{eff,0}\right| \leq \left|h_{eff,0} \cdot \varepsilon\right|$$

Two pathways are present:

- Pathway 1.6 (P 1.6). If Equation 1022 is true, the algorithm stops;
- Pathway 2.6 (P 2.6). When Equation 1022 is false, the algorithm moves to Block 2 (step a) of Section 1 of Appendix R). the current number of iteration (n) increases of 1 and $h_{eff,0}$ is equal to h_{eff};

A^B and A^R are equal to zero for oblate ellipsoidal and for spherical storage containers.

1.1. Algorithm of the wet walls temperature

The T_w^L algorithm is one the sub-algorithm of the h_{eff} algorithm, as it is explained in Figure 222. Due to the *hypothesis of unique wet wall* (assumption c) of Section 6.1 of Chapter 4), the bottom and wet side wall have the same wall temperature, which is called wet wall temperature (T_w^L). This temperature is homogeneous in the wet walls, due to the hypothesis of homogeneity (assumption a) of Section 1.1). This wall temperature can be computed form the energy balance equation at the wet walls (Equation 221). To do that, the average heat transfer coefficients at the bottom ($\bar{h}_w^B$) and the wet side wall ($\bar{h}_w^{SL}$) are required. The values of these coefficients are computed with the difference in temperature between the wet walls and the liquid. Hence, the calculation procedure is iterative. The equations and variables of this procedure are reported in Table 252.

Table 252. Equation and variables of $\boldsymbol{T_w^L}$ algorithm.

Variable	Equation	Formula
T_w^L	Equation 1023	$f_w^L = \left(\bar{h}_w^{SL} \cdot A^{SL} + \bar{h}_w^B \cdot A^B\right) \cdot (T_w^L - T^L) - h_{eff} \cdot [(A^{SL} + A^B) \cdot (T^W - T_w^L)]$
$\bar{h}_w^B$	Equation 203	Semi-empirical approach (see Section 4.6)
$\bar{h}_w^{SL}$	Equation 208	Boundary layer approach (see Section 4.6)

Equation 1023 is deduced from Equation 221. The Newton-Raphson method with finite difference approach (see Section 2 of Appendix I) is suitable to solve Equation 1023. As consequence, T_w^L algorithm uses this numerical method, which is described in Section 2 of Appendix I. T_w^L is the objective variable and Equation 1023 is the objective function. This method requires the first guess value of the objective variable and the intermediate variables to quickly and stably converge. The intermediate variables and the first guess value are calculated as described in Table 253.

Table 253. Equations to compute the first guess value of $\boldsymbol{T_w^L}$ and the intermediate variables.

Variable	Name	Equation	Formula
First intermediate variable of the wet walls temperature	$T_{w,1}^L$	Equation 1024	$T_{w,1}^L = 1.001 \cdot T_{w,0}^L$
Second intermediate variable of the wet walls temperature	$T_{w,2}^L$	Equation 1025	$T_{w,2}^L = 0.999 \cdot T_{w,0}^L$
First guess value of the wet walls temperature	$T_{w,0}^L$	Equation 1026	$T_{w,0}^L = \dfrac{T_{w,0}^B + T_{w,0}^{SL}}{2}$
First guess value of the wet side wall temperature	$T_{w,0}^{SL}$	Equation 1027	$T_{w,0}^{SL} = T^L + \dfrac{\dot{Q}_w^{SL,0}}{\bar{h}_w^{SL} \cdot A^{SL}}$
First guess value of the bottom wall temperature	$T_{w,0}^B$	Equation 1028	$T_{w,0}^B = T^L + \dfrac{\dot{Q}_w^{B,0}}{\bar{h}_w^B \cdot A^B}$
First guess value of the wet side wall heat flow	$\dot{Q}_w^{SL,0}$	Equation 1029	$\dot{Q}_w^{SL,0} = \dfrac{A^{SL}}{A^B + A^{SL}} \cdot \dot{Q}_{w,0}^L$
First guess value of the bottom heat flow	$\dot{Q}_w^{B,0}$	Equation 1030	$\dot{Q}_w^{B,0} = \dfrac{A^B}{A^B + A^{SL}} \cdot \dot{Q}_{w,0}^L$
First guess value of the wet walls heat flow	$\dot{Q}_{w,0}^L$	Equation 1031	$\dot{Q}_{w,0}^L = h_{eff} \cdot (A^{SL} + A^B) \cdot (T^W - T^L)$

Equation 1024, Equation 1026 and Equation 1025 are arbitrary taken. Equation 1027 and Equation 1028 are deduced from the definition of heat flow[141]. Equation 1029 and Equation 1030 are obtained from Equation 1031 considering that the heat flows $\dot{Q}_w^{B,0}$ and $\dot{Q}_{w,0}^L$ are proportional to the surface area of the bottom and of the side wall, respectively. Equation 1031 is deduced from definition of heat flow, considering that T_w^L is equal to T^L. In Equation 1027 and Equation 1028, $\bar{h}_w^B$ and $\bar{h}_w^{SL}$ are computed with the heat flows $\dot{Q}_w^{B,0}$ and $\dot{Q}_{w,0}^L$, respectively. The semi-empirical approach and the boundary layer approach are used for $\bar{h}_w^B$ and $\bar{h}_w^{SL}$, respectively.

The input and the output variables of this algorithm are reported in Table 254.

---

[141] Heat flow definition : $\dot{Q} = h \cdot A \cdot \Delta T$

Table 254. Input and output of T_w^L algorithm.

Variables	Description
Inputs	The effective heat transfer coefficient (h_{eff}), wet side wall and bottom surface areas (A^{SL} and A^B), external wall temperature (T^W), thermo-physical properties, filling ratio, saturated liquid temperature, relative tolerance (ε_2) and absolute tolerance (ε_1) and number of iteration (N_I)
Output	wet walls temperature (T_w^L)

The values of the absolute and relative tolerance are respectively 10^{-10} and 10^{-5}.

T_w^L algorithm is presented in Figure 223.

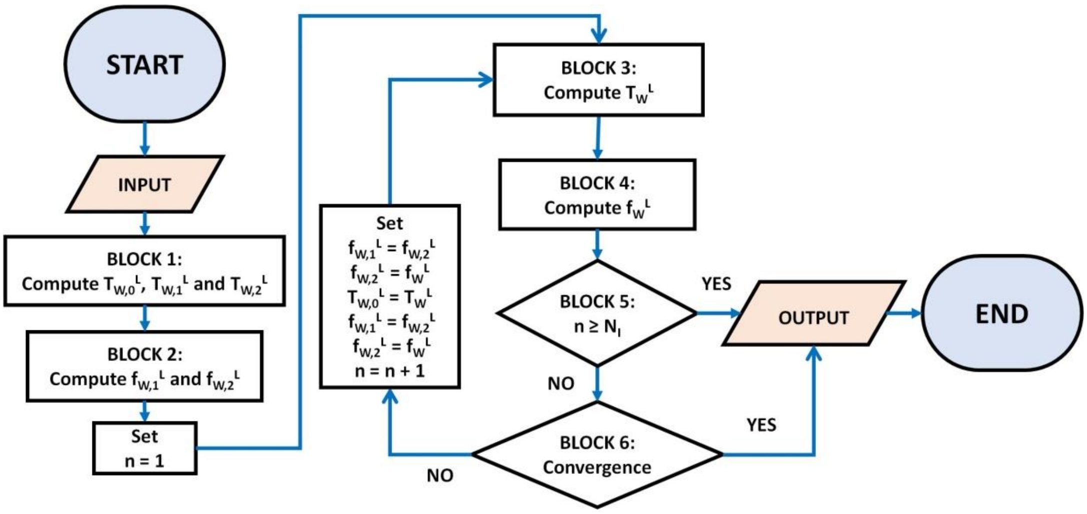

Figure 223. T_W^L algorithm.

T_w^L algorithm is composed of the following steps:

a) BLOCK 1. The first guess value and the intermediate variables are computed with the equations of Table 253;

b) BLOCK 2. The value of the objective functions at $T_{w,1}^L$ and $T_{w,2}^L$ ($f_{w,1}^L$ and $f_{w,2}^L$) are computed with Equation 1023;

c) BLOCK 3. The objective variable T_w^L is determined with Equation 1032;

Equation 1032
$$T_w^L = T_{w,1}^L - f_{w,1}^L \cdot \frac{T_{w,2}^L - T_{w,1}^L}{f_{w,2}^L - f_{w,1}^L}$$

d) BLOCK 4. The objective function f_w^L is determined with Equation 1023, with the value of T_w^L;

e) BLOCK 5. Two pathways are present, as function of the value of the current number of iteration (n):
   - Pathway 1.5 (P 1.5). If n is higher or equal to the number of iteration (N_I), the algorithm stops;
   - Pathway 2.5 (P 2.5). When the current number of iteration is lower than N_I, the algorithms move to Block 6 (step f) of Section 1.1 of Appendix R);

f) BLOCK 6. Two convergence criteria are defined with Equation 1033 and with Equation 1034, respectively;

Equation 1033
$$|f_w^L| \leq \varepsilon_1$$

Equation 1034
$$\left|T_{w,0}^L - T_w^L\right| \leq \left|T_{w,0}^L \cdot \varepsilon_2\right|$$

Two pathways are present:

- Pathway 1.6 (P 1.6). If Equation 1033 and Equation 1034 are true, the algorithm stops;
- Pathway 2.6 (P 2.6). If Equation 1033 is false or Equation 1034 is false, the algorithms move to Block 3 (step c) of Section 1.1 of Appendix R). The current number of the iteration increases of 1, and $T^L_{w,1}$, $T^L_{w,2}$, $T^L_{w,0}$, $f^L_{w,1}$ and $f^L_{w,2}$ are respectively equal to $T^L_{w,2}$, T^L_w, T^L_w, $f^L_{w,2}$ and f^L_w;

The wet walls temperature algorithm is used in the α algorithm too.

1.2. Algorithm of the corrective coefficient beta

The behaviour of cryogenic liquid can be affected by the dry side wall-to-interface heat transfer. This heat flows depends on the gradient of the dry side wall temperature near the interface, and on the thickness of the side wall. Due to hypothesis of total homogeneity (assumption a) of Section 1.1), this gradient is neglected. This thickness is calculated, introducing an uncertainty on the performance of the model, as described in Section 8 of Chapter 2. Hence, a corrective coefficient, called β, is required and it is calculated with the β algorithm. This coefficient can be computed with the energy balance equation at the steady state vapour (Equation 217). In Equation 217, the Boil-Off Gad flow ($\dot{m}_{BOG}$) is required and this variable is computed with the mass balance equation of steady state vapour (Equation 218). In Equation 218, the net mass flow is calculated with the interface energy balance (Equation 219). Hence, the system of equations and variables of β algorithm is the one reported in Table 255.

Table 255. Equations and variables of $\boldsymbol{\beta}$ algorithm.

Variable	Name	Equation	Formula
Corrective coefficient	β	Equation 1035	$f^V_w = h_{eff} \cdot (A^{SV} + A^R) \cdot (T^W - T^{SV}_w) - \beta \cdot \dot{Q}^{LV}_w - \dot{Q}^V_I$ $+\dot{m}_{BOG} \cdot \left[\tilde{h}^V_S(P) - \tilde{h}^V(T^V, P)\right]$
Boil-Off Gas flow	$\dot{m}_{BOG}$	Equation 1036	$\dot{m}_{BOG} = \frac{\dot{Q}^V_I + \dot{Q}^L_w + \beta \cdot \dot{Q}^{LV}_w}{\Delta\widetilde{H}_{EV}(P^V)}$
Heat flow between the wet walls and the liquid	$\dot{Q}^L_w$	Equation 1037	$\dot{Q}^L_w = h_{eff} \cdot (A^{SL} + A^B) \cdot (T^w - T^L_w)$

$\dot{Q}^V_I$ and $\dot{Q}^{LV}_w$ are computed as described in Section 5.2 and 4.5. T^{SV}_w of Equation 1035 is computed with the algorithm of the dry side wall temperature (see Section 1.3 of Appendix R). Equation 1035 is deduced from energy balance equation at the steady state vapour (Equation 217). Equation 1036 is obtained from the mass balance equation of steady state vapour (Equation 218) and from the interface energy balance (Equation 219). The corrective coefficient β is the objective variable and Equation 1035 is the objective function. Due to the nature of the objective function, β algorithm is solved by means of the Newton-Raphson method with finite difference approach (see Section 2 of Appendix I). This method requires a first guess value of the objective function and the intermediate variables. The intermediate variables can be calculated from the first guess value. This value can be calculated by simplifying Equation 1035. $\dot{m}_{BOG}$ of Equation 1035 can be calculated with Equation 1036 and Equation 1035 can be written as follows:

Equation 1038

$$f^V_w = h_{eff} \cdot (A^{SV} + A^R) \cdot (T^W - T^{SV}_w) - \beta \cdot \dot{Q}^{LV}_w - \dot{Q}^V_I + \frac{\dot{Q}^V_I + \dot{Q}^L_w + \beta \cdot \dot{Q}^{LV}_w}{\Delta\widetilde{H}_{EV}(P^V)} \cdot \left[\tilde{h}^V_S(P) - \tilde{h}^V(T^V, P)\right]$$

The terms $\beta \cdot \dot{Q}^{LV}_w$, $\dot{Q}^V_I$ and $\dot{Q}^L_w$ of Equation 1038 are grouped and Equation 1038 can be written as:

Equation 1039

$$f_w^V = h_{eff} \cdot (A^{SV} + A^R) \cdot (T^W - T_w^{SV}) - \beta \cdot \dot{Q}_w^{LV} \cdot \left(1 + \frac{\Delta\widetilde{H}_V}{\Delta\widetilde{H}_{EV}(P^V)}\right) - \dot{Q}_w^L \cdot \frac{\Delta\widetilde{H}_V}{\Delta\widetilde{H}_{EV}(P^V)} - \dot{Q}_I^V \cdot \left(1 + \frac{\Delta\widetilde{H}_V}{\Delta\widetilde{H}_{EV}(P^V)}\right)$$

$\Delta\widetilde{H}_V$ is equal to the difference $-\left[\tilde{h}_S^V(P) - \tilde{h}^V(T^V, P)\right]$. If f_w^V is equal to zero, the first guess value and intermediate variables can be computed with the equations of Table 256.

Table 256. Equations to compute the first guess value of $\boldsymbol{T_w^L}$ and the intermediate variables.

Variable	Name	Equation	Formula
First intermediate variable of coefficient β	β_1	Equation 1040	$\beta_1 = 0.999 \cdot \beta_0$
Second intermediate variable of coefficient β	β_2	Equation 1041	$\beta_2 = 1.001 \cdot \beta_0$
First guess value of coefficient β	β_0	Equation 1042	$\beta_0 = \dfrac{h_{eff} \cdot (A^{SV} + A^R) \cdot (T^W - T_w^{SV}) - \dot{Q}_w^L \cdot \frac{\Delta\widetilde{H}_V}{\Delta\widetilde{H}_{ev}} - \dot{Q}_I^V \cdot \left(1 + \frac{\Delta\widetilde{H}_V}{\Delta\widetilde{H}_{ev}}\right)}{\dot{Q}_w^{LV} \cdot \left(1 + \frac{\Delta\widetilde{H}_V}{\Delta\widetilde{H}_{ev}}\right)}$

Equation 1042 is deduced from Equation 1039. In Equation 1042, T_w^{SV} is calculated as follows:

Equation 1043

$$T_w^{SV} = T^W - \frac{\dot{Q}_{IN} - \dot{Q}_w^L}{h_{eff} \cdot (A^{SV} + A^R)}$$

In Equation 1043, the difference $\dot{Q}_{IN} - \dot{Q}_w^L$ is equal to the heat flow between the environment and the dry walls (dry side and roof). Equation 1043 is deduced from the definition of heat flow.

As it is indicated in Table 255 and in Table 256, the input and output variables required are reported in Table 257.

Table 257. Input and output of $\boldsymbol{T_w^L}$ algorithm.

Variables	Description
Inputs	The effective heat transfer coefficient (h_{eff}), wet side wall, dry side wall, bottom and roof surface areas (A^{SL}, A^{SV}, A^B and A^R), external wall temperature (T^W), thermo-physical properties, filling ratio, saturated liquid temperature, vapour temperature, wet walls temperature (T_w^L), relative tolerance (ε_2) and absolute tolerance (ε_1) and number of iteration (N_I)
Output	Corrective coefficient (β)

Figure 224 describes the β algorithm.

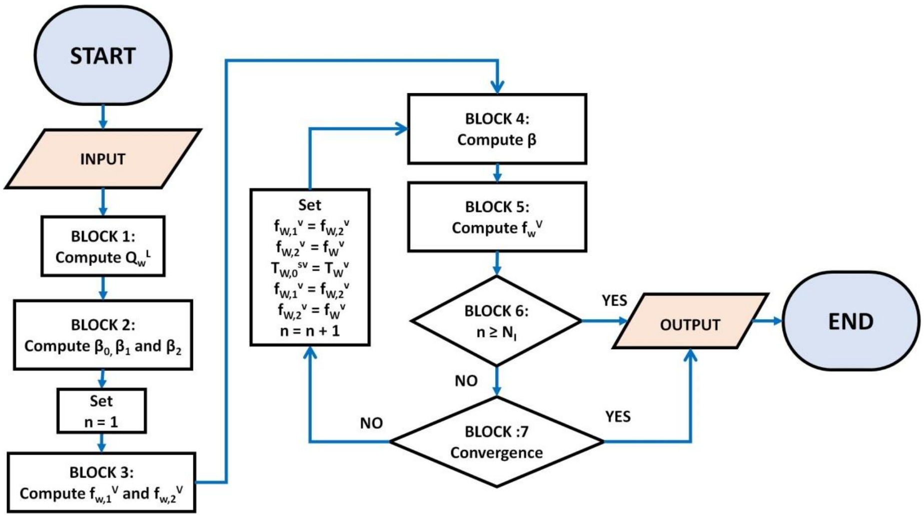

Figure 224. Algorithm to compute $\boldsymbol{\beta}$.

The β algorithm is composed by the following steps:

a) BLOCK 1. The wet walls-to-liquid heat input ($\dot{Q}_w^L$) is computed with Equation 1037. T_w^L of Equation 1037 is computed with the wet wall temperature algorithm, as explained in Section 1.1 of Appendix R);
b) BLOCK 2. The first guess value of the corrective coefficient β (β_0) and the intermediate variables β_1 and β_2 are computed with the equations of Table 256;
c) BLOCK 3. The values of the objective function $f_{w,1}^V$ and $f_{w,2}^V$ are computed with Equation 1035, respectively using the values of β_1 and β_2;
d) BLOCK 4. The value of the corrective coefficient β is computed with Equation 1044.

Equation 1044
$$\beta = \beta_1 - f_{w,1}^V \cdot \frac{\beta_2 - \beta_1}{f_{w,2}^V - f_{w,1}^V}$$

e) BLOCK 5. The objective function $f_w^V$is computed with Equation 1035 at β;
f) BLOCK 6. Two pathways are present, as function of the value of the current number of iteration (n):
   - Pathway 1.6 (P 1.6). if n is higher or equal to the number of iteration (N_I), the algorithm stops;
   - Pathway 2.6 (P 2.6). When the current number of iteration is lower than N_I, the algorithms move to Block 7 (step g) of Section 1.2 of Appendix R);
g) BLOCK 7. Two convergence criteria are defined with Equation 1045 and with Equation 1046, respectively;

Equation 1045
$$|f_w^V| \le \varepsilon_1$$

Equation 1046
$$|\beta_0 - \beta_0| \le |\beta_0 \cdot \varepsilon_2|$$

Two pathways are present:
   - Pathway 1.7 (P 1.7). If Equation 1045 and Equation 1046 are true, the algorithm stops;
   - Pathway 2.7 (P 2.7). If Equation 1045 is false or Equation 1046 is false, the algorithm moves to Block 3 (step d) of Section 1.2 of Appendix R). The current number of the iteration increases of 1, and β_1, β_2, β_0, $f_{w,1}^V$ and $f_{w,2}^V$ are respectively equal to β_2, β, β, $f_{w,2}^V$ and f_w^V;

β algorithm is used in the h_{eff} algorithm at Block 3 (step c) of Section 1 of Appendix R).

1.3.Algorithm of dry side wall temperature

The T_w^{SV} algorithm is one the sub-algorithm of the h_{eff} algorithm, as it is explained in Figure 222. This algorithm computes the dry side wall temperature (T_w^{SV}). This variable can be computed from the dry side wall-to-vapour heat flow ($\dot{Q}_w^{SV}$), which is computed from energy balance equations at the dry side wall (Equation 222). In Equation 222, the dry side wall temperature (T_w^{SV}) and the dry side wall-to-vapour heat transfer coefficient ($\bar{h}_w^{SV}$) are required. Hence, T_w^{SV} is computed with an iterative procedure that requires the equation and the variables of Table 258.

Table 258. Variables and equations of $\boldsymbol{T_w^{SV}}$ algorithm.

Variable	Equation	Formula

Table 258. Variables and equations of $\boldsymbol{T_w^{SV}}$ algorithm.

$\dot{Q}_{LV}^{SV}$	Equation 1047	$f_w^{SV} = \dot{Q}_{LV}^{SV} + \beta \cdot \dot{Q}_w^{LV} - h_{eff} \cdot (A^{SV} + A^R) \cdot (T^W - T_w^{SV})$
$\bar{h}_w^{SV}$	Equation 208	Boundary layer approach (see Section 4.6). The heat flow $\dot{Q}_{LV}^{SV}$ is used as input parameter of this approach.
T_w^{SV}	Equation 1048	$T_w^{SV} = T^V + \frac{\dot{Q}_w^{SV}}{A^{SV} \cdot \bar{h}_w^{SV} \cdot \alpha}$

The corrective coefficient α is equal to 1 due to the hypothesis of exact heat transfer coefficient (assumption e) of Section 6.1). The variable $\dot{Q}_w^{LV}$ is computed as explained in Section 4.5. As it is indicated by Table 258, the objective variable is $\dot{Q}_w^{SV}$ because T_w^{SV} can be computed from Equation 1048. So, the objective variable is Equation 1047, which is deduced form energy balance equation at the dry side wall (Equation 222). Due to the nature of the objective function (Equation 1047), the method of Netwon-Rhapson with finite difference approach (see Section 2 of Appendix R) is used in the T_w^{SV} algorithm. This method requires the first guess value of the objective variables and the intermediate variables. This first guess and the intermediate variables are computed with the equations of Table 259.

Table 259. Equations to compute the first guess value of $\boldsymbol{T_w^{SV}}$ and the intermediate variables.

Variable	Name	Equation	Formula
First intermediate variable of the dry side wall-to-vapour heat flow	$\dot{Q}_w^{SV,1}$	Equation 1049	$\dot{Q}_w^{SV,1} = 0.999 \cdot \dot{Q}_w^{SV,0}$
Second intermediate variable of the dry side wall-to-vapour heat flow	$\dot{Q}_w^{SV,2}$	Equation 1050	$\dot{Q}_w^{SV,2} = 1.001 \cdot \dot{Q}_w^{SV,0}$
First guess value of the dry side wall-to-vapour heat flow	$\dot{Q}_w^{SV,0}$	Equation 1051	$\dot{Q}_w^{SV,0} = h_{eff} \cdot (A^{SV} + A^R) \cdot (T^W - T^V) - \beta \cdot \dot{Q}_{LV}^{w}$

Equation 1049 and Equation 1050 are arbitrary defined. Equation 1051 is deduced from energy balance equation at the dry side wall (Equation 222).

The input and the output variable of T_w^{SV} algorithm are the ones reported in Table 260, due to the variables required to solve the objective function (Equation 1047).

Table 260. Input and output of $\boldsymbol{T_w^{SV}}$ algorithm.

Variables	Description
Inputs	The effective heat transfer coefficient (h_{eff}), dry side wall and roof surface areas (A^{SV} and A^R), external wall temperature (T^W), thermo-physical properties, filling ratio, vapour temperature, relative tolerance (ε_2) and absolute tolerance (ε_1) and number of iteration (N_I)
Output	Dry side wall temperature (T_w^{SV})

The values of the absolute and relative tolerance are respectively 10^{-10} and 10^{-5}. T_w^{SV} algorithm is presented in Figure 225.

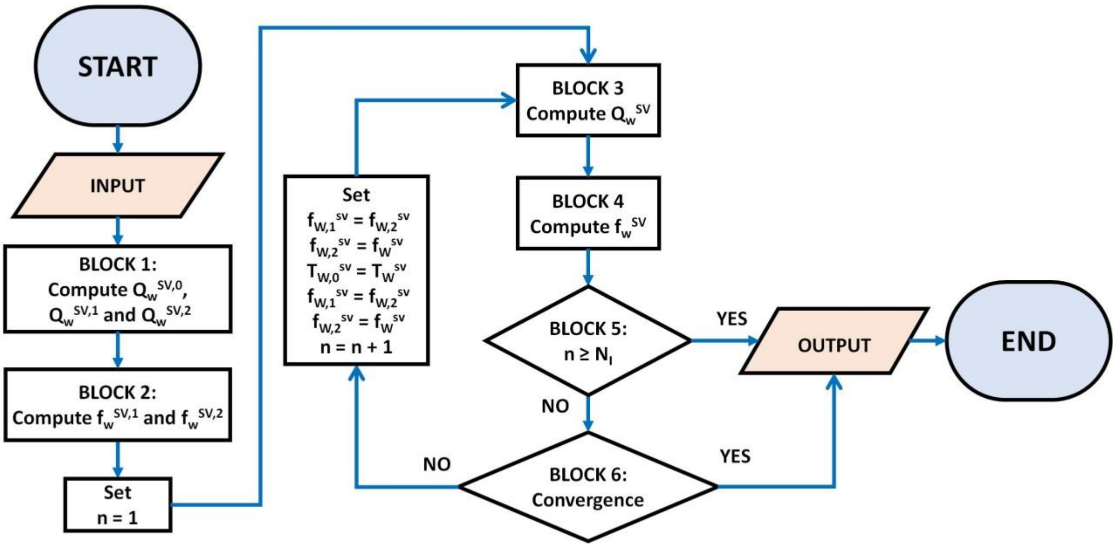

Figure 225. Algorithm to compute T_w^{SV}.

The T_w^{SV} algorithm is composed by the following steps:

a) BLOCK 1. The first guess value ($\dot{Q}_w^{SV,0}$) and the intermediate variables ($\dot{Q}_w^{SV,1}$ and $\dot{Q}_w^{SV,2}$) are computed with equations of Table 259;

b) BLOCK 2. The values of the objective function $f_w^{SV,1}$ and $f_w^{SV,2}$ are calculated with Equation 1035, respectively at $\dot{Q}_w^{SV,1}$ and at $\dot{Q}_w^{SV,2}$. The dry side wall temperature and the average heat transfer coefficient are computed with the equations of Table 258;

c) BLOCK 3. The objective variable $\dot{Q}_w^{SV}$ is determined with Equation 1052;

Equation 1052
$$\dot{Q}_w^{SV} = \dot{Q}_w^{SV,1} - f_w^{SV,1} \cdot \frac{\dot{Q}_w^{SV,2} - \dot{Q}_w^{SV,1}}{f_w^{SV,2} - f_w^{SV,1}}$$

d) BLOCK 4. The value of the objective function f_w^{SV} is calculated with Equation 1035. The dry side wall temperature and the average heat transfer coefficient are computed with the equations of Table 258;

e) BLOCK 5. Two pathways are present, as function of the value of the current number of iteration (n):
   - Pathway 1.5 (P 1.5). if n is higher or equal to the number of iteration (N_I), the algorithm stops;
   - Pathway 2.5 (P 2.5). when the current number of iteration is lower than N_I, the algorithms move to Block 6 (step f) of Section 1.3);

f) BLOCK 6. Two convergence criteria are respectively defined with Equation 1053 and with Equation 1054;

Equation 1053
$$|f_w^{SV}| \leq \varepsilon_1$$

Equation 1054
$$\left|\dot{Q}_w^{SV,0} - \dot{Q}_w^{SV}\right| \leq \left|\dot{Q}_w^{SV,0} \cdot \varepsilon_2\right|$$

Two pathways are present:
   - Pathway 1.6 (P 1.6). if Equation 1053 and Equation 1054 are true, the algorithm stops;
   - Pathway 2.6 (P 2.6). If Equation 1053 is false or Equation 1054 is false, the algorithms move to Block 3 (step c) of Section 1.3). The current number of the

iteration increases of 1, and $T_{w,1}^{SV}$, $T_{w,2}^{SV}$, $T_{w,0}^{SV}$, $f_{w,1}^{SV}$ and $f_{w,2}^{SV}$ are respectively equal to $T_{w,2}^{SV}$, T_{w}^{SV}, T_{w}^{SV}, $f_{w,2}^{SV}$ and f_{w}^{SV};

T_w^{SV} algorithm is applied in the h_{eff} algorithm and in the β algorithm

2. Algorithm of corrective coefficient alpha

The corrective coefficient α is introduced to correct the dry side wall-to-vapour heat transfer, due to the homogeneity hypothesis (assumption a) of Section 1.1). This correction is applied for the test at low filling ratio (Test 2) because α is equal to 1 for the test at high filling ratio (Test 1).

At the dry side wall, the thermal distribution of the heat flows is described with the energy balance equation of the dry side wall (Equation 222). In Equation 222, the term $h_{eff} \cdot (A^{SV} + A^{R}) \cdot (T^{W} - T_w^{SV})$ can be substituted with the difference between the overall heat input ($\dot{Q}_{IN}$) and wet walls-to-liquid heat flow ($\dot{Q}_w^L$). Hence, the corrective coefficient α can be computed as follows:

Equation 1055
$$\alpha = \frac{\dot{Q}_{IN} - \dot{Q}_w^L - \beta \cdot \dot{Q}_w^{LV}}{A^{SV} \cdot \bar{h}_w^{SV} \cdot (T_w^{SV} - T^V)}$$

$\dot{Q}_w^L$ is computed with is computed with Equation 1037. T_w^L of Equation 1037 is computed with the wet wall temperature algorithm, as explained in Section 1.1 of Appendix R. $\dot{Q}_w^{LV}$ is calculated as described in Section 4.5. $\bar{h}_w^{SV}$ is computed with the boundary layer approach, using the difference in temperatures between the dry side wall and the vapour ($T_w^{SV} - T^V$) as input parameter (see Section 4.5). T_w^{SV} can be estimated with Equation 1043. β is computed with Equation 1042. Hence, the input and output variables of the α algorithm are reported in Table 261.

Table 261. Input and output of $\boldsymbol{\alpha}$ algorithm.

Variables	Description
Inputs	The effective heat transfer coefficient (h_{eff}), wet dry side wall, dry side wall, bottom and roof surface areas (A^{SV}, A^{SL}, A^B and A^R), external wall temperature (T^W), thermo-physical properties, filling ratio, vapour temperature
Output	Corrective coefficient (α)

The algorithm to compute α is reported in Figure 226.

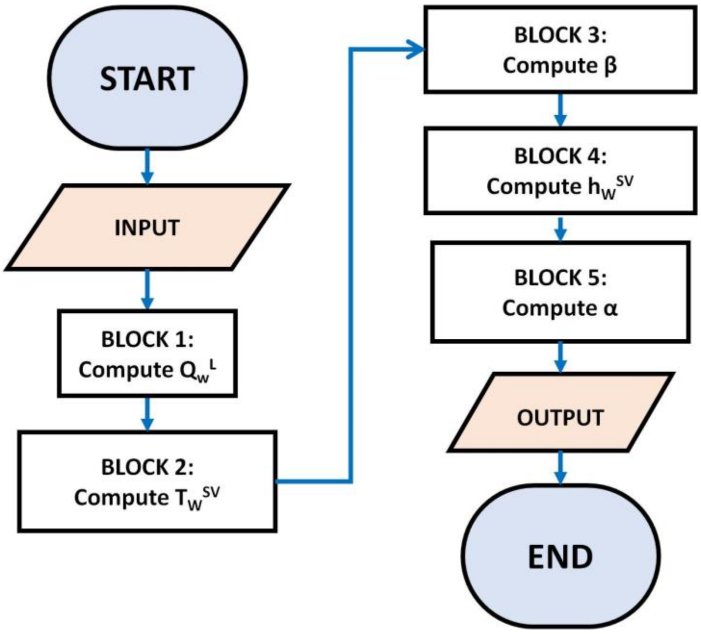

Figure 226. Algorithm to compute $\boldsymbol{\alpha}$.

α algorithm is composed by the following steps:

a) BLOCK 1. The wet walls-to-liquid heat input ($\dot{Q}_w^L$) is computed with Equation 1037. T_w^L of Equation 1037 is computed with the wet wall temperature algorithm, as explained in Section 1.1 of Appendix R;
b) BLOCK 2. The dry side wall temperature (T_w^{SV}) can be estimated with Equation 1043;
c) BLOCK 3. The corrective coefficient β is computed with Equation 1042;
d) BLOCK 4. The dry side wall-to-vapour heat transfer coefficient ($\bar{h}_w^{SV}$) is computed with the boundary layer approach (see Section 4.5);
e) BLOCK 5. The value of α is calculated with Equation 1055.

α algorithm does not require iterative procedure as for h_{eff} algorithm.

Appendix S

Statistical errors and post-treating of the results

The results of the homogeneous model (H model) are compared with the ones of equilibrium model (EQ model), by using the statistical errors. The results have to be post-treated to be used for this comparison.

Section 1 describes the statistical errors and Section 2 presents the post-treating.

1. Statistical errors

The accuracy of each model in calculating the time-evolutions of pressure, liquid and vapour temperatures, and filling ratio is computed with the statistical errors. These errors are the Average Absolute Deviation (AAD), the Bias and the Maximum Absolute Deviation (MAD). These errors are reported in Table 262.

Table 262. Types of numerical errors.

Errors	Description	Symbol	Equations	Formula
Average absolute deviation	It's the average of the relative deviation respect to the experimental data	AAD	Equation 1056	$ARD = \frac{1}{N_{EXP}} \cdot \sum_{i=1}^{N_{EXP}} \lvert\xi_i\rvert$
Bias	It's is the average of the relative error	$BIAS$	Equation 1057	$BIAS = \frac{1}{N_{EXP}} \cdot \sum_{i=1}^{N_{EXP}} \xi_i$
Maximum absolute relative deviation	It's the maximum value of the relative error	MAD	Equation 1058	$MAD = \max[\lvert\xi_i\rvert]$

N_{EXP} is the number of the experimental data. ξ_i is the relative error and it is defines as the ratio between the difference in value between the model and the experiments, and the value of the experimental data, as follows:

Equation 1059
$$\xi_i = \frac{y_i - y_i^{EXP}}{y_i^{EXP}}$$

y_i is the computed value and y_i^{EXP} is the experimental value.

2. Post-treating of the results

The values of pressure, liquid and vapour temperatures, and liquid volume, thus liquid level, are calculated with the solver of Ordinary Differential Equations (ODEs) system. In the equilibrium model (EQ model), only the pressure and the liquid volume are obtained with the ODE system solver. The other variables are deduced form therm. Hence, the values of this variable cannot be computed at the exact time at which the experimental values are measured. As consequence, the results have to be post-treated to compute the values of these variables at the exact measuring time of the experimental data. This calculation is done with a linear interpolation between the time-point before and the time-point after the measuring time-point, as follows:

Equation 1060
$$y_i = \frac{y_{t_{i+1}} - y_{i-1}}{t_{i+1} - t_{i-1}} \cdot \left(t_i^{EXP} - t_{i-1}\right) + y_{i-1}$$

y_i is the value of the compute variable at the measuring time-point and it is used in Equation 1059. t_i^{EXP} is the measuring time, t_{i+1} and t_{i-1} are respectively the time-point before and the time-point after t_i^{EXP}. $y_{t_{i+1}}$ and y_{i-1} are the values of the computed variable at t_{i+1} and t_{i-1}, respectively.

Appendix T

Algorithm of the dry side wall boundary layer of the homogeneous model 2.0 (H 2.0 model)

In the homogeneous model 2.0 (H 2.0 model), the calculation of the variables U and δ_M is impacted by the bulk ullage temperature gradient (Equation 226). Hence, only the algorithm of Integration Boundary Layer (IBL) approach of the dry side wall is modified respect to the version used in the homogeneous model (H model). The inputs and output variables of this algorithm are reported in Table 263.

Table 263. Input and output of the IBL approach of the dry side wall.

Variable	Description
Input	State variables and thermo-physical properties (see Table 62 and Table 49), heat flows at the surface or the surface wall temperature, gravity acceleration, length of the side wall (L_c), diameter at every sub-layer (a_n), the discretized length of the side ($dL_{c,n}$) and the bulk temperature gradient.
Output	boundary layer variables (Table 62)

The diameter at every sub-layer and the discretized length of the side are calculated as it is explained in Section 3.4.1 of Chapter 4. As it is reported in Table 263, the input and the output are the ones of the IBL approach of the H model, but the bulk ullage temperature gradient is added as inputs variables in the IBL approach of dry side wall of H 2.0 model.

In the H model, the algorithm of IBL approach (see Section 2 of Appendix P) can be divided into three steps:

a) The definition of the heat mode;
b) The calculation of the variables U and δ_M;
c) The calculation of the remaining boundary layer variables (see Table 62), using the variables U and δ_M;

Hence, only the step of the calculation of the variables U and δ_M (step b) of Appendix T) is impacted by the bulk ullage temperature gradient. This calculation is done with the algorithm of the numerical integration (see 2.1 of Appendix P), which numerically integrates the conservation laws (Equation 178 and Equation 179) of the boundary layer along the side wall. One of the steps of the algorithm of the numerical integration is the integration algorithm of the sub-layer (see Section 2.1.4 of Appendix P), which computes the values of the variables U and δ_M in the sub-layer. One of the steps of the integration algorithm of the sub-layer is the calculation of the number of the sub-space-points, which spatially discretize the sub-layer of the boundary layer. Hence, only this step, which is the Block 2 of the integration algorithm of the sub-layer, is changed. In Block 2 of the integration algorithm of the sub-layer, the value of this number is equal to 10. As consequence, the structures of integration algorithm of the sub-layer, of integration algorithm of the sub-layer and of algorithm of the numerical integration do not change in the H 2.0 model.

Appendix U

Algorithm of the dry side wall heat flow of the homogeneous model 2.0

The structure of the algorithm to compute the dry side wall-to-vapour heat flow is based on the Newton-Raphson with finite difference method (see Section 2 of Appendix I) to increase the stability of the iterative procedure. The increment of the stability is required because the bulk ullage temperature gradient is considered in the calculation of the boundary layer variables U and δ_M, thus the computation of the heat transfer coefficient $\bar{h}_w^{SV}$. Hence, the input and out variables are Table 264.

Table 264. Input and output variables of $\dot{Q}_w^{SV}$ algorithm.

Variables	**Description**
Input	Thermo-physical properties, effective heat transfer coefficient (h_{eff}), the corrective coefficients α and β, surface area of the dry side wall (A^{SV}), external wall temperature (T^W), vapour temperature (T^V), number of iteration (N_I), the values of the absolute tolerance (ε_1) and of relative tolerance (ε_2), and the bulk ullage temperature gradient.
Output	heat flow between the dry side wall and the vapour ($\dot{Q}_w^{SV}$), dry side wall temperature (T_w^{SV}) and heat transfer coefficient ($\bar{h}_w^{SV}$)

The values of the absolute and relative tolerance are respectively 10^{-10} and 10^{-5}. As it is indicated in Table 264, the input and the output are the ones of the algorithm of the dry side wall-to-vapour heat flow of the H model (see Section 3 of Appendix Q), except for the bulk ullage temperature gradient and the values of the absolute and relative tolerance.

The Newton-Raphson with finite difference method requires an objective function and an objective variable. The objective variable is the heat flow $\dot{Q}_w^{SV}$ and the objective function is described as follows:

Equation 1061 $$f_w^{SV} = h_{eff} \cdot (A^{SV} + A^R) \cdot (T^w - T_w^{SV}) - \left[\dot{Q}_w^{SV} + \beta \cdot \dot{Q}_w^{LV}\right]$$

Equation 1061 is obtained from the energy balance equation at the dry side wall (Equation 262). In Equation 1061, T_w^{SV} is computed with Equation 261.

The algorithm to compute $\dot{Q}_w^{SV}$ can be structured as illustrated in Figure 227.

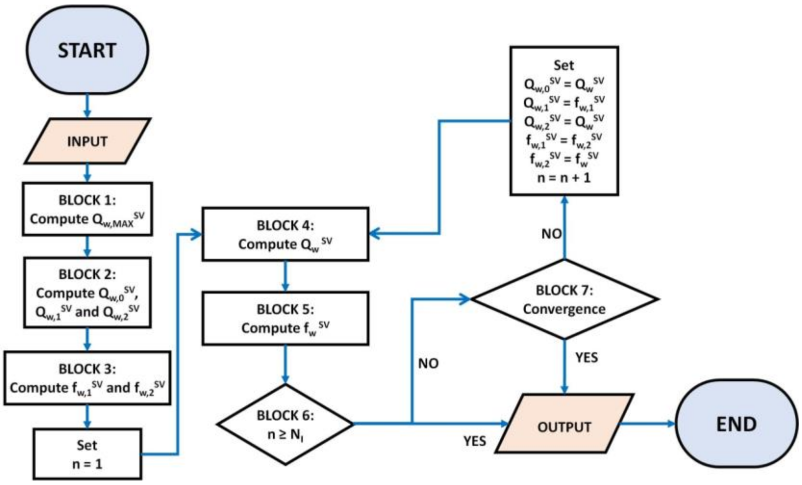

Figure 227. Algorithm of the dry side wall-to-vapour heat transfer.

This algorithm is composed by the following steps:

a) BLOCK 1. The maximum heat input at the bottom ($\dot{Q}_{w,MAX}^{SV}$) is calculated with Equation 267.

b) BLOCK 2. The first guess value ($\dot{Q}_w^{SV,0}$) and, the intermediate variables of the heat input ($\dot{Q}_w^{SV,1}$and $\dot{Q}_w^{SV,2}$) are computed with the equations of Table 94;

c) BLOCK 3. The values of the objective function ($f_w^{SV,1}$ and $f_w^{SV,2}$) are computed at $\dot{Q}_w^{SV,1}$ and $\dot{Q}_w^{SV,2}$, with Equation 1061. The dry side wall temperature is calculated with Equation 261. The value of the current iteration (n) is equal to 1.

d) BLOCK 4. The heat input is computed with Equation 1062.

Equation 1062
$$\dot{Q}_w^{SV} = \dot{Q}_w^{SV,1} - f_w^{SV,1} \cdot \frac{\dot{Q}_w^{SV,2} - \dot{Q}_w^{SV,1}}{f_w^{SV,2} - f_w^{SV,1}}$$

e) BLOCK 5. The objective function (f_w^{SV}) is computed with Equation 1061. The dry side wall temperature is calculated with Equation 261.

f) BLOCK 6. Two pathways are present, according to the value of the current iteration:
  - Pathways 1.7 (P 1.7): if the current number of iteration is higher or equal to the number of iteration, the mathematical procedure stops.
  - Pathways 2.7 (P 2.7): when the current number is lower than the number of iteration, the algorithm moves to Block 7 (step g) of Appendix U).

g) BLOCK 7. The convergence criteria are defined by Equation 1063 and by Equation 1064.

Equation 1063
$$|f_w^{SV}| \leq \varepsilon_1$$

Equation 1064
$$\left|\dot{Q}_w^{SV,0} - \dot{Q}_w^{SV}\right| \leq \left|\dot{Q}_w^{SV,0} \cdot \varepsilon_2\right|$$

Two pathways are presents:

- Pathway 1.8 (P 1.8): If Equation 1063 and Equation 1064 hold true, the algorithm stops;
- Pathway 2.8 (P 2.8): If Equation 1063 is false or Equation 1064 is false, the algorithm starts at Block 4 (step d) of Appendix U). $\dot{Q}_w^{SV,0}$, $\dot{Q}_w^{SV,1}$, $\dot{Q}_w^{SV,2}$, $f_w^{SV,1}$ and $f_w^{SV,2}$ are respectively equals to $\dot{Q}_w^{SV}$, $\dot{Q}_w^{SV,2}$, $\dot{Q}_w^{SV}$, $f_w^{SV,2}$ and f_w^{SV}.

The algorithm proposed here is to reach convergence in less than 10 iterations. The computational time of this algorithm is significant because of the numerical solution of the storage boundary layer model.

Appendix V

Algorithm of the net mass flow of the homogeneous model 2.0

The vapour-to-interface heat flow ($\dot{Q}_I^V$) depends on the fluid-motions of the ullage, as it is indicated by Equation 275. The descending flow of Equation 275 is computed with Equation 276. If this equation is applied to the interface sub-layer, the descending mass flow can be computed as follows:

Equation 1065 $$\dot{m}_2^D = \dot{m}_1^{BL} - \dot{m}_N$$

$\dot{m}_1^{BL}$ is computed with the equations of Table 92. The net mass flow ($\dot{m}_N$) can be computed as done in the homogeneous model (H model), thus as it is reported below:

Equation 1066 $$\dot{m}_N = \frac{\dot{Q}_I^L + \dot{Q}_W^{LV} + \dot{Q}_I^V}{\Delta\widetilde{H}_{EV}}$$

Hence, the vapour-to-interface heat flow depends on the net mass flow and $\dot{m}_N$ is affected by $\dot{Q}_I^V$. As consequence, an iterative procedure is required and it is called algorithm of the net mass flow. The objective variable of this algorithm is the net mass flow ($\dot{m}_N$).

Due to the hypothesis of local thermodynamic equilibrium (assumption d) of Section 1.2 of Chapter 5), the energy balance at the interface of the homogeneous model 2.0 (H 2.0 model) is similar to the one of the H model. Hence, this equation can be described as follows:

Equation 1067 $$\dot{Q}_I^L + \dot{Q}_W^{LV} + \dot{Q}_I^V - \dot{m}_N \cdot \Delta\widetilde{H}_{EV} = 0$$

As consequence, the objective function of this iterative procedure is reported below:

Equation 1068 $$f_I = \dot{Q}_I^L + \dot{Q}_W^{LV} + \dot{Q}_I^V - \dot{m}_N \cdot \Delta\widetilde{H}_{EV}$$

As it is indicated by Equation 1067, the algorithm of the net mass flow can be based on the Newton-Raphson with finite difference method (see Section 2 of Appendix I). Hence, the input and the output of the algorithm of the net mass flow are the ones reported in Table 265.

Table 265. Input and output of the algorithm of the net mass flow.

Variables	**Description**
Input	Thermo-physical properties, interface surface area (A^I), vapour temperature (T^V), liquid temperature (T^L), interface temperature (T^I), the boundary layer mass flow and temperature at the last sub-layer of wet side wall boundary layer ($\dot{m}_I^{BL}$) and (T_{BL}^I), number of iteration (N_I), the dry side wall-to-interface heat flow ($\dot{Q}_w^{LV}$) and the values of the absolute tolerance (ε_1) and of relative tolerance (ε_2), and the bulk ullage temperature gradient.
Output	Liquid-to-interface heat flow ($\dot{Q}_I^L$), vapour-to-interface heat flow ($\dot{Q}_I^V$) and net mass flow ($\dot{m}_N$)

The values of the absolute and relative tolerance are respectively 10^{-10} and 10^{-5}. The Newton-Raphson with finite difference method requires a first guess value of the objective function and the intermediate variables, as it is explained in Section 2 of Appendix I. To increases the stability and the speed of convergence this algorithm should be computed considering the physics of the heat transfer at the interface. The vapour-to-interface heat flow transfers the heat that enters in the ullage to the interface. Hence, its maximum value is the dry side wall-to-interface heat flow ($\dot{Q}_w^{SV}$) and the maximum value of the net mass flow can be calculated, as follows:

Equation 1069
$$\dot{m}_{N,MAX} = \frac{\dot{Q}_I^L + \dot{Q}_W^{LV} + \dot{Q}_w^{SV}}{\Delta\widetilde{H}_{EV}}$$

Due to the fluid-motion of the ullage, the vapour-to-interface heat flow cannot transfer the energy coming from the dry walls (dry side wall and roof). Hence, the minimum value of the vapour-to-interface heat flow is zero and the minimum value of the net mass flow can be computed as follows:

Equation 1070
$$\dot{m}_{N,MIN} = \frac{\dot{Q}_I^L + \dot{Q}_W^{LV}}{\Delta\widetilde{H}_{EV}}$$

As consequence, the first guess value of the net mass flow can be computed using the minimum and the maximum values of $\dot{m}_N$, as follows:

Equation 1071
$$\dot{m}_{N,0} = \frac{\dot{m}_{N,MIN} + \dot{m}_{N,MAX}}{2}$$

The intermediate variables can be calculated from the first guess value of the net mass flow, as follows:

Equation 1072
$$\dot{m}_{N,1} = 0.999 \cdot \dot{m}_{N,0}$$

Equation 1073
$$\dot{m}_{N,2} = 1.001 \cdot \dot{m}_{N,0}$$

The algorithm to compute the net mass flow is illustrated in Figure 228.

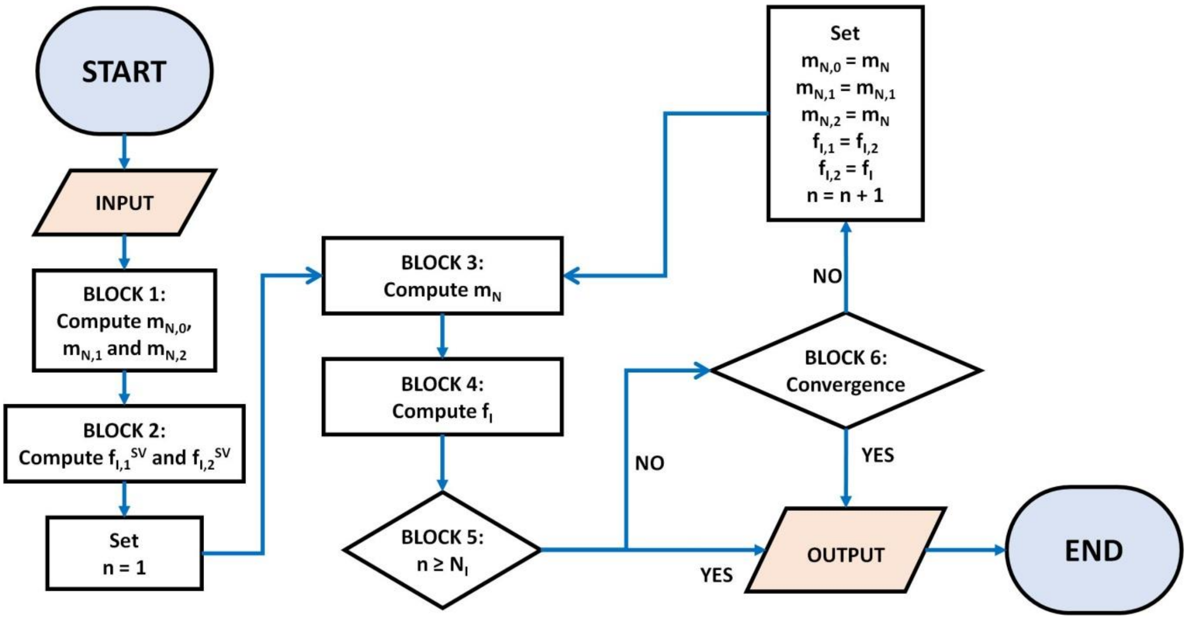

Figure 228. Algorithm to compute the net mass flow.

The algortimh of the net mass flow is composed by the following steps:

a) BLOCK 1. The first guess value ($\dot{m}_{N,0}$) is calculated with Equation 1071 and, the intermediate variables of the heat input ($\dot{m}_{N,1}$ and $\dot{m}_{N,2}$) are computed with Equation 1072 and Equation 1073;
b) BLOCK 2. The values of the objective function ($f_{I,1}$ and $f_{I,2}$) are computed at $\dot{m}_{N,1}$ and $\dot{m}_{N,2}$, with Equation 1068. The value of the current iteration (n) is equal to 1.
c) BLOCK 3. The heat input is computed with Equation 1074.

Equation 1074
$$\dot{m}_N = \dot{m}_{N,1} - f_{I,1} \cdot \frac{\dot{m}_{N,2} - \dot{m}_{N,1}}{f_{I,2} - f_{I,1}}$$

d) BLOCK 4. The objective function (f_I) is computed with Equation 1074;
e) BLOCK 5. Two pathways are present, according to the value of the current iteration:
  - Pathways 1.7 (P 1.7): if the current number of iteration is higher or equal to the number of iteration, the mathematical procedure stops.
  - Pathways 2.7 (P 2.7): when the current number is lower than the number of iteration, the algorithm moves to Block 6 (step f) of Appendix V).

f) BLOCK 6. The convergence criteria are defined by Equation 1075 and by Equation 1076.

Equation 1075
$$|f_I| \leq \varepsilon_1$$

Equation 1076
$$\left|\dot{m}_{N,0} - \dot{m}_N\right| \leq \left|\dot{m}_{N,0} \cdot \varepsilon_2\right|$$

Two pathways are presents:

  - Pathway 1.8 (P 1.8): If Equation 1075 and Equation 1076 hold true, the algorithm stops;
  - Pathway 2.8 (P 2.8): If Equation 1075 is false or Equation 1076 is false, the algorithm starts at Block 4 (step d) of Appendix V). $\dot{m}_{N,0}$, $\dot{m}_{N,1}$, $\dot{m}_{N,2}$, $f_{I,1}$ and $f_{I,2}$ are respectively equals to $\dot{m}_N$, $\dot{m}_{N,2}$, $\dot{m}_N$, $f_{I,2}$ and f_I.

This algorithms requires three iteration to converge. Thus, this algortimh quickly converges.

Appendix Z

Beta algorithm of alpha algorithm of Boil-Off Rate model of the homogeneous model 2.0

As it is explained in Section 5, the structure of the Boil-Off Rate (BOR) model of the homogeneous (H 2.0) model is the one of the BOR model of homogeneous model (H model). The main difference in the BOR model between H 2.0 and H models is the steady state energy balance equation of the ullage (Equation 278). Hence, the structure of the beta algorithm of h_{eff} algorithm does not change. In the α algorithm, the beta coefficient is calculated with a formula in the BOR model of H model. Since the steady state energy balance equation of the ullage (Equation 278) is different from the one of H model, the beta coefficient is computed with an specific algorithm in the α algorithm of BOR model of H 2.0 model.

Section 1 describes the objective function and the objective variable of β algorithm of α algorithm. Section 2 presents the input and the output of this algorithm. Section 3 explains the structure of β algorithm of α algorithm.

1. Objective function and objective variable

β algorithm of α algorithm of Boil-off rate (BOR) model of homogeneous model 2.0 (H 2.0 model) compute the bet coefficient. Hence, this coefficient is the objective variable of this algorithm. Considering that β algorithm of α algorithm of BOR model of H 2.0 model is based on the steady state energy balance equation at the ullage (Equation 278), the objective variable of this algorithm is the following:

Equation 1077

$$
\begin{gathered}
f_w^V = \dot{m}_N \cdot \left(\tilde{h}_S^V - \tilde{h}_1^V\right) - \dot{Q}_I^V + \dot{Q}_w^{SV} \\
+\sum_{i=1}^{N^+}\left[\dot{m}_i^{BL} \cdot \tilde{h}_i^V\right] - \sum_{i=1}^{N^-}\left[\dot{m}_i^{BL} \cdot \tilde{h}_i^V\right] + \sum_{i=1}^{N^V}\left[F_{i+1}^{D,+} \cdot \dot{m}_{i+1}^D \cdot \left(\tilde{h}_{i+1}^V - \tilde{h}_i^V\right)\right] \\
-\sum_{i=1}^{N^V}\left[F_{i+1}^{D,-} \cdot \dot{m}_{i+1}^D \cdot \left(\tilde{h}_i^V - \tilde{h}_{i+1}^V\right)\right]
\end{gathered}
$$

To use Equation 1077, the net mass flow ($\dot{m}_N$), the descending flows ($\dot{m}_i^D$) and the bulk-to-boundary layer mass flow ($\dot{m}_i^{BL}$), the virtual temperature profile of the ullage to compute the specific enthalpy, the dry side wall-to-vapour heat flow ($\dot{Q}_w^{SV}$) and the vapour-to-interface heat flow ($\dot{Q}_I^V$) are required. The net mass flow can be computed with the algorithm of Appendix V. The heat flow $\dot{Q}_I^V$ can be calculated as it is explained in Section 4.2 of Chapter 5. The mass flow $\dot{m}_i^{BL}$ can be computed with the Storage Boundary Layer (SBL) model and the descending flows are computed with Equation 276. The heat flow $\dot{Q}_w^{SV}$ is computed as follows:

Equation 1078

$$\dot{Q}_w^{SV} = h_{eff} \cdot \left(A^{SV} + A^R\right) \cdot \left(T^w - T_w^{SV}\right) - \beta \cdot \dot{Q}_w^{LV}$$

Equation 1078 is deduced from the energy conservation law of the dry side wall (Equation 262). $\dot{Q}_w^{LV}$ is computed with the Storage Heat Transfer (SHT) model (see Section 4.5 of Chapter 4) with the bulk temperature gradient. This gradient is computed with Equation 226, using the experimental value of ullage temperature and filling ratio of Test 2. h_{eff} is computed with the h_{eff} algorithm, using the experimental values of ullage temperature, BOR, filling ratio and pressure of Test 1 (high filling ratio). A^{SV} and A^{R} are respectively the surface area of the dry side wall and of the roof. T^{w} is the external temperature and T_{w}^{SV} is the dry side wall temperature. This temperature is calculated as done in the H model, thus as follows:

Equation 1079
$$T_{w}^{SV} = T^{w} - \frac{\dot{Q}_{IN} - \dot{Q}_{w}^{L}}{h_{eff} \cdot (A^{SV} + A^{R})}$$

Equation 1079 is deduced from the definition of heat flow, applied at the dry side wall. $\dot{Q}_{IN}$ is the overall heat input, measured during Test 2 (low filling ratio) and $\dot{Q}_{w}^{L}$ is the wet walls (wet side wall and bottom)-to-liquid heat flow. This heat flow is calculated as done in the H model, thus as follows:

Equation 1080
$$\dot{Q}_{w}^{L} = h_{eff} \cdot (A^{SL} + A^{B}) \cdot (T^{w} - T_{w}^{L})$$

T_{w}^{L} is the wet walls temperature and it is calculated with T_{w}^{L} algorithm of H model (see Section 1.1 of Appendix R). A^{SL} and A^{B} are respectively the surface area of wet side wall and bottom.

2. Input and output

As it is indicated in Equation 1077, the input and the output variable of β algorithm of α algorithm are the one reported in Table 266.

Table 266. Input and output of $\boldsymbol{\beta}$algorithm of $\boldsymbol{\alpha}$ algorithm.

Variable	Description
Input	Experimental values of ullage temperature, pressure, filling ratio and heat inputs (or BOR) at Test 2 (low filling ratio), effective heat transfer coefficient (h_{eff}), surface area of each surface of the storage container (A^{SL}, A^{B}, A^{SV} and A^{R}), the wet walls temperature (T_{w}^{L}) and the external temperature (T^{w}) and the values of the absolute tolerance (ε_1) and of relative tolerance (ε_2),
Output	Value of beta coefficient (β)

The values of the absolute and relative tolerance are respectively 10^{-10} and 10^{-5}.

3. Structure of the algorithm

Since the objective function is Equation 1077, the β algorithm of α algorithm can be developed using the Newton-Raphson with finite difference (see Section 2 of Appendix I). This method requires a first guess value of the objective function and the intermediate variables. If the computed thickness of side wall is equal to the one of the storage container. If the calculated dry side wall temperature gradient is equal to the real one, the value of the beta coefficient is equal to 1. Hence, the equation of Table 267 can be used to compute the first guess value and the intermediate variables.

Table 267. First guess value and intermediate variables of $\boldsymbol{\beta}$.

Variables	Name	Equation	Formula
first guess value of beta coefficient	β_0	Equation 1081	$\beta_0 = 1$
First intermediate variable of beta coefficient	β_1	Equation 1082	$\beta_1 = 0.999 \cdot \beta_0$
Second intermediate variable of beta coefficient	β_2	Equation 1083	$\beta_2 = 1.001 \cdot \beta_0$

The structure of the β algorithm of α algorithm is illustrated in Figure 229.

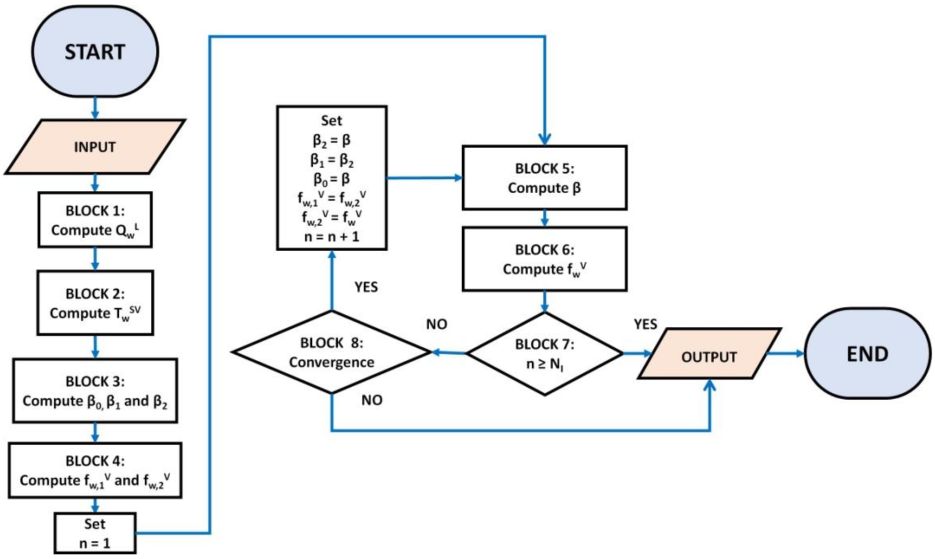

Figure 229. Structure of $\boldsymbol{\beta}$ algorithm of $\boldsymbol{\alpha}$ algorithm.

This algortimh is composed by the following steps:

a) BLOCK 1. The wet walls-to-liquid heat flow ($\dot{Q}_w^L$) is calculated with Equation 1080;
b) BLOCK 2. The dry side wall temperature (T_w^{SV}) is calculated with Equation 1079;
c) BLOCK 3. The first guess value (β_0) and, the intermediate variables of the heat input (β_1 and β_2) are computed with the equations of Table 267;
d) BLOCK 4. The values of the objective function ($f_{w,1}^V$ and $f_{w,2}^V$) are computed at β_1 and β_2, with Equation 1077. The value of the current iteration (n) is equal to 1.
e) BLOCK 5. The beta coefficient is computed with Equation 1084.

Equation 1084 $$\beta = \beta_1 - f_{w,1}^V \cdot \frac{\beta_2 - \beta_1}{f_{w,2}^V - f_{w,1}^V}$$

f) BLOCK 6. The objective function (f_w^V) is computed with Equation 1077;
g) BLOCK 7. Two pathways are present, according to the value of the current iteration:
    - Pathways 1.7 (P 1.7): if the current number of iteration is higher or equal to the number of iteration, the mathematical procedure stops.
    - Pathways 2.7 (P 2.7): when the current number is lower than the number of iteration, the algorithm moves to Block 8 (step h) of Section 3 of Appendix Z).
h) BLOCK 8. The convergence criteria are defined by Equation 1085 and by Equation 1086.

Equation 1085 $$|f_w^V| \leq \varepsilon_1$$

Equation 1086 $$|\beta_0 - \beta| \leq |\beta_0 \cdot \varepsilon_2|$$

Two pathways are presents:

- Pathway 1.8 (P 1.8): If Equation 1085 and Equation 1086 hold true, the algorithm stops;
- Pathway 2.8 (P 2.8): If Equation 1085 is false or Equation 1086 is false, the algorithm starts at Block 4 (step e) of Section 3 of Appendix Z). β_0, β_1, β_2, $f_{w,1}^V$ and $f_{w,2}^V$ are respectively equals to β, β_2, β, $f_{w,2}^V$ and f_w^V.

This algorithm takes around 10 iterations to converge. The number of the iteration is equal to the maximum one, when the value of beta is close to zero

Appendix AA

Geometrical formulas of liquid stratification model

The geometrical formulas of the liquid stratification model are deduced from the geometry of the storage container. Section 1 describes the equation to compute the volume of the bulk of the sub-layer. Section 2 presents the equations to calculate the mass of the sub-layer ($m_{n_L}^{L}$). Section 3 describes the formulas to compute the geometrical coefficient Z_{n_L}. Section 4 presents the general formulas of the geometry.

1. Estimation of the volume of the sub-layer bulk

The liquid volume is discretized in sub-layer as it is reported in Figure 230. In Figure 230, the blue rectangles are the sub-layers and the black border is the wall of the storage container. The yellow dashed line is the interface. The vertical orange lines are the liquid heights respect to the bottom. The green lines are the interface surface area of each sub-layer.

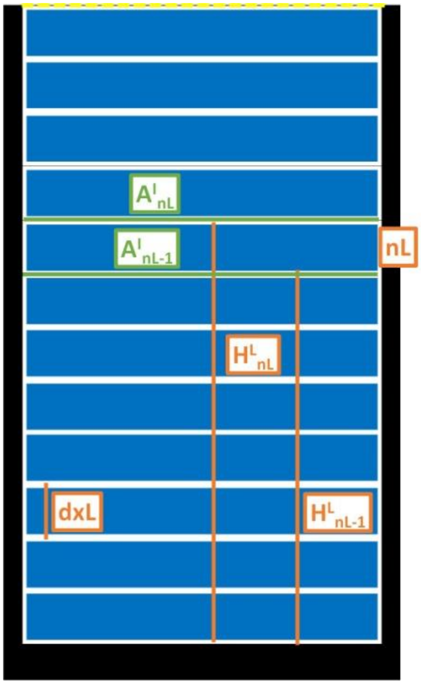

a)

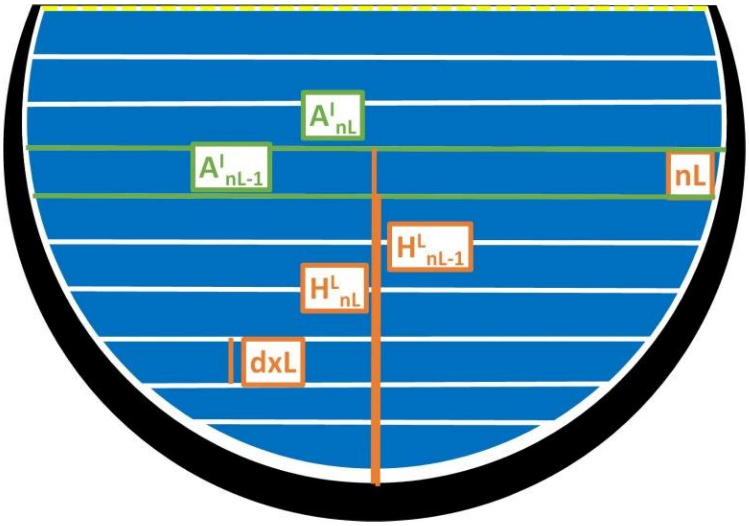

b)

Figure 230. Discretized liquid volume: a) vertical cylindrical tank with flat bottom and roof; b) sphere and oblate.

As reported in Figure 230, the volume of the sub-layer can be estimated as the difference in volumes between the value at the height $H_{n_L}^{L}$ and the value at height $H_{n_L-1}^{L}$. So, the volume of the sub-layer can be estimated with Equation 1087.

Equation 1087 $$V_{n_L}^{SL} = V^{L}\left(H_{n_L}^{L}\right) - V^{L}\left(H_{n_L-1}^{L}\right)$$

The sub-layer is composed by the boundary layer and the bulk. So, the volume of the sub-layer bulk ($V_{n_L}^{BK}$) is the difference in volume between the sub-layer and the boundary layer, as described by Equation 1088.

Equation 1088 $$V_{n_L}^{BK} = V_{n_L}^{SL} - V_{n_L}^{BL}$$

$V_{n_L}^{BL}$ is the volume of the boundary layer of the sub-layer.

2. Estimation of the mass of the sub-layer bulk

The mass of the sub-layer is estimated as the product between the density and the volume of the sub-layer, as indicated by Equation 1089.

Equation 1089 $$m_{n_L}^{L} = V_{n_L}^{L} \cdot \rho^{L}$$

ρ^{L} is the liquid density computed at the average values of temperature and pressure.

3. Estimation of the geometrical coefficient

The estimation of the geometrical coefficient changes with the geometry of the storage container. This coefficient can be computed as indicated in Table 268.

Table 268. Geometrical formulas to compute $\boldsymbol{Z_{n_L}}$.

Vertical cylinder with flat bottom and roof	Equation 1090	$Z_{n_L} = A^{I}$
Sphere and oblate ellipsoid	Equation 1091	$Z_{n_L} = 6 \cdot \frac{V^{TOT}}{H^{TOT}} \cdot \left[2 \cdot \frac{dxL}{H^{TOT}} \cdot \left(\frac{1}{2} + N\right) - 3 \cdot \left(\frac{dxL}{H^{TOT}}\right)^{2} \cdot \left(\frac{1}{3} + N^{2} + N\right)\right]$

H^{TOT} is the internal height of the storage container. N is equal to $[n_L - 1]$. The mathematical procedures to obtain Equation 1090 and Equation 1091 are respectively explained in Section 3.1 and 3.2. Both mathematical procedures consider that the time derivate of the volume of the boundary layer of the sub-layer is negligible due to the hypothesis of liquid discretisation (assumption b) of Section 1.2 of Chapter 6).

3.1. Vertical cylinder with flat bottom and roof

For a vertical cylinder, the internal section does not change with the distance from the bottom, as indicated in Figure 230 (a). As consequence, Equation 1087 can be written as indicated in Equation 1092.

Equation 1092 $$V_{n_L}^{SL} = A^{I} \cdot \left(H_{n_L}^{L} - H_{n_{L-1}}^{L}\right)$$

The difference $\left(H_{n_L}^{L} - H_{n_{L-1}}^{L}\right)$ is equal to dxL. Hence, the time derivate of $V_{n_L}^{SL}$ can be computed as described by Equation 1093.

Equation 1093 $$\frac{\partial V_{n_L}^{SL}}{\partial t} = A^{I} \cdot \frac{\partial dxL}{\partial t}$$

Hence, the geometrical coefficient Z_{n_L} is equal to A^{I}.

3.2. Sphere and oblate ellipsoid

The internal section of the storage container change with the distance from the bottom, as indicated in Figure 230 (b) for sphere and oblate ellipsoid. So, Equation 1087 can be written as described by Equation 1094.

Equation 1094 $$V_{n_L}^{SL} = 6 \cdot V^{TOT} \cdot \left\{\left(\frac{H_{n_L}^{L}}{H^{TOT}}\right)^{2} \cdot \left[\frac{1}{2} - \frac{1}{3} \cdot \left(\frac{H_{n_L}^{L}}{H^{TOT}}\right)\right] - \left(\frac{H_{n_L-1}^{L}}{H^{TOT}}\right)^{2} \cdot \left[\frac{1}{2} - \frac{1}{3} \cdot \left(\frac{H_{n_L-1}^{L}}{H^{TOT}}\right)\right]\right\}$$

$H_{n_L}^{L}$ is equal to $\left[H_{n_L-1}^{L} + dxL\right]$, which is equal to $[dxL \cdot (n_L - 1) + dxL]$ and Equation 1094 can be determined with Equation 1095.

Equation 1095
$$V_{n_L}^{SL} = 6 \cdot V^{TOT} \cdot \left\{ \left(\frac{dxL \cdot (n_L - 1) + dxL}{H^{TOT}} \right)^2 \cdot \left[\frac{1}{2} - \frac{1}{3} \cdot \left(\frac{dxL \cdot (n_L - 1) + dxL}{H^{TOT}} \right) \right] - \left(\frac{dxL \cdot (n_L - 1)}{H^{TOT}} \right)^2 \cdot \left[\frac{1}{2} - \frac{1}{3} \cdot \left(\frac{dxL \cdot (n_L - 1)}{H^{TOT}} \right) \right] \right\}$$

The term dxL is grouped in Equation 1095 and the volume of the sub-layer can be estimated with Equation 1096.

Equation 1096
$$V_{n_L}^{SL} = 6 \cdot V^{TOT} \cdot \left[\left(\frac{dxL}{H^{TOT}} \right)^2 \cdot \left(\frac{1}{2} + N \right) - \left(\frac{dxL}{H^{TOT}} \right)^3 \cdot \left(N^2 + N + \frac{1}{3} \right) \right]$$

The time derivate of Equation 1096 is done and Equation 1097 is obtained.

Equation 1097
$$\frac{\partial V_{n_L}^{SL}}{\partial t} = 6 \cdot \frac{V^{TOT}}{H^{TOT}} \cdot \left[\frac{2 \cdot dxL}{H^{TOT}} \cdot \left(\frac{1}{2} + N \right) - 3 \cdot \left(\frac{dxL}{H^{TOT}} \right)^2 \cdot \left(N^2 + N + \frac{1}{3} \right) \right] \cdot \frac{\partial dxL}{\partial t}$$

From Equation 1097, the coefficient $Z_{n_L}$is obtained.

4. General geometrical formulas

The liquid stratification model (LS model) requires geometrical formulas to compute the total volume, the internal surface and the filling ratio. These geometrical formulas are reported in Table 269.

Table 269. Geometrical formulas of LS model.

Geometrical Variables	Name	Equations	Formulas
General			
Liquid height at sub-layer	$H_{n_L}^L$	Equation 1098	$H_{n_L}^L = dxL \cdot n_L$
Filling ratio at sub-layer	LF_{n_L}	Equation 1099	$LF_{n_L} = \frac{H_{n_L}^L}{H^L}$
Vertical cylinder with flat bottom and flat roof			
Total liquid volume	V^L	Equation 1100	$V^L = \sum_{n_L=1}^{N^L} V_{n_L}^L = \frac{\pi \cdot D^2}{4} \cdot H^L$
Volume of liquid sub-layer	$V_{n_L}^L$	Equation 1101	$V_{n_L}^L = \frac{\pi \cdot D^2}{4} \cdot H_{n_L}^L$
Wet side wall at sub-layer	$A_{n_L}^{SL}$	Equation 1102	$A_{n_L}^{SL} = \pi \cdot D \cdot H_{n_L}^L$
Wet side wall of sub-layer	$dA_{n_L}^{SL}$	Equation 1103	$dA_{n_L}^{SL} = A_{n_L}^{SL} - A_{n_L-1}^{SL} = \pi \cdot D \cdot dxL$
Oblate ellipsoid with two equal semi axis			
Wet side wall at sub-layer	$A_{n_L}^{SL}$	Equation 1104	$A_{n_L}^{SL} = A^S \cdot LF_{n_L}$
Wet side wall of sub-layer	$dA_{n_L}^{SL}$	Equation 1105	$dA_{n_L}^{SL} = A^S \cdot \left(LF_{n_L} - LF_{n_L-1} \right)$
Interface section	A^I	Equation 1106	$A^I = \pi \cdot {D_{MAX}}^2 \cdot LF \cdot (1 - LF)$

Appendix AB

Liquid pressure profile

The liquid pressure in each sub-layer increases from the interface to the bottom, due to the hydrostatic effect, as it is described:

Equation 1107 $$P_{n_L}^L = P^V + g \cdot \rho^L \cdot (H^L - H_{n_L}^L)$$

H^L is the overall liquid height and $H_{n_L}^L$ is the liquid height of the sub-layer "n_L". The density of the liquid depends on the average liquid pressures, with is calculated from the values of the liquid pressure in each sub-layers. Hence, an iterative procedure is required to compute the liquid pressure in each sub-layer and this pressure is computed with the algorithm reported in Figure 231.

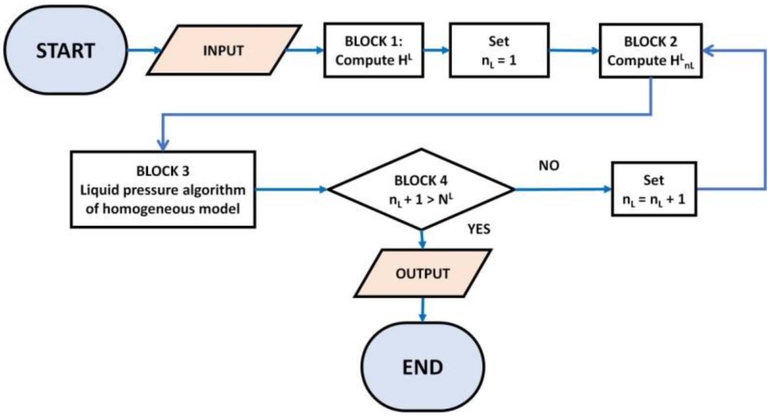

Figure 231. Algorithm to compute the liquid temperature in each sub-layer.

The input variables of this algorithm are the number of liquid sub-layer, the variable of state of the liquid stratification model and the inputs of the algorithm of the liquid pressure of the homogeneous model. The output is the values of the liquid pressure in each sub-layer. The algorithm of Figure 231 is composed by the following steps:

a) BLOCK 1: The total liquid height (H^L) is computed as follows:

   Equation 1108 $$H^L = N^L \cdot dxL$$

   The number of sub layer (n_L) is set equal to 1;

b) BLOCK 2: the liquid deep ($H_{n_L}^L$) is calculated as follows:

   Equation 1109 $$H_{n_L}^L = H^L - dxL \cdot \left(n_L - \frac{1}{2}\right)$$

c) BLOCK 3: The algorithm of the liquid pressure of homogeneous model is applied (see Section 4 of Appendix L);

d) BLOCK 4: the number of the current sub-layer (n_L) is compared with the number of the sub-layer (N^L). Two pathways are present:
   - Pathway 1.4 (P.14): n_L is higher or equal to N^L, indicating that the liquid pressure is calculated in all the sub-layers. Thus, the algorithm stops ;
   - Pathway 2.4 (P 2.4): the current number of the sub-layer is lower than the number of the sub-layer. The algorithm starts at Block 2 (step b) of Appendix AB), increasing the number of the current sub-layer of 1.

Appendix AC

Mathematical steps of the mathematical procedure of the liquid stratification model

The mathematical procedure is composed of height steps, as it is described in Figure 128. In each of these steps, equations are presented and explained, but the mathematical steps to obtain them are not explained. These mathematical steps are described here.

Section 1, 2, 3 and 4 describes the mathematical steps to deduce the simplified form of the conservation laws, the descending flow equations, the pressure-thickness equations, and the pressure-evolution, thickness-evolution, inlet liquid flow and boil-off gas equations, respectively.

1. Mathematical steps of the simplified form of the conservation laws

The simplified form of the conservation laws are balance equations that depends only on the time-derivates of the temperatures and of the pressure, as it is described in Section 2.4. The simplified form of the conservation laws, which are reported in Table 123, can be divided into the mass ullage, the energy ullage, the liquid mass and the liquid energy balance equations. The ullage mass balance equation is Equation 330 and the ullage energy balance equation is Equation 331, which is obtained as it is explained in Chapter 5. The liquid mass balance equations are Equation 332, Equation 334, Equation 336, Equation 338, Equation 340, Equation 344, Equation 346, Equation 348, Equation 350, Equation 352, Equation 354, Equation 356, Equation 358, Equation 360, Equation 362, Equation 364 and Equation 366. The liquid energy balance equations are Equation 333, Equation 335, Equation 337, Equation 339, Equation 341, Equation 345, Equation 347, Equation 349, Equation 351, Equation 353, Equation 355, Equation 357, Equation 359, Equation 361, Equation 363, Equation 365 and Equation 367.

Section 1.1, 1.2 and 1.3 respectively present the mathematical steps to deduce the simplified forms of the ullage mass conservation laws, of the liquid mass conservation laws and of the liquid energy conservation laws.

1.1. Mathematical steps of the simplified form of the ullage mass conservation laws

The ullage mass is the product between the ullage volume and the vapour density. The density of a pure fluid is a function of temperature and pressure. Hence, the time-derivate of the ullage mass can be computed as follows:

Equation 1110
$$\frac{\partial m^V}{\partial t} = \rho^V \cdot \frac{\partial V^V}{\partial t} + V^V \cdot \left[\left.\frac{\partial \rho^V}{\partial T^V}\right|_{P^V} \cdot \frac{\partial T^V}{\partial t} + \left.\frac{\partial \rho^V}{\partial P^V}\right|_{T^V} \cdot \frac{\partial P^V}{\partial t} \right]$$

The variable $\frac{\partial m^V}{\partial t}$ of the ullage mass conservation law (Equation 97) can be substituted by Equation 1110 and this conservation laws can be written as follows:

Equation 1111
$$\rho^V \cdot \frac{\partial V^V}{\partial t} + V^V \cdot \left[\left.\frac{\partial \rho^V}{\partial T^V}\right|_{P^V} \cdot \frac{\partial T^V}{\partial t} + \left.\frac{\partial \rho^V}{\partial P^V}\right|_{T^V} \cdot \frac{\partial P^V}{\partial t} \right] = \dot{m}_{IN}^V + \dot{m}_N - \dot{m}_{BOG}$$

Due to the conservation law of the volume (Equation 288), the variation of the ullage volume must be balanced by the variation of the liquid volume. Hence, the variable $\frac{\partial V^V}{\partial t}$ of Equation 692 can be substituted with Equation 288. So, the ullage mass conservation law can be written as follows:

Equation 1112
$$-\rho^V \cdot \left(\sum_{n_L=1}^{N^L} \frac{\partial V_{n_L}^L}{\partial t} \right) + V^V \cdot \left[\frac{\partial \rho^V}{\partial T^V}\bigg|_{P^V} \cdot \frac{\partial T^V}{\partial t} + \frac{\partial \rho^V}{\partial P^V}\bigg|_{T^V} \cdot \frac{\partial P^V}{\partial t} \right] = \dot{m}_{IN}^V + \dot{m}_N - \dot{m}_{BOG}$$

The derivate $\frac{\partial V_{n_L}^L}{\partial t}$ can be computed as product between the geometrical coefficient Z_{nL}^L (see Appendix Appendix AB) and the time-derivate of the thickness of the sub-layers ($\frac{\partial dxL}{\partial t}$). The simplified form of the vapour mass conservation law (Equation 330) is then obtained by substituting $\frac{\partial V_{n_L}^L}{\partial t}$ with the product $Z_{nL}^L \cdot \frac{\partial dxL}{\partial t}$ in Equation 890.

1.2.Mathematical steps of the simplified form of the liquid mass conservation laws

The conservation laws of liquid mass of Table 157 can be generalized as follows:

Equation 1113
$$\frac{\partial m_{n_L}^{B,L}}{\partial t} = K_{n_L}$$

K_{n_L} is the right part of the conservation laws of liquid mass of Table 157 and it contains the convective mass flows.

As for the ullage mass, the mass of the bulk liquid sub layer is the product of the volume of the bulk sub-layer and of the density. Hence, the time derivate of the mass of the bulk liquid sub layer can be computed with Equation 1114, which can be applied for the interface, the core and the bottom sub-layers.

Equation 1114
$$\frac{\partial m_{n_L}^{B,L}}{\partial t} = \rho^L \cdot \frac{\partial V_{n_L}^{B,L}}{\partial t} + V_{n_L}^L \cdot \left[\frac{\partial \rho^L}{\partial T^L}\bigg|_{P^V} \cdot \frac{\partial T_{n_L}^{B,L}}{\partial t} + \frac{\partial \rho^L}{\partial P^V}\bigg|_{T^L} \cdot \frac{\partial P^V}{\partial t} \right]$$

So, the variable $\frac{\partial m_{n_L}^{SBL}}{\partial t}$ of Equation 1113 can be computed with Equation 1114 and the generalized conservation laws of liquid mass of Table 157 (Equation 1113) can be written as follows:

Equation 1115
$$\rho^L \cdot \frac{\partial V_{n_L}^{B,L}}{\partial t} + V_{n_L}^L \cdot \left[\frac{\partial \rho^L}{\partial T^L}\bigg|_{P^V} \cdot \frac{\partial T_{n_L}^{B,L}}{\partial t} + \frac{\partial \rho^L}{\partial P^V}\bigg|_{T^L} \cdot \frac{\partial P^V}{\partial t} \right] = K_{n_L}$$

The time-derivate of the volume of bulk of the liquid sub-layer ($\frac{\partial V_{n_L}^{B,L}}{\partial t}$) is equal to the time derivate of the volume of the liquid sub-layer ($\frac{\partial V_{n_L}^L}{\partial t}$) because the transient of the boundary layer of the sub-layer is neglected as it is explained in Section 1.3. The variable $\frac{\partial V_{n_L}^{B,L}}{\partial t}$ is equal to $Z_{nL}^L \cdot \frac{\partial dxL}{\partial t}$, as it is explained in Section 1.1 of Appendix AC. So, Equation 1115 can be written as follows:

Equation 1116
$$\rho^L \cdot Z_{nL}^L \cdot \frac{\partial dxL}{\partial t} + V_{n_L}^L \cdot \left[\frac{\partial \rho^L}{\partial T^L}\bigg|_{P^V} \cdot \frac{\partial T_{n_L}^{B,L}}{\partial t} + \frac{\partial \rho^L}{\partial P^V}\bigg|_{T^L} \cdot \frac{\partial P^V}{\partial t} \right] = K_{n_L}$$

If the variable K_{n_L} is substituted with the convective mass flow of the conservation laws of liquid mass of Table 157, the simplified form of the liquid mass conservation laws of Table 123 is obtained.

1.3. Mathematical steps of the simplified form of the liquid energy conservation laws

The conservation laws of liquid energy of Table 157 can be generalized as follows:

Equation 1117
$$\frac{\partial \tilde{H}_{n_L}^{B,L}}{\partial t} = Y_{n_L}$$

Y_{n_L} is the right part of the conservation laws of liquid energy of Table 157 and it contains the enthalpy flow of the convective mass flows, the wet wall-to-liquid heat flow and the intra-layer heat flows.

The enthalpy of the bulk of the sub-layer ($\tilde{H}_{n_L}^{B,L}$) is the product between the mass of the bulk of the sub-layer ($m_{n_L}^{B,L}$) and the specific enthalpy of the bulk of the sub-layer ($\tilde{h}_{n_L}^{B,L}$). This specific enthalpy is a function of the liquid pressure of the sub-layer and of the temperature of the bulk of the sub-layer ($T_{n_L}^{B,L}$). As consequence, the time derivate of the enthalpy of the bulk of the sub-layer ($\frac{\partial \tilde{H}_{n_L}^{B,L}}{\partial t}$) can be computed as follows:

Equation 1118
$$\frac{\partial \tilde{H}_{n_L}^{B,L}}{\partial t} = m_{n_L}^{B,L} \cdot \left[C_P^L \cdot \frac{\partial T_{n_L}^{B,L}}{\partial t} + \left.\frac{\partial \tilde{h}_{n_L}^{B,L}}{\partial P^V}\right|_{T_{n_L}^{B,L}} \cdot \frac{\partial P^V}{\partial t} \right] + \frac{\partial m_{n_L}^{B,L}}{\partial t} \cdot \tilde{h}_{n_L}^{B,L}$$

Equation 1118 can be applied to the interface, core and bottom sub-layer. So, the generalized conservation law of liquid energy of Table 157 (Equation 1117) can be written as follows:

Equation 1119
$$m_{n_L}^{B,L} \cdot \left[C_P^L \cdot \frac{\partial T_{n_L}^{B,L}}{\partial t} + \left.\frac{\partial \tilde{h}_{n_L}^{B,L}}{\partial P^V}\right|_{T_{n_L}^{B,L}} \cdot \frac{\partial P^V}{\partial t} \right] + \frac{\partial m_{n_L}^{B,L}}{\partial t} \cdot \tilde{h}_{n_L}^{B,L} = Y_{n_L}$$

The time-derivate of the mass of the bulk of the sub-layer ($\frac{\partial m_{n_L}^{B,L}}{\partial t}$) can be computed with the generalized conservation law of liquid mass (Equation 1113). Equation 1119 can be written as follows:

Equation 1120
$$m_{n_L}^{B,L} \cdot \left[C_P^L \cdot \frac{\partial T_{n_L}^{B,L}}{\partial t} + \left.\frac{\partial \tilde{h}_{n_L}^{B,L}}{\partial P^V}\right|_{T_{n_L}^{B,L}} \cdot \frac{\partial P^V}{\partial t} \right] = Y_{n_L} - K_{n_L} \cdot \tilde{h}_{n_L}^{B,L}$$

The variables Y_{n_L} and K_{n_L} depends on the flow distribution in the liquid, as it is described by the control volumes of Figure 36. The simplified form of the energy conservation laws of the liquid of Table 123 can be deduced from Equation 1120, by substituting the variables Y_{n_L} and K_{n_L} with the enthalpy flows and with convective flows of each case, respectively.

2. Mathematical steps of the descending flow equations

As said in Section 2.6, the equations of the first descending flow (FDF) and of core descending flow (CDF) can be deduced from the linear form of the conservation laws (Table 123) and from the temperature equations of the liquid (Equation 435, Equation 436 and Equation 437).

Section 2.1 and 2.2 describes the mathematical steps of the first descending flow (Equation 459) and of the core descending flow, respectively.

2.1.Mathematical steps of the first descending flow

The accumulation of mass in the bottom sub-layer can be described with linear form of the liquid mass conservation law (Equation 373), as function of the time-derivates of the ullage pressure ($\frac{\partial P^V}{\partial t}$), of the thickness of the sub-layer ($\frac{\partial dxL}{\partial t}$) and of the bulk temperature of the sub-layer ($\frac{\partial T_1^{B,L}}{\partial t}$). The time-derivate of the bulk temperature of the sub-layer can be computed with the first sub-layer liquid temperature evolution ($T^L{}_1$-e) equation (Equation 435). So, the time-derivate $\frac{\partial T_1^{B,L}}{\partial t}$ can be substituted with Equation 435 and the linear form of the liquid mass conservation law can be written as follows:

Equation 1121

$$B_1^{HL}\cdot\left(A^{''TL}_{1}\cdot\frac{\partial P^V}{\partial t}+C^{''TL}_{1}\cdot\frac{\partial dxL}{\partial t}+D^{''TL}_{1}\cdot\dot{m}_2^{D,L}+F^{''TL}_{1}+G^{''TL}_{1}\cdot\dot{m}_{IN}^{L}+H^{''TL}_{1}\cdot\dot{m}_{OUT}^{L}\right)+$$
$$A_1^{HL}\cdot\frac{\partial P^V}{\partial t}+C_1^{HL}\cdot\frac{\partial dxL}{\partial t}+D_1^{HL}\cdot\dot{m}_2^{D,L}+F_1^{HL}+G_1^{HL}\cdot\dot{m}_{IN}^{L}+H_1^{HL}\cdot\dot{m}_{OUT}^{L}=0$$

In Equation 1121, the variables $\frac{\partial P^V}{\partial t}$, $\frac{\partial dxL}{\partial t}$, $\dot{m}_2^{D,L}$, $\dot{m}_{IN}^{L}$ and $\dot{m}_{OUT}^{L}$ can be grouped and the linear form of the liquid mass conservation law can be written as follows:

Equation 1122

$$\left(B_1^{HL}\cdot A^{''TL}_{1}+A_1^{HL}\right)\cdot\frac{\partial P^V}{\partial t}+\left(B_1^{HL}\cdot C^{''TL}_{1}+C_1^{HL}\right)\cdot\frac{\partial dxL}{\partial t}$$
$$+\left(B_1^{HL}\cdot D^{''TL}_{1}+D_1^{HL}\right)\cdot\dot{m}_2^{D,L}+B_1^{HL}\cdot F^{''TL}_{1}+F_1^{HL}+\left(B_1^{HL}\cdot G^{''TL}_{1}+G_1^{HL}\right)\cdot\dot{m}_{IN}^{L}$$
$$+\left(B_1^{HL}\cdot H^{''TL}_{1}+H_1^{HL}\right)\cdot\dot{m}_{OUT}^{L}=0$$

Term $\left(B_1^{HL}\cdot D^{''TL}_{1}+D_1^{HL}\right)\cdot\dot{m}_2^{D,L}$ can be moved to the right part of Equation 373. Then, the equation obtained is divided by $-\left(B_1^{HL}\cdot D^{''TL}_{1}+D_1^{HL}\right)$. So, Equation 1121 can be written as follows:

Equation 1123

$$\dot{m}_2^{D,L}=-\frac{\left(B_1^{HL}\cdot A^{''TL}_{1}+A_1^{HL}\right)\cdot\frac{\partial P^V}{\partial t}+\left(B_1^{HL}\cdot C^{''TL}_{1}+C_1^{HL}\right)\cdot\frac{\partial dxL}{\partial t}}{\left(B_1^{HL}\cdot D^{''TL}_{1}+D_1^{HL}\right)}$$
$$-\frac{B_1^{HL}\cdot F^{''TL}_{1}+F_1^{HL}\cdot\dot{m}_{OUT}^{L}}{\left(B_1^{HL}\cdot D^{''TL}_{1}+D_1^{HL}\right)}-\frac{\left(B_1^{HL}\cdot G^{''TL}_{1}+G_1^{HL}\right)\cdot\dot{m}_{IN}^{L}+\left(B_1^{HL}\cdot H^{''TL}_{1}+H_1^{HL}\right)\cdot\dot{m}_{OUT}^{L}}{\left(B_1^{HL}\cdot D^{''TL}_{1}+D_1^{HL}\right)}$$

If the coefficients of Table 130 are used in Equation 1121, the equation of the first descending flow (FDF) equation (Equation 459) is obtained.

2.2.Mathematical steps of the core descending flow

The linear form of the conservation laws of mass of the core sub-layer (Equation 375) computes the accumulation of mass in the bulk of the core sub-layers as function of the of the time-derivates of the ullage pressure ($\frac{\partial P^V}{\partial t}$), of the thickness of the sub-layer ($\frac{\partial dxL}{\partial t}$) and of the bulk temperature of the sub-layer ($\frac{\partial T_{n_L}^{B,L}}{\partial t}$). this time-derivate can be computed with the core sub-layer liquid temperature evolution ($T^L{}_{nL}$-e) equation (Equation 436). So, Equation 375 can be written as follows:

Equation 1124

$$B_{n_L}^{HL}\cdot\left(A^{''TL}_{n_L}\cdot\frac{\partial P^V}{\partial t}+C^{''TL}_{n_L}\cdot\frac{\partial dxL}{\partial t}+D^{''TL}_{n_L}\cdot\dot{m}_{n_L+1}^{D,L}+E^{''TL}_{n_L}\cdot\dot{m}_{n_L}^{D,L}+F^{''TL}_{n_L}\right)+$$
$$A_{n_L}^{HL}\cdot\frac{\partial P^V}{\partial t}+C_{n_L}^{HL}\cdot\frac{\partial dxL}{\partial t}+D_{n_L}^{HL}\cdot\dot{m}_{n_L+1}^{D,L}+E_{n_L}^{HL}\cdot\dot{m}_{n_L}^{D,L}+F_{n_L}^{HL}=0$$

The variables $\frac{\partial P^V}{\partial t}$, $\frac{\partial dxL}{\partial t}$, $\dot{m}^{D,L}_{n_L+1}$ and $\dot{m}^{D,L}_{n_L}$ can be grouped and Equation 375 can be written as follows:

Equation 1125
$$\left(B^{HL}_{n_L}\cdot {A''}^{TL}_{n_L}+A^{HL}_{n_L}\right)\cdot\frac{\partial P^V}{\partial t}+\left(B^{HL}_{n_L}\cdot {C''}^{TL}_{n_L}+C^{HL}_{n_L}\right)\cdot\frac{\partial dxL}{\partial t}$$
$$+\left(B^{HL}_{n_L}\cdot {D''}^{TL}_{n_L}+D^{HL}_{n_L}\right)\cdot\dot{m}^{D,L}_{n_L+1}+\left(B^{HL}_{n_L}\cdot {E''}^{TL}_{n_L}+E^{HL}_{n_L}\right)\cdot\dot{m}^{D,L}_{n_L}+B^{HL}_{n_L}\cdot {F''}^{TL}_{n_L}+F^{HL}_{n_L}=0$$

The term $\left(B^{HL}_{n_L}\cdot {D''}^{TL}_{n_L}+D^{HL}_{n_L}\right)\cdot\dot{m}^{D,L}_{n_L+1}$ is moved to the left part of the Equation 1125. Then, the obtained equation is divided by $-\left(B^{HL}_{n_L}\cdot {D''}^{TL}_{n_L}+D^{HL}_{n_L}\right)$. Equation 1125 can be written as follows:

Equation 1126
$$\dot{m}^{D,L}_{n_L+1}=-\frac{\left(B^{HL}_{n_L}\cdot {A''}^{TL}_{n_L}+A^{HL}_{n_L}\right)\cdot\frac{\partial P^V}{\partial t}+\left(B^{HL}_{n_L}\cdot {C''}^{TL}_{n_L}+C^{HL}_{n_L}\right)\cdot\frac{\partial dxL}{\partial t}}{\left(B^{HL}_{n_L}\cdot {D''}^{TL}_{n_L}+D^{HL}_{n_L}\right)}$$
$$-\frac{\left(B^{HL}_{n_L}\cdot {E''}^{TL}_{n_L}+E^{HL}_{n_L}\right)\cdot\dot{m}^{D,L}_{n_L}+B^{HL}_{n_L}\cdot {F''}^{TL}_{n_L}+F^{HL}_{n_L}}{\left(B^{HL}_{n_L}\cdot {D''}^{TL}_{n_L}+D^{HL}_{n_L}\right)}$$

If the coefficients of Table 130 are used in Equation 1126 and in Equation 1121, the equation of the core descending flow (CDF) equation (Equation 460) is obtained.

3. Mathematical steps of the pressure-thickness equations

As it is indicated in Table 131, there are two pressure-thickness equations, respectively called vapour pressure-thickness equation and liquid pressure-thickness equation. Both equations can be deduced from the linear form of the conservation laws (Table 123).

Section 3.1 and 3.2 respectively describe the mathematical steps to obtain the vapour and the liquid pressure-thickness equations.

3.1.Mathematical steps of the vapour pressure-thickness equations

The linear form of the ullage energy conservation law (Equation 368) can compute the accumulation of the mass in the ullage. This equation is a function of the time-derivates of the pressure ($\frac{\partial P^V}{\partial t}$) and of the ullage temperature ($\frac{\partial T^V}{\partial t}$), which can be computed with the vapour temperature equation (Equation 438). So, the time-derivate $\frac{\partial T^V}{\partial t}$ can be substituted with Equation 438 and Equation 369 can be written as follows:

Equation 1127
$$B^P\cdot\left[A''^{TV}\cdot\frac{\partial P^V}{\partial t}+C''^{TV}\cdot\frac{\partial dxL}{\partial t}+D''^{TV}\cdot\dot{m}^V_{IN}+E''^{TL}\cdot\dot{m}_{BOG}+F''^{TV}\right]+$$
$$A^P\cdot\frac{\partial P^V}{\partial t}+C^P\cdot\frac{\partial dxL}{\partial t}+D^P\cdot\dot{m}^V_{IN}+E^P\cdot\dot{m}_{BOG}+F^P=0$$

The variables $\frac{\partial P^V}{\partial t}$, $\frac{\partial dxL}{\partial t}$, $\dot{m}^V_{IN}$, E''^{TL} and F''^{TV} can be grouped and Equation 1127 can be written as follows:

Equation 1128
$$\left(A^P+B^P\cdot A''^{TV}\right)\cdot\frac{\partial P^V}{\partial t}+\left(C^P+B^P\cdot C''^{TV}\right)\cdot\frac{\partial dxL}{\partial t}+\left(D^P+B^P\cdot D''^{TV}\right)\cdot\dot{m}^V_{IN}$$
$$+\left(E^P+B^P\cdot E''^{TL}\right)\cdot\dot{m}_{BOG}+F^P+B^P\cdot F''^{TV}=0$$

The vapour pressure-thickness equation (Equation 467) is obtained by using the coefficients of Table 132 into Equation 1128.

3.2. Mathematical steps of the liquid pressure-thickness equations

To deduce the descending flow equations of Table 129, the linear form of the mass conservation law of Table 124 are used from the bottom sub-layer to the sub-layer before the interface sub-layer. Hence, the linear form of the mass conservation law of the interface sub-layer (Equation 371) can be used to deduce the liquid pressure-thickness conservation equation (Equation 468). Equation 371 is composed by three variables: the time-derivate of the pressure ($\frac{\partial P^V}{\partial t}$), the time-derivate of the bulk liquid temperature of the interface sub-layer ($\frac{\partial T^{B,L}_{N^L}}{\partial t}$), the time-derivate of the thickness ($\frac{\partial dxL}{\partial t}$) and the descending flow at the interface sub-layer ($\dot{m}^{D,L}_{N^L}$). The time-derivate $\frac{\partial T^{B,L}_{N^L}}{\partial t}$ can be computed with the interface sub-layer temperature evolution equation (Equation 437). So, Equation 371 can be written as follows:

Equation 1129
$$B^{HL}_{N^L}\cdot\left[A''^{TL}_{N^L}\cdot\frac{\partial P^V}{\partial t}+C''^{TL}_{N^L}\cdot\frac{\partial dxL}{\partial t}+E''^{TL}_{N^L}\cdot\dot{m}^{D,L}_{N^L}+F''^{TL}_{N^L}\right]+$$
$$A^{HL}_{N^L}\cdot\frac{\partial P^V}{\partial t}+C^{HL}_{N^L}\cdot\frac{\partial dxL}{\partial t}+E^{HL}_{N^L}\cdot\dot{m}^{D,L}_{N^L}+F^{HL}_{N^L}=0$$

The variables $\frac{\partial P^V}{\partial t}$, $\frac{\partial dxL}{\partial t}$ and $\dot{m}^{D,L}_{N^L}$ can be grouped and Equation 1129 can be written as follows:

Equation 1130
$$\left(A^{HL}_{N^L}+A''^{TL}_{N^L}\cdot B^{HL}_{N^L}\right)\cdot\frac{\partial P^V}{\partial t}+\left(C^{HL}_{N^L}+C''^{TL}_{N^L}\cdot B^{HL}_{N^L}\right)\cdot\frac{\partial dxL}{\partial t}$$
$$+\left(F^{HL}_{N^L}+F''^{TL}_{N^L}\cdot B^{HL}_{N^L}\right)+\left(E^{HL}_{N^L}+E''^{TL}_{N^L}\cdot B^{HL}_{N^L}\right)\cdot\dot{m}^{D,L}_{N^L}=0$$

The coefficients of Table 132 ($A''^{HL}_{N^L}$, $C''^{HL}_{N^L}$, $E''^{HL}_{N^L}$ and $F''^{HL}_{N^L}$) can be used in Equation 1130 and the mass conservation laws of the interface sub-layer can be written as follows:

Equation 1131
$$A''^{HL}_{N^L}\cdot\frac{\partial P^V}{\partial t}+C''^{HL}_{N^L}\cdot\frac{\partial dxL}{\partial t}+E''^{HL}_{N^L}\cdot\dot{m}^{D,L}_{N^L}+F''^{HL}_{N^L}=0$$

In Equation 1131, the descending flow at the interface sub-layer ($\dot{m}^{D,L}_{N^L}$) can be computed with the core descending flow equation (Equation 460), applied at the sub-layer "N^L-1". So, the descending flow $\dot{m}^{D,L}_{N^L}$ depends on the descending flow $\dot{m}^{D,L}_{N^L-1}$, which can be computed with core descending flow equation (Equation 460), applied at the sub-layer "N^L-2". Hence, the descending flow $\dot{m}^{D,L}_{N^L}$ can be computed as follows:

Equation 1132
$$\dot{m}^{D}_{N^L}=\frac{\partial P^V}{\partial t}\cdot\left[\sum_{n_L=1}^{N^L-1}A''^{HL}_{n_L}\cdot\left(\prod_{j=n_L+1}^{N^L-1}E''^{HL}_{j}\right)\right]$$
$$+\frac{\partial dxL}{\partial t}\cdot\left[\sum_{n_L=1}^{N^L-1}C''^{HL}_{n_L}\cdot\left(\prod_{j=n_L+1}^{N^L-1}E''^{HL}_{j}\right)\right]+\left[\sum_{n_L=1}^{N^L-1}F''^{HL}_{n_L}\cdot\left(\prod_{j=n_L+1}^{N^L-1}E''^{HL}_{j}\right)\right]$$
$$+\left(\prod_{n_L=2}^{N^L}E''^{HL}_{n_L}\right)\cdot G''^{HL}_{1}\cdot\dot{m}^{L}_{IN}+\left(\prod_{n_L=2}^{N^L}E''^{HL}_{n_L}\right)\cdot H^{HL}_{1}\cdot\dot{m}^{L}_{OUT}$$

So, Equation 1131 can be written as follows:

Equation 1133
$$A''^{HL}_{N^L}\cdot\frac{\partial P^V}{\partial t}+C''^{HL}_{N^L}\cdot\frac{\partial dxL}{\partial t}+F''^{HL}_{N^L}$$

$$+E''^{HL}_{N^L}\cdot\left\{\frac{\partial P^V}{\partial t}\cdot\left[\sum_{n_L=1}^{N^L-1}A''^{HL}_{n_L}\cdot\left(\prod_{j=n_L+1}^{N^L-1}E''^{HL}_{j}\right)\right]+\frac{\partial dxL}{\partial t}\cdot\left[\sum_{n_L=1}^{N^L-1}C''^{HL}_{n_L}\cdot\left(\prod_{j=n_L+1}^{N^L-1}E''^{HL}_{j}\right)\right]\right.$$
$$+\left[\sum_{n_L=1}^{N^L-1}F''^{HL}_{n_L}\cdot\left(\prod_{j=n_L+1}^{N^L-1}E''^{HL}_{j}\right)\right]+\left(\prod_{n_L=2}^{N^L}E''^{HL}_{n_L}\right)\cdot G''^{HL}_{1}\cdot\dot{m}^L_{IN}+\left(\prod_{n_L=2}^{N^L}E''^{HL}_{n_L}\right)$$
$$\left.\cdot H^{HL}_1\cdot\dot{m}^L_{OUT}\right\}=0$$

The variables $\frac{\partial P^V}{\partial t}$ and $\frac{\partial dxL}{\partial t}$ can be grouped in Equation 1133 and Equation 1133 can be written as follows:

Equation 1134

$$\left\{A''^{HL}_{N^L}+E''^{HL}_{N^L}\cdot\left[\sum_{n_L=1}^{N^L-1}A''^{HL}_{n_L}\cdot\left(\prod_{j=n_L+1}^{N^L-1}E''^{HL}_{j}\right)\right]\right\}\cdot\frac{\partial P^V}{\partial t}+$$
$$\left\{C''^{HL}_{N^L}+E''^{HL}_{N^L}\cdot\left[\sum_{n_L=1}^{N^L-1}C''^{HL}_{n_L}\cdot\left(\prod_{j=n_L+1}^{N^L-1}E''^{HL}_{j}\right)\right]\right\}\cdot\frac{\partial dxL}{\partial t}+$$
$$F''^{HL}_{N^L}+E''^{HL}_{N^L}\cdot\left[\sum_{n_L=1}^{N^L-1}F''^{HL}_{n_L}\cdot\left(\prod_{j=n_L+1}^{N^L-1}E''^{HL}_{j}\right)\right]+$$
$$E''^{HL}_{N^L}\cdot\left\{\left(\prod_{n_L=2}^{N^L}E''^{HL}_{n_L}\right)\cdot G''^{HL}_{1}\cdot\dot{m}^L_{IN}+\left(\prod_{n_L=2}^{N^L}E''^{HL}_{n_L}\right)\cdot H^{HL}_1\cdot\dot{m}^L_{OUT}\right\}=0$$

The coefficients of Table 132 (A''^{HL}, C''^{HL}, F''^{HL}, G''^{HL} and H''^{HL}) can be sued in Equation 1134 and the liquid pressure-thickness equation (Equation 468) is obtained.

4. Mathematical steps of the pressure-evolution, thickness-evolution, inlet liquid flow and boil-off gas equations

As it is reported in Table 133, the pressure-evolution (P-e), the thickness-evolution (dxL-e), the inlet liquid flow (ILF) and boil-off gas (BOG) equations of the self-pressurisation are different from the one used for the steady state, even if these equations are deduced from the pressure-thickness equations (Table 131). In the steady state, the pressure and the liquid volume are fixed and the time derivate of these variables are equal to zero. So, the pressure-thickness equations (Table 131) can be used to deduce the ILF and the BOG equations. In the self-pressurisation (mode 4), the inlet liquid and the BOG flows ($\dot{m}^L_{IN}$ and $\dot{m}_{BOG}$) are equal to zero because the storage container is close and the pressure-thickness equations (Table 131) can be used to deduce the P-e and the dxL-e equations.

Section 4.1, 4.2, 4.3 and 4.4 respectively explain the mathematical steps to deduce the BOG equation at the steady state (Equation 485), the ILF equation (Equation 490) at steady state, the dxL-e equation (Equation 488) during the self-pressurisation and the P-e equation (Equation 483) during the self-pressurisation.

4.1.Boil-off gas equation at steady state

The vapour-thickness equation (Equation 467) is a function of the time-derivate of the ullage pressure ($\frac{\partial P^V}{\partial t}$), of the time-derivate of the thickness ($\frac{\partial dxL}{\partial t}$), of the inlet vapour flow ($\dot{m}^V_{IN}$) and of the boil-off gas ($\dot{m}_{BOG}$). The variable $E''^P\cdot\dot{m}_{BOG}$ of Equation 467 can be moved to the right part and Equation 467 can be written as follows:

Equation 1135
$$A^{\prime\prime P} \cdot \frac{\partial P^{V}}{\partial t} + C^{\prime\prime P} \cdot \frac{\partial dxL}{\partial t} + D^{\prime\prime P} \cdot \dot{m}_{IN}^{V} + F^{\prime\prime P} = -E^{\prime\prime P} \cdot \dot{m}_{BOG}$$

If the left and the right part of Equation 1135 are divided by "$-E^{\prime\prime P}$", the boil-off gas (BOG) equation (Equation 485) is obtained.

4.2. Inlet liquid flow equation at steady state

The liquid pressure-thickness equation (Equation 468) depends on the time-derivate of the ullage pressure ($\frac{\partial P^{V}}{\partial t}$), on the time-derivate of the thickness ($\frac{\partial dxL}{\partial t}$), and on the inlet and outlet liquid flows ($\dot{m}_{IN}^{L}$ and $\dot{m}_{OUT}^{L}$). The variable $G^{\prime\prime HL} \cdot \dot{m}_{IN}^{L}$ of Equation 468 can be moved to the right part and Equation 468 can be written as follows:

Equation 1136
$$A^{\prime\prime HL} \cdot \frac{\partial P^{V}}{\partial t} + C^{\prime\prime HL} \cdot \frac{\partial dxL}{\partial t} + F^{\prime\prime HL} + H^{\prime\prime HL} \cdot \dot{m}_{OUT}^{L} = -G^{\prime\prime HL} \cdot \dot{m}_{IN}^{L}$$

If the left and the right parts of Equation 1136 are divided by "$-G^{\prime\prime HL}$", the inlet liquid flow (ILF) equation (Equation 490) is obtained.

4.3. Thickness-evolution equations during the self-pressurisation

The liquid pressure-thickness equation (Equation 468) is a function of the time-derivate of the ullage pressure ($\frac{\partial P^{V}}{\partial t}$), of the time-derivate of the thickness ($\frac{\partial dxL}{\partial t}$), and of the inlet and outlet liquid flows ($\dot{m}_{IN}^{L}$ and $\dot{m}_{OUT}^{L}$). The variable $\frac{\partial dxL}{\partial t} \cdot C^{\prime\prime HL}$ can be moved to the right part of Equation 468, which can be written as follows:

Equation 1137
$$A^{\prime\prime HL} \cdot \frac{\partial P^{V}}{\partial t} + F^{\prime\prime HL} + G^{\prime\prime HL} \cdot \dot{m}_{IN}^{L} + H^{\prime\prime HL} \cdot \dot{m}_{OUT}^{L} = -\frac{\partial dxL}{\partial t} \cdot C^{\prime\prime HL}$$

If the right and the left part of Equation 1137 are divided by "$-C^{\prime\prime HL}$", the thickness-evolution (dxL-e) equation (Equation 488) is obtained.

4.4. Pressure-evolution equations during the self-pressurisation

The vapour-thickness equation (Equation 467) is a function of the time-derivate of the ullage pressure ($\frac{\partial P^{V}}{\partial t}$), of the time-derivate of the thickness ($\frac{\partial dxL}{\partial t}$), of the inlet vapour flow ($\dot{m}_{IN}^{V}$) and of the boil-off gas ($\dot{m}_{BOG}$). The time-derivate $\frac{\partial dxL}{\partial t}$ can be computed with the thickness-evolution (dxL-e) equation (Equation 488). So, the vapour-thickness equation can be written as follows:

Equation 1138
$$\begin{gathered} A^{\prime\prime P} \cdot \frac{\partial P^{V}}{\partial t} + D^{\prime\prime P} \cdot \dot{m}_{IN}^{V} + E^{\prime\prime P} \cdot \dot{m}_{BOG} + F^{\prime\prime P} \\ -\frac{C^{\prime\prime P}}{C^{\prime\prime HL}} \cdot \left[A^{\prime\prime HL} \cdot \frac{\partial P^{V}}{\partial t} + F^{\prime\prime HL} + G^{\prime\prime HL} \cdot \dot{m}_{IN}^{L} + H^{\prime\prime HL} \cdot \dot{m}_{OUT}^{L} \right] = 0 \end{gathered}$$

The time derivate $\frac{\partial P^{V}}{\partial t}$ is grouped in Equation 1138 and Equation 1138 can be written as follows:

Equation 1139
$$\begin{gathered} \left(A^{\prime\prime P} - \frac{C^{\prime\prime P}}{C^{\prime\prime HL}} \cdot A^{\prime\prime HL} \right) \cdot \frac{\partial P^{V}}{\partial t} + D^{\prime\prime P} \cdot \dot{m}_{IN}^{V} + E^{\prime\prime P} \cdot \dot{m}_{BOG} + F^{\prime\prime P} + \\ \frac{C^{\prime\prime P}}{C^{\prime\prime HL}} \cdot [F^{\prime\prime HL} + G^{\prime\prime HL} \cdot \dot{m}_{IN}^{L} + H^{\prime\prime HL} \cdot \dot{m}_{OUT}^{L}] = 0 \end{gathered}$$

The variable $\left(A''^{P} - \frac{C''^{P}}{C''^{HL}} \cdot A''^{HL}\right) \cdot \frac{\partial P^{V}}{\partial t}$ is moved to the right part of Equation 1139 and Equation 1139 can be written as follows:

Equation 1140

$$\frac{C''^{P}}{C''^{HL}} \cdot [F''^{HL} + G''^{HL} \cdot \dot{m}_{IN}^{L} + H''^{HL} \cdot \dot{m}_{OUT}^{L}] + \\ D''^{P} \cdot \dot{m}_{IN}^{V} + E''^{P} \cdot \dot{m}_{BOG} + F''^{P} = -\left(A''^{P} - \frac{C''^{P}}{C''^{HL}} \cdot A''^{HL}\right) \cdot \frac{\partial P^{V}}{\partial t}$$

The left and the right part of Equation 1140 are divided by "$-\left(A''^{P} - \frac{C''^{P}}{C''^{HL}} \cdot A''^{HL}\right)$" and the pressure-evolution (P-e) equation (Equation 483) is obtained.

Appendix AD

Algorithm to compute the direction of the descending flows

As it is explained in Section 3 of Chapter 6, the direction and the values of the descending flows have to be computed with an iterative procedure because the coefficients of the descending flow (Table 130) are computed with the direction of these flows. The input and the output of this procedure are reported in Table 270.

Table 270. Input and output of the algoritm to compute the direction of the descending flows.

Variable	Description
Input	The coefficients $A^{HL}_{n_L}$, $B^{HL}_{n_L}$ and $C^{HL}_{n_L}$ of Table 42, the values of the mass flow exchanged between the boundary layer and the bulk ($\dot{m}^{BL}_{n_L}$) and the values of the rising flow of the bottom ($\dot{m}^{B}_{n_L}$ and $\dot{m}^{B}_{n_L-1}$).
Output	The direction of the descending mass flows.

The structure of this iterative procedure is described in Figure 232.

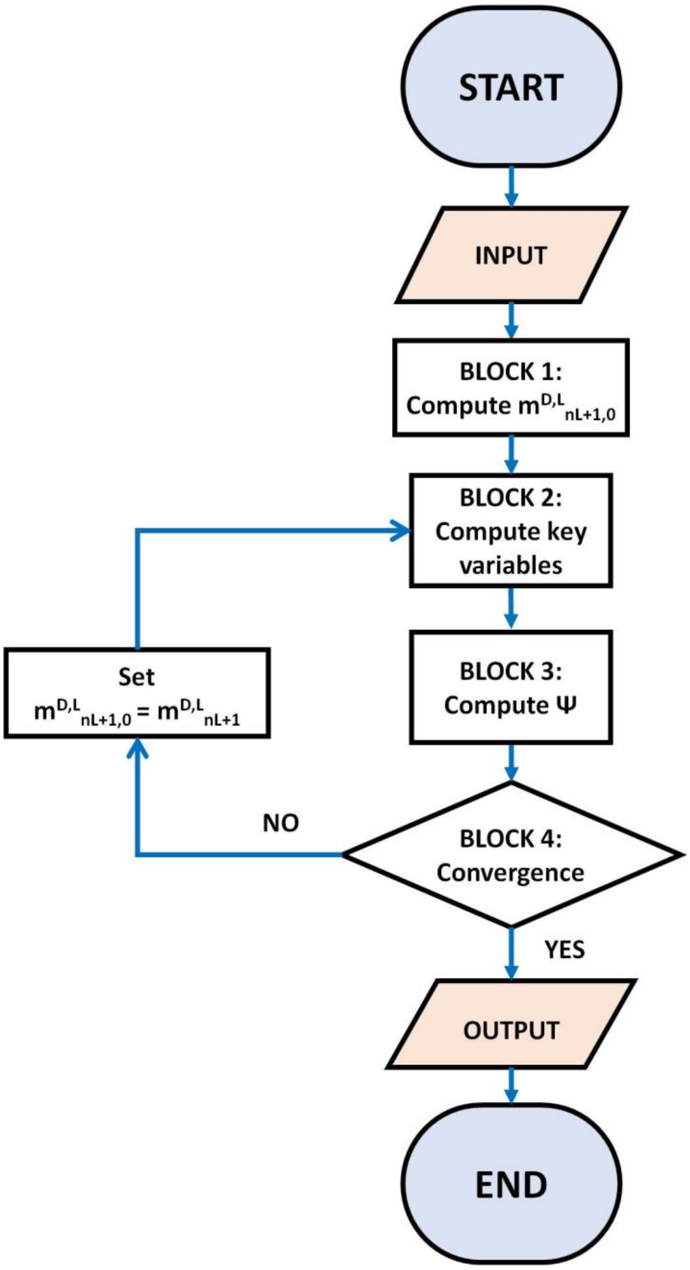

Figure 232. Structure of the algorithm of the direction of the descending flow.

The algoritmh is composed by the following steps:

a) BLOCK 1. The first guess values of the descending flows are computed with the equations of Table 136. If the value is positive, the direction is downward. If the value is negative, the direction is upward;
b) BLOCK 2. The indipendent variables are computed with the equations of Table 118. If the value of the descending flows is positive, the direction is downward and, if it is the negative, the direction is upward.
c) BLOCK 3. The variable Ψ is computed as follows:

Equation 1141
$$\Psi = \sum_{n_L=2}^{N^L} F_{n_L}$$

$F_{n_L}$is computed with the equations of Table 271.

Table 271. Equations to compute $\boldsymbol{F_{n_L}}$.

Equation	Formula	Condition
Equation 1142	$F_{n_L} = 1$	$\dot{m}_{n_L+1,0}^{D,L} \cdot \dot{m}_{n_L+1,2}^{D,L} < 0$
Equation 1143	$F_{n_L} = 0$	$\dot{m}_{n_L+1,0}^{D,L} \cdot \dot{m}_{n_L+1,2}^{D,L} \geq 0$

$\dot{m}_{n_L+1,0}^{D,L}$ and $\dot{m}_{n_L+1,2}^{D,L}$ are first guess value and the values of Block 2 of the descending flow, respectively. The condition of Equation 1142 indicates that the direction of $\dot{m}_{n_L+1,0}^{D,L}$ is equal to the direction of $\dot{m}_{n_L+1,2}^{D,L}$ because they have the same sign. The condition of Equation 1143 points out that the direction of $\dot{m}_{n_L+1,0}^{D,L}$ is not equal to the direction of $\dot{m}_{n_L+1,2}^{D,L}$ because they have not the same sign.

d) BLOCK 4. The convergence criterion is defined as follows:

Equation 1144
$$\Psi \geq 0$$

So, two pathways are present:
- Pathway 1.4 (P 1.4): Equation 1144 is true and the algorithm stops;
- Pathway 2.4 (P 2.4): Equation 1144 is false, indicating the direction of the descending flow changed from the ones of Block 1 (step a) of Appendix AD) to the ones of Block 2 (step b) of Appendix AD), at least in one sub-layer. So, the first guess value of the descending flow is equal to the value of the descending flow computed at Block 2 (step b) of Appendix AD). The algorithm re-starts at Block 2 (step b) of Appendix AD)

This algortimh usually converges in less than 3 iterations because the first guess value of the directions of the descending flow are close to the final values.

Appendix AE

Algorithm to compute the wet side wall-to-liquid heat flows

As it is described in Section 3.2.1 of Chapter 6, the calculation of the wet side wall-to-liquid heat flows ($\dot{Q}_{w,n_L}^{SL}$) and the temperatures of the sub-layer of the wet side wall (T_{w,n_L}^{SL}) can be done with an iterative procedure because the heat transfer coefficient (h_{w,n_L}^{SL}) depends on these heat flows. As it is indicated by the energy conservation laws at the wet side wall (Table 139), the input and the output of this iterative procedure are the ones reported in Table 272.

Table 272. Input and output of the algorithm that computes $\dot{\boldsymbol{Q}}_{\boldsymbol{w,n_L}}^{\boldsymbol{SL}}$.

Variable	Description
Input	Effective heat transfer coefficient (h_{eff}), surface are of the side wall of the sub-layer (A_{w,n_L}^{SL}), thermo-physical properties, dry side wall-to-interface heat flow ($\dot{Q}_W^{LV}$), the bulk temperature of the liquid sub-layer ($T_{n_L}^{SBL}$), bulk temperature gradient of the liquid, the number of iteration (N_I) and the values of the relative and absolute tolerance (ε_1 and ε_2).
Output	Heat flow $\dot{Q}_{w,n_L}^{SL}$, heat transfer coefficients h_{w,n_L}^{SL} and temperatures T_{w,n_L}^{SL}

The values of the relative and absolute tolerances are respectively 10^{-5} and 10^{-10}. The number of iteration is 100. Considering the energy conservation laws at the wet side wall of Table 139, the objective function of this iterative procedure can de described by the ones of Table 273. In Table 273, the objective variables of this iterative procedure are reported.

Table 273. Objective function and variable of the algorithm that computes $\dot{\boldsymbol{Q}}_{\boldsymbol{w,n_L}}^{\boldsymbol{SL}}$.

Objective variables	Equation	Formulas
$\dot{Q}_{w,N^L}^{SL}$	Equation 1145	$f_{w,N^L}^{SL} = h_{eff} \cdot A_{N^L}^{SL} \cdot \left(T^W - T_{w,N^L}^{SL}\right) + \dot{Q}_W^{LV} - A_{N^L}^{SL} \cdot h_{w,N^L}^{SL} \cdot (T_{w,N^L}^{SL} - T_{N^L}^{SBL})$
$\dot{Q}_{w,n_L}^{SL}$	Equation 1146	$f_{w,n_L}^{SL} = h_{eff} \cdot A_{n_L}^{SL} \cdot \left(T^W - T_{w,n_L}^{SL}\right) - A_{n_L}^{SL} \cdot h_{w,n_L}^{SL} \cdot (T_{w,n_L}^{SL} - T_{n_L}^{SBL})$

The temperature T_{w,n_L}^{SL} and T_{w,N^L}^{SL} are calculated with Equation 533. As it is indicated by the equations of Table 273, the method of Netwon-Rhapson with finite difference approach (see Section 2 of Appendix I) can be used to compute the objective variables. For this type of numerical method, the first guess values of the heat flows of the wet side wall and the maximum values of these variables are required to stabilize the numerical procedure. The heat transfer properties of the liquid are high and the temperature of the wet side wall is almost equal to the temperature of the liquid. So, the first guess value of the objective variables can be computed with the equations of Table 274.

Table 274. First guess value of the objectives variables of the algorithm that computes $\dot{\boldsymbol{Q}}_{\boldsymbol{w,n_L}}^{\boldsymbol{SL}}$.

Equation	Formula
Equation 1147	$\dot{Q}_{w,N^L}^{SL,0} = h_{eff} \cdot A_{N^L}^{SL} \cdot \left(T^W - T_{N^L}^{SBL}\right) + \dot{Q}_W^{LV}$
Equation 1148	$\dot{Q}_{w,n_L}^{SL,0} = h_{eff} \cdot A_{n_L}^{SL} \cdot \left(T^W - T_{n_L}^{SBL}\right)$

In the wet side wall, the heat enters from the environment and from the dry side wall. As consequence, the maximum value of the wet side wall-to-liquid heat flow can be computed as follows:

$$\text{Equation 1149} \qquad \dot{Q}_{w,n_L}^{SL,MAX} = h_{eff} \cdot A_{n_L}^{SL} \cdot \left(T^W - T_{n_L}^{SBL}\right) + \dot{Q}_W^{LV}$$

Equation 1149 is applied to all the sub-layers of the wet side wall. The method of Netwon-Rhapson with finite difference approach requires the values of the intermediate variables to compute the derivate of the objective function. These variables are computed with the equations of Table 275.

Table 275. Equations to compute the intermediate variables of the algorithm that computes $\dot{\boldsymbol{Q}}_{\boldsymbol{w,n_L}}^{\boldsymbol{SL}}$.

Equation	Formula

Table 275. Equations to compute the intermediate variables of the algorithm that computes $\boldsymbol{\dot{Q}_{w,n_L}^{SL}}$.

Equation 1150	$\dot{Q}_{w,n_L}^{SL,1} = 0.999 \cdot \dot{Q}_{w,n_L}^{SL,0}$
Equation 1151	$\dot{Q}_{w,n_L}^{SL,2} = 1.001 \cdot \dot{Q}_{w,n_L}^{SL,0}$

The equations of Table 275 are used for all the sub-layers of the wet side wall.

The structure of the algorithm of the wet side wall-to-liquid heat transfer of LS model is described in Figure 233.

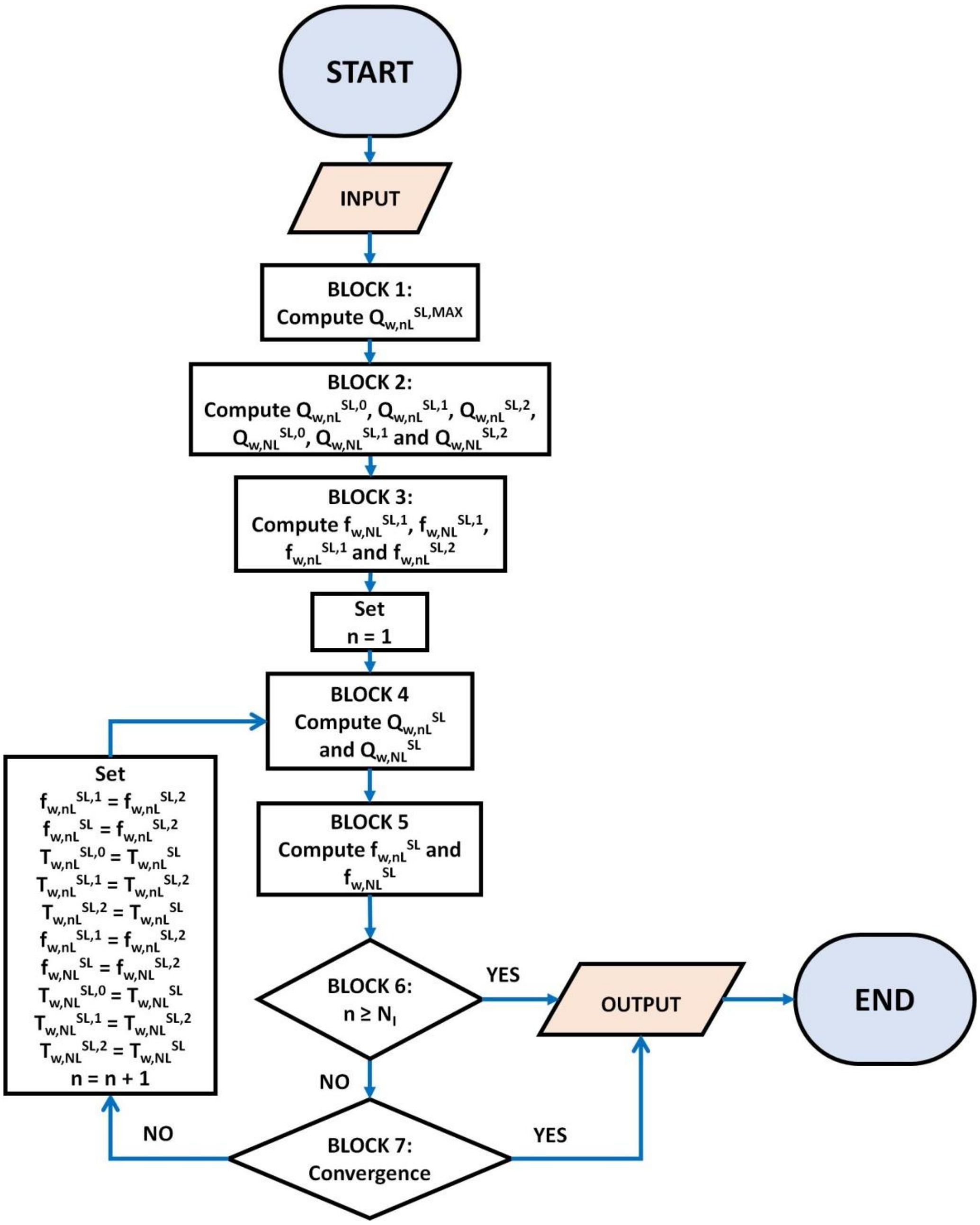

Figure 233. Algorithm of the model of the wet side wall heat transfer.

The mathematical steps of this algorithm are the following:

a) BLOCK 1. The maximum values of the objective variable are computed with Equation 1149 for all the sub-layers of the wet side wall;

b) BLOCK 2. The first guess values of the objective variables are calculated with the equations of Table 274. The values of the intermediate variables are computed with the equations of Table 275 for all the sub-layers of the wet side wall.

c) BLOCK 3. The values of the objective functions are computed with the values of the intermediate variables using the equations of Table 273. The current number of the iteration (n) is equal to 1.

d) BLOCK 4. The wet side wall-to-liquid heat flow is computed as follows:

Equation 1152
$$\dot{Q}_{w,n_L}^{SL} = \dot{Q}_{w,n_L}^{SL,1} - f_{w,n_L}^{SL,1} \cdot \frac{\dot{Q}_{w,n_L}^{SL,2} - \dot{Q}_{w,n_L}^{SL,1}}{f_{w,n_L}^{SL,2} - f_{w,n_L}^{SL,1}}$$

Equation 1152 is applied for all the sub-layer of the wet side wall.

e) BLOCK 5. The values of the objective function are computed with the values of the wet side wall-to-liquid heat flows of BLOCK 4 (step d) of Appendix AE), using the equations of Table 273;

f) BLOCK 6. Two pathways exist as function of the current number of iteration:
    - Pathway 1.6 (P 1.6): If the current number of iteration is lower than the maximum number of iteration, the mathematical procedure goes to BLOCK 7 (step g) of Appendix AE);
    - Pathway 2.6 (P 2.6): If the current number of iteration is higher or equal to the maximum number of iteration, the mathematical procedure stops;

g) BLOCK 7. The convergence criteria are defined by Equation 1153 and by Equation 1154 for all the sub-layers of the wet side wall.

Equation 1153
$$\left|f_{w,n_L}^{SL}\right| \leq \varepsilon_1$$

Equation 1154
$$\left|\dot{Q}_{w,n_L}^{SL,0} - \dot{Q}_{w,n_L}^{SL}\right| \leq \left|\dot{Q}_{w,n_L}^{SL,0} \cdot \varepsilon_2\right|$$

Two pathways are present:

- Pathway 1.7 (P 1.7): Equation 1153 and Equation 1154 are true for all the sub-layers of the et side wall;
- Pathway 2.7 (P 2.7): the convergence criteria are not respected for at least one of the sub-layer. $\dot{Q}_{w,n_L}^{SL,0}$, $\dot{Q}_{w,n_L}^{SL,1}$ and $\dot{Q}_{w,n_L}^{SL,2}$ are respectively equals to $\dot{Q}_{w,n_L}^{SL}$, $\dot{Q}_{w,n_L}^{SL,2}$ and $\dot{Q}_{w,n_L}^{SL}$. $f_{w,n_L}^{SL,1}$ and $f_{w,n_L}^{SL,2}$ are respectively equals to $f_{w,n_L}^{SL,2}$ and f_{w,n_L}^{SL}. The algorithm starts at Block 4 (step d) of Appendix AE);

This algorithm usually converges within the 10 iterations. The computational time of this algorithm is high because (i) the numerical integration algorithm of the storage Boundary Layer (see Section 2 of Appendix P) is executed for computing the heat transfer coefficient with the boundary layer approach (see Section 4.6 of Chapter 4) and (ii) because of the discretisation of the wet side wall, which increases the number of variables and iterations.

Bibliography

[1] G. C. Vliet, J. J. Brogan, T. S. Sheppard, F. H. Morse, et F. L. Hines, « Stratified Layer Flow Model - A Numerical Approach to Temperature Stratification in Liquids Contained in Heated Vessels », Aerospace Sciences Meeting, New York, p. 1-12, 1964.

[2] M. J. Daigle, V. N. Smelyanskiy, J. Boschee, et M. Foygel, « Temperature Stratification in a Cryogenic Fuel Tank », Journal of Thermopysics and Heat Transfer, p. 116-126, 2013.

[3] S. Z. S. Al Ghafri et al., « Advanced boil-off gas studies of liquefied natural gas used for the space and energy industries », Acta Astronautica, 2022.

[4] R. Rohde, « Global Temperature Report for 2020 », Berkely Earth. [En ligne]. Disponible sur: http://berkeleyearth.org/global-temperature-report-for-2020/

[5] The Core Writing Team, R. K. Pachauri, et L. Meyer, « Climate Change 2014 - Synthesis Report ». International Panel on Climate Change, 2015.

[6] O. Edenhofer et al., « Climate Change 2014 Mitigation of Climate Change - Working Group III Contribution to the Fifth Assessment Report of the Intergovernmental Panel on Climate Change ». Cambridge University Press, 2014.

[7] « Bio-LNG in transport: Making climate neutrality a reality », European Bio gas, 2020. [En ligne]. Disponible sur: https://www.europeanbiogas.eu/wp-content/uploads/2020/11/BioLNG-in-Transport_Making-Climate-Neutrality-a-Reality.pdf

[8] National Institute of Standard and Technology, REFPROP.

[9] « Natural gas Fuel Basics ». U.S. Departement of Energy. Consulté le: 18 avril 2023. [En ligne]. Disponible sur: https://afdc.energy.gov/fuels/natural_gas_basics.html

[10] US Departement of Energy Efficiency & Renewable energy, « Hydrogen Storage », Washington, D C. Consulté le: 30 novembre 2022. [En ligne]. Disponible sur: https://www.energy.gov/eere/fuelcells/hydrogen-storage

[11] H. Roussel, « Ukraine : deux autres méthaniers avec du gaz russe attendus au terminal de Montoir-de-Bretagne », France bleu. Consulté le: 23 octobre 2023. [En ligne]. Disponible sur: https://www.francebleu.fr/infos/economie-social/ukraine-deux-autres-methaniers-avec-du-gaz-russe-attendus-au-terminal-de-montoir-de-bretagne-1646684482

[12] A. Swanger, « World's Largest Liquid Hydrogen Tank Nears Completion ». Cryogenic Society of America, 6 mai 2022. Consulté le: 1 décembre 2022. [En ligne]. Disponible sur: https://www.cryogenicsociety.org/index.php?option=com_dailyplanetblog&view=entry&year=2022&month=05&day=05&id=48:world-s-largest-liquid-hydrogen-tank-nears-completion

[13] « Le biométhane liquéfié comme énergie : une première pour l'industrie », Engie. Consulté le: 23 octobre 2023. [En ligne]. Disponible sur: https://www.engie.fr/actualites/biomethane-liquefie-premiere-industrie/

[14] « LNG Tüp Sistemleri », Keyes Engineering. Consulté le: 23 octobre 2023. [En ligne]. Disponible sur: http://www.keyesengineering.com/tr/lng-tup-sistemleri

[15] S. Mokhatab, J. Y. Mak, J. V. Valappil, et D. A. Wood, Handbook of Liquefied Natural Gas. Oxford: Gulf Professional Publishing, 2014.

[16] « Private communication ».

[17] S. Kamiya, M. Nishimura, et E. Harada, « Study on Introduction of CO2Free Energy to Japan with Liquid Hydrogen », Physics Procedia, p. 11-19, 2015.

[18] T. Fuji et H. Imura, « Natural Convection Heat Transfer From a Plate with Arbitrary Inclination », International Journal of Heat Mass Transfer, p. 755-767, 1972.

[19] A. H. Persad et C. A. Ward, « Expressions for the Evaporation and Condensation Coefficients in the Hertz-Knudsen Relation », Chemical Review, p. 7727−7767, 2016.

[20] C. Beduz et R. G. Scurlock, « Evaporation Mechanism and Instability in Cryogenic Liquis », Advances in Cryogenic Engineering, New York, p. 1749-1757, 1994.

[21] C. Beduz, R. Rebiai, et R. G. Scurlock, « Thermal Overfill and the Surface Vaporisation of Cryogenic Liquids Under Storage Conditions. », Advances in Cryogenic Engineering, Boston, p. 795-803, 1984.

[22] M. C. M. Atkinson-Barr, « Studies by Experimental Simulation of Rollover and Surface Vaporisation of Cryogens », University of Southampton, Institute of Cryogenics, Southampton, 1989.

[23] V. V. Osipov et C. B. Muratov, « Dynamic condensation blocking in cryogenic refueling », Applied Physics Letters, 2008.

[24] M. Seo et S. Jeong, « Analysis of self-pressurization phenomenon of cryogenic fluid storage tank with thermal diffusion model », Cryogenics, vol. 50, nº 9, Art. nº 9, sept. 2010, doi: 10.1016/j.cryogenics.2010.02.021.

[25] M. Kang, J. Kim, H. You, et D. Chang, « Experimental investigation of thermal stratification in cryogenic tanks », Exp. Therm. Fluid Sci., vol. 96, p. 371-382, sept. 2018, doi: 10.1016/j.expthermflusci.2017.12.017.

[26] F. Perez et al., « Measurements of boil-off gas and stratification in cryogenic liquid nitrogen with implications for the storage and transport of liquefied natural gas », p. 1-13, 2021.

[27] M. Hasan M., C. Lin S., et N. Van Dresar T., « Self-Pressurization of a Flightweight Liquid Hydrogen Storage Tank Subjected to Low Heat Flux », NASA, Technical Memorandum 103804, 1991.

[28] N. Van Dresar T., C. Lin S., et M. Hasan M., « Self-Pressurization of a Flightweight Liquid Hydrogen Tank: Effects of Fill Level at Low Wall Heat Flux », NASA, Technical Memorandum 105411, 1992.

[29] J. C. Aydelott, « Normal Gravity Self-Pressurization of 9-Inch-(23 cm) Diameter Spherical Liquid Hydrogen tank », National Aeronautics and Space Administration, Lewis Research Center, Cleveland, Ohio, Technical Note NASA TN D-4171, 1967.

[30] J. C. Aydelott et C. M. Spuckler, « Effect of size on normal-gravity self-pressurisation of spherical liquid hydrogen tankage », National Aeronautics and Space Administration, Lewis Research Center, Cleveland, Ohio, Technical Note NASA TN D-5196, 1969.

[31] B. H. Anderson et M. J. Kolar, « Experimental Investigation of the Behaviour of a Confined Fluid subjected to nonuniform source and wall heating », National Aeronautics and Space Administration, Lewis Research Center, Cleveland, Ohio, D-2079, nov. 1963.

[32] R. G. Schwind et G. C. Vliet, « Observation and Interpretations of Natural Convection and Stratification in Vessels », Proceedings of the 1964 Heat Transfer and Fluid Mechanics Institute W. H. Giedt and S. Levy, eds., Stanford University Press, p. 51-68, 1964.

[33] E. R. F. Winter et R. J. Schoenhals, « Analytical and Experimental Studies of Thermal Stratification Phenomena », Purdue University, Indiana, Final report 5, 1972.

[34] S. Z. S. Al Ghafri et al., « Advanced boil-off gas studies for liquefied natural gas », Applied Thermal Engineering, p. 1-13, 2021.

[35] M. S. Islam et R. G. Scurlock, « Qualitative details of the complex flow in cryogenic vapour columns », Cryogenics, p. 655-660, 1977.

[36] J. Boardman, « Heat Transfer in Cryogenic Vapour Columns », University of Southampton, Institute of Cryogenics, 1974.

[37] G. Beresford, « Laser Droplet Velocity in cryogenic vapour columns », University of Southampton, Institute of Cryogenics, 1984.

[38] G. G. Dimopolous et C. A. Frangopoulos, « A Dynamic Model for Liquefied Natural Gas Evaporation During Marine Transportation », International Journal of Thermodynamics, p. 123-131, 2008.

[39] A. A. Wordu et B. Peterside, « Estimation of Boil-off-Gas BOG from Refrigerated Vessels in Liquefied Natural Gas Plant », International Journal of Engineering and Technology, p. 44-49, 2013.

[40] M. Miana, R. del Hoyo, V. Rodrigálvarez, J. R. Valdés, et R. Llorens, « Calculation models for prediction of Liquefied Natural Gas (LNG) ageing during ship transportation », Applied Energy, p. 1687-1700, 2010.

[41] M. Miana, V. Rodrigálvarez, et R. del Hoyo Alonso, « Comparison of evaporation rate and heat flow models for prediction of Liquefied Natural Gas (LNG) ageing during ship transportation », Fuel, mars 2016. [En ligne]. Disponible sur: DOI: 10.1016/j.fuel.2016.02.070

[42] J. M. Shah et J. J. Aarts, « Effect of Weathering of LNG in storage tanks », Advances in Cryogenic Engineering, p. 253-260, 1995.

[43] C. Migliore, C. Tubilleja, et V. Vesovic, « Weathering prediction model for stored liquefied natural gas (LNG) », Journal of Natural Gas Science and Engineering, p. 570-580, 2015.

[44] C. M. Cappello, « Modelling the weathering process of stored liquefied natural gas (LNG) », Imperial College of London, Department of Earth Science and Engineering, London, 2016.

[45] L. A. Pellegrini, S. Moioli, F. Brignoli, et C. Bellini, « LNG Technology: The Weathering in Above-Ground Storage Tanks », Industrial & engineering Chemistry Research, p. 3931−3937, 2014.

[46] C. Migliore, A. Salehi, et V. Vesovic, « A non-equilibrium approach to modelling the weathering of stored Liquefied Natural Gas (LNG) », Energy, p. 684-692, 2017.

[47] R. N. Krikkis, « A thermodynamic and heat transfer model for LNG ageing during ship transportation. Towards an efficient boil-off gas management », Cryogenics, p. 76-83, 21 avril 2018.

[48] F. Huerta et V. Vesovic, « A realistic vapour phase heat transfer model for the weathering of LNG stored in large tanks », Energy, vol. 174, p. 280-291, mai 2019, doi: 10.1016/j.energy.2019.02.174.

[49] Y. Qu, I. Noba, X. Xu, R. Privat, et J.-N. Jaubert, « A thermal and thermodynamic code for the computation of Boil-Off Gas – Industrial applications of LNG carrier », Cryogenics, vol. 99, p. 105-113, avr. 2019, doi: 10.1016/j.cryogenics.2018.09.002.

[50] F. Ovidi, E. Pagni, G. Landucci, L. Tognotti, et C. Galletti, « CFD Modelling of Vertical LNG Tanks Adopted in Heavy Trucks Refuelling Stations », CHEMICAL ENGINEERING TRANSACTIONS, p. 547-552, 2018.

[51] S. Roh, G. Son, G. Song, et J. Bae, « Numerical study of transient natural convection in a pressurized LNG storage tank », Applied Thermal Engineering, p. 209-220, 2013.

[52] Q. Chen, J. Wegrzyn, et V. Prasad, « Analysis of temperature and pressure changes in liquefied natural gas (LNG) cryogenic tanks », Cryogenics, p. 701-709, 2004.

[53] Gi. E. Scarponi, G. Landucci, F. Ovidi, et V. Cozzani, « Lumped Model for the Assessment of the Thermal and Mechanical Response of LNG Tanks Exposed to Fire », Chemical Engineering Transactions, p. 307-313, 2016.

[54] B. Jung et al., « Prediction model of LNG weathering using net mass and heat transfer », Energy, p. 1-11, 2022.

[55] C.-S. Lin et M. Hasan, « Numerical investigation of the thermal stratification in cryogenic tanks subjected to wall heat flux », in 26th Joint Propulsion Conference, Orlando,FL,U.S.A.: American Institute of Aeronautics and Astronautics, juill. 1990. doi: 10.2514/6.1990-2375.

[56] T. L. Hardy et T. M. Tomsik, « Prediction of the Ullage Gas Thermal Stratification in a NASP Vehicle Propellant Tank Experimental Simulation Using FLOW-3D », National Aeronautics and Space Administration, Lewis Research Center, Cleveland, Ohio, Technical Memorandum 103217, 1990.

[57] M. Kassemi et O. Kartuzova, « Effect of interfacial turbulence and accommodation coefficient on CFD predictions of pressurization and pressure control in cryogenic storage tank », Cryogenics, p. 138-153, 2016.

[58] G. D. Grayson et J. Navickas, « Interaction between Fluid-dynamic and Thermodynamic Phenomena in a Cryogenic Upper Stage », AIAA 28th Thermophysics Conference, Orlando,FL,U.S.A., p. 1-10, 1993.

[59] M. Kassemi, O. Kartuzova, et S. Hylton, « Validation of two-phase CFD models for propellant tank self-pressurization: Crossing fluid types, scales, and gravity levels », Cryogenics, vol. 89, p. 1-15, janv. 2018, doi: 10.1016/j.cryogenics.2017.10.019.

[60] L. Wang, Y. Li, C. Li, et Z. Zhao, « CFD investigation of thermal and pressurization performance in LH2 tank during discharge », Cryogenics, vol. 57, p. 63-73, oct. 2013, doi: 10.1016/j.cryogenics.2013.05.005.

[61] J. M. Ruder, « Stratification in a Pressurized Container with Sidewall Heating », AIAA Journal, Technical Notes, p. 135-137, 1964.

[62] D. O. Barnett, T. W. Winstead, et L. S. McReynolds, « An Investigation of liquid-hydrogen stratifiaction in large cylindrical tank of the saturn configuration », Advances in Cryogenic Engineering, p. 314-324, 1964.

[63] S. Gursu, S. A. Sherif, T. N. Veziroglu, et J. W. Sheffield, « Analysis and Optimization of Thermal Stratification and Self-Pressurization Effects in Liquid Hydrogen Storage Systems—Part 1: Model Development », J. Energy Resour. Technol., vol. 115, n° 3, Art. n° 3, 1993, doi: 10.1115/1.2905997.

[64] S. Gursu, S. A. Sherif, T. N. Veziroglu, et J. W. Sheffield, « Analysis and Optimization of Thermal Stratification and Self-Pressurization Effects in Liquid Hydrogen Storage Systems—Part 2: Model Results and Conclusions », J. Energy Resour. Technol., vol. 115, n° 3, Art. n° 3, 1993, doi: 10.1115/1.2905998.

[65] R. W. Arnett et R. O. Voth, « A computer program for the calculation of thermal stratification and self-pressurization in a liquid hydrogen tank », National Aeronautics and Space Administration (NASA), Washington, D C, Contractor Report 2026, 1972.

[66] M. E. M. Stewart, « Pressurization of a Flightweight, Liquid Hydrogen Tank: Evaporation & Condensation at a Liquid/Vapor Interface », American Institute of Aeronautics and Astronautics (NASA), p. 1-17, 2017.

[67] M. E. M. Stewart et J. P. Moder, « Self-Pressurization of a Flightweight, Liquid Hydrogen Tank: Simulation and Comparison with Experiments », American Institute of Aeronautics and Astronautics, p. 1-14, 2017.

[68] S. P. Kumar, B. V. S. S. S. Prasad, G. Venkatarathnam, K. Ramamurthi, et S. S. Murthy, « Influence of surface evaporation on stratification in liquid hydrogen tanks of different aspect ratios », International Journal of Hydrogen Energy, p. 1954-1960, 2006.

[69] P. N. Estey, D. H. Lewis Junior, et M. Connor, « Prediction of a Propellant Tank Pressure History Using State Space Methods », Journal of Spacecraft and Rockets, p. 49-54, 1983.

[70] V. V. Osipov, M. J. Daigle, C. B. Muratov, M. Foygel, V. N. Smelyanskiy, et M. D. Watson, « A Dynamical Model of Rocket Propellant Loading with Liquid Hydrogen », NASA, 2011.

[71] Z. Liu et Y. Li, « Thermal physical performance in liquid hydrogen tank under constant wall temperature », Renewable Energy, p. 601-612, 2019.

[72] S. Z. S. Al Ghafri et al., « Modelling of Liquid Hydrogen Boil-Off », Energies, p. 1-16, 2022.

[73] G. Petitpas, « Simulation of boil-off losses during transfer at a LH2 based hydrogen refueling station », International Journal of Hydrogen Energy, p. 21451-21463, 2018.

[74] A. F. Schmidt, J. R. Purcell, W. A. Wilson, et R. V. Smith, « An Experimental Study Concerning the Pressurization and Stratification of Liquid Hydrogen », Journal of Resources of the National Bureau of Standards, p. 81-87, 1961.

[75] J. H. Robbins et A. C. Rogers Jr, « An Analysis on Predicting Thermal Stratification in Liquid Hydrogen », Journal of Spacecraft, p. 40-45, 1966.

[76] M. Epstein, H. K. Georgius, et R. E. Ardenson, « A generalized propellant tank-pressurization analysis », International Advances in Cryogenic Engineering, Plenum Press, New York, p. 290-302, 1965.

[77] Z. Wang, A. Sharafian, et W. Mérida, « Non-equilibrium thermodynamic model for liquefied natural gas storage tanks », Energy, p. 116412, janvier 2020.

[78] C. Wang, J. Yonglin, et Y. Fu, « Dynamic modeling and analysis of LNG fuel tank pressurization under marine conditions », Energy, p. 1-12, 2021.

[79] M. Seo et S. Jeong, « Thermodynamic Analysis of Self Pressurized liquid nitrogen cryogenic Storage Tank », Conference Paper.

[80] Z. Wang, A. Sharafian, et W. Mérida, « Thermal stratification and rollover phenomena in liquefied natural gas tanks », Energy, p. 1-21, 2022.

[81] M. Miana, R. Legorburo, D. Díez, et Y. H. Hwang, « Calculation of Boil-Off Rate of Liquefied Natural Gas in Mark III tanks of ship carriers by numerical analysis », Appl. Therm. Eng., vol. 93, p. 279-296, janv. 2016, doi: 10.1016/j.applthermaleng.2015.09.112.

[82] A. Saleem, S. Farooq, I. A. Karimi, et R. Banerjee, « A CFD simulation study of boiling mechanism and BOG generation in a full-scale LNG storage tank », Comput. Chem. Eng., vol. 115, p. 112-120, juill. 2018, doi: 10.1016/j.compchemeng.2018.04.003.

[83] K. J. Kountz, « Weathering of LNG in On-Board Storage Tanks », Institute of gas technology, Final report, 1999.

[84] A. Aspelund, G. A. Gjøvåg, P. Nekså, et K. Kolsaker, « LNG-chain, a calculation tool for natural gas quality in small scale LNG distribution chains », Proc. 21th Int. Cryog. Eng. Conf. (ICEC-21), Prage, 2007.

[85] K. McKinley, « Densities of liquefied natural gas and of low molecular weight hydrocarbons », Conference Densities of liquefied natural gas and of low molecular weight hydrocarbons, Chicago.

[86] J. Heestand, C. W. Shipman, et J. W. Meader, « A Predictive Model for Rollover in Stratified LNG Tanks », AlChE Journal, p. 199-207, mars 1983.

[87] B. Kozanoglu et F. Rubio, « The characteristic length on natural convection from a horizontal heated plate facong downwards », Thermal Science, p. 555-561, 2014.

[88] J. I. Hochstein, H.-C. Ji, et J. C. Aydelott, « Prediction of Self-Pressurization Rate ofCryogenic Propellant Tankage », Journal of Propulsion, p. 11-17, 1990.

[89] J. I. Hochstein, H.-C. Ji, et J. C. Aydelott, « Effect of subcooling on the on-orbit pressursation rate of cryogenic propellant tankage », American Institute of Aeronautics and Astronautics, p. 1-9, 1986.

[90] W. U. Notardonato, A. M. Swanger, J. E. Fesmire, K. M. Jumper, W. L. Johnson, et T. M. Tomsik, « Zero boil-off methods for large-scale liquid hydrogen tanks using integrated refrigeration and storage », IOP Conf. Series: Materials Science and Engineering, 2017. [En ligne]. Disponible sur: doi:10.1088/1757-899X/278/1/012012

[91] Kang, « Experimental investigation of thermal stratification in cryogenic tanks », Experimental Thermal and Fluid Science, p. 371-382, 2018.

[92] C. Ludwig, M. E. Dreyer, et E. J. Hopfinger, « Pressure variations in a cryogenic liquid storage tank subjected to periodic excitations », International Journal of Heat and Mass Transfer, p. 223-234, 2013.

[93] W. H. Lee, « A Pressure Iteration Scheme for Two-Phase Flow Modelin », Los Alamos, New Mexico 87545, USA, p. 407-431, 1979.

[94] G. Greg Harper et C. Charles Powars, « Advanced liquid natural gas onboard storage system », Golden, CO, 2003. [En ligne]. Disponible sur: https://doi.org/10.2172/835120

[95] M. Konopka, P. Noeding, J. Klatte, et P. Behruzi, « Analysis of LN2 filling, draining, stratification and sloshing experiments », 46th AIAA Fluid Dynamics Conference, 2016.

[96] J. A. Sarsten, « LNG stratification and rollover », Pipeline Gas Journal, 1972.

[97] W. C. Y. Lee, « An Approximate Method for Obtaining Rain Rate Statistics for Use in Signal Attenuation Estimating », IEEE Transactions on Antennas and Propagation, 1979. [En ligne]. Disponible sur: 10.1109/TAP.1979.1142100

[98] H. B. Squire, Modern Developments in Fluid Dynamics. London and New York: Oxford University Press, 1938.

[99] E. R. Eckert et T. W. Jackson, « Analysis of Turbulent Free-convection Boundary Layer on Flat Plate », National Advisory Committee for Aeronautics (NACA), Lewis Flight Propulsion Laboratory, Cleveland, Ohio, Technical Note 1015, 1951.

[100] D. M. Tellep et E. Y. Harper, « Approximate Analysis of Propellant Stratification », AIAA Journal, Technical Notes and Comments, p. 1954-1956, 1963.

[101] G. C. Vliet, « Stratification with Bottom Heating », Journal of Spacecraft, p. 1142-1144, 1966.

[102] S. E. Hurd et E. Y. Harper, « Liquid Propellant Stratification with Sidewall and Bottom Heating », Journal of Spacecraft, Engineering Notes, p. 220-222, 1968.

[103] J. Shi, M. Bi, et X. Yang, « Experimental research on thermal stratification of liquefied gas in tanks under external thermal attack », Exp. Therm. Fluid Sci., vol. 41, p. 77-83, sept. 2012, doi: 10.1016/j.expthermflusci.2012.03.013.

[104] J. Shi, J. Ren, P. Liu, et M. Bi, « Experimental research on the effects of fluid and heater on thermal stratification of liquefied gas », Experimental Thermal and Fluid Science, p. 29-36, 2013.

[105] S. Seo, W. Jang, J. Kim, J. Ryu, et C. Chang, « Experimental study on heating type pressurization of liquid applicable to LNG fueled shipping », Applied Thermal Engineering, p. 837-845, 2017.

[106] D. O. Barnett, « Liquid nitrogen stratification analysis and experiments in a partially filled spherical container », Advances in Cryogenic Engineering, p. 174-187, 1995.

[107] S. C. Huntley, « Temperature-Pressure-Time relationship in a closed cryogenic container », Advances in Cryogenic Engineering, p. 342-352, 1960.

[108] C. Ludwig et M. E. Dreyer, « Investigations on thermodynamic phenomena of the active-pressurization process of a cryogenic propellant tank », Cryogenics, p. 1-16, 2014.

[109] S. B. Vishnu, S. Bhowmick, et B. T. Kuzhiveli, « Experimental and Numerical Investigation of Stratification and Self pressurization in a High Pressure Liquid Nitrogen Storage Tank », Energy Sources Part A: Recovery, Utilization, and Environmental Effects, p. 1-15, 2019.

[110] S. P. Muraleedharan, J. Joseph, A. Chollackal, J. Peter, et D. K. Agarwal, « Experimental investigation of thermal stratification in cryogenic tank subjected to multi-species bubbling », Journal of Thermal Analysis and Calorimetry, p. 1-11, 2023.

[111] M. P. Segel, « Experimental study of the phenomena of stratificaiton and pressurization of liquid hydrogen ».

[112] D. H. Liebenberg et F. J. Edeskuty, « Pressurisation analysis of a large-scale liquid hydrogen dewar », International Advances in Cryogenic Engineering, Plenum Press, p. 284-289, 1965.

[113] J. W. Tatom, W. H. Brown, L. H. Knight, et E. F. Coxe, « Analysis of thermal stratification of liquid hydrogen in rocket propellant tanks », Advances in Cryogenic Engineering, p. 265-272, 1964.

[114] T. E. Bailey et R. F. Fearn, « Analytical and experimental determination of liquid-hydrogen temperature stratification », Advances in Cryogenic Engineering, p. 254-264, 1964.

[115] J. C. Aydelott, « Effect of gravity on self-pressurisation of spherical liquid-hydrogen tankage », National Aeronautics and Space Administration, Lewis Research Center, Cleveland, Ohio, Technical Note NASA TN D-4286, 1967.

[116] J. C. Aydelott et C. M. Spuckler, « Venting of hydrogen tankage », National Aeronautics and Space Administration, Lewis Research Center Cleveland, Ohio, Technical Note NASA TN D-5263, 1969.

[117] W. U. Notardonato, A. M. Swanger, J. E. Fesmire, K. M. Jumper, W. L. Johnson, et T. M. Tomsik, « Final test results for the ground operations demonstration unit for liquid hydrogen », Cryogenics, p. 147-155, 2017.

[118] W. U. Notardonato, W. L. Johnson, A. M. Swanger, et T. M. Tomsik, « Ground operations demonstration unit for liquid hydrogen initial test results », IOP Conf. Series: Materials Science and Engineering, p. 1-9, 2015.

[119] A. M. Swanger, W. U. Notardonato, J. E. Fesmire, K. M. Jumper, W. L. Johnson, et T. M. Tomsik, « Large scale production of densified hydrogen to the triple point and below », IOP Conf. Series: Materials Science and Engineering, 2017. [En ligne]. Disponible sur: 10.1088/1757-899X/278/1/012013

[120] R. Siegel, « Analysis of Laminar and Turbulent Free Convection From a Smooth Vertical Plate With Uniform Heat Dissipation Per Unit Surface Area », General Engineering Laboratory Library, General Electric Co., New York, Technical Information Series R54GL89, 1954.

[121] National Institute of Standard and Technology, Chemistry WebBook. https://webbook.nist.gov/chemistry/.

[122] Z. Wang, A. Sharafian, et W. Mérida, « Thermal stratification and rollover phenomena in liquefied natural gas tanks », Energy, vol. 238, p. 121994, janv. 2022, doi: 10.1016/j.energy.2021.121994.

[123] W. Haoren et al., « Theoretical investigation on heat leakage distribution between vapor and liquid in liquid hydrogen tanks », International Journal of Hydrogen Energy, 2023.

[124] M. Kang, J. Kim, H. You, et D. Chang, « Experimental investigation of thermal stratification in cryogenic tanks », Experimental Thermal and Fluid Science, p. 371-382, 2018.

[125] O. Kunz, R. Klimeck, W. Wagner, et M. Jaeschke, « The GERG-2004 Wide-Range Reference Equation of State for Natural Gases and Other Mixtures », GERG Technical Monograph 15Fortschr.-Ber. VDI, VDI-Verlag, Düsseldorf, 2007.

[126] R. Span, E. W. Lemmon, R. T. Jacobsen, W. Wagner, et A. Yokozeki, « A Reference Equation of State for the Thermodynamic Properties of Nitrogen for Temperatures from 63.151 to 1000 K and Pressures to 2200 MPa », Journal of Physical and Chemical Reference Data 29, p. 1-74, 2000.

[127] J. W. Leachman, R. T. Jacobsen, S. G. Penoncello, et E. W. Lemmon, « Fundamental Equations of State for Parahydrogen, Normal Hydrogen, and Orthohydrogen », Journal of Physical and Chemical Reference Data, p. 721-748, 2009.

[128] E. W. Lemmon et R. T. Jacobsen, « Viscosity and Thermal Conductivity Equations for Nitrogen, Oxygen, Argon, and Air », International Journal of Thermophysics, Vol. 25, p. 1-49, 1 janvier 2004.

[129] C. D. Muzny, M. L. Huber, et A. F. Kazakov, « Correlation for the Viscosity of Normal Hydrogen Obtained from Symbolic Regression », Journal of Chemical and Engineering Data, p. 969-979, 2013.

[130] M. J. Assael, J. A. M. Assael, M. L. Huber, R. A. Perkins, et Y. Takata, « Correlation of the Thermal Conductivity of Normal and Parahydrogen from the Triple Point to 1000 K and up to 100 MPa) », Journal of Physical and Chemical Reference Data 29, p. 1-13, 2011.

[131] W. H. Press et S. A. Teukolsky, « Adaptive Stepsize Runge-Kutta Integration », Computers in Physics, 1992. [En ligne]. Disponible sur: https://doi.org/10.1063/1.4823060

[132] L. B. Evans, R. C. Reid, et E. M. Drake, « Transient Natural Convection in a Vertical Cylinder », AlChE Journal.

[133] E. M. Drake, « Transient Natural Convection of Fluids Within Vertical Cylinder », Massachusetts Institute of Technology, 1958.

[134] R. B. Bird, W. E. Stewart, et E. N. Lightfoot, Transport Phenomena, 2^{e} éd. John Wiley & Sons, Inc, 2002.

[135] Y. A. Cengel, Heat Transfer - A Pratical Approach, Second.

[136] Z. Wang, A. Sharafian, et W. Mérida, « Non-equilibrium thermodynamic model for liquefied natural gas storage tanks », Energy, p. 1-20, 2020.

[137] H. Hertz, « Ueber die Verdunstung der Flüssigkeiten, insbesondere des Quecksilbers, im luftleeren Raume », Ann. Phys., p. 177-193, 1882.

[138] M. Fishenden et O. A. Saunders, An Introduction to Heat transfer. Oxford and New York, 1950.

[139] R. G. Scurlock, Stratification, Rollover and Handling of LNG, LPG and Other Cryogenic Liquid Mixtures. Springer, 2016. [En ligne]. Disponible sur: DOI 10.1007/978-3-319-20696-7

[140] R. H. Perry, D. W. Green, et J. O. Maloney, Perry’s Chemical Enginners’ Handbook, 7th éd. New York: McGrawHill, 1999.

[141] ASME Boiler & Pressure Vessel Code. American Society of Mechanical Enginners (ASME).

[142] H. D. Kweon, J. W. Kim, O. Song, et D. Oh, « Determination of true stress-strain curve of type 304 and 316 stainless steels using a typical tensile test and finite element analysis », Nuclear Engineering and Technology, p. 647-656, 2021.

[143] G. A. Olchowy et J. V. Sengers, « A Simplified Representation for the Thermal Conductivity of Fluids in the Critical Region », International Journal of Thermophysics, p. 417-426, 1989.

[144] W. H. McAdams, Heat Transmission. 1954.

[145] J. P. Hartnett et T. F. Irvine Jr, Advances in Heat Transfer, vol. 4. New York: Academic Press, 1967.

Communications

Articles

Campestrini M., Hoceini S., Stringari P., Baiguini N., On the crystallization of solid formers during liquefaction of gases. Fluid Phase Equilibria, February 2023, volume 570, 113774.

Baiguini N., Stringari P., Campestrini M., Tawk R., Malvos H., Discretized Model for LNG storage in Small Scale Tanks – Laying the First Brick. 28th World Gas Conference Proceedings, 2022.

Baiguini N., Stringari P., Campestrini M., Tawk R., Modelling of storage of pure cryogenic liquids in static small scale storage containers: liquid stratification model. Energies, 2024 (paper under reviwing).

Conferences

Baiguini N., Stringari P., Campestrini M., Tawk R., Discrete model for the behaviour of cryogenic liquids in small-scale tanks. Poster, 31th ESAT 2011, virtual conference, 5-9 July, Paris, France.

Baiguini N., Stringari P., Campestrini M., Tawk R., A model for LNG storage in SS tanks. Poster, 28th World Gas Conference, 2022, 23-27 May, Daegu, Korea.

Baiguini N., Stringari P., Campestrini M., Tawk R., Malvos H., Discretized Model for LNG storage in Small Scale Tanks – Laying the First Brick. Presentation, 28th World Gas Conference, 2022, 23-27 May, Daegu, Korea.

Baiguini N., Stringari P., Campestrini M., Tawk R., Modelling cryogenic fluids for application to LNG as fuen in Small-scale tanks. Poster, 5th European Gas Technology Conference, 2022, 14-15 June, Hamburg, Germany.

Baiguini N., Stringari P., Campestrini M., Tawk R., Modelling cryogenic fluids for application to LNG as fuen in Small-scale tanks. Presentation, 5th European Gas Technology Conference, 2022, 14-15 June, Hamburg, Germany.

Professional presentations

Baiguini N., Small-scale liquefied natural gas: experimental tests and modelling of storage tanks. Presentation, 21th Jannuary 2018, Centre of Thermodynamics of Processes.

Baiguini N., Model of storage of LNG in small-scale tank. Presentation, 23th June 2020, Centre of Thermodynamics of Processes.

Baiguini N., Modelling of small-scale storage of cryogenic liquids. Presentation, 21th June 2021, Centre of Thermodynamics of Processes.

Professional reports

Baiguini N., Literature Review – Gas condensation. Bibliography study, Engie Lab Crigen, 2019.

Baiguini N., Gas condensation model implementation. Report, Engie Lab Crigen, 2019.

Baiguini N., Tawk R., Improvement of Smart gauge V1 and development of Smart gauge V2. Annual report, Engie Lab Crigen, 2019.

Baiguini N., Note on experimental data. Report, Engie Lab Crigen, 2019.

Baiguini N., Progess note for third year of the thesis on Small-scale LNG storage, Annual report, Engie Lab Crigen, 2021.

Baiguini N., Development of cryogenic liquid behaviour’s analytical model. Annual report, Engie Lab Crigen, 2021.

RÉSUMÉ

De nouveaux axes de recherche apparaissent dans le cadre du marché Small Scale (SS) (ou marché de détail) de fluides cryogéniques. Ce marché repose, entre autres, sur le stockage de liquides cryogéniques dans des réservoirs SS (< 100 m^3) et nécessite des modèles fiables capables de prédire certaines propriétés (comme la température, la pression et le taux de remplissage) dont l'évolution temporelle est une conséquence des phénomènes de stockage propres aux réservoirs SS : la stratification thermique dans le liquide et dans le ciel vapeur, l’auto-pressurisation et le vieillissement.

L'objectif de cette thèse est le développement d'un modèle prenant en compte de tels phénomènes et capable de reproduire les profils expérimentaux de température et de pression relatifs au stockage SS de l'azote liquide et de l'hydrogène liquide.

Bien que les profils expérimentaux de température du liquide ne soient pas prédits avec précision, la dernière version du modèle surmonte avec succès certains problèmes critiques des versions précédentes, notamment en matière de prédiction de l'auto-pressurisation. Avant d'étendre le modèle au comportement de mélanges cryogéniques (comme le gaz naturel liquéfié) dans les réservoirs SS, d'autres pistes d’amélioration du modèle ont été suggérées. De plus, une conception préliminaire d'un réservoir SS pour la mesure de toutes les propriétés nécessaires à la validation du modèle a été proposée.

MOTS CLÉS

Stockage des liquides cryogéniques, petite-échelle, stratification thermique, auto-pressurisation, hydrogène liquide, azote liquide.

ABSTRACT

Small Scale (SS) applications in energy and transport sectors rest on the storage of cryopgeinc liquids in SS tanks and requires reliable models capable of predicting some physical variables (like temperature, pressure and filling ratio) whose time-evolution is a consequence of storage phenomena peculiar to SS tanks, such as thermal stratification in liquid and in the ullage, self-pressurisation and ageing.

The objective of this thesis is the development of a model that considers such phenomena and capable of reproducing experimental temperature and pressure profiles related to the SS storage of liquid nitrogen and liquid hydrogen.

Despite experimental liquid temperature profiles are not accurately predicted, the last version of the model successfully overcomes some critical issues of the previous ones especially in predicting the self-pressurisation. Before extending the model to the behaviour of cryogenic mixtures (like liquefied natural gas) in SS tanks, further modelling improvements have been suggested. Furthermore, a preliminary design of a SS tank for the measurement off all the properties that are needed for model validation has been proposed.

KEYWORDS

Cryogenic liquids storage, small scale, thermal stratification, self-pressurisation, liquid hydrogen, liquid nitrogen